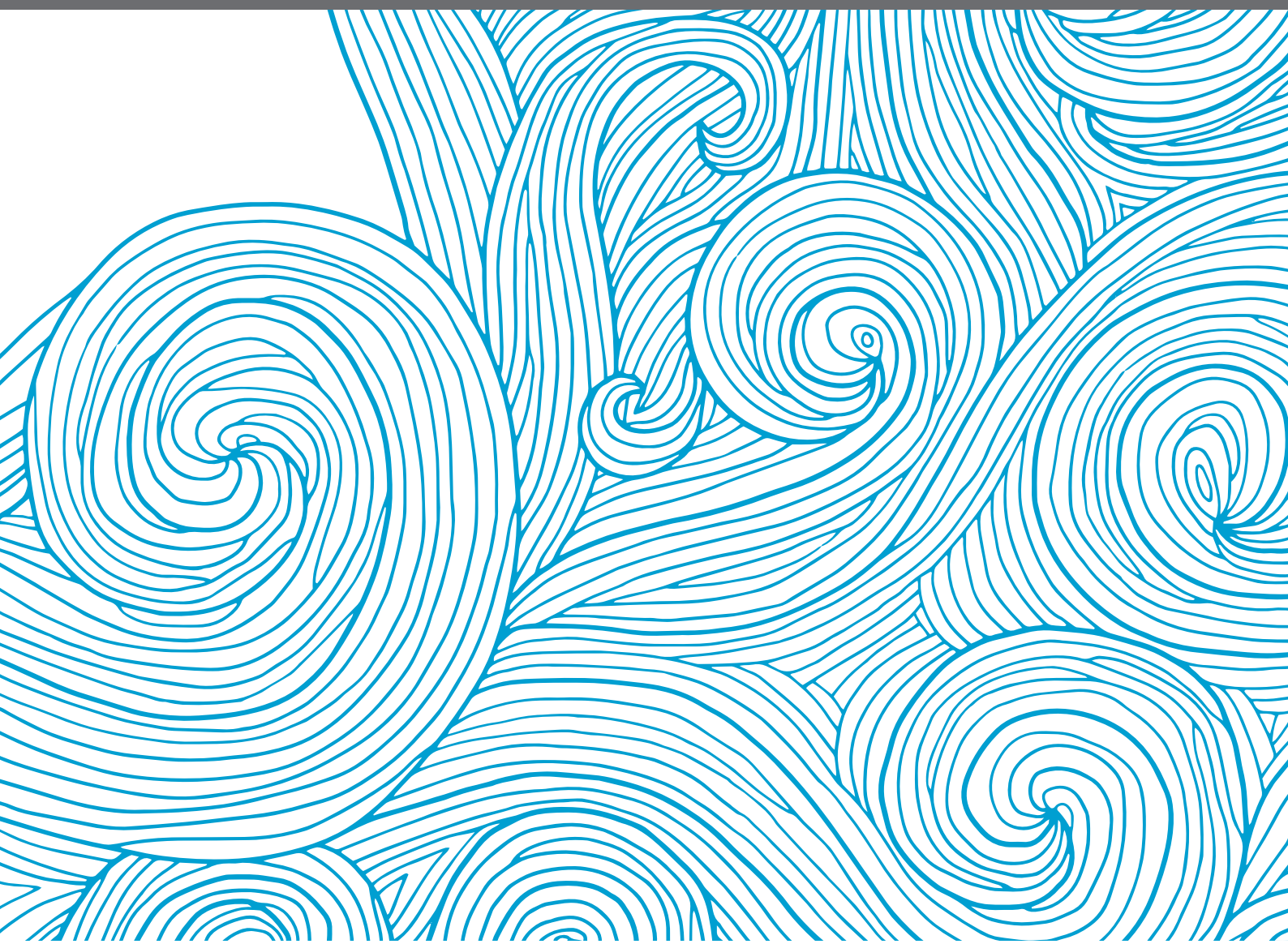
LIVING ALONG GRADIENTS: PAST, PRESENT, FUTURE

EDITED BY: Ulrich Bathmann, Hendrik Schubert, Elinor Andrén, Laura Tuomi, Teresa Radziejewska, Karol Kulinski and Irina Chubarenko

PUBLISHED IN: Frontiers in Marine Science and Frontiers in Earth Science



frontiers Research Topics



frontiers

Frontiers eBook Copyright Statement

The copyright in the text of individual articles in this eBook is the property of their respective authors or their respective institutions or funders. The copyright in graphics and images within each article may be subject to copyright of other parties. In both cases this is subject to a license granted to Frontiers.

The compilation of articles constituting this eBook is the property of Frontiers.

Each article within this eBook, and the eBook itself, are published under the most recent version of the Creative Commons CC-BY licence. The version current at the date of publication of this eBook is CC-BY 4.0. If the CC-BY licence is updated, the licence granted by Frontiers is automatically updated to the new version.

When exercising any right under the CC-BY licence, Frontiers must be attributed as the original publisher of the article or eBook, as applicable.

Authors have the responsibility of ensuring that any graphics or other materials which are the property of others may be included in the CC-BY licence, but this should be checked before relying on the CC-BY licence to reproduce those materials. Any copyright notices relating to those materials must be complied with.

Copyright and source acknowledgement notices may not be removed and must be displayed in any copy, derivative work or partial copy which includes the elements in question.

All copyright, and all rights therein, are protected by national and international copyright laws. The above represents a summary only. For further information please read Frontiers' Conditions for Website Use and Copyright Statement, and the applicable CC-BY licence.

ISSN 1664-8714
ISBN 978-2-88963-468-2
DOI 10.3389/978-2-88963-468-2

About Frontiers

Frontiers is more than just an open-access publisher of scholarly articles: it is a pioneering approach to the world of academia, radically improving the way scholarly research is managed. The grand vision of Frontiers is a world where all people have an equal opportunity to seek, share and generate knowledge. Frontiers provides immediate and permanent online open access to all its publications, but this alone is not enough to realize our grand goals.

Frontiers Journal Series

The Frontiers Journal Series is a multi-tier and interdisciplinary set of open-access, online journals, promising a paradigm shift from the current review, selection and dissemination processes in academic publishing. All Frontiers journals are driven by researchers for researchers; therefore, they constitute a service to the scholarly community. At the same time, the Frontiers Journal Series operates on a revolutionary invention, the tiered publishing system, initially addressing specific communities of scholars, and gradually climbing up to broader public understanding, thus serving the interests of the lay society, too.

Dedication to Quality

Each Frontiers article is a landmark of the highest quality, thanks to genuinely collaborative interactions between authors and review editors, who include some of the world's best academicians. Research must be certified by peers before entering a stream of knowledge that may eventually reach the public - and shape society; therefore, Frontiers only applies the most rigorous and unbiased reviews.
Frontiers revolutionizes research publishing by freely delivering the most outstanding research, evaluated with no bias from both the academic and social point of view. By applying the most advanced information technologies, Frontiers is catapulting scholarly publishing into a new generation.

What are Frontiers Research Topics?

Frontiers Research Topics are very popular trademarks of the Frontiers Journals Series: they are collections of at least ten articles, all centered on a particular subject. With their unique mix of varied contributions from Original Research to Review Articles, Frontiers Research Topics unify the most influential researchers, the latest key findings and historical advances in a hot research area! Find out more on how to host your own Frontiers Research Topic or contribute to one as an author by contacting the Frontiers Editorial Office: researchtopics@frontiersin.org

LIVING ALONG GRADIENTS: PAST, PRESENT, FUTURE

Topic Editors:
Ulrich Bathmann, Leibniz Institute for Baltic Sea Research (LG), Germany
Hendrik Schubert, University of Rostock, Germany
Elinor Andrén, Södertörn University, Sweden
Laura Tuomi, Finnish Meteorological Institute, Finland
Teresa Radziejewska, University of Szczecin, Poland
Karol Kulinski, Institute of Oceanology (PAN), Poland
Irina Chubarenko, P.P. Shirshov Institute of Oceanology (RAS), Russia

Citation: Bathmann, U., Schubert, H., Andrén, E., Tuomi, L., Radziejewska, T., Kulinski, K., Chubarenko, I., eds. (2020). Living Along Gradients: Past, Present, Future. Lausanne: Frontiers Media SA. doi: 10.3389/978-2-88963-468-2

Table of Contents

06 ***Editorial: Living Along Gradients: Past, Present, Future***
Ulrich Bathmann, Hendrik Schubert, Elinor Andrén, Laura Tuomi, Teresa Radziejewska, Karol Kulinski and Irina Chubarenko

PART I
MONITORING AND ASSESSMENT

09 ***Argo Floats as a Novel Part of the Monitoring the Hydrography of the Bothnian Sea***
Noora Haavisto, Laura Tuomi, Petra Roiha, Simo-Matti Siiriä, Pekka Alenius and Tero Purokoski

21 ***Estimating Currents From Argo Trajectories in the Bothnian Sea, Baltic Sea***
Petra Roiha, Simo-Matti Siiriä, Noora Haavisto, Pekka Alenius, Antti Westerlund and Tero Purokoski

33 ***Summer Distribution of Total Suspended Matter Across the Baltic Sea***
Dmytro Kyryliuk and Susanne Kratzer

49 ***Study on Different Fractions of Organic Molecules in the Baltic Sea Surface Microlayer by Spectrophoto- and Spectrofluorimetric Methods***
Violetta Drozdowska, Piotr Kowalczuk, Marta Konik and Lidia Dzierzbicka-Glowacka

61 ***In Search of a Field-Based Relationship Between Benthic Macrofauna and Biogeochemistry in a Modern Brackish Coastal Sea***
Mayya Gogina, Marko Lipka, Jana Woelfel, Bo Liu, Claudia Morys, Michael E. Böttcher and Michael L. Zettler

79 ***Metrology for pH Measurements in Brackish Waters—Part 1: Extending Electrochemical pH_T Measurements of TRIS Buffers to Salinities 5–20***
Jens D. Müller, Frank Bastkowski, Beatrice Sander, Steffen Seitz, David R. Turner, Andrew G. Dickson and Gregor Rehder

91 ***Metrology of pH Measurements in Brackish Waters—Part 2: Experimental Characterization of Purified meta-Cresol Purple for Spectrophotometric pH_T Measurements***
Jens D. Müller and Gregor Rehder

100 ***Middle to Late Holocene Variations in Salinity and Primary Productivity in the Central Baltic Sea: A Multiproxy Study From the Landsort Deep***
Falkje van Wirdum, Elinor Andrén, Denise Wienholz, Ulrich Kotthoff, Matthias Moros, Anne-Sophie Fanget, Marit-Solveig Seidenkrantz and Thomas Andrén

122 ***Monitoring of Marine Biofilm Formation Dynamics at Submerged Solid Surfaces With Multitechnique Sensors***
Maciej Grzegorczyk, Stanisław Józef Pogorzelski, Aneta Pospiech and Katarzyna Boniewicz-Szmyt

138 ***Long-Term Mean Circulation of the Baltic Sea as Represented by Various Ocean Circulation Models***
Manja Placke, H. E. Markus Meier, Ulf Gräwe, Thomas Neumann, Claudia Frauen and Ye Liu

158 ***Assessment of Uncertainties in Scenario Simulations of Biogeochemical Cycles in the Baltic Sea***
H. E. Markus Meier, Moa Edman, Kari Eilola, Manja Placke, Thomas Neumann, Helén C. Andersson, Sandra-Esther Brunnabend, Christian Dieterich, Claudia Frauen, René Friedland, Matthias Gröger, Bo G. Gustafsson, Erik Gustafsson, Alexey Isaev, Madline Kniebusch, Ivan Kuznetsov, Bärbel Müller-Karulis, Michael Naumann, Anders Omstedt, Vladimir Ryabchenko, Sofia Saraiva and Oleg P. Savchuk

187 ***Assessment of Eutrophication Abatement Scenarios for the Baltic Sea by Multi-Model Ensemble Simulations***
H. E. Markus Meier, Moa K. Edman, Kari J. Eilola, Manja Placke, Thomas Neumann, Helén C. Andersson, Sandra-Esther Brunnabend, Christian Dieterich, Claudia Frauen, René Friedland, Matthias Gröger, Bo G. Gustafsson, Erik Gustafsson, Alexey Isaev, Madline Kniebusch, Ivan Kuznetsov, Bärbel Müller-Karulis, Anders Omstedt, Vladimir Ryabchenko, Sofia Saraiva and Oleg P. Savchuk

PART II
MAJOR BALTIC INFLOWS AND THEIR IMPACT

211 ***Major Baltic Inflow Statistics – Revised***
Volker Mohrholz

227 ***Propagation of Impact of the Recent Major Baltic Inflows From the Eastern Gotland Basin to the Gulf of Finland***
Taavi Liblik, Michael Naumann, Pekka Alenius, Martin Hansson, Urmas Lips, Günther Nausch, Laura Tuomi, Karin Wesslander, Jaan Laanemets and Lena Viktorsson

250 ***Impact of the Major Baltic Inflow in 2014 on Manganese Cycling in the Gotland Deep (Baltic Sea)***
Olaf Dellwig, Bernhard Schnetger, David Meyer, Falk Pollehne, Katharina Häusler and Helge W. Arz

270 ***Impact of a Major Inflow Event on the Composition and Distribution of Bacterioplankton Communities in the Baltic Sea***
Benjamin Bergen, Michael Naumann, Daniel P. R. Herlemann, Ulf Gräwe, Matthias Labrenz and Klaus Jürgens

PART III
COASTAL WATERS AND LAGOONS

284 ***Understanding the Coastal Ecocline: Assessing Sea–Land Interactions at Non-tidal, Low-Lying Coasts Through Interdisciplinary Research***
Gerald Jurasinski, Manon Janssen, Maren Voss, Michael E. Böttcher, Martin Brede, Hans Burchard, Stefan Forster, Lennart Gosch, Ulf Gräwe, Sigrid Gründling-Pfaff, Fouzia Haider, Miriam Ibenthal, Nils Karow, Ulf Karsten, Matthias Kreuzburg, Xaver Lange, Peter Leinweber, Gudrun Massmann, Thomas Ptak, Fereidoun Rezanezhad, Gregor Rehder, Katharina Romoth, Hanna Schade, Hendrik Schubert, Heide Schulz-Vogt, Inna M. Sokolova, Robert Strehse, Viktoria Unger, Julia Westphal and Bernd Lennartz

306 ***Impact of Macrofaunal Communities on the Coastal Filter Function in the Bay of Gdansk, Baltic Sea***
Franziska Thoms, Christian Burmeister, Joachim W. Dippner, Mayya Gogina, Urszula Janas, Halina Kendzierska, Iris Liskow and Maren Voss

325 ***Sub-marine Continuation of Peat Deposits From a Coastal Peatland in the Southern Baltic Sea and its Holocene Development***
Matthias Kreuzburg, Miriam Ibenthal, Manon Janssen, Gregor Rehder, Maren Voss, Michael Naumann and Peter Feldens

337 ***Continuous and High Transport of Particles and Solutes by Benthos in Coastal Eutrophic Sediments of the Pomeranian Bay***
Martin Powilleit and Stefan Forster

350 ***Phosphorus Contents Re-visited After 40 Years in Muddy and Sandy Sediments of a Temperate Lagoon System***
Maximilian Berthold, Dana Zimmer, Volker Reiff and Rhena Schumann

364 ***Solute Reservoirs Reflect Variability of Early Diagenetic Processes in Temperate Brackish Surface Sediments***
Marko Lipka, Jana Woelfel, Mayya Gogina, Jens Kallmeyer, Bo Liu, Claudia Morys, Stefan Forster and Michael E. Böttcher

384 ***Nutrient Retention in the Swedish Coastal Zone***
Moa Edman, Kari Eilola, Elin Almroth-Rosell, H. E. Markus Meier, Iréne Wåhlström and Lars Arneborg

406 ***Two Non-indigenous Dreissenids (*Dreissena polymorpha *and* D. rostriformis bugensis*) in a Southern Baltic Coastal Lagoon: Variability in Populations of the "Old" and a "New" Immigrant***
Brygida Wawrzyniak-Wydrowska, Teresa Radziejewska, Anna Skrzypacz and Adam Woźniczka

PART IV
ANTHROPOGENIC INFLUENCE

420 ***Assessment of the Influence of Dredge Spoil Dumping on the Seafloor Geological Integrity***
Joonas J. Virtasalo, Samuli Korpinen and Aarno T. Kotilainen

435 ***Influence of Surfactant Concentration and Temperature Gradients on Spreading of Crude-Oil at Sea****
Katarzyna Boniewicz-Szmyt and Stanisław Józef Pogorzelski

446 ***Secondary Microplastics Generation in the Sea Swash Zone With Coarse Bottom Sediments: Laboratory Experiments***
Irina Efimova, Margarita Bagaeva, Andrei Bagaev, Alexander Kileso and Irina P. Chubarenko

frontiers in Marine Science

EDITORIAL
published: 10 January 2020
doi: 10.3389/fmars.2019.00801

Editorial: Living Along Gradients: Past, Present, Future

*Ulrich Bathmann[1], Hendrik Schubert[2], Elinor Andrén[3], Laura Tuomi[4], Teresa Radziejewska[5], Karol Kulinski[6] and Irina Chubarenko[7]**

[1] Leibniz-Institute for Baltic Sea Research, Warnemünde, Germany, [2] Institute of Biosciences, Ecology, University of Rostock, Rostock, Germany, [3] School of Natural Sciences, Technology and Environmental Studies, Södertörn University, Huddinge, Sweden, [4] Marine Research Unit, Finnish Meteorological Institute, Helsinki, Finland, [5] Institute of Marine and Environmental Sciences, University of Szczecin, Szczecin, Poland, [6] Marine Biogeochemistry Laboratory, Institute of Oceanology of the Polish Academy of Sciences, Sopot, Poland, [7] Laboratory for Marine Physics, Shirshov Institute of Oceanology of the Russian Academy of Sciences, Moscow, Russia

Keywords: Baltic Sea, coastal seas, hypoxia, major baltic inflow, eutrophication

Editorial on the Research Topic

Living Along Gradients: Past, Present, Future

The Baltic Sea is a geologically and evolutionarily young part of the coastal ocean that experienced, in its past, several severe environmental changes. In its present state, the Baltic Sea is characterized by both horizontal and vertical gradients of environmental conditions. As a huge estuary, it shows a west to east/south to north surface salinity gradient from 24 in Kattegat to nearly freshwater in the Bothnian Bay. The vertical salinity and oxygen gradients result in stratification which causes hypoxic and sulfidic anoxic conditions in deep basins. These gradient systems are impacted by natural and anthropogenic changes due to physico-chemical driving forces, varying over time and space. Gradient environments produce an imprint on both the structure and function of the biological systems and influence biogeochemical cycling. Besides, coastal seas in general and the Baltic Sea in particular, experience constant and direct influence from land with consequences to matter and energy cycles, biogeochemical interactions, energy fluxes, and sediment dynamics.

"Living along gradients: past, present, future" in the Baltic are today's very important aspects that rise questions like which of the effects we are detecting occur naturally, and which are driven by human activities. Deciphering past environmental changes and their causes provide keys to understand and simulate possible future scenarios, all of which should rise societal awareness and implementation of appropriate marine and coastal policies. Present-day knowledge on the dynamics of gradient systems, on the processes that affect the coastal sea environment, the results of interaction between coastal seas and society, the detection or reconstruction of past and present changes on time scales from inter-annual to millennial, and future change models are summarized here, with the idea to stimulate scientific exchange on most complex questions, addressing them from different perspectives.

MONITORING AND ASSESSMENT

Modern strategies, concepts, and tools are addressed in this paper collection, including operational oceanography, observational approaches, *in-situ* technologies, development of sensors and methods for their calibration, experimental studies, and numerical modeling.

Results of environmental monitoring using Argo floats are reported based on their operation in the Bothnian Sea in 2012–2017 (Haavisto et al.; Roiha et al.).

Distribution of total suspended matter across the Baltic Sea is evaluated by Kyryliuk and Kratzer who used remote sensing data of summer composites for 2009, 2010, 2011 and a 3-year summer mean (2009–2011).

OPEN ACCESS

Edited and reviewed by:
Charitha Bandula Pattiaratchi, University of Western Australia, Australia

****Correspondence:***
Irina Chubarenko
irina_chubarenko@mail.ru

Specialty section:
This article was submitted to Coastal Ocean Processes, a section of the journal Frontiers in Marine Science

Received: *09 December 2019*
Accepted: *12 December 2019*
Published: *10 January 2020*

Citation:
Bathmann U, Schubert H, Andrén E, Tuomi L, Radziejewska T, Kulinski K and Chubarenko I (2020) Editorial: Living Along Gradients: Past, Present, Future. Front. Mar. Sci. 6:801. doi: 10.3389/fmars.2019.00801

Different fractions of surfactants, collected during three research cruises in coastal and open waters of the Baltic Sea are analyzed by spectrophoto- and spectrofluorimetric methods by Drozdowska et al. Sediment cores, obtained during several cruises in the southern Baltic Sea in different seasons of 2014–2016 years, are used by Gogina et al. for the investigation of pore-water biogeochemistry and associated nutrient fluxes across the sediment-water interface.

An important problem of reliable calibration of pH instruments in the low-salinity range of brackish water is addressed by Müller et al. and Müller and Rehder.

The increase in the extent of hypoxic bottom areas in the Baltic Sea during recent decades seems to be attributed to anthropogenic forcing. In their study in the Landsort Deep, van Wirdum et al. analyse past periods of hypoxic conditions in the Baltic Sea, caused by changing climate conditions during the Holocene Thermal Maximum and Medieval Climate Anomaly.

An experimental study of biofilm formation on artificial (glass, metal, plastic) and biotic (wood, macrophytes) solid substrata deployed at a depth of 0.5 m in several locations in near-shore waters of the Gulf of Gdansk is presented by Grzegorczyk et al.

The skill of the state-of-the-art ocean circulation models GETM (General Estuarine Transport Model), RCO (Rossby Centre Ocean model), and MOM (Modular Ocean Model) to represent hydrographic conditions and the mean circulation of the Baltic Sea is investigated by Placke et al.

A review paper by Meier et al. assesses knowledge acquired from available literature about future scenario simulations of biogeochemical cycles in the Baltic Sea and their uncertainties, and recommends that the models' skill for the Baltic Sea region and the spread in scenario simulations (differences among the projected changes) be regularly evaluated (by comparing with observations).

Meier et al. assess the impact of the Baltic Sea Action Plan implementation on the future environmental status of the Baltic Sea and analyze the available uncoordinated multi-model ensemble simulations for the Baltic Sea region in the twenty-first century.

MAJOR BALTIC INFLOWS AND THEIR IMPACT

An inflow of saline and oxygenated oceanic water is an oceanographic process of a key importance for the functioning of the Baltic Sea ecosystem. Major Baltic Inflows (MBI) transport large amounts of saline water into the Baltic, having a significant impact on physics, biogeochemistry, and marine life.

Mohrholz presents a reconstruction of a continuous series of barotropic inflows from the Belt Sea and the Sound for the period from 1887 till present, based on long-term data series of the sea level, river discharge, and salinity. Increased eutrophication during the last century is suggested as the main driver of the temporal and spatial spreading of suboxic and anoxic conditions in the deep layer of the Baltic Sea.

Propagation of the MBI signal from the Eastern Gotland Basin to the Gulf of Finland is dealt with by Liblik et al. based on *in-situ* measurements from January 2014 to March 2017, merging Estonian, Swedish, German, and Finnish oceanographic data sets. The impact of the 2014 MBI which brought saline and oxygenated water into the basins of the central Baltic Sea, is revealed by the manganese cycling (Dellwig et al.) and by the composition and distribution of bacterioplankton communities (Bergen et al.).

COASTAL WATERS AND LAGOONS

Coastal zones link terrestrial and marine ecosystems, providing a unique environment that is under increasing anthropogenic pressure. Knowledge on the influences from the catchment, including land-ocean interactions, hydrology, and supply of various substances is important for understanding the role of coastal processes affecting the land-locked marine systems.

An interdisciplinary approach to the investigation of interactions between land and sea at shallow coasts is proposed in the Hypothesis-and-Theory paper (Jurasinski et al.). Sea–land interactions are far-reaching, occurring on either side of the interface, and can only be understood when both long-term and event-based patterns at different spatial scales are taken into account in interdisciplinary research that involves marine and terrestrial expertise.

The impact of macrofaunal communities on the coastal filter function is investigated by Thoms et al. who used faunistic, porewater, and bottom water data obtained during three cruises to the Gulf of Gdansk. Diffusive porewater nutrient fluxes are calculated and related to the total net fluxes.

Sub-marine continuation of peat deposits from a coastal peatland in the southern Baltic Sea and its Holocene development is considered by Kreuzburg et al. Based on on- and offshore sediment cores and geo-acoustic surveys, the present Heiligensee and Hütelmoor peat deposits (Northern Germany) are found to continue more than 90 m in front of the coastline.

Results on bioirrigation and reworking of sediments by benthic macrofauna in coastal eutrophic sediments of the Pomeranian Bay (southern Baltic Sea) are presented and discussed by Powilleit and Forster.

Sediments in eutrophic systems, suffering from long-lasting anthropogenically elevated nutrient inputs, are assumed to be an important internal nutrient source. Phosphorus content is re-evaluated after 40 years by Berthold et al. in muddy and sandy sediments of the Darß-Zingst Bodden chain, a typical temperate lagoon system of the southern Baltic Sea.

Coastal marine sediments are a hotspot of organic matter degradation. Lipka et al. investigate, on a seasonal basis, the key mineralization processes in sediments (permeable sands to fine grained muds) of a shallow (15–45 m water depth) coastal area of the southern Baltic Sea.

Nutrient retention in the Swedish coastal zone is estimated by Edman et al., who found that only significantly less than a half of the nutrient input from land can be assumed to be exported from coastal waters to the open sea.

Monthly samples in 2015–2017 from the Szczecin Lagoon (a southern Baltic coastal lagoon) allowed Wawrzyniak-Wydrowska et al. to report on changes in the abundance and biomass of two co-occurring non-indigenous dreissenids (*Dreissena polymorpha* and *D. rostriformis bugensis*), suspected of being competitors.

ANTHROPOGENIC INFLUENCE

The European Marine Strategy Framework Directive requires the development of suitable indicators for regular reporting on the environmental state and achievement of a good environmental status of EU's marine waters by 2020. In search of such an indicator, Virtasalo et al. present a study of Vuosaari and Uusikaupunki-D offshore dumping sites in Finland (northern Baltic Sea), aimed at assessing the influence of dredge spoil dumping on the seafloor geological integrity.

Properties of contaminants in the marine environment can be effectively studied under controlled laboratory conditions. Boniewicz-Szmyt and Pogorzelski describe laboratory experiments on the contaminant spreading kinetics, using crude oils surfactant-containing sea water of well-controlled thermo-elastic surface properties as an example. Fragmentation common commercial synthetic polymers (polyethylene, polypropylene, and polystyrene) in the sea swash zone is analyzed by Efimova et al. based on experiments in a rotating laboratory mixer. A time-dependent increase in the weight and number of the microplastic particles generated as well the link between them are important for field monitoring and numerical modeling of plastic contamination in the marine environment.

The volume summarizes the progress that has been achieved in broadening our knowledge on the structure and functioning of the present-day Baltic Sea ecosystems, and on its underpinnings based on recent and more distant past. Projections onto the ecosystem's future are discussed, which will depend on how well the present ecosystem is appreciated and managed. The knowledge summarized in this volume is by no means a closed chapter. The Baltic Sea continues to be intensively studied and we look forward to new insights the coming years will bring. In particular, we hope for significant insights from the novel joint Baltic Sea and North Sea Research and Innovation Programme (BANOS), expected to run from 2021 onwards, which will assume a high level of scientific, administrative and financial integration and should open new horizons for development of EU and national policies and strategies, with a particular consideration of Europe's blue growth strategy in the northern European regional seas.

AUTHOR CONTRIBUTIONS

All authors listed have made a substantial, direct and intellectual contribution to the work, and approved it for publication.

ACKNOWLEDGMENTS

We thank all authors, reviewers, and editors who have contributed to this Research Topic.

Conflict of Interest: The authors declare that the research was conducted in the absence of any commercial or financial relationships that could be construed as a potential conflict of interest.

Copyright © 2020 Bathmann, Schubert, Andrén, Tuomi, Radziejewska, Kulinski and Chubarenko. This is an open-access article distributed under the terms of the Creative Commons Attribution License (CC BY). The use, distribution or reproduction in other forums is permitted, provided the original author(s) and the copyright owner(s) are credited and that the original publication in this journal is cited, in accordance with accepted academic practice. No use, distribution or reproduction is permitted which does not comply with these terms.

frontiers in Marine Science

ORIGINAL RESEARCH
published: 18 September 2018
doi: 10.3389/fmars.2018.00324

Argo Floats as a Novel Part of the Monitoring the Hydrography of the Bothnian Sea

Noora Haavisto[1†], Laura Tuomi[1], Petra Roiha[1], Simo-Matti Siiriä[1], Pekka Alenius[1] and Tero Purokoski[2]*

[1] Department of Marine Research, Finnish Meteorological Institute, Helsinki, Finland, [2] Department of Observation Services, Finnish Meteorological Institute, Helsinki, Finland

We made an assessment of the hydrography in the Bothnian Sea based on data collected by the Argo floats during the first 6 years of operation in the Bothnian Sea (2012–2017). We evaluated the added value of Argo data related to the pre-existing monitoring data. The optimal usage and profiling frequency of Argo floats was also evaluated and the horizontal and vertical coverage of the profiles were assessed. For now we lose 4 m of data from the surface due to sensor design and some meters from the bottom because of the low resolution of available bathymetry data that is used to avoid bottom collisions. Mean monthly temperature and salinity close to surface and below halocline from the float data were within the boundaries given in literature, although some variation was lost due to scarcity of winter profiles. The temporal coverage of the Argo data is much better than that of ship monitoring, but some spatial variability is lost since the floats are confined in the over 100 m deep area of the Bothnian Sea. The possibility to adjust the float profiling frequency according to weather forecasts was successfully demonstrated and found a feasible way to get measurements from storms and other short term phenomena unreachable with research vessels. First 6 years of operation have shown that Argo floats can be successfully operated in the challenging conditions of the Bothnian Sea and they are shown to be an excellent addition to the monitoring network there. With multiple floats spread in the basin we can increase our general knowledge of the hydrographic conditions and occasionally get interesting data related to intrusions and mixing during high wind events and other synoptic scale events.

Keywords: Bothnian Sea, hydrography, Argo floats, Baltic Sea, monitoring, instrument

OPEN ACCESS

Edited by:
Pengfei Xue,
Michigan Technological University,
United States

Reviewed by:
Begoña Pérez-Gómez,
Puertos del Estado, Madrid, Spain

****Correspondence:***
Laura Tuomi
laura.tuomi@fmi.fi

†Present Address:
Noora Haavisto,
Tvärminne Zoological Station, Faculty of Biological and Environmental Sciences, University of Helsinki, Helsinki, Finland

Specialty section:
This article was submitted to Coastal Ocean Processes, a section of the journal Frontiers in Marine Science

Received: *29 March 2018*
Accepted: *23 August 2018*
Published: *18 September 2018*

Citation:
Haavisto N, Tuomi L, Roiha P, Siiriä S-M, Alenius P and Purokoski T (2018) Argo Floats as a Novel Part of the Monitoring the Hydrography of the Bothnian Sea. Front. Mar. Sci. 5:324. doi: 10.3389/fmars.2018.00324

1. INTRODUCTION

The physical properties of the water masses and the changes in them have been monitored in the Bothnian Sea since the late 19th century (Pettersson and Ekman, 1897). Ocean observation techniques have evolved during the past century from manual shipborne water sampling to ever more precise and autonomous measurements with modern electronic devices. In the last 40 years CTD (Conductivity-Temperature-Depth) profiling from research vessels has been the most common practice of standard monitoring. Moored instruments at surface, at certain depths and profiling moorings are also used along with remote sensing. Various remotely operable platforms for measuring hydrography, for example Argo floats, gliders and wave gliders, have become widely used. The most commonly used is the Argo float. There are close to 4,000 floats spread in the

oceans worldwide as a part of the International Argo Program, but they have seen little use in shallow coastal seas. For example Grayek et al. (2015) and Kassis et al. (2015) have deployed floats in relatively small basins in the Cretan Sea and the Black Sea, but these areas are much deeper than the Bothnian Sea.

Monitoring of the sea is essential for gaining knowledge of the past and present state and changes of the water column, and the effect of climate change on our sea areas. At present the Finnish monitoring of the Bothnian Sea hydrography in the open sea areas is the responsibility of the Finnish Meteorological Institute and the monitoring is done in co-operation with the Finnish Environment Institute three times a year as a part of the Helsinki Comission (HELCOM) monitoring programme COMBINE (HELCOM, 2014).

Although monitoring aims at providing long time series from fixed locations to evaluate the long-term changes in the state of the Bothnian Sea, for many applications measurements with higher temporal resolution that reflect the course of seasonal cycles of temperature and salinity are needed. Even higher temporal resolution, with observation interval being a day or in some cases even less allows us to record phenomena happening in short time scales, and helps to put the sparse ship monitoring data into context in relation to the seasonal cycles. Improving modeled forecasts by data assimilation and validation also require frequent *in-situ* data. Argo floats provide a relatively cost efficient method for measuring with high temporal resolution in the open sea.

The Finnish Meteorological Institute (FMI) first tested an Argo float in the Baltic Sea in 2011 and has operated them in the Bothnian Sea and the Gotland deep since 2012 as a part of Euro-Argo ERIC. We now have an operational float in the Bothnian Bay as well. The characteristics of the Baltic Sea present challenges to float operations, but the floats have been found to function adequately there. Their data has already been used for model validation (Westerlund and Tuomi, 2016) and the deep water circulation in the Bothnian Sea was assessed from their drift speed by Roiha et al. (2018).

In this study we assess the hydrography of the Bothnian Sea based on the first 6 years of Argo data. The added value of Argo floats to the existing monitoring network, that in the open sea consists only of ship observations from regular monitoring cruises, is evaluated and different options for Argo float use in the Bothnian Sea are compared. Finally we make suggestions for further development of the monitoring network in the Bothnian Sea.

1.1. The Bothnian Sea

The Bothnian Sea is a shallow semi-enclosed sub-basin of the Baltic Sea. It is connected to the Baltic Sea Proper only through narrow straits through the Åland Sea (the Southern Quark) and the shallow Archipelago Sea connecting it to the northern Baltic Sea Proper (**Figure 1**). The water in the basin, as in the entire Baltic Sea, is brackish due to large river runoff and limited inflow of saline water from the Baltic Proper. The surface area of the Bothnian Sea is 64,886 km^2 and the mean depth is 66 m (Fonselius, 1996), with an over 100 m deep area reaching from the sill to Åland Sea along the Finnish coast to North-Northeast (referred to as the Bothnian Sea deep in this work), and shallower banks with numerous shoals on the Swedish side called Finngrunden banks. The deepest point in the Bothnian Sea is the Ulvö deep next to the northern Swedish coast.

A weak halocline on average at 50–60 m separates the deep water from the mixed layer in the Bothnian Sea. The mixed layer overturns in the spring and autumn, and in the summer a thermocline of 15 m depth on average forms. The Bothnian Sea is at least partially covered by sea ice every winter. Fresh water runoff from land dominates the mixed layer, while the deep water is replenished by inflow of saline water from above the halocline in the northern Baltic Sea Proper (Håkansson et al., 1996; Hietala et al., 2007). There is a N-S gradient in salinity in the Bothnian Sea, with more saline water in the South and along the Finnish coast, than in the North and down the Swedish coast. The surface salinity ranges from 4.8 to 6.0 g kg^{-1} and the bottom salinity is between 6.4 and 7.2 g kg^{-1} (Bock, 1971). The average temperature at the surface reaches 16 °C in the summer, and the bottom temperature varies between 1.5 and 4.5 °C (Haapala and Alenius, 1994).

1.2. Argo Floats in the Bothnian Sea

Argo floats are designed for open ocean, where proximity to shoreline or bottom depth do not have to be considered. The specific features of the Bothnian Sea, such as seasonal ice cover, relatively small size of the basin and low salinity, present challenges for the operation of floats. There are risks of the float touching the bottom and getting stuck, drifting to even shallower waters and on shore, and hitting seasonal ice cover.

Seasonal differences in the Bothnian Sea stratification present a challenge for the float diving. A large change in the float density may be needed to penetrate the seasonal thermocline and the halocline, but in spring and autumn only a small float density change may result in sinking straight to the bottom in the overturned water column. To address this problem Purokoski et al. (2013) modified APEX float's diving algorithm to respond faster to pressure change. This method worked, but it increased the energy consumption of the float and therefore was not applied in further missions to increase the mission duration.

To prevent collision with seasonal ice cover, the float can be commanded to cut the ascent at a certain threshold of temperature. So far 0–1 °C has been used depending on the conditions, but more ice winters are needed to find an optimal value. If the float does not reach the surface it saves the data and sends it when the GPS connection has been established next time. The ice avoidance limits data coverage of the upper water column during ice season.

When operating in small basins, it is beneficial to have some control on the drifting of the floats, so that they do not drift to shallow coastal waters. It was found that driving the floats to the vicinity of the bottom between the measurement cycles worked well, and also in some cases lead to nearly stationary floats. An advantage with operating so close to shore is that the floats can be retrieved for maintenance after each mission and redeployed. On the other hand the floats in the Bothnian Sea require in general much more operator time than the usual open ocean floats.

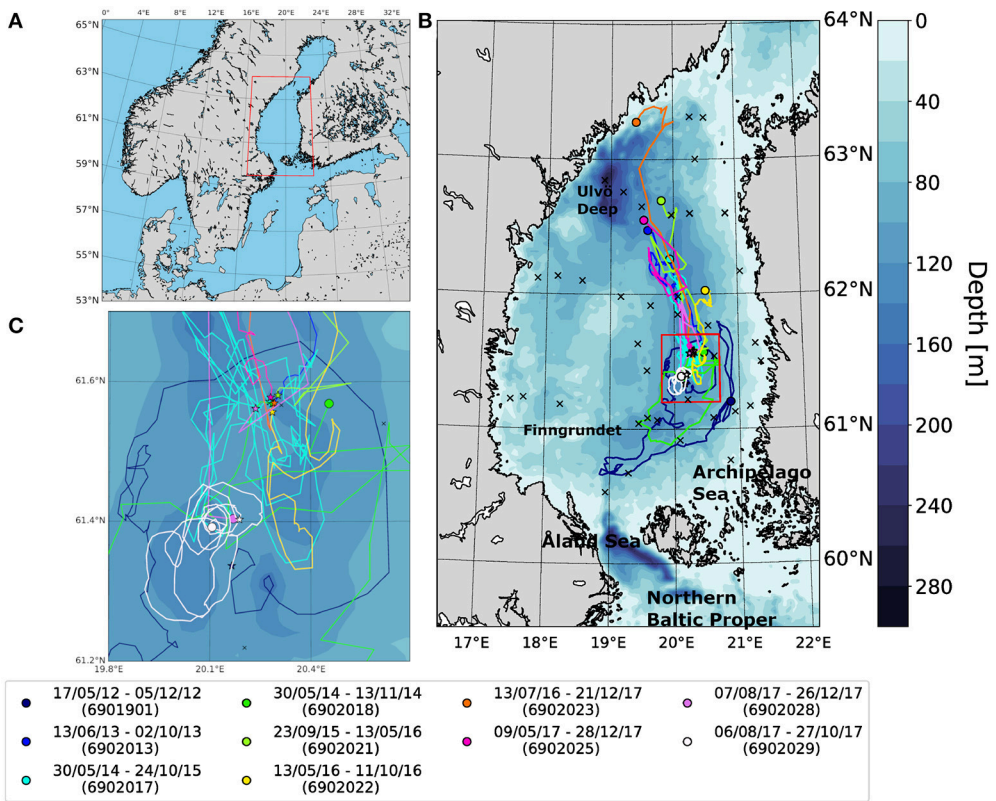


FIGURE 1 | (A) Bothnian Sea location in the Baltic Sea **(B)**, Argo float drift routes in the Bothnian Sea, and **(C)** a zoomed in map of the deployment area. The colors indicate separate deployments, and the stars and circles represent the deployment point ant the point of float retrieval or of latest profile, respectively. The black x:s show locations of CTD-profiles measured in the Bothnian Sea deep during 2012–2017. The bathymetry data is from Seifert et al. (2001).

2. OBSERVATIONS AND METHODS

2.1. Argo Data

The Argo profiles used in the analysis of this paper were collected in the Bothnian Sea in 2012 –2017. The data is from 10 different deployments, six of which were done with reused floats. In Argo system the floats are identified with unique WMO numbers that are related to the deployments rather than the physical float themselves. The floats used were 2,000 m APEX floats by Teledyne Webb Research. The details of the used floats and their measured parameters are listed in **Table 1**. For detailed information of the sensors and Argo float structure and operation see Teledyne Webb Research, Inc. (2013). The data is freely available at Argo (2000)[1].

Altogether 1,280 float cycles were recorded over the 6 years period, of which 1,083 resulted in a profile of the water column. Here unsuccessful cycles were defined as profiles with only up to four measurement points in the entire water column. The percentage of failed profiles varies between deployments (**Table 2**). Most of these failed profiles were due to float being temporarily stuck in the bottom or the float not diving properly from the surface in the first place. The sampling resolution was 2 dbar except for profiles less than 50 m deep, for which the sampling resolution is 5 dbar due to a software bug in the floats. In this paper "delayed mode" data was used whenever available, and only data with a quality flag 1 or 2 were used (see Argo Data Management Team, 2017 for details). Missing

TABLE 1 | Details of the Argo floats used in the Bothnian Sea 2012–2017.

		APE1	APE2	HAPE1	BAPE2
Model		APEX-APF9I			
Communications and positioning		Two-way Iridium Short Burst Data (SBD), GPS			
Measured parameters		Pressure, temperature, salinity		+ oxygen	+ fluorecence, turbidity
Sensors		Sea-Bird SBE-41CP		+ Aanderaa Optode 4330	+ WET Labs FLbb
Additional spesifications	Ice avoidance algorithm	x		x	x
			Modified pressure detection algorithm by FMI and Aalto University		

Extended from Roiha et al. (2018).

[1]http://www.coriolis.eu.org/Data-Products/Data-Delivery/Argo-floats-by-WMO-number

TABLE 2 | Argo float deployments in the Bothnian Sea in 2012–2017.

WMO	Float	Cycles	Recorded profiles	Mean cycle length [d]	Mean profile depth [dbar]	Bottom hits [%]	Mission timespan
6901901	APE1	314	247	1	59	0	17.05.2012–05.12.2012
6902013	APE2	119	119	1	77	0	13.06.2013–02.10.2013
6902017	APE1	176	173	2	115	13	30.05.2014–24.10.2015
6902018	BAPE2	58	50	4	93	30	30.05.2014–13.11.2014
6902021	BAPE2	49	42	7	105	5	23.09.2015–13.05.2016
6902022	APE2	217	215	0.5	101	10	13.05.2016–11.10.2016
6902023	APE1	103	40	7	89	69	13.07.2016–31.12.2017
6902025	HAPE1	49	47	7	108	19	09.05.2017–31.12.2017
6902028	BAPE2	31	20	7	111	38	07.08.2017–31.12.2017
6902029	APE2	160	159	0.5	118	-	06.08.2017–27.10.2017

Bolded missions were ongoing at the end of the year 2017. Bottom hit here means that the float had a bottom contact some time during a measurement cycle. The table is modified and extended from Roiha et al. (2018).

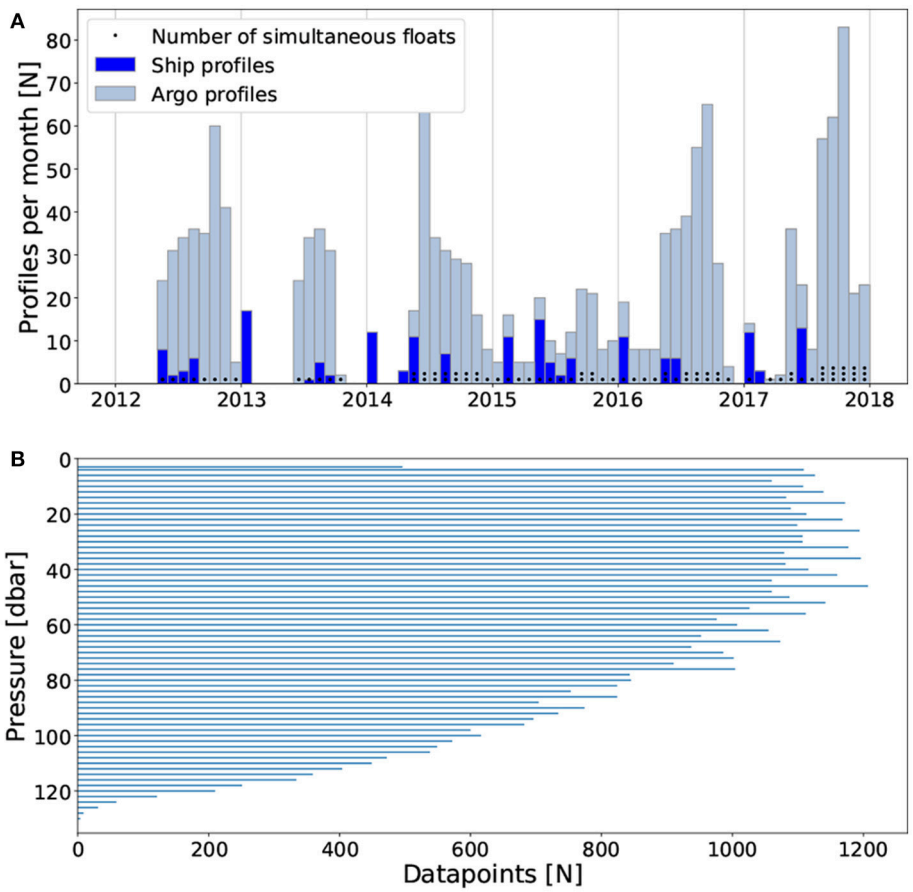


FIGURE 2 | (A) Number of measured Argo profiles (gray) and CTD profiles (blue) per month in the Bothnian Sea for 2012–2017. The black dots represent the amount of simultaneous floats each month. **(B)** Number of measurements per depth with a 2 dbar resolution with the Argo floats during 2012–2017.

latitude and longitude information for cycles that didn't reach the surface were interpolated for the purpose of density and salinity calculations.

Most of the Argo profiles were measured during the ice free season, and since 2014 continuous measurements have been made with at least one float over wintertime, although there are some short gaps in 2016–2017 where the mission 6902023 didn't provide profiles due to it being temporarily stuck in the bottom (**Figure 2A**). The mean deepest measurement point per profile for all missions was at 94 dbar, and the mean deepest

measurement point per profile of each mission varied from 59 (6901901) to 118 dbar (6902029) (**Table 2**) depending on the drifting area and target pressure relative to bathymetry. The deepest pressure measured at was 130 dbar (26.10.2017, 6902029).

All the floats were deployed inside an area of 615 km^2 with maximum 28 km between the deployment points (**Figure 1**). The floats mostly stayed confined in the Bothnian Sea deep basin. Two floats had a cyclonic drift path along isobaths in the southern Bothnian Sea (missions 6901901 and 6902018), one was almost stationary with maximum distance between profiles being 24 km (6902029), and the rest followed the deep toward North-Northeast. There were three simultaneous deployments in the autumn of 2017 (6902025, 6902028, and 6902029) with 6902028 and 6902029 close to each other and 6902025 more to the North (locations of the floats shown in **Figure 1**). A fourth float, mission 6902023, was also active during the same period, but it was stuck in the bottom from May to December 2017.

During the first two missions (6901901 and 6902013) the park pressure of the floats was kept at around 80 dbar to avoid bottom contacts. Due to this, approximately a 30 m deep layer above the bottom was not observed. For the rest of the missions the floats were kept closer to bottom, on average 10 m away, for better steering. This also resulted in more frequent bottom contacts (**Table 2**). Due to the high profiling frequency for mission 6902029 it was difficult to estimate the amount of bottom contacts since it spent such a short time at the park pressure between profiles. On average 4 m from surface was not measured due to CTD sensor design. In this work "near surface" refers to the shallowest available data point in the Argo profiles. Gridded bathymetry data from Seifert et al. (2001)[2] was used to estimate the depth at profile locations.

The ice avoidance algorithm preventing the floats from colliding with sea ice got it's first operational test during winter 2016–2017, when float 6902023 drifted under sea ice from February to April. The partial profiles it measured during that time show that the algorithm did detect the cold water mass and cut the float ascent as planned.

2.2. CTD Data

CTD data used here for comparison was measured on the Finnish research vessel RV Aranda in the Bothnian Sea 1998–2017. A Seabird CTD probe was installed on Aranda in 1997 so this 20 year period gives us a consistent data set to compare with. Since Finland is responsible for monitoring of the Bothnian Sea together with Sweden, and the deep area of the basin is mostly located in Finnish waters, most of the deep CTD profiles from the Bothnian Sea are included in the data set and give a comprehensive picture of the availability of CTD profiles in the area. The average number of CTD profiles per month was 3 for 1998–2017 and 2 for 2012–2017, although it greatly varies depending on monitoring and research campaign timing with usually around 4 months in a year having any measurements (**Figure 2A**). The locations of the profiles in 2012–2017 are shown in **Figure 1**.

2.3. Variables and Units

Density and absolute salinity for the Argo and CTD profiles were calculated using the Python implementation[3] of the Thermodynamic Equation Of Seawater– 2010 (TEOS-10) (IOC et al., 2010). All salinity data presented in this work are in absolute salinity, but the values from literature are presented as they were in the original work, which was usually practical salinity. The difference of absolute salinity and practical salinity is approximately 0.1 with absolute salinity being higher, and this is taken into account in the comparisons. Temperature shown is the *in situ* temperature, except for T-S diagrams, for which potential temperature calculated according to TEOS-10 was applied.

Since the amount of Argo and CTD profiles greatly varies between seasons and the same month of different years, the monthly mean values shown were calculated by first averaging over each month with data (or using the profile as is for months with only one profile) and then taking the mean over the years for each month. The monthly means were considered valid up to 100 dbar depth, below which there were only scattered datapoints (**Figure 2B**). Winter means were calculated for 2014–2017 due to lack of winter profiles before 2014, while other seasons also include years 2012 and 2013. Halocline and thermocline depths were calculated as the depth of maximum gradient of salinity and temperature. Seasonal halocline was excluded from the analysis by using measurements only under thermocline when it existed.

3. RESULTS

3.1. Hydrography Based on Argo Data

Six summers and 3 year-round (2014–2017) cycles of temperature and salinity in the water column were measured during 2012–2017. Near surface temperature varied from 0.1 °C (10.3.2017, float 6902023) to 22.7 °C (28.7.2014, float 6902017), and the seasonal variation reached to almost 100 dbar depth during winter 2014–2015 (**Figure 3**). In 2014, the near surface temperature was overall much higher than in the other years, up to 3 °C higher than in the second warmest summer 2016, and up to 6 °C warmer than the average of the warmest month, August (**Figure 4A**). Monthly mean temperature (2012–2017 average for ice-free season and 2014–2017 average for winter months) close to surface varied between 1.7 and 16.8 °C with highest temperatures in August and lowest in March before the spring overturning, and the mean temperature at 100 dbar was between 3.6 and 4.5 °C. The depth of 100 dbar was chosen to represent deep water, since it was the deepest HELCOM standard depth with measurements for every month of the year, and it was always below the calculated halocline depth. Thermocline development varied between years, starting in May with strongest stratification (−2.0 °C/m) in August, after which the thermocline started to decay. The mean depth of the thermocline in August varied between 13 dbar (2014) and 22 dbar (2013 and 2016). The mean thermocline depth in August over the whole Argo dataset was 18 dbar (**Figure 5**).

[2]https://www.io-warnemuende.de/topography-of-the-baltic-sea.html

[3]https://anaconda.org/pypi/gsw

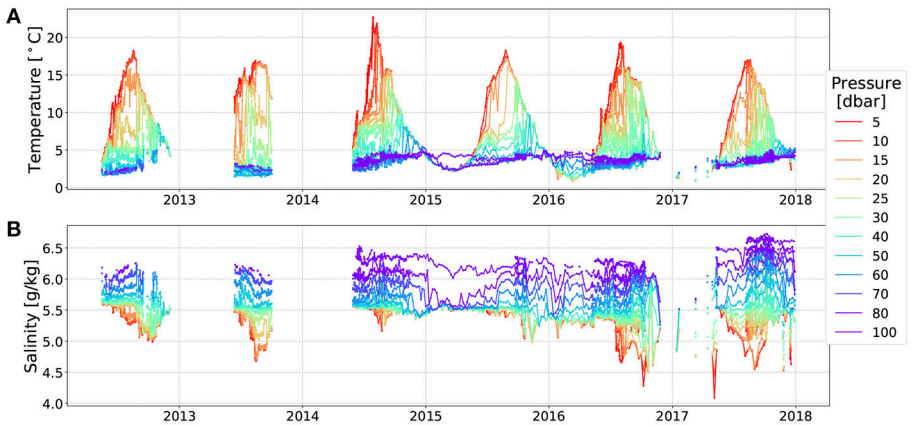


FIGURE 3 | Time series of **(A)** temperature and **(B)** salinity at HELCOM standard depths from the Argo floats.

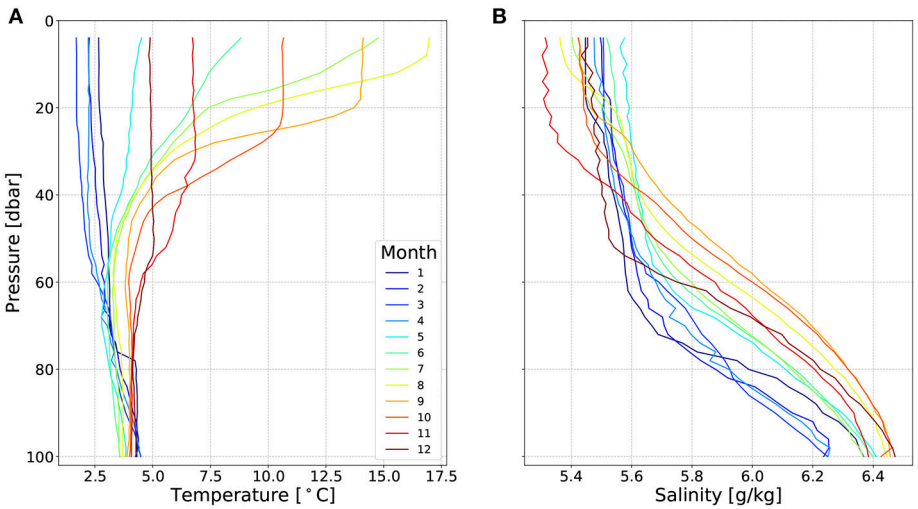


FIGURE 4 | Monthly mean profiles of **(A)** temperature and **(B)** salinity from Argo data. Profiles for months 1–4 include only 2015–2017 data due to lack of profiles and the other months include the entire dataset period of 2012–2017. Data above 4 dbar and below 100 dbar were cut off due to sparse measurements.

Measured salinity range close to surface was from 4.18 g kg^{-1} (5.5.2017, float 6902023) to 5.74 g kg^{-1} (2.6.2012, float 6901901) (**Figure 3B**). For 100 dbar depth the minimum and maximum values were 5.99 g kg^{-1} (18.11.2016, float 6902023) and 6.83 g kg^{-1} (7.10.2017, float 6902028), respectively. The variation of the monthly mean of salinity close to surface was 5.31–5.60 g kg^{-1} with highest values in May before the thermocline has developed and lowest in August when the thermocline restricts the mixing of freshwater runoff with the underlaying watermass. At 100 dbar the range of monthly mean salinity was 6.24–6.47 g kg^{-1} with highest values in the autumn and lowest in the spring around the time of spring overturning **Figure 4B**. The halocline was on average deepest, at 90 dbar, in February, and shallowest, at about 58 dbar, in August, when the thermocline was the strongest (**Figure 5**). The average halocline depth for the entire period 2012–2017 was at 67 dbar. Salinity below the halocline along the Bothnian Sea deep area was 0.33 g kg^{-1} higher in 2017 than in in 2012–2016, whereas the halocline depth has shallowed since 2015, when the mean below halocline salinity was lowest (**Figure 3B**).

The mean temperatures measured with the floats fit to those commonly presented in literature for the Bothnian Sea (Lentz, 1971), although the summer mean temperature is a couple of degrees warmer and bottom temperature variation is smaller. The record warm year 2014 showed as high near surface and mixed layer temperature, and this is reflected in the results. The smaller bottom variation compared to previously presented is most likely explained by sparse winter profiles and the lack of profiles from the shallow edge of the Archipelago Sea, where seasonal mixing can reach the bottom easier. Salinity both close to surface and below halocline was also on average in the limits of what is presented in Bock (1971) but the values were mostly at the lower end of the range and variation smaller. This is probably also caused by scarcity of profiles close to the sill to the Åland Sea. The

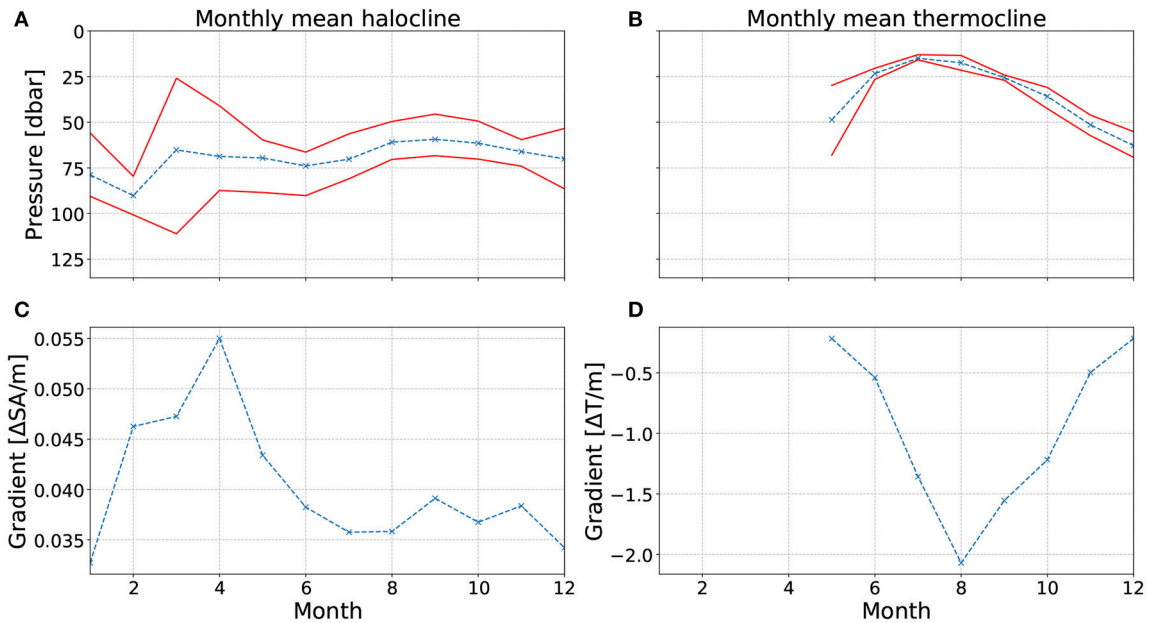


FIGURE 5 | Monthly means of **(A)** halocline and **(B)** thermocline depth and the strength of **(C)** salinity and **(D)** temperature gradients at the pycnocline depths calculated from Argo data. Means for months 1–4 include only 2015–2017 data due to lack of profiles and the other months include the entire dataset period of 2012–2017. The red lines in **(A,B)** show the maximum and minimum depths of halocline and thermocline for each month.

monthly halocline depth here was similar to those presented by Haapala and Alenius (1994), although here the maximum depth of the halocline occurred earlier in the Spring (**Figure 5**). This is most likely also due to the small amount of winter profiles, which amplifies the impact of the available years.

The mean salinity below the halocline in 2017 was 0.3 g kg^{-1} higher than between 1998 and 2016, both compared to the CTD data and the Argo profile data. Compared to the long time series of salinity from the Bothnian Sea from 1900's onwards the salinity in 2017 is well inside the observed variability, but still highest in the Bothnian Sea during the 21'st century. The drivers for this salinity change could be many and certainly require further research. One reason might be the major Baltic inflows (MBI) in 2014–2016, which pushed saline water from the Northern Baltic Proper to the Gulf of Finland, where record high bottom salinities were measured in the end of 2016. The MBI's could have had an impact on the Bothnian Sea bottom salinity as well, although the water has to pass multiple sills to reach the basin. However, a change in the halocline depth or it's salinity could influence the Bothnian Sea, since the deep water of the Bothnian Sea originates from the water above the Southern Quark sill depth of 60–70 m in the Northern Baltic Proper (Hietala et al., 2007). Also, change in wind conditions or runoff from land may also have affected the change in stratification in the Bothnian Sea. In a modeling study by Väli et al. (2013) a strong negative correlation between accumulated river runoff and below halocline salinity, as well as westerly winds and below halocline salinity were found. Compared to the climatological period 1981–2010 during 2017 there were 2–3% more westerly winds and less easterly winds, but the accumulated precipitation along the Finnish coast of the Gulf of Bothnia was smaller than the rest of 2010's and the 1981–2010 average. Especially in Oulu and Vaasa, the yearly precipitation was on average 118% of the normal period average, while in 2017 it was 95%[4].

3.2. Spatial and Temporal Scale Variability From Argo Profiles

We analyzed areal similarity and the significance of the profiling frequency in the Bothnian Sea by comparing three simultaneous missions from autumn 2017 between 06.08.–27.10.2017 (6902025, 6902028 and 6902029). In the Baltic Sea the size of an area where the water mass can be regarded as homogeneous in a climatological sense was defined as 30'x1° (latitude x longitude) or 55x55 km by Haapala and Alenius (1994). The same definition seems to apply for the short term Argo data as well. Floats 6902028 and 6902029 were within 50 km radius from each other for 75% of the duration of mission 6902029, with the maximum distance between them being 61 km. The hydrographic features their data showed were very similar (**Figure 6**). Float 6902025 drifted more to the north, with a 50–100 km distance to the other floats, to an area with less saline water above halocline. The north-south gradient in salinity is known to be dominant in the Bothnian Sea (for example Janssen et al., 1999). The shape of the T-S-diagram for float 6902025 is similar to those of 6902028 and 6902029, which indicates that the temperature dynamics in the open sea along the Bothnian Sea deep are not strongly dependent of latitude.

[4]http://en.ilmatieteenlaitos.fi/statistics-from-1961-onwards

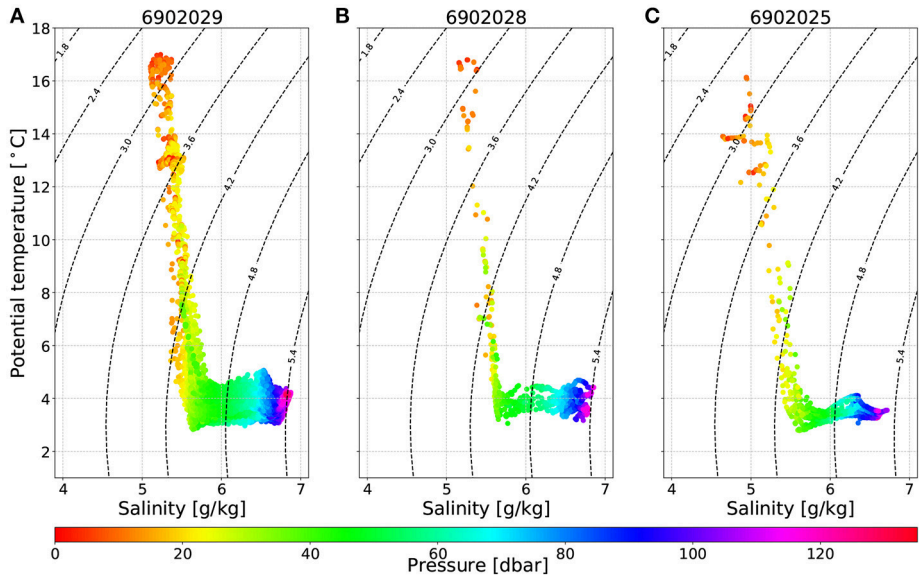


FIGURE 6 | T-S diagrams of for deployments **(A)** 6902029, **(B)** 6902028, and **(C)** 6902025. Colors show pressure of measurement points.

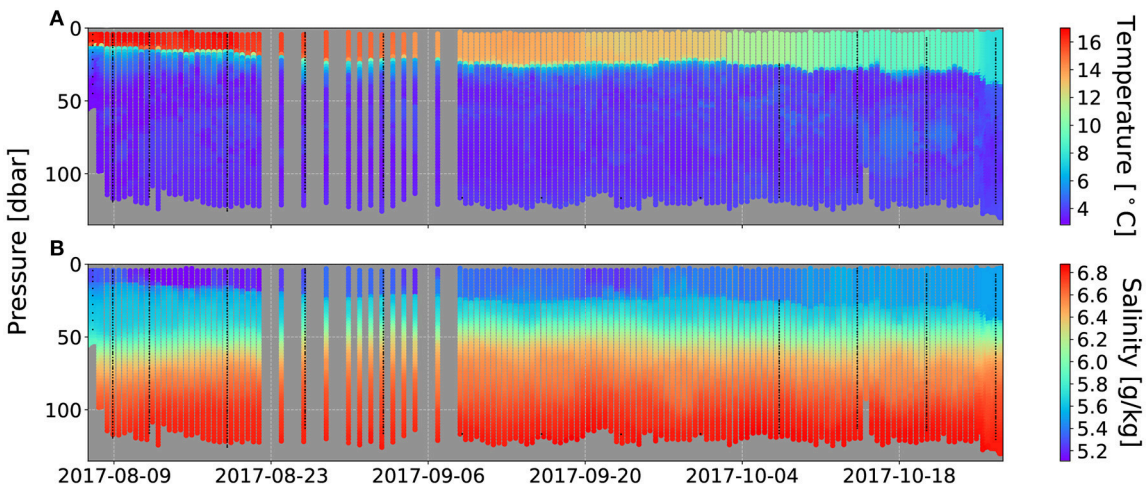


FIGURE 7 | (A) Temperature and **(B)** absolute salinity profiles from float 6902029. Black dotted lines show timing of profiles of float 6902028 during the same period. The gray shade is the background color and indicates that no data is available.

The high profiling frequency, one cycle every day (**Table 2**), of float 6902029 revealed more fluctuation in water temperature and variation in salinity above the halocline, than what float 6902028 captured with a weekly profiling schedule (**Figure 7**). The cooling of the mixed layer and the decay of the thermocline were recorded in more detail than previously has been possible in this area.

In the end of October float 6902029 was set to do continuous profiling to capture a predicted storm. The resulting dataset has profiles every 2 h and it is the first of it's kind in the Bothnian Sea. It reveals a 10 dbar deepening of the thermocline from 30 to 40 dbar, and a cooling of the mixed layer by 0.9 °C in 24 h between 25.-26.10.2017. This successful short term event monitoring with continuous profiling is a good example of the different observation routines possible with Argo floats with two-way communication. The storm was noticed in the forecast in time and the new settings for the float were delivered before the storm reached the Bothnian Sea. A profiling resolution of 2–3 h, which is likely the fastest possible with the depth range of 100–150 m, was achieved.

There was a lot of variation in the surface mixed layer salinity, with values ranging from 5.11 to 5.54 g kg^{-1} during the 2.5 months. In August there was a 5 day period with 1.5 g kg^{-1} less saline water in the surface mixed layer than the surrounding

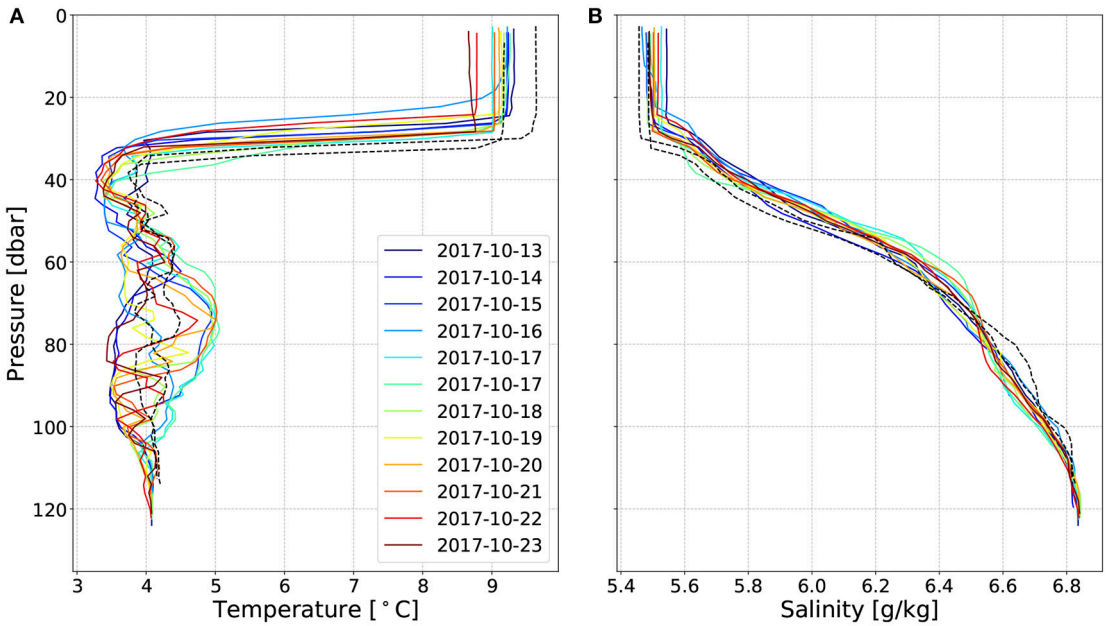


FIGURE 8 | (A) Temperature and **(B)** salinity profiles measured by float 6902029 between 13.-24.10.2017. The dashed black lines show the profiles from float 6902028 from the same time period.

days, which could be an advected lens of less saline water. An oscillation of the halocline depth between 40 and 60 dbar was also observed during the mission.

After October 15, 2017 two lenses of relatively warm water were measured below the halocline between 60 and 100 dbar (**Figure 8**). The temperature of these lenses was up to 5.1 °C, while the mean temperature of the layer was 3.8 °C. The event lasted around 10 days, after which the ambient temperature returned close to the mean. The float drifted approximately 9 km during the event. Prevailing wind direction at Märket automatic weather station between 5.–10.10. was between NW–NE and on the 13.10. there were 15 m s^{-1} winds from the North. These northerly winds may have caused downwelling on the Swedish side of the Bothnian Sea and at the edge of Finngrunden shoals. The float drifted close to the eastern edge of Finngrunden for the entire mission (white line in **Figure 1**).

Most of these phenomena were either completely missed with float 6902028 because of them falling in between profiles (see the black dots in **Figure 7**), or their duration and magnitude was not fully captured. For example the storm was left in between profiles, as well as the warm water lenses.

4. DISCUSSION

4.1. Argo Floats vs Traditional Ship Monitoring

After the start of regular Argo observations in the Bothnian Sea in 2012, 166 ship borne CTD profiles have been measured. Only three monitoring stations coincide with the Argo float deployment area (red rectangle in **Figure 1**), and six out of the 166 CTD profiles were measured at these stations. The most commonly visited standard monitoring stations SR5, F26, and US5B fall outside the main Argo drifting areas. Since temporal coverage of Argo floats in the Bothnian Sea is much larger than that of shipborne CTD profiling (**Figure 2**), Argo floats can capture extreme values, as well as synoptic to storm scale dynamics which are not possible to obtain with seasonal ship monitoring.

Because Argo floats measure more frequently, they capture the warming of the mixed layer and the development of the thermocline in early summer, the temperature maximum and variation during summer, and the cooling and decay of the thermocline in the autumn, whereas the ship monitoring brings out at best only the interannual variability of the water column at certain monitoring stations. Usually the summer COMBINE monitoring cruises take place in June and August, so the highest surface temperature, that occurs at the edge of July-August, and thermocline strength are often missed. During 2012–2017 the Argo floats recorded up to 5°C warmer temperatures in the surface layer than ship monitoring (**Figure 9A**). On the other hand minimum temperatures captured by ship profiling were lower than those by Argo floats in the entire water column. This can be mainly explained by the temporal coverage of the Argo data, since until now, there is very little data from winter time. The wider range in temperature in the CTD profiles below 80 dbar could be explained with spatial variation, the CTD data covers the Southern Quark better than the Argo data. Due to the larger areal coverage of the ship monitoring data, it includes data from shallower areas, where the use of Argo float is not optimal and also from deeper areas, such as the Ulvö deep, which have not yet been monitored with Argo floats. When only the area in which the Argo floats are deployed and from where there is most

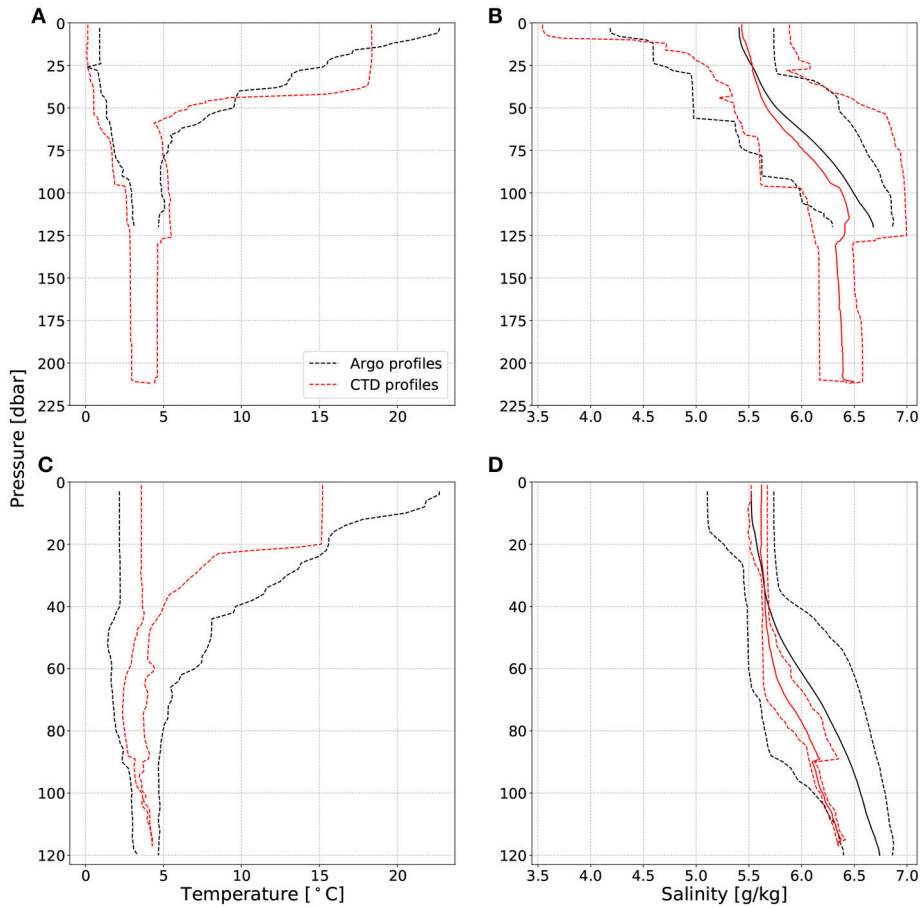


FIGURE 9 | Ranges (dashed lines) and means (solid lines in **B,D**) of **(A,C)** temperature and **(B,D)** salinity data from Argo data (black) and ship CTD (red) from **(A,B)** the entire Bothnian Sea and from **(C,D)** the Argo float deployment area shown as a red rectangle in **Figure 1** between 2012 and 2017. The locations of the CTD profiles are also shown in **Figure 1**.

data available (the zoomed in area in **Figure 1**) is considered, then the variability captured with Argo floats is 10°C more than with CTD (**Figure 9**).

The range of salinity in the entire Bothnian Sea was larger in the CTD data than in the Argo data, especially close to surface, where CTD profiles show up to 1 g kg^{-1} lower values. Since a horizontal gradient in salinity exists in the Bothnian Sea, it is to be expected that with a ship, not confined in the deep area, the extreme values are better reached. Argo floats recorded less saline cases between 10 – 75 dbar, but their profile mean was higher than that of the shipborne CTD profiles. However, in the float deployment area it can be seen that the temporal variability in salinity is much better captured by the Argo floats.

4.2. Monitoring Bothnian Sea Hydrography as a Whole

We have presented in this paper a new addition to the monitoring of the Bothnian Sea hydrography, the Argo floats. However, there are also other new automated measurement systems, such as gliders, that deserve to be mentioned and discussed . And also existing *in-situ* moorings, satellite data and FerryBox systems that already are, in addition to the traditional research vessel monitoring, an essential part of the monitoring of the state of the Bothnian Sea.

Due to the seasonal ice cover in the Bothnian Sea, maintenance of *in-situ* moorings is challenging and therefore they are currently limited only to few operational surface temperature buoys, located close to the shoreline and two wave buoys, which also include a temperature sensor. These surface buoys operate only during the ice-free season and need to be recovered well before the ice season starts. Therefore, they do not cover the full seasonal cycle, but provide a good overview of the late spring, summer, and autumn SST dynamics at their locations.

FerryBox systems offer continuous data from the near-surface level from designated ship routes. Presently there is one FerryBox operating in the Gulf of Bothnia (route Gothenburg-Kemi-Oulu-Lübeck-Gothenburg). The quality of the temperature and salinity measurements has been found good by Karlson et al. (2016) when compared to other field measurements and together with other measurements to complement the traditional monitoring data in the Baltic Sea.

In addition to these *in-situ* measurements, satellites provide a good coverage of the sea surface. Sea surface temperature has been observed with satellites for a long time and daily SST maps are provided in services such as the Copernicus Marine and Environment Monitoring System (CMEMS)[5]. Also SSS can be obtained from satellites, but presently the resolution and quality of the products are not good enough in the Baltic Sea, but maybe new progress will improve that (Olmedo et al., 2016).

To obtain more T-S-profile measurements, FMI has recently started to operate a glider to measure the hydrography in the southeastern part of the Bothnian Sea. Presently there have been two measurement campaigns during Autumns 2016 and 2017 (Alenius et al., 2018). Compared to Argo floats that drift freely with currents, the gliders can be navigated along predetermined routes. The vertical coverage of measurements is slightly better than with Argos, since the FMI glider has an altimeter, which allows the glider to dive close, c. 3–5 m, to the bottom. The ice season sets limits to the operation of gliders in the northern Baltic Sea. Liblik et al. (2016) state in their analysis of the potential of underwater gliders in global observing system that under ice operations have still been limited for gliders, but shown to be feasible by e.g., Beszczynska Möller et al. (2011). The gliders have not yet been used for regular monitoring in the Baltic Sea, but have shown their potential to be a good addition to the monitoring. They are, however, significantly more expensive than Argo floats and require more piloting and maintenance.

The present state-of-the-art 3D ocean models, such as the NEMO-Nordic Hordoir et al. (2018), are able to depict the Baltic Sea hydrography fairly well. For example Westerlund and Tuomi (2016) have shown that the vertical temperature and salinity structure and the seasonal development of thermocline in the Bothnian Sea were modeled with relatively good accuracy. However, they also showed, with the help of Argo float data, that there is a need for improvement in the model physics and parameterization in order to better describe the complex stratification conditions of the Baltic Sea. The accuracy of the 3D models can be improved by introducing assimilation of both surface and profile data as has been shown e.g., by Axell and Liu (2016) in the Baltic Sea.

5. CONCLUSION

Hydrography of the Bothnian Sea during 2012–2017 was estimated based on Argo data as a separate dataset, and then Argo data were compared to CTD profiles from the same time period and to historical CTD measurements.

For the first time we were able to observe the seasonal cycle of the water column in the open sea areas of the Bothnian Sea on a weekly scale. The timing of spring and autumn overturning and the development and decay of the thermocline can now be followed in much more detail than is possible with ship monitoring. With continuous *in-situ* profiling the phase of the yearly thermal cycle of the water column can be followed and compared to previous years to monitor changes in the cycle, much like Leppäranta et al. (1988) did with the ice season. This knowledge can be used to predict, for example, the upcoming ice winter or timing and magnitude of summer algae blooms.

The Argo floats seem to work well as an independent monitoring system for temperature dynamics in the Bothnian Sea. Since salinity is a more conservative and location dependent variable, the gradual changes in it may be better observed with long term station monitoring, but small and short scale phenomena are captured well. It was shown that the float profiling schedule is flexible and can be adjusted to fit the needs of both standard monitoring and short term event observation. The possibility to adjust the float behavior according to weather forecasts provides a great method to (a) achieve long term deployments with weekly profiles and longer battery life with still the option to get occasional fast profiling sequences and (b) get data from storms where normal research vessel operations would be difficult or not possible. There are very little measured T-S-profiles from storm situations in the Bothnian Sea. Achieving data from upper mixed layer dynamics during a storm will give valuable data e.g., for process studies and model development.

The Argo floats and ship monitoring supplement each other. The long time series from fixed monitoring stations with high vertical resolution from ships gives reference to the magnitude of short term variability measured with Argo floats, and the spatially variable high temporal resolution profiling with Argo floats gives insight of the possible phenomena behind anomalies seen in the temporally sparse monitoring data. The floats also contribute to the long term standard monitoring time series whenever they drift past a monitoring station. The Argo floats are confined in the deep area of the Bothnian Sea, so their data mostly represents the South-North variability in the water column.

For now, we have missed the top 4 m of the water column because of the limitation set by the CTD sensor design. Switching to an alternative sensor would enable even better monitoring of the mixed layer, which would then make prediction of for example algal blooms easier. Gaining weekly to daily sea surface observations would also support validation of sea surface remote sensing.

Despite the challenging environment in the Bothnian Sea, the Argo floats were found to function well and they have become an important part of the monitoring network. Even though the floats often touch the bottom and occasionally get stuck in the bottom, they have so far always managed to free themselves. The ice avoidance algorithm was also determined to be functioning as expected and we have managed to retrieve all our floats so far.

For future work it would be interesting to assess the Bothnian Sea observing system in it's current state as done by Grayek et al. (2015) in the Black Sea to see what improvements could be made regarding the now existing Argo operations. Grayek et al. (2015) concluded that for the Black Sea a good amount of floats is 10 and that adding more floats instead of increasing profiling frequency gives best results at least for data assimilation. Most important questions are how many floats are enough to capture the instantaneous state of

[5]http://marine.copernicus.eu

the Bothnian Sea sufficiently, and what is the best profiling frequency for long term monitoring and for the needs of forecasting.

AUTHOR CONTRIBUTIONS

NH wrote the first draft with significant help from LT and was the main responsible for the analysis of the observation data and producing the illustrations. PR, S-MS, LT, and PA contributed to the illustrations. Background research was mainly done by NH, PR, and PA. TP was responsible for the technical support and acquisition of data. All authors contributed to the evaluation of the data, wrote sections for this manuscript and revised and approved the sent version.

ACKNOWLEDGMENTS

The Argo data used in this work were collected and made freely available by the International Argo Program and the national programs that contribute to it. (http://www.argo.ucsd.edu, http://argo.jcommops.org). The Argo Program is part of the Global Ocean Observing System. This work has been partly supported by the Strategic Research Council at the Academy of Finland, project SmartSea (grant number 292 985).

REFERENCES

Alenius, P., Tikka, K., Lips, U., Tuomi, L., Purokoski, T., Roiha, P., et al. (2018). "Euro-Argo in work and new potential of gliders in the Baltic Sea BOOS," in *Operational Oceanography serving Sustainable Marine Development. Proceedings of the Eight EuroGOOS International Conference*, eds E. Buch, V. Fernández, D. Eparkhina, and Gorringe, P., and G. Nolan (Bergen), 143–148.

Argo (2000). *Argo Float Data and Metadata From Global Data Assembly Centre (Argo GDAC).* SEANOE.

Argo Data Management Team (2017). *Argo User's Manual V3.2.* http://doi.org/10.13155/29825

Axell, L., and Liu, Y. (2016). Application of 3-d ensemble variational data assimilation to a baltic sea reanalysis 1989–2013. *Tellus A Dynam. Meteorol. Oceanogr.* 68:24220. doi: 10.3402/tellusa.v68.24220

Beszczynska Möller, A., Woodgate, R., Lee, C., Melling, H., and Karcher, M. (2011). A synthesis of exchanges through the main oceanic gateways to the Arctic Ocean. *Oceanography* 24, 82–99. doi: 10.5670/oceanog.2011.59

Bock, K. H. (1971). Monatskarten des salzgehalten der ostsee, dargestellt für verschiedene tiefenhorisonte [monthly salinity maps of the Baltic Sea for different depths]. *Deutsch. Hydrogr. Z. Ergänzungshäft Reihe B* 12, 1–147.

Fonselius, S. (1996). *Västerhavets och Östersjöns Oceanografi*. Norrköping: SMHI.

Grayek, S., Stanev, E. V., and Schulz-Stellenfleth, J. (2015). Assessment of the Black Sea observing system. A focus on 2005-2012 Argo campaigns. *Ocean Dynam.* 65, 1665–1684. doi: 10.1007/s10236-015-0889-8

Håkansson, B., Alenius, P., and Brydsten, L. (1996). Physical Environment in the Gulf of Bothnia. *Ambio*, 8, 5–12.

Haapala, J., and Alenius, P. (1994). Temperature and salinity statistics for the northern Baltic Sea 1961-1990. *Finnish Mar. Res.* 262, 51–121.

HELCOM (2014). *Manual for Marine Monitoring in the COMBINE Programme of HELCOM*. HELCOM.

Hietala, R., Lundberg, P., and Nilsson, J. A. (2007). A note on the deep-water inflow to the Bothnian Sea. *J. Mar. Syst.* 68, 255–264. doi: 10.1016/j.jmarsys.2006.12.004

Hordoir, R., Axell, L., Höglund, A., Dieterich, C., Fransner, F., Gröger, M., et al. (2018). Nemo-Nordic 1.0: a NEMO based ocean model for Baltic & North Seas, research and operational applications. *Geosci. Model Dev Discuss.* 2018, 1–29. doi: 10.5194/gmd-2018-2

IOC, SCOR, and IAPSO (2010). *The International Thermodynamic Equation of Seawater – 2010: Calculation and Use of Thermodynamic Properties.* Number 56 in Intergovernmental Oceanographic Commission, Manuals and Guides. UNESCO.

Janssen, F., Schrum, C., and Backhaus, J. O. (1999). A climatological data set of temperature and salinity for the Baltic Sea and the North Sea. *Deutsch. Hydrogr. Z.* 51:5.

Karlson, B., Andersson, L., Kaitala, S., Kronsell, J., Mohlin, M., Seppälä, J., et al. (2016). A comparison of FerryBox data vs. monitoring data from research vessels for near surface waters of the Baltic Sea and the Kattegat. *J. Mar. Syst.* 162, 98–111. doi: 10.1016/j.jmarsys.2016.05.002

Kassis, D., Korres, G., Petihakis, G., and Perivoliotis, L. (2015). Hydrodynamic variability of the Cretan Sea derived from Argo float profiles and multi-parametric buoy measurements during 2010–2012. *Ocean Dynam.* 65, 1585–1601. doi: 10.1007/s10236-015-0892-0

Lentz, W. (1971). Monatskarte der Temperatur der Ostsee dargestellt für verschiedene Tiefenhorisonte [Monthly maps of the temperature of the Baltic Sea for different depths]. *Deutsch. Hydrogr. Z. Ergänzungshäft Reihe B* 11, 1–148.

Leppäranta, M., Palosuo, E., Grönvall, H., Kalliosaari, S., and Seinä, A. (1988). Itämeren jäätalven vaiheet (leveyspiiristä 57°N pohjoiseen) [Ice phases in the Baltic Sea, north of latitude 57°N]. *Finnish Mar. Res.* 254, 1–83.

Liblik, T., Karstensen, J., Testore, P., Alenius, P., Hayes, D., Ruiz, S., et al. (2016). Potential for an underwater glider component as part of the Global Ocean Observing System. *Methods Oceanogr.* 17, 50–82. doi: 10.1016/j.mio.2016.05.001

Olmedo, E., Martínez, J., Umbert, M., Hoareau, N., Portabella, M., Ballabrera-Poy, J., et al. (2016). Improving time and space resolution of SMOS salinity maps using multifractal fusion. *Remote Sens. Environ.* 180, 246–263. doi: 10.1016/j.rse.2016.02.038

Pettersson, O. and Ekman, G. (1897). *De Hydrografiska Förändringarne Inom Nordsjöns Och Östersjöns Områade Under Tiden 1893-1897*, volume 29 of *Kongliga Svenska Vetenskaps-Akademiens Handlingar*. Kungl. boktryckeriet. P.A. Norstedt & Söner.

Purokoski, T., Aro, E., and Nummelin, A. (2013). First long-term deployment of Argo Float in Baltic Sea. *Sea Technol.* 54, 41–44.

Roiha, P., Siiriä, S., Alenius, P., Haavisto, N., Westerlund, A., and Purokoski, T. (2018). Estimating currents from Argo Trajectories in the Bothnian Sea, Baltic Sea. *Front. Mar. Sci.* 5:308. doi: 10.3389/fmars.2018.00308

Seifert, T., Tauber, F., and Kayser, B. (2001). "A high resolution spherical grid topography of the Baltic Sea - 2nd Edn.," in *Baltic Sea Science Congress* (Stockholm), Poster #147. Available online at: www.io-warnemuende.de/iowtopo

Teledyne Webb Research, Inc. (2013). *APF-11 APEX Profiling Float User Manual, Rev. 2 Edn*. North Falmouth.

Väli, G., Meier, H. E. M., and Elken, J. (2013). Simulated halocline variability in the Baltic Sea and its impact on hypoxia during 1961–2007. *J. Geophys. Res. Oceans* 118, 6982–7000. doi: 10.1002/2013JC009192

Westerlund, A., and Tuomi, L. (2016). Vertical temperature dynamics in the Northern Baltic Sea based on 3d modelling and data from shallow-water Argo floats. *J. Mar. Syst.* 158, 34–44. doi: 10.1016/j.jmarsys.2016.01.006

Conflict of Interest Statement: The authors declare that the research was conducted in the absence of any commercial or financial relationships that could be construed as a potential conflict of interest.

Copyright © 2018 Haavisto, Tuomi, Roiha, Siiriä, Alenius and Purokoski. This is an open-access article distributed under the terms of the Creative Commons Attribution License (CC BY). The use, distribution or reproduction in other forums is permitted, provided the original author(s) and the copyright owner(s) are credited and that the original publication in this journal is cited, in accordance with accepted academic practice. No use, distribution or reproduction is permitted which does not comply with these terms.

frontiers in Marine Science

ORIGINAL RESEARCH
published: 12 September 2018
doi: 10.3389/fmars.2018.00308

Estimating Currents From Argo Trajectories in the Bothnian Sea, Baltic Sea

Petra Roiha[1], Simo-Matti Siiriä[1], Noora Haavisto[1,2], Pekka Alenius[1], Antti Westerlund[1] and Tero Purokoski[1]*

[1] Marine Research Unit, Finnish Meteorological Institute, Helsinki, Finland, [2] Tvärminne Zoological Station, University of Helsinki, Helsinki, Finland

Argo floats have been used in the environmental monitoring of the very shallow Bothnian Sea, a sub-basin of the Baltic Sea, for 5 years as part of the Finnish Euro-Argo programme. The Bothnian Sea is so far considered to be an environmentally healthy part of the Baltic Sea because the deep waters of the basin are well-ventilated by inflowing oxygen-rich saltier and heavier surface layer waters of the Baltic Sea proper. Thus the deep water flow is of interest in the Bothnian Sea. In this study, we used Argo float data from six different long-term missions, from 111 to 512 days, to analyze the deep-water flow in the Bothnian Sea where no continuous monitoring of currents exist. We estimated mainly the flow below the expected halocline from the paths of the floats. We analyzed the movements statistically and estimated the error caused by the surface drift of the floats during their stay at the surface by using 3D hydrodynamic model results as reference data. Our results show a northward flowing resultant current in the deep trench of the Bothnian Sea. There seemed to be very little exchange between coastal zone and open-sea waters in deeper layers. The drifting speed of the floats in the deep layers of Bothnian Sea generally was around 2 cm/s but instantaneous speeds of up to 30 cm/s in the middle-layer (50 dbars) were observed. In the Bothnian Sea deep, the deep trench on the Finnish side of the Bothnian Sea, the vast majority of the observations showed deep currents from south to north, with the same average speed of around 2 cm/s but the instantaneous maximum was smaller at 13 cm/s. Our study indicates that the routine Argo float observations can be used to get information on the deep currents in the basin in addition to hydrographic observations.

Keywords: autonomous, measurement device, real-time, ocean observations, circulation, environmental monitoring, hydrography

OPEN ACCESS

Edited by:
Elinor Andrén, Södertörn University, Sweden

Reviewed by:
Taavi Liblik, Tallinn University of Technology, Estonia
Alexander B. Rabinovich, P.P. Shirshov Institute of Oceanology (RAS), Russia

****Correspondence:***
Petra Roiha
petra.roiha@fmi.fi

Specialty section:
This article was submitted to Coastal Ocean Processes, a section of the journal Frontiers in Marine Science

Received: *13 March 2018*
Accepted: *10 August 2018*
Published: *12 September 2018*

Citation:
Roiha P, Siiriä S-M, Haavisto N, Alenius P, Westerlund A and Purokoski T (2018) Estimating Currents From Argo Trajectories in the Bothnian Sea, Baltic Sea. Front. Mar. Sci. 5:308. doi: 10.3389/fmars.2018.00308

1. INTRODUCTION

The Baltic Sea is a small shallow sea that consists of several basins with most of the deeper parts separated from each other by underwater sills. The water quality of the deep waters of the basins differ considerably from each other, although the whole Baltic Sea is more or less under loads from the land. For example, the marine ecosystems change because of nutrient and energy fluxes between the surface and benthos; the local climate and ice conditions depend on the energy storage of the sea and its movements. To know the deep currents and their variations is to be aware of potential changes in the environment.

The dynamics of the deep areas of the Baltic Sea are still partly poorly known due to the limited quantity of measurements in these areas. Most of the studies that enlighten the deeper water layer dynamics concentrate on the Baltic Proper (e.g., Wieczorek, 2012), southern Baltic Sea (e.g., Bulczak et al., 2016), and Gulf of Finland (e.g., Suhhova et al., 2018) and are often related to examining the influence of major Baltic inflows on the deep water (Meier et al., 2006). Subsurface currents transport energy and substances, and they also have an effect on ecosystems by transporting the matter and the organisms.

The Bothnian Sea, a large sub-basin of the Baltic Sea, has been considered to be an environmentally healthy part of the vulnerable Baltic Sea, which suffers from environmental problems, the most severe of which is the oxygen deficit in the deep waters of the Baltic Sea Proper. Some concern on the slight worsening of the deep-water oxygen conditions in the Bothnian Sea was expressed by Raateoja (2013). The general understanding of the dynamics of the deep waters of the Bothnian Sea is that oxygen-rich saltier and heavier water from the surface layer of the Baltic Sea proper flow in to the Bothnian Sea and sinks toward the bottom and continues toward the north along the bottom, thus ventilating the deep-waters there (Hietala et al., 2007). This deep-water flow is of interest and should be monitored. However, there is no monitoring of currents in that open-sea area.

Kuosa et al. (2017) have studied the development of the Gulf of Bothnia ecosystem and concluded that variation in deep-water inflow from the Baltic Proper has an effect on phyto- and zooplankton communities in the Bothnian Sea.

The Finnish Meteorological Institute (FMI) has operated Argo floats in the Bothnian Sea already for 5 years as part of the Finnish Euro-Argo contribution. On average year the Bothnian Sea freezes almost completely (SMHI, 1982) and the floats are equipped with ice-avoidance algorithm. When ice avoidance is used the float is given a temperature value near freezing temperature (in the Bothnian Sea 0.25–0.5°C). If the float detects freezing water it stops profiling and returns to the parking depth. In this study period no ice-avoidance was needed as the missions were performed in either ice-free period or in the area with no ice. However, the ice-avoidance was tested during this study with test value around 3°C.

In this paper we study the possibility to utilize the Bothnian Sea Argo float data to estimate the deep currents below the pycnocline and thus add the value of the regular monitoring with these instruments. We analyzed the 5 years data of Argo float measurements from 2012 to 2016 to study the deep water movements in the Bothnian Sea in order to gain understanding of the processes affecting ecosystems there now and to be able in the future to predict the changes in the physical conditions. This type of data has far too coarse time resolution to reflect internal oscillations in the basin, like inertial ones and Bothnian Sea seiches. The results reflect more the net water transport in the deep layer.

1.1. The Bothnian Sea

The Bothnian Sea is located in the northern part of the Baltic Sea (**Figure 1**). It is generally shallow, with an average depth of 66 m, but it is divided topographically different sections. There is relatively straight forward sloping bottom on the eastern side of the basin and an arch-shaped deep trench with maximum depth of 293 m in the north-western part of the basin. The area of the basin is 64 886 km^2 (Fonselius, 1996). The surface salinity in the open sea area is 5–6 and the deep-water salinity is 6–7 (Fonselius and Valderrama, 2003). The shoreline is near, and the area is important for marine traffic, nature conservation and fishing activities (Backer and Frias, 2013).

The northern parts and the coastal areas of the basin freeze or are near to the freezing point during the winter. The upper layer temperature is then smaller than maximum density temperature. In spring the surface temperature increases toward maximum density temperature, which causes overturning. In summer the temperature is greater than maximum density temperature and a seasonal thermocline forms. When the surface layer cools in the autumn toward maximum density temperature the surface layer overturns again. In winter the upper and deep layers are separated by a weak halocline, which also is a pycnocline, at somewhere between 70 and 90 m depths. The winter time convection reaches this pycnocline as interpreted from Argo data in the Bothnian Sea (Haavisto et al., 2018) and data from fixed oceanographic station at Utö (Haapala and Alenius, 1994).

The Bothnian Sea is a basin that is behind several smaller basins and sills that prevent the direct deep water flow from the Baltic Sea Proper. Thus the deep waters in the Bothnian Sea are formed during the winter from surface water from the Baltic Proper (Leppäranta and Myrberg, 2009). In last 20 years the saline water inflow to the deep layers of the Bothnian Sea has increased potentially by changes in sea-level dynamics in the Baltic Proper or the salinity content of the inflowing water (Raateoja, 2013). The deep water in the Gulf of Bothnia is mainly cooled winter water from the Gotland Sea, that has sunk over the southern Åland sill (Marmefelt and Omstedt, 1993). During the summer the deep water system resembles the deep water system in the Baltic Proper, with a strong thermocline and dicothermal layer. Then the direct wind mixing can only effect the layer that is on top of the thermocline, and deeper mixing can only happen when the thermocline disappears during spring and autumn overturning. This has a significant effect on the microbial ecosystem on the surface layer and oxygen conditions in the bottom layer (Raateoja, 2013).

The currents are induced in the sea by four different mechanisms: wind stress, sea surface tilt, horizontal thermohaline gradient of density and tidal forces (Leppäranta and Myrberg, 2009). The currents are altered by Coriolis acceleration, topography and friction. The period of the inertial oscillation is around 13.75 h in the southern Bothnian Sea and around 13.44 h in the Northern Bothnian Sea. River run-off could also change the local sea-level height and thus the currents. The passing low pressure cells often cause seiches in the Bothnian Sea. The theoretical uninodal seiche period for the Baltic Proper–Bothnian Sea system is 35.6 h and water-level observations suggest it might be as long as 39 h (Leppäranta and Myrberg, 2009). With Merian formula we may estimate that the uninodal seiche period accross the Bothnian Sea is 4.4 h and along the Bothnian Sea 7 h. A northerly wind also drives the surface layer toward the south and west, causing upwelling on

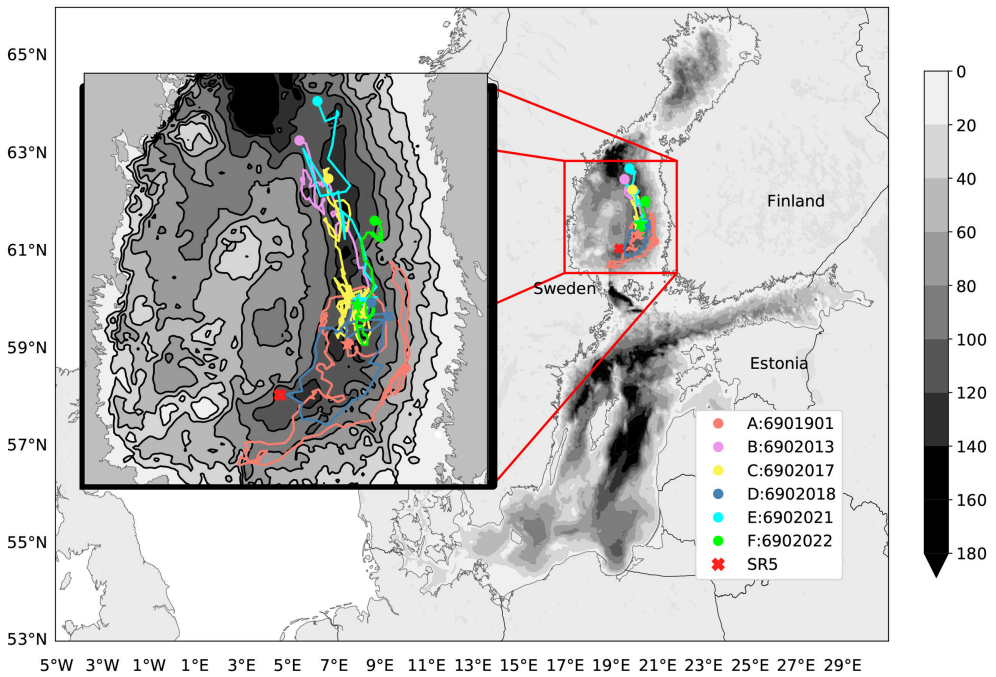


FIGURE 1 | Map of Argo missions in the Bothnian Sea 2012–2016. The deployment site of the floats is in a deep part of the Bothnian Sea. The starting and ending points are marked with stars and circles, respectively.The gray-scale shows the bathymetry. The cross marks the HELCOM continuous monitoring station, SR5.

the Finnish coast. The compensating current in the deep layer then flows toward the north.

The general concepts of the circulation in the Gulf of Bothnia were laid down in the early 20th century when Witting (1912) and Palmén (1930) studied the currents using observations from drift cards, ship borne current measurements and from light ships. They noticed that the main feature in the Bothnian Sea surface and near surface was a cyclonic circulation moving water to the north on the Finnish side of the basin and southwards on the Swedish side. Witting's works indicated two main circulation cells, one in the northern part of the Bothnian Sea and the other in the southern part. Palmén , however, concluded that there is only one basin-wide circulation cell, and that concept has been the basis of the general thinking since the 1930s.

Witting (1912) described the surface circulation separately for June, August, October and from June to October. He described the deep water movements in connection to water transports and gave figures for transports in spring and autumn. In that description the deep water transport goes down to the deep trench of the Bothnian Sea and rises upwards on the Swedish side where the depth of the sea is smaller. In both seasons the deep water transport is toward north.

The data on the deep water currents in the Bothnian Sea is sparse, and most of the measurements are concentrated in the southern part near the Understen–Märket trench, where the water exchange between the Baltic Sea Proper and the Bothnian Sea is taking place. Witting and Pettersson (1925) were the first to analyze the deep currents in that area in two short campaigns in the early 1920s. In the 1950s Hela (1958) studied the hydrography of the area. In the 1960s Palosuo (1964) studied the water exchange in the Åland Sea and the Quark and the routes of the water in the upper layers (15–40 m) of the Bothnian Sea.

In 1991 the Gulf of Bothnia Year programme aimed at a better understanding of the processes affecting on the ecosystem. This programme also included an intensive field observation of currents (e.g., Uotila et al., 1996). Coastal-open sea exchange processes as well as deep-sea mixing processes were scrutinized by using moored current meters and thermistor chains among others to gain insight into the structure and dynamics of the whole water column (Murthy et al., 1993). The current meter data from 8 and 60 m depth from a station with bottom depth of 112 m, showed mainly northward going currents at both depth levels even in summer and inertial oscillations were sometimes present at both depths. Unfortunately even those datasets cannot answer to the question if there exists a two layer flow in the area under conditions when there is clear summer stratification.

Hietala et al. (2007) performed a measurement campaign with R/V Aranda to study with ship-mounted acoustic Doppler current profiler (ADCP) the currents in the Understen–Märket trench. 3D hydrodynamic modeling studies have also been executed to understand the water movements (e.g., Myrberg and Andrejev, 2006). These studies concentrate mainly on the near surface layers because there has not been good long-term observational data on the currents in the whole water column. The models today have achieved a certain maturity, but alongside the models we need observations to improve our understanding on the movement of water masses in the whole water column.

Mesoscale phenomena on the surface have been also studied by remote sensing methods (Kahru et al., 1995), but those methods do not tell what happens in the deep layers.

1.2. Argo Floats

In the 1990s the time was right to start a global pursuit to automatically monitor the oceans' evolving temperature and salinity fields (Riser et al., 2016). The first global pursuit to survey the physical properties of the world oceans was the World Ocean Circulation Experiment (WOCE) (Woods, 1985). The global Argo programme was launched after WOCE and has been working since the year 2000 and it aims at real time monitoring of the world's oceans including sea areas that are difficult to reach by other means. Nowadays the main task of the floats is to measure the vertical distribution of basic hydrography fields and up to 80 additional parameters (Carval et al., 2015) at regular intervals and upload the data right after the measurements to the Internet. The floats have mostly been used in Open Ocean in areas where the depth is much more that 1,000 m. In between the profile measurements, the floats drift freely with currents deep below the surface (Argo, 2000).

In general, floats are designed to be used in oceans where there is no danger of hitting the bottom or being hit by a ship while on the surface. Normally there is no need to change the diving parameters during the mission, and a one-way satellite transmission from float to shore is sufficient.

Usually the floats drift for about 10 days at a depth from 1 to 2 km. While ascending, they collect profiles of at least the temperature and salinity, but other sensors might be included too. Once the float is at the surface, the measurement data as well as the float's GPS position is transmitted to the data collector via satellite. All the data from Argo floats is transmitted by satellite and made available in a public database. Thus, continuous measurement data becomes available from sea areas where *in-situ* observations otherwise would be sparse (Le Traon, 2013). Currently, almost all deployed floats are in the deep oceans, with only a few operating in shallow, marginal seas.

The floats are successfully used to study currents in the deep oceans and shelf seas for example in the Black Sea (Korotaev et al., 2006), the Nordic Seas (Lavender et al., 2005; Voet et al., 2010), and the Mediterranean Sea (Menna and Poulain, 2010), too. The methods for analyzing the deep currents from the Argo data have been developed during the years (e.g., Park et al., 2005) In this study, we used the Argo data for the first time in analyzing currents in a shallow brackish water basin. With this data, we are able to achieve time series that cover most of the ice free seasons in the Bothnian Sea.

The Baltic Sea has a different operating environment than the oceans. With the aim of preventing the float from hitting the bottom and from drifting to shore, a much more active involvement with the float's mission is required. Therefore, to be able to change the diving parameters of the float, two-way satellite communication and short dive cycles are necessary requirements (Purokoski et al., 2013). The main cost of operating the floats is the manpower needed to keep watch on the floats. Benefit for this is the ability to react to interesting phenomena and increasing the observation frequency when needed.

The Finnish Meteorological Institute has used Argo floats in monitoring the Baltic Sea since the year 2012. At least two Argo floats have been continuously in the sea in the Gotland Deep, Baltic Sea Proper and in the Bothnian Sea. In our early Bothnian Sea Argo float missions, the floats were taken out from the sea for the ice-covered season, but later in the years 2015 and 2016 the floats have been equipped with ice avoidance system and they stay there also during the winter and a potentially ice-covered period. The floats have been measuring in the areas where there are routine HELCOM monitoring stations but no dense time series. As the floats are kept away from the coast, they can be used to estimate the water movements in areas where so far only short-term deep current measurements have been done.

2. MATERIALS AND METHODS

2.1. Bothnian Sea Argo Floats and Missions

In January 2011, FMI received two floats specifically balanced for use in sea areas around Finland. These APEX (Autonomous Profiling Explorer) floats were manufactured by Teledyne Webb Research Corp. (East Falmouth, Massachusetts). Both of the floats were equipped with basic Sea-Bird Electronics Inc. (Bellevue, Washington) SBE 41CP CTD (Conductivity-Temperature-Depth) sensors and a two-way Iridium satellite transmitter. Later a bio-optical float was also deployed to the Bothnian Sea (**Table 1**). The floats were especially balanced to function in brackish water. Since 2012, the measuring activity has been continuous.

There were altogether six missions in the years 2012–2016 done by three different floats (**Table 2**). FMI recovers the floats after missions and reuses them after service. Five of the missions were launched between mid-May and mid-June and one mission was launched in September. All the missions were launched near the same location in the middle of the Bothnian Sea deep to avoid bottom contact and collision with vessels. The deployment area is relatively deep and has a level bottom. During the winter time the ice avoidance was also tested in open water with ice avoidance temperature higher than exact ice avoidance temperature, but the largest number of observations are from the summer season. In later years, the number of winter measurements has also been increasing due to positive experiences with the ice-avoidance algorithm (**Figure 2**).

The typical measuring cycle starts when a float starts the diving procedure. When reaching the target pressure, the float stays at that depth, measuring pressure and temperature. After a pre-set diving time the float starts to measure the profile. Unlike the ocean, the profile is started from the parking depth (**Figure 3**). During the missions, the floats sometimes stayed on the surface during the diving cycle, hit the bottom, or did not send the complete log file. These occasions are removed from the analyzed datasets (**Table 2**).

From the Argo logs we can directly access the diving time, the time floated at the parking depth and the ascending time. When we know the total cycle time, we can estimate the time spent at the surface from those values.

TABLE 1 | Technical details of the floats used in this study.

	APE1	APE2	BAPE2
Modifications		Modified pressure detection algorithm by FMI and Aalto University	
Model	APEX-APF91		
Sensors	Temperature, conductivity, pressure		+ Oxygen sensor Aanderaa Optode 4330, + fluorescence sensor and turbidity sensor Wetlabs FLbb.
Communications	2-way Iridium satellite		

All three floats had a 2-way satellite connection and CTD equipment. APE2 had also modified pressure detection, and BAPE2 had additional oxygen, fluorescence and turbidity sensors.

TABLE 2 | Some statistics of Argo measurements in the Bothnian Sea 2012–2016.

Mission	Float	Beginning	End	Total cycles	Valid cycles	Median parking pressure (dbar)	Median speed (cm/s)	Standard deviation of speed (cm/s)
A : 6901901	APE1	2012-05-17	2012-12-05	314	198	68	3.3	4.8
B : 6902013	APE2	2013-06-13	2013-10-02	120	115	77	2.4	2.1
C : 6902017	APE1	2014-05-30	2015-10-04	177	170	117	1.7	1.5
D : 6902018	BAPE2	2014-05-30	2014-11-14	62	27	95	3.0	2.2
E : 6902021	BAPE2	2015-09-23	2016-05-13	49	38	106	2.2	1.2
F : 6902022	APE2	2016-05-13	2016-10-11	217	214	101	0.9	1.4

The WMO number of missions, float name, starting and ending dates of the missions, total number of observation cycles, number of quality controlled cycles, median parking pressure, estimated median speed per mission and its standard deviation.

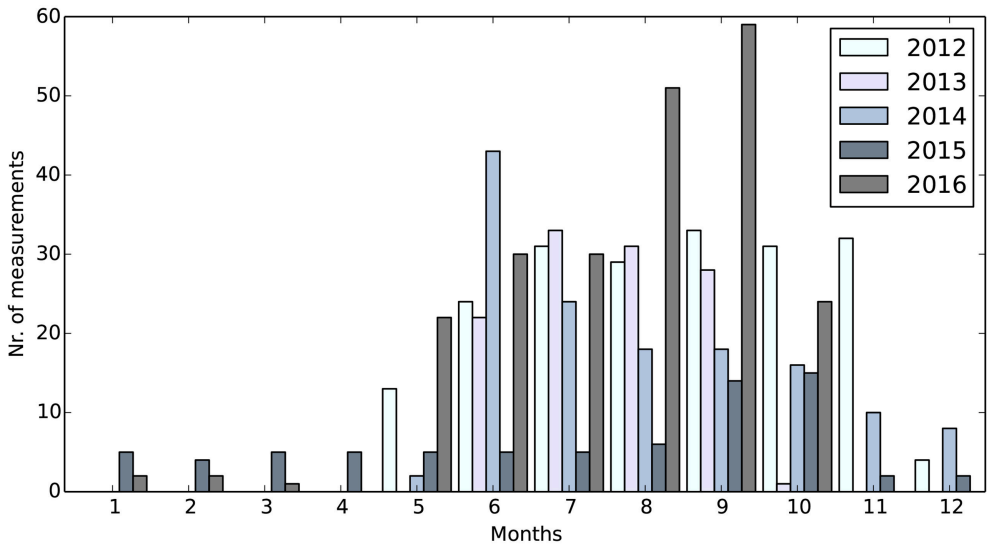


FIGURE 2 | Number of Argo cycles per month and per year in the Bothnian Sea, 2012–2016.

2.2. Hydrodynamic Model Configuration Used for Error Analysis

For comparing estimated velocities from floats and analyzing surface drift errors we used a 2 nautical mile set-up of the NEMO 3D ocean model (V3.6) covering the Baltic Sea and North Sea area. We ran the model for the year 2014. This set-up was documented and validated for mixing in Westerlund and Tuomi (2016) and for the currents in Westerlund et al. (2018) and is based on the NEMO Nordic configuration by Hordoir et al. (2013, 2015).

The vertical resolution of this set-up starts from 3 m on the surface, and increases with depth. The temporal resolution of the model is 15 min and the values are saved as 1 day averages. The bathymetry of the set-up was updated to the latest version of the NEMO Nordic bathymetry. River run-offs and precipitation fields were climatological. We used forecasts

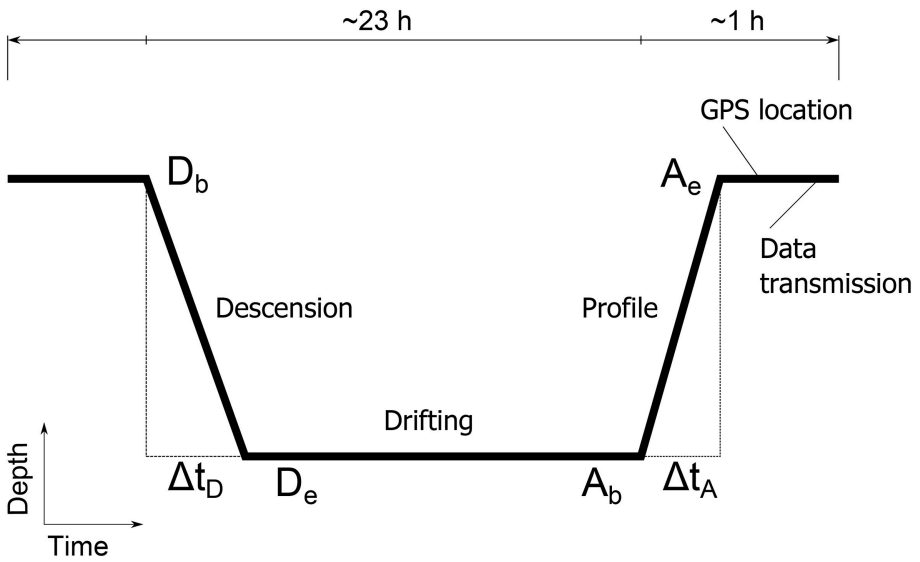


FIGURE 3 | Schematic diagram of the APEX cycle during the first mission in the Baltic Sea. The time scale is much shorter than in the deep ocean Argo measurements. The parking depth also is the same as the depth where the profile starts. D_b is the beginning of the descension and D_e is the end. A_b and A_e are the beginning and the end of ascension, respectively, and Δt_D and Δt_A are the times used for descension and ascension, respectively.

from the FMI numerical weather prediction system HIRLAM (HIRLAM-B, 2015) as forcing. Forcing was read into the NEMO run with the CORE bulk formulae (Large and Yeager, 2004).

3. RESULTS

We divided our analysis of deep-water currents in two sections. First we wanted to get an overall impression of the deep currents and their statistics in the Bothnian Sea in general and analyze the extreme velocities with results from a hydrodynamic model. The second topic was to analyze specifically the deep flow in the Bothnian Sea deep, which is the deepest trench along the basin, and the flow persistence there.

3.1. Measurements and Current Estimations in the Bothnian Sea in General

In the Bothnian Sea the floats median diving pressure was 93 dbar and median cycle length was 24 h, varying from around 2 h to 7 days. Diving pressures were chosen so, that the estimated distance from bottom remained roughly 30 m in the first two missions A (6901901) and B (6902013) (**Figure 1**) and 10 m in the rest of the missions, based on known topography. For further description of the bottom distance see (Haavisto et al., 2018). The shortest cycles are used when the float has been deployed and recovered to ensure that the float can receive commands via satellite. The typical distance the float moved was 2 to 3 km per cycle and typical estimated speed around 2 cm/s (**Table 2**), which has been considered to be typical residual speed in the deep waters. Seventy-five percent of the estimated velocities were under 3.5 cm/s. High velocities over 10 cm/s were very rare, only 3% of the cases and were only observed during the first mission at a fairly shallow depth, median 47 dbars. The highest estimated speed was 30 cm/s toward south at 50 dbar depth near to Finnish coast in a situation where sea level was going down in the Gulf of Bothnia. The floats' paths followed usually the expected northward going resultant current in the deep layers of the Bothnian Sea. The first mission A (6901901) had a shallower average drifting depth than the others (**Figure 1**).

We compared the speeds from the NEMO model to the estimated speeds in each measurement way point in the model layer that corresponded to the diving pressure of the float. The model was run from June to December 2014. The model results cannot be compared directly to speed estimations, because the time scale of events suitable to be investigated by this model is limited by the structure of the model configuration and available inputs for the model. Overall, comparison of modeled currents to observed ones always constitutes a challenge. To be able to estimate the scale of the speeds we analyzed the speed distributions from the model and observations. In two cases the speeds either modeled by NEMO or estimated from Argo trajectories represents the highest 5% of the speeds (**Figure 4**).

In the study period there were three occasions, where there were steady hard winds over period of several days. During all these three events the estimated maximum speeds were over 7 cm/s. On the surface, hard constant northward winds cause upwellings on the Finnish coast of the Bothnian Sea and the low pressure system tilts the water level in the basin speeding the deep currents northward.

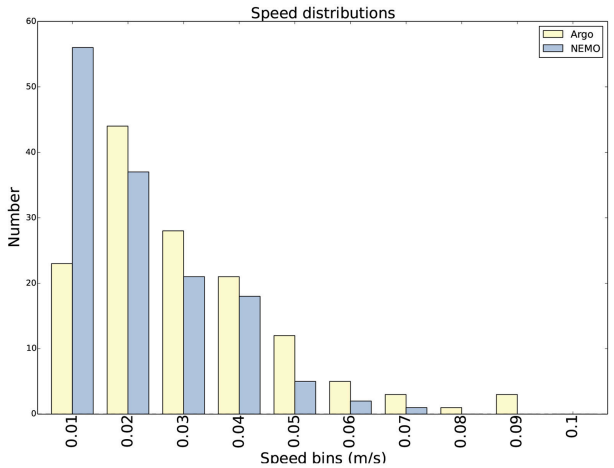


FIGURE 4 | Comparison of APEX parking pressure speed distribution versus respective NEMO speed distribution from June 2014 to December 2014.

In the beginning of June 2014, there was a steady northern wind, exceeding a daily average of 14 m/s at four coastal weather stations along the Finnish coast on June 13. The tide gauges on Gulf of Bothnia registered a rapid water level drop during this event. The Argo float reached the speed of 8 cm/s to N-N-E at an average pressure of 110 dbars. The cycle length was 24 h.

On September 20–22 2014, there was a deep low pressure system passing over Sweden, which caused hard northerly winds, speeds exceeding 26 m/s at the Swedish coastal weather stations in the Bothnian Sea. This low pressure system affected water levels throughout the Gulf of Bothnia where there was a sudden drop in water level and afterwards a very quick rise. The sea surface temperatures also dropped rapidly and we could see an upwelling event in the south-eastern coast of Bothnian Sea. This event also affected on the estimated velocity of the Argo float. The highest speed was 7.6 cm/s to N-N-W at the average diving pressure of 117 dbars during a 48-h cycle.

During this 7 months study period, there was one occasion where southern hard winds were dominant from October 22 to November 4. The float moved at the fastest 8 cm/s to N-N-E in the diving pressure of 100 dbars. This is probably due to weakened stratification, which allows the wind to affect deeper layers than in the summer time when the water column is heavily stratified and wind effect is limited on the mixed layer. The Ekman transport has an effect on the right hand direction from the wind direction.

We may argue that both estimations show exceptionally high speeds during these events and our current estimation from the float trajectories is valid. On the last occasion the wind direction was southward and the model could not show a clear signal of higher current speeds. This could be due to issues in weather forcing and the fact that the routes of the low pressure cells may not be described exactly by the weather models, the poorly known bathymetry in the area or the model's inadequacies to produce correct stratification in the autumn.

3.2. Measurements and Current Estimations in the Bothnian Sea Deep

The Bothnian Sea Deep is a passage for deep water (**Figure 5**). Our datasets have 257 cycles from this deep. On average, the buoys drifted at 106 dbar pressure, while the maximum diving pressure was 126 dbar. The minimum pressure of 51 dbar was reached while deployed in June 2013. The shallow parking pressure was set to avoid bottom contact during the first dive (Siiriä in submitted). The median cycle time was 24 h. When ice avoidance was tested, the cycle time was as long as 7 days.

On average, the speed estimated from float movement was 2 cm/s, while the temporary maximum was 13 cm/s. The main directions of the currents were along the north-south axis, with the major part of observations showing northward movement. The N-W to N sector covers 37% of all the observed directions, while the sector S-S-W to S-S-E sector covers around 22% of all directions (**Figure 6**).

The average speeds were calculated for the area (**Figure 7**). The diving cycles below 90 dbars were selected to represent the deep currents. We divided the area to a 3′ latitude × 6′ longitude grid and computed the number of observations and average current speed in each grid box. The average speed was calculated as follows:

$$\bar{u} = \frac{1}{N}\sum_{n=1}^{N} u_n \tag{1}$$

and

$$\bar{v} = \frac{1}{N}\sum_{n=1}^{N} v_n, \tag{2}$$

where $\bar{u}$ and $\bar{v}$ are the average eastward and northward components of velocity, u_n and v_n are the respective components of the velocity in a single cycle, and N is the number of cycles. Cases where there have been fewer than three measurement have been discarded. From the Equations (1, 2) we see that the average movement is measured as distance/time. Each dive has the same weight regardless of the diving time, as the float likely moves back and forth between the dives. Therefore a longer diving time would not indicate the actual drift direction with a higher probability than a short one.

The persistency R of the current was also calculated by dividing the mean vector speed by the average scalar speed as presented by Palmén (1930)

$$R = \frac{\sqrt{\bar{u}^2 + \bar{v}^2}}{\frac{1}{N}\sum\sqrt{u_n^2 + v_n^2}} \tag{3}$$

Most of the averaged velocities have a a stronger northward component in the area, even though the averaged velocities are fairly small. Only the south-west corner of the studied area appears to have a stronger southward component.

We analyzed also the persistence of the flows in different grid boxes. In this study the persistence varied between 17 and 96% per cell in the grid boxes that had over 8 measurements (i.e., the float had measured the averaged currents a week or longer). In

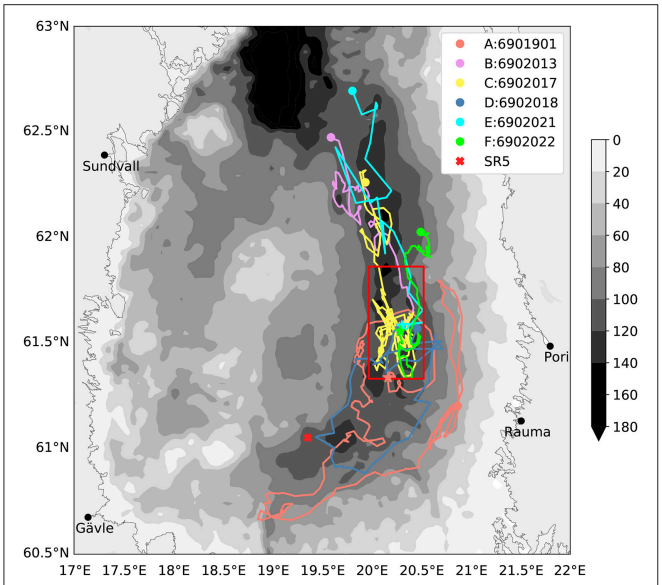


FIGURE 5 | Argo cycles in Bothnian Sea deep area. There were altogether 257 measurement cycles analyzed for this study. The bathymetry is shown in grayscale and the studied area is marked with red box. The routes of the missions are are marked with colors.

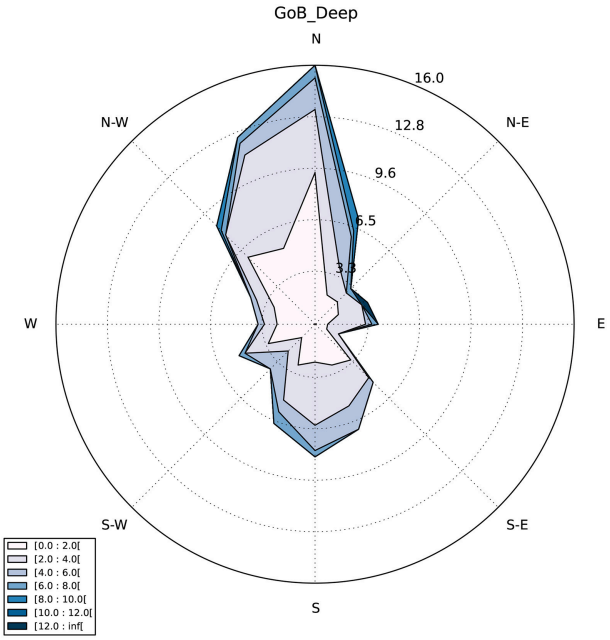


FIGURE 6 | Velocity distribution of the Apex missions in the Gulf of Bothnia Deep. The colors show the estimated speed (cm/s) and the curves show the percentage of the measurements in different directions.

common place, the measurement per grid box are consecutive so it is possible that synoptic scale weather phenomena is one explanatory factor for persistent current. Within this method we are able to study effects of the synoptic scale weather effects to the Bothnian Sea.

In the southern part of the study area the persistence is in general fairly small and the directions of the estimated current changes quite often. However, in the middle part of the area the currents are fairly persistently flowing toward north. This is probably partly due to the directing effect of the bottom bathymetry.

3.3. Estimating Possible Source of Errors

Katsumata and Yoshinari (2010) have analyzed the possible sources of errors in measurement in Argo drifting. These are positioning errors, internal clock drift, and unknown surface drift before submerging and after surfacing. In this paper, we took a deeper look on surface drift because unlike the other sources of error, it is not as randomly distributed as the other errors. It is possibly the biggest source of error due to the fact that floats in the Bothnian Sea spend a fairly long portion of their mission time on the surface compared to Argos in the ocean.

The distance drifted needs to be estimated from a model or by estimating the velocity shear in the upper water column (Lebedev et al., 2007). In this study we have estimated the scale of the surface drift from the NEMO implementation in FMI. For this study, we analyzed the year 2014 from the model and observations and estimated the scale of the surface drift by calculating the drifted distance from the model at the surfacing point for each cycle. To avoid excessive error from surface drifting, we removed the measurements that stayed in the surface

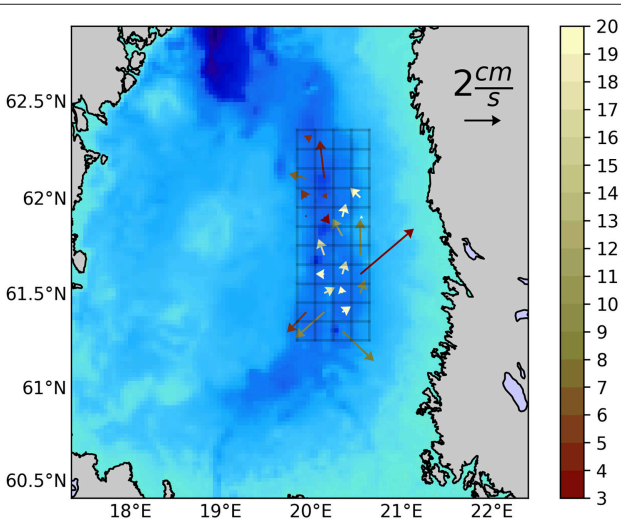


FIGURE 7 | Average Argo velocities for the drifting depth (>90 dbar) in the Bothnian Sea Deep. The length of the arrow indicates the average speed, and the color indicates the number of observations in a grid box. The lighter the color, the more observations.

layer (<20 dbars), where wind has a strong effect on the float movements.

In the depth range of the Bothnian Sea Deep, roughly 100 m, the Argo floats take on average 15 min to reach the parking depth. In general, the speed goal for descending and ascending is 8 cm/s. The exact speed cannot be determined because the first pressure

check is done 15 min after the diving procedure starts. In that time the float has usually reached the target depth.

In this study the surface drift time was around 50 min varying from 25 to 166 min depending on how quickly the floats gets the GPS position and how quickly it succeeds in getting the data connection. Another factor that affects the surface drift time is the depth of the profile and hence the amount of data to be sent. The float drifts an unknown distance while ascending, descending and while at the surface, since it reports its location only once per cycle, just before diving.

From the pressure data we assumed that the median amount of time spent in parking pressure was 95% of the total cycle time varying from 90 to 99% from mission to mission. The median value of surface drift time was 2.8% of the cycle, varying from 1 to 4% from mission to mission. The standard deviation for park time is 6% and for surface drift 3.4%. The rest of the cycle is descending (Δt_D) and ascending (Δt_A) (**Figure 3**).

We were able to evaluate the drifting speed on surface in few cases, as the floats stay on surface for few hours, before recovery transmitting their location roughly once in 10 min. These occasions gave average surface drifting speed of 9 cm/s (lowest 3.2 cm/s, highest 15.5 cm/s). We also estimated the surface drift from model run of the year 2014. On every cycle the float surface time was multiplied by the model surface velocities. This gives us the rough estimation of the scale of surface drift and cannot be understood as the exact drift due to the limitations of the hydrodynamic model. The median value with this method was around 100 m per cycle and maximum 540 m. In this estimation the median value for the distance traveled on the surface is 5%. In comparison, the size of float's internal GPS sensor error is less than 15 m. One must notice that most of the surface drift values are beyond the resolution of current regional 3D models.

4. DISCUSSION

Finnish Meteorological Institute has used Argo floats in hydrographic monitoring of the Bothnian Sea for over 6 years. The floats have measured hundreds of profiles in all seasons and we have got lots of new data from the open sea conditions and physics of the Bothnian Sea. Alongside the hydrographic data we have collected a unique dataset of over 700 estimates of the drifting velocity of the floats in their parking depths. We have analyzed those velocity estimates and their uncertainties to see if they are useful and give added value to the monitoring program.

In our measuring strategy the floats stay at maximum pressure and measure the profile from there to the surface. The pressure is defined according to the estimated topography of the area where the float is. Thus the parking depth should represent the deepest layer of the area and drift there the deep currents. The average parking pressure of our whole data set was 90 dbars, but there were differences from mission to mission. In the first two missions the average parking pressure was around 70 dbars, but later on we kept the floats deeper, at more than 95 dbars, even up to 113 dbars pressure.

It should be noted that the observation strategy was not specifically planned for measuring the drift. Thus the time step between observations varies a lot, from a few hours to several days. However, In half of the cases the time step was around one day and in 16% of the cases half a day, which both are much shorter than time steps in conventional Argo float measurements.

The aim of this study was to analyse how well these measurements describe the deep water currents and what kind of uncertainties remains. Therefore we compared our results to the earlier studies in the area.

As shown in the introduction and description of the Bothnian Sea, the general circulation of the sea was described already in the early 1900's. Those descriptions were based on current measurements from research ship and light ships. Some decades later Palosuo (1964) studied the hydrography of the Bothnian Sea and found the cyclonic circulation in the upper layers (15–40 m).

Strong efforts were put to the Gulf of Bothnia in its specific study year 1991. In that context Alenius (1993) concluded that the 60 m currents in the southern Bothnian Sea, on station SR5, were more variable in direction and speed than on coastal stations being less than 20 cm/s with northward currents dominating. Current measurements were done in 1990 and 1991 with Aanderaa RCM-4 and RCM-7 current meters at station SR5 (61.0520N, 19.3555E) (**Figure 1**) in the central southern Bothnian Sea (Alenius, 1993) for several months in both years with 10 and 15 min time steps. The data consists of over 33,000 individual observations from 113 m depth. In almost half of the observations, the current speed was below the threshold speed, 1.1 cm/s, of the current meters, which makes impossible to estimate the true average speed there. The mean current speed from data including the threshold speed was 4.5 cm/s. There exists also ADCP data and ship measurements from the Bothnian Sea Hietala et al. (2007).

We detected a northward resultant current in the Bothnian Sea deep in accordance with the earlier studies. Our results of current direction and speed were in line with present knowledge in that area. Analysis of the persistence of the deep currents showed that there were some areas where the flow was fairly persistent and the flow toward the north was notably constant.

This is partly due to the topographical steering of the deep area. In the literature we could find values for persistence of the surface currents in the area, which are typically between 20 and 40% (Leppäranta and Myrberg, 2009) or 20 and 90% (Witting, 1912). In general, the deep currents are more persistent than upper layer currents in the open sea.

Our analysis of persistence for the currents shows values that are in accordance of the values found in early literature. The limited number of drift estimates filter out possible short time scale motions which makes difficult to generalize our persistence results. Further studies are needed to analyze the persistence on the longer time scales.

The overall properties of the currents estimated from Argo float trajectories are similar enough to the earlier studies to give confidence that Argo data is useful in describing at least the net transport of the deep waters in the Bothnian Sea. However, because the floats leave the parking depth water mass when they measure the vertical profile, the water mass where they return after the profile measurement and consequent surface drift, is not exactly the same than where they were before. How this affects the results remains to be studied.

Argo float drift is not the best method to describe extreme velocity cases, though such cases may be important in shaping the underwater environment. The strong currents feed energy for the mixing processes, shape the bottom and move matter. The suspension and resuspension caused by friction and turbulence is an important factor in nutrient cycling. These extreme deep currents are difficult to study with hydrodynamic models because of their small scale. With Argo float data, we may still get more accurate information about the strength of the currents.

One major source of error in the deep current estimate is the surface drift of the float, when it determines its position and sends the data and receives instructions. The float can also drift horizontally during the ascent and descent from and to the parking depth. This may especially be the case in measurements in the shallow sea and short time steps between the profiles. For using the floats specifically for deep flow measurements, one should optimize the measurement interval so that our resolution is fine enough to be in the scale of the deep water phenomena to be studied and large enough in comparison to the surface drift so that the error does not overwhelm the whole estimation.

We used surface drift estimates from numerical model and data from the recovery of the floats in our error estimation. During the recovery the float records its position with 10–15 min intervals and sends typically several positions values during the drift at the surface. This is the best estimate of the float's surface drift, for the float behaves similarly during the mission.

The data collected in the recovery includes only fairly calm wind situations so it would be beneficial to measure the surface drift also in windy situations to achieve the speed range of the wind driven drift.

We are still on the way of studying other methods to estimate the surface drift of our floats and how it really affects to the estimates of deep currents.

5. CONCLUSIONS

Our aim was to study how well Argo float measurements describe the deep water currents and what kind of uncertainties remains. As the drift of the float follows the water mass, we conclude that we have caught the water mass movements of the deep water in the Bothnian Sea, which is essential for the long-term environmental conditions in the basin.

Argo floats have been used for years in the ocean monitoring for their reliability, affordability, weather independence, and real-time data sending after profiling.In this study we have shown that they are usable also for current estimation in the very shallow semi-enclosed sea as the Baltic Sea.

In shallow waters the Argo floats have still limitations, some of which may be resolved in the future. The strength and weakness of Argos is that they are not stationary. Larger areas can be covered with the floats, but the prevailing currents steer their movement mostly. We can steer the floats in some degree by adjusting the cycle length and the diving pressure or by keeping the float at the surface when it drifts to the desired direction there, but the true destination remains still dependent on the currents and winds.

For shallow water the lack of altimeter in the float forces to define the parking pressure by relying on the existing bathymetric data, which is not always accurately known. Thus the very near-bottom currents remain out of sight of the floats.

Even though the floats are used for routine monitoring, their capacity allows to react to differing conditions and increase the observing frequency when needed. Coordinated use of Argo floats and other autonomous vehicles, like gliders, increase the monitoring and research possibilities even further.

In the future with better GPS positioning at the surface we can reduce the error in deep water flow estimates and we can get surface drift estimates, too. With these features we may give new use for the Argo data in monitoring and this comes without any extra costs. Argo floats have become an integral part of the Baltic Sea monitoring and they serve scientific research, too.

The next step is the optimizing of the number of floats as well as their measuring frequency as already studied in the Black Sea (Grayek et al., 2015). Optimization depends on many factors, such as whether studying long-term changes in the current field or quick changes caused by low pressure systems.

In order to be able to detect mesoscale phenomena, we need to have measurements in time interval of days and spatial scale of kilometres, which can be easily achieved by Argo measurements as shown in our study. These mesoscale phenomena are for example eddies, lenses of different water masses and effects of mixing in the water column during the storms. These measurements can be used as well in analysing the present conditions as well as in developing the hydrodynamic models, forecasts, and scenario studies for the future.

We may also use the Argo data to estimate the age of the water in the basin, as is done with models by Myrberg and Andrejev (2006) Also, the data may be used to study, for example, the salinity changes and oxygen conditions under the halocline and the accumulation of environmentally harmful substances in the deep areas.

By combining Argo data with other *in-situ* measurements and hydrodynamic model results we could get a more complete picture of the water movements in the Gulf of Bothnia. Argos have been used already before in the ocean to characterize the interplay of the different water masses and currents (e.g., Gasparin et al., 2011).

These measurements could also be assimilated into forecasting systems with hydrodynamical models to gain a better understanding of the dynamics in the deep areas (e.g., Taillandier et al., 2010). The better we understand the connections between the sea and the atmosphere, the better we can estimate the effects of the changing climate on the biotic and abiotic environment.

AUTHOR CONTRIBUTIONS

All authors contributed to planning of this study. PR wrote the first draft and did largely the analyses for the observations and model results. S-MS and NH contributed on analyses and illustrations. PR, NH, and PA did literature and background research. AW did the 3D modeling for this study and contributed on analyzing the model results. TP participated significantly on

acquisition of the data and evaluation of the measurements with PR and NH. All authors wrote sections for this manuscript and revised and approved the final version.

ACKNOWLEDGMENTS

These data were collected and made freely available by the International Argo Program and the national programs that contribute to it (http://www.argo.ucsd.edu, http://argo.jcommops.org). The Argo Program is part of the Global Ocean Observing System. The authors want to thank Laura Tuomi for enabling and commenting this work and Eemeli Aro for technical support in the early phases of the Baltic Sea Argo monitoring. This work has been partly supported by the Strategic Research Council at the Academy of Finland, project SmartSea (grant number 292 985).

REFERENCES

Alenius, P. (1993). "Finnish Eulerian current measurements," in *The Gulf of Bothnia Year 1991. Physical Transport Experiments*, SMHI Reports Oceanography (Norrköping: Swedish Meteorological and Hydrological Institute), 30–40.

Argo (2000). *Argo float data and metadata from global data assembly centre (Argo GDAC)*. SEANOE. doi: 10.17882/42182

Backer, H. and Frias, M. (2013). *Planning the Bothnian Sea–Key Findings of the Plan Bothnia project*. Plan Bothnia.

Bulczak, A., Rak, D., Schmidt, B., and Beldowski, J. (2016). Observations of near-bottom currents in Bornholm Basin, Slupsk Furrow and Gdansk Deep. *Deep Sea Res. II Top. Stud. Oceanogr.* 128, 96–113. doi: 10.1016/j.dsr2.2015.02.021

Carval, T., Keeley, B., Takatsuki, Y., Yoshida, T., Loch, S., Schmid, C., et al. (2015). *ARGO User's Manual, Version 3.2*. (Ifremer). doi: 10.13155/29825

Fonselius, S., and Valderrama, J. (2003). One hundred years of hydrographic measurements in the Baltic Sea. *J. Sea Res.* 49, 229–241. doi: 10.1016/S1385-1101(03)00035-2

Fonselius, S. H. (1996). *Västerhavets Och Östersjöns Oceanografi*. Norrköping: SMHI.

Gasparin, F., Ganachaud, A., and Maes, C. (2011). A western boundary current east of New Caledonia: observed characteristics. *Deep Sea Res. I Oceanogr. Res. Pap.* 58, 956–969. doi: 10.1016/j.dsr.2011.05.007

Grayek, S., Stanev, E. V., and Schulz-Stellenfleth, J. (2015). Assessment of the Black Sea observing system. A focus on 2005-2012 Argo campaigns. *Ocean Dyn.* 65, 1665–1684. doi: 10.1007/s10236-015-0889-8

Haapala, J., and Alenius, P. (1994). Temperature and salinity statistics for the northern Baltic Sea 1961-1990. *Finn. Mar. Res.* 262, 51–121.

Haavisto, N., Tuomi, L., Roiha, P., Siiriä, S.-M., Alenius, P., and Purokoski, T. (2018). Argo floats as a novel part of the monitoring the hydrography of the Bothnian Sea. *Front. Mar. Sci.* 5:324. doi: 10.3389/fmars.2018.00324

Hela, I. (1958). A hydrographical survey of the waters in the Åland Sea. *Geophysica* 6, 219–242.

Hietala, R., Lundberg, P., and Nilsson, J. A. (2007). A note on the deep-water inflow to the Bothnian Sea. *J. Mar. Syst.* 1, 255–264. doi: 10.1016/j.jmarsys.2006.12.004

HIRLAM-B (2015). *System Documentation*. Technical report, HIRLAM Consortium.

Hordoir, R., Axell, L., Löptien, U., and Dietze, H. (2015). Influence of sea level rise on the dynamics of salt inflows in the Baltic Sea. *J. Geophys. Res.* 120, 6653–6668. doi: 10.1002/2014JC010642

Hordoir, R., Dieterich, C., Basu, C., Dietze, H., and Meier, H. (2013). Freshwater outflow of the Baltic Sea and transport in the Norwegian current: a statistical correlation analysis based on a numerical experiment. *Contin. Shelf Res.* 64, 1–9. doi: 10.1016/j.csr.2013.05.006

Kahru, M., Håkansson, B., and Rud, O. (1995). Distributions of the sea-surface temperature fronts in the Baltic Sea as derived from satellite imagery. *Contin. Shelf Res.* 15, 663–679.

Katsumata, K., and Yoshinari, H. (2010). Uncertainties in global mapping of Argo drift data at the parking level. *J. Oceanogr.* 66, 553–569. doi: 10.1007/s10872-010-0046-4

Korotaev, G., Oguz, T., and Riser, S. (2006). Intermediate and deep currents of the Black Sea obtained from autonomous profiling floats. *Deep Sea Res. II Top. Stud. Oceanogr.* 53, 1901–1910. doi: 10.1016/j.dsr2.2006.04.017

Kuosa, H., Fleming-Lehtinen, V., Lehtinen, S., Lehtiniemi, M., Nygård, H., Raateoja, M., et al. (2017). A retrospective view of the development of the Gulf of Bothnia ecosystem. *J. Mar. Syst.* 167, 78–92. doi: 10.1016/j.jmarsys.2016.11.020

Large, W. G., and Yeager, S. G. (2004). *Diurnal to Decadal Global Forcing for Ocean and Sea-Ice Models: the Data Sets and Flux Climatologies*. NCAR Technical Note, NCAR/TN-460+STR, CGD Division of the National Center for Atmospheric Research.

Lavender, K. L., Owens, W. B., and Davis, R. E. (2005). The mid-depth circulation of the subpolar North Atlantic Ocean as measured by subsurface floats. *Deep Sea Res. I Oceanogr. Res. Pap.* 52, 767–785. doi: 10.1016/j.dsr.2004.12.007

Le Traon, P. Y. (2013). From satellite altimetry to Argo and operational oceanography: three revolutions in oceanography. *Ocean Sci.* 9, 901–915. doi: 10.5194/os-9-901-2013

Lebedev, K. V., Yoshinari, H., Maximenko, N. A., and Hacker, P. W. (2007). *Yomaha'07: Velocity Data Assessed from Trajectories of Argo Floats at Parking Level and at the Sea Surface*. International Pacific Research Center (IPRC) Technical Note.

Leppäranta, M., and Myrberg, K. (2009). *Physical Oceanography of the Baltic Sea*. Berlin: Springer. doi: 10.1007/978-3-540-79703-6

Marmefelt, E., and Omstedt, A. (1993). Deep water properties in the Gulf of Bothnia. *Contin. Shelf Res.* 13, 169–187.

Meier, H. E. M., Feistel, R., Piechura, J., Arneborg, L., Burchard, H., Fiekas, V., et al. (2006). Ventilation of the Baltic Sea deep water: a brief review of present knowledge from observations and models. *Oceanologia* 48, 133–164.

Menna, M., and Poulain, P. M. (2010). Mediterranean intermediate circulation estimated from Argo data in 2003-2010. *Ocean Sci.* 6, 331–343. doi: 10.5194/os-6-331-2010

Murthy, R., Håkansson, B., and Alenius, P. (1993). *The Gulf of Bothnia Year 1991 Physical Transport Experiments*. Technical Report 15, SMHI, Norrköping.

Myrberg, K., and Andrejev, O. (2006). Modelling of the circulation, water exchange and water age properties of the Gulf of Bothnia. *Oceanologia* 48S, 55–74.

Palmén, E. (1930). Untersuchungen über die Strömungen in den Finnland umgebenden Meeren. *Soc. Sci. Fenn. Comm. Phys. Math.* 12, 1–82.

Palosuo, E. (1964). A description of the seasonal variations of water exchange between the Baltic Proper and the Gulf of Bothnia. *Merentutkimuslaitoksen Julkaisu 215* 32, 1–32.

Park, J. J., Kim, K., King, B. A., and Riser, S. C. (2005). An advanced method to estimate deep currents from profiling floats. *J. Atmos. Ocean. Technol.* 22, 1294–1304. doi: 10.1175/JTECH1748.1

Purokoski, T., Aro, E., and Nummelin, A. (2013). First long-term deployment of Argo float in Baltic Sea Argo's inaugural operation in shallow, low-salinity water. *Sea Technol.* 54, 41–44.

Raateoja, M. (2013). Deep-water oxygen conditions in the Bothnian Sea. *Boreal Environ. Res.* 18, 235–250.

Riser, S. C., Freeland, H. J., Roemmich, D., Wijffels, S., Troisi, A., Belbeoch, M., et al. (2016), Fifteen years of ocean observations with the global Argo array, *Nat. Clim. Change* 6, 145–153, doi: 10.1038/nclimate2872

SMHI (1982). "Climatological ice atlas for the Baltic Sea, Kattegat, Skagerrak and lake Vänern (1963-1979)," in *Swedish Meteorological and Hydrological Institute & Institute of Marine Research, Finland*. Norrköping.

Suhhova, I., Liblik, T., Madis-Jaak, L., and Urmas, L. (2018). A descriptive analysis of the linkage between the vertical stratification and current oscillations in the Gulf of Finland. *Boreal Environ. Res.* 23, 83–103.

Taillandier, V., Dobricic, S., Testor, P., Pinardi, N., Griffa, A., Mortier, L., et al. (2010). Integration of Argo trajectories in the Mediterranean forecasting system and impact on the regional analysis of the western Mediterranean circulation. *J. Geophys. Res. Oceans* 115:C03007. doi: 10.1029/2008JC005251

Uotila, J., Launiainen, J., and Vihma, T. (1996). Analysis of the surface drift currents in the Bothnian Sea. *Oceanogr. Lit. Rev.* 5:432.

Voet, G., Quadfasel, D., Mork, K. A., and Søiland, H. (2010). The mid-depth circulation of the Nordic Seas derived from profiling float observations. *Tellus A* 62, 516–529.

Westerlund, A., Tuomi, L., Alenius, P., Miettunen, E., and Vankevich, R. E. (2018). Attributing mean circulation patterns to physical phenomena in the Gulf of Finland. *Oceanologia* 60, 16–31. doi: 10.1016/j.oceano.2017.05.003

Westerlund, A., and Tuomi, L. (2016). Vertical temperature dynamics in the Northern Baltic Sea based on 3D modelling and data from shallow-water Argo floats. *J. Mar. Syst.* 158, 34–44. doi: 10.1016/j.jmarsys.2016.01.006

Wieczorek, G. (2012). *Spatiotemporal Scales of the Deep Circulation in the Eastern Gotland Basin/Baltic Sea*. Ph.D. thesis.Meereswissenschaftliche Berichte MARINE SCIENCE REPORTS No. 88 Leibniz-Institut für Ostseeforschung Warnemünde.

Witting, R. (1912). *Zusammenfassende übersicht der Hydrographie des Bottnischen und Finnischen Meerbusens und der Nördlichen Ostsee*. Finnländische hydrographisch-biologische Untersuchungen.

Witting, R. and Pettersson, H. (1925). Thalassologische Beobachtungen im Ålandsmeer und Schärenmeer in juli 1922 und juli 1923. *Merentutkimuslaitoksen Julkaisuja* 30, 1–39.

Woods, J. D. (1985). The world ocean circulation experiment. *Nature* 314:501.

Conflict of Interest Statement: The authors declare that the research was conducted in the absence of any commercial or financial relationships that could be construed as a potential conflict of interest.

Copyright © 2018 Roiha, Siiriä, Haavisto, Alenius, Westerlund and Purokoski. This is an open-access article distributed under the terms of the Creative Commons Attribution License (CC BY). The use, distribution or reproduction in other forums is permitted, provided the original author(s) and the copyright owner(s) are credited and that the original publication in this journal is cited, in accordance with accepted academic practice. No use, distribution or reproduction is permitted which does not comply with these terms.

frontiers in Marine Science

ORIGINAL RESEARCH
published: 09 January 2019
doi: 10.3389/fmars.2018.00504

Summer Distribution of Total Suspended Matter Across the Baltic Sea

*Dmytro Kyryliuk and Susanne Kratzer**

Department of Ecology Environment and Plant Sciences, Stockholm University, Stockholm, Sweden

There are three optical in-water components that, besides water itself, govern the under-water light field: phytoplankton, total suspended matter (TSM), and colored dissolved organic matter (CDOM). In essence, it is the spectral absorption and scattering properties of each optical component that govern the underwater light field, and also the color of the sea that we can perceive, and that can also be measured remotely from space. The Baltic Sea is optically dominated by CDOM, apart from cyanobacteria blooms that often cover most of the Baltic proper during summer. Remote sensing images of TSM reveal large-and mesoscale features and currents, especially in the Southern Baltic, which are influenced both by atmospheric Rossby waves and the Coriolis force. In coastal waters, the optical properties are strongly influenced by inorganic suspended matter, which may originate from coastal erosion and from run-off from land, streams, and rivers. In this paper, we evaluate the distribution of TSM across the Baltic Sea using remote sensing data and statistically compare the TSM loads in the different Helsinki Commission (HELCOM)-defined basins. The total suspended matter (TSM) loads during summer vary substantially in the different basins, with the south-eastern Baltic overall being most influenced by cyanobacteria blooms. The Gdansk basin and the Gulf of Riga were distinguished both by relatively high TSM loads with high standard deviations, indicating strong fluvial input and/or resuspension of sediments. We also evaluate a coastal TSM transect in Himmerfjärden bay, which is located at the Swedish East coast in the Western Gotland Basin. The effect of wind-wave stirring on the distribution of TSM from source (shore) to sink (open sea) can be assessed using satellite data from European Space Agency's (ESA) MEdium Resolution Imaging Spectrometer (MERIS) mission (2002–2012) with 300 m resolution. The TSM transect data from areas with low wind exposure and a stable thermocline showed a gradient distribution perpendicular to the coast for summer seasons 2009, 2010, 2011, and a 3-year summer composite, confirming a previous bio-optical study from the Western Gotland basin.

Keywords: Baltic Sea basin, total suspended matter, spatial distribution, MERIS data, coastal influence, resuspension

OPEN ACCESS

Edited by:
Teresa Radziejewska, University of Szczecin, Poland

Reviewed by:
P. R. Renosh, UMR7093 Laboratoire d'Océanographie de Villefranche (LOV), France
Roman Marks, University of Szczecin, Poland

****Correspondence:***
Susanne Kratzer
susanne.kratzer@su.se

Specialty section:
This article was submitted to Coastal Ocean Processes, a section of the journal Frontiers in Marine Science

Received: *22 May 2018*
Accepted: *14 December 2018*
Published: *09 January 2019*

Citation:
Kyryliuk D and Kratzer S (2019) Summer Distribution of Total Suspended Matter Across the Baltic Sea. Front. Mar. Sci. 5:504. doi: 10.3389/fmars.2018.00504

INTRODUCTION

Marine waters are usually divided into optical case 1 and optical case 2 waters (Morel and Prieur, 1977). Optical case 1 waters are waters where the optical properties, are dominated by phytoplankton and co-varying colored dissolved organic matter (CDOM), besides the optical properties of water itself. Typical examples of case 1 waters are clear ocean waters, and the clearest water known is the Sargasso Sea (Kirk, 1985). Optical case 2 waters are coastal waters that are influenced by terrestrial run-off, and thus are optically also influenced by total suspended matter (TSM, also termed suspended particulate matter, SPM) and by CDOM. Baltic Sea waters are generally classified as optical case 2 waters with a relatively strong optical influence from CDOM (Kowalczuk et al., 2006; Kratzer and Tett, 2009; Kratzer and Moore, 2018). Many marine waters, however, are also strongly influenced by TSM, especially waters that have a strong tidal influence where the resuspension of sediments may reach much further off-shore than in the Baltic Sea. In some coastal areas, there is also a strong influence of TSM due to both high river run-off and tidal influence. Examples for this are the Thames Estuary where, according to Devlin et al. (2008) estuarine waters typically have much higher concentrations of TSM (8.2–73.8 gm^{-3}) compared to coastal waters (3.0–24.1 gm^{-3}). Off-shore waters showed concentrations of up to 9.3 gm^{-3} which is much higher than found in the Baltic Sea. Kratzer and Tett (2009), for example found that in summer (Western Gotland Basin) the measured TSM ranged from only 0.48–1.34 gm^{-3} in the open sea ($n = 18$) and 0.48–2.77 gm^{-3} in coastal areas ($n = 22$). Kratzer and Moore (2018) found a range of 0.44 gm^{-3}-4.82 gm^{-3} in the open sea ($n = 43$) with a median of 1.00 gm^{-3} and 0.48–3.36 gm^{-3} in coastal areas ($n = 55$) with a median of 1.62 gm^{-3}. High TSM values in the open sea were usually related to very high chl-a concentrations during the occurrence of cyanobacteria blooms in summer. Harvey (2015) and Harvey et al. (2018) measured ranges of 0.5–21.7 gm^{-3} in the W Gotland Basin by including areas with stronger terrestrial influence such as Bråviken and Nyköping bay. **Table 1** gives an overview of TSM measured *in situ* in different sub-basins of the Baltic Sea. There are some areas in the world with much higher terrestrial influence. For example, the Rio de Plata at the border between Argentina and Uruguay has shown to have very high turbidity ranging from 62–185 NTU, and the Gironde Estuary in southwest France showed ranges of 41–988 FNU (Dogliotti et al., 2015).

In essence, it is the spectral absorption and scattering properties of each optical component that govern the underwater light field, and also the reflectance, i.e., the color of the sea that we can perceive, and that can also be measured remotely from space. Colored dissolved organic matter (CDOM) absorbs light, especially in the blue part of the visible spectrum. The absorption curve follows a logarithmic decline (Kirk, 1985). Because of the high absorption in the blue and green parts of the spectrum CDOM makes the water look more yellow—or even brown at very high CDOM concentrations. The strong absorption of CDOM also makes the water look darker as it reflects much less light. Inorganic suspended matter mostly scatters light, whereas organic suspended matter mostly absorbs light and behaves optically in a similar way to CDOM. Due to the strong scattering of light, inorganic suspended matter usually increases the brightness of a satellite image. Phytoplankton mostly absorbs light in the blue and in the red part of the spectrum due to the absorption of chlorophyll pigments. Carotenoid pigments also absorb in the blue-green and are usually correlated to chlorophyll-a. Phycobilin pigments are usually found in cyanobacteria and in the Baltic Sea, they tend to absorb light in the 560 and 620 nm region (Kratzer, 2000). CDOM originates mostly from terrestrial plants on land and usually indicates input of freshwater. Inorganic suspended matter indicates land drainage and wind-stirring in shallow waters (Kratzer and Tett, 2009). Total suspended matter (TSM) is strongly correlated to turbidity (Kari et al., 2017) which is a supportive parameter in the EU Marine Strategy Framework Directive Annex III (2008), especially in coastal waters. Phytoplankton is affected by anthropogenic nutrients from land and thus indicates the productive status of the pelagic ecosystem (Kratzer and Tett, 2009). Chl-a is often used as a proxy for phytoplankton biomass and an indicator for eutrophication.

In this study we focus on TSM as can be used as an indicator for the extent of coastal waters in a bio-optical model developed in the Baltic Sea. Kratzer and Tett (2009) used TSM to define the breadth of coastal waters using the inorganic fraction as an indicator. It was found that inorganic suspended matter tends toward zero at a distance of tens of kilometer from the shore. Inorganic suspended matter is also the optical component that showed a clear difference in distribution between inner

TABLE 1 | Comparison of the ranges of TSM concentrations [TSM] in different sub-basins of the Baltic Sea.

Baltic Sea area	[TSM]	References
Unit	g m^{-3}	
Arkona Sea	0.7–9.0	Ohde et al., 2007; Fleming-Lehtinen and Laamanen, 2012
Bornholm Sea	0.4–5.0	Ohde et al., 2007
Gotland Sea	3.0–6.0	Ohde et al., 2007
Pomeranian Bight, Germany	0.5–20.0	Kowalczuk et al., 2005; Ohde et al., 2007
Gulf of Gdansk Poland	0.4–15.7	Wasmund et al., 2001; Kowalczuk et al., 2005; Wozniak et al., 2011
SE Baltic Sea, Lithuanian coast	1.1–32.0	Wasmund et al., 2001; Vaičiute et al., 2012
Pärnu Bay, Estonia	5.0–24.3	Alikas et al., 2015
Gulf of Riga, Estonia	10.0–24.0	Toming et al., 2009; Fleming-Lehtinen and Laamanen, 2012; Raag et al., 2014
Gulf of Finland	0.8–20.0	Koponen et al., 2007; Vazyulya et al., 2014
NW Baltic proper	0.5–21.7	Harvey, 2015
Öre Estuary, Bothnian Sea, SE	0.2–20.9	Harvey, 2015

The table is based on in situ measurements found in the literature.

coastal and open sea waters. The trendline showed a relatively steep decline in the inner Himmerfjärden bay, and off the cost with a much flatter trendline. All optical components were best described with a polynomial function when moving from the shore (source) to Landsort deep (sink) Kratzer and Tett (2009). This was explained due to the fact that the Baltic Sea has almost no tidal influence, making diffusion the main physical force for the distribution of particles. Also, the W Gotland Basin has relatively low influence from wind forcing when, for example, compared to the Southern Baltic Sea (Danielsson et al., 2007). The wind field has shown to have a strong effect on the resuspension patterns in the Baltic proper. Kuhrts et al. (2004) found that sediment transport is generally smaller in summer because of lower winds. In wintertime, the wind forcing is stronger and due to the vertical mixing and enhanced vertical current shear, the resuspension of sediment is stronger. The authors also found that the transport of sedimentary material over longer distances occurs only under extreme wind events that are relatively rare. There are several mechanisms that may induce currents in the Baltic Sea: wind stress at the sea surface, surface pressure gradients, thermohaline horizontal gradients of density, as well as tidal forces. All these currents are also influenced by Coriolis acceleration, as well as bottom topography and friction, forming a general (cyclonic) circulation in the stratified system (Myrberg and Lehmann, 2013), generating mesoscale eddies. These physical processes are often shown on satellite images depicting cyanobacteria blooms in the Baltic Sea (Kahru et al., 2007; Kratzer et al., 2011, 2014; Kahru and Elmgren, 2014). These processes may also carry suspended matter up to 150 km off-shore (Kyryliuk, 2014), especially in the Southern Baltic Sea.

HELCOM's Monitoring and Assessment Strategy

One of the Helsinki Commission's (HELCOM) Monitoring and Assessment Strategy objectives is "to facilitate the implementation of the ecosystem approach, covering the whole Baltic Sea, including coastal and open waters" and "to enable the provision of data and information that links pressures on land, from the atmosphere, in coastal areas and at sea to their impacts on the marine environment" (HELCOM, 2013). The HELCOM Strategy aims to provide assessment and monitoring of data that can be utilized for both international assessment by HELCOM as well as for monitoring on a national level. The strategy is designed in such a way that insures both data production and dissemination of information by the Contracting Parties of the EU Member States and fulfilling the requirements of several EU directives such as the Marine Strategy Framework Directive (MSFD), the Water Framework Directive (WFD), the Habitats and Birds Directives, the EU Strategy for the Baltic Sea Region (EUSBSR), and the EU Integrated Maritime Policy (HELCOM, 2013). Foremost, the Strategy is aimed to support ecosystem-based Maritime Spatial Planning (MSP) in the Baltic Sea by enabling high-quality spatial data and assessment tools for the purposes envisioned for MSP. This latter aim led to the formation of the idea to investigate whether the use of TSM data derived from MERIS can be used in the sense of MSP as a "high-quality spatial data" and as an assessment tool, covering the last assessment period of HELCOM.

For the purposes of regional assessment HELCOM sub-divides Baltic Sea into the different sub-basins. Those basins are described in the document "HELCOM sub-divisions of the Baltic Sea" (Attachment 4; HELCOM, 2013), following distinctive hierarchical levels of sub-division, depending on management needs. For the purposes of this study the sub-division of the Baltic Sea into 16 sub-basins is used (**Table 2**) in order to comply with general management practices in the Baltic Sea basin.

Aims and Objectives

It is the aim of this study to (1) evaluate the difference in TSM loads in the different sub-basins of the Baltic Sea and to compare them statistically. In order to do this, data from the MEdium Resolution Imaging Spectrometer (MERIS with 300 m resolution) was used. MERIS was developed by the European Space Agency (ESA) and was launched on ENVISAT in early 2002 and operated until early 2012. The MERIS data was used to generate TSM composites of all viable MERIS scenes from summers 2009, 2011, and 2011. These yearly summer composites were then aggregated into a 3-year summer composite (2009–2011), which gives a seasonal overview of TSM distribution across the different Baltic Sea basins. This 3-year summer composite was then divided into the different HELCOM sub-basins for statistical comparison. Furthermore, it is the aim (2) to evaluate the differences in coastal distribution patterns along a transect reaching from the inner Himmerfjärden bay out into the open sea, thus covering a range of coastal to off-shore water types. As the distribution of TSM in the southwestern Baltic Sea is highly influenced by meso-scale eddies we focus here on a transect set in the W Gotland Basin. We also (3) discuss how

TABLE 2 | Nomenclature of sub-basins of the Baltic Sea according to HELCOM.

HELCOM-ID	Name
SEA-001	Kattegat
SEA-002	Great Belt
SEA-003	The Sound
SEA-004	Kiel Bay
SEA-005	Bay of Mecklenburg
SEA-006	Arkona Basin
SEA-007	Bornholm Basin
SEA-008	Gdansk Basin
SEA-009	Eastern Gotland Basin
SEA-010	Western Gotland Basin
SEA-011	Gulf of Riga
SEA-012	Northern Baltic Proper
SEA-013	Gulf of Finland
SEA-014	Aland Sea
SEA-015	Bothnian Sea
SEA-016	The Quark
SEA-017	Bothnian Bay

the concentrations derived from MERIS data compare to *in situ* data found in the literature, and discuss the application of this approach in environmental monitoring and management of the Baltic Sea.

MATERIALS AND METHODS

Area of Investigation

The Baltic Sea is a brackish ecosystem with many distinguishable characteristics, and is sometimes described as a large fjord-like estuary with brackish water, driven by river run-off, and weather conditions over the Baltic Sea-North Sea region (Kullenberg and Jacobsen, 1981; Voipio, 1981). The Baltic is, however, much larger and deeper than an average estuary and has narrow and shallow connections with the North Atlantic Ocean. In this respect, it would be more similar to a gigantic threshold fjord with a series of sub-basins (Snoeijs-Leijonmalm et al., 2017).

Overall, the Baltic Sea is characterized by a permanent halocline with higher saline waters in the bottom layers (originating from the North Sea), and brackish waters in the top layers. High fluvial input to the surface layers creates a strong north-south facing horizontal salinity gradient across the Baltic Sea basin. For example, the salinity is about 3–2 g kg^{-1} in the Bothnian Bay, and about 8–6 g kg^{-1} in the Baltic Proper. The Baltic Sea topography is divided into a series of basins separated by shallow areas, and has a mean depth of 56 m, where nearly 17% of the area are no more than 10 m deep (Kullenberg and Jacobsen, 1981). With 459 m depth, Landsort Deep in the NW Baltic proper is the deepest part of the Baltic Sea. The main circulation in the Baltic Sea is driven by wind and deviations in atmospheric pressure (Leppäranta and Myrberg, 2009). The Northern Baltic is dominated by Precambrian and Paleozoic bed rock whilst the Southern areas of the Baltic Sea bottoms consist mostly of alluvial sediments (Kullenberg and Jacobsen, 1981). Large amounts of river discharge, especially in the Southern Baltic bring in high levels of humic substances and suspended matter, which from an ocean color point of view, makes the Baltic Sea comprise optical case 2 waters, i.e., waters that, besides being optically dominated by phytoplankton may also contain large amounts of TSM and CDOM (Kratzer et al., 2003; Harvey, 2015; Kopelevich et al., 2016).

Himmerfjärden (HF) is a north-south facing, elongated bay located in the Northern Baltic Proper about 60 km south of Stockholm, Sweden (Engqvist, 1996) (**Figure 1**). HF is optically dominated by the absorption of CDOM (g440) ranging from 0.3–1.2 m^{-1} (Kratzer and Moore, 2018) and TSM load ranges from 0.5–2.7 gm^{-3} with a polynomial gradient toward the open sea (Kratzer and Tett, 2009). Himmerfjärden receives a relatively minor freshwater input from lake Mälaren, however it is also under strong influence from the third largest sewage treatment plant in the Stockholm region (Franzén et al., 2011). The bay has been extensively studied for over 30 years and is regularly monitored by the Marine Monitoring Group at Stockholm University (SU) and since the late 90s also investigated by the Marine Remote Sensing Group (SU), combining dedicated optical campaigns with satellite data (e.g., Envisat/MERIS, Sentinel-2/MSI, and Sentinel-3/OLCI).

Geolocation and Radiometric Correction

Full Resolution (FR) 300 m Level-2 (L2) MERIS data processed by Brockmann Consult (BC), Germany, was provided by Brockmann Geomatics AB. The delivered L2 data had been geo-located with the Accurate MERIS Ortho-Rectified Geo-location Operational Software (AMORGOS), developed by ACRI-ST in France (Manual and Document, 2007; Patrice et al., 2011). AMORGOS generates slightly improved accuracy, and a much better overall quality of the geocorrection was achieved (Philipson et al., 2014). Further, the raw data was converted from digital numbers to Top-Of-the-Atmosphere (TOA) radiances measured in $mWm^{-2}sr^{-1}$ nm^{-1}, and corrected for the so-called "Smile Effect" (Bourg et al., 2008), and for adjacency effects from land using the Improved Contrast between Ocean and Land processor (ICOL); (Santer and Zagolski, 2009).

Level-2 Processing

Level-2 processing usually consists of atmospheric correction and the retrieval of water constituent concentrations. The derived products are L2 remote sensing reflectances at the Bottom-Of-Atmosphere (BOA) as well as bio-geophysical products, such as chlorophyll-a, TSM and CDOM (Philipson et al., 2014). During recent years, besides the ESA's standard MERIS Ground Segment (MEGS) processor a number of coastal and inland L2 processors have been developed, and the results have been steadily improved for coastal and Baltic Sea waters (Schiller and Doerffer, 1999; Kratzer et al., 2011; Beltrán-Abaunza et al., 2014). The coastal Water Properties Processor from Free University Berlin (FUB) (Schroeder et al., 2007) is used in this study and has been well-tested for the Baltic Sea (Kratzer and Vinterhav, 2010; Beltrán-Abaunza et al., 2014). Total suspended matter (TSM) derived using the FUB algorithm is lower than when using the standard processor MEGS. However, the TSM concentration derived by MEGS were associated with significant spatial noise and data quality flags tend to remove up 60% of pixels than when compared to the L1P CoastColour data pre-processing quality flagging combined with the FUB algorithm (Brockmann Consult, 2014). The rigorous flagging by MEGS may be explained by the fact that MEGS was initially developed using primarily North Sea data, and thus was not adapted to the optical complexity of the Baltic Sea and the high ranges in CDOM. The FUB processor, in contrast, was trained on a wider range of optical water types and produced more coherent images for the Baltic Sea, with less spatial noise (Beltrán-Abaunza et al., 2014).

A variety of valid-pixel expressions were applied during flagging and were combined with additional quality flags that had been developed by ESA's CoastColour project (http://www.coastcolour.org/). This allowed to keep valid pixels that otherwise would be removed by the rigorous flagging provided by the standard processor, MEGS. Additionally, the data derived from the FUB showed a more accurate spectral shape of the reflectance spectrum, with a slight, but spectrally consistent off-set when compared to *in situ* reflectance data (Beltrán-Abaunza et al., 2014), and therefore provide more realistic spectral signatures than other coastal processors tested in the region. FUB is also more accurate in retrieving chlorophyll-a concentrations.

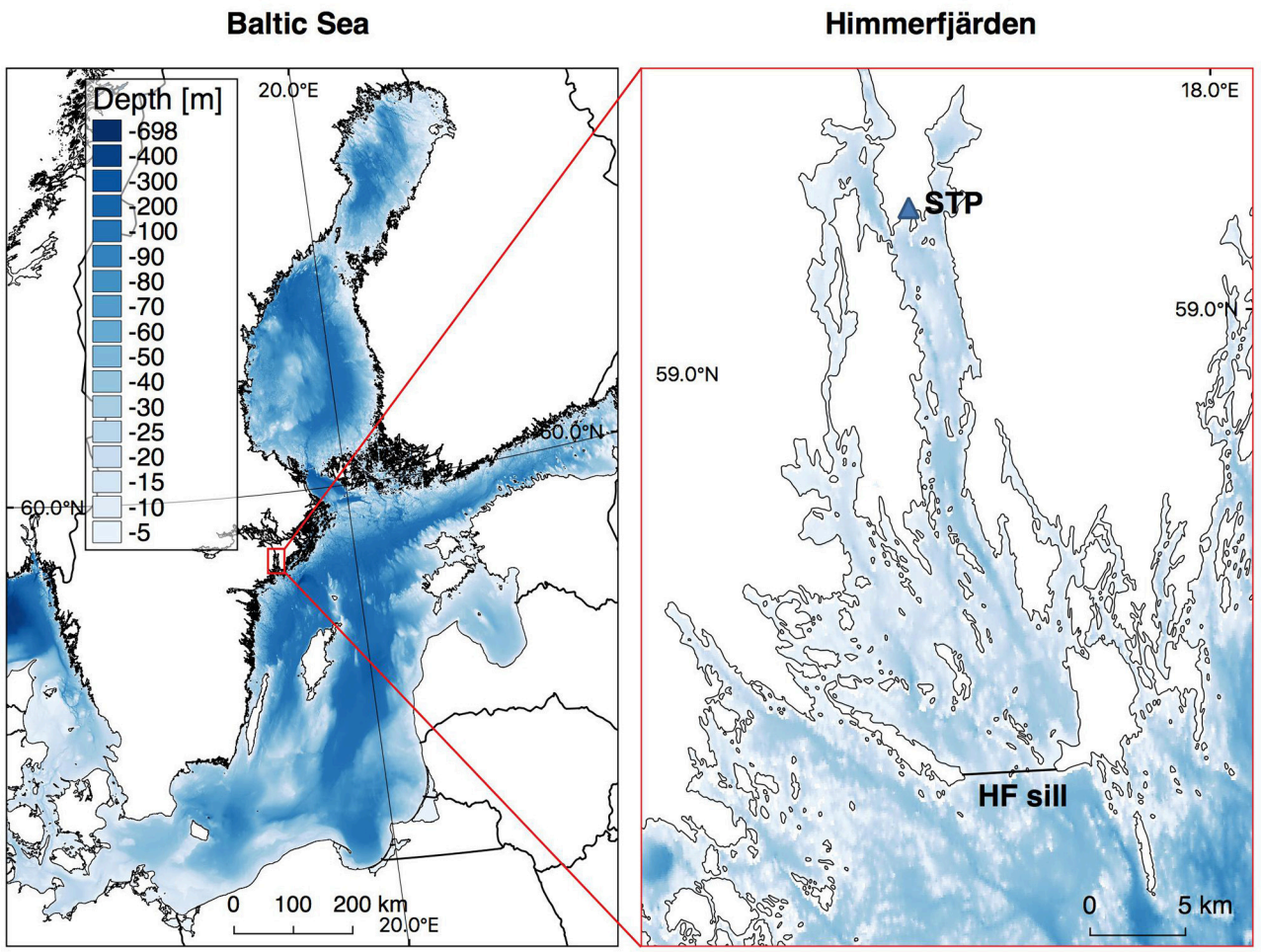


FIGURE 1 | Area of investigation. Baltic Sea and Himmerfjäaden bay (HF), Swedish coastal areas. STP: Sewage Treatment Plant. Bathymetry data (Shom, 2018); (http://portal.emodnet-bathymetry.eu/). European coastline shapefile (European Environment Agency; https://www.eea.europa.eu/ds_resolveuid/06227e40310045408ac8be0d469e1189). Country boundaries (Natural Earth; https://www.naturalearthdata.com/downloads/10m-cultural-vectors/10m-admin-0-boundary-lines/).

Also, generally, FUB generated the best results for all tested areas (including Swedish lakes and coastal waters) and has therefore been used for implementation in the Swedish coastal observational system (www.vattenkvalitet.se).

Level-3 Processing, Mosaic, and Binning

Usually, a single MERIS overpass does not cover the entire Baltic Sea. In order to derive a full image of the Baltic Sea it was required to derive a mosaic composite image of at least 2 MERIS scenes. These scenes can further be spatially and temporally binned and are generally referred to as Level-3 (L3) data. The L3 "binning function" is used to derive averaged weekly, monthly, or yearly images (composites) of the TSM L2 data. Binning thus refers to the process of attributing the contribution of all L2 pixels in satellite coordinates to a fixed L3 grid using a geographic reference system. A sinusoidal projection is used to generate a L3 grid comprising a fixed number of equal area bins with global coverage.

TSM and HELCOM Sub-basins

Summer composites each for 2009, 2010, 2011 and a 3-year summer mean (2009–2011) of TSM concentrations (i.e., L3 TSM) were generated for the whole Baltic Sea. In order to map and compare the distribution of TSM concentrations in each basin according to the HELCOM division of the Baltic Sea, the HELCOM sub-basins were superimposed over a 3-year composite covering the Baltic Sea, excluding the Bothnian Bay and parts of the Gulf of Finland due to artifacts caused by processing errors. Each pixel contained a value representing the average TSM concentrations in gm^{-3} over a 3-year period (summer).

In order to compare the different HELCOM basins the statistics were derived for each basin as follows. Each sub-basin definition was used as a polygon to extract the corresponding pixels and to derive the descriptive statistics, i.e., the mean, median, minimum, maximum, the percentiles (p_{90}, p_{95}), the standard deviation (SD) and the number of pixels (N), respectively for each basin, and presented in **Table 3**. Then,

TABLE 3 | TSM concentration per sub-basin derived from a 3-year TSM summer composite.

HELCOM sub-basin	Indicator	Mean	Median	Min.	Max.	p_{90}	p_{95}	SD	N (pixels)
SEA-001 Kattegat	TSM	0.96	0.41	0.11	49.69	1.20	1.89	3.04	478,859
SEA-002 Great Belt	TSM	0.97	0.40	0.09	44.29	1.20	2.92	2.61	202,181
SEA-003 The_Sound	TSM	1.10	0.32	0.14	36.46	0.79	4.46	3.54	17,798
SEA-004 Kiel Bay	TSM	0.47	0.36	0.15	26.66	0.55	0.76	0.79	65,467
SEA-005 Bay of Mecklenburg	TSM	0.66	0.38	0.16	36.73	0.89	1.44	1.50	86,705
SEA-006 Arkona Basin	TSM	1.11	0.44	0.09	50.04	0.94	2.69	3.71	336,633
SEA-007 Bornholm Basin	TSM	0.84	0.64	0.11	35.11	0.88	1.13	1.29	811,175
SEA-008 Gulf of Gdansk	TSM	2.80	1.20	0.47	27.62	9.51	13.39	3.90	111,292
SEA-009 Eastern Gotland Basin	TSM	1.16	0.82	0.34	48.59	1.01	1.21	2.12	1,507,151
SEA-010 Western Gotland Basin	TSM	0.80	0.75	0.10	32.58	0.88	0.94	0.55	703,007
SEA-011 Gulf of Riga	TSM	1.56	0.95	0.21	41.23	2.75	4.15	2.00	356,623
SEA-012 Northern Baltic Proper	TSM	0.86	0.85	0.10	49.60	0.99	1.04	0.54	701,042
SEA-013 Gulf of Finland	TSM	1.10	0.94	0.17	35.18	1.32	1.85	0.76	276,207
SEA-014 Aland Sea	TSM	0.91	0.75	0.09	34.83	1.27	1.65	0.71	348,717
SEA-015 Bothnian Sea	TSM	0.60	0.56	0.13	36.58	0.71	0.82	0.36	1,371,625
SEA-016 The Quark	TSM	0.73	0.56	0.15	27.33	1.19	1.78	0.70	192,800

based on these statistics, a box-and-whisker plot (showing the median and interquartile range as well as upper and lower fences) was made for each basin (using R-studio 3.4.1; {raster} package; Hijmans et al., 2017). Next, a coastal transect through Himmerfjärden bay and out to the open sea was investigated in order to evaluate the distribution of particles close to the shore. TSM values were extracted from 2009 to 2011, and from a 3-year summer composite using a transect mask (in SNAP 6.0) and were then plotted against the horizontal distance from the sewage treatment plant in the inner-most part of the bay. Then, descriptive statistical parameters (mean, median, min., max., SD, and N of pixels) were derived for each transect.

RESULTS

The binned summer composites of TSM concentrations (**Figure 2**, upper panels) show that the distribution pattern and the coverage of filamentous cyanobacteria varies from year to year. The 3-year composite (lower panel) averaging all viable summer data (2009–2011) shows the distribution of TSM corresponding to the previous HELCOM assessment period which spanned over a five-year period (2007–2011). According to HELCOM, at least 3 consecutive years within a five-year period should be assessed in order to account for natural variability in the data. In the coastal areas, the composites indicate increased TSM due to coastal run-off, but also depict off-shore production by filamentous cyanobacteria that are usually dominant during the summer months. The summer composite from 2009 is heavily influenced by cyanobacteria blooms in the Baltic proper, with highest concentrations in Western Gotland Basin. The composite from summer 2010 showed higher TSM in the Southern Baltic (especially in the Eastern Gotland Basin), highlighting mixing processes between off-shore blooms and wind-driven resuspension of sediments. Summer 2011 was somewhat less affected by the off-shore production of filamentous cyanobacteria, apart from distinctly higher concentrations in the Northern Baltic Proper with extension towards the Gulf of Finland. The Western Baltic (along the Swedish, Danish and German coasts) showed lower TSM concentrations apart from the Pomeranian Bight. In the Bothnian Sea, there are usually no blooms of filamentous cyanobacteria detected, and the increased values of TSM on a strip along the Finnish coast observed throughout all summer seasons may indicate the influence of fluvial input and/or of other phytoplankton species. The 3-year composite in the lower panel in **Figure 2** summarizes the distribution of TSM in the Baltic Sea over the 3-year period, and shows the average concentrations over the three chosen years. This 3-year summer composite was then superimposed by a shapefile, containing the last HELCOM sub-divisions of the Baltic Sea (**Table 2**; **Figure 3**). The box-and-whisker plots for the different basins (**Figure 4**), indicate a parabolic increase in the ranges of TSM concentration from the most Western basin up to the Baltic proper, and again decreasing values further up North, through the Bothnian Sea (SEA-015) and The Quark (SEA-016). The Gulf of Gdansk (Basin SEA-008) with its strong fluvial input and the shallow Gulf of Riga (SEA-011) showed a much wider range of TSM (0.47–27.6 gm^{-3}, and 0.21–41.2 gm^{-3}), and the highest Median values, 1.2 gm^{-3} and 0.95gm^{-3}, respectively,

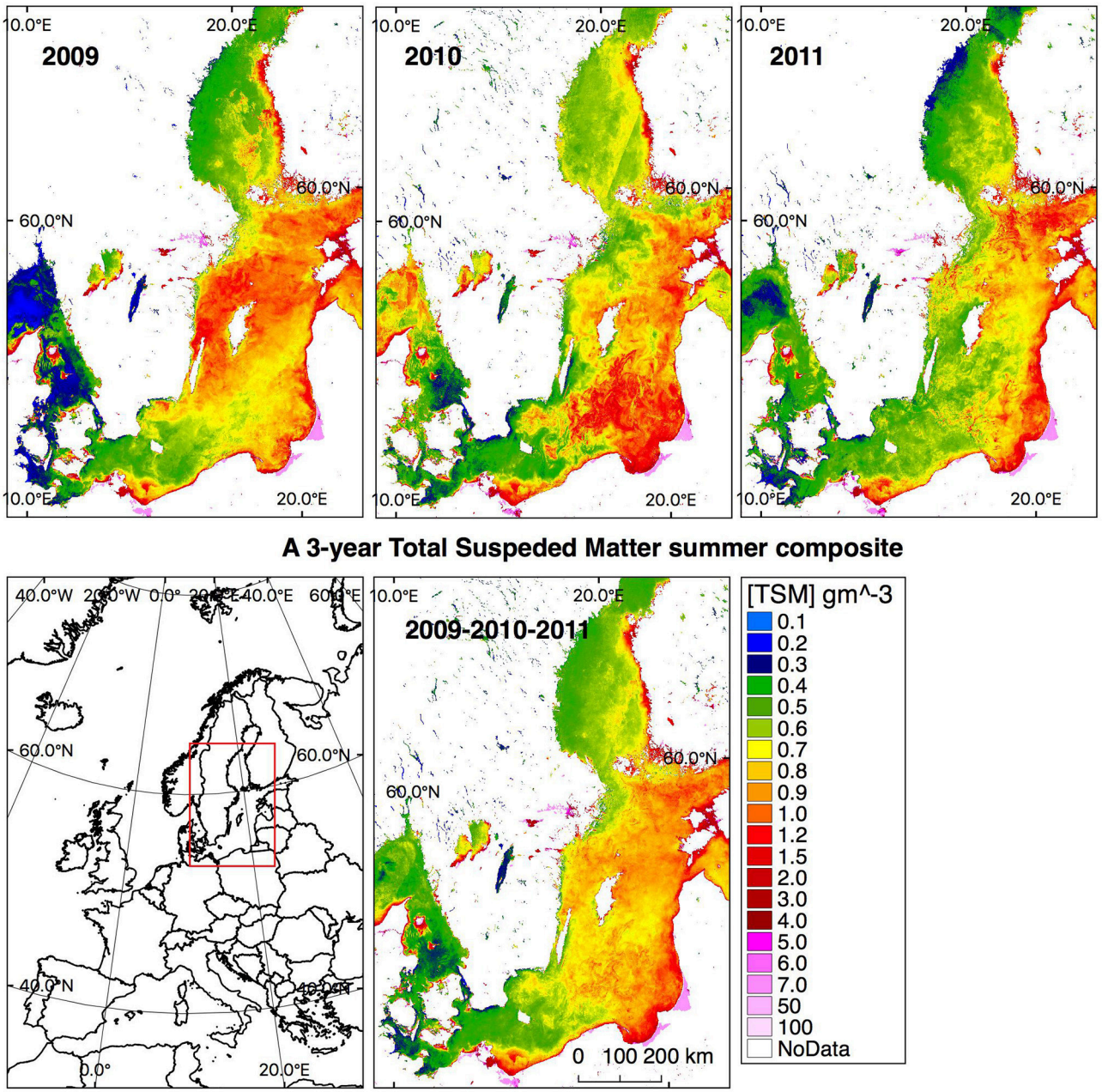


FIGURE 2 | Total Suspended Matter mean summer concentrations (gm^{-3}) in 2009, 2010, 2011, and a 3-year summer composite in the Baltic Sea. Countries (https://www.naturalearthdata.com/downloads/10m-cultural-vectors/10m-admin-0-countries/).

than found in other basins. Furthermore, the Eastern Gotland Basin (SEA-009) showed a significantly higher median value (0.82 gm^{-3}), than the Western Gotland Basin (SEA-010); (0.75 gm^{-3}), the latter showing very similar median values as found in the Åland Sea. The Eastern Gotland basin (SEA-009) and the Northern Baltic Proper (SEA-012) showed a very similar range of sediment loads and median values that do not differ significantly: 0.82 gm^{-3} vs. 0.85 gm^{-3}, respectively. The Gulf of Finland (SEA-013) is also characterized by somewhat higher values (median: 0.94 gm^{-3}), possibly due to the very strong inflow of sediments loads from the Niva river in the Eastern Gulf of Finland (close to St. Petersburg).

In order to evaluate the differences in coastal distribution patterns, a transect was extracted through Himmerfjärden bay from each composite (2009–2011), and also from the 3-year seasonal composite (2009–2011). Each transect represents a

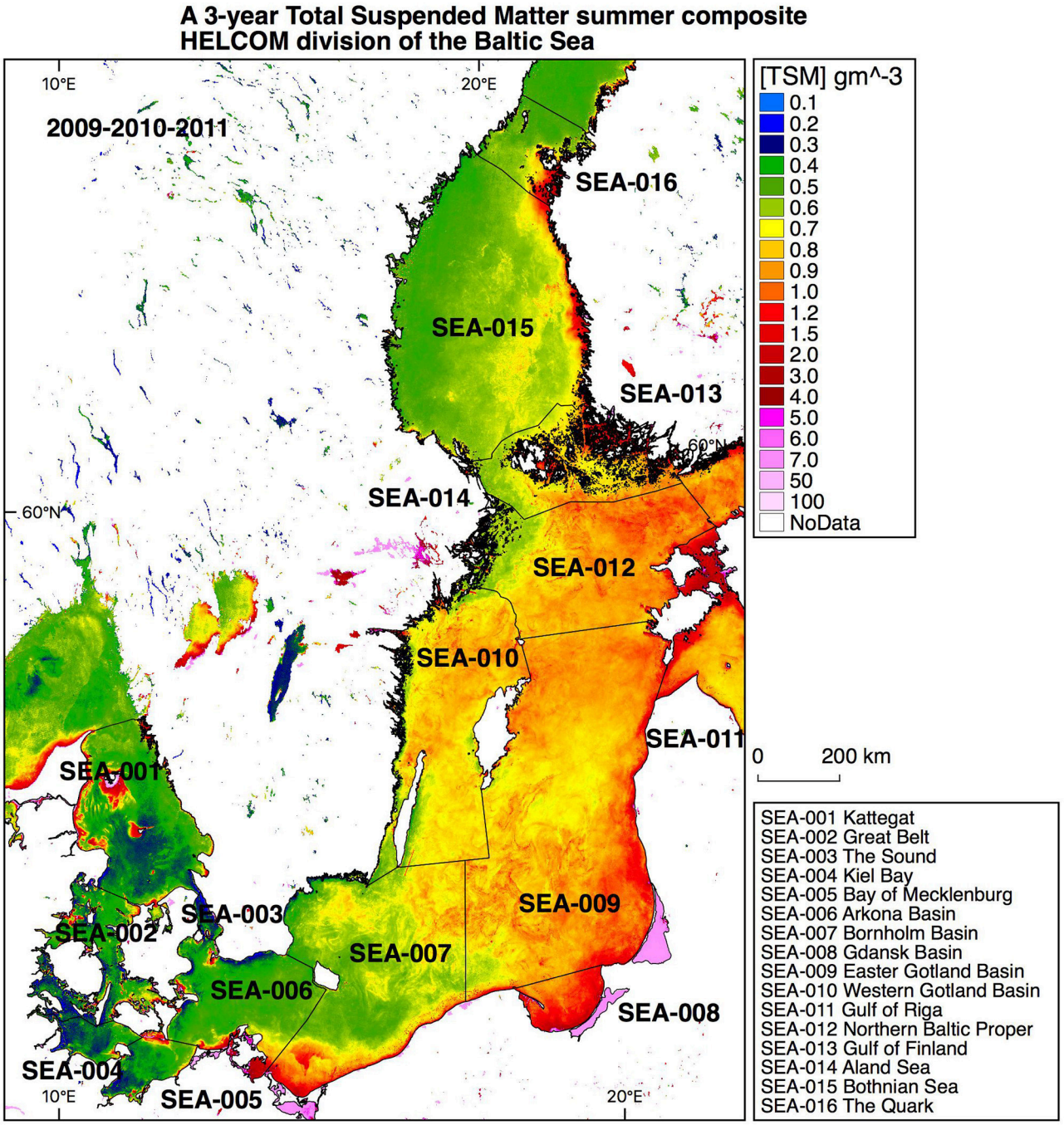


FIGURE 3 | A 3-year TSM summer composite superimposed by HELCOM sub-basins (http://metadata.helcom.fi/geonetwork/srv/eng/catalog.search#/metadata/d4b6296c-fd19-462c-94d2-4c81b9313d77).

gradient from the inner-most part of Himmerfjärden bay, toward the open sea. The values extracted along the coastal-open sea transect are shown in **Figure 5**. The extracted TSM concentrations were plotted against the distance to the Himmerfjärden Sewage Treatment Plant (STP) situated in the inner bay (**Figure 1**, right panel). The descriptive statistical parameters i.e., the mean, median, minimum, maximum, the standard deviation (SD) and the number of pixels (N), respectively, for each season along the transect were derived and summarized in **Table 4**. The TSM values extracted along the transect indicate that the mean concentrations in the summer seasons 2009 and 2011 were almost the same, whereas the median was higher (1.07 gm^{-3}) during 2011. The summer season 2010 was described by lower TSM concentrations and variability along

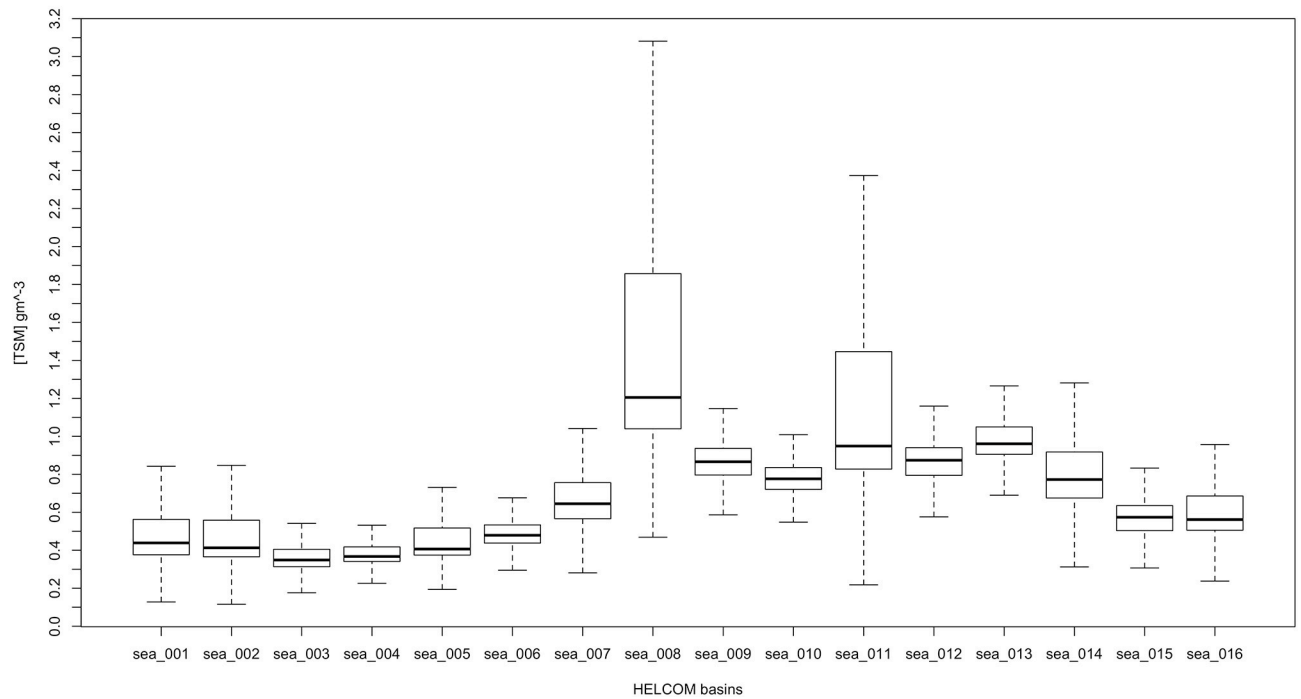


FIGURE 4 | Box-and-whisker plot comparison of TSM concentrations (box: interquartile range; horizontal line: median; whiskers: upper and lower fence) between HELCOM basins for a 3-year summer composite.

the transect. There was a clear decline of TSM concentrations at a distance of about 30 km from the sewage treatment plant. This corresponds to the mouth of Himmerfjärden, that is delineated by a sill and by Askö island (**Figure 1**, right panel). The concentrations further off-shore decrease asymptotically. Summer 2011 was strongly influenced by open sea production (i.e., a cyanobacteria bloom) that is clearly visible on the map (**Figure 2** top right panel; **Figure 4**), and represented on the corresponding plot by high variability in concentrations both before and after the 30 km mark. The transect extracted from the 3-year composite shows the mean coastal gradient of TSM distribution along the coast with a median concentration of 0.9 gm^{-3} and a mean of 1.0 gm^{-3}, which is within ranges of the median (1.5 gm^{-3}; 2008–2014) and mean (1.4 gm^{-3}; 2001–2002) measured *in situ* in this area (Kratzer and Tett, 2009; Kari et al., 2017), although the values derived from MERIS are underestimated by approximately 1/3.

In the following we compare the TSM concentrations derived from the 3-year summer composite and extracted for the different HELCOM sub-basin to *in situ* measured values found in the literature. Arkona Basin (SEA-004): 0.1–50.4 gm^{-3} derived from satellite vs. 0.7–9.0 gm^{-3} (Ohde et al., 2007; Fleming-Lehtinen and Laamanen, 2012). Bornholm Basin (SEA-007): 0.1–35.1 gm^{-3} vs. 0.4–5.0 gm^{-3} (Ohde et al., 2007; Fleming-Lehtinen and Laamanen, 2012) and 0.5–20.0gm^{-3} (Ohde et al., 2007; Fleming-Lehtinen and Laamanen, 2012). Eastern Gotland Basin (SEA-009): 0.3–48.5 gm^{-3} vs. 3.0–6.0 gm^{-3} (Ohde et al., 2007; Fleming-Lehtinen and Laamanen, 2012); and 1.1–32.0 gm^{-3} (Wasmund et al., 2001; Vaičiute et al., 2012). Gulf of Gdansk (SEA-008): 0.5–27.6 gm^{-3} vs. 0.4–15.7 gm^{-3} (Ohde et al., 2007; Fleming-Lehtinen and Laamanen, 2012). Gulf of Riga (SEA-011): 0.2–41.2 gm^{-3} vs. 10.0 - 24.0 gm^{-3} (Toming et al., 2009; Fleming-Lehtinen and Laamanen, 2012; Raag et al., 2014). Gulf of Finland (SEA-013): 0.2–35.1 gm^{-3} vs. 0.8–20.0 gm^{-3} (Toming et al., 2009; Fleming-Lehtinen and Laamanen, 2012; Raag et al., 2014). Western Gotland Basin (SEA-010): 0.1–32.5 gm^{-3} vs. 0.5–21.7 gm^{-3} (Toming et al., 2009; Fleming-Lehtinen and Laamanen, 2012; Raag et al., 2014). Bothnian Sea (SEA-015) 0.1–36.5 gm^{-3} vs. 0.2–20.9 gm^{-3} (Toming et al., 2009; Fleming-Lehtinen and Laamanen, 2012; Raag et al., 2014). Overall, it may be stated that the ranges of TSM measured *in situ* are also covered by the 3-year composite MERIS data. However, for each basin the satellite data shows a much higher range.

DISCUSSION

Recent advances in ocean color remote sensing led to the development of reliable coastal processors such as the coastal water properties processor developed by Free University of Berlin (FUB). This processor allows for the reliable retrieval of in-water constituents from satellite data also over optically-complex waters with high CDOM absorption. The use of the FUB processor here to derived TSM combined with data quality flags developed in the CoastColor project (C2R CoastColor) allowed to derive a 3-year summer composite, covering almost the whole Baltic Sea. The frequent cloud cover (40–55%) during

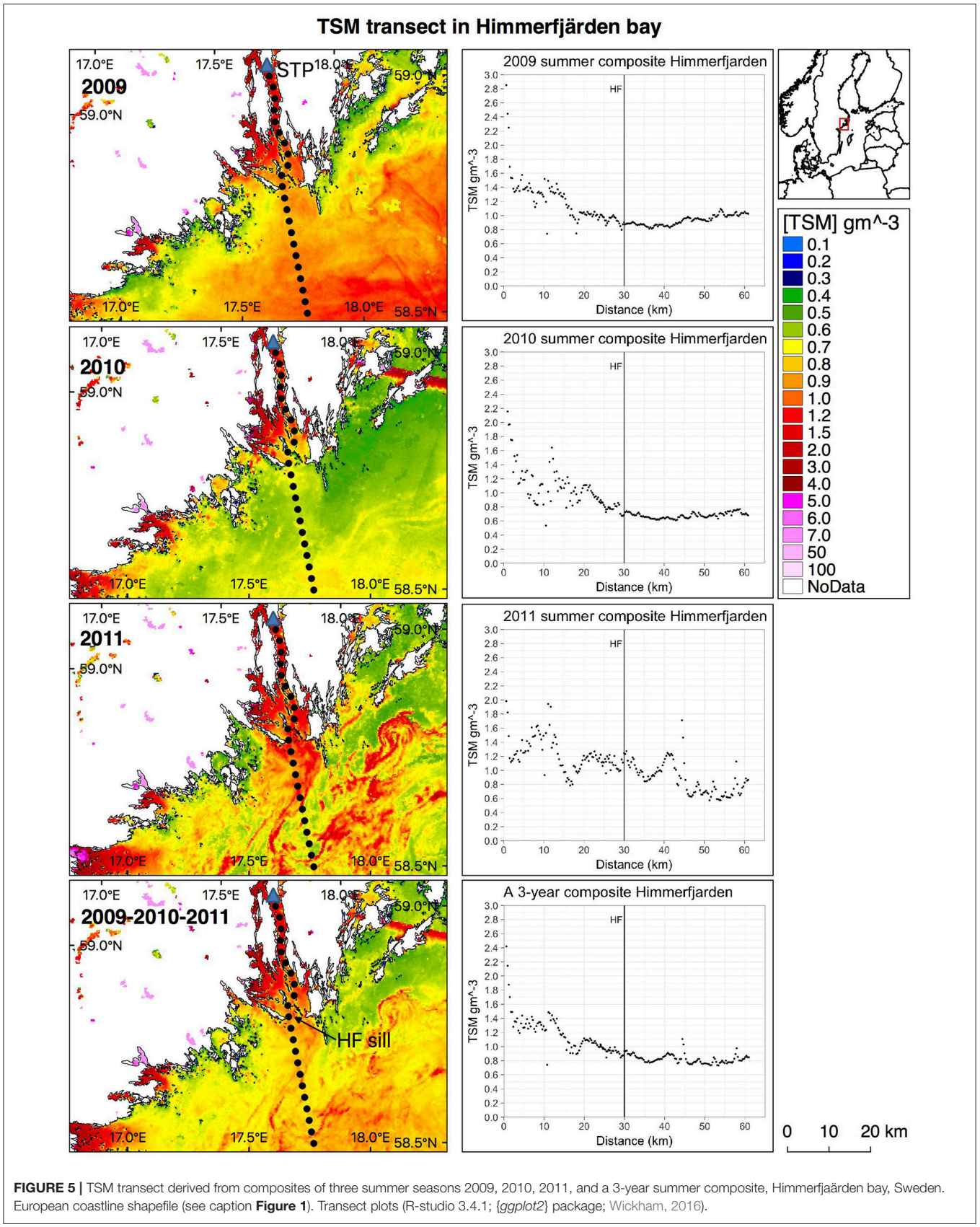


FIGURE 5 | TSM transect derived from composites of three summer seasons 2009, 2010, 2011, and a 3-year summer composite, Himmerfjaärden bay, Sweden. European coastline shapefile (see caption **Figure 1**). Transect plots (R-studio 3.4.1; {*ggplot2*} package; Wickham, 2016).

TABLE 4 | Comparison of TSM concentration per transect derived from summer seasons 2009–2011 and a 3-year summer composite.

Season	Mean	Median	Min.	Max.	SD	N (pixels)
2009	1.06	0.98	0.74	2.85	0.28	208
2010	0.86	0.74	0.53	2.15	0.30	205
2011	1.05	1.07	0.58	1.98	0.31	207
3-year composite	0.99	0.91	0.73	2.42	0.27	208

the summer period in the Baltic Sea (Karlsson, 2003), makes it a challenge to get cloudless images and to evaluate the spatial distribution of in-water constitutes e.g., TSM on a daily-basis. In order to get full spatial coverage of the entire basin it is required to aggregate several daily images together into weekly, monthly or seasonal averages. Often, there are not enough complete daily scenes to produce representative monthly averages. Those scenes, however, can be accounted for in the seasonally-averaged summer composite presented in this study. There are statistical methods (Poggio et al., 2012; Weiss et al., 2014; Land et al., 2018), to fill in the gaps caused by flagged pixels (e.g., cloud flags), but these methods may also be prone to error.

The TSM images derived from MERIS data and presented here showed to be relevant for mapping areas with high run-off and also highlight regional differences in coastal influence, such as in the Western Baltic Sea (**Figure 3**). TSM also indicates large-scale oceanographic features, such as eddies influencing the TSM distribution in the Southern and Eastern Baltic Sea, and carrying the sediments off-shore, and also further up North along the Eastern Baltic coast. The typical long-term mean horizontal current field in the Baltic Sea has a weak cyclonic pattern, creating anti-clockwise, rotation across the Baltic proper (Kullenberg, 1981; Stigebrandt, 2001). This rotation leads to the so-called Swedish current that transports surface waters up North (on the Eastern side of the Basin), and down south all along the Swedish coast (Voipio, 1981). TSM is also indicative of meso-scale features generated by atmospheric Rossby, i.e., planetary atmospheric waves caused by the Coriolis acceleration as well as by bottom topography and friction (Lehmann and Myrberg, 2008). Another common phenomenon is coastal upwelling, usually observed in the summer season along the Baltic Sea coastline at distances of approximately 10–20 km off-shore (Lehmann and Myrberg, 2008). The overlap between coastal sediment plumes and currents carrying suspended matter both further off-shore, and further up North along the Finnish coast is visible on the TSM composites (**Figures 2**, **3**). Strong wind-wave stirring in the Southern Baltic keeps small and medium sized particles (Danielsson et al., 2007) as well as organic suspended matter longer in suspension, and moves them further off-shore.

Besides depicting large-scale phenomena, seasonal averages also allow for a comparison between summer seasons from different years, and also aggregation into longer time-periods, such as the 3-year summer composite presented in this study. These images may be used in management as complimentary information for the status classification of the Baltic Sea e.g., in the periodic assessments done by HELCOM.

Comparison of Different Baltic Sea Basins

The superimposing of the HELCOM division of the Baltic Sea into 16 sub-basins allowed to evaluate the 3-year summer composite of TSM with respect to HELCOM basins. Concentrations in the different basins were then compared statistically. **Figure 4** illustrates that the ranges of TSM concentrations vary between basins, indicating the presence of cyanobacteria blooms as well as influence from physical processes such as wind-wave stirring and resuspension of sediments in shallow areas (Jönsson, 2005; Danielsson et al., 2007). Danielsson et al. (2007) found that these events have seasonal patterns with higher resuspension frequency in winter due to stronger current velocities. They also found that grain size had a strong effect, with fine sediments and medium sand having a considerable higher percentage of resuspension than larger grain sizes. As cyanobacteria and other phytoplankton are mostly made up of organic matter, and sometimes even may have positive buoyancy–e.g., due to the gas vacuoles in filamentous cyanobacteria (Walsby et al., 1995), they can be carried much further off-shore, following the dominant oceanographic currents.

The Gulf of Gdansk (sea_009) and Gulf of Riga (sea_011) include wider ranges of TSM, compared to the other basins. Both are coastal basins that are relatively shallow (the Gulf of Gdansk has a mean depth of 57 m and the Gulf of Riga 23 m) and may be exposed to strong wind-wave stirring, keeping the suspended matter in suspension (Danielsson et al., 2007). These processes, in turn, are manifested in higher concentrations of TSM, and the mean values are depicted in the satellite images (**Figure 2**), and are statistically compared in **Table 3**. The Gulf of Gdansk also receives considerable amounts of terrestrial input from the Vistula river (Szymczak and Galinska, 2013). The Gulf of Riga was only partially captured by the analyzed composite and the results may thus not capture the full variability of TSM in this basin. This highlights the challenges collecting remote sensing data in the Baltic Sea region—which has a relatively high occurrence of cloud cover (Karlsson, 2003).

In the Northwestern Baltic proper TSM concentrations are generally much lower and reach much less further off-shore than in the Southern and Southeastern Baltic proper. Also, the sea bottom here predominantly consists of exposed rock and mud, whereas the bottom substrate in S and SE Baltic proper is dominant by sand and mud (Al-Hamdani and Reker, 2007). In the Southern Baltic Sea, the TSM concentrations are presumably higher due to the higher run-off from large rivers in the Southern Baltic (i.e., the Vistula and the Order) and due to stronger wind exposure (Danielsson et al., 2007). Here, wind-wave stirring may keep the heavier particles in suspension longer and carry it further off-shore by the surface currents. The southern Baltic Sea is also characterized by a different morphology, hydrology and bottom topography. The coast is rather exposed to wind and there are only a limited number of large bays (such as the Gulf of Riga and the Gulf of Gdansk). The NW Baltic has a completely different morphology with a large number of elongated bays that often consist of small sub-basins intersected by sills, and it is less exposed to wind (Danielsson et al., 2007). Heavy inorganic particles thus tend to fall out here in the inner basins.

It is also the combination of bottom topography and river run-off that seem to determine the TSM loads in the more coastal basins in the Southern and in the Eastern Baltic. Large rivers (i.e., the Oder and Vistula in the South as well as the Neva in the East) bring in large amounts of anthropogenic loads from densely populated areas in Poland, Germany and Russia. **Figures 3**, **4** show that the Gulf of Gdansk (SEA-008), the Eastern Gotland Basin (SEA-009), and the Gulf of Riga (SEA-11) stick out with clearly elevated values of TSM. For the Gulf of Gdansk and the Gulf of Riga, this may be attributed to strong coastal influence and shallow bottom topography—especially in the Gulf of Riga- as well as cyanobacterial production during summer. In the off-shore areas of the Eastern Gotland Basin (SEA-009) cyanobacterial production seems to dominate the picture. The Northern Baltic proper (SEA-12) the Eastern Gotland Basin (SEA-009) and the Western Gotland Basin (SEA-010) showed similar patterns of off-shore TSM that seem to be strongly influenced by cyanobacteria blooms. The Arkona Basin (SEA-006) and the Bothnian Sea (SEA-015) seem least influenced by wind-driven resuspension and/or blooms of filamentous cyanobacteria. Filamentous cyanobacteria generally do not tend to bloom in the Gulf of Bothnia, which may be partially attributed to phosphate limitation (Snoeijs-Leijonmalm et al., 2017). Also, the lower water temperatures (subarctic, boreal climate) and the low salinities (ranging from 1.8 g kg^{-1} up North in the Bothnian Bay to 6.6 g kg^{-1} in the Bothnian Sea), as well as the low water transparencies (Snoeijs-Leijonmalm et al., 2017) may limit cyanobacterial growth (Lehtimaki et al., 1997). The accumulation patterns of particulate matter are strongly related both to sediment type and basin depth (Leipe et al., 2011). The Arkona Basin (SEA-006) basin, however, is relatively shallow with a mean depth of 23 m. Despite the shallowness, Leipe et al. (2011) found relatively low accumulation rates of particulate organic matter in the Arkona Sea. The authors state that large differences in the accumulation and burial rates of organic matter cannot always be fully explained by regional differences in surface-water productivity. The deep water transport in the Baltic Sea happens in a cascade-like manner from the shallower into the deeper basins (Voipio, 1981) and suspended sediments thus tend to accumulate in the deepest basins such as the Gotland basin (Leipe et al., 2011).

Trend in Himmerfjärden Bay

The inner coastal to off-shore transects extracted from the TSM composites from the 3 different summer seasons in Himmerfjärden showed that TSM follows a rather steep decrease inside Himmerfjärden bay, tending toward an asymptotic line in the open sea. This trend was first observed and described by Kratzer and Tett (2009), using *in situ* data from summer, and is now confirmed here by transects derived from MERIS data, indicating a similar distribution trend. Kratzer and Tett (2009) showed that the high concentrations of TSM in the inner bay are mostly caused by inorganic particles which fall out rather steeply in the inner bay. The TSM found in the open sea consisted mostly of organic particles (including phytoplankton), which tend to be lighter, and thus can be carried further off-shore. These trends were recently confirmed in a spring study by Kari et al. (2018), which also confirmed a much higher percentage of inorganic material in the inner bay during spring time. These patterns again seem to be governed by a combination of bottom topography (small sub-basins intersected by sills) and the relatively low wind forcing in the NW Baltic Sea.

The *in situ* TSM transect described by Kratzer and Tett (2009) was derived from the mean of 4 optical transects measured during June 2001 and August 2002, and thus originated both from different years and from different summer months. Compared to the TSM transects derived from MERIS data, the *in situ* transects were spatially sparse (3–5 optical station in each transect with about 15–20 km distance between stations). In contrast, the transects derived from MERIS TSM composites were derived from full spatial resolution data (300 m pixels), allowing to derive a continuous set of TSM concentrations, and to fill in the gaps between the *in situ* sampling stations. The results shown in **Figure 5** demonstrate that there is a consistent trend with higher values in the inner bay that is also persistent through different summer seasons. The study by Kari et al. (2018) confirmed that the same spatial pattern is also found in spring with slightly higher ranges of TSM due to the influence from ice thawing. The higher range of values in coastal waters can be attributed to the influence from land (erosion and run-off). The strong variability of TSM in the open sea during summer can be mostly explained by the variability in cyanobacteria biomass (Kratzer and Tett, 2009; Beltrán-Abaunza et al., 2016; Kari et al., 2017).

The remote sensing approach also allows to retrieve and assess the variability and distribution of TSM concentrations between stations. As *in situ* measurements are relatively expensive and much more time consuming, one usually samples at a much lower spatial, and temporal resolution than possible to retrieve from satellite data (Beltrán-Abaunza et al., 2016; Harvey et al., 2018). Additionally, similar transects derived in other regions of the Baltic Sea allow to spatially evaluate the contribution of river run-off and coastal resuspension (Kyryliuk, 2014). For example, rivers that flow through agricultural landscapes transport suspended sediments and nutrients. Agricultural run-off rich in nutrients as well as industrial discharges are prime contributors of phosphorus and nitrogen into surface waters that may also affect off-shore eutrophication (Voipio, 1981). Suspended matter often contains phosphorus and is transported from coastal areas into the open Baltic Sea, following currents. The sediment transport is also influenced by wind-stirring as wind may cause resuspension of sediments that, in turn, may affect the nutrient dynamics (Danielsson et al., 2007). All these processes are reflected in the TSM patterns that are visible from space and can be quantified and mapped. As TSM and total phosphate are correlated (Beusekom and Jonge, 1994), one possibly could also use satellite-derived TSM as a proxy for phosphorus distribution in coastal areas or in different basins of the Baltic Sea.

Furthermore, TSM is highly related to turbidity as TSM scatters light and turbidity is a measure of particle scatter. This relationship has been studied by Kari et al. (2017) and

has shown to be robust across the Baltic Sea. The authors developed a regional algorithm between TSM and turbidity in the Baltic Proper and tested the algorithm on independent datasets, including a dataset from Lithuanian coastal waters and the Curonian Lagoon with very large ranges of TSM (0.6–24.0 gm^{-3} and 1.8–34.0 gm^{-3}, respectively). The r^2 for the TSM-turbidity relationship was found to be 0.93 (Kari et al., 2017; Kari, 2018). According to the nomenclature of the EU Water Framework Directive TSM could also be described as a physio-chemical parameter. Turbidity is listed in the EU Marine Strategy Framework directive as one of the mandatory variables to be measured and monitored in coastal waters (Marine Strategy Framework Directive Annex III, 2008). The concentrations of TSM—and thus turbidity—can also be used as an indicator for coastal water masses (Capello et al., 2004; Kratzer and Tett, 2009; Almroth-Rosell et al., 2011).

A number of studies have been conducted in recent years (**Table 1**) where researchers measured TSM *in situ* in different Baltic Sea basins. Although monitoring campaigns and oceanographic cruises are quite regular in the Baltic Sea, they still cannot achieve the same temporal and spatial coverage as satellite data. *In situ* campaigns usually cover open sea station as well as coastal areas. They most often take place in spring in order to track the development of the spring bloom (that consists mostly of diatoms and dinoflagellates), and then later in summer to cover the cyanobacteria blooms. However, sampling campaigns are logistically rather complex and are associated with high costs and usually limited to a set of pre-defined stations that are revisited yearly to keep track of the annual variability of water quality variables. These spatially sparse monitoring stations are often considered to be representative for each basin. However, in reality they are only very limited point measurements and even sometimes only represent one point in time in the respective basin. The Baltic Sea, however, is highly variable and dynamic, as shown in **Figure 2**, and what happens between stations or where measurements are not performed at all is often assumed or calculated by means of numerical modeling (Savchuk, 2018), which, again, is often based on a restricted number (both in space and in time) of empirical/measured data.

Ocean color data provides us with waters quality indicators (e.g., CDOM, chl-a, TSM and Secchi depth) that are also routinely measured *in situ* (Kratzer et al., 2016). Extensive validation campaigns and development of improved algorithms to derive the inherent optical properties and in-water constituents from remote sensing reflectance data allows to derive water quality indicators reliably and with full spatial resolution (300 m) on a Baltic Sea wide scale (Kutser et al., 2005; Ohde et al., 2007; Kratzer et al., 2008, 2011; Kutser, 2009; Kratzer and Vinterhav, 2010; Vaičiute et al., 2012; Beltrán-Abaunza et al., 2014; Kahru and Elmgren, 2014; Hieronymi et al., 2017; Kari et al., 2017; Kratzer and Moore, 2018). This body of recent research demonstrates that the remote sensing approach corresponds to the MSP needs for high quality data and assessment tools with high temporal and spatial resolution.

Furthermore, GIS analysis of MERIS-derived TSM data allows to retrieve concentrations for any bay, estuary or basin larger than 300 m. The HELCOM sub-divisions of the Baltic Sea comes with a shapefile that can be used to derive basin-specific concentrations, to statistically estimate the difference between those basins, and also to evaluate how those concentrations compare to what is found in the literature. The comparison here showed that concentrations derived from the TSM composite indicate much wider ranges than measured *in situ* and found in the literature (see **Tables 1**, **3**), possibly due to a better spatial coverage by satellite data. However, the very high ranges may also be due to inclusion of very near-shore areas (pixels), where TSM retrieval may be influenced by the so-called land-adjacency effect, i.e., the high reflectance from land that may influence near-shore water pixels. This, in turn may lead to erroneously high values of TSM concentrations (Toming et al., 2017). Statistically, this can be accounted for by either using the median values (accounting for non-normal distribution of the data), or by using the 90 or 95 percentiles excluding the extreme values, and thus accounting for errors associated with land-adjacency effects and values that are beyond the training range of a given processor.

CONCLUSION

The use of the FUB processor on MERIS data over the Baltic Sea allowed to map the summer distribution of TSM over the last 3 years of the ENVISAT mission. This time span also fell within HELCOM's previous assessment period (2007–2011). The problems related to frequent cloud cover in the Baltic Sea, leading to limited coverage of individual MERIS scenes, could be overcome by producing averaged summer composite using the L3 binning approach. This allowed to map the TSM distribution almost across the entire Baltic Sea basin (apart from some areas in the Gulf of Riga and the Gulf of Finland due extensive cloud cover). The summer composites from 2009 to 2011 were aggregated into a single 3-year summer season composite, representing average spatial patterns of TSM distribution over this time period. These composites demonstrate how ocean color remote sensing data can provide additional information for Baltic Sea research and management. It allows to understand and investigate large-scale phenomena, from river discharge and phytoplankton blooms, to meso-scale features, depicting the mean current-fields of the Baltic Sea, to the monitoring of coastal waters. The main advantage to conventional monitoring efforts is a synoptic and potentially full-scale coverage of the Baltic Sea with good spatial and temporal resolution (Kratzer et al., 2014; Harvey et al., 2018). The additional use of GIS allowed to divide the 3-year summer composite into sub-basins according to HELCOM designated basins, and to derive descriptive statistics for each corresponding basin, and to perform a spatial trend analysis on an extracted coastal transects from Himmerfjärden bay and adjacent areas. TSM particles followed a steep decline in the inner-most part of the bay and converted toward relatively low open sea values ranging from about 0.5–0.7 gm^{-3}. The trend showed to fluctuate, depending on the conditions during the respective summer season, e.g., due to variability in precipitation, run-off and coastal primary production as well as the influence of off-shore production- e.g., cyanobacterial blooms- further

off the coast. The transects confirmed observations and trends previously made using *in situ* measurements, namely a rather steep decline of TSM in inner coastal bay, tending toward an open sea threshold. Such data extracted from coastal transects may play a role in estimating water exchange rates within coastal and open sea systems, and the ecological state of these systems. Furthermore, this approach allowed to fill in gaps between monitoring stations, describing coastal trends with good spatial resolution and coverage. TSM concentration extracted from a 3-year summer composite showed to be coherent with values found in the literature, however with somewhat larger ranges.

AUTHOR CONTRIBUTIONS

All authors listed have made a substantial, direct and intellectual contribution to the work, and approved it for publication.

FUNDING

This research was funded by Swedish National Space Board (SNSB) contract no. Dnr. 165/11 and Dnr. 175/17, European Space Agency (ESA)/ESRIN contract no. 21524 and by SU's strategic project Baltic Ecosystem Adaptive Management (BEAM), application no. 2009-3435-13495-18.

ACKNOWLEDGMENTS

The satellite imagery and detailed information on data processing was provided by Dr. Petra Phillipson, Brockmann Geomatics, Sweden AB. Thanks to Brockmann Consult, Germany for data processing up to Level-2 (Pre-processing and FUB). Thanks to Kari Eilola for helpful comments on a previous version of the manuscript.

REFERENCES

Al-Hamdani, Z., and Reker, J. (eds.). (2007). *Towards marine landscapes in the Baltic Sea*. Balance interim report #10. Copenhagen. Available online at: http://balance-eu.org/xpdf/balance-interim-report-no-10.pdf (Accessed December 20, 2018).

Alikas, K., Kratzer, S., Reinart, A., Kauer, T., and Paavel, B. (2015). Robust remote sensing algorithms to derive the diffuse attenuation coefficient for lakes and coastal waters. *Limnol. Oceanogr. Methods* 13, 402–415. doi: 10.1002/lom3.10033

Almroth-Rosell, E., Eilola, K., Hordoir, R., Meier, M. H. E., and Hall, P. (2011). Transport of fresh and resuspended particulate organic material in the Baltic Sea — a model study. *J. Mar. Syst.* 87, 1–12. doi: 10.1016/j.jmarsys.2011.02.005

Beltrán-Abaunza, J. M., Kratzer, S., and Brockmann, C. (2014). Evaluation of MERIS products from Baltic Sea coastal waters rich in CDOM. *Ocean Sci.* 10, 377–396. doi: 10.5194/os-10-377-2014

Beltrán-Abaunza, J. M., Kratzer, S., and Höglander, H. (2016). Using MERIS data to assess the spatial and temporal variability of phytoplankton in coastal areas. *Int. J. Remote Sens.* 38, 2004–2028. doi: 10.1080/01431161.2016.1249307

Beusekom, J. E. E., and Jonge, V. N. (1994). The role of suspended matter in the distribution of dissolved inorganic phosphate, iron and aluminium in the Ems estuary. *Netherlands J. Aquat. Ecol.* 28, 383–395. doi: 10.1007/BF02334208

Bourg, L., D'Alba, L., and Colagrande, P. (2008). *MERIS Smile Effect Characterization and Correction*. Paris: ESA. Available online at: https://earth.esa.int/documents/700255/707220/MERIS_Smile_Effect.pdf/a1e7cbd0-2f1e-40f2-a5bc-92f5dab1ee43 (Accessed December 20, 2018).

Brockmann Consult (2014). *DUE CoastColour Product User Guide Deliverable DEL-21. 33.*

Capello, M., Budillon, G., Ferrari, M., and Tucci, S. (2004). Suspended matter variability in relation to water masses in Terra Nova Bay (Ross Sea-Antarctica). *Chem. Ecol.* 20, S7–S18. doi: 10.1080/02757540410001664620

Danielsson, Å., Jönsson, A., and Rahm, L. (2007). Resuspension patterns in the Baltic proper. *J. Sea Res.* 57, 257–269. doi: 10.1016/j.seares.2006.07.005

Devlin, M. J., Barry, J., Mills, D. K., Gowen, R. J., Foden, J., Sivyer, D., et al. (2008). Relationships between suspended particulate material, light attenuation and Secchi depth in UK marine waters. *Estuar. Coast. Shelf Sci.* 79, 429–439. doi: 10.1016/j.ecss.2008.04.024

Dogliotti, A. I., Ruddick, K. G., Nechad, B., Doxaran, D., and Knaeps, E. (2015). A single algorithm to retrieve turbidity from remotely-sensed data in all coastal and estuarine waters. *Remote Sens. Environ.* 156, 157–168. doi: 10.1016/j.rse.2014.09.020

Engqvist, A. (1996). Long-term nutrient balances in the eutrophication of the Himmerfjärden estuary. *Estuar. Coast. Shelf Sci.* 42, 483–507. doi: 10.1006/ecss.1996.0031

Fleming-Lehtinen, V., and Laamanen, M. (2012). Long-term changes in Secchi depth and the role of phytoplankton in explaining light attenuation in the Baltic Sea. *Estuar. Coast. Shelf Sci.* 102–103, 1–10. doi: 10.1016/j.ecss.2012.02.015

Franzén, F., Kinell, G., Walve, J., Elmgren, R., and Söderqvist, T. (2011). Participatory social-ecological modeling in eutrophication management: the case of Himmerfjärden, Sweden. *Ecol. Soc.* 16:art27. doi: 10.5751/ES-04394-160427

Harvey, E. T., Walve, J., Andersson, A., Karlson, B., and Kratzer, S. (2018). The effect of optical properties on secchi depth and implications for eutrophication management. *Front. Mar. Sci.* 5:496. doi: 10.3389/fmars.2018.00496

Harvey, T. (2015). *Bio-optics, Satellite Remote Sensing and Baltic Sea Ecosystems: Applications for Monitoring and Management.* Doctoral dissertation, Department of Ecology, Environment and Plant Sciences, Stockholm University. Available online at: http://www.diva-portal.org/smash/record.jsf?pid=diva2%3A849120&dswid=3680 (Accessed December 20, 2018).

HELCOM (2013). *HELCOM Monitoring and Assessment Strategy*. HELCOM Minist. Decralation.

Hieronymi, M., Müller, D., and Doerffer, R. (2017). The OLCI Neural Network Swarm (ONNS): a bio-geo-optical algorithm for open ocean and coastal waters. *Front. Mar. Sci.* 4:140. doi: 10.3389/fmars.2017.00140

Hijmans, R. J., van Etter, J., Cheng, J., Mattiuzzi, M., Summer, M., Greenberg, J. A., et al. (2017). *Geographic Data Analysis and Modeling*. R CRAN Proj. Available online at: http://rspatial.org/ (Accessed December 20, 2018).

Jönsson, A. (2005). *Model Studies of Surface Waves and Sediment Resuspension in the Baltic Sea*. Available online at: http://www.diva-portal.org/smash/get/diva2:20699/FULLTEXT01.pdf.

Kahru, M., and Elmgren, R. (2014). Multidecadal time series of satellite-detected accumulations of cyanobacteria in the Baltic Sea. *Biogeosciences* 11, 3619–3633. doi: 10.5194/bg-11-3619-2014

Kahru, M., Savchuk, O. P., and Elmgren, R. (2007). Satellite measurements of cyanobacterial bloom frequency in the Baltic Sea: interannual and spatial variability. *Mar. Ecol. Prog. Ser.* 343, 15–23. doi: 10.3354/meps06943

Kari, E. (2018). *Light Conditions in Seasonally Ice-Covered Waters : Within the Baltic Sea Region*. Available online at: http://su.diva-portal.org/smash/get/diva2:1221600/FULLTEXT01.pdf

Kari, E., Kratzer, S., Beltrán-Abaunza, J. M., Harvey, E. T., and Vaičiute, D. (2017). Retrieval of suspended particulate matter from turbidity – model development, validation, and application to MERIS data over the Baltic Sea. *Int. J. Remote Sens.* 38, 1983–2003. doi: 10.1080/01431161.2016.1230289

Kari, E., Merkouriadi, I., Leppäranta, M., Walve, J., and Kratzer, S. (2018). Development of under-ice stratification in Himmerfjärden bay, north-western Baltic proper, and their effect on the phytoplankton spring bloom. *Mar J. Syt.* 186, 85–95. doi: 10.1016/j.jmarsys.2018.06.004

Karlsson, K.-G. (2003). A 10 year cloud climatology over Scandinavia derived from NOAA advanced very high resolution radiometer imagery. *Int. J. Climatol.* 23, 1023–1044. doi: 10.1002/joc.916

Kirk, J. T. O. (1985). Light and photosynthesis in aquatic ecosystems. *Int. Rev. der gesamten Hydrobiol. und Hydrogr*. 70, 897–898. doi: 10.1002/iroh.19850700619

Kopelevich, O. V., Vazyulya, S. V., Sheberstov, S. V., and Bukanova, T. V. (2016). Suspended matter in the surface layer of the southeastern Baltic from satellite data. *Oceanology* 56, 46–54. doi: 10.1134/S0001437016010069

Koponen, S., Attila, J., Pulliainen, J., Kallio, K., Pyhälahti, T., Lindfors, A., et al. (2007). A case study of airborne and satellite remote sensing of a spring bloom event in the Gulf of Finland. *Cont. Shelf Res.* 27, 228–244. doi: 10.1016/j.csr.2006.10.006

Kowalczuk, P., Olszewski, J., Darecki, M., and Kaczmarek, S. (2005). Empirical relationships between coloured dissolved organic matter (CDOM) absorption and apparent optical properties in Baltic Sea waters. *Int. J. Remote Sens.* 26, 345–370. doi: 10.1080/01431160410001720270

Kowalczuk, P., Stedmon, C. A., and Markager, S. (2006). Modeling absorption by CDOM in the Baltic Sea from season, salinity and chlorophyll. *Mar. Chem.* 101, 1–11. doi: 10.1016/j.marchem.2005.12.005

Kratzer, S. (2000). *Bio-Optical Studies of Coastal Waters*. Ph.D. Thesis, School of Ocean Sciences, University of Wales, Bangor, UK. Available online at: http://www.isni.org/isni/0000000136024205

Kratzer, S., Alikas, K., Harvey, T., Beltrán-Abaunza, J. M., Morozov, E., Mustapha, S. B., et al. (2016). "Multitemporal remote sensing of coastal waters," in *Multitemporal Remote Sensing: Methods and Applications*, ed. Y. Ban (Cham: Springer International Publishing), 391–426. doi: 10.1007/978-3-319-47037-5_19

Kratzer, S., Brockmann, C., and Moore, G. (2008). Using MERIS full resolution data to monitor coastal waters - A case study from Himmerfjarden, a fjord-like bay in the northwestern Baltic Sea. *Remote Sens. Environ.* 112, 2284–2300. doi: 10.1016/j.rse.2007.10.006

Kratzer, S., Ebert, K., and Sørensen, K. (2011). "Monitoring the bio-optical state of the Baltic Sea ecosystem with remote sensing and autonomous *in situ* techniques," in *The Baltic Sea Basin*, eds. J. Harff, S. Björck, and P. Hoth (Berlin; Heidelberg: Springer), 407–435. doi: 10.1007/978-3-642-17220-5_20

Kratzer, S., Håkansson, B., and Sahlin, C. (2003). Assessing Secchi and photic zone depth in the Baltic Sea from satellite data. *J. Hum. Environ.* 32, 577–585. doi: 10.1639/0044-7447(2003)032[0577:asapzd]2.0.co;2

Kratzer, S., and Moore, G. (2018). Inherent optical properties of the baltic sea in comparison to other seas and oceans. *Remote Sens.* 10:418. doi: 10.3390/rs10030418

Kratzer, S., and Tett, P. (2009). Using bio-optics to investigate the extent of coastal waters: a Swedish case study. *Hydrobiologia* 629, 169–186. doi: 10.1007/s10750-009-9769-x

Kratzer, S., Therese Harvey, E., and Philipson, P. (2014). The use of ocean color remote sensing in integrated coastal zone management—A case study from Himmerfjärden, Sweden. *Mar. Policy* 43, 29–39. doi: 10.1016/j.marpol.2013.03.023

Kratzer, S., and Vinterhav, C. (2010). Improvement of MERIS level 2 products in baltic sea coastal areas by applying the improved Contrast between Ocean and Land Processor (ICOL) - Data analysis and validation. *Oceanologia* 52, 211–236. doi: 10.5697/oc.52-2.211

Kuhrts, C., Fennel, W., and Seifert, T. (2004). Model studies of transport of sedimentary material in the western Baltic. *J. Mar. Syst.* 52, 167–190. doi: 10.1016/j.jmarsys.2004.03.005

Kullenberg, G. (1981). Chapter 3 Physical Oceanography. *Elsevier Oceanogr. Ser.* 30, 135–181. doi: 10.1016/S0422-9894(08)70140-5

Kullenberg, G., and Jacobsen, T. S. (1981). The Baltic Sea: an outline of its physical oceanography. *Mar. Pollut. Bull.* 12, 183–186. doi: 10.1016/0025-326X(81)90168-5

Kutser, T. (2009). Passive optical remote sensing of cyanobacteria and other intense phytoplankton blooms in coastal and inland waters. *Int. J. Remote Sens.* 30, 4401–4425. doi: 10.1080/01431160802562305

Kutser, T., Pierson, D. C., Kallio, K. Y., Reinart, A., and Sobek, S. (2005). Mapping lake CDOM by satellite remote sensing. *Remote Sens. Environ.* 94, 535–540. doi: 10.1016/j.rse.2004.11.009

Kyryliuk, D. (2014). *Total suspended matter derived from MERIS data as an indicator of coastal processes in the Baltic Sea*. Independen. Available online at: http://su.diva-portal.org/smash/get/diva2:1060672/FULLTEXT01.pdf

Land, P. E., Shutler, J. D., and Smyth, T. J. (2018). Correction of sensor saturation effects in MODIS oceanic particulate inorganic carbon. *IEEE Trans. Geosci. Remote Sens.* 56, 1466–1474. doi: 10.1109/TGRS.2017.2763456

Lehmann, A., and Myrberg, K. (2008). Upwelling in the Baltic Sea - A review. *J. Mar. Syst.* 74, 3–12. doi: 10.1016/j.jmarsys.2008.02.010

Lehtimaki, J., Moisander, P., Sivonen, K., and Kononen, K. (1997). Growth, nitrogen fixation, and nodularin production by two baltic sea cyanobacteria. *Appl. Environ. Microbiol.* 63, 1647–1656.

Leipe, T., Tauber, F., Vallius, H., Virtasalo, J., Uścinowicz, S., Kowalski, N., et al. (2011). Particulate organic carbon (POC) in surface sediments of the Baltic Sea. *Geo Mar. Lett.* 31, 175–188. doi: 10.1007/s00367-010-0223-x

Leppäranta, M., and Myrberg, K. (2009). *Physical Oceanography of the Baltic Sea*. Berlin; Heidelberg: Springer Berlin Heidelberg. doi: 10.1007/978-3-540-79703-6

Manual, S. U., and Document, I. C. (2007). *The AMORGOS MERIS CFI (Accurate MERIS Ortho-Rectified Geo-location Operational Software) Software User Manual & Interface Control Document*. Manual, Software User Document Control.

Marine Strategy Framework Directive Annex III (2008). Directive 2008/56/EC of the European Parliament and of the Council. *Off. J. Eur. Union* 164, 19–40. Available online at: https://eur-lex.europa.eu/legal-content/EN/TXT/PDF/?uri=CELEX:32008L0056&from=EN (Accessed December 20, 2018).

Morel, A., and Prieur, L. (1977). Analysis of variations in ocean color. *Limnol. Oceanogr.* 22, 709–722. doi: 10.4319/lo.1977.22.4.0709

Myrberg, K., and Lehmann, A. (2013). "Topography, hydrography, circulation and modelling of the Baltic Sea," in *Preventive Methods for Coastal Protection*, eds T. Soomere, and E. Quak (Heidelberg: Springer International Publishing), 31–64. doi: 10.1007/978-3-319-00440-2_2

Ohde, T., Siegel, H., and Gerth, M. (2007). Validation of MERIS Level-2 products in the Baltic Sea, the Namibian coastal area and the Atlantic Ocean. *Int. J. Remote Sens.* 28, 609–624. doi: 10.1080/01431160600972961

Patrice, B., Amberg, V., Bourg, L., PETIT, D., Huc, M., Miras, B., et al. (2011). Geolocation assessment of MERIS GlobCover orthorectified products. *IEEE Trans. Geosci. Remote Sens.* 49, 2972–2982. doi: 10.1109/TGRS.2011.2122337

Philipson, P., Sandström, A., Asp, A., Axenrot, T., Kinnerbäck, A., and Ragnarsson-Stabo, H. (2014). *MERIS and Hydroacoustic Data for Fisheries Management, Assessment Of Ecosystem Status and Identification of Essential Habitats in Sweden's Large Lakes*. Project Report, Swedish National Space Board.

Poggio, L., Gimona, A., and Brown, I. (2012). Spatio-temporal MODIS EVI gap filling under cloud cover: an example in Scotland. *ISPRS J. Photogramm. Remote Sens.* 72, 56–72. doi: 10.1016/j.isprsjprs.2012.06.003

Raag, L., Sipelgas, L., and Uiboupin, R. (2014). Analysis of natural background and dredging-induced changes in TSM concentration from MERIS images near commercial harbours in the Estonian coastal sea. *Int. J. Remote Sens.* 35, 6764–6780. doi: 10.1080/01431161.2014.963898

Santer, R., and Zagolski, F. (2009). *ICOL-Improve Contrast between Ocean & Land, ATBD (Algorithm Theoretical Basis Document)-MERIS Level-1C, Version: 1.1*. Available online at: http://www.brockmann-consult.de/beam-wiki/download/attachments/13828113/ICOL_ATBD_1.1.pdf (Accessed December 20, 2018).

Savchuk, O. P. (2018). Large-Scale Nutrient Dynamics in the Baltic Sea, 1970–2016. *Front. Mar. Sci.* 5:95. doi: 10.3389/fmars.2018.00095

Schiller, H., and Doerffer, R. (1999). Neural network for emulation of an inverse model operational derivation of Case II water properties from MERIS data. *Int. J. Remote Sens.* 20, 1735–1746. doi: 10.1080/014311699212443

Schroeder, T., Behnert, I., Schaale, M., Fischer, J., and Doerffer, R. (2007). Atmospheric correction algorithm for MERIS above case-2 waters. *Int. J. Remote Sens.* 28, 1469–1486. doi: 10.1080/01431160600962574

Shom (2018). Shom (Service Hydrographique et Océanographique de la Marine) (2018). *EMODnet Digital Bathymetry (DTM* 2018). doi: 10.12770/18ff0d48-b203-4a65-94a9-5fd8b0ec35f6

Snoeijs-Leijonmalm, P., Schubert, H., and Radziejewska, T. (2017). *Biological oceanography of the Baltic Sea*. Dordrecht: Springer Science & Business Media. doi: 10.1007/978-94-007-0668-2

Stigebrandt, A. (2001). "Physical oceanography of the Baltic Sea," in *A Systems Analysis of the Baltic Sea*, eds F. V Wulff, L. A. Rahm, and P. Larsson (Berlin; Heidelberg: Springer), 19–74. doi: 10.1007/978-3-662-04453-7_2

Szymczak, E., and Galinska, D. (2013). Sedimentation of suspensions in the Vistula River mouth. *Oceanol. Hydrobiol. Stud.* 42, 195–201. doi: 10.2478/s13545-013-0075-x

Toming, K., Arst, H., Paavel, B., Laas, A., and Nõges, T. (2009). Spatial and temporal variations in coloured dissolved organic matter in large and shallow Estonian waterbodies. *Boreal Environ. Res.* 14, 959–970. Available online at: https://helda.helsinki.fi/bitstream/handle/10138/233610/ber14-6-959.pdf?sequence=1 (Accessed December 20, 2018).

Toming, K., Kutser, T., Uiboupin, R., Arikas, A., Vahter, K., and Paavel, B. (2017). Mapping water quality parameters with Sentinel-3 Ocean and Land Colour Instrument imagery in the Baltic Sea. *Remote Sens.* 9:1070. doi: 10.3390/rs9101070

Vaičiute, D., Bresciani, M., and Bučas, M. (2012). Validation of MERIS bio-optical products with in situ data in the turbid Lithuanian Baltic Sea coastal waters. *J. Appl. Remote Sens.* 6, 63568–63561. doi: 10.1117/1.JRS.6.063568

Vazyulya, S., Khrapko, A., Kopelevich, O., Burenkov, V., Eremina, T., and Isaev, A. (2014). Regional algorithms for the estimation of chlorophyll and suspended matter concentration in the Gulf of Finland from MODIS-Aqua satellite data. *Oceanologia* 56, 737–756. doi: 10.5697/oc.56-4.737

Voipio, A. (1981). "The Baltic Sea," in *Elsevier Oceanography Series*, Vol. 30 (Amsterdam: Elsevier).

Walsby, A. E., Hayes, P. K., and Boje, R. (1995). The gas vesicles, buoyancy and vertical distribution of cyanobacteria in the Baltic Sea. *Eur. J. Phycol.* 30, 87–94. doi: 10.1080/09670269500650851

Wasmund, N., Andrushaitis, A., Łysiak-Pastuszak, E., Müller-Karulis, B., Nausch, G., Neumann, T., et al. (2001). Trophic status of the south-eastern Baltic Sea: a comparison of coastal and open areas. *Estuar. Coast. Shelf Sci.* 53, 849–864. doi: 10.1006/ecss.2001.0828

Weiss, D. J., Atkinson, P. M., Bhatt, S., Mappin, B., Hay, S. I., and Gething, P. W. (2014). An effective approach for gap-filling continental scale remotely sensed time-series. *ISPRS J. Photogramm. Remote Sens.* 98, 106–118. doi: 10.1016/j.isprsjprs.2014.10.001

Wickham, H. (2016). *ggplot2: Elegant Graphics for Data Analysis.* New York, NY: Springer-Verlag. Available online at: http://ggplot2.org

Wozniak, S. B., Meler, J., Lednicka, B., Zdun, A., and Ston-Egiert, J. (2011). Inherent optical properties of suspended particulate matter in the southern Baltic Sea. *Oceanologia* 53, 691–729. doi: 10.5697/oc.53-3.691

Conflict of Interest Statement: The authors declare that the research was conducted in the absence of any commercial or financial relationships that could be construed as a potential conflict of interest.

Copyright © 2019 Kyryliuk and Kratzer. This is an open-access article distributed under the terms of the Creative Commons Attribution License (CC BY). The use, distribution or reproduction in other forums is permitted, provided the original author(s) and the copyright owner(s) are credited and that the original publication in this journal is cited, in accordance with accepted academic practice. No use, distribution or reproduction is permitted which does not comply with these terms.

frontiers in Marine Science

ORIGINAL RESEARCH
published: 04 December 2018
doi: 10.3389/fmars.2018.00456

Study on Different Fractions of Organic Molecules in the Baltic Sea Surface Microlayer by Spectrophoto- and Spectrofluorimetric Methods

Violetta Drozdowska[1], Piotr Kowalczuk[2], Marta Konik[2] and Lidia Dzierzbicka-Glowacka[1]*

[1] Physical Oceanography Department, Institute of Oceanology, Polish Academy of Sciences, Sopot, Poland, [2] Marine Physics Department, Institute of Oceanology, Polish Academy of Sciences, Sopot, Poland

The sea surface microlayer (SML), created by surface active organic molecules (called: surfactants), is a highly active interface between the sea and the atmosphere. In this study we used the absorption and fluorescence analysis of organic matter collected in the SML and in subsurface layer, of 1 m depth, to describe the changes in molecular size and weight and the composition of surfactants. Data were collected during three research cruises in coastal zone and open waters of the Baltic Sea. The values of the CDOM absorption coefficient were higher in the SML about 29% (in the UV light) to 17% (in a blue spectral range), that reveal dominance of low molecular weighted CDOM molecules, absorbing in the UV light, in the SML. The spectral slope coefficients at different spectral ranges, $S_{\Delta\lambda}$ increased with salinity, while the slope coefficient for 350–400 nm reach lower values by 10.5% in SML compared to SS, caused by an effect of irradiation on the SML. The fluorescence intensities of the main peaks at Excitation Emission Matrix spectra belonging to the main fluorescing components of marine organic matter, called: *A*, *C*, *M*, *T*, were higher in SML by 41, 43, 41, and 14% compared to SS. The ratio of fluorescence intensities, $(M+T)/(A+C)$ and humification index, *HIX*, in the SML were, respectively, higher by 17.9% and lower by 10.7% compared to SS. These relationships reveal more intensive process of *in situ* produced components in the SML as well as faster removal of humic components of high MW in the SML. We have observed an increase of spectral slope ratio, S_R, ($S_{275-295} > S_{350-400}$) with increasing salinity (from 4.5 to 7.94 of practical salinity), being proof that the samples acquire more marine in character. The S_R increased with salinity 33.5 and 23.6% in the SML and SS, respectively, and their maximal values in open water were still maintained. The fluorescence intensity of all FDOM peaks decreased in the same salinity gradient. The decrease rate was higher in SML for the fluorescing peaks by 34, 36, and 26% for *A*, *C*, and *M*, respectively than in the SS. Decrease rate indicated the susceptibility to photochemical degradation of respective peaks. This effect was strongest for C, while T peak was almost unbleached. The fluorescence intensity decrease rate was smaller in SS what indicated shielding effect of the SML.

Keywords: surfactants, fluorescence, absorption, sea surface microlayer, the Baltic Sea, CDOM, FDOM

OPEN ACCESS

Edited by:
Laura Tuomi,
Finnish Meteorological Institute, Finland

Reviewed by:
Manuel Dall'Osto,
Instituto de Ciencias del Mar (ICM), Spain
X. Antón Álvarez-Salgado,
Instituto de Investigaciones Marinas, Spain

****Correspondence:***
Violetta Drozdowska
drozd@iopan.pl

Specialty section:
This article was submitted to Marine Biogeochemistry, a section of the journal Frontiers in Marine Science

Received: *30 April 2018*
Accepted: *13 November 2018*
Published: *04 December 2018*

Citation:
Drozdowska V, Kowalczuk P, Konik M and Dzierzbicka-Glowacka L (2018) Study on Different Fractions of Organic Molecules in the Baltic Sea Surface Microlayer by Spectrophoto- and Spectrofluorimetric Methods. Front. Mar. Sci. 5:456. doi: 10.3389/fmars.2018.00456

INTRODUCTION

The sea surface microlayer (SML), commonly defined as the upper 0–1 mm of the surface ocean (Liss and Duce, 1997) is described by different physical properties than the underlying layers due to the molecules that form the surface film (Hardy, 1982). The SML is almost ubiquitous and covers most of the surface of the ocean, even under conditions of high turbulence (Cunliffe et al., 2013). The SML is created by the surface active organic molecules, called surfactants, characterized by an amphiphilic structure, i.e., with hydrophobic and hydrophilic heads. The hydrophobic properties of the surfactants cause the aquatic environment to push them to the interfacial boundary, to minimize the internal energy of the aqueous system. The SML interacts with the surface accumulation of organic matter produced by biological processes in the underlying water column (Galgani et al., 2016; Kurata et al., 2016). The SML also accumulates a variety of colloidal and particulate organic matter that may be substrates for bacterioneuston, and therefore the SML is called as a complex hydrate "gel" of macromolecules and colloidal material (Sieburth, 1983).

The organic matter in the sea have the allochthonous (from terrestrial input) and autochthonous (derived from primary production in the water column) origin and dissipate due to loss of material at the sea surface by microbial degradation, chemical and photo-chemical processes and loss due to absorption and adsorption onto particles (Aiken et al., 1985; Tilstone et al., 2010; Cunliffe et al., 2011; Cunliffe et al., 2013; Engel et al., 2017). The main mechanism that affects the organic matter in the surface top layer of the ocean is the sunlight. The loss of the color (photobleaching) occurs simultaneously with photochemical modification in the organic molecules. Large organic molecules undergo photochemical and biological degradation, that changes their optical properties and the depth of penetration of solar radiation into the sea, especially in the UV and PAR spectral range. Studies on a role of DOM in limiting the light penetration into the sea (Williamson, 1995; Zepp et al., 1998) and its utilization (Kirk, 1994), reactivity (Williams et al., 2010; Zhang et al., 2013) and transport of inorganic and organic pollutants (Chin et al., 1994; Miller and Zepp, 1995; Stedmon et al., 2003; Pastuszak et al., 2012) are carried out intensively in various marine basins.

The organic matter dynamics are often studied by the changes in chromophoric or fluorophoric fractions of DOM (i.e., CDOM or FDOM) (Boehme and Wells, 2006; Hudson et al., 2007; Cisek et al., 2010; Williams et al., 2010; Drozdowska et al., 2013, 2017). CDOM absorbs light in the UV and visible region and its absorption spectrum decreases exponentially toward longer wavelengths. CDOM participates in various photochemical reactions, including the production of CO and dissolved inorganic carbon (Gao and Zepp, 1998; Szymczycha et al., 2017) and remineralization of terrestrial DOM in a system of the Baltic Sea (Kuliński et al., 2016). The photochemical reactions transform it into smaller and more bio-available forms, and photo-bleaching is recognized as the most important sink for CDOM in the ocean (Zhou and Mopper, 1997; Moran et al., 2000; Goldstone et al., 2004; Zhang et al., 2013; Gonsior et al., 2014; Timko et al., 2015). A specific structure of the energy levels of the complex CDOM molecules results in a specific spectral distribution of the light intensity. Absorption and fluorescence spectra may allow the identification of chromophores and fluorophores belonging to the organic molecules and their sources (Højerslev, 1974, 1988; Coble, 1996; Chari et al., 2012). Changes in the values of the spectral slope coefficients varied inversely proportionally to the CDOM molecular mass (Amon and Budeus, 2003; Twardowski et al., 2004; Helms et al., 2008). According to the experiments carried out by Helms et al. (2008) the values of $S_{275-295}$ and S_R should be higher in the SML due to more effective photobleaching process in the SML. Earlier studies have proposed that the UV-Vis absorption spectra of CDOM at longer wavelengths (>350 nm) originate from a continuum of charge transfer (CT) states between a large number of charge acceptors and charge donors (Del Veccio and Blough, 2004). The absorption at shorter wavelengths, in the UV, should rather be a superposition of discrete chromophores. This suggests a different optical and molecular origin of the absorption signals recorded for the same sample. The UV irradiation influences chromophores, associated with HMW CDOM, and destroys them resulting in a shift from a pool of HMW to LMW of CDOM molecules. Photobleaching process, more effective in the SML, influences the mass balance between high-molecular weighted (HMW) CDOM and low-molecular weighted (LMW) CDOM in the surface layers. The amplitude of $a_{CDOM}(\lambda)$ curve is a proxy for concentration of CDOM, the spectral slope is often used as a proxy for CDOM composition, including the ratio of fulvic to humic acids and molecular weight (Carder et al., 1989; Blough and Green, 1995; Twardowski et al., 2004).

The other method for identification complex and labile organic matter compounds is the fluorescence spectroscopy. Coble (1996) attributed the distinct fluorescence intensity peaks of Excitation Emission Matrix to different types of fluorophores found in natural waters; where peak A (ex./em. – excitation and emission – 250/437 nm) is attributed to terrestrial UV humic like substances; peak C (ex./em. 310/429 nm) represents terrestrial visible-humic like substances; peak M (ex./em. 300/387 nm) characterizes marine humic like substances; and peak T (ex./em. 270/349 nm) represents proteinaceous substances (Zhang et al., 2013). Fluorescence intensities of the main FDOM components: A, C, M, and T (in R.U.) can be used as a proxy of FDOM concentration (Kowalczuk et al., 2005; Loiselle et al., 2009; Drozdowska and Fateyeva, 2013; Drozdowska and Józefowicz, 2015; Drozdowska et al., 2017). Additionally, several fluorescing indices help in describing the FDOM sources. The humification index, *HIX*, reflects the structural changes that occurred during the humification process, causing an increase in both aromaticity (the ratio C/H) and condensation in DOM molecules (Williams et al., 2010; Chen et al., 2011; Chari et al., 2012). Another fluorescent index allowing description of the DOM composition and source is the $(M + T)/(A + C)$ ratio.

The absorption and fluorescence spectra allow the identification of the sources of organic matter. Additionally, several absorption ($S_{\Delta\lambda}$ in different spectral ranges and a slope ratio) and fluorescence (the ratio of the fluorescence intensities $(M + T)/(A + C)$ and *HIX*) indices help in describing the

changes in molecular size and weight as well as in composition of organic matter.

The Baltic Sea is semi-enclosed sea with the limited water exchange with the Atlantic through the Danish Straits and it has unique optical properties because of a very high input of fresh water from the large surrounding drainage area (Lepparanta and Myrberg, 2009). Previous studies proved that the optical properties of the Baltic Sea water are determined to a large extent by light absorption by CDOM (Højerslev, 1989). Maximum freshwater runoff occurs in April/May and coincidents with phytoplankton blooms. In the winter, wind-driven mixing leads to the vertical thermohaline circulation that reduce biological activity and riverine outflow and results in clearer surface waters (Olszewski et al., 1992; Kowalczuk, 1999; Kowalczuk et al., 2010). CDOM has a significant influence on the spectral properties of the apparent optical properties of the Baltic Sea water (Darecki et al., 2003; Kowalczuk et al., 2005).

Absorption and fluorescence investigations, presented herein, included the open and coastal regions of the Baltic Sea. Measurements were carried out along the transect from the Vistula river outlet to the open sea (Gdansk Deep) and along the transect running across the Baltic Proper, on the section from the Arkona Basin to the Gdansk Deep, i.e., in a coastal zone as well as far from the estuaries and lands. The fluorescence and absorption measurements of the samples collected from a SML and sub-surface layer (SS), at a depth of 1 m, during three research cruises in the Baltic Sea were carried out on 'raw' and filtered samples, to test how the filtration process affects the results of surfactant concentration and composition. One of the main goals of our work is to characterize the specific luminescent properties of molecules present in the SML. While the SML is a complex of dissolved and colloidal and particulate organic matter (Sieburth, 1983) the filtration process was omitted in a part of our laboratory procedures, so as not to get rid of the essential ingredients of the "gel."

The authors have conducted research on the SML properties in the several estuaries of the southern Baltic Sea for almost 10 years (Drozdowska et al., 2013, 2015, 2017; Drozdowska and Józefowicz, 2015). But the results concerned the coastal zone only. The new dataset, as the results from the cruises in 2015 and 2016 concerning spatially and hydrological diverse areas, prompted us to perform comparative analyzes of the results. The objectives of the research is to determine what physical parameters of the environment affect the composition of surfactants, where there is no significant impact of rivers. The main objectives are (i) to detect any changes in surfactant concentration and composition in the open sea and in coastal waters and which components predominate in open water; (ii) to evaluate/estimate differences in spectroscopic properties performed on 'raw' and filtered samples.

MATERIALS AND METHODS

Field Works and Sampling

Sampling of the seawater probes for studying the absorption and fluorescence properties of organic matter in the SML and SS were carried out during three cruises: one in a summer (7–10 June) 2015 on a board of R/V Academik Ioffe, and two in an autumn 2016 on R/V Oceania (**Figure 1**). During the research cruise in June 2015, sampling was made on 25 stations, across the transect through the Baltic Proper from the Arkona Basin through Bornholm Basin and Slupsk Furrow to the Gdansk Deep. The ship was slowing down on the stations allowing the surface water to be collected into the wide container. Next, after 15 min, the newly formed SML was collected by the Glass Plate (Falkowska, 1999). The collected samples were prepared to laboratory measurements. The samples collected on the first three stations, on 7 June, were frozen, while the next samples (collected in 8–10 June) were put to a refrigerator and were analyzed immediately after the end of the cruise in a lab, within 48 h after sampling. During two research cruises in 2016: on 24 September and 2 November, samplings were conducted across the transect from the Vistula River outlet, to the open waters in Gdansk Deep. The seawater samples from SML were collected by the Garrett Screen (Garrett, 1965; Carlson, 1982), mesh 18. The screen was firstly immersed in the water, parallel to the sea surface, to stabilize the surface microfilm and carefully raised in a horizontal position. Then water was poured to a polyethylene bottle. In September and November' 2016, the samples from the SS, using a Niskin bottle, were taken as well. Sampling by stainless-steel Garrett Screen, GS, yields the collection of a relatively thick layer compared to Glass Plate, GP, sampling technique, which may cause the differences in the results. However, screen samples are characterized by a higher degree of dilution with underlying water, hence the quantity of organic molecules is rather representative for the thinner thickness of the water layer. Additionally, the results of absorption and fluorescence measurements concerning the station in the open Baltic Sea, collected by GP on R/V Akademik Ioffe, do not differ from those concerning the last station of the transect V (at the Gdansk Deep) by GS on R/V Oceania. Each time about 1 L of the SML water was collected. Sampling during the cruises in 2016 were done at the last day of the cruise and the lab analyses were performed at the next day, so within 24 h after sampling. The part of water samples were passed through Sartorius 0.2 μm pore cellulose membrane filters to remove bigger and fine-sized particles. The 'raw' and filtered water samples were stored in the dark at 4°C until analysis in the land-based laboratory. On every station during the cruises the hydrographic data, of the upper layer of 1 m, were recorded; on R/V Akademik Ioffe by a Idronaut 320+ while on R/V Oceania with a SeaBird SBE 911+ CTD system. Moreover the meteorological observations were made to control the state of the sea, and during our experiments sea state was beneath 4B and a lack of the precipitation.

Laboratory Measurements

Spectrophotometric and spectrofluorometric measurements of seawater samples were performed in the laboratories of the Institute of Oceanology, the Polish Academy of Sciences. Before any spectroscopic measurements, the water samples were left to warm up to room temperature. The absorption and fluorescence analysis were performed on the 'raw' and filtered samples, except for a summer' 2015, when the fluorescence measurements

were performed on the 'raw' samples only. During the other experiments the measurements on 'raw' and filtered water samples from the SML and SS were carried out simultaneously.

Absorption Measurements and Absorption Indices

CDOM absorption spectra were measured on Perkin Elmer Lambda 650 spectrophotometer in the spectral range 240–700 nm. For measurements the quartz 10 cm cuvettes were used and an ultrapure Milli-Q water was used as a reference signal. The recorded absorbance $A(\lambda)$ spectra were processed to get the curves of the CDOM absorption coefficients $a_{CDOM}(\lambda)$, m^{-1}. Next, a non-linear least-squares fitting method was applied (Stedmon et al., 2000; Kowalczuk et al., 2006) to calculate the spectral slope coefficient, $S_{\Delta\lambda}$, in the several spectral ranges: 275–295 and 350–400 nm, $S_{275-295}$ and $S_{350-400}$, respectively. The dimensionless parameter called "a slope ratio," S_R, as a ratio of two spectral slope coefficients, $S_{275-295}$ and $S_{350-400}$, was calculated as well. The detailed procedure is described in the papers by Kowalczuk et al. (2009) and Drozdowska et al. (2017).

Fluorescence Measurements and Fluorescence Indices

The 3D-fluorescence spectra (EEM) were carried out on Varian Cary Eclipse scanning spectrofluorometer in a 1 cm path length quartz cuvette using a 4 mL sample volume. Series of emission scans (280–600 nm at 2 nm resolution) over an excitation wavelength range from 250 to 500 nm at 10 nm increments were measured. The instrument was configured to collect the signal using maximum lamp energy and 5 nm band pass on both the excitation and emission monochromators. The results of fluorescence measurements were not corrected by the inner filter effect that may lead to the re-absorption of the emitted light (for the samples with CDOM absorption coefficient $> 10\ m^{-1}$). To normalize the EEM spectra of seawater samples, the fluorescence EEM spectrum of Milli-Q water, as a blank sample, was measured using the same instrumental set-up. The intensity of the Milli-Q water Raman signal, as the integral in the spectral range: 374–424 nm of the Raman emission spectrum, exited at 350 nm, (Murphy et al., 2010) was calculated. The blank Milli-Q EEM spectrum was subtracted from the all EEM spectra of seawater samples. Then all blank corrected EEMs of seawater sample spectra were normalized to Milli-Q water Raman emission [scaled to Raman units (R.U.)] by dividing the resulting spectra by calculated Raman emission intensity value. The procedure is described in details in the literature (Drozdowska et al., 2013, 2017).

The humification index, *HIX*, is calculated as a ratio of two fluorescence bands, in the near-visible and UV-A range of the fluorescence spectrum excited at 255 nm (Zsolnay et al., 1999; Glatzel et al., 2003). That is a ratio of a fluorescence intensity at a blue-part of the spectrum, at: 435–480 nm to a fluorescence intensity at the UV-A part: 330–346 nm. *HIX* is directly proportional to the humic content of DOM, where *HIX* values around 1–2 are associated with non-humified plant materials while values >10 are commonly reported for fulvic acid extracts (Zsolnay et al., 1999; Williams et al., 2010).

The fluorescent index, the $(M + T)/(A + C)$ ratio, allows description of the DOM composition and source. The $(M + T)/(A + C)$ ratio is a derivative of the β/α ratio, proposed by Parlanti et al. (2000); where β region, the emission at 380 nm, is divided by α region, the emission band between 420 and 435 nm – for excitation at 310 nm. The fluorescence intensities, ratio, $(M + T)/(A + C)$, allows the assessment of the relative contribution of dissolved organic matter recently produced *in situ*, M and T, to humic substances characterized by highly complex high-molecular-weighted (HMW) structures, A and C (Parlanti et al., 2000; Osburn et al., 2009; Wilson and Xenopoulos, 2009; Williams et al., 2010; Drozdowska et al., 2015). Values of the ratio >1 indicate the predominant amount of autochthonous DOM molecules, while values of <0.6 indicate the allochthonous ones (Huguet et al., 2009). The $(M + T)/(A + C)$ ratio is correlated positively with bacterial production of terrestrial DOM and indicate the presence of microbially derived DOM (peak T) in aquatic ecosystems (McKnight et al., 2001). Additionally, the ratio is well-correlated with a photobleaching and points to a decrease in terrestrial components (A and C) decomposed by the irradiation (Williams et al., 2010).

RESULTS

Analysis of the Absorption Data

The absorption spectra recorded for the samples collected from the SML and SS during three Baltic cruises show the differences in the slope of the curves as well as in the values of the spectral distribution of the absorption coefficient for different seasons and studied areas. The lowest values of CDOM absorption coefficient were recorded for the Baltic Proper, in June, due to the largest distance from lands and river outflows and in November, due to low biology activity and reduced river water inflows. The CDOM absorption coefficient recorded for 'raw' and filtered samples at the same station show higher values for 'raw' samples, with the exception for short-UV spectral region, where the higher values are reached for the filtered samples. Moreover, the curves of the spectral resolution of the CDOM absorption coefficient for the samples collected at the very mouth of the river have less inclined shape, what means a presence of a greater amount of components absorbing at longer wavelengths, 300–400 nm (Grzybowski, 2000; Twardowski et al., 2004; Helms et al., 2008).

Figure 2 presents the relation between salinity and CDOM absorption coefficient at several wavelengths for 'raw' and filtered samples collected from the SML and SS during Baltic cruises. The graph shows the decrease of CDOM absorption coefficient, along with an increase in salinity. As one can see, the CDOM absorption coefficient decreases and the fastest decrease (the highest value of a linear regression coefficient) occurs at the UV range, wavelengths 254 nm, while the slowest one at the longer wavelength, 410 nm, in both SML and SS (Twardowski et al., 2004; **Table 1**).

The CDOM absorption coefficient has lower values for filtered waters in the entire examined light spectrum. The wavelength

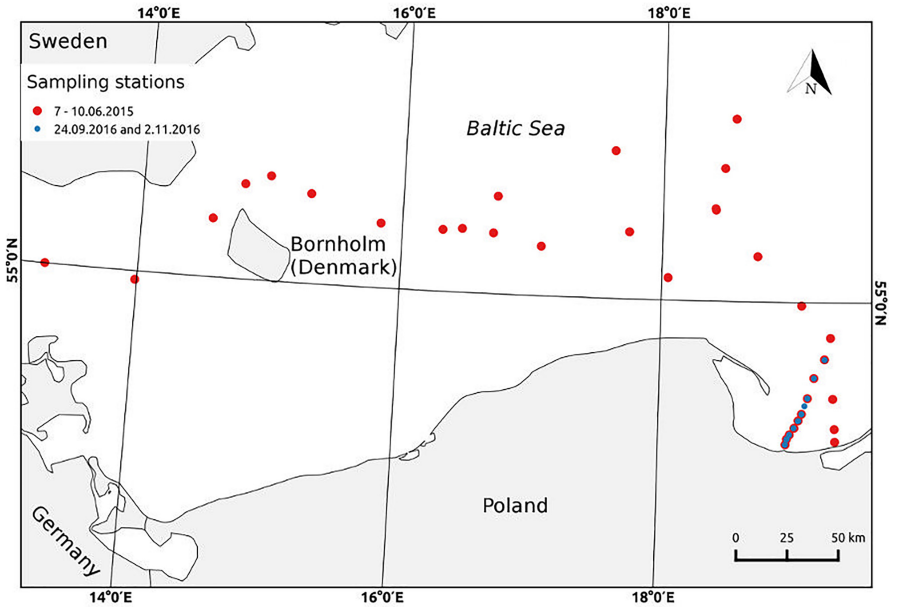


FIGURE 1 | Map of sampling stations during the cruises in June' 2015, on R/V Akademik Ioffe (red dots) and in September and November' 2016 on R/V Oceania (blue dots).

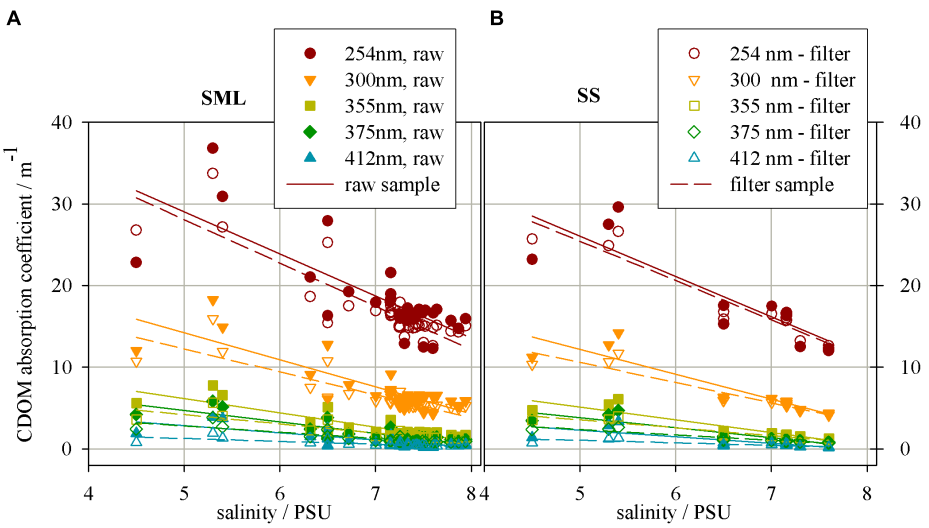


FIGURE 2 | The relation between salinity and CDOM absorption coefficient in different wavelength for the samples collected from **(A)** a surface microlayer (SML) and **(B)** a depth of 1 m (SS), for 'raw' and filtered samples.

254 nm was chosen due to specific electron transition occuring in the region of the UV range, for some aromatic hydrocarbons. These molecules are the precursor for components of certain types of humic substances (particularly those derived from terrestrial sources).

Differences between the values of regression coefficients between SML and SS as well as filtered and 'raw' samples are clearly visible (see **Table 1**). However, due to the uncertainty (standard deviations) of the obtained regression coefficients, it was necessary to check the hypothesis that these coefficients are significantly different. We put the null hypothesis H_0 that the coefficients are equal and tested this hypothesis. Significance tests were calculated for the linear correlations between salinity and the values of CDOM absorption coefficient yielded for different samples. The significant ratio, SR, was calculated as follows:

$SR = |a_1 - a_2|/\sqrt{(S_{a_1})^2 + (S_{a_2})^2}$; where a_1 and a_2 – regression coefficients of the two relations, S_{a_1} and S_{a_2} – the standard deviation of the regression coefficients. If $SR > 1.96$ it means that we can reject the hypothesis H_0 that the regression coefficient are equal at $P < 0.05$.

TABLE 1 | The relation between salinity and the CDOM absorption coefficients (**Figure 2**).

For $a_{CDOM}(\lambda)$	Linear regression coefficients between $a_{CDOM}(\lambda)$ and salinity; $a_{CDOM}(\lambda) = a \cdot Salinity + b$					
	a (Sa)	b (Sb)	r^2	a (Sa)	b (Sb)	r^2
λ/nm	SML – 'raw' samples			SML – filtered samples		
254	−5.13 (0.73)	54.68 (5.24)	0,54	−5.31 (0.50)	54.6 (3.6)	0,76
300	−3.32 (0.38)	30.82 (2.7)	0,67	−2.81 (0.29)	26.25 (2.05)	0,73
355	−1.76 (0.17)	14.96 (1.24)	0,74	−1.13 (0.11)	9.86 (0.81)	0,74
375	−1.4 (0.14)	11.69 (0.99)	0,73	−0.87 (0.078)	6.71 (0.56)	0,75
412	−0.89 (0.12)	7.29 (0.89)	0,55	−0.35 (0.053)	3.01 (0.38)	0,55
λ/nm	SS – 'raw' samples			SS – filtered samples		
254	−4.93 (0.77)	50.67 (5.25)	0,76	−4.82 (0.42)	49.5 (2.84)	0,91
300	−3.05 (0.37)	27.49 (2.53)	0,84	−2.48 (0.24)	23.02 (1.62)	0,89
355	−1.56 (0.19)	12.89 (1.29)	0,84	−0.97 (0.09)	8.39 (0.63)	0,89
375	−1.23 (0.16)	9.99 (1.1)	0,82	−0.67 (0.062)	5.72 (0.42)	0,9
412	−0.79 (0.17)	6.21 (1.16)	0,62	−0.31 (0.06)	2.56 (0.38)	0,69

Firstly, the calculations of the H_0 were made for the absorption results. The values of *SR* referring to the differences between the regression coefficients for filtered and 'raw' samples, for the SML or SS separately, are <1.96 in the UV spectral range, in both layers. Thus, the differences between filter and 'raw' samples are at the UV light (254 and 300 nm) statistically irrelevant. The values of *SR*, are >1.96 at blue/visible light (355, 375, and 412 nm), that support the significant differences between filtered and 'raw' samples, both in the SML and SS. Next, the tests of significant differences for the regression coefficients for the SML and SS samples were calculated, for the filtered and 'raw' ones separately. The *SR* is about 1 (less than 1.96) in the all spectral range, so the differences between the regression coefficients for the SML and SS are irrelevant at $P < 0.05$, for both, the filter and 'raw' samples.

Analysis of the Fluorescence Data

Studies on 3D fluorescence spectra allowed following changes in the intensity of emission bands belonging to the fluorophores A, C, M, and T. Peak intensity values (in R.U.) of the fluorescence bands of the basic FDOM components decreased with increasing salinity both in the SML and SS, **Figures 3A** and **B**, respectively. The linear regression coefficients of the relation between fluorescence intensity and salinity reach higher values in the SML waters than SS. The values of linear regression analysis are included in **Table 2**. The analysis of fluorescence spectra also allowed following the changes in the percentage composition of the main components of FDOM (in %) occurring in SML and SS, as shown in **Figures 3C** and **D**, respectively. A percentile contribution of the main FDOM fluorophores, calculated as the ratio of the respective peak intensity (A, C, M, or T) to the sum ($A + C + M + T$) of all peak intensities, gives information about the relative changes of a fluorophore composition in a sample. Changes in the share of individual components in the SML and SS, both in 'raw' and filtered samples, are presented in **Figure 3**.

It can be seen that the fluorescence intensity of a component A decreases faster then C and next M, while T component decreases the most slowly with an increase of salinity (their regression coefficients, a, are as follow: −0.47, −0.3, −0.19, and −0.06 for the SML and −0.35, −0.22, −0.15, and −0.06 for the SS, respectively). All linear regression coefficients were higher in the SML except of T component, for which they were similar in both layers, for both 'raw' and filtered samples (**Table 2**, **Figures 3A**, **B**). Moreover, the percentile composition of the main FDOM components in 'raw' samples in the SML shows that the share of components A and M is almost constant, only C decreases and T increases with salinity. While, in SS the share of components A, M, and C almost do not change throughout the studied area, while T increases (**Figures 3C,D**).

Due to the standard deviations of the regression coefficients, put in **Table 2**, it is necessary to check the hypothesis that the regression coefficients for different relations are significantly different. The values of the *SR* calculated for the differences between the regression coefficients for filtered and 'raw' samples, in the SML and SS separately, show that $SR < 1.96$ in the all fluorescent components (i.e., A, C, M, and T). Thus, the differences between the regression coefficients for filter and 'raw' samples, are statistically insignificant. Next, the tests of significant differences between the regression coefficients between the SML and SS samples, were calculated, for the filtered and 'raw' ones separately. The *SR* ratio oscillate between 1.23–1.79, except the component T (0.23–0.41). Thus, the values of $SR < 1.96$, so the differences between the regression coefficients for the SML and SS are insignificant for both, the filter and 'raw' samples at $P < 0.05$.

Analysis of the Absorption Indices

Figure 4 shows the values of the slope coefficients, $S_{275-295}$ and $S_{350-400}$ (in nm^{-1}) in different wavelength ranges, respectively: 275–295 nm, 350–400 nm as well as the dimensionless parameter called "a slope ratio," S_R. The slope ratio coefficient, as the ratio of two spectral slope coefficients, $S_{275-295}$ and $S_{350-400}$,

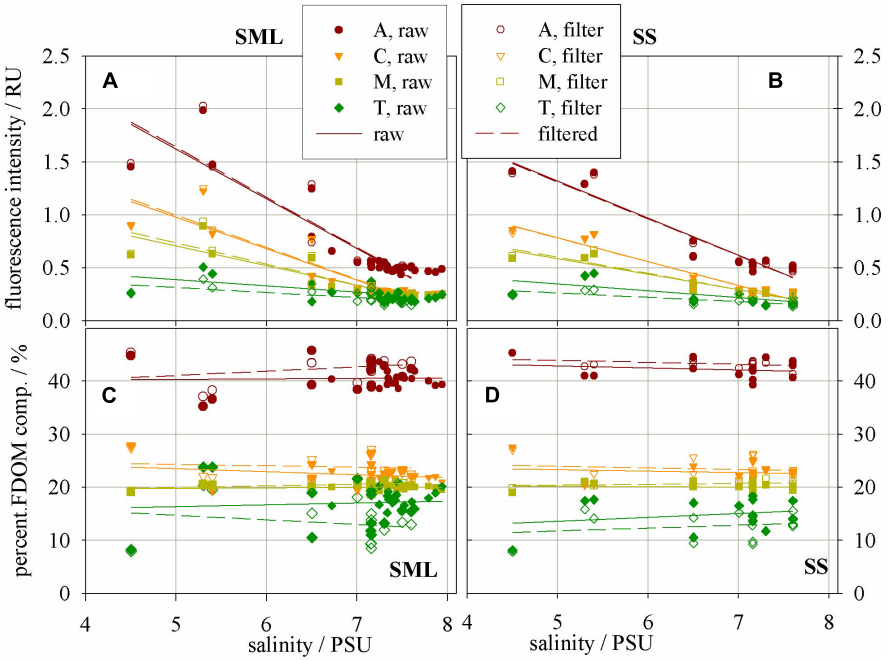


FIGURE 3 | Fluorescence intensity – a proxy of concentration of fluorophores – the main FDOM components in **(A)** SML and **(B)** SS; Percentage composition of the main FDOM components in **(C)** SML and **(D)** SS.

TABLE 2 | The relation between salinity and the fluorescence intensities of FDOM components (**Figure 3**).

Linear regression coefficients between FDOM component and salinity; *fl.intens.*(*FDOM comp.*) = *a* · *Salinity* + *b*						
	a (Sa)	**b (Sb)**	r^2	**a (Sa)**	**b (Sb)**	r^2
FDOM component	**SML – 'raw' samples**			**SML – filtered samples**		
A	−0,47 (0.066)	3.97 (0.45)	0,81	−0,47 (0.07)	4.0 (0.46)	0,80
C	−0,30 (0.043)	2.46 (0.29)	0,80	−0,3 (0.04)	2.51 (0.3)	0,80
M	−0,0.19 (0.03)	1.64 (0.21)	0,75	−0,20 (0.03)	1.73 (0.23)	0,74
T	−0,0.06 (0.027)	0.68 (0.18)	0,28	−0.05 (0.018)	0.55 (0.12)	0,37
FDOM component	**SS – 'raw' samples**			**SS – filtered samples**		
A	−0,35 (0.031)	3.07 (0.21)	0,91	−0,35 (0.03)	3,05 (0.19)	0,93
C	−0,22 (0.02)	1.91 (0.13)	0,91	−0,22 (0.02)	1,9 (0.13)	0,92
M	−0,15 (0.013)	1.31 (0.09)	0,90	−0,15 (0.015)	1,37 (0.1)	0,89
T	−0.064 (0.018)	0.67 (0.12)	0,49	−0.04 (0.008)	0,47 (0.05)	0,68

TABLE 3 | The equations related to **Figure 4**.

$a_{CDOM}(\lambda) = 2.303 \times A(\lambda)/l$ $A(\lambda)$ – the corrected spectrophotometer absorbance at wavelength λ l – the optical path length [m]; quartz cuvette – 10 *cm*	Eq. 1
The CDOM absorption curve: $a_{CDOM}(\lambda) = a_{CDOM}(\lambda_0)e^{S(\lambda_0-\lambda)} + K$, $\lambda_0 - 350\,nm$, K – background constant, S and K – estimated simultaneously via non-linear regression using Eq. 2 in the spectral range (300–600 nm)	Eq. 2
Linear regression coefficients between the slope coefficient, S, in different ranges, $\Delta\lambda$, and salinity: $S_{\Delta\lambda} = a \cdot Salinity + b$	Eq. 3

is calculated for the SML and SS. The values of the all slope factors increase with increasing salinity. The values of the spectral slope coefficients in the range 275–295 and 350–400 nm increase with salinity, while in the UV range faster, both in 'raw' and filtered samples in the SML and SS. It occurs under the irradiation causing increasing of $S_{275-295}$ and decreasing of $S_{350-400}$. Generally, during irradiation chromophores associated with HMW CDOM are destroyed during photobleaching process that

gives result in a shift of a significant portion of CDOM molecules from HMW to LMW phase (**Figures 4A**,**B**). In the SML the values of $S_{275-295}$ and $S_{350-400}$ (in nm^{-1}) change in a range 0.0093 to 0.0218 and 0.0085 to 0.019, respectively, while in the SS they change in the ranges: 0.010 to 0.022 and 0.009 to 0.0171, respectively. In the filtered samples the values of spectral slope coefficients in the SML and SS are closed to each other. The values of the spectral slope coefficient $S_{275-295}$ in filtered samples change in the range 0.0178 to 0.0243 and from 0.0192 to 0.0236 for the SML and SS, respectively, while a coefficient $S_{350-400}$ changes in the ranges 0.0171 to 0.0.0233 and 0.0171 to 0.0226 in the SML and SS, respectively. Thus, the changes of a spectral slopes in the study area, with salinity, for the 'raw' samples yielded about 100%, while in the filtered ones 25–35% only, both in the SML and SS.

The results of S_R both in the 'raw' and filtered samples give the values >1, that means a near shore (marine-like) character of the samples (Helms et al., 2008). What is more, the values of S_R in 'raw' samples change in a range from 1.093 to 1.513 and from 1.145 to 1.485 in the SML and SS, respectively. While the ranges of the values of S_R in the filtered samples for the SML and SS are much narrower and the range limits lay close to each other, from 1.029 to 1.3737 for the SML and from 1.027 to 1.269 for the SS. However, the percentile changes of MW in the SML and SS reflected by S_R yield 33.5 and 23.6% for filtered water, respectively and 38.5 and 29.6% for 'raw' ones. Thus, the changes of MW between the SML and SS, both for filtered and 'raw' samples, reveal about 10% and the changes are related to shift in molecular weight caused by photobleaching in the SML.

Analysis of the Fluorescence Indices

The **Figure 5** presents the humification index as well as the ratio of fluorescence intensities at peaks of the main FDOM components in the SML and SS (**Figures 5A** and **B**, respectively), as the results of the degradation processes. The values of *HIX* index are smaller in 'raw' samples, which means that the denominator has a higher value (more component T in 'raw' than in filtered samples). The humification index, *HIX*, changed in the SML in a range from 3.8 to 17.9, while in the SS it ranged from 6.09 to 18.68. *HIX* index achieved a little higher values in the SS than in the SML. Additionally, *HIX* index achieved higher values for both, SML and SS, for filtered samples. The one exception, for filtered samples, are the results obtained for the station at the very mouth of the river. On the graphs on **Figure 5** the changes of the ratio of the fluorescence intensities of FDOM components created in the sea, M and T, to the sum of fluorescence intensity of the components brought in by rivers, A and C, are presented as well. The values of the ratio $(M + T)/(A + C)$, for 'raw' samples, vary in the SML in a range 0.39 to 0.8 while in the SS from 0.36 to 0.63. The results obtained for filtered ones in the SML varied in a range: 0.38 to 0.69,

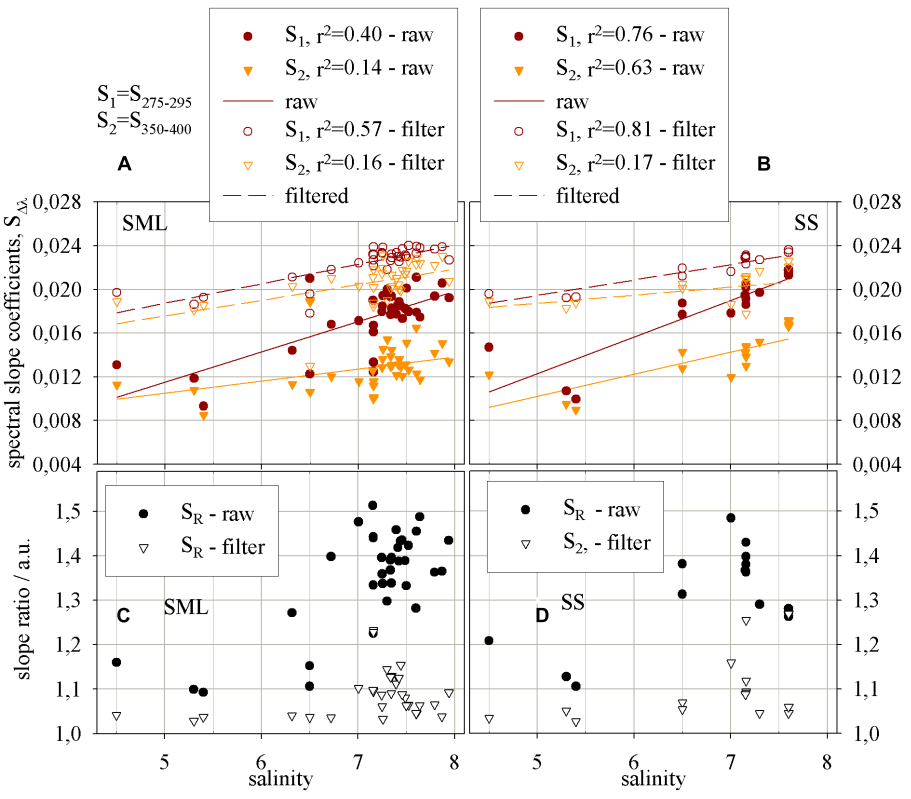


FIGURE 4 | The relations, for the SML and SS, respectively, between salinity and **(A,B)** the spectral slope and **(C,D)** the slope ratio coefficients. Spectral slope coefficients increase (i.e., molecular weight decreases) with raising salinity, for 'raw' and filtered samples, in **(A)** the SML and **(B)** SS. The report of the equations applied to reach the results presented on the graphs – **Table 3**.

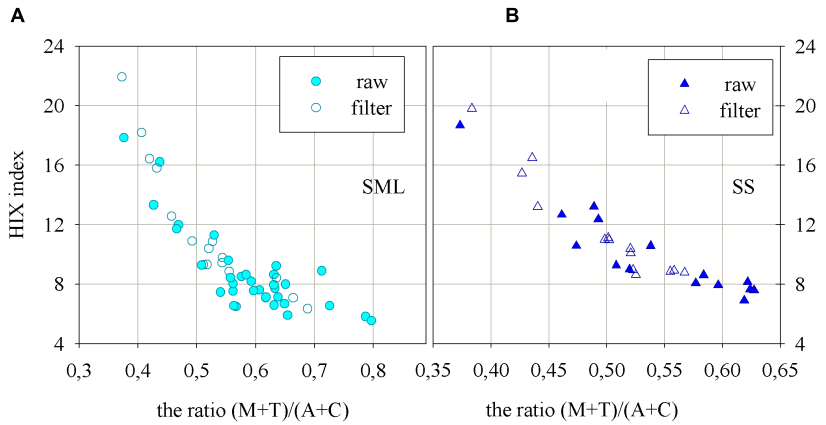


FIGURE 5 | The relation between the ratio of fluorescence intensities of the main components of FDOM, $(M + T)/(A + C)$, and humification index, *HIX*, for the **(A)** SML and **(B)** SS water.

while in the SS: 0.38 to 0.58. The results of the ratio of the fluorescence intensities show higher values in the SML than in the SS and a little higher values in the 'raw' samples than in filtered ones.

DISCUSSION AND CONCLUSION

Our experimental results address two aspects of surfactant photochemistry in brackish sea environments: (i) the influence of photochemical processes on terrestrially derived light-absorbing and fluorescing material resident in the study aquatic system and (ii) what corrections and changes are made by using the 'raw' and filtered water samples when studying the properties and concentrations of surfactants (the molecules of surface-active organic matter).

The CDOM absorption coefficients as well as the fluorescence intensity of FDOM components decrease with increase of salinity. The decrease of the values of the CDOM absorption coefficient reveals the fastest decrease (the highest value of a linear regression coefficient) at the UV range, at the wavelength 254 nm, while the slowest one at the longer wavelength, 410 nm, in both SML and SS. In the UV range some aromatic hydrocarbons, that are the precursor for components of terrestrial humic-like substances, absorb. The highest decrease of the fluorescence intensity of the main FDOM components occurred for a UV-absorbing terrestrial humic-like, component A, then a visible-absorbing terrestrial humic-like, component C, and the slowest decrease for marine humic-like component, M. While protein-like component, T, stayed almost unbleached through the all salinity gradient. The results of fluorescence measurements should be corrected using the inner filter effect that may cause the re-absorption of the emitted light by organic matter in the samples characterized by the CDOM absorption coefficient >10 m^{-1}. However, the inner filter correction was not applied and this can affect the fluorescence of peaks A and T in three stations near the mouth of the Vistula. The regression coefficient for the relation between salinity and the fluorescence intensities of the FDOM components indicate higher values in the SML then in SS. The organic molecules of terrestrial origin are decomposed under the influence of the light more effectively (Chin et al., 1994; Chen et al., 2011; Zhang et al., 2013).

Our studies indicate that photochemical processes that affect the surface ocean, observed during a day-light period (either low-intensity or high-intensity irradiance) more efficiently remove colored and fluorescent components from DOM pool in the SML than SS, like it was explored by Moran et al. (2000). The results confirm the dominant share of the terrestrial humic-like molecules in the all studied area, especially in the SML, also in the open surface waters of the Baltic Sea.

The analysis of absorption data allows concluding that the magnitude of absorption coefficient (molar absorptivity) in the UV is indicative of both the degree of humification that has occurred and the contribution of terrestrial materials present in the organic matter sources (Tilstone et al., 2010). The relative amount of aromatic moieties in aquatic fulvic acids increases with increasing molecular weight (Chin et al., 1994; Chari et al., 2012). The analysis of the slope factors of the $a_{CDOM}(\lambda)$ curve, which change inversely proportional to the molecular mass of the absorbing molecules, indicates the presence of DOM molecules with lower molecular weight in the SML than in SS in the all studied regions of the Baltic Sea.

The analysis of the EEM spectra indicates the higher intensities in the fluorescence spectra for the SML than SS samples. Additionally, the most dynamic portion of the absorbing and fluorescing organic matter are the components C and T, that has been previously attributed to fluorescence from terrestrial humic-like material and aromatic amino acids, respectively (Coble, 1996). The explanation of such changes in C component is a photobleaching process, because C fluorophore is in somewhat more susceptible to photochemical degradation than A and M fluorophores (Moran et al., 2000). An increase in amino acid fluorescence (peak T) indicates probably that bacterial transformation of non-photodegradable estuarine DOM can be a source of new fluorophores. T fluorophores also appeared to

be less susceptible to photodegradation (Moran et al., 2000). The elevated values of humification index, *HIX*, in the SS indicate presence of molecules of higher molecular weight that are more condensed, with higher aromaticity, in the SS than in the SML. The ratio $(M + T)/(A + C)$ indicates higher values in the SML because of the bigger amount of T component and lower amount of terrestrial humic substances disintegrated using photobleaching process in the SML (Williams et al., 2010). What is more, the values of the ratio $(M + T)/(A + C)$ are <1, that indicates the significant participation of allochthonous DOM molecules in the SML, even in the open waters of the Baltic Sea.

Humification index, *HIX* is well-related to the ratio $(M + T)/(A + C)$, and in proportional dependence to the terrestrial constituents of organic matter as well. Humification index, *HIX* well-correlates with concentration of terrestrial DOM, means that much of stream DOM in the studied areas of the Baltic Sea originated from humic-like terrestrial material, similarly like it was reported for a lake water (Williams et al., 2010).

The filtering process slightly affects the results of absorption measurements by lowering the $a_{CDOM}(\lambda)$ values of the filtered samples, except for the UV region, and by changing the shape of the curve. The reason of the weak signal in 'raw' samples in the UV may result from the biology processes of living organisms due to disintegration of absorbing aromatic particles by, i.e., fungi, active in degradation and mineralization of humic substances contained in 'raw' samples (Khundzhua et al., 2013). Anyway, the differences between the absorption spectra of the 'raw' and filtered samples occur mainly in the short UV spectral range only. However, these differences do not cause significant changes in the absorption indices, because they are calculated on the basis of the shapes of the spectra (in other words: are based on the relative differences between the values of CDOM absorption coefficient in the central part of the measuring range (Grzybowski, 2000; Twardowski et al., 2004; Helms et al., 2008). The absorption coefficient has higher values for 'raw' samples in both the SML and SS. While, the filtration process almost does not affect the decrease rate of fluorescence intensities, with the exception of T component. The differences between EEM spectra recorded for 'raw' and filtered samples in the studied fluorescence spectra lay in the region of T component mainly. The protein-like molecules, T component, recently produced in the sea in biological and photodegradation processes are the main component of the "gel" and the most effectively retain on the filter. Additionally, the filtration process influences the percentile composition of A and T in the SML, while in the SS it does not play any role.

The analysis of the slope factors of the $a_{CDOM}(\lambda)$ curve, which are inversely proportional to the molecular mass of the absorbing molecules, indicates the presence of lower MW CDOM and little differentiated molecules in filtered samples. While, in the 'raw' samples there were both HMW molecules in areas of low salinity and a LMW ones in the open sea. The *HIX* index achieved a little higher values in filtered samples, while the ratio $(M + T)/(A + C)$ reached lower results in the filtered ones. Thus, the absorption and fluorescence indices show sensitivity to the filtration, due to the presence of molecules with high molecular mass and complex hydrate "gel" ones or lack thereof in the SML.

The results of marine measurements carried out in coastal and open waters of the Baltic Sea constitute a continuous and consistent sequence of data describing absorption and fluorescence properties of marine surfactants. The quantities describing surfactants, studied in the Gulf of Gdansk and Gdansk Deep and in the Baltic Proper, confirm the dominant share of the terrestrial humic-like molecules in the all studied regions of the Baltic Sea. Moreover, the results obtained at the most saline and distant from land-based sources and shoreline, maintain their almost invariable values in the all open waters. Finally, the authors concluded that the degradation processes of the organic molecules contained in the SML and SS proceed at different rates. Hence, the DOM molecules included in the SML may specifically modify the physical processes associated with the sea surface layer.

AUTHOR CONTRIBUTIONS

VD designed the experiments, performed the field and laboratory works, and wrote the paper. PK provided laboratory instrumentation for spectroscopic analysis, gave scientific guidance, and contributed to the paper. MK and LD-G contributed to data analyzing of the laboratory data. All authors reviewed and commented on the paper.

FUNDING

This work was partly supported by Institute of Oceanology Polish Academy of Sciences and the National Centre for Research and Development within the BIOSTRATEG III (Program No. BIOSTRATEG3/343927/3/NCBR/2017).

ACKNOWLEDGMENTS

The authors thank to the scientific team of the research vessels MS Akademik Ioffe and MS/Y Oceania.

REFERENCES

Aiken, G. R., McKnight, D. M., Wershaw, R. L., and MacCarthy, P. (1985). *Humic Substances in Soil, Sediment and Water: Geochemistry, Isolation and Characterization*. New York, NY: Wiley-Lnterscience. doi: 10.1029/2002JC001594

Amon, R. M. W., and Budeus, G. (2003). Dissolved organic carbon distribution and origin in the Nordic Seas: exchanges with the Arctic Ocean and the North Atlantic. *J. Geophy. Res.* 108:3221. doi: 10.1029/2002JC001594

Blough, N. V., and Green, S. A. (1995). "Spectroscopic characterization and remote sensing of nonliving organic matter," in *Role of Nonliving Organic Matter in the Earth's Carbon Cycle*, eds R. G. Zepp and C. Sonntag (New York, NY: Wiley), 23–45.

Boehme, J., and Wells, M. (2006). Fluorescence variability of marine and terrestrial colloids: examining size fractions of chromophoric dissolved organic matter

in the Damariscotta River estuary. *Mar. Chem.* 101, 95–103. doi: 10.1016/j.marchem.2006.02.001

Carder, K. L., Steward, R. G., Harvey, G. R., and Ortner, P. B. (1989). Marine humic and fulvic acids: their effects on remote sensing of ocean chlorophyll. *Limnol. Oceanogr.* 34, 68–81. doi: 10.4319/lo.1989.34.1.0068

Carlson, D. J. (1982). A field evaluation of plate and screen microlayer sampling techniques. *Mar. Chem.* 11, 189–208. doi: 10.1016/0304-4203(82)90015-9

Chari, N. V., Sarma, H. K., Pandi, S. R., and Murthy, K. N. (2012). Seasonal and spatial constraints of fluorophores in the Midwestern Bay of Bengal by PARAFAC analysis of excitation emission matrix spectra. *Estuar. Coast. Shelf Sci.* 100, 162–171. doi: 10.1016/j.ecss.2012.01.012

Chen, H., Zheng, B., Song, J., and Qin, Y. (2011). Correlation between molecular absorption spectral slope ratios and fluorescence humification indices in characterizing CDOM. *Aquat. Sci.* 73, 103–112. doi: 10.1007/s00027-010-0164-5

Chin, Y.-P., Aiken, G., and O'Loughlin, E. (1994). Molecular weight, polydispersity, and spectroscopic properties of aquatic humic substances. *Environ. Sci. Technol.* 28, 1853–1858. doi: 10.1021/es00060a015

Cisek, M., Colao, F., Demetrio, E., Di Cicco, A., Drozdowska, V., Fiorani, L., et al. (2010). Remote and local monitoring of dissolved and suspended fluorescent organic matter off the Svalbard. *J. Optoelectron. Adv. Mater.* 12, 1604–1618.

Coble, P. (1996). Characterization of marine and terrestrial DOM in seawater using excitation-emission matrix spectroscopy. *Mar. Chem.* 51, 325–346. doi: 10.1016/0304-4203(95)00062-3

Cunliffe, M., Upstill-Goddard, R. C., and Murrell, J. C. (2011). Microbiology of aquatic surface microlayers. *FEMS Microbiol. Rev.* 35, 233–246. doi: 10.1111/j.1574-6976.2010.00246.x

Cunliffe, M. A., Engel, S., Frka, S., Gašparović, B., Guitart, C., Murrell, J. C., et al. (2013). Sea surface microlayers: a unified physicochemical and biological perspective of the air–ocean interface. *Prog. Oceanogr.* 109, 104–116. doi: 10.1016/j.pocean.2012.08.004

Darecki, M., Weeks, A., Sagan, S., Kowalczuk, P., and Kaczmarek, S. (2003). Optical characteristics of two contrasting case 2 waters and their influence on remote sensing algorithms. *Cont. Shelf Res.* 23, 237–250. doi: 10.1016/S0278-4343(02)00222-4

Del Veccio, R., and Blough, N. V. (2004). On the origin of the optical properties of humic substances. *Environ. Sci. Technol.* 38, 3885–3891. doi: 10.1021/es049912h

Drozdowska, V., and Fateyeva, N. L. (2013). "Spectrophotometric study of natural Baltic surfactants – results of marine Experiments," in *Hydrobiology in Environment Protection*, eds T. M. Traczewska and B. Hanus-Lorenz (Wrocław: PWR Press), 25–33.

Drozdowska, V., Freda, W., Baszanowska, E., Rudź, K., Darecki, M., Heldt, J. R., et al. (2013). Spectral properties of natural and oil polluted Baltic seawater – results of measurements and modeling. *Eur. Phys. J. Spec. Top.* 222, 1–14. doi: 10.1140/epjst/e2013-01992-x

Drozdowska, V., and Józefowicz, M. (2015). Spectroscopic studies of marine surfactants in the southern Baltic Sea. *Oceanologia* 57, 159–167. doi: 10.1016/j.oceano.2014.12.002

Drozdowska, V., Kowalczuk, P., and Józefowicz, M. (2015). Spectrofluorometric characteristics of fluorescent dissolved organic matter in a surface microlayer in the Southern Baltic coastal waters. *J. Eur. Opt. Soc. Rapid. Publ.* 10:15050. doi: 10.2971/jeos.2015.15050

Drozdowska, V., Wróbel, I., Markuszewski, P., Makuch, P., Raczkowska, A., and Kowalczuk, P. (2017). Study on organic matter fractions in the surface microlayer in the Baltic Sea by spectrophotometric and spectrofluorometric methods. *Ocean Sci.* 13, 633–647. doi: 10.5194/os-13-633-2017

Engel, A., Bange, H. W., Cunliffe, M., Burrows, S. M., Friedrichs, G., Galgani, L., et al. (2017). The ocean's vital skin: toward an integrated understanding of the sea surface microlayer. *Front. Mar. Sci.* 4:165. doi: 10.3389/fmars.2017.00165

Falkowska, L. (1999). Sea surface microlayer: a field evaluation of teflon plate, glass plate and screen sampling techniques. Part 2. Dissolved and suspended matter. *Oceanologia* 41, 223–240.

Galgani, L., Piontek, J., and Engel, A. (2016). Biopolymers form a gelatinous microlayer at the air-sea interface when Arctic sea ice melts. *Sci. Rep.* 6:29465. doi: 10.1038/srep29465

Gao, H., and Zepp, R. G. (1998). Factors influencing photoreactions of dissolved organic matter in a coastal river of the southeastern United States. *Environ. Sci. Technol.* 32, 2940–2946. doi: 10.1021/es9803660

Garrett, W. D. (1965). Collection of slick-forming materials from the sea surface. *Limnol. Oceanogr.* 10, 602–605. doi: 10.4319/lo.1965.10.4.0602

Glatzel, S., Kalbitz, K., Dalva, M., and Moore, T. (2003). Dissolved organic matter properties and their relationship to carbon dioxide efflux from restored peat bogs. *Geoderma* 113, 397–411. doi: 10.1016/S0016-7061(02)00372-5

Goldstone, J. V., Del Vecchio, R., Blough, N. V., and Volker, B. M. (2004). A multicomponent model of chromophoric dissolved organic matter photobleaching. *Photochem. Photobiol.* 80, 52–60. doi: 10.1562/TM-03-17.1

Gonsior, M., Schmitt-Kopplin, P., Stavklint, H., Richardson, S. D., Hertkorn, N., and Bastviken, D. (2014). Changes in dissolved organic matter during the treatment processes of a drinking water plant in Sweden and formation of previously unknown disinfection byproducts. *Environ. Sci. Technol.* 48, 12714–12722. doi: 10.1021/es504349p

Grzybowski, W. (2000). Effect of short-term sunlight irradiation on absorbance spectra of chromophoric organic matter dissolved in coastal and riverine water. *Chemosphere* 40, 1313–1318. doi: 10.1016/S0045-6535(99)00266-0

Hardy, J. T. (1982). The sea-surface microlayer e biology, chemistry and anthropogenic enrichment. *Prog. Oceanogr.* 11, 307–328. doi: 10.1016/0079-6611(82)90001-5

Helms, J. R., Stubbins, A., Ritchie, J. D., Minor, E. C., Kieber, D. J., and Mopper, K. (2008). Absorption spectral slopes and slope ratios as indicators of molecular weight, source, and photobleaching of chromophoric dissolved organic matter. *Limnol. Oceanogr.* 53, 955–969. doi: 10.4319/lo.2008.53.3.0955

Højerslev, N. K. (1974). Inherent and apparent properties of the Baltic, Rep. *Inst. Phys. Oceanogr.* 23:88.

Højerslev, N. K. (1988). Natural occurrences and optical effects of Gelbstoff, Rep. *Inst. Phys. Oceanogr.* 50:30.

Højerslev, N. K. (1989). Surface water-quality studies in the interior marine environment of Denmark. *Limnol. Oceanogr.* 34, 1630–1639. doi: 10.4319/lo.1989.34.8.1630

Hudson, N., Baker, A., and Reynolds, D. (2007). Fluorescence analysis of dissolved organic matter in natural, waste and polluted waters – a review. *River Res. Appl.* 23, 631–649. doi: 10.1002/rra.1005

Huguet, A., Vacher, L., Relexans, S., Saubusse, S., Froidefond, J. M., and Parlanti, E. (2009). Properties of fluorescent dissolved organic matter in the Gironde Estuary. *Org. Geochem.* 40, 706–719. doi: 10.1016/j.orggeochem.2009.03.002

Khundzhua, D. A., Patsaeva, S. V., Terekhova, V. A., and Yuzhakov, V. I. (2013). Spectral characterization of fungal metabolites in aqueous medium with humus substances. *J. Spectrosc.* 2013:538608. doi: 10.1155/2013/538608

Kirk, J. T. O. (1994). *Light and Photosynthesis in Aquatic Ecosystems*. New York, NY: Cambridge University Press. doi: 10.1017/CBO9780511623370

Kowalczuk, P. (1999). Seasonal variability of yellow substance absorption in the surface layer of the Baltic Sea. *J. Geophys. Res. Ocean* 104, 30047–30058. doi: 10.1029/1999JC900198

Kowalczuk, P., Durako, M. J., Young, H., Kahn, A. E., Cooper, W. J., and Gonsior, M. (2009). Characterization of dissolved organic matter fluorescence in the South Atlantic Bight with use of PARAFAC model: interannual variability. *Mar. Chem.* 113, 182–196. doi: 10.1016/j.marchem.2009.01.015

Kowalczuk, P., Stedmon, C. A., and Markager, S. (2006). Modelling absorption by CDOM in the Baltic Sea from season, salinity and chlorophyll. *Mar. Chem.* 101, 1–11. doi: 10.1016/j.marchem.2005.12.005

Kowalczuk, P., Ston-Egiert, J., Cooper, W. J., Whitehead, R. F., and Durako, M. J. (2005). Characterization of chromophoric dissolved organic matter (CDOM) in the Baltic Sea by excitation emission matrix fluorescence spectroscopy. *Mar. Chem.* 96, 273–292. doi: 10.1016/j.marchem.2005.03.002

Kowalczuk, P., Zabłocka, M., Sagan, S., and Kuliński, K. (2010). Fluorescence measured in situ as a proxy of CDOM absorption and DOC concentration in the Baltic Sea. *Oceanologia* 52, 431–471. doi: 10.5697/oc.52-3.431

Kuliński, K., Hammer, K., Schneider, B., and Schulz-Bull, D. (2016). Remineralization of terrestrial dissolved organic carbon in the Baltic Sea. *Mar. Chem.* 181, 10–17. doi: 10.1016/j.marchem.2016.03.002

Kurata, N., Kate Vella, K., Hamilton, B., Shivji, M., Soloviev, A., Matt, S., et al. (2016). Surfactant-associated bacteria in the near-surface layer of the ocean. *Sci. Rep.* 6:19123. doi: 10.1038/srep19123

Lepparanta, M., and Myrberg, K. (2009). *Physical Oceanography of the Baltic Sea*. Heidelberg: Springer, 378. doi: 10.1007/978-3-540-79703-6

Liss, P. S., and Duce, R. A. (1997). *The Sea Surface and Global Change*. Cambridge: Cambridge University Press. doi: 10.1017/CBO9780511525025

Loiselle, S. A., Bracchini, L., Dattilo, A. M., Ricci, M., Tognazzi, A., Cózar, A., et al. (2009). The optical characterization of chromophoric dissolved organic matter using wavelength distribution of absorption spectral slopes. *Limnol. Oceanogr.* 54, 590–597. doi: 10.4319/lo.2009.54.2.0590

McKnight, D. M., Boyer, E. W., Westerhoff, P. K., Doran, P. T., Kulbe, T., and Andersen, D. T. (2001). Spectrofluorometric characterization of dissolved organic matter for indication of precursor organic material and aromaticity. *Limnol. Oceanogr.* 46, 38–48. doi: 10.4319/lo.2001.46.1.0038

Miller, W. L., and Zepp, R. G. (1995). Photochemical production of dissolved inorganic carbon from terrestrial organic matter: significance to the oceanic organic carbon cycle. *Geophys. Res. Lett.* 22, 417–420. doi: 10.1029/94GL03344

Moran, M. A., Sheldon, W. M. Jr., and Zepp, R. G. (2000). Carbon loss and optical property changes during long-term photochemical and biological degradation of estuarine dissolved organic matter. *Limnol. Oceanogr.* 45, 1254–1264. doi: 10.4319/lo.2000.45.6.1254

Murphy, K. R., Butler, K. D., Spencer, R. G. M., Stedmon, C. A., Boehme, J. R., and Aiken, G. R. (2010). Measurement of dissolved organic matter fluorescence in aquatic environments: an interlaboratory comparison. *Environ. Sci. Technol.* 44, 9405–9412. doi: 10.1021/es102362t

Olszewski, J., Sagan, S., and Darecki, M. (1992). Spatial and temporal changes in some optical parameters in the southern Baltic. *Oceanologia* 33, 87–103.

Osburn, C. L., O'Sullivan, D. W., and Boyd, T. J. (2009). Increases in the longwave photobleaching of chromophoric dissolved organic matter in coastal waters. *Limnol. Oceanogr.* 54, 145–159. doi: 10.4319/lo.2009.54.1.0145

Parlanti, E., Worz, K., Geoffroy, L., and Lamotte, M. (2000). Dissolved organic matter fluorescence spectroscopy as a tool to estimate biological activity in a coastal zone submitted to anthropogenic inputs. *Org. Geochem.* 31, 1765–1781. doi: 10.1016/S0146-6380(00)00124-8

Pastuszak, M., Stålnacke, P., Pawlikowski, K., and Witek, Z. (2012). Response of Polish rivers (Vistula, Oder) to reduced pressure from point sources and agriculture during the transition period (1988–2008). *J. Mar. Syst.* 94, 157–173. doi: 10.1002/etc.3519

Sieburth, J. M. (1983). "Microbiological and organic-chemical processes in the surface and mixed layers," in *Air-Sea Exchange of Gases and Particles*, eds P. S. Liss and W. G. N. Slinn (Hingham, MA: Reidel Publishers Co), 121–172.

Stedmon, C. A., Markager, S., and Bro, R. (2003). Tracing dissolved organic matter in aquatic environments using a new approach to fluorescence spectroscopy. *Mar. Chem.* 82, 239–254. doi: 10.1021/acs.est.8b02648

Stedmon, C. A., Markager, S., and Kaas, H. (2000). Optical properties and signatures of chromophoric dissolved organic matter (CDOM) in Danish coastal waters. *Estuar. Coast. Shelf Sci.* 51, 267–278. doi: 10.1006/ecss.2000.0645

Szymczycha, B., Winogradow, A., Karol Kuliński, K., Koziorowska, K., and Pempkowiak, J. (2017). Diurnal and seasonal DOC and POC variability in the land-locked sea. *Oceanologia* 59, 379–388. doi: 10.1016/j.oceano.2017.03.008

Tilstone, G. H., Angel-Benavides, I. M., Pradhan, Y., Shutler, J. D., Groom, S., and Sathyendranath, S. (2010). An assessment of chlorophyll-a algorithms available for SeaWiFS in coastal and open areas of the Bay of Bengal and Arabian Sea. *Remote Sens. Environ.* 115, 2277–2291. doi: 10.1016/j.rse.2011.04.028

Timko, S., Maydanov, A., Pittelli, S. L., Conte, M. H., Cooper, W. J., Koch, B. P., et al. (2015). Depth-dependent photodegradation of marine dissolved organic matter. *Front. Mar. Sci.* 2:66. doi: 10.3389/fmars.2015.00066

Twardowski, M. S., Boss, E., Sullivan, J. M., and Donaghay, P. L. (2004). Modeling the spectra shape of absorption by chromophoric dissolved organic matter. *Mar. Chem.* 89, 69–88. doi: 10.1016/j.marchem.2004.02.008

Williams, C. J., Yamashita, Y., Wilson, H. F., Jaffé, R., and Xenopoulos, M. A. (2010). Unraveling the role of land use and microbial activity in shaping dissolved organic matter characteristics in stream ecosystems. *Limnol. Oceanogr.* 55, 1159–1171. doi: 10.4319/lo.2010.55.3.1159

Williamson, C. E. (1995). What role does UV-B radiation play in freshwater ecosystems? *Limnol. Oceanogr.* 40, 386–392. doi: 10.4319/lo.1995.40.2.0386

Wilson, H. F., and Xenopoulos, M. A. (2009). Effects of agricultural land use on the composition of fluvial dissolved organic matter. *Nat. Geosci.* 2, 37–41. doi: 10.1038/ngeo391

Zepp, R. G., Callaghan, T. V., and Erickson, D. J. (1998). Effects of enhanced solar ultraviolet radiation on biogeochemical cycles. *J. Photochem. Photobiol. B Biol.* 46, 69–82. doi: 10.1007/BF02986960

Zhang, Y., Liu, X., Osburn, C. L., Wang, M., Qin, B., and Zhou, Y. (2013). Photobleaching response of different sources of chromophoric dissolved organic matter exposed to natural solar radiation using absorption and excitation–emission matrix spectra. *PLoS One* 8:e77515. doi: 10.1371/journal.pone.0077515

Zhou, X. L., and Mopper, K. (1997). Photochemical production of low-molecular-weight carbonyl compounds in seawater and surface microlayer and their air-sea exchange. *Mar. Chem.* 56, 201–213. doi: 10.1016/S0304-4203(96)00076-X

Zsolnay, A., Baigar, E., Jimnez, M., Steinweg, B., and Saccomandi, F. (1999). Differentiating with fluorescence spectroscopy the sources of dissolved organic matter in soils subjected to drying. *Chemosphere* 38, 45–50. doi: 10.1016/S0045-6535(98)00166-0

Conflict of Interest Statement: The authors declare that the research was conducted in the absence of any commercial or financial relationships that could be construed as a potential conflict of interest.

Copyright © 2018 Drozdowska, Kowalczuk, Konik and Dzierzbicka-Glowacka. This is an open-access article distributed under the terms of the Creative Commons Attribution License (CC BY). The use, distribution or reproduction in other forums is permitted, provided the original author(s) and the copyright owner(s) are credited and that the original publication in this journal is cited, in accordance with accepted academic practice. No use, distribution or reproduction is permitted which does not comply with these terms.

frontiers in Marine Science

ORIGINAL RESEARCH
published: 19 December 2018
doi: 10.3389/fmars.2018.00489

In Search of a Field-Based Relationship Between Benthic Macrofauna and Biogeochemistry in a Modern Brackish Coastal Sea

Mayya Gogina[1], Marko Lipka[2], Jana Woelfel[3], Bo Liu[2†], Claudia Morys[4†], Michael E. Böttcher[2] and Michael L. Zettler[1]*

[1] Biological Oceanography, Leibniz Institute for Baltic Sea Research (IOW), Warnemünde, Germany, [2] Geochemistry & Isotope Biogeochemistry, Leibniz Institute for Baltic Sea Research (IOW), Warnemünde, Germany, [3] Chemical Oceanography, Leibniz Institute for Baltic Sea Research (IOW), Warnemünde, Germany, [4] Institute for Biosciences - Marine Biology, University of Rostock, Rostock, Germany

OPEN ACCESS

Edited by:
Teresa Radziejewska,
University of Szczecin, Poland

Reviewed by:
Oleg P. Savchuk,
Stockholm University, Sweden
Brygida Wawrzyniak-Wydrowska,
University of Szczecin, Poland

***Correspondence:**
Mayya Gogina
mayya.gogina@io-warnemuende.de

†Present Address:
Bo Liu,
Marine Geochemistry,
Alfred-Wegener-Institute for Polar and Marine Research (AWI), Bremerhaven, Germany
Claudia Morys,
Department of Estuarine and Delta Systems, NIOZ Netherlands Institute for Sea Research, Utrecht University,Yerseke, Netherlands

Specialty section:
This article was submitted to Coastal Ocean Processes, a section of the journal Frontiers in Marine Science

Received: 30 April 2018
Accepted: 04 December 2018
Published: 19 December 2018

Citation:
Gogina M, Lipka M, Woelfel J, Liu B, Morys C, Böttcher ME and Zettler ML (2018) In Search of a Field-Based Relationship Between Benthic Macrofauna and Biogeochemistry in a Modern Brackish Coastal Sea. Front. Mar. Sci. 5:489. doi: 10.3389/fmars.2018.00489

During several cruises in the southern Baltic Sea conducted in different seasons from 2014 to 2016, sediment cores were collected for the investigation of pore-water biogeochemistry and associated nutrient fluxes across the sediment-water interface. Six stations were positioned along a salinity gradient (ranging from 22 to 8) and covered various sedimentary habitats ranging from mud to sand. Integrated fluxes of nutrients in the supernatant water and sediment oxygen consumption were additionally derived from incubations of intact sediment cores. Subsequently, sediment from the pore-water and incubation cores was sieved for taxonomic identification and estimation of benthic macrofauna density. This combined dataset was used to determine the dominant factors influencing the vertical distribution of geochemical parameters in the pore-waters of the studied habitats and to find similarities and patterns explaining significant variations of solute fluxes across the sediment-water interface. A statistical relationship between the thickness of sulfide-free surface sediments, solute fluxes of sulfide, ammonium, and phosphate as well as oxygen consumption and taxonomic and functional characteristics of macrobenthic communities were tested. Our data and modeling results indicate that bioturbation and bioirrigation alter near-surface pore-water nutrient concentrations toward bottom water values. Besides sediment properties and microbial activity, the biogeochemical fluxes can further be explained by the functional structure of benthic macrofauna. Community bioturbation potential, species richness, and biomass of biodiffusers were the best proxies among the tested set of biotic and abiotic parameters and could explain 63% of multivariate total benthic flux variations. The effects of macrobenthos on ecosystem functioning differ between sediment types, specific locations and seasons. Both, species distribution and nutrient fluxes are temporally dynamic. Those natural patterns, as well as potential anthropogenic and

natural disturbances (e.g., fishery, storm events), may cause impacts on field data in a way beyond our present capability of quantitative prediction, and require more detailed seasonal studies. The data presented here adds to our understanding of the complexity of natural ecosystem functioning under anthropogenic pressure.

Keywords: benthic macrofauna, ecosystem functioning, nutrient fluxes, sediment biogeochemistry, pore-water gradients, Baltic Sea

INTRODUCTION

Ecosystem functioning, defined as stocks and fluxes of energy and material within and across the boundaries of a given system and its relative stability over time (Paterson et al., 2012), is mediated by diverse biological communities (Snelgrove et al., 2018). Among all the interconnected processes and ecosystem components, marine benthic macrofauna is involved in the provision of ecosystem services as sediment (de)stabilization, food webs, nutrients cycling, and transport. It has long been demonstrated that the biogeochemistry of coastal sediments is strongly influenced by the presence and activity of benthic invertebrates (Gray, 1974; Rhoads, 1974; Haese, 2006; Snelgrove et al., 2018). Though this is recognized, the actual quantitative estimates linking major parameters describing macrofaunal community inhabiting the sediment (such as its taxonomic and functional diversity and density) with nutrient fluxes within the sediment-water interface (SWI) are still sporadic and scarce. Most of the published data is based on laboratory or mesocosm experiments (e.g., Mermillod-Blondin et al., 2004; Bonaglia et al., 2013). In respect of the Baltic Sea, the results of several field studies have now been published, e.g., for the Danish Sounds and for the Archipelago Sea (Hansen and Kristensen, 1997; Karlson et al., 2007; Delefosse and Kristensen, 2012; Norkko et al., 2012). Gammal et al. (2017) emphasized the increase of solute effluxes of phosphate and ammonium from sediments with decreased macrofaunal activity induced by coastal hypoxia in the western Gulf of Finland. The recent study in the Bay of Gdansk by Thoms et al. (2018) determined the greatest impact of macrofauna on sedimentary fluxes at stations where communities were dominated by deep-burrowing polychaetes. The authors suggested that these communities can serve as a descriptive indicator to estimate the extent of the coastal filter, where organic matter is reworked and relatively large amounts of nutrients (NH_4^+, NO_3^-, PO_4^{3-}, SiO_2) are released into the bottom water. Organic matter and nutrients cannot accumulate in the sediment because they are immediately used. They are buried by deep-burrowing fauna, but are also made available again to microbial degradation, therefore high turnover rates are induced due to particle mixing and surface increment (Rusch et al., 2006).

The effects of changes in benthic macrofaunal activity (both bioturbation and bioirrigation) on biogeochemical cycling are not firmly established, and few quantitative rules exist to predict their role (Mermillod-Blondin et al., 2004; Braeckman et al., 2010). Several reviews have attempted to consolidate the recent findings related to diverse ecosystems [for instance with a focus on the role of invasive ecosystem engineers by Guy-Haim et al. (2017)]. There is a certain lack of consensus even with regard to the direction of the effects. Increased faunal activity imply more intense redistribution of sediment particles, oxygenation of the sediment, decline of hydrogen sulfide, reduction of phosphate release into the bottom water (as phosphates are accumulated in the sediment bound to iron minerals), general decrease of the ammonium outflux, and an increase in the dinitrogen gas efflux due to coupled nitrification/denitrification in bioturbated sediments (Karlson et al., 2007; Norkko et al., 2012; Janas et al., 2017). Contradicting with the above, other authors (e.g., Pelegri and Blackburn, 1994; Mermillod-Blondin et al., 2004; Jordan et al., 2009; Gilbertson et al., 2012) describe the increased ammonium flux from the sediment to the overlying water column observed in the presence of burrowing invertebrates. In the Gulf of Finland, Maximov et al. (2014) found evidence for an effect of an increased population of invasive polychaete *Marenzelleria* spp. on binding of phosphate in sediments and reducing eutrophication conditions. This all suggests not only natural variability in nutrient cycling between regions, but also high context-dependency due to the complex interplay of multiple processes even on a very local scale (e.g., within few kilometers or less, Gammal et al., 2017), making basin scale extrapolations difficult.

There is a lack of such estimates, especially based on field data (*in situ* derived), in respect of the German part of the south-western Baltic Sea. This underlines the importance of further field studies and quantitative estimates, crucial for understanding and parameterization of the biogeochemical processes in order to support scientifically sound ecosystem management, to ensure the health of the Baltic Sea ecosystem and to mitigate unfavorable changes.

Overall physical transports between the free water column and sediment interstitial water, low in diffusion-dominated and high in advection-dominated habitats, control microbial activity inside sediments (Aller, 1994). According to Mermillod-Blondin (2011) bioturbation (particle mixing) and biodeposition (settling of feces and pseudofeces) produced by benthic invertebrates may play a bigger role in diffusion-dominated habitats where they can significantly modify water and particle fluxes at the water–sediment interface, whereas only slight influence of ecosystem engineers is expected in advection dominated habitats predominantly controlled by hydrological processes. Here it is important to specify that generally diffusion is the transport of dissolved material along a concentration gradient due to random movement. Advection is the transport of both dissolved material and its solvent. This includes hydrodynamics, bioturbation, bioirrigation, bottom trawling, and every process that is moving

the pore water itself together with chemical species dissolved in it. However, Mermillod-Blondin (2011) referred *"diffusion-dominated habitats"* to marine coastal benthic environments with fine sediment texture and low physical exchange of water between bottom water and interstitial water, characterized by low interstitial flow rates. In contrast, "a*dvection-dominated habitats*" were defined as benthic environments (in shallow areas) characterized by coarser permeable sandy sediments, where high rates of movement of solutes with water are driven by hydraulic gradients. With this definition Mermillod-Blondin (2011) suggested that with high interstitial flows arising due to high rates of hydrological exchanges, bioturbation by invertebrates can only moderately modify the water circulation patterns in sediments. This study highlighted the need to test this general framework on a wide range of marine (and freshwater) habitats by quantifying the interactions between the functional traits of species and the fluxes of water and particles at the SWI.

Linking the detailed biological and chemical information is a crucial step toward a mechanistic understanding of the role of macrofauna in the marine sediments biogeochemistry and nutrient cycles. In this context, the present study aims to interpret field data obtained within a 21 month period during several cruises from sandy and muddy sediments of the southern Baltic Sea. Research was carried out within the interdisciplinary research project SECOS ("The Service of Sediments in German Coastal Seas"), aiming to determine and understand the performance of marine sediments in the German part of the Baltic Sea. The main objectives of this case study were (1) to determine the (regional and context-dependent) quantitative relationships between biogeochemical solute fluxes and macrofaunal data derived from the sediment cores, and (2) to analyze the relevance of descriptors and indicators of benthic communities functional structure that significantly influence sediment biogeochemistry. Our study is centered around the key research question: what interactions (if any) occur between the macrobenthos composition and quantitative changes in solute fluxes in muddy and sandy habitats (under modern anthropogenic impacts)? In order to address it, the following hypotheses were set off and tested based on the available data: (H1) the signals of intensive faunal bioturbation activity are reflected in pore-water profiles, (H2) there is significant correlation between biogenic mixing depth and sulfide appearance depths, (H3) the variability of biogeochemical patterns can at least partly be explained by functional structure of macrofauna.

MATERIALS AND METHODS

Study Area

In the southern Baltic Sea (**Figure 1**), the shallow areas along the shore and on top of the offshore glacial elevations are characterized by a mosaic of coarse sediments and sands, whereas increasing water depths and finer and more organic-rich muddy sediments generally dominate in the deeper basins and bays. Fine sands cover about 32% of the German EEZ, mud up to 25% (Tauber, 2012). Near-bottom salinity and oxygen concentration are the major factors influencing species richness and composition of macrozoobenthic communities in the area (Zettler et al., 2017). Salinity declines from 20–25 in the western part of Kiel Bay to 7–8 in the Oder Bank. The water exchange between the western Baltic and the Baltic Proper is inhibited by the Darss and Drodgen Sills, usually causing the

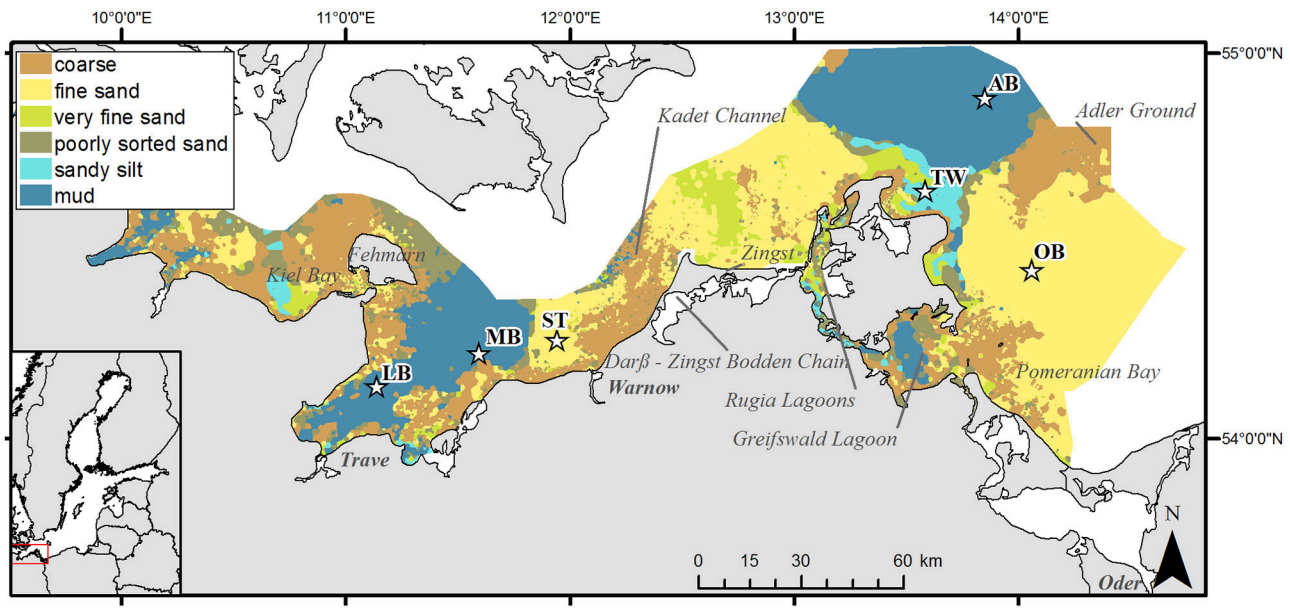


FIGURE 1 | Map of the study area in the south-western Baltic Sea with locations of sampling stations. Background colors show the distribution of sediment types after Tauber (2012). The number of cores obtained during each sampling event is given in **Table 1**. Geographic locations: LB, Bay of Lübeck; MB, Bay of Mecklenburg; ST, Stoltera; TW, Tromper Wiek; AB, Arkona Basin; OB, Oder Bank.

highest temporal variability of salinity in the western part of the study area. However, due to the influence of major Baltic Inflow event in December 2014 (Mohrholz et al., 2015) during SECOS cruises the variability of salinity was clearly higher in AB than in LB and MB (**Table 1**). Aperiodic seasonal oxygen depletion events occur in the deeper areas of the Kiel Bay, the Bay of Mecklenburg and in the Arkona Basin, and have negative effects on the diversity and density of soft-bottom fauna (Arntz, 1981). Such oxygen depletion event was observed in our study during the cruise EMB111 at stations MB, LB, ST, and AB, when only OB stations remained oxygenated (see **Table 1**).

TABLE 1 | The number of cores obtained for porewater analysis and incubation experiment during each sampling event as well as values (mean ± standard deviation) of physical, chemical, and sedimentary variables measured at each station.

Station/Area		**LB**	**MB**	**AB**	**TW**	**ST**	**OB**
Cruise ID	**Season dates**	**N Porewater cores**					
ALK434	Spring 2014 28.03–09.04.	1	1	3	2	2	1
POS475	Autumn 2014 27.09–12.10.	1	1			1	3
EMB100	Spring 2015 09.04–23.04.		2	2	1	2	2
EMB111	Autumn 2015 25.08–07.09.	1	1	1	1	1	1
MSM50	Winter 2016 06.01–24.01.	1	1	1	1	1	1
Cruise ID		**N Incubated cores/N oxic cores considered in this study**					
EMB100			3/3	3/3		2/2	2/2
EMB111*		3/1	3/1	3/0		3/0	3/1
MSM50		4/2		4/2		4/2	4/2
	Incubation temperature [°C]	**Ambient near-bottom salinity/temperature [°C]/oxygen [ml/l] from ship CTD at station during sampling event**					
EMB100	4 ± 1.2		20.5/4.3/5.15	15/4.8/6.31		16.2/5.1/8.43	8.3/5.8/8.53
EMB111*	10 ± 1	16.9/13.3/3.45	20.4/12.6/1.18	12.7/8.5/1.75		18.3/13.5/1.2	8/18.3/6.02
MSM50	4 ± 1	21.4/3.7/7.26		19/8.3/4.71		19.3/3.7/7.90	8.6/2.1/9.18
Variables		**Mean ± standard deviation**					
Sediment type		**Mud**	**Mud**	**Mud**	**Silt**	**Sand**	**Sand**
Depth [m]		23.1	26.4	45.6	29.1	18.6	15.7
Salinity (near bottom)		20.6 ± 2.5	21.7 ± 1.3	16.9 ± 3.7	9.8 ± 1.4	19.4 ± 2.4	8 ± 0.5
Temperature (near bottom) [°C]		9.2 ± 5.4	8.2 ± 4.9	6.8 ± 1.9	7.7 ± 5.6	8.6 ± 5.1	9.6 ± 7.1
Total organic content [%]		12.1 ± 1.6	10.9 ± 1.5	14.3 ± 4.4	3.2 ± 0.7	0.8 ± 0.3	0.4 ± 0.3
Oxygen (near bottom) [ml/l]		4.6 ± 2.4	4.5 ± 2.6	4.9 ± 2.2	7.4 ± 1.4	6.1 ± 2.9	7.7 ± 1.4
Chl a (0–0.5 cm) [μg 0.5 cm^3]		9.6 ± 3	8.3 ± 3.4	4.2 ± 1.8	8.9	5.6 ± 1.5	4 ± 0.4
Median grain size [μm]		17.8 ± 1.3	18 ± 2.4	19 ± 2.4	44 ± 5.9	156 ± 12.6	171.2 ± 30.8
Fraction finer 63 μm [%]		99.7 ± 0.1	99.5 ± 0.3	99.5 ± 0.5	70.8 ± 8.1	11.8 ± 3.8	6.6 ± 5.5
Skewness [phi]		−0.6 ± 0	−0.6 ± 0.1	−0.7 ± 0	−0.7 ± 0.1	−0.6 ± 0.2	−0.2 ± 0.3
Sorting [phi]		1.4 ± 0	1.4 ± 0.1	1.4 ± 0	1.3 ± 0.1	0.7 ± 0.1	0.6 ± 0.1
Sediment water content in top 20 cm, [%]		75.7 ± 2.7	74.9 ± 4.1	76.4 ± 4.0	31.4 ± 6.5	21.8 ± 3.0	20.2 ± 0.8

Stations abbreviations are as follows: LB, Bay of Lübeck; MB, Bay of Mecklenburg; ST, Stoltera; TW, Tromper Wiek; AB, Arkona Basin; OB, Oder Bank.

**During cruise EMB111 hypoxic conditions were observed at all stations with the exception of OB, most incubated cores with initially hypoxic conditions were excluded from the analysis (initial bottom water oxygen concentrations [μmol/l]: all AB and ST cores hypoxic: 54–75; MB: 2 cores hypoxic 40–45, 1 core: 100; LB: 2 cores hypoxic: 48–60, 1 core: 195, OB: 2 cores hypoxic, 1 core: 300). For comparison initial bottom water oxygen concentrations ranged during EMB100 between 195 and 370 μmol/l, during MSM50 - between 199 and 333 μmol/l.*

It is important to mention that the presence of anthropogenic effects (bottom trawling traces) was clearly observed at station MB during side-scan sonar survey (Lipka et al., 2018; see Bunke, 2018). Further, at the shallow OB station, sediments rearrangements during short-term natural physical events (e.g., storms) are known to occur (Mohrholz et al., 2015; Lipka et al., 2018).

Biogeochemical Data

Several research cruises were carried out between April 2014 and January 2016 with research vessels "Alkor" (ALK434), "Poseidon" (POS475), "Elisabeth Mann Borgese" (EMB100, EMB111), and "Maria S. Merian" (MSM50), see **Table 1**. During each cruise and at each visited location, sediment sampling was carried out by collecting up to eight parallel short sediment cores with a multicorer in acrylic tubes (60 cm long, 10 cm internal diameter). Cores disturbed during sampling (e.g., with shattered or inclined sediment-water interface) were discarded.

Pore-water (PW) samples were taken immediately after recovery of cores from 1, 2, 3, 4, 5, 7, 9, 11, 15, and 20 cm below and from bottom water right above the SWI using rhizons (with 0.2 μm pore size of the filter membrane) attached to clean syringes (Seeberg-Elverfeldt et al., 2005). About 10 ml pore-water were extracted from each depth (up to 20 cm below the sediment surface) after discarding the first 1–2 ml. A detailed description of the sampling procedure and pore-water analysis is given in Lipka et al. (2018). Following the methods described in Kowalski et al. (2012) and Reyes et al. (2016), the concentrations of the major, minor and trace elements (including total P, Fe, and Si) dissolved in pore-water, were measured by inductively coupled plasma optical emission spectroscopy (ICP-OES; Thermo, iCAP 6300 Duo, Thermo Fisher Scientific GmbH, Dreieich, Germany), NO_3^- and NH_4^+ concentrations—using QuAAtro nutrient analyser (SEAL analytical) as described in Winde et al. (2014) and H_2S (sum of the dissolved sulfide species) concentrations—photometrically according to Cline (1969). Benthic solute reservoirs were calculated as depth integrated concentrations in the pore-waters of the top 10 cm surface sediments considering porosity that was determined as outlined in Lipka et al. (2018).

Incubation (INC) of intact short sediment cores (10–20 top centimeter of the sediment column) with naturally inhabiting macrofaunal communities was carried out on board of the research vessel to estimate the total oxygen uptake and total benthic fluxes of NH_4, PO_4, and Si. The volume of each "incubation chamber" (height of sediment as well as of the water phase) was determined and integrated into the calculations. Cores were incubated at constant temperature (4°C, except for during EMB111 in autumn 2015–10°C, see **Table 1** for more details) in darkness for 5–10 days. Stirring mechanisms were used to homogenize the water column for analyses without resuspension of sediment particles, keeping the bottom water movement close to natural conditions. In the closed incubation chambers, overlaying water oxygen was measured using in-core attached optode spots (Fibox 4 sensor system, PreSens Precision Sensing GmbH, Regensburg, Germany): in each core, optical phase values were logged with a 5 s rate for 5–10 min three to five times a day. These values were converted into oxygen concentrations and adjusted to prevailing temperature and salinity using the mathematical conversion matrix of the manufacturer PreSens. Incubation periods under oxic conditions ranged from 3 to 10 days during EMB100, from 1.5 to 6.5 days during EMB111 when hypoxic conditions were observed at all stations with the exception of OB, and from 3 to 6 days during MSM50 cruise.

Sensor calibrations of both O_2 procedures were performed in ambient sea water (100% atmospheric saturation) aerated for 30 min, and in saturated seawater sodium dithionite solution (0% oxygen), cross checked by Winkler titration (Winkler, 1888). The deviations of oxygen concentrations measured several seconds apart were 0.2%.

For nutrient analysis, supernatant water sampling was performed every 12 to 24 h. The stirrer was switched off during the sampling to prevent intermixing of the sampled water with injected reservoir water for volume compensation. About 10 ml was filled into various sample tubes for subsequent analysis of main and trace element concentrations, sulfide/sulfate concentrations, dissolved inorganic carbon (DIC) concentration, and on-board nutrient analysis (see above). For more details on the incubation setup see Lipka et al. (2018).

Concentration changes of the bottom water solutes over time were evaluated via linear regression. Net flux rates (e.g., total oxygen uptake, TOU) were calculated using the slope ($R^2 > 0.85$, $p < 0.1$), separately for oxic (>89 μM O_2), hypoxic (<89 μM O_2) and anoxic phases, corrected for the surface area to volume ration of each chamber. Because the effects of macrofauna activity under natural conditions were of interest, only oxic phase fluxes of O_2, NH_4, PO_4, and Si derived for the 21 cores incubated under oxic conditions were used in this study. Nutrient fluxes were calculated from linear increase or decrease of concentration vs. time, taking into account the volume of water above the incubated sediment.

Macrofaunal Data and Macrobenthic Parameters Tested

Macrozoobenthic samples were collected from short cores after completing the pore-water analysis or incubation. Thus, our data represents 2 sets: PW-dataset with 36 cores from 6 stations (**Figure 1**) and 5 sampling campaigns (March/April 2014, September/October 2014, April 2015, August/September 2015, and January 2016) analyzed for pore-water nutrients and diffusive fluxes; and INC-dataset with 41 cores incubated on board to estimate the total oxygen uptake and total benthic fluxes of NH_4, PO_4, and Si (of which only 21 are included in the evaluation) from 5 stations sampled during 3 latter cruises (see **Table 1**). The area covered by each core (10 cm inner diameter) was 0.00785 m^2. For macrofauna sampling sediment from the cores was sieved using a 1.0 mm sieve mesh size and samples were preserved in 4% buffered formaldehyde–seawater solution. In the laboratory, the organisms were sorted, identified to species level (with the exception of genus *Phoronis* and family Naididae), counted and weighted. The nomenclature was cross-checked following the World Register of Marine Species (WoRMS Editorial Board, 2018). Abundance and biomass data

were standardized to an area of 1 m^2. Ash-free dry weight (AFDW) biomass (used here in the analysis) was estimated from the wet weight (determined including calcareous structures, without tubes) using species-specific conversion factors from the in-house list of the Leibniz Institute for Baltic Sea Research, Warnemünde (includes over 500 species, based on 15,000 measurements after drying at 60°C for 24 h and ignition at 500°C for 5 h).

Additionally, at every station and sampling event, at least 3 replicate samples were collected by the Van Veen grab (sampling area 0.1 m^2). The samples were processed in the same way as described above for the short cores. Considering the patchy distribution of benthic assemblages (especially at finer scales, even in homogenous habitats) and in order to keep the amount of analysis feasible, this study is mainly focused on the collation of macrofaunal and biogeochemical data obtained directly from the same short cores. Therefore, the data from grab samples (referred to as VV) was used here only occasionally for comparative purposes (some more details on this data can be found in Gogina et al., 2017).

General descriptors of macrofaunal community considered in the analysis were species richness, total macrofaunal biomass and abundance. The metric of bioturbation potential (Solan et al., 2004) was used as proxy for sediment mixing activity:

$$BP_c = \sum_{i=1}^{n} BP_{pi}, \text{ where } BP_{pi} = (B_i/A_i)^{0.5} * A_i * M_i * R_i$$

Where B_i is AFDW biomass in g/m^2 and A_i is abundance (in ind/m^2) of the ith species, respectively. M_i and R_i are categorical scores reflecting increasing mobility and sediment reworking, respectively (indicating for M_i: 1—living in a fixed tube, 2—limited movement, 3—slow, free movement through the sediment, 4—free three dimensional movement via burrow system; for R_i: 1—epifauna that bioturbate at the sediment–water interface, 2—surficial modifiers, 3—upward and downward conveyors, 4—biodiffusors, 5—regenerators that excavate holes, transferring sediment at depth to the surface). M_i and R_i scores applied in this study are published in Gogina et al. (2017). BP_{pi} summed across all species in a sample gives an estimate of community-level bioturbation potential, BP_c

Quantitative services for ecosystem functioning provided by macrofauna vary mainly due to differences in biomass and burial depth between communities. Vertically resolved information on the distribution of organisms at various sediment depths in the PW and INC cores was lacking (but see Morys et al., 2017 for high resolution macrofauna depth distribution in spring 2014). In order to estimate the differences in the potential mixing depth for analyzed cores, an empirical equation that provides an estimate of biogenic mixing depth (BMD) based on the BPc published in Solan et al. (2004), i.e., BMD = 4.55 + 0.719*logBPc, was used. It should be noted that this metric is only a proxy, and is therefore not a precise match with the real sediment depth at which individuals were occurring.

To express the community functional structure in the analyzed cores, we used the biological traits approach (BTA) with a selected set of traits relevant for actuating flows of chemical substances, particularly fluxes of solutes, across the SWI and generally important for species-environmental relationships (Bremner et al., 2006; van der Linden et al., 2017). **Table 2** provides the full list of 8 traits and 32 modalities considered. Based on the affinity of species to a particular modality of each trait, partial BTA scores, ranging from 0 (no affinity) to 1 (exclusive affinity), are assigned for each species so that the sum of scores of all modalities of each trait would sum to one. This "fuzzy coding" approach allows each taxon and each biological trait to have the same weight in further analysis (Chevenet et al., 1994; Bremner et al., 2006; van der Linden et al., 2017). To code the taxa by their functional traits we have used scores published in Gogina et al. (2014).

Accompanying Environmental Data

Environmental characteristics (**Table 1**) were measured at each sampling event parallel to the collection of cores. Water depth,

TABLE 2 | Biological traits used to describe functional structure of macrofauna community.

General trait	Modalities	Code
Motility	Sedentary	mot.sed
	Limited free movement	mot.lim
	Freely motile in or on sediment	mot.fre
	Semi-pelagic	mot.spel
Feeding	Suspension	feed.sus
	Deposit feeder	feed.dep
	Predator	feed.pre
	Scavenger	feed.sca
	Grazer	feed.gra
Habitat structure	Permanent burrow	struc.bur
	Hole, pit or non-permanent burrow	struc.pit
	Tube	struc.tub
	Creating troughs or trampling across sediment surface	struc.tra
	Forming biogenic epibenthic structures	struc.epi
Sediment transport	Surface-to-deep	sed.sd
	Deep-to-surface	sed.ds
	Surface mixing	sed.sm
	Deep mixing	sed.dm
	No transport	sed.no
Size	Small (<5 mm longest dimension)	size.s
	Medium (5–20 mm longest dimension)	size.m
	Large (>20 mm longest dimension)	size.l
Position in sediment	Protruding surface	pos.pro
	Attached	pos.att
	Oxygenated zone	pos.oxy
	Below the oxygenated zone	pos.sox
Larvae	Planktonic	lar.pla
	Benthic	lar.ben
Longevity (yr)	≤2	long.2
	2–5	long.5
	6–0	long.10
	10+	long.10p

near bottom water salinity and temperature were obtained from ship CTD. Near bottom oxygen concentration was derived using Winkler titration. One sample was taken at each sampling event for the determination of sediment characteristics (organic content, fraction finer 63 μm, median grain size, sorting, skewness). Chlorophyll a content of top 0.5 cm of sediment was determined as described in Morys et al. (2016). Sediment water contents of the freezed (under −20°C) and vacuum-dried samples were calculated gravimetrically by Bunke (2018).

Data Interpretation and Statistical Analysis

Pore-water profiles for separate cores were visually compared against the BPc values based on animals found in particular PW-cores, which represented a proxy for potential faunal activity.

Results of Shapiro-Wilk test of normality indicated that the null hypothesis of data originating from a normal distribution could be rejected for all but three variables (total NH_4 flux, species richness, and near-bottom oxygen concentrations). Therefore, only non-parametric methods could be allied to test for significant differences in geochemical, environmental and macrozoobenthic parameters between sediment types, sampling sites, and seasons.

Correlations between macrofaunal parameters such as the number of species, abundance, biomass, BPc, and pore-water reservoirs and solute fluxes at SWI were tested by Spearman correlation coefficients with p-value approximated by permutation. A significance level threshold of $p \leq 0.05$ was assumed for all the analyses. Software PRIMER 7 (Clarke et al., 2014) and PERMANOVA+ (Anderson et al., 2008) were used to test the differences of functional traits structure between stations (settings: unrestricted permutation of raw data, number of permutations = 9999, estimation of P-values based on Monte Carlo simulations to overcome the problem of low number of replicates).

Fuzzy Correspondence Analysis (FCA, Chevenet et al., 1994) was applied to ordinate and explore biological traits structure (see section Macrofaunal data and macrobenthic parameters tested) in PW cores, using R-package "ade4" (Dray and Dufour, 2007). FCA is able to incorporate discrete fuzzy coded biological traits variables and apply corrections to account for the fact that each biological trait has multiple trait modalities that sum to no more than one. FCA ordination of cores and traits was obtained using Euclidean distances from relative frequencies of traits weighted by AFDW biomass. The result is an ordination plot where each point represents the biomass-weighted trait composition of each core, and proximity of points on the plot corresponds to structural similarity. FCA allows extraction of variability covered by each ordination axis and correlation ratios of each trait with principal axes.

To determine the set of environmental abiotic and biological variables (that reflect faunal metabolic and bioturbation activity) that best explain the multivariate variation of oxygen consumption and total benthic fluxes measured in incubation experiments, we performed a distance-based linear model permutation test (DistLM with dbRDA, McArdle and Anderson, 2001) employing the routine from the PRIMER 7 with PERMANOVA+ add-on. A similarity matrix based on the Euclidean distance of normalized total multivariate fluxes (total oxygen uptake and total benthic fluxes of NH_4, PO_4, and Si) data was obtained for 21 incubation cores. Highly correlated predictor variables were removed from the analysis (correlation coefficient ≥ 0.90), retaining: sediment grain size fraction below 63 μm, CTD derived near-bottom water salinity, oxygen concentrations, temperature, BPc, biomass (AFDW) of upward and downward conveyors, biomass of biodiffusers and biomass of suspension feeders and species richness (Nsp) of fauna colonizing the particular core (see **Appendix 4**). Step-wise selection criterion procedure based on 9,999 random permutations and the adjusted R^2 was used to determine the best set of predictors (similar to the approach used in Belley and Snelgrove, 2016). Variables showing significance levels above the threshold ($p > 0.05$) in the marginal test were excluded from the final model. Scatter plots of macrofaunal BPc against total solute fluxes were produced to aid interpretation of results.

To provide clear definitions, "diffusive fluxes" here are referred to the (theoretical) proportion of the flux that is only driven by molecular movements without any rearrangement of the solvent. This flux can only be reliably measured if advective processes can be largely excluded because advective fluxes have a great influence on the concentration gradients and therefore on the calculated diffusive fluxes. "Total fluxes," estimated from incubation experiments, and denote the fluxes of dissolved chemical species by both advection of water (e.g., by organisms, via hydro-irrigation or due to relocation of pore-water and particles in surface sediments by human activities) and simple molecular diffusion across sediment-water interface. Total fluxes are the fluxes measured by incubation or estimated from process rates (like oxygen consumption) under the assumption that a steady state prevails. "Advective fluxes" in this study denote the transport of dissolved materials across sediment-water interface due to the transport of water by non-diffusive processes such as bioirrigation and bioturbation by burrowing organisms, hydro-irrigation and antropogenic activities like bottom trawling. Here "advective fluxes" are estimated as difference of total and diffusive fluxes. However, this estimate of the advective flux component using the difference of total and diffusive fluxes is only feasible for parameters that are not much involved in secondary reactions such as redox-reactions. An example of a reaction that excludes estimates of advective component of phosphate fluxes in our data is the reoxidation of Fe at the SWI resulting in the diffusive flux directed not toward the water column, but into the oxic zone of Fe-oxide precipitation, located somewhere in the top millimeters of sediment (Lipka et al., 2018). Similar secondary processes might occur with NH_4 that seems to be consumed in the oxic bottom waters during incubation experiments (see e.g., **Figure 6B**). Thus, out of the parameters covered with total fluxes measurements in our study arguably only Si seems suitable to separately estimate the advective flux. Our intention was to check if the effect of macrofaunal activity (expressed by BPc, abundance and biomass) on advective component of the Si flux is more distinct compared to that on the total or diffusive Si fluxes. As diffusive and total fluxes were derived from different cores (with

high variability between the parallels), for this estimate the only option was the use of averages of the two methods for each site and sampling campaign.

RESULTS

Pore-Water Profiles and Faunal Bioturbation Activity (PW Cores)

In total, 1,151 individuals representing 42 taxa (excluding the records of uncountable species—Bryozoa and Hydrozoa—from two OB, two LB, and one ST core from spring 2014 and autumn 2015) were identified in 36 PW cores (**Appendix 1**). Overall, Gastropoda were the most abundant, particularly at sandy OB and silty TW, followed by Bivalvia (most abundant at sandy ST, muddy AB, and MB sites) and Polychaeta (most abundant at muddy LB and second-most abundant at TW and ST). Polychaeta was also the most diverse group (represented by 20 taxa), followed by Bivalvia (8 species) and Gastropoda (3 species only).

To explore the effect of macrofaunal activity on the dynamic of nutrients in pore-waters we have compared the vertical concentration profiles of the cores with the lowest and highest BPc values within our PW-dataset. Pore-water concentration profiles of NH_4, P, H_2S, Fe, and H_4SiO_4 were plotted against the corresponding BPc values in **Figures 2**, **3**. Generally, cores with higher BPc values display pore water concentration profiles with declining gradients toward SWI and concentrations that are closer to bottom water values, and therefore lower benthic solute reservoirs in the top centimeters. In typical nutrient-poor sandy sediments of OB site (**Figure 3**) cores indicating higher BPc showed deeper throughout mixing and more peaks, suggesting more intensive mixing, and active transport mechanism. This is visible in the two parallel cores OB2 and OB3 from EMB100 (**Figure 3**). Core OB3 indicated an overall second highest BPc (3,122) in PW-dataset (exceeded only slightly by the BPc value for core OB5 collected in January 2016, 3,288), with larger (>5 mm) individuals of deeper-dwelling bivalve *Mya arenaria* contributing most to this value.

A similar pattern was evidenced for pore-water cores from muddy stations. From three parallel AB cores from ALK434 cruise AB3 had the lowest of three BPc values (110, determined by only 3 single individuals of *Diastylis rathkei*, *Scoloplos armiger*, and *Nephtys hombergii* with total biomass of 2.5 mg) and showed near-surface peaks in P, Fe^{2+},and H_4SiO_4 profiles (**Figure 2**). On the contrary, AB1 and AB2 displayed the highest BPc values recorded at this station (991, with the highest contribution of 10 individuals of *Limecola balthica* and 10 individuals of *Scoloplos armiger*, and 744 mostly shaped by large single individual of *Nephtys ciliata* and 5 *L. balthica*, respectively), corresponding with lower P, H_4SiO_4 and NH_4 reservoirs. AB1 showed no peaks in P, Fe^{2+}, and H_4SiO_4 profiles, whereas peaks in AB2 occurred in deeper sediment layers and were less pronounced compared to those in AB3. In the example of two parallel cores from the sandy ST site collected in spring 2015 (ST4_EMB100 and ST5_EMB100, **Figure 3**), despite the higher BPc in core ST4 (where surficial modifiers *Arctica islandica* and *L. balthica* contributed most), the presence of one individual of *N. hombergii* in core ST5 seemed to have a greater effect on the Si and P profiles.

However, this relation is not always preserved. Generally, at muddy stations MB and LB biomass was dominated by Cumacea followed by Polychaeta. Sediments from two parallel MB cores from EMB100 cruise were nearly devoid of macrofauna (only one organism of surficial biodiffusor *Diastylis rathkei* was found in core MB2), and thus biogenic mixing by macrofauna is not expected here (**Figure 2**). Yet, despite the occurrence of peak and high concentrations of Fe in MB3 profile close to the sediment surface, detection of H_2S only below 10 cm sediment depth suggests possible impact of disturbance of sediment surface (for example by bottom trawling, known to be common for this area).

Sulfide Appearance Depth vs. Biogenic Mixing Depth

Biogenic mixing depth BMD, calculated based on BPc values of the community inhabiting each core, was used as proxy for macrofaunal burial depth. It was highest in sands and lowest in muds, with silt cores showing intermediate values (**Figure 4**). BMD significantly and positively correlated to sulfide appearance depths ($R = 0.65$, $p < 0.01$), suggesting the direct impact of faunal mixing. Cores from sandy stations also showed the largest variability in observed sulfide appearance depths values.

Functional Structure and Benthic Solute Reservoirs

The functional structure of macrofauna inhabiting the cores from the PW-dataset corresponded to changes in sediment type with sandy stations clustering on the left part of the ordination plot and muddy and silt stations located more to the right along the first FAC axis (**Figure 5**, **Table 3**). PERMANOVA analysis confirmed that differences in biomass-weighted trait data were significant between mud and sand cores ($t = 4.02$, $P_{(perm)} = 0.001$) as well as between sand and silt cores ($t = 2.07$, $P_{(perm)} = 0.029$), but not between mud and silt cores ($t = 0.18$, $P_{(perm)} = 0.957$). The co-structure between species biomass weighted trait-by-station arrays and pore-water solute reservoirs data set was not random [Monte-Carlo test: coinertia = 0.238 (coefficient of correlation between the two tables); $p = 0.004$].

The sediment gradient from sand to mud was associated with a change from suspension to deposit feeding and a declining role of species penetrating below the oxygenated zone as well as species with large individual sizes. It corresponded to the increase of benthic solute reservoirs of ammonium, phosphate and silica in the top 10 cm of sediment (confirmed by significant positive correlation with FCA1, **Table 3**, see also **Appendix 3**), and the respective diffusive fluxes out of the sediments (supported by significant negative correlations with FCA1, **Table 3**). The FCA2 axis displayed only a weak significant correlation with Fe reservoir significantly declined along with FCA2 together with biomass of semipelagic taxa, taxa creating permanent burrows, and those contributing to deep-to-surface sediment transport.

Incubation (INC) Cores

A total of 21 incubations under oxic conditions spanned 5 sites and 3 seasons. In total, we identified 1,584 individuals

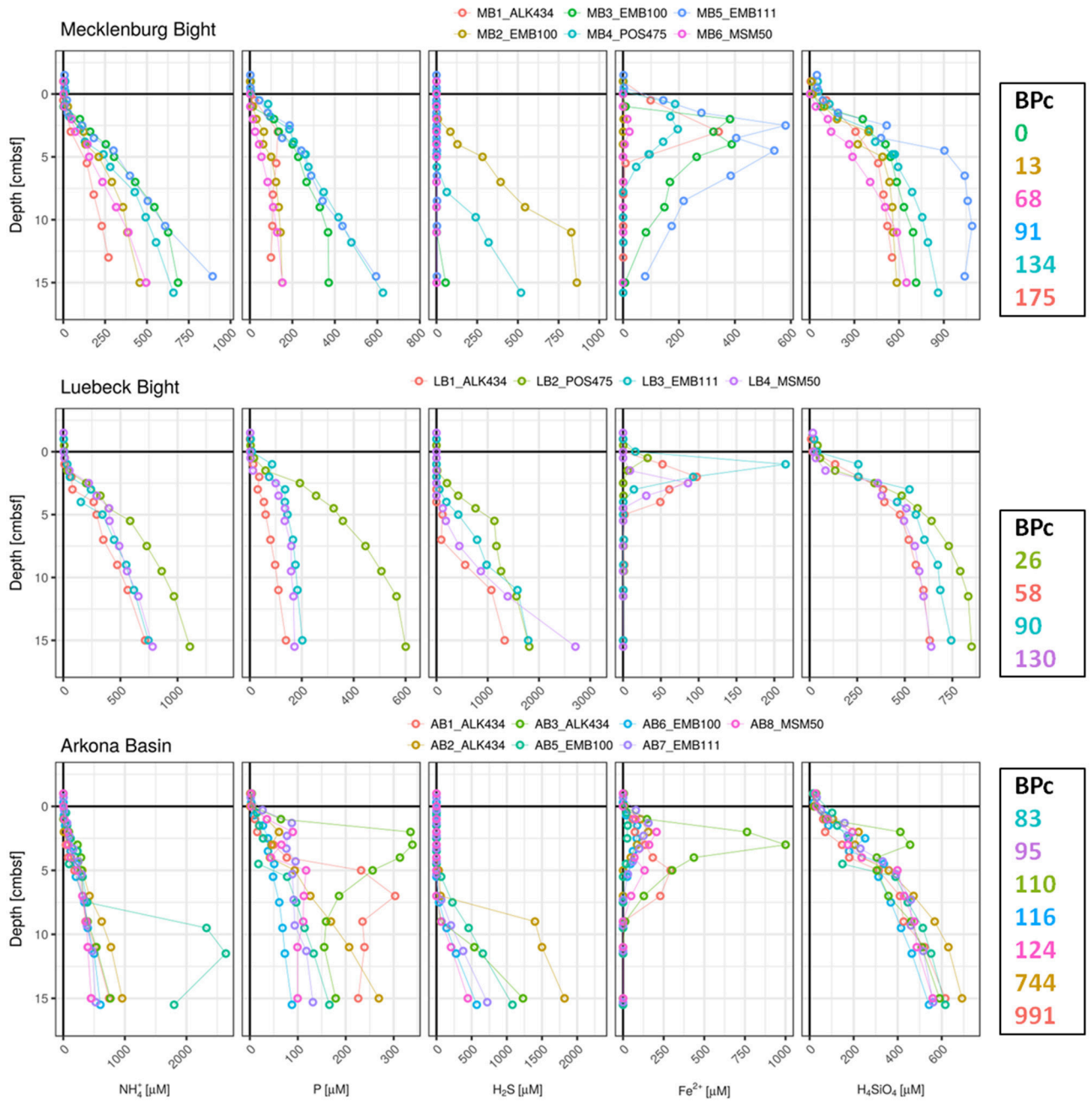


FIGURE 2 | Pore-water profiles of NH_4^+, P, H_2S, Fe^{2+}, and H_4SiO_4 for sediment cores collected from mud stations plotted against the BPc values defined by the colonizing benthic macrofauna community. Note the differences in axes scales. Cores are labeled according to sampling station (first 2 characters), followed by one character indicating core ID number, whereas the last 6 characters represent the cruise ID (respective seasons are indicated in **Table 1**).

representing 30 taxa (**Appendix 1**, **Data Sheet 2**). Overall in INC cores the most diverse class was Polychaeta, Bivalvia dominated the biomass, whereas Gastropoda were the most abundant. *Peringia ulvae* followed by *Mya arenaria* and *Cerastoderma glaucum* occurred in the highest densities in OB cores. Biomass was dominated by *C. glaucum*, *L. balthica,* and *M. arenaria*. At our sandy stations, functional richness, species richness, and density were significantly higher than in the adjacent muddy sediments (independent 2-group Mann-Whitney *U*-Test based on 33 PW cores, excluding TW cores: W = 24, W = 22.5 and W = 11, respectively, p-value ≤ 0.001).

PERMANOVA performed on Bray-Curtis similarity matrices of log (x+1) transformed AFDW data with pacifier variables (to account for cores without macrofauna), indicated significant

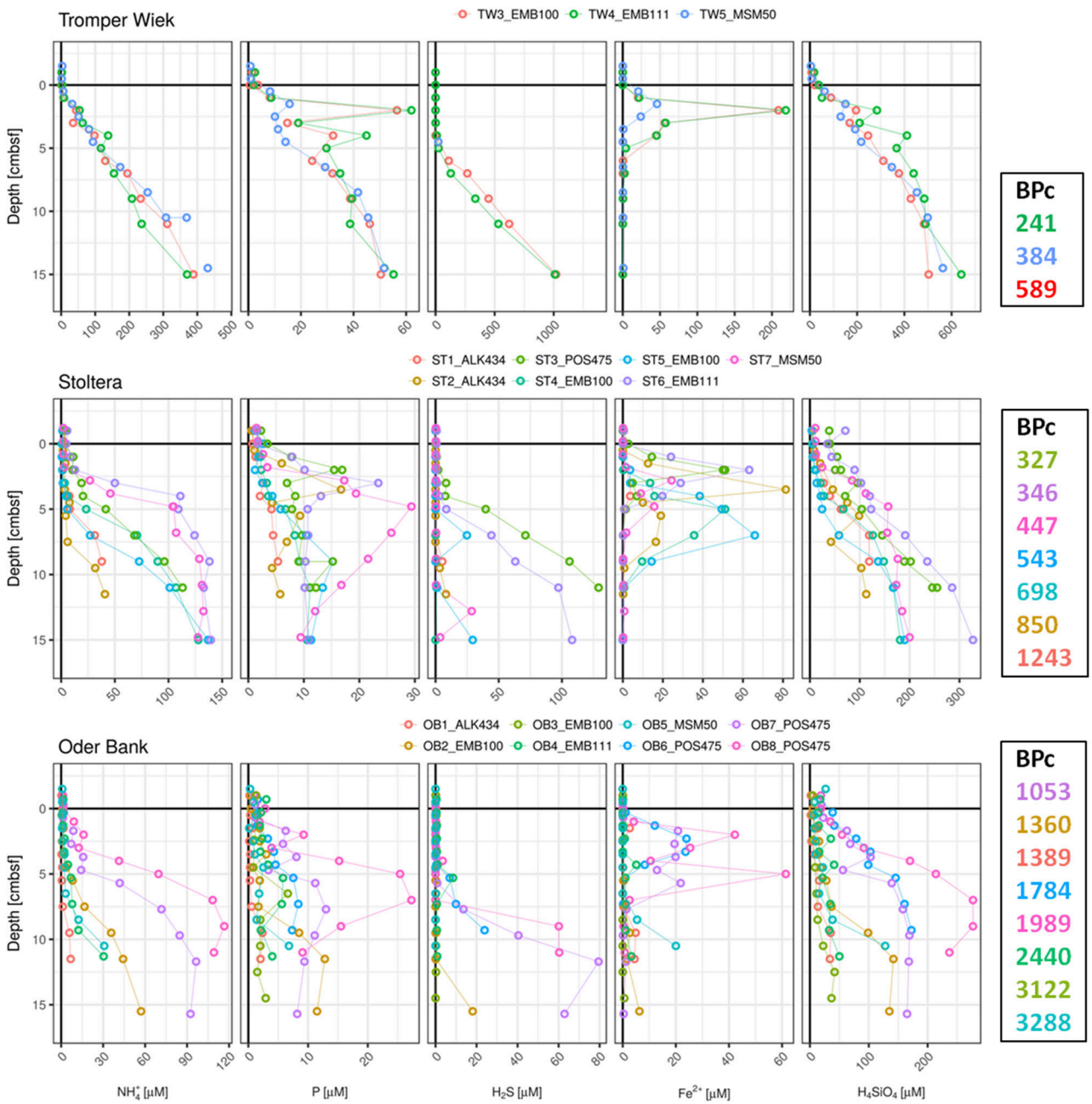


FIGURE 3 | Pore-water profiles of NH_4^+, P, H_2S, Fe^{2+}, and H_4SiO_4 for sediment cores collected from silt and sand stations plotted against the BPc values defined by the colonizing benthic macrofauna community. Note the differences in axes scales. Cores are labeled according to sampling station (first 2 characters), followed by one character indicating core ID number, whereas the last 6 characters represent the cruise ID (respective seasons are indicated in **Table 1**).

differences in macrofauna composition among the 5 sampling sites and thus significantly greater variability in assemblages among sites than within sites ($P_{(perm)} < 0.01$). Pair-wise comparisons showed significantly ($P_{(perm)} < 0.05$) different benthic communities for all but three pairs of sites (AB and MB, $P_{(perm)} = 0.421$; LB and MB, $P_{(perm)} = 0.196$; LB and ST, $P_{(perm)} = 0.177$). Results of the Monte-Carlo permutation test further indicated distinct statistically significant differences of macrofauna composition expressed in AFDW biomass only between the OB and the other 4 stations.

PERMANOVA performed on Euclidean similarity matrix of normalized benthic total fluxes data indicated significant differences in benthic fluxes among the sampling sites and also significantly greater variability in flux among sites than

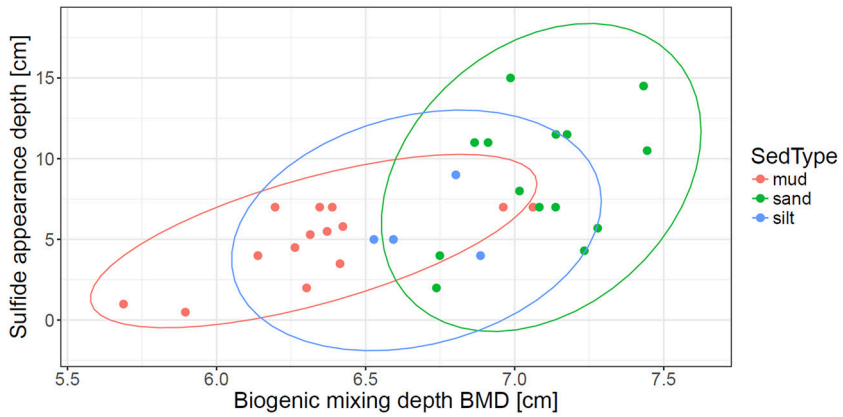


FIGURE 4 | Biogenic mixing depth (BMD) values derived based on bioturbation potential (BPc) of the community inhabiting each core after Solan et al. (2004) plotted against sulfide appearance depths values (determined from pore-water profiles).

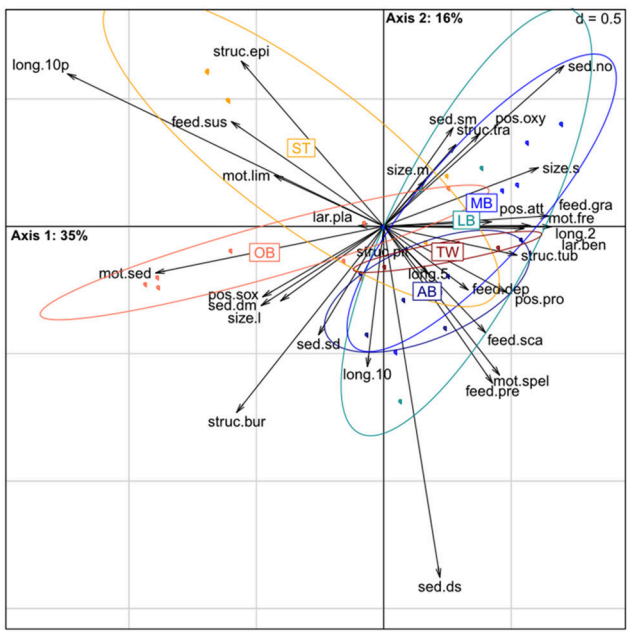


FIGURE 5 | Results of Fuzzy Correspondence Analysis on macrofauna data for pore-water (PW) cores. 2D ordination of samples based on trait categories exhibited by the communities (weighted by the untransformed biomass); samples (points) are grouped (circles) for stations, arrows point to the center of gravity of the samples presenting that category modality. Ellipses show the 95% confidence intervals. First axis explained 35% of total variation of the trait data, second axis−16%. See **Table 2** for traits abbreviations.

within sites [$P_{(perm)} < 0.05$, **Table 1**]. Pair-wise comparisons with the Monte-Carlo test showed that benthic fluxes at LB differed significantly from fluxes measured at AB and ST [AB, $P_{(perm)} = 0.019$; ST, $P_{(perm)} = 0.039$], but no significant difference was found with fluxes at MB or OB. Pair-wise comparisons also showed that benthic fluxes at MB differed significantly from fluxes measured at AB and ST, that were also significantly different from each other [MB and AB, $P_{(perm)} = 0.025$; MB and ST, $P_{(perm)} = 0.03$; AB and ST, $P_{(perm)} = 0.007$] (data displayed in **Figure 6**).

Analysis of outliers performed for each station separately highlighted that core OB1_spr15 showed extremely high BPc, total AFDW as well as AFDW of bivalves and species attributed to biodiffusers (R4), which in turn associated with extremely high values of oxygen uptake and release of PO_4, NH_4, and Si. Results of DistLM obtained on a dataset excluding outliers showed that log-transformed BPc, species richness (Nsp) and biomass of biodiffusers were the best proxies among the tested set of biotic and abiotic parameters and could explain 63.6% of the multivariate total benthic flux variations (**Appendix 4**).

For a set of 21 incubated cores, the only significant values of Spearman rank correlation found for benthic fluxes and macrofaunal parameters were between total Si flux and BPc ($r = 0.470$, $p = 0.032$) and between Si flux and species richness Nsp ($r = -0.442$, $p = 0.045$). Correlation between NH_4 flux and AFDW of biodiffusors (R4afdw) was negative and close to significance threshold ($r = -0.423$, $p = 0.056$). No consistent relationship between ammonium fluxes measured in INC-dataset and the presence and biomass of infauna creating permanent burrows was found. For two parallel cores from the OB station sampled in spring 2015, the two overall highest values of NH_4 release were measured. In this case, increase of ammonium release corresponded with increased BPc observed in the cores (**Figure 6B**). Despite the presence of burrowing invertebrates and the second-high BPc values in both OB cores from winter 2016, only one of them displayed significant release of ammonium from the sediment, whereas for the other incubated core, no significant flux across the SWI could be detected. Moreover, even though burrowing macrofauna was present at OB in autumn 2015, sediment uptake of ammonium from the overlaying water was measured during the incubation. This was also the case at AB station in spring 2015 and winter 2016, though biomass of burrowing infauna (or species scored as biodiffusors) in AB cores was comparatively low (**Appendix 5**).

TABLE 3 | Correlation ratios of biological traits for the FCA ordination, that corresponds to the proportion of variance on each axis that can be explained by the trait modalities (abbreviation as in **Table 2**) within each trait.

	Axis1	Axis2		Axis1	Axis2
Correlation ratios			Spearman rank correlation (continued)		
Mot	**0.35**	0.04	**feed.sus**	**−0.74**	0.18
Feed	**0.23**	0.12	**feed.dep**	**−0.57**	−0.26
Struc	0.08	0.11	feed.pre	**−0.37**	−0.31
Sed	0.10	**0.20**	feed.sca	**−0.43**	−0.24
Size	0.17	0.06	feed.gra	−0.32	−0.03
Pos	**0.19**	0.10	**struc.bur**	**−0.48**	**−0.48**
Lar	0.05	0.00	**struc.pit**	**−0.79**	0.02
Long	**0.57**	0.16	struc.tub	−0.31	0
Eigenvalues	0.218	0.099	**struc.tra**	**−0.66**	0.28
Percent of Variance	35.07	15.98	**struc.epi**	**−0.6**	0.22
Total Inertia		0.622	**sed.sd**	**−0.62**	−0.26
Spearman rank correlations			sed.ds	**−0.4**	**−0.52**
DIC	**0.52**	−0.09	**sed.sm**	**−0.66**	0.27
Fe	0.05	**−0.37**	**sed.dm**	**−0.85**	−0.1
H_2S	**0.51**	−0.07	sed.no	0.13	0.16
Mn	0.34	−0.01	size.s	**−0.42**	0.06
NH_4	**0.64**	0.05	**size.m**	**−0.6**	0.19
PO_4	**0.53**	−0.04	**size.l**	**−0.82**	−0.07
Si	**0.62**	0.01	pos.pro	**−0.41**	−0.29
H_2S_diffl	**−0.36**	−0.1	pos.att	**−0.4**	0.04
Mn_diffl	**−0.43**	0.17	**pos.oxy**	**−0.56**	0.28
NH_4_diffl	**−0.66**	0	**pos.sox**	**−0.85**	−0.07
PO_4_diffl	**−0.67**	−0.02	**lar.pla**	**−0.83**	0
Si_diffl	**−0.53**	0.11	lar.ben	−0.46	−0.09
SO_4_diffl	-0.21	0.22	long.2	−0.26	−0.15
TA_diffl	**−0.51**	−0.02	long.5	−0.38	0.02
mot.sed	**−0.83**	0.02	long.10	−0.68	−0.33
mot.lim	**−0.77**	0.11	long.10p	−0.64	0.28
mot.fre	**−0.51**	−0.1			
mot.spel	**−0.41**	**−0.47**			

*Highest ratios for each axis are in bold. The respective eigenvalues and percent of variance explained are given for each axis. The total inertia (in parentheses) represents the total variance accounted for in an ordination (**Figure 4**). The spearman rank correlations (significant in bold) between each axis scores and sediment reservoirs (variables DIC to Si) and diffusive fluxes (variables abbreviated with "diffl"), as well as correlations with each trait modality, are listed.*

Estimate of Advective Flux Component and Effect of Macrofaunal Activity

The results of comparing the effects of macrofaunal activity on the total, diffusive and advective components of the Si flux are presented in **Figure 7** and **Table 4**. As we expected, the most pronounced effect was the positive correlation between advective flux component and infauna activity expressed by bioturbation potential (and, to a smaller degree, abundance and biomass), while the diffusive flux negatively correlated with benthos activity. When muddy and sandy sites were considered separately, no significant effects were found for muddy stations. Looking into more detail, at muddy LB site in autumn 2015 only 65% of Si flux was due to advection and it corresponded with very low bioturbation potential of infauna enclosed in INC cores. In contrast, during winter 2016, diffusive Si fluxes were close to 0, therefore advection was nearly 100%, and BPc in INC cores was comparatively high (mostly due to biomass of bivalve *A. islandica* that could mix surficial sediments). At MB station in spring 2015 high total and low diffusive Si fluxes resulted in rather high advective flux component (75%), but the lowest macrozoobenthos activity was recorded in INC and PW cores (however, in Van Veen garb samples from MB site collected on same occasion AFDW biomass was rather high, mainly again due to *A. islandica* exceeding 10 g/m^2). For sandy stations alone, advective component displayed correlation only with biomass averaged across incubated cores, and this relation was negative.

DISCUSSION

Previous studies have established that macrofaunal reworking, including bioturbation, can cause much higher nutrient flux from sediments into the water column than molecular diffusion

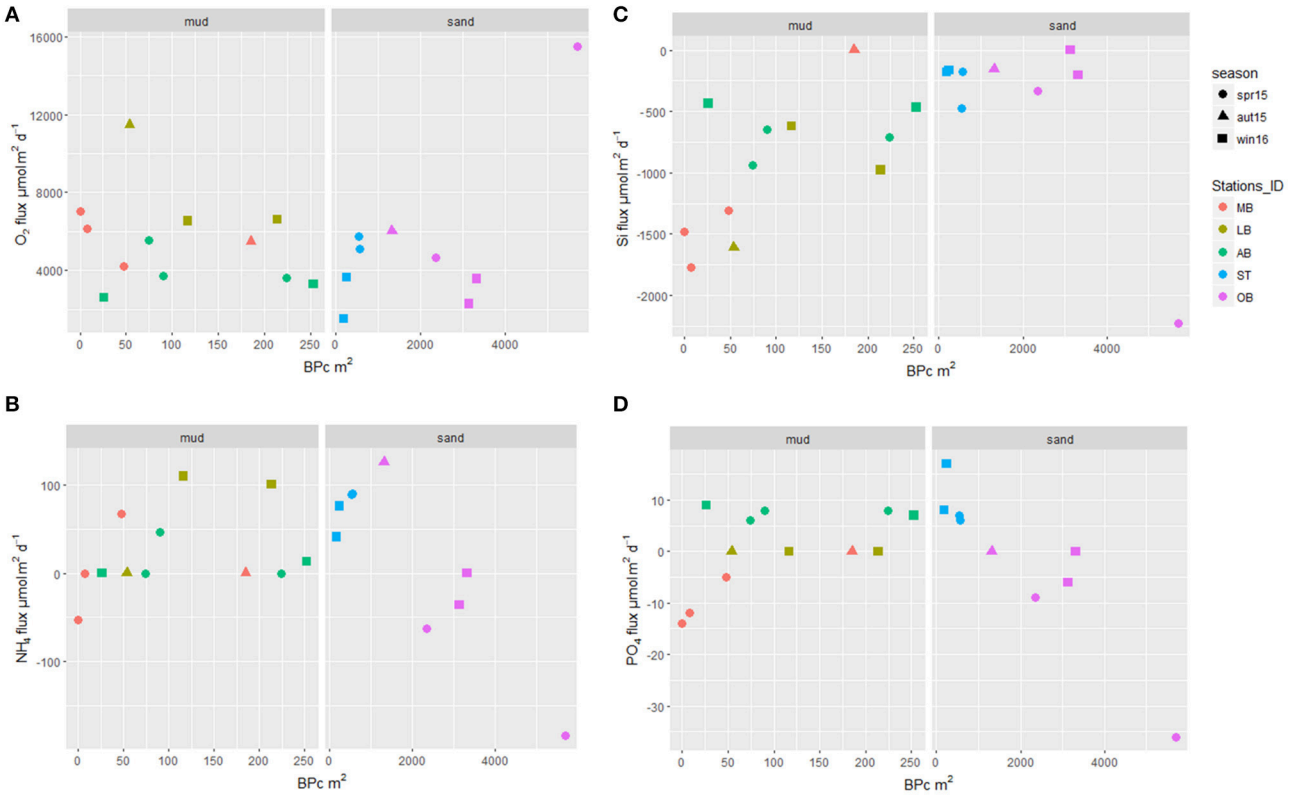


FIGURE 6 | Total oxygen uptake **(A)**, NH_4 **(B)**, Si **(C)** and PO_4 **(D)** total solute fluxes [µmol m^2/day] across the SWI (negative values indicate release from the sediment) derived from incubation of natural cores (Lipka et al., 2018), plotted against community bioturbation potential BPc. Different colors indicate different stations, different symbols show seasonal variability.

in coastal areas (Mortimer et al., 1999; Christensen et al., 2000). Bioirrigation generates transport of pore-water especially in the presence of tube-dwelling animals or gallery-building biodiffusers (Aller, 1982; Kristensen, 2001; Shull et al., 2009; Braeckman et al., 2010). Where macrofauna is abundant, oxygen is introduced punctually deeper into the sediment surface, therefore shifting the sulfidic zone downwards. Although this is recognized, actual quantitative field estimates are scarce.

It is suggested that functional group composition of biota is the most critical aspect of biodiversity for ecosystem functioning in the context of global biogeochemical cycles (Snelgrove et al., 2018). We attempted to identify the main players responsible for altered geochemical profiles and looked for similarities and patterns explaining significant alterations of calculated fluxes across the SWI in the south-western Baltic Sea. Taxonomic and functional identities, estimates of abundance, biomass and community bioturbation potential were used to assess the role of macrofauna in variation of pore-water reservoirs, oxygen uptake and total nutrient efflux. The first general observation is that data scatters a lot over time, differences in scale and from repetitions.

Among the possible reasons explaining why the interpretation of data reveals no clear strong dependencies are three major points: (1) the activity of organisms has stochastic nature, it is not constant and mixing, pumping, and respiration work of individuals captured in the analyzed cores may be reduced in intensity or ceased, especially under stressed conditions associated with sampling procedures; (2) human induced impacts on the seafloor such as trawling fishery evidenced e.g., in the Bay of Mecklenburg (that were not quantitatively captured by our analysis) may overwhelm the coupling of macrofauna activity and sedimentary biogeochemistry; (3) marine microorganisms are a major component of global nutrient cycles (Arrigo, 2005), whereas macrozoobenthos is only a mediator of bacterial-induced processes in benthic-pelagic coupling (Yazdani Foshtomi et al., 2015). Leuzinger et al. (2011) found that the magnitude of responses decline in higher order interactions and suggest that global scale impacts on the ecosystem may be dampened as a result of positive and negative drivers of change.

Parameters like salinity, temperature and oxygen affect both redox-reactions and animal distribution, density and behavior (Gogina et al., 2014; Gammal et al., 2017). During autumn 2015, our study observed oxygen depletion at all stations with the exception of OB, and near-bottom water temperature was much warmer compared to the other cruises (**Table 1**). Hypoxia could be stimulated by an inflow of North Sea waters into the Baltic Sea in December 2014 that terminated a decade of continuously increasing oxygen deficiency in the central deep basins (Mohrholz et al., 2015). According to findings of

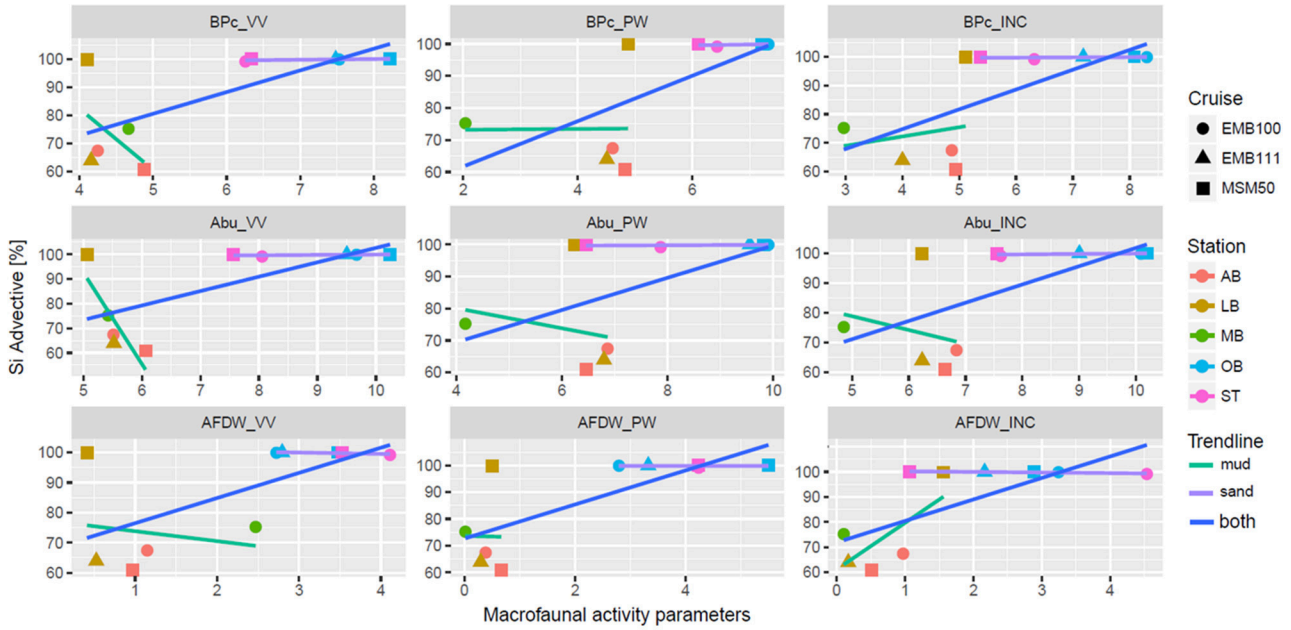


FIGURE 7 | Estimate of advective component (in %) of Si total fluxes at different sites and seasons (EMB100–spring 2015, EMB111–autumn 2015, MSM50–winter 2016) plotted against log-transformed major macrofaunal parameters (BPc_VV, BPc_PW, BPc_INC—community bioturbation potential estimated per m^2 based on Van Veen Grab (0.1 m^2) samples (VV), pore-water (PW) cores set and incubation (INC) cores set, respectively, Abu refers to respective abundance [ind/m^2] and AFDW—to biomass [AFDW g/m^2].

TABLE 4 | Spearman rank correlation coefficients between the estimated total, diffusive, and advective fluxes, as well as advective component of Si, and general macrofaunal parameters (averaged per cruise and site).

	BPc_VV	BPc_PW	BPc_INC	Abu_VV	Abu_PW	Abu_INC	AFDW_VV	AFDW_PW	AFDW_INC
SPEARMAN RANK CORRELATION, BOTH MUD AND SAND SITES (*N* = 11 SAMPLING EVENTS)									
totSi	−0.57	−0.36	−0.54	−0.55	−0.31	−0.31	**−0.67**	**−0.62**	−0.42
difSi	**−0.63**	**−0.8**	**−0.72**	−0.55	−0.33	**−0.75**	−0.42	**−0.83**	**−0.66**
advSi	−0.41	−0.17	−0.34	−0.41	−0.17	−0.16	−0.53	−0.49	−0.2
SiAdv%	**0.68**	**0.74**	**0.74**	0.58	0.42	**0.67**	0.62	**0.68**	0.61
SPEARMAN RANK CORRELATION, MUD SITES (*N* = 6 SAMPLING EVENTS)									
totSi_ink	**−0.79**	−0.5	**−0.82**	−0.71	−0.24	−0.24	−0.64	−0.68	−0.54
difSi_pw	−0.21	**−0.89**	−0.57	−0.07	0.38	−0.65	−0.11	**−0.79**	−0.64
advSi	−0.71	−0.54	**−0.86**	**−0.79**	−0.4	−0.31	−0.54	−0.71	−0.57
SiAdvToTot	0.09	0.49	0.49	−0.14	−0.41	0.17	0.37	0.26	0.54
SPEARMAN RANK CORRELATION, SAND SITES (*N* = 5 SAMPLING EVENTS)									
totSi_ink	−0.4	0.2	0.1	−0.3	0.1	−0.3	−0.1	−0.6	0.5
difSi_pw	−0.6	0.2	0	−0.3	0	−0.3	0.1	−0.4	0.7
advSi	−0.4	0.2	0.1	−0.3	0.1	−0.3	−0.1	−0.6	0.5
SiAdvToTot	0.45	−0.11	−0.11	0.11	−0.11	0.11	−0.22	0.11	**−0.89**

Values marked in bold are significant. Advective fluxes (advSi) are estimated as difference between total (totSi) and diffusive fluxes (difSi). The advective component (SiAdv%) is calculated as the percentage of advective flux in the total flux. Macrofaunal parameters: BPc_VV, BPc_PW, BPc_INC, bioturbation potential based on Van Veen Grab samples (VV); PW indicates pore-water cores set and INC, incubation cores set, respectively. Abu refers to abundance [ind/m^2] and AFDW, to biomass [AFDW g/m^2].

Braeckman et al. (2010) faunal simulation can double benthic microbial respiration and mineralization especially in summer, whereas in winter, before the spring phytoplankton bloom, faunal effects can be negligible. The authors explained the strong summer effect by reference to higher macrobenthic activity owing to the elevated temperature and better animals' conditions (enhanced metabolism). Perhaps due to the complexity of interactive effects, we were unable to find distinct seasonal patterns in our data. Indeed, at LB station we observed the highest total oxygen uptake in autumn 2015 among muddy

sites, corresponding with one of the lowest BPc values, whereas at MB site intermediate total oxygen uptake was found in the core with the highest BPc (**Figure 6**). The absence of abiotic variables in the best solution of our DistLM model (to explain the multivariate patterns of variation of oxygen consumption and total benthic fluxes measured in incubation experiments, see **Data sheet 2**) could be due to the fact that in our case information on macrofauna was resolved to the core level whereas abiotic variables were measured at coarser spatial scale (per station and sampling event), that can explain the low predictive power of the latter in this limited dataset. On the other hand, it can also be due to the close linkage between species and their environment, that the former well mirroring the latter (in agreement with Belley and Snelgrove, 2016).

Estuarine ecosystems are subjected to a high degree of variability in their environmental conditions due to usually large areas with shallow water depth, freshwater and seawater inputs, as well as climatic and anthropogenic impacts. van der Linden et al. (2017) found polychaetes to display higher levels of functional diversity compared to mollusc group in tropical estuaries. Whereas infaunal activity inherently contributes to increased solute exchange between the sediment and the overlying water, the contribution of the underlying drivers varies among functional groups through increased diffusive fluxes, advective pore water bioirrigation (Kristensen et al., 2012), and animal excretion. Mermillod-Blondin et al. (2004) showed that in diffusion dominated systems *Cerastoderma edule* acted as a biodiffuser in the top 2 cm of the sediment, but had little effect on O_2 consumption, water exchange across SWI, microbial characteristics, and release of nutrients from the sediment. In contrast, *Corophium volutator* and *Hediste diversicolor* build burrows in the sediment that allows transport of surface particles into biogenic structures and enhanced solute exchange. *H. diversicolor* typically bury down to 10 cm, maximal—down to 30 cm sediment depth (Zettler et al., 1994). *C. glaucum* (having traits similar to *C. edule*) and *H. diversicolor* were also typically present in INC cores from our OB station (see **Appendix 2**), together with another burrowing polychaetes *Marenzelleria viridis*. Particularly in the core OB1, where overall highest nutrient fluxes released from the sediments were observed, *H. diversicolor* contributed up to 11% to total biomass (with 3.8 g AFDW/m^2) and dominated the BPc (with a share of 24%), whereas *C. glaucum* had the share of 26% in biomass (with 9.1 g AFDW/m^2) and 18% in BPc.

Norkko et al. (2013) depicted the number of large bivalves as the best predictor of ecosystem functioning. In our data, bivalves that can reach individual sizes exceeding 5 mm (at their longest dimension) are represented by *A. islandica*, *C. glaucum, L. balthica* and deep-dwelling (down to 25 cm sediment depth) *M. arenaria*. Increased biomass of *A. islandica* (e.g., ST cores from spring 2015 and winter 2016) was observed along with a declining release of ammonium and phosphate, whereas higher abundance of *M. arenaria* coincided with a significant increase of ammonium and phosphate total fluxes out of the sediment at OB site. Also, sulfide appearance depth showed a strong positive correlation with abundance of *M. arenaria* (see **Appendix 6**). At muddy stations, total phosphate release was recorded only in cores from the MB site where no bivalves were present (with the exception of 1 small individual of *Corbula gibba* having AFDW biomass of 0.22 mg). The only incubated core from MB station that displayed no phosphate release was inhabited by one relatively large (15 mg) individual of *N. hombergii*. This all suggests the importance of both tube dwelling and burrowing polychaetes and bivalves acting as biodiffusors.

The significant positive relationship between biogenic mixing depth *sensu* Solan et al. (2004) and sulfide appearance depth found in our study is in agreement with findings of Sturdivant and Shimizu (2017) who showed a match between the burrow depth and the aRPD values (apparent color redox-potential discontinuity). Our results also support the conclusions of the previous studies that found BPc to be a good proxy for ecosystem efficiency (e.g., Baldrighi et al., 2017). According to Cozzoli (2016), metabolic energy will be spent on sediment reworking independent of the type of bioturbation, in order to obtain food, resulting in sediment mixing and the exposure of fine particles to the surface, where they can be resuspended. The ability to spend this energy will scale with metabolism, and therefore it is natural to expect a scaling of ecosystem engineering with body size and abundance.

We have tested the effect of macrofaunal activity (expressed by abundance, biomass and BPc that includes both) on the advective component of the Si flux and compared it to the effect on the total and diffusive Si fluxes. In accordance with our expectations, the most pronounced effect was the positive correlation between the advective flux component and infauna activity expressed by bioturbation potential (and, to a smaller degree, abundance and biomass), while the diffusive flux negatively correlated with benthos activity, suggesting that gradients were leveled out by advective processes (see **Appendix 7**). In line with Huettel et al. (1998), advective transport processes were the most important in controlling total fluxes in permeable sediments. However, the significance of the relationship between advective component and macrofaunal activity in our data did not preserve when sandy and muddy sites were treated separately (for sandy cores, only the negative correlation with biomass was significant).

Based on this study and the high variability of data, it is difficult to predict implications that can be expected if the invertebrate community of those typical habitats of the south-western Baltic Sea would change (e.g., due to climatic variability or human-induced pressures). Generally, increased biodiversity enhances ecosystem functioning due to increased probability of the presence of species fulfilling particular functions (Magurran, 2012). Our study was ultimately constrained spatially (to our set of sampling stations) and temporally (by the onset of cruises with respective conditions of preceding inflow, seasonal hypoxia in autumn 2015 and/or storms). Both species distributions as well as nutrient fluxes are temporally dynamic (**Figure 6**) and those natural patterns inhibit clear interpretation of presented field data, i.e., this is an example of the need for more repeated samplings and replicates at these areas of high spatio-temporal variability there is a need of more repeated samplings and replicates (but see Bolam et al., 2002). Nevertheless, such data free from experimental

manipulations (such as de-oxygenation or defaunation) presents valuable information on the true complexity of ecosystem functioning in the natural system (Carpenter, 1996). The description of the variability itself has a value as a source of documented information for the future generalizations (Coble et al., 2016). Until a great deal of empirical experience is collected, we do not know whether a given example of structure is extraordinary, or it is a mere trivial expression of something which we may learn to expect all the time (Hutchinson, 1953).

Overall, from the parameters tested, bioturbation potential was identified as the best proxy for variation in pore-water reservoirs of biogeochemical components compared to available abiotic proxies, abundance, or biomass parameters (in total or considered separately for different functional groups). This was anticipated due to high scoring of deep-burrowing and bioturbating taxa (particularly large individuals) that have a major influence on all oxygen-dependent biogeochemical processes, supporting the importance of functional groups (Bolam et al., 2002).

Small-scale disturbances such as hypoxia (observed during EMB111 cruise in autumn 2015), sediment transport due to currents, trawling or storms, may play a driving, often diminishing, role for biodiversity in general and bioturbation in particular (Villnäs et al., 2013; Gogina et al., 2017). These disturbances also affect fluxes in and out of the sediment (Villnäs et al., 2013). Whereas the mixing effect of physical disturbance can be similar to bioturbation, the effects of species respiration or enlarged pool of their metabolic waste products, such as ammonium (Thoms et al., 2018), is likely to be different. This highlights the complexity of ecosystem function relationships in the soft sediment benthos.

Another, more important factor that may impact the biogeochemical sediment services that has to be considered in future studies is the abundance, community structure and activity of microorganisms, that are particularly active in muddy and sandy surface sediments and cause the liberation of metabolites to the pore-waters (Llobet-Brossa et al., 1998, 2002; Sahm et al., 1999; de Beer et al., 2005), therefore creating the disequilibrium physicochemical environment that promotes element fluxes within the sediments and across the sediment-water interface (Boudreau, 1997). A further factor that may impact the transport processes of electrons in the surface sediment and may have to be addressed in future studies is the activity of cable bacteria (van de Velde et al., 2017).

Despite of our initial expectation, no clear relationships and consistent patterns were found between major macrobenthic parameters and biogeochemical fluxes at stations of the same sediment type. However, we should not ignore this absence of correlations even if it does not meet the general expectation, and therefore we find reporting of these negative results here particularly important. For example, Jacquot et al. (2018) also reported the lack of the relationship between macrofauna and denitrification they were aiming to find, and suggested that macrofaunal density and/or burrowing activity should be above some threshold to increase bioturbation or irrigation to sufficient levels to affect denitrification (see also **Appendix 8**).

CONCLUSIONS AND PERSPECTIVES

Our data indicates that bioturbation and bioirrigation alter near-surface pore-water profiles of nutrients toward bottom water signals. Biogeochemical fluxes can partly be explained by functional structure of macrofauna, with community bioturbation potential performing as the best proxy among the tested set of biotic and abiotic variables. The effects of macrobenthos on benthic solute reservoirs and total fluxes differed between sediment types, specific locations, and seasons. High complexity and variability in spatial and temporal distribution, anthropogenic influence (e.g., fishery) and short-term physical events (e.g., storms) hinder interpretability of collected data. Thus, the outcomes of this case study are context dependent, but the search and exploration of similar parallel datasets combining characterization of biogeochemical processes across the sediment-water interface should be continued at different scales: in the study area as well as other regions. Ideally, microbiological data should be included in the analysis, to reveal significant relationships, address their generality and better capture the natural variability and various hidden mechanisms.

AUTHOR CONTRIBUTIONS

The contributions of the authors are: MG, ML, JW, MB, and MZ designed the study. MG did macrofauna sampling, most of the analysis and calculations and wrote the paper. ML carried out sediment sampling and pore-water analysis. ML and JW conducted the incubation experiments, and ML performed the fluxes calculations. BL contributed to modeling the impact of physical disturbances on pore-water profiles. CM contributed the chlorophyll a data and was involved in sampling and analysis. All authors contributed to writing, review and editing, read the text and agreed about the final version of the manuscript.

FUNDING

This work was supported by the German Federal Ministry for Education and Research: KÜNO Projects SECOS (03F0666) and SECOS-Synthese (03F0738).

ACKNOWLEDGMENTS

We greatly acknowledge the valuable support of all IOW colleagues deployed in field sampling and laboratory analyses, in particular, Anne Köhler and Iris Schmiedinger, and the captains and crews of RVs Elisabeth Mann Borgese, Poseidon, Alkor, and Maria S. Merian. We greatly acknowledge the comments by two reviewers and the editor Teresa Radziejewska that helped to considerably improve this manuscript. We express our thanks to Irina Steinberg for correcting the English.

SUPPLEMENTARY MATERIAL

The Supplementary Material for this article can be found online at: https://www.frontiersin.org/articles/10.3389/fmars.2018.00489/full#supplementary-material

REFERENCES

Aller, R. C. (1982). "The effects of macrobenthos on chemical properties of marine sediment and overlying water," in *Animal–Sediment Relations. Topics in Geobiology*, Vol 100, eds P.L. McCall and M. J. S. Tevesz (Boston, MA: Springer), 53–102.

Aller, R. C. (1994). Bioturbation and remineralization of sedimentary organic matter: effects of redox oscillation. *Chem. Geol.* 114, 331–345. doi: 10.1016/0009-2541(94)90062-0

Anderson, M. J., Gorley, R. N., and Clarke, K. R. (2008). *PERMANOVA+ for PRIMER Guide to Software and Statistical Methods*. Plymouth: PRIMER-E Ltd.

Arntz, W. E. (1981). "Biomass zonation and dynamics of macrozoobenthos in an area stressed by oxygen deficiency," in *Stress Effects on Natural Ecosystems*, eds G. Barrett and R. Rosenberg (Chichester: John Wiley and Sons), 179–200.

Arrigo, K. R. (2005). Marine microorganisms and global nutrient cycles. *Nature* 437, 349–355. doi: 10.1038/nature04159

Baldrighi, E., Giovannelli, D., D'Errico, G., Lavaleye, M., and Manini, E. (2017). Exploring the relationship between macrofaunal biodiversity and ecosystem functioning in the deep sea. *Front. Mar. Sci.* 3:198. doi: 10.3389/fmars.2017.00198

Belley, R., and Snelgrove, P. V. R. (2016). Relative contributions of biodiversity and environment to benthic ecosystem functioning. *Front. Mar. Sci.* 3:242. doi: 10.3389/fmars.2016.00242

Bolam, S. G., Fernandes, T. F., and Huxham, M. (2002). Diversity, biomass and ecosystem processes in the marine benthos. *Ecol. Monogr.* 72, 599–615. doi: 10.1890/0012-9615(2002)072[0599:DBAEPI]2.0.CO;2

Bonaglia, S., Bartoli, M., Gunnarsson, J. S., Rahm, L., Raymond, C., Svensson, O., et al. (2013). Effect of reoxygenation and *Marenzelleria* spp. Bioturbation on Baltic Sea sediment metabolism. *Mar. Ecol. Prog. Ser.* 482, 43–55. doi: 10.3354/meps10232

Boudreau, B. P. (1997). *Diagenetic Models and their Implementations*. Berlin: Springer Verlag.

Braeckman, U., Provoost, P., Gribsholt, B., Van Gansbeke, D., Middelburg, J. J., Soetaert, K., et al. (2010). Role of macrofauna functional traits and density in biogeochemical fluxes and bioturbation. *Mar. Ecol. Prog. Ser.* 399, 173–186. doi: 10.3354/meps08336

Bremner, J., Rogers, S., and Frid, C. (2006). Methods for describing ecological functioning of marine benthic assemblages using Biological Traits Analysis (BTA). *Ecol. Indic.* 6, 609–622. doi: 10.1016/j.ecolind.2005.08.026

Bunke, D. (2018). *Sediment Mixing Processes and Accumulation Patterns in The South-Western Baltic Sea*. Dissertation, University of Greifswald.

Carpenter, S. R. (1996). Microcosm experiments have limited relevance for community and ecosystem ecology. *Ecol.* 77, 677–680. doi: 10.2307/2265490

Chevenet, F., Doledec, S., and Chessel, D. (1994). A fuzzy coding approach for the analysis of long-term ecological data. *Freshw. Biol.* 31, 295–309. doi: 10.1111/j.1365-2427.1994.tb01742.x

Christensen, B., Vedel, A., and Kristensen, E. (2000). Carbon and nitrogen fluxes in sediment inhabited by suspension-feeding (*Nereis diversicolor*) and non-suspension-feeding (*N. Virens)* polychaetes. *Mar. Ecol. Prog. Ser.* 192, 203–217. doi: 10.3354/meps192203

Clarke, K. R., Gorley, R. N., Somerfield, P. J., and Warwick, R. M. (2014). *Change in Marine Communities: An Approach to Statistical Analysis and Interpretation*. Plymouth: PRIMER-E.

Cline, J. D. (1969). Spectrophotometric determination of hydrogen sulfide in natural waters. *Limnol. Oceanogr.* 14, 454–458. doi: 10.4319/lo.1969.14.3.0454

Coble, A. A., Asch, R. G., Rivero-Calle, S., Heerhartz, S. M., Holding, J. M., Kremer, C. T., et al. (2016). Climate is variable, but is our science? *Limnol. Oceanogr. Bull.* 25, 71–76. doi: 10.1002/lob.10115

Cozzoli, F. (2016). *Modelling Biota-Sediment Interactions in Estuarine Environments*. Dissertation, Nijmegen: Radboud University.

de Beer, D., Wenzhöfer, F., Ferdelman, T. G., Boehme, S. E., Hüttel, M., Van Beusekom, J. E. E., et al. (2005). Transport and mineralization in North Sea sandy intertidal sediments, Sylt-Rømø Basin, Wadden Sea. *Limnol. Oceanogr.* 50, 113–127. doi: 10.4319/lo.2005.50.1.0113

Delefosse, M., and Kristensen, E. (2012). Burial of *Zostera marina* seeds in sediment inhabited by three polychaetes: laboratory and field studies. *J. Sea Res.* 71, 41–49. doi: 10.1016/j.seares.2012.04.006

Dray, S., and Dufour, A. B. (2007). The ade4 package: implementing the duality diagram for ecologists. *J. Stat. Softw.* 22, 1–20. doi: 10.18637/jss.v022.i04

Gammal, J., Norkko, J., Pilditch, C. A., and Norkko, A. (2017). Coastal hypoxia and the importance of benthic macrofauna communities for ecosystem functioning. *Estuaries Coast.* 40, 457–468. doi: 10.1007/s12237-016-0152-7

Gilbertson, W. W., Solan, M., and Prosser, J. I. (2012). Differential effects of microorganism–invertebrate interactions on benthic nitrogen cycling. *FEMS Microbiol. Ecol.* 82, 11–22. doi: 10.1111/j.1574-6941.2012.01400.x

Gogina, M., Darr, A., and Zettler, M. L. (2014). Approach to assess consequences of hypoxia disturbance events for benthic ecosystem functioning. *J. Mar. Syst.* 129, 203–213. doi: 10.1016/j.jmarsys.2013.06.001

Gogina, M., Morys, C., Forster, S., Gräwe, U., Friedland, R., and Zettler, M. L. (2017). Towards benthic ecosystem functioning maps: quantifying bioturbation potential in the German part of the Baltic Sea. *Ecol. Ind.* 73, 574–588. doi: 10.1016/j.ecolind.2016.10.025

Gray, J. S. (1974). Animal-sediment relationships. *Oceanogr. Mar. Biol. Ann. Rev.* 12, 223–261.

Guy-Haim, T., Lyons, D., Kotta, J., Ojaveer, H., Queiros, A., Chatzinikolaou, E., et al. (2017). Diverse effects of invasive ecosystem engineers on marine biodiversity and ecosystem functions: a global review and meta-analysis. *Glob. Change Biol.* 24, 906–924. doi: 10.1111/gcb.14007

Haese, R. R. (2006). "The biogeochemistry of iron," in *Marine Geochemistry*, eds H. D. Schulz, and M. Zabel (Berlin: Springer), 241–270.

Hansen, K., and Kristensen, E. (1997). Impact of macrofaunal recolonization on benthic metabolism and nutrient fluxes in a shallow marine sediment previously overgrown with macroalgal mats. *Estuar. Coast. Shelf Sci.* 45, 613–628. doi: 10.1006/ecss.1996.0229

Huettel, M., Ziebis, W., Forster, S., and Luther, G. W. (1998). Advective transport affecting metal and nutrient distributions and interfacial fluxes in permeable sediments. *Geochim. Cosmochim. Acta* 62, 613–631. doi: 10.1016/S0016-7037(97)00371-2

Hutchinson, G. E. (1953). The concept of pattern in ecology. *Proc. Acad. Nat. Sci. Philadelphia* 105, 1–12.

Jacquot, M. P., Dorgan, K. M., Mortazavi, B., Kleinhuizen, A. A., and Clemo, W. C. (2018). Macrobenthic community structure and influence on denitrification capacity in soft sediments (Mobile Bay, Alabama, USA). *Mar. Ecol. Prog. Ser.* 605, 17–35. doi: 10.3354/meps12759

Janas, U., Bonsdorff, E., Warzocha, J., and Radziejewska, T. (2017). "Deep soft seabeds," in *Biological Oceanography of the Baltic Sea,* eds. P. Snoeijs-Leijonmalm, H. Schubert, and T. Radziejewska (Springer), 359–385.

Jordan, M. A., Welsh, D. T., Dunn, R. J. K., and Teasdale, P. R. (2009). Influence of Trypaea australiensis population density on benthic metabolism and nitrogen dynamics in sandy estuarine sediment: a mesocosm simulation. *J. Sea. Res.* 61, 144–152. doi: 10.1016/j.seares.2008.11.003

Karlson, K., Bonsdorff, E., and Rosenberg, R. (2007). The impact of benthic macrofauna for nutrient fluxes from Baltic Sea sediments. *AMBIO* 36, 161–167. doi: 10.1579/0044-7447(2007)36[161:TIOBMF]2.0.CO;2

Kowalski, N., Dellwig, O., Beck, M., Grunwald, M., Dürselen, C.-D., Badewien, T. H., et al. (2012). A comparative study of manganese dynamics in the water column and sediments of intertidal systems of the North Sea. *Estuar. Coast. Shelf Sci.* 100, 3–17. doi: 10.1016/j.ecss.2011.03.011

Kristensen, E. (2001). Impact of polychaetes (*Nereis* spp. and *Arenicola marina*) on carbon biogeochemistry in coastal marine sediments. *Geochem. Trans.* 2, 92–103. doi: 10.1186/1467-4866-2-92

Kristensen, E., Penha-Lopes, G., Delefosse, M., and Valdemarsen, T. (2012). What is bioturbation? The need for a precise definition for fauna in aquatic sciences. *Mar. Ecol. Prog. Ser.* 446, 285–302. doi: 10.3354/meps09506

Leuzinger, S., Lou, Y. Q., Beier, C., Dieleman, W., Vicca, S., and Körner, C. (2011). Do global change experiments overestimate impacts on terrestrial ecosystems? *Trends Ecol. Evol.* 26, 236–241. doi: 10.1016/j.tree.2011.02.011

Lipka, M., Woelfel, J., Gogina, M., Kallmeyer, J., Liu, B., Morys, C., et al. (2018). Solute reservoirs reflect variability of early diagenetic processes in temperate brackish surface sediments. *Front. Mar. Sci.* 5:1. doi: 10.3389/fmars.2018.00413

Llobet-Brossa, E., Rabus, R., Böttcher, M. E., Könneke, M., Finke, N., Schramm, A., et al. (2002). Community structure and activity of sulfate-reducing bacteria in an intertidal surface sediment: a multi-method approach. *Aquat. Microb. Ecol.* 29, 211–226. doi: 10.3354/ame029211

Llobet-Brossa, E., Rosselló-Mora, R., and Amann, R. (1998). *Microbial community* composition of Wadden Sea sediments as revealed by fluorescence *in situ* hybridization. *Appl. Environ. Microbiol.* 64, 2691–2696.

Magurran, A. E. (2012). "Biodiversity in the context of ecosystem function," in *Marine Biodiversity and Ecosystem Functioning: Frameworks, Methodologies, and Integration,* eds. M. Solan, R. J. Aspden, and D. M. Paterson (Oxford: Oxford University Press), 16–23. doi: 10.1093/acprof:oso/9780199642250.003.0002

Maximov, A. A., Eremina, T. R., Lange, E. K., Litvinchuk, L. F., and Maximova, O. B. (2014). Regime shift in the ecosystem of the eastern Gulf of Finland caused by the invasion of the polychaete *Marenzelleria arctia*. *Oceanology* 54, 46–53. doi: 10.1134/S0001437013060052

McArdle, B. H., and Anderson, M. J. (2001). Fitting multivariate models to semi-metric distances: a comment on distance-based redundancy analysis. *Ecology* 82, 290–297. doi: 10.1890/0012-9658(2001)082[0290:FMMTCD]2.0.CO;2

Mermillod-Blondin, F. (2011). The functional significance of bioturbation and biodeposition on biogeochemical processes at the water–sediment interface in freshwater and marine ecosystems. *J. N. Am. Benthol. Soc.* 30, 770–778. doi: 10.1899/10-121.1

Mermillod-Blondin, F., Rosenberg, R., François-Carcaillet, F., Norling, K., and Mauclaire, L. (2004). Influence of bioturbation by three benthic infaunal species on microbial communities and biogeochemical processes in marine sediment. *Aquat. Microb. Ecol.* 36, 271–284. doi: 10.3354/ame036271

Mohrholz, V., Naumann, M., Nausch, G., Krüger, S., and Gräwe, U. (2015). Fresh oxygen for the Baltic Sea – an exceptional saline inflow after a decade of stagnation. *J. Mar. Sys.* 148, 152–166. doi: 10.1016/j.jmarsys.2015.03.005

Mortimer, R. J. G., Davey, J. T., Krom, M. D., Watson, P. G., Frinkers, P. E., and Clifton, R. J. (1999). The effect of macrofauna on porewater profiles and nutrient fluxes in the intertidal zone of the Humber estuary. *Estuar.Coast. Shelf Sci.* 48, 683–699. doi: 10.1006/ecss.1999.0479

Morys, C., Forster, S., and Graf, G. (2016). Variability of bioturbation in various sediment types and on different spatial scales in the Southwestern Baltic Sea. *Mar. Ecol. Progr. Ser.* 557, 31–49. doi: 10.3354/meps11837

Morys, C., Powilleit, M., and Forster, S. (2017). Bioturbation in relation to the depth distribution of macrozoobenthos in the southwestern Baltic Sea. *Mar. Ecol. Prog. Ser.* 579, 19–36. doi: 10.3354/meps12236

Norkko, A., Villnäs, A., Norkko, J., Valanko, S., and Pilditch, C. (2013). Size matters: implications of the loss of large individuals for ecosystem function. *Sci. Rep.* 3:2646. doi: 10.1038/srep02646

Norkko, J., Reed, D. C., Timmermann, K., Norkko, A., Gustafsson, B. G., Bonsdorff, E., et al. (2012). A welcome can of worms? Hypoxia mitigation by an invasive species. *Glob. Change Biol.* 18, 422–434. doi: 10.1111/j.1365-2486.2011.02513.x

Paterson, D. M., Defew, E. C., and Jabour, J. (2012). "Ecosystem functioning and co-evolution of terminology in marine science and management," in *Marine Biodiversity and Ecosystem Functioning: Frameworks, Methodologies, and Integration*, eds. M. Solan, R.J. Aspden, and D.M. Paterson. (Oxford: Oxford University Press), 24–33.

Pelegri, S. P., and Blackburn, T. H. (1994). Bioturbation effects of the amphipod Corophium volutator on microbial nitrogen transformations in marine-sediments. *Mar. Biol.* 121, 253–258. doi: 10.1007/BF00346733

Reyes, C., Dellwig, O., Dahnke, K., Gehre, M., Noriega-Ortega, B. E., Böttcher, M. E., et al. (2016). Bacterial communities potentially involved in iron-cycling in Baltic Sea and North Sea sediments revealed by pyrosequencing. *FEMS Microbiol. Ecol.* 92:fiw054. doi: 10.1093/femsec/fiw054

Rhoads, D. C. (1974). Organism-sediment realtions on the muddy sea floor. *Oceanogr. Mar. Biol. Ann. Rev.* 12, 263–300.

Rusch, A., Huettel, M., Wild, C., and Reimers, C. (2006). Benthic oxygen consumption and organic matter turnover in organic-poor, permeable shelf sands. *Aquat. Geochem.* 12, 1–9. doi: 10.1007/s10498-005-0784-x

Sahm, K., MacGregor, B. J., Jørgensen, B. B., and Stahl, D. A. (1999). Sulphate *reduction* and vertical distribution of sulphate-*reducing* bacteria quantified by rRNA slot-blot hybridization in a coastal marine sediment. *Environ. Microbiol.* 1, 65–74. doi: 10.1046/j.1462-2920.1999.00007.x

Seeberg-Elverfeldt, J., Schlüter, M., Feseker, T., and Kölling, M. (2005). Rhizon sampling of porewaters near the sediment-water interface of aquatic systems. *Limnol. Oceanogr. Methods* 3, 361–371. doi: 10.4319/lom.2005.3.361

Shull, D., Benoit, J., Wojcik, C., and Senning, J. R. (2009). Infaunal burrow ventilation and pore-water transport in muddy sediments. *Estuar. Coast. Shelf Sci.* 83, 277–286. doi: 10.1016/j.ecss.2009.04.005

Snelgrove, P. V. R., Soetaert, K., Solan, M., Thrush, S., Wei, C.-L., Danovaro, R., et al. (2018). Global carbon cycling on a heterogeneous seafloor. *Trends. Ecol. Evol.* 33, 96–105. doi: 10.1016/j.tree.2017.11.004

Solan, M., Cardinale, B. J., Downing, A. L., Engelhardt, K. A. M., Ruesink, J. L., and Srivastava, D. S. (2004). Extinction and ecosystem function in the marine benthos. *Science* 306, 1177–1180. doi: 10.1126/science.1103960

Sturdivant, S. K., and Shimizu, M. S. (2017). *In situ* organism-sediment interactions: bioturbation and biogeochemistry in a highly depositional estuary. *PLoS ONE* 12:e0187800. doi: 10.1371/journal.pone.0187800

Tauber, F. (2012). *Meeresbodensedimente in der deutschen Ostsee. Bundesamt für Seeschifffahrt und Hydrographie, Hamburg*. Available online at: www.bsh.de/de/Produkte/Karten/Geologische_Karten/index.jsp

Thoms, F., Burmeister, C., Gogina, M., Janas, U., Kendzierska, H., Liskow, I., et al. (2018). Impact of macrofaunal communities on the coastal filter function in the Bay of Gdansk, Baltic Sea. *Front. Mar. Sci.* 5:201. doi: 10.3389/fmars.2018.00201

van de Velde, S., Callebaut, I., Gao, Y., and Meysman, F. (2017). Impact of electrogenic sulfur oxidation on trace metal cycling in a coastal sediment. *Chem. Geol.* 452, 9–23. doi: 10.1016/j.chemgeo.2017.01.028

van der Linden, P., Marchini, A., Smith, C. J., Dolbeth, M., Simone, L. R. L., Marques, S. J., et al. (2017). Functional changes in polychaete and mollusc communities in two tropical estuaries. *Estuar. Coast. Shelf Sci.* 187, 67–83. doi: 10.1016/j.ecss.2016.12.019

Villnäs, A., Norkko, J., Hietanen, S., Josefson, A. B., Lukkari, K., and Norkko, A. (2013). The role of recurrent disturbances for ecosystem multifunctionality. *Ecology* 94, 2275–2287. doi: 10.1890/12-1716.1

Winde, V., Böttcher, M. E., Escher, P., Böning, P., Beck, M., Liebezeit, G., et al. (2014). Tidal and spatial variations of $DI^{13}C$ and aquatic chemistry in a temperate tidal basin during winter time. *J. Mar. Sys.* 129, 394–402. doi: 10.1016/j.jmarsys.2013.08.005

Winkler, L. (1888). Die Bestimmung des in Wasser Gelösten Sauerstoffes. *Berichte der Deutschen Chemischen Gesellschaft* 21, 2843–2855. doi: 10.1002/cber.188802102122

WoRMS Editorial Board (2018). *World Register of Marine Species*. Available online at: http://www.marinespecies.org at VLIZ

Yazdani Foshtomi, M., Braeckman, U., Derycke, S., Sapp, M., Van Gansbeke, D., Sabbe, K., et al. (2015). The link between microbial diversity and nitrogen cycling in marine sediments is modulated by macrofaunal bioturbation. *PLoS ONE* 10:e0130116. doi: 10.1371/journal.pone.0130116

Zettler, M. L., Bochert, R., and Bick, A. (1994). Röhrenbau und Vertikalverteilung von *Marenzelleria viridis* (Polychaeta: Spionidae) in einem inneren Küstengewässer der südlichen Ostsee. *Rostocker Meeresbiologische Beiträge* 2, 215–225.

Zettler, M. L., Friedland, R., Gogina, M., and Darr, A. (2017). Variation in benthic long-term data of transitional waters: is interpretation more than speculation? *PLoS ONE* 12:e0175746. doi: 10.1371/journal.pone.0175746

Conflict of Interest Statement: The authors declare that the research was conducted in the absence of any commercial or financial relationships that could be construed as a potential conflict of interest.

Copyright © 2018 Gogina, Lipka, Woelfel, Liu, Morys, Böttcher and Zettler. This is an open-access article distributed under the terms of the Creative Commons Attribution License (CC BY). The use, distribution or reproduction in other forums is permitted, provided the original author(s) and the copyright owner(s) are credited and that the original publication in this journal is cited, in accordance with accepted academic practice. No use, distribution or reproduction is permitted which does not comply with these terms.

frontiers in Marine Science

ORIGINAL RESEARCH
published: 10 July 2018
doi: 10.3389/fmars.2018.00176

Metrology for pH Measurements in Brackish Waters—Part 1: Extending Electrochemical pH_T Measurements of TRIS Buffers to Salinities 5–20

Jens D. Müller[1], Frank Bastkowski[2], Beatrice Sander[2], Steffen Seitz[2], David R. Turner[3], Andrew G. Dickson[4] and Gregor Rehder[1]*

[1] Department of Marine Chemistry, Leibniz Institute for Baltic Sea Research Warnemünde, Rostock, Germany, [2] Department of Physical Chemistry, Physikalisch-Technische Bundesanstalt, Braunschweig, Germany, [3] Department of Marine Sciences, University of Gothenburg, Gothenburg, Sweden, [4] Marine Physical Laboratory, Scripps Institution of Oceanography, University of California, San Diego, La Jolla, CA, United States

OPEN ACCESS

Edited by:
Eric 'Pieter Achterberg, GEOMAR Helmholtz-Zentrum für Ozeanforschung Kiel, Germany

Reviewed by:
Marta Plavsic, Rudjer Boskovic Institute, Croatia
Stathys Papadimitriou, National Oceanography Centre Southampton, United Kingdom
Socratis Loucaides, National Oceanography Centre Southampton, United Kingdom

***Correspondence:**
Frank Bastkowski
frank.bastkowski@ptb.de

Specialty section:
This article was submitted to Marine Biogeochemistry, a section of the journal Frontiers in Marine Science

Received: *26 January 2018*
Accepted: *03 May 2018*
Published: *10 July 2018*

Citation:
Müller JD, Bastkowski F, Sander B, Seitz S, Turner DR, Dickson AG and Rehder G (2018) Metrology for pH Measurements in Brackish Waters—Part 1: Extending Electrochemical pH_T Measurements of TRIS Buffers to Salinities 5–20. Front. Mar. Sci. 5:176. doi: 10.3389/fmars.2018.00176

Harned cell pH_T measurements were performed on 2-amino-2-hydroxymethyl-1,3-propanediol (TRIS) buffered artificial seawater solutions in the salinity range 5–20, at three equimolal buffer concentrations (0.01, 0.025, 0.04 mol·kg-H_2O^{-1}), and in the temperature range 278.15–318.15 K. Measurement uncertainties were assigned to the pH_T values of the buffer solutions and ranged from 0.002 to 0.004 over the investigated salinity and temperature ranges. The pH_T values were combined with previous results from literature covering salinities from 20 to 40. A model function expressing pH_T as a function of salinity, temperature and TRIS/TRIS·H^+ molality was fitted to the combined data set. The results can be used to reliably calibrate pH instruments traceable to primary standards and over the salinity range 5–40, in particular, covering the low salinity range of brackish water for the first time. At salinities 5–20 and 35, the measured dependence of pH_T on the TRIS/TRIS·H^+ molality enables extrapolation of quantities calibrated against the pH_T values, e.g., the dissociation constants of pH indicator dyes, to be extrapolated to zero TRIS molality. Extrapolated quantities then refer to pure synthetic seawater conditions and define a true hydrogen ion concentration scale in seawater media.

Keywords: Harned cell, traceability, primary standard, TRIS, pH, total scale, brackish water, seawater

INTRODUCTION

Changes in seawater pH are linked to changes in the concentration of dissolved inorganic carbon and alkalinity. Precise and accurate pH measurements are therefore an ideal tool to investigate two processes of global importance: (i) Ocean acidification, caused by the uptake of anthropogenic carbon dioxide (CO_2) from the atmosphere (Le Quéré et al., 2016), can be directly traced by pH measurements in open ocean environments (Byrne et al., 2010). (ii) The investigation of biogeochemical transformations can be supported by pH measurements, as any production or mineralization of organic matter is inevitably coupled to the uptake and release of CO_2.

In many brackish water systems, intense biogeochemical transformations cause pronounced pH fluctuations superimposed on long-term pH trends due to the uptake of anthropogenic CO_2

(Hofmann et al., 2011). Accurate traceable and direct pH measurements are essential in deciphering the impact of both drivers. Furthermore, open ocean and brackish waters differ with respect to two characteristics of alkalinity, which underlines the need for accurate and traceable pH measurements in the latter waters. Firstly, alkalinity levels in brackish waters can change on time scales of ocean acidification. For example, Müller et al. (2016) reported an increase in alkalinity over the past two decades for the Baltic Sea, one of the world's largest estuarine systems, that significantly buffered the acidification caused by anthropogenic CO_2 uptake. Consequently, acidification trends cannot reliably be predicted from changes in pCO_2 as is the case in open ocean waters with stable alkalinity levels (Doney et al., 2009), but require direct pH measurements. Secondly, brackish waters are typically characterized by high loads of dissolved organic matter that contribute significantly to alkalinity, which results in erroneous results if alkalinity is used as an input parameter for CO_2 system calculations (Kulinski et al., 2014). Under such conditions, accurate and precise pH measurements are extremely valuable for a complete determination of the CO_2 system. It was shown that this can in principle be achieved by spectrophotometric pH measurements, because the methods work reliably even in the presence of high amounts of dissolved organic matter (Müller et al., 2018).

According to its definition on the activity scale, $pH = -\log_{10}(a_{H^+})$, pH involves a single ion quantity and is as such immeasurable by any thermodynamically valid method (Buck et al., 2002). pH measurements according to the IUPAC recommendation require conventions which are only valid for ionic strength ≤ 0.1 mol·kg^{-1}. For measurements in seawater with a higher ionic strength it is convenient to measure pH on scales that refer to the hydrogen ion concentration. The definition of such concentration scales requires the definition of a standard composition of seawater, because hydrogen ions are in equilibrium with other acid base components in seawater. pH_T, where the index T denotes the total pH scale, has become a widely accepted convention within the scientific community (Dickson et al., 2015). According to its definition, $pH_T = -\log_{10}\left\{\left[H^+\right]\left(1+\frac{\left[SO_4^{2-}\right]_T}{K_{HSO_4^-}}\right)\right\}$, it accounts for the concentrations of both, the free hydrogen ions, $\left[H^+\right]$, and hydrogen sulfate ions, expressed as the total sulfate concentration $\left[SO_4^{2-}\right]_T$ divided by the dissociation constant of hydrogen sulfate $K_{HSO_4^-}$. The latter contribute to the acidity of the solution by the potential to transfer further hydrogen ions to other proton acceptors.

In order to assure comparability of pH_T measurement results, internationally accepted primary pH_T standards are essential. Currently the de facto standards are TRIS (2-amino-2-hydroxymethyl-1,3-propanediol) buffered artificial seawater (ASW) solutions (DelValls and Dickson, 1998; Pratt, 2014) in the salinity (S) range 20–40, where pH_T values have been measured using an electrochemical setup comprising Harned cells. This setup represents a primary method for pH measurements (Buck et al., 2002). In oceanographic practice, pH_T is typically measured by other methods such as spectrophotometry (Clayton and Byrne, 1993; Liu et al., 2011) and Ion Selective Field Effect Transistor (ISFET) (Martz et al., 2010). The spectrophotometric pH_T measurement relies on pH indicator dyes such as m-Cresol Purple (mCP). Standard buffer solutions with well-defined, traceable pH_T values are required for the physico-chemical characterization of the purified dyes. This characterization was previously achieved for the indicator mCP in the salinity range 20–40 and temperatures from 273.15 to 308.15 K (Liu et al., 2011), based on the TRIS buffer characterization by DelValls and Dickson (1998). Recently, similar standards were achieved for sea-ice brines with temperatures as low as the freezing point by a successive characterization of hypersaline TRIS buffers (Papadimitriou et al., 2016) and–based on those buffer solutions—the extended characterization of mCP (Loucaides et al., 2017).

Up to now, Harned cell measurements on TRIS buffered ASW solutions in the lower salinity range ($S < 20$) have not been made. Consequently, spectrophotometrically obtained pH_T values in this salinity range were not traceable to a primary pH_T standard. Mosley et al. (2004) provided an interim solution by interpolating the pH_T values of TRIS buffered ASW solutions for the salinity range 0–20. The interpolation was based on the results for $S = 20$–40 of DelValls and Dickson (1998) and for TRIS in pure water by Bates and Hetzer (1961). Although the solutions of Bates and Hetzer (1961) contained no other salts, (Mosley et al., 2004) interpreted the buffer ionic strength as salinity, leading to questionable accuracy. Moreover, non-purified dye was used for the mCP characterization and measurements were conducted only at 298.15 K (Mosley et al., 2004). Consequently, spectrophotometric pH_T measurements in brackish waters with salinity below 20 were not traceable to a primary pH_T standard and results were subject to an unknown degree of measurement uncertainty.

To fill this gap, we present Harned cell pH_T measurement results in the salinity range 5–20 and, in addition, at 35 for assessment of consistency with the previous results of DelValls and Dickson (1998) and Pratt (2014). In particular, we discuss issues of buffer solution preparation in the low salinity range, which differs significantly from that in the upper salinity range and affects pH_T measurements. Measurements were performed in the temperature range 278.15 to 318.15 K. All buffer solutions were prepared at three equimolal concentrations of TRIS/TRIS·H^+, which allows extrapolation of calibration parameters determined in these solutions to pure artificial seawater conditions as recommended by Nemzer and Dickson (2005). We combined our results with those of DelValls and Dickson (1998) to derive a consistent pH_T model for the salinity range 5–40, which is a prerequisite to comparing pH_T values measured in ocean and brackish waters.

MATERIALS AND METHODS

Scope and Concept

We prepared and analyzed TRIS buffered ASW solutions (ASW/TRIS-HCl) with salinities $S = 5$, 10, 15, 20, and 35. Preparing low-saline buffer solutions for subsequent calibration

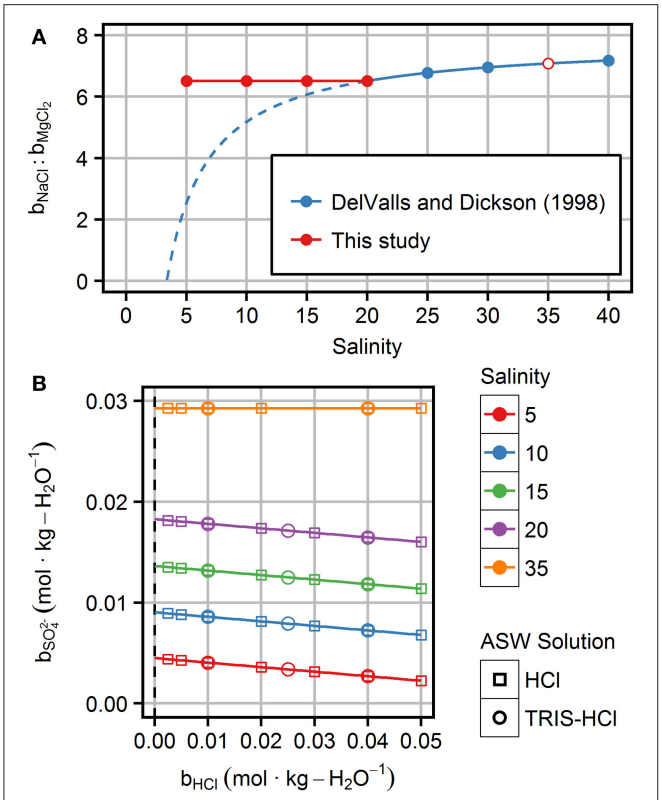


FIGURE 1 | Characteristics of artificial seawater solutions prepared in this study: **(A)** Cation composition represented by b_{NaCl}: b_{MgCl_2} molality ratios for ASW solutions with a HCl molality of 0.04 mol·kg-H_2O^{-1}. The cation ratios as prepared in this study (red) are compared to those proposed by DelValls and Dickson (1998)—actually prepared: blue circles and solid line; recipe hypothetically applied for lower salinities: dashed blue line. **(B)** Sulfate molality, $b_{SO_4^{2-}}$, as a function of HCl molality and salinity. Squares represent HCl solutions in ASW to measure the standard potential of the Harned cell, $E^{*\circ}$. Circles indicate the three investigated TRIS/TRIS·H^+ molalities.

of pH instruments includes a general problem: HCl added contribute significantly to the ionic strength of the buffer solution. An equivalent amount of salt components of the ASW matrix has to be removed to ensure constant ionic strength. Consequently, the solution composition used for the calibration of any pH instrument differs from the seawater to be analyzed. For a classical equimolal TRIS/TRIS·H^+ buffer with a molality of 0.04 mol·kg-H_2O^{-1} (DelValls and Dickson, 1998), the ionic strength contribution ranges from 5 to 10% for salinities of 40–20. The impact of this ionic strength contribution on the determination of the dissociation constant of mCP has not yet been assessed. Even though it might be negligible within the overall uncertainty of seawater pH_T measurements at salinities above 20, this assumption is critical at lower salinities since the contribution of the buffer substance increases with decreasing salinity. This problem is inevitable and counteracting it by reducing the concentration of the buffer component comes at the cost of reduced buffer stability. To account for this problem, equimolal buffer consisting of TRIS and protonated TRIS

TABLE 1 | Reference solution composition computed according to DelValls and Dickson (1998) for $S = 20$ and $b_{HCl} = 0.04$ mol·kg-H_2O^{-1}.

Component	Molality (mol·kg-H_2O^{-1})
NaCl	0.20061
Na_2SO_4	0.01647
KCl	0.00595
$MgCl_2$	0.03080
$CaCl_2$	0.00605

(TRIS·H^+) each at molalities of 0.04, 0.025, and 0.01 mol·kg-H_2O^{-1} were prepared and individual pH_T values measured. This allows extrapolation of the measured quantities to zero TRIS/TRIS·H^+ molality (Müller and Rehder, 2018).

The relative composition of the salts (NaCl, $MgCl_2$, Na_2SO_4, $CaCl_2$, and KCl) that form the ASW matrix is an associated problem. DelValls and Dickson (1998) computed the salt composition by first scaling a TRIS-free reference composition from $S = 35$ to the target salinity. Afterwards, the amount of NaCl was reduced by the amount of HCl added to maintain the nominal ionic strength. If a specific HCl concentration, e.g., 0.04 mol·kg-H_2O^{-1}, is adjusted, this approach implies changing the ratios between Na^+ and other cations at different salinities. For salinities of 20–40 those changes are small (**Figure 1A**). However, toward lower salinities the differences in the cation ratios become more pronounced. At a salinity of ~4, NaCl would be entirely replaced by HCl when preparing solutions according to DelValls and Dickson (1998). Therefore, only our buffers at $S = 35$ and the buffer at $S = 20$ with equimolal TRIS/TRIS·H^+ molality of 0.04 mol·kg-H_2O^{-1} have been prepared according to the recipe of DelValls and Dickson (1998) in order to achieve best comparability to previous studies. The recipe was modified to achieve constant ratios between the ASW salts for all other buffer solutions.

Preparation of the TRIS-HCl and HCl Solutions in Artificial Seawater

We have chosen the composition proposed by DelValls and Dickson (1998) for $S = 20$ and HCl molality $b_{HCl} = 0.04$ mol·kg-H_2O^{-1} as the reference composition of ASW (**Table 1**). Based on the reference composition at $S = 20$, the concentrations of all ASW salts were varied proportionally to compensate for the HCl ionic strength contribution and achieve target salinities. This proportional variation of the molality b of any salt component x (NaCl, $MgCl_2$, Na_2SO_4, $CaCl_2$, and KCl) was computed as a function of S and b_{HCl} according to:

$$b_x(S,\ b_{HCl}) = \frac{I\,(S) - b_{HCl}}{I\,(20) - 0.04\ \text{mol}\cdot\text{kg-H}_2\text{O}^{-1}} \cdot b_x(20,\ 0.04\ \text{mol}\cdot\text{kg-H}_2\text{O}^{-1}) \quad (1)$$

where b_{HCl} is the target molality of HCl in mol·kg-H_2O^{-1} (which is identical to $b_{TRIS/TRIS\cdot H^+}$), 0.04 mol·kg-H_2O^{-1} refers to b_{HCl} in the reference solution, b_x (20, 0.04 mol·kg-H_2O^{-1}) is the molality of salt x in the reference solution summarized in **Table 1**, and I is

the ionic strength calculated from the target salinity S by:

$$I(S) = \frac{19.919 \cdot S}{1000 - 1.00192 \cdot S} \quad (2)$$

Based on the reference composition of ASW according to DelValls and Dickson (1998), Equation (2) achieves proportional scaling of ionic strength in moles per kg solution with salinity (nominator) and conversion to ionic strength in moles per kg water (denominator). Coefficients in Equation (2) are based on IUPAC 2013 atomic weights (Meija et al., 2016).

For measurements of pH_T with Harned cells it is necessary to determine the standard potential of the silver-silver chloride (Ag|AgCl) electrodes. This can be achieved by measurements of a serial dilution of HCl in the respective solution (see chapter "Determination of pH_T" below). Therefore, HCl solutions were prepared in ASW (ASW/HCl) at b_{HCl} of 0.0025, 0.005, 0.01, 0.02, 0.03, 0.04, and 0.05 mol·kg-H_2O^{-1} at each target salinity according to Equations (1) and (2) and **Table 1**.

Our preparation method of ASW/TRIS-HCl and ASW/HCl solutions has the following implications at salinities ≤ 20:

- Constant ratios of the ASW salt components at all salinities and HCl molalities, which is reflected in the b_{NaCl}: b_{MgCl_2} ratio (**Figure 1A**).
- Variable chloride and sulfate molality at a given salinity, because more sulfate is removed at higher HCl (**Figure 1B**). This change in sulfate molality requires corrections (see "Sulfate correction for effective $E^{*\circ}$ values" below).

All solutions were prepared from stock solutions of NaCl, KCl, $CaCl_2$, $MgCl_2$, Na_2SO_4, TRIS and HCl that have been gravimetrically prepared with ultrapure water (see supplement). All weighings were performed using an analytical balance (Sartorius Genius) and were buoyancy corrected. The air density for buoyancy correction was calculated from the atmospheric conditions measured with a combined humidity and temperature sensor (Almemo) as well as a barometer (Setra Systems).

The various salts, NaCl, KCl, $CaCl_2$, $MgCl_2$ (originating from MV laboratories Inc., Frenchtown, NJ, USA and kindly supplied from METAS, Switzerland), and Na_2SO_4 (originating from Merck), were characterized by coulometric measurements (see supplement: Tables S1, S2.1). NaCl and KCl were dried at 383 K for 2 h before use. $CaCl_2$ and $MgCl_2$ are hygroscopic. Hence, stock solutions were prepared and characterized using ion chromatography (see supplement: Table S2.1). TRIS was purchased from NIST (SRM 723e). No losses of TRIS weight on drying over magnesium perchlorate could be detected in the range of weighing uncertainty. The HCl stock solution was prepared from Titrisol ampoules (Merck). The HCl stock solution molality was assayed by potentiometric titration against the stock solution of TRIS SRM 723e (see supplement). The titration of the HCl against the TRIS stock solution ensures equimolal TRIS/TRIS·H^+ ratios in the produced buffer solutions. All dilutions were carried out with ultrapure water obtained from a Milli-Q system. Actual salinities of the ASW/TRIS-HCl solutions were calculated from the actual ionic strength based on weighings according to Equation (2).

Harned Cell Measurements

The pH_T values of the ASW/TRIS-HCl solutions were calculated from measured potentials using Harned cells (Harned and Owen, 1958), which consist of a platinum hydrogen electrode and an Ag|AgCl reference electrode. Both electrodes are placed into a U-tube measurement cell. Both electrodes are in direct contact with the solution measured, i.e., there is no electrolyte bridge or a similar junction necessary to connect the electrodes electrically. The cells also comprise a unit for humidification of the hydrogen gas (see picture of the Harned measurement cell in Figure S1). The cell voltage was measured after temperature stabilization using a digital voltmeter (Agilent A3458) and corrected for the actual partial pressure of the hydrogen gas p_{H2} (Hills and Ives, 1951). Details of the Harned cell setup and the cell voltage correction are given in the supplement.

Measurements of the artificial seawater solutions containing TRIS-HCl were always measured in triplicate while artificial seawater solutions containing different HCl molalities were measured only once in most of the cases (see Tables S5.1, S5.2 in the Supplement).

Determination of pH_T

pH_T is defined on an amount content basis (moles per kilogram solution). However, the electrochemical measurement of pH_T is established via the molality-based expression of pH_b (DelValls and Dickson, 1998) according to:

$$pH_b = \frac{E_{ASW/TRIS-HCl} - E^{*\circ}}{\frac{RT\ln 10}{F}} + \log_{10}\left(\frac{b^\circ_{Cl^-}}{b}\right) \quad (3)$$

with the electric Harned cell potential $E_{ASW/TRIS-HCl}$ of the buffered artificial seawater solution, the standard potential $E^{*\circ}$ of the Ag|AgCl electrode in pure ASW of the same nominal salinity, the molality b_{Cl^-} of chloride in the solution and the standard molality $b^\circ = 1$ mol·kg-H_2O^{-1}. The expression of pH_b in Equation (3) assumes that the activity coefficient of HCl in the buffer solution is the same as its trace value in the pure artificial seawater (see section Discussion).

$E^{*\circ}$ was determined at each salinity and temperature from measured potentials $E_{ASW/HCl}$ of 7 ASW solutions with HCl molalities ranging from 0.0025 to 0.05 mol·kg-H_2O^{-1}. Therefore, E' values were calculated from measured $E_{ASW/HCl}$ according to Equation (4):

$$E' = E_{ASW/HCl} + \frac{RT\ln 10}{F} \cdot \log_{10}\left(\frac{b_{HCl} \cdot b_{Cl^-}}{(b^\circ)^2}\right) \quad (4)$$

with b_{HCl} the molality of HCl. $E^{*\circ}$ was determined as the intercept at zero HCl molality of a second order polynomial fitted to E' as a function of b_{HCl}.

The pH_b value derived from Equation (3) is molality-based, while pH_T is defined in terms of the amount content (moles per kg solution). Therefore, pH_T has to be calculated from pH_b (DelValls and Dickson, 1998) according to:

$$pH_T = pH_b - \log_{10}(1 - 0.00106 \cdot S) \quad (5)$$

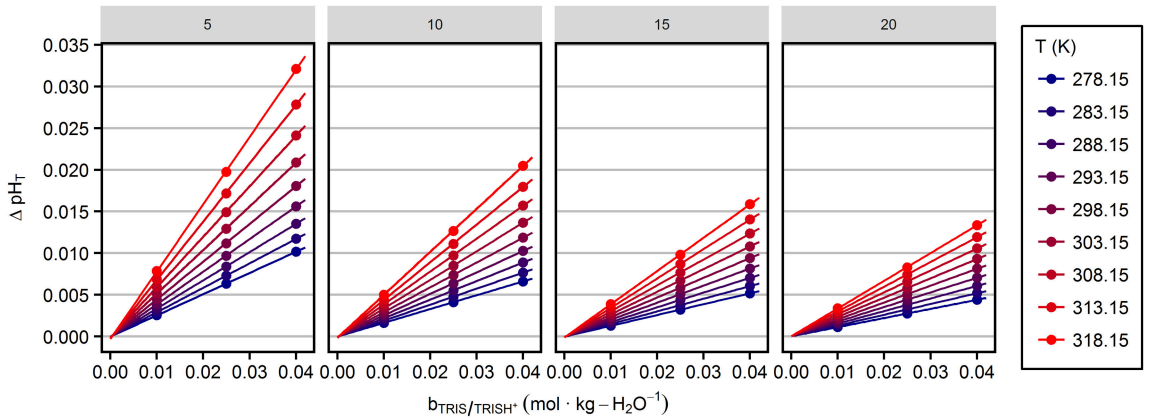


FIGURE 2 | Correction of pH_T terms due to changes in the total sulfate concentration as a function of TRIS/TRIS·H$^+$ molality. Panels represent the four investigated salinities indicated at the top. Lines indicate the linear behavior at various temperatures.

where the term 1 – 0.00106·S expresses the relation between salinity and the water content of the pure ASW solution, ω_{H_2O}. The latter is defined as mass water per mass solution (see section Discussion).

Twelve Harned cells have been used to measure the potential of 12 solutions simultaneously to reduce measurement time. Measurements of ASW/HCl solution to determine $E^{*\circ}$ were not carried out in the same measurement run as the potential measurements of the ASW/TRIS-HCl solutions for practical reasons. To ensure that the electrochemical properties of the Ag|AgCl electrodes is, within the uncertainty limits, the same for all solutions, the potentials of these electrodes were measured against a master Ag|AgCl electrode. The master electrode was always stored in 0.005 M hydrochloric acid and was considered to be stable in potential with time. The comparison measurements of all electrodes against the master electrode were performed in the same HCl solution before each measurement run and found to differ not more than 85 μV, corresponding to around 0.0015 in terms of pH.

The uncertainties of the measured pH_T values were determined for all temperatures, salinities and TRIS/TRIS·H$^+$ molalities according to the Guide to the expression of uncertainty in measurement (https://www.bipm.org/en/publications/guides/) using a Monte Carlo method in Mathematica (for details see Supplement) (ISO/IEC, 2008).

Sulfate Correction for Effective E*° Values

$E^{*\circ}$ of an Ag|AgCl electrode that is immersed in artificial seawater containing sulfate can be expressed as (DelValls and Dickson, 1998):

$$E^{*\circ} = E^{\circ} - \frac{2RT}{F}\ln\gamma_{\pm}(\mathrm{HCl}) + \frac{RT}{F}\ln\left(1 + \frac{b_{SO_4^{2-},T}}{K_{HSO_4^-}}\right) \quad (6)$$

where E° is the potential of the Harned cell under standard conditions, $\gamma_{\pm}$(HCl) is the trace activity coefficient of HCl in ASW, $b_{SO_4^{2-},T}$ is the total sulfate molality and $K_{HSO_4^-}$ is the limiting molality quotient for hydrogen sulfate in artificial seawater medium.

It is assumed that $E^{*\circ}$, determined at a particular salinity and temperature, remains unchanged if some of the artificial seawater salts are replaced with TRIS-HCl such that the ionic strength is unchanged. However, in this study the TRIS-HCl addition was compensated by a proportional reduction of all ASW salts to keep the ratios of cations constant. Consequently, the sulfate concentration was also reduced. The change in sulfate concentration requires a correction so that the effective $E^{*\circ}$ corresponds to the respective ASW/TRIS-HCl solutions ($E^{*\circ}$(ASW/TRIS-HCl)) and not to the infinite dilution of HCl solutions to pure ASW condition (E^{*} (ASW)). According to Equation (3) the required correction can be expressed as:

$$\Delta pH_T = \frac{F}{RT\ln 10}\left(E^{*\circ}(\mathrm{ASW}) - E^{*\circ}\left(\mathrm{ASW/TRIS\text{ - }HCl}\right)\right) \quad (7)$$

$E^{*\circ}$(ASW) and $E^{*\circ}$(ASW/TRIS-HCl) in Equation (7) can be expressed by applying Equation (6), where $b_{SO_4^{2-},T}$ is replaced by $b_{SO_4^{2-},T}(ASW)$ and $b_{SO_4^{2-},T}$(ASW/TRIS-HCl), respectively. The former describes the sulfate molality in pure ASW and the latter describes the sulfate molality in ASW containing TRIS-HCl. $K_{HSO_4^-}$ is assumed constant for a given temperature and salinity according to Dickson (1990). Thus,

$$\Delta pH_T = \log_{10}\left(1 + \frac{b_{SO_4^{2-},T}(\mathrm{ASW})}{K_{HSO_4^-}}\right) - \log_{10}\left(1 + \frac{b_{SO_4^{2-},T}(\mathrm{ASW/TRIS\text{-}HCl})}{K_{HSO_4^-}}\right) \quad (8)$$

The values of ΔpH_T calculated for the solution compositions of this study are displayed in **Figure 2** and referred to as sulfate corrections hereafter. This correction does not account for any changes in the activity coefficients implicit in Equation 6 (see section Discussion).

TABLE 2 | Coefficients for the pH_T model (Equation 10). Test value: pH_T = 8.0703 at $S = 20$, $T = 298.15$ K, and $b_{TRIS/TRIS\cdot H^+}$ = mol·kg-H_2O^{-1}.

Coefficient	Value
a	−327.3307
b_1	−2.400270
b_2	$8.124630 \cdot 10^{-2}$
b_3	$-9.635344 \cdot 10^{-4}$
c_1	$-9.103207 \cdot 10^{-2}$
c_2	$-1.963311 \cdot 10^{-3}$
c_3	$6.430229 \cdot 10^{-5}$
c_4	$-7.510992 \cdot 10^{-7}$
d_1	56.92797
d_2	$5.235889 \cdot 10^{-1}$
d_3	$-1.7602 \cdot 10^{-2}$
d_4	$2.082387 \cdot 10^{-4}$
e	11382.97
f_1	−2.417045
f_2	$7.645221 \cdot 10^{-2}$
f_3	$1.122392 \cdot 10^{-2}$
f_4	$-3.248381 \cdot 10^{-4}$
g_1	−4.161537
g_2	$6.143395 \cdot 10^{-2}$

Fitting Combined pH_T Results for the Salinity Range 5–40

In order to derive a common expression of pH_T as a function of salinity, temperature and TRIS/TRIS·H^+ molality over the largest range of conditions, the sulfate-corrected pH_T data from this study in the salinity range 5–20 were combined with previous pH_T data in the salinity range 20–40. The latter were calculated from potentials given in **Table 2** of DelValls and Dickson (1998) and corresponding $E^{*\circ}$ values from Dickson (1990) according to Equations (3) and (5). Only measurements in the temperature range investigated in this study (278.15–318.15 K) were included in the combined data set.

The following expression of pH_T as a function (f) of S, T and $b_{TRIS/TRIS\cdot H^+}$ was specified as a full model and fitted to the combined data set:

$$pH_T = f\left\{\left[\left(1 + S + S^2 + S^3\right)\cdot\left(1 + T + \ln(T) + \frac{1}{T}\right)\right] + \left[\left(b_{TRIS/TRIS\cdot H^+} + b^2_{TRIS/TRIS\cdot H^+}\right)\cdot(1 + S + T + S\cdot T)\right]\right\} \quad (9)$$

The first part of this full model includes all combinations of the terms of a third order salinity polynomial with the terms of the physico-chemical expression of the temperature dependence of dissociation constants. This first part of Equation (9) deviates from the model fitted by DelValls and Dickson in their Equation (18) only by the higher order of the salinity polynomial. The second part of Equation (9) accounts for the dependence of pH_T on the TRIS/TRIS·H^+ molality. The total number of terms of the full model given in Equation (9) is 24.

The fit of the full model was obtained by generalized linear modeling with the "stats" package of the statistical programming language "R" (R Core Team, 2014). The model was fitted to the mean pH_T values at each combination of target salinity, temperature, and TRIS/TRIS·H^+ molality. Mean pH_T values were weighted by the respective standard measurement uncertainty (Table S6) as $1/u(pH_T)^2$. The temperature dependency of measurement uncertainty found in this study at salinities 20 and 35 was fitted with a linear model and the same uncertainty was assigned to the data of DelValls and Dickson (1998). After fitting the full model (Equation 9), insignificant terms were removed by stepwise variable selection in both directions based on the Akaike information criterion. The removal of insignificant terms was performed with the "stepAIC" function from the R package "MASS," and resulted in an expression with 19 terms given below in Equation (10).

RESULTS

pH_T of TRIS Buffers

The pH_T values of the equimolal TRIS buffered ASW solutions at salinities 5, 10, 15, 20, and 35, temperatures from 278.15 to 318.15 K in intervals of 5 K, as well as equimolal TRIS/TRIS·H^+ molalities 0.04, 0.025, and 0.01 mol·kg-H_2O^{-1} are given in Table S6, the corresponding electric potentials of all solutions measured are given in Table S5.1 in the Supplemental Material.

Figure 3 shows mean pH_T values (triplicate measurements) of ASW/TRIS-HCl solutions as a function of temperature (278.15 – 318.15 K), for salinities 5, 10, 15, and 20 and at equimolal TRIS/TRIS·H^+ molality 0.04 mol·kg-H_2O^{-1}. pH_T decreased almost linearly from around 8.7 to 7.5 with increasing temperature (around -0.03 K^{-1}). The investigation of the pH_T dependence on temperature at other TRIS/TRIS·H^+ molalities showed no significant difference from the results shown in **Figure 3**.

Figure 4 displays in more detail the dependence of pH_T on salinity and TRIS/TRIS·H^+ molality, including previous results from DelValls and Dickson (1998). pH_T values shown in **Figure 4** were corrected for minor difference (<0.06 K) between the actual measurement temperature (Table S6) and the target temperature indicated at the top of the panels to achieve a consistent presentation with the model results. At low temperatures pH_T decreased with decreasing salinity. Toward higher temperatures, the lowest pH_T values were found at intermediate salinities.

The expanded measurement uncertainty (coverage factor k = 2) of pH_T was found to range between 0.002 and 0.004, with the highest uncertainties at salinity 5 and 15 (Figure S3). The uncertainty of pH_T significantly increased with temperature at salinity 5 (Figure S3), whereas the temperature dependence of the measurement uncertainty was much less pronounced at higher salinities.

It was found that the uncertainty of the pH_T values was dominated by the uncertainty contributions of the standard potential of the silver-silver chloride electrodes, $E^{*\circ}$, with relative contributions of 55–95% (Figure S4). The determination of $E^{*\circ}$

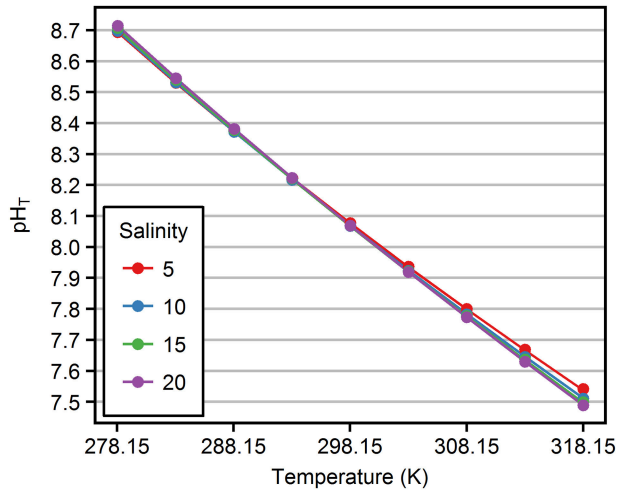


FIGURE 3 | pH_T values as a function of temperature. Circles represent mean measured pH_T for $b_{TRIS/TRIS\cdot H^+} = 0.04$ mol·kg-H_2O^{-1} and salinities 5–20 (color). Lines indicate the fitted pH_T model at respective conditions. Measurement uncertainties are <0.005 and cannot be visualized due to the scaling of the y-axis.

was found to be sensitive to the extrapolation to zero HCl molality. The highest uncertainties of $E^{*\circ}$ were found at salinities 5 and 15 (Figure S4) resulting in the highest pH_T uncertainties being found at these salinities (Figure S3).

The second most important uncertainty contribution was that of the cell potential measured in the buffer solutions, $E_{ASW/TRIS-HCl}$, ranging between 5 and 35% (Figure S4). The uncertainty of the measurement temperature T contributed 1–4% and the molalities of the NaCl, and $MgCl_2$ stock solutions contributed in sum 1–7% to the pH_T measurement uncertainty. All other contributions to the measurement uncertainty were <1%.

pH_T Model

The pH_T model fitted to the combined data set including results from this study and DelValls and Dickson (1998) is expressed in Equation (10). The parameters T and $b_{TRIS/TRIS\cdot H^+}$ in Equation (10) were multiplied with 1/K and 1/mol·kg-H_2O^{-1}, respectively, to derive dimensionless quantities. The corresponding dimensionless coefficients are given in **Table 2**.

pH_T values predicted by this model are displayed along with mean pH_T values in **Figures 3** and **4**. Residuals of triplicate pH_T measurements from the model are shown in **Figure 5**, along with expanded measurement uncertainties (coverage factor $k = 2$). No uncertainties are available for the results of DelValls and Dickson (1998). Therefore, we interpolated our uncertainties determined at salinity 20 and 35 to provide a rough estimate of the consistency between measurement results and residuals in the salinity range 20–40. The dependency of the measurement uncertainty on $b_{TRIS/TRIS\cdot H^+}$ is negligible (Figure S3) and therefore not displayed in **Figure 5**. The residuals are within the range of the expanded measurement uncertainty, except for a few results at lowest TRIS/TRIS·H^+ molality and salinities 15 and 20 (**Figure 5**).

$$\begin{aligned} pH_T = {} & a + \left(b_1 \cdot S + b_2 \cdot S^2 + b_3 \cdot S^3\right) \\ & + \left(c_1 \cdot T + c_2 \cdot S \cdot T + c_3 \cdot S^2 \cdot T + c_4 \cdot S^3 \cdot T\right) \\ & + \left(d_1 \cdot \ln(T) + d_2 \cdot S \cdot \ln(T) + d_3 \cdot S^2 \cdot \ln(T)\right. \\ & \left. + d_4 \cdot S^3 \cdot \ln(T)\right) + \left(e \cdot \frac{1}{T}\right) \\ & + \left(f_1 \cdot b_{TRIS/TRIS\cdot H^+} + f_2 \cdot b_{TRIS/TRIS\cdot H^+} \cdot S\right. \\ & \left. + f_3 \cdot b_{TRIS/TRIS\cdot H^+} \cdot T + f_4 \cdot b_{TRIS/TRIS\cdot H^+} \cdot S \cdot T\right) \\ & + \left(g_1 \cdot b^2_{TRIS/TRIS\cdot H^+} + g_2 \cdot b^2_{TRIS/TRIS\cdot H^+} \cdot S\right) \end{aligned} \quad (10)$$

DISCUSSION

Measurement Uncertainty and pH_T Model

The deviations of measured pH_T values from the pH_T model (Equation 10, **Table 2**) agree well with the range of the expanded measurement uncertainty (**Figure 5**), i.e., they are not significantly higher or lower. This indicates that the model represents the experimental results well, and does not overfit the data.

The deviations from the model reveal a minor salinity-dependent pattern. In the salinity range 5–20, there is a tendency toward positive offsets at $S = 15$ and negative offsets at $S = 20$. As this tendency exists for the pH_T of all TRIS/TRIS·H^+ molalities and replicates, the patterns must have a common cause, which is likely to be the determination of the standard potential of the silver-silver chloride electrodes, $E^{*\circ}$. The determination of $E^{*\circ}$ represents the major contribution to the measurement uncertainty (55–95%, Figure S4) and was only performed once for each combination of temperature and salinity. The uncertainty in the $E^{*\circ}$ determination is presumably related to the extrapolation to pure ASW conditions, which is especially sensitive to the E' measurements (Equation 4) at lowest HCl molalities. The model deviations reveal slightly positive offsets at $S = 25$ and 30, which is very similar to the patterns displayed in Figure 2B of DelValls and Dickson (1998).

No pronounced temperature-dependence of the residuals exists, except at salinity 5 and $b_{TRIS/TRIS\cdot H^+} = 0.04$ mol·kg-H_2O^{-1}, where a positive offset increases to a maximum of 0.004 at highest temperatures.

Comparison to Previous Studies

The highest deviation between pH_T values measured in this study and by DelValls and Dickson (1998) across all temperatures, at salinities 20 and 35, and $b_{TRIS/TRIS\cdot H^+} = 0.04$ mol·kg-H_2O^{-1} is 0.0025 at $S = 35$ and $T = 288.15$ K. The deviations are therefore within the extended measurement uncertainty of the method.

At salinities ≥ 20, excellent agreement was found between our pH_T model at $b_{TRIS/TRIS\cdot H^+} = 0.04$ mol·kg-H_2O^{-1} and the model defined in Equation (18) of DelValls and Dickson (1998).

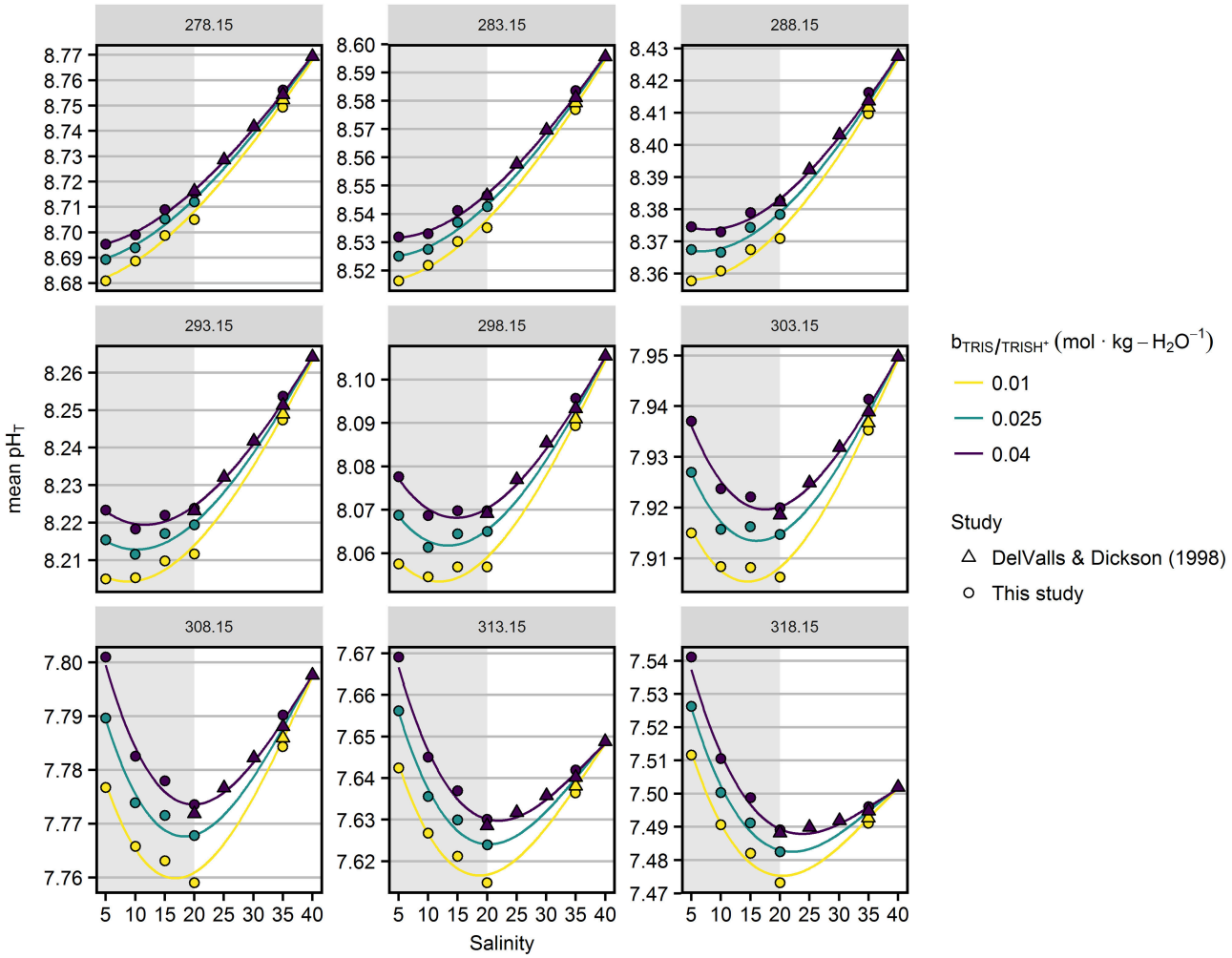


FIGURE 4 | Mean pH_T values as a function of salinity (x-axis), temperatures (in K, indicated at the top of the panels) and TRIS/TRIS·H^+ molalities (color). Circles represent results from this study highlighted by the gray area, triangles refer to DelValls and Dickson (1998). Lines represent the pH_T model (Equation 10) fitted to the combined data set.

Differences are <0.001 for the entire salinity range 20–40 and the temperature range 278.15–318.15 K (Figure S5). Within the range of the extended measurement uncertainty both models do not differ. The residuals from the model fitted in this study are larger than those presented in Figure 2 of DelValls and Dickson (1998), presumably a result of the larger range of salinities and the included dependency of pH_T on TRIS/TRIS·H+ molality in our model.

Our pH_T model at $b_{TRIS/TRIS\cdot H^+} = 0.04$ mol·kg-H_2O^{-1} and 298.15 K and the model by Mosley et al. (2004) agree within 0.002 in the salinity range 20–40 (Figure S5), which is not surprising, because both models are based on the same results of DelValls and Dickson (1998). However, in the salinity range 5–20, where Mosley et al. (2004) interpolated the pH_T of TRIS buffer solutions between the results of DelValls and Dickson (1998) for S>20 and the results of Bates and Hetzer (1961) in pure water, deviations increase up to 0.009 (Figure S5) and highlight the shortcomings of the interim solution.

Correction of E*° for Changes in Sulfate Concentration and Activity Coefficients

Changes in the sulfate concentration between pure ASW and ASW/TRIS-HCl solutions were corrected in this study according to Equation (8) (**Figure 2**). However, determined $E^{*\circ}$ values do not exactly correspond to the values required for pH_T calculation in Equation (3), because changes in activity coefficients between pure ASW and ASW/TRIS-HCl solutions remain unaccounted for, namely:

(1) Changes in the value of $K_{HSO_4^-}$ arising from changes in the activity coefficients of H^+, SO_4^{2-} and HSO_4^-
(2) Changes in the activity coefficients of H^+ and Cl^-

This limitation was previously discussed (e.g., Nemzer and Dickson, 2005; Dickson et al., 2015) and applies to all currently available experimental pH_T measurements of TRIS buffered ASW solutions. The activity changes can only be corrected with

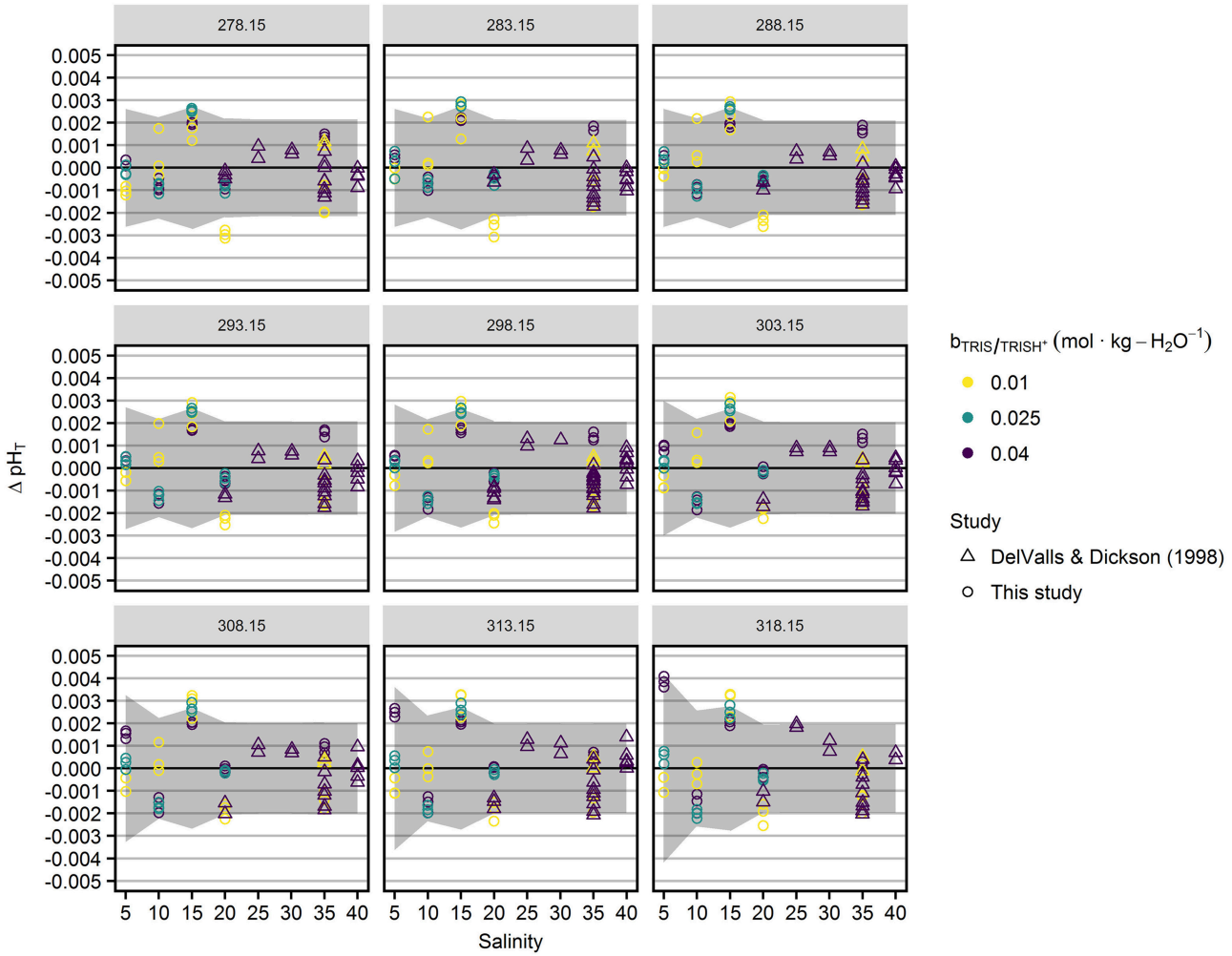


FIGURE 5 | Residuals of pH_T values from the model (Equation 10, **Table 2**, **Figure 4**), $\Delta pH_T = pH_{T,\ measured} - pH_{T,\ model}$, as a function of salinity (x-axis), temperatures (in K, indicated at the top of the panels), and TRIS/TRIS·H^+ molalities (color). Circles represent results from this study, triangles refer to DelValls and Dickson (1998). The gray areas indicate the expanded (coverage factor $k = 2$) measurement uncertainty of pH_T.

estimates from a speciation model. Gallego-Urrea and Turner (2017) have recently developed optimized Pitzer coefficients for TRIS in artificial seawater at 298.15 K, using the artificial seawater model of Waters and Millero (2013). According to Gallego-Urrea and Turner (2017), pH_T correction terms, addressing the above mentioned effects (1) and (2), were calculated for the results of this study at 298.15 K. Those ΔpH_T values from the speciation model differed from the applied sulfate corrections shown in **Figure 2** by <0.002, indicating that changes in sulfate concentration dominate over the effect of changes in the activity coefficient.

However, the Pitzer coefficients for TRIS buffered ASW solutions are restricted to 298.15 K (Gallego-Urrea and Turner, 2017) due to scarcity of experimental data for other temperatures and can therefore not be applied consistently to the full temperature range covered in this study. The development of accurate Pitzer models for TRIS in artificial seawater over an extended temperature range is a main focus of the SCOR Working Group 145 "Modelling Chemical Speciation in Seawater to Meet Twenty first Century Needs" (http://marchemspec.org/).

It should be noted that the neglected effect of changes in activity coefficients does not impact the calibration of pH instruments, if those are performed at variable TRIS/TRIS·H^+ molality and extrapolated to zero TRIS (see section: Calibration of pH instruments).

Conversion Between pH_b and pH_T

The conversion of pH from the molality to the amount content scale (from pH_b to pH_T) was calculated as the negative decadic logarithm of

$$\omega_{H_2O} = 1 - 0.00106 \cdot S \quad (11)$$

according to DelValls and Dickson (1998). ω_{H_2O} represents the mass of water per mass solution and the given relationship

between ω_{H_2O} and salinity refers to the composition of pure ASW. As pointed out by Pratt (2014), ω_{H_2O} in pure ASW is not exactly identical to ω_{H_2O} of the corresponding ASW/TRIS-HCl solution, due to the difference of the total mass of solution per amount of water after replacing some of the ASW salts with TRIS/HCl. As a result, for solutions with a TRIS molality of 0.04 mol·kg-H_2O^{-1}, the pH conversion based on the actually weighed buffer composition gives 0.003 and 0.004 higher pH_T values at salinity 35 and 5, respectively, compared to those using Equation (4). Obviously, the conversion error decreases toward lower TRIS molality. To be consistent with the pH_T results measured previously and to perform the pH_T-fit on a consistent database we have also used Equation (4) for the correction, even though we deem the conversion based on the actually weighed buffer composition more appropriate.

It should be noted that preliminary results obtained with the speciation model by Gallego-Urrea and Turner (2017) indicate that the correction of changes in activity coefficients between pure ASW and ASW/TRIS-HCl solutions, which has been neglected in this study due to the restriction of model results to 298.15 K, is around −0.005 at $S = 35$ and $b_{TRIS/TRIS\cdot H^+} = 0.04$ mol·kg-H_2O^{-1}. This is in a similar order of magnitude, but with opposite sign compared to the effect of pH scale conversion according to Equation (11). Therefore, if adequate activity coefficients were available, superposition of the pH scale conversion using the actual buffer composition and the correction of changes in activity coefficients would be expected to provide pH_T values that are within the range of uncertainties of the pH_T value we have presented here.

In any case, the choice of the scale conversion does not impact the calibration of pH instruments, if they are performed at variable TRIS/TRIS·H^+ molality and extrapolated to zero TRIS (see chapter: Calibration of pH instruments).

Calibration of pH Instruments

We recommend the use of TRIS buffered ASW solutions as prepared in this study as pH_T-standards for future calibration of pH instruments in the salinity range 5–20, with assigned pH_T values according to Equation (10) and **Table 2**. Moreover, this approach also allows for a consistent assignment of pH_T values without discontinuity or significant differences to previous results in the salinity range 20–40 when buffer solutions are prepared according to DelValls and Dickson (1998).

As discussed in the previous two chapters, the composition of TRIS buffer solutions differs from that of pure ASW. The contribution of TRIS-HCl to the total ionic strength increases toward lower salinities and:

(1) affects the pH_T values of the buffer solutions (**Figure 4**),
(2) requires corrections of the $E^{*\circ}$ differences between pure ASW and ASW/TRIS-HCl,
(3) affects ω_{H_2O} and therefore the scale conversion between pH_b and pH_T, and
(4) impacts the calibration quantity of any pH instrument, such as the determination of dissociation constants of pH indicator dyes.

Uncertainties in (2) and (3) result in uncertainties of the assigned pH_T values of the buffer solutions. However, it must be emphasized that effects (1)–(4) do not affect the calibration of pH instruments, if they include the extrapolation of calibrated parameters, e.g., the dissociation constant of mCP (Müller and Rehder, 2018), to pure ASW conditions. The extrapolated quantity refers to an exact definition of the total hydrogen ion concentration scale without constraints (Nemzer and Dickson, 2005; Dickson et al., 2015). Therefore, we recommend calibration of pH instruments in the salinity range 5–20 at the three TRIS/TRIS·H^+ molalities reported in this study and extrapolation of the results to zero TRIS/TRIS·H^+ molality. However, the dependence of pH_T on TRIS/TRIS·H^+ in Equation (10) is strictly valid only for salinities 5–20 and 35, due to the lack of experimental data at other salinities. It must also be noted that no uncertainties have been calculated for the coefficients listed in **Table 2**, since no uncertainties have been available for the results of DelValls and Dickson (1998). We recommend assigning uncertainties to pH_T values corresponding to those given Table S6 if Equation (10) is used to calculate pH_T values.

Recommendations for the Preparation of TRIS Buffer Solutions

To replicate the TRIS buffer solutions characterized in this study, we recommend production of stock solutions for the salt components of the ASW matrix. The impact of salt impurities on buffer pH_T has not yet been systematically studied. Therefore, we recommend using salts of the highest purity grade, although the contribution of ASW composition to the measurement uncertainty budget is assumed to be small. The stock solution of HCl should be titrated against the TRIS stock solution with potentiometric or colorimetric (e.g., methyl red) endpoint detection. This ensures an exact equimolal TRIS:TRIS·H^+ ratio, which is essential for reproducing the correct pH_T value. Finally, all TRIS containing solutions should be handled so as to avoid uptake of atmospheric CO_2. Ideally, the headspace of the containers should be flushed with humidified argon.

Solution Composition Concept and Relevance to Natural Waters

Alternative strategies for the solution composition applied in this study would result in pronounced changes in cation ratios at low salinity (**Figure 1**). Based on current knowledge it is impossible to quantify the effect of such changes of cation ratios on TRIS buffer pH_T, because information is lacking on the sensitivity of the TRIS·H^+ dissociation constant on the ionic composition of the matrix. As a future experimental approach to this open question it would be informative to perform electrochemical pH_T measurement of TRIS buffered solutions in variable ASW matrices.

Characterized buffer solutions in various ASW matrices would enable studies of the impact of solution composition on the measurement signals of other pH instruments, including the dissociation behavior of mCP. Such experiments could shed light on the ultimate question of how representative pH_T measurements are for various natural brackish and

freshwaters that differ in ionic composition (Feistel et al., 2010). Currently, it remains impossible to estimate the uncertainty of pH measurements arising from differences in the ionic composition of natural brackish water samples and the simplified composition of buffer solutions prepared in ASW matrix based on experimental data. A more detailed discussion of this issue is given in "Metrology for pH Measurements in Brackish Waters—Part 2: Experimental Characterization of Purified meta-Cresol Purple for Spectrophotometric pH_T Measurements" by Müller and Rehder (2018).

CONCLUSION

This study extends the characterization of TRIS buffer solutions by Harned cell measurements to brackish waters and provides a consistent pH_T model for the salinity range 5–40. It is emphasized that minor assumptions and uncertainties remain in the pH_T assignment and restrict the accuracy of all currently available TRIS buffer characterizations. However, these limitations do not affect the calibration of other pH instruments, if calibration results are extrapolated to zero buffer molality, which is especially important at low salinities. This study provides the required characterization of buffer solutions with variable TRIS molality in the salinity range 5–20. Measurements with pH instruments that have been calibrated against the buffer concentration represent currently the only access to the total hydrogen ion concentration without constraints.

DATA AVAILABILITY STATEMENT

All datasets [GENERATED/ANALYZED] for this study are included in the manuscript and the supplementary files.

AUTHOR CONTRIBUTIONS

JM: contributed to the research idea and plan, participated in the characterization of chemicals used, analyzed and interpreted the results and is first main author (shared authorship with FB) of the manuscript; FB: contributed to the research plan, analyzed and interpreted the measurement results and is the second main author (shared authorship with JM) of the manuscript; BS: contributed to the research plan, performed the measurements and revised the manuscript; SS: contributed to the research plan, analyzed and interpreted the measurement results and revised the manuscript; DT: contributed in performing the research activities, in the interpretation of the results and revision of the manuscript; AD: contributed to the research plan, interpreted the results and revised the manuscript; GR: contributed to the research plan and revised the manuscript.

FUNDING

AD was supported by the US National Science Foundation, Grant No. OCE-1657799. Physikalisch-Technische Bundesanstalt (PTB). The research leading to this manuscript has received funding from BONUS, the joint Baltic Sea research and development program (Art 185), funded jointly from the European Union's Seventh Program for research, technological development and demonstration and from the German Federal Ministry of Education and Research through Grant No. 03F0689A (BONUS PINBAL).

ACKNOWLEDGMENTS

We acknowledge the Swiss Federal Institute of Metrology (METAS) for providing characterized salts. The quality of this paper gained from scientific discussions with Bernd Schneider, Robert H. Byrne, Kenneth W. Pratt, Regina Easley, and Michael DeGrandpre. We thank Franko Schmähling for valuable recommendations concerning appropriate fitting procedures.

SUPPLEMENTARY MATERIAL

The Supplementary Material for this article can be found online at: https://www.frontiersin.org/articles/10.3389/fmars.2018.00176/full#supplementary-material

REFERENCES

Bates, R. G., and Hetzer, H. B. (1961). Dissociation constant of the protonated acid form of 2-amino-(hydroxymethyl)-1,3-propanediol [trishydroxymethyl)-aminomethane] and related thermodynamic quantities from 0 to 50°. *J. Phys. Chem.* 65, 667–671. doi: 10.1021/j100822a017

Buck, R. P., Rondinini, S., Covington, A. K., Baucke, F. G. K., Brett, C. M. A., Camoes, M. F., et al. (2002). Measurement of pH. Definition, standards, and procedures (IUPAC recommendations 2002). *Pure Appl. Chem.* 74, 2169–2200. doi: 10.1351/pac200274112169

Byrne, R. H., Mecking, S., Feely, R. A., and Liu, X. (2010). Direct observations of basin-wide acidification of the North Pacific Ocean. *Geophys. Res. Lett.* 37:L0260. doi: 10.1029/2009GL040999

Clayton, T. D., and Byrne, R. H. (1993). Spectrophotometric seawater pH measurements — total hydrogen-ion concentration scale calibration of m-cresol purple and at-sea results. *Deep Sea Res. Part I Oceanogr. Res. Pap.* 40, 2115–2129. doi: 10.1016/0967-0637(93)90048-8

DelValls, T. A., and Dickson, A. G. (1998). The pH of buffers based on 2-amino-2-hydroxymethyl-1,3-propanediol ('tris') in synthetic sea water. *Deep Sea Res. Part I Oceanogr. Res. Pap.* 45, 1541–1554. doi: 10.1016/S0967-0637(98)00019-3

Dickson, A. G. (1990). Standard potential of the reaction: AgCl(s) + ½H_2(g) = Ag(s) + HCl(aq), and the standard acidity constant of the ion HSO_4^- in synthetic sea water from 273.15 to 318.15 K. *J. Chem. Thermodynamics* 22, 113–127. doi: 10.1016/0021-961490074-Z

Dickson, A. G., Camões, M. F., Spitzer, P., Fisicaro, P., Stoica, D., Pawlowicz, R., et al. (2015). Metrological challenges for measurements of key climatological observables. Part 3: seawater pH. *Metrologica* 53, R26–R39. doi: 10.1088/0026-1394/53/1/R26

Doney, S. C., Fabry, V. J., Feely, R. A., and Kleypas, J. A. (2009). Ocean acidification: the other CO_2 problem. *Ann. Rev. Mar. Sci.* 1, 169–192. doi: 10.1146/annurev.marine.010908.163834

Feistel, R., Weinreben, S., Wolf, H., Seitz, S., Spitzer, P., Adel, B., et al. (2010). Density and absolute salinity of the Baltic Sea 2006–2009. *Ocean Sci.* 6, 3–24. doi: 10.5194/os-6-3-2010

Gallego-Urrea, J. A., and Turner, D. R. (2017). Determination of pH in estuarine and brackish waters: Pitzer parameters for Tris buffers and

dissociation constants for *m*-cresol purple at 298.15 K. *Mar. Chem.* 195, 84–89. doi: 10.1016/j.marchem.2017.07.004

Hills, G. J., and Ives, D. J. G. (1951). 69. The hydrogen-calomel cell. Part I. The hydrogen electrode. *J. Chem. Soc.* 318, 305–310. doi: 10.1039/JR9510000305

Hofmann, G. E., Smith, J. E., Johnson, K. S., Send, U., Levin, L. A., Micheli, F., et al. (2011). High-frequency dynamics of ocean pH: a multi-ecosystem comparison. *PLoS ONE* 6:e28983. doi: 10.1371/journal.pone.0028983

Harned, H. S., and Owen, B. B. (1958). *The Physical Chemistry of Electrolytic Solutions, Chap. 14.* New York, NY: Reinhold.

ISO/IEC (2008). Guide to the expression of uncertainty in measurement (2008), Guide 98-3, Geneva, Switzerland

Kulinski, K., Schneider, B., Hammer, K., Machulik, U., and Schulz-Bull, D. (2014). The influence of dissolved organic matter on the acid–base system of the Baltic Sea. *J. Mar. Syst.*. 132, 106–115. doi: 10.1016/j.jmarsys.2014.01.011

Le Quéré, C., Andrew, R. M., Canadell, J. G., Sitch, S., Korsbakken, J. I., Peters, G. P., et al (2016). Global carbon budget 2016. *Earth Syst. Sci. Data* 8, 605–649. doi: 10.5194/essd-8-605-2016

Liu, X., Patsavas, M. C., and Byrne, R. H. (2011). Purification and characterization of meta-cresol purple for spectrophotometric seawater pH measurements. *Environ. Sci. Technol.*. 45, 4862–4868. doi: 10.1021/es200665d

Loucaides, S., Rèrolle, V. M. C., Papadimitriou, S., Kennedy, H., Mowlem, M. C., Dickson, A. G., et al. (2017). Characterization of meta-Cresol Purple for spectrophotometric pH measurements in saline and hypersaline media at sub-zero temperatures. *Sci. Rep.* 7, 1–11. doi: 10.1038/s41598-017-02624-0

Martz, T. R., Connery, J. G., and Johnson, K. S. (2010). Testing the Honeywell Durafet for seawater pH applications. *Limnol. Oceanogr. Methods* 8, 172–184. doi: 10.4319/lom.2010.8.172

Meija, J., Coplen, T. B., Berglund, M., Brand, W. A., De Bièvre, P., Gröning, M., et al. (2016). Atomic weights of the elements 2013 (IUPAC Technical Report). *Pure Appl. Chem.* 88, 265–291. doi: 10.1515/pac-2015-0305

Mosley, L. M., Husheer, S. L. G., and Hunter, K. A. (2004). Spectrophotometric pH measurement in estuaries using thymol blue and m-cresol purple. *Mar. Chem.* 91, 175–186. doi: 10.1016/j.marchem.2004.06.008

Müller, J. D., and Rehder, G. (2018) Metrology for pH measurements in brackish waters - part 2: experimental characterization of purified m-Cresol Purple for spectrophotometric pHT measurements. *Front. Mar. Sci.* 5:177. doi: 10.3389/fmars.2018.00177

Müller, J. D., Schneider, B., Aßmann, S., and Rehder, G. (2018). Spectrophotometric pH measurements in the presence of dissolved organic matter and hydrogen sulfide. *Limnol. Oceanogr. Methods* 16, 68–82. doi: 10.1002/lom3.10227

Müller, J. D., Schneider, B., and Rehder, G. (2016). Long-term alkalinity trends in the Baltic Sea and their implications for CO_2-induced acidification. *Limnol. Oceanogr.* 61, 1984–2002. doi: 10.1002/lno.10349

Nemzer, B. V., and Dickson, A. G. (2005). The stability and reproducibility of Tris buffers in synthetic seawater. *Mar. Chem.* 96, 237–242. doi: 10.1016/j.marchem.2005.01.004

Papadimitriou, S., Loucaides, S., Rérolle, V., Achterberg, E. P., Dickson, A. G., Mowlem, M., et al. (2016). The measurement of pH in saline and hypersaline media at sub-zero temperatures: characterization of Tris buffers. *Mar. Chem.* 184, 11–20. doi: 10.1016/j.marchem.2016.06.002

Pratt, K. (2014). Measurement of pH_T values of Tris buffers in artificial seawater at varying mole ratios of Tris:Tris·HCl. *Mar. Chem.* 162, 89–95. doi: 10.1016/j.marchem.2014.03.003

R Core Team (2014). *R: A Language and Environment for Statistical Computing*. Available online at: http://www.r-project.org/

Waters, J. F., and Millero, F. J. (2013). The free proton concentration scale for seawater pH. *Mar. Chem.* 149, 8–22. doi: 10.1016/j.marchem.2012.11.003

Conflict of Interest Statement: The authors declare that the research was conducted in the absence of any commercial or financial relationships that could be construed as a potential conflict of interest.

Copyright © 2018 Müller, Bastkowski, Sander, Seitz, Turner, Dickson and Rehder. This is an open-access article distributed under the terms of the Creative Commons Attribution License (CC BY). The use, distribution or reproduction in other forums is permitted, provided the original author(s) and the copyright owner(s) are credited and that the original publication in this journal is cited, in accordance with accepted academic practice. No use, distribution or reproduction is permitted which does not comply with these terms.

frontiers in Marine Science

ORIGINAL RESEARCH
published: 10 July 2018
doi: 10.3389/fmars.2018.00177

Metrology of pH Measurements in Brackish Waters—Part 2: Experimental Characterization of Purified meta-Cresol Purple for Spectrophotometric pH_T Measurements

Jens D. Müller and Gregor Rehder*

Department of Marine Chemistry, Leibniz Institute for Baltic Sea Research Warnemünde, Rostock, Germany

Spectrophotometric pH measurements allow for an accurate quantification of acid-base equilibria in natural waters, provided that the physico-chemical properties of the indicator dye are well known. Here we present the first characterization of purified m-Cresol Purple (mCP) directly linked to a primary pH standard in the salinity range 5–20. Results were obtained from mCP absorption measurements in TRIS buffer solutions. The pH_T of identical buffer solutions was previously determined by Harned cell measurements in a coordinated series of experiments. The contribution of the TRIS/HCl component to the ionic strength of the buffer solutions increases toward lower salinity: This was taken into account by extrapolating the determined pK_2e_2 to zero buffer concentration, thereby establishing access to a true hydrogen ion concentration scale for the first time. The results of this study were extended with previous determinations of pK_2e_2 at higher and lower salinity and a pK_2e_2 model was fitted to the combined data set. For future investigations that include measurements in the salinity range 5–20, pH_T should be calculated according to this pK_2e_2 model, which can also be used without shortcomings for salinities 0–40 and temperatures from 278.15 to 308.15 K. It should be noted that conceptual limitations and methodical uncertainties are not yet adequately addressed for pH_T determinations at very low ionic strength.

Keywords: m-Cresol Purple, brackish water, estuaries, spectrophotometric pH measurements, traceability, primary standard, TRIS buffer

OPEN ACCESS

Edited by:
Eric' Pieter Achterberg, GEOMAR Helmholtz-Zentrum für Ozeanforschung Kiel, Germany

Reviewed by:
Manab Kumar Dutta, Xiamen University, China
Robert H. Byrne, University of South Florida, United States

****Correspondence:***
Jens D. Müller
jens.mueller@io-warnemuende.de

Specialty section:
This article was submitted to Marine Biogeochemistry, a section of the journal Frontiers in Marine Science

Received: *26 January 2018*
Accepted: *03 May 2018*
Published: *10 July 2018*

Citation:
Müller JD and Rehder G (2018) Metrology of pH Measurements in Brackish Waters—Part 2: Experimental Characterization of Purified meta-Cresol Purple for Spectrophotometric pH_T Measurements. Front. Mar. Sci. 5:177. doi: 10.3389/fmars.2018.00177

INTRODUCTION

pH is a master variable of seawater analysis. It allows the tracking of numerous biogeochemical processes, including organic matter production and mineralization, and is the most direct measure for ocean acidification (Byrne et al., 2010; Byrne, 2014). Several methods have been developed to determine pH, ranging from glass electrodes (Easley and Byrne, 2012), to ISFET sensors (Martz et al., 2010) and to pH optodes (Clarke et al., 2015). However, spectrophotometric pH measurements have proven to be the most precise and accurate method and are often considered to be a reference method (Liu et al., 2011; Byrne, 2014). Müller et al. (2018a) recently demonstrated

that the method works reliably in the presence of high concentrations of dissolved organic matter and hydrogen sulfide and therefore supports full CO_2 system characterizations even under challenging conditions typical for brackish waters.

Spectrophotometric pH measurements rely on the addition of pH-sensitive indicator dyes, like m-Cresol Purple (mCP), to a water sample. The dye changes its color with sample pH. Those color changes are reflected in the absorbance spectra of the dye as changes in the peak absorbance ratio R, which depends on physico-chemical properties of the dye molecule (Clayton and Byrne, 1993; Liu et al., 2011). The accurate determination of acid-base equilibria in seawater—including the speciation of the CO_2 system—and the determination of long-term acidification trends require knowledge of the dye's dissociation constant and absorbance behavior. In order to ensure comparability of pH measurement results, the determination of the dissociation constant should be traceable to a fully characterized primary pH standard, e.g., by Harned cell measurements (Buck et al., 2002; Dickson et al., 2016).

In previous studies, reliable determinations of the dissociation and absorption behavior of mCP have been established in the salinity range 20–40 (Liu et al., 2011) and for river water conditions (Lai et al., 2016, 2017). The characterization experiments involved measurements of buffer solutions with pH assigned by Harned cell measurements (e.g., DelValls and Dickson, 1998) to determine the dissociation constant. Such buffer solutions were previously not available for salinities between 0 and 20. Mosley et al. (2004) provided an interim solution for this brackish water gap and characterized mCP for the full salinity range. However, the uncertainty of this characterization remained large, mainly due to (i) the interpolation of unknown TRIS buffer pH values between salinity 5 and 20, (ii) the lack of seawater salts in the salinity range 0.06–2, and (iii) the use of non-purified mCP. Further, the characterization was restricted to 298.15 K. Douglas and Byrne (2017b) combined the previous characterizations of purified mCP (Liu et al., 2011; Lai et al., 2016, 2017) with the results of Mosley et al. (2004) and modeled mCP properties over the full salinity and temperature range after correcting for dye impurities (Douglas and Byrne, 2017a). Nevertheless, a direct experimental characterization of purified mCP in brackish waters traceable to a primary pH standard was still missing, making it impossible to quantify the accuracy of spectrophotometric pH measurements in brackish waters. Uncertainties remained especially large at temperatures different from 298.15 K, due to the absence of experimental data.

To overcome these limitations, a concerted series of experiments was performed, which included two work packages:

1. Prior to the experiments presented here, Harned cell measurements of TRIS buffered artificial seawater (ASW) solutions were preformed to determine pH values on the total scale (pH_T) at salinities ranging from 5 to 20, temperatures from 278.15 to 318.15 K and equimolal TRIS/TRIS·H^+ molalities of 0.01, 0.025, and 0.04 mol·kg-H_2O^{-1} (Müller et al., 2018b).
2. Here we present the experimental determination of the mCP dissociation behavior in brackish waters based on spectrophotometric measurements performed with the newly available TRIS buffers.

The obtained characterization of mCP in the salinity range 5–20 was combined with previous results at higher and lower salinity, to derive a model for the dissociation behavior covering the full salinity and temperature range. This model was evaluated in comparison to previous characterizations, with special emphasizes to remaining uncertainties for spectrophotometric pH measurements at very low ionic strength.

MATERIALS AND METHODS

Theory

The basic principles of spectrophotometric pH measurements have been described extensively before (Clayton and Byrne, 1993; Mosley et al., 2004; Liu et al., 2011). In brief, the measurements are based on the addition of a pH-sensitive indicator dye to a water sample. The second dissociation constant, pK_2, of the diprotic dye mCP lies in the pH range typical for seawater. In this case, the solution pH can be expressed as:

$$pH = pK_2 + \log_{10}\left(\frac{[I^{2-}]}{[HI^{-}]}\right) \quad (1)$$

where $[HI^-]$ and $[I^{2-}]$ are the concentrations of the monoprotonated and deprotonated species of the indicator dye, respectively. The concentration ratio $[HI^-]/[I^{2-}]$ can be determined by absorbance (A) measurements, because HI^- and I^{2-} have two clearly distinguishable absorbance maxima (**Figure 1**) at wavelength $\lambda_1 = 434$ nm and $\lambda_2 = 578$ nm, respectively (Clayton and Byrne, 1993). However, the absorbance spectra of both indicator species overlap. Therefore, at both wavelength λ_1 and λ_2 the absorbance A_λ needs to be expressed by the Lambert-Beer-law describing the additive absorbance contribution, $A_\lambda\left(I^{2-}\right) + A_\lambda\left(HI^{-}\right)$, of both species as:

$$A_\lambda = \left(\varepsilon_\lambda\left(HI^{-}\right)\cdot\left[HI^{-}\right] + \varepsilon_\lambda\left(I^{2-}\right)\cdot\left[I^{2-}\right]\right)\cdot d \quad (2)$$

where $\varepsilon_\lambda(X)$ are the molar extinction coefficients of the indicator species X at wavelength λ, and d is the cuvette length.

After combining Equations (1) and (2), and with algebraic manipulation, the pH of the solution can be expressed as:

$$pH = pK_2 + \log_{10}\left(\frac{R - e_1}{e_2 - e_3\cdot R}\right) \quad (3)$$

where $R = A_{578}/A_{434}$ is the ratio of the absorbance measured at the two peak wavelengths (dashed lines in **Figure 1**) and $e_1 = \varepsilon_{578}(HI^-)/\varepsilon_{434}(HI^-)$, $e_2 = \varepsilon_{578}(I^{2-})/\varepsilon_{434}(HI^-)$ and $e_3 = \varepsilon_{434}(I^{2-})/\varepsilon_{434}(HI^-)$ are the molar absorptivity ratios (Clayton and Byrne, 1993; Mosley et al., 2004).

The molar absorptivity ratios e_2 and e_3 include molar extinction coefficients of both mCP species, HI^- and I^{2-}. Therefore, the separate determination of e_2 and e_3 would require the combination of measurements obtained in high and low pH

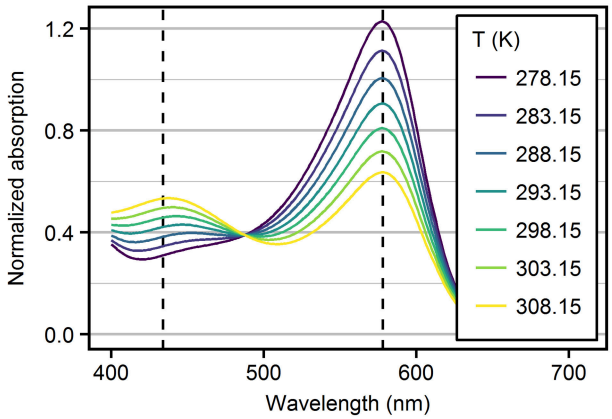


FIGURE 1 | Absorbance spectra of mCP recorded in TRIS ASW solutions ($S = 10$, $b_{TRIS/TRIS\cdot H^+} = 0.04$ mol·kg-H_2O^{-1}) as a function of temperature. Spectra are normalized to the absorption at the isosbestic wavelength at 488 nm. Dashed lines mark the wavelengths of HI^- and I^{2-} peak absorbances.

solutions. Liu et al. (2011) avoided this by rearranging Equation (3) to:

$$pH = pK_2e_2 + \log_{10}\left(\frac{R - e_1}{1 - \frac{e_3}{e_2}\cdot R}\right) \quad (4)$$

The salinity and temperature dependence of the term pK_2e_2 can be determined from measurements in buffer solutions with a known pH, provided that e_1 and e_3/e_2 are known. Determined pK_2e_2 values refer to the same pH scale that was assigned to the pH buffer solutions. Currently, the total pH scale (pH_T) is a widely accepted standard in oceanography. According to its definition, $pH_T = -log_{10}\left\{\left[H^+\right]\cdot\left(1+\left[SO_4^-\right]_T/K_{HSO_4^-}\right)\right\}$, it accounts for the concentrations of both, the free hydrogen ions, $\left[H^+\right]$, and hydrogen sulfate ions, expressed as the total sulfate concentration $\left[SO_4^-\right]_T$ divided by the dissociation constant of hydrogen sulfate $K_{HSO_4^-}$ (Müller et al., 2018b). Previously, the required seawater buffer solutions with pH values assigned on the total scale were only available at salinities ≥ 20 (DelValls and Dickson, 1998).

Buffer Solutions

TRIS buffered ASW solutions were prepared at salinities 5, 10, 15, 20, and at 35 for consistency assessments with previous results, according to Müller et al. (2018b). At each salinity, three buffer solutions contained equimolal TRIS/$TRISH^+$ molalities ($b_{TRIS/TRIS\cdot H^+}$) of 0.01, 0.025, 0.04 mol·kg-H_2O^{-1}. This allows the impact of the solution composition on the pH_T of the buffers and on the dissociation behavior of the dye to be corrected by extrapolation of the determined pK_2e_2 values to zero TRIS/$TRISH^+$ molality. The preparation and bottling of the buffer solutions was performed by the national metrological institute of Germany, Physikalisch-Technische Bundesanstalt (PTB), in parallel (same lab, day, stock solutions, and person, but separate weighings) to the preparation of identical buffer solutions for Harned cell pH_T measurements (Müller et al., 2018b). Solutions prepared at PTB were stored in 500 mL glass bottles (Schott DURAN, GL 45 polypropylene screw caps). The headspace was filled with humidified Argon gas (Argon 5.0, 99.999% purity, Linde AG, Pullach, Germany) in order to avoid CO_2 uptake from the atmosphere. Solutions were shipped to the Leibniz Institute for Baltic Sea Research in Warnemünde (IOW) for spectrophotometric measurements. The headspace was refilled with humidified Argon whenever bottles were opened to take subsamples.

Spectrophotometric Measurements

In the buffer solutions described above, absorbance spectra of mCP were recorded at seven temperatures from 278.15 to 308.15 K in intervals of 5 K. Measurements were performed with an instrument set-up as described by Carter et al. (2013). The system consisted of an Agilent 8453 diode array spectrophotometer (Santa Clara, US) and a cylindrical, jacketed, flow-through cuvette (path length 100 mm, inner diameter 5 mm, custom made by Hellma Analytics, Müllheim, Germany). The mantle of the cuvette was permanently flushed with water from a Julabo F30 heating circulator (Seelbach, Germany). Temperature was measured with a Pt resistance thermometer (Burster Kelvimat 4306 equipped with needle probe 42905, Gernsbach, Germany) calibrated at IOW's calibration lab with an uncertainty of 0.02 K. The needle probe was inserted in the water stream just behind the cuvette. Measured temperatures were within ±0.05 K of the target values. Before analysis, buffer solutions were brought to within 1 K of the analysis temperature in a separate temperature bath. The cuvette was filled and emptied with a computer-controlled syringe pump. The Agilent 8453 spectrometer was operated with both the tungsten- and the deuterium lamp switched on. More details on the measurement procedure are given in Carter et al. (2013).

All measurements were performed with purified mCP (Liu et al., 2011) kindly provided by the lab of Robert H. Byrne, Univ. of South Florida. A 2 mM stock solution of the dye was prepared by dissolving 0.08 g mCP in 100 mL deionized water. For better dissolution and pH adjustment, the stock solution was sonicated and 3.25 mL of 0.1 M NaOH were added to achieve a pH of around 8.

Spectrometers are known to behave non-linearly at high and low absorbances. For mCP absorbance spectra, this is critical for the strong absorbance of I^{2-} at 578 nm (**Figure 1**), especially at high pH in cold TRIS buffer solutions. To avoid non-linear behavior, absorbances at 578 nm were limited to values around 1 by adjusting the added amount of mCP. However, this may result in low absorbance at 434 nm. The most critical conditions were encountered at salinity 35 and 278.15 K with an absorbance ratio around 5 (Figure S1).

The spectrometer performance was verified by running the self-test of the instrument (deuterium lines test for wavelength accuracy and reproducibility; as well as noise-, baseline flatness-, and stability tests). Wavelength accuracy was

further verified by measurements of Holmium oxide standards (Certified Reference Materials, Type 667-UV5, Holmium Liquid Filter; Hellma Analytics, Mühlheim, Germany). Furthermore, spectrophotometric comparison measurements were performed under conditions with well-defined solution pH and dye characteristics. This refers to measurements at 298.15 K of TRIS buffer solutions (batch T27 and T30) provided by the lab of Andrew G. Dickson (Univ. of California). Further, measurements performed on own TRIS buffer solutions at salinity 20 and 35 were compared with previous results of Liu et al. (2011), that were obtained in identical experiments, at temperatures from 278.15 to 303.15 K.

Determination of pK_2e_2

pH_T values of TRIS buffer solutions used in this study to calculate pK_2e_2 were assigned by Harned cell measurement (Table S1) according to Müller et al. (2018b). The determination of pK_2e_2 from known pH_T values and corresponding R ratios was obtained from Equation (4) written in the following form:

$$pK_2e_2 = pH_T - \log_{10}\left(\frac{R - e_1}{1 - \frac{e_3}{e_2} \cdot R}\right) \quad (5)$$

Equation (5) requires knowledge of the absorptivity ratios e_1 and e_2/e_3. As proposed by Douglas and Byrne (2017b), the absorptivity ratios by Liu et al. (2011) according to Equations (6) and (7):

$$e_1 = -0.007762 + 4.5174 \cdot 10^{-5} \cdot T \quad (6)$$

$$\frac{e_3}{e_2} = -0.020813 + 2.60262 \cdot 10^{-4} \cdot T + 1.0436 \cdot 10^{-4} \cdot (S - 35) \quad (7)$$

were applied for the salinity range 5–20, although originally determined for salinities >20. Deviations between the salinity-dependent e_2/e_3 of Liu et al. (2011) extrapolated to $S = 0$, and e_2/e_3 determined by Lai et al. (2016) for freshwater conditions are presumably related to differences in the determination procedure. Only Liu et al. (2011) applied an iterative process to derive e_3/e_2 values that account for all absorbing species in solution, (R.H. Byrne, pers. comm.).

pK_2e_2 values were determined from measured R and pH_T data for all buffer solutions as described above. At each combination of salinity and temperature, the change of pK_2e_2 with TRIS/$TRISH^+$ molality was determined by linear regression analysis. The determined slope was used to correct individual pK_2e_2 values to zero TRIS/$TRIS{\cdot}H^+$ molality (Figure S2).

Fitting a pK_2e_2 Model to a Combined Data Set Including Previously Published Results

pK_2e_2 results determined in this study at salinities 5–20 were combined with previously published results to derive a complete characterization of mCP from ocean to river water. In order to include the measurement uncertainty of previous work, we calculated pK_2e_2 values from individual data rather than fitted equations given in the respective publications. The following data were included:

- For salinities 20, 30, 35, and 40 and temperatures from 278.15 to 308.15 K, pK_2e_2 values were calculated from Table S4 in the supporting information of Liu et al. (2011).
- For salinities between 0.06 and 4.03 and 298.15 K, impurity-corrected results based on Mosley et al. (2004) were taken from Table 1 in Douglas and Byrne (2017b). An offset of +0.0065 pH units was observed at $S = 5$ between the results of Douglas and Byrne (2017b) and this study. This offset was added to all pK_2e_2 values at salinities from 0.06 to 4.03. This correction is smaller than the uncertainty in the data (see discussion) and allows for a pK_2e_2 fit without a discontinuity.
- For salinity 0 and temperatures from 281.2 to 303.2 K, pK_2e_2 was calculated from the measured dissociation constant at infinite dilution, pK_I^0 (C. Lai and M. DeGrandpre, pers. comm.), and e_2 (Table 2 in Lai et al., 2016) as $pK_I^0 - log_{10}(e_2)$.

The following full model, expressing pK_2e_2 as a function (f) of S, T, was fitted to the combined data set:

$$pK_2e_2 = f\left\{\left(1 + S^{0.5} + S + S^{1.5} + S^2 + S^{2.5}\right) \cdot \left(1 + T + ln\,(T) + \frac{1}{T}\right)\right\} \quad (8)$$

Equation (8) includes 24 terms representing all combinations of the terms of a fifth order $S^{0.5}$ polynomial and the terms of the physico-chemical expression of the temperature dependence of dissociation constants. The salinity polynomial in Equation (8) is identical to that fitted by Douglas and Byrne (2017b). Expressions with identical temperature dependence were previously fitted to pK_2e_2 results (Liu et al., 2011) and TRIS buffer pH_T data (DelValls and Dickson, 1998).

The fit was obtained by generalized linear modeling with the "stats" package of the statistical programming language "R" (R Core Team, 2014). After fitting the full model (Equation 8), insignificant terms were removed by stepwise variable selection in both directions based on the Akaike information criterion. The removal of terms was performed with the "stepAIC" function from the R package "MASS" and resulted in a pK_2e_2 model with 19 terms (Equation 9).

RESULTS

Extrapolation of pK_2e_2 to Zero Buffer Concentration

At each combination of temperature and salinity, pK_2e_2 was determined at three different TRIS/$TRISH^+$ molalities, 0.01, 0.025, and 0.04 mol·kg-H_2O^{-1}. The pK_2e_2 values were extrapolated linearly to zero TRIS/$TRISH^+$ molality (Figure S2). The mean slope of this extrapolation ranged from 0.3 to −0.07 mol^{-1}·kg-H_2O at salinities 5 and 35, respectively. For a TRIS/$TRISH^+$ molality of 0.04 mol·kg-H_2O^{-1}, this slope corresponds to a mean pK_2e_2 correction ranging from 0.012 to −0.003 at salinities 5 and 35, respectively (Figure S3). The standard deviation of the residuals from the linear

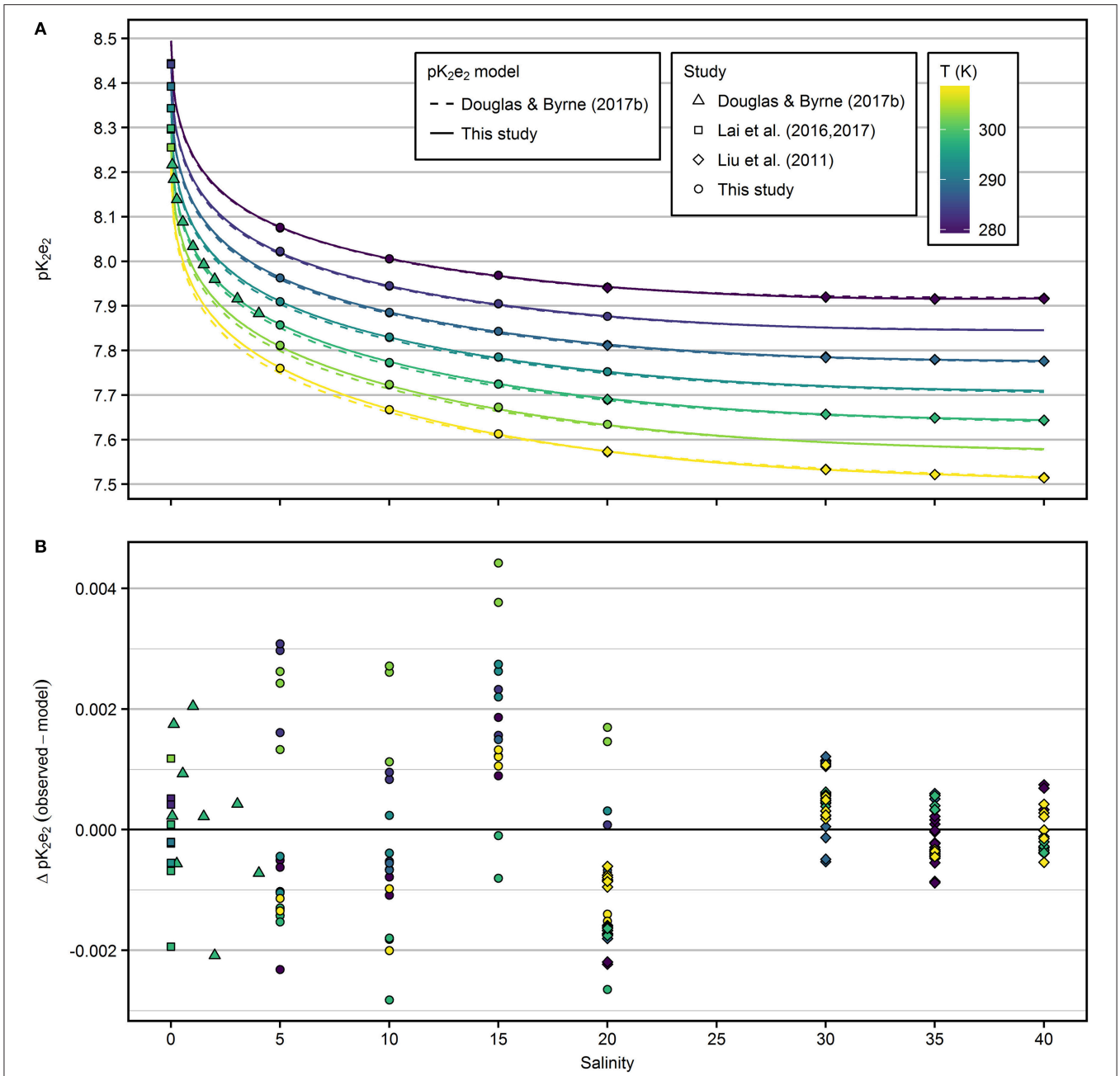


FIGURE 2 | (A) pK_2e_2 of mCP as a function of salinity and temperature. Results from this study (salinity range 5–20) were combined with previous results and fitted to a common pK_2e_2 model (solid lines). Dashed lines represent the pK_2e_2 model by Douglas and Byrne (2017b). **(B)** Residuals from the model fitted in this study.

extrapolation fit was <0.001 for all combinations of temperature and salinity. The pK_2e_2 value determined at $S = 20$ and a TRIS/TRISH$^+$ molality of 0.025 mol·kg-H_2O^{-1} deviated from the value interpolated between the results at TRIS/TRISH$^+$ molalities of 0.01 and 0.04 mol·kg-H_2O^{-1} by more than three times the standard deviation of all measurements, and was removed for further analysis without knowing the source of error.

pK_2e_2 Results and Model

The extrapolated pK_2e_2 values of mCP determined in this study at $S = 20$ and $T = 308.15$ K and at $S = 5$ and 278.15 K ranged from 7.57 to 8.08 (**Figure 2A**). The salinity-dependence of pK_2e_2 increases toward lower salinity. The dependence on temperature is almost linear at constant salinity. The pK_2e_2 model fitted to the combined data set, including results from this study and from that of Douglas and Byrne (2017b), Lai et al. (2016, 2017), and Liu

TABLE 1 | Coefficients of equation 9 fitted to the combined data set displayed in **Figure 2A**.

Coefficient	Value
a_0	$1.08071477 \cdot 10^{3}$
a_1	$-1.35394946 \cdot 10^{-1}$
a_2	$-1.98063716 \cdot 10^{2}$
a_3	$6.31924397 \cdot 10^{1}$
a_4	−5.18141866
b_1	$-2.66457425 \cdot 10^{4}$
b_2	$5.08796578 \cdot 10^{3}$
b_3	$-1.62454827 \cdot 10^{3}$
b_4	$1.33276788 \cdot 10^{2}$
c_1	$-1.89671212 \cdot 10^{2}$
c_2	$3.49038762 \cdot 10^{1}$
c_3	$-1.11336508 \cdot 10^{1}$
c_4	$9.12761930 \cdot 10^{-1}$
d_1	$3.27430677 \cdot 10^{-1}$
d_2	$-7.51448528 \cdot 10^{-4}$
d_3	$3.94838229 \cdot 10^{-4}$
d_4	$-6.00237876 \cdot 10^{-2}$
d_5	$1.90997693 \cdot 10^{-2}$
d_6	$-1.56396488 \cdot 10^{-3}$

Control value for pK_2e_2 at S = 20 and T = 298.15 K is 7.6920.

et al. (2011) is given in Equation (9) with respective coefficients given in **Table 1**.

$$\begin{aligned} pK_2e_2 = {} & a_0 + a_1 \cdot S^{0.5} + a_2 \cdot S^{1.5} + a_3 \cdot S^2 + a_4 \cdot S^{2.5} \\ & + b_1 \cdot \mathrm{T}^{-1} + b_2 \cdot S^{1.5} \cdot \mathrm{T}^{-1} + b_3 \cdot S^2 \cdot \mathrm{T}^{-1} \\ & + b_4 \cdot S^{2.5} \cdot \mathrm{T}^{-1} \\ & + c_1 \cdot \ln(\mathrm{T}) + c_2 \cdot S^{1.5} \cdot \ln(\mathrm{T}) + c_3 \cdot S^2 \cdot \ln(\mathrm{T}) \\ & + c_4 \cdot S^{2.5} \cdot \ln(\mathrm{T}) \\ & + d_1 \cdot T + d_2 \cdot S^{0.5} \cdot T + d_3 \cdot S \cdot T + d_4 \cdot S^{1.5} \cdot T \\ & + d_5 \cdot S^2 \cdot T + d_6 \cdot S^{2.5} \cdot T \end{aligned} \quad (9)$$

Residuals from the fitted pK_2e_2 model (**Figure 2B**) are within ±0.005 for the entire salinity and temperature range.

Agreement With Previous Studies

In the salinity range 5–20, the pK_2e_2 model of Douglas and Byrne (2017b) agrees with the new model presented in this study within 0.008 at 298.15 K (Figure S4). At salinity 20, deviations are within 0.004. At salinity 5 and 308.15 K, the largest offset between both models was observed with 0.013 higher pK_2e_2 values predicted by the model fitted in this study.

In the salinity range 20–40, the pK_2e_2 model of Liu et al. (2011) agrees with the model presented in this study within 0.002 across all temperatures (Figure S4). At freshwater conditions, pK_2e_2 calculated according to Lai et al. (2017) agrees with the model presented in this study within 0.006 across all temperatures (Figure S4).

The residuals from the model (**Figure 2B**) are larger at salinities ≤20, compared to the residuals at salinities >20. However, the precision achieved within each group of salinity, temperature and TRIS/TRISH$^+$ is <0.001 and comparable for the results of this study and those of Liu et al. (2011). The higher residuals at lower salinities reflect the uncertainty in the pH_T determination by Harned cell measurements (compare residuals in Figure 5 of Müller et al., 2018a), which was not included in previous studies when pH_T values of buffer solutions were calculated from fitted models.

For a direct comparison to previous results, spectrophotometric pH_T values calculated according to Liu et al. (2011) were determined in TRIS buffer solutions (batch T27 and T30) purchased from the laboratory of Andrew G. Dickson (Scripps Institution of Oceanography). Results were highly reproducible and consistently 0.005–0.006 pH units lower than TRIS pH_T values calculated according to DelValls and Dickson (1998) at 298.15 K. For own TRIS buffer solutions at salinity 20 and 35, spectrophotometric pH_T values calculated according to Liu et al. (2011) were 0.002 to 0.008 pH units lower than pH_T values determined by Harned cell measurements over the temperature range from 278.15 to 308.15 K.

DISCUSSION

Advantages of a Coordinated Experimental Concept

The experiments presented here were part of a coordinated measurement program covering the preparation of TRIS buffered ASW solutions, pH_T determination by Harned cell measurements and subsequent recording of mCP absorption spectra. This reduces uncertainties included in all previous experiments, in which the required analysis of the buffer solutions (e.g., DelValls and Dickson, 1998) and subsequent mCP characterizations (e.g., Liu et al., 2011) were performed in separate experiments. Nemzer and Dickson (2005) found TRIS buffer pH to vary by up to 0.0034, even when carefully prepared in the same laboratory, and argued that an error of only 0.23% in the TRIS/TRISH$^+$ ratio will result in an error of 0.001 in pH. Müller et al. (2018b) and this study reduced this uncertainty by titrating the TRIS- against the HCl-stock solution and subsequently preparing all buffers from the same stock solution. Further, in this study we determined pK_2e_2 based on pH_T values individually assigned by Harned cell measurements to the same batch of buffer solution, whereas previous studies had to rely on pH_T values calculated from fitted models.

Correcting the Contribution of TRIS and HCl to the Ionic Composition of the Buffer Solutions

The ionic composition of buffered ASW solutions differs from that of pure ASW solutions, due to the replacement of seawater salts by TRIS and HCl at a given ionic strength. The relative contribution of the buffer components increases toward lower salinity. This can only to a certain degree be circumvented by

lower buffer concentrations, because solutions with lower buffer concentrations are less stable and reproducible. The inevitable difference in solution composition has two effects: (i) The pH_T of the buffer solution changes with the concentration of the buffer and assigned pH_T values do not exactly correspond to the total hydrogen ion concentration scale (see discussion in Nemzer and Dickson, 2005; Dickson et al., 2016; Müller et al., 2018b). (ii) The difference in solution composition affects the pK_2e_2 of mCP. However, both effects (i) and (ii) are corrected when calibration results are extrapolated to zero buffer concentration, as done in this study for the first time.

At salinity 35, we found the pK_2e_2 correction to be < 0.005 for a 0.04 mol·kg-H_2O^{-1} TRIS/$TRISH^+$ molality. Although this effect might be small in comparison to other sources of uncertainty, similar extrapolation experiments as performed in this study are required to accurately determine pH_T at salinities 20–40. More pronounced pK_2e_2 corrections needed to be applied at lower salinity and amounted to as much as 0.02 for a TRIS/$TRISH^+$ molality of 0.04 mol·kg^{-1} at 308.15 K (Figure S3).

Performing the required extrapolation, this study presents the first attempt to determine pK_2e_2 values that allow measurements of pH on a true total hydrogen ion concentration scale referring to the reference ASW composition in the salinity range 5–20. In contrast, the mCP characterization by Mosley et al. (2004) did not account for the ionic strength contribution of TRIS/$TRISH^+$, despite covering salinities as low as 0.06. Furthermore, at salinities below 2, TRIS/$TRISH^+$ represented the only contribution to ionic strength in the experiments performed by Mosley et al. (2004) but was still interpreted in terms of salinity, based on the results of Bates and Hetzer (1961). In view of these uncertainties, our pK_2e_2 model is strictly valid only for salinities as low as 5 and the reported ASW solutions composition. For salinities below 5, the pK_2e_2 models reported in this study and that of Douglas and Byrne (2017b) are associated with similar uncertainties, going back to the limitations in the study of Mosley et al. (2004).

Spectrophotometric pH Measurements at Very Low Ionic Strength

Similar to the pK_2e_2 extrapolation performed in this study, Lai et al. (2016) determined changes of the dissociation constant of mCP of ∼0.02 when decreasing the phosphate buffer concentration by only ∼0.005 mol·kg^{-1} under freshwater conditions. This highlights the potential sensitivity of the dissociation behavior of mCP on the ionic composition of the sample at low ionic strength. It remains to be studied, whether the dissociation behavior of mCP is controlled only by the ionic strength of the solution or whether the ionic composition plays a significant role. If the latter is the case, it would be questionable, whether an accuracy in the order of a few thousands of pH units can ever be achieved at very low ionic strength, without knowing the ionic composition of the sample. This is a consequence of the more general problem to determine salinity from conductivity measurements in low-saline water with variable composition (Feistel et al., 2009; Wright et al., 2011). Lai et al. (2016) started to address this issue by comparing spectrophotometric pH measurements with two different indicator dyes, phenol red and mCP, on seven different freshwater samples. They found pH results that agreed within ±0.01. Those results indicate same ionic interactions of both dyes, i.e., similar activity coefficients in similar media, but do not allow for an independent assessment of the accuracy of the results. Potential approaches to improve the understanding of mCP behavior in very low-saline and river water conditions include: (i) traceable characterization experiments at variable buffer concentrations and ionic composition of the salt matrix, and (ii) estimation of the effects of solution composition changes on the dyes dissociation behavior with Pitzer models (Turner et al., 2016).

Observed Offsets in pH_T Comparison Measurements

Performing comparison measurements with TRIS buffers provided by Dickson's laboratory, our pH_T values calculated according to Liu et al. (2011) were consistently lower by 0.005 at 298.15 K. Over the full temperature range, pH_T values determined in own TRIS buffer solutions were 0.002 to 0.008 lower. Similar offsets were reported by Carter et al. (2013), but the reason for this offset could not be determined. Obviously, lower determined pH_T values result from a lower R-ratio in Equation (4). Vice versa, lower R-ratios applied in Equation (5) lead to slightly higher pK_2e_2 values. In accordance with the comparison measurement, we determined slightly higher pK_2e_2 values compared to previous results (Liu et al., 2011) at finite buffer concentration. Interestingly, our extrapolation to zero TRIS/$TRISH^+$ molality compensates for this offset to the results of Liu et al. (2011) at salinity 20 (**Figure 2**). In contrast, at salinity 35 the correction has an opposite sign and observed pH_T differences do not cancel out. Due to the scarce amount of data at salinities >20 obtained in this study, we included only the results by Liu et al. (2011) into our combined data set.

Model Evaluation and Recommendation

The pK_2e_2 model by Douglas and Byrne (2017b) agrees surprisingly well with the results presented in this study, although previous experimental data in the salinity range 5–20, going back to the results of Mosley et al. (2004), were limited to 298.15 K and associated to several uncertainties. However, differences between both models (> 0.01) are larger than the measurement uncertainty of the method (Carter et al., 2013). In addition, the pK_2e_2 model presented in this study fits the results of Liu et al. (2011) almost as well as the original model (residuals within ± 0.002), and therefore better than the model of Douglas and Byrne (2017b), who found residuals > 0.003.

Therefore, we recommend to use the pK_2e_2 model presented in this study for all spectrophotometric pH measurements in brackish water that cover salinities below 20. Due to the excellent agreement with the results of Liu et al. (2011), the pK_2e_2 model

presented in this study can also be applied for pH calculations at salinities >20 without constraints. However, the uncertainty of this model is as large as that of Douglas and Byrne (2017b) for salinities well below 5.

CONCLUSION

In this study, we provided the experimental basis to directly link spectrophotometric pH_T measurements in the salinity range 5–20 to Harned cell pH_T determinations of TRIS buffered artificial seawater solutions. We combined the derived pK_2e_2 estimates of mCP with the results from previous studies and fitted a pK_2e_2 model as a function of temperature and salinity to the combined data set. We recommend using the new pK_2e_2 model for all measurements in brackish waters that include samples with salinities below 20. Measurements under fully marine conditions can be performed without compromise compared to previous pK_2e_2 models. For $S < 5$, the model faces the same problems as in previous work, but is potentially better suited for pH measurements near 5. For near river water conditions, the impact of ionic composition on spectrophotometric pH determination remains to be studied to answer the question whether spectrophotometric measurements can produce accurate pH results without knowledge of the exact ionic composition of the sample.

AUTHOR CONTRIBUTIONS

JM: Initiation and concept of the study, experimental work, data analysis and interpretation, manuscript preparation; GR: Coordinator of the research project BONUS PINBAL providing the framework for this work, involved in the outline of the manuscript and the interpretation of the data.

ACKNOWLEDGMENTS

The quality of this paper gained from scientific discussions with Bernd Schneider.

The research leading to this manuscript has received funding from BONUS, the joint Baltic Sea research and development programme (Art 185), funded jointly from the European Union's Seventh Programme for research, technological development and demonstration and from the German Federal Ministry of Education and Research through Grant No. 03F0689A (BONUS PINBAL) and Grant No. 03F0773A (BONUS INTEGRAL).

SUPPLEMENTARY MATERIAL

The Supplementary Material for this article can be found online at: https://www.frontiersin.org/articles/10.3389/fmars.2018.00177/full#supplementary-material

REFERENCES

Bates, R. G., and Hetzer, H. B. (1961). Dissociation constant of the protonated acid form of 2-amino-2-(hydroxymethyl)- 1, 3-propanediol [tris- hydroxymethyl) -aminomethane] and related thermodynamic quantities from 0 to 50°. *J. Phys. Chem.* 65, 667–671. doi: 10.1021/j100822a017

Buck, R. P., Rondinini, S., Covington, A. K., Baucke, F. G. K., Brett, C. M. A., Camoes, M. F., et al. (2002). Measurement of pH. Definition, standards, and procedures (IUPAC Recommendations 2002). *Pure Appl. Chem.* 74, 2169–2200. doi: 10.1351/pac200274112169

Byrne, R. H. (2014). Measuring ocean acidification: new technology for a new era of ocean chemistry. *Environ. Sci. Technol.* 48, 5352–60. doi: 10.1021/es405819p

Byrne, R. H., Mecking, S., Feely, R. A., and Liu, X. (2010). Direct observations of basin-wide acidification of the North Pacific Ocean. *Geophys. Res. Lett.* 37:L02601. doi: 10.1029/2009GL040999

Carter, B. R., Radich, J. A., Doyle, H. L., and Dickson, A. G. (2013). An automated system for spectrophotometric seawater pH measurements. *Limnol. Oceanogr. Methods* 11, 16–27. doi: 10.4319/lom.2013.11.16

Clarke, J. S., Achterberg, E. P., Rérolle, V. M., Abi Kaed Bey, S., Floquet, C. F. A., and Mowlem, M. C. (2015). Characterisation and deployment of an immobilised pH sensor spot towards surface ocean pH measurements. *Anal. Chim. Acta* 897, 69–80. doi: 10.1016/j.aca.2015.09.026

Clayton, T. D., and Byrne, R. H. (1993). Spectrophotometric seawater pH measurements : total hydrogen results. *Deep Sea Res. Part I Oceanogr. Res. Pap.* 40, 2115–2129. doi: 10.1016/0967-0637(93)90048-8

DelValls, T. A., and Dickson, A. G. (1998). The pH of buffers based on 2-amino-2-hydroxymethyl-1,3-propanediol ("tris") in synthetic sea water. *Deep Sea Res. Part I Oceanogr. Res. Pap.* 45, 1541–1554.

Dickson, A. G., Camões, M. F., Spitzer, P., Fisicaro, P., Stoica, D., Pawlowicz, R., et al. (2016). Metrological challenges for measurements of key climatological observables. Part 3: seawater pH. *Metrologia* 53, R26–R39. doi: 10.1088/0026-1394/53/1/R26

Douglas, N. K., and Byrne, R. H. (2017a). Achieving accurate spectrophotometric pH measurements using unpurified meta-cresol purple. *Mar. Chem.* 190, 66–72. doi: 10.1016/j.marchem.2017.02.004

Douglas, N. K., and Byrne, R. H. (2017b). Spectrophotometric pH measurements from river to sea: calibration of mCP for $0 \leq S \leq 40$ and $278.15 \leq T \leq 308.15$ K. *Mar. Chem.* 197, 64–69. doi: 10.1016/j.marchem.2017.10.001

Easley, R. A., and Byrne, R. H. (2012). Spectrophotometric calibration of pH electrodes in seawater using purified m-cresol purple. *Environ. Sci. Technol.* 46, 5018–5024. doi: 10.1021/es300491s

Feistel, R., Weinreben, S., Wolf, H., Seitz, S., Spitzer, P., Adel, B., et al. (2009). Density and Absolute Salinity of the Baltic Sea 2006–2009. *Ocean Sci.* 6, 3–24. doi: 10.5194/os-6-3-2010

Lai, C., DeGrandpre, M. D., Wasser, B. D., Brandon, T. A., Clucas, D. S., Jaqueth, E. J., et al. (2016). Spectrophotometric measurement of freshwater pH with purified meta-cresol purple and phenol red. *Limnol. Oceanogr. Methods* 14, 864–873. doi: 10.1002/lom3.10137

Lai, C., DeGrandpre, M. D., Wasser, B. D., Brandon, T. A., Clucas, D. S., Jaqueth, E. J., et al. (2017). Corrigendum to: spectrophotometric measurement of freshwater pH with purified meta-cresol purple and phenol red: freshwater pH with purified indicators (Limnology and Oceanography: Methods, (2016), 14, 12, (864-873), 10.1002/lom3.10137). *Limnol. Oceanogr. Methods* 15:903. doi: 10.1002/lom3.10210

Liu, X., Patsavas, M. C., and Byrne, R. H. (2011). Purification and characterization of meta-cresol purple for spectrophotometric seawater pH measurements. *Environ. Sci. Technol.* 45, 4862–4868. doi: 10.1021/es200665d

Martz, T. R., Connery, J. G., and Johnson, K. S. (2010). Testing the Honeywell Durafet for seawater pH applications. *Limnol. Oceanogr. Methods* 8, 172–184. doi: 10.4319/lom.2010.8.172

Mosley, L. M., Husheer, S. L. G., and Hunter, K. A. (2004). Spectrophotometric pH measurement in estuaries using thymol blue and m-cresol purple. *Mar. Chem.* 91, 175–186. doi: 10.1016/j.marchem.2004.06.008

Müller, J. D., Bastkowski, F., Sander, B., Seitz, S., Turner, D. R., Dickson, A. G., et al. (2018b). Metrology for pH measurements in brackish waters–part 1: extending electrochemical pH_T measurements of TRIS buffers to salinities 5–20. *Front. Mar. Sci.* 5:176. doi: 10.3389/fmars.2018.00176

Müller, J. D., Schneider, B., Aßmann, S., and Rehder, G. (2018a). Spectrophotometric pH measurements in the presence of dissolved organic matter and hydrogen sulfide. *Limnol. Oceanogr. Methods* 16, 68–82. doi: 10.1002/lom3.10227

Nemzer, B. V., and Dickson, A. G. (2005). The stability and reproducibility of Tris buffers in synthetic seawater. *Mar. Chem.* 96, 237–242. doi: 10.1016/j.marchem.2005.01.004

R Core Team (2014). *R: A Language and Environment for Statistical Computing*. Available online at: http://www.r-project.org/

Turner, D. R., Achterberg, E. P., Chen, C.-T. A., Clegg, S. L., Hatje, V., Maldonado, M. T., et al. (2016). Toward a quality-controlled and accessible pitzer model for seawater and related systems. *Front. Mar. Sci.* 3:139. doi: 10.3389/fmars.2016.00139

Wright, D. G., Pawlowicz, R., McDougall, T. J., Feistel, R., and Marion, G. M. (2011). Absolute salinity, "density salinity" and the reference-composition salinity scale: present and future use in the seawater standard TEOS-10. *Ocean Sci.* 7, 1–26. doi: 10.5194/os-7-1-2011

Conflict of Interest Statement: The authors declare that the research was conducted in the absence of any commercial or financial relationships that could be construed as a potential conflict of interest.

The handling Editor declared a past collaboration with the authors.

Copyright © 2018 Müller and Rehder. This is an open-access article distributed under the terms of the Creative Commons Attribution License (CC BY). The use, distribution or reproduction in other forums is permitted, provided the original author(s) and the copyright owner(s) are credited and that the original publication in this journal is cited, in accordance with accepted academic practice. No use, distribution or reproduction is permitted which does not comply with these terms.

frontiers in Marine Science

ORIGINAL RESEARCH
published: 18 February 2019
doi: 10.3389/fmars.2019.00051

Middle to Late Holocene Variations in Salinity and Primary Productivity in the Central Baltic Sea: A Multiproxy Study From the Landsort Deep

Falkje van Wirdum[1], Elinor Andrén[1], Denise Wienholz[2], Ulrich Kotthoff[2,3], Matthias Moros[4], Anne-Sophie Fanget[5], Marit-Solveig Seidenkrantz[6,7] and Thomas Andrén[1]*

[1] School of Natural Sciences, Technology and Environmental Studies, Södertörn University, Huddinge, Sweden, [2] Institute for Geology, University of Hamburg, Hamburg, Germany, [3] Center of Natural History, University of Hamburg, Hamburg, Germany, [4] Leibniz Institute for Baltic Sea Research Warnemünde, Rostock, Germany, [5] CEFREM, University of Perpignan, Perpignan, France, [6] Centre for Past Climate Studies, Department of Geoscience, Aarhus University, Aarhus, Denmark, [7] iCLIMATE Aarhus University Interdisciplinary Centre for Climate Change, Aarhus, Denmark

OPEN ACCESS

Edited by:
Marta Marcos,
Universitat de les Illes Balears, Spain

Reviewed by:
Oscar E. Romero,
University of Bremen, Germany
Ole Bennike,
Geological Survey of Denmark and Greenland, Denmark
Ieva Grudzinska,
Helmholtz Association of German Research Centers (HZ), Germany

***Correspondence:**
Falkje van Wirdum
falkje@gmail.com

Specialty section:
This article was submitted to Coastal Ocean Processes, a section of the journal Frontiers in Marine Science

Received: 04 May 2018
Accepted: 30 January 2019
Published: 18 February 2019

Citation:
van Wirdum F, Andrén E, Wienholz D, Kotthoff U, Moros M, Fanget A-S, Seidenkrantz M-S and Andrén T (2019) Middle to Late Holocene Variations in Salinity and Primary Productivity in the Central Baltic Sea: A Multiproxy Study From the Landsort Deep. Front. Mar. Sci. 6:51. doi: 10.3389/fmars.2019.00051

Anthropogenic forcing has led to an increased extent of hypoxic bottom areas in the Baltic Sea during recent decades. The Baltic Sea ecosystem is naturally prone to the development of hypoxic conditions due to its geographical, hydrographical, geological, and climate features. Besides the current spreading of hypoxia, the Baltic Sea has experienced two extensive periods of hypoxic conditions during the Holocene, caused by changing climate conditions during the Holocene Thermal Maximum (HTM; 8–4.8 cal ka BP) and the Medieval Climate Anomaly (MCA; 1–0.7 cal ka BP). We studied the variations in surface and bottom water salinity and primary productivity and their relative importance for the development and termination of hypoxia by using microfossil and geochemical data from a sediment core retrieved from the Landsort Deep during IODP Expedition 347 (Site M0063). Our findings demonstrate that increased salinity was of major importance for the development of hypoxic conditions during the HTM. In contrast, we could not clearly relate the termination of this hypoxic period to salinity changes. The reconstructed high primary productivity associated with the hypoxic period during the MCA is not accompanied by considerable increases in salinity. Our proxies for salinity show a decreasing trend before, during and after the MCA. Therefore, we suggest that this period of hypoxia is primarily driven by increasing temperatures due to the warmer climate. These results highlight the importance of natural climate driven changes in salinity and primary productivity for the development of hypoxia during a warming climate.

Keywords: paleoceanography, hypoxia, geochemistry, diatoms, foraminifera, palynomorphs, IODP Expedition 347

INTRODUCTION

Oxygen concentrations have been declining worldwide in both the open oceans and coastal waters since the mid-20th century (Breitburg et al., 2018). Hypoxia (<2 mg/l dissolved oxygen) has become common in coastal seas, deteriorating ecosystem structure and functioning (Zhang et al., 2010). This spreading of hypoxia during recent decades has been associated with human activities and

global climate warming (Diaz and Rosenberg, 2008). Hypoxia is a severe environmental problem in the Baltic Sea (**Figure 1**), where over 20% of all known coastal hypoxic sites are located (Conley et al., 2011). This marginal sea is considered a key area for studying the factors governing hypoxia (Carstensen et al., 2014).

The Baltic Sea is a semi-enclosed brackish sea connected to the North Sea through the Little and Great Belts and the Öresund (**Figure 1**). With a mean depth of 54 m and an area of 393,000 km^2 (Leppäranta and Myrberg, 2009), its basin is overall relatively small and shallow. The deepest sub-basin is the Landsort Deep (459 m, **Figure 1**). Natural climate forcing regulates the water exchange between the North Sea and the Baltic Sea, which is of high importance for the environmental conditions throughout the basin (Elken and Matthäus, 2008). Inflows from the North Sea affect the salt and oxygen concentrations in the deep waters (Mohrholz et al., 2015). Stronger salinity stratification and increased primary productivity have been identified as two important climatic forcing factors in driving hypoxia before intense human impact (Papadomanolaki et al., 2018), yet their relative importance is not fully understood (Zillén et al., 2008; Schimanke et al., 2012; Jokinen et al., 2018). Nine coastal countries surround the Baltic Sea and over 85 million people inhabit its drainage basin. At present, anthropogenic forcing exerts a wide variety of pressures on the Baltic Sea ecosystem (Helcom, 2017). A major threat to the ecosystem is eutrophication, caused by excessive input of nutrients to the sea (Andersen et al., 2017). This has a positive feedback on the spreading of hypoxic zones (Zillén and Conley, 2010). Both natural and human-induced changes of the Baltic Sea ecosystem play a role in the current spreading of hypoxic zones (Zillén and Conley, 2010; Meier et al., 2017), but their relative importance is difficult to separate.

We aim to establish the natural variability in environmental conditions in the Baltic Proper (**Figure 1**) during the middle and late Holocene (respectively, 8.2 – 4.2 cal ka BP and 4.2 ka BP - present; Walker et al., 2012) using a multiproxy approach. We focus on reconstructing variability in salinity and primary productivity and establishing their roles in driving redox conditions in the Landsort Deep (**Figure 1**). Variations in the assemblage and concentrations of fossil diatoms, silicoflagellates, dinoflagellate cysts (hereafter dinocysts), and *Radiosperma corbiferum* (hereafter *Radiosperma*) reflect changes in surface water salinity. In contrast, benthic foraminiferal concentrations reflect variations in bottom water salinity and oxygenation and can thus pinpoint intrusions of well-oxygenated saline water to the sea floor. Lithological characteristics of sediments allow for interpretations of redox conditions at the sediment-water interface. Diatom concentration and biogenic silica content of the sediments provide information on changes in diatom production. The total carbon content of the sediments represents changes in gross primary production. Relative pollen abundances are applied as indicators of terrestrial ecosystem and climate change.

This study provides information needed for assessing the consequences of ongoing and future changes in salinity and primary productivity for the Baltic Sea ecosystem. Ongoing anthropogenic and natural climate forcing on the Baltic Sea ecosystem are expected to increase primary productivity (Meier et al., 2011b, 2012; Storch von et al., 2015). Whether, the salinity of the Baltic Sea will increase or decrease is uncertain (Meier et al., 2011a, 2017). Assessing the impact of such changes on redox conditions in the water column can be projected to present and future changes in the Baltic Sea ecosystem and used to design action plans to improve its status by adjusting human actions.

REGIONAL SETTING

Present Baltic Sea

The salt balance of the Baltic Sea is governed by evaporation (Leppäranta and Myrberg, 2009); freshwater input from rivers and precipitation (Bergstrom and Carlsson, 1994); and saline inflows from the North Sea (Mohrholz et al., 2015), which maintain the brackish character of the basin. Such inflows are forced either by wind and differences in air pressure (Matthäus, 2006) or by the salinity gradient between the Baltic Sea and Kattegat (**Figure 1**; Mohrholz et al., 2006). In the Baltic Proper (**Figure 1**) surface water salinity is on average 7 and bottom water salinities vary between 11 and 13 (Mohrholz et al., 2015). This vertical salinity gradient results in the presence of a permanent halocline (at c. 60 m water depth), which isolates bottom waters from surface waters. Therefore, ventilation of the deeper waters strongly depends on marine inflows (**Figure 1C**).

Only episodic large inflows of highly saline and oxygenated water can renew the deep waters in the Baltic Proper (Matthäus et al., 2008). These events, known as major Baltic inflows, occur mainly during winter and depend on the prevailing wind-regime (Matthäus, 2006; Mohrholz et al., 2015). Although these inflows bring in oxygen to the deep waters, they also cause increased stability of stratification. This results in stagnation of the bottom waters for several years (Matthäus et al., 2008). Therefore, marine inflows do not necessarily lead to improved oxygen conditions and can actually result in an expansion of hypoxic areas (Conley et al., 2002; Meier et al., 2017; Neumann et al., 2017).

During periods of high primary productivity organic matter sinks into the stratified deeper waters, where it is decomposed. The limited bottom water ventilation does not replenish the bottom waters with sufficient oxygen to compensate for the oxygen consumed during organic matter degradation (Reissmann et al., 2009). Anoxic bottom conditions lead to regeneration and enrichment of phosphorous in the bottom waters (Jilbert et al., 2011), which alters the ratio of phosphorous to nitrogen available for primary producers. The limiting nutrient for phytoplankton production during spring in the Baltic Proper is nitrogen (Granéli et al., 1990; Lignell et al., 2003; Tamminen and Andersen, 2007; Walve and Larsson, 2010). After the spring phytoplankton bloom, surface waters become nitrogen depleted. During summer, the excess phosphate available leads to potentially harmful blooms of nitrogen-fixing bacteria, which fertilize

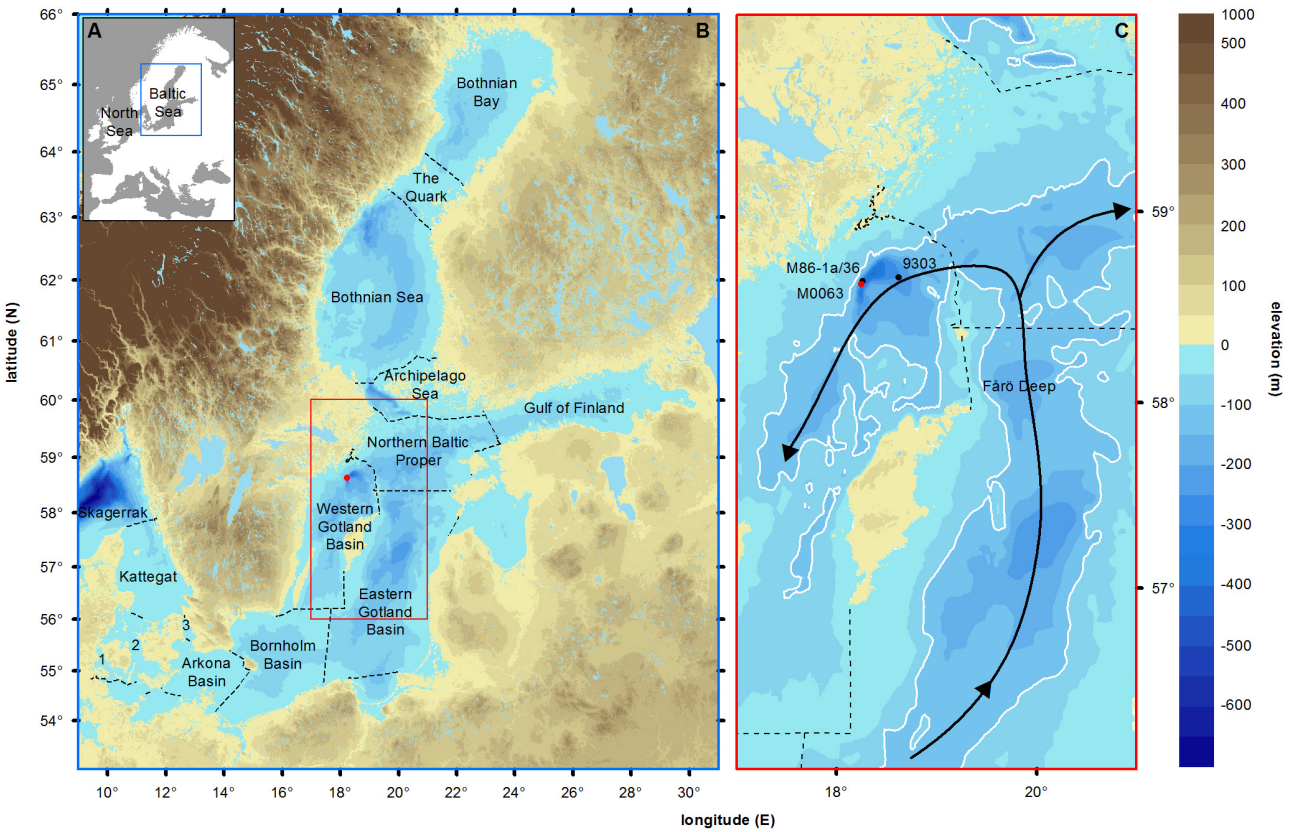


FIGURE 1 | (A) Map of Europe showing the semi-enclosed position of the Baltic Sea. **(B)** Land elevation (brown shades, meters), bathymetry (blue shades, meters) and main sub-basins of the Baltic Sea (dotted lines, according to HELCOM). Skagerrak and Kattegat form the transition zone to the North Sea. The Little Belt (1), Great Belt (2), and Öresund (3) form the connections to the North Sea. The Arkona Basin, Bornholm Basin, Eastern Gotland Basin, Northern Baltic Proper and Western Gotland Basin form the Baltic Proper. The Bothnian Sea, The Quark and the Bothnian Bay form the Gulf of Bothnia. **(C)** Inset of the studied area. The red dot represents the studied Integrated Ocean Drilling Program Expedition 347 site M0063 (Landsort Deep, 58°37.350'N, 18°15.260'E, Andrén et al., 2015). The black dots represent the sites 435-2 (Warden et al., 2017) and 9303 (Bianchi et al., 2000), used for comparison of carbon data and corresponding ages to data of core M0063D. White lines indicate 100 m depth contours. Black arrows show the directions of inflowing deep-water. Geospatial data are provided by HELCOMs Map and Database Service (http://maps.helcom.fi).

the sea with nitrogen (Kononen, 2001; Vahtera et al., 2007; Funkey et al., 2014).

Historical Hypoxia in the Baltic Sea

The Baltic Sea has experienced periods of hypoxia before the most recent expansion, which allows the study of driving mechanisms for hypoxic conditions in the past. During the past 16,000 years, the Baltic Sea basin has undergone several brackish and freshwater phases, due to the interplay of the gradual melting of the Scandinavian Ice Sheet, subsequent glacio-isostatic uplift, and changes in eustatic sea level (Björck, 1995; Andrén et al., 2011; Rosentau et al., 2017). These natural climate-driven processes led to variations in water exchange with the North Sea, which in turn led to variations in salinity, aquatic productivity, and oxygen conditions in the Baltic basin. In addition to the current hypoxic period, two distinct intervals of hypoxia during the last c. 8000 years are recorded in the sediments of the Baltic Sea (Zillén et al., 2008). Past periods of hypoxia can be recognized in sediment cores as laminated deposits (Jonsson et al., 1990). These laminations show a distinct pattern of seasonal sediment layers, undisturbed by bottom dwelling organisms.

Hypoxia Between c. 8–4 ka BP

The first period of hypoxia has been dated to c. 8–4 cal ka BP (Zillén et al., 2008). This period coincided with the Holocene Thermal Maximum (HTM, c. 8–4.8 cal ka BP, Seppä et al., 2015). During the HTM, a stable, warm, and dry climate prevailed in northern Europe (Seppä et al., 2009; Renssen et al., 2012; Borzenkova et al., 2015). Maximum salinities were reached in the Baltic Sea during the HTM (Gustafsson and Westman, 2002; Emeis et al., 2003). Combined effects of isostatic rebound and eustatic sea level rise led to increased sill depths of the Baltic basin (Andrén et al., 2011) promoting the inflow of saline waters from the North Sea. The dry conditions during the HTM reduced freshwater discharge to the basin which led to higher salt concentrations (Gustafsson and Westman, 2002; Snowball et al., 2004).

Though marine inflows supplied the bottom waters with oxygen, a halocline developed at the same time and stratified

the water column (Carstensen et al., 2014). This stratification led to the development of hypoxic conditions at the sea floor. A subsequent increased bioavailability of phosphorus regenerated from sediments augmented primary productivity at the sea surface, and in turn amplified hypoxic conditions (Sohlenius et al., 2001; Jilbert and Slomp, 2013). After the HTM, land uplift exceeded eustatic sea level rise, and shallowing of the sills resulted in a gradual decrease in salinity (Andrén et al., 2011). The termination of this period of hypoxia has been associated with climate cooling and reduced salinity and subsequent reduced water-column stratification (Carstensen et al., 2014).

Hypoxia Between c. 2–0.8 ka BP

The second period of hypoxia is recorded in the Baltic proper between 2 and 0.8 ka BP (Zillén et al., 2008), partly coinciding with the Roman Warm Period and the Medieval Climate Anomaly (MCA). Pollen-inferred temperature reconstructions from Northern Europe (Seppä et al., 2009) show a warm climate anomaly between c. 3 and 1 ka BP. Temperature peaks around c. 2 ka BP, likely reflecting the Roman Warm Period (c. 2.5–1.6 ka BP; Mann, 2007). The MCA (c. 1–0.7 ka BP; Mann et al., 2009) is observed as a pronounced warm period in multiproxy databases, albeit not as warm as present-day (Mann et al., 2008, 2009). Salinity reconstructions for the Baltic Sea hitherto show no agreement during this hypoxic period. Emeis et al. (2003) show a steady increase in salinity that commenced c. 3 ka BP, whereas Gustafsson and Westman (2002) show that a steady decrease started c. 2 ka BP. Whether salinity played a role in the development of past hypoxic periods is unknown (Meier et al., 2017).

A positive correlation between sea surface temperature and both organic carbon and hypoxia in the Eastern Gotland Basin has been found by Kabel et al. (2012). The increase in organic carbon is partly explained by the surface water temperatures being warm enough for massive cyanobacteria blooms (Kabel et al., 2012). In addition, increased biogenic silica suggests that diatom productivity contributed to the increase in organic carbon as well. Increased primary production leads to increased oxygen consumption in bottom waters and thereby contributed to the development of hypoxic conditions. Kabel et al. (2012) link the spread of hypoxia during this period to increased surface water temperatures, influencing deep-water oxygenation through increased primary productivity. A model based on pollen-records from Sweden suggests that land-use intensified between c. 1–0.5 ka BP. This has been related to an expansion of the population during the MCA in the Baltic Sea drainage area (Åkesson et al., 2015). Therefore, it has been suggested that human-induced eutrophication may have played a role in sustaining hypoxic conditions in the Baltic Sea (Zillén et al., 2008; Zillén and Conley, 2010).

Oxic conditions recorded between c.750 and 50 years BP, coincide with a general cooling climate trend, with coldest conditions during the Little Ice Age (LIA; 550–250 yr BP; Mann et al., 2009). The record of Kabel et al. (2012) shows a decline in organic carbon during the LIA, which is associated to decreased sea surface temperatures, unfavorable for cyanobacteria. This oxic period also covers a period of a decline in the human population in the Baltic Sea region, due to the Black Death (600–400 years BP; Lagerås, 2007). It is debated whether this population decline led to decreased anthropogenic forcing on the Baltic Sea ecosystem, allowing for the return of oxic conditions (Zillén et al., 2008). Noticeably, the roles of salinity, primary productivity and eutrophication in the development of hypoxic conditions between c. 2 and 0.8 ka BP and in the return to oxic conditions have not yet been resolved.

Study Site

Landsort Deep, which reaches a maximum water depth of 459 m, is located in the Western Gotland Basin (**Figure 1**), along a fault line that has been deepened by glacial erosion (Flodén and Brännström, 1965). The trench is relatively narrow, with a sill depth of 138 m (Lepland and Stevens, 1998). Today, a permanent halocline exists around 50–80 m water depth, which prevents mixing of surface and bottom waters. This is also illustrated by the vertical salinity gradient: surface water salinity in the Landsort Deep is on average 7, while the salinity in the deepest part of the basin is on average 11 (Viktorsson, 2018). Due to minimal vertical mixing, Landsort Deep depends on major Baltic inflows for deep-water renewal. The geography and geometry (i.e., a cleft shaped with very steep walls) of Landsort Deep make it function as a depocenter where post-glacial mud accumulates. The high sedimentation rate in this basin has resulted in a 30 m thick sediment archive for the past c. 8000 years.

MATERIALS AND METHODS

Material

During the Integrated Ocean Drilling Program (IODP) Expedition 347 in 2013 onboard the R/V *Greatship Manisha*, sediment cores were recovered from five holes at site M0063 in the central part of Landsort Deep (**Figure 1**; Andrén et al., 2015). Seismic profiles have been acquired to select the most suitable drilling target for obtaining the longest undisturbed post-glacial sequence (**Supplementary Figure S1**, Andrén et al., 2015).The results presented in this study are based on analyses on sediment samples from Hole D (58°37.350′N, 18°15.260′E), which was cored using a hydraulic piston corer at a water depth of 437.1 m. Hole D was drilled to a total depth of 86.8 m below seafloor (mbsf). In this study, we focus on sediments from the upper 30 mbsf, which encompass the Mid and Late Holocene.

Adjustment of the Depth Scale

Due to the organic-rich sediments at site M0063, the dissolved methane-gas content in the sediments was considerably high. As gas was released during the recovery process, the cores experienced expansion, resulting in extensive sediment loss at the first hole. Therefore, subsequent holes were cored using an adjusted coring strategy, where only 2 m of sediments was drilled in 3.3 m liners, allowing for expansion of sediments without losing sediments (Andrén et al., 2015). Due to this adjusted coring method, the initial meters below seafloor (mbsf) depth scale had to be adjusted to get a best estimate of initial sediment position at the time of coring, prior to recovery and decompression. Based

on the mean gamma density profiles of cores from Hole D, Obrochta et al. (2017) obtained an expansion function that was used to develop a new depth scale, expressed as "adjusted meters below seafloor" (ambsf), including quantification of uncertainty.

Lithostratigraphy

Based on Hole D, the sediment record of site M0063 was divided into seven lithostratigraphic units, covering the Late Glacial and Holocene (Andrén et al., 2015). Here, sediment samples from Unit 1 (Subunits a–d) and Subunits 2a,b have been investigated (**Figure 2**).

Unit 2 is composed of gray clay. Subunit 2b (33.29–27.59 ambsf) consists of homogeneous gray clay. In Subunit 2a (27.59–25.06 ambsf) the dark gray clay is characterized by weak iron sulfide-stained laminations. Unit 1 consists of organic-rich clays, with homogeneous, weakly laminated and distinct laminated intervals. Prominent colorful laminated organic-rich clays characterize Subunit 1d (25.06–18.16 ambsf). Subunit 1c (18.16–5.23 ambsf) is composed of more homogeneous black organic-rich clays, though some weak laminations are visible. Subunit 1b (5.23–4.13 ambsf) shows laminations in the black clay. Subunit 1a (4.13–0 ambsf) is composed of black organic-rich clay, no sedimentary features are visible, probably because this section experienced a high degree of gas expansion.

Methods

Age-Depth Model

One sample of benthic foraminifera was dated but found to be coated with calcite which resulted in a too young age. Due to the lack of datable macrofossils, a total of 13 bulk sediment samples from core M0063D have been radiocarbon analyzed by Beta Analytic (**Table 1**). An age-depth model was presented by Obrochta et al. (2017) based on 7 of these dates. Using this age-depth model on our proxies gave less reliable results and we therefore decided to scrutinize the 13 dated levels to produce an alternative model. By studying the sediment core images, several dates were rejected as they were from sediments that might have been disturbed during the coring process. One date (Beta418038;1720 $\pm$ 30) from possibly disturbed sediment, however, is backed by a very similar one from core M0063C (Beta 418207; 1760 $\pm$ 30) at similar depth, 5.835 ambsf and 5.22 mcd, respectively, and was therefore included. The presented age-depth model for site M0063 (**Figure 2**) is based on 5 calibrated radiocarbon dates (^{14}C dates published in Obrochta et al., 2017) from the upper $\sim$27 ambsf (**Table 1**). It is worth noting that the age-depth model assumes that the top of the core has an age of $-$63 year BP as the year of coring was 2013. Considering the coring method, however, it is not likely that the very soft and water saturated very topmost sediments were recovered (Andrén et al., 2015).

The age-depth modeling was performed using the age-modeling software CLAM version 2.2 (Blaauw, 2010). Linear interpolation was carried out between dated levels with 10000 iterations using a specially generated calibration dataset based on the IntCal 13 calibration curve (Reimer et al., 2013). A reservoir age (R) and a standard deviation of 900 and 500 ^{14}C years, respectively, were used in this age-depth model. These constraints have been used to make our alternative age-depth model comparable to the one presented by Obrochta et al. (2017) and are based on the regional bulk sediment R variability given by Lougheed et al. (2017). All subsequent ages discussed refer to calibrated ages in years before AD 1950 (cal ka BP). The mean sedimentation rate in the upper c. 27 ambsf is 3.5 mm/yr with the highest rate, 8.7 mm/y, recorded between c. 14.9 and 19.3 ambsf.

Siliceous Microfossils

A total of 54 sediment samples from the upper 30 ambsf (c. 50 cm resolution) were freeze-dried, after which a known weight of sediment was subsampled for the preparation of samples for diatom analysis. Diatom suspensions were prepared according to standard procedures (Battarbee, 1986), and microspheres were added to allow for diatom concentration reconstructions following Battarbee and Kneen (1982). Samples were analyzed for siliceous microfossils using an Olympus BX 51 light microscope with Nomarski differential interference contrast at 1000x magnification and oil immersion. Counting procedures were carried out according to Schrader and Gersonde (1978). When possible, at least 300 diatom valves (excluding *Chaetoceros* spp. resting spores) were counted and identified to species level in each sample. If diatom abundance was too low to reach 300 valves in one slide, a total of at least 1000 microspheres was counted. Diatom valves were identified to species level according to Cleve-Euler (1951; 1952; 1953a, b, 1955); Krammer and Lange-Bertalot (1975; 1988; 1991a, b); Snoeijs (1993); Snoeijs and Vilbaste (1994); Snoeijs and Kasperovičienė (1996); Snoeijs and Potapova (1995); Snoeijs and Balashova (1998); Witkowski et al. (2000).

Chaetoceros spp. resting spores were counted as well, but not identified to species level, except for *Chaetoceros mitra* epivalves. Since the hypovalves of *C. mitra* were not distinguished from other *Chaetoceros* spp. resting spores, only the presence of *C. mitra* is used. The group *Chaetoceros* spp. resting spores will from now on be addressed as resting spores and include *Chaetoceros mitra*. Silicoflagellates and ebridians were counted and identified to species level.

The relative abundance (%) of the diatom taxa was calculated including resting spores in the total diatom sum. For the diatom stratigraphy the diatom species that have a relative abundance of at least 4% in one level were plotted, after confirming that no important indicator species were left out due to this cut. Life-forms (benthic or pelagic) and salinity preferences (**Supplementary Table S1**) of the diatom taxa were obtained from the intercalibration guides of Snoeijs (1993); Snoeijs and Vilbaste (1994); Snoeijs and Potapova (1995); Snoeijs and Kasperovičienė (1996); Snoeijs and Balashova (1998). The diatom species present, were grouped into four different salinity affinity groups, i.e., freshwater (F), brackish-freshwater (BF), and brackish-marine (BM), and a group unknown (U). Group U contains both species with unknown affinity, and diatoms that could not be identified to species level. Relative abundances of the salinity affinity groups were calculated. The ratio of benthic to pelagic diatom taxa (B/P ratio) was calculated using relative abundances. Absolute abundances of siliceous microfossils were calculated according to Battarbee and Kneen (1982) and expressed in numbers of valves per gram dry weight (gdw).

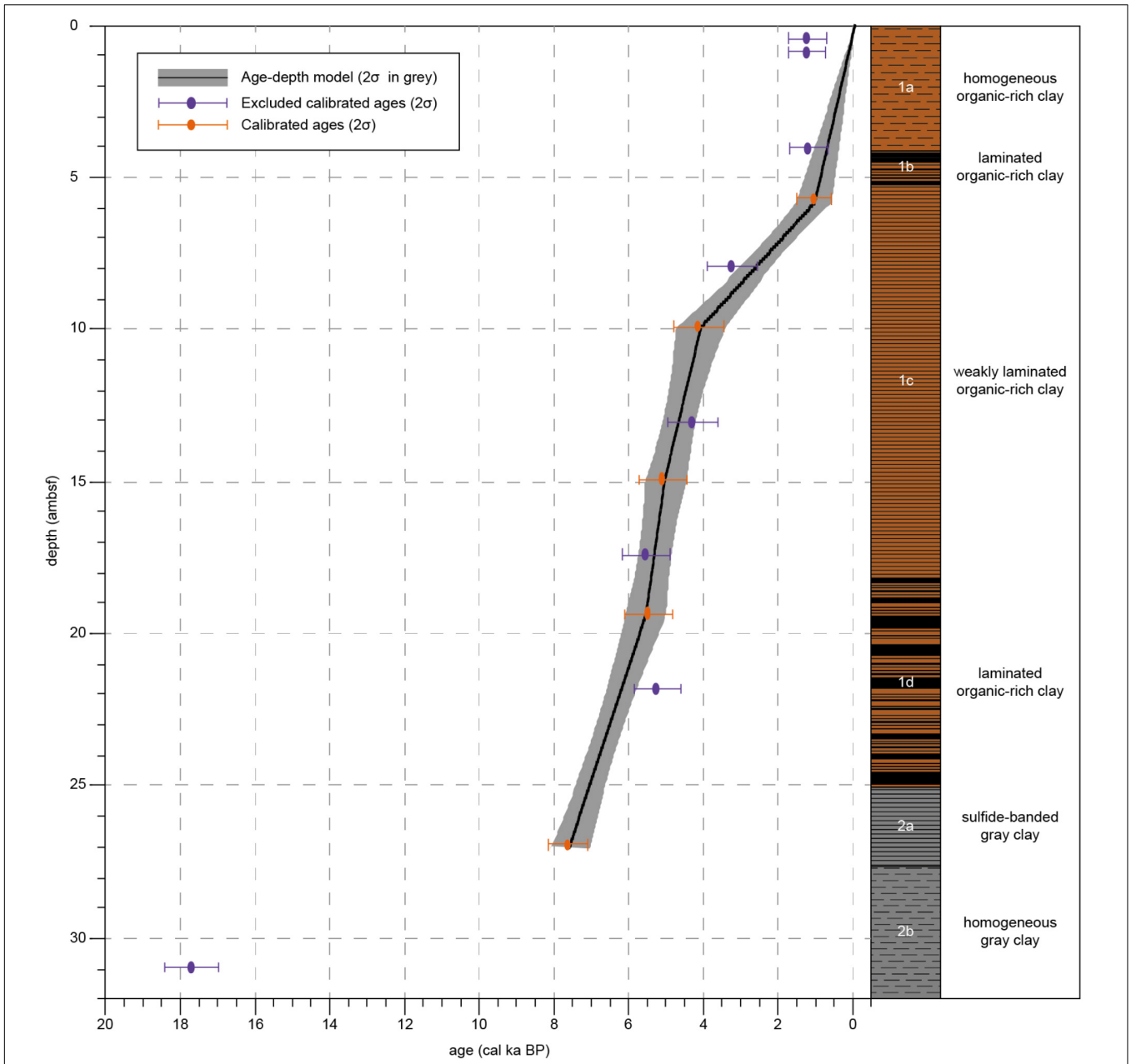


FIGURE 2 | Calibrated sample ages, age-depth model and lithology for Integrated Ocean Drilling Program Expedition 347 Core M0063D. Calibrated ages (2σ) of samples that have been excluded from the age-depth model are indicated in purple. Calibrated ages (2σ) of samples that have been used for the age-depth model are indicated in orange. The black line represents the age-depth model, the gray area represents 2σ. Lithology and sedimentological units are obtained from Andrén et al. (2015).

Terrestrial and Marine Palynomorphs

For the analysis of terrestrial and marine palynomorph assemblages, 35 samples of c. 1 cm thickness were subsampled from 0 to c. 25 ambsf (c. 100 cm resolution). Pilot studies (Andrén et al., 2015) indicated that material between c. 25 and 30 ambsf (Unit 2) was barren of well-preserved palynomorphs. Per sample, 1 to 6 g of sediment was processed using standard palynological techniques for marine sediments (HCl and HF treatment and sieving with 7-μm mesh; Kotthoff et al., 2008). *Lycopodium* marker spores were added to the samples to calculate palynomorph concentrations (Stockmarr, 1971). Approximately 200 pollen grains were identified and counted per sample under 400 to 1000x magnification. Differentiation of triporate grains of *Carpinus* and *Corylus*, was based on general shape (triangular-flattened versus spheroidal), while size could only be used to some degree (compare section "Pollen"). Organic-walled dinocysts and *Radiosperma* were also determined and counted. The concentration of *Radiosperma* is given in specimens

TABLE 1 | Calibrated radiocarbon dates from Integrated Ocean Drilling Program Expedition 347 Site M0063, Hole D bulk sediment samples.

Laboratory ID	Core	Section	Top (cm)	Bottom (cm)	Center Depth (mbsf)	Center Depth (ambsf)	^{14}C Age (year BP)	1σ (year)	Mean calibrated age (year BP)	2σ (year)	Reservoir Age (^{14}C years)	Standard Deviation (^{14}C years)
-	-	-	-	-	-	0	-	-	-63	2	900	500
Beta418053	1	1	142	143	1.425	0.485	1940	30	1216	520	900	500
Beta418036	1	2	95	96	2.455	1.011	1810	30	1221	489	900	500
Beta418037	3	2	25	26	4.65	4.164	1890	30	1184	505	900	500
Beta418038	4	1	60	61	6.105	5.835	1720	30	1026	472	900	500
Beta418039	5	1	80	81	8.305	8.014	3660	30	3214	671	900	500
Beta418040	6	1	73	74	10.235	9.94	4320	30	4122	677	900	500
Beta418041	7	2	85	85.5	13.7125	13.126	4590	30	4271	675	900	500
Beta418042	8	2	35	36	15.355	14.94	5120	30	5074	635	900	500
Beta418043	9	2	79	80	17.795	17.439	5480	30	5532	638	900	500
Beta418044	10	3	16	16.5	20.5125	19.371	5390	30	5457	641	900	500
Beta418045	12	1	112	113	22.625	21.887	5220	30	5224	638	900	500
Beta418046	15	1	17	18	27.175	27.05	7380	30	7617	529	900	500
Beta418047	17	1	22	23	31.225	31.053	15.220	60	17684	719	900	500

Note: The samples in shaded rows have been included for age-depth modeling.

per gram dry weight of sediment (gdw). Since the amount of dinocysts varied greatly over the analyzed material, with several samples being almost barren, we could not aim at counting a fixed sum of dinocysts per samples. Therefore, good preservation of dinocysts under hypoxic conditions may result in artificial peaks in laminated sediments. To avoid this artifact we present dinocysts percentages in relation to the pollen sum [in accordance with Kotthoff et al. (2017)]. The general development of dinocysts concentrations is described in the results section. We have measured the process length of encountered *O. centrocarpum* cysts. The average spine length encountered is 3.96 μm, which is in accordance with findings by Willumsen et al. (2013). However, since the number of specimens measured is low we do not present a process-length plot in the results section.

Benthic Foraminifera

A total of 191 samples of 2-cm core length (20 ml sediment) were prepared for foraminiferal analyses (c. 20 cm resolution). The samples were weighted wet and washed through sieves with mesh sizes of 63, 100, and 1000 μm. The sample fractions were subsequently dried at 40°C and weighed. The 100–1000 μm fraction was used for the foraminiferal assemblage analysis; all foraminifera present in this fraction were counted. Benthic foraminifera were identified to species level to exclude reworked Quaternary and pre-Quaternary specimens from calculations of the abundance of allochthonous benthic foraminifera. These benthic foraminiferal concentrations were calculated as number of specimens per gram wet weight of sediment (gww).

Geochemistry

For geochemistry, a total of 203 samples from the upper 30 ambsf were analyzed for carbon and biogenic silica content (c. 20 cm resolution). Total carbon (TC) was measured on dry samples using a Euro EA from Hekatech; and an EA 1110 CHN from CE-Instruments (GC-based methods). Since sediments from the open Baltic Sea contain almost no carbonate carbon (Andrén et al., 2015; Hardisty et al., 2016; Warden et al., 2017; Häusler et al., 2018), trends in TC were regarded as trends in organic carbon. Biogenic silica (BSi) was determined after basic extraction: 50 mg of dry sample matter was treated with 100 ml 1 M NaOH for 40 min at 80°C in shaking steel backers. The resulting suspensions were then centrifuged, filtrated, and prepared for Si-analysis with ICP-OES. The method was developed and modified as proposed by Müller and Schneider (1993), and quality assurance was tested by including standard material from Conley (1998).

RESULTS

Age-Depth Model

The homogeneous clay in Unit 2b was not suitable for radiocarbon dating (**Table 1**), due to the low content of organic carbon in the sediments (**Figure 5**; Olsson, 1979). Therefore, no reliable ages could be obtained for Subunit 2b and for the lower limit of Subunit 2a. According to the age-depth model (**Figure 2**), sediments in lithological Subunit 1d were deposited between 7.1 and 5.4 cal ka BP, Subunit 1c between 5.4 and 0.9 cal ka BP, Subunit 1b between 0.9 and 0.7 cal ka BP, and Subunit 1a between 0.7 cal ka BP and present-day.

Siliceous Microfossils

The samples analyzed in Subunit 2b are all barren of siliceous microfossils (**Figures 3–5**), this is likely a combined effect of poor diatom preservation and low diatom production, since the carbon content is low as well. In Subunit 2a diatom preservation is considered moderate to good. This subunit is characterized by a shift from a complete freshwater diatom assemblage to an assemblage with more brackish-marine diatom species (**Figure 4**). No silicoflagellates (**Figure 4**) nor ebridians

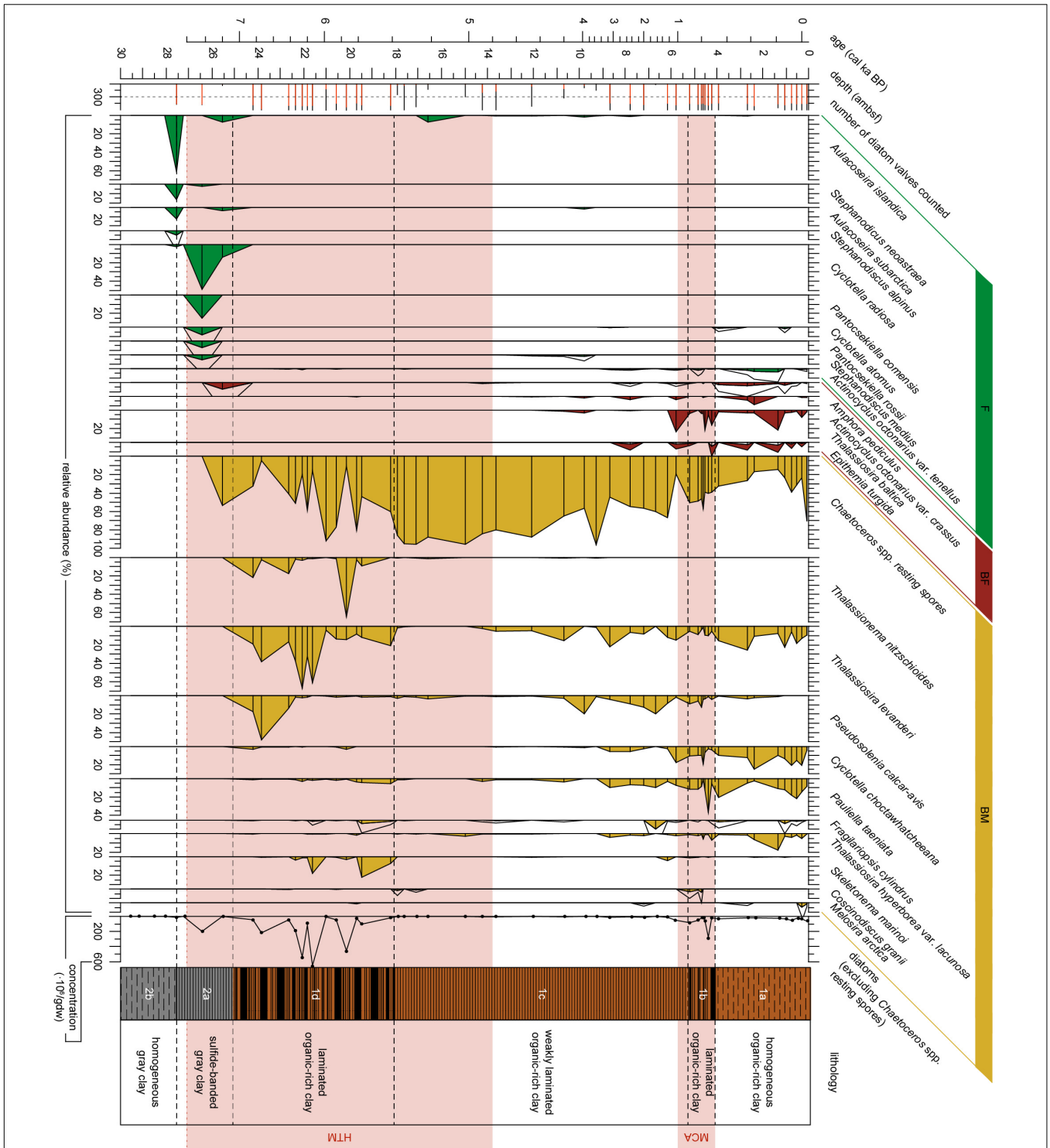


FIGURE 3 | Diatom stratigraphy for the upper ~27 ambsf (adjusted meters below seafloor) of Integrated Ocean Drilling Program Expedition 347 core M0063D. The number of diatoms counted are indicated in red for diatom valves other than *Chaetoceros* spp. resting spores, the black bars indicate the number of *Chaetoceros* spp. resting spores counted, the dotted vertical line represents a count of 300. Relative abundances (%) of diatom taxa with an abundance of 4% or greater in any sample versus depth (ambsf) are plotted as filled areas, for diatom species with a relative abundance <10% a 4x exaggeration is added by the black line. Analyzed levels are indicated by black bars. Diatoms are arranged by their environmental preference with respect to salinity (F, Freshwater affinity; BF, Brackish-Freshwater affinity; BM, Brackish-Marine affinity), and by their first occurrence. Absolute abundance of vegetative diatom valves in millions of valves per gram dry weight (gdw). The warm climate anomalies Holocene Thermal Maximum (HTM, 8–4.8 cal ka BP, Seppä et al., 2009) and Medieval Climate Anomaly [MCA, 1.0 - 0.7 cal ka BP(MCA, 1.0 – 0.7 cal ka BP, Mann et al., 2009)] are represented by the light red areas. Lithology and sedimentological units are obtained from Andrén et al. (2015).

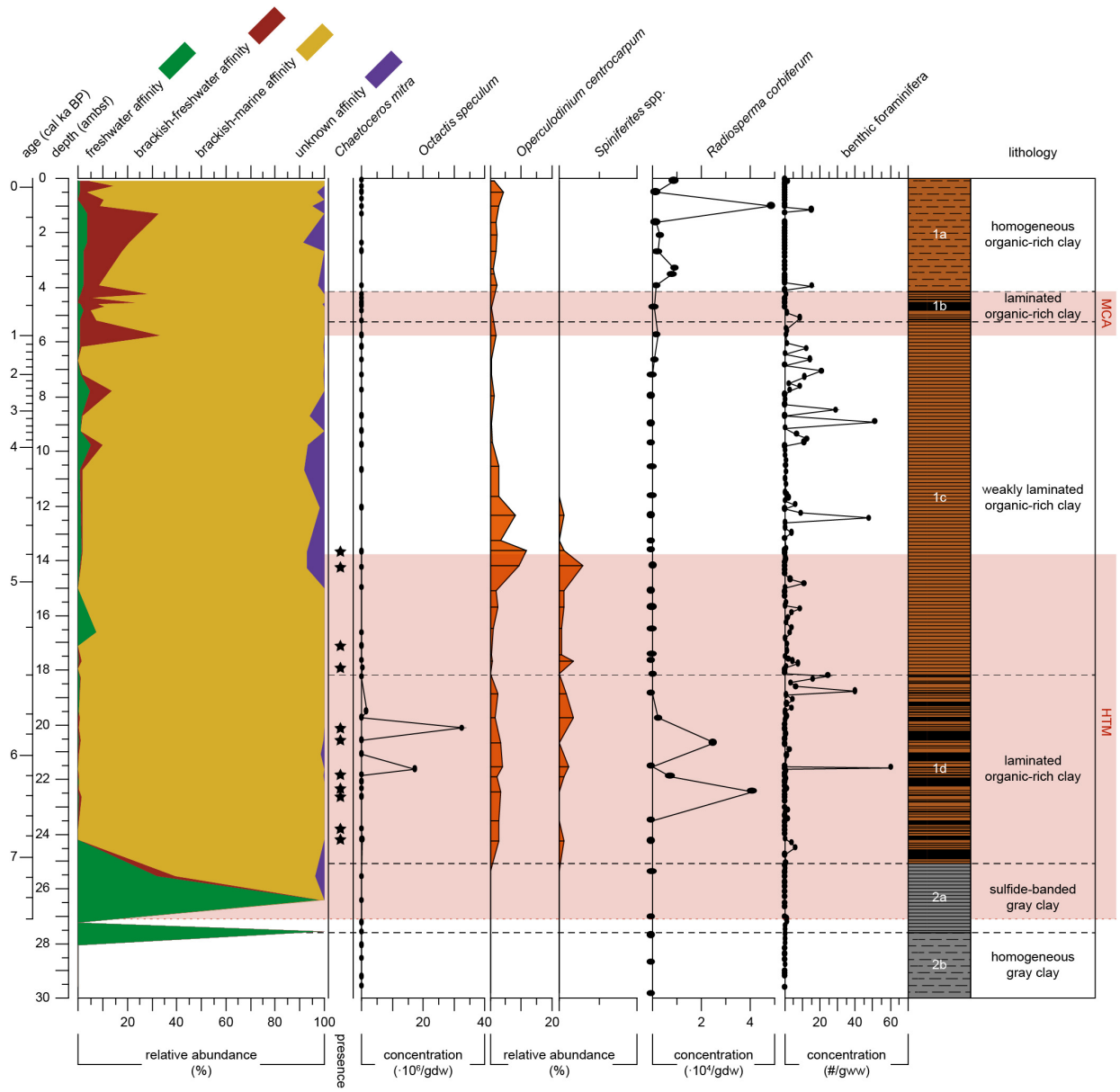


FIGURE 4 | Proxy records for salinity of Integrated Ocean Drilling Program Expedition 347 core M0063D plotted versus depth (adjusted meters below seafloor). Relative abundance of diatom salinity-based affinity groups (i.e., freshwater. brackish-freshwater. brackish-marine and unknown) are plotted as different color-filled areas. Presence of *Chaetoceros mitra* resting spores are indicated by black dots. Absolute abundance of the silicoflagellate *Octatis speculum* [× 10^6 skeletons/gram dry weight (gdw)]. Relative abundances (% related to pollen sum) of dinoflagellate cysts *Operculodinium centrocarpum* and *Spiniferites* spp. Absolute abundances of *Radiosperma corbiferum* (× 10^4/gdw). Absolute abundance of benthic foraminifera in number per gram wet weight (gww). The warm climate anomalies Holocene Thermal Maximum (HTM, 8–4.8 cal ka BP, Seppä et al., 2009) and Medieval Climate Anomaly [MCA, 1.0 – 0.7 cal ka BP(MCA, 1.0 – 0.7 cal ka BP, Mann et al., 2009)] are represented by the light red areas. Lithology and sedimentological units are obtained from Andrén et al. (2015).

are present (**Figure 5**). At 27.6 ambsf the freshwater pelagic taxa *Aulacoseira islandica* and *Stephanodiscus neoastraea* dominate the assemblage (**Figure 3**). A completely barren sample is found at 27.2 ambsf (**Figure 3**). At 26.4 ambsf (7.4 cal ka BP) the diatom concentration increases (**Figure 5**) and the assemblage is still characterized by freshwater species, this time dominated by *Cyclotella radiosa* and *Pantocsekiella comensis* (**Figure 3**). At c. 25.6 ambsf (7.2 cal ka BP), the diatom concentration is too low to reach 300 counts (**Figure 3**). The brackish-freshwater epiphyte *Amphora pediculus* is recorded for the first time in the stratigraphy (**Figure 3**). Brackish-marine *Chaetoceros* spp. resting spores also have their first occurrence here, albeit in low abundances (**Figure 5**).

Subunit 1d (7.1–5.4 cal ka BP) is dominated by brackish-marine diatom taxa (**Figure 4**), with no freshwater species present (**Figure 3**). Diatom preservation is good in this subunit.

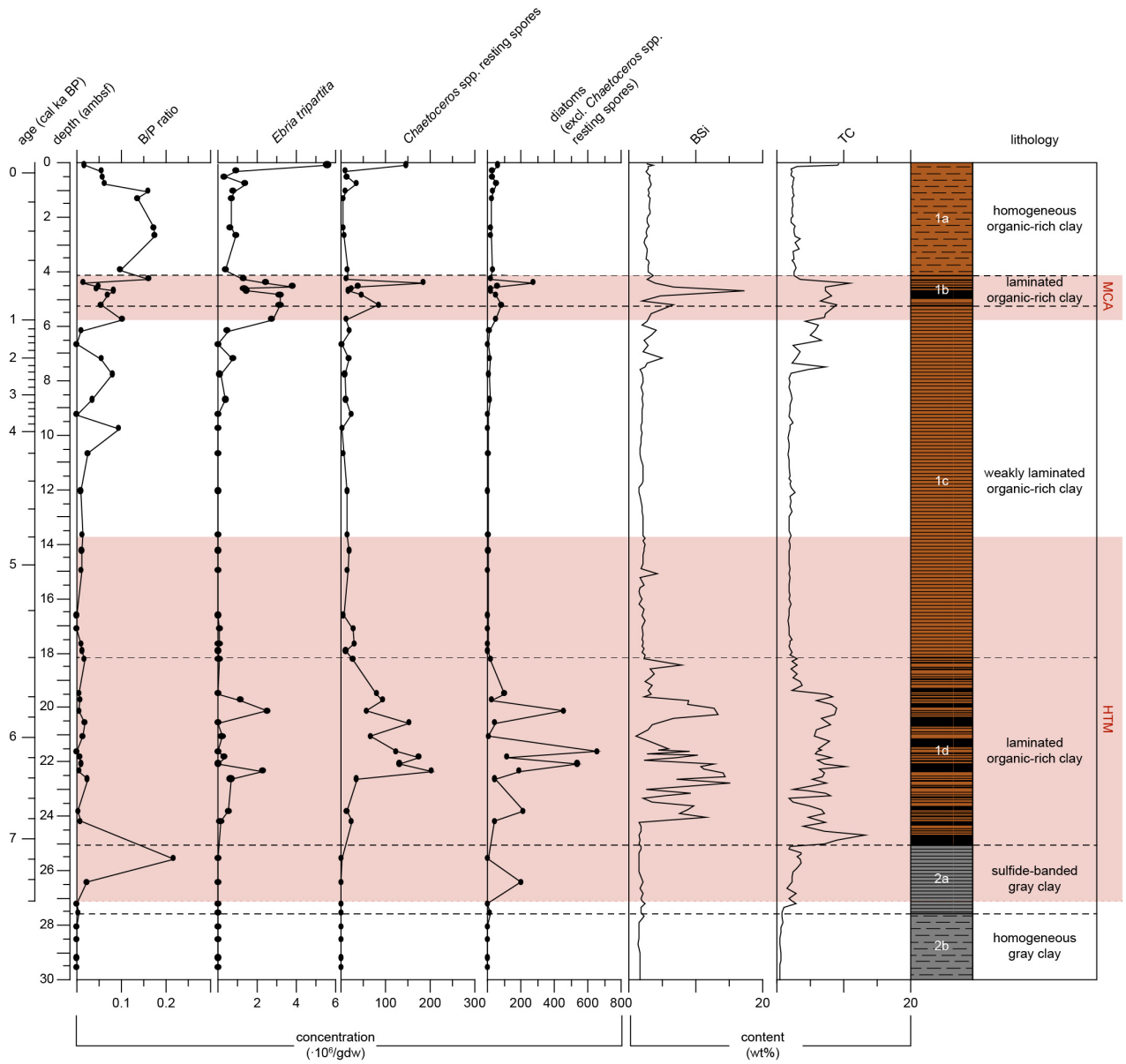


FIGURE 5 | Proxy records for primary productivity of Integrated Ocean Drilling Program Expedition 347 core M0063D plotted versus depth (adjusted meters below seafloor). The ratio of benthic to pelagic diatoms (B/P ratio) has no unit. Absolute abundance of *Ebria tripartita*, *Chaetoceros* spp. resting spores and vegetative diatom valves in millions of valves per gram dry weight (gdw). Biogenic silica (BSi) and total carbon (TC) content of the sediments (wt%). The warm climate anomalies Holocene Thermal Maximum (HTM, 8–4.8 cal ka BP, Seppä et al., 2009) and Medieval Climate Anomaly [MCA, 1.0 – 0.7 cal ka BP(MCA, 1.0 - 0.7 cal ka BP, Mann et al., 2009)] are represented by the light red areas. Lithology and sedimentological units are obtained from Andrén et al. (2015).

The brackish-marine pelagic taxa *Pseudosolenia calcar-avis*, *Thalassiosira levanderi*, *Skeletonema marinoi,* and *Thalassionema nitzschioides* all have their highest relative abundances in this zone (**Figure 3**). The marine pelagic silicoflagellate *Octactis speculum* only occurs here, and *Chaetoceros mitra* resting spores mainly occur in this subunit (**Figure 4**). The ebridian *Ebria tripartita* occurs in relatively high numbers at 22.3 (6.3 cal ka BP) and 20.1 (5.7 cal ka BP) ambsf (**Figure 5**). Concentrations of both resting spores and other diatom valves are highest in this Subunit (**Figure 5**).

Subunit 1c (5.4–0.9 cal ka BP) is still dominated by brackish-marine diatom species (**Figure 4**). However, the concentration of diatom valves other than *Chaetoceros* spp. resting spores between 18 and 9 ambsf (5.4–3.4 cal ka BP) is too low to reach 300 counts. *Chaetoceros* spp. resting spores dominate the diatom assemblage (**Figure 3**), though its concentration is relatively low compared to Subunit 1d (**Figure 5**). In this part of Subunit 1c the more heavily silicified diatom species might be over-represented, due to dissolution of the more finely silicified diatom species. Between 8.7 and 5.2 ambsf (3.1–0.9 cal ka BP), the

number of brackish-freshwater taxa increases (**Figure 4**.), diatom preservation is moderate, with relatively high fragmentation of valves. *Thalassionema nitzschioides* is no longer present, whereas *Thalassiosira levanderi* and *Pseudosolenia calcar-avis* are still abundant, albeit with a lower relative abundance compared to Subunit 1d (**Figure 3**). Increased abundances of *Cyclotella choctawhatcheeana*, *Pauliella taeniata*, *Fragilariopsis cylindrus*, *Thalassiosira baltica* and *Thalassiosira hyperborea* var. *lacunosa* are recorded (**Figure 3**). The B/P ratio, concentrations of *Ebria tripartita*, and both resting spores and other diatom valves show an increasing trend towards the top of this subunit (**Figure 5**).

Subunit 1b (0.9–0.7 cal ka BP) is characterized by a relatively high abundance of the brackish-freshwater taxon *Thalassiosira baltica* and sea-ice associated taxon *Pauliella taeniata* (**Figure 3**). The brackish-marine pelagic taxa *Thalassiosira levanderi*, *Pseudosolenia calcar-avis*, and *Cyclotella choctawhatcheeana* are all relatively abundant in this Subunit (**Figure 3**). The concentration of *Ebria tripartita* is relatively high, as well as the concentrations of both resting spores and other diatoms (**Figure 5**). Preservation of diatom valves is good in this subunit.

Subunit 1a (0.7 cal ka BP-present) is characterized by increasing abundances of fresh- and brackish-freshwater diatom species (**Figure 3**). The relative abundances of the pelagic freshwater taxon *Actinocyclus octonarius* var. *tenellus*, brackish-freshwater taxon *A. octonarius* var. *crassus*, brackish-freshwater epiphytes *Epithemia turgida* and *Amphora pediculus* increase (**Figure 3**). *Thalassiosira baltica* decreases, though increasing again at 1.3 ambsf (0.2 cal ka BP). *Thalassiosira levanderi, Pauliella taeniata*, and *Cyclotella choctawhatcheeana* contribute considerably to the assemblage. *Thalassiosira hyperborea* var. *lacunosa* increases towards the top whereas *Pseudosolenia calcar-avis* decreases (**Figure 3**). The B/P ratio is highest in this subunit, *Ebria tripartita* is present in intermediate numbers, both resting spore and vegetative diatom abundance are relatively low (**Figure 5**). At 1.0 ambsf (0.3 cal ka BP), the relative abundance of freshwater and brackish-freshwater taxa decreases (**Figure 4**). The brackish-marine species *Pseudosolenia calcar-avis* and *Thalassionema nitzschioides* are not present. The benthic to planktic ratio decreases towards the core top, whereas concentrations of both *Ebria tripartita* and resting spores show an increase in the uppermost sample, the diatom concentration increases as well, albeit not as much (**Figure 5**). Preservation of diatom valves is considered moderate to good in this subunit.

Pollen

Samples are almost barren of pollen in Unit 2 but appear, except for *Picea,* all at the same level at 25.4 ambsf (7.1 cal ka BP) in Subunit 2b (**Figure 6**). Pollen preservation was good in nearly all samples, but grains appeared smaller than in recent samples in several cases. In Unit 1, pollen grains are frequent and well preserved. The pollen spectra for Subunit 1d (7.1–5.4 cal ka BP) shows a general dominance of *Pinus* (pine) pollen grains, but lower percentages than the following subunits. *Picea* (spruce) is almost absent in this unit. Pollen of warmth loving broad-leaved trees such as *Alnus* (alder), *Quercus* (oak), *Ulmus* (elm), *Carpinus* and *Corylus* (hornbeam and hazel, combined in Coryloideae), and *Tilia* (linden), show relatively high percentages in Subunit 1d compared to the units above. Poaceae pollen percentages vary around 1.3 % in this unit. The transition to Subunit 1c (5.4 cal ka BP) is marked by an increase in bisaccate pollen (*Pinus* and *Picea*), with *Pinus* percentages >50% and a general decrease in several broad-leaved-tree pollen, particularly *Alnus* and *Corylus*, and, slightly later, *Tilia* (**Figure 6**). *Corylus* and *Ulmus* show generally lower percentages in Subunit 1c compared to the lower subunit, while *Picea* is consistently present, with a slight increasing trend. One sample at 12.3 ambsf (4.5 cal ka BP) reveals particularly high *Pinus* values, paired with decreases in pollen of several broad-leaved taxa. Subunit 1b (0.9–0.7 cal ka BP) is only reflected in one sample of the palynological record (**Figure 6**). It is characterized by particularly low *Pinus* occurrences and a relative increase in *Picea*, *Betula*, and *Alnus*. Subunit 1a (0.7 cal ka BP-present) shows an increase in *Betula* and *Alnus* at 2.7 ambsf (0.4 cal ka BP). A decrease in *Betula* and *Alnus* follows and is coeval with an increase of bisaccate pollen. In the uppermost sample *Betula* increased again and is coeval with a decrease in *Pinus* (**Figure 6**). Pollen of herb taxa and Poaceae (grasses) are generally rare (usually < 2%) in this record, which is in accordance with other Holocene records from the central Western Baltic (e.g., Påhlsson and Bergh Alm, 1985; Thulin et al., 1992). Only in the uppermost samples (<2 ambsf, 0.3 cal ka BP), Poacea pollen show average percentages >2%, coevally with a decrease in pollen of broad-leaved trees.

Marine Palynomorphs

Dinocyst concentration is generally low in the analyzed samples (on average < 2000 cysts/gdw compared to ∼65000 pollen grains/gdw). A record from the Fårö Deep (**Figure 1**) shows significantly higher concentrations (Willumsen et al., 2013). In our record two cyst types of gonyaulacoid dinoflagellates have been found in certain intervals in higher occurrences. These belong to the taxa *Operculodinium centrocarpum* and *Spiniferites* spp. *Lingulodinium* cysts, which are known from the southwestern Baltic Sea (Kotthoff et al., 2017), were not encountered. This is in accordance with results of Ning et al. (2016), who found *Lingulodinium* cysts in only very low concentrations in a coastal sediment core from the Western Gotland Basin. The concentration of *Radiosperma* in certain units is higher compared to the record from Fårö Deep (Willumsen et al., 2013).

Dinocysts and *Radiosperma* are not present in Unit 2. In Subunit 1d (7.1–5.4 cal ka BP), both *Spiniferites* spp. and *O. centrocarpum* are present (**Figure 4**), but the abundances of *Spiniferites* spp. cysts compared to pollen grains are low (<2%). *Radiosperma* concentration shows two peaks, which are coeval with particularly low *Spiniferites* spp. values. In the lower part of Subunit 1c (c. 5.4–4.4 cal ka BP), the relative abundance of dinocysts compared to pollen increases to the highest values within the record (>10% at 13.6 ambsf; 4.8 cal ka BP; **Figure 4**). The absolute abundance of dinocysts is slightly lower compared to Subunit 1d. In the upper part (4.4–0.9 cal ka BP) of Subunit 1c *Spiniferites* spp. is not present, and both relative (**Figure 4**) and absolute abundances of *O. centrocarpum* are low. Remains of *Radiosperma* are almost absent in Subunit 1c, though its

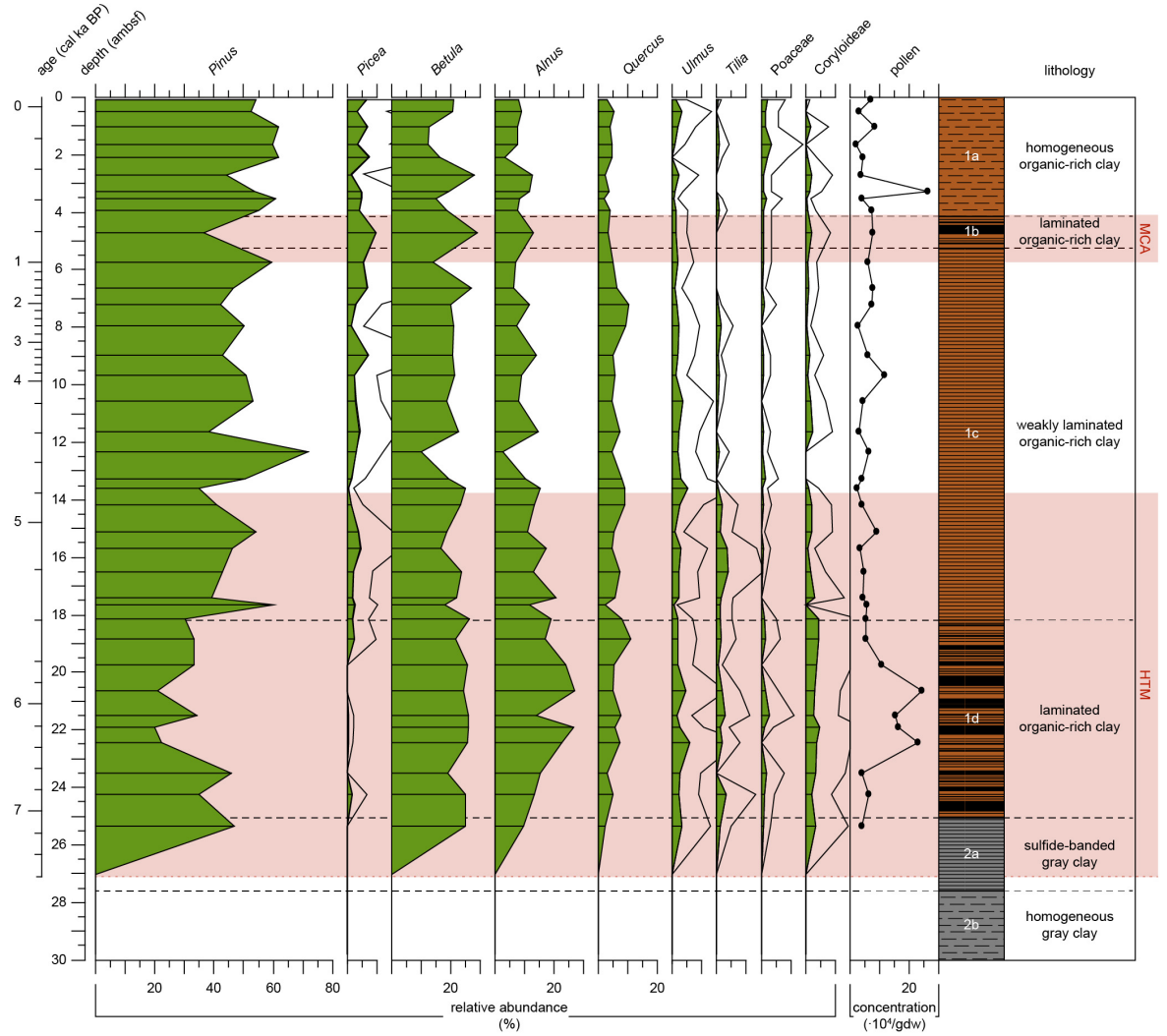


FIGURE 6 | Pollen record of Integrated Ocean Drilling Program Expedition 347 core M0063D plotted versus depth (adjusted meters below seafloor). Relative abundance of selected pollen taxa (%) indicated by green-filled areas, abundances of pollen taxa that have a relative abundance <10% are in addition 4x exaggerated (black line). *Carpinus* and *Corylus* (hornbeam and hazel) are combined in the group Coryloideae. Analyzed levels are indicated by the black lines. Pollen concentrations in x 10^4/gram dry weight. The warm climate anomalies Holocene Thermal Maximum (HTM, 8–4.8 cal ka BP, Seppä et al., 2009) and Medieval Climate Anomaly [MCA, 1.0 – 0.7 cal ka BP(MCA, 1.0 – 0.7 cal ka BP, Mann et al., 2009)] are represented by the light red areas. Lithology and sedimentological units are obtained from Andrén et al. (2015).

concentration increases slightly in the uppermost part (from 2.0 cal ka BP).

Subunit 1b (0.9–0.7 cal ka BP) reveals no particular difference to the subunits underneath. Subunit 1a shows a higher concentration of *Radiosperma* within the samples, with two peaks at 3.3 (0.6 cal ka BP) and 1.0 ambsf (0.1 cal ka BP, **Figure 4**). *Spiniferites* spp. remains absent in Subunits 1b and 1a, while *O. centrocarpum* shows increasing relative values compared to pollen grains within Subunit 1a (0.7 cal ka BP-present).

Benthic Foraminifera

Total foraminiferal abundances are overall low throughout core M0063 (**Figure 4**). Only calcareous benthic foraminifera are present in the samples. Foraminifera are only found in relatively high concentrations in certain intervals, and many samples are found to be barren. The specimens are generally not well-preserved, which indicates some effect of carbonate dissolution. Three different allochthonous species have been identified, the dominant species is *Elphidium clavatum,* with *Elphidium albiumbilication* and *Elphidium incertum* also present in lower numbers in intervals where foraminifera are most abundant. In addition, the samples also contain some reworked glacial Quaternary (e.g., *Cassidulina reniforme*) and pre-Quaternary (mainly upper Cretaceous) species that have not been included in the analyses.

Foraminifera are present in low but very gradually increasing numbers in Subunit 2b (**Figure 4**). In subunit 2a a first, minor peak in concentration occurs at c. 27.2 ambsf. In Unit

1, low foraminiferal abundances are regularly interrupted by foraminiferal abundance peaks. Clusters of such peaks in benthic foraminiferal concentrations are common from the top (7.1 cal ka BP) of Subunit 1d until the end of Subunit 1b (0.7 cal ka BP) with maximum occurrences between 19–18 ambsf (Subunit 1d/1c, 5.5–5.4 cal ka BP), at 12.8 ambsf (Subunit 1c, 4.6 cal ka BP), and 9.8–5 ambsf (Subunit 1c/1b, 3.9–0.9 cal ka BP).

Geochemistry

Biogenic Silica (BSi)

In Unit 2 the biogenic silica content is relatively low, varying between 1.3 and 3.0 wt% (**Figure 5**). In Subunit 1d, at 24.0 ambsf (6.8 cal ka BP) a sudden increase is recorded, i.e., from 1.4 to 11.5 wt%. In Subunit 1d (7.1–5.4 cal ka BP), biogenic silica content is on average relatively high (6.0 wt%), shifting between maxima of 15.0 wt%, and minima as low as 1.0 wt%. In the lower part (5.4–2.3 cal ka BP) of Subunit 1c, values are relatively stable, on average 2.0 wt%. An increasing trend is recorded in the upper part of Subunit 1c, starting at 7.5 ambsf (2.3 cal ka BP). In Subunit 1b, the highest biogenic silica content is recorded (17.3 wt%, 0.8 cal ka BP). In Subunit 1a values are again relatively stable, on average 2.9 wt%.

Total Carbon (TC)

In Subunit 2b, the carbon content is low, on average 0.7 wt% (**Figure 5**). In Subunit 2a, values increase to an average of 2.8 wt%. In Subunit 1d (7.1–5.4 cal ka BP) a sudden increase in carbon from 1.8 to 13.2 wt% is recorded, the latter is the maximum value in this record. In this subunit values are high, on average 6.7 wt%, though they are shifting between minima of 1.9 wt% and maxima of 13.2 wt%. At 19.4 ambsf (0.6 cal ka BP) a sharp decrease is recorded from 7.4 to 2.3 wt%. In the lower part (5.4–2.4 cal ka BP) of Subunit 1c, values are relatively stable, on average 2 wt%. In the upper part of Subunit 1c, values gradually increase, starting at 7.7 ambsf (2.4 cal ka BP). In Subunit 1b, values continue to gradually increase to a peak of 10.9 wt% (0.8 cal ka BP). After this peak, values decrease once again and are relatively stable in Subunit 1a, with an average of 2.6 wt%. In the uppermost sediments, carbon content increases to values as high as 9.3 wt%.

DISCUSSION

Accuracy of the Age-Depth Model

The lithology, age-depth model, and diatom stratigraphy of M0063D confirm that the studied sediments were deposited during the Holocene, more specifically the Ancylus Lake and Littorina Sea stages (e.g., Lepland et al., 1999; Westman and Sohlenius, 1999; Andrén et al., 2000b) as well as more recent years. However, considering uncertainties introduced by both bulk reservoir ages and core expansion due to escaping gas, the accuracy of our age-depth model needs to be addressed. Therefore, we compare our organic matter record to that of two records in the vicinity of site M0063 (**Supplementary Figure S2**). Radiocarbon dating for core 9303 (250 m water depth; **Figure 1**; Bianchi et al., 2000) was carried out using bulk sediments, whereas for core M86-1a/36 (437 m water depth; **Figure 1**; Häusler et al., 2017) benthic foraminifera were used. This comparison reveals an age discrepancy at the termination of the high primary productivity period commonly attributed to the HTM. Our age-depth model suggests that this period ends at 5.4 cal ka BP, whereas organic matter content in the other records remains relatively high until c. 4 cal ka BP. Since it is highly unlikely that organic matter production has been this dissimilar between neighboring sites, we consider our age-depth model to be inaccurate in this part of the record. Four bulk sediment samples between 14.5 and 21.9 ambsf all have ages between c. 5.1 and 5.5 ^{14}C ka BP (**Table 1**), this indicates that bulk sediment ages in this section are less reliable. Pollen data from Lakes Holtjärnen and Klotjärnen in eastern Sweden (Giesecke, 2005) imply consistent occurrences of *Picea* around 5.2 cal ka BP, while records from the south coast of Sweden (compare e.g., Yu et al., 2005) show even later consistent occurrences. In western Estonia, Latvia and Lithuania *Picea* was well established at c. 6 cal ka BP (Giesecke and Bennett, 2004) and the pollen could very well have been transported to site M0063 both with wind and water currents. In our marine pollen record, *Picea* occurrences without interruptions start at ∼5.8 cal ka BP (**Figure 6**). Even if the appearance of *Picea* cannot be used as a precise marker, these findings support our assumption that for the interval of the HTM, our age model implies too old ages. Accordingly, we conclude that the exact timing of the termination of this high primary productivity period in our record is not provided by our age-depth model. Nevertheless, this inaccuracy does not hinder discussing mechanisms responsible for observed changes in our proxy records.

Environmental Conditions in the Landsort Deep During the Middle and Late Holocene

Subunit 2b

The low carbon and biogenic silica content of the sediments and the low diatom abundance (**Figure 5**) indicate low primary productivity during deposition of Subunit 2b (**Table 2**). The homogeneous gray clays of Subunit 2b suggest a well-mixed and oxygenated water column (**Table 2**). However, very low abundances of benthic foraminifera (**Figure 4**) suggest minor marine influence in the bottom waters of Landsort Deep. Due to the absence of siliceous microfossils interpretations regarding surface water salinity cannot be made (**Figures 3**, **4**).

Low organic content and a well-oxygenated water body have been found characteristic for the Ancylus Lake stage (Sohlenius et al., 1996, 2001), a freshwater stage lasting from c. 10.7 to 9.8 ka BP (Andrén et al., 2011). Based on our proxy records, we suggest that the sediments in Subunit 2b cover part of the Ancylus Lake stage. A water body filled with discharged clay particles from the melting ice sheet led to a reduced extent of the photic zone (Winterhalter, 1992). Deglaciated land areas were exposed to wave action, which resulted in erosion of pristine soils into the water body. It is unlikely that the sediments in Subunit 2b are barren of siliceous microfossils only due to low primary production, since several studies show varying abundances of diatoms in the open Baltic Sea during the Ancylus Lake stage

TABLE 2 | Summary of salinity, primary productivity and bottom water oxygenation interpretations for Integrated Ocean Drilling Program Expedition 347 site M0063.

Sedimentological unit	Lithology	Age (cal ka BP)	Bottom water salinity	Surface water salinity	Primary productivity	Marine influx	Bottom water oxygenation
1a	homogeneous organic-rich clay	0.7 cal ka BP - close to present	brackish conditions (similar to present-day)	brackish conditions (similar to present-day)	intermediate	sporadic	hypoxic/oxic
1b	laminated organic-rich clay	0.9–0.7 cal ka BP	gradually decreasing	gradually decreasing	high	sporadic	hypoxic
1c	weakly laminated organic-rich clay	5.4–0.9 cal ka BP	gradually decreasing to brackish conditions	gradually decreasing to brackish conditions	2.4–0.9 cal ka BP: gradually increasing 5.4–2.4 cal ka BP: intermediate	frequent	hypoxic/oxic
1d	laminated organic-rich clay	7.1–5.4 cal ka BP	brackish-marine conditions (highest salinities reached)	brackish-marine conditions (highest salinities reached)	high	intermediate	hypoxic
2a	sulfide-banded gray clay	not dated	brackish conditions	gradually increasing to brackish conditions	gradually increasing	sporadic	oxic
2b	homogeneous gray clay	not dated	freshwater to brackish conditions	freshwater conditions	low	sporadic	oxic

Note: Lithology and sedimentological units are obtained from Andrén et al. (2015).

(Lepland et al., 1999; Westman and Sohlenius, 1999; Andrén et al., 2000a,b). Therefore, we presume diatom valves have been poorly preserved in this subunit due to dissolution.

Subunit 2a

The carbon content shows an increase around 7.6 cal ka BP, and gradually increases throughout Subunit 2a (**Figure 5**), indicating increased gross primary productivity (**Table 2**), hence nutrient availability. The large clear-water lake diatom species present in the oldest sediments of Subunit 2a (**Figure 3**), such as *Aulacoseira islandica* and *Stephanodiscus neoastraea*, demonstrate freshwater conditions in the surface waters. A minor peak in benthic foraminifera concentration at c. 7.6 cal ka BP Subunit 2a (**Figure 4**) signals a first minor influx of saline water to the deeper waters, while surface waters were still fresh (**Table 2**). After this first occurrence, benthic foraminifera become absent until c. 7.1 cal ka BP. The absence of marine palynomorphs (**Figure 4**) show surface water salinities are relatively low until c. 7.1 cal ka BP (**Table 2**). However, the diatom assemblage (**Figure 3**) implies considerable changes in surface water conditions and nutrient conditions from 7.4 to 7.1 cal ka BP.

In our record, the planktic species *Cyclotella radiosa* and *Pantocsekiella comensis* dominate the diatom assemblage at 7.4 cal ka BP (**Figure 3**). A similar assemblage is recorded between c. 8.2–7.9 cal ka BP in a sediment core from the Archipelago Sea (Tuovinen et al., 2008) and has been related to increased surface water salinity. Winder et al. (2009) have found that intensified stratification of the water column selects for the *Cyclotella* genus. The genus *Cyclotella* is also known to be a good competitor for nitrogen (Winder and Hunter, 2008), hence a nitrogen limited primary production may have allowed the fast-growing *C. radiosa* and *P. comensis* to dominate the diatom community. The shift from an oligotrophic freshwater diatom assemblage to an assemblage dominated by *Cyclotella* species coincides with a peak in diatom concentration (**Figure 5**). We suggest that both increased surface water salinity and nutrient availability played a role in this shift in species composition. Although the sample at 7.2 cal ka BP was almost barren of diatoms, the presence and *Chaetoceros* spp. resting spores (**Figure 3**) is indicative of a gradually increasing surface water salinity (**Table 2**).

The very low diatom abundance, increase in diatom diversity, and an assemblage dominated by periphytic fresh- and brackish-freshwater diatom species have been found characteristic for the Initial Littorina Sea stage in the open Baltic Sea (Westman and Sohlenius, 1999; Andrén et al., 2000a,b; Sohlenius et al., 2001). This stage is the time-transgressive transitional phase between the Ancylus Lake stage and Littorina Sea stage (Andrén, 1999; Andrén et al., 2000a,b), often referred to as the Mastogloia Sea in the coastal zone (Miettinen, 2004). Andrén et al. (2000a) identified the Initial Littorina Sea stage in a diatom record from the Eastern Gotland Basin and dated it to last from c. 8.3–7 cal ka BP. During this stage brackish conditions developed gradually throughout the basin, due to the interplay between sea level rise and subsidence of sills in the Danish Straits (Sohlenius et al., 2001). The sediments almost barren of diatoms deposited during this transitional stage have been suggested to be related to the effects of resuspension of sediments due to marine water inflow (Westman and Sohlenius, 1999). The occurrence of benthic species is likely due to increased transport form littoral zones, due to a changing surface circulation caused by the transgression of the Baltic Sea.

Subunit 1d (c. 7.1–5.4 cal ka BP)

The laminated sediments of Subunit 1d (**Figure 2**) imply hypoxic conditions prevailed during the time of deposition (**Table 2**). Carbon content shows a sharp increase at 7.1 cal ka BP, and remains relatively high until c. 5.6 cal ka BP (**Figure 5**). It has been argued that organic carbon is better preserved during anoxic bottom conditions, and therefore higher organic carbon values do not necessarily indicate increased primary productivity (Sohlenius et al., 2001). However, our data also show a sharp increase in biogenic silica and diatom concentration at 6.8 cal ka BP (**Figure 5**), which points to increased diatom productivity (**Table 2**). In addition, the concentrations of both *Ebria tripartita* and *Chaetoceros* spp. resting spores increase at 6.4 cal ka BP. Ebridians are cosmopolitan, marine, heterotrophic flagellates that have a rather widespread distribution (Korhola and Grönlund, 1999). It is suggested that ebridians are indicative for increased nutrient levels (Witkowski and Pempkowiak, 1995). The formation of *Chaetoceros* spp. resting spores are considered as indicators of previous high primary productivity events that resulted in nitrogen depletion in high salinity environments (Oku and Kamatani, 1997). Vegetative cells of the genus *Chaetoceros* are very lightly silicified, and therefore rarely found in the sediment record, in contrast their resting spores are heavily silicified and usually well preserved.

The species composition of the brackish-marine diatom assemblage (**Figure 3**) implies the highest surface water salinities indicated in our samples (**Table 2**). *Pseudosolenia calcar-avis* is a common marine species in tropical and subtropical waters (Viličić et al., 2009), and does not occur in the present Baltic Sea (Snoeijs and Kasperovičienė, 1996). *Thalassionema nitzschioides* is a widely distributed marine neritic species (Hasle and Syvertsen, 1997), favored by both warm and saline water conditions. At present it is not occurring in basins north of the Bornholm Basin (Snoeijs and Vilbaste, 1994). *Chaetoceros mitra* (**Figure 4**) is common in the present North Sea, but not found in the Baltic Sea nowadays, due to its low salinity (Snoeijs and Kasperovičienė, 1996; Hasle and Syvertsen, 1997). Resting spores of this species are only present in the older part of the Littorina Sea stage (Andrén et al., 2000a,b; Witak et al., 2011). *Octactis speculum* is an exclusively marine pelagic silicoflagellate requiring high salinity (Chang et al., 2017). In this core it is only present between c. 6.8 and 5.4 cal ka BP (**Figure 4**). Similar siliceous microfossil assemblages were found in other studies from the Baltic Proper (Thulin et al., 1992; Westman and Sohlenius, 1999; Andrén et al., 2000a), and are suggested to reflect maximum marine conditions during the Littorina Sea stage. Relatively saline surface water conditions are also indicated in our record by the first appearance of marine palynomorphs at c. 7.1 cal ka BP (**Figure 4**). *Radiosperma* is generally more abundant in our record compared to that of the Fårö Deep (Willumsen et al., 2013), where an increase in concentration was recorded at c. 8 cal ka BP. Ning et al. (2017) find an increase in *Radiosperma* at c. 7 cal ka BP in the Blekinge coast. In our record an increase is recorded at c. 6.5 cal ka BP (**Figure 4**). These differences in timing suggest that water depth and/or distance to the coast is an important factor in the distribution of this taxon.

Benthic foraminiferal concentrations fluctuate in this subunit. A minor peak at c. 6.9 cal ka BP (**Figure 4**)indicates the onset of relatively consistently reoccurring events of influx of saline water from the North Sea (**Table 2**). The still relatively low concentrations of benthic foraminifera after this peak are likely a result of a stratified water column with unfavorable oxygen conditions for benthic foraminifera. Periods with low bottom-water oxygenation would cause decrease or disappearance of benthic foraminifera, while periods of higher bottom-water oxygen concentration would allow the re-establishment of a benthic foraminiferal fauna. The high carbon content and lithology of the sediment also points towards low bottom-water oxygenation. It may have resulted in dissolution of foraminiferal tests accentuating the low number of calcareous benthic foraminifera in the deposits. The varying foraminiferal concentrations throughout this period point to fluctuating influence from the North Sea (**Table 2**).

Subunit 1c (c. 5.4–0.9 cal ka BP)

Carbon and biogenic silica content, and diatom concentrations are relatively low between 5.4 and 2.4 cal ka BP (**Figure 5**). The presence of *Chaetoceros* spp. resting spores, albeit in low numbers, suggests a slightly higher primary productivity compared to the Initial Littorina Sea stage. Although interpretations are not accurate due to small diatom concentrations, some implications for changing surface water salinity are provided by the diatom record. *Chaetoceros* spp. resting spores, *Chaetoceros mitra* resting spores, and the proboscis of *Pseudosolenia calcar-avis* are relatively heavily silicified and are thus expected to be preserved in the sediments. Whereas *Chaetoceros* spp. resting spores are abundant in most of this sequence, *Pseudosolenia calcar-avis* is only found in low numbers, and *Chaetoceros mitra* resting spores do not appear after c. 4.7 cal ka BP. This suggests a decrease in surface water salinities (**Table 2**), which is supported by the absence of the heavily silicified silicoflagellate *Octactis speculum* (**Figure 4**). The absence of *Radiosperma* may also point to lower salinity (**Figure 4**). Ning et al. (2017) find a similar decrease slightly earlier (c. 6.5 cal ka BP) at the Blekinge coast of Sweden. The absolute abundance of dinocysts within this interval is lower than in the sediments below, but this may be a preservation signal. The increase in relative abundance of dinocysts (**Figure 4**) indicates that the salinity of the surface waters is still high enough for both *Spiniferites* spp. and *O. centrocarpum* until c. 4.4 cal ka BP. These relatively high values of *Spiniferites* compared to the rest of the record are again in accordance with findings by Ning et al. (2017). After c. 4.4 cal ka BP, less saline surface water conditions probably lead to the decrease in *Operculodinium* and absence of *Spiniferites* cysts.

At c. 4.4 cal ka BP the diatom assemblage has an increased abundance of brackish-freshwater diatom taxa, and benthic diatom taxa are present (**Figure 3**). It is unlikely that benthic diatoms were abundant in the autochthonous living diatom assemblage in Landsort Deep because the photic zone cannot have reached such depths. The increased benthic to pelagic diatom ratio (**Figure 5**) therefore most likely indicates a change in the circulation pattern, bringing in benthic diatoms from the

littoral zone, due to transgression and/or increased discharge from land. Concurrently, the appearance of more brackish-freshwater diatom taxa suggests a decreased salinity in the surface waters. *Pseudosolenia calcar-avis* occurs in this sequence, whereas other taxa which were abundant during the most marine phase have disappeared (e.g., *Thalassionema nitzschioides, Chaetoceros mitra* resting spores, *Octactis speculum*). Among the marine palynomorphs, *Spiniferites* cysts also vanished, and both *Operculodinium* cysts and *Radiosperma* decreased in abundance. This infers a drop in surface water salinities, although surface waters were still more saline than seen in the area today, since *P. calcar-avis* is still present. In contrast, the benthic foraminifera show a more consistent, albeit still fluctuating, presence in the sediments between c. 5.4 and 0.9 cal ka BP. This may, to some extent, be due to reduced post-mortem dissolution, but may also be linked to increased bottom-water ventilation either from increased subsurface inflow of marine waters or increased wind speeds.

Carbon and biogenic silica content show an increasing trend starting at c. 2.4 cal ka BP and coincide with increasing concentrations of *Ebria tripartita*. Diatom concentrations do not demonstrate any pronounced increases in this time-span, which may be a bias of the relatively high fragmentation of the diatom frustules in this sequence. *Cyclotella choctawhatcheeana* becomes one of the major contributors in the diatom assemblage from here on. This is a diatom taxon which has been referred to as a warm-water species (Hällfors, 2004), though also associated with anthropogenic disturbances and increasing eutrophication in the Baltic Sea (Andrén et al., 2000a; Weckström and Juggins, 2006). Based on these findings, we suggest that primary productivity increased during this period (**Table 2**).

Subunit 1b (c. 0.9–0.7 cal ka BP)

The highest carbon content is recorded in this subunit, at c. 0.8 cal ka BP (**Figure 5**) and coincides with a peak in diatom abundance. Biogenic silica also has a distinct peak, though slightly earlier. The discrepancy between these peaks remains unclear from this study. These peaks and the increased concentrations of *Ebria tripartita* and *Chaetoceros* spp. resting spores suggest increased primary productivity during this period (**Table 2**).

The diatom record shows no clear signs of increased surface water salinity compared to Subunit 1c (**Figure 3**). Diatom species *Thalassiosira baltica*, *Pauliella taeniata,* and *Thalassiosira hyperborea* var. *lacunosa* have been associated with sea ice (Snoeijs and Weckström, 2010). The increased abundance of these species and the accompanying decrease of *Pseudosolenia calcar-avis* illustrate decreased surface water salinities and a more extensive ice-coverage during winters. Relatively low abundances of *Operculodinium* cysts and *Radiosperma* (**Figure 4**) do not point to increased surface water salinities either. Benthic foraminiferal concentrations are relatively low, though a peak at c. 0.9 cal ka BP (**Figure 4**) indicates bottom water oxygenation (**Table 2**).

Subunit 1a (c. 0.7 cal ka BP-Present)

Carbon and biogenic silica content show a decreasing trend, though still slightly higher compared to before Subunit 1b (**Figure 5**). Resting spore and *Ebria tripartita* concentrations show a similar decreasing trend, ebridians are present in higher numbers compared to before Subnit 1b. This decreased but slightly higher primary productivity (**Table 2**) might be a combined influence of both a cooler climate and increased anthropogenic influence. The pollen record (**Figure 6**) corroborates an anthropogenic influence; even though cereal taxa have not been distinguished from other Poaceae in the framework of this project, we suggest that the consistent occurrence of Poaceae pollen with values around 2% in the upper two ambsf, combined with decreased percentages of broad-leaved trees such as *Quercus*, may point to increased land use. Such an increase is also consistent with findings by Påhlsson and Bergh Alm (1985).

Between c. 0.9 and 0.2 cal ka BP, brackish-freshwater diatom species increase in abundance (**Figure 4**). The small centric diatom taxa *Cyclotella choctawhatcheeana* and *Thalassiosira levanderi* have a relatively high abundance, and the freshwater taxon *Cyclotella atomus* appears, though in low relative abundances (**Figure 3**). Ice-associated species *Thalassiosira baltica* and *Thalassiosira hyperborea* var. *lacunosa* also increase throughout this sequence. This suggests a further decrease in surface water salinity and more extensive ice-coverage during winter (**Table 2**). The minor relative increase of *Operculodinium* cysts remains unclear in this context but could be tied to changes in water temperature. The increase in *Radiosperma* cannot be interpreted unequivocally since its biology is not completely understood (compare e.g., Brenner, 2001; and Ning et al., 2017). It may be that this taxon took profit from the change to brackish-fresh conditions for a short interval while the conditions during subunit 1c were probably too marine. In the most recent sequence in this record (c. 0.2 cal ka BP-present), *Pseudosolenia calcar-avis* is not present any longer, most likely surface salinity reached present-day levels. Benthic foraminiferal concentrations are low throughout Subunit 1a (**Figure 4**), indicating reduced bottom water ventilation (**Table 2**).

During the last c. 150 years of the sediment record, pelagic diatoms show an increased abundance compared to the older part of Subunit 1a (**Figure 5**). Such a change in B/P ratio has been found in other studies as well (Andrén, 1999; Andrén et al., 2000a,b), and is interpreted as a result of increased nutrient availability. Increased nutrient load leads to turbid waters and a shallower photic zone, unfavorable for benthic species. Increasing abundance of *Ebria tripartita*, *Chaetoceros* resting spores and increased carbon content (**Figure 5**) do support increased nutrient availability, hence increased primary productivity (**Table 2**).

Implications for the Development of Hypoxic Conditions in the Landsort Deep

The laminated Subunits 1d and 1b illustrate that the two main periods of hypoxia found throughout the Baltic Proper (Zillén et al., 2008) are recorded in our sediment core from the Landsort Deep. Here we discuss the relative importance of observed changes in salinity and primary productivity in relation to these

two periods of hypoxia. A summary of our findings is presented in **Table 2**.

Hypoxia During the Holocene Thermal Maximum

Our proxy records show that bottom waters were the first to become more saline, followed by gradually increasing primary productivity and eventually surface waters becoming more saline before the onset of laminated sediments in Subunit 1d (**Table 2**). This succession can be explained by the establishment of a warmer climate commonly attributed to the HTM. In our pollen record (**Figure 6**), Subunit 1d is characterized by a higher pollen concentration compared to subsequent intervals. Broad-leaved tree pollen such as *Alnus*, *Ulmus*, *Tilia*, and *Corylus* all have relatively high relative abundances (compare to Seppä et al., 2015). Seppä et al. (2009) reconstructed warmer and/or more humid conditions until c. 5.8 ka BP compared to the conditions afterwards.

Increasing sill depths in the Baltic basin enhanced the inflow of saline and oxygenated water from the North Sea. Frequent inflows to the Baltic basin led to gradually increasing primary productivity by enhancing the availability of phosphorous. Marine water itself is enriched in phosphorous (Bianchi et al., 2000) but it also reduces binding of phosphorous in sediments (Caraco et al., 1990). Excess availability of phosphorous results in a nitrogen limited primary production. This, and higher surface water temperatures, favor nitrogen fixing cyanobacteria blooms (Bianchi and McCave, 1999; Kabel et al., 2012). The increase in carbon in our record is not accompanied by an increase in biogenic silica. Therefore, primary production might have been dominated by cyanobacteria rather than diatoms. The idea of a phosphorous-enriched water column is supported by the abundance of *Cyclotella* spp. around 7.4 cal ka BP. Reconstructed sea surface temperatures in a parallel core (M0063C) show that the threshold temperature for cyanobacteria was reached in Subunit 2a (Papadomanolaki et al., 2018). In the same parallel core high molybdenum concentrations are recorded in Subunit 2a and 1d (Hardisty et al., 2016), which have been suggested to be indicative for the presence of cyanobacteria blooms (Kunzendorf et al., 2001).

A halocline developed due to the inflow of highly saline North Sea water into the deep waters of the Baltic Sea basin. As soon as the water column became stratified and bottom waters became hypoxic several feedback mechanisms amplified the release of phosphorous from sediments (Emeis et al., 2000; Slomp, 2013). The sudden increase and peak in carbon content at the onset of the laminated sequence was likely due to a sudden release of phosphorus from the sediments during the transition from oxic to anoxic bottom water conditions (Emeis et al., 2000). Phosphorous continued to be released due to the establishment of hypoxic conditions and amplified primary productivity. The decomposition of organic material produced in turn sustains hypoxic conditions in the bottom waters.

The return to only weakly laminated sediments in Subunit 1c are related to the termination of this extensive hypoxic period. Similar sequences have been found in other records of the Baltic Basin (Westman and Sohlenius, 1999; Andrén et al., 2000a; Zillén et al., 2008), dated to c. 4–2 ka BP. Westman and Sohlenius (1999) suggest this homogeneous section was a result of a quick regression at the Öresund, which led to a decrease in inflowing marine waters, which in turn led to decreased nutrient upwelling, hence decreased primary productivity, allowing bottom waters to become oxic again and recolonization of burrowing animals. Furthermore, humid climate conditions (Zillén et al., 2008) likely led to more freshwater input from the drainage area resulting in decreased surface water salinity.

Our pollen record shows a relative increase in the taphonomically more robust bisaccate pollen grains (particularly *Pinus*) which probably points to less warm/humid conditions in summer for the time interval reflected in Subunit 1. We cannot completely rule out, though, that this relative increase of taphonomically more robust bisaccate grains may to some degree be caused by the end of dysoxic conditions in the sediments. Our proxy record suggests gradually decreasing surface water salinities in Subunit 1c, but the very low abundances of siliceous microfossils do not allow for reliable interpretations. The still relatively high abundance of marine palynomorphs demonstrate that surface water salinities did not drop to very low values. This is supported by the findings of Papadomanolaki et al. (2018), who found no considerable changes in surface water salinity. The fluctuating abundance of benthic foraminifera indicate fluctuating salinity and/or oxygen conditions at the sea floor. In contrast, primary productivity decreased considerably. Therefore, it is likely that it was not decreased salinity that was responsible for the termination of this hypoxic period (Subunit 1d) but rather decreased temperatures.

Hypoxia During the Medieval Climate Anomaly

The second period of prominent laminated sediments (Subunit 1b) is commonly attributed to changing climate conditions during the MCA. Benthic foraminiferal concentrations confirm reduced bottom-water oxygenation. The MCA is reflected in the pollen record as increased percentages of warmth-loving taxa like *Alnus* at the cost of taxa like *Pinus* (**Figure 6**). As for the previous hypoxic period, a gradual development in our proxy records is apparent and starts in the top of Subunit 1c.

The increasing B/P ratio and the highly fragmented diatom frustules in the upper sediments of Subunit 1c suggest increased influence from the littoral zone. As discussed before, the increasing abundance of *C. choctwhatcheeana* could point to eutrophication. Therefore, the increasing primary productivity during this period may be related to more nutrient input from land. This increased nutrient input could be due to increased freshwater discharge from the drainage area as a result of humid climate conditions, and/or human-induced eutrophication. Increased freshwater discharge would lead to both freshening of surface waters and a changed water circulation. Zillén and Conley (2010) suggest that anthropogenic forcing through increased nutrient input from the drainage area might have influenced the primary productivity in the Baltic Sea during these times. Recent studies from the Finnish and Swedish coast find no evidence of anthropogenic forcing during the MCA (Jokinen et al., 2018; Ning et al., 2018).

The diatom stratigraphy suggests that hypoxic conditions in Subunit 1b have not been due to pronounced salinity changes, but rather due to increased primary productivity. In addition to the above discussed possible increased nutrient load from land the warmer climate itself has likely played a major role in this increased productivity. The warmer conditions during this period led to increased production of organic carbon resulting in more oxygen consumption during degradation. The increased oxygen consumption in the deeper waters stratified the water column which further promoted hypoxia at the bottom waters and increased primary production in the surface waters due to the release of phosphorus. Cyanobacteria might once again have had a major contribution to the organic carbon pool during this time, due to the phosphorous-enrichment and warmer sea surface temperatures (Kabel et al., 2012). In M0063C high molybdenum concentrations were recorded in this subunit (Hardisty et al., 2016), and thus support the idea of cyanobacteria blooms during this time. The increase in absolute abundance of *Chaetoceros* resting spores could be pointing to a nitrogen depleted sea.

Primary productivity significantly decreased after this period of hypoxia, and the homogeneous sediments of Subunit 1a suggest increased bottom-water ventilation. Benthic foraminiferal concentrations are, however relatively low. The diatom assemblage reflects gradually decreasing surface water salinities getting close to the present-day values. The termination of this hypoxic period is likely due to the cooling of the climate after the MCA.

CONCLUSION

Based on microfossil, carbon, and silica data we reconstructed the variability in surface and bottom water salinity and primary productivity in the Landsort Deep over the past c. 7600 years. We assessed the relative importance of such changes for the establishment and termination of hypoxic conditions at the sea floor and conclude the following:

1. increased bottom water salinity set the stage for the development of hypoxic conditions during the Holocene Thermal Maximum
2. the return to oxic conditions after this first period of hypoxia is mainly due to decreased surface water temperatures
3. no considerable changes in salinity are recorded before, during and, after the hypoxic period attributed to the Medieval Climate Anomaly

Our results emphasize the impact of natural climate forcing on the development of hypoxic conditions in the Baltic Sea. Although human-induced eutrophication is likely the most important forcing factor of the current spreading of hypoxia, future changes in salinity and productivity induced by both naturally and anthropogenically forced climate dynamics, can be of similar importance. Hence, a good understanding of such climatic processes is of importance when designing action plans to improve the status of the Baltic Sea ecosystem.

AUTHOR CONTRIBUTIONS

TA, EA, and FvW contributed to the conception and design of the study. FvW performed the siliceous microfossil analysis. UK and DW performed the palynomorph analysis. A-SF performed the foraminiferal analysis. MM performed the geochemistry analysis. TA provided the age-depth model. FvW harmonized all data, provided figures, and wrote the first draft of the manuscript. TA, UK, DW, M-SS, and MM wrote sections of the manuscript. All authors contributed to manuscript revision, read and approved the submitted version.

FUNDING

This research was supported by the Foundation for Baltic and East European Studies (Grants 1562/3.1.1/2013 and 2207/3.1.1/2014), the Swedish Research Council (Grant 826-2012-5114), the Carlsberg Foundation (IVAR-347 project) and Geocenter Denmark (DAN-IODP-SEIS project), the Independent Research Fund Denmark (Grant 7014-00113B, G-Ice), and the German Research Foundation (DFG, projects Ko3944/6-1 and Ko3944/8–1).

ACKNOWLEDGMENTS

This study used samples from IODP Expedition 347, and we are very grateful to IODP and ESSAC for funding and organizing the expedition. We thank the crew and science party of IODP Exp. 347, as well as the technical staff at MARUM, Bremen, for their support during the expeditions off- and onshore phases. We are also grateful for technical support from the different laboratories involved in the study. Karen Luise Knudsen is thanked for discussion on foraminiferal species taxonomy and ecology. We also thank the reviewers and editor for giving constructive input which has helped to improve the manuscript.

SUPPLEMENTARY MATERIAL

The Supplementary Material for this article can be found online at: https://www.frontiersin.org/articles/10.3389/fmars.2019.00051/full#supplementary-material

REFERENCES

Åkesson, C., Nielsen, A. B., Broström, A., Persson, T., Gaillard, M. J., and Berglund, B. E. (2015). From landscape description to quantification: a new generation of reconstructions provides new perspectives on Holocene regional landscapes of SE Sweden. *Holocene* 25, 178–193. doi: 10.1177/0959683614556552

Andersen, J. H., Carstensen, J., Conley, D. J., Dromph, K., Fleming-Lehtinen, V., Gustafsson, B. G., et al. (2017). Long-term temporal and spatial trends in eutrophication status of the Baltic Sea: eutrophication in the Baltic Sea. *Biol. Rev.* 92, 135–149. doi: 10.1111/brv.12221

Andrén, E. (1999). *Holocene Environmental Changes Recorded by Diatom Stratigraphy in the Southern Baltic Sea*. Stockholm: Stockholm University.

Andrén, E., Andrén, T., and Kunzendorf, H. (2000a). Holocene history of the Baltic Sea as a background for assessing records of human impact in the sediments of the Gotland Basin. *Holocene* 10, 687–702. doi: 10.1191/0959683009 4944

Andrén, E., Andrén, T., and Sohlenius, G. (2000b). The holocene history of the southwestern Baltic Sea as reflected in a sediment core from the Bornholm Basin. *Boreas* 29, 233–250. doi: 10.1111/j.1502-3885.2000.tb00 981.x

Andrén, T., Björck, S., Andrén, E., Conley, D., Zillén, L., and Anjar, J. (2011). "The development of the Baltic Sea Basin during the last 130 ka," in *The Baltic Sea Basin*, eds J. Harff, S. Björck, and P. Hoth (Berlin: Springer), 75–97.

Andrén, T., Jørgensen, B. B., Cotterill, C., Green, S., and the Iodp Expedition 347 Scientists. (2015). *Proc. IODP*. College Station TX: Integrated Ocean Drilling Program.

Battarbee, R. W. (1986). "Diatom analysis," in *Handbook of Holocene Palaeoecology and Palaeohydrology*, ed. B. E. Berglund (Chichester: Wiley), 527–570.

Battarbee, R. W., and Kneen, M. J. (1982). The use of electronically counted microspheres in absolute diatom analysis. *Limnol. Oceanogr.* 27, 184–188. doi: 10.4319/lo.1982.27.1.0184

Bergstrom, S., and Carlsson, B. (1994). River runoff to the Baltic Sea: 1950-1990. *AMBIO* 23, 280–287.

Bianchi, G. G., and McCave, I. N. (1999). Holocene periodicity in North Atlantic climate and deep-ocean flow south of Iceland. *Nature* 397, 515–517. doi: 10. 1038/17362

Bianchi, T. S., Engelhaupt, E., Westman, P., Andrén, T., Rolff, C., and Elmgren, R. (2000). Cyanobacterial blooms in the Baltic Sea: natural or human-induced? *Limnol. Oceanogr.* 45, 716–726. doi: 10.4319/lo.2000.45.3. 0716

Björck, S. (1995). A review of the history of the Baltic Sea, 13.0-8.0 ka BP. *Quat. Int.* 27, 19–40. doi: 10.1016/1040-6182(94)00057-C

Blaauw, M. (2010). Methods and code for 'classical' age-modelling of radiocarbon sequences. *Quat. Geochronol.* 5, 512–518. doi: 10.1016/j.quageo.2010. 01.002

Borzenkova, I., Zorita, E., Borisova, O., Kalniņa, L., Kisielienė, D., Koff, T., et al. (2015). "Climate change during the holocene (Past 12,000 Years)," in *Proceedings of the Second Assessment of Climate Change for the Baltic Sea Basin Regional Climate Studies*, (Cham: Springer), 25–49. doi: 10.1007/978-3-319-16006-1_2

Breitburg, D., Levin, L. A., Oschlies, A., Grégoire, M., Chavez, F. P., Conley, D. J., et al. (2018). Declining oxygen in the global ocean and coastal waters. *Science* 359:eaam7240. doi: 10.1126/science.aam7240

Brenner, W. (2001). Organic-walled microfossils from the central Baltic Sea, indicators of environmental change and base for ecostratigraphic correlation. *Baltica* 14, 40–51.

Caraco, N., Cole, J., and Likens, G. E. (1990). A comparison of phosphorus immobilization in sediments of freshwater and coastal marine systems. *Biogeochemistry* 9, 277–290. doi: 10.1007/BF00000602

Carstensen, J., Conley, D. J., Bonsdorff, E., Gustafsson, B. G., Hietanen, S., Janas, U., et al. (2014). Hypoxia in the Baltic Sea: biogeochemical cycles, benthic fauna, and management. *AMBIO* 43, 26–36. doi: 10.1007/s13280-013-0474-7

Chang, F. H., Sutherland, J., and Bradford-Grieve, J. (2017). Taxonomic revision of dictyochales (Dictyochophyceae) based on morphological, ultrastructural, biochemical and molecular data. *Phycol. Res.* 65, 235–247. doi: 10.1111/pre. 12181

Cleve-Euler, A. (1951). *Die Diatomeen von Schweden und Finnland. T. 1*. Stockholm: Almqvist & Wiksell.

Cleve-Euler, A. (1952). *Die Diatomeen von Schweden und Finnland. T. 5, Schluss*. Stockholm: Almqvist & Wiksell.

Cleve-Euler, A. (1953a). *Die Diatomeen von Schweden und Finnland. T. 2, Arraphideae, Brachyraphideae*. Stockholm: Almqvist & Wiksell.

Cleve-Euler, A. (1953b). *Die Diatomeen von Schweden und Finnland. T. 3, Monoraphideae, Biraphideae 1*. Stockholm: Almqvist & Wiksell.

Cleve-Euler, A. (1955). *Die Diatomeen von Schweden und Finnland. T. 4, Biraphideae 2*. Stockholm: Almqvist & Wiksell.

Conley, D. J. (1998). An interlaboratory comparison for the measurement of biogenic silica in sediments. *Mar. Chem.* 63, 39–48. doi: 10.1016/S0304-4203(98)00049-8

Conley, D. J., Carstensen, J., Aigars, J., Axe, P., Bonsdorff, E., Eremina, T., et al. (2011). Hypoxia is increasing in the coastal zone of the Baltic Sea. *Environ. Sci. Technol.* 45, 6777–6783. doi: 10.1021/es201212r

Conley, D. J., Humborg, C., Rahm, L., Savchuk, O. P., and Wulff, F. (2002). Hypoxia in the Baltic Sea and basin-scale changes in phosphorus biogeochemistry. *Environ. Sci. Technol.* 36, 5315–5320. doi: 10.1021/es025 763w

Diaz, R. J., and Rosenberg, R. (2008). Spreading dead zones and consequences for marine ecosystems. *Science* 321, 926–929. doi: 10.1126/science.115 6401

Elken, J., and Matthäus, W. (2008). "Physical system description," in *Proceedings of the Assessment of Climate Change for the Baltic Sea Basin Regional Climate Studies*, (Berlin: Springer), 379–389.

Emeis, K. C., Struck, U., Blanz, T., Kohly, A., and Voβ, M. (2003). Salinity changes in the central Baltic Sea (NW Europe) over the last 10000 years. *Holocene* 13, 411–421. doi: 10.1191/0959683603hl634rp

Emeis, K. C., Struck, U., Leipe, T., Pollehne, F., Kunzendorf, H., and Christiansen, C. (2000). Changes in the C, N, P burial rates in some Baltic Sea sediments over the last 150 years—relevance to P regeneration rates and the phosphorus cycle. *Mar. Geol.* 167, 43–59. doi: 10.1016/S0025-3227(00) 00015-3

Flodén, T., and Brännström, B. (1965). En thumperprofil genom landsortsdjupet. *Geol. Fören. Stockh. Förh.* 87, 337–346. doi: 10.1080/1103589650944 8917

Funkey, C. P., Conley, D. J., Reuss, N. S., Humborg, C., Jilbert, T., and Slomp, C. P. (2014). Hypoxia sustains cyanobacteria blooms in the Baltic Sea. *Environ. Sci. Technol.* 48, 2598–2602. doi: 10.1021/es404395a

Giesecke, T. (2005). Holocene dynamics of the southern boreal forest in Sweden. *Holocene* 15, 858–872. doi: 10.1191/0959683605hl859ra

Giesecke, T., and Bennett, K. D. (2004). The holocene spread of *Picea abies* (L.) *Karst.* in Fennoscandia and adjacent areas. *J. Biogeogr.* 31, 1523–1548. doi: 10.1111/j.1365-2699.2004.01095.x

Granéli, E., Wallström, K., Larsson, U., Granéli, W., and Elmgren, R. (1990). Nutrient limitation of primary production in the Baltic Sea Area. *AMBIO* 19, 142–151.

Gustafsson, B. G., and Westman, P. (2002). On the causes for salinity variations in the Baltic Sea during the last 8500 years. *Paleoceanography* 17, 12.1–12.14. doi: 10.1029/2000PA000572

Hällfors, G. (2004). "Checklist of Baltic Sea phytoplankton species (including some heterotrophic protistan groups)," in *Proceedings of the Baltic Sea Environmental*, (Helsinki: HELCOM).

Hardisty, D. S., Riedinger, N., Planavsky, N. J., Asael, D., Andrén, T., Jørgensen, B. B., et al. (2016). A holocene history of dynamic water column redox conditions in the Landsort Deep, Baltic Sea. *Am. J. Sci.* 316, 713–745. doi: 10.2475/08.2016.01

Hasle, G. R., and Syvertsen, E. E. (1997). "Chapter 2 - marine diatoms," in *Identifying Marine Phytoplankton*, ed. C. R. Tomas (San Diego, CA: Academic Press), 5–385.

Häusler, K., Dellwig, O., Schnetger, B., Feldens, P., Leipe, T., Moros, M., et al. (2018). Massive Mn carbonate formation in the Landsort Deep (Baltic Sea): hydrographic conditions, temporal succession, and Mn budget calculations. *Mar. Geol.* 395, 260–270. doi: 10.1016/j.margeo.2017.10.010

Häusler, K., Moros, M., Wacker, L., Hammerschmidt, L., Dellwig, O., Leipe, T., et al. (2017). Mid- to late Holocene environmental separation of the northern and central Baltic Sea basins in response to differential land uplift. *Boreas* 46, 111–128. doi: 10.1111/bor.12198

Helcom. (2017). *First Version of the "State of the Baltic Sea" report - June 2017 - to be Updated in 2018*. Available at: http://stateofthebalticsea.helcom.fi

Jilbert, T., and Slomp, C. P. (2013). Iron and manganese shuttles control the formation of authigenic phosphorus minerals in the euxinic basins of the Baltic Sea. *Geochim. Cosmochim. Acta* 107, 155–169. doi: 10.1016/j.gca.2013. 01.005

Jilbert, T., Slomp, C. P., Gustafsson, B. G., and Boer, W. (2011). Beyond the Fe-P-redox connection: preferential regeneration of phosphorus from organic matter as a key control on Baltic Sea nutrient cycles. *Biogeosciences* 8, 1699–1720. doi: 10.5194/bg-8-1699-2011

Jokinen, S. A., Virtasalo, J. J., Jilbert, T., Kaiser, J., Dellwig, O., Arz, H. W., et al. (2018). A 1500-year multiproxy record of coastal hypoxia from

the northern Baltic Sea indicates unprecedented deoxygenation over the 20th century. *Biogeosciences* 15, 3975–4001. doi: 10.5194/bg-2018-25

Jonsson, P., Carman, R., and Wulff, F. (1990). Laminated sediments in the baltic: a tool for evaluating nutrient mass balances. *AMBIO* 19, 152–158.

Kabel, K., Moros, M., Porsche, C., Neumann, T., Adolphi, F., Andersen, T. J., et al. (2012). Impact of climate change on the Baltic Sea ecosystem over the past 1,000 years. *Nat. Clim. Change* 2, 871–874. doi: 10.1038/nclimate1595

Kononen, K. (2001). Eutrophication, harmful algal blooms and species diversity in phytoplankton communities: examples from the Baltic Sea. *AMBIO J. Hum. Environ.* 30, 184–189. doi: 10.1579/0044-7447-30.4.184

Korhola, A., and Grönlund, T. (1999). Observations of *Ebria tripartita* (Schumann) lemmermann in baltic sediments. *J. Paleolimnol.* 21, 1–8. doi: 10.1023/A:1008019504122

Kotthoff, U., Groeneveld, J., Ash, J. L., Fanget, A. S., Krupinski, N. Q., Peyron, O., et al. (2017). Reconstructing Holocene temperature and salinity variations in the western Baltic Sea region: a multi-proxy comparison from the little belt (IODP expedition 347, Site M0059). *Biogeosciences* 14, 5607–5632. doi: 10.5194/bg-14-5607-2017

Kotthoff, U., Pross, J., Müller, U. C., Peyron, O., Schmiedl, G., Schulz, H., et al. (2008). Climate dynamics in the borderlands of the aegean sea during formation of sapropel S1 deduced from a marine pollen record. *Quat. Sci. Rev.* 27, 832–845. doi: 10.1016/j.quascirev.2007.12.001

Krammer, K., and Lange-Bertalot, H. (1975). *Süsswasserflora von Mitteleuropa. Bd 2, Bacillariophyceae, T. 1, Naviculaceae*. Stuttgart: Fischer.

Krammer, K., and Lange-Bertalot, H. (1988). *Süsswasserflora von Mitteleuropa. Bd 2, Bacillariophyceae, T. 2, Bacillariaceae, Epithemiaceae,Surirellaceae*. Stuttgart: Fischer.

Krammer, K., and Lange-Bertalot, H. (1991a). *Süsswasserflora von Mitteleuropa. Bd 2, Bacillariophyceae, T. 3, Centrales, Fragilariaceae, Eunotiaceae*. Stuttgart: Fischer.

Krammer, K., and Lange-Bertalot, H. (1991b). *Süsswasserflora von Mitteleuropa. Bd 2, Bacillariophyceae, T. 4, Achnanthaceae: Kritische Ergänzungen zu Navicula (Lineolatae) und Gomphonema*. Stuttgart: Fischer.

Kunzendorf, H., Voss, M., Brenner, W., Andrén, T., and Vallius, H. (2001). Molybdenum in sediments of the central Baltic Sea as an indicator for algal blooms. *Baltica* 14, 123–130.

Lagerås, P. (2007). *The Ecology of Expansion and Abandonment: Medieval and Post-Medieval Agriculture and Settlement in a Landscape Perspective*. Stockholm: Riksantikvarieämbetet.

Lepland, A., Heinsalu, A., and Stevens, R. L. (1999). The pre-Littorina diatom stratigraphy and sediment sulphidisation record from the west-central Baltic Sea: Implications of the water column salinity variations. *GFF* 121, 57–65. doi: 10.1080/11035899901211057

Lepland, A., and Stevens, R. L. (1998). Manganese authigenesis in the Landsort Deep, Baltic Sea. *Mar. Geol.* 151, 1–25. doi: 10.1016/S0025-3227(98)00046-2

Leppäranta, M., and Myrberg, K. (2009). *Physical Oceanography of the Baltic Sea*. Berlin: Springer-Verlag. doi: 10.1007/978-3-540-79703-6

Lignell, R., Seppälä, J., Kuuppo, P., Tamminen, T., Andersen, T., and Gismervik, I. (2003). Beyond bulk properties: responses of coastal summer plankton communities to nutrient enrichment in the northern Baltic Sea. *Limnol. Oceanogr.* 48, 189–209. doi: 10.4319/lo.2003.48.1.0189

Lougheed, B. C., Obrochta, S. P., Lenz, C., Mellström, A., Metcalfe, B., Muscheler, R., et al. (2017). Bulk sediment 14C dating in an estuarine environment: how accurate can it be: estuarine bulk sediment 14C dating. *Paleoceanography* 32, 123–131. doi: 10.1002/2016PA002960

Mann, M. E. (2007). Climate over the past two millennia. *Annu. Rev. Earth Planet. Sci.* 35, 111–136. doi: 10.1146/annurev.earth.35.031306.140042

Mann, M. E., Zhang, Z., Hughes, M. K., Bradley, R. S., Miller, S. K., Rutherford, S., et al. (2008). Proxy-based reconstructions of hemispheric and global surface temperature variations over the past two millennia. *Proc. Natl. Acad. Sci.* 105, 13252–13257. doi: 10.1073/pnas.0805721105

Mann, M. E., Zhang, Z., Rutherford, S., Bradley, R. S., Hughes, M. K., Shindell, D., et al. (2009). Global signatures and dynamical origins of the little ice age and medieval climate anomaly. *Science* 326, 1256–1260. doi: 10.1126/science.1177303

Matthäus, W. (2006). *The History of Investigation of Salt Water Inflows into the Baltic Sea- from the Early Beginning to Recent Results*. Warnemünde: Baltic Sea Research Institute Warnemünde.

Matthäus, W., Nehring, D., Feistel, R., Nausch, G., Mohrholz, V., and Lass, H. U. (2008). "The inflow of highly saline water into the Baltic Sea," in *State and Evolution of the Baltic Sea, 1952-2005: A Detailed 50-Year Survey of Meteorology and Climate, Physics, Chemistry, Biology, and Marine Environment*, eds R. Feistel, G. Nausch, and N. Wasmund (Hoboken, NJ: John Wiley & Sons, Inc), 265–309. doi: 10.1002/9780470283134.ch10

Meier, H. E. M., Andersson, H. C., Eilola, K., Gustafsson, B. G., Kuznetsov, I., Müller-Karulis, B., et al. (2011a). Hypoxia in future climates: a model ensemble study for the Baltic Sea. *Geophys. Res. Lett.* 38:L24608. doi: 10.1029/2011GL049929

Meier, H. E. M., Eilola, K., and Almroth, E. (2011b). Climate-related changes in marine ecosystems simulated with a 3-dimensional coupled physical-biogeochemical model of the Baltic Sea. *Clim. Res.* 48, 31–55. doi: 10.3354/cr00968

Meier, H. E. M., Höglund, A., Eilola, K., and Almroth-Rosell, E. (2017). Impact of accelerated future global mean sea level rise on hypoxia in the Baltic Sea. *Clim. Dyn.* 49, 163–172. doi: 10.1007/s00382-016-3333-y

Meier, H. E. M., Hordoir, R., Andersson, H. C., Dieterich, C., Eilola, K., Gustafsson, B. G., et al. (2012). Modeling the combined impact of changing climate and changing nutrient loads on the Baltic Sea environment in an ensemble of transient simulations for 1961–2099. *Clim. Dyn.* 39, 2421–2441. doi: 10.1007/s00382-012-1339-7

Miettinen, A. (2004). Holocene sea-level changes and glacio-isostasy in the Gulf of Finland, Baltic Sea. *Quat. Int.* 120, 91–104. doi: 10.1016/j.quaint.2004.01.009

Mohrholz, V., Dutz, J., and Kraus, G. (2006). The impact of exceptionally warm summer inflow events on the environmental conditions in the Bornholm Basin. *J. Mar. Syst.* 60, 285–301. doi: 10.1016/j.jmarsys.2005.10.002

Mohrholz, V., Naumann, M., Nausch, G., Krüger, S., and Gräwe, U. (2015). Fresh oxygen for the Baltic Sea — an exceptional saline inflow after a decade of stagnation. *J. Mar. Syst.* 148, 152–166. doi: 10.1016/j.jmarsys.2015.03.005

Müller, P. J., and Schneider, R. (1993). An automated leaching method for the determination of opal in sediments and particulate matter. *Deep Sea Res. Part Oceanogr. Res. Pap.* 40, 425–444. doi: 10.1016/0967-0637(93)90140-X

Neumann, T., Radtke, H., and Seifert, T. (2017). On the importance of major baltic inflows for oxygenation of the central Baltic Sea. *J. Geophys. Res. Oceans* 122, 1090–1101. doi: 10.1002/2016JC012525

Ning, W., Andersson, P. S., Ghosh, A., Khan, M., and Filipsson, H. L. (2017). Quantitative salinity reconstructions of the Baltic Sea during the mid-Holocene. *Boreas* 46, 100–110. doi: 10.1111/bor.12156

Ning, W., Ghosh, A., Jilbert, T., Slomp, C. P., Khan, M., Nyberg, J., et al. (2016). Evolving coastal character of a Baltic Sea inlet during the Holocene shoreline regression: impact on coastal zone hypoxia. *J. Paleolimnol.* 55, 319–338. doi: 10.1007/s10933-016-9882-6

Ning, W., Nielsen, A. B., Ivarsson, L. N., Jilbert, T., Åkesson, C. M., Slomp, C. P., et al. (2018). Anthropogenic and climatic impacts on a coastal environment in the Baltic Sea over the last 1000 years. *Anthropocene* 21, 66–79. doi: 10.1016/j.ancene.2018.02.003

Obrochta, S. P., Andrén, T., Fazekas, S. Z., Lougheed, B. C., Snowball, I., Yokoyama, Y., et al. (2017). The undatables: quantifying uncertainty in a highly expanded late glacial-holocene sediment sequence recovered from the deepest Baltic Sea basin—IODP Site M0063. *Geochem. Geophys. Geosyst.* 18, 858–871. doi: 10.1002/2016GC006697

Oku, O., and Kamatani, A. (1997). Resting spore formation of the marine planktonic diatom *Chaetoceros anastomosans* induced by high salinity and nitrogen depletion. *Mar. Biol.* 127, 515–520. doi: 10.1007/s002270050040

Olsson, I. (1979). A warning against radiocarbon dating of samples containing little carbon. *Boreas* 8, 203–207. doi: 10.1111/j.1502-3885.1979.tb00801.x

Påhlsson, I., and Bergh Alm, K. (1985). Pollen-analytical studies of the cores 14103-3 and 14102-1 from the Western Baltic. *Striae* 23, 74–82.

Papadomanolaki, N. M., Dijkstra, N., van Helmond, N. A. G. M., Hagens, M., Bauersachs, T., Kotthoff, U., et al. (2018). Controls on the onset and termination

of past hypoxia in the Baltic Sea. *Palaeogeogr. Palaeoclimatol. Palaeoecol.* 490, 347–354. doi: 10.1016/j.palaeo.2017.11.012

Reimer, P. J., Bard, E., Bayliss, A., Beck, J. W., Blackwell, P. G., Ramsey, C. B., et al. (2013). IntCal13 and Marine13 radiocarbon age calibration curves 0–50,000 years cal BP. *Radiocarbon* 55, 1869–1887. doi: 10.1016/j.dib.2018.10.040

Reissmann, J. H., Burchard, H., Feistel, R., Hagen, E., Lass, H. U., Mohrholz, V., et al. (2009). Vertical mixing in the Baltic Sea and consequences for eutrophication – a review. *Prog. Oceanogr.* 82, 47–80. doi: 10.1016/j.pocean.2007.10.004

Renssen, H., Seppä, H., Crosta, X., Goosse, H., and Roche, D. M. (2012). Global characterization of the holocene thermal maximum. *Quat. Sci. Rev.* 48, 7–19. doi: 10.1016/j.quascirev.2012.05.022

Rosentau, A., Bennike, O., Uścinowicz, S., and Miotk-Szpiganowicz, G. (2017). "The Baltic Sea basin," in *Submerged Landscapes of the European Continental Shelf*, eds N. C. Flemming, J. Harff, D. Moura, A. Burgess, and G. N. Bailey (Hoboken, NJ: John Wiley & Sons Ltd).

Schimanke, S., Meier, H. E. M., Kjellström, E., Strandberg, G., and Hordoir, R. (2012). The climate in the Baltic Sea region during the last millennium simulated with a regional climate model. *Clim. Past* 8, 1419–1433. doi: 10.5194/cp-8-1419-2012

Schrader, H. J., and Gersonde, R. (1978). "Diatoms and silicoflagellates," in *Micropaleontological Counting Methods and Techniques: an Exercise on an Eight Metres Section of the Lower Pliocene of Capo Rossello, Sicily Utrecht Micropaleontological Bulletins*, eds W. J. Zachariasse, W. R. Riedel, A. Sanfilippo, R. R. Schmidt, M. J. Brolsma, and H. J. Schrader (Utrecht: Schotanus and Jens).

Seppä, H., Bjune, A. E., Telford, R. J., Birks, H. J. B., and Veski, S. (2009). Last nine-thousand years of temperature variability in Northern Europe. *Clim. Past Discuss.* 5, 1521–1552. doi: 10.5194/cpd-5-1521-2009

Seppä, H., Schurgers, G., Miller, P. A., Bjune, A. E., Giesecke, T., Kühl, N., et al. (2015). Trees tracking a warmer climate: the holocene range shift of hazel (*Corylus avellana*) in northern Europe. *Holocene* 25, 53–63. doi: 10.1177/0959683614556377

Slomp, C. P. (2013). Reconstructing the history of euxinia in a coastal sea. *Geology* 41, 523–524. doi: 10.1130/focus0420131.1

Snoeijs, P. (1993). *Intercalibration and Distribution of Diatom Species in the Baltic Sea*, Vol. 1. Uppsala: Opulus press.

Snoeijs, P., and Balashova, N. (1998). *Intercalibration and Distribution of Diatom Species in the Baltic Sea*, Vol. 5. Uppsala: Opulus press.

Snoeijs, P., and Kasperovičienė, J. (1996). *Intercalibration and Distribution of Diatom Species in the Baltic Sea*, Vol. 4. Uppsala: Opulus press.

Snoeijs, P., and Potapova, M. (1995). *Intercalibration and Distribution of Diatom Species in the Baltic Sea*, Vol. 3. Uppsala: Opulus press.

Snoeijs, P., and Vilbaste, S. (1994). *Intercalibration and Distribution of Diatom Species in the Baltic Sea*, Vol. 2. Uppsala: Opulus press.

Snoeijs, P., and Weckström, K. (2010). "Diatoms and environmental change in large brackish-water ecosystems," in *The Diatoms: Applications for the Environmental and Earth Sciences*, eds J. P. Smol and E. F. Stoermer (Cambridge: Cambridge University Press), 287–308. doi: 10.1017/CBO9780511763175.016

Snowball, I., Korhola, A., Briffa, K. R., and Koç, N. (2004). "Holocene climate dynamics in Fennoscandia and the North Atlantic," in *Past Climate Variability Through Europe and Africa Developments in Paleoenvironmental Research*, eds R. W. Battarbee, F. Gasse, and C. E. Stickley (Dordrecht: Springer), 465–494.

Sohlenius, G., Emeis, K. C., Andrén, E., Andrén, T., and Kohly, A. (2001). Development of anoxia during the Holocene fresh–brackish water transition in the Baltic Sea. *Mar. Geol.* 177, 221–242. doi: 10.1016/S0025-3227(01)00174-8

Sohlenius, G., Sternbeck, J., Andrén, E., and Westman, P. (1996). Holocene history of the Baltic Sea as recorded in a sediment core from the Gotland Deep. *Mar. Geol.* 134, 183–201. doi: 10.1016/0025-3227(96)00047-3

Stockmarr, J. (1971). Tablets with spores used in absolute pollen analysis. *Pollen Spores* 13, 615–621.

Storch von, H., Omstedt, A., Pawlak, J., and Reckermann, M. (2015). "Introduction and Summary," in *Proceedings of the Second Assessment of Climate Change for the Baltic Sea Basin Regional Climate Studies*, (Cham: Springer), 1–22.

Tamminen, T., and Andersen, T. (2007). Seasonal phytoplankton nutrient limitation patterns as revealed by bioassays over Baltic Sea gradients of salinity and eutrophication. *Mar. Ecol. Prog. Ser.* 340, 121–138. doi: 10.3354/meps340121

Thulin, B., Possnert, G., and Vuorela, I. (1992). Stratigraphy and age of two postglacial sediment cores from the Baltic Sea. *Geol. Fören. Stockh. Förh.* 114, 165–180. doi: 10.1080/11035899209453882

Tuovinen, N., Virtasalo, J. J., and Kotilainen, A. T. (2008). Holocene diatom stratigraphy in the Archipelago Sea, northern Baltic Sea. *J. Paleolimnol.* 40, 793–807. doi: 10.1007/s10933-008-9199-1

Vahtera, E., Conley, D. J., Gustafsson, B. G., Kuosa, H., Pitkänen, H., Savchuk, O. P., et al. (2007). Internal ecosystem feedbacks enhance nitrogen-fixing cyanobacteria blooms and complicate management in the Baltic Sea. *AMBIO* 36, 186–194. doi: 10.1579/0044-7447(2007)36[186:IEFENC]2.0.CO;2

Viktorsson, L. (2018). Hydrography and Oxygen in the Deep Basins. HELCOM Balt. Sea Environ. Fact Sheets. Available at: http://www.helcom.fi/baltic-sea-trends/environment-fact-sheets/ [accessed April 25, 2018].

Viličić, D., Djakovac, T., Burić, Z., and Bosak, S. (2009). Composition and annual cycle of phytoplankton assemblages in the northeastern Adriatic Sea. *Bot. Mar.* 52, 291–305. doi: 10.1515/bot.2009.004

Walker, M. J. C., Berkelhammer, M., Björck, S., Cwynar, L. C., Fisher, D. A., Long, A. J., et al. (2012). Formal subdivision of the holocene series/epoch: a discussion paper by a working group of INTIMATE (Integration of ice-core, marine and terrestrial records) and the subcommission on quaternary stratigraphy (International commission on stratigraphy). *J. Quat. Sci.* 27, 649–659. doi: 10.1002/jqs.2565

Walve, J., and Larsson, U. (2010). Seasonal changes in Baltic Sea seston stoichiometry: the influence of diazotrophic cyanobacteria. *Mar. Ecol. Prog. Ser.* 407, 13–25. doi: 10.3354/meps08551

Warden, L., Moros, M., Neumann, T., Shennan, S., Timpson, A., Manning, K., et al. (2017). Climate induced human demographic and cultural change in northern Europe during the mid-Holocene. *Sci. Rep.* 7:15251. doi: 10.1038/s41598-017-14353-5

Weckström, K., and Juggins, S. (2006). Coastal diatom–environment relationships from the Gulf of Finland, Baltic Sea1. *J. Phycol.* 42, 21–35. doi: 10.1111/j.1529-8817.2006.00166.x

Westman, P., and Sohlenius, G. (1999). Diatom stratigraphy in five offshore sediment cores from the northwestern Baltic proper implying large scale circulation changes during the last 8500 years. *J. Paleolimnol.* 22, 53–69. doi: 10.1023/A:1008011511101

Willumsen, P. S., Filipsson, H. L., Reinholdsson, M., and Lenz, C. (2013). Surface salinity and nutrient variations during the littorina stage in the fårö deep, Baltic Sea: surface salinity and nutrient variations, Littorina Stage, Baltic Sea. *Boreas* 42, 210–223. doi: 10.1111/j.1502-3885.2012.00286.x

Winder, M., and Hunter, D. A. (2008). Temporal organization of phytoplankton communities linked to physical forcing. *Oecologia* 156, 179–192. doi: 10.1007/s00442-008-0964-7

Winder, M., Reuter, J. E., and Schladow, S. G. (2009). Lake warming favours small-sized planktonic diatom species. *Proc. R. Soc. B Biol. Sci.* 276, 427–435. doi: 10.1098/rspb.2008.1200

Winterhalter, B. (1992). Late-quaternary stratigraphy of Baltic Sea basins - a review. *Bull. Geol. Soc. Finl.* 64, 189–194. doi: 10.17741/bgsf/64.2.007

Witak, M., Dunder, J., and Leśniewska, M. (2011). Chaetoceros resting spores as indicators of Holocene paleoenvironmental changes in the Gulf of Gdańsk, southern Baltic Sea. *Oceanol. Hydrobiol. Stud.* 40:21. doi: 10.2478/s13545-011-0037-0

Witkowski, A., Lange-Bertalot, H., and Metzeltin, D. (2000). *Diatom Flora of Marine Coasts / Iconographia Diatomologica*, Vol. 7. Ruggell: Gantner.

Witkowski, A., and Pempkowiak, J. (1995). Reconstructing the development of human impact from diatoms and 210Pb sediment dating (The gulf of Gdańsk — Southern Baltic Sea). *Geogr. Pol.* 65, 63–78.

Yu, S. Y., Berglund, B. E., Sandgren, P., and Fritz, S. C. (2005). Holocene palaeoecology along the Blekinge coast, SE Sweden, and implications for climate and sea-level changes. *Holocene* 15, 278–292. doi: 10.1191/0959683605hl792rp

Zhang, J., Gilbert, D., Gooday, A. J., Levin, L., Naqvi, S. W. A., Middelburg, J. J., et al. (2010). Natural and human-induced hypoxia and consequences for coastal areas: synthesis and future development. *Biogeosciences* 7, 1443–1467. doi: 10.5194/bg-7-1443-2010

Zillén, L., and Conley, D. J. (2010). Hypoxia and cyanobacteria blooms - are they really natural features of the late Holocene history of the Baltic Sea? *Biogeosciences* 7, 2567–2580. doi: 10.5194/bg-7-2567-2010

Zillén, L., Conley, D. J., Andrén, T., Andrén, E., and Björck, S. (2008). Past occurrences of hypoxia in the Baltic Sea and the role of climate variability, environmental change and human impact. *Earth Sci. Rev.* 91, 77–92. doi: 10.1016/j.earscirev.2008.10.001

Conflict of Interest Statement: The authors declare that the research was conducted in the absence of any commercial or financial relationships that could be construed as a potential conflict of interest.

Copyright © 2019 van Wirdum, Andrén, Wienholz, Kotthoff, Moros, Fanget, Seidenkrantz and Andrén. This is an open-access article distributed under the terms of the Creative Commons Attribution License (CC BY). The use, distribution or reproduction in other forums is permitted, provided the original author(s) and the copyright owner(s) are credited and that the original publication in this journal is cited, in accordance with accepted academic practice. No use, distribution or reproduction is permitted which does not comply with these terms.

frontiers in Marine Science

ORIGINAL RESEARCH
published: 10 October 2018
doi: 10.3389/fmars.2018.00363

Monitoring of Marine Biofilm Formation Dynamics at Submerged Solid Surfaces With Multitechnique Sensors

Maciej Grzegorczyk[1], *Stanisław Józef Pogorzelski*[1], *Aneta Pospiech*[2] *and Katarzyna Boniewicz-Szmyt*[3]*

[1] *Institute of Experimental Physics, Faculty of Mathematics, Physics and Informatics, University of Gdańsk, Gdańsk, Poland,* [2] *Institute of Geography, Faculty of Geography and Oceanography, University of Gdańsk, Gdańsk, Poland,* [3] *Department of Physics, Gdynia Maritime University, Gdynia, Poland*

OPEN ACCESS

Edited by:
Karol Kulinski,
Institute of Oceanology (PAN), Poland

Reviewed by:
Violetta Drozdowska,
Institute of Oceanology (PAN), Poland
Ian R. Jenkinson,
Chinese Academy of Sciences, China

***Correspondence:**
Katarzyna Boniewicz-Szmyt
kbon@am.gdynia.pl

Specialty section:
This article was submitted to Coastal Ocean Processes, a section of the journal Frontiers in Marine Science

Received: *16 April 2018*
Accepted: *20 September 2018*
Published: *10 October 2018*

Citation:
Grzegorczyk M, Pogorzelski SJ, Pospiech A and Boniewicz-Szmyt K (2018) Monitoring of Marine Biofilm Formation Dynamics at Submerged Solid Surfaces With Multitechnique Sensors. Front. Mar. Sci. 5:363. doi: 10.3389/fmars.2018.00363

Biofouling on artificial and biotic solid substrata was studied in several locations in near-shore waters of the Baltic Sea (Gulf of Gdansk) during a three-year period with contact angle wettability, confocal microscopy and photoacoustic spectroscopy techniques. As a reference, the trophic state of water body was determined from chemical analyses according to the following parameters: pH, dissolved O_2, phosphate, nitrite, nitrate, ammonium concentrations, and further correlated to the determined biofilm characterizing parameters by means of Spearman's rank correlation procedure. Biofilm adhesive surface properties (surface free energy, work of adhesion) were obtained with the contact angle hysteresis (CAH) approach using an automatic captive bubble solid surface wettability sensor assigned for *in-situ*, on-line, and quasi-continuous measurements of permanently submerged samples (Pogorzelski et al., 2013; Pogorzelski and Szczepanska, 2014). From confocal reflection microscopy (COCRM) data, characteristic biofilm structural signatures such as biovolume, substratum coverage fraction, area to volume ratio, spatial heterogeneity, mean thickness, and roughness) were determined at different stages of microbial colony development. Photosynthetic properties [photosynthetic energy storage (ES), photoacoustic amplitude and phase spectra] of biofilm communities exhibited a seasonal variation, as indicated by a novel closed-cell type photoacoustic spectroscopy (PAS) system. Mathematical modeling of a marine biofilm under steady state was undertaken with two adjustable parameters, of biological concern i.e., the specific growth rate and induction time, derived from simultaneous multitechnique signals. A set of the established biofilm structural and physical parameters could be modern water body trophic state indexes.

Keywords: baltic waters, submerged substrata biofilm, multitechnique biofilm parameters, biofilm growth model, trophic state indexes, marine bioassessment indicators

INTRODUCTION

Steps of biofilm formation are illustrated in **Figure 1A** (Rubio, 2002). The characteristic formation time scale is apparently related to the length scale of the organisms forming the biofilm colony on solid submersed surfaces (**Figure 1B**). The biofilm development at solid substrata in aquatic environments is presented as a sequence of phases starting from the formation of a conditioning film via microfouling to complex mature macrofouling organisms community. Various time scales for biofilm-related processes were found (Picioreanu et al., 1998). Periphyton is a complex mixture of algae, cyanobacteria, heterotrophic microbes, and detritus this is attached to submerged surfaces in most aquatic ecosystems (Dang and Lovell, 2016). Microbial substrata colonization leads to production of particular substances named extracellular polymeric substances (EPS) consisting of proteins, glycoproteins, glycolipids, extracellular DNA, polysaccharides etc. EPS is critical in the formation of microcolony aggregates acting as a binding hydrated and heterogeneous matrix or "glue" which holds microbes together, and bind them to the submersed substratum (Flemming, 2009). Periphyton serves as an indicator of water quality because:

- it has naturally high number of species;
- it has a fast response to changes;
- it is easy to sample;
- it is known for tolerance/sensitivity to change.

There are several factors affecting the marine biofilm adhesion, apart from the surface free energy of substrata (Zhao et al., 2005), like surface electricity, surface architecture, temperature, fluid shear stress or contact time (Thomas and Muirhead, 2009).

A short generation time, sessile nature and fast responsiveness to environmental conditions make biofilms being water chemistry bioindicators particularly suitable as a monitoring tool in Baltic Sea eutrophication studies. There are several methods used in biofilm formation studies, for a review see (Azeredo et al., 2017). The contact angle (CA) captive bubble technique (Pogorzelski et al., 2013, 2014) adapted here allows the outermost biofilm surface wettability evolution to be monitored quasi-continuously and *in-situ* at subsequent stages of the biofilm formation starting from the molecular adsorption phase (second-minute time scale) to the final mature stage of the marine biofilm cycle. Geometric, structural and biological, commonly evaluated biofilm characteristics like: biovolume, coverage fraction, area to volume ratio, spatial heterogeneity, number of species, mean thickness, roughness, fractal dimension in 2D etc. were on-line determined from confocal reflection microscopy (COCRM) data (Inaba et al., 2013), processed with graphical programs (COMSTAT, ImageJ, CMEIAS, PHLIP etc.). Biofilm is also a photosynthetic system containing a mixture of pigments (Schagerl and Donabaum, 2003).The photosynthetic properties (photosynthetic energy storage ES, photoacoustic amplitude, and phase spectra) of biofilm communities should reveal a seasonal variation, as studied here, by a novel closed-cell type photoacoustic spectroscopy (PAS) system (Szurkowski et al., 2001). The main aim of the work is to demonstrate a close correlation between the biofilm structural state derived from multitechnique physical sensors and the standard water body trophic state indicators on the basis of comprehensive measurements performed in near-shore shallow waters of the Baltic Sea (Gulf of Gdansk). The analyses established a several biological compounds composing the biofilm (bacteria, micro-algae and ConA-stained EPS), which demonstrated differentiated growth rate values evaluated with multi-sensor signals. The biofilm growth kinetics curve was approximated with Gompertz functions (Zwietering et al., 1990), where the specific growth rates μ_i and induction times λ_i where introduced from the simultaneous multi-technique data. Moreover, knowledge of three-dimensional structure of the biofilm and the distribution of species concerned is crucial in managing and preventing uncontrolled colonization of great practical value for undersea engineering constructions.

It should be pointed out that so many methods and several parameters were measured since the biofilm structure, composition, state of evolution, photosynthetic system features respond to environmental stresses in a very complex way. In addition, not all the selected quantities turned out to be sensitive enough in trophic state monitoring.

MATERIALS AND METHODS

Materials-Biofilm Sample Collection

Several artificial solid substrata (glass, metallic, polymeric) and biotic (wood, macrophytes) of varying surface energy placed in a transparent plastic loaded box were deployed at a depth of 0.5 m in near-shore waters of the southern Baltic Sea, for a certain time (**Figure 2A**).

The solid substrata had a form of rectangular plates (dimensions: $77 \times 26 \times 1.5$ mm) or disks (diameter $= 1.8$ mm, thickness $= 0.1$ mm) were mounted in a plastic holders oriented perpendicularly (**Figure 2B**). The artificial model substrata were cleaned by immersion in a methanol/chloroform mixture (1:2 v/v) and toluene; subsequently the samplers were dried before deployment (**Figure 2C**). Biofilm accumulation time was ranging from 1 to 24 days; probes were studied every month from May to November, 2016. Biofilm samples (5–10 from the particular location) together with the adjacent water were collected in a plastic bottle, not allowed to dry out, and further processed under laboratory conditions within an hour after collection. The submerged macrophyte (*Potamogeton lucens*) was also used as the model natural substrates. However, as a natural material, a large diversity in the surface morphology of the macrophyte leaf surface was reflected in a large variability of the particular parameter values measured. Biofilm wet weight (BWW) was chosen as a direct biofilm collection efficiency indicator of the studied samples (Simões et al., 2007), determined by weighting (microbalance; $\Delta m = \pm 10^{-4}$ g) a biofilm material scratched with a scalpel from the known film-covered area A (a few cm^2).

METHODS

Evaluations of Water Body Trophic State

For contact angle wettability studies, seawater samples were collected in near-shore coastal locations [at Gdansk, Sopot,

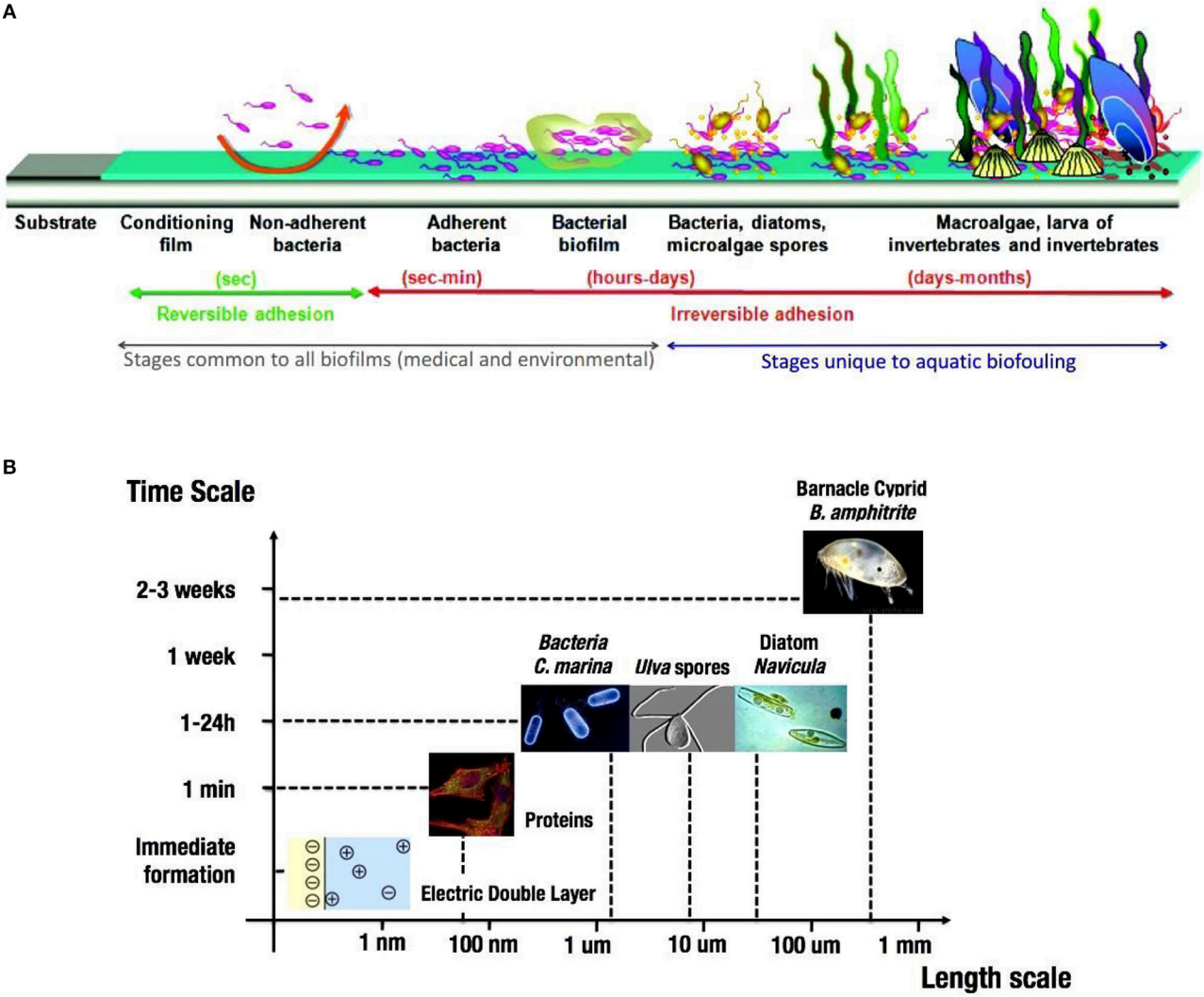


FIGURE 1 | (A) Stages of biofilm formation (modified after Rubio, 2002). **(B)** Characteristic time of biofilm formation vs. length scale of organism's colony (data taken from Dang and Lovell, 2016).

Gdynia (southern Baltic Sea)] had pH 8.2–8.6 ± 0.1 and surface tension γ_{LV} = 69.2–73.3 ± 0.1 mJ m^{-2} at 20°C, were used as the model water phase. The surface tension γ_{LV} was measured *in situ* with a Bubble Pressure Tensiometer BP2100 (PocketDyne, Krűss, Germany). A trophic status of the water body was determined according to the following parameters: pH, dissolved O_2, phosphate (PO_4^{3-}), nitrite (NO_2^-), nitrate (NO_3^-), ammonium (NH_4^+), and Secchi depth. The seawater chemical parameters were also taken from SatBałtyk System data base (available at http://satbaltyk.iopan.gda.pl). Average values of the trophic state indexes (TSI) were calculated according to Carlson (1977). Relationships between the physicochemical variables and the biofouled solid substrata wettability, geometric – morphological, and photoacoustic spectra parameters were analyzed by Spearman's rank correlation routine.

Contact Angle Captive Bubble Apparatus

The solid surface wettability, in particular the surface free energy, is commonly derived from static contact angle measurements by means of several theoretical approaches (Gindl et al., 2001).

In contrast, CA hysteresis (CAH= $\Theta_A - \Theta_R$) formalism developed by Chibowski (2003) allows the apparent surface free energy of the solid γ_{SV} to be determined, and is based on the three measurable quantities: the dynamic contact angles (advancing- Θ_A and receding- Θ_R), and the surface tension of the probe liquid γ_{LV}. The CA captive bubble experimental set-up together with the operational procedure was described in detail elsewhere (Pogorzelski et al., 2013, 2014). The gas bubble at the end of the micropipette touching the studied surface is compressed to determine Θ_R. In the next step, the bubble is drawn up and Θ_A was measured by means of ImageJ program applied to images taken by a side-situated camera (**Figures 3A,B**).

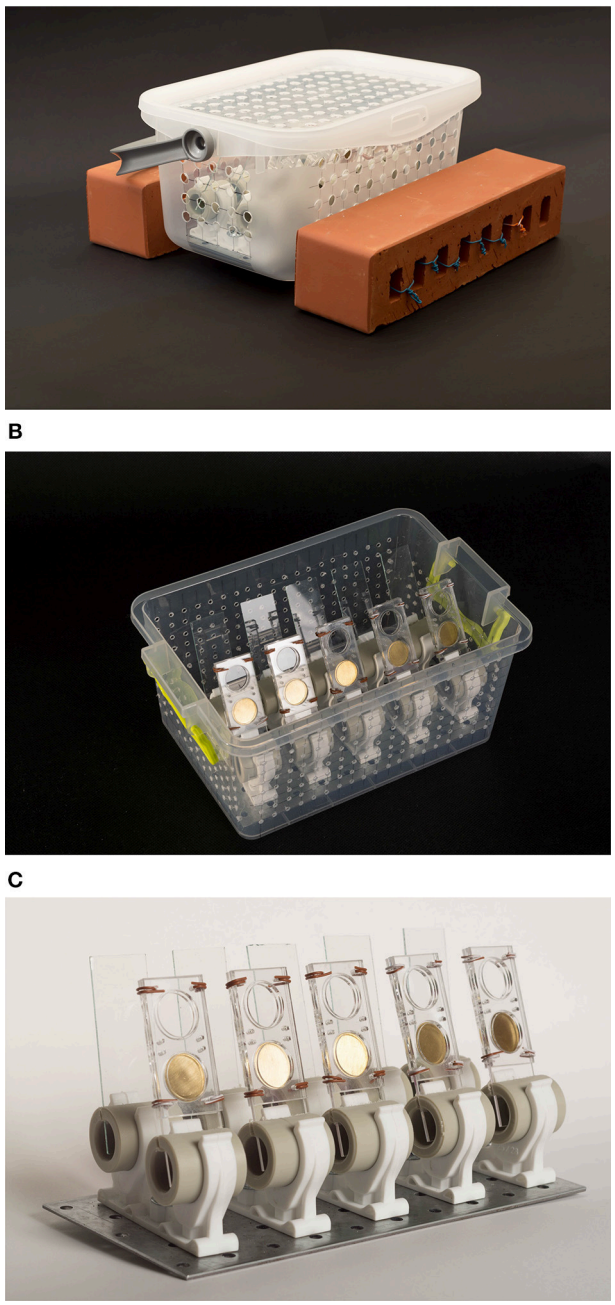


FIGURE 2 | Biofilm sampling devices: **(A)** loaded sampling substrata carrier ready to deployment; **(B)** perpendicularly-oriented rectangular plates or disks placed in a plastic box; **(C)** sampling substrata plastic holders.

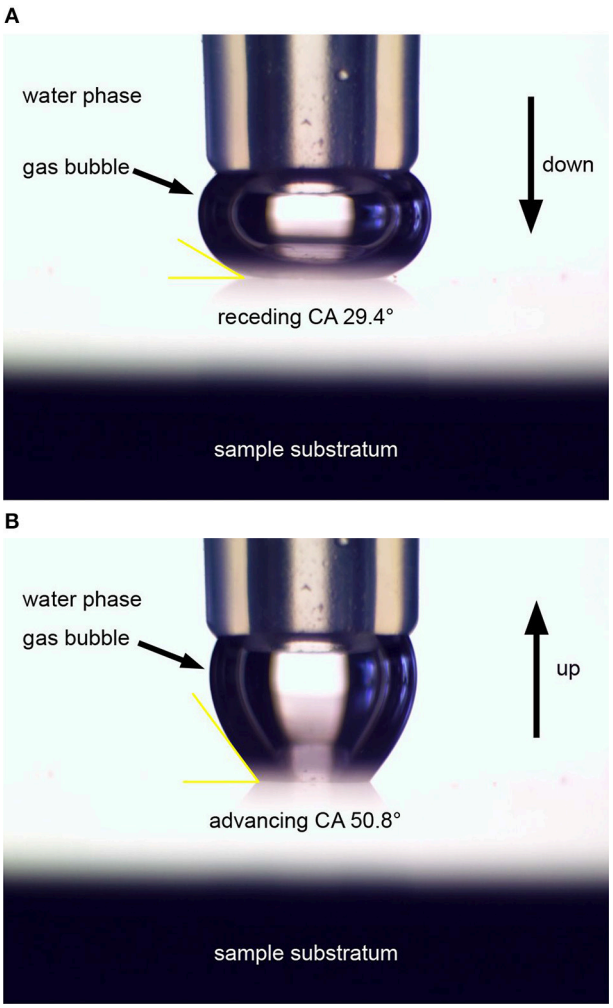


FIGURE 3 | Determination of dynamic CAs with a captive bubble technique for fully-hydrated biofouled surfaces: **(A)** receding CA; **(B)** advancing CA.

In these studies, the novel automated, computer-operated version of the system is shown in **Figure 4**. The outermost biofouled glass plate surface (4) is sensed with a gas bubble formed at the tip of a microsiringe, placed in a water tank (1). Captive bubble microsyringe set-up (2–3) is computer-controlled. The digital cameras (5) allow one to CA determination. A Long-axis microscope is used for selection the area to be studied (5–6). The surface wettability mapping is realized with a step motor + gear utility by positioning the sensing tip along x-y axes (7).

The peristaltic pump+tubes (8, 10) are used to control the water flow circulation in a measuring cell which is illuminated with a diffused light source.

The apparent solid surface free energy γ_{SV} and the remaining wettability parameters can be expressed with the following equations (Chibowski, 2003, 2007):

$$\text{Adsorbed matter 2D film pressure}: \Pi = \gamma_{LV}(\cos\Theta_R - \cos\Theta_A)$$

$$\text{Apparent surface energy}: \gamma_{SV} = \Pi(1+\cos\Theta_A)^2/[(1+\cos\Theta_R)^2 - (1+\cos\Theta_A)^2]$$

$$\text{Adhesion work}: W_A = \gamma_{LV}(1+\cos\Theta_A)$$

$$\text{Cohesion work}: W_C = 2\gamma_{LV}$$

$$\text{Spreading work}: W_S = W_A - W_C$$

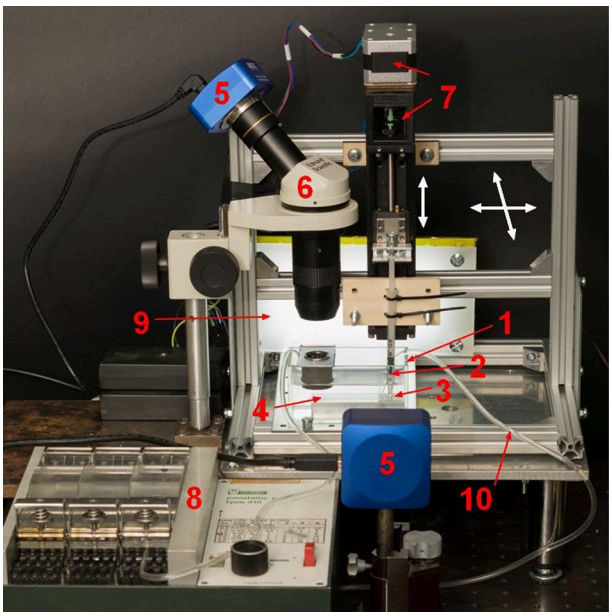


FIGURE 4 | Elements of the automatic, captive bubble CA determination system (for description see text).

where: Θ_A is the advancing contact angle, Θ_R - the receding contact angle, CAH = Θ_A- Θ_R is the contact angle hysteresis, and γ_{LV} is the surface tension of test liquid.

Confocal Microscopy Technique

Confocal laser scanning microscopy (Axiovert 200M, Carl Zeiss, Germany), working in the reflection mode configuration (Inaba et al., 2013), was a tool for the biofilm surface architecture analyses.

The flow cell is also used for continuous microscopic observations of biofilm formation and structure evolution on glass slides under particular shear water flow rates controlled with a peristaltic pump (Yawata et al., 2016). More detailed surface geometric, structural and morphological signatures are evaluated with advanced image analysis programs (COMSTAT, CMEIAS, PHLIP, ImageJ).

In particular, ImageJ allows to create image stacks (z axis) leading to 3D projections of the surface morphology by means of confocal microscopy registrations. The obtained 3D images can reveal details of biofilm matrix geometry, and further used in combination with fluorescence staining visualization, makes the concentration distribution of particular biofilm species like bacteria, algae, or ions to be quantified (Swearingen et al., 2016).

Photoacoustic Spectroscopy System

Photosynthesis generates phenomena which may be detected with a photoacoustic technique. Light energy converted to heat leads to the thermal expansion of tissue, liquids and gases, and is termed the photothermal signal. This is generated when the photosynthetic sample is irradiated by a light pulse. Not all of the light energy absorbed by the sample tissue stored as the process products. The variable unused fraction of the absorbed beam is converted to heat leading to a detectable pressure drop. When a photosynthetic system is illuminated by a pulsed light source, the resulting photosynthetic photolysis of water causes the evolution of a burst of gaseous O_2. The process results in an increase in pressure which is detected by a microphone as a photobaric signal (Pinchasov et al., 2005).

In the photoacoustic spectroscopy (PAS) the thermal diffusion length μ (a certain sample thickness,which affects the signal amplitude at a fixed modulation frequency, can be written: $\mu = (\alpha / \pi f)1/2$ where: $\alpha = k / \rho c$ is the thermal diffusivity ($m^2 s^{-1}$), k is the thermal conductivity (J s^{-1} m^{-1} K^{-1}), c is the specific heat capacity (J kg^{-1} K^{-1}), ρ is the density (kg m^{-3}), f is the frequency of light modulation (varied from 1 to 1kHz). The amplitude of PA signal is proportional to the optical density of the sample (index s) $p_A \sim \mu_S / k_S$ (Szurkowski et al., 2001). By changing the frequency of light modulation, the PA depth profile can provide information on the location of pigments in the biofilm structure (Charland and Leblanc, 1993). The application of different photoacoustic spectroscopy systems for analytical measurements is recently reviewed in (Haisch, 2012).

Interpretation of the data is based on the results originating from a classical Rosencweig-Gersho model (Rosencwaig, 1980). The PAS experimental arrangement constructed for these biofilm studies was described in detail elsewhere (Szurkowski et al., 2000).

The modulated light beam illuminating the biofouled sample placed in a closed-type PA cell leads to the light energy absorption in such a photosynthetic system composed of pigments. There are two parts of the absorbed energy emission, the first one is emitted as the thermal signal (originating from the thermal deactivation of pigments), and the second one spent in photochemical processes (emission of oxygen). Both kinds of emissions and the subsequent acoustic pressure are detected using a microphone. Energy storage (ES) was determined, by measuring heat emission in a closed-type PA cell exposed to modulated and non-modulated background light, as the ratio (A-B)/A * 100(%). A is the PA signal originated from the modulated light switched on together with the non-modulated background light of 2000 μmol photons m^{-2} s^{-1}, whereas B is the PA signal when the cell is illuminated only with the modulated light beam. The modulated light intensity was 25 μmol photons m m^{-2} s^{-1}. The strong background light applied to the sample leads to the saturation state of the photochemical reactions in the sample. Such a strong irradiation increases the conversion effectiveness of the adsorbed light energy to heat to almost 100%. Under the applied condition, the maximal PA is obtained proportional to the modulated light absorption in the probe. All the measurements were performed at room temperature using the measuring light wavelength of 680 nm, for the modulation frequency of 80 Hz i.e., height enough to neglect the oxygen signal contribution, as assumed by others (Veeranjaneyulu et al., 1991). The PA signal amplitude and phase is evaluated by means of the phase-sensitive method realized using a lock-in amplifier. A schematic diagram of the PA system is shown in **Figure 5A** with a laboratory-build closed-type photoacoustic cell, presented in **Figure 5B**.

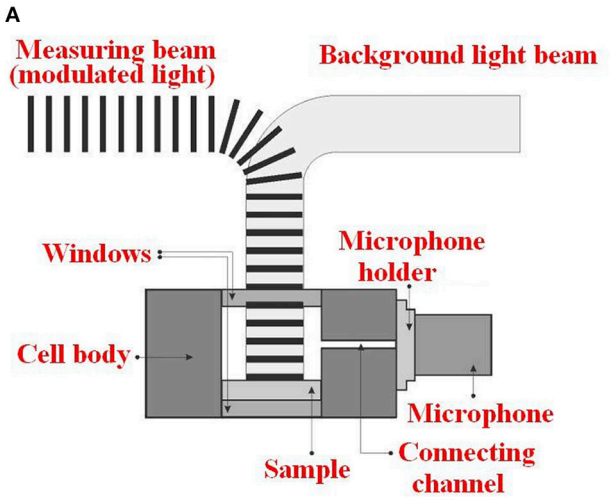


FIGURE 5 | (A) Schematic diagram of PA system. **(B)** Laboratory-built closed-type photoacoustic cell.

As an abiotic substratum for biofilm collection, disks of the same diameter = 18 mm made of glass, aluminum, and brass were chosen. Samples from the seawater planktonic phase were processed following the procedure introduced by Carpentier et al. (1989), where the filtered biological material covered a membrane filter (Sartorius SM 11306). A piece (15 mm ring in diameter) was cut out from the filter, for further PA measurements. Samples made of marine seaweed *Fucus vesiculosus*, *Cladophora sp.*, *Enteromorpha sp.* algae collected at the same location were also studied with the photoacoustic spectroscopy technique, for comparison.

RESULTS AND DISCUSSION

Wettability of Biofouled Surfaces

Since the marine biofouled solid substrata stand for highly heterogeneous, fully-hydrated and porous interfacial systems, the particular CA measuring technique i.e., a captive bubble method turned out to give accurate and reproducible results (Pogorzelski et al., 2013).

CA changes resulting from a variety of fouling conditions are discussed in Thomas and Muirhead (2009). In general, surface fouling can decrease CA when crystalline structures or biofilms are formed. However, at late stages of biofilm formation the outermost surface is enriched in EPS of polymeric and hydrophobic nature. Such a surface coverage has lower γ_{SV} and higher CA, as observed in this study.

In the previous marine biofilm wettability studies), dynamics of the selected parameters variability, for samples registered in the short-time marine biofilm formation interval (to 80 min.), is depicted in Figures 3A–D of Pogorzelski and Szczepanska (2014). The particular biofilm development stages can be identified. At short times, an increase of the both dynamic CAs points to the conditioning film formation step, and after $t = 20$ min. a tendency to attain the constant CA value can be noticed. **Figure 3B** reveals two CAH minima at $t = 5$ and 43 min., which seems to be related to the best-release surface feature. In addition, the time interval between the both stages $\Delta t = 38$ min. could be related to the growth rates ($\sim 1/\Delta t = 2.78 \times 10^{-4}$ s^{-1}) of the microorganisms colony, since the similar values were reported for *Cyanobacteria* (8×10^{-6} s^{-1}) and EPS (12×10^{-6} s^{-1}) in Wanner et al. (2006). Gao and McCarthy (2006) argued that CAH is closely related to the bioadhesion of OM to the solid substratum. It was evidenced that CAH less than 10°Could lead to removal of biofilm covering submerged macrophyte leaf blades by shear water flow (Genzer and Efimenko, 2006). Schmidt et al. (2004) found that the bioadhesive properties the surface are correlated to CAH rather than to the surface energies of the coatings. The outermost surface appeared to be most hydrophobic (minimal γ_{SV}) at $t = 43$ min., as shown in Figure 3C, which is correlated with the maximum at Π (t) plot from Figure 3D i.e., the mature biofilm stage, where the surface bioaccumulation ($\sim\Pi$) attains the saturation value. Finlay et al. (2002) addressed the solid surface energy effect on biofilm accumulation using a variety of model materials of differentiated hydrophobicity. As a result, the hydrophobic surfaces tend to accumulate polymeric-like compounds whereas the hydrophilic ones are enriched in polar biomaterials (Krishnan et al., 2008). The lowest bioadhesion is foreseen for solid substrata with γ_{SV} from the range [20–30 mJ m^{-2}; Baier (1970)]. The model substrata used here had surface energy values: 58.8 (wood), 55.9 (glass), 43.3 (aluminum), 41.8 (brass), and 38.6 (stainless steel) mJ m^{-2}, and demonstrated significant bioaccumulation. 2D adsorptive film pressure Π, according to the Gibbs adsorption theory (Adamson and Gast, 1997), is related to the surface adsorption Γ (Gibbs excess) $\sim\Pi/RT$, where: R is the gas constant and T is the absolute temperature. Our comprehensive biofilm studies confirmed that the biofilm wet weight (BWW) was positively correlated to Π. An increase of surface roughness (derived from confocal microscopic studies) resulted in CAH ↑. Bioaccumulation progressing in time of biofilm formation (expressed by BWW) pointed to the hydrophobization (γ_{SV} ↓) of the outermost biofilm surface likely enriched in EPS compounds. It should be pointed out that several other factors which could affect the biofilm formation process and final composite structure like surface energy, electricity, shear flow velocity, roughness etc., as can

be learned in Zhao et al. (2005) and Thomas and Muirhead (2009).

A general trend in the wettability parameters variability can be noticed: $\Theta_A \uparrow$, $\Theta_R \uparrow$, CAH $\uparrow$, $\Pi \uparrow$ $\gamma_{SV} \downarrow$, $W_A \downarrow$, and W_S become more negative with an increase of the biofilm age at longer time-scale periods (days).

The biofilm treatment procedure has a significant influence on CA, vacuum drying of fouled surfaces increases CA by about 8° (Donlan, 2002). Surface roughness is another important factor influencing CA, especially on a complex surface of biofilms. In tests, where defect heights was used in ratio to capillary length, larger defect heights served to increase CA, likely creating pinning edges (Cubaud et al., 2001). In Thomas and Muirhead (2009), the empirical equation for CA was developed with two parameters characterizing the biofouled surface i.e., the area fraction fouled f_{fouled}, and d/l_{cap}-the ratio of defect height to capillary length, which supports the observation that wastewater fouling can generally decrease CA from the baseline on a clean but corrugate surface. Biofouling studies of six different abiotic substrata with varying surface energy (18–40 mJ m^{-2}) and surface roughness (45–175 μm) were performed in coastal sea waters (Lakshmi et al., 2012). The correlation analyses performed on biofilm parameters (carbo hydrate, total viable bacterial count, organic matter etc.) exhibited that surface energy and CA are highly correlated, viable count of bacteria was positively correlated to surface energy ($R = 0.69$). The attachment of macrofouler and the surface characteristics are also well correlated with surface energy and roughness.

A large variety of organisms can compose the marine biofilm colony of different size and shape like: bacteria (1 μm), yeast (3–5 μm), fungi (12–18 μm), algae (∼25 μm), cilitae (>200 μm) living apart from macroorganisms (barancles or seaweeds) that is important in the light of surface roughness of substrata to be inhabited (Wanner et al., 2006).

Data on the marine organisms classes and their occurrence in different seasons at the south Baltic region can be found in Kautsky and Kautsky (2000). In the study area, monocell algae were present composing microphytobenthos. *Diatomophyceae* and *Dinophyceae* dominated phytoplankton of the Baltic with a significant account of *Cyanobacteria*. Seasonality of organisms taxes can be noticed: diatoms are found in spring, *Cyanophyta* in summer, and diatoms prevail in autumn.

Spearman's rank correlation coefficients (R) between the trophic status indicators and the surface wettability parameters of the glass substrata submerged in Baltic Sea coastal waters are listed in **Table 1**. All the parameters are negatively correlated to Secchi depth, although the absolute values indicated a strong correlation effect only for the wettability parameters: CAH, γ_{SV}, Π (with R = 0.68–0.96). The remaining ones i.e., W_A are W_S are much less correlated to the trophic status indicators ($R =$ 0.40–0.69). Moreover, the wettability parameters are correlated to each other (data not shown here). That concerns Θ_A, Θ_R, CAH, and W_A. It may be concluded that a set of the surface wettability parameters can be limited only to the uncorrelated quantities since the other ones born no more information on the solid surface/water phase interactions. A larger comprehensive data set is required to establish the functional relations between the trophic status parameters and the surface wettability energetic ones of practical value.

TABLE 1 | Spearman's rank correlation coefficients between the trophic status indicators and wettability parameters of glass substrata submerged in Baltic Sea coastal waters.

Trophic State Indicators	CAH (deg)	Π (mNm^{-1})	γ_{SV} ($mJ\ m^{-2}$)	W_A ($mJ\ m^{-2}$)	W_S ($mJ\ m^{-2}$)
1. pH	0.631	0.673	0.712	0.551	0.684
2. Dissolved O_2 (mg dm^{-3})	0.845	0.781	0.893	0.613	0.697[b]
3. Secchi depth (m)	−0.621	−0.755	−0.825	−0.654	−0.715
4. Total P (mg dm^{-3})	0.751	0.912[a]	0.789	0.572	0.542[b]
5. Total N (mg dm^{-3})	0.824	0.933[a]	0.726	0.683	0.402[b]

[a]$p < 0.05$, $n = 9$; [b]$p < 0.01$, $n = 6$.

So far, the wetting properties of solid substrata (minerals) found in marine waters affected by natural surfactant adsorption were determined under laboratory using the dynamic CA approach (Mazurek et al., 2009). Recently, the condition level of submerged in sea water surfaces were evaluated via the surface wettability parameters (Pogorzelski et al., 2013). Moreover, the novel contact angle hysteresis methodology based on wettability energetics allowed us to quantify the atmospheric environment pollution impacts on *Pinus Silvestris L.* needles (Pogorzelski et al., 2014), and seems to be a technique of general concern applicable to a large variety of complex interfacial systems.

Confocal Microscopy Biofilm Characterization

The non-invasive visualization of biofilm development by applying the technique of continuous-optimizing confocal refection microscopy (COCRM) was used to derive the input biofilm features essential in mathematical modeling of biofilm formation kinetics (Inaba et al., 2013).

Confocal microscopy sections (along z-axis with a 3 μm separation) through a marine biofilm on glass (14 – day formation time) from top (1) to bottom (11) are shown in **Figure 6A**; HF represents a split of an image stock from (1) to (11) derived with Helicon Focus program covering area 425 × 570 μm. 3D reconstructed surface morphology exhibiting an exopolymer matrix with water cannels was obtained by ImageJ program (**Figure 6B**). Much more detailed information on the particular biofilm architecture can be obtained using several image processing programs applied to 3D stacks of biofilm images, as demonstrated in Heydorn et al. (2000), Mueller et al. (2006); Lamprecht et al. (2007) and Dazzo (2010). For instance, the use of PHLIP permitted the dynamics and spatial separation of diatoms, bacteria, and organic and inorganic components to be followed (Mueller et al., 2006).

The geometric-morphological biofilm parameters, for the particular structure in **Figure 6**, are as follows: mean thickness = 14.2 μm, biovolume = 46,700 μm^3, coverage area fraction f =

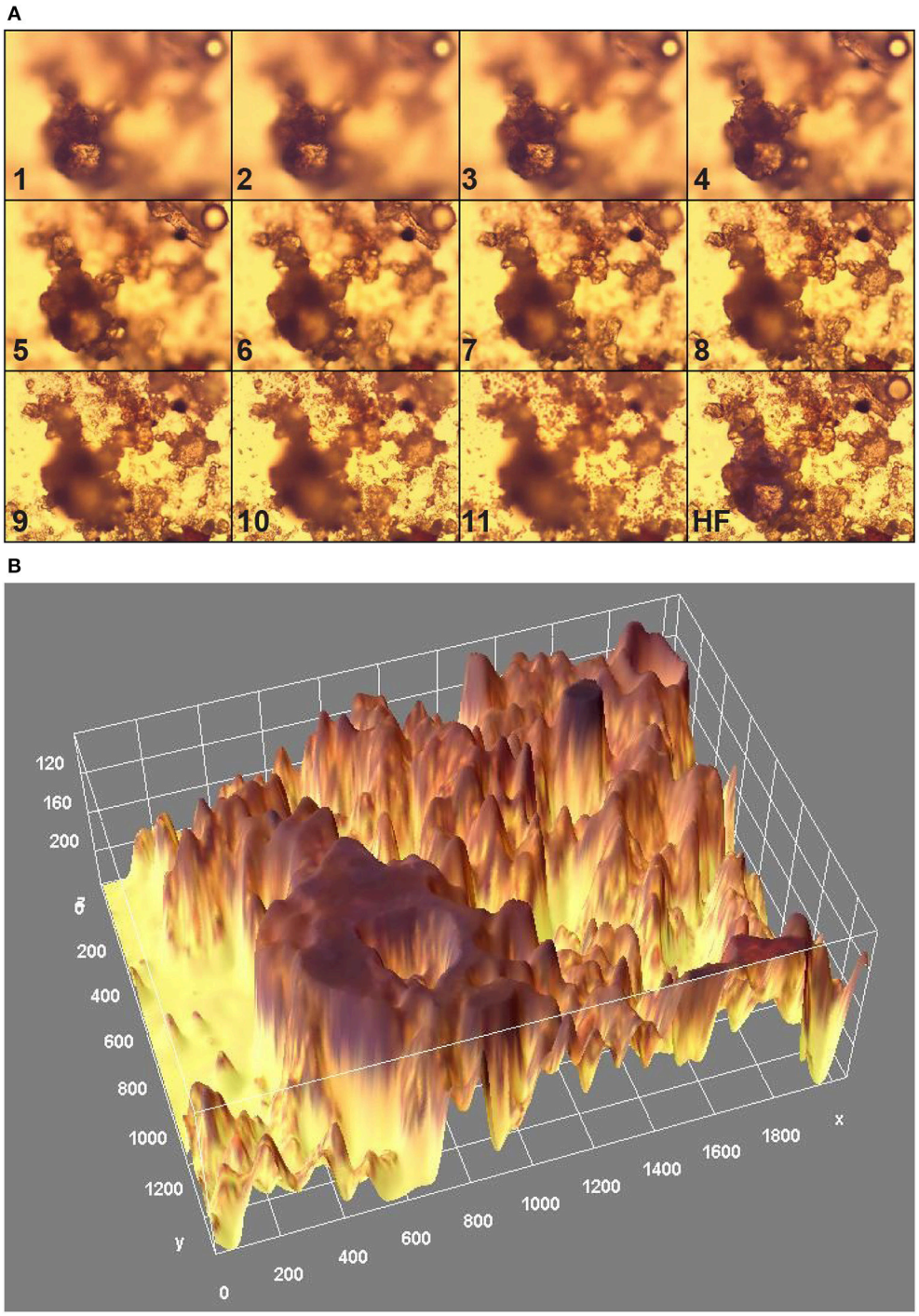


FIGURE 6 | Optical confocal microscopy sections through a marine biofilm on glass: **(A)** stock of sections from (1) to (11) spitted to (HR) with Helicon Focus routine; z-axis separation = 3 μm, **(B)** 3D reconstructed surface architecture with ImageJ program from HF covering area = 425 × 570 μm (Magnification = 400 times; x, y, and z axes in pixels i.e., 180 pixels = 50 μm).

60.2 %, roughness parameter r = 0.49, fractal dimension = 1.36, Hopkins aggregation index = 2.89.

The fractal dimension (varying between 1 and 2) reflects a contact line complexity of the object with the surrounding area, higher values point to a more developed border line (Yang et al., 2000). Hopkins' index is a measure of biofilm colony dispersion state, for randomly distributed structures is <2 (Dazzo, 2010).

Generally, the algal community evaluated to larger species which correlated to an increase in biovolume ($R = 0.96$), and demonstrated the biofilm thickness grow ($R = 0.87$) with time. Bacteria were appeared at measurable quantities close to the solid surface, whereas microalgae occupied intermediate parts of the layered structure. EPS covered the outermost surface of the microcolony exposed to the surrounding water. The principal biofilm compounds demonstrated differentiated kinetics with the time elapsed. A clear transition was observed from a heterotrophic community (enriched in bacteria) to an autotrophic community consisting largely of diatoms. The biofilm development leads to an increase in its heterogeneity since a strong correlation between roughness and biovolume was noticed.

Not all the structural-geometric biofilm parameters are useful as the novel water body trophic status indicators. These comprehensive studies demonstrated that a strong positive correlation appeared between: biovolume vs. biofilm wet mass (BWW) ($R = 0.78$), coverage fraction f vs. BWW ($R = 0.82$), biofilm thickness vs. Π ($R = 0.86$), and biofilm thickness vs. γ_{SV} ($R = -0.83$).

An attempt was made to map the surface spatial heterogeneity with both the captive bubble wettability sensor, and confocal microscopy system on the same biofilm-covered glass sample. The biofilm thickness along the straight line marked on the glass slide surface (**Figure 7A**) correlates well with the surface pressure Π (x-axis) profile (compare **Figures 7B**,**C**); although the thickness is apparently negatively related to the surface energy of the sample (**Figure 7D**).

Modeling of Biofilm Formation Dynamics

There are two commonly-used biofilm modeling techniques based on a dynamic systems formalism where the concentrations variability of the species are expressed with different relations and a so-called individual—based approach which appears to be of particular value in describing multicomponent systems undergoing several structural transitions of differentiated time-scales (Garrett et al., 2008; Lodhi, 2010).

The model analyzed in this report is based on the general principle of mass conservation for soluble and particulate biofilm components (Wanner et al., 2006).

The biofilm formation process in a seawater environment is a complex phenomenon, where several species are involved like: bacteria, fungi, diatoms, protozoans, larvae, and algal spores (Railkin, 2004). In addition, the process is mediated by physicochemistry of a substratum along with the environmental conditions such as a nutrient level, pH, dissolved O_2, light availability, sample depth, and temperature (Chiu et al., 2005).

From the previous work (Pogorzelski and Szczepanska, 2014), the CA wettability sensor appeared to be effective in *in-situ* and continuously biofilm formation studies and was used here simultaneously with a fluorescence-based microscopy technique. The experimental methodology and data evaluation procedure was adapted after (Fischer et al., 2014) to identify the known phases of biofilm development and to determine the specific growth rates μ, and the conditioning or induction times λ, where Gomperts sigmoidal function was selected to describe a specimen growth curve (Zwietering et al., 1990). The specific growth rate starts at a value of zero and then accelerates to a maximum value μ_m in a certain period of time, resulting in a lag time (λ). Values of μ_m and λ were recovered from the growth dynamics curve G(t), as presented in Fischer et al. (2014). The colony organism growth curves can show a decline that leads to different μ and λ values.

The experimental observations in these studies revealed that in natural multispecies ecosystems, the surface colonization kinetics ought to be approximated with at least three Gompertz functions that remained in agreement with previous findings of Fischer et al. (2014). A split of G(t) functions is required to display the main steps of microcolony formation (Fischer et al., 2014):

$$G(t) = \sum_{i=1}^{3} g_i(t) \text{ where} \tag{1}$$

$$g_i(t) = (A_i - A_{i-1}) \exp\left\{-\exp\left[\frac{\mu_i \cdot e}{A_i - A_{i-1}}(\lambda_i - t) + 1\right]\right\}$$

Here, $g_i(t)$ is a logarithmic function of the biofilm signal (film-covered area fraction f) corresponding to the sigmoidal growth taking place in the *i*th stage of biofilm development. The remaining parameters are defined in Fischer et al. (2014).

The biofilm structure development dynamics was followed simultaneously with three sensors (confocal microscopy, wettability CA technique, and photoacoustic spectroscopy) to validate the model and determine the biologically significant parameters. For instance, EPS deposition pattern in a biofilm can be quantifiable by application of potassium permanganate, $KMnO_4$, yielding brown MnO_2 precipitate deposition on the EPS, which was evaluated using data from a reflection detector (Swearingen et al., 2016). On the basis of an increase in the red band PA spectra from chlorophyll-containing cells, the growth in a cell size was determined.

An exemplary marine biofilm growth curve is shown in **Figure 8**. From the plot, biological parameters μ_i and λ_i were derived, as shown in Figure 1 of Zwietering et al. (1990), for the main stages of the biofilm establishment and identified specimens. They are collected in **Table 2**, and remain in agreement with the published data by others on the time-scale of transition processes in biofilms (Wanner et al., 2006; Klapper and Dockey, 2010).

At least, seven main phases of marine biofilm structure can be defined (Fischer et al., 2014), and four identified in our studies are visualized in **Figure 8** as insets. Starting from the biochemical conditioning (phase I), subsequently a pioneer attachment phase appears (phase II) followed by the adaptation phase (phase III). The exponential-like accumulation growth stage (phase IV) leads to the asymptotic maximal bacterial cell density (in phase V). In this phase, the surface is to a great extend colonized by unicellular diatoms. The presence of phase VI is attributed to the accumulation of eukaryotic microorganisms, and finally phase VII representing the exponential accumulation stage of, which stand for the pseudo-stationary stage of mature biofilm structure. The latter phases are mediated by environment-specific

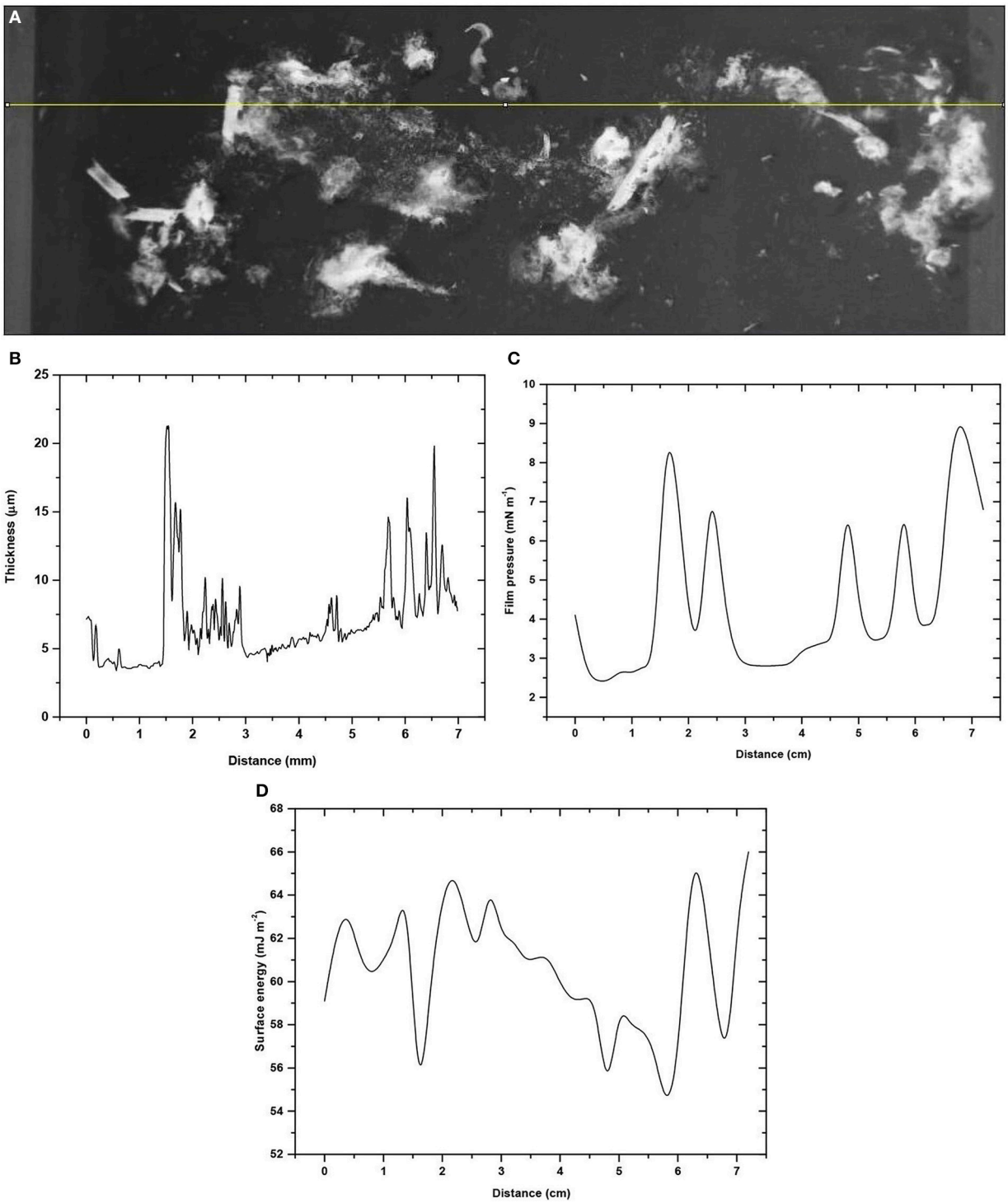


FIGURE 7 | Spatial mapping of marine biofilm heterogeneity on glass. **(A)** Optical profile along a horizontal line. **(B)** Biofilm thickness profile from confocal microscopy. **(C)** Surface pressure and **(D)** Surface energy profiles both derived with the wettability captive bubble sensor.

factors like seasonal, local and biological activity in seawater and plankton availability. It should be born in mind that not all the phase may necessarily occur in particular marine ecosystems. Biofilm formation dynamics studies performed in a low primary production season (November-December) demonstrated no settlements of larger microorganisms. The similarity of biofilms on different substrata in seawater was observed for early stages of a colony formation (up to 4 d), where a conditioning film of organic matter is quickly generated. This film masks the surface chemistry of the substratum (Jones et al., 2007). As a result,

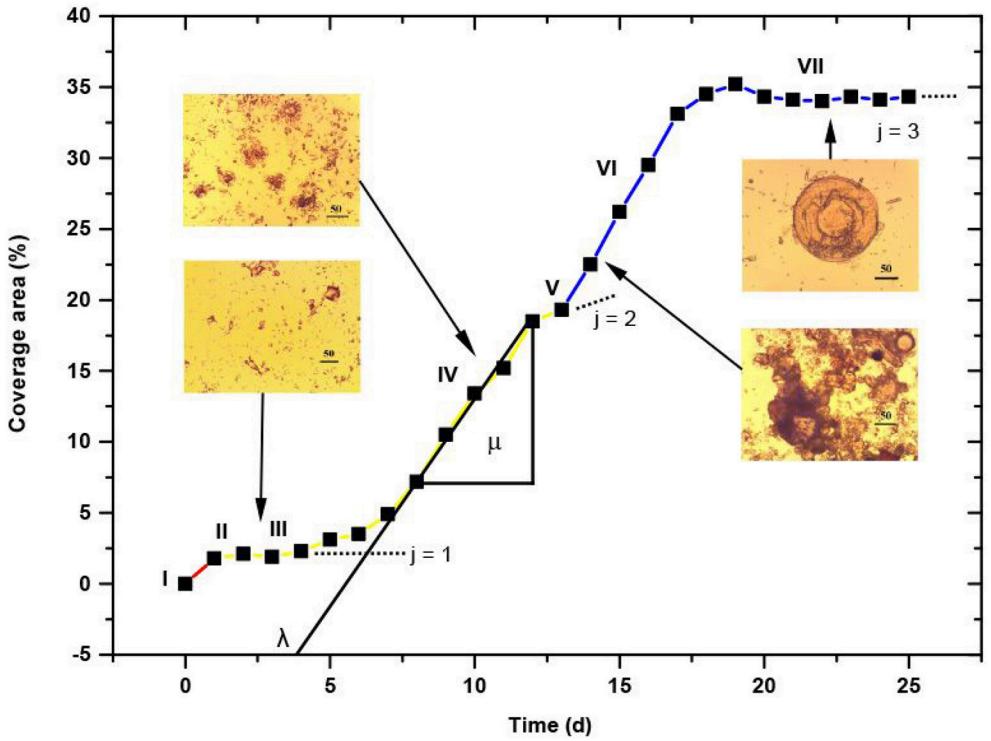


FIGURE 8 | Marine biofilm growth curve (coverage area fraction vs. time) fitted with three Gompertz functions. Red, orange and blue line parts correspond to the main stages of biofilm establishment. I-VII seven main phases of biofilm formation dynamics. Microscopic images of four characteristic stages of the growth phases (Magnification 400 x, bars correspond to 50 μm) are shown as insets.

TABLE 2 | Characteristic time-dependent features of marine biofilm formation.

No	Biofilm process time scale	Sensor
1	Biochemical preconditioning to 5 min. $\mu = 0.27 \pm 0.09\ h^{-1}$	Contact Angle
2	Initial bacteria colonization 5 to 40 min.	Contact Angle, Confocal Microscopy
3	Bacteria colonization cycle 1 h	Contact Angle
4	Cyanobacteria growth 34.5 h	PA Spectroscopy
5	EPS growth 23 h; $\lambda_1 = 2.8 \pm 0.2$ d, $\mu_1 = 0.56 \pm 0.12\ d^{-1}$ $\lambda_2 = 6.4 \pm 0.4$ d, $\mu_2 = 0.27 \pm 0.82\ d^{-1}$	Confocal Microscopy Contact Angle
6	EPS death 11.5 d	Confocal Microscopy, Contact Angle
7	Diatom growth 57 d	PA Spectroscopy, Confocal Microscopy
8	Diatom consumption 12.5 d	PA Spectroscopy

colonizing bacteria could perceive them as similar, and other factors as electricity, roughness, color etc. could mediate further colonization.

Chlorophyll a is most commonly used to estimation of algal biomass, thus the *Chlorophyll* content may be inversely proportional to light intensity. Chemical composition of biofilms can be used as an indicator of nutrient uptake efficiency. Largely, elemental ratios of nutrients such as carbon and nitrogen (C/N), and nitrogen and phosphorus (N/P) are calculated (Burns and Ryder, 2001).

Biofilm as a Photosynthetic System

Energy Storage ES of Biofilms

Photoacoustic PA technique turned out to be an effective tool in photosynthetic systems investigations particularly to direct determination of ES (Carpentier et al., 1989; Veeranjaneyulu et al., 1991), and oxygen emission in untouched leaves (Poulet et al., 1983; Mauzerall, 1990).

The energy storage of the sample indicated a linear dependence on the photosynthetic system capacity taken at the maximum rate corresponding to stable photochemical products generation (Szurkowski and Tukaj, 1995).

The exemplary energy storage (ES) determination plot is shown in **Figure 9**, for a biofilm sample stored in Baltic Sea coastal waters for 14 days (studied on August 25, 2015).

Short-time ES evolution studies showed the fast ES increase up to 3–4 h then reaching an almost constant value in the middle of the biofilm cycle. ES measurements were carried out for the sample in its steady state. ES data were evaluated at different seasons, for biofilms collected at solid substrata (glass, macrophyte leaves), and organic matter filtered from a planktonic phase met at adjacent waters, for comparison, are summarized in **Table 3**.

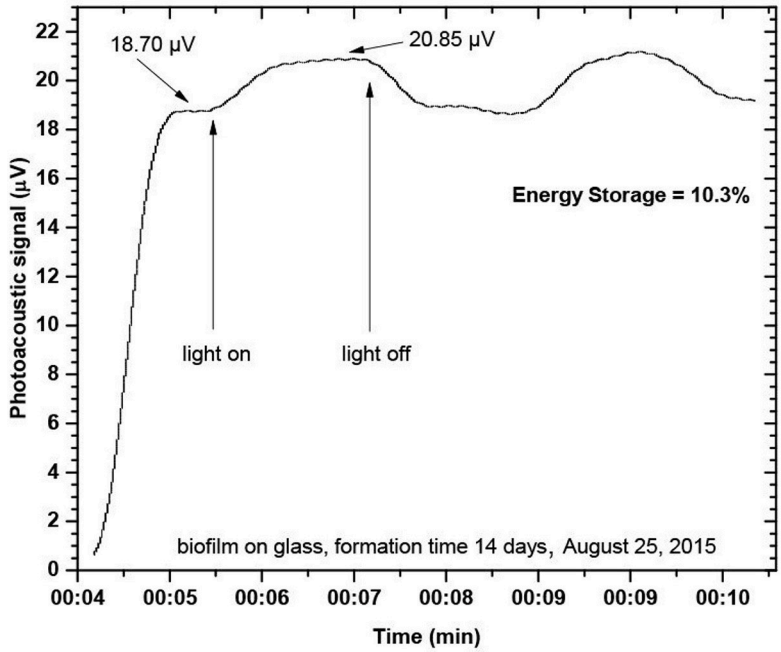


FIGURE 9 | Photoacoustic ES plot, for marine biofilm collected at a glass substratum (Baltic Sea, Gulf of Gdansk, sample age- 14 days).

TABLE 3 | ES of marine photosynthetic systems studied in Baltic Sea coastal waters registered along a time period from spring to autumn seasons.

No.	Species	Energy storage (%)
1	Biofilm on glass (14-d formation; Baltic Sea; 27 July 2015)	18.4 ± 4.6
2	Planktonic phase (50 cm^3 volume deposition on membrane filter; 27 July 2016; Baltic Sea)	15.1 ± 2.8
	Planktonic phase (150 cm^3 volume deposition on membrane filter; 25 August 2016; Baltic Sea)	10.3 ± 1.9
	Planktonic phase (150 cm^3 volume deposition on membrane filter; 23 September 2016; Baltic Sea)	10.4 ± 1.6
	Planktonic phase (250 cm^3 volume deposition on membrane filter; 21 October 2016; Baltic Sea)	6.2 ± 1.1
3	Biofilm on glass (14-d formation; August, 2015)	19.6 ± 5.0
4	Biofilm on glass (14-d formation; September, 2015)	21.3 ± 5.6
5	Biofilm on glass (14-d formation; October, 2015)	20.5 ± 4.6
6	Biofilm on glass (14-d formation; November, 2015)	12.2 ± 4.8
Macroalgae		
7	*Cladophora sp.* (July, 2015)	23.1 ± 4.0
8	*Fucus vesiculosus* (July, 2015)	21.8 ± 5.2
9	*Zostera marina* (July, 2015)	11.3 ± 3.5

Generally, ES values were higher, for a season of high primary production. The maximum was attained in September, for biofilm on glass samples, although for the planktonic phase matter it was observed in late July. In addition, ES values were found higher by a factor of 1.5–2, for the biofilm settled on solid substrata, in particular on biotic macroalgae blades, for probes taken at the same place, time, and environmental conditions. The obtained ES values lie in the range reported by Cullen (1990). Comprehensive algal (*Macrocystis pyrifera* and *Ulva sp.*) studies revealed similar ES variability (Herbert et al., 1990). Seasonal O_2 and ES evolution during the cell cycle of green alga *Scendesmus aramtus* was already characterized by photoacoustic spectroscopy (Szurkowski et al., 2001). ES could be an indicator of water pollution, as demonstrated by Szurkowski and Tukaj (1995), for plants exposed to contamination. They are lower than or equal to those measured for samples in a pollution-free environment. The best correlation between ES and pollution levels was obtained for a batch culture of green microalgae *Scenedesmus armatus* (Szurkowski and Tukaj, 1995).

It can be noted that photosynthetic energy storage efficiency mediates the development of phytoplankton cultures. All the abiotic environmental factors like: temperature, nutrient availability and contamination level will be reflected in detectable changes in photosynthetic energy storage efficiency of phytoplankton, and further affects the total biomass and composition of biofilm cultures (Pinchasov et al., 2007). The effect of nutrient limitation on relative photosynthetic efficiency was exhibited as a significant drop in ES (by 50%) in P- limited, and (by 60%) in N-limited algal cultures, as compared to the reference one (Pinchasov et al., 2005). In the photoacoustic method, ES efficiency is independent of chlorophyll concentration, and the observed ES decrease did not result from death of some cells within the population but due to inactivation of increasing fractions of the photosynthetic units.

PA Spectral Characteristics of Biofilms

Bioptical properties of a microorganism colony at solid substrata were already studied with acoustic spectroscopy methods (Schmid, 2006; Bageshwar et al., 2010) apart from the conventional optical ones (Ionescu et al., 2012). The photo thermal signal amplitude can be a good measure of the culture biomass, dimensions of the cells and oxygen evolution therein (Szurkowski et al., 2001). Periphyton is a complex mixture of algae, cyanobacteria, heterotrophic microbes, and detritus containing a mixture of pigments (see in **Figure 10**, where the combined absorption spectra of natural pigments, modified after (Schagerl and Donabaum, 2003; Schagerl et al., 2003) are shown.

The high correlation between the photosynthetically active biomass, expressed in *Chlorophyll a* content, and the absorption coefficient at the corresponding absorption wavelength of *Chl a* (673 nm) already made possible the estimation of biomass from reflectance measurements (Kazemipour et al., 2011).

Exemplary marine biofilm on glass PA amplitude (blue) and phase (red) spectra obtained in summer **(A)** and autumn **(B)** seasons are shown in **Figure 11**. In determining a photoacoustic spectrum, the original photoacoustic signal has to be divided by the spectrum of the excitation light beam (routinely by the spectrum of the reference sample i.e., carbon black) in order to eliminate a discrepancy attributed to differential light intensity throughout the source spectrum (Rosencwaig, 1980), so the PA amplitude is in (a.u.). The spectrum exhibits three maxima at wavelengths ca 430, 490, and 690 nm. The first and third of these maxima corresponds to absorption by *Chlorophyll a*, that at

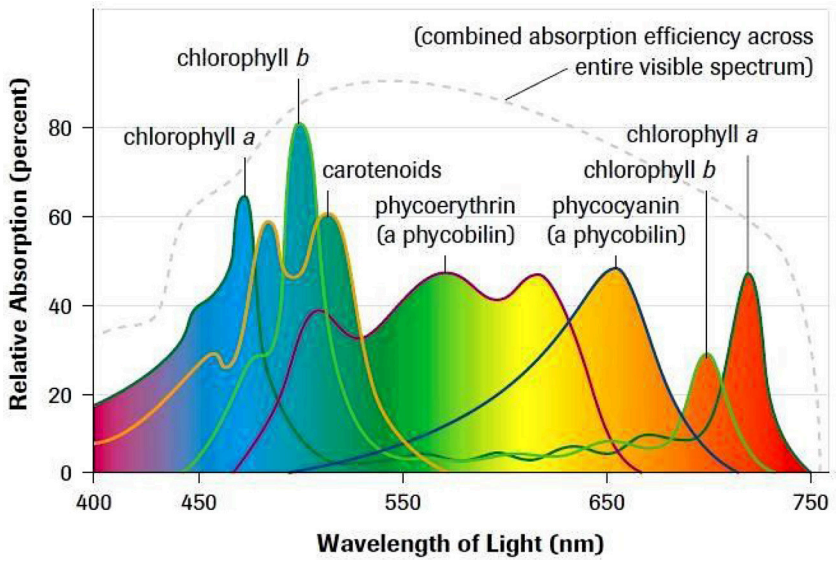


FIGURE 10 | Natural pigments absorption spectra, where the accessory pigments are combined with *Chlorophylls a and b*; modified after (Schagerl et al., 2003).

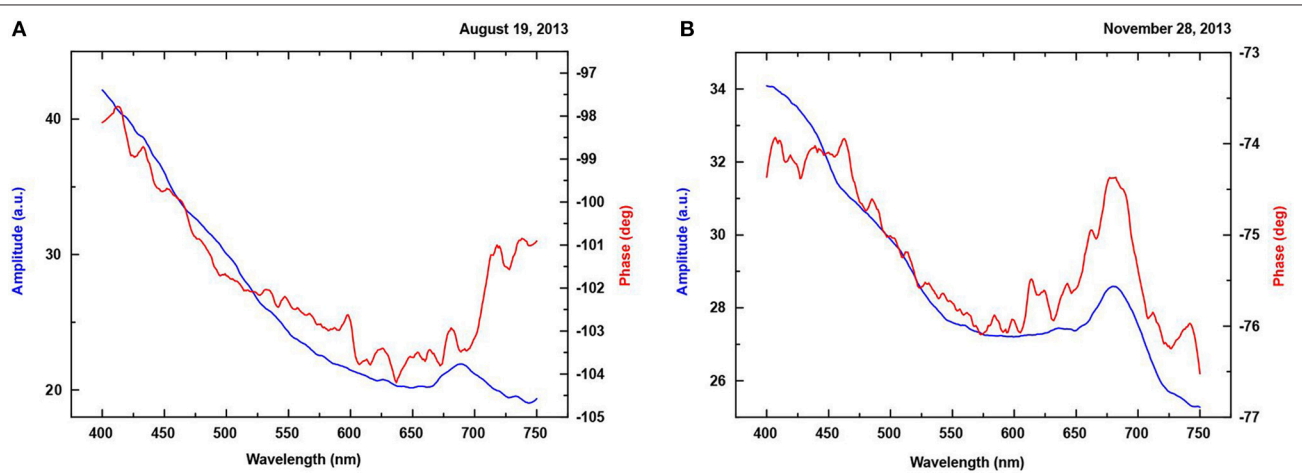


FIGURE 11 | Marine biofilm PA amplitude and phase spectra registered at the same station (Orlowo, Gulf of Gdansk, biofilm age-−14 days, collected on glass) in different seasons: **(A)** summer and **(B)** autumn.

480–490 nm to absorption of pigments accessory to *Chlorophyll a*.

Significant differences between PA amplitude spectra can be noticed. The lower maximum, for *Chlorophyll a* at 675 nm, for the sample collected on 19 Sept. 2013 in reference to the one on 28 Nov., 2013 can result from: 1. a lower *Chl. a* content in this time or 2. Very effective process of oxygen production (Szurkowski et al., 2001). A seasonal succession of phytoplankton groups in the studied water body (Fischer et al., 2014), reveals the presence of cyanobacteria, dinoflagellates, and bacillariophyceae in September but diatoms are found only in November. It should be noticed that the PA amplitude is dependent on the photoacoustically-induced heat production (proportional also to biomass) but the PA signal phase is proportional to oxygen production effectiveness (Poulet et al., 1983). The phase of the PA signal is more sensitive to the changes of optical and thermal properties of the layered sample than the magnitude of the PA signal (Du et al., 1995). The absolute value of the PA signal phase increment is caused by the additional signal due to the oxygen evolution. It means that the lower PA amplitude maximum in September does not result from the lower algae content in the biofilm but from the fact that a significant part of the heat energy was spent on the photosynthesis process (oxygen production). This statement was confirmed by the PA signal phase spectra. The maximal phase change, observed in September, was about 6° (from -104° to -98°) but in November only 3° (from -77° to -74°). It points to the higher oxygen production in the photosynthetic biofilm system taking place in September.

Since cyanobacteria are incorporated into the biofilm structure together with green bacteria containing *Chlorophyll a* (Ionescu et al., 2012), the biofilm pigment composition can be derived from the spectral maxima ratio: (*Bacteriochlorphyll c*/*Chlorophyll a*), (Kazemipour et al., 2011).

Effectiveness of the photosynthetic part of biomass accumulation in a biofilm structure is a substratum-specific quantity, as demonstrated in **Figure 12**. The peak values in the PA signal amplitude spectra maximum at ∼680 nm were found highest for a biotic substratum (wood), lower for the filtered planktonic phase, and lowest for the metallic abiotic surfaces. A close positive correlation was found between the said spectral peak value and BWW (R= 0.89). Such a relation is helpful in the best efficient collecting sampler material selection (depending on surface free energy, roughness, surface electricity etc.), for a particular water body (sea, inland waters).

The photoacoustic parameters (ES and PA signal amplitude spectra maxima, in particular) turned out to be unequivocally related to the biofilm structural signatures (free energy of the outermost biofilm surface, biofilm wet weight, fractional biofilm area coverage). In conclusion, the photoacoustic method proves to be a source of valuable information on the photosynthetic apparatus of biofilm colony (as ES, diffusion parameters, photochemical loss) during its life cycle not accessible by other methods.

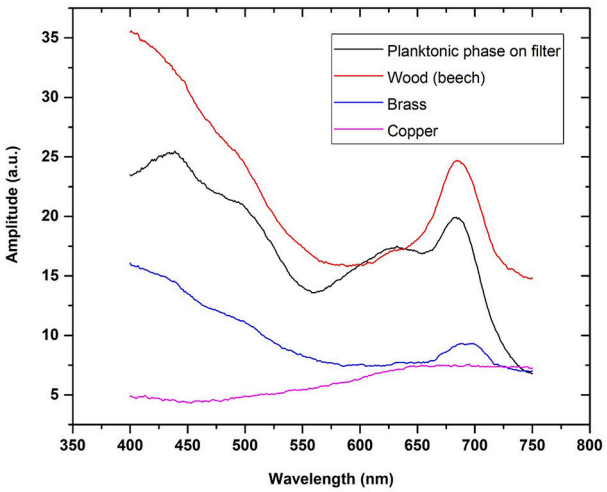


FIGURE 12 | Biofilm substratum effect on PA signal amplitude spectra. Biofilm samplers deployed in Baltic Sea coastal waters; sampling time 14 days.

CONCLUSIONS

The CA wettability sensor is capable of quasi-continuous biofilm evolution monitoring from the conditioning film stage to fully-developed 3D structured multispecies clusters. *In-situ* and *on-line* measurements can be performed on permanently submerged solid substrata, so-called biointerfaces (epilithon, epixylon, epipsammon, and epiphylon).

Confocal reflection microscopy assisted with imaging picture processing allowed us to indentify known phases of a biofilm development and to determine parameters of biological meaning (specific growth rates, induction time) applying a superposition of Gompertz functions to mathematical modeling of biofilm growth dynamics.

3D biofilm architecture can be quantified with several structural-geometric parameters (biovolume, roughness, thickness, substratum coverage, fractal dimension, Hopkins aggregation index etc.) which turned out to be unequivocally related to physicochemical surface properties of the substratum and environmental conditions, finally correlated to the trophic state indicators of the sea water body.

PA spectroscopy spectra and ES values of the biofilm photosynthetic system exhibited seasonal changes related to OM accumulation, and the transition of biofilm colony community from autotrophic to heterotrophic organisms. It can be expected that the level of main nutrients attributed to biofilm growth (nitrogen and phosphorus), are the principal factors mediating its biomass and ES efficiency. Variability of ES within hours to days is accompanied by changes in biomass or taxonomic composition.

Nutrient limitation and anthropogenic eutrophication are among others the most important factors determining the overall status of water bodies which can be followed by ES efficiency of biofilm cultures.

Cross-correlations found between the chemical water body trophic state indicators and the structural-geometric-wettability-photoacoustic biofilm parameters derived from physical sensing techniques made a promising starting point to propose modern indicators useful in marine waters bioassessment. However, the functional dependences remain to be established, on the larger data base, to apply the results in real ocean science and engineering.

AUTHOR CONTRIBUTIONS

MG prepared the experimental set-up, performed photoacoustic spectroscopy and confocal microscopy measurements and data evaluations. SP formulated work concept, created theoretical background, analyzed and discussed results. AP performed seawater chemical analyses and trophic state evaluations. KB-S performed correlation analyses, searched for literature background interpretation, wrote manuscript. The manuscript has been read and approved by all the listed authors, and the order of authors in the article was also approved.

FUNDING

This work was financially supported by the University of Gdańsk (contract number: DS 530-5200-D464-17).

REFERENCES

Adamson, A. W., and Gast, A. P. (1997). *Physical Chemistry of Surfaces.* 6th Edn Newyork, NY: Wiley and Sons

Azeredo, J., Azevedo, N. F., Braindet, R., Cerca, N., Coenye, T., Costa, A. R., et al. (2017). Critical review on biofilm methods. *Crit. Rev. Microbiol.* 43, 313–351. doi: 10.1080/1040841X.2016.1208146

Bageshwar, D. V., Pawar, A. S., Khanvilkar, V. V., and Kadam, V. J. (2010). Photoacoustic spectroscopy and its applications – a tutorial review. *Eurasian J. Anal. Chem.* 5, 187–203.

Baier, R. E. (1970). "Surface properties influencing biological adhesion," in *Adhesion in Biological Systems,* ed R. S. Many (New York, NY: Academic Press Inc), 15–48.

Burns, A., and Ryder, D. S. (2001). Potential for biofilms as biological indicators in Australian riverine systems. *Ecol. Manage. Restor.* 2, 53–63. doi: 10.1046/j.1442-8903.2001.00069.x

Carlson, R. E. (1977). A tropic state index for lakes. *Limnol. Oceanogr.* 22, 361–639. doi: 10.4319/lo.1977.22.2.0361

Carpentier, R., Leblanc, R. M., and Mimeault, M. (1989). Photoacoustic detection of photosynthetic energy storage in photosystem II submembrane fractions. *Biochim. Biophys. Acta* 808, 293–299. doi: 10.1016/0005-2728(85)90012-X

Charland, M., and Leblanc, R. M. (1993). Photoacoustic spectroscopy applied to biological systems. *Bull. Inst. Chem. Res. Kyoto Univ*. 71, 226–244.

Chibowski, E. (2003). Surface free energy of a solid from contact angle hysteresis. *Adv. Colloid Interf. Sci.* 103, 149–172. doi: 10.1016/S0001-8686(02)00093-3

Chibowski, E. (2007). On some relations between advancing, receding and Young's contact angles. *Adv. Colloid Interf. Sci.* 133, 51–59. doi: 10.1016/j.cis.2007.03.002

Chiu, J. M. Y., Thiyagarajan, V., Tsoi, M. M. Y., and Qian, P. Y. (2005). Qualitative and quantitative changes in marine biofilms as a function of temperature and salinity in summer and winter. *Biofilms* 2, 183–195. doi: 10.1017/S147905050500195X

Cubaud, T., Fermigier, M., and Jenffer, P. (2001). Spreading of large drops on patterned surfaces. *Oil Gas Sci. Technol.* 56, 23–31. doi: 10.2516/ogst:2001003

Cullen, J. J. (1990). On models of growth and photosynthesis in phytoplankton. *Deep-Sea Res.* 37, 667–683. doi: 10.1016/0198-0149(90)90097-F

Dang, H., and Lovell, C. R. (2016). Microbial surface colonization and biofilm development in marine environments. *Microbiol. Mol. Biol. Rev.* 80, 91–138. doi: 10.1128/MMBR.00037-15

Dazzo, F. B. (2010). "CMEIAS Digital microscopy and quantitative image analysis of microorganisms," in *Microscopy: Science, Technology, Applications and Education*, eds A. Mendez-Vilaz and J. Diaz (Badajoz: Formatex Research Center), 1083–1090.

Donlan, R. M. (2002). Biofilms: microbial life on surfaces. *Emerg. Infect. Dis.* 8, 881–890. doi: 10.3201/eid0809.020063

Du, H., Fang, W., and Zheng, J. J. (1995). Photoacoustic phase spectrum of a layered sample. *Appl. Phys. A* 60, 419–423. doi: 10.1007/BF01538344

Finlay, J. A., Callow, M. E., Ista, L. K., Lopez, G. P., and Callow, J. A. (2002). The influence of surface wettability on the adhesion strength of settled spores of the green alga *Enteromorpha* and the diatom *Amphora*. *Integr. Comp. Biol.* 42, 1116–1122. doi: 10.1093/icb/42.6.1116

Fischer, M., Friedrichs, G., and Lachnit, T. (2014). Fluorescent-based quasicontinuous and in situ monitoring of biofilm formation dynamics in natural marine environments. *Appl. Environ. Microbiol.* 80, 3721–3728. doi: 10.1128/AEM.00298-14

Flemming, H. C. (2009). "Why microorganisms live in biofilms and the problem of biofouling," in *Marine and Industrial Biofouling,* eds H. C. Fleming, R. Venkatesan, and K. E. Cooksey (Berlin; Heidelberg: Springer), 3–12.

Gao, L., and McCarthy, T. J. (2006). Contact angle hysteresis explained. *Langmuir* 22, 6234–6237. doi: 10.1021/la060254j

Garrett, T. R., Bhakoo, M., and Zhang, Z. (2008). Bacterial adhesion and biofilms on surfaces. *Prog. Nat. Sci.* 18, 1049–1056. doi: 10.1016/j.pnsc.2008.04.001

Genzer, J., and Efimenko, K. (2006). Recent developments in superhydrophobic surfaces and their relevance to marine fouling: a review. *Biofouling* 22, 339–360. doi: 10.1080/08927010600980223

Gindl, M., Sinn, G., Gindl, W., Reiterer, A., and Tschegg, S. (2001). A comparison of different methods to calculate the surface free energy of wood using contact angle measurements. *Colloids Surf. A* 181, 279–287. doi: 10.1016/S0927-7757(00)00795-0

Haisch, C. (2012). Photoacoustic spectroscopy for analytical measurements. *Meas. Sci. Technol.* 23:17. doi: 10.1088/0957-0233/23/1/012001.

Herbert, S. K., Fork, D. C., and Malkin, S. (1990). Photoacoustic measurements *in vivo* of energy storage by cycling electron flow in algae and higher plants. *Plant Physiol.* 94, 926–934. doi: 10.1104/pp.94.3.926

Heydorn, A., Nielsen, A. T., Hentzer, M., Sternberg, C., Givskov, M., Ersbøll, B. K., et al. (2000). Quantification of biofilm structures by the novel computer program COMSTAT. *Microbiology* 146, 2395–2407. doi: 10.1099/00221287-146-10-2395

Inaba, T., Ichihara, T., Yawata, Y., Toyofuku, M., Uchiyama, H., and Nomura, N. (2013). Three-dimensional visualization of mixed species biofilm formation together with its substratum. *Microb. Immunol.* 57, 589–593. doi: 10.1111/1348-0421.12064

Ionescu, D., Siebert, C., Polerecky, L., Munwes, Y. Y., Lott, C., Häusler, S., et al. (2012). Microbial and chemical characterization of underwater fresh water springs in the . *PLoS ONE* 7:e38319. doi: 10.1371/journal.pone.0038319

Jones, P. R., Cottrel, M. T., Kirchman, D. L., and Dexter, S. C. (2007). Bacterial community structure of biofilms on artificial surfaces in an estuary. *Microb. Ecol.* 53, 153–162. doi: 10.1007/s00248-006-9154-5

Kautsky, L., and Kautsky, N. (2000). "The Baltic Sea, including Bothnian Sea and Bothnian Bay," in *Seas at the Millennium: an Environmental Evaluation,* ed C. R. R. Sheppard (Amsterdam: Elsevier Science Ltd.,), 121–133.

Kazemipour, F., Meleder, V., and Launeau, P. (2011). Optical properties of microphytobenthic biofilms (MPBOM): biomass retrieval implication. *J. Quant. Spectrosc. Radiat. Transf.* 112, 131–142. doi: 10.1016/j.jqsrt.2010.08.029

Klapper, I., and Dockey, J. (2010). Mathematical description of microbial biofilms. *SIAM Rev.* 52, 221–265. doi: 10.1137/080739720

Krishnan, S., Weinman, C. J., and Ober, C. K. (2008). Advances in polymers for anti-biofouling surfaces. *J. Mater. Chem.* 18, 3405–3413. doi: 10.1039/b801491d

Lakshmi, K., Muthukumar, T., Doble, M., Vedaprakash, L., Kruparathnam, C., Dineshram, R., et al. (2012). Influence of surface characteristics on biofouling formed on polymers exposed to coastal sea waters of India. *Colloids Surf. B* 91, 205–211. doi: 10.1016/j.colsurfb.2011.11.003

Lamprecht, M. R., Sabatini, D. M., and Carpenter, A. E. (2007). CellProfiler: free, versatile software for automated biological image analysis. *BioTechniques* 42, 71–75. doi: 10.2144/000112257

Lodhi, H. M. (2010). *Adavances in Computational Systems Biology*. New York, NY: John Wiley & Sons 1–17.

Mauzerall, D. C. (1990). Determination of oxygen emission and uptake in leaves by pulsed, time resolved photoacoustics. *Plant Physiol.* 94, 278–283. doi: 10.1104/pp.94.1.278

Mazurek, A., Pogorzelski, S. J., and Boniewicz-Szmyt, K. (2009). Adsorption of natural surfactants present in sea waters at surfaces of minerals: contact angle measurements. *Oceanologia* 51, 377–403. doi: 10.5697/oc.51-3.377

Mueller, L. N., de Brouwer, J. F. C., Almeida, J. S., Stal, L. J., and Xavier, J. B. (2006). Analysis of a marine phototrophic biofilm by confocal laser scanning microscopy using the new image quantification software PHLIP. *BMC Ecol.* 6:1. doi: 10.1186/1472-6785-6-1

Picioreanu, C., van Loosdrecht, M. C., and Heijnen, J. J. (1998). Two-dimensional model of biofilm detachment caused by internal stress from liquid flow. *Biotech. Bioeng.* 72, 205–218. doi: 10.1002/1097-0290(20000120)72:2<205::AID-BIT9>3.0.CO;2-L

Pinchasov, Y., Kotliarevsky, D., Dubinsky, Z., Mauzerall, D. C., and Feitelson, J. (2005). Photoacoustics as a diagnostic tool for probing the physiological status of phytoplankton. *Isreael J. Plant Sci.* 53, 1–10. doi: 10.1560/4DVV-JT78-G7VW-QTFM

Pinchasov, Y., Porat, R., Zur, B., and Dubinsky, Z. (2007). Photoacoustics: a novel tool for the determination of photosynthetic energy storage efficiency in phytoplankton. *Hydrobiologia* 579, 251–256. doi: 10.1007/s10750-006-0408-5

Pogorzelski, S. J., Mazurek, A. Z., and Szczepanska, A. (2013). *In-situ* surface wettability parameters of submerged in brackish water surfaces derived from captive bubble contact angle studies as indicators of surface condition level. *J. Mar. Syst.* 119–120, 50–60. doi: 10.1016/j.jmarsys.2013.03.011

Pogorzelski, S. J., Rochowski, P., and Szurkowski, J. (2014). *Pinus sylvestris* L. needle surface wettability parameters as indicators of atmospheric environment pollution impacts: novel contact angle hysteresis methodology. *Appl. Surf. Sci.* 292, 857– 866. doi: 10.1016/j.apsusc.2013.12.062

Pogorzelski, S. J., and Szczepanska, A. (2014). On-line and *in-situ* kinetics studies of biofilm formation on solid marine submerged substrata by contact angle wettability and microscopic techniques, IEEE Conference Publications, Baltic International Symposium (BALTIC), 2014 IEEE/OES, IEEE *Xplore*, 1–8.

Poulet, P., Cohen, D., and Malkin, S. (1983). Photoacoustic detection of photosynthetic oxygen evolution from leaves. Quantitative analysis by phase and amplitude measurements. *Biochim. Biophys. Acta* 724, 433–446. doi: 10.1016/0005-2728(83)90104-4

Railkin, A. (2004). *Marine Biofouling: Colonization Processes and Defenses*. Boca Raton, FL: CRC Press 25–31.

Rosencwaig, A. (1980). *Photoacoustics and Photoacoustic Spectroscopy,* New York, NY: Wiley Interscience Publication.

Rubio, C. (2002). These de l' Universite de Paris VI.

Schagerl, M., and Donabaum, K. (2003). Patterns of major photosynthetic pigments in freshwater algae. 1. Cyanoprokaryota, Rhodophyta and Cryptophyta. *Ann. Limnol.- Int. J. Lim.* 39, 35–47. doi: 10.1051/limn/2003003

Schagerl, M., Pichler, C., and Donabaum, K. (2003). Patterns of major photosynthetic pigments in freshwater algae. 2. Dinophyta, Euglenophyta, Chlorophyceae and Charales. *Ann. Limnol.- Int. J. Lim.* 39, 49–62. doi: 10.1051/limn/2003005

Schmid, T. (2006). Photoacoustic spectroscopy for process analysis. *Anal. Bioanal. Chem.* 384, 1071–1086. doi: 10.1007/s00216-005-3281-6

Schmidt, D. L., Brady, R. F., Lam, K., Schmidt, D. C., and Chaudhury, M. K. (2004). Contact angle hysteresis, adhesion, and marine biofouling. *Langmuir* 20, 2830–2836. doi: 10.1021/la035385o

Simões, M., Cieto, S., Pereira, M. O., and Viera, M. J. (2007). Influence of biofilm composition on the resistance to detachment. *Water Sci. Technol.* 55, 473–480. doi: 10.2166/wst.2007.293

Swearingen, M. C., Mehta, A., Mehta, A., Nistico, L., Hill, P. J., and Falzarano, A. R. (2016). A novel technique using potassium permanganate and reflectance confocal microscopy to image biofilm extracellular polymeric matrix reveals non-eDNA networks in Pseudomonas aeruginosa biofilms *FEMS Pathog. Dis.*74:ftv104. doi: 10.1093/femspd/ftv104

Szurkowski, J., Bańcik-Remisiewicz, A., Matusiak, K., and Tukaj, Z. (2001). Oxygen evolution and photosynthetic energy storage during the cell cycle of green alga *Scenedesmus armatus* characterized by photoacoustic spectroscopy. *J. Plant Physiol.* 158, 1061–1067. doi: 10.1078/0176-1617-00244

Szurkowski, J., Pawelska, I., Wartewig, S., and Pogorzelski, S. J. (2000). Photoacoustic study of the interaction between thin oil layers with water. *Acta Physica Polonica A* 97, 1073–1082. doi: 10.12693/APhysPolA.97.1073

Szurkowski, J., and Tukaj, Z. (1995). Characterization by photoacoustic spectroscopy of the photosynthetic *Scenedesmus armatus* system affected by fuel oil contamination. *Arch. Environ. Contam. Toxicol.* 29, 406–410. doi: 10.1007/BF00212508

Thomas, E., and Muirhead, D. (2009). Impact of wastewater fouling on contact angle. *Biofouling* 25, 445–454. doi: 10.1080/08927010902875105

Veeranjaneyulu, K., Charland, M., Charlebois, D., and Leblanc, R. M. (1991). Photosynthetic energy storage of Photosystem I and II in the spectral range of photosynthetically active radiation in intact sugar maple leaves. *Photosyn. Res.* 30, 131–138. doi: 10.1007/BF00042011

Wanner, O., Eberl, H., Morgenroth, E., Noguera, D., Picioreanu, C., Rittmann, B., et al. (2006). *Mathematical Modeling of Biofilms*, IWA Scientific and Technical Report No. 18, IWA Publishing, 36.

Yang, X., Beyenal, H., Harkin, G., and Lewandowski, Z. (2000). Quantifying biofilm structure using image analysis. *J. Microbiol. Methods* 39, 109–119. doi: 10.1016/S0167-7012(99)00097-4

Yawata, Y., Nguyen, J., Stocker, R., and Rusconi, R. (2016). Microfluidic studies of biofilm formation in dynamic environments. *J. Bacteriol.* 198, 2589–2595. doi: 10.1128/JB.00118-16

Zhao, Q., Liu, Y., Wang, C., Wang, S., and Muller-Steinhagen, H. (2005). Effect of surface free energy on the adhesion of biofouling and crystalline fouling. *Chem. Eng. Sci.* 60, 4858–4865. doi: 10.1016/j.ces.2005.04.006

Zwietering, M. H., Jongenburger, I., Romboust, F. M., and van 't Riet, K. (1990). Modeling of the bacterial growth curve. *Appl. Environ. Microbiol.* 56, 1875–1881.

Conflict of Interest Statement: The authors declare that the research was conducted in the absence of any commercial or financial relationships that could be construed as a potential conflict of interest.

The reviewer VD and handling editor declared their shared affiliation.

Copyright © 2018 Grzegorczyk, Pogorzelski, Pospiech and Boniewicz-Szmyt. This is an open-access article distributed under the terms of the Creative Commons Attribution License (CC BY). The use, distribution or reproduction in other forums is permitted, provided the original author(s) and the copyright owner(s) are credited and that the original publication in this journal is cited, in accordance with accepted academic practice. No use, distribution or reproduction is permitted which does not comply with these terms.

frontiers in Marine Science

ORIGINAL RESEARCH
published: 13 September 2018
doi: 10.3389/fmars.2018.00287

Long-Term Mean Circulation of the Baltic Sea as Represented by Various Ocean Circulation Models

Manja Placke[1], H. E. Markus Meier[1,2], Ulf Gräwe[1], Thomas Neumann[1], Claudia Frauen[1] and Ye Liu[2]*

[1] *Department of Physical Oceanography and Instrumentation, Leibniz Institute for Baltic Sea Research Warnemünde, Rostock, Germany,* [2] *Department of Research and Development, Swedish Meteorological and Hydrological Institute, Norrköping, Sweden*

The skill of the state-of-the-art ocean circulation models GETM (General Estuarine Transport Model), RCO (Rossby Centre Ocean model), and MOM (Modular Ocean Model) to represent hydrographic conditions and the mean circulation of the Baltic Sea is investigated. The study contains an assessment of vertical temperature and salinity profiles as well as various statistical time series analyses of temperature and salinity for different depths at specific representative monitoring stations. Simulation results for 1970–1999 are compared to observations from the Baltic Environmental Database (BED). Further, we analyze current velocities and volume transports both in the horizontal plane and through three transects in the Baltic Sea. Simulated current velocities are validated against 10 years of Acoustic Doppler Current Profiler (ADCP) measurements in the Arkona Basin and 5 years of mooring observations in the Gotland Basin. Furthermore, the atmospheric forcing datasets, which drive the models, are evaluated using wind measurements from 28 automatic stations along the Swedish coast. We found that the seasonal cycle, variability, and vertical profiles of temperature and salinity are simulated close to observations by RCO with an assimilation setup. All models reproduce temperature well near the sea surface. Salinity simulations are of lower quality from GETM in the northern Baltic Sea and from MOM at various stations. Simulated current velocities lie mainly within the standard deviation of the measurements at the two monitoring stations. However, sea surface currents and transports in the ocean interior are significantly larger in GETM than in the other models. Although simulated hydrographic profiles agree predominantly well with observations, the mean circulation differs considerably between the models highlighting the need for additional long-term current measurements to assess the mean circulation in ocean models. With the help of reanalysis data ocean state estimates of regions and time periods without observations are improved. However, due to the lack of current measurements only the baroclinic velocities of the reanalyses are reliable. A substantial part of the differences in barotropic velocities between the three ocean models and reanalysis data is explained by differences in wind velocities of the atmospheric forcing datasets.

Keywords: Baltic Sea, ocean circulation model assessment, hydrographic conditions, mean circulation, current velocity measurements

OPEN ACCESS

Edited by:
Laura Tuomi,
Finnish Meteorological Institute, Finland

Reviewed by:
Lígia Pinto,
Instituto Superior Técnico, Universidade de Lisboa, Portugal
Ivica Vilibic,
Institute of Oceanography and Fisheries, Croatia

****Correspondence:***
Manja Placke
manja.placke@io-warnemuende.de

Specialty section:
This article was submitted to Coastal Ocean Processes, a section of the journal Frontiers in Marine Science

Received: *25 April 2018*
Accepted: *27 July 2018*
Published: *13 September 2018*

Citation:
Placke M, Meier HEM, Gräwe U, Neumann T, Frauen C and Liu Y (2018) Long-Term Mean Circulation of the Baltic Sea as Represented by Various Ocean Circulation Models. Front. Mar. Sci. 5:287. doi: 10.3389/fmars.2018.00287

INTRODUCTION

Understanding of ocean climate requires, *inter alia*, knowledge of long-term variability in transports of volume, heat, salt, and matter by highly varying currents. The Baltic Sea as a semi-enclosed sea in Northern Europe covers an area of approximately 420,000 km^2 and is subdivided into several basins (see **Figure 1**) which formed after the last glaciation. With an average depth of only 54 m the Baltic Sea is strongly responding to atmospheric influences. It is characterized by an intense freshwater supply from the difference between precipitation and evaporation over the sea surface and the inflow from a variety of surrounding rivers. For the period 1970 to 1999 the total runoff into the Baltic Sea including Kattegat amounts to 15,500 m^3 s^{-1} (calculated from Meier and Döscher, 2002, c.f. Bergström and Carlsson, 1994) with an error of about ± 600 m^3 s^{-1} (Omstedt and Nohr, 2004). Another significant feature are salt water exchanges with the World Ocean via the North Sea in the west. This leads to a gradient in salinity from west to northeast and hence strong stratification in the Baltic Sea interior. Atmospheric winds strongly influence both salt water inflows into this very shallow and tide-less sea and coastal upwelling. In turn, precipitation and wind depend on the large-scale atmospheric circulation which is characterized by, e.g., the North Atlantic Oscillation (NAO) and related storm tracks.

The first diagnostic model of the horizontal summer circulation in the Baltic Sea which based upon the geostrophic balance was applied by Sarkisyan et al. (1975). With the help of a three-dimensional (3D) circulation model based upon the primitive equations Lehmann and Hinrichsen (2000) calculated the mean circulation and its stability during four consecutive years from 1992 to 1995. Despite the large variability in atmospheric forcing, like wind and sea level pressure, they found rather stable annual mean circulation patterns with only some inter-annual variations in the magnitude of the basin-wide cyclonic gyre transports.

Also with diagnostic models Stigebrandt (1987) and Elken (1996) calculated the interleaving of saline water into the eastern Gotland Basin deep water. They found maxima in 60–65 and 90–110 m depth, respectively, indicating small- and medium-size inflows ventilating the halocline and a secondary maximum at the bottom of the Gotland Basin indicating Major Baltic Inflows (MBIs) (Matthäus and Franck, 1992). Similar results were reported from 3D circulation modeling (Meier and Kauker, 2003). Approximately, these transports below the Ekman layer form the lower branch of the estuarine circulation in the Baltic Sea.

Further analysis of the wind-driven and thermohaline (or estuarine) circulation of the Baltic Sea was performed by Döös et al. (2004), who calculated the overturning stream function on a transect along the axis of the Baltic Sea in temperature, salinity or density coordinates instead of depth and estimated the residence time with Lagrangian particles released in Öresund, Great Belt and at the mouth of the river Neva. According to Döös et al. (2004) the residence time of particles released in the entire water volume of the Baltic Sea amounts to 26–29 years.

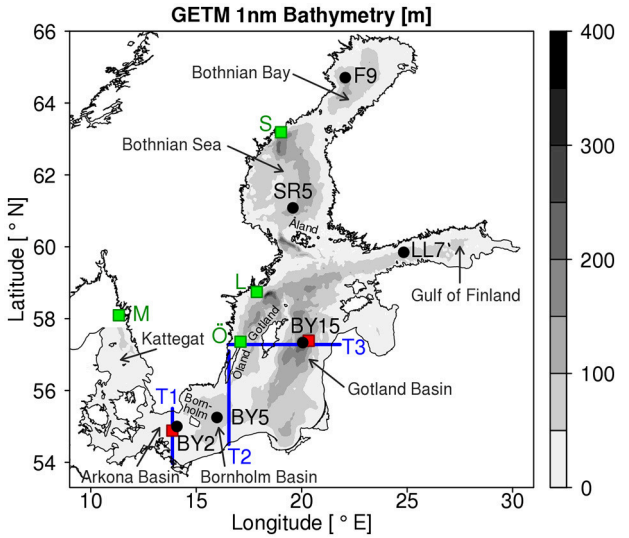


FIGURE 1 | Locations of the used monitoring stations for the assessment of temperature and salinity (black dots) and current velocities (red squares) as well as the analyzed transects (blue lines) in the Baltic Sea. The background color (gray shading) shows the bathymetry [m] from the GETM-1 nm-run. Exemplary stations for atmospheric wind data comparison are shown as green squares. See text for further information.

A useful tool to quantify time scales of water masses and to describe the circulation is the concept of age (e.g., Deleersnijder et al., 2001), that has been introduced into 3D Baltic Sea models, e.g., by Andrejev et al. (2004a,b) for the Gulf of Finland, by Meier (2005, 2007) for the entire Baltic Sea, and by Myrberg and Andrejev (2006) for the Gulf of Bothnia. Using a passive tracer for the age, which is the time elapsed since a water parcel left the sea surface, Meier (2005) quantified the sensitivity of the Baltic deep water ventilation with respect to changes in freshwater supply, wind speed and sea level amplitude in Kattegat. He found that changes of fresh- or saltwater inflow or low-frequency wind longer than the turnover time scale may cause the Baltic Sea to drift into a new state with significantly changed salinity but with only slightly altered stability and deep water ventilation. The vertical overturning circulation is partially recovered. By contrast, long-term changes of the high-frequency wind affect mixing and by that deep water ventilation significantly.

From these earlier studies, Elken and Matthäus (2008) draw a schematic view of the large-scale circulation in the Baltic Sea including entrainment, diffusion and upwelling. However, recent observations suggest that probably the understanding of the overturning circulation has to be revised because lateral mixing and mixing at the sloping bottom are one order of magnitude larger than vertical mixing in the stratified interior (Holtermann and Umlauf, 2012; Holtermann et al., 2012). Hence, mixing parameterizations in ocean circulation models need to be revised, especially if the driving processes are not properly resolved.

The focus of the present study is on the assessment of state-estimates of the Baltic Sea generated by various ocean circulation models with differing vertical coordinates, differing mixing parameterizations as well as distinct atmospheric and

hydrological forcing in the light of how good physical conditions and processes are reproduced and how suitable the models are for detailed investigations in the Baltic Sea region. For this purpose, we have selected three state-of-the-art ocean circulation models, namely the General Estuarine Transport Model (GETM; Burchard and Bolding, 2002; Gräwe et al., 2015, 2016), the Rossby Centre Ocean model (RCO; Meier et al., 2003; Meier, 2007), and the Modular Ocean Model (MOM; Neumann et al., 2002; Griffies, 2004). These models are originally developed for different purposes and have been used previously in numerous process and climate studies for the Baltic Sea and other coastal seas. Their capability to simulate the evolution, variability, and vertical profiles of temperature and salinity as well as mean large-scale circulation patterns and volume transports for the present-day time period from 1970 through 1999 is investigated qualitatively and quantitatively.

In this regard, we assess the model results with respect to observations and also have a closer look into the atmospheric wind forcing which is used for driving the ocean models. Since there are no long-term observational datasets with high spatial and temporal resolution, we rely on existing reanalyses. However, even the resolution of most state-of-the-art reanalysis datasets, like for example ERA-Interim (Dee et al., 2011), is still too coarse to drive high-resolution regional ocean models (e.g., Meier et al., 2011). Therefore, regional climate models are used to perform a downscaling of the global reanalyses (Samuelsson et al., 2011; Geyer, 2014).

Note, that we do not perform a model intercomparison due to the different model setups, grid resolutions, vertical coordinates, parameterizations of sub-grid scale processes as well as atmospheric and hydrological forcing. Hence, we can only speculate about the causes for differences in model results. As all models have been calibrated to monitoring data of temperature and salinity, the aim of the study is to analyze uncertainties in the modeling of the resulting mean circulation, which is of great importance for climate studies. Although model results are strictly speaking not comparable, we will show that nevertheless interesting conclusions for the modeling of the mean circulation can be drawn. Thus, our intention is to compare state estimates, rather than models following Pätsch et al. (2017) for the North Sea or Myrberg et al. (2010) for the Gulf of Finland on shorter time scales. For instance, in the latter study it was concluded that the performance of the models was generally satisfactory although simulated vertical profiles of temperature and salinity were biased compared to observations particularly in the eastern Gulf of Finland.

The manuscript is organized as follows. In section Methods the data base including brief descriptions of the used ocean circulation models and their setups, the observational datasets, the statistical evaluation measures, and the experimental strategy are described. An evaluation of the model simulations together with the observations is presented in section Results. This assessment contains vertical profiles of temperature and salinity at specific representative monitoring stations in the Baltic Sea as well as statistical time series analyses of temperature and salinity at different depths. The dynamics represented by the models are investigated by an analysis of patterns of horizontal surface current and volume transport. Further, mean current velocities and volume transports at selected cross sections perpendicular to the estuarine flow are analyzed and statistics of current velocities at two monitoring stations are performed. That section is completed by an evaluation of the atmospheric wind data. In section Discussion causes for the differences in the mean circulation between the models are discussed. Section Summary, Conclusions, and Outlook summarizes and concludes the present study and reveals prospects for future investigations.

METHODS

Ocean Circulation Models

For the present assessment three state-of-the-art ocean circulation models were investigated. The General Estuarine Transport Model (GETM; Burchard and Bolding, 2002; Hofmeister et al., 2010; Gräwe et al., 2015, 2016) is a three-dimensional baroclinic open source model with hydrostatic and Boussinesq assumptions and was mainly developed for shallow sea applications. GETM uses terrain-following vertically adaptive coordinates and applies an Arakawa C-grid for horizontal coordinates with free-slip lateral boundary conditions. The used mixing parameterization in vertical direction was a two-equation k-ε turbulence model coupled to an algebraic second-moment closure. Lateral diffusion of momentum, salinity and temperature was carried out along the model layers with a harmonic Smagorinsky diffusivity and a turbulent Prandtl number of three. The model version used in this study had 50 vertical layers and used a horizontal resolution of 1 nautical mile (nm). The minimum thickness of vertical layers was limited to 50 cm. The same held for the thickness of the surface layer to have a better representation/computation of the surface fluxes. The model domain comprised the Baltic Sea and was a reduced version of the setup of Gräwe et al. (2015). Atmospheric forcing data were taken from the coastDat2 hindcast dataset (Geyer, 2014), which is a regional downscaling of the global NCEP/NCAR reanalysis (Kalnay et al., 1996) with spectral nudging, and which has a spatial resolution of about 24 km (0.22°). River runoff was based on HELCOM (2015). Output of the present GETM version were daily mean data along selected transects and at individual stations, but also full 3D monthly means of temperature, salinity, currents and heat/salt fluxes. For the present study, data output on the vertically adaptive coordinates had been interpolated to a regular vertical grid with 2 m resolution.

The Rossby Centre Ocean model (RCO) is a Bryan-Cox-Semtner primitive equation circulation model with a free surface (Killworth et al., 1991) and a lateral open boundary in the Kattegat (Meier et al., 2003), which was originally intended for large-scale ocean simulations of the Baltic Sea. Subgrid-scale mixing was parameterized using a turbulence closure scheme of the k-ε type with flux boundary conditions to include the effect of a turbulence enhanced layer due to breaking surface gravity waves and a parameterization for breaking internal waves (Meier, 2001). No explicit horizontal diffusion was applied whereas a harmonic parameterization of the horizontal viscosity was chosen (Meier, 2007). In vertical direction level coordinates were

used and in horizontal direction simulations were based on an Arakawa B-grid with no-slip lateral boundary conditions. In this study simulations were used from a conventional setup (Eilola et al., 2011; Löptien and Meier, 2011) and an assimilation/reanalysis setup by Liu et al. (2017, see also Liu et al., 2013, 2014) which in the following will be referred to as RCO and RCO-A, respectively. In RCO-A all temperature and salinity profiles from the Swedish Ocean Archive (SHARK; http://sharkweb.smhi.se) available during 1970–1999 were assimilated using the ensemble optimal interpolation method (Liu et al., 2017). Detailed numbers of the used observed profiles per sub-basin and year can be found in Liu et al. (2017, their Figure 2). Note, that the data assimilation integrates the information from both model and observations to provide the best estimation of ocean state. But nevertheless RCO-A differs from observations as the used assimilation system is not perfect and measurements for assimilation are neither available continuously nor do they cover the entire model domain. Further, RCO-A utilized the same ocean model as in RCO simulations except that the bathymetry of Słupsk Channel was deeper for RCO-A than for RCO. This methodical deepening in RCO-A served as a tool for optimizing salinity in the central and northern Baltic Sea. However, it turned out that the impact of deepening the Słupsk Channel on salinity was negligible. Both model setups had a vertical resolution of 3 m and a horizontal resolution of 2 nm. As atmospheric forcing regionalized ERA40 data (Uppala et al., 2005) using the Rossby Centre Atmosphere model version 3 (RCA3; see Meier et al., 2011; Samuelsson et al., 2011) were used. Due to the known underestimation of the wind speed in RCA3 compared to observations the simulated wind speed was corrected using the gustiness of the wind (Höglund et al., 2009; Meier et al., 2011). The river runoff was based on Bergström and Carlsson (1994). The data used here had a two-daily time resolution.

The Modular Ocean Model (MOM version 5.1) is a circulation model which was also developed for large-scale ocean simulations (e.g., Pacanowski and Griffies, 2000; Griffies, 2004) and had been adapted to the Baltic Sea with an explicit free surface, an open boundary condition with respect to the North Sea, and freshwater riverine input (e.g., Neumann et al., 2017). The used mixing parameterizations are the K profile parameterization (KPP; Large et al., 1994) in vertical direction and the Smagorinsky scheme (Smagorinsky, 1963) in horizontal direction. MOM used vertical level coordinates on z*-layers and an Arakawa B-grid in the horizontal plane with no-slip lateral boundary conditions. In this study the horizontal resolution was 3 nm and the vertical layer thickness varied between 0.5 m at the surface and about 2 m at depths greater than approximately 50 m. Similar as in the GETM simulations, coastDat2 data were taken as atmospheric forcing and HELCOM data as river runoff data. The original time resolution of the data at single stations was hourly. Full 3D data fields had monthly resolution.

For a consistent assessment the different horizontal and vertical grid resolutions of the used ocean models needed to be considered carefully. In order to evaluate wind-driven and baroclinic circulation patterns and volume transports as well as the bathymetry of the entire Baltic Sea, we used a uniform horizontal grid resolution of 2 nm for all models, i.e., current velocities from RCO simulations remained on their original grid, whereas velocities simulated by GETM and MOM were interpolated to that grid. The calculation of the volume transports was then done by multiplying the velocities and the interpolated velocities, respectively, by the zonal and meridional distances of the 2-nm grid. Differences of horizontal surface current patterns between RCO-A and each of the other models were determined by subtracting the magnitudes of the respective velocity vectors. For the analysis of zonal or meridional currents through transects we interpolated current speeds simulated by MOM on z*-layers to a regular vertical resolution of 2 m. For RCO in both setups and GETM with their regular vertical grids no adjustment was needed.

Observations

Temperature and Salinity

For assessing the physical conditions simulated by the selected ocean circulation models we took the Baltic Environmental Database (BED; http://nest.su.se/bed) of the Baltic Nest Institute, Stockholm, into account which is a collection of quality controlled hydrographic and biogeochemical data around the Baltic Sea. In the present study post-processed monthly averages were used which cover the time period from 1970 to 2008 (Gustafsson and Rodriguez-Medina, 2011). These data were available every 5 m near the surface, every 10 m between 20 and 100 m depth, and for stations reaching even deeper data were predominantly available every 25 m. At these standard depths observations of temperature, salinity, and many other parameters were gathered which lie between 1 m above and 1 m below that depth. For the present study we considered data from the monitoring stations BY2 in the Arkona Basin (55.0°N, 14.1°E), BY5 at Bornholm Deep (55.3°N, 16.0°E), BY15 at Gotland Deep (57.3°N, 20.0°E), LL7 in the Gulf of Finland (59.9°N, 24.8°E), SR5 in the Bothnian Sea (61.1°N, 19.6°E), and F9 in the Bothnian Bay (64.7°N, 22.1°E). Their locations are illustrated in **Figure 1** as black dots. The selected stations cover conditions in the southern, the central, and the northern Baltic Sea and differ primarily in the influence of salt water inflows, thermal conditions due to insolation, and characteristics of currents. The average numbers of observations per depth used for temperature and salinity at these monitoring stations are ∼1,500 at BY2, ∼4,250 at BY5, ∼1,100 at BY15, ∼640 at LL7, ∼360 at SR5, and ∼300 at F9. A detailed listing of samples per parameter, depth, and station is given in Gustafsson and Rodriguez-Medina (2011). Note, that the observed profiles assimilated into RCO-A are a sub-set of the BED database.

Current Velocity

For the evaluation of simulated current velocities we used measurements which were performed (a) with an Acoustic Doppler Current Profiler (ADCP) at the Arkona monitoring station of the Marine Environment Observation Network (MARNET) and (b) with a subsurface mooring close to Gotland Deep. Their locations are shown as red squares in **Figure 1**. The Arkona station (54.9°N, 13.9°E) is operated since the year 2003 on behalf of the Federal Maritime and Hydrographic Agency of Germany (BSH) by the Leibniz Institute for Baltic Sea Research

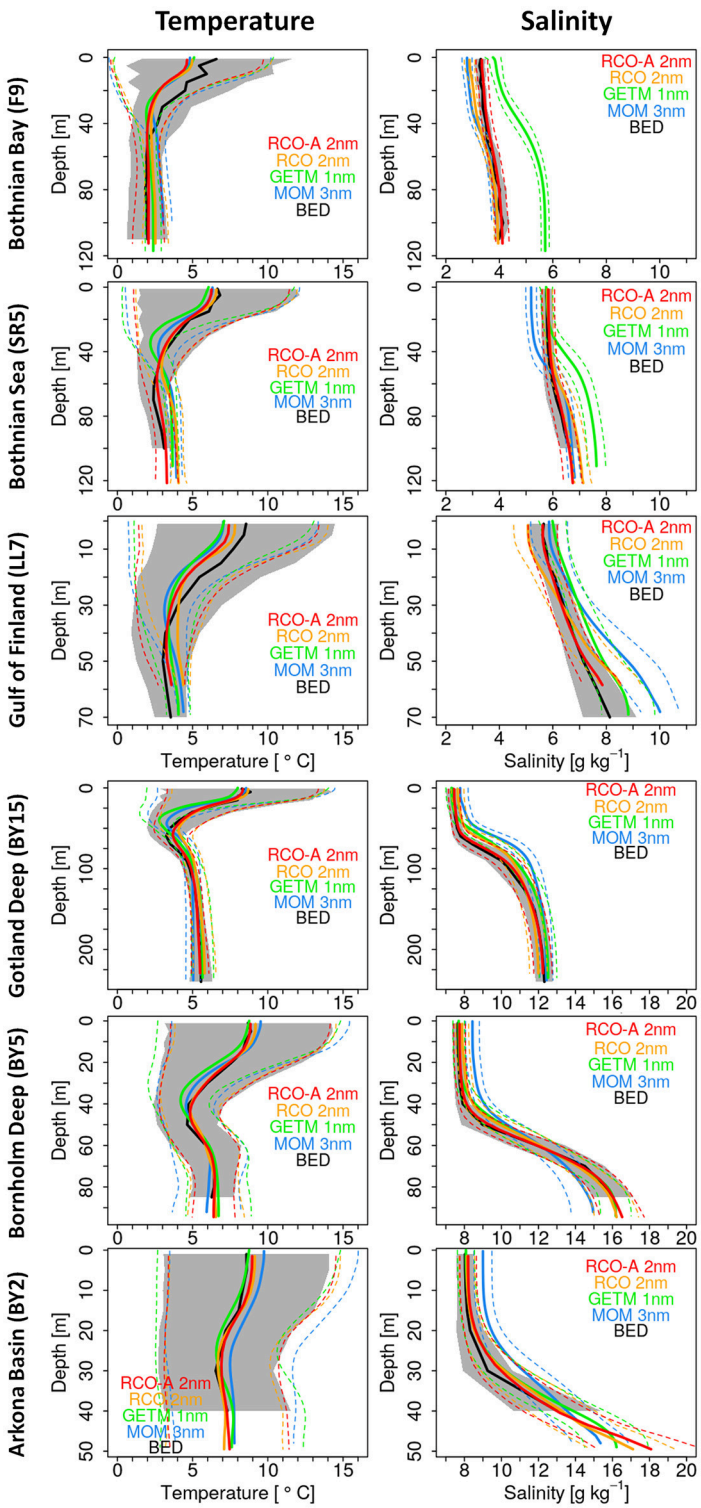


FIGURE 2 | Thirty-year mean vertical profiles of sea temperature (**left**) and salinity (**right**) from BED observation data (black) and the ocean models RCO-A (red), RCO (orange) both with 2 nm horizontal resolution, GETM (green) with 1 nm resolution, and MOM (blue) with 3 nm resolution for the time period from 1970 through 1999. Results for the monitoring stations BY2 in the Arkona Basin, BY5 at Bornholm Deep, BY15 at Gotland Deep, LL7 in the Gulf of Finland, SR5 in the Bothnian Sea, and F9 in the Bothnian Bay are displayed from bottom to top. Mean values are illustrated by solid lines. Standard deviations are indicated by the gray-shaded area for the BED data and by the colored dashed lines for the models. The depth ranges are adjusted to the maximum water depth at each station and therefore differ for the individual stations. Note, that the value range for salinity is different for the southern and the northern stations.

Warnemünde (IOW). It works autonomous and is equipped with a variety of instruments (Krüger, 2000). For the present study ADCP measurements of hourly current velocity were considered for the time period from 2005 through 2014.

These 10 years were also covered by GETM and MOM simulations whereas model runs of RCO-A and RCO were not available during that time. Therefore, a comparable 10-year time period from 1990 through 1999 was used for the statistical analysis of these models. For the comparison with the ADCP data model results had been taken from 3D fields at approximately the same location as the observations. Model results from GETM and MOM were only considered when observations were available. For RCO-A and RCO which do not cover the same time period, we shortened the 10-year time series by the length of the measurement gaps.

The Gotland mooring is deployed northeast of Gotland Deep (57.4°N, 20.3°E) and was equipped with current meters (Aanderaa RCM-7 and/or RCM-9). It measured temperature, current speed, and current direction with a sampling interval of 1 h. For this study we used daily averages of zonal and meridional currents at 204 m depth (Hagen and Feistel, 2004) for the years 2000 until the end of 2004. During these 5 years simulations were available for GETM, MOM, and RCO. Again, for RCO-A, we chose an equivalent 5-year time period, namely from 1995 through 1999, as the simulations of this model finished at the end of 1999. The respective depths from the simulations for the comparison with the mooring measurements were 204 m for GETM, 205 m for MOM, and 205.5 m for RCO-A and RCO. Datasets from the models were taken from 3D fields at the same location as the observations for GETM, RCO-A, and RCO. As the bathymetry in MOM is shallower than in the other models at the location of the mooring, the next wet grid point further west from the mooring was chosen which is located at 20.2°E.

Wind Velocity

For the estimation of how close the two atmospheric wind forcing datasets RCA3-ERA40 and coastDat2 are to reality, we compared them to wind measurements from 28 automatic stations along the Swedish coast for the time period from 1996 through 2008 (Höglund et al., 2009). The observations were available as hourly 10-minute averages. The temporal resolution of CoastDat2 was hourly whereas RCA3-ERA40 had only 3-hourly resolution. Hence, for a direct comparison of forcing and measured data, daily averages had been computed for the three datasets. In order to compare the station-based observations to the gridded reanalysis datasets, the nearest grid point away from land had been manually selected from the models for each station. Exemplary mean annual cycles of wind speed were investigated at the stations Skagsudde at the northern Bothnian Sea coast (63.2°N, 19.0°E), Landsort at the northwestern central Baltic coast (58.7°N, 17.9°E), Ölands Norra Udde at the northern tip of the island Öland (57.4°N, 17.1°E), and Måseskär at the eastern coast of the Skagerrak (58.1°N, 11.3°E). Their locations are shown in **Figure 1** as green squares with abbreviations S (Skagsudde), L (Landsort), Ö (Ölands Norra Udde), and M (Måseskär).

Evaluation Measures

Taylor Diagram

The evaluation of simulated temperature and salinity included the use of Taylor diagrams (Taylor, 2001). A Taylor diagram combines standard deviation, Pearson correlation coefficient, and centered root mean square (RMS) difference in a single diagram. The Pearson correlation coefficient represents the similarity in pattern between the simulated and observed time series. It is depicted by straight lines which are related to the azimuthal angle. Values from 0 to 1 stand for no correlation up to 100% accordance. The standard deviation of each model time series was calculated relative to the standard deviation of the observations in order to allow a unified representation of the different model results in one Taylor diagram. This normalized standard deviation is proportional to the radial distance from the origin of the diagram. For results close to the arc with the relation of 1 between the standard deviations of simulated and observed time series, the pattern variations in the model are correct, i.e., they are of similar amplitude as in the observations. The centered RMS difference in the simulated time series is proportional to the distance from the intersection of that arc with the x-axis. A perfect agreement between model results and observations would be located directly at that intersection meaning that the correlation of both time series is highest and the RMS error in the model time series is lowest. For details the reader is referred to Taylor (2001).

Cost Function

As Taylor diagrams do not consider offsets of modeled and observed time series, a cost function as an additional statistical measure for the quality of the simulated results was taken into account. Following Eilola et al. (2011) this cost function (C) was computed for each model (i) from

$$C_i = \left| \frac{M_i - B}{STD} \right| \tag{1}$$

with M_i and B being the monthly mean values of the individual models and of the BED validation data set, respectively, and STD being the standard deviation of the observations. The cost function values were calculated for each depth considered in the Taylor diagrams and assess the correspondence between simulations and observations as follows: $0 \leq C < 1$ represents good quality, $1 \leq C < 2$ represents reasonable quality, and all $C \geq 2$ signify poor agreement. Hence, a good accordance occurs if the long-term mean of a model does not deviate more than plus or minus one standard deviation from the mean of the BED validation data.

Based on the statistical measures which are included in the Taylor diagrams, an extended cost function was computed. Here we took three terms into account for differences between mean values, standard deviations as well as the RMS error

$$CM_i = \frac{1}{3}\left(\left| \frac{M_i - B}{STD} \right| + \left| \frac{STD_i - STD}{STD} \right| + \left| \frac{RMSE_i}{STD} \right| \right) \tag{2}$$

Here, STD_i and $RMSE_i$ are the standard deviation and the centered root mean square error of each model, respectively.

Experimental Strategy

In order to assess the quality of the ocean circulation models RCO (both in a conventional setup and an assimilation setup which is referred to RCO-A), GETM, and MOM (see section Methods) for application in the Baltic Sea, a 30-year time period from 1970 through 1999 was analyzed. We focused on the models' ability to simulate temperature and salinity as realistic as possible when compared to observations gathered in the BED validation dataset. This assessment included the investigation of vertical profiles as well as statistical time series analysis for different depths at certain monitoring stations in the Baltic Sea.

In a further step horizontal patterns of surface current velocities and depth-integrated volume transports as simulated by the different models for the entire Baltic Sea were assessed and compared to the reanalysis RCO-A. We also analyzed the vertical structure of simulated currents through three transects in the Baltic Sea. These transects were located in the Arkona Basin (from 53.8 to 55.5°N, at 13.9°E), at the western entrance of Słupsk Channel (from 54.5 to 57.1°N, at 16.6°E), and in the Gotland Basin (at 57.3°N, from 16.5 to 21.8°E). They are illustrated in **Figure 1** as the blue lines T1, T2, and T3, respectively. The Słupsk transect T2 was exceptional in that its northern region between Sweden and Öland was only an open channel in the GETM simulations such that the northern and southern parts of this transect both contributed to the volume transport. In contrast, in RCO-A, RCO, and MOM the northern and southern part of the Słupsk transect were separated by a land connection between Sweden and the southern part of Öland such that only the southern part contributed to the entire volume transport. Hence, for calculation of the vertical profile of volume transport through T2 the entire transect was considered for GETM, but only the southern part of it for the other models.

Finally, current velocities measured by an ADCP and a mooring at two different monitoring stations were compared to the model results and the atmospheric wind forcing data driving the ocean models were analyzed.

RESULTS

Temperature and Salinity at Monitoring Stations

Mean Profiles

Figure 2 shows the 30-year mean vertical profiles of temperature and salinity with their standard deviations at the six monitoring stations. Mean values and standard deviations were calculated from monthly averages of each year from 1970 through 1999, i.e., 360 data profiles were included for averaging. Mean temperatures at the considered stations cover a range from approximately 2 to 9.5°C with maximum standard deviations of close to 6°C near the sea surface. The temperature at about 0 to 20 m depth is well represented by all models at the stations BY5, BY15, and SR5. There the maximum deviations between each model mean and the observational mean are smaller than 1°C. However, the near-surface temperature fits also well at BY2 for RCO-A, RCO, and GETM whereas it is slightly overestimated by more than 1°C by MOM. At LL7 and F9 the near-surface temperature is underestimated by all models by up to 2°C.

The thermocline stretches on average from 20 to 40–60 m depth depending on each station. For most of the stations, the simulated thermocline by GETM and MOM lies somewhat higher (10 to 20 m closer to the sea surface) than in the BED validation data. Below the thermocline, RCO-A fits almost perfect to the observations at all stations, whereas RCO, GETM, and MOM slightly overestimate temperature by up to 1.5°C at the northern stations. At very large depths (like for BY15 and SR5), all models have standard deviations smaller than 1°C.

The 30-year mean vertical salinity profiles cover a range of approximately 3 to 9 g kg^{-1} at the surface and 4 to 18 g kg^{-1} at the bottom. At most of the stations the standard deviations of the BED data and the model simulations are predominantly much smaller than 1 g kg^{-1}. Exceptions are BY2 and LL7 as well as the bottommost depth range at BY5, where standard deviations are up to 3 g kg^{-1} in maximum. Simulated mean salinity by RCO rarely exceeds the standard deviation of the BED dataset. This also holds for GETM at the southern stations, but at the northern stations GETM partly overestimates the observations by up to 2 g kg^{-1} although the near-surface salinity is well reproduced. MOM salinity simulations deviate more often from the observed means and their standard deviations at all stations with maximum underestimation by 1 g kg^{-1} at SR5 at the surface and maximum overestimation by 2 g kg^{-1} at LL7 near the bottom.

In summary, simulated means by RCO partly exceed the range covered by the standard deviation of the BED validation data. Means simulated by GETM and MOM exceed the BED standard deviations more often than RCO at various depths, but GETM has an overall better agreement with the observations than MOM. The almost perfect agreement between RCO-A and BED profiles at the monitoring locations are expected as the observed profiles which were assimilated into RCO-A are a sub-set of the BED database.

Mean Seasonal Cycle

For Gotland Deep (BY15), which is the second deepest location in the Baltic Sea, we further assessed the model results at the sea surface in detail. **Figure 3** shows the 30-year mean annual cycles of monthly sea surface temperature (SST) and sea surface salinity (SSS) with their standard deviations. The mean temperature stretches from approximately 1–3°C in March to 17–18°C in August. RCO overestimates the mean SST by 0.5 to almost 1.5°C from January to July with the maximum occurring in June. For August to December the RCO simulations are similar to those of RCO-A. GETM and MOM show a different behavior with underestimation of mean temperature by 0.5 to almost 1.5°C from November to March and an overestimation by 0.5–3°C from May to August. Thereby MOM simulations of mean temperature lie almost continuously within the observed standard deviation (except for June) while GETM simulations exceed the observed standard deviation from November to February as well as in June. Largest absolute differences between RCO-A and BED data amount to 0.5°C.

The mean observed SSS shows only a weak annual cycle with values of approximately 7.1–7.6 g kg^{-1} peaking in April

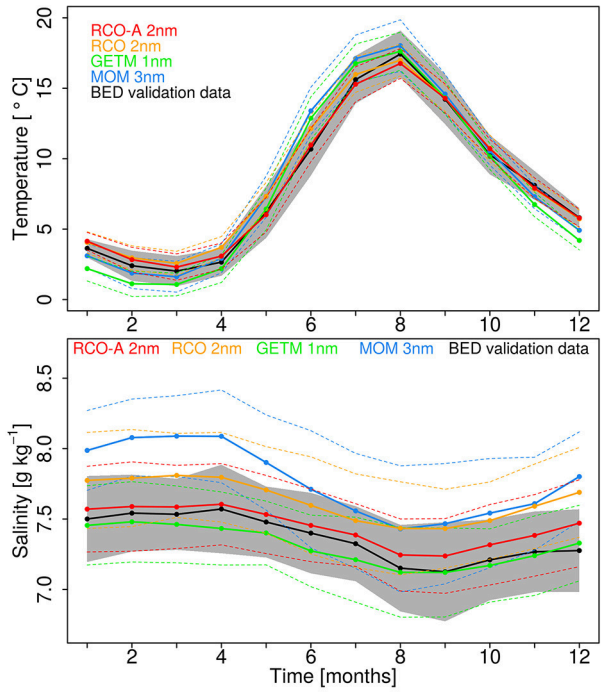


FIGURE 3 | Thirty-year mean annual cycles of monthly sea surface temperature (**top**) and salinity (**bottom**) from BED observation data (black) and the ocean models RCO-A (red), RCO (orange), GETM (green), and MOM (blue) at the monitoring station Gotland Deep (BY15) for the time period from 1970 to 1999. Mean values are illustrated by solid lines. Standard deviations are indicated by the gray-shaded area for the BED data and by the colored dashed lines for the models.

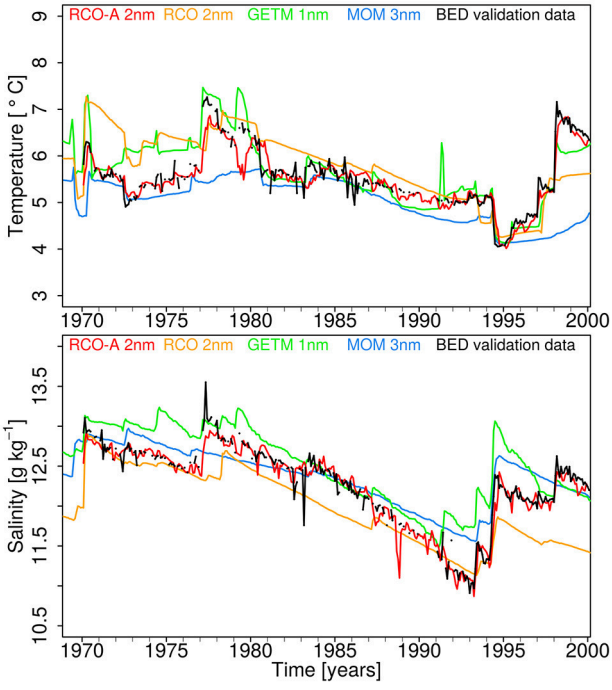


FIGURE 4 | Monthly mean temperature (**top**) and salinity (**bottom**) from BED observation data (black) and the ocean models RCO-A (red), RCO (orange), GETM (green), and MOM (blue) at 225 m depth at Gotland Deep (BY15) for the years from 1970 to 1999.

and lowest values in September. GETM reproduces these values almost perfectly with a minor underestimation of about 0.1 g kg^{-1} from January to August. The mean SSS simulated by RCO shows a comparable annual cycle as in the observations, but with a positive offset of about 0.2–0.4 g kg^{-1}. Hence, the RCO simulations lie approximately at the upper standard deviation of the BED validation dataset or slightly above it. MOM overestimates the mean observed SSS more than RCO, namely by about 0.3–1.1 g kg^{-1}, and shows an annual cycle with stronger magnitudes. The values only lie within the upper observed standard deviation from July to September and otherwise above it. Overall, the standard deviations of the BED validation data and the models are of similar magnitude. SSSs in RCO-A are slightly higher throughout the year by about 0.1–0.2 g kg^{-1} than in the observations.

Interannual Variability

We further analyzed temperature and salinity in the deep water at BY15, which is approximately at 225 m depth in the models. **Figure 4** shows time series of monthly mean values for 1970 through 1999. During this time period the observed bottom temperature varies between about 4 and 7°C with the minimum occurring from 1994 to 1995 and two maxima occurring in 1977 and 1998. The observed deep water salinity is lowest in 1993 with 10.9 g kg^{-1} and highest in 1977 with 13.6 g kg^{-1}. For both temperature and salinity, RCO-A agrees very well with the BED data both in magnitude and variability. Sudden changes in temperature and salinity like for instance at the beginning of 1994 or 1998 are reproduced very realistically.

The other models partly reproduce observed magnitudes very well, but do not show the strong variability which is visible in the BED and RCO-A data. RCO and GETM over- or underestimate temperature at 225 m depth from time to time by up to 1.5°C. MOM underestimates temperature almost continuously by about 0.5 to 2.5°C in maximum. Salinity at 225 m depth is predominantly underestimated by RCO and overestimated by GETM and MOM with maximum deviations from the observations of about 1 g kg^{-1}. The best accordance of models and observations occurs in the time period from 1983 through 1986 where GETM and MOM simulate the observed salinity decrease precisely.

Statistical Evaluation

In order to assess the capability of the single models to simulate the temporal evolution of temperature and salinity at various depths at each monitoring station within the 30-year time period, we applied Taylor diagrams and cost functions. The Taylor diagrams for temperature in **Figure 5** show an overall similar distribution of near-surface values which lie accumulated close to the brown reference point (which has a normalized standard

deviation of 1 and a correlation of 100%). This indicates the high quality of all simulations near the sea surface. The correlations of the SST time series even lie in general between 95 and 98%, the RMS errors are smaller than 0.3, and the normalized standard deviations for SST are closest to 1 at BY2, BY5, LL7, and F9.

At larger depths the temperature correlations generally become worse and show a larger spread around the solid black arc, which represents a normalized standard deviation of 1. Moreover, the model results partly also show RMS errors greater than 1. The highest correlations always occur for RCO-A, the lowest predominantly for GETM or MOM.

The good reproduction of the near-surface temperature simulations is supported by the cost function in **Figure 6**. For all models and at all stations, the temperature cost function values at 0, 15, and 30 m depth lie between 0 and 1, which represents good quality. At larger depths the different capabilities of the individual models to simulate temperature become obvious. RCO-A has overall very low cost function values between 0 and 0.5, which emphasizes the excellent quality of this reanalysis dataset. For RCO, GETM, and MOM the temperature cost function below 30 m depth lies mainly between 0 and 1 and maximizes for all models at 80 m depth at BY15 and SR5. There, values are partly up to 2, which still represents reasonable quality.

For salinity the Taylor diagrams and cost function values reveal stronger differences between the assessed models. RCO-A stands out at almost all stations with highest correlations over all depths and the smallest spread of the values around the normalized standard deviation of 1. The respective cost function values are predominantly smaller than 0.5, which underlines the very good accordance of reanalyzed salinity in RCO-A with the BED dataset.

The statistics of the salinity simulations by RCO and GETM are almost comparable to each other with RCO revealing an overall slightly better quality than GETM. Their correlations lie predominantly between 50 and 90%. Most deviations from the normalized standard deviation of 1 are about ± 0.25 and RMS errors lie between 0.4 and 0.9. The cost function values lie predominantly between 0 and 1.5, but also reveal some shortcomings of these two models in simulating salinity at certain depths and stations.

Compared to the other models, salinity is represented worst by MOM. This arises from the predominantly low correlations in the Taylor diagrams (which mainly lie below 80%), the strong deviations from the normalized standard deviation of 1 (values up to about 0.7), and the high RMS errors (0.5 up to 1.3). Similarly, the cost function shows poor agreement (values greater than 2) at a variety of depths for the six monitoring stations. An interesting feature is that salinity simulations by MOM seem to be better at larger depths than toward the surface.

The above findings are also confirmed by the mean cost function value CM over all stations and all depths for temperature and salinity (Equation 2, see **Table 1**). Also for this mean cost function RCO-A reveals lowest values. RCO and GETM are mid-table and MOM reveals highest values and hence lowest quality. Overall, the mean cost function values for temperature have a smaller spread than those for salinity for the three model simulations and the reanalysis.

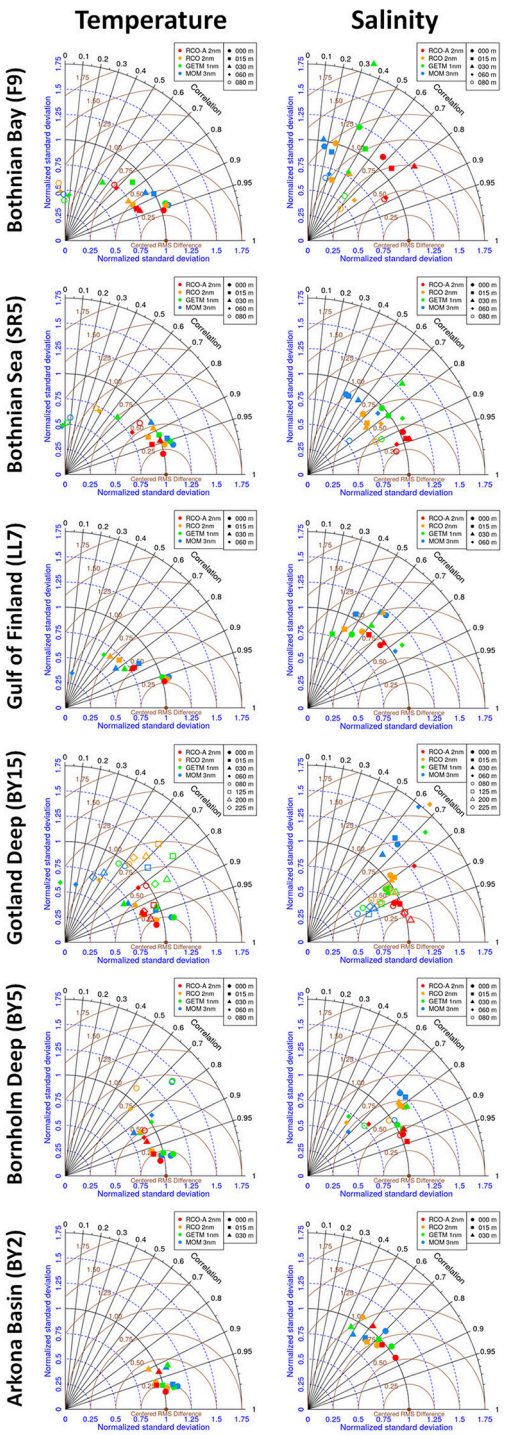


FIGURE 5 | Taylor diagrams derived from monthly time series of sea temperature (**left**) and salinity (**right**) from 1970 to 1999 at particular standard depths at BY2 in the Arkona Basin, BY5 at Bornholm Deep, BY15 at Gotland Deep, LL7 in the Gulf of Finland, SR5 in the Bothnian Sea, and F9 in the Bothnian Bay. Correlation, normalized standard deviation, and centered RMS difference of the simulated time series from the ocean models RCO-A (red), RCO (orange), GETM (green), and MOM (blue) compared to the BED observation data are shown. Different plotting symbols refer to the single depths. See text for more details.

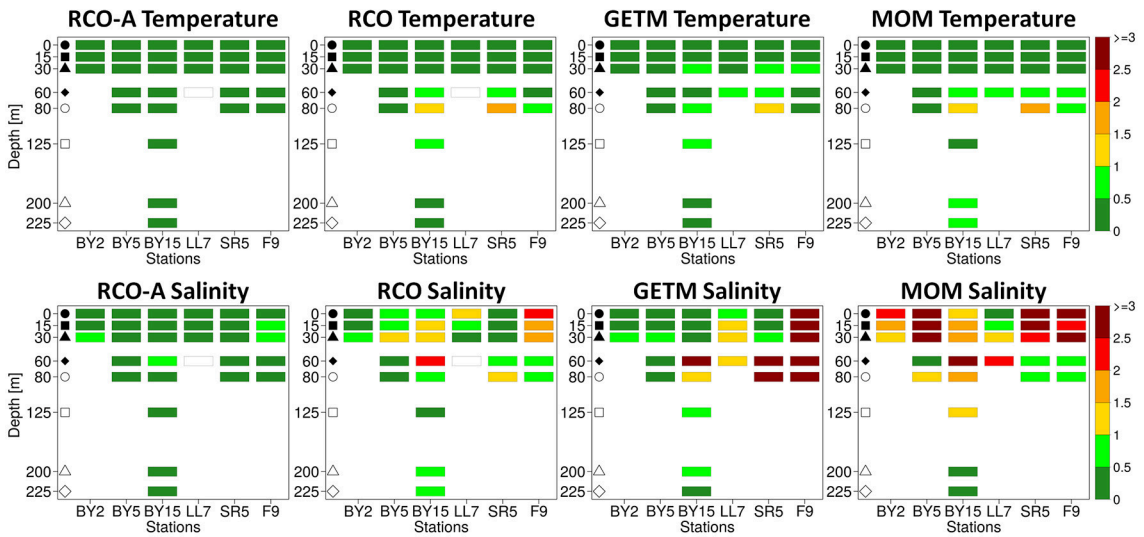


FIGURE 6 | Cost function values derived from monthly time series of sea temperature (**top**) and salinity (**bottom**) from 1970 to 1999 at the six monitoring stations BY2, BY5, BY15, LL7, SR5, and F9. Results from the ocean models RCO-A, RCO, GETM, and MOM (from left to right) compared to the BED observation data are shown at the same depths as illustrated in the Taylor diagrams in **Figure 5**. The symbols in the left part of each diagram refer to the depth-dependent plotting symbols from the Taylor diagrams. Blank bins for RCO-A and RCO at LL7 and 60 m depth are due to missing data of these models at this location. See text for more details.

TABLE 1 | Mean cost function values CM for temperature and salinity determined from Equation 2 for the ocean models RCO-A, RCO, GETM, and MOM.

	RCO-A	RCO	GETM	MOM
Temperature	0.39	0.46	0.48	0.51
Salinity	0.45	0.64	0.90	0.96

Mean Circulation

Horizontal Surface Current Patterns

For the assessment of the mean circulation of the entire Baltic Sea there currently exists still no comprehensive data product from measurements which could be involved. Therefore, we chose RCO-A with assimilated data as a reference for the following analyses even though this model does not reflect the true reality. Differences between model results which arise in the following underline the need for more long-term and large-scale current measurements. **Figure 7** shows the 30-year mean values of the surface current velocity averaged over the upper 10 m and of the volume transport integrated over the whole depth range (surface to bottom) as well as the used bathymetry of RCO-A. For the other models differences of these parameters from the results of RCO-A are illustrated. Large areas of the Baltic Sea surface reveal surface velocities between 0 and 3 cm s^{-1} from RCO-A. Maxima of up to almost 28 cm s^{-1} appear in the Kattegat, values of up to 17 cm s^{-1} and 13 cm s^{-1} in the Øresund and Great Belt, respectively, and there are several channel-like regions throughout the whole Baltic Sea with enhanced current velocities of about 5–8 cm s^{-1} on average. Further conspicuous maxima occur for instance northwest of the island Bornholm, at the southern tip of the island Öland or approximately between Sweden and the Åland Islands.

The difference between the surface current pattern simulated by RCO and that simulated by RCO-A shows—when compared to the other models—relatively small deviations of about ±4 cm s^{-1} in maximum and 0.2 cm s^{-1} on average. GETM and RCO-A surface currents differ stronger throughout the whole Baltic Sea with −12 cm s^{-1} as negative maximum and 25 cm s^{-1} as positive maximum. The average deviation is 0.7 cm s^{-1}. The surface speed difference between MOM and RCO-A reveals predominantly negative values, i.e., MOM simulates mainly smaller current speeds than RCO-A. The maximum negative and positive difference is about −10 cm s^{-1} and 12 cm s^{-1}, respectively, and the average deviation is approximately −0.4 cm s^{-1}.

Horizontal Transport Patterns and Bathymetry

The depth-integrated volume transport simulated by RCO-A has values of 0–6,000 m^3 s^{-1} on average and maximizes in Gotland Basin (values of up to 39,000 m^3 s^{-1}), Bornholm Basin (about 24,000 m^3 s^{-1}), and Arkona Basin (about 14,000 m^3 s^{-1}) with an almost closed counterclockwise gyre each. Further minor maxima appear at Landsort Deep, around the Åland Islands as well as in the northern Bothnian Sea. In general, the patterns of the depth-integrated volume transport for the other models are quite similar in the Gotland Basin but, again, the deviations from RCO to RCO-A are smallest throughout the whole Baltic Sea and largest differences occur for GETM. The pattern of the differences between RCO and RCO-A is comparable to the corresponding pattern seen for their surface velocity. Maximum positive deviations of about 12,000 m^3 s^{-1} and negative deviations of almost −17,000 m^3 s^{-1} occur around Słupsk Channel in the southern Baltic Sea. This is possibly mainly due to the fact that the bathymetry of Słupsk Channel is

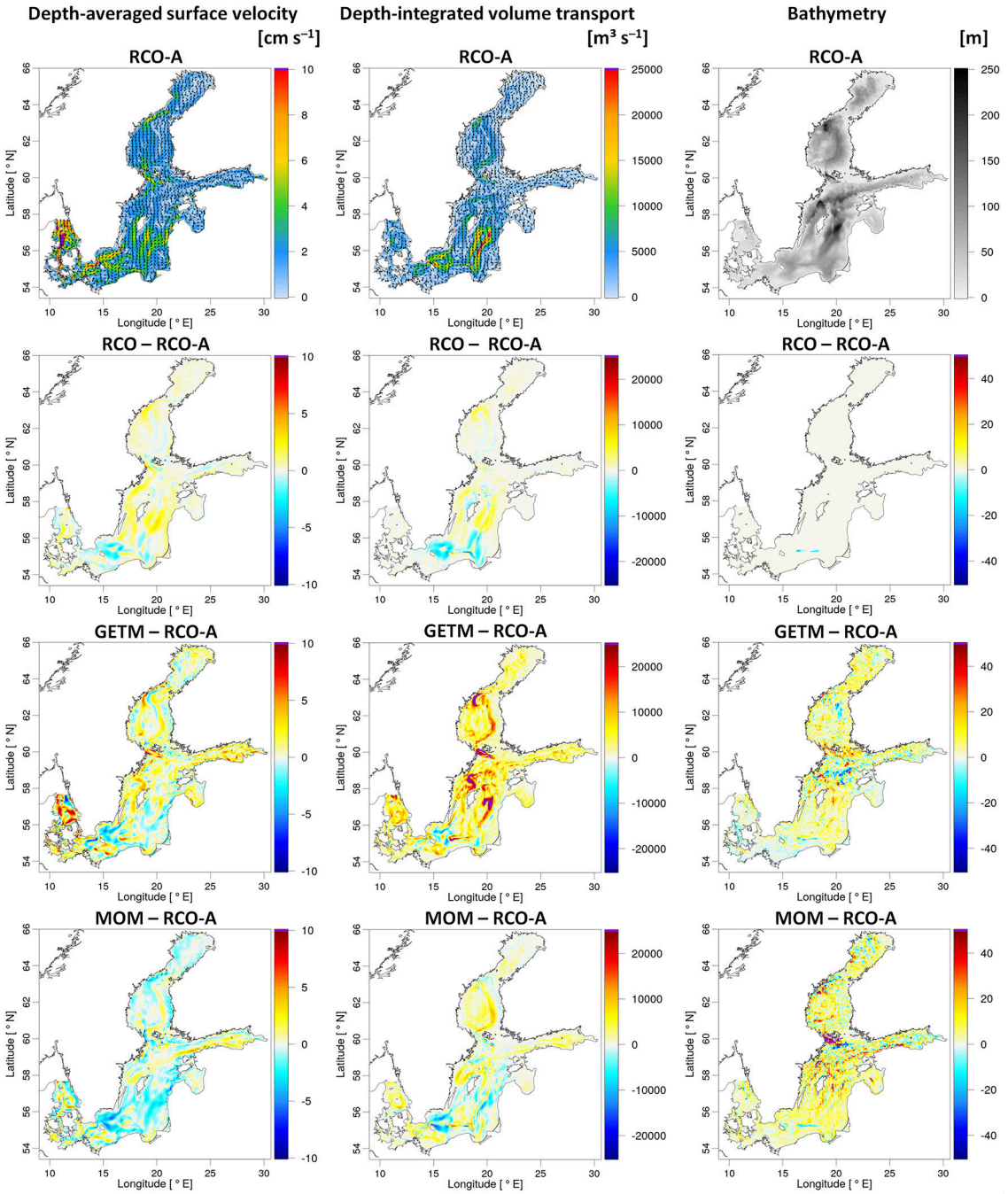


FIGURE 7 | Thirty-year mean surface velocity averaged from the Baltic Sea surface down to 10 m depth (**left**) and volume transport integrated from the surface to the bottom (**middle**) as well as the used model bathymetry (**right**) for the years 1970 through 1999. In the top panels absolute values from the model RCO-A are displayed. Arrows show the direction of velocity and transport, respectively, at every 5th model grid point. The panels below show the differences of the individual models RCO, GETM, and MOM from RCO-A, respectively. Values exceeding the maximum positive plotting range are drawn in purple.

deeper for RCO-A than for RCO (see **Figure 7**). On average, the basin wide deviation of the depth-integrated volume transport of RCO-A and RCO is zero.

The depth-integrated volume transport simulated by GETM is significantly higher than that simulated by RCO-A. On average, the deviation is almost 4,000 $m^3\ s^{-1}$ throughout the whole Baltic Sea. Most negative deviations occur in Bornholm Basin with values of up to −13,000 $m^3\ s^{-1}$. The strongest positive deviations are found at Landsort Deep (∼ 94,000 $m^3\ s^{-1}$), between Sweden and the Åland Islands (∼ 80,000 $m^3\ s^{-1}$), in the northern

Bothnian Sea ($\sim$ 52,000 m^3 s^{-1}), at Gotland Deep ($\sim$ 42,000 m^3 s^{-1}), and at the northern edge of Kattegat ($\sim$ 30,000 m^3 s^{-1}). For MOM the deviations to RCO-A are again smaller than those from GETM to RCO-A with an average value of about 600 m^3 s^{-1}. Most of the negative deviations occur in Bornholm Deep (maximizing in about $-23{,}000$ m^3 s^{-1}) as well as in Gotland Basin. Positive deviations are found throughout the whole Baltic Sea and maximize in the Bothnian Sea, between Sweden and Gotland and at Słupsk Channel.

Local differences of depth-integrated volume transport do not necessarily result from differences in bathymetries. A direct coherence of bathymetry and volume transport occurs obviously along Słupsk Channel where volume transports simulated by RCO, GETM, and MOM differ from RCO-A. However, many other regions throughout the entire Baltic Sea which are characterized by strong volume transport differences coincide with small differences between model bathymetries (e.g., in Bornholm Basin, central Gotland Basin or in the southeastern Bothnian Sea). The other way around, big differences in the bathymetries of GETM or MOM versus RCO-A which occur for instance in the northeastern Gotland Basin and toward the Gulf of Finland are not characterized by very strong volume transport differences. And in the region between Sweden and the Åland Islands the bathymetry difference between GETM and RCO-A is smaller than that between MOM and RCO-A, but GETM shows much higher volume transport differences to RCO-A than MOM. Hence, the used bathymetries are individually adapted to the numerical solvers of each model for optimal representation of the physical conditions, and their patterns do not necessarily affect local current or volume transport patterns as these are compensated by the large-scale circulation.

Currents Through Transects

Figure 8 shows the mean current velocities through the three transects as simulated by the ocean circulation models. Positive values indicate eastward currents for Arkona and Słupsk transect

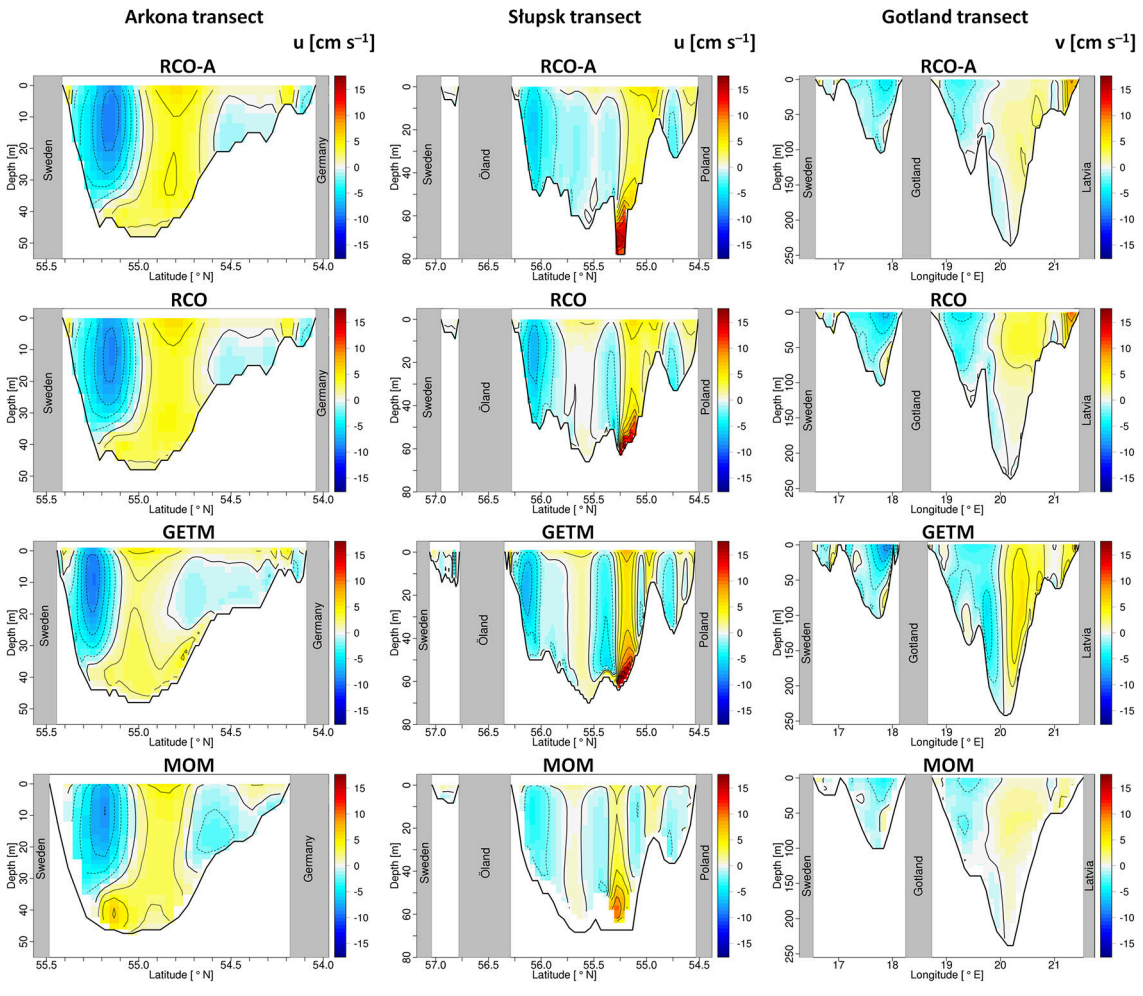


FIGURE 8 | Mean current velocities orthogonal through Arkona transect (**left**), Słupsk transect (**middle**), and Gotland transect (**right**) for the time period from 1970 to 1999 for the models RCO-A, RCO, GETM, and MOM. Positive values denote eastward velocity for Arkona and Słupsk transect and northward velocity for Gotland transect. Isolines are drawn every 2 cm s^{-1} (solid for positive values, dashed for negative values). Plotting range is ± 17.3 cm s^{-1}. Note, that the shown transects cover different depth ranges.

(T1 and T2 in **Figure 1**) and northward currents for Gotland transect (T3 in **Figure 1**), respectively.

The 30-year mean zonal velocity through the Arkona transect as simulated by all models shows the gyre-like structure which was already seen in the surface velocity and the depth-integrated volume transport in **Figure 7**. The current is westward directed (negative) in the northern part of the transect maximizing approximately between 5 and 15 m depth at about -9 cm s^{-1} for RCO-A, RCO, and GETM and at about -7 cm s^{-1} for MOM. In the middle part of the transect the current is eastward directed (positive) and almost constant over depth. However, for RCO-A and RCO a maximum of approximately 5 cm s^{-1} appears at the surface whereas MOM simulates a maximum of almost 7 cm s^{-1} below the westward directed current in the north. The southern region of the Arkona transect is characterized by a near-surface eastward current above a westward current as well as a westward coastline-current. Overall, the currents in the southern region are weaker than the gyre in the north. The center of this gyre lies at about 55 °N for RCO-A, RCO, and MOM, whereas it is slightly shifted toward the north by GETM.

The zonal current through Słupsk transect as simulated by RCO-A is predominantly westward (negative) in the northern part with a maximum of approximately -6 cm s^{-1} near Öland. Approximately in the center between Öland and Poland currents are eastward (positive) with a strong maximum of almost 16 cm s^{-1} within the pronounced Słupsk Channel (which has a depth of almost 80 m for RCO-A) and a weaker maximum of almost 6 cm s^{-1} at the surface. Toward Poland the currents alternate. Principally, RCO, GETM, and MOM show comparable current patterns, but their westward directed northern current is interrupted by a weak eastward current at about 55.7°N each. RCO and GETM simulate partly stronger magnitudes than RCO-A and have their maximum at the entrance of the Słupsk channel between 50 and 60 m depth. MOM has the weakest current velocities throughout the whole Słupsk transect.

Meridional currents through Gotland transect reveal the gyre around Gotland Deep. Between Sweden and Gotland all models simulate predominantly southward (negative) current velocities, which are strongest for GETM (-9 cm s^{-1}) and RCO (-7 cm s^{-1}) and weakest for MOM (-3 cm s^{-1}). Between Gotland and Latvia the gyre structure is visible. In principle, the patterns simulated by RCO-A, RCO, and MOM are similar with MOM having the weakest magnitudes. GETM simulates the gyre with a slight shift to the east (such that it is centered directly at Gotland Deep over the whole depth range) and with stronger current velocities than the other models (values up to about ± 5 cm s^{-1}).

Volume Transports Through Transects

Figure 9 shows the simulated 30-year mean vertical profiles of volume transport per depth interval which had been integrated horizontally along the three transects each. For the Arkona transect the vertical profiles of all models are very similar with maximum outflows from the Baltic Sea of about $-1{,}900$ to $-1{,}700$ m^2 s^{-1} between 10 and 15 m depth and maximum inflows of about 1,300 to almost 1,600 m^2 s^{-1} at around 40 m depth. Near the sea surface all models simulate inflows into the Baltic Sea with GETM having the strongest magnitudes.

At Słupsk transect the vertical structure of volume transport per depth interval is in principle comparable to that at Arkona transect, but due to the greater depth the maxima are located further down. Hence, the maximum outflow occurs at around 25 m depth for all models. The maximum inflow takes place near the surface as well as between 50 and 60 m depth for RCO, GETM, and MOM, but at about 70 m depth for RCO-A. The corresponding outflow magnitudes reach from almost $-1{,}900$ m^2 s^{-1} for RCO-A to about $-1{,}300$ m^2 s^{-1} for MOM. At the largest depths the inflow maximizes at about 1,600 m^2 s^{-1} for RCO and almost 1,800 m^2 s^{-1} for GETM.

Compared to Arkona and Słupsk transects the mean vertical profiles of volume transport per depth interval at Gotland transect have a different shape. Maximum outflow from the northern Baltic Sea takes place near the sea surface and inflow into the northern Baltic Sea occurs at depths below about 30 m for RCO, GETM, and MOM, but at depths below about 60 m for RCO-A. The maximum outflow ranges from almost $-2{,}200$ m^2 s^{-1} for GETM to about $-1{,}400$ m^2 s^{-1} for RCO-A and RCO. The inflow maximizes at about 300 m^2 s^{-1} for RCO and GETM, almost 400 m^2 s^{-1} for MOM, and over 500 m^2 s^{-1} for RCO-A.

When only the eastern part of the Gotland transect is considered, i.e., the region between Gotland and Latvia, the vertical profiles differ from the profiles for the whole transect between the surface and approximately 110 m depth. Due to the exclusion of the western part of this transect, which is dominated by southward currents and hence outflow (see **Figure 8**), the Gotland East transect is characterized by inflow into the northern Baltic Sea over the whole depth range except for MOM. The stronger volume transport per depth interval between the surface and 50 m depth simulated by RCO-A, RCO, and GETM is due to the enhanced northward current at the eastern coast near Latvia, which is strongest pronounced in RCO near the sea surface. Therefore, RCO maximizes in about 1,200 m^2 s^{-1} at the sea surface. At the same place RCO-A and GETM reveal inflows of about 400–500 m^2 s^{-1} while MOM simulates maximum outflow of about -600 m^2 s^{-1}. The vertical profile of RCO is comparable to that by Meier and Kauker (2003, their Figure 13) even though they used a different horizontal resolution and showed total mean horizontally integrated transports (in m^3 s^{-1}).

Table 2 summarizes the mean total volume transports through the Gotland transect calculated from the vertical profiles shown in **Figure 9** by taking the vertical resolutions of the individual models into account and summing over depth. The outflow above the reversal depth of each profile has comparable values of about $-30{,}000$ m^3 s^{-1} for RCO, GETM, and MOM. In RCO-A a deeper located reversal depth coincides with a higher outflow of about $-36{,}000$ m^3 s^{-1}. The inflow below the reversal depth is again similar for RCO, GETM, and MOM (approximately 17,000 m^3 s^{-1}), but consequently higher for RCO-A (21,000 m^3 s^{-1}). The corresponding differences of outflow and inflow reveal the total mean volume transport through the Gotland transect which is smallest for MOM ($-12{,}000$ m^3 s^{-1}) and highest for RCO-A ($-15{,}000$ m^3 s^{-1}). In all three models, these numbers are in accordance to the freshwater balance, i.e., the sum of river runoff and precipitation minus evaporation north of the transect T3 equals the net outflow through T3 (**Table 2**) in due consideration

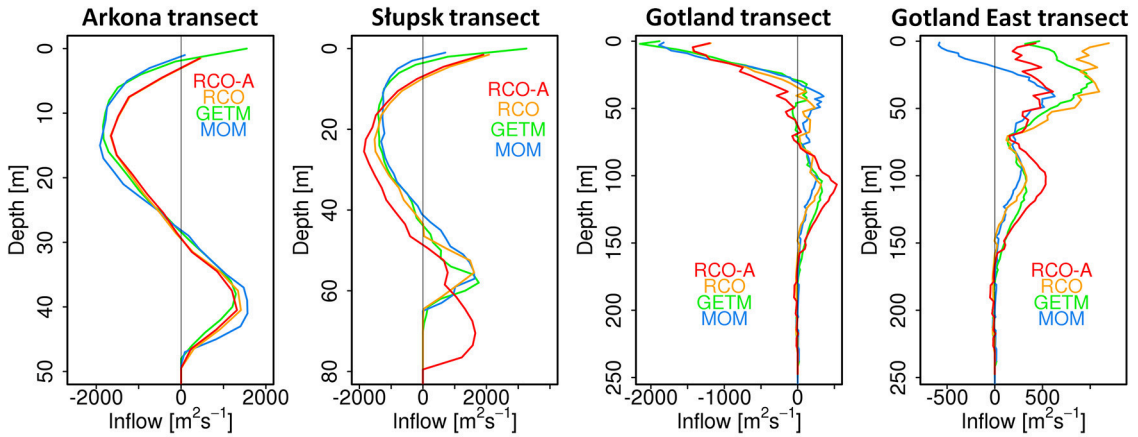


FIGURE 9 | Vertical profiles of horizontally integrated flows per unit depth along Arkona, Słupsk, and Gotland transect as well as along the eastern part of the Gotland transect only (between Gotland and Latvia) as simulated by the ocean models RCO-A (red), RCO (orange), GETM (green), and MOM (blue) for the time period from 1970 to 1999. Note the different depth ranges of the individual transects.

TABLE 2 | Mean volume transports through Gotland transect calculated from the vertical profiles shown in **Figure 9** for the ocean models RCO-A, RCO, GETM, and MOM as well as runoff and precipitation (P) minus evaporation (E) for this transect (numbers rounded to thousands).

	Reversal depth [m]	Outflow above [m^3 s^{-1}]	Inflow below [m^3 s^{-1}]	Net outflow [m^3 s^{-1}]	Runoff [m^3 s^{-1}]	P minus E [m^3 s^{-1}]	Total runoff [m^3 s^{-1}]	Total P minus E [m^3 s^{-1}]
RCO-A	63	−36,000	21,000	−15,000	−12,000	–	−16,000	–
RCO	34	−28,000	15,000	−13,000	−12,000	−1,000*	−16,000	−2,000*
GETM	29	−31,000	17,000	−14,000	−14,000	−1,000	−17,000	−1,000
MOM	30	−30,000	18,000	−12,000	−11,000	−1,000	−15,000	−2,000

*Numbers in the last two columns relate to the entire Baltic Sea including the Kattegat. (*according to Meier and Döscher, 2002. For RCO-A P minus E is not available).*

of the error owing to the rounding of numbers to thousands. However, in RCO-A the freshwater balance might not be closed due to the data assimilation.

Additionally, the 30-year mean depth-integrated volume transport per unit length for the Gotland transect is shown in **Figure 10**. For all models the transport is predominantly southward directed (negative) between Sweden and the western coast of Gotland. The magnitudes for RCO-A, RCO, and GETM are close to each other while MOM simulates a smaller transport. Between the eastern coast of Gotland and Latvia the structure of the gyre is visible with southward transport in the western part and northward transport in the eastern part. Here, the transports differ more for the individual models with strongest magnitudes simulated by GETM and smallest ones by MOM. The results of RCO-A and RCO are similar. Analogous 30-year mean depth-integrated volume transports per unit length for Arkona and Słupsk transects (not shown) reflect the patterns from **Figure 8**, which were described before.

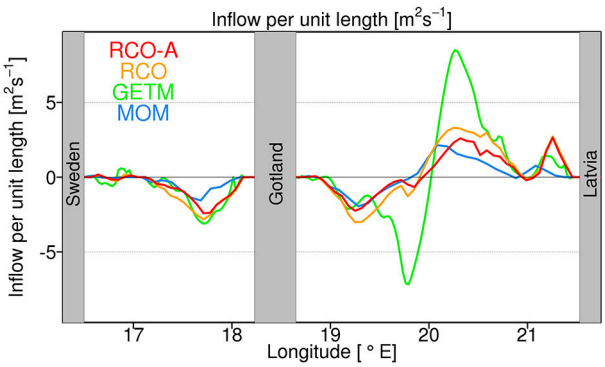


FIGURE 10 | Depth-integrated flows per unit length orthogonal through Gotland transect as simulated by the ocean models RCO-A (red), RCO (orange), GETM (green), and MOM (blue) for the time period from 1970 to 1999.

Evaluation of Simulated Currents

The simulated currents were validated against ADCP measurements in the Arkona Basin (approximately in the center of the Arkona transect T1) and against mooring measurements near Gotland Deep (almost in the center of the eastern part of the Gotland transect T3; see **Figure 1**).

Arkona Basin

The statistics of the ADCP measurements are shown on the left-hand side of **Figure 11** and were based on monthly averages of all

datasets at a depth of 10 m below the surface. The 10-year mean observed zonal current velocity is close to 1.5 cm s^{-1} and has a standard deviation of about ±9 cm s^{-1}. RCO-A, RCO, and MOM simulate a somewhat higher mean zonal current (about 3 cm s^{-1}) and a smaller standard deviation in the same order of magnitude as the mean. For GETM the zonal current at this location in the Arkona Basin varies around zero with a standard deviation of ±5 cm s^{-1}. The relative frequency of the observed and simulated zonal currents shows a good agreement between GETM and the ADCP measurements and clarifies also the similarity of RCO-A, RCO, and MOM with their higher means and smaller spread. Note, that some few ADCP outlier values between 62.5 and 67.5 cm s^{-1} are not shown in the histogram.

The mean meridional current velocities observed and simulated at 10 m depth are more in accordance to each other. The ADCP measurements vary around a mean value of 2 cm s^{-1} with a standard deviation of about ±4 cm s^{-1}. GETM lies very close to these values. MOM shows a similar variation as in the observations, but varies around a mean value of 4 cm s^{-1}. RCO-A and RCO have means of about 2.5 cm s^{-1} with a standard deviation in the order of this mean. The respective relative frequencies reflect the relatively good agreement of the models with the measurements.

Gotland Basin

The statistics of the mooring observations near Gotland Deep shown on the right-hand side of **Figure 11** are also based on monthly averages of all datasets, but at 204 m depth. The 5-year mean zonal current velocities and their standard deviations are very close to zero for both the mooring observations and the model simulations. The small deviation range is reflected by the relative frequency as well. Greater differences between measurements and models occur for the meridional current velocity. From the mooring observations it varies around a mean value of 3 cm s^{-1} with a standard deviation of about ± 2 cm s^{-1}. In contrast, the models simulate again mean values around zero and standard deviations smaller than ±1 cm s^{-1}.

Evaluation of the Atmospheric Wind Data

Finally, the wind velocities of RCA3-ERA40 and coastDat2, which drive the ocean circulation models, were evaluated. The mean statistics over all stations along the Swedish coast which have been considered for this analysis are summarized in **Table 3**. They reveal partly substantial differences between

TABLE 3 | Mean zonal wind speed (u), meridional wind speed (v), and total wind speed (ws) with their standard deviations (σ) for observations, coastDat2, and RCA3-ERA40 dataset as well as mean and root mean square difference (RMSD) between the reanalysis datasets (rea) and the observations (obs) for zonal, meridional, and total wind speed.

	Observations		coastDat2		RCA3-ERA40	
	Mean	**σ**	**Mean**	**σ**	**Mean**	**σ**
u	1.02	3.90	0.98	4.18	1.18	3.73
v	0.66	4.09	0.36	4.33	0.41	3.81
ws	5.81	2.68	5.94	2.89	5.18	2.67
			Mean	**RMSD**	**Mean**	**RMSD**
$u_{rea} - u_{obs}$		–	−0.04	1.99	0.16	2.39
$v_{rea} - v_{obs}$		–	−0.30	2.09	−0.24	2.56
$ws_{rea} - ws_{obs}$		–	0.14	1.86	−0.62	2.26

Calculations are done over all stations for the time period 1996–2008. The unit of all parameters is [m s^{-1}].

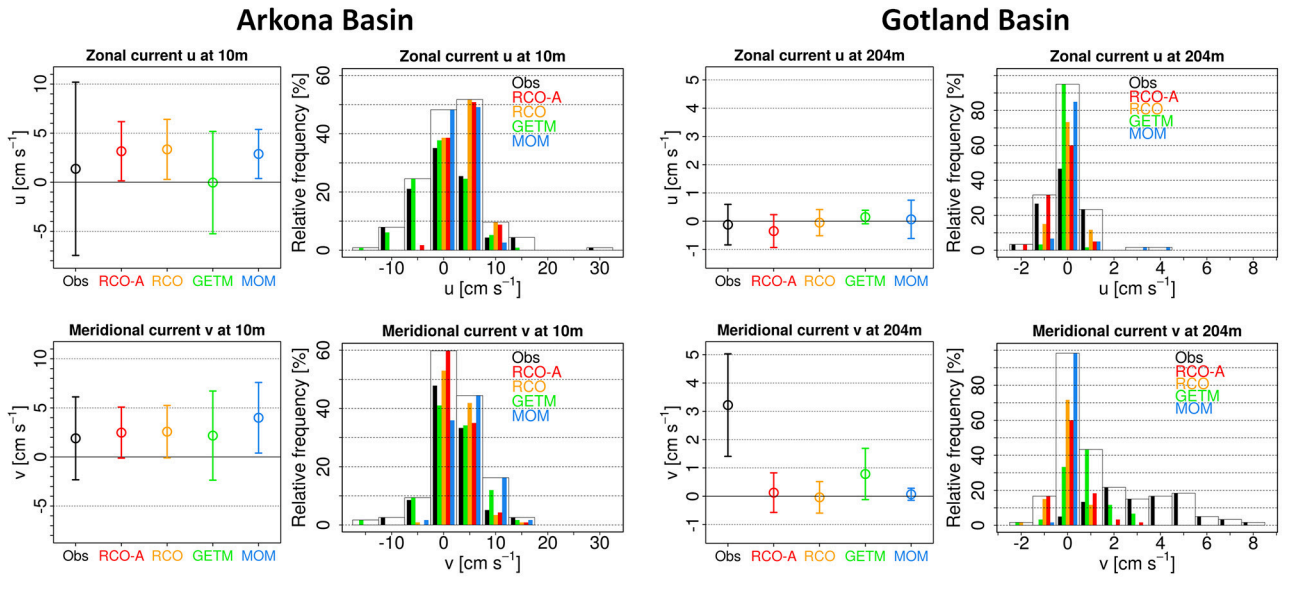


FIGURE 11 | Mean current velocities with their standard deviations as well as relative frequency of these velocities from observations (black) and model simulations (colors) in the Arkona Basin at 10 m depth (**left**) and in the Gotland Basin at 204 m depth (**right**). Results for zonal components are shown in the top panels and for meridional components in the bottom panels. See text for further information.

observations and the forcing data. The mean zonal wind from both reanalysis datasets and the observations is directed eastward and is of the same magnitude. The mean meridional wind is directed northward, but the reanalysis datasets reproduce weaker magnitudes than in the observations. The strongest difference occurs for the mean wind speed, which is slightly overestimated by coastDat2 but largely underestimated by RCA3-ERA40. With some exceptions this also holds true for the individual stations. Also, root mean square differences (RMSDs), both for the wind components and for the wind speed, are larger in the RCA3-ERA40 than in the coastDat2 dataset.

As an example the mean annual cycles of the wind speed at four stations along the Swedish coast are presented in **Figure 12**. At Skagsudde both reanalysis datasets agree well with the observations, but at the other three stations (Landsort, Ölands Norra Udde, and Måseskär) RCA3-ERA40 systematically underestimates the mean wind speed throughout the whole year. CoastDat2 is closer to the observations but also underestimates the mean wind speed at Landsort and Måseskär and overestimates it in autumn and winter at Ölands Norra Udde.

DISCUSSION

In this assessment the best results comparing observed and simulated temperature and salinity profiles are found for RCO-A. However, this finding is not surprising as the reanalysis temperature and salinity observations have been assimilated. The utilized observations are a sub-set of the BED database, that has been used in this study for the evaluation. Nevertheless, RCO simulations are very good even without data assimilation. Compared to models with level coordinates in vertical direction like RCO and MOM, GETM has the advantage of vertically adaptive coordinates, that minimizes spurious numerical mixing across isopycnals (diapycnical mixing) in the ocean interior (Gräwe et al., 2015). This reduced numerical mixing might cause the too shallow thermocline (**Figure 2**). The mixing in the surface well mixed layer is currently too low, which opens the possibility to see effects of additional parameterizations for surface waves effects and Langmuir-circulation. Although numerical mixing is still present in GETM, this mixing might mimic the effects of physical mixing, however, very likely for the wrong reason. Anyhow, this mixing in GETM corresponds better to recent observations than deep water mixing parameterizations used in level coordinate models (Holtermann and Umlauf, 2012; Holtermann et al., 2012, 2014, 2017).

Due to the assimilation of temperature and salinity measurements, we presume that in RCO-A the baroclinic part of the simulated current velocity fields is close to observations and can be used as a reference. However, the barotropic part, which is forced by the curl of the wind stress (calculated from wind velocity) minus the curl of the bottom drag, is not affected by the data assimilation and consequently not constrained by temperature and salinity observations.

In the following, selected hypotheses about the differences in both hydrography and circulation between the models are presented:

1. As all models reproduce temperature much better than salinity, it seems to be easier to calibrate the heat balance of Baltic Sea models than the water balance. However, in detail there are differences between the models. Largest mean biases in temperature are found in GETM perhaps because the parameterizations of the surface heat fluxes are not adopted to Baltic Sea conditions. Smallest biases and the most realistic mean seasonal cycle in temperature are found for RCO, which applies bulk formulae developed from flux measurements from the Baltic Sea region (Meier et al., 2003).
2. Although bottom salinities at Bornholm Deep and Gotland Deep are somewhat better reproduced in GETM than in RCO or MOM (with a more acceptable halocline depth in GETM and RCO than in MOM), in the Bothnian Sea and Bothnian Bay large biases were found in GETM. These problems might be caused by a different type of deep water formation process in the northern Baltic Sea (Bothnian Sea and Bothnian Bay) compared to the Baltic proper (Bornholm Basin and Gotland Basin). In the Baltic proper the deep water is renewed by saltwater intrusions from the North Sea, whereas in the Bothnian Sea and Bothnian Bay deep water might be formed by convection caused by cooling and brine release related to ice formation. Perhaps the present version of GETM with its thermodynamic sea ice model is not yet optimized for the latter process.
3. Mean surface velocities are much stronger in GETM than in the other models. A likely explanation is the zooming of the layers in GETM toward the surface. Here the minimum layer thickness can reach 50 cm, allowing a better representation of the wind shear effect in the surface layer. A further reason might be the larger wind speeds of the atmospheric forcing in GETM at least compared to RCO and RCO-A. Whether the stronger barotropic velocities in GETM are more realistic than in the other models cannot be decided as mentioned above. Since MOM is also driven by coastDat2 winds but simulates a weaker barotropic circulation than GETM, either the bottom drag or the horizontal viscosity together with the lateral drag (no-slip versus free-slip) in MOM is significantly larger than in GETM.
4. We identified several features of the currents differing among the models. For instance, the northward directed coastal current along the eastern Baltic Sea coast is more spatially centered and stronger in RCO and RCO-A than in GETM and MOM. Another detail is the stronger eastward flow through the Słupsk Channel in RCO and GETM than in MOM. Although in RCO-A the western sill of the Słupsk Channel was locally deepened, the results in that region do not differ much between RCO and RCO-A and the change in topography has no larger effect. Further, the barotropic circulation in Arkona Basin is stronger in RCO and RCO-A than in MOM and GETM perhaps because of the differing atmospheric forcing.
5. The vertical overturning or estuarine circulation is stronger in RCO-A than in MOM, GETM, or RCO perhaps because horizontal density gradients in RCO-A are larger than in the other models. The magnitude of the deep water ventilation is considerably affected by the use of data assimilation suggesting that internal pressure gradients still differ substantially among

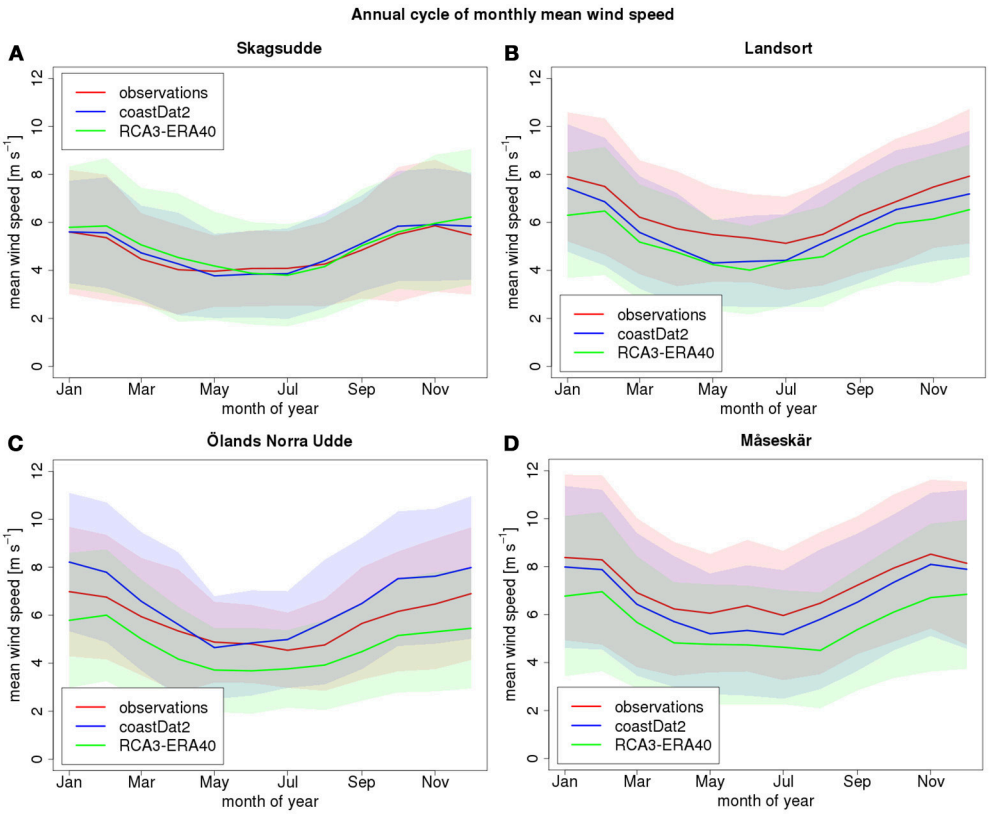


FIGURE 12 | Annual cycle of monthly mean wind speed at selected stations around the Baltic Sea for the observations (red), coastDat2 (blue), and RCA3-ERA40 (green): **(A)** Skagsudde, **(B)** Landsort, **(C)** Ölands Norra Udde, and **(D)** Måseskär. The solid lines indicate the monthly mean and the shading indicates ±1 standard deviation.

the models although at least GETM and RCO show acceptable agreement with observed temperature and salinity profiles at monitoring stations. Hence, a good agreement between model results and observed temperature and salinity profiles measured by Taylor diagrams and cost functions is only a necessary but not a sufficient condition for a realistically simulated thermohaline circulation. Note, that river runoff differs between the models (**Table 2**). For the halocline ventilation the results by RCO-A are close to the results from the diagnostic model by Elken (1996) (see also Meier, 2000, 2005; Meier and Kauker, 2003). Assuming geostrophically balanced currents, Elken (1996) calculated the mean flow east of Gotland between the transport minimum in 60 m depth and the sea bottom. An important question for future research is which data and quality measures are needed to evaluate the performance of climate models with respect to the estuarine overturning circulation properly.

6. The presented version of MOM performed worse in the Baltic proper compared to GETM or RCO/RCO-A. A possible reason might be that the calibration in MOM is less optimized. As both vertical (z-level) and horizontal (Arakawa B-grid) coordinates are similar in MOM and RCO there are no reasons to assume that MOM with the same forcing, model setup, sub-grid scale parameterizations and parameter settings will not perform at least as good as RCO. Earlier simulations suggest that differences due to the horizontal resolution between 1 and 3 nm are less important.

SUMMARY, CONCLUSIONS, AND OUTLOOK

Summary

The present study deals with an assessment of the long-term mean circulation of the Baltic Sea as a classical example of a coastal sea as represented by various ocean circulation models, namely RCO (both in a conventional setup and an assimilation / reanalysis setup which is referred to RCO-A), GETM, and MOM. The capability of these models to represent physical conditions and processes of the Baltic Sea is investigated for a 30-year time period from 1970 through 1999. Simulations of temperature and salinity at monitoring stations are investigated by vertical profiles and statistical time series analysis at various depths taking Taylor diagrams and cost functions into account. As a reference dataset for comparisons post-processed observations of BED are used.

The main result is that observed temperature and salinity data are most realistically reproduced by the RCO-A reanalysis, which holds for temporal evolution, variability, and vertical profiles of

these parameters. GETM and RCO show more deviations from the observations than RCO-A at certain monitoring stations and certain depths, but they still agree better with the BED data than MOM. In general, all models reproduce temperature well between the surface and 20 m depth. Salinity simulations are of predominantly good to reasonable quality for RCO and GETM independently of the depth except for stations which are located far north. The strongest deviations from observations occur for salinity simulated by MOM.

The investigation of the wind-driven circulation for the upper 10 m below the sea surface and of the depth-integrated volume transport for the entire Baltic Sea shows partly differing circulation patterns for the different models with GETM revealing strongest differences to RCO-A and greatest volume transports in the central Baltic Sea. The best agreement of currents and transport is found between RCO and RCO-A as expected.

Furthermore, mean current velocities and flows through three transects in the Arkona Basin, at the western entrance of Słupsk Channel, and in the Gotland Basin are examined. In general, all considered models show similar patterns at Arkona and Słupsk transect even though the location and magnitude of some circulation patterns varies. Smallest differences to RCO-A are found for RCO and strongest deviations occur for GETM. Numbers of near-surface outflows and inflows below the reversal depth disagree between RCO-A on the one hand and RCO, GETM, and MOM on the other hand.

The evaluation of simulated zonal and meridional current velocities from the used models with ADCP and mooring measurements at two monitoring stations shows an overall acceptable accordance. The model mean current velocities lie predominantly well within the standard deviation of the measurements except for the meridional current velocity near Gotland Deep. However, more observations from other depths are needed in order to allow a comprehensive evaluation.

The evaluation of the used atmospheric forcing datasets reveals that the mean wind speed is slightly overestimated by coastDat2, which drives the ocean circulation models GETM and MOM, but significantly underestimated by RCA3-ERA40, which is used for driving RCO-A and RCO.

Conclusions

The main conclusions of this study are:

1. Regardless of the chosen vertical coordinate system (z-level or vertically adaptive coordinates) and horizontal resolution (grid size between 1 and 3 nm) temperature and salinity observations at monitoring stations are reasonably reproduced by state-of-the-art regional ocean circulation models on a 30-year time scale provided that model setup and parameter calibration are correctly done.
2. Both the mean wind-driven and thermohaline circulation differ considerably between the models highlighting the need for additional long-term current measurements to assess the mean circulation in ocean models.
3. Model results with data assimilations provide the best available datasets to assess ocean models. However, data assimilation of temperature and salinity observations alone cannot constrain the mean currents. In addition to more current measurements, river runoff and wind velocity data need to be assessed more carefully because the datasets utilized in the various models differ considerably. These differences may explain some of the discovered differences in the ocean currents.

Outlook

These findings raise the question which model results represent the correct mean circulation of the entire Baltic Sea and its climate variability. To study the mean circulation and its variability further suitable long-term, high-frequency automated *in situ* observations for current velocity at additional stations are needed. Also, the potential location of new moorings will be calculated from model differences. In addition, the variability and sensitivity of the meridional overturning circulation to changes in atmospheric and hydrological forcing and saltwater inflows into the Baltic Sea will be investigated.

We propose to extend the Baltic Sea model assessment as an activity of the Baltic Earth program (Earth System Science for the Baltic Sea region, see http://www.baltic.earth) and invite other modeling groups to participate with their model results in the assessment following the methods and protocol of this study.

DATA AVAILABILITY STATEMENT

Observations from the Baltic Environmental Database (BED) are publicly available from http://nest.su.se/bed. The raw data supporting the conclusions of this manuscript will be made available by the authors, without undue reservation, to any qualified researcher.

AUTHOR CONTRIBUTIONS

MP and HEMM developed the concept of this study and worked predominantly on the manuscript. MP performed the main part of the data analysis and figure preparation. HEMM prepared the RCO model data and organized the corresponding database. UG prepared and provided the GETM data and contributed with ideas for the manuscript concept. TN processed and improved the MOM data during the analysis process. CF performed the comparison of the atmospheric wind data. YL prepared and provided the RCO-A reanalysis data. All authors contributed to manuscript revision, read and approved the submitted version.

FUNDING

YL was supported by the Swedish Research Council (VR) within the project Reconstruction and projecting Baltic Sea climate variability 1850-2100 (grant no. 2012-2117) and by the Swedish Research Council for Environment, Agricultural Sciences and Spatial Planning (FORMAS) within the project Cyanobacteria life cycles and nitrogen

fixation in historical reconstructions and future climate scenarios (1850-2100) of the Baltic Sea (grant no. 214-2013-1449).

ACKNOWLEDGMENTS

The research presented in this study is part of the Baltic Earth program. We thank the Federal Maritime and Hydrographic Agency Hamburg and Rostock (BSH) for financing and for supporting the operation of the MARNET stations in the western Baltic. We also thank our colleagues from the department of instrumentation at IOW for their relentless commitment before, during, and after monitoring ship cruises, and in particular Dr. Eberhard Hagen, Günter Plüschke, and Toralf Heene for providing the measurement data. Further, we acknowledge the support of the IOW IT department for managing the archive of long-term measurement data (see http://iowmeta.io-warnemuende.de). Temperature and salinity data used for evaluation are open access and were extracted from the Baltic Environmental Database (BED, http://nest.su.se/bed) at Stockholm University and all data providing institutes (listed at http://nest.su.se/bed/ACKNOWLE.shtml) are kindly acknowledged. The model development and simulations for GETM and MOM were performed with resources provided by the North-German Supercomputing Alliance (HLRN). We thank Uwe Schulzweida, the R Core Team, and the Unidata development team (and all involved developers/contributors) for maintaining the open source software packages Climate Data Operators (cdo), the statistical computing language R, and netCDF, respectively.

REFERENCES

Andrejev, O., Myrberg, K., Alenius, P., and Lundberg, P. A. (2004a). Mean circulation and water exchange in the Gulf of Finland–a study based upon three-dimensional modeling. *Boreal Environ. Res.* 9, 1–16.

Andrejev, O., Myrberg, K., and Lundberg, P. A. (2004b). Age and renewal time of water masses in a semi-enclosed basin–application to the Gulf of Finland. *Tellus A* 56, 548–558. doi: 10.3402/tellusa.v56i5.14435

Bergström, S., and Carlsson, B. (1994). River runoff to the Baltic Sea—1950-1990. *Ambio* 23, 280–287.

Burchard, H., and Bolding, K. (2002). *GETM–A General Estuarine Transport Model: Scientific Documentation.* Technical Report EUR 20253 EN, European Commission.

Dee, D. P., Uppala, S. M., Simmons, A. J., Berrisford, P., Poli, P., Kobayashi, S., et al. (2011). The ERA-Interim reanalysis: configuration and performance of the data assimilation system. *Q. J. R. Meteorol. Soc.* 137, 553–597. doi: 10.1002/qj.828

Deleersnijder, E., Campin, J.-M., and Delhez, E. J. M. (2001). The concept of age in marine modeling: I. Theory and preliminary model results. *J. Marine Syst.* 28, 229–267. doi: 10.1016/S0924-7963(01)00026-4

Döös, K., Meier, H. E. M., and Döscher, R. (2004). The Baltic haline conveyer belt or the overturning circulation and mixing in the Baltic. *AMBIO* 33, 261–266. doi: 10.1579/0044-7447-33.4.261

Eilola, K., Gustafsson, B. G., Kuznetsov, I., Meier, H. E. M., Neumann, T., and Savchuk, O. P. (2011). Evaluation of biogeochemical cycles in an ensemble of three state-of-the-art numerical models of the Baltic Sea. *J. Marine Syst.* 88, 267–284. doi: 10.1016/j.jmarsys.2011.05.004

Elken, J. (1996). *Deep Water Overflow, Circulation and Vertical Exchange in the Baltic Proper.* Report Series No.6 (Tallinn: Estonian Marine Institute), 91.

Elken, J., and Matthäus, W. (2008). "Baltic Sea oceanography," in *BALTEX Assessment of Climate Change for the Baltic Sea Basin (BACC)*, ed H. von Storch (Berlin: Springer), 379–386.

Geyer, B. (2014). High-resolution atmospheric reconstruction for Europe 1948-2012: coastDat2. *Earth Syst. Sci. Data* 6, 147–164. doi: 10.5194/essd-6-147-2014

Gräwe, U., Flöser, G., Gerkema, T., Duran-Matute, M., Badewien, T. H., Schulz, E., et al. (2016). A numerical model for the entire Wadden Sea: skill assessment and analysis of hydrodynamics. *J. Geophys. Res. Oceans* 121, 5231–5251. doi: 10.1002/2016JC011655

Gräwe, U., Holtermann, P., Klingbeil, K., and Burchard, H. (2015). Advantages of vertically adaptive coordinates in numerical models of stratified shelf seas. *Ocean Model.* 92, 56–68. doi: 10.1016/j.ocemod.2015.05.008

Griffies, S. M. (2004). *Fundamentals of Ocean Climate Models.* Princeton, NJ: Princeton University Press.

Gustafsson, B. G., and Rodriguez-Medina, M. (2011). *Validation data set compiled from Baltic Environmental Database, (Version 2, January 2011).* Baltic Nest Institute Technical Report No.2, (Stockholm).

Hagen, E., and Feistel, R. (2004). Observations of low-frequency current fluctuations in deep water of the Eastern Gotland Basin/Baltic Sea. *J. Geophys. Res.* 109:C03044. doi: 10.1029/2003JC002017

HELCOM (2015). "Updated fifth Baltic Sea pollution load compilation (PLC-5.5)," in *Baltic Sea Environment Proceedings No. 145*, 1–142.

Hofmeister, R., Burchard, H., and Beckers, J.-M. (2010). Non-uniform adaptive vertical grids for 3D numerical ocean models. *Ocean Model.* 33, 70–86. doi: 10.1016/j.ocemod.2009.12.003

Höglund, A., Meier, H. E. M., Broman, B., and Kriez, E. (2009). *Validation and Correction of Regionalised ERA-40 Wind Fields Over the Baltic Sea using the Rossby Centre Atmosphere Model RCA3.0.* Rapport Oceanografi No. 97. Norrköping: SMHI.

Holtermann, P. L., Burchard, H., Gräwe, U., Klingbeil, K., and Umlauf, L. (2014). Deep-water dynamics and boundary mixing in a nontidal stratified basin: a modeling study of the Baltic Sea. *J. Geophys. Res. Oceans* 119, 1465–1487. doi: 10.1002/2013JC009483

Holtermann, P. L., Prien, R., Naumann, M., Mohrholz, V., and Umlauf, L. (2017). Deepwater dynamics and mixing processes during a major inflow event in the central Baltic Sea. *J. Geophys. Res. Oceans* 122, 6648-6667. doi: 10.1002/2017JC013050

Holtermann, P. L., and Umlauf, L. (2012). The Baltic sea tracer release experiment: 2. mixing processes. *J. Geophys. Res.* 117:C01022. doi: 10.1029/2011JC007445

Holtermann, P. L., Umlauf, L., Tanhua, T., Schmale, O., Rehder, G., and Waniek, J. J. (2012). The Baltic sea tracer release experiment: 1. mixing rates. *J. Geophys. Res.* 117:C01021. doi: 10.1029/2011JC007439

Kalnay, E., Kanamitsu, M., Kistler, R., Collins, W., Deaven, D., Gandin, L., et al. (1996). The NCEP/NCAR 40-year reanalysis project. *Bull. Am. Meteorol. Soc.* 77, 437–471. doi: 10.1175/1520-0477(1996)077<0437:TNYRP>2.0.CO;2

Killworth, P. D., Stainforth, D., Webb, D. J., and Paterson, S. M. (1991). The development of a free-surface Bryan-Cox-Semtner ocean model. *J. Phys. Oceanogr.* 21, 1333–1348. doi: 10.1175/1520-0485(1991)021<1333:TDOAFS>2.0.CO;2

Krüger, S. (2000). "Basic shipboard instrumentation and fixed automatic stations for monitoring in the Baltic Sea," in *The Ocean Engineering Handbook*, ed El-Hawary (Boca Raton, FL: CRC Press LLC, N. W. Corporate Blvd), 52.

Large, W. G., McWilliams, J. C., and Doney, S. C. (1994). Oceanic vertical mixing: a review and a model with a nonlocal boundary layer parameterization. *Rev. Geophys.* 32, 363–403. doi: 10.1029/94RG01872

Lehmann, A., and Hinrichsen, H.-H. (2000). On the wind driven and thermohaline circulation of the Baltic Sea. *Phys. Chem. Earth* 25, 183–189. doi: 10.1016/S1464-1909(99)00140-9

Liu, Y., Meier, H. E. M., and Axell, L. (2013). Reanalyzing temperature and salinity on decadal time scales using the ensemble optimal interpolation data assimilation method and a 3-D ocean circulation model of the Baltic Sea. *J. Geophys. Res. Oceans* 118, 5536–5554. doi: 10.1002/jgrc.20384

Liu, Y., Meier, H. E. M., and Eilola, K. (2014). Improving the multiannual, high-resolution modelling of biogeochemical cycles in the Baltic Sea by using data assimilation. *Tellus A* 66:1. doi: 10.3402/tellusa.v66.24908

Liu, Y., Meier, H. E. M., and Eilola, K. (2017). Nutrient transports in the Baltic Sea–results from a 30-year physical-biogeochemical reanalysis. *Biogeosciences* 14, 2113–2131.doi: 10.5194/bg-14-2113-2017

Löptien, U., and Meier, H. E. M. (2011). The influence of increasing water turbidity on the sea surface temperature in the Baltic Sea: a model sensitivity study. *J. Marine Syst.* 88, 323–331. doi: 10.1016/j.jmarsys.2011.06.001

Matthäus, W., and Franck, H. (1992). Characteristics of major Baltic inflows–a statistical analysis. *Cont. Shelf Res.* 12, 1375–1400. doi: 10.1016/0278-4343(92)90060-W

Meier, H. E. M. (2000). *The Use of the κ-ε Turbulence Model within the Rossby Centre Regional Ocean Climate Model: Parameterization Development and Results.* Reports Oceanography No. 28, Norrköping: SMHI, 81.

Meier, H. E. M. (2001). On the parameterization of mixing in three-dimensional Baltic Sea models. *J. Geophys. Res.* 106, 30997–31016. doi: 10.1029/2000JC000631

Meier, H. E. M. (2005). Modeling the age of Baltic Sea water masses: quantification and steady state sensitivity experiments. *J. Geophys. Res.* 110:C02006. doi: 10.1029/2004JC002607

Meier, H. E. M. (2007). Modeling the pathways and ages of inflowing salt- and freshwater in the Baltic Sea. *Estuar. Coast. Shelf Sci.* 74, 610–627. doi: 10.1016/j.ecss.2007.05.019

Meier, H. E. M., and Döscher, R. (2002). Simulated water and heat cycles of the Baltic Sea using a 3D coupled atmosphere-ice-ocean model. *Boreal Env. Res.* 7, 327–334.

Meier, H. E. M., Döscher, R., and Faxén, T. (2003). A multiprocessor coupled ice-ocean model for the Baltic Sea: application to salt inflow. *J. Geophys. Res.* 108:3273. doi: 10.1029/2000JC000521

Meier, H. E. M., Höglund, A., Döscher, R., Andersson, H., Löptien, U., and Kjellström, E. (2011). Quality assessment of atmospheric surface fields over the Baltic Sea from an ensemble of regional climate model simulations with respect to ocean dynamics. *Oceanologia* 53, 193–227. doi: 10.5697/oc.53-1-TI.193

Meier, H. E. M., and Kauker, F. (2003). Modeling decadal variability of the Baltic Sea: 2. Role of freshwater inflow and large-scale atmospheric circulation for salinity. *J. Geophys. Res.* 108:3368.doi: 10.1029/2003 JC001799

Myrberg, K., and Andrejev, O. (2006). Modelling of the circulation, water exchange and water age properties of the Gulf of Bothnia. *Oceanologia* 48, 55–74.

Myrberg, K., Ryabchenko, V., Isaev, A., Vankevich, R., Andrejev, O., Bendtsen, J., et al. (2010). Validation of three-dimensional hydrodynamic models of the Gulf of Finland. *Boreal Environ. Res.* 15, 453–479.

Neumann, T., Fennel, W., and Kremp, C. (2002). Experimental simulations with an ecosystem model of the Baltic Sea: A nutrient load reduction experiment. *Global Biogeochem. Cycles* 16, 7-1–7-19. doi: 10.1029/2001GB001450

Neumann, T., Radtke, H., and Seifert, T. (2017). On the importance of Major Baltic Inflows for oxygenation of the central Baltic Sea. *J. Geophys. Res. Oceans* 122, 1090–1101. doi: 10.1002/2016JC012525

Omstedt, A., and Nohr, C. (2004). Calculating the water and heat balances of the Baltic Sea using ocean modelling and available meteorological, hydrological and ocean data. *Tellus A* 56, 400–414. doi: 10.3402/tellusa.v56i4.14428

Pacanowski, R. C., and Griffies, S. M. (2000). *MOM 3.0 Manual.* Technical Report, Geophysical Fluid Dynamics Laboratory.

Pätsch, J., Burchard, H., Dieterich, C., Gräwe, U., Gröger, M., Mathis, M., et al. (2017). An evaluation of the North Sea circulation in global and regional models relevant for ecosystem simulations. *Ocean Model.* 116, 70–95. doi: 10.1016/j.ocemod.2017.06.005

Samuelsson, P., Jones, C. G., Willén, U., Ullerstig, A., Gollvik, S., Hansson, U., et al. (2011). The Rossby Centre Regional Climate model RCA3: model description and performance. *Tellus A* 63, 4–23. doi: 10.1111/j.1600-0870.2010.00478.x

Sarkisyan, A. S., Staskwiecz, A., and Koalik, Z. (1975). Diagnostic computation of the summer circulation in the Baltic Sea. *Oceanologia* 15, 653–656.

Smagorinsky, J. (1963). General circulation experiments with the primitive equations: 1. The basic experiment. *Monthly Weather Rev.* 91, 99–164. doi: 10.1175/1520-0493(1963)091<0099:GCEWTP>2.3.CO;2

Stigebrandt, A. (1987). Computations of the flow of dense water into the Baltic Sea from hydrographical measurements in the Arkona Basin. *Tellus A* 39A, 170–177.

Taylor, K. E. (2001). Summarizing multiple aspects of model performance in a single diagram. *J. Geophys. Res.* 106, 7183–7192. doi: 10.1029/2000JD900719

Uppala, S. M., KÅllberg, P. W., Simmons, A. J., Andrae, U., Bechtold, V. D. C., Fiorino, M., et al. (2005). The ERA-40 re-analysis. *Q. J. R. Meteorol. Soc.* 131, 2961–3012. doi: 10.1256/qj.04.176

Conflict of Interest Statement: The authors declare that the research was conducted in the absence of any commercial or financial relationships that could be construed as a potential conflict of interest.

Copyright © 2018 Placke, Meier, Gräwe, Neumann, Frauen and Liu. This is an open-access article distributed under the terms of the Creative Commons Attribution License (CC BY). The use, distribution or reproduction in other forums is permitted, provided the original author(s) and the copyright owner(s) are credited and that the original publication in this journal is cited, in accordance with accepted academic practice. No use, distribution or reproduction is permitted which does not comply with these terms.

frontiers in Marine Science

REVIEW
published: 04 March 2019
doi: 10.3389/fmars.2019.00046

Assessment of Uncertainties in Scenario Simulations of Biogeochemical Cycles in the Baltic Sea

H. E. Markus Meier[1,2], Moa Edman[2], Kari Eilola[2], Manja Placke[1], Thomas Neumann[1], Helén C. Andersson[2], Sandra-Esther Brunnabend[1], Christian Dieterich[2], Claudia Frauen[1], René Friedland[1], Matthias Gröger[2], Bo G. Gustafsson[3,4], Erik Gustafsson[3], Alexey Isaev[5], Madline Kniebusch[1], Ivan Kuznetsov[6], Bärbel Müller-Karulis[3], Michael Naumann[1], Anders Omstedt[7], Vladimir Ryabchenko[5], Sofia Saraiva[8] and Oleg P. Savchuk[3]*

[1] Department of Physical Oceanography and Instrumentation, Leibniz Institute for Baltic Sea Research Warnemünde, Rostock, Germany, [2] Department of Research and Development, Swedish Meteorological and Hydrological Institute, Norrköping, Sweden, [3] Baltic Nest Institute, Stockholm University, Stockholm, Sweden, [4] Tvärminne Zoological Station, University of Helsinki, Hanko, Finland, [5] Shirshov Institute of Oceanology, Russian Academy of Sciences, Moscow, Russia, [6] Institute of Coastal Research, Helmholtz-Zentrum Geesthacht, Geesthacht, Germany, [7] Department of Marine Sciences, University of Gothenburg, Göteborg, Sweden, [8] MARETEC, Instituto Superior Técnico, University of Lisbon, Lisbon, Portugal

OPEN ACCESS

Edited by:
Karol Kulinski,
Institute of Oceanology (PAN), Poland

Reviewed by:
Gennadi Lessin,
Plymouth Marine Laboratory, United Kingdom
Artur Piotr Palacz,
International Ocean Carbon Coordination Project (IOCCP), Poland

***Correspondence:**
H. E. Markus Meier
markus.meier@io-warnemuende.de

Specialty section:
This article was submitted to Coastal Ocean Processes, a section of the journal Frontiers in Marine Science

Received: *19 August 2018*
Accepted: *28 January 2019*
Published: *04 March 2019*

Citation:
Meier HEM, Edman M, Eilola K, Placke M, Neumann T, Andersson HC, Brunnabend S-E, Dieterich C, Frauen C, Friedland R, Gröger M, Gustafsson BG, Gustafsson E, Isaev A, Kniebusch M, Kuznetsov I, Müller-Karulis B, Naumann M, Omstedt A, Ryabchenko V, Saraiva S and Savchuk OP (2019) Assessment of Uncertainties in Scenario Simulations of Biogeochemical Cycles in the Baltic Sea. Front. Mar. Sci. 6:46. doi: 10.3389/fmars.2019.00046

Following earlier regional assessment studies, such as the Assessment of Climate Change for the Baltic Sea Basin and the North Sea Region Climate Change Assessment, knowledge acquired from available literature about future scenario simulations of biogeochemical cycles in the Baltic Sea and their uncertainties is assessed. The identification and reduction of uncertainties of scenario simulations are issues for marine management. For instance, it is important to know whether nutrient load abatement will meet its objectives of restored water quality status in future climate or whether additional measures are required. However, uncertainties are large and their sources need to be understood to draw conclusions about the effectiveness of measures. The assessment of sources of uncertainties in projections of biogeochemical cycles based on authors' own expert judgment suggests that the biggest uncertainties are caused by (1) unknown current and future bioavailable nutrient loads from land and atmosphere, (2) the experimental setup (including the spin up strategy), (3) differences between the projections of global and regional climate models, in particular, with respect to the global mean sea level rise and regional water cycle, (4) differing model-specific responses of the simulated biogeochemical cycles to long-term changes in external nutrient loads and climate of the Baltic Sea region, and (5) unknown future greenhouse gas emissions. Regular assessments of the models' skill (or quality compared to observations) for the Baltic Sea region and the spread in scenario simulations (differences among projected changes) as well as improvement of dynamical downscaling methods are recommended.

Keywords: Baltic Sea, nutrients, eutrophication, climate change, future projections, uncertainties, ensemble simulations

INTRODUCTION

Due to its location (**Figure 1**) and physical characteristics, the semi-enclosed Baltic Sea is vulnerable to external pressures such as eutrophication, pollution or global warming (e.g., Jutterström et al., 2014). The Baltic Sea is surrounded by a large catchment that is populated with about 90 million people (Ahtiainen and Öhman, 2014). In particular, the southern Baltic Sea region is characterized by a high population density and intensive agricultural activities causing anthropogenic loads of nutrients and pollutants (Hong et al., 2012; HELCOM, 2015, 2018a). During the 1950s and 1960s, agriculture in the Baltic Sea region was facilitated by both mechanization and greatly increased fertilizer application, thus causing an increase in nutrient input from the southern agricultural landscapes (Gustafsson et al., 2012). The progressing urbanization was initially not accompanied by appropriate wastewater treatment and led to a further increase in nutrient loads. Since the 1980s, riverborne nutrient loads and the atmospheric deposition of nitrogen decreased as a consequence of an expanded wastewater treatment and reduced fertilizer usage in the Baltic Sea region (Savchuk et al., 2012b; HELCOM, 2015, 2018b; Savchuk, 2018).

To project the future environmental status of the Baltic Sea and to support marine management with nutrient load abatement strategies such as the Baltic Sea Action Plan (BSAP) of the Helsinki Commission (HELCOM) (HELCOM, 2007a,b, 2013a,b), scenario simulations have been developed taking both changing climate and changing anthropogenic nutrient loads into account (e.g., Meier et al., 2011b; Neumann et al., 2012; Omstedt et al., 2012; Saraiva et al., 2018, 2019). For a summary of available future scenario simulations of the biogeochemical cycles of the Baltic Sea, the reader is referred to **Table 1**.

One aim of scenario simulations of the Baltic Sea ecosystem is to provide decision makers with reliable information about multiple stressors (e.g., Jutterström et al., 2014). Hence, dynamical downscaling of global climate change may contribute, in particular, to the development of an improved BSAP in future climate and, in general, to an improved holistic marine management because of the long response time scale of the Baltic Sea of about 30 years (e.g., Omstedt and Hansson, 2006a,b). In this context, the assessment of uncertainties (or knowledge gaps) of scenario simulations is of utmost importance (Mastrandrea et al., 2010).

In general, uncertainties in scenario simulations (here defined as the variances of mean changes between future and historical climates) are caused by climate model uncertainties, by unknown future greenhouse gas (GHG) emissions (or concentrations) and by natural variability (Hawkins and Sutton, 2009). Natural variability has two contributions, i.e. unforced internal and externally driven variations such as solar variability and volcanic eruptions. The latter source of uncertainty is usually neglected, since scenario simulations are not predictions but projections of only anthropogenic climate change (Rummukainen, 2016b). In addition to these three distinct sources inherent to all climate projections, uncertainties in regional projections comprise even the experimental setup of the downscaling approach including for instance lateral boundary conditions such as the global mean sea level rise (Meier et al., 2017) and initial conditions (including the spin up strategy), or unknown regional nutrient load scenarios (Zandersen et al., 2019). Further, insufficient process descriptions in state-of-the-art biogeochemical models for the Baltic Sea such as unknown bioavailable fractions of external nutrient loads (e.g., Eilola et al., 2011), the insufficient description of non-Redfield stoichiometry (e.g., Fransner et al., 2018) and benthic macrofauna (Timmermann et al., 2012), the missing impact of invasive species (e.g., Holopainen et al., 2016; Isaev et al., 2017), the implicit description of the microbial loop (e.g., Wikner and Andersson, 2012), and the lacking top-down cascade in the food web including the impact of fishing (e.g., Niiranen et al., 2013; Nielsen et al., 2017; Bauer et al., 2018, in press) contribute to the overall uncertainties of projections.

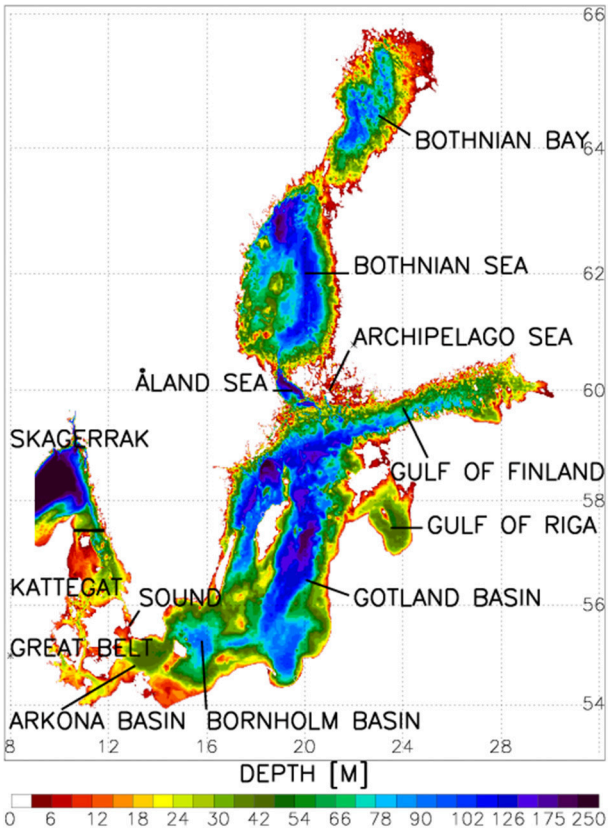


FIGURE 1 | Bottom topography of the Baltic Sea. The Baltic proper comprises the Arkona Basin, Bornholm Basin and Gotland Basin. The solid line marks the border between Kattegat and Skagerrak which is the lateral boundary in BALTSEM and other Baltic Sea models (see text).

In this study, we identify, discuss and rank uncertainties in scenario simulations of the Baltic Sea by assessing the existing literature and by expert judgment. The purpose of the review is to better understand the various sources of uncertainties and to identify knowledge gaps.

In the following two sections, results of scenario simulations of biogeochemical cycles in the Baltic Sea (Background) and the methods used for the projections of coastal seas (Dynamical Downscaling Methods) are reviewed. Further, uncertainties of

TABLE 1 | Dynamical downscaling experiments for the Baltic Sea for the twenty-first century (BSM, Baltic Sea Model; LSM, Land Surface Model; RCM, Regional Climate Model; GCM, global General Circulation Model; GHG, Greenhouse Gas).

	BSM physics	BSM biogeo-chemistry	LSM	RCM	GCM	Time slice	Bias correction	GHG emission scenario	Nutrient load scenario	Related publications
1	PROBE-Baltic	No	HBV	RCA0	HadCM2	1980–1990 and 2039–2100	no	1%/year increased equivalent CO_2	no	Omstedt et al., 2000
2	RCO	No	HBV	RCA0	HadCM2	1980–1989 and 2091–2100	no	150% increased equivalent CO_2	no	Haapala et al., 2001; Meier, 2002a,b
3	RCAO	No	HBV	RCAO	ECHAM4/OPYC3, HadAM3H	1961–1990 and 2071–2100	no	A2, B2	no	Döscher and Meier, 2004; Meier et al., 2004a,b; Räisänen et al., 2004; Meier, 2006
4	RCO	SCOBI	HBV	RCAO	ECHAM4/OPYC3, HadAM3H	1961–1990 and 2071–2100	Delta-change with historical reconstruction as reference	A2, B2	no	Meier, 2006; Meier et al., 2011a
5	MOM	ERGOM	STAT_S	CCLM	ECHAM5/MPI-OM	1960–2100	no	A1B, B1	REF	Neumann, 2010
6	RCO	SCOBI	STAT	RCAO	HadCM3, ECHAM5/MPI-OM	1961–2099	Wind speed correction	A1B, A2	BSAP, CLEG, REF, BAU	Eilola et al., 2012, 2013; Meier et al., 2012a
7	RCO	SCOBI	B-HYPE	RCAO	HadCM3, ECHAM5/MPI-OM	1961–2099	Wind speed correction	A1B, A2	BSAP, CLEG, REF, BAU	Meier et al., 2012b
8	BALTSEM	BALTSEM	STAT	RCAO	HadCM3, ECHAM5/MPI-OM	1961–2099	Wind speed correction	A1B, A2	BSAP, CLEG, REF, BAU	Meier et al., 2011b
9	MOM	ERGOM	STAT	RCAO	HadCM3, ECHAM5/MPI-OM	1961–2099	Wind speed correction	A1B	BSAP, REF, BAU	Meier et al., 2011b; Neumann et al., 2012
10	MOM	ERGOM	Data constant	CCLM	ECHAM5/MPI-OM	1960–2100	no	A1B, B1	BSAP, REF	Friedland et al., 2012; Schernewski et al., 2015
11	PROBE-Baltic	PROBE-Baltic	CSIM	RCA3	ECHAM5/MPI-OM	1960–2100	Delta-change with ERA-40 reference	A2, A1B, B1	BSAP, REF, BAU	Omstedt et al., 2012
12	COHERENS	OXYCON	Data constant	Operational atmosphere model Brandt et al., 2001	No	2001–2003	Sensitivity experiment	Idealized (T = +3°C)	no	Bendtsen and Hansen, 2013

(Continued)

TABLE 1 | Continued

	BSM physics	BSM biogeo-chemistry	LSM	RCM	GCM	Time slice	Bias correction	GHG emission scenario	Nutrient load scenario	Related publications
13	GETM	ERGOM	B-HYPE	RCAO	HadCM3	1997–2006 and 2090–2099	initial conditions from MOM-ERGOM	A1B	BAU	Lessin et al., 2014
14	RCA4-NEMO	No	River flow 10% increase	RCA4-NEMO	ECHAM5/MPI-OM	1961-2100	no	A1B	no	Bülow et al., 2014
15	ECOSMO	ECOSMO	River flow constant	no	BCM, ECHAM5/MPI-OM, IPSL-CM4 (CMIP3) and NorESM, MPI-ESM, IPSL-CM5 (CMIP5)	1970–1999 and 2070-2099	Delta-change with NCEP/NCAR reference	A1B, RCP 4.5	Nutrient loads constant	Pushpadas et al., 2015
16	ECOSMO	ECOSMO	River flow constant	no	IPSL-CM4	1981–2000 and 2080–2099	Delta-change with NCEP/NCAR reference	A1B	Nutrient loads constant	Holt et al., 2016
17	SPBEM	SPBEM	STAT	RCAO	HadCM3, ECHAM5/MPI-OM	1961–2099	Wind speed correction	A1B, A2	BSAP, REF	Ryabchenko et al., 2016
18	RCO	SCOBI	Data	Historical reconstruction	No	1850–2008	Sensitivity experiment	Idealized (SSH $= +1$ *m*)	REF	Meier et al., 2017
19	RCO	SCOBI	E-HYPE	RCA4-NEMO	MPI-ESM-LR, EC-EARTH, IPSL-CM5A-MR, HadGEM2-ES	1975–2100	Wind speed correction	RCP 4.5, RCP 8.5	BSAP, REF, Worst Case	Saraiva et al., 2018, 2019
20	RCA4-NEMO	No	River flow 10% increase	RCA4-NEMO	MPI-ESM-LR, HadGEM2-ES, EC-EARTH, GFDL-ESM2M, IPSL-CM5A-MR	1961–2100	no	RCP 8.5	no	Gröger et al., under review

For model acronyms see ***Table 3***.

scenario simulations are qualitatively assessed and their sources are discussed (Results of the Assessment of Uncertainties). Identified or hypothesized uncertainties are related to (1) lack of observations for model calibration, (2–3) differences between projections of General Circulation or Global Climate Models (GCMs) and Regional Climate Models (RCMs), (4) unknown changes in the regional water cycle, (5) natural variability, (6) unknown bioavailable fractions of nutrient loadings from land and the unknown impact of changing climate on nutrient loads, (7) unknown future GHG emission or concentration scenarios, (8) unknown initial conditions of nutrient pools in the water and sediment or unsuitable spin-up simulations due to lack of observations, (9) differences in Global Mean Sea Level (GMSL) projections, (10) lateral boundary conditions, (11) bias correction, (12) differences between projections of the Baltic Sea Models (BSMs), (13) unknown processes of the carbon cycle, and (14) weighting of ensemble members (**Table 2**). Finally, we discuss methods to estimate and to narrow uncertainties in projections. Weighting is regarded both as a source of uncertainty and as an opportunity to narrow uncertainty. An example illustrating the spread in projected hypoxic area for the Baltic Sea is presented as **Supplementary Material**. Here, hypoxic area is defined as the area of bottom water with an oxygen concentration less than 2 mL L^{-1}. Conclusions finalize the review. Acronyms used in this study are explained in **Table 3**.

TABLE 2 | Sources of uncertainty addressed by this study and selected key references of the Baltic Sea. For details, the reader is referred to the text.

	Source of uncertainty	References
1	Insufficient number of observational data for model calibration	Savchuk, 2018
2	Differences between projections caused by GCMs	Saraiva et al., 2019; Déqué et al., 2012
3	Differences between projections caused by RCMs	Christensen and Christensen, 2007; Déqué et al., 2012
4	Unknown changes in the regional water cycle	BACCII Author Team, 2015
5	Natural variability	Kjellström et al., 2011
6	Unknown bioavailable fractions of nutrient loadings from land and the unknown impact of changing climate on nutrient loads	Eilola et al., 2011; Arheimer et al., 2012; Saraiva et al., 2018, 2019; Zandersen et al., 2019
7	Unknown future GHG emission or concentration scenarios	Nakićenović et al., 2000; Moss et al., 2010
8	Unknown initial conditions of nutrient pools in the water and sediment or unsuitable spin-up simulations due to lack of observations	Meier et al., 2012c
9	Differences in GMSL projections	Saraiva et al., 2019
10	Lateral boundary conditions	This study
11	Bias correction	Rechid et al., 2016; Schrum et al., 2016
12	Differences between projections of the BSMs	Meier et al., 2011b
13	Unknown processes of the carbon cycle	Omstedt et al., 2012
14	Weighting of ensemble members	Meier et al., 2018a

BACKGROUND

For the Baltic Sea and North Sea regions detailed assessments of scenario simulations are available (BACC Author Team, 2008; BACCII Author Team, 2015; Schrum et al., 2016; cf. Omstedt, 2017; cf. Räisänen, 2017). Since the first quantitative scenario simulations of biogeochemical cycles in the Baltic Sea did not become available until the year 2010, only the BACCII Author Team (2015) discussed the results of projections of the marine ecosystem published before the year 2012. In the following, we summarize these results of the BACCII Author Team (2015) and of the more recent literature.

Changes in Hydrodynamics

The BACCII Author Team (2015) essentially confirmed the results by the BACC Author Team (2008) concerning water temperature, salinity, sea ice, storm surges and sea level. The projections suggest that the future Baltic Sea would be warmer (between 1.9° and 3.2°C on average) and fresher (between 0.6 and 4.2 g kg^{-1} on average) than in present climate with a substantial decline in sea-ice cover (between 46 and 77%) and increased storm surges (cf. Meier et al., 2018a). The latter will probably be caused rather by sea-level rise than by increased wind speed (Gräwe et al., 2013). Sea levels are rising primarily as a result of thermal expansion and the loss of land-based ice sheets at global scale (Stocker et al., 2013). Sea levels in the Baltic Sea will follow the global trends but changes will partly be compensated by land-uplift essentially in the northern parts of the Baltic Sea (BACCII Author Team, 2015). Due to the isostatic adjustment after the last glaciation of Fennoscandia, the land is rising with maximum land uplift in the Bothnian Bay close to the Swedish city Luleå of about 0.8 m per century. In the southern Baltic Sea and Kattegat region, land uplift is close to zero.

Newer studies on past and future sea level variability are based on advanced methods and confirm earlier results (e.g., Johansson et al., 2014; Karabil et al., 2017a,b, 2018). Also for sea ice, new projections have been carried out taking the latest results of the Coupled Model Intercomparison Project (CMIP), i.e., CMIP5, into account (e.g., Luomaranta et al., 2014; Seitola et al., 2015). Further, comprehensive work on coastline changes was done (e.g., Harff et al., 2017).

During winter, future runoff may increase in the northern Baltic Sea region whereas in the southern Baltic Sea region the summer runoff will very likely decrease (BACCII Author Team, 2015). The total runoff into the Baltic Sea is projected to increase but figures vary substantially depending on the climate model, GHG emission scenario and downscaling method between about 1 and 21% (Meier et al., 2012c; Donnelly et al., 2014; Saraiva et al., 2019). As most of the variability in salinity is explained by the variability in freshwater supply (Meier and Kauker, 2003a; Schimanke and Meier, 2016), projected salinities are lower than in present climate but the spread among projections is large (Meier et al., 2006). Further, Hordoir et al. (2018) suggested that

TABLE 3 | List of acronyms, their explanation and references (in alphabetical order).

Acronym	Explanation	Comment	References
BED	Baltic Environmental Database	Marine observational data from the Baltic Sea monitoring programs	http://nest.su.se/bed/
B-HYPE, E-HYPE	Hydrological predictions for the environment applied for the Baltic Sea, Europe	process-based multi-basin model for the land surface	http://hypeweb.smhi.se, Arheimer et al., 2012; Donnelly et al., 2013, 2017; Hundecha et al., 2016
BSAP	Baltic Sea Action Plan	Nutrient load abatement strategy for the Baltic Sea	HELCOM, 2013b
CCLM	COSMO Climate Limited-area Modeling community	Regional climate model	https://www.clm-community.eu/
CLEG, REF, BAU	Current Legislation, Reference, Business-As-Usual	Nutrient load scenarios	Meier et al., 2012a
CMIP	Coupled Model Intercomparison Project of the World Climate Research Programme (WRCP)	GCM/ESM results from CMIP2, CMIP3 and CMIP5 are used	https://www.wcrp-climate.org/wgcm-cmip
COHERENS-OXYCON	OXYgen CONsumption model	Coupled hydrodynamical–ecological model for regional and shelf seas coupled to a pelagic and benthic oxygen consumption model	Luyten et al., 1999; Bendtsen and Hansen, 2013
CSIM	Catchment Simulation Model	Hydrological model for river runoff, carbon and nutrient fluxes	Mörth et al., 2007
EC-EARTH	European countries earth system model	ESM, CMIP5	https://www.knmi.nl
ECHAM4/OPYC3	Max Planck Institute global climate model	GCM	Roeckner et al., 1999
ECHAM5-MPI-OM	Max Planck Institute global climate model	GCM, CMIP3	Roeckner et al., 2006 Jungclaus et al., 2006
ECOSMO	Ecosystem model	Coupled physical-biogeochemical ocean circulation model for the North Sea and Baltic Sea	Schrum, 1997; Daewel and Schrum, 2013
ERA-40	40-year reanalysis of the European Center for Medium Range Weather Forecast	Reanalysis data used for instance as atmospheric forcing for ocean models	Uppala et al., 2005
ESM	Earth System Model	Model applied for global climate simulations including the carbon cycle	Heavens et al., 2013
GCM	General Circulation Model	Model applied for global climate simulations	Meehl et al., 2004
GETM	General Estuarine Transport Model	3D hydrodynamic model for coastal oceans	https://getm.eu/
GFDL-ESM2M	Geophysical Fluid Dynamics Laboratory Earth System Model	ESM, CMIP5	https://www.gfdl.noaa.gov/earth-system-model/
HadAM3H	Hadley Center high-resolution Atmosphere Model, component of HadCM3	GCM	Gordon et al., 2000[a]
HadCM2	Hadley Center Climate Model	GCM, Global ocean-atmosphere circulation model	Johns et al., 1997; Mitchell and Johns, 1997
HadCM3	Hadley Center Global Climate Model	GCM, CMIP3	Gordon et al., 2000
HadGEM2-ES	Hadley Center Global Environment Model version 2 – Earth System	ESM, CMIP5	http://www.metoffice.gov.uk
HBV	Hydrologiska Byråns Vattenbalansavdelning	Large-scale hydrological model for river runoff	Graham, 1999
IOW	Leibniz Institute for Baltic Sea Research Warnemünde	German research institute	http://io-warnemuende.de
IOWMETA	Leibniz Institute for Baltic Sea Research Warnemünde Data Portal	Marine observational data from the German monitoring program	http://iowmeta.io-warnemuende.de
IPCC	Intergovernmental Panel on Climate Change	Performed assessment reports of past and future changes in 1990, 1995, 2001, 2008, 2013 *inter alia* based upon CMIP results	http://www.ipcc.ch
IPSL-CM4	Institute Pierre Simon Laplace Climate Model	ESM	Marti et al., 2006
IPSL-CM5A-MR	Institut Pierre Simon Laplace Climate Model - Medium Resolution	ESM, CMIP5	https://www.ipsl.fr/en/
MPI-ESM-LR	Max Planck Institute Earth System Model - Low Resolution	ESM, CMIP5	https://www.mpimet.mpg.de

(Continued)

TABLE 3 | Continued

Acronym	Explanation	Comment	References
NCEP/NCAR	National Centers for Environmental Prediction (NCEP) and the National Center for Atmospheric Research (NCAR)	Atmospheric reanalysis data used *inter alia* as atmospheric forcing for ocean models (1948-present)	Kalnay et al., 1996, https://www.esrl.noaa.gov/psd/data/reanalysis/reanalysis.shtml
RCA0	Rossby Center Atmosphere Model version 0	Regional Climate Model	Räisänen et al., 2001; Rummukainen et al., 2001
RCA3	Rossby Center Atmosphere Model version 3	Regional climate model	Samuelsson et al., 2011
RCA4-NEMO	Rossby Center Atmosphere model version 4 – Nucleus for European Modeling of the Ocean	Coupled atmosphere-ocean model applied for the Baltic Sea and North Sea	Dieterich et al., 2013; Kupiainen et al., 2014; Wang et al., 2015; Madec and The NEMO team, 2016
RCAO	Rossby Center Atmosphere Ocean Model	Regional climate model	Döscher et al., 2002
RCM	Regional Climate Model	Regional atmosphere or coupled atmosphere-ocean model applied for dynamical downscaling of changing climate	Rummukainen, 2010, 2016a; Feser et al., 2011; Rockel, 2015; Rummukainen et al., 2015; Schrum, 2017
RCO-SCOBI, BALTSEM, MOM-ERGOM, PROBE, SPBEM	Model abbreviations	Coupled physical-biogeochemical models for the Baltic Sea	Meier et al. (2018a, this research topic), their Tables 1, 2 and references therein
RCP	Representative Concentration Pathway	Greenhouse gas concentration scenario	Moss et al., 2010; Van Vuuren et al., 2011
RCSM	Regional Climate System Model	Regional coupled atmosphere–sea-ice–ocean–wave–land surface–atmospheric chemistry–marine ecosystem model	Giorgi and Gao, 2018
SHARK	Swedish Ocean Archive	Marine observational data from the Swedish monitoring program	https://sharkweb.smhi.se/
SMHI	Swedish Meteorological and Hydrological Institute	Swedish center for weather forecasts and climate scenarios	http://www.smhi.se
SRES	Special Report on Emission Scenarios	Described greenhouse gas emission scenarios, e.g. A1B, A2, B2, B1	Nakićenović et al., 2000
SSP	Shared socio-economic pathways	Narratives of socio-economic changes, here downscaled to the Baltic Sea region	O'Neill et al., 2014
STAT	Hydrological model	Statistical model for river runoff calculated from precipitation and evaporation over land	Meier et al., 2012a
STAT_S	Hydrological model	Statistical model for river runoff calculated from the soil model of the RCM	Neumann, 2010
UERRA	Uncertainties in Ensembles of Regional Re-Analyses	Atmospheric reanalysis data used *inter alia* as atmospheric forcing for ocean models	http://www.uerra.eu/
Worst Case	Worst Case scenario	Nutrient load scenario	Saraiva et al., 2018

[a] *For the explanation, why HadAM3H instead of HadCM3 was used, the reader is referred to Räisänen et al. (2004).*

the estuarine overturning of the Baltic Sea would slow down in warmer climate although the causes are not well understood.

Changes in Biogeochemical Cycles

Changing hydrographic conditions due to changing climate will affect biogeochemical cycles in many ways (e.g., BACCII Author Team, 2015). Higher water temperatures may cause increased algae production and increased remineralization of dead organic material and will reduce the air-sea fluxes of oxygen (Meier et al., 2011b). Furthermore, warming will preferentially favor cyanobacteria blooms compared to the blooms of other phytoplankton species such as diatoms, flagellates and others. The spring bloom is expected to start (and end) earlier (depending on the nutrient and light conditions), and nitrogen fixation might increase (Neumann, 2010; Meier et al., 2012b; Neumann et al., 2012). Indeed, both long-term remote sensing data and BALTSEM (Savchuk, 2002; Gustafsson, 2003; Savchuk et al., 2012a) simulations indicate prolongation of the marine vegetation season in the 2010s comparing to the 1970s, shifting of the annual biomass maximum from spring to summer with the cyanobacteria bloom occurring by half a month earlier, and a tripling of the simulated nitrogen fixation and net primary production (Kahru et al., 2016).

Related to higher air temperatures in future climate is a shrinking sea-ice cover in the northern Baltic Sea that will lead to an earlier onset of the spring bloom due to improved light conditions (Eilola et al., 2013). Due to the reduced sea-ice cover, winds and wave-induced resuspension may increase, causing an increased transport of nutrients from the productive coastal zone into the deeper areas of the northern Baltic Sea. Scenario simulations suggest that increased winter mixing (due to shrinking sea-ice cover) and increased freshwater supply may cause a reduced stratification in the Gulf of Finland (Meier et al., 2011b, 2012a). The reduced sea-ice cover therefore partly

counteracts eutrophication because the increased vertical mixing improves oxygen conditions in lower layers.

For the southern Baltic Sea regions without regular seasonal sea-ice cover, it is unclear whether mixing and light conditions will change in future climate because projected changes in wind and cloud cover over the Baltic Sea are uncertain (Räisänen et al., 2004; Kjellström et al., 2011). In a recent study by Gröger et al. (manuscript under review), a consistent northward shift in the mean summer position of the westerly winds was found causing an increase of the wind speed in particular over the southwestern Baltic Sea. For mixing, wind speed extremes are important. However, projected changes in wind speed extremes have a large spread among scenario simulations (Nikulin et al., 2011).

Increasing river runoff together with increased precipitation extremes may reinforce river-borne nutrient loads (Stålnacke et al., 1999; Arheimer et al., 2012; Meier et al., 2012b). However, other drivers than climate change such as sewage treatment and livestock density may become even more important controlling the changes in nutrient loads (e.g., Humborg et al., 2007). Humborg et al. (2007) speculated that riverborne nitrogen loads might increase due to higher livestock densities whereas phosphorus and silica fluxes may decrease due to improved sewage treatment. Such changes would have significant impact on phytoplankton communities. However, these projections do not consider the impact of changing climate on terrestrial biogeochemical processes, which may counteract other anthropogenic effects (Arheimer et al., 2012). Since the 1980, observed phosphorus and nitrogen loads decreased as a response to nutrient load abatement measures (Gustafsson et al., 2012) whereas silicate concentrations showed no significant changes in the northern Baltic proper, Gulf of Finland and Åland Sea during 1979–2011 (Suikkanen et al., 2013). In present climate, silicate is not regarded as limiting nutrient.

As the Baltic Sea is shallow with a mean depth of only 52 m, the nutrient exchange between sediment and water column and resuspension of organic matter are important processes for the biogeochemical cycling. Eilola et al. (2012) suggested that in future climate the exchange between shallow and deeper waters might intensify and that the internal removal of phosphorus might become weaker because of an increased production in the coastal zone and expanding oxygen depletion in the deep water, respectively.

How saltwater inflows may change is unclear (Schimanke et al., 2014). In present climate, no statistically significant trends were found (Mohrholz, 2018). However, global mean sea level rise may enhance the salt transport into the Baltic Sea causing increased stratification, reduced deep water ventilation and expanding hypoxia in the Baltic proper (Meier et al., 2017).

The rising atmospheric CO_2 concentration will lead to a decrease in pH (Omstedt et al., 2012), while eutrophication and enhanced biological production would enhance the seasonal cycle of pH. Eutrophication in the Gulf of Finland is projected to increase assuming a "business-as-usual" (BAU) nutrient load scenario (Lessin et al., 2014). This scenario is characterized by decreasing bottom oxygen concentrations, more frequent anoxic conditions, and increasing phosphate and decreasing nitrate concentrations below 60 m depth. These changes may cause a considerable increase in nitrogen fixation.

In a recent study, a decline in oxygen concentrations in the Bothnian Sea during the last 20 years was found (Ahlgren et al., 2017). This finding is surprising because the Bothnian Sea was so far considered to be oligotrophic. The oxygen depletion was primarily a consequence of warmer water temperature. Further causes were an increase in dissolved organic carbon (DOC) and the import of nutrients from adjacent sub-basins.

Finally, it should be noted that in future climate also the ecosystem structure and functioning is projected to change (BACCII Author Team, 2015). An example is the recent study by Vuorinen et al. (2015), who analyzed the effects of salinity changes on the distribution of marine species. They found a critical shift in the salinity range between 5 and 7 g kg^{-1}, which is a threshold for both freshwater and marine species distributions and diversity. Andersson et al. (2015) provided an overview about future climate change scenarios for the Baltic Sea ecosystem, both for southern and northern sub-basins, and concluded that climate change is likely to have large effects on the marine ecosystem. For instance, in the north heterotrophic bacteria might be favored by allochthonous organic matter, while phytoplankton production may be reduced. In scenario simulations with biogeochemical models, the impact of changing ecosystem structure and function on the biogeochemical cycles are not considered, representing a source of uncertainty.

Changes in Hypoxic Area

Changes in hydrographic conditions and changes in external nutrient loads may cause changes in oxygen depletion and hypoxic area. Meier et al. (2011b) showed with the aid of a multi-model ensemble that hypoxic area might expand in future climate because of increased nutrient loads due to enhanced river runoff, reduced air-sea fluxes and accelerated recycling of organic matter due to higher water temperatures. More frequent and longer lasting periods of hypoxia in future climate (Neumann et al., 2012) may lead to larger phosphorus fluxes from the sediment into the water column (or reduced retention capacity of the sediment) and intensified eutrophication (Meier et al., 2012c; Ryabchenko et al., 2016). Recently, Meier et al. (2018d) found that after saltwater inflows under contemporary environmental conditions oxygen consumption rates in the deep water were accelerated compared to less eutrophied conditions. This acceleration further amplifies deoxygenation in the Baltic Sea and counteract natural ventilation. The reason is that water of inflow events originates mainly from the Baltic surface layer and contains under contemporary environmental conditions, *inter alia,* higher concentrations of organic matter, zooplankton and higher trophic levels (causing increased heterotrophic oxygen consumption).

Hypoxia is an important indicator of ecosystem health but also a challenge for modeling. In the **Supplementary Material**, results of past and future changes in hypoxic area of various scenario simulations are summarized.

DYNAMICAL DOWNSCALING METHODS

In this section, various dynamical downscaling methods used to perform Baltic Sea projections are reviewed. In general, the

dynamical downscaling method uses high-resolution regional simulations to dynamically extrapolate the effects of large-scale climate variability to regional or local scales of interest (**Figure 2A**). Regional climate atmosphere models have an added value compared to global climate models with respect to the representation of orographic details, the land-sea mask, sea surface boundary conditions (sea surface temperature (SST) and sea ice), more detailed vegetation and soil characteristics, and extremes, e.g., cyclones (e.g., Rummukainen, 2010, 2016a; Feser et al., 2011; Rockel, 2015; Rummukainen et al., 2015). Corresponding arguments apply for regional climate ocean models (e.g., Meier, 2002a). From the ocean perspective, historically the main requests from the regional atmospheric forcing were proper wind fields and atmospheric surface variables that take the changing sea-ice cover in the Baltic Sea under global warming into account (Meier et al., 2011c; their Figure 3). Due to the ice-albedo feedback in the northern Baltic Sea (Bothnian Bay, see **Figure 1**) winter mean changes in SST and wind speed may differ between individual scenario simulations performed with uncoupled (atmosphere) and coupled (atmosphere–sea-ice–ocean) regional climate models by more than 3°C and 1 m s^{-1}, respectively (Meier et al., 2011c; their Figures 10, 11). Even larger discrepancies were reported from the European PRUDENCE project (Christensen and Christensen, 2007) emphasizing the added value of coupled RCMs. However, the added value of the usage of coupled RCMs or Regional Climate System Models (RCSMs; Giorgi and Gao, 2018) is often overshadowed by the uncertainties from the lateral boundary data from the GCMs or the experimental setup (Schrum, 2017; Mathis et al., 2018).

The first scenario simulations of the Baltic Sea based upon coupled physical-biogeochemical ocean circulation models were performed by Neumann (2010) and Meier et al. (2011a). Earlier scenario simulations that have been developed since the end of the 1990s focussed only on hydrodynamic changes in the Baltic Sea (**Table 1**). Neumann (2010) performed transient simulations for the period 1960–2100 with an ecosystem model driven by the atmospheric and hydrological forcing from a regional climate atmosphere model with sea surface and lateral boundary data from a global climate model, which is in turn driven by two GHG emission scenarios (A1B and B1, see Nakićenović et al., 2000).

Meier et al. (2011a) performed six 30-year time slice experiments driven by two regionalized GCMs, i.e. two control simulations representing present climate (1961–1990) and four simulations with A2 or B2 emission scenario, representing the climate of the late twenty-first century (2071–2100). To regionalize global climate change, the regional coupled atmosphere–sea-ice–ocean model by Döscher et al. (2002) with lateral boundary data from the two GCMs was applied (Räisänen et al., 2004).

Meier et al. (2011a) applied the delta approach for the time slice experiments considering only climatological monthly mean changes of the atmospheric and hydrological forcing together with the reconstructed variability of the period 1969–1998. Hence, they assumed that on interannual and longer time scales the temporal variability of the forcing does not change in future climate.

In recent years, the dynamical downscaling approaches used in these two pioneering studies by Neumann (2010) (**Figure 2B**) and Meier et al. (2011a) (**Figure 2C**) were significantly improved (**Table 1**). For instance, improved versions of GCMs or Earth System Models (ESMs) and RCMs (i.e., coupled atmosphere–sea-ice–ocean models), historical spin up of the BSM, transient simulations (instead of time slices), limited usage of bias correction, expanded multi-model ensembles, more plausible nutrient load scenarios and updated GHG concentration scenarios characterize the latest scenario simulations (e.g., Saraiva et al., 2018, 2019). Since uncertainties are considerable and large ensembles of scenario simulations are needed to estimate uncertainties, the sizes of the ensembles were enlarged with time (e.g., Meier et al., 2011b, 2018a; Omstedt et al., 2012; Holt et al., 2016; Saraiva et al., 2019).

Figure 2 shows various experimental setups of the dynamical downscaling approach. Ideally, boundary data from available GCMs or ESMs would be used to force a RCSM, i.e., a regional coupled atmosphere–sea-ice–land surface–ocean model including the regional carbon and nutrient cycles (Giorgi and Gao, 2018). Hence, changes in atmospheric, hydrological and nutrient forcing of the coastal sea of interest, in this case the Baltic Sea, would be calculated by the RCSM based upon global GHG emission (Nakićenović et al., 2000) or concentration (Moss et al., 2010) scenarios and regional nutrient load scenarios (Zandersen et al., 2019). In case of the ecosystem model comprising even higher trophic levels (e.g., Niiranen et al., 2013; Bauer et al., 2018, in press), also fishery scenarios would be needed (cf. Rose et al., 2010). Regional scenarios of nutrient loads and fishery would be consistently downscaled from global Shared Socio-economic Pathways (SSPs) (Van Vuuren et al., 2011; O'Neill et al., 2014; see Zandersen et al., 2019).

Although the dynamical downscaling approach was improved in recent years, existing methods do not follow the ideal experimental setup described above (**Figure 2A**) and results still suffer from shortcomings. For instance, the work by Saraiva et al. (2018, 2019) employed a hydrological and biogeochemical Land Surface Model (LSM), E-HYPE (Arheimer et al., 2012; Donnelly et al., 2013), separated from the RCSM (**Figure 2D**). In a first step, the scenario simulations with a coupled atmosphere–sea-ice–ocean model (RCA4-NEMO, Dieterich et al., 2013; Gröger et al., 2015; Wang et al., 2015; see **Table 1**) were carried out. Surface fields of precipitation and air temperature over land were stored, bias corrected and used to force the uncoupled E-HYPE model that calculates runoff and nutrient loads into the Baltic Sea (Hundecha et al., 2016). In a second step, the atmospheric forcing from RCA4-NEMO and river runoff and nutrient loads from E-HYPE were used to force the simulations of the coupled physical-biogeochemical model RCO-SCOBI (Meier et al., 2003; Eilola et al., 2009; see **Table 1**). The reason for the choice of this more complicated and not straightforward approach is that RCA4-NEMO included neither a LSM (just a river routing scheme, see Wang et al., 2015) nor a module for marine biogeochemistry. In addition, the atmospheric deposition of nitrogen was prescribed following the nutrient load scenarios of optimistic conditions (BSAP), reference or "current" conditions (REF) and "worst case" conditions (Worst Case) (Saraiva et al., 2018).

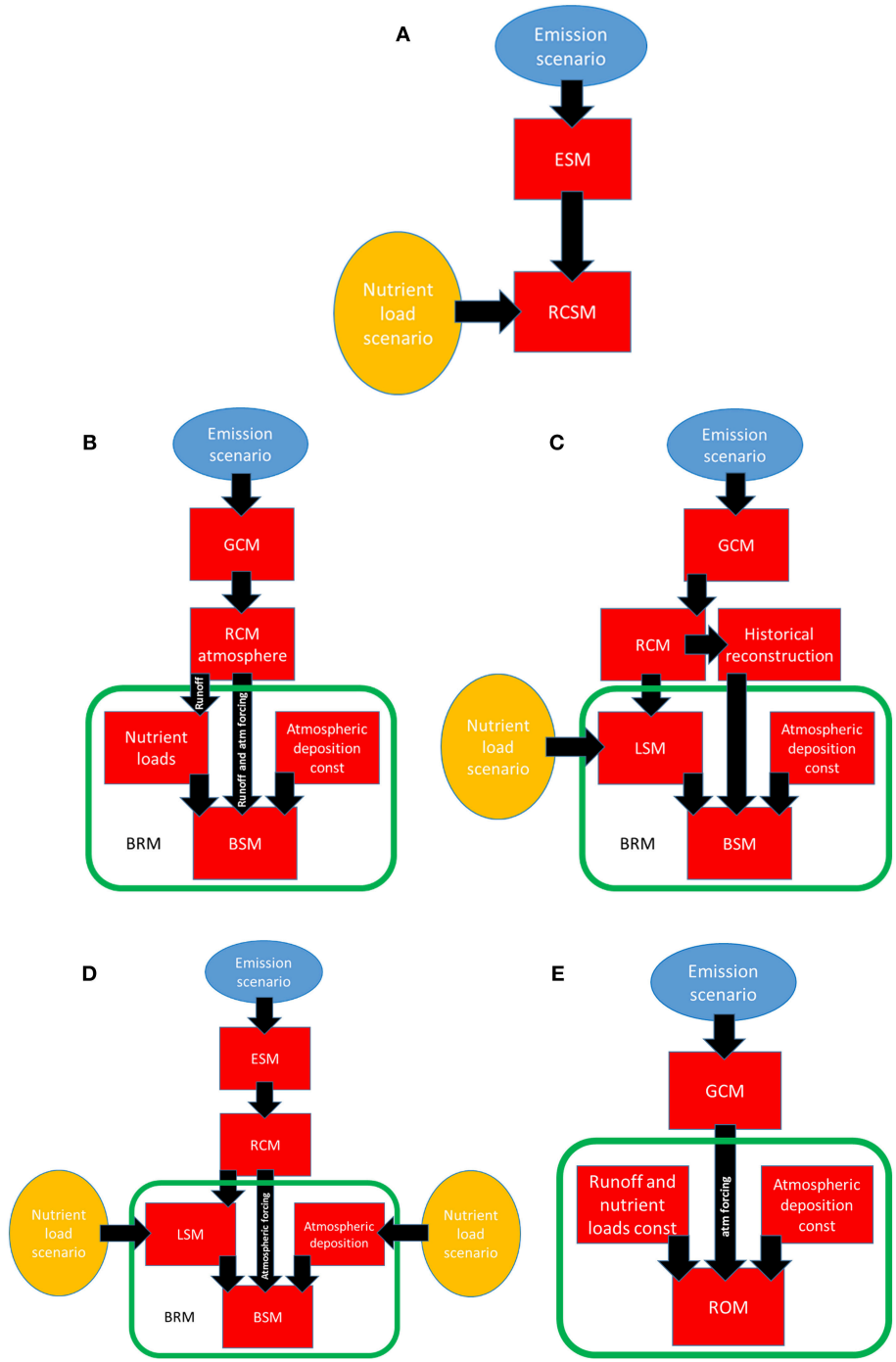


FIGURE 2 | (A) Hierarchy of models in the dynamical downscaling approach (ESM, Earth System Model; RCSM, Regional Climate System Model including atmosphere, sea ice, ocean, land surface and terrestrial vegetation, atmospheric chemistry, marine biogeochemistry, food web, fishery). **(B)** Hierarchy of models in the dynamical downscaling approach used, e.g., by Neumann (2010) (GCM, General Circulation Model or Global Climate Model; RCM, Regional Climate Model, i.e., a regional atmosphere model; BSM, Baltic Sea Model; BRM, Baltic Region Model including a BSM and data sets for riverine nutrient loads calculated from the product of river runoff and climatological river nutrient concentration and atmospheric deposition). **(C)** Hierarchy of models in the dynamical downscaling approach used, e.g., by Meier et al. (2011a). Monthly mean changes in atmospheric surface fields were added to a historical reconstruction that forces a Baltic Sea model (LSM, Land Surface Model; BRM, Baltic Region Model including a BSM, LSM, and data sets for atmospheric deposition). **(D)** Hierarchy of models in the dynamical downscaling approach used, e.g., by Saraiva et al. (2018). **(E)** Hierarchy of models in the dynamical downscaling approach used, e.g., by Holt et al. (2016) (ROM, Regional Ocean Model for the Black Sea, Barents Sea, North Sea and Baltic Sea, and Northwest European Continental Shelf).

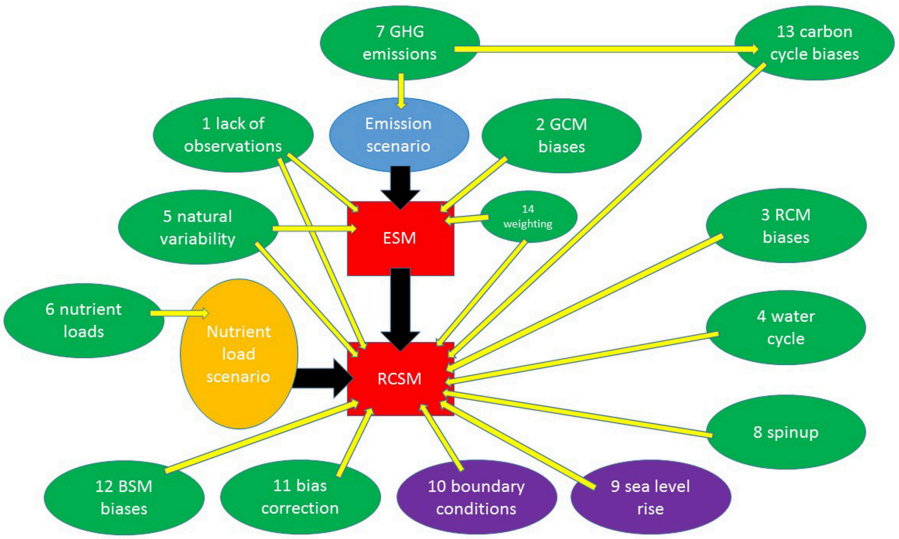


FIGURE 3 | Hierarchy of models in the dynamical downscaling approach as shown by **Figure 2** and selected sources of uncertainties as discussed in the text.

Another approach, that does not follow the ideal experimental setup shown in **Figure 2A**, omitting even a regional atmosphere climate model was presented by Holt et al. (2016) and Pushpadas et al. (2015) (**Figure 2E**).

In addition to the models described above, long-records of homogenous observational datasets, e.g., monitoring data, are needed for the development of scenario simulations because climate models have to be calibrated and evaluated for past and present climate variability before they can be used for future projections. In this study, uncertainties related to differing numbers of observations contained in various databases are discussed (**Table 4**). The insufficient temporal and spatial data coverage may cause errors of integrated data products such as nutrient pools that are used for model calibration and evaluation (**Table 5**).

RESULTS OF THE ASSESSMENT OF UNCERTAINTIES

Estimating Uncertainties

Meier et al. (2012c) compared reconstructed past variations and future projections of the Baltic Sea ecosystem and described considerable uncertainties due to model biases, unknown initial conditions, and unknown GHG emission and nutrient load scenarios. Therefore, the significance of scenario simulations is strongly related to the inherent uncertainties. Within the used model chain the assumptions taken, the dynamic behavior of the considered system itself and existing knowledge gaps constitute several sources of uncertainties. They may add up and pollute the simulation results. Finally, conclusions may become weak or are even impossible. However, for marine management combined climate and nutrient load scenario simulations are of utmost importance because of the long time scales of marine biogeochemical cycles. Hence, to be useful in the decision-making process projections have to consider the range of uncertainty. The challenge for research is to discover how *a priori* assumptions (like unknown future scenarios) affect uncertainty and how uncertainty can be reduced. With this information some management questions can still be answered with the help of scenario simulations despite considerable uncertainties.

Uncertainties of future projections are large, as shown by Meier et al. (2018a). Several differing sources may contribute to these uncertainties (**Figure 3**, **Table 2**). Nevertheless, Meier et al. (2018a) showed that in a relatively large ensemble of scenario simulations based on six coupled physical-biogeochemical models of the Baltic Sea the signal-to-noise ratios of temperature and salinity at the surface and in the deep water in Bornholm Basin, Gotland Basin, Gulf of Finland, Bothnian Sea and Bothnian Bay (for the locations see **Figure 1**) are larger than 1 (Meier et al., 2018a; their Figure 8). Here, the signal-to-noise ratio is defined as the absolute value of the ratio between the ensemble mean change and the standard deviation of the mean changes between future and historical climates calculated from all ensemble members, i.e. the ensemble spread.

However, for biogeochemical variables, such as deep water oxygen concentrations and winter mean surface concentrations of nitrate and phosphate, the signal-to-noise ratios are mostly smaller than 1 suggesting that changes are not significant (Meier et al., 2018a; their Figure 8). Similar results were found by Meier et al. (2012c their Figure 2) using three coupled physical-biogeochemical models of the Baltic Sea.

Uncertainties in scenario simulations have been studied before (e.g., Räisänen, 2001; Hawkins and Sutton, 2009; Rummukainen, 2016b; Ruosteenoja et al., 2016). Hawkins and Sutton (2009) identified three sources of uncertainty in global temperature projections, i.e. model uncertainty, scenario uncertainty and internal variability (see introduction). They

TABLE 4 | Total amount of stations ("station" is a vertical profile sampled; it could be just temperature measured every few centimeters or a full set at standard depths; it could also include multi-day intensive stations with profiles taken every few hours) in different datasets: (1) The data archive (http://iowmeta.io-warnemuende.de) of the Leibniz Institute for Baltic Sea Research Warnemünde (IOW), (2) the Swedish Ocean Archive (SHARK, https://sharkweb.smhi.se/) operated by the Swedish Meteorological and Hydrological Institute (SMHI), and (3) the Baltic Environmental Database (BED, http://nest.su.se/bed) at Stockholm University.

	IOW	SHARK	BED
1970–2015	757	365	2604
1970–1999	270	198	1571

(BED numbers include stations from IOW and SHARK and are cleaned of "duplicate" identical stations coming from different providers).

TABLE 5 | Average (2000–2010) basin-wide annual mean concentrations (mmol m^{-3}) estimated from different datasets (see **Table 4**).

	IOW	SHARK	BED
Nitrate+nitrite	2.49 ± 0.66	3.18 ± 0.60	3.36 ± 0.41
Phosphate	1.00 ± 0.04	1.09 ± 0.07	1.01 ± 0.06

applied a statistical formalism based upon average variances of simulated climate change of a smoothed fit of the original time series and variances of the residuals across scenarios and time. They concluded that for lead times of the next few decades or shorter the dominant contributions to the total uncertainty are internal variability and model uncertainty. The importance of internal variability increases at regional compared to global scales and at time scales shorter than a few decades. Consistent with these results, in many studies the statistical significance of simulated climate change between future and past time slices (usually of a 30-year period) was calculated from a Student's *t*-test (e.g., Räisänen et al., 2004). For longer lead times the dominant sources of uncertainty are model uncertainty and scenario uncertainty according to Hawkins and Sutton (2009). Finally, they concluded that the uncertainties from internal variability and model uncertainty are potentially reducible through better initialization of climate predictions (e.g., Smith et al., 2007; Meehl et al., 2009) and progress in model development although the advantages of improved models are not yet visible (Knutti and Sedláček, 2013).

In a first attempt to quantify uncertainties in scenario simulations of the Baltic Sea, Saraiva et al. (2019) analyzed uncertainties of projected temperature, salinity, primary production, nitrogen fixation and hypoxic area from an ensemble of 21 scenario simulations and two sensitivity experiments using one BSM, one RCM, one hydrological model, four GCMs, two GHG concentration scenarios (i.e., the Representative Concentration Pathways RCP 4.5 and RCP 8.5, see Moss et al., 2010) and three regional nutrient load scenarios ranging from plausible low to high values following Zandersen et al. (2019). Saraiva et al. (2019) analyzed uncertainties at the end of the twenty-first century and consequently neglected the uncertainty from natural variability (Hawkins and Sutton, 2009). Hence, for scenario simulations of the Baltic Sea comprehensive, quantitative analyses of the sources of uncertainty are still not available.

Sources of Uncertainties

Observations

The mechanisms of eutrophication are better explained by total amounts (pools) of nutrients in the aquatic system rather than by concentrations at specific locations because of large horizontal gradients. Therefore, an assessment of uncertainties in the pools reconstructed from observations and used for calibration and validation of the models is very important. The extent of such uncertainties can be demonstrated by a comparison of basin-wide mean concentrations of oxidized nitrogen (NO_3+NO_2) and phosphate for the Baltic proper from different measurement datasets for 2000–2010, the time interval reasonably covered by the national monitoring schemes (Savchuk, 2018). The datasets differ in station distributions and number of observations (**Table 4**). The comparison suggests that there are systematic differences between the pools reconstructed from the various datasets, larger for oxidized nitrogen than for phosphate (**Table 5**).

Global Climate Models

Over the Baltic Sea region, 60–70% of the uncertainty in the 4th decade of the projection and still 40–50% in the 9th decade is due to GCM uncertainties (Hawkins and Sutton, 2009; their Figure 6). GCMs and ESMs are usually not tuned to perform well in a specific region but rather to reproduce the dynamics of large-scale key climate processes. Furthermore, the tuning strategy can differ significantly among different modeling groups (e.g., Hourdin et al., 2017; Schmidt et al., 2017) and often the model's climate sensitivity plays a significant role in model calibration (e.g., Mauritsen et al., 2012). Moreover, the long-term development of global models often follows a trend toward more complexity, i.e., inclusion of more processes and more climate components leading to more comprehensive ESMs (see, e.g., the special issue on the development of the MPI-ESM model in Journal of Advances in Modeling Earth Systems[1]. However, the advances in global climate modeling will not necessarily translate into a better climate representation on the regional scale. A big problem for the Baltic Sea region still is that it is either not at all spatially resolved or only treated as a lake (e.g., Sein et al., 2015). Thus, even in those GCMs, where the Baltic Sea is included, it does not benefit from the interactive air-sea coupling due to the coarse resolution. Therefore, there is growing evidence that for dynamical downscaling of climate scenarios for the Baltic Sea the use of regional coupled atmosphere-ocean models is beneficial compared to standalone models (e.g., Tian et al., 2013; Gröger et al., 2015).

The number of GCMs that can be downscaled for the region of interest is usually too small to estimate uncertainties. This requires defining criteria for a careful selection of available GCM scenarios. Very recently methods were developed for GCM

[1]available online: https://agupubs.onlinelibrary.wiley.com/doi/toc/10.1002/(ISSN)1942-2466.MPIESM1).

selection that suggest to select a subset of models that best represents the whole spectrum of available GCMs (e.g., Wilcke and Bärring, 2016). In retrospect, the method by Wilcke and Bärring (2016) motivates the selection of GCMs by Saraiva et al. (2019) who estimated uncertainties in Baltic Sea ecosystem projections due to GCM deficiencies. Saraiva et al. (2019) selected four out of the five GCMs identified by Wilcke and Bärring (2016) to best represent the optimal number of clusters for the spread in projections.

Regional Climate Models

The choice of RCM contributes to the uncertainty of simulated climate in the Baltic Sea first and foremost through the representation of natural variability (Van der Linden and Mitchell, 2009) because biogeochemical cycles in the Baltic Sea are sensitive to atmospheric conditions on shorter time scales, for example, through Major Baltic Inflows (Matthäus and Franck, 1992), storm-induced mixing (Reissmann et al., 2009) or upwelling (Vahtera et al., 2005).

Projections with RCMs inherit the model uncertainty from the GCMs that are used as boundary forcing for the RCMs. In addition, strategies, how the equations are discretized and how sub-grid scale processes are parameterized, contribute to the uncertainties originating from RCMs. Déqué et al. (2007) and Déqué et al. (2012) studied projections of temperature and precipitation over the European region in ensembles of different RCMs driven by different GCMs to determine the contributions of GCM and RCM model uncertainties to the total spread in the projections. They found that in general the GCM has a larger contribution to the spread. This should come as no surprise since RCMs are developed and tuned for a specific region, whereas GCMs need to perform reasonably well everywhere and are mostly tuned to the large open ocean areas. While the choice of the GCM becomes important on seasonal and longer time scales, on shorter time scales the RCM uncertainty dominates. Weekly to hourly time scales are important, for instance, for large salt water inflows, upwelling and mixing.

It has been shown by Deser et al. (2014) that uncertainty on a regional scale can be connected to the natural variability of the system. Different patterns of atmospheric variability like Scandinavian blocking[2] or a potential shift in the storm track and its effect on the Baltic Sea ecosystem have not been investigated so far. It is conceivable that the choice of the GCM and RCM and even the combination of different GCM/RCM pairs might lead to different representations of these patterns. In order to quantify this added uncertainty, specific experiments need to be carried out for future, more detailed assessments.

Since state-of-the-art multi-model ensembles are using only a selected number of RCMs to drive the Baltic Sea ecosystem models, the uncertainty that stems from the choice of the RCMs is undersampled. Studies like the PRUDENCE project (Christensen and Christensen, 2007) or the CORDEX effort (Jacob et al., 2014) showed that, for example, uncertainties in projections of precipitation are mainly dominated by the RCM in the Baltic Sea drainage basin. One of the most important factors that governs the interaction between the atmosphere and the marine ecosystem is the wind at the atmosphere-ocean interface. The surface wind is also one of those variables that on a regional scale are very much dependent on the choice of the RCM and do affect the solution of the marine ecosystem. On the other hand, integrated measurements like the bottom salinity in the Gotland Basin provide a good test to assess the credibility of a specific RCM and marine ecosystem combination for hindcast periods where reanalyses are available to drive the RCM.

Finally, the choice of the size of the RCM domain is a source of uncertainty. For instance, the freshwater balance of the Mediterranean Sea depends on storm tracks over the North Atlantic, which representation are dependent on the resolution of the models (Gimeno et al., 2012). In addition, atmosphere-ocean feedbacks potentially outside the coupled model domain of the RCM may affect cyclones and heavy precipitation events (Ho-Hagemann et al., 2017).

Regional Water Balance

The global water balance is dominated by precipitation and evaporation at the ocean–atmosphere interface. In coastal seas, such as the Baltic Sea, the land influence is high and on long time scales, the net precipitation over land is balanced by the river runoff to the sea. The precipitation and evaporation rates are strongly influenced by the mid latitudes' low-pressure systems and related trajectories. Fresh water that precipitates over the Baltic Sea catchment area may come from surrounding sea areas such as the Atlantic Ocean, North Sea, Barents Sea or Mediterranean Sea (e.g., Sepp et al., 2018). Long-term changes in the frequency of cyclones and their trajectories are of major importance for the hydrological cycle and for example, the number of cyclones over the Baltic Sea has increased, especially during winter (e.g., Sepp et al., 2005; BACCII Author Team, 2015). During past decades, efforts have been made to analyze the hydrological cycle in the Baltic Basin area by using hydrological models calculating the fresh water drainage to the Baltic Sea (e.g., Graham, 1999). Coastal ocean models were then used to evaluate the water balance calculation (see reviews in Omstedt et al., 2004, 2014) based on available data including salinity measurements. Modeling the Baltic Sea allowed consistent estimates of in- and outflows for closing the hydrological cycles and a possibility to estimate uncertainties with regard to the fresh water cycle in the Baltic Basin area. In the model study by Omstedt and Nohr (2004), all available data were integrated indicating that the long-term net water balances (mean errors over decadal time scales) could be estimated within an error of about $\pm$ 600 $m^3 s^{-1}$ or 4% of the total river runoff (15,000 $m^3 s^{-1}$). By introducing atmospheric and land surface models (e.g., Jacob, 2001; Bengtsson, 2010) it was possible to achieve reasonable estimates of the net fresh water outflow from the Baltic Sea if the atmospheric model was driven by observations based on reanalyzed data at the lateral boundaries. However, estimates on model uncertainties were not analyzed.

Biases and inconsistent climate signals have been reported based on present state-of-the-art RCMs (e.g., Turco et al.,

[2]Scandinavian blocking is a large-scale, persistent atmospheric pattern of high pressure over Scandinavia that redirects migrating cyclones. The range of typical time scales of blocking is several days to even weeks.

2013). From model calculations on different levels of complexity, the uncertainty in RCMs was estimated using the BALTEX box concept (Raschke et al., 2001). Further, it was shown that especially for climate change impact studies downscaling methods using RCMs still indicate a need for improvement (Omstedt et al., 2000, 2012; Lind and Kjellström, 2009; Donnelly et al., 2014; BACCII Author Team, 2015). For example, Omstedt et al. (2012) showed that without bias corrections related to the fresh water inflow the biogeochemical calculations in the BSMs would be poor. In addition, Donnelly et al. (2014) found that the climate sensitivity of their hydrological model also depends on the bias correction method applied to precipitation and air temperature from the driving RCM.

Natural Variability

The Baltic Sea is affected by internal modes of variability of atmospheric large-scale circulation such as the North Atlantic Oscillation (NAO, e.g., Tinz, 1996; Omstedt and Chen, 2001; Andersson, 2002; Meier and Kauker, 2002; Chen and Omstedt, 2005; Löptien et al., 2013) or decadal and centennial variations related to ocean-atmosphere interactions in the adjacent Atlantic (e.g., Kauker and Meier, 2003; Meier and Kauker, 2003a,b; Hansson and Omstedt, 2008; Schimanke and Meier, 2016; Börgel et al., 2018). Therefore, in order to distinguish natural variations from anthropogenic induced changes, it is crucial to determine the magnitude of natural variability of physical and ecosystem characteristics undisturbed of anthropogenic influence, even though the projected impact of climate change at the end of the century can be expected to be substantially larger than the variability that has been recorded during the historical period.

Previous downscaling studies usually attempted to estimate natural variability from reanalysis data or hindcast simulations by downscaling GCM simulations of the historical period (e.g., Holt et al., 2012; Sein et al., 2015; Wang et al., 2015). In addition, the ensemble approach was applied to distinguish between natural variability and the climate change signal although the number of ensemble members was limited (e.g., three members in Kjellström et al., 2011; Omstedt et al., 2012).

However, anthropogenic influence has already started during the historical period and common hindcast simulations mostly cover the period since 1960. Observation based estimates indicate that the global mean temperature rises at rates between 0.15° and 0.2°C per decade since the seventies of the previous century (e.g., Hansen et al., 2010). Thus, the currently observed warming has already reached about half of the rates which are expected even for the strongest warming projections reported by the assessments of the IPCC, e.g., 0.34°C per decade for the A2 scenario (Meehl et al., 2007) or 0.37°C per decade for the RCP 8.5 scenario (Table 12.2 in Collins et al., 2013). Therefore, estimates of natural variability inferred from any hindcast simulation are already strongly affected by climate warming.

An alternative approach to quantitatively estimate natural variability has been presented by Tinker et al. (2015) and Tinker et al. (2016). They used the regionalized climate from HadCM3 applied to POLCOMS for the northwestern European shelf to downscale 146 years out of a long-term, pre-industrial control simulation from the HadCM3 global climate model. Such a control simulation is unaffected by anthropogenic forcing and thus represents natural variability as realistic as possible. Accordingly, it can even be used to estimate significance of changes simulated during the historical period. The long duration of this simulation likewise allows determining natural variability at low frequencies, which is typically related to the ocean with its higher internal inertia.

An even longer simulation of pre-industrial climate of the Baltic Sea for the period 950-1800 AD was carried out by Schimanke and Meier (2016). These model data allowed to analyze the low-frequency natural climate variability of the Baltic Sea. For instance, Börgel et al. (2018) showed that the Atlantic Multidecadal Oscillation (Knight et al., 2005) has a significant impact on Baltic Sea salinity variations on time scales of 60–90 and 120–180 years for the periods 1450–1650 and 1150–1400, respectively. However, as every GCM generates its own variability characteristics one would have to apply the dynamical downscaling procedure for every individual GCM control climate used in regional multi-GCM ensembles, which makes it computationally quite expensive.

Nutrient Loads and Bioavailability

Although being derived from the same original data (e.g., Savchuk et al., 2012b), different external nutrient inputs were used to calibrate the BSMs, with most important differences originating from the differing assumptions on the bioavailable fractions of land loads taking coastal nutrient retention into account. Especially significant are the differences in terrestrial phosphorus inputs, reaching up to 50% in historical model simulations (Eilola et al., 2011; Meier et al., 2018a; their Figure 3). Recently, Asmala et al. (2017) estimated from up-scaled observations that the coastal filter of the entire Baltic Sea removes 16% of nitrogen (N) and 53% of phosphorus (P) inputs from land, with archipelagos being the most important phosphorus traps. BSMs covering the entire Baltic Sea do not resolve the processes of the coastal zone properly, although shallow areas are included and calibrated to remove "enough" nutrients in the coastal zone to achieve correct nutrient concentrations in the water column of the open sea in present climate. For the entire Swedish coastline, Edman et al. (2018) estimated from a high-resolution coastal zone model the average nutrient filter efficiency to be about 54 and 70% for nitrogen and phosphorus, respectively. As a result, the total amounts and the N:P ratio of nutrients actually entering the open sea biogeochemical cycle are substantially different between the models, which is a source of systematic quantitative differences in scenario responses to projected changes given in absolute amounts.

For instance, in the BALTSEM model the decrease of phosphorus bioavailability from the current 100% would be simply equivalent to a reduction of external input. As had already been shown by Savchuk and Wulff (1999) and was repeatedly confirmed since then, e.g., by hundreds of numerical experiments performed for the revision of the BSAP (Gustafsson and Mörth,

2014), such reduction would result in a weakening of the "vicious circle"[3], which is a positive feedback mechanism that impedes the switch from eutrophic to oligotrophic conditions (Vahtera et al., 2007), and would have similar consequences to those already described with the BSAP scenario.

Atmospheric nitrogen depositions amount up to more than 25% of the total loads (HELCOM, 2015). Estimates of atmospheric loads are based on atmospheric transport models calibrated against monitored nitrogen deposition. Modeling relies on emission and land use data. Since not only the HELCOM area contributes to the deposition, also data from outside the HELCOM area and from shipping are used. Past reconstructions may involve larger uncertainties due to missing forcing data and reliable model simulations. Most data have to be considered as rough estimates (Gustafsson et al., 2012).

Some LSMs like HYPE (Arheimer et al., 2012; Donnelly et al., 2013) are process-based and calculate the impact of changing climate on nutrient loads. For instance, Arheimer et al. (2012) suggested that due to the changing climate the total load from the catchment area to the Baltic Sea will decrease for nitrogen and increase for phosphorus in the future. Their scenario simulations indicate that the impact of climate change may be of the same order of magnitude as the expected nitrogen reductions from the measures simulated such as wastewater treatment and agricultural practices. Whereas the knowledge about soil processes on shorter time scales is available, the response to changing climate on longer time scales such as centennial is lacking. Due to sparse observations of long-term trends in the nutrient storage in soil caused by changing climate and land use management, simulated changes in LSMs are difficult to validate.

Emission Scenarios

For addressing uncertainty, new GHG emission scenarios are designed regularly within the framework of CMIP. During phase 3 of CMIP scenarios were defined that provide a range of slower and faster increasing emissions from 2001 onward leading to maximal atmospheric CO_2 concentrations at the end of the twenty-first century (Nakićenović et al., 2000). These scenarios did not include any specific mitigation actions to explicitly reduce emissions but rely more on scenarios for economic growth.

For CMIP5 models, RCPs were developed and define a maximum radiative forcing of GHGs at a certain time with decreasing forcing afterwards. For example, RCP 2.6 has its biggest radiative forcing ($\sim$3 W m^{-2}) in the middle of the twenty-first century and thereafter it decreases slightly to 2.6 W m^{-2} at the end of the century. Thus, when comparing different RCP scenarios, the maximal climate response can be expected at different times depending on the respective RCP. Existing radiative transfer models estimate a present day radiative forcing due to CO_2 of 1.8 W m^{-2} and a combined effect of all GHGs of 2.25 W m^{-2} (Myhre et al., 1998). More recent estimates of the total radiative forcing from 26 GHGs amount to 2.83 W m^{-2} (see Myhre et al., 2013; their Table 8.2, p. 678). It is therefore rather unlikely that RCP 2.6 can be achieved. Hence, this scenario was neglected in most of the previous studies (e.g., Meier et al., 2018a; Saraiva et al., 2018, 2019).

By contrast, the moderate to high radiative forcing scenarios RCP 4.5, RCP 6.0, and RCP 8.5 reach their respective maximum in radiative forcing at the end of the twenty-first century. All RCP scenarios start from the historical period, which ends in 2005. Not considered yet in scenario simulations are the most recent emission scenarios developed in the framework of CMIP6. They are defined from 2015 onward (Eyring et al., 2016) and include a by far more comprehensive suite of possible SSPs compared to the previous phases of CMIP (O'Neill et al., 2014).

The two most commonly used RCP scenarios in Baltic Sea projections, RCP 4.5 and RCP 8.5, are those projections in the CMIP5 program that are included in the core set of experiments (Taylor et al., 2012). In terms of CO_2 emissions, the RCP 8.5 scenario corresponds to the 90th percentile of the scenarios that have been considered for the development of the RCPs (Moss et al., 2010). It represents non-climate policy and high population scenarios. The socio-economic scenario in RCP 8.5 is not unique. Different SSPs would be consistent with this RCP. However, RCP 8.5 may be characterized by fossil fuel dominated economy, high-energy consumption and medium agricultural land use. The RCP 4.5 scenario is a typical mitigation scenario where CO_2 emissions are stabilized after 2080 (Moss et al., 2010). It is compatible with different climate policy scenarios, such as the B1 scenario of the Special Report of Emission Scenarios (SRES) (Nakićenović et al., 2000). It assumes that the population has reached its peak around 2080 at 9 billion people. In the RCP 4.5 scenario, energy consumption is much lower (three fifth) than in RCP 8.5 and coal, oil, gas, bio-energy and nuclear power contribute with roughly equal amounts. Agricultural land use in RCP 4.5 is very low (Van Vuuren et al., 2011).

A noteworthy difference to the currently available RCP scenarios is that the core SSPs, as defined in the CMIP6 ScenarioMIP (Scenario Model Intercomparison Project, O'Neill et al., 2016), include protocols for overshoot scenarios and long-term scenarios that proceed up to 300 years into the future. This refers to the fact that some high impact and non-linear climate responses (e.g., Liu et al., 2017) can occur on time scales beyond the common projection period until 2100. In this long-term perspective, the uncertainty due to the use of different global models is expected to be large, which demands for a high number of ensemble members to be considered in future regional studies.

Initial Conditions

Both, multicomponent ESMs as well as high resolution RCMs have their own internal dynamics and certainly their own individual biases. Therefore, it is highly unlikely that the prescribed initial fields are in phase with internal model dynamics. Especially in the Baltic Sea, which has longer flushing

[3]The "vicious circle" is a feedback mechanism that sustains eutrophication in the Baltic Sea and similar systems (Vahtera et al., 2007; Savchuk, 2018). Increased nutrient loads lead to increased algae blooms, mineralization and oxygen consumption in the water column and sediments. Expanding hypoxia increases removal of nitrogen by denitrification, thus decreasing the N:P ratio. Under anoxic conditions, the phosphorus retention capacity of sediments is considerably reduced causing increased phosphorus fluxes from the sediments into the water column. Deficit of nitrogen and increased availability of phosphate enhance nitrogen fixation by cyanobacteria making nitrogen available for other phytoplankton species and thus reinforcing eutrophication.

times than many other shelf seas (e.g., the North Sea), this can result in more or less strong model drifts (e.g., Gustafsson et al., 1998; Omstedt et al., 2000; Meier, 2002a). This applies even more to biogeochemical variables involved in carbon and nutrient cycling, and especially to the sediments.

Two approaches have been reported in the literature to overcome this problem: (1) Prolonged spin up runs applying repeated forcing according to present day climate (e.g., Meier, 2007; Lessin et al., 2014), or (2) starting the simulation long before the time period of interest using reconstructed forcing data (e.g., Gustafsson et al., 2012; Meier et al., 2018a,b,c).

The initialization problem becomes more prominent when downscaling GCM climate scenarios. Any initialization from runs other than the corresponding historical run of the global GCM will result in a more or less strong perturbation due to the switch in atmospheric forcing. To remedy this problem, different kinds of bias correction methods have been developed (e.g., Meier, 2006; Meier et al., 2011a; Holt et al., 2012; Mathis et al., 2013; Pushpadas et al., 2015). The general rationale behind those methods is that global GCMs are considered to be sufficiently good to simulate global climate change but are biased on the regional scales (see sub-section on bias correction).

Filtering of nutrients in the coastal zone or burial in the sediments have very long time scales. Hence, the spin up period in many of the state-of-the-art ensemble simulations is too short.

Global Mean Sea Level Rise

Projections of GMSL change range from 0.26 to 0.82 m for the period 2081–2100 relative to 1986–2005 (Stocker et al., 2013). They are dependent on the choice of the emission scenario (Schrum et al., 2016) and natural climate forcing (e.g., solar variability). For the next decades climate variability is already committed by today's GHG levels, whereas long-term projections are more uncertain (Rummukainen, 2016b). A less likely, higher increase in GMSL cannot be ruled out due to possible additional ice sheet contributions (BACCII Author Team, 2015; Schrum et al., 2016).

Uncertainties in GMSL change projections and the different projected spatial patterns arise from the limited capability of the models to simulate climate system processes and natural variability (e.g., El Niño–Southern Oscillation (ENSO) or NAO on regional scales) as the non-linear system of equations has to be solved numerically and is therefore an approximation (Schrum et al., 2016). Horizontal and vertical resolutions are defining the capability of simulating climate system processes and are limited by the available computational resources. In addition, different numerical techniques, parameterizations and model approaches lead to additional uncertainties, which are not well estimated in most studies (Schrum et al., 2016).

Beside the uncertainty of future GMSL change itself, its influence on the Baltic Sea is also uncertain, as only a few studies have investigated this question. Using a process-oriented model Gustafsson (2004) investigated the sensitivity of Baltic Sea salinity to large perturbations in climate such as changes in GMSL and freshwater supply. He found that a rise in GMSL of about + 1 m would lead to a sea surface salinity increase from 8 to 9 g kg^{-1} in the southern Baltic proper. Hordoir et al. (2015) investigated the influence of GMSL change on saltwater inflows into the Baltic Sea. They performed idealized model sensitivity experiments using a regional ocean general circulation model covering the North Sea and the Baltic Sea. They found that GMSL rise leads to a non-linear increase in salt inflow caused by increased cross-sections and reduced mixing in the Danish straits (Hordoir et al., 2015). However, Arneborg (2016) disproved the interpretation of the results of Hordoir et al. (2015) by arguing that the increased salt inflow caused by GMSL rise is not originating from reduced mixing but is due to a higher increase of barotropic volume fluxes in the Sound than in the Belt Sea.

A study by Meier et al. (2017) investigated the influence of GMSL rise of 0.5 m or 1.0 m on the water exchange between the North Sea and the Baltic Sea and the state of hypoxic areas in the Baltic Sea using a coupled physical-biogeochemical model. Saraiva et al. (2019) even combined scenario simulations with a 1.0 m higher mean sea level. Both studies found a linear increase in salt inflow with increasing cross section and higher stratification in the Baltic Sea and hence increased hypoxic bottom areas. From the performed idealized sensitivity experiments where only time-independent sea level anomalies were added, uncertainties of the scenario simulations by Saraiva et al. (2019) were estimated. However, the simulations overestimate the impact of GMSL rise because they do not take the transient behavior of changing climate into account (Meier et al., 2017).

Uncertainty in Nutrient Concentrations at the Lateral Boundary in the Northern Kattegat/Skagerrak

Regional ocean models usually have a boundary to connecting oceans or seas. Consequently, information at the boundary from outside the model domain is needed. In the case of the Baltic Sea, the effect of the open boundary may be limited due to the bathymetry of the narrow and shallow Danish straits, which confine the exchange between the Baltic Sea and the open ocean. Nevertheless, the effective net import of nitrogen from Kattegat into the Baltic Sea accounts for up to 100 ktons $year^{-1}$ (Radtke and Maar, 2016)[4]. Here, we will discuss the impact of uncertain information about nutrient concentrations for simulations of the Baltic Sea.

Sources of uncertainty in boundary conditions

According to several earlier estimates, the water masses at the entrance to the Kattegat consist of about 80% of Atlantic waters from the central North Sea, while German Bight and Baltic waters contribute only about 10% each (e.g., Aarup et al., 1996; Kristiansen and Aas, 2015). Despite a marked decrease of nutrient concentrations in the Dutch coastal areas, almost returning to the pre-industrial levels with slightly higher N:P ratio (e.g., Troost et al., 2014; Burson et al., 2016), the concentrations in the offshore areas of the German Bight, where the Jutland Coastal Current originates, have not changed much since the known regime shift in the late 1980s (e.g., Lenhart et al., 2010; Topcu et al., 2011).

[4]The net import from Kattegat amounts to about 11-14 % of the total bioavailable riverborne nitrogen load during 1980-2005 according to Meier et al. (2018a).

A relative stability of the Skagerrak nutrient status has already been demonstrated by Skogen et al. (2004), when drastic reductions of 50% of riverine nutrient input to the North Sea resulted in only about 5% decrease of the simulated primary production in the Skagerrak, which was far less than the natural interannual variations. Less than 15% reduction of primary production has also been simulated with similar nutrient load reductions in several models covering the entire North Sea (Lenhart et al., 2010). Scenario simulations with 50% reductions of the North Sea nitrogen and phosphorus river loads performed with a biogeochemical model for the coupled North Sea - Baltic Sea area resulted in a decrease of the winter surface nitrate and phosphate concentrations at the Skagerrak-Kattegat boundary of 10–20% and 5–10%, respectively (Kuznetsov et al., 2016). The change in nutrient concentrations in the North Sea, Skagerrak and Kattegat due to nutrient load reductions in North Sea rivers is small because of the large exchange of the North Sea water with the Atlantic.

As trends in nutrient concentrations in Atlantic waters filling the southern and central parts of the North Sea have not been observed yet (Radach and Pätsch, 1997; Laane et al., 2005), nutrient concentrations in Skagerrak are usually assumed to be constant. However, as was demonstrated by scenario simulations with a global coupled physical-biogeochemical model with finer resolved northwestern European shelf, the projected warming and freshening sharpens stratification and reduces the upward mixing of nutrient-rich waters along the continental shelf break and their import into the North Sea (Gröger et al., 2013). Consequently, nutrient concentrations in the open North Sea are about halved and primary production is significantly decreased. Recent scenario simulations suggest that the variability in net primary production in the North Sea will rapidly increase after 2080 (Mathis et al., 2019). This non-linear effect is explained by the threshold when the mixed layer depth in the eastern North Atlantic reaches the shelf break causing high-frequent changes in nutrient transports into the North Sea. The impact of such changes for the Baltic Sea has so far not been explored. However, as the nutrient inventory of the Baltic Sea is rather controlled by riverine input and interaction with sediments the effect might probably be small. Efforts to reduce the currently high input of anthropogenic nutrients from, *inter alia*, fertilizers could give rise to a more prominent role of boundary conditions in the eastern North Sea region in future (see the discussion below).

Impact of uncertainty in boundary conditions

In order to demonstrate the uncertainties introduced into scenario simulations that keep the nutrient inputs from Skagerrak unchanged, BALTSEM simulations have been performed for 300 years under repeated present climate and the contemporary nutrient inputs to the Baltic Sea (HELCOM, 2015) have been kept unchanged except for the inputs through the Skagerrak-Kattegat boundary. Two scenarios have been implemented with reduced boundary nutrient concentrations from the very start of the simulations: "North Sea" (20% nitrogen and 10% phosphorus reduction) and "Atlantic" (50% nitrogen and 50% phosphorus reduction). The comparison of these scenarios to the reference run, where the Skagerrak concentrations are kept unchanged, shows much larger changes in the Kattegat compared to the Gotland Sea, especially in the more plausible "North Sea" scenario (**Table 6**).

TABLE 6 | Relative changes (in %) of the average (2050–2300) of annual mean nutrient concentrations and integral fluxes induced by the "North Sea" and "Atlantic" scenario reductions of the nitrogen and phosphorus imports from Skagerrak.

BALTSEM basin	TN	TP	PP	NF
NORTH SEA SCENARIO (2.9% N AND 4.0% P OF THE TOTAL LOAD)				
Central Kattegat	−10.8%	−7.5%	−11.7%	−4.9%
Gotland Sea	+1.4%	−1.2%	−2.3%	−2.2%
ATLANTIC SCENARIO (7.2% N AND 20.1% P OF THE TOTAL LOAD)				
Central Kattegat	−30.2	−37.5	−40.4	−55.8
Gotland Sea	+7.3	−5.2	−10.2	−10.1

TN, total nitrogen; TP, total phosphorus; PP, net primary production; NF, nitrogen fixation. The total load to the entire Baltic Sea comprises nutrient inputs from land, via atmosphere, and through the Skagerrak-Kattegat boundary.

The weak response of the Baltic Sea as a whole is explained by the filtering capacity of the shallow and narrow Danish straits. However, in the "Atlantic" scenario the import to the Arkona Basin is reduced by 24 and 28%, i.e., by one half of the relative reductions at the boundary. This small sensitivity might change if the GMSL increases. It is remarkable that even minor reductions of both phosphorus inputs and concentrations lead to a decline of primary production and hypoxic area in the Baltic Sea with a consecutive decrease of denitrification and increase of the phosphorus sediment retention, which in consequence could also be considered as a weakening of the "vicious circle" (Vahtera et al., 2007). Compared to all other uncertainties and overall changes projected by the entire ensemble of available scenario simulations (Meier et al., 2018a), the uncertainties originating from the prescribed nutrient imports from the North Sea can be considered as insignificant. Differences among the models are probably small because the same observations from Kattegat or Skagerrak are used at the lateral boundaries.

Bias Correction

To reduce biases, BSMs and LSMs might be forced by trends calculated from the RCMs/GCMs rather than directly by biased RCM/GCM climates (Rechid et al., 2016; Schrum et al., 2016). However, this method cannot account for biases in wind direction (in earlier studies only wind speed was corrected, e.g., Höglund et al., 2009; Meier et al., 2011c), which may be important in the context of saltwater inflows to the Baltic Sea. Furthermore, atmospheric boundary variables are not independent of each other and their relationships are in most cases non-linear. Hence, the bias corrected forcing variables are in most cases physically not consistent. Further, in case of the Baltic Sea deep water one has to consider that the high sensitivity of inflows to atmospheric forcing (e.g., Schimanke et al., 2014) requires to force and initialize the model with data as close as possible to the forcing data set to which model parameters were originally tuned to. These forcing data are usually various kinds of global (e.g., NCEP/NCAR, Kalnay et al., 1996; ERA-40, Uppala et al., 2005)

or regional (e.g., UERRA[5]) atmospheric reanalysis data sets (e.g., Omstedt et al., 2005), gridded observations (e.g., Meier et al., 2003; Omstedt and Hansson, 2006a,b; Meier, 2007), and reconstructions (e.g., Gustafsson et al., 2012; Meier et al., 2012c; Meier et al., 2018b).

On the other hand, bias correction will facilitate the comparison of large ensembles applying multiple driving GCMs (as it removes the individual GCM biases, which must be expected to differ among GCMs) and allows starting the model from conditions as realistic as possible (e.g., Meier et al., 2006; Pushpadas et al., 2015; Holt et al., 2016).

Different Responses/Sensitivity in Baltic Sea Models and Processes

Uncertainties are introduced by both the LSM and the BSM. Since the physical basics of the hydrodynamic modeling are well known, differences in model results emerge merely from the applied numerical approximation of the differential equations and the parameterization of sub-grid scale processes (e.g., Myrberg et al., 2010) or from the atmospheric forcing (Placke et al., 2018). In addition, the model setup like the bathymetry, the open boundary conditions or the treatment of runoff may introduce different model results. Owing to their nature, biogeochemical models are flawed due to the complexity of processes involved and knowledge gaps in their details and parameterizations. The uncertainties in the representation of biogeochemical processes in BSMs were discussed by Eilola et al. (2011). They concluded from the analysis of hindcast simulations of three different BSMs that the largest uncertainties are related to the initial conditions in the early 1960s (the start period of their simulations), the bioavailability of nutrients in land runoff (see section discussion above), the parameterization of sediment fluxes and the turnover of nutrients in the sediments, and the nutrient cycling in the Gulf of Bothnia.

Despite simplification, implemented sediment parameterizations produce biogeochemical fluxes that are reasonably comparable in hindcast simulations to available measurements. However, the integral amounts of sediment nutrients differ between models manifold, which greatly affects the carrying capacity of sediments as ecosystem's memory and makes the response time in projections rather uncertain (Eilola et al., 2011).

Usually in BSMs the response of benthic communities to changing environmental conditions is neglected (e.g., Neumann et al., 2002; Savchuk, 2002; Eilola et al., 2009). Timmermann et al. (2012) showed that benthic fauna has an impact on nutrient sediment fluxes and the feedback between eutrophication and hypoxia. However, Timmermann et al. (2012) concluded that quantitative studies how benthic fauna would affect the system over large spatial and temporal scales are still missing. In particular, the benthic influence on algal blooms and fish populations is quantitatively unknown. Recent simplified simulations of invasive polychaete *Marenzelleria* spp. in the Gulf of Finland with the SPBEM model demonstrated that the effect would also be similar to a weakening of the "vicious circle" (Isaev et al., 2017).

Models generally strongly underestimate phytoplankton primary production in the Bothnia Bay. For instance, the spring-to-summer reduction of surface nitrate concentration simulated with BALTSEM (8 to 5 μmol L^{-1}) is about a half of the one estimated from measurements (8 to 2 μmol L^{-1}) (Savchuk et al., 2012a). Here, the unknown or poorly parameterized biogeochemical processes might be related to large pools of humic substances, poorer light climate, the relative distribution of bacterial vs. phytoplankton-based production, and the severe phosphorus limitation of the phytoplankton development (Eilola et al., 2011). The assumption on variable phytoplankton stoichiometry instead of the fixed Redfield ratio allowed to somewhat reduce the selected model-data differences (Fransner et al., 2018). However, the implemented parameterizations have yet to be tested in the southern sub-basins of the Baltic Sea. On the other hand, a southward export of nitrogen, underutilized in the Bothnian Bay, is largely assimilated already in the Bothnian Sea.

State-of-the-art models have been developed and evaluated to the present eutrophic situation in the Baltic Sea (Eilola et al., 2011). Evaluation of simulated model results from more oligotrophic pre-industrial times to present (Gustafsson et al., 2012) is therefore important for the assessment of model performance and uncertainties. Historical observations, e.g., of harmful cyanobacteria blooms, are however scarce (Finni et al., 2001) and from pelagic observations we mainly have an understanding about the situation during the eutrophic period in the Baltic Sea. Long records of Secchi depth and oxygen concentrations give some support for historical reconstructions from 1850 forward (Hansson and Gustafsson, 2011; Gustafsson et al., 2012; Meier et al., 2012c, 2018b,c,d; HELCOM, 2013c; Carstensen et al., 2014), but no information about the nutrient cycling or the occurrence of cyanobacteria blooms. Thus, it is difficult to assess the model performance under different forcing conditions like oligotrophic nutrient loads or different climate.

Further, the link to top-down ecosystem pressures and bio-economic scenarios in state-of-the-art BSMs is usually missing. In the recent review by Nielsen et al. (2017), a big number of bio-economic models operating in scenario mode in the Baltic Sea was reviewed. However, these models did not contain a coupled physical-biogeochemical component. Although the approach of end-to-end ecosystem models was already developed many years ago (Fulton, 2010), only a few studies about bottom-up linkages are available for the Baltic Sea (Niiranen et al., 2013; Bauer et al., 2018, in press; Bossier et al., 2018). Usually, state-of-the-art BSMs do not consider higher trophic levels (e.g., Neumann et al., 2002; Savchuk, 2002; Eilola et al., 2009).

Concerning model biases, temperature and salinity dependencies of some key biogeochemical and food web processes are not well understood. For instance, higher temperatures accelerate bacterial mineralization of phosphorus in the bottom sediments, but the overall rate is unknown. Furthermore, Meier et al. (2011b) showed by comparison of scenario simulations with three BSMs, that sensitivities of the ecosystem response to nutrient load changes differ considerably

[5]http://www.uerra.eu/

among the models. For instance, they found large differences in bottom oxygen concentration changes. For a given nutrient load scenario the discrepancies are largest in regions along the slopes of the Baltic proper and Gulf of Finland that are affected by the varying position and strength of the halocline. The reasons are runoff and wind speed changes that differ among the climate projections. In addition, the sensitivity of the halocline depth to changes in runoff and wind speed differs among the various BSMs. Further, the sensitivity to changes in nutrient loads (BSAP, REF, and BAU) varies considerably among the models. Despite these uncertainties, all three models agree astonishingly well in their overall response of the ecosystem to changes in the external nutrient supply because the response to nutrient load changes is even larger than the spread of the projections. For instance, Meier et al. (2011b) found that in future climate the BSAP is very likely not as efficient as in present climate and perhaps will not lead to any improvement at all under the prescribed experimental setup. In this respect, all three models agreed.

Carbon Cycle Uncertainties

State-of-the-art marine biogeochemical models are often expanded to include the carbon cycle explicitly (e.g., Omstedt et al., 2009; Edman and Omstedt, 2013; Kuznetsov and Neumann, 2013; Gustafsson et al., 2014a,b).

Measurements of carbonate system parameters in the Baltic Sea cover more than one hundred years. As demonstrated by Müller et al. (2016), total alkalinity (A_T) measurements from 1995 and onwards are particularly consistent (in terms of precision), while measurements, e.g., during the 1965–1995 period, are generally less certain. There are also cases where the handling of sulfidic water samples may have resulted in a considerable underestimation of A_T concentrations (Ulfsbo et al., 2011). These issues have implications for hindcast modeling studies as well as model validation.

Another source of uncertainty is the influence of organic alkalinity. The Baltic Sea is heavily influenced by riverborne loads of organic material. If the alteration of the acid-base balance caused by organic acids is not taken into account in carbonate system calculations, the calculations are unreliable. A bulk dissociation constant and average DOC fraction that contributes to the organic alkalinity have been defined for Baltic Sea waters (Kulinski et al., 2014; Ulfsbo et al., 2015), but spatial differences and temporal changes are as yet not described in detail. Riverine A_T as well as dissolved inorganic carbon concentrations and loads are in addition expected to change in the future as a result of both changes in weathering induced by rising air temperatures, and changes in precipitation patterns (Omstedt et al., 2012).

Omstedt et al. (2015) estimated that the acidification due to the atmospheric deposition of acids peaked around 1980, with a cumulative pH decrease of approximately 0.01 in surface waters and a cumulative reduction of A_T of approximately 30 μmol kg^{-1}. The effect on pH is approximately one order of magnitude less than the cumulative acidification due to increased atmospheric CO_2 concentrations.

The CO_2 exchange between air and sea depends directly on the difference between CO_2 partial pressure (pCO_2) in air and surface water respectively. To reproduce observed pCO_2 by means of model simulations has however proven to be a difficult task. Particularly the main mechanism behind the observed pCO_2 drawdown in surface waters during the productive season has been discussed quite extensively. Processes that could contribute include (1) cold nitrogen fixation by cyanobacteria as well as nutrient replenishment in sunlit layers by migrating plankton organisms (Eggert and Schneider, 2015); (2) efficient utilization of dissolved organic nutrients by phytoplankton (Edman and Anderson, 2014); (3) excessive CO_2 consumption and DOC exudation by phytoplankton, as well as (4) flexible phytoplankton cell stoichiometry (Kreus et al., 2015; Fransner et al., 2018). In addition, the calculated air-sea CO_2 flux is sensitive to the choice of exchange parameterization (Norman et al., 2013; Gustafsson et al., 2015). Fransner et al. (2018) showed for the northern Baltic Sea that beyond non-Redfield stoichiometry an extensive extracellular DOC production contributes to the low observed surface pCO2 during the vegetation period.

In several modeling studies (e.g., Omstedt et al., 2009; Edman and Omstedt, 2013; Gustafsson et al., 2014a) the riverine A_T concentrations were calibrated (based on Hjalmarsson et al. (2008)) so that observed A_T in different sub-basins could be reproduced by the models. These calibrated values are however in many cases considerably higher than the concentrations obtained from measurements (Gustafsson et al., 2014b). This implies either that the quality of measured riverine concentrations is questionable, or that there are other A_T sources in the Baltic Sea that are not accounted for in the model calculations. None of the system-scale physical-biogeochemical BSMs is for example capable of explicitly simulating the coupled phosphorus-iron-sulfur cycling and related A_T production and consumption in sediments. Potentially, A_T generation coupled to anaerobic mineralization processes in sediments (e.g., pyrite burial) could be a significant missing link (Gustafsson et al., 2014b). It is reasonable to assume that this A_T production/consumption depends largely on both sedimentation rate and the expansion of hypoxic and anoxic sediment areas (cf. Reed et al., 2016). Sedimentation rates and hypoxic areas ultimately depend on the magnitude of external nutrient loads, and these loads differ largely in the different future scenarios. The potential impact of changing climate on future A_T concentrations is unknown.

Weighting

Weighting may add another level of uncertainty to the generation of ensemble-based climate projections because the choice and combination of applied metrics is subjective (Christensen et al. (2010). Weigel et al. (2010) discussed the generic risks if weights do not appropriately represent the true underlying uncertainties, e.g., due to large internal variability. However, weighting may also narrow uncertainty by removing outliers as discussed below.

Meier et al. (2018a) analyzed weighted and unweighted changes from an "ensemble of opportunity", i.e., from an ensemble of uncoordinated experiments from various projects. They found that the skills of the scenario simulations during the historical climate (1980–2005) differ considerably between the models and that the variances of mean changes between historical and future (2072–2097) climates are relatively large depending on the location and variable. Here, skill (or performance of the

simulation) is defined as any measure of the agreement between the predictand, i.e., the climate model results during the historical period, and a set of observations, i.e. monitoring data from selected stations of temperature, salinity and phosphate, nitrate, ammonium, oxygen and hydrogen sulfide concentrations. Meier et al. (2018a) evaluated the skills of 29 climate simulations of six BSMs driven by various GCMs and RCMs and by various land surface or hydrological models. The skill was represented in terms of two metrics, the annual or seasonal mean absolute error and the Pearson correlation coefficient measuring the similarity in the shape of mean profiles. As the results of several tested metrics do not differ considerably, Meier et al. (2018a) concluded that weighting may reduce the uncertainties of the projections in the northern Baltic Sea where the discrepancies between weighted and unweighted ensembles are larger and where the skills of the models are lower than in the southern Baltic Sea (Eilola et al., 2011). In the southern Baltic Sea, projections in weighted and unweighted ensembles are rather similar. Hence, Meier et al. (2018a) concluded that the rigorous implementation of the BSAP would result in a significantly improved environmental status in the southern Baltic Sea despite the counteracting impact of changing climate and despite the large uncertainties. However, the relationship between spread and skill is still unknown and deserves further research (Hawkins and Sutton, 2009).

DISCUSSIONS

In the following, we discuss methods to estimate uncertainty ranges and to reduce uncertainties in projections based on ensemble modeling and weighting of ensemble members.

Estimating Uncertainties

The first attempt by Saraiva et al. (2019) to estimate ranges of uncertainty in projections for the Baltic Sea was based upon the analysis of variances of 30-year mean changes of selected variables between future and historical climates. They found that the response of biogeochemical fluxes, such as primary production and nitrogen fixation, and deep water oxygen conditions, to changing climate depend mainly on the nutrient load scenario. In the case of high nutrient loads (the so-called "fossil-fueled" scenario), the impact of the changing climate on biogeochemical cycles would be considerable whereas in the case of low loads (the BSAP scenario) the impact of changing climate would be negligible (cf. Saraiva et al., 2018). Hence, the dominant source of uncertainty is very likely related to the nutrient load scenario. For primary production, the second largest source of uncertainty was the unknown greenhouse gas concentration scenario and, for nitrogen fixation and hypoxic area, the second largest source originated from the climate model uncertainties, i.e., from model deficiencies affecting *inter alia* projected stratification changes (Saraiva et al., 2019). Finally, also the large spread in GMSL rise of one meter affected the uncertainties of nitrogen fixation and hypoxic area in agreement with the results by Meier et al. (2017).

In the study by Meier et al. (2018a), the ensemble spread was significantly larger than by Saraiva et al. (2019), as qualitatively illustrated by hypoxic area in the **Supplementary Material**, because the "ensemble of opportunity" contained both response and scenario uncertainties (Parker, 2013) whereas the ensemble by Saraiva et al. (2019) only partly reflected these uncertainties. According to Parker (2013) response uncertainty is the insufficiently known model sensitivity under a specified scenario and scenario uncertainty refers to the unknown GHG emissions and other external forcings such as nutrient loads. However, in all available ensemble studies of the Baltic Sea the response uncertainty might be underestimated because the models have the same NPZD (Nutrients-Phytoplankton-Zooplankton-Detritus) structure and were not independently developed. Hence, Parker (2013) recommended working more on structural uncertainty, i.e., the uncertainty about the form of the model equations and how they should be solved computationally.

Since Saraiva et al. (2019) underestimated uncertainties in their quantitative assessment by neglecting natural variability and BSM biases, ways forward toward more complete, quantitative assessment of uncertainties would be to apply the method by Hawkins and Sutton (2009) to newly designed, coordinated multi-model ensemble simulations for the Baltic Sea for 1850–2100 (including a suitable spin up). Hawkins and Sutton (2009) defined the internal variability for each model as the variance of the residuals from a smoothed fit of the projection, estimated independently of scenario and lead time. Since the importance of internal variability increases at smaller spatial scales and shorter time scales, it would be interesting to calculate not only the partitioning of uncertainty with time but also the growth of uncertainty from global to regional scales by comparing the variances of GCMs, RCMs, and BSMs.

Potentials to Narrow Uncertainties

As the quality of scenario simulations differs considerably, a strategy might be to reduce the spread in projections (i.e., the uncertainty) by weighting the ensemble members according to their skill during the historical period. The calculated skills might also be used to exclude members with insufficient quality from the ensemble by defining a certain threshold for the applied metric. However, the choice of an appropriate skill metric is subjective as mentioned above. Hence, the calculated weights would depend on the metric and consequently on the specific application. In the northern Baltic Sea, weighting has probably a larger impact on projections of the biogeochemical cycles than in the southern Baltic Sea because of the large impact of the physics. Climate sensitivity depends on feedback mechanisms that differ in different climate states. Hence, skill is at least a necessary (but not a sufficient) condition for the correct climate sensitivity and higher skill reduces uncertainty (Hawkins and Sutton, 2009). Highly sensitive sub-basins are more affected by model deficiencies than other sub-basins. In the northern Baltic Sea, the ice-albedo feedback affects temperature changes, which in turn affect biogeochemical processes (e.g., growth rates, remineralization rates). Further, in present climate the northern sub-basins are weakly stratified. Hence, increased runoff may further reduce the stratification, e.g., in the Gulf of Finland and Bothnian Bay, and consequently

enhance the vertical flux of oxygen with the result of improved bottom oxygen concentrations (Meier et al., 2011b). Thus, the large spread in runoff projections causes large uncertainty in oxygen concentrations and biogeochemical cycling because many processes are highly redox-dependent. Due to these feedback mechanisms, weighting may reduce uncertainties by removing outliers. In summary, results of the few available Baltic Sea studies confirm that equally weighted multi-model ensemble means outperform the results of the single ensemble members supporting the multi-model ensemble approach (e.g., Eilola et al., 2011) and that optimal weighting may in principle further reduce the response uncertainty.

Further research on structural uncertainties identified by this review may potentially lead to a reduction of the overall uncertainty in projections. Taking the specific characteristics of the Baltic Sea into account and focusing on the regional scale, the latter might be possible by improving process descriptions in BSMs in particular in the northern Baltic Sea but also elsewhere (see the unknown small-scale processes with impact on the entire system such as sediment-water fluxes and nutrient retention in the sediments under no. 12 and 13, **Table 2**); by performing sufficiently long model spin ups without switching the atmospheric forcing from historical reconstructions to climate model results during the simulation (no. 8, see **Supplementary Material**); by improved calculation of bioavailable loads or by accounting for the entire total loads by modeling dissolved organic nutrients as separate variables (Gustafsson et al., 2014a; Vladimirova et al., 2018) (no. 6); by investigating the filter capacity of the coastal zone in the Baltic Sea as in Edman et al. (2018) under different climates (no. 6); by improving the water cycle in RCMs and its response to changing climate (no. 4); and by consideration of GMSL at the lateral boundary of the BSMs (no. 9). As an effort of the scientific community, rigorous statistical and process-based quality controls of models implemented for projections by using available long-term observations (e.g., Eilola et al., 2011; Placke et al., 2018) may lead, extending the discussion on weighting, to a reduction of uncertainties (such as no. 3, 12, 13). For this purpose, more research on the relationship between skill and spread would be needed. Consequently, bias corrections, which are inherent sources of uncertainty in projections (no. 11), are not recommended and should be avoided whenever possible because they may change the models' sensitivity to changes in the forcing.

How Does Uncertainty Affect the Use of Scenarios in Decision-Making and Future Research?

With 43% of the European Union (EU) population living in coastal regions, it is recognized, e.g., in EU Blue Growth strategies that marine areas offer many opportunities for further exploitation to enhance citizens' health, wellbeing and prosperity. However, as these benefits co-exist alongside hazards and risks that may be exacerbated by climate change and other anthropogenic pressures, these opportunities need to be addressed collectively in a science based integrated management approach to ensure a sustainable exploitation of the sea affected by climate change (Jutterström et al., 2014). The way forward is to climate-proof the ongoing implementation of policies, conventions and frameworks for protection of the marine environment, such as HELCOM's BSAP, The Marine Strategy Framework Directive and The Water Framework directives. Hence, projections will be needed even if their uncertainties are considerable. For the implementation of the BSAP, it will have large economic consequences if additional measures are required to reach good environmental status in future climate. Hence, for research it is of utmost importance to quantify uncertainty, to understand the sources of uncertainty and to narrow uncertainty.

How Can We Deal With Uncertainties in Scenario Simulations?

To quantify uncertainty, large multi-model ensembles of scenario simulations are needed. All projections should be presented together with uncertainty ranges. To raise the credibility of models we suggest to perform regular assessments of models and scenario simulations. Regular information about current knowledge on climate change, e.g., presented in publicly available assessments and fact sheets, and a regular dialog on uncertainty between science and policy makers, e.g., within an expert network on climate change, may help to discuss the usage of models and their uncertainties and to weigh the resources spent for mitigation.

CONCLUSIONS

We discussed various sources of uncertainties in projections. Although quantitative estimates are lacking, we estimate based on expert judgment of the authors that the biggest uncertainties are caused by (1) unknown current and future bioavailable nutrient loads from land and atmosphere, (2) the experimental setup of the dynamical downscaling (including the spin up strategy), (3) differences between the projections of the GCMs and RCMs, in particular, with respect to GMSL rise and regional water cycle, (4) differing model-specific responses of the simulated biogeochemical cycles to long-term changes in external nutrient loads and climate of the Baltic Sea region, and (5) unknown future greenhouse gas emissions.

Despite considerable uncertainties in scenario simulations of biogeochemical cycles, a list of potentials to narrow uncertainties was identified. As already during the historical period differences between applied bioavailable nutrient loads and the various experimental setups cause large model biases compared to observations, improvements in spin up, atmospheric forcing, bioavailable nutrient load data set, and model calibration may lead to reduced model biases and reduced spread in projections.

We conclude that assessments of scenario simulations and knowledge syntheses such as this review have the potential to narrow uncertainty ranges. Analyses of state-of-the-art multi-model ensemble scenario simulations, thorough assessments of the results and common workshops will result in research proposals for improving models, experimental strategies and weighting procedures to narrow uncertainties.

DATA AVAILABILITY

Observations from the Baltic Environmental Database (BED) are publicly available from http://nest.su.se/bed. Model codes and data used for the analysis of this study are available from the authors upon request.

AUTHOR CONTRIBUTIONS

Conception and design of the assessment were discussed during two Baltic Earth workshops in Norrköping, Sweden (March 2014) and Warnemünde, Germany (November 2016) in which most of the authors participated. HM developed the idea of the study and coordinated the project. ME and MP helped with preparatory data analysis of model results developed by HM, ME, KE, TN, HA, CD, RF, BG, EG, AI, IK, BM-K, AO, VR, SS and OS. KE, TN, S-EB, CD, CF, MG, BG, EG, IK, AO, VR, and OS wrote sections of the manuscript. MK and MP compiled relevant literature and prepared the reference list. MN helped with the observational data. The final version of the manuscript was edited by OS and HM. All authors contributed to manuscript revision, read and approved the submitted version.

FUNDING

The research presented in this study is part of the Baltic Earth program (Earth System Science for the Baltic Sea region, see http://www.baltic.earth) and was funded by the BONUS BalticAPP (Well-being from the Baltic Sea–applications combining natural science and economics) project which has received funding from BONUS, the joint Baltic Sea research and development programme (Art 185), funded jointly from the European Union's Seventh Programme for research, technological development and demonstration and from the Swedish Research Council for Environment, Agricultural Sciences and Spatial Planning (FORMAS, grant no. 942-2015-23). Additional support by FORMAS within the project Cyanobacteria life cycles and nitrogen fixation in historical reconstructions and future climate scenarios (1850–2100) of the Baltic Sea (grant no. 214-2013-1449) and by the Stockholm University's Strategic Marine Environmental Research Funds Baltic Ecosystem Adaptive Management (BEAM) is acknowledged. The Baltic Nest Institute is supported by the Swedish Agency for Marine and Water Management through their grant 1:11 - Measures for marine and water environment. AI and VR were funded in the framework of the state assignment of FASO Russia (theme No. 0149-2019-0015).

ACKNOWLEDGMENTS

The observational data used for the analysis of nutrient content and lateral boundary conditions are open access and were extracted from the Baltic Environmental Database (BED, http://nest.su.se/bed) at Stockholm University and all data providing institutes (listed at http://nest.su.se/bed/ACKNOWLE.shtml) are kindly acknowledged. BED contains observations, *inter alia*, from the national, long-term environmental monitoring programs such as the Swedish Ocean Archive (SHARK, https://sharkweb.smhi.se/) operated by the Swedish Meteorological and Hydrological Institute (SMHI) or the German Baltic Sea monitoring data archive (http://iowmeta.io-warnemuende.de) operated by the Leibniz Institute for Baltic Sea Research Warnemünde (IOW) (**Table 4**). Berit Recklebe is acknowledged for editing the reference list. The constructive comments from two reviewers helped to improve the manuscript considerably.

SUPPLEMENTARY MATERIAL

The Supplementary Material for this article can be found online at: https://www.frontiersin.org/articles/10.3389/fmars.2019.00046/full#supplementary-material

REFERENCES

Aarup, T., Holt, N., and Højerslev, N. (1996). Optical measurements in the North Sea-Baltic Sea transition zone. II. Water mass classification along the Jutland west coast from salinity and spectral irradiance measurements. *Cont. Shelf Res.* 16, 1343–1353. doi: 10.1016/0278-4343(95)00076-3

Ahlgren, J., Grimvall, A., Omstedt, A., Rolff, C., and Wikner, J. (2017). Temperature, DOC level and basin interactions explain the declining oxygen concentrations in the Bothnian Sea. *J. Mar. Syst.* 170, 22–30. doi: 10.1016/j.jmarsys.2016.12.010

Ahtiainen, H., and Öhman, M. C. (2014). *Ecosystem Services in the Baltic Sea: Valuation of Marine and Coastal Ecosystem Services in the Baltic Sea*. Vol. 563 *of Report TemaNord*. Copenhagen: Nordic Council of Ministers. doi: 10.6027/TN2014-563

Andersson, A., Meier, H. E. M., Ripzsam, M., Rowe, O., Wikner, J., Haglund, P., et al. (2015). Future climate change scenarios for the Baltic Sea ecosystem and impacts for management. *Ambio* 44 (Suppl. 3):S345S356. doi: 10.1007/s13280-015-0654-8

Andersson, H. C. (2002). Influence of long-term regional and large-scale atmospheric circulation on the Baltic sea level. *Tellus A* 54, 76–88. doi: 10.3402/tellusa.v54i1.12125

Arheimer, B., Dahné, J., and Donnelly, C. (2012). Climate change impact on riverine nutrient load and land-based remedial measures of the Baltic Sea Action Plan. *Ambio* 41, 600–612. doi: 10.1007/s13280-012-0323-0

Arneborg, L. (2016). Comment on "Influence of sea level rise on the dynamics of salt inflows in the Baltic Sea" by R. Hordoir, L. Axell, U. Löptien, H. Dietze, and I. Kuznetsov. *J. Geophys. Res.* 121, 2035–2040. doi: 10.1002/2015JC011451

Asmala, E., Carstensen, J., Conley, D. J., Slomp, C. P., Stadmark, J., and Voss, M. (2017). Efficiency of the coastal filter: nitrogen and phosphorus removal in the Baltic Sea. *Limnol. Oceanogr.* 62. doi: 10.1002/lno0.10644

BACC Author Team (2008). *Assessment of Climate Change for the Baltic Sea Basin. Regional Climate Studies*. Berlin; Heidelberg: Springer-Verlag. doi: 10.1007/978-3-540-72786-6

BACCII Author Team (2015). *Second assessment of Climate Change for the Baltic Sea Basin. Regional Climate Studies*. Springer: Cham. doi: 10.1007/978-3-319-16006-1

Bauer, B., Gustafsson, B. G., Hyytiäinen, K., Meier, H. E. M., Müller-Karulis, B., and Saraiva, S., et al. (in press). What are potential future states of the Baltic Sea food web? *Ambio*.

Bauer, B., Meier, H. E. M., Casini, M., Hoff, A., Margonski, P., Orio, A., et al. (2018). Reducing eutrophication increases spatial extent of communities supporting

commercial fisheries: a model case study. *ICES J. Mar. Sci.* 75, 1306–1317. doi: 10.1093/icesjms/fsy023.

Bendtsen, J., and Hansen, J. L. (2013). Effects of global warming on hypoxia in the Baltic Sea–North Sea transition zone. *Ecol. Model.* 264, 17–26. doi: 10.1016/j.ecolmodel.2012.06.018

Bengtsson, L. (2010). The global atmospheric water cycle. *Environ. Res. Lett.* 5:025202. doi: 10.1088/1748-9326/5/2/025202

Börgel, F., Frauen, C., Neumann, T., Schimanke, S., and Meier, H. E. M. (2018). Impact of the Atlantic Multidecadal Oscillation on Baltic Sea Variability. *Geophys. Res. Lett*. 45, 9880–9888. doi: 10.1029/2018GL078943

Bossier, S., Palacz, A. P., Nielsen, J. R., Christensen, A., Hoff, A., Maar, M., et al. (2018). The Baltic Sea Atlantis: an integrated end-to-end modelling framework evaluating ecosystem-wide effects of human-induced pressures. *PLoS ONE* 13:e0199168. doi: 10.1371/journal.pone.0199168

Brandt, J., Christensen, J. H., Frohn, J. H., Palmgren, F., Berkowicz, F., and Zlatev, Z. (2001). Operational air pollution forecasts from European to local scale. *Atmos. Environ.* 35, 91–98. doi: 10.1016/S1352-2310(00)00415-5

Bülow, K., Dieterich, C., Elizalde, A., Gröger, M., Heinrich, H., Hüttl-Kabus, S., et al. (2014). *Comparison of Three Regional Coupled Ocean Atmosphere Models for the North Sea Under Today's and Future Climate Conditions*. KLIWAS Zeitschriftenreihe 27/2014. Koblenz: Bundesanstalt für Gewässerkunde.

Burson, A., Stomp, M., Akil, L., Brussaard, C. P., and Huisman, J. (2016). Unbalanced reduction of nutrient loads has created an offshore gradient from phosphorus to nitrogen limitation in the North Sea. *Limnol. Oceanogr.* 61, 869–888. doi: 10.1002/lno.10257

Carstensen, J., Andersen, J. H., Gustafsson, B. G., and Conley, D. J. (2014). Deoxygenation of the Baltic Sea during the last century. *Proc. Natl. Acad. Sci. U.S.A.* 111, 5628–5633. doi: 10.1073/pnas.1323156111

Chen, D., and Omstedt, A. (2005). Climate-induced variability of sea level in Stockholm: influence of air temperature and atmospheric circulation. *Adv. Atmospher. Sci.* 22, 655–664. doi: 10.1007/BF02918709

Christensen, J. H., and Christensen, O. B. (2007). A summary of the PRUDENCE model projections of changes in European climate by the end of this century. *Clim. Change* 81, 7–30. doi: 10.1007/s10584-006-9210-7

Christensen, J. H., Kjellström, E., Giorgi, F., Lenderink, G., and Rummukainen, M. (2010). Weight assignment in regional climate models. *Clim. Res.* 44, 179–194. doi: 10.3354/cr00916

Collins, M., Knutti, R., Arblaster, J., Dufresne, J.-L., Fichefet, T., Friedlingstein, P., et al. (2013). "Long-term climate change: projections, commitments and irreversibility." in *Climate Change 2013: The Physical Science Basis. IPCC Working Group I Contribution to IPCC AR5*, eds T. F. Stocker, D. Quin, G. K. Plattner, M. Tignor, S. K. Allen, J. Boschung, A. Nauels, Y. Xia, V. Bex and P. M. Midgley (Cambridge; New York, NY: Cambridge University Press), 1029–1136.

Daewel, U., and Schrum, C. (2013). Simulating long-term dynamics of the coupled North Sea and Baltic Sea ecosystem with ECOSMO II: model description and validation. *J. Mar. Sys.* 119–120, 30–49. doi: 10.1016/j.jmarsys.2013.03.008

Déqué, M., Rowell, D., Lüthi, D., Giorgi, F., Christensen, J., Rockel, B., et al. (2007). An intercomparison of regional climate simulations for Europe: assessing uncertainties in model projections. *Clim. Change* 81, 53–70. doi: 10.1007/s10584-006-9228-x

Déqué, M., Somot, S., Sanchez-Gomez, E., Goodess, C., Jacob, D., Lenderink, G., et al. (2012). The spread amongst ENSEMBLES regional scenarios: regional climate models, driving general circulation models and interannual variability. *Clim. Dyn.* 38, 951–964. doi: 10.1007/s00382-011-1053-x

Deser, C., Phillips, A. S., Alexander, M. A., and Smoliak, B. V. (2014). Projecting North American climate over the next 50 years: uncertainty due to internal variability. *J. Clim.* 27, 2271–2296. doi: 10.1175/JCLI-D-13-00451.1

Dieterich, C., Schimanke, S., Wang, S., Väli, G., Liu, Y., Hordoir, R., et al. (2013). *Evaluation of the SMHI Coupled Atmosphere-Ice-Ocean Model RCA4-NEMO*, Vol. 47 *of Report Oceanography.* Norrköping: SMHI.

Donnelly, C., Arheimer, B., Capell, R., Dahn,é, J., and Strömqvist, J. (2013). "Regional overview of nutrient load in Europe – challenges when using a large-scale model approach, E-HYPE," in *Proceedings of H04, IAHS-IAPSO-IASPEI Assembly*, Vol. 361 (Gothenburg: IHS Publication), 49–58.

Donnelly, C., Greuell, W., Andersson, J., Gerten, D., Pisacane, G., Roudier, P., et al. (2017). Impacts of climate change on European hydrology at 1.5, 2 and 3 degrees mean global warming above preindustrial level. *Clim. Change* 143, 13–26. doi: 10.1007/s10584-017-1971-7

Donnelly, C., Yang, W., and Dahn,é, J. (2014). River discharge to the Baltic Sea in a future climate. *Clim. Change* 122, 157–170. doi: 10.1007/s10584-013-0941-y

Döscher, R., and Meier, H. E. M. (2004). Simulated sea surface temperature and heat fluxes in different climates of the Baltic Sea. *Ambio* 33, 242–248. doi: 10.1579/0044-7447-33.4.242

Döscher, R., Willén, U., Jones, C., Rutgersson, A., Meier, H. E. M., Hansson, U., et al. (2002). The development of the regional coupled ocean-atmosphere model RCAO. *Boreal Environ. Res.* 7, 183–192.

Edman, M., Eilola, K., Almroth-Rosell, E., Meier, H. E. M., Wåhlström, I., and Arneborg, L. (2018). Nutrient retention along the Swedish coastline. *Front. Mar. Sci.* 5:415. doi: 10.3389/fmars.2018.00415

Edman, M., and Omstedt, A. (2013). Modeling the dissolved CO_2 system in the redox environment of the Baltic Sea. *Limnol. Oceanogr.* 58, 74–92. doi: 10.4319/lo.2013.58.1.0074

Edman, M. K., and Anderson, L. G. (2014). Effect on pCO_2 by phytoplankton uptake of dissolved organic nutrients in the Central and Northern Baltic Sea, a model study. *J. Mar. Syst.* 139, 166–182. doi: 10.1016/j.jmarsys.2014.06.004

Eggert, A., and Schneider, B. (2015). A nitrogen source in spring in the surface mixed-layer of the Baltic Sea: evidence from total nitrogen and total phosphorus data. *J. Mar. Syst.* 148, 39–47. doi: 10.1016/j.jmarsys.2015.01.005

Eilola, K., Almroth-Rosell, E., Dieterich, C., Fransner, F., Höglund, A., and Meier, H. E. M. (2012). Modeling nutrient transports and exchanges of nutrients between shallow regions and the open Baltic Sea in present and future climate. *Ambio* 41, 586–599. doi: 10.1007/s13280-012-0317-y

Eilola, K., Gustafsson, B. G., Kuznetsov, I., Meier, H. E. M., Neumann, T., and Savchuk, O. P. (2011). Evaluation of biogeochemical cycles in an ensemble of three state-of-the-art numerical models of the Baltic Sea. *J. Mar. Syst.* 88, 267–284. doi: 10.1016/j.jmarsys.2011.05.004

Eilola, K., Mårtensson, S., and Meier, H. E. M. (2013). Modeling the impact of reduced sea ice cover in future climate on the Baltic Sea biogeochemistry. *Geophys. Res. Lett.* 40, 149–154. doi: 10.1029/2012GL054375

Eilola, K., Meier, H. E. M., and Almroth, E. (2009). On the dynamics of oxygen, phosphorus and cyanobacteria in the Baltic Sea; A model study. *J. Mar. Syst.* 75, 163–184. doi: 10.1016/j.jmarsys.2008.08.009

Eyring, V., Bony, S., Meehl, G. A., Senior, C. A., Stevens, B., Stouffer, R. J., et al. (2016). Overview of the Coupled Model Intercomparison Project Phase 6 (CMIP6) experimental design and organization. *Geosci. Model Dev.* 9, 1937–1958. doi: 10.5194/gmd-9-1937-2016

Feser, F., Rockel, B., von Storch, H., Winterfeldt, J., and Zahn, M. (2011). Regional climate models add value to global model data: a review and selected examples. *Bull. Am. Meteorol. Soc.* 92, 1181–1192. doi: 10.1175/2011BAMS3061.1

Finni, T., Kononen, K., Olsonen, R., and Wallström, K. (2001). The history of cyanobacterial blooms in the Baltic Sea. *Ambio* 30, 172–178. doi: 10.1579/0044-7447-30.4.172

Fransner, F., Gustafsson, E., Tedesco, L., Vichi, M., Hordoir, R., Roquet, F., et al. (2018). Non-Redfieldian dynamics explain seasonal pCO_2 drawdown in the Gulf of Bothnia. *J. Geophys. Res. Oceans* 123, 166–188. doi: 10.1002/2017JC013019

Friedland, R., Neumann, T., and Schernewski, G. (2012). Climate change and the Baltic Sea action plan: model simulations on the future of the western Baltic Sea. *J. Mar. Syst.* 105, 175–186. doi: 10.1016/j.jmarsys.2012.08.002

Fulton, E. A. (2010). Approaches to end-to-end ecosystem models. *J. Mar. Syst.* 81, 171–183. doi: 10.1016/j.jmarsys.2009.12.012

Gimeno, L., Stohl, A., Trigo, R. M., Dominguez, F., Yoshimura, K., Yu, L., et al. (2012). Oceanic and terrestrial sources of continental precipitation. *Rev. Geophys.* 50:RG4003. doi: 10.1029/2012RG000389

Giorgi, F., and Gao, X.-J. (2018). Regional earth system modeling: review and future directions. *Atmos. Oceanic Sci. Lett.* 11, 189–197. doi: 10.1080/16742834.2018.1452520

Gordon, C., Cooper, C., Senior, C. A., Banks, H., Gregory, J. M., Johns, T. C., et al. (2000). The simulation of SST, sea ice extents and ocean heat transports in a version of the Hadley Centre coupled model without flux adjustments. *Clim. Dyn.* 16, 147–168. doi: 10.1007/s003820050010

Graham, P. (1999). Modeling runoff to the Baltic Sea. *Ambio* 28, 328–334.

Gräwe, U., Friedland, R., and Burchard, H. (2013). The future of the western Baltic Sea: two possible scenarios. *Ocean Dyn.* 63, 901–921. doi: 10.1007/s10236-013-0634-0

Gröger, M., Dieterich, C., Meier, H. E. M., and Schimanke, S. (2015). Thermal air–sea coupling in hindcast simulations for the North Sea and Baltic Sea on the NW European shelf. *Tellus A* 67:26911. doi: 10.3402/tellusa.v67.26911

Gröger, M., Maier-Reimer, E., Mikolajewicz, U., Moll, A., and Sein, D. (2013). NW European shelf under climate warming: implications for open ocean-shelf exchange, primary production, and carbon absorption. *Biogeosciences* 10, 3767–3792. doi: 10.5194/bg-10-3767-2013

Gustafsson, B. G. (2003). *A Time-Dependent Coupled-Basin Model for the Baltic Sea.* Report C47, Earth Sciences Centre, Göteborg University, Göteborg.

Gustafsson, B. G. (2004). Sensitivity of Baltic Sea salinity to large perturbations in climate. *Clim. Res.* 27, 237–251. doi: 10.3354/cr027237

Gustafsson, B. G., and Mörth, C. M. (2014). *Revision of the Maximum Allowable Inputs and Country Allocation Scheme of the Baltic Sea Action Plan*. Baltic Nest Institute, Stockholm University.

Gustafsson, B. G., Schenk, F., Blenckner, T., Eilola, K., Meier, H. E. M., Müller-Karulis, B. , et al. (2012). Reconstructing the development of Baltic Sea eutrophication 1850–2006. *Ambio* 41, 534–548. doi: 10.1007/s13280-012-0318-x

Gustafsson, E., Deutsch, B., Gustafsson, B. G., Humborg, C., and Mörth, C.-M. (2014a). Carbon cycling in the Baltic Sea - The fate of allochthonous organic carbon and its impact on air-sea CO_2 exchange. *J. Mar. Syst.* 129, 289–302. doi: 10.1016/j.jmarsys.2013.07.005

Gustafsson, E., Omstedt, A., and Gustafsson, B. G. (2015). The air-water CO_2 exchange of a coastal sea - A sensitivity study on factors that influence the absorption and outgassing of CO_2 in the Baltic Sea. *J. Geophys. Res.* 120, 5342–5357. doi: 10.1002/2015JC010832

Gustafsson, E., Wällstedt, T., Humborg, C., Mörth, C.-M., and Gustafsson, B. G. (2014b). External total alkalinity loads versus internal generation: the influence of nonriverine alkalinity sources in the Baltic Sea. *Global Biogeochem. Cycles* 28, 1358–1370. doi: 10.1002/2014GB004888

Gustafsson, N., Nyberg, L., and Omstedt, A. (1998). Coupling of a high-resolution atmospheric model and an ocean model for the Baltic Sea. *Month. Weather Rev.* 126, 2822–2846. doi: 10.1175/1520-0493(1998)126<2822:COAHRA>2.0.CO;2

Haapala, J., Meier, H. E. M., and Rinne, J. (2001). Numerical investigations of future ice conditions in the Baltic Sea. *Ambio* 30, 237–244. doi: 10.1579/0044-7447-30.4.237

Hansen, J., Ruedy, R., Sato, M., and Lo, K. (2010). Global surface temperature change. *Rev. Geophys.* 48:RG4004. doi: 10.1029/2010RG000345

Hansson, D., and Gustafsson, E. (2011). Salinity and hypoxia in the Baltic Sea since A.D. 1500. *J. Geophys. Res.* 116:C03027. doi: 10.1029/2010JC006676

Hansson, D., and Omstedt, A. (2008). Modelling the Baltic Sea ocean climate on centennial time scale: temperature and sea ice. *Clim. Dyn.* 30, 763–778. doi: 10.1007/s00382-007-0321-2

Harff, J., Furmanczyk, K., and von Storch, H. (2017). *Coastline Changes of the Baltic Sea from South to East: Past and Future Projection*. Cham: Springer International Publishing. doi: 10.1007/978-3-319-49894-2

Hawkins, E., and Sutton, R. (2009). The potential to narrow uncertainty in regional climate predictions. Bull. Am. Meteorol. Soc. 90, 1095–1108. doi: 10.1175/2009BAMS2607.1

Heavens, N. G., Ward, D. S., and Natalie, M. M. (2013). Studying and projecting climate change with earth system models. *Nat. Educ. Knowl.* 4:4.

HELCOM (2007a). "Baltic Sea action plan," in HELCOM Ministerial Meeting 2007 (Krakow).

HELCOM (2007b). "Towards a Baltic Sea unaffected by Eutrophication. Helcom overview 2007," in *Background Document for the HELCOM Ministerial Meeting* (Helsinki).

HELCOM (2013a). "Approaches and methods for eutrophication target setting in the Baltic Sea region," in *Baltic Sea Environment Proceedings,* Vol. 133. (Helsinki).

HELCOM (2013b). *Copenhagen Ministerial Declaration, HELCOM Ministerial Meeting* (Copenhagen).

HELCOM (2013c). "Summary report on the development of revised Maximum Allowable Inputs (MAI) and updated Country Allocated Reduction Targets (CART) of the Baltic Sea Action Plan," in *Background Document for the 2013 HELCOM Ministerial Meeting* (Helsinki).

HELCOM (2015). "Updated Fifth Baltic Sea pollution load compilation (PLC-5.5)," in *Baltic Sea Environment Proceedings No. 145* (Helsinki).

HELCOM (2018a). "Sources and pathways of nutrients to the Baltic Sea," in *Baltic Sea Environment Proceedings No. 153* (Helsinki).

HELCOM (2018b). "Inputs of Nutrients to the Subbasins," in *HELCOM Core Indicator Report.* Available online at: http://www.helcom.fi/baltic-sea-trends/indicators/inputs-of-nutrients-to-the-subbasins (Accessed Dec 5, 2018).

Hjalmarsson, S., Wesslander, K., Anderson, L. G., Omstedt, A., Perttila, M., and Mintrop, L. (2008). Distribution, long-term development and mass balance calculation of total alkalinity in the Baltic Sea. *Cont. Shelf Res.* 28, 593–601. doi: 10.1016/j.csr.2007.11.010

Höglund, A., Meier, H. E. M., Broman, B., and Kriezi, E. (2009). *Validation and Correction of Regionalised ERA-40 Wind Fields Over the Baltic Sea Using the Rossby Centre Atmosphere model RCA3.0, Rapport Oceanografi 97.* SMHI: Norrköping.

Ho-Hagemann, H. T. M., Gröger, M., Rockel, B., Geyer, B., Zahn, M., and Meier, H. E. M. (2017). Effects of air-sea coupling over the North Sea and the Baltic Sea on simulated summer precipitation over Central Europe. *Clim. Dyn.* 49, 3851–3876. doi: 10.1007/s00382-017-3546-8

Holopainen, R., Lehtiniemi, M., Meier, H. E. M., Albertsson, J., Gorokhova, E., Kotta, J., et al. (2016). Impacts of changing climate on the non-indigenous invertebrates in the northern Baltic Sea by end of the 21st century. *Biol. Invasions* 18, 3015–3032. doi: 10.1007/s10530-016-1197-z

Holt, J., Butenschoen, M., Wakelin, S. L., Artioli, Y., and Allen, J. I. (2012). Oceanic controls on the primary production of the northwest European continental shelf: model experiments under recent past conditions and a potential future scenario. *Biogeosciences* 9, 97–117. doi: 10.5194/bg-9-97-2012

Holt, J., Schrum, C., Cannaby, H., Daewel, U., Allen, I., Artioli, Y., et al. (2016). Potential impacts of climate change on the primary production of regional seas: a comparative analysis of five European seas. *Prog. Oceanogr.* 140, 91–115. doi: 10.1016/j.pocean.2015.11.004.

Hong, B., Swaney, D. P., Mörth, C.-M., Smedberg, E., Hägg, H. E., Humborg, C., et al. (2012). Evaluating regional variation of net anthropogenic nitrogen and phosphorus inputs (NANI/NAPI), major drivers, nutrient retention pattern and management implications in the multinational areas of Baltic Sea basin. *Ecol. Model.* 227, 117–135. doi: 10.1016/j.ecolmodel.2011.12.002

Hordoir, R., Axell, L., Löptien, U., Dietze, H., and Kuznetsov, I. (2015). Influence of sea level rise on the dynamics of salt inflows in the Baltic Sea. *J. Geophys. Res. Oceans* 120, 6653–6668. doi: 10.1002/2014JC010642

Hordoir, R., Höglund, A., Pemberton, P., and Schimanke, S. (2018). Sensitivity of the overturning circulation of the Baltic Sea to climate change, a numerical experiment. *Clim. Dyn.* 50, 1425–1437. doi: 10.1007/s00382-017-3695-9

Hourdin, F., Mauritsen, T., Gettelman, A., Golaz, J.-C., Balaji, V., Duan, Q., et al. (2017). The art and science of climate model tuning. *Bull. Am. Meteorol. Soc.* 98, 589–602. doi: 10.1175/BAMS-D-15-00135.1

Humborg, C., Mörth, C.-M., Sundbom, M., and Wulff, F. (2007). Riverine transport of biogenic elements to the Baltic Sea – past and possible future perspectives. *Hydrol. Earth Syst. Sci.* 11, 1593–1607. doi: 10.5194/hess-11-1593-2007

Hundecha, Y., Arheimer, B., Donnelly, C., and Pechlivanidis, I. (2016). A regional parameter estimation scheme for a pan-European multi-basin model. *J. Hydrol. Reg. Stud.* 6, 90–111. doi: 10.1016/j.ejrh.2016.04.002

Isaev, A. V., Eremina, T. R., Ryabchenko, V. A., and Savchuk, O. P. (2017). Model estimates of the impact of bioirrigation activity of *Marenzelleria* spp. on the Gulf of Finland ecosystem in a changing climate. *J. Mar. Syst.* 171, 81–88. doi: 10.1016/j.jmarsys.2016.08.005

Jacob, D. (2001). A note to the simulation of the annual and inter-annual variability of the water budget over the Baltic Sea drainage basin. *Meteorol. atmosphere. Phys.* 77, 61–73. doi: 10.1007/s007030170017

Jacob, D., Petersen, J., Eggert, B., Alias, A., Christensen, O. B., Bouwer, L. M., et al. (2014). EURO-CORDEX: new high-resolution climate change projections for European impact research. *Reg. Environ. Change* 14, 563–578. doi: 10.1007/s10113-013-0499-2

Johansson, M. M., Pellikka, H., Kahma, K. K., and Ruosteenoja, K. (2014). Global sea level rise scenarios adapted to the Finnish coast. *J. Mar. Syst.* 129, 35–46. doi: 10.1016/j.jmarsys.2012.08.007

Johns, T. C., Carnell, R. E., Crossley, J. F., Gregory, J. M., Mitchell, J. F. B., Senior, C. A., et al. (1997). The second Hadley Centre coupled ocean-atmosphere

GCM: model description, spinup and validation. *Clim. Dyn.* 13, 103–134. doi: 10.1007/s003820050155

Jungclaus, J. H., Botzet, M., Haak, H., Keenlyside, N., Luo, J.-J., Latif, M., et al. (2006). Ocean circulation and tropical variability in the coupled ECHAM5/MPI-OM. *J. Clim.* 19, 3952–3972. doi: 10.1175/JCLI3827.1

Jutterström, S., Andersson, H., Omstedt, A., and Malmaeus, J. (2014). Multiple stressors threatening the future of the Baltic Sea - Kattegat marine ecosystem: implications for policy and management actions. *Mar. Pollut. Bull.* 86, 468–480. doi: 10.1016/j.marpolbul.2014.06.027

Kahru, M., Elmgren, R., and Savchuk, O. P. (2016). Changing seasonality of the Baltic Sea. *Biogeosciences* 13, 1009–1018. doi: 10.5194/bg-13-1009-2016

Kalnay, E., Kanamitsu, M., Kistler, R., Collins, W., Deaven, D., Gandin, L., et al. (1996). The NCEP/NCAR 40-year reanalysis project. *Bull. Am. Meteorol. Soc.* 77, 437–471. doi: 10.1175/1520-0477(1996)077<0437:TNYRP>2.0.CO;2

Karabil, S., Zorita, E., and Baehr, J. (2017a). Mechanisms of variability in decadal sea-level trends in the Baltic Sea over the 20th century. *Earth Syst. Dyn.* 8, 1031–1046. doi: 10.5194/esd-8-1031-2017

Karabil, S., Zorita, E., and Baehr, J. (2017b). Mechanisms of *Sea Level Variability* in the Baltic Sea *Region* for the *Period* 1850-2100. Doctoral dissertation, Universität Hamburg, Hamburg.

Karabil, S., Zorita, E., and Hünicke, B. (2018). Contribution of atmospheric circulation to recent off-shore sea-level variations in the Baltic Sea and the North Sea. *Earth Syst. Dyn.* 9, 69–90. doi: 10.5194/esd-9-69-2018

Kauker, F., and Meier, H. E. M. (2003). Modeling decadal variability of the Baltic Sea: 1. Reconstructingatmospheric surface data for the period 1902-1998. *J. Geophys. Res. Oceans* 108:3267. doi: 10.1029/2003JC001797

Kjellström, E., Nikulin, G., Hansson, U. L. F., Strandberg, G., and Ullerstig, A. (2011). 21st century changes in the European climate: uncertainties derived from an ensemble of regional climate model simulations. *Tellus A* 63, 24–40. doi: 10.1111/j.1600-0870.2010.00475.x

Knight, J. R., Allan, R. J., Folland, C. K., Vellinga, M., and Mann, M. E. (2005). A signature of persistent natural thermohaline circulation cycles in observed climate. *Geophys. Res. Lett.* 32:L20708. doi: 10.1029/2005GL024233

Knutti, R., and Sedláček, J. (2013). Robustness and uncertainties in the new CMIP5 climate model projections. *Nat. Clim. Chang.* 3:369. doi: 10.1038/nclimate1716

Kreus, M., Schartau, M., Engel, A., Nausch, M., and Voss, M. (2015). Variations in the elemental ratio of organic matter in the central Baltic Sea: Part I-Linking primary production to remineralization. *Cont. Shelf Res.* 100, 25–45. doi: 10.1016/j.csr.2014.06.015

Kristiansen, T., and Aas, E. (2015). Water type quantification in the Skagerrak, the Kattegat and off the Jutland west coast. *Oceanologia* 57, 177–195. doi: 10.1016/j.oceano.2014.11.002

Kulinski, K., Schneider, B., Hammer, K., Machulik, U., and Schulz-Bull, D. (2014). The influence of dissolved organic matter on the acid–base system of the Baltic Sea. *J. Mar. Syst.* 132, 106–115. doi: 10.1016/j.jmarsys.2014.01.011

Kupiainen, M., Jansson, C., Samuelsson, P., Jones, C.,Willén, U., et al. (2014). *Rossby Centre Regional Atmospheric Model, RCA4, Rossby Center News Letter*. Norrköping: SMHI. Available online at: http://www.smhi.se/en/Research/Research-departments/climate-research-rossby-centre2-552/1.16562

Kuznetsov, I., Eilola, K., Dieterich, C., Hordoir, R., Axell, L., Höglund, A., et al. (2016). *Model Study on the Variability of Ecosystem Parameters in the Skagerrak-Kattegat Area, Effect of Load Reduction in the North Sea and Possible Effect of BSAP on Skagerrak-Kattegat Area*. Rapport Oceanografi 119, SMHI, Norrköping.

Kuznetsov, I., and Neumann, T. (2013). Simulation of carbon dynamics in the Baltic Sea with a 3D model. *J. Mar. Syst.* 111, 167–174. doi: 10.1016/j.jmarsys.2012.10.011

Laane, R., Brockmann, U., van Liere, L., and Bovelander, R. (2005). Immission targets for nutrients (N and P) in catchments and coastal zones: a North Sea assessment. *Estuar. Coast. Shelf Sci.* 62, 495–505. doi: 10.1016/j.ecss.2004.09.013

Lenhart, H.-J., Mills, D. K., Baretta-Bekker, H., van Leeuwen, S. M., van der Molen, J., Baretta, J. W., et al. (2010). Predicting the consequences of nutrient reduction on the eutrophication status of the North Sea. *J. Mar. Syst.* 81, 148–170. doi: 10.1016/j.jmarsys.2009.12.014

Lessin, G., Raudsepp, U., Maljutenko, I., Laanemets, J., Passenko, J., and Jaanus, A. (2014). Model study on present and future eutrophication and nitrogen fixation in the Gulf of Finland, Baltic Sea. *J. Mar. Syst.* 129, 76–85. doi: 10.1016/j.jmarsys.2013.08.006

Lind, P., and Kjellström, E. (2009). Water budget in the Baltic Sea drainage basin: evaluation of simulated fluxes in a regional climate model. *Boreal Environ. Res.* 14, 56–67.

Liu, W., Xie, S.-P., Liu, Z., and Zhu, J. (2017). Overlooked possibility of a collapsed Atlantic Meridional Overturning Circulation in warming climate. *Sci. Adv.* 3:e1601666. doi: 10.1126/sciadv.1601666

Löptien, U., Mårtensson, S., Meier, H. E. M., and Höglund, A. (2013). Long-term characteristics of simulated ice deformation in the Baltic Sea (1962-2007). *J. Geophys. Res.* 118, 801–815. doi: 10.1002/jgrc.20089

Luomaranta, A., Ruosteenoja, K., Jylh,ä, K., Gregow, H., Haapala, J., and Laaksonen, A. (2014). Multimodel estimates of the changes in the Baltic Sea ice cover during the present century. *Tellus A* 66:22617. doi: 10.3402/tellusa.v66.22617

Luyten, P. J., Jones, J. E., Proctor, R., Tabor, A., Tett, P., and Wild-Allen, K. (1999). *COHERENS– a Coupled Hydrodynamical–Ecological Model for Regional and Shelf Seas: User Documentation*. MUMM Report. Management Unit of the Mathematical Models of the North Sea. 914.

Madec, G., and The NEMO team (2016). *NEMO Ocean Engine*. version 3.6 stable. Note du Pôle de modélisation. Institut Pierre-Simon Laplace (IPSL)-LOCEAN. Paris. No 27. Available online at: https://www.nemo-ocean.eu/wp-content/uploads/NEMO_book.pdf

Marti, O., Braconnot, P., Bellier, J., Benshila, R., Bony, S., Brockmann, P., et al. (2006). *The New IPSL Climate System Model: IPSL-CM4.* Note du Pole de Modelisation 26. Institut Pierre-Simon Laplace (IPSL).

Mastrandrea, M. D., Field, C. B., Stocker, T. F., Edenhofer, O., Ebi, K. L., Frame, D. J., et al. (2010). Guidance Note for Lead Authors of the IPCC Fifth Assessment Report on Consistent Treatment of Uncertainties. Intergovernmental Panel on Climate Change (IPCC). Available online at: http://www.ipcc.ch

Mathis, M., Elizalde, A., and Mikolajewicz, U. (2018). Which complexity of regional climate system models is essential for downscaling anthropogenic climate change in the Northwest European Shelf? *Clim. Dyn.* 50, 2637–2659. doi: 10.1007/s00382-017-3761-3

Mathis, M., Elizalde, A., and Mikolajewicz, U. (2019). The future regime of Atlantic nutrient supply to the Northwest European Shelf. *J. Mar. Syst.* 189, 98–115. doi: 10.1016/j.jmarsys.2018.10.002

Mathis, M., Mayer, B., and Pohlmann, T. (2013). An uncoupled dynamical downscaling for the North Sea: method and evaluation. *Ocean Model.* 72, 153–166. doi: 10.1016/j.ocemod.2013.09.004

Matthäus, W., and Franck, H. (1992). Characteristics of major Baltic inflows - a statistical analysis. *Cont. Shelf Res.* 12, 1375–1400. doi: 10.1016/0278-4343(92)90060-W

Mauritsen, T., Stevens, B., Roeckner, E., Crueger, T., Esch, M., Giorgetta, M., et al. (2012). Tuning the climate of a global model. *J. Adv. Model. Earth Syst.* 4:M00A01. doi: 10.1029/2012MS000154

Meehl, G., Stocker, T., Collins, W., Friedlingstein, P., Gaye, A., Gregory, J., et al. (2007). "Global Climate Projections." in *Climate Change 2007: the Physical Science Basis. Contribution of Working Group I to the Fourth Assessment Report of the Intergovernmental Panel on Climate Change*, eds S. Solomon, D. Quin, M. Manning, K. Averyt, M. Marquis, K. B. Averyt, M. Tignor and H. L. Miller (Cambridge: New York, NY: Cambridge University Press), 747–845.

Meehl, G. A., Goddard, L., Murphy, J., Stouffer, R. J., Boer, G., Danabasoglu, G., et al. (2009). Decadal prediction: can it be skillful? *Bull. Am. Meteorol. Soc.* 90, 1467–1486. doi: 10.1175/2009BAMS2778.1

Meehl, G. A., Washington, W. M., Ammann, C. M., Arblaster, J. M., Wigley, T. M. L., and Tebaldi, C. (2004). Combinations of natural and anthropogenic forcings in twentieth-century climate. *J. Clim.* 17, 3721–3727. doi: 10.1175/1520-0442(2004)017<3721:CONAAF>2.0.CO;2

Meier, H. E. M. (2002a). Regional ocean climate simulations with a 3D ice-ocean model for the Baltic Sea. Part 1: Model experiments and results for temperature and salinity. *Clim. Dyn.* 19, 237–253. doi: 10.1007/s00382-001-0224-6

Meier, H. E. M. (2002b). Regional ocean climate simulations with a 3D ice-ocean model for the Baltic Sea. Part 2: Results for sea ice. *Clim. Dyn.* 19, 255–266. doi: 10.1007/s00382-001-0225-5

Meier, H. E. M. (2006). Baltic Sea climate in the late twenty-first century: a dynamical downscaling approach using two global models and two emission scenarios. *Clim. Dyn.* 27, 39–68. doi: 10.1007/s00382-006-0124-x

Meier, H. E. M. (2007). Modeling the pathways and ages of inflowing salt- and freshwater in the Baltic Sea. *Estuar. Coast. Shelf Sci.* 74, 610–627. doi: 10.1016/j.ecss.2007.05.019

Meier, H. E. M., Andersson, H. C., Arheimer, B., Blenckner, T., Chubarenko, B., Donnelly, C., et al. (2012c). Comparing reconstructed past variations and future projections of the Baltic Sea ecosystem – first results from multi-model ensemble simulations. *Environ. Res. Lett.* 7:034005. doi: 10.1088/1748-9326/7/3/034005

Meier, H. E. M., Andersson, H. C., Eilola, K., Gustafsson, B. G., Kuznetsov, I., Müller-Karulis, B., et al. (2011b). Hypoxia in future climates: a model ensemble study for the Baltic Sea. *Geophys. Res. Lett.* 38:L24608. doi: 10.1029/2011GL049929

Meier, H. E. M., Broman, B., and Kjellström, E. (2004a). Simulated sea level in past and future climates of the Baltic Sea. *Clim. Res.* 27, 59–75.

Meier, H. E. M., Döscher, R., and Faxén, T. (2003). A multiprocessor coupled ice-ocean model for the Baltic Sea: application to salt inflow. *J. Geophys. Res. Oceans* 108:3273. doi: 10.1029/2000JC000521

Meier, H. E. M., Döscher, R., and Halkka, A. (2004b). Simulated distributions of Baltic seaice in warming climate and consequences for the winter habitat of the Baltic ringed seal. *Ambio* 33, 249–256.

Meier, H. E. M., Edman, M., Eilola, K., Placke, M., Neumann, T., Andersson, H., et al. (2018a). Assessment of eutrophication abatement scenarios for the Baltic Sea by multi-model ensemble simulations. *Front. Mar. Sci.* 5:440. doi: 10.3389/fmars.2018.00440

Meier, H. E. M., Eilola, K., and Almroth, E. (2011a). Climate-related changes in marine ecosystems simulated with a three-dimensional coupled biogeochemical-physical model of the Baltic Sea. *Clim. Res.* 48, 31–55. doi: 10.3354/cr00968

Meier, H. E. M., Eilola, K., Almroth-Rosell, E., Schimanke, S., Kniebusch, M., Höglund, A., et al. (2018b). Disentangling the impact of nutrient load and climate changes on Baltic Sea hypoxia and eutrophication since 1850. *Clim. Dyn.* 1–22. doi: 10.1007/s00382-018-4296-y

Meier, H. E. M., Eilola, K., Almroth-Rosell, E., Schimanke, S., Kniebusch, M., Höglund, A., et al. (2018c). Correction to: Disentangling the impact of nutrient load and climate changes on Baltic Sea hypoxia and eutrophication since 1850. *Clim. Dyn.* 1–3. doi: 10.1007/s00382-018-4483-y

Meier, H. E. M., Höglund, A., Döscher, R., Andersson, H., Löptien, U., and Kjellström, E. (2011c). Quality assessment of atmospheric surface fields over the Baltic Sea of an ensemble of regional climate model simulations with respect to ocean dynamics. *Oceanologia* 53, 193–227. doi: 10.5697/oc.53-1-TI.193

Meier, H. E. M., Höglund, A., Eilola, K., and Almroth-Rosell, E. (2017). Impact of accelerated future GMSL rise on hypoxia in the Baltic Sea. *Clim. Dyn.* 49, 163–172. doi: 10.1007/s00382-016-3333-y

Meier, H. E. M., Hordoir, R., Andersson, H., Dieterich, C., Eilola, K., Gustafsson, B. G., et al. (2012a). Modeling the combined impact of changing climate and changing nutrient loads on the Baltic Sea environment in an ensemble of transient simulations for 1961-2099. *Clim. Dyn.* 39, 2421–2441. doi: 10.1007/s00382-012-1339-7

Meier, H. E. M., and Kauker, F. (2002). *Simulating Baltic Sea climate for the Period 1902-1998 With the Rossby Centre Coupled Ice-Ocean Model*. Reports Oceanography No.30, SMHI, Norrköping.

Meier, H. E. M., and Kauker, F. (2003a). Modeling decadal variability of the Baltic Sea: 2. Role of freshwater inflow and large-scale atmospheric circulation for salinity. *J. Geophys. Res. Oceans* 108:3368. doi: 10.1029/2003JC001799

Meier, H. E. M., and Kauker, F. (2003b). Sensitivity of the Baltic Sea salinity to the freshwater supply. *Clim. Res.* 24, 231–242. doi: 10.3354/cr024231

Meier, H. E. M., Kjellström, E., and Graham, L. P. (2006). Estimating uncertainties of projected Baltic Sea salinity in the late 21st century. *Geophys. Res. Lett.* 33:L15705. doi: 10.1029/2006GL026488

Meier, H. E. M., Müller-Karulis, B., Andersson, H. C., Dieterich, C., Eilola, K., Gustafsson, B. G., et al. (2012b). Impact of climate change on ecological quality indicators and biogeochemical fluxes in the Baltic Sea: a multi-model ensemble study. *Ambio* 41, 558–573. doi: 10.1007/s13280-012-0320-3

Meier, H. E. M., Väli, G., Naumann, M., Eilola, K., and Frauen, C. (2018d). Recently accelerated oxygen consumption rates amplify deoxygenation in the Baltic Sea. *J. Geophys. Res. Oceans* 123, 3227–3240. doi: 10.1029/2017JC013686

Mitchell, J. F. B., and Johns, T. C. (1997). On modification of global warming by sulfate aerosols. *J. Clim.* 10, 245–267. doi: 10.1175/1520-0442(1997)010<0245:OMOGWB>2.0.CO;2

Mohrholz, V. (2018). Major baltic inflow statistics – revised. *Front. Mar. Sci.* 5:384. doi: 10.3389/fmars.2018.00384

Mörth, C.-M., Humborg, C., Eriksson, E., Danielsson, A., Medina, R., Löfgren, S., et al. (2007). Modeling riverine nutrient transport of the Baltic Sea: a large-scale approach. *Ambio* 36, 124–133. doi: 10.1579/0044-7447(2007)36[124:MRNTTT]2.0.CO;2

Moss, R. H., Edmonds, J. A., Hibbard, K. A., Manning, M. R., Rose, S. K., Van Vuuren, D. P., et al. (2010). The next generation of scenarios for climate change research and assessment. *Nature* 463, 747–756. doi: 10.1038/nature08823

Müller, J. D., Schneider, B., and Rehder, G. (2016). Long-term alkalinity trends in the Baltic Sea and their implications for CO2-induced acidification. *Limnol. Oceanogr.* 61, 1984–2002. doi: 10.1002/lno.10349

Myhre, G., Highwood, E. J., Shine, K. P., and Stordal, F. (1998). New estimates of radiative forcing due to well mixed greenhouse gases. *Geophys. Res. Lett.* 25, 2715–2718. doi: 10.1029/98GL01908

Myhre, G., Shindell, D., Bréon, F.-M., Collins, W., Fuglestvedt, J., Huang, J., et al. (2013). "Anthropogenic and natural radiative forcing," in *Climate Change 2013: The Physical Science Basis. IPCC Working Group I Contribution to IPCC AR5,* eds T. F. Stocker, D. Quin, G. K. Plattner, M. Tignor, S. K. Allen, and J. Boschung, A. Nauels, Y. Xia, V. Bex and P. M. Midgle (Cambridge; New York, NY: Cambridge University Press), 659–740

Myrberg, K., Ryabchenko, V., Isaev, A., Vankevich, R., Andrejev, O., Bendtsen, J., et al. (2010). Validation of three-dimensional hydrodynamic models of the Gulf of Finland. *Boreal Environ. Res.* 15, 453–479.

Nakićenović, N., Alcamo, J., Grubler, A., Riahi, K., Roehrl, R., Rogner, H.-H., et al. (2000). *Special Report on Emissions Scenarios (SRES), a Special Report of Working Group III of the Intergovernmental Panel on Climate Change*. Cambridge University Press.

Neumann, T. (2010). Climate-change effects on the Baltic Sea ecosystem: a model study. *J. Mar. Syst.* 81, 213–224. doi: 10.1016/j.jmarsys.2009.12.001

Neumann, T., Eilola, K., Gustafsson, B., Müller-Karulis, B., Kuznetsov, I., Meier, H. E. M., et al. (2012). Extremes of temperature, oxygen and blooms in the Baltic Sea in a changing climate. *Ambio* 41, 574–585. doi: 10.1007/s13280-012-0321-2

Neumann, T., Fennel, W., and Kremp, C. (2002). Experimental simulations with an ecosystem model of the Baltic Sea: a nutrient load reduction experiment. *Global Biogeochem. Cycles* 16, 7-1-7-19. doi: 10.1029/2001GB001450

Nielsen, J. R., Thunberg, E., Holland, D. S., Schmidt, J. O., Fulton, E. A., Bastardie, F., et al. (2017). Integrated ecological–economic fisheries models—Evaluation, review and challenges for implementation. *Fish Fish.* 1–29. doi: 10.1111/faf.12232

Niiranen, S., Yletyinen, J., Tomczak, M. M., Blenckner, T., Hjerne, O., MacKenzie, B., et al. (2013). Combined effects of global climate change and regional ecosystem drivers on an exploited marine food web. *Glob. Chang. Biol.* 19, 3327–3342. doi: 10.1111/gcb.12309

Nikulin, G., Kjellström, E., Hansson, U. L. F., Strandberg, G., and Ullerstig, A. (2011). Evaluation and future projections of temperature, precipitation and wind extremes over Europe in an ensemble of regional climate simulations. *Tellus A* 63, 41–55. doi: 10.1111/j.1600-0870.2010.00466.x

Norman, M., Rutgersson, A., and Sahlée, E. (2013). Impact of improved air-sea gas transfer velocity on fluxes and water chemistry in a Baltic Sea model. *J. Mar. Syst.* 111, 175–188. doi: 10.1016/j.jmarsys.2012.10.013

Omstedt, A. (2017). "The development of climate science of the Baltic Sea Region," in *Oxford Research Encyclopedia of Climate Science* (Oxford: Oxford University Press). doi: 10.1093/acrefore/9780190228620.013.654

Omstedt, A., and Chen, D. (2001). Influence of atmospheric circulation on the maximum ice extent in the Baltic Sea. *J. Geophys. Res. Oceans* 106, 4493–4500. doi: 10.1029/1999JC000173

Omstedt, A., Chen, Y., and Wesslander, K. (2005). A comparison between the ERA40 and the SMHI gridded meteorological databases as applied to Baltic Sea modelling. *Hydrol. Res.* 36, 369–380.

Omstedt, A., Edman, M., Claremar, B., Frodin, P., Gustafsson, E., Humborg, C., et al. (2012). Future changes in the Baltic Sea acid–base (pH) and oxygen balances. *Tellus B* 64:19586. doi: 10.3402/tellusb.v64i0.19586

Omstedt, A., Edman, M., Claremar, B., and Rutgersson, A. (2015). Modelling the contributions to marine acidification from deposited SOx, NOx, and NHx in the Baltic Sea: Past and present situations. *Cont. Shelf Res.* 111, 234–249. doi: 10.1016/j.csr.2015.08.024

Omstedt, A., Elken, J., Lehmann, A., and Piechura, J. (2004). Knowledge of the Baltic Sea physics gained during the BALTEX and related programmes. *Prog. Oceanogr.* 63, 1–28. doi: 10.1016/j.pocean.2004.09.001

Omstedt, A., Gustafsson, B., Rodhe, J., and Walin, G. (2000). Use of Baltic Sea modelling to investigate the water cycle and the heat balance in GCM and regional climate models. *Clim. Res.* 15, 95–108. doi: 10.3354/cr015095

Omstedt, A., Gustafsson, E., and Wesslander, K. (2009). Modelling the uptake and release of carbon dioxide in the Baltic Sea surface water. *Cont. Shelf Res.* 29, 870–885. doi: 10.1016/j.csr.2009.01.006

Omstedt, A., and Hansson, D. (2006a). The Baltic Sea ocean climate system memory and response to changes in the water and heat balance components. *Cont. Shelf Res.* 26, 236–251. doi: 10.1016/j.csr.2005.11.003

Omstedt, A., and Hansson, D. (2006b). Erratum to:"The Baltic Sea ocean climate system memory and response to changes in the water and heat balance components":[Continental Shelf Research 26 (2)(2006) 236–251]. *Cont. Shelf Res.* 26, 1685–1687. doi: 10.1111/j.1600-0870.2004.00070.x

Omstedt, A., Humborg, C., Pempkowiak, J., Perttilä, M., Rutgersson, A., Schneider, B., et al. (2014). Biogeochemical control of the coupled CO_2-O_2 system of the Baltic Sea: a review of the results of Baltic-C. *Ambio* 43, 49–59. doi: 10.1007/s13280-013-0485-4

Omstedt, A., and Nohr, C. (2004). Calculating the water and heat balances of the Baltic Sea using ocean modelling and available meteorological, hydrological and ocean data. *Tellus A* 56, 400–414. doi: 10.3402/tellusa.v56i4.14428

O'Neill, B. C., Kriegler, E., Riahi, K., Ebi, K. L., Hallegatte, S., Carter, T. R., et al. (2014). A new scenario framework for climate change research: the concept of shared socioeconomic pathways. *Clim. Change* 122, 387–400. doi: 10.1007/s10584-013-0905-2

O'Neill, B. C., Tebaldi, C., van Vuuren, D. P., Eyring, V., Friedlingstein, P., Hurtt, G., et al. (2016). The scenario model intercomparison project (ScenarioMIP) for CMIP6. *Geosci. Model Dev.* 9, 3461–3482. doi: 10.5194/gmd-9-3461-2016

Parker, W. S. (2013). Ensemble modeling, uncertainty and robust predictions. Wiley Interdiscip. Rev. Clim. Change 4, 213–223. doi: 10.1002/wcc.220

Placke, M., Meier, H. E. M., Gräwe, U., Neumann, T., Frauen, C., and Liu, Y. (2018). Long-term mean circulation of the Baltic Sea as represented by various ocean circulation models. *Front. Mar. Sci.* 5:287. doi: 10.3389/fmars.2018.00287

Pushpadas, D., Schrum, C., and Daewel, U. (2015). Projected climate change impacts on North Sea and Baltic Sea: CMIP3 and CMIP5 model based scenarios. *Biogeosci. Discuss.* 12, 12229–12279. doi: 10.5194/bgd-12-12229-2015

Radach, G., and Pätsch, J. (1997). Climatological annual cycles of nutrients and chlorophyll in the North Sea. *J. Sea Res.* 38, 231–248. doi: 10.1016/S1385-1101(97)00048-8

Radtke, H., and Maar, M. (2016). Estimating the effective nitrogen import: an example for the North Sea-Baltic Sea boundary. *J. Geophys. Res.* 121, 2562–2575. doi: 10.1002/2016JG003516

Räisänen, J. (2001). CO_2-induced climate change in CMIP2 experiments: quantification of agreement and role of internal variability. *J. Clim.* 14, 2088–2104. doi: 10.1175/1520-0442(2001)014<2088:CICCIC>2.0.CO;2

Räisänen, J. (2017). "Future climate change in the Baltic Sea Region and environmental impacts," in *Oxford Research Encyclopedia of Climate Science* (Oxford: Oxford University Press), 37. doi: 10.1093/acrefore/9780190228620.013.634

Räisänen, J., Hansson, U., Ullerstig, A., Döscher, R., Graham, L. P., Jones, C., et al. (2004). European climate in the late twenty-first century: regional simulations with two driving global models and two forcing scenarios. *Clim. Dyn.* 22, 13–31. doi: 10.1007/s00382-003-0365-x

Räisänen, J., Rummukainen, M., and Ullerstig, A. (2001). Downscaling of greenhouse gas induced climate change in two GCMs with the Rossby Centre regional climate model for northern Europe. *Tellus A* 53, 168–191. doi: 10.1034/j.1600-0870.2001.00168.x

Raschke, E., Meywerk, J., Warrach, K., Andrea, U., Bergström, S., Beyrich, F., et al. (2001). The Baltic Sea Experiment (BALTEX): a European contribution to the investigation of the energy and water cycle over a large drainage basin. *Bull. Am. Meteorol. Soc.* 82, 2389–2413. doi: 10.1175/1520-0477(2001)082<2389:TBSEBA>2.3.CO;2

Rechid, D., Meier, H. E. M., Schrum, C., Rummukainen, M., Moseley, C., Bülow, K., et al. (2016). "Annex 2: Climate Model Simulations for the North Sea Region," in *North Sea Region Climate Change Assessment*, eds M. Quante and F. Colijn (Cham: Springer International Publishing).

Reed, D. C., Gustafsson, B. G., and Slomp, C. P. (2016). Shelf-to-basin iron shuttling enhances vivianite formation in deep Baltic Sea sediments. *Earth Planet. Sci. Lett.* 434, 241–251. doi: 10.1016/j.epsl.2015.11.033

Reissmann, J. H., Burchard, H., Feistel, R., Hagen, E., Lass, H. U., Mohrholz, V., et al. (2009). Vertical mixing in the Baltic Sea and consequences for eutrophication - A review. *Prog. Oceanogr.* 82, 47–80. doi: 10.1016/j.pocean.2007.10.004

Rockel, B. (2015). The regional downscaling approach: a brief history and recent advances. *Curr. Clim. Change Rep.* 1, 22–29. doi: 10.1007/s40641-014-0001-3

Roeckner, E., Bengtsson, L., Feicther, J., Lelieveld, J., and Rodhe, H. (1999). Transient climate change simulations with a coupled atmosphere-ocean GCM including the tropospheric sulfur cycle. *J. Clim.* 12, 3004–3032. doi: 10.1175/1520-0442(1999)012<3004:TCCSWA>2.0.CO;2

Roeckner, E., Brokopf, R., Esch, M., Giorgetta, M., Hagemann, S., and Kornblueh, S. (2006). Sensitivity of simulated climate to horizontal and vertical resolution in the ECHAM5 atmosphere model. *J. Clim.* 19, 3771–3791. doi: 10.1175/JCLI3824.1

Rose, K. A., Allen, J. I., Artioli, Y., Barange, M., Blackford, J., Carlotti, F., et al. (2010). End-to-end models for the analysis of marine ecosystems: challenges, issues, and next steps. *Mar. Coast. Fisher.* 2, 115–130. doi: 10.1577/C09-059.1

Rummukainen, M. (2010). State-of-the-art with Regional Climate Models. *Wiley Interdisc. Rev. Clim. Change* 1, 82–96. doi: 10.1002/wcc.8

Rummukainen, M. (2016a). Added value in regional climate modeling. *Wiley Interdisc. Rev. Clim. Change* 7, 145–159. doi: 10.1002/wcc.378

Rummukainen, M. (2016b). "Annex 3: Uncertainties in Climate Change Projections," in *North Sea Region Climate Change Assessment*, eds M. Quante and F. Colijn (Cham: Springer International Publishing), 505–513.

Rummukainen, M., Räisänen, J., Bringfelt, B., Ullerstig, A., Omstedt, A., Willén, U., et al. (2001). A regional climate model for northern Europe - model description and results from the downscaling of two GCM control simulations. *Climate Dynamics* 17, 339–359. doi: 10.1007/s003820000109

Rummukainen, M., Rockel, B., Bärring, L., Christensen, J. H., and Reckermann, M. (2015). Twenty-first-century challenges in regional climate modeling. *Bull. Am. Meteorol. Soc.* 96, ES135–ES138. doi: 10.1175/BAMS-D-14-00214.1

Ruosteenoja, K., Jylh,ä, K., and Kämäräinen, M. (2016). Climate projections for Finland under the RCP forcing scenarios. *Geophysica* 51, 17–50.

Ryabchenko, V., Karlin, L., Isaev, A., Vankevich, R., Eremina, T., Molchanov, M., et al. (2016). Model estimates of the eutrophication of the Baltic Sea in the contemporary and future climate. *Oceanology* 56, 36–45. doi: 10.1134/S0001437016010161

Samuelsson, P., Jones, C. G., Willén, U., Ullerstig, A., Gollvik, S., Hansson, U., et al. (2011). The Rossby Centre Regional Climate model RCA3: model description and performance. *Tellus A* 63, 4–23. doi: 10.1111/j.1600-0870.2010.00478.x

Saraiva, S., Meier, H. E. M., Andersson, H., Höglund, A., Dieterich, C., Hordoir, R., et al. (2018). Baltic Sea ecosystem response to various nutrient load scenarios in present and future climates. *Clim. Dyn.* 1–19. doi: 10.1007/s00382-018-4330-0

Saraiva, S., Meier, H. E. M., Andersson, H. C., Höglund, A., Dieterich, C., Gröger, M., et al. (2019). Uncertainties in projections of the Baltic Sea ecosystem driven by an ensemble of global climate models. *Front. Earth Sci.* 6:244. doi: 10.3389/feart.2018.00244

Savchuk, O., and Wulff, F. (1999). "Modelling regional and large-scale response of Baltic Sea ecosystems to nutrient load reductions." in *Biological, Physical and Geochemical Features of Enclosed and Semi-enclosed Marine Systems,* ed E. M. Blomqvist (Dordrecht: Springer), 35–43. doi: 10.1007/978-94-017-0912-5_5

Savchuk, O. P. (2002). Nutrient biogeochemical cycles in the Gulf of Riga: scaling up field studies with a mathematical model. *J. Mar. Syst.* 32, 253–280. doi: 10.1016/S0924-7963(02)00039-8

Savchuk, O. P. (2018). Large-Scale Nutrient Dynamics in the Baltic Sea, 1970–2016. *Front. Mar. Sci.* 5:95. doi: 10.3389/fmars.2018.00095

Savchuk, O. P., Gustafsson, B. G., Medina, M. R., Sokolov, A., and Wulff, F. (2012b). *External Nutrient Loads to the Baltic Sea, 1970-2006.* Baltic Nest Institute Technical Report No. 5, 22.

Savchuk, O. P., Gustafsson, B. G., and Müller-Karulis, B. (2012a). *BALTSEM: A Marine Model for Decision Support Within the Baltic Sea Region*. Baltic Nest Institute Technical Report No. 7, 55.

Schernewski, G., Friedland, R., Carstens, M., Hirt, U., Leujak, W., Nausch, G., et al. (2015). Implementation of European marine policy: new water quality targets for German Baltic waters. *Marine Policy* 51, 305–321. doi: 10.1016/j.marpol.2014.09.002

Schimanke, S., Dieterich, C., and Meier, H. E. M. (2014). An algorithm based on sea-level pressure fluctuations to identify major Baltic inflow events. *Tellus A* 66:23452. doi: 10.3402/tellusa.v66.23452

Schimanke, S., and Meier, H. E. M. (2016). Decadal-to-centennial variability of salinity in the Baltic Sea. *J. Clim.* 29, 7173–7188. doi: 10.1175/JCLI-D-15-0443.1

Schmidt, G. A., Bader, D., Donner, L. J., Elsaesser, G. S., Golaz, J.-C., Hannay, C., et al. (2017). Practice and philosophy of climate model tuning across six US modeling centers. *Geosci. Model Dev.* 10, 3207–3223. doi: 10.5194/gmd-10-3207-2017

Schrum, C. (1997). "A coupled ice–ocean model for the North Sea and the Baltic Sea," in *Sensitivity of North Sea, Baltic Sea and Black Sea to Anthropogenic and Climatic Changes in NATO ASI Series*, eds E. Özsoy, and A. Mikaelyan, A., (Dordrecht, Boston, MA: Kluwer Academic Publishers), 311–325.

Schrum, C. (2017). "Regional Climate Modeling and Air-Sea Coupling." in *Oxford Research Encyclopedia of Climate Science* (Oxford: Oxford University Press). doi: 10.1093/acrefore/9780190228620.013.3

Schrum, C., Lowe, J., Meier, H. E. M., Grabemann, I., Holt, J., Mathis, M., et al. (2016). "Projected Change - North Sea." in *North Sea Region Climate Change Assessment,* eds M. Quante and F. Colijn (Cham: Springer International Publishing), 175–217. doi: 10.1007/978-3-319-39745-0

Sein, D. V., Mikolajewicz, U., Gröger, M., Fast, I., Cabos, W., Pinto, J. G., et al. (2015). Regionally coupled atmosphere-ocean-sea ice-marine biogeochemistry model ROM: 1. Description and validation. *J. Adv. Model. Earth Syst.* 7, 268–304. doi: 10.1002/2014MS000357

Seitola, T., Ukkonen, P., Karpechko, A., Ruosteenoja, K., and Gregow, H. (2015). "Co-variability of North Atlantic Oscillation and maximumsea ice extent in the Baltic Sea in CMIP5 Climate Models," in *OTC Arctic Technology Conference. Offshore Technology Conference* (Copenhagen). Available online at: http://toc.proceedings.com/26328webtoc.pdf

Sepp, M., Post, P., and Jaagus, J. (2005). Long-term changes in the frequency of cyclones and their trajectories in Central and Northern Europe. *Hydrol. Res.* 36, 297–309. doi: 10.2166/nh.2005.002

Sepp, M., Post, P., Mändla, K., and Aunap, R. (2018). On cyclones entering the Baltic Sea region. *Boreal Environ. Res.* 23, 1–14.

Skogen, M. D., Søiland, H., and Svendsen, E. (2004). Effects of changing nutrient loads to the North Sea. *J. Mar. Syst.* 46, 23–38. doi: 10.1016/j.jmarsys.2003.11.013

Smith, D. M., Cusack, S., Colman, A. W., Folland, C. K., Harris, G. R., and Murphy, J. M. (2007). Improved surface temperature prediction for the coming decade from a global climate model. *Science* 317, 796–799, doi: 10.1126/science.1139540

Stålnacke, P., Grimvall, A., Sundblad, K., and Tonderski, A. (1999). Estimation of riverine loads of nitrogen and phosphorus to the Baltic Sea 1970–1993. *Environ. Monit. Assess.* 58, 73–200. doi: 10.1023/A:1006073015871

Stocker, T., Qin, D., Plattner, G.-K., Alexander, L., Allen, S., Bindoff, N., et al. (2013). "Technical summary, in Climate Change 2013: the Physical Science Basis," in *Contribution of Working Group I to the Fifth Assessment Report of the Intergovernmental Panel on Climate Change*, eds T. F. Stocker, D. Quin, G. K. Plattner, M. Tignor, S. K. Allen, J. Boschung, A. Nauels, Y. Xia, V. Bex and P. M. Midgle (Cambridge: Cambridge University Press). 33–115. doi: 10.1017/CBO9781107415324

Suikkanen, S., Pulina, S., Engström-Öst, J., Lehtiniemi, M., and Lehtinen, S. (2013). Climate Change and Eutrophication Induced Shifts in Northern Summer Plankton Communities. *PLoS ONE* 8:e66475. doi: 10.1371/journal.pone.0066475

Taylor, K. E., Stouffer, R. J., and Meehl, G. A. (2012). An overview of CMIP5 and the experiment design. *Bull. Am. Meteorol. Soc.* 93, 485–498. doi: 10.1175/BAMS-D-11-00094.1

Tian, T., Boberg, F., Christensen, O. B., Christensen, J. H., She, J., and Vihma, T. (2013). Resolved complex coastlines and land–sea contrasts in a high-resolution regional climate model: a comparative study using prescribed and modelled SSTs. *Tellus A* 65:19951. doi: 10.3402/tellusa.v65i0.19951

Timmermann, K., Norkko, J., Janas, U., Norkko, A., Gustafsson, B. G., and Bonsdorff, E. (2012). Modelling macrofaunal biomass in relation to hypoxia and nutrient loading. *J. Mar. Syst.* 105, 60–69. doi: 10.1016/j.jmarsys.2012.06.001

Tinker, J., Lowe, J., Holt, J., Pardaens, A., and Wiltshire, A. (2015). Validation of an ensemble modelling system for climate projections for the northwest European shelf seas. *Prog. Oceanogr.* 138, 211–237. doi: 10.1016/j.pocean.2015.07.002

Tinker, J., Lowe, J., Pardaens, A., Holt, J., and Barciela, R. (2016). Uncertainty in climate projections for the 21st century northwest European shelf seas. *Prog. Oceanogr.* 148, 56–73. doi: 10.1016/j.pocean.2016.09.003

Tinz, B. (1996). On the relation between annual maximum extent of ice cover in the Baltic Sea and sea level pressure as well as air temperature field. *Geophysica* 32, 319–341.

Topcu, D., Behrendt, H., Brockmann, U., and Claussen, U. (2011). Natural background concentrations of nutrients in the German Bight area (North Sea). *Environ. Monit. Assess.* 174, 361–388. doi: 10.1007/s10661-010-1463-y

Troost, T., De Kluijver, A., and Los, F. (2014). Evaluation of eutrophication variables and thresholds in the Dutch North Sea in a historical context—a model analysis. *J. Mar. Syst.* 134, 45–56. doi: 10.1016/j.jmarsys.2014.01.015

Turco, M., Sanna, A., Herrera, S., Llasat, M.-C., and Gutiérrez, J. M. (2013). Large biases and inconsistent climate change signals in ENSEMBLES regional projections. *Clim. Change* 120, 859–869. doi: 10.1007/s10584-013-0844-y

Ulfsbo, A., Hulth, S., and Anderson, L. G. (2011). pH and biogeochemical processes in the Gotland Basin of the Baltic Sea. *Mar. Chem.* 127, 20–30. doi: 10.1016/j.marchem.2011.07.004

Ulfsbo, A., Kulinski, K., Anderson, L. G., and Turner, D. R. (2015). Modelling organic alkalinity in the Baltic Sea using a Humic-Pitzer approach. *Mar. Chem.* 168, 18–26. doi: 10.1016/j.marchem.2014.10.013

Uppala, S. M., Kållberg, P. W., Simmons, A. J., Andrae, U., Bechtold, V. C., Fiorino, M., et al. (2005). The ERA40 reanalysis. *Q. J. R. Meteorol. Soc.* 131, 2961–3012. doi: 10.1256/qj.04.176

Vahtera, E., Conley, D. J., Gustafsson, B. G., Kuosa, H., Pitkänen, H., Savchuk, O. P., et al. (2007). Internal ecosystem feedbacks enhance nitrogen-fixing cyanobacteria blooms and complicate management in the Baltic Sea. *Ambio* 36, 186–194. doi: 10.1579/0044-7447(2007)36[186:IEFENC]2.0.CO;2

Vahtera, E., Laanemets, J., Pavelson, J., Huttunen, M., and Kononen, K. (2005). Effect of upwelling on the pelagic environment and bloom-forming cyanobacteria in the western Gulf of Finland, Baltic Sea. *J. Mar. Syst.* 58, 67–82. doi: 10.1016/j.jmarsys.2005.07.001

Van der Linden, P., and Mitchell, J. F. B. (2009). *ENSEMBLES: Climate Change and Its Impacts-Summary of Research and Results From the ENSEMBLES Project.* Available Online at: http://mfkp.org/INRMM/article/14257308; https://web.archive.org/web/20170116182610/http://ensembles-eu.metoffice.com/docs/Ensembles_final_report_Nov09.pdf

Van Vuuren, D. P., Edmonds, J., Kainuma, M., Riahi, K., Thomson, A., Hibbard, K., et al. (2011). The representative concentration pathways: an overview. *Clim. Change* 109:5. doi: 10.1007/s10584-011-0148-z

Vladimirova, O. M., Eremina, T. R., Isaev, A. V., Ryabchenko, V. A., and Savchuk, O. P. (2018). Modelling dissolved organic nutrients in the Gulf of Finland. *Fundament. Appl. Hydrophys.* 11 , 90–101. doi: 10.7868/S2073667318040111

Vuorinen, I., Hänninen, J., Rajasilta, M., Laine, P., Eklund, J., Montesino-Pouzols, F., et al. (2015). Scenario simulations of future salinity and ecological consequences in the Baltic Sea and adjacent North Sea areas - implications for environmental monitoring. *Ecol. Indic.* 50, 196–205. doi: 10.1016/j.ecolind.2014.10.019

Wang, S., Dieterich, C., Döscher, R., Höglund, A., Hordoir, R., Meier, H. E. M., et al. (2015). Development and evaluation of a new regional coupled atmosphere–ocean model in the North Sea and Baltic Sea. *Tellus A* 67:24284. doi: 10.3402/tellusa.v67.24284

Weigel, A., Knutti, R., Liniger, M. A., and Appenzeller, C. (2010). Risks of model weighting in multimodel climate projections. *J. Clim.* 23 , 4175–4197. doi: 10.1175/2010JCLI3594.1

Wikner, J., and Andersson, A. (2012). Increased freshwater discharge shifts the trophic balance in the coastal zone of the northern Baltic Sea. *Glob. Chang. Biol.* 18, 2509–2519. doi: 10.1111/j.1365-2486.2012.02718.x

Wilcke, R. A. I., and Bärring, L. (2016). Selecting regional climate scenarios for impact modelling studies. *Environ. Model. Softw.* 78, 191–201. doi: 10.1016/j.envsoft.2016.01.002

Zandersen, M., Hyytiainen, K., Meier, H. E. M., Tomzcak, M., Bauer, B., Haapasaari, P., et al. (2019). Extending shared socioeconomic pathways for the Baltic Sea region for use in studying regional environmental problems. *Reg. Environ. Change*. 1–14. doi: 10.1016/j.gloenvcha.2015.04.004

Conflict of Interest Statement: The authors declare that the research was conducted in the absence of any commercial or financial relationships that could be construed as a potential conflict of interest.

Copyright © 2019 Meier, Edman, Eilola, Placke, Neumann, Andersson, Brunnabend, Dieterich, Frauen, Friedland, Gröger, Gustafsson, Gustafsson, Isaev, Kniebusch, Kuznetsov, Müller-Karulis, Naumann, Omstedt, Ryabchenko, Saraiva and Savchuk. This is an open-access article distributed under the terms of the Creative Commons Attribution License (CC BY). The use, distribution or reproduction in other forums is permitted, provided the original author(s) and the copyright owner(s) are credited and that the original publication in this journal is cited, in accordance with accepted academic practice. No use, distribution or reproduction is permitted which does not comply with these terms.

frontiers in Marine Science

ORIGINAL RESEARCH
published: 28 November 2018
doi: 10.3389/fmars.2018.00440

Assessment of Eutrophication Abatement Scenarios for the Baltic Sea by Multi-Model Ensemble Simulations

H. E. Markus Meier[1,2], Moa K. Edman[2], Kari J. Eilola[2], Manja Placke[1], Thomas Neumann[1], Helén C. Andersson[2], Sandra-Esther Brunnabend[1], Christian Dieterich[2], Claudia Frauen[1], René Friedland[1], Matthias Gröger[2], Bo G. Gustafsson[3,4], Erik Gustafsson[3], Alexey Isaev[5], Madline Kniebusch[1], Ivan Kuznetsov[6], Bärbel Müller-Karulis[3], Anders Omstedt[7], Vladimir Ryabchenko[5], Sofia Saraiva[8] and Oleg P. Savchuk[3]*

[1] Department of Physical Oceanography and Instrumentation, Leibniz Institute for Baltic Sea Research Warnemünde, Rostock, Germany, [2] Department of Research and Development, Swedish Meteorological and Hydrological Institute, Norrköping, Sweden, [3] Baltic Nest Institute, Stockholm University, Stockholm, Sweden, [4] Tvärminne Zoological Station, University of Helsinki, Hanko, Finland, [5] Shirshov Institute of Oceanology, Russian Academy of Sciences, Moscow, Russia, [6] Institute of Coastal Research, Helmholtz-Zentrum Geesthacht, Geesthacht, Germany, [7] Department of Marine Sciences, University of Gothenburg, Göteborg, Sweden, [8] MARETEC, Instituto Superior Técnico, University of Lisbon, Lisbon, Portugal

OPEN ACCESS

Edited by:
Karol Kulinski,
Institute of Oceanology (PAN), Poland

Reviewed by:
Gennadi Lessin,
Plymouth Marine Laboratory, United Kingdom
Athanasios Thomas Vafeidis, Christian-Albrechts-Universität zu Kiel, Germany
Letizia Tedesco, Finnish Environment Institute (SYKE), Finland

***Correspondence:**
H. E. Markus Meier
markus.meier@io-warnemuende.de

Specialty section:
This article was submitted to Coastal Ocean Processes, a section of the journal Frontiers in Marine Science

Received: *17 April 2018*
Accepted: *31 October 2018*
Published: *28 November 2018*

Citation:
Meier HEM, Edman MK, Eilola KJ, Placke M, Neumann T, Andersson HC, Brunnabend S-E, Dieterich C, Frauen C, Friedland R, Gröger M, Gustafsson BG, Gustafsson E, Isaev A, Kniebusch M, Kuznetsov I, Müller-Karulis B, Omstedt A, Ryabchenko V, Saraiva S and Savchuk OP (2018) Assessment of Eutrophication Abatement Scenarios for the Baltic Sea by Multi-Model Ensemble Simulations. Front. Mar. Sci. 5:440. doi: 10.3389/fmars.2018.00440

To assess the impact of the implementation of the Baltic Sea Action Plan (BSAP) on the future environmental status of the Baltic Sea, available uncoordinated multi-model ensemble simulations for the Baltic Sea region for the twenty-first century were analyzed. The scenario simulations were driven by regionalized global general circulation model (GCM) data using several regional climate system models and forced by various future greenhouse gas emission and air- and river-borne nutrient load scenarios following either reference conditions or the BSAP. To estimate uncertainties in projections, the largest ever multi-model ensemble for the Baltic Sea comprising 58 transient simulations for the twenty-first century was assessed. Data from already existing simulations from different projects including regionalized GCM simulations of the third and fourth assessment reports of the Intergovernmental Panel on Climate Change based on the corresponding Coupled Model Intercomparison Projects, CMIP3 and CMIP5, were collected. Various strategies to weigh the ensemble members were tested and the results for ensemble mean changes between future and present climates are shown to be robust with respect to the chosen metric. Although (1) the model simulations during the historical period are of different quality and (2) the assumptions on nutrient load levels during present and future periods differ between models considerably, the ensemble mean changes in biogeochemical variables in the Baltic proper with respect to nutrient load reductions are similar between the entire ensemble and a subset consisting only of the most reliable simulations. Despite the large spread in projections, the implementation of the BSAP will lead to a significant improvement of the environmental status of the Baltic Sea according to both weighted and unweighted ensembles. The results emphasize the need for investigating ensembles with many members and rigorous assessments of models' performance.

Keywords: Baltic Sea, nutrients, eutrophication, climate change, future projections, uncertainties, ensemble simulations

INTRODUCTION

The Baltic Sea is a semi-enclosed coastal sea located in northern Europe and extending from about 54°N to almost 66°N (**Figure 1**). The long meridional extension determines substantial gradients in seasonal patterns of the thermal regime both in the sea and at its watershed. Water exchange of the almost non-tidal Baltic Sea with the open ocean is limited by the shallow and narrow Danish straits to the west, while the rivers, situated mostly in the northeast, annually bring in fresh water in amount equivalent to about 1/40 of the sea volume. Such geographical settings generate an estuarine water circulation along a chain of depressions separated by the shallower sills and resulting in large horizontal and vertical gradients of salinity (e.g., Stigebrandt, 2001; Leppäranta and Myrberg, 2009; Omstedt et al., 2014a). The sub-basins of the Baltic Sea are the Arkona, Bornholm, and Gotland basins, Gulf of Riga, Gulf of Finland, Bothnian Sea and Bothnian Bay (**Figure 1**). While the southern sub-basins are characterized by a pronounced, perennial halocline separating a surface and deep layer, the northern sub-basins, Bothnian Sea and Bothnian Bay, have a weaker, seasonal halocline with a well-mixed water column during winter. In present climate, the northern sub-basins, Gulf of Finland, Bothnian Sea and Bothnian Bay, are seasonally ice-covered on average.

In the Baltic Sea, patterns of species diversity are controlled by freshwater supply from the large catchment area and salt water inflows from the North Sea (Remane and Schlieper, 1971). Large landscape and land use gradients are found also over the Baltic Sea drainage basin, from densely populated southern areas with its intensive agriculture to almost deserted northern rocks, forests and wetlands. Such unique combination of natural and socio-economic features determines strong geophysical, biogeochemical, and ecosystem gradients (Schneider et al., 2017; Snoeijs-Leijonmalm and Andrén, 2017) that are very challenging to numerical modeling, especially to simulations involving scenarios of both climate (e.g., temperature and precipitation) and anthropogenic (e.g., nutrient inputs) changes (e.g., Vuorinen et al., 2015; Meier et al., 2018b).

To project future changes of the Baltic Sea scenario simulations have been developed during the past decade using coupled physical-biogeochemical models of varying complexity (BACC Author Team, 2008; BACC II Author Team, 2015). From recent transient scenario simulations for the period 1960–2100 it was found that water temperatures will increase and sea-ice cover will decrease in the future (BACC II Author Team, 2015). For instance, Meier (2006) calculated between the periods 1961–1990 and 2071–2100 an increase in volume averaged temperature between 1.9 and 3.2°C with an ensemble mean change of 2.5°C and a decline in sea-ice extent between 46 and 77% with an ensemble mean reduction of 62%. According to the BACC II Author Team (2015) salinity is projected to decrease due to the increased total annual river discharge. Future projections suggest that during winter runoff from the northern parts of the Baltic Sea catchment area will increase while during summer the runoff from the southern regions will decrease. From the overall increased total annual runoff, for instance Meier (2006) calculated a decrease in volume averaged salinity between 0.6 and 4.2 g kg^{-1} with an ensemble mean reduction of 2.3 g kg^{-1}. Although in general wind changes over the Baltic Sea are small (Kjellström et al., 2011; Nikulin et al., 2011), higher wind speeds can be expected in regions where the sea-ice is projected to disappear on average affecting, e.g., currents, wind waves and resuspension (Eilola et al., 2013). However, sea level rise has a greater potential to increase surge levels than projected wind speed changes (Gräwe and Burchard, 2012).

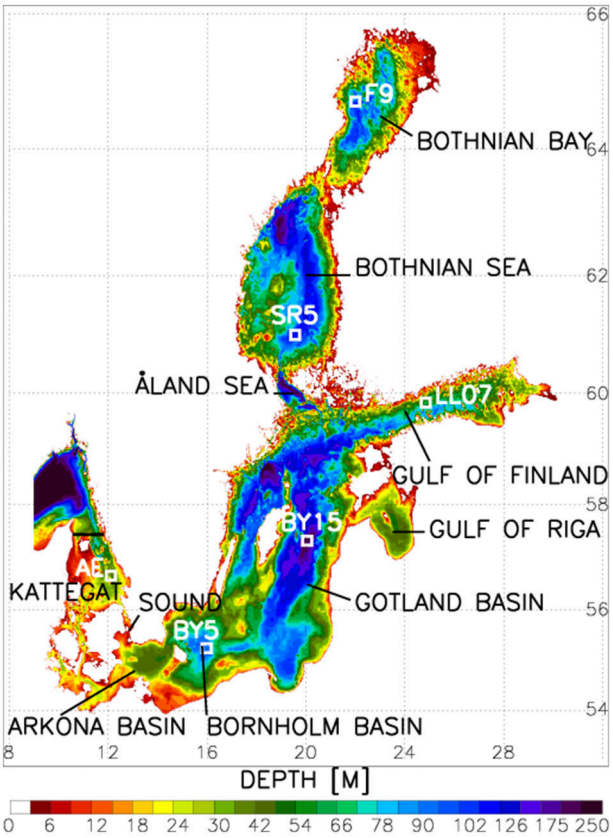


FIGURE 1 | Bottom topography of the Baltic Sea and locations of the monitoring stations Anholt East in Kattegat (AE), Bornholm Deep (BY5), Gotland Deep (BY15), LL07 in the Gulf of Finland, SR5 in the Bothnian Sea and F9 in the Bothnian Bay. The Baltic proper comprises the Arkona Basin, Bornholm Basin and Gotland Basin.

The intensity and frequency of salt water inflows are projected to remain unchanged (Gräwe et al., 2013) or to slightly increase (Schimanke et al., 2014). However, in the latter study rising global mean sea level (GMSL) and changes in river runoff were not considered. Recent publications suggest that at least in sensitivity experiments exploring the impact of high-end projections following the Intergovernmental Panel on Climate Change (IPCC, 2007) GMSL rise will cause significant increases in (1) frequency and magnitude of salt water inflows (Hordoir et al., 2015; Arneborg, 2016), (2) salinity, and (3) phosphate concentrations in the Baltic Sea as a consequence of increased cross sections in the Danish straits, and will contribute to (4) increased hypoxia and anoxia (Meier et al., 2017). In these

simulations, the increased phosphate concentrations in the water column originate from the fluxes between water column and sediment.

According to the BACC II Author Team (2015) climate change is likely to exacerbate eutrophication effects in the Baltic Sea because of (1) increased external nutrient loads due to increased runoff, (2) reduced oxygen flux from the atmosphere to the ocean, and (3) intensified internal nutrient cycling due to increased water temperatures (e.g., Meier et al., 2011, 2012a; Neumann et al., 2012; Omstedt et al., 2012). In the Baltic proper, higher water temperatures lead to faster phytoplankton growth and increased remineralization rates causing not only intensified nutrient cycling in the euphotic zone but also enhanced nutrient flows from the sediments due to a reduction in the nutrient retention capacity of the sediments (Meier et al., 2012b) caused by increased bacterial activity (e.g., Wulff et al., 2001). However, in the northern Baltic Sea phytoplankton production may actually be reduced in future climate due to increased allochthonous organic matter (Andersson et al., 2015).

Nutrient loads from land may vary differently than the volume flow due to changing soil moisture and soil temperature in future climate. Arheimer et al. (2012) found decreasing total nitrogen (N) and increasing total phosphorus (P) loads. According to their analysis, warmer temperatures may reinforce both denitrification causing N removal from the storage in water compartments and remineralization causing P accumulation in the water flow toward the sea.

Whether primary production and hypoxic area will increase in future climate will depend to a large extent on the nutrient load and greenhouse gas (GHG) emission or concentration scenarios (Meier et al., 2011; Saraiva et al., 2018). Future climate change will amplify oxygen depletion. Its impact on biogeochemical cycles is greater in the case of higher rather than lower nutrient loads. However, it has to be considered that the response of nutrient pools in the Baltic Sea to nutrient load changes will take several decades (Savchuk, 2018; and references therein).

In regions, such as the Bothnian Sea and the western Gulf of Finland, that may become on average ice-free in future climate, phytoplankton in spring will start growing earlier as a consequence of the shrinking sea-ice cover and improved light conditions and will decrease earlier due to earlier nutrient depletion (Eilola et al., 2013; their Figure 2F).

Neumann et al. (2012) suggested that also cyanobacteria blooms in the Baltic proper might occur earlier in summer. Such projected extension of the growth season and changes of the seasonal phytoplankton dynamics have already been detected in long-term satellite measurements (Kahru et al., 2016). Similar changes in seasonal dynamics of the surface water temperature are also reconstructed from field observations in all the major Baltic Sea basins but the corresponding changes in nutrient dynamics are not evident (Savchuk, 2018).

Concerning acidification the BACC II Author Team (2015) concluded that the rising atmospheric CO_2 mainly controls future pH changes in Baltic Sea surface water and that eutrophication and enhanced biological production are not affecting the annual mean pH, but may amplify the seasonal cycle by increased production and remineralization (Omstedt et al., 2012). Depending on the CO_2 emission scenario the pH of Baltic sea water will likely decrease further in the future.

The Baltic Sea is surrounded by nine riparian countries and therefore success of environmental management depends on concerted efforts of these countries. To facilitate this, all countries and the European Union (EU) have agreed to cooperate under the statutes of the Helsinki Convention and the implementation of the convention is coordinated by the Helsinki Commission (HELCOM). In addition, eight of the countries are EU member states and need to implement the Marine Strategy Framework and Water Framework directives (cf. Tedesco et al., 2016). A major step forward in the marine management was taken when the HELCOM Baltic Sea Action Plan (BSAP) was agreed by the HELCOM Contracting Parties in 2007 (HELCOM, 2007a,b) including concrete steps toward improved environmental status. One of the main components of the BSAP is a quantitative nutrient reduction scheme based on the ecosystem approach to management, providing reduction requirements per country and sub-basin, so called Country Allocated Nutrient Reduction Targets (CART) that should be achieved in order to mitigate eutrophication effects for the Baltic Sea. The reduction requirements were revised in 2013 based on new information (HELCOM, 2013a,b). The BSAP nutrient reduction scheme is based on the following steps (HELCOM, 2007a,b): (1) The politically agreed environmental objectives are translated into quantitative targets on observable variables in the sea (Secchi depth, Chl-a concentration, nutrient concentrations, oxygen deficit), (2) a biogeochemical model is used to estimate the maximum inputs per major sub-basin (so called Maximum Allowable Inputs, MAI) that will eventually lead to the achievement of target levels, and (3) the responsibility to perform the reduction necessary to achieve MAI for each sub-basin is shared between the countries (CART).

The assumptions how the MAI is implemented differ among the available scenario simulations. In some studies it was assumed that the nutrient loads after the year 2021 follow precisely the MAI (Friedland et al., 2012; Saraiva et al., 2018), whereas in other studies the impact of changing climate on the nutrient loads caused by the increased runoff and changes in other land surface processes is considered (Meier et al., 2011, 2012a; Neumann et al., 2012; BACC II Author Team, 2015).

In this pilot study, we assess the quality of available, state-of-the-art scenario simulations during the historical period 1980–2005 with the aim to reduce uncertainties and to raise confidence in projections of biogeochemical cycles. Henceforth, uncertainty is defined as the spread in future projections within an ensemble of scenario simulations expressed by the standard deviation of mean changes. Following climate modelers' terminology, we differentiate between scenario simulations (numerical model calculations based upon given assumptions) and scenarios (assumptions on nutrient load or radiative forcing that are not part of the applied model). We focus on the comparison between reference conditions from the recent past (1980–2005) and two nutrient load scenarios (REF and BSAP) for future climates (2072–2097). The REF scenario assumes unchanged reference conditions from the past also for future conditions.

From the analysis of the scenario simulations, we would like to answer the question whether current nutrient load abatement strategies, such as the BSAP (HELCOM, 2007a,b, 2013a,b) will meet their objectives of restored water quality status despite changing climate taking the uncertainties of the projections into account. For this aim, we analyzed results of scenario simulations performed in a number of international projects, such as ABNORMAL (Skogen et al., 2014), AMBER (Vuorinen et al., 2015), ECOSUPPORT (Meier et al., 2014), INFLOW (Kotilainen et al., 2014), Baltic-C (Omstedt et al., 2014b) and BONUS BalticAPP (Saraiva et al., 2018; Saraiva et al., submitted).

The nutrient load scenarios, REF and BSAP, correspond only to two out of five available Shared Socioeconomic Pathways (SSPs, O'Neill et al., 2014), i.e., SSP2 and SSP1, respectively (Zandersen et al., submitted manuscript) and do not represent the actual range of uncertainty. However, as we only focus on the question whether the BSAP will work in future climate taking plausible climate projections into account, nutrient load scenarios representing the other SSPs are not investigated. For comparison, only SSP2 (here defined as REF) is used as a business-as-usual scenario.

In an attempt to reduce uncertainties, we weighted the various scenario simulations with respect to the quality of simulated temperature, salinity and dissolved inorganic nitrogen, phosphorus and oxygen concentrations during the historical period (1980–2005) using available data of the national, long-term environmental monitoring programs in all Baltic Sea countries and using various metrics. Hence, we studied the future changes and its spreads of the whole ensemble and of a subset of scenario simulations with by definition "acceptable" quality to investigate whether the results of the projections depend on the quality of the models. In this approach, the definition and the assessment of the quality of the models are based on the evaluation of a cost function penalizing annual and seasonal mean biases normalized with the standard deviations of observations (e.g., Eilola et al., 2011; Skogen et al., 2014; Edman et al., 2018).

The paper is organized as follows. In section Methods, the involved global and regional climate models, the Baltic Sea models, the nutrient load and GHG emission scenarios, the list of investigated scenario simulations and the method of weighting the ensemble are introduced. In section Results, results of selected scenario simulations and of ensembles of weighted and unweighted scenario simulations are presented. In section Discussion, the advantages and disadvantages of weighting are discussed. In section Conclusions, some conclusions of the study are drawn.

METHODS

Climate Models

We collected data from scenario simulations of six coupled physical-biogeochemical Baltic Sea Models (BSMs, see **Table 1**) driven by eight climate models (**Table 2**). Each climate model consists of a global General Circulation Model (GCM) or ESM (Earth System Model including also the carbon cycle), a regional climate atmosphere or atmosphere-ocean model (RCM), a land surface model (LSM) and one or two GHG emission scenarios. From all models, we defined eight subsets, each consisting of a combination of one BSM and one LSM. Henceforth, these subsets are called Baltic Region Models (BRMs) or Model A to H (**Table 2**). For each BRM the ensemble means of all scenario simulations were calculated for REF and BSAP nutrient load scenarios. The hierarchy of models used to carry out the scenario simulations is summarized in **Figure 2**.

The projections are based on regionalized GCM results of the third and fourth assessment reports of the (IPCC, 2007, 2013)

TABLE 1 | Baltic Sea models (N, nitrogen; P, phosphorus; Si, silica; CTC, total inorganic carbon; ATC, total alkalinity; PHY, phytoplankton; O_2, oxygen (or hydrogen sulfide); D, dead organic matter; Z, zooplankton; H, horizontal; V, vertical; BGC, biogeochemical cycling; OBC, open boundary conditions; T, temperature; S, salinity; BED, Baltic Environmental Database).

	Model A–C	Model D	Model E	Model F	Model G	Model H
Resolution H	3.7 km	5.6 km	1.8–5.6 km	13 sub-basins	13 sub-basins	9.3 km
Resolution V	3 m	1.5–5 m	1.5–5 m	Variable	1–5 m	2–5 m
Sea-ice	Hibler-type	Hibler-type	Hibler-type	Parametrized	Parametrized	Hibler-type
BGC pelagic	2xN, P, 3xPHY, Z, O_2, D (DN, DP in Model C)	2xN, P, 3xPHY, Z, O_2, D	2xN, P, 3xPHY, Z, O_2, D	2xN, P, Si, 3xPHY, Z, O_2, DN, DP, DS	2xN, P, CTC, ATC, 2xPHY, O_2	2xN, P, Si, 3xPHY, Z, O_2, DN, DP, DS
BGC sediment	N, P	N, P	N, P	N, P, Si	Burial	N, P, Si
Resuspension	Explicit from waves	Explicit from waves	Explicit from waves	Implicit	Implicit	Explicit from waves
OBC T, S, nutrients	Kattegat Climatology (seasonal profiles)	Skagerrak Climatology (seasonal profiles)	Skagerrak Climatology (seasonal profiles)	Kattegat Climatology (monthly profiles)	Kattegat Climatology (constant deep water values)	Kattegat Climatology (monthly profiles)
Initial conditions	Present climate (Model A and B) Historical spinup (Model C)	Present climate	Present climate	Historical spinup	Historical spinup	Present climate (BED)

TABLE 2 | List of scenario simulations (BRM, Baltic Region Model; BSM, Baltic Sea Model; LSM, land surface model; RCM, regional climate model; GCM, global general circulation model).

No.	BRM	BSM	LSM	RCM	GCM	Emission scenario	References
1	A	RCO-SCOBI	STAT	RCAO	HadCM3	A1B	Meier et al. (2012a)
2					ECHAM5/MPI-OM-r3		
3					ECHAM5/MPI-OM-r1		
4					ECHAM5/MPI-OM-r1	A2	
5	B	RCO-SCOBI	B-HYPE	RCAO	HadCM3	A1B	Meier et al. (2012b)
6					ECHAM5/MPI-OM-r3		
7					ECHAM5/MPI-OM-r1		
8					ECHAM5/MPI-OM-r1	A2	
9	C	RCO-SCOBI	E-HYPE	RCA4-NEMO	MPI-ESM-LR	RCP 4.5	Saraiva et al. (2018), Saraiva et al., submitted manuscript
10						RCP 8.5	
11					EC-EARTH	RCP 4.5	
12						RCP 8.5	
13					IPSL-CM5A-MR	RCP 4.5	
14					HadGEM2-ES	RCP 4.5	
15						RCP 8.5	
16	D	ERGOM	STAT	RCAO	HadCM3	A1B	Neumann et al. (2012), Meier et al. (2011)
17					ECHAM5/MPI-OM-r3		
18	E	ERGOM2	Data	CCLM	ECHAM5/MPI-OM-r1	A1B	Friedland et al. (2012)
19					ECHAM5/MPI-OM-r2		
20					ECHAM5/MPI-OM-r1	B1	
21	F	BALTSEM	STAT	RCAO	HadCM3	A1B	Meier et al. (2011)
22					ECHAM5/MPI-OM-r3		
23					ECHAM5/MPI-OM-r1		
24					ECHAM5/MPI-OM-r1	A2	
25	G	PROBE-Baltic	CSIM	RCA3	ECHAM5/MPI-OM-r1	A1B (REF) and B1 (BSAP, only one) realization	Omstedt et al. (2012)
26					ECHAM5/MPI-OM-r2		
27					ECHAM5/MPI-OM-r3		
28	H	SPBEM	STAT	RCAO	HadCM3	A1B	Ryabchenko et al. (2016)
29					ECHAM5/MPI-OM-r3		

based on the Coupled Model Intercomparison Projects, CMIP3 and CMIP5, respectively. Regionalized model data from both CMIPs were analyzed together because otherwise the size of our ensemble would be too small. Knutti and Sedláček (2013) showed that the projected changes in the global patterns of air temperature and precipitation between CMIP3 and CMIP5 are remarkably similar and that the local model spread has not changed much motivating our approach to analyze both sets of scenario simulations together. Two GCMs from CMIP3, i.e., ECHAM5/MPI-OM (Jungclaus et al., 2006; Roeckner et al., 2006) and HadCM3 (Gordon et al., 2000), were used. For ECHAM5/MPI-OM three realizations (ECHAM5/MPI-OM-r1, -r2, -r3) based on the same model version but with differing initial conditions were available to study the impact of natural variability on the projections (e.g., Meier et al., 2012a). From CMIP5 four ESMs were used: MPI-ESM-LR (Block and Mauritsen, 2013; Stevens et al., 2013; https://www.mpimet.mpg.de), EC-EARTH (Hazeleger et al., 2012; https://www.knmi.nl), IPSL-CM5A-MR (Marti et al., 2010; Hourdin et al., 2013; http://icmc.ipsl.fr/) and HadGEM2-ES (Jones et al., 2011; http://www.metoffice.gov.uk). For the dynamical downscaling two uncoupled RCMs (CCLM, Rockel et al., 2008; RCA3, Samuelsson et al., 2011) and two coupled RCMs (RCAO, Döscher et al., 2002; RCA4-NEMO, Gröger et al., 2015; Wang et al., 2015) were applied.

Baltic Region Models

For climate studies in the Baltic Sea region, BSMs and LSMs of varying complexity are applied (BACC II Author Team, 2015). BSMs are either (1) process-oriented, spatially integrated (e.g., Omstedt, 2015) or (2) three-dimensional, spatially resolved ocean circulation models (e.g., Griffies, 2004). From precipitation and air temperature LSMs calculate river runoff and river-borne nutrient loads from land to sea. LSMs are statistical models with simple assumptions on related nutrient loads (e.g., Meier et al., 2012a) or process-based models that consider biogeochemical cycles in vegetation and soils (e.g., Arheimer et al., 2012). In the following, the eight BRMs of this study are introduced (see also **Tables 1**, **2**).

Model A to C: The Rossby Centre Ocean model (RCO) is a Bryan-Cox-Semtner primitive equation circulation model coupled to a Hibler-type sea-ice model with elastic-viscous-plastic rheology and open boundary conditions in the northern Kattegat (Meier et al., 2003). RCO is coupled to the Swedish Coastal and Ocean BIogeochemical model (SCOBI) describing

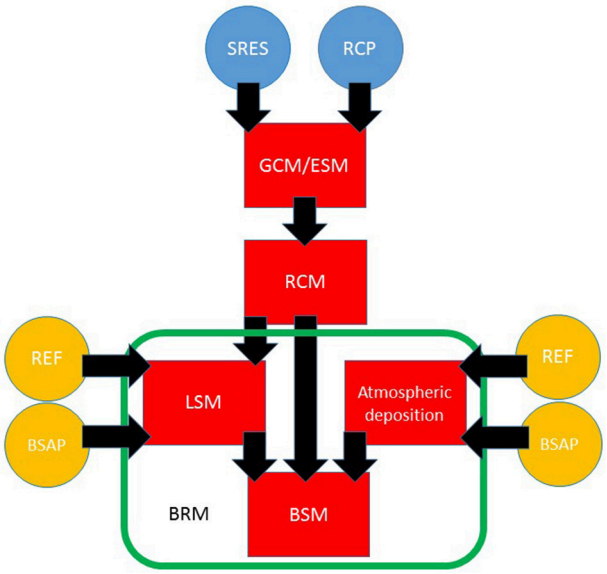


FIGURE 2 | Model hierarchy consisting of a global General Circulation Model (GCM) or Earth System Model (ESM), a Regional Climate Model (RCM), a Land Surface Model (LSM), a Baltic Sea Model (BSM) and scenarios for radiative forcing according to Representative Concentration Pathways (RCPs) or the Special Report on Emission Scenarios (SRES) and nutrient loads (Reference–REF and Baltic Sea Action Plan–BSAP). A Baltic Region Model (BRM) comprises one BSM and one LSM. For details see text.

nitrogen and phosphorus cycling in the water and sediment (Eilola et al., 2009). Boundary conditions at the sea floor are provided by a simple, vertically integrated sediment module. With the help of a simplified wave model, the combined effect of waves and current induced shear stress is considered to calculate resuspension of organic matter (Almroth-Rosell et al., 2011). The horizontal and vertical resolutions of RCO-SCOBI are about 3.7 km and 3 m, respectively. RCO-SCOBI was driven with (1) a statistical model for runoff and nutrient loads (STAT) and CMIP3 forcing (Model A, Meier et al., 2012a) and two versions of a process-based LSM, i.e., (2) B-HYPE (Arheimer et al., 2012) and CMIP3 forcing (Model B, Meier et al., 2012b), and (3) E-HYPE (Donnelly et al., 2013, 2014, 2017; Hundecha et al., 2016) and CMIP5 forcing (Model C, Saraiva et al., submitted).

Model D and E: The Ecological ReGional Ocean Model (ERGOM, see www.ergom.net) is a marine biogeochemical model coupled with an ocean general circulation model and a Hibler-type sea-ice model (MOM, Griffies, 2004). ERGOM describes the pelagic and benthic cycling of nitrogen and phosphorus with emphasis on changing redox conditions. Boundary conditions at the sea floor are provided by a simple, vertically integrated sediment module. With the help of a simplified wave model, resuspension of organic matter is calculated. The horizontal resolution of the model is about 5.6 km; the vertical resolution is 1.5 m in the upper 30 m and below that depth gradually increasing up to 5 m (Eilola et al., 2011; Neumann et al., 2012). A second model setup based on ERGOM was used ("ERGOM 2"), which has a finer horizontal resolution of 1.8 km in the southwestern Baltic Sea and 5.6 km elsewhere with a transition zone in between (Friedland et al., 2012; Schernewski et al., 2015). ERGOM and ERGOM2 were driven by the hydrological model STAT and by observed river runoff and nutrient loads from the end of the twentieth century, respectively. Both models are driven by CMIP3 regionalizations.

Model F: BALTSEM (BAltic sea Long-Term large-Scale Eutrophication Model; Savchuk, 2002; Gustafsson, 2003; Gustafsson et al., 2012; Savchuk et al., 2012) resolves the Baltic Sea spatially in 13 dynamically interconnected and horizontally averaged sub-basins with high vertical resolution, albeit morphometrically different from PROBE (see below). BALTSEM has a dynamical sea-ice model for leads (Nohr et al., 2009). Simulations were done using the NP version of the model, which describes nitrogen, phosphorus and silica cycles driven by water transports and biogeochemical fluxes. The sediment module is similar to the one used by Model C based on Savchuk (2002). Oxygen is a prognostic variable coupled to the production and remineralization of organic matter. BALTSEM scenario simulations were driven by STAT and CMIP3 forcing.

Model G: The PROBE-Baltic model is a fully coupled physical-biogeochemical model that resolves the Baltic Sea into 13 sub-basins with natural boundaries following the ecosystem-based regions and with high vertical and temporal resolutions for each sub-basin (Omstedt, 2015). The coupling of sub-basins is ensured through simplified strait flow models. The one-dimensional sea-ice model is based upon Omstedt and Nyberg (1996). The PROBE-Model system includes the carbon, nitrogen and phosphorus dynamics under both oxic and anoxic conditions (Edman and Omstedt, 2013). PROBE scenario simulations were driven by the Catchment Simulation Model, CSIM (Mörth et al., 2007; Omstedt et al., 2012), and CMIP3 forcing.

Model H: The St. Petersburg Baltic Eutrophication Model (SPBEM) is a coupled three-dimensional eco-hydrodynamic model with a modular structure. The hydrodynamic module of the model consists of models simulating the circulation patterns of the sea and sea-ice (Neelov et al., 2003; Myrberg et al., 2010). The biogeochemical module consists of pelagic and benthic models that are largely similar to BALTSEM (e.g., Savchuk, 2002). The horizontal resolution of the implemented version of SPBEM is 9.3 km; the vertical resolution is 2 m in the upper 100 m and 5 m in the lower layers (Ryabchenko et al., 2016). SPBEM scenario simulations were driven by STAT and CMIP3 forcing.

All BSMs except PROBE-Baltic are also described and compared by Tedesco et al. (2016).

Nutrient Load Scenarios

The nutrient loads of the two scenarios, REF and BSAP, differ considerably among the models both during historical and future periods, in particular for phosphorus (**Figure 3**). These differences are explained by differing assumptions on bioavailable fractions of nutrient loadings from land (Eilola et al., 2011). However, even for the same BSM the nutrient loads vary because of differing LSMs with differing historical loads and climate sensitivities. For instance, in Model C phosphorus loads are 24% larger than in Model A during the historical period. Under the

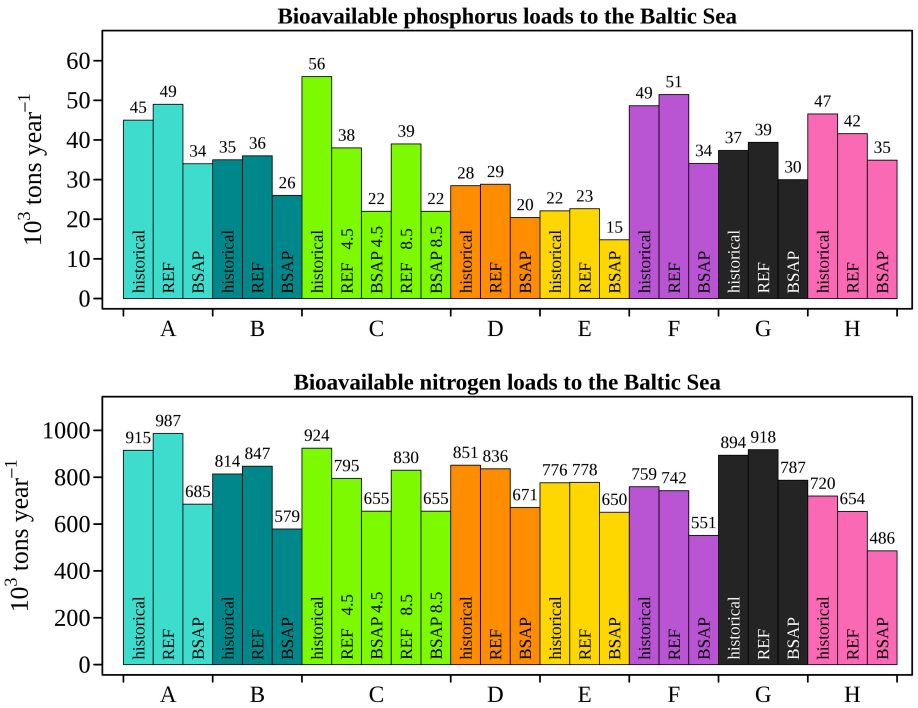


FIGURE 3 | Projected ensemble means of total (land and atmosphere) bioavailable annual nutrient loads (phosphorus–upper panel, nitrogen–lower panel) to the Baltic Sea in historical (1980–2005) and future (2072–2097) climates for the scenarios REF and BSAP. At the x-axis the scenario simulations of Model A to H are listed (with a color code as in the other figures of this study). Note that for Model C projections driven by both RCP 4.5 and RCP 8.5 are shown. Model A (RCO-SCOBI coupled to STAT), B (RCO-SCOBI coupled to B-HYPE), C (RCO-SCOBI coupled to E-HYPE), D (ERGOM coupled to STAT), E (ERGOM2 using data), F (BALTSEM coupled to STAT), G (PROBE-Baltic coupled to CSIM), and H (SPBEM coupled to STAT).

REF scenario both increasing and decreasing nutrient loads in future climate compared to the historical period are applied. In all models the BSAP scenario is characterized by lower nutrient loads compared to the historical period although the relative changes between future and historical periods differ. In some scenario simulations it is assumed that the BSAP is implemented as planned whereas in other LSMs the effects of increased runoff and changing soil processes in future climate are considered, counteracting the reduction in riverine nutrient concentrations (Meier et al., 2011). For instance, in Model A and C phosphorus loads are reduced in the BSAP scenario by 24 and 61% in the future compared to the historical period, respectively. The differences between the changes in nitrogen loads in Model A and C are smaller and the changes amount to 26 and 30%, respectively. Corresponding scenarios for the atmospheric nitrogen and phosphorus deposition are used (**Figure 3**).

Greenhouse Gas Emission Scenarios

The GHG emission scenarios differ among the scenario simulations. The concept of the GHG emission scenarios changed between CMIP3 and CMIP5. Whereas, in CMIP3 GHG emission scenarios by Nakicenovic et al. (2000), such as A1B, A2 and B1 were applied, the emissions in CMIP5 were based on Representative Concentration Pathways (RCPs) corresponding to a radiative forcing at the end of the century of 4.5 and 8.5 Wm^{-2}, respectively (Moss et al., 2010). For instance, the difference in global temperature change between A1B and A2 are significantly smaller than between RCP 4.5 and RCP 8.5 (Rogelj et al., 2012; their Figure 3). As the results of ECHAM5/MPI-OM A1B and A2 are rather similar we used just one ensemble for Model A, B, and F following Meier et al. (2011). For Model E and C we combined scenario simulations under A1B and B1 and RCP 4.5 and RCP 8.5, respectively. The impact on nutrient loads in Model C under RCP 4.5 and RCP 8.5 is illustrated in **Figure 3**. Hence, the ensemble mean changes of these models follow a mean GHG emission scenario. In case of Model G, we followed the strategy of the original study by Omstedt et al. (2012). Thus, the REF and BSAP nutrient load scenarios were combined with A1B and B1 GHG emission scenarios, respectively.

Setup of the Scenario Simulations

The 58 scenario simulations from various projects collected for this study (**Table 2**) were not coordinated. Hence, the setups of the simulations, such as initial and lateral boundary conditions, nutrient loads and bioavailable fractions differ (**Table 1**; **Figure 3**) and a model intercomparison is impossible. For the latter, model simulations with the same external forcing, initial conditions and internally used datasets, such as the bathymetry would be required (cf. Placke et al., 2018; this research topic).

All scenario simulations are transient runs that start in the time interval 1958–1975 and terminate at the end of the twenty-first century. In case of the Model C and F a spinup

was performed using reconstructed atmospheric, hydrological and nutrient load forcing since 1850 (Gustafsson et al., 2012; Meier et al., 2012c, 2018b; Schenk and Zorita, 2012). In case of Model G, even a long-term spinup since 1500 was performed (Hansson and Gustafsson, 2011). In all models at the lateral boundaries in Kattegat or Skagerrak climatological observations with differing resolution were prescribed or nudged throughout the entire simulation. In 1975 (Model C), 1961 (Model F) or 1958 (Model G) the atmospheric forcing switched from reconstructed to climate model data. Henceforth, the simulations during the historical period are called control simulations.

All projections were published in peer-reviewed literature and are *a priori* regarded as equally plausible. Nevertheless, in the assessment of this study the performance of the various control simulations was evaluated to investigate whether the quality of the control simulations and the spread of the projections are connected. The assessment was done both for each of the 29 control simulations and for the eight BRMs. The latter approach (clustering by BRMs) assumes that the largest uncertainty in biogeochemical cycling during the control period originates from process descriptions in the Baltic Sea and from the runoff and nutrient loads from land. The clustering of scenario simulations by BRMs was performed for clarity of the presentation but does not influence the main conclusions of this study. As most of the earlier studies considered at least the ensemble mean and a high-end climate scenario, the impact of climate change is considered in all BRM simulations approximately in the same way. However, we are aware that scenario simulations of the third and fourth assessment reports of the (IPCC, 2007, 2013) differ. For instance, the warming of the A1B emission scenario is in between the corresponding air temperature changes in RCP 4.5 and RCP 8.5 scenarios (Knutti and Sedláček, 2013). Nevertheless, authors of previous studies have used both A1B and RCP 4.5 as representatives of the ensemble mean (e.g., Meier et al., 2012a; Saraiva et al., 2018). Hence, we consider this choice as part of the uncertainty in Baltic Sea projections. Sources of uncertainties are not investigated here and will be studied separately.

Observations

For the model evaluation observed and simulated annual and seasonal mean profiles of temperature, salinity and oxygen, ammonium, nitrate and phosphate concentrations at the monitoring stations Anholt East (AE), Bornholm Deep (BY5), Gotland Deep (BY15), Gulf of Finland (LL07), Bothnian Sea (SR5), and Bothnian Bay (F9) were compared (**Figure 1**). The inter-annual variability of the simulated variables was not assessed. The mean profiles were calculated for the historical period. In this study, post-processed data from the Baltic Environmental Database (BED) were used (Gustafsson and Rodriguez Medina, 2011). Data are available every 5 m near the surface, every 10 m between 20 and 100 m depth, and for stations reaching even deeper data are predominantly available every 25 m. At these standard depths, observations are gathered from a depth range of one meter above and one meter below the standard depth.

In this study, the model-data comparison is restricted to abiotic natural prototypes that are rather unequivocally represented in the models. In contrast to some other formulations (e.g., Baird et al., 2013; Vichi et al., 2015; Butenschön et al., 2016), none of our models explicitly simulates the chlorophyll cell quota as a separate model variable. Meanwhile, the stoichiometric ratio between chlorophyll and other characteristics of phytoplankton biomass varies both between and within algae species in dependence on ambient environment and the recent history of populations, for instance, in the range from 20 to 100 (g C:g Chl-a) as a conservative estimate (e.g., Wasmund and Siegel, 2008; Spilling et al., 2014; Jakobsen and Markager, 2016). Within the large meridional and phenological Baltic Sea gradients, the usage of fixed conversion from biomass simulated in nitrogen or carbon units to chlorophyll concentration would introduce an unknown inherent uncertainty, thus unnecessarily compromising judgement of the model's plausibility. In addition, the models represent horizontally and vertically averaged values (of different degree depending on grid sizes) while observations are pointwise and may be affected by small-scale patchiness, which may be especially pronounced for the biological components.

Cost Function and Weighting

Two skill metrics were combined to define a cost function for the control simulations. The vertical and seasonal mean bias, $C > 0$, is the average of all $i = 1, \ldots, n$ absolute differences between model, P_i, and observation, O_i, averages at each depth and time of the year divided by the standard deviation, σ, of the observations.

$$C = \frac{\sum_{i=1}^{n} \left| \frac{P_i - O_i}{\sigma(O_i)} \right|}{n} \tag{1}$$

The Pearson correlation coefficient, $R > 0$, measures the similarity in the shape of the mean profiles, i.e., how well the simulated and observed vertical mean profiles and seasonal cycles agree.

$$R = \frac{\sum_{i=1}^{n} \left(P_i - \overline{P}\right)\left(O_i - \overline{O}\right)}{\left| \sqrt{\sum_{i=1}^{n} \left(P_i - \overline{P}\right)^2 \sum_{i=1}^{n} \left(O_i - \overline{O}\right)^2} \right|} \tag{2}$$

We tested various differing normalized cost functions, CQ, such as

$$CQ = \sqrt{\left(\left(\frac{C}{2}\right)^2 + \left(\frac{3\ (1-R)}{2}\right)^2\right)} \tag{3}$$

based on annual and seasonal means. If $R = 1$ (perfect agreement in the shape of the profiles or seasonal cycle), a mean bias of the model results smaller than two standard deviations of the observations, which is regarded as an acceptable quality according to Eilola et al. (2011), would result in a cost function $CQ < 1$. If $C = 0$ (no mean bias), a correlation coefficient of $R > 1/3$ would result in $CQ < 1$. For most variables and for all investigated monitoring stations the annual mean bias is a more restrictive skill metric than the correlation coefficient (not shown). As the outcomes for CQ do not differ much regardless of

the choice of the metric, in this study the following cost function based on annual mean variables was used:

$$CQ = \left(\frac{C}{2}\right)^2 \quad (4)$$

For C < 2 or CQ < 1, the quality was regarded as acceptable (Eilola et al., 2011). Thus, per definition model results are acceptable when the mean biases during the control period are less than two standard deviations of the observations on average. This criterion was defined as the threshold for a model simulation to be included in the weighted ensemble. Members of the ensemble with CQ > 1 were disregarded. From the cost functions weights, W_{jkl}, for each control simulation j per station k and variable l were calculated according to

$$W_{jkl} = \frac{1 - CQ_{jkl}}{\sum_{j'}(1 - CQ_{j'kl})} \quad (5)$$

Finally, for each run of Model A to H one cost function and one weight is calculated by averaging all cost functions of all stations and variables. The calculation of the combined cost functions and combined weights is done without the monitoring station Anholt East (AE) because for some of the BSMs this station is located near the model's lateral boundary.

RESULTS

Evaluation and Weighting

In the following, we discuss results of the weighted and unweighted ensemble means at Gotland Deep compared to annual or winter mean observations (**Figure 4**). After 1990, annual mean sea surface temperature (SST) observations are usually within one standard deviation of the climate model results, which is regarded as good. Note that prior to 1990 the annual mean SST calculated from observations might be biased due to missing observations. This also applies to all other variables with a pronounced seasonal cycle. Sea surface salinity (SSS) is overestimated during the historical period by several models indicating problems with the representation of the pronounced vertical gradients in the Baltic Sea. Due to spurious numerical mixing the vertical salt flux might be too large (Rennau and Burchard, 2009). In two of the simulations, SSS amounts to 12–13 g kg^{-1} instead of 7 g kg^{-1} in observations whereas the other simulations are much closer to observations (not shown). The weighted ensemble means of simulated SSS are close to observations whereas unweighted ensemble means overestimate observations considerably. Also for deep water temperature and oxygen concentration slight differences between weighted and unweighted ensemble means are found. The weighted ensemble mean deep water is warmer and more oxygenated. For all other variables, the two ensemble figures are relatively close to each other. As the pronounced decadal variations in deep water temperature and salinity, deep water oxygen concentration and surface water phosphate concentration, such as the stagnation period during 1983–1993, cannot be reproduced by climate simulations, deviations between ensemble mean model results and observations are expected. Weighted and unweighted ensemble mean deep water salinities are close to observations. Finally, there is a tendency of under- and overestimated winter mean surface dissolved inorganic nitrogen (DIN, i.e., nitrate and ammonium) and phosphorus (DIP, i.e., phosphate) concentrations, respectively.

For most simulations and monitoring stations, the values of the normalized cost function (Equations 1, 4) are lower for temperature and higher for salinity and phosphate (**Figure 5**). Further, cost functions are smaller in the southwestern and higher in the northern Baltic Sea with some exceptions, such as salinity. These results indicate smaller mean biases of the historical model results for temperature relative to salinity and phosphate and a better model representation of the southern relative to the northern Baltic Sea in accordance to Eilola et al. (2011). The horizontal and vertical stratification in the Baltic Sea is dominated by salinity gradients, which are controlled by freshwater supply from rivers, salt water inflows from the Kattegat, intrusions into the Gotland Basin and mixing while temperature gradients are predominantly controlled by air-sea fluxes. The northern Baltic Sea (in particular the Bothnian Bay) is perhaps more difficult to simulate because of, *inter alia,* the seasonal sea-ice cover and seasonal vertical stratification, a P-limited environment, a more important microbial loop, and a larger CDOM contribution limiting light conditions (e.g., Andersson et al., 2015). Recently, Fransner et al. (2018) showed that non-Redfieldian dynamics explain the seasonal pCO_2 cycle in the Bothnian Sea and Bothnian Bay. However, most biogeochemical models of the Baltic Sea are based on Redfield stoichiometry (e.g., Savchuk, 2002; Eilola et al., 2009; Neumann et al., 2012; Omstedt et al., 2012; Ryabchenko et al., 2016).

If we neglect the station in Kattegat for the following discussion, oxygen concentrations are more accurately simulated in the Bornholm Basin and Gotland Basin than in the Gulf of Finland, Bothnian Sea and Bothnian Bay (**Figure 5**). In most sub-basins and most simulations, DIN concentrations are of acceptable quality except in the Bothnian Bay. In several simulations, phosphate concentrations in the Gotland Basin, Gulf of Finland, Bothnian Sea and Bothnian Bay are biased. However, the magnitude of the cost function varies considerably among the models.

An exception is the monitoring station Anholt East (AE) in Kattegat (**Figure 5**). The poor results of some control simulations at this station (Model A and B for oxygen and Model B and C for phosphate) might indicate problems of the corresponding setups at the lateral boundaries of the model domain.

No control simulation fulfills the criterion CQ < 1 (Equation 4, mean model bias smaller than two standard deviations of the observations on average) at all stations and for all variables and there is no unambiguously best or worst model. The cost functions (**Figure 5**) and related weights (**Figure 6**) vary substantially between the variables and stations. For all variables the number of simulations considered for the calculation of the weights are much smaller in the northern than in the southern Baltic Sea (**Figure 6**). For instance, in the Bornholm Basin

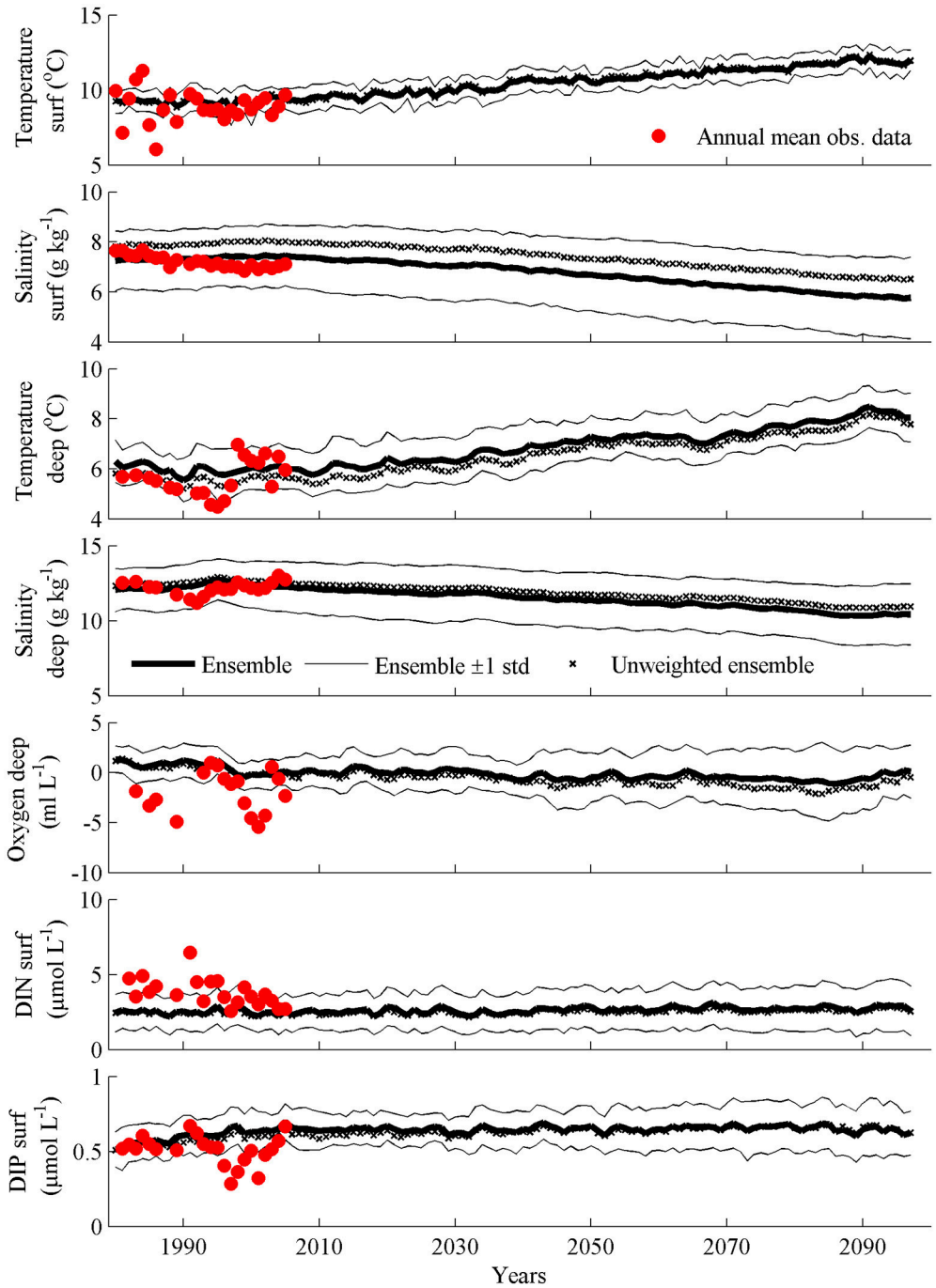


FIGURE 4 | Simulated (black lines) and observed (red circles) annual mean water temperatures (in °C) and salinities (in g kg^{-1}) at Gotland Deep in the surface (surf) and deep layer (deep), annual mean oxygen concentrations (in mL O_2 L^{-1}) in the deep layer, and winter (December-February) mean dissolved inorganic nitrogen (in mmol N m^{-3}) and phosphorus (in mmol P m^{-3}) concentrations in the surface layer. Data have been extracted from the models' top grid cell for the surface layer (surf) and for the grid cell closest to 200 m for the deep layer (deep). Shown are the weighted and unweighted ensemble means and plus/minus one standard deviations of all simulations performed with Model A to H for the period 1980–2097. In all scenario simulations, the REF nutrient load scenario is applied.

all 29 control simulations perform acceptably for temperature, oxygen, DIN and DIP concentrations. A corresponding number of simulations for salinity is 20. However, for the same variables in the Bothnian Bay we found that only 18 (temperature), 19 (salinity), 16 (oxygen concentration), 10 (DIN concentration), and 7 (phosphate concentration) simulations are of acceptable quality. For phosphate in the Bothnian Bay the 7 acceptable simulations were performed with only one BRM (Model C).

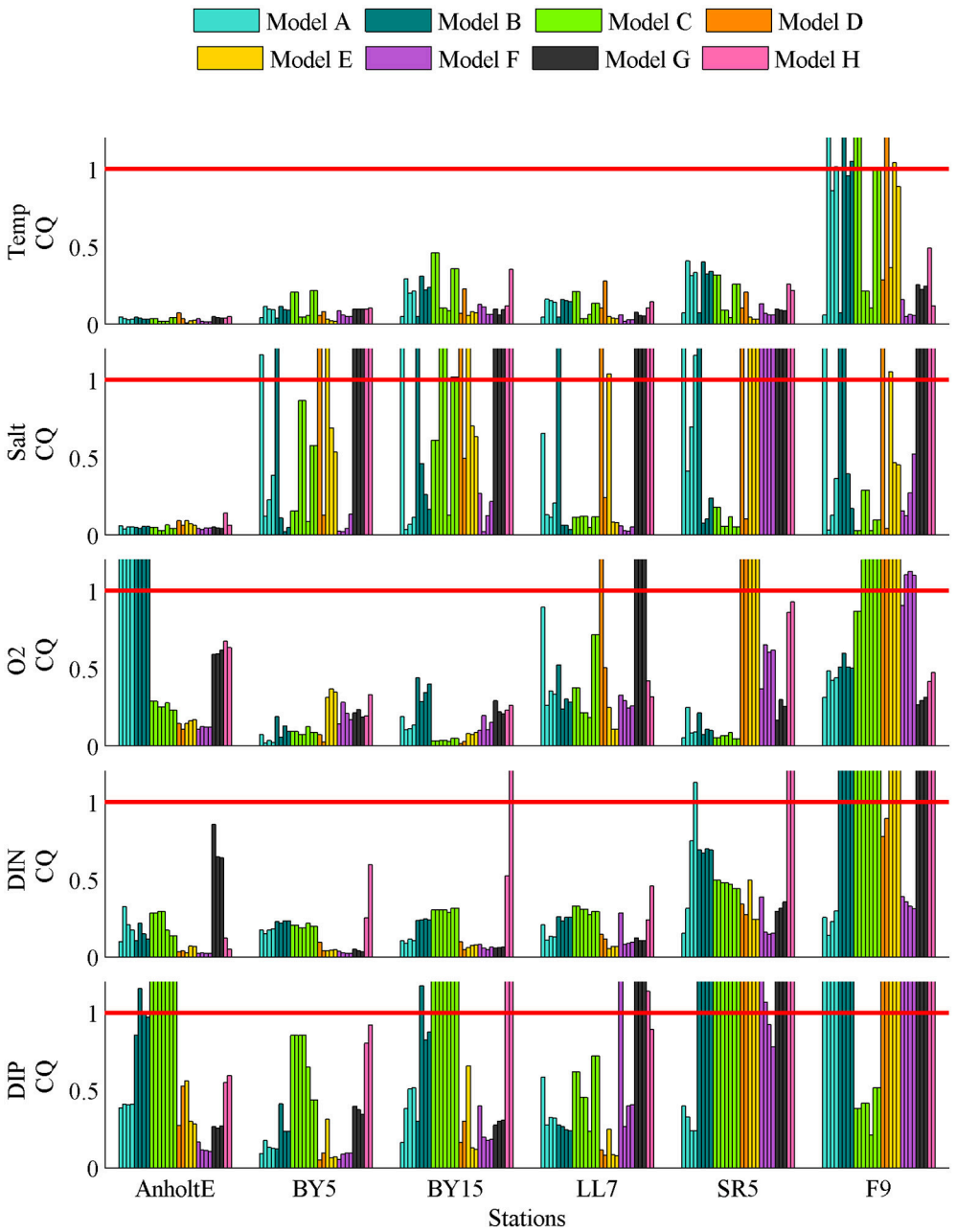


FIGURE 5 | Normalized cost function (Equation 4) for temperature, salinity, oxygen, DIN and DIP concentrations at the monitoring stations Anholt East (AE), Bornholm Deep (BY5), Gotland Deep (BY15), Gulf of Finland (LL07), Bothnian Sea (SR5), and Bothnian Bay (F9) for all scenario simulations of Model A to H during the historical period 1980–2005. Only simulations with a cost function value, *CQ*, smaller than one (red line) for all stations and all variables are considered for the weighted ensemble.

When results of the simulations are weighted for each variable independently, ensemble mean results would be rather artificial because the weighted variables are not dynamically consistent anymore. In this case, the number of simulations contributing to the weights for each variable and station would be different (**Figure 6**). Hence, for each Model A to H we combined the weights for each simulation by calculating the averages over all stations, simulations and variables. Following this strategy the combined cost function with the criterion $CQ < 1$ suggests that 17 out of 29 scenario simulations are of acceptable quality (**Figure 7**). These simulations belong to four BRMs, i.e., Model A, B, C, and F, that are of acceptable quality. Indeed, the cost functions vary considerably between the simulations. Only two out of six BSMs dominate

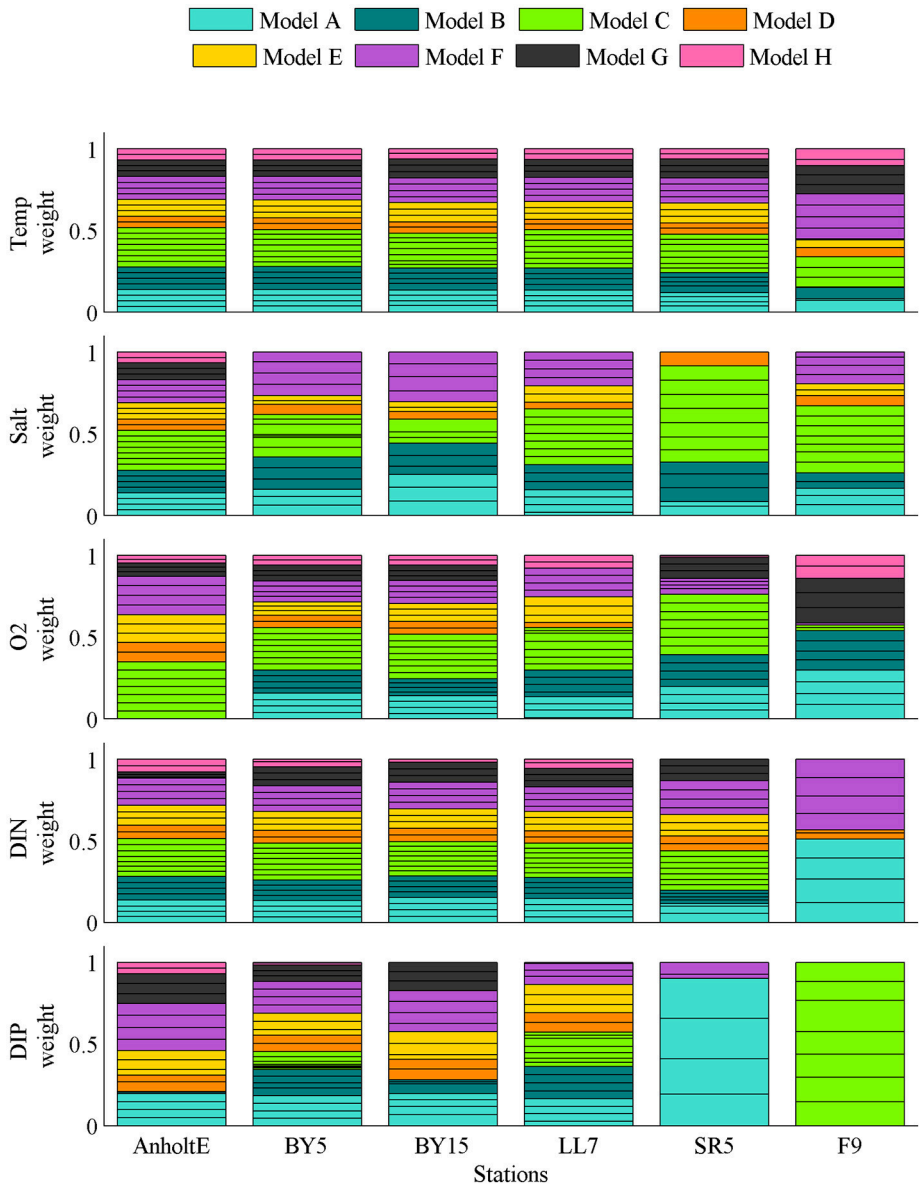


FIGURE 6 | Weights (Equation 5) for each variable, station and scenario simulation of Model A to H.

the sum of all weights and, consequently, the ensemble mean.

Projections

Figure 4 shows the ensemble mean and spread of all scenario simulations driven with various greenhouse gas emission and nutrient load scenarios at Gotland Deep to illustrate the wide range of the responses. In the unweighted and weighted ensembles projected changes at the end of the century are not necessarily larger than the biases during the historical period, i.e., the signal-to-noise ratio is relatively small (**Figure 4**). In particular, considerable differences between the means of weighted and unweighted model results for SSS are found. Nevertheless, both weighted and unweighted ensemble mean model results clearly show increased temperatures, decreased salinities, decreased deep water oxygen concentrations and increased surface water phosphate concentrations.

Figure 8 shows the weighted and unweighted ensemble mean changes between future and historical periods (including also various GHG emission scenarios) for the nutrient load scenarios REF and BSAP. Annual surface and bottom water temperatures increased by about 2–3 and 1–2°C in the weighted ensemble mean, respectively. Surface temperature changes are slightly larger in the northern than in the southern Baltic Sea because of the ice-albedo effect (Meier et al., 2012a). A contrary behavior was found for bottom temperatures with slightly smaller changes

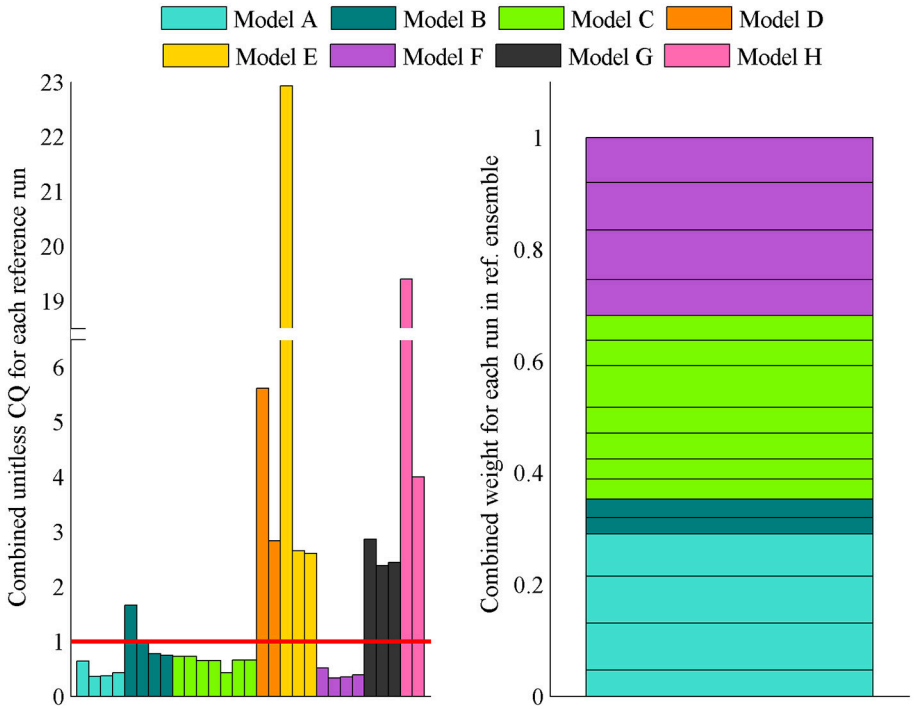


FIGURE 7 | Combined cost function calculated from all variables and stations. Shown are the results for all 29 control simulation of Model A to H.

in the northern than in the southern Baltic Sea perhaps because of warm salt water inflows from Kattegat that only affect the Baltic proper and Gulf of Finland directly (Matthäus and Franck, 1992). Annual surface and bottom salinity changes amount to about −1 to −1.5 and −1 to −2 g kg^{-1}, respectively. Salinity changes both at the surface and at the bottom are slightly smaller in the northern than in the southern Baltic Sea in accordance with results by Meier (2006) because salinity changes due to increased river runoff are smaller in case of smaller salinities (Meier and Kauker, 2003).

For annual mean deep water oxygen and winter mean surface nitrate and phosphate concentrations the weighted and unweighted ensemble mean changes depend on the nutrient load scenario (**Figure 8**). In both REF ensembles we found decreased deep water oxygen concentrations in the Baltic proper (at BY5 and BY15) perhaps reflecting (1) increased nutrient loads compared to the historical period in some of the projections (**Figure 3**), (2) increased temperature dependent stratification (**Figures 9**, **10**), and (3) the impact of warming as explained by Meier et al. (2011). However, in the Gulf of Finland (at LL07) oxygen concentrations increase and decrease in the weighted and unweighted ensembles, respectively (for an explanation see below). In BSAP oxygen concentrations increase at all stations in both ensembles due to the decreased nutrient loads.

There are slight increases in winter mean surface nitrate concentrations in both REF and BSAP except at BY5 and BY15 in case of BSAP in the weighted ensemble (**Figure 8**). In REF winter surface phosphate concentrations increase in the Baltic proper and decrease at LL07 and SR5 in the weighted ensemble. The latter decrease might be explained by smaller stratification and improved oxygen conditions in the deep water. Correspondingly, winter mean surface phosphate concentrations decrease at LL07 and SR5 in the unweighted ensemble following the changes in oxygen concentrations. In BSAP phosphate concentrations decrease at all stations in both ensembles. However, the changes at F9 are small. In summary, the changes in oxygen and phosphate concentrations qualitatively agree in the Baltic proper in the two ensembles but may differ in the northern Baltic Sea and Gulf of Finland with respect to their sign. However, the dominant impact of the BSAP on changes in biogeochemical variables compared to the changes in REF is clearly visible in both ensembles.

Further, the standard deviations of the changes of biogeochemical variables in simulations with an acceptable CQ are generally smaller than in the entire ensemble (**Figure 8**). Note, that the standard deviations of temperature and salinity changes in REF and BSAP are not identical because for Model G the REF ensemble consists of three simulations under the A1B scenario whereas the BSAP ensemble consists of only one simulation under the B1 scenario (**Table 2**).

The changes of profiles in the two ensembles of weighted and unweighted scenario simulations show some differences (**Figures 9**–**13**) but overall the responses to nutrient load changes in the Baltic proper (at BY5 and BY15, see **Figure 1**) are similar (**Figures 9**, **10**). An exception is the northern Baltic Sea, in particular in the Gulf of Finland (station LL07, **Figure 11**) and

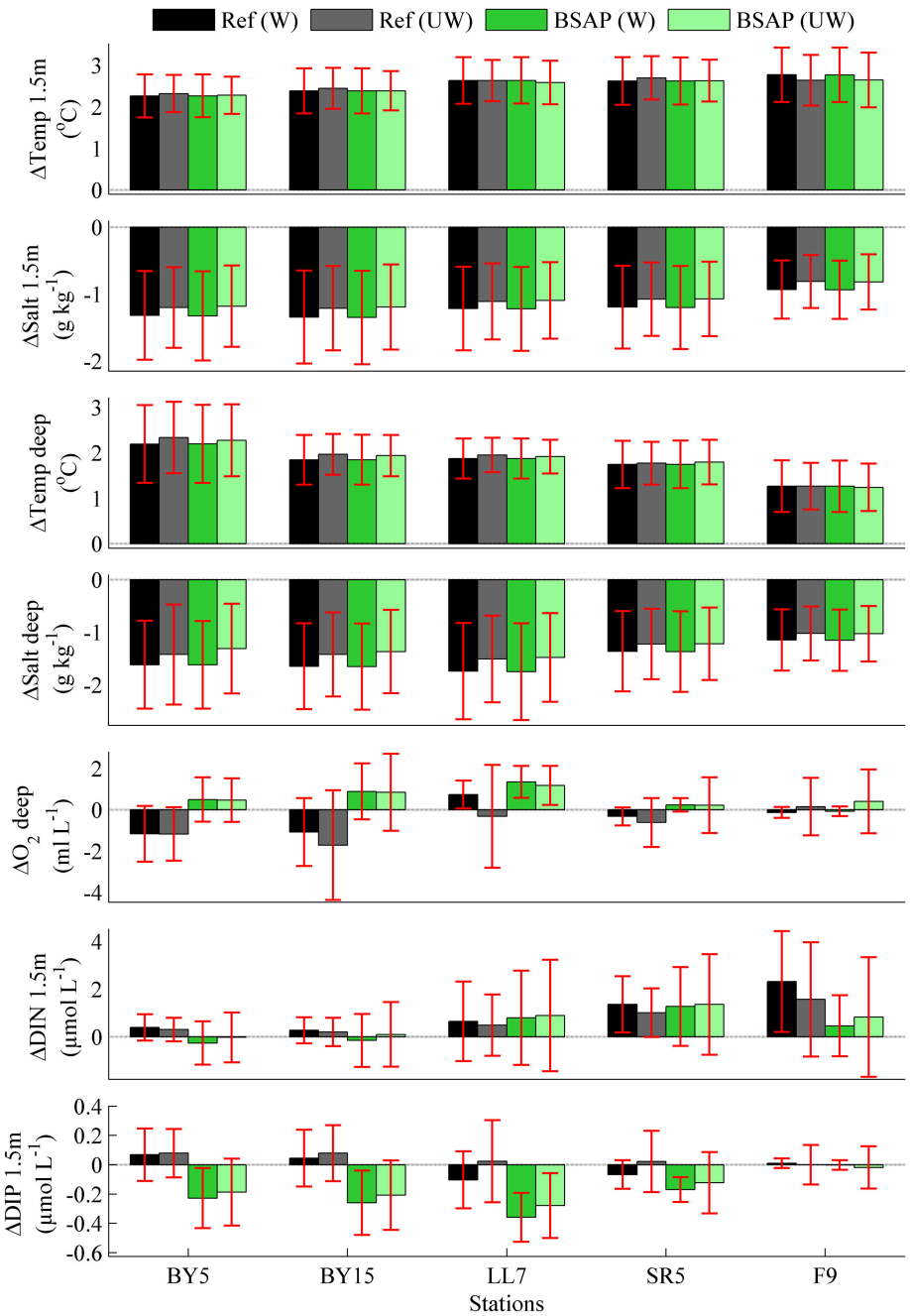


FIGURE 8 | Weighted and unweighted ensemble mean changes and standard deviations (represented by error bars) in REF and BSAP scenario simulations for temperature, salinity, oxygen, dissolved inorganic nitrogen and phosphorus concentrations at the monitoring stations BY5, BY15, LL07, SR5 and F9 at 1.5 and 200 m depth. Data have been extracted from the models' top grid cell for the surface layer (1.5 m) and for the grid cell closest to 200 m or the deepest grid cell for the deep layer (deep). "W" and "UW" refer to weighted and unweighted ensemble mean results.

Bothnian Bay (station F9, **Figure 13**), where we found larger differences between the two ensembles. The differences are relatively small for changes in temperature and salinity but larger for the biogeochemical variables (oxygen, DIN and DIP concentrations) in the deep water. Note that the spread of the changes in biogeochemical variables is larger in the deep water with larger oxygen variations than in the surface layer indicating an uncertainty in the fluxes between water column and sediment and between the surface and deep layer. For instance, in the unweighted ensemble the increase in mean oxygen concentration of the deep water at LL07 is by about 2 mL L^{-1} larger in BSAP than in REF whereas in the weighted ensemble the increase in

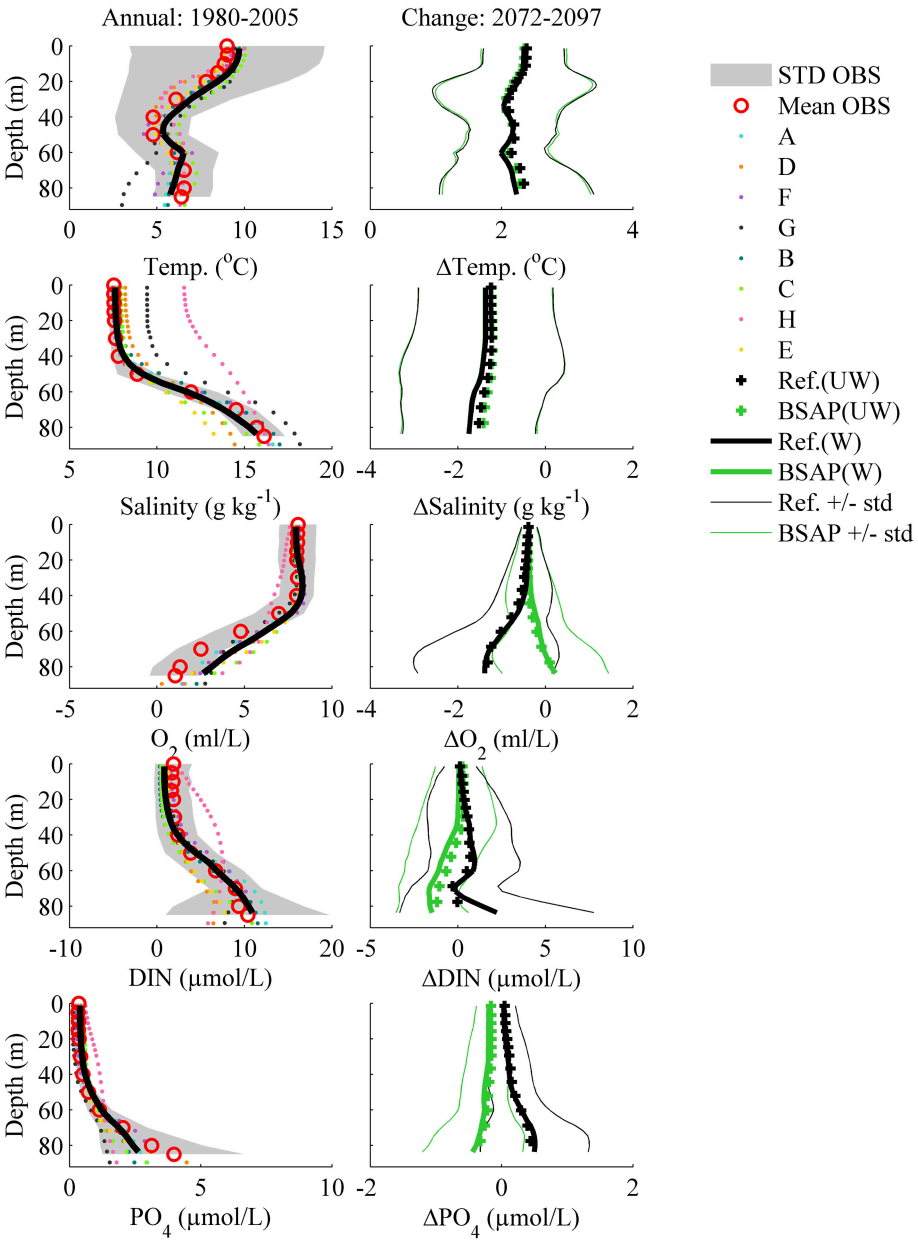


FIGURE 9 | Mean observed and simulated profiles in the control runs for each variable and each Model A to H at Bornholm Deep (BY5) for the period 1980–2005 (left panels). The ensemble mean value (thick black line) is calculated from the weighted model results. In addition, the unweighted (plus signs) and weighted (thick solid lines) ensemble mean changes and standard deviations between the future (2072–2097) and present (1980–2005) climates in REF and BSAP scenario simulations are shown (right panels). Standard deviations are calculated from the two ensembles without weighting.

oxygen concentration is much smaller. In the latter (weighted) ensemble, mean oxygen concentrations in both REF and BSAP are higher than in the unweighted ensemble with large impact on the simulated changes in biogeochemical cycles. In the Bothnian Sea (station SR5) the differences between weighted and unweighted ensembles are slightly larger than in the Baltic proper (**Figure 12**). Hence, weighting does not change the overall conclusion for the eutrophied Baltic proper (without the Gulf of Finland) whether the BSAP will work in future climates or not. However, in the northern Baltic Sea, such as the Bothnian Bay and the Gulf of Finland weighting matters.

DISCUSSION

Weighting

The weighting of model results from multi-model ensembles was investigated before (e.g., Christensen et al., 2010; Räisänen et al., 2010). The aim of weighting is to improve the estimates

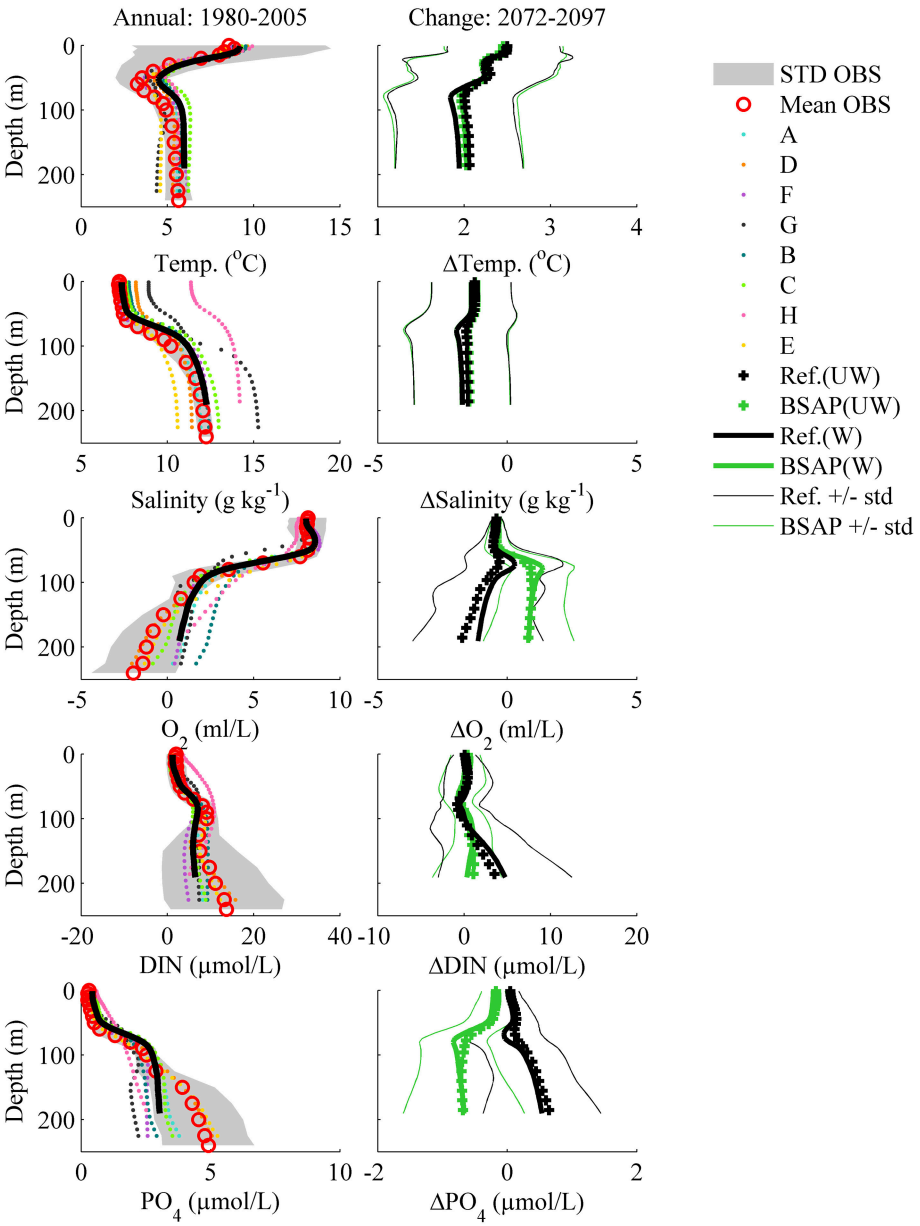


FIGURE 10 | Mean observed and simulated profiles in the control runs for each variable and each Model A to H at Gotland Deep (BY15) for the period 1980–2005 (left panels). The ensemble mean value (thick black line) is calculated from the weighted model results. In addition, the unweighted (plus signs) and weighted (thick solid lines) ensemble mean changes and standard deviations between the future (2072–2097) and present (1980–2005) climates in REF and BSAP scenario simulations are shown (right panels). Standard deviations are calculated from the two ensembles without weighting.

of climate change impacts and to reduce the ensemble spread by excluding (or giving lower weight to) ensemble members with insufficient performance in the control simulation of historical climate. Weighting assumes that there is a relationship between biases in historical climate and ensemble mean changes and their spread in future climate. Christensen et al. (2010) found that weighting adds another level of uncertainty to the generation of ensemble-based climate projections because the choice and combination of applied metrics is subjective. They concluded that there is no evidence of an improved description of mean climate states using weighted in comparison to unweighted ensembles. Räisänen et al. (2010) came to similar conclusions but found a not negligible decrease in cross-correlation error and that their method could potentially be improved.

In this study, we compared a large multi-model ensemble of scenario simulations with a subset of models with better performance than the entire ensemble. The simulated variables within the ensemble subset are dynamically

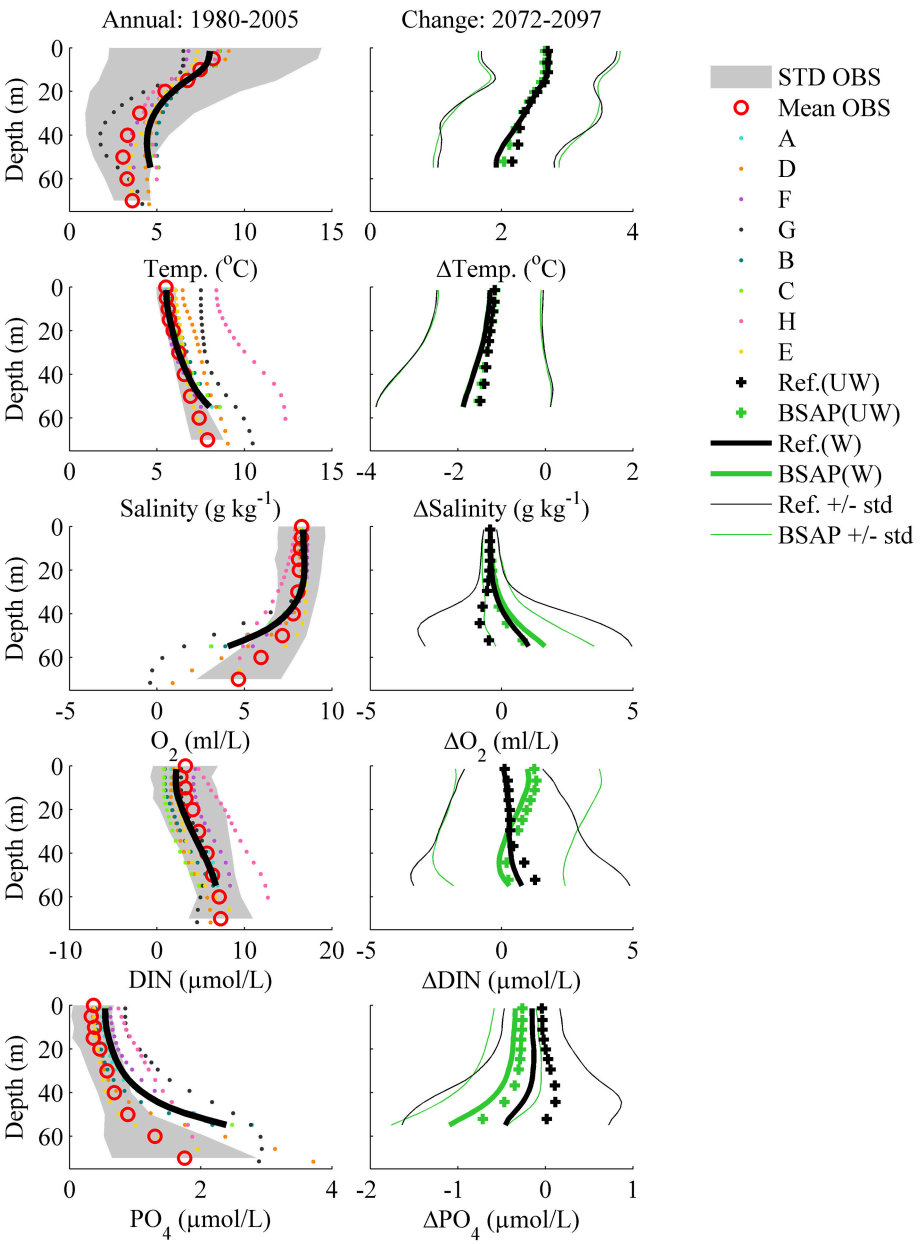


FIGURE 11 | Mean observed and simulated profiles in the control runs for each variable and each Model A to H at LL07 in the Gulf of Finland for the period 1980–2005 (left panels). The ensemble mean value (thick black line) is calculated from the weighted model results. In addition, the unweighted (plus signs) and weighted (thick solid lines) ensemble mean changes and standard deviations between the future (2072–2097) and present (1980–2005) climates in REF and BSAP scenario simulations are shown (right panels). Standard deviations are calculated from the two ensembles without weighting.

consistent because we have not weighted the variables and stations independently but calculated a combined weight per simulation.

From this procedure, we may confirm the conclusions from the earlier studies. For the REF and BSAP scenarios the ensemble mean changes in future climate projections of these two ensembles are similar for the Baltic proper (**Figures 9**, **10**) and Bothnian Sea (**Figure 12**). However, also in the sub-basins with larger discrepancies between weighted and unweighted ensembles the BSAP scenario will lead to an improved environmental status compared to REF despite the large spread in the ensembles. The results of the projections are robust with respect to the choice of the cost function or metric. However, we have only tested a limited number of metrics that measure the performance of the annual and seasonal mean states. For instance, an assessment of the frequency and intensity of extremes was not done.

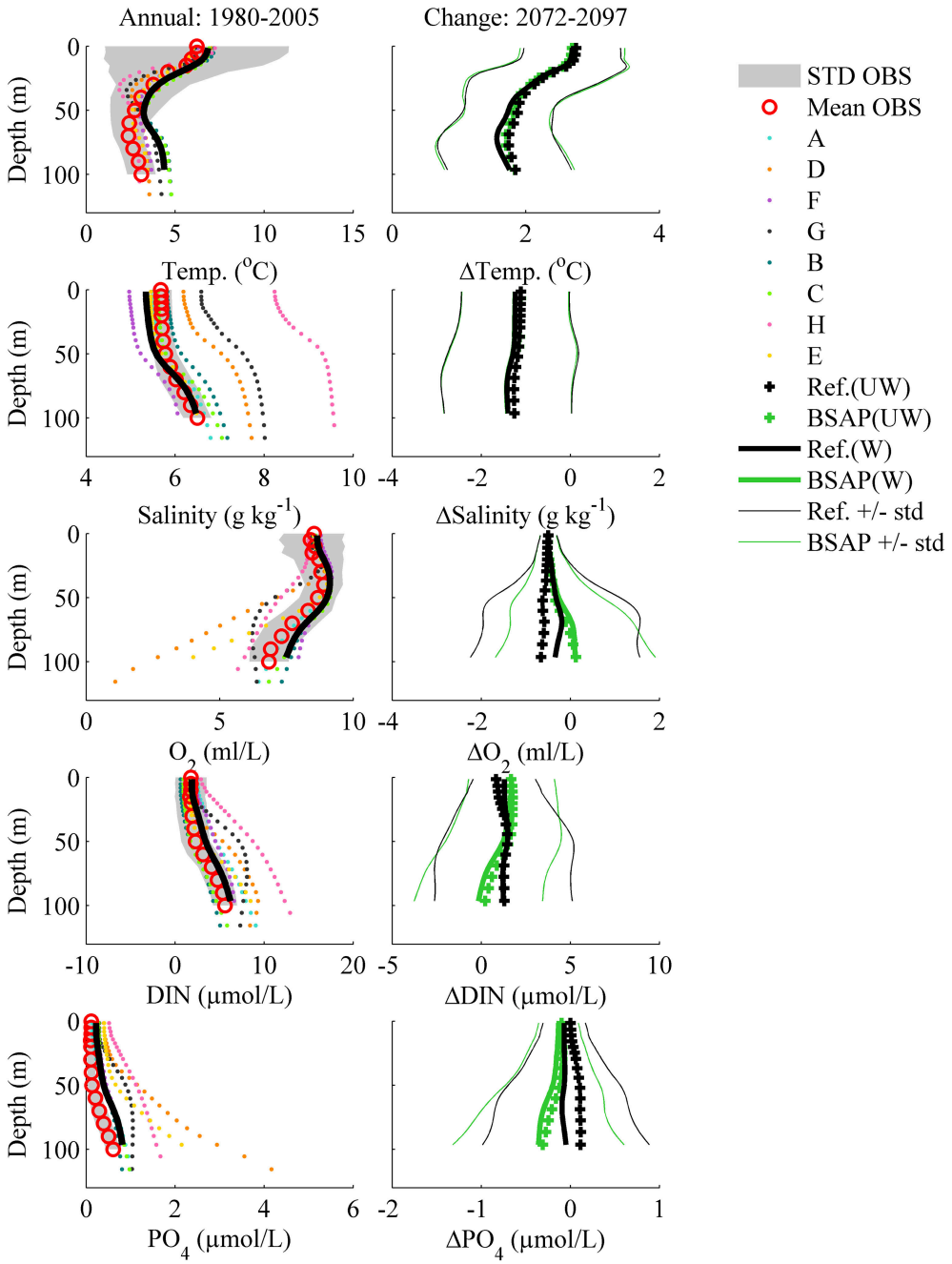


FIGURE 12 | Mean observed and simulated profiles in the control runs for each variable and each Model A to H at SR5 in the Bothnian Sea for the period 1980–2005 (left panels). The ensemble mean value (thick black line) is calculated from the weighted model results. In addition, the unweighted (plus signs) and weighted (thick solid lines) ensemble mean changes and standard deviations between the future (2072–2097) and present (1980–2005) climates in REF and BSAP scenario simulations are shown (right panels). Standard deviations are calculated from the two ensembles without weighting.

Biases and Sensitivities

The effect of weighting is to remove the impact from outlier models that do not perform well (either at stations or variables). As for many variables (except salinity and phosphate concentration), the model skills in the southern Baltic Sea are acceptable, differences between weighted and unweighted ensemble means are not expected (**Figure 5**). If the weighted and unweighted ensemble means in historical climate are close to each other, model errors will not be correlated and will compensate each other. On the other hand, stations and depths with large model biases indicate locations affected by physical or

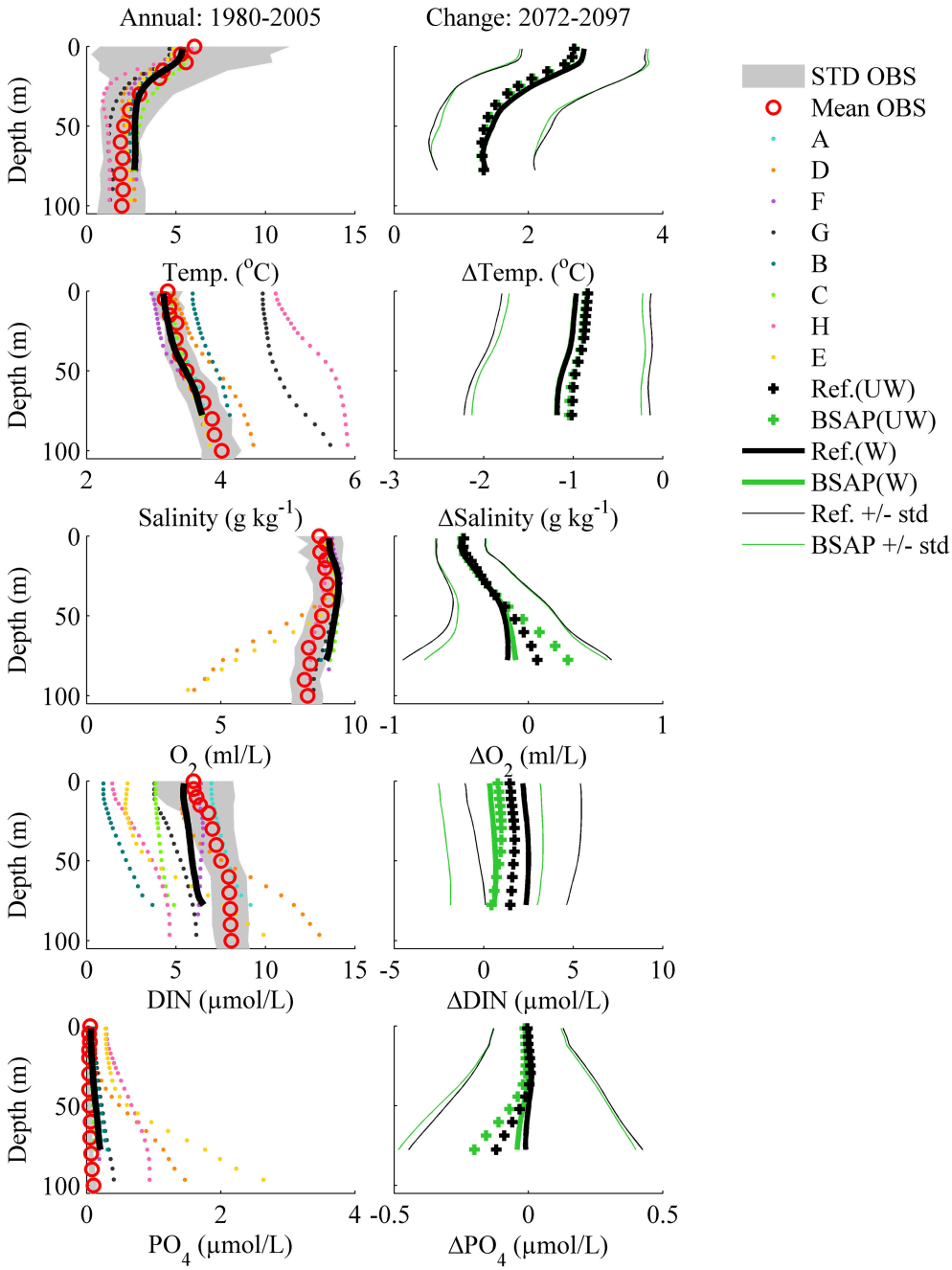


FIGURE 13 | Mean observed and simulated profiles in the control runs for each variable and each Model A to H at F9 in the Bothnian Bay for the period 1980–2005 (left panels). The ensemble mean value (thick black line) is calculated from the weighted model results. In addition, the unweighted (plus signs) and weighted (thick solid lines) ensemble mean changes and standard deviations between the future (2072–2097) and present (1980–2005) climates in REF and BSAP scenario simulations are shown (right panels). Standard deviations are calculated from the two ensembles without weighting.

biogeochemical processes that are not well-understood or not well-resolved, such as steep slopes and large gradients in hydrography.

We also found that the ensemble mean changes in weighted and unweighted ensembles differ in the northern Baltic Sea, in particular in the Gulf of Finland (**Figure 11**). This might indicate that in the northern Baltic Sea the response of biogeochemical cycles to changing climate and changing nutrient loads depends more on the mean conditions during the historical period than in the southern Baltic Sea, i.e., the system response in the northern Baltic Sea is more non-linear than in the southern Baltic Sea. If the response to changing climate and changing nutrient loads

is overwhelmingly non-linear, the differences between weighted and unweighted ensemble mean changes might be considerable.

The larger discrepancy between weighted and unweighted ensembles in the northern sub-basins might be caused by two reasons, i.e., (1) the ice-albedo feedback and (2) changes in river runoff. *Ad* (1): Due to the ice-albedo feedback small differences in the scenario simulations of the GCMs might cause large differences in the projected changes in sea-ice cover, warming of the water column, light conditions, resuspension, mixing, stratification, and primary production in the Baltic Sea (e.g., Eilola et al., 2013). *Ad* (2): In the Gulf of Finland, the sub-basin with the largest discrepancies between weighted and unweighted ensembles, increased freshwater supply will cause a weaker vertical stratification, improved oxygen conditions, changes in redox-dependent biogeochemical processes and water-sediment fluxes. The considerable spread in runoff projections (e.g., Meier et al., 2006, 2012b) may cause substantial differences in stratification and consequently in biogeochemical cycling due to changing redox conditions. For instance, the runoff changes between 2069–2098 and 1976–2005 calculated with the LSM E-HYPE driven by the regionalized ESMs MPI-ESM-LR, EC-EARTH, IPSL-CM5A-MR and HadGEM2-ES under the RCP 4.5 scenario amount to 1, 7, 21, and 14%, respectively (Saraiva et al., submitted). Corresponding figures for MPI-ESM-LR, EC-EARTH and HadGEM2-ES under RCP 8.5 are 15, 6, and 20%, respectively.

Further, the weighting method described here does not evaluate the climate sensitivity of the models. For such an evaluation much longer control simulations than those presented here for the period 1980–2005 including some trend analysis would be required driven by regionalized climate model data and evaluated with observations that do not exist. Our method may rank a model high, that may show an acceptable performance during the historical climate but may still have wrong climate sensitivity and, *vice versa*, a model with bad performance in present climate may work well in future climate. Our assumption that an acceptable performance during historical climate is a necessary condition for correct climate sensitivity cannot be verified.

Benchmarking and Quality Labeling of Projections

It should be emphasized that this study is an assessment of existing scenario simulations and not an assessment of BSMs because the identified errors might originate from the dynamical downscaling approach including BSMs, LSMs, RCMs, and GCMs/ESMs. Recently, an assessment of hindcast simulations of ocean models was performed (Placke et al., 2018; this research topic). Assessments foster model development, *inter alia,* to improve scenario simulations. However, to reduce uncertainties in scenario simulations their sources (as discussed by Meier et al., submitted manuscript; this research topic) have to be identified and possibly removed.

Estimating Uncertainties

For the estimation of uncertainties multi-model ensembles are needed. Due to limited computer resources, the number of climate projections is generally too small to access uncertainties adequately. Thus, an important question is how many members of an ensemble are really needed and whether an appropriately chosen sub-set of the ensemble may represent the uncertainty of the full ensemble (Wilcke and Bärring, 2016).

We have not addressed the differences in uncertainties between weighted and unweighted ensembles. However, a careful evaluation of all components of the model system may lead to a reduced number of ensemble members and to improved estimates of future projections. For the investigation of quality, we selected annual and seasonal mean variables. However, this choice does not guarantee more reliable climate sensitivity. To improve our approach we may evaluate also longer simulations including historical trends in eutrophication and changing climate constraining the long-term sensitivity of the models. So far, the climate sensitivity of the Baltic Sea has not been assessed thoroughly. However, recently historical reconstructions since 1850 became available that might be used, for instance together with light ship observations, for this purpose (Meier et al., 2012c, 2018a,b). However, such an evaluation of simulated past changes may not be sufficient for the evaluation of climate sensitivities that control the much larger changes in physical variables that are expected in future climate. Nevertheless, our assessment may contribute to improved credibility of scenario simulations.

CONCLUSIONS

In the present work eight differing BRMs applied in 58 transient scenario simulations representing modeling efforts in Sweden, Germany, Russia, Finland, Denmark, Poland and Estonia were assessed. This is the first time that such a large ensemble of different projections was investigated. From this study, we draw the following conclusions:

1. Differences between state-of-the-art scenario simulations for the Baltic Sea both during historical and future climates are considerable. Some models perform better than others in comparison to available monitoring data from 1980 to 2005.
2. In the eutrophied Baltic proper (excluding the Gulf of Finland) the ensemble mean changes in biogeochemical variables between REF and BSAP scenarios are similar between weighted and unweighted ensembles. Hence, weighting does not qualitatively affect ensemble mean changes. A relatively small number of models with acceptable quality compared to observations seems to be representative for the entire ensemble although more systematic research on this topic is needed. In the ensemble mean calculated from all unweighted simulations, model biases seem to compensate each other for most variables and locations. The results do not depend significantly on the choice of metric (for those that were tested).
3. Although uncertainties are large, we conclude that the rigorous implementation of the BSAP will result in improved environmental conditions despite the counteracting impact of changing climate. Hence, management questions can be answered despite considerable uncertainties.

4. Earth system modeling activities in the Baltic Sea region are intensive and of acceptable quality for some models. However, there is a strong need for regular assessments (like the pilot study presented here) that support (1) the modeling community with forcing and scenario data and with improved modeling tools and (2) marine management with improved best estimates of climate change impacts and their uncertainties.

DATA AVAILABILITY STATEMENT

Observations from the Baltic Environmental Database (BED) are publicly available from http://nest.su.se/bed. Model codes and data used for the analysis of this study are available from the authors upon request.

AUTHOR CONTRIBUTIONS

Conception and design of the assessment were discussed during two Baltic Earth workshops in Norrköping, Sweden (March 2014) and Warnemünde, Germany (November 2016) in which most of the authors participated. HM developed the idea of the study and coordinated the project. ME analyzed and visualized the ensemble simulations and compared model results to observations. MP and KE contributed with data analysis and visualization of nutrient loads. HM wrote the first draft of the manuscript and analyzed model sensitivities. KE, TN, S-EB, CD, CF, MG, BG, EG, IK, AO, BMK, VR, and OS wrote sections of the manuscript. HA, HM, ME, KE, RF, BG, AI, IK, AO, SS, and OS performed model experiments, and extracted and processed data from scenario simulations used for the analysis of this study. MK compiled relevant literature and prepared the reference list. The final version of the manuscript was edited by CF and HM. All authors contributed to manuscript revision, read and approved the submitted version.

FUNDING

The research presented in this study is part of the Baltic Earth program (Earth System Science for the Baltic Sea region, see http://www.baltic.earth) and was funded by the BONUS BalticAPP (Well-being from the Baltic Sea–applications combining natural science and economics) project which has received funding from BONUS, the joint Baltic Sea research and development programme (Art 185), funded jointly from the European Union's Seventh Programme for research, technological development and demonstration and from the Swedish Research Council for Environment, Agricultural Sciences and Spatial Planning (FORMAS, grant no. 942-2015-23). Additional support by FORMAS within the project Cyanobacteria life cycles and nitrogen fixation in historical reconstructions and future climate scenarios (1850–2100) of the Baltic Sea (grant no. 214-2013-1449) and by the Stockholm University's Strategic Marine Environmental Research Funds Baltic Ecosystem Adaptive Management (BEAM) is acknowledged. The Baltic Nest Institute is supported by the Swedish Agency for Marine and Water Management through their grant 1:11–Measures for marine and water environment. AI and VR were funded in the framework of the state assignment of FASO Russia (theme No. 0149-2018-0014). AI and VR were additionally supported by the grant 14-50-00095 of the Russian Science Foundation. The publication of this article was funded by the Open Access Fund of the Leibniz Association in Germany.

ACKNOWLEDGMENTS

The observational data used for the weighting, analysis of nutrient content and lateral boundary conditions are open access and were extracted from the Baltic Environmental Database (BED, http://nest.su.se/bed) at Stockholm University and all data providing institutes (listed at http://nest.su.se/bed/ACKNOWLE.shtml) are kindly acknowledged. BED contains observations, *inter alia*, from the national, long-term environmental monitoring programs, such as the Swedish Ocean Archive (SHARK, http://sharkweb.smhi.se) operated by the Swedish Meteorological and Hydrological Institute (SMHI) or the German Baltic Sea monitoring data archive (http://iowmeta.io-warnemuende.de) operated by the Leibniz Institute for Baltic Sea Research Warnemünde (IOW). We thank the reviewers for constructive comments that helped to improve our manuscript.

REFERENCES

Almroth-Rosell, E., Eilola, K., Hordoir, R., Meier, H. E. M., and Hall, P. O. J. (2011). Transport of fresh and resuspended particulate organic material in the Baltic Sea–a model study. *J. Mar. Syst.* 87, 1–12. doi: 10.1016/j.jmarsys.2011.02.005

Andersson, A., Meier, H. E. M., Ripszam, M., Rowe, O., Wikner, J., Haglund, P., et al. (2015). Future climate change scenarios for the Baltic Sea ecosystem and impacts for management. *Ambio* 44, 345–356. doi: 10.1007/s13280-015-0654-8

Arheimer, B., Dahné, J., and Donnelly, C. (2012). Climate change impact on riverine nutrient load and land-based remedial measures of the Baltic Sea Action Plan. *Ambio* 41, 600–612. doi: 10.1007/s13280-012-0323-0

Arneborg, L. (2016). Comment on "Influence of sea level rise on the dynamics of salt inflows in the Baltic Sea" by R. Hordoir, L. Axell, U. Löptien, H. Dietze, and I. Kuznetsov. *J. Geophys. Res.* 121, 2035–2040. doi: 10.1002/2015JC011451

BACC Author Team (2008). "Assessment of climate change for the Baltic Sea basin," in *Regional Climate Studies* (Berlin Heidelberg: Springer), 474.

BACC II Author Team (2015). "Second assessment of climate change for the Baltic Sea Basin," in *Regional Climate Studies* (Cham: Springer).

Baird, M. E., Ralph, P. J., Rizwi, F., Wild-Allen, K., and Steven, A. D. L. (2013). A dynamic model of the cellular carbon to chlorophyll ratio applied to a batch culture and a continental shelf ecosystem. *Limnol. Oceanogr.* 58, 1215–1226. doi: 10.4319/lo.2013.58.4.1215

Block, K., and Mauritsen, T. (2013). Forcing and feedback in the MPI-ESM-LR coupled model under abruptly quadrupled CO_2. *J. Adv. Model. Earth Syst.* 5, 676–691. doi: 10.1002/jame.20041

Butenschön, M., Clark, J., Aldridge, J. N., Allen, J. I., Artioli, Y., Blackford, J., et al. (2016). ERSEM 15.06: a generic model for marine biogeochemistry and the ecosystem dynamics of the lower trophic levels. *Geosci. Model Dev.* 9, 1293–1339. doi: 10.5194/gmd-9-1293-2016

Christensen, J. H., Kjellström, E., Giorgi, F., Lenderink, G., and Rummukainen, M. (2010). Weight assignment in regional climate models. *Clim. Res.* 44, 179–194. doi: 10.3354/cr00916

Donnelly, C., Arheimer, B., Capell, R., Dahné, J., and Strömqvist, J. (2013). "Regional overview of nutrient load in Europe–challenges when using a large-scale model approach, E-HYPE," in *Proceedings of H04, IAHS-IAPSO-IASPEI Assembly*, Gothenburg, Sweden (IAHS Publ. 361, 2013), 49–58.

Donnelly, C., Greuell, W., Andersson, J., Gerten, D., Pisacane, G., Roudier, P., et al. (2017). Impacts of climate change on European hydrology at 1.5, 2 and 3 degrees mean global warming above preindustrial level. *Clim. Change* 143, 13–26. doi: 10.1007/s10584-017-1971-7

Donnelly, C., Yang, W., and Dahné, J. (2014). River discharge to the Baltic Sea in a future climate. *Clim. Change* 122, 157–170. doi: 10.1007/s10584-013-0941-y

Döscher, R., Willén, U., Jones, C., Rutgersson, A., Meier, H. E. M., Hansson, U., et al. (2002). The development of the regional coupled ocean-atmosphere model RCAO. *Boreal Environ. Res.* 7, 183–192.

Edman, M., Eilola, K., Almroth-Rosell, E., Meier, H. E. M., Wåhlström, I., and Arneborg, L. (2018). Nutrient retention in the Swedish coastal zone. *Front. Mar. Sci.* 5:415. doi: 10.3389/fmars.2018.00415

Edman, M., and Omstedt, A. (2013). Modeling the dissolved CO_2 system in the redox environment of the Baltic Sea. *Limnol. Oceanogr.* 58, 74–92. doi: 10.4319/lo.2013.58.1.0074

Eilola, K., Gustafsson, B. G., Kuznetsov, I., Meier, H. E. M., Neumann, T., and Savchuk, O. P. (2011). Evaluation of biogeochemical cycles in an ensemble of three state-of-the-art numerical models of the Baltic Sea. *J. Mar. Syst.* 88, 267–284. doi: 10.1016/j.jmarsys.2011.05.004

Eilola, K., Mårtensson, S., and Meier, H. E. M. (2013). Modeling the impact of reduced sea ice cover in future climate on the Baltic Sea biogeochemistry. *Geophys. Res. Lett.* 40, 149–154. doi: 10.1029/2012GL054375

Eilola, K., Meier, H. E. M., and Almroth, E. (2009). On the dynamics of oxygen, phosphorus and cyanobacteria in the Baltic Sea; A model study. *J. Mar. Syst.* 75, 163–184. doi: 10.1016/j.jmarsys.2008.08.009

Fransner, F., Gustafsson, E., Tedesco, L., Vichi, M., Hordoir, R., Roquet, F., et al. (2018). Non-Redfieldian dynamics explain seasonal pCO_2 drawdown in the Gulf of Bothnia. *J. Geophys. Res.* 123, 166–188. doi: 10.1002/2017JC013019

Friedland, R., Neumann, T., and Schernewski, G. (2012). Climate change and the Baltic Sea action plan: Model simulations on the future of the western Baltic Sea. *J. Mar. Syst.* 105, 175–186. doi: 10.1016/j.jmarsys.2012.08.002

Gordon, C., Cooper, C., Senior, C. A., Banks, H., Gregory, J. M., Johns, T. C., et al. (2000). The simulation of SST, sea ice extents and ocean heat transports in a version of the Hadley Centre coupled model without flux adjustments. *Clim. Dyn.* 16, 147–168. doi: 10.1007/s003820050010

Gräwe, U., and Burchard, H. (2012). Storm surges in the Western Baltic Sea: the present and a possible future. *Clim. Dyn.* 39, 165–183. doi: 10.1007/s00382-011-1185-z

Gräwe, U., Friedland, R., and Burchard, H. (2013). The future of the western Baltic Sea: two possible scenarios. *Ocean Dyn.* 63, 901–921. doi: 10.1007/s10236-013-0634-0

Griffies, S. M. (2004). *Fundamentals of Ocean Climate Models*. Princeton, NJ: Princeton University Press.

Gröger, M., Dieterich, C., Meier, H. E. M., and Schimanke, S. (2015). Thermal air–sea coupling in hindcast simulations for the North Sea and Baltic Sea on the NW European shelf. *Tellus A Dyn. Meteorol. Oceanogr.* 67:26911. doi: 10.3402/tellusa.v67.26911

Gustafsson, B. G. (2003). *A Time-Dependent Coupled-Basin Model for the Baltic Sea*. Report C47, Earth Sciences Centre, Göteborg University, Göteborg.

Gustafsson, B. G., and Rodriguez Medina, M. (2011). *Validation Data Set Compiled From Baltic Environmental Database Version 2*. Baltic Nest Institute Technical Report No. 2, Stockholm University.

Gustafsson, B. G., Schenk, F., Blenckner, T., Eilola, K., Meier, H. E. M., Müller-Karulis, B., et al. (2012). Reconstructing the development of Baltic Sea eutrophication 1850–2006. *Ambio* 41, 534–548. doi: 10.1007/s13280-012-0318-x

Hansson, D., and Gustafsson, E. (2011). Salinity and hypoxia in the Baltic Sea since A.D. 1500. *J. Geophys. Res.* 116:C03027. doi: 10.1029/2010JC006676

Hazeleger, W., Wang, X., Severijns, C., Stefănescu, S., Bintanja, R., Sterl, A., et al. (2012). EC-Earth V2. 2: description and validation of a new seamless earth system prediction model. *Clim. Dyn.* 39, 2611–2629. doi: 10.1007/s00382-011-1228-5

HELCOM (2007a). *Baltic Sea Action Plan, HELCOM Ministerial Meeting 2007*, Krakow, Poland.

HELCOM (2007b). "Towards a Baltic Sea unaffected by eutrophication," in *Helcom Overview 2007, Background document for the HELCOM Ministerial Meeting* (Krakow). (Accessed November 15, 2007), 35.

HELCOM (2013a). "Approaches and methods for eutrophication target setting in the Baltic Sea region," in *Baltic Sea Environment Proceedings* (Helsinki), 133.

HELCOM (2013b). *Copenhagen Ministerial Declaration, HELCOM Ministerial Meeting*, Copenhagen, Denmark.

Hordoir, R., Axell, L., Löptien, U., Dietze, H., and Kuznetsov, I. (2015). Influence of sea level rise on the dynamics of salt inflows in the Baltic Sea. *J. Geophys. Res.* 120, 6653–6668. doi: 10.1002/2014JC010642

Hourdin, F., Foujols, M.-A., Codron, F., Guemas, V., Dufresne, J.-L., Bony, S., et al. (2013). Impact of the LMDZ atmospheric grid configuration on the climate and sensitivity of the IPSL-CM5A coupled model. *Clim. Dyn.* 40, 2167–2192. doi: 10.1007/s00382-012-1411-3

Hundecha, Y., Arheimer, B., Donnelly, C., and Pechlivanidis, I. (2016). A regional parameter estimation scheme for a pan-European multi-basin model. *J. Hydrol. Regional Stud.* 6, 90–111. doi: 10.1016/j.ejrh.2016.04.002

IPCC (2007). *The Fourth Assessment Report of the Intergovernmental Panel on Climate Change*. Geneva, Switzerland.

IPCC (2013). *Climate Change 2013–The Physical Science Basis: Working Group I Contribution to the Fifth Assessment Report of the Intergovernmental Panel on Climate Change*. Cambridge University Press.

Jakobsen, H. H., and Markager, S. (2016). Carbon-to-chlorophyll ratio for phytoplankton in temperate coastal waters: seasonal patterns and relationship to nutrients. *Limnol. Oceanogr.* 61, 1853–1868. doi: 10.1002/lno.10338

Jones, C. D., Hughes, J. K., Bellouin, N., Hardiman, S. C., Jones, G. S., Knight, J., et al. (2011). The HadGEM2-ES implementation of CMIP5 centennial simulations. *Geosci. Model. Dev.* 4, 543–570. doi: 10.5194/gmd-4-543-2011

Jungclaus, J. H., Keenlyside, N., Botzet, M., Haak, H., Luo, J.-J., Latif, M., et al. (2006). Ocean circulation and tropical variability in the coupled model ECHAM5/MPI-OM. *J. Clim.* 19, 3952–3972. doi: 10.1175/JCLI3827.1

Kahru, M., Elmgren, R., and Savchuk, O. P. (2016). Changing seasonality of the Baltic Sea. *Biogeosciences* 13, 1009–1018. doi: 10.5194/bg-13-1009-2016

Kjellström, E., Nikulin, G., Hansson, U., Strandberg, G., and Ullerstig, A. (2011). 21st century changes in the European climate: uncertainties derived from an ensemble of regional climate model simulations. *Tellus* 63, 24–40. doi: 10.1111/j.1600-0870.2010.00475.x

Knutti, R., and Sedláček, J. (2013). Robustness and uncertainties in the new CMIP5 climate model projections. *Nat. Clim. Change* 3:369. doi: 10.1038/nclimate1716

Kotilainen, A. T., Arppe, L., Dobosz, S., Jansen, E., Kabel, K., et al. (2014). Echoes from the past: a healthy Baltic Sea requires more effort. *Ambio* 43, 60–68. doi: 10.1007/s13280-013-0477-4

Leppäranta, M., and Myrberg, K. (2009). *Physical Oceanography of the Baltic Sea. Geophysical Sciences*. Berlin: Springer.

Marti, O., Braconnot, P., Dufresne, J.-L., Bellier, J., Benshila, R., Bony, S., Brockmann, P., Cadule, P., Caubel, A., Codron, F., et al. (2010). Key features of the IPSL ocean atmosphere model and its sensitivity to atmospheric resolution. *Clim. Dyn.* 34, 1–26. doi: 10.1007/s00382-009-0640-6

Matthäus, W., and Franck, H. (1992). Characteristics of major Baltic inflows–a statistical analysis. *Cont. Shelf Res.* 12, 1375–1400.

Meier, H. E. M. (2006). Baltic Sea climate in the late twenty-first century: a dynamical downscaling approach using two global models and two emission scenarios. *Clim. Dyn.* 27, 39–68. doi: 10.1007/s00382-006-0124-x

Meier, H. E. M., Andersson, H. C., Arheimer, B., Blenckner, T., Chubarenko, B., Donnelly, C., et al. (2012c). Comparing reconstructed past variations and future projections of the Baltic Sea ecosystem–first results from multi-model ensemble simulations. *Environ. Res. Lett.* 7:034005. doi: 10.1088/1748-9326/7/3/034005

Meier, H. E. M., Andersson, H. C., Arheimer, B., Donnelly, C., Eilola, K., Gustafsson, B. G., et al. (2014). Ensemble modeling of the Baltic Sea ecosystem to provide scenarios for management. *Ambio* 43, 37–48. doi: 10.1007/s13280-013-0475-6

Meier, H. E. M., Andersson, H. C., Eilola, K., Gustafsson, B. G., Kuznetsov, I., Müller-Karulis, B., et al. (2011). Hypoxia in future climates: a model ensemble study for the Baltic Sea. *Geophys. Res. Lett.* 38:L24608. doi: 10.1029/2011GL049929

Meier, H. E. M., Döscher, R., and Faxén, T. (2003). A multiprocessor coupled ice-ocean model for the Baltic Sea: application to salt inflow. *J. Geophys. Res.* 108:3273. doi: 10.1029/2000JC000521

Meier, H. E. M., Eilola, K., Almroth-Rosell, E., Schimanke, S., Kniebusch, M., Höglund, A., et al. (2018b). Disentangling the impact of nutrient load and climate changes on Baltic Sea hypoxia and eutrophication since 1850. *Clim. Dyn.* doi: 10.1007/s00382-018-4296-y

Meier, H. E. M., Höglund, A., Eilola, K., and Almroth-Rosell, E. (2017). Impact of accelerated future global mean sea level rise on hypoxia in the Baltic Sea. *Clim. Dyn.* 49, 163–172. doi: 10.1007/s00382-016-3333-y

Meier, H. E. M., Hordoir, R., Andersson, H., Dieterich, C., Eilola, K., Gustafsson, B. G., et al. (2012a). Modeling the combined impact of changing climate and changing nutrient loads on the Baltic Sea environment in an ensemble of transient simulations for 1961–2099. *Clim. Dyn.* 39, 2421–2441. doi: 10.1007/s00382-012-1339-7

Meier, H. E. M., and Kauker, F. (2003). Sensitivity of the Baltic Sea salinity to the freshwater supply. *Clim. Res.* 24, 231–242. doi: 10.3354/cr024231

Meier, H. E. M., Kjellström, E., and Graham, L. P. (2006). Estimating uncertainties of projected Baltic Sea salinity in the late 21st century. *Geophys. Res. Lett.* 33:L15705. doi: 10.1029/2006GL026488

Meier, H. E. M., Müller-Karulis, B., Andersson, H. C., Dieterich, C., Eilola, K., Gustafsson, B. G., et al. (2012b). Impact of climate change on ecological quality indicators and biogeochemical fluxes in the Baltic Sea: a multi-model ensemble study. *Ambio* 41, 558–573. doi: 10.1007/s13280-012-0320-3

Meier, H. E. M., Väli, G., Naumann, M., Eilola, K., and Frauen, C. (2018a). Recently accelerated oxygen consumption rates amplify deoxygenation in the Baltic Sea. *J. Geophys. Res.* 123, 3227–3240. doi: 10.1029/2017JC013686

Mörth, C.-M., Humborg, C., Eriksson, H., Danielsson, Å., Rodriguez Medina, M., et al. (2007). Modeling riverine nutrient transport to the Baltic Sea: a large-scale approach. *Ambio* 36, 124–133. doi: 10.1579/0044-7447(2007)36[124:MRNTTT]2.0.CO;2

Moss, R. H., Edmonds, J. A., Hibbard, K. A., Manning, M. R., Rose, S. K., Van Vuuren, D. P., et al. (2010). The next generation of scenarios for climate change research and assessment. *Nature* 463, 747–756. doi: 10.1038/nature08823

Myrberg, K., Ryabchenko, V., Isaev, A., Vankevich, R., Andrejev, O., Bendtsen, J., et al. (2010). Validation of three-dimensional hydrodynamic models of the Gulf of Finland. *Boreal Environ. Res.* 15, 453–479.

Nakicenovic, N., Alcamo, J., Grubler, A., Riahi, K., Roehrl, R., Rogner, H.-H., et al. (2000). *Special Report on Emissions Scenarios (SRES), A Special Report of Working Group III of the Intergovernmental Panel on Climate Change*. Cambridge University Press.

Neelov, I. A., Eremina, T. R., Isaev, A. V., Ryabchenko, V. A., Savchuk, O. P., and Vankevich, R. E. (2003). A simulation of the Gulf of Finland ecosystem with 3-D model. *Proc. Estonian Acad. Sci. Biol. Ecol.* 52, 346–359.

Neumann, T., Eilola, K., Gustafsson, B., Müller-Karulis, B., Kuznetsov, I., Meier, H. E. M., et al. (2012). Extremes of temperature, oxygen and blooms in the Baltic Sea in a changing climate. *Ambio* 41, 574–585. doi: 10.1007/s13280-012-0321-2

Nikulin, G., Kjellström, E., Hansson, U., Strandberg, G., and Ullerstig, A. (2011). Evaluation and future projections of temperature, precipitation and wind extremes over Europe in an ensemble of regional climate simulations. *Tellus* 63, 41–55. doi: 10.1111/j.1600-0870.2010.00466.x

Nohr, C., Björk, G., and Gustafsson, B. G. (2009). A dynamic sea ice model based on the formation direction of leads. *Cold Regions Sci. Technol.* 58, 36–46. doi: 10.1016/j.coldregions.2009.04.005

Omstedt, A. (2015). *Guide to Process Based Modeling of Lakes and Coastal Seas. Geophysical Sciences*. Berlin Heidelberg: Springer, 258.

Omstedt, A., Edman, M., Claremar, B., Frodin, P., Gustafsson, E., Humborg, C., et al. (2012). Future changes in the Baltic Sea acid–base (pH) and oxygen balances. *Tellus B Chem. Phys. Meteorol.* 64:19586. doi: 10.3402/tellusb.v64i0.19586

Omstedt, A., Elken, J., Lehmann, A., Leppäranta, M., Meier, H. E. M., Myrberg, K., et al. (2014a). Progress in physical oceanography of the Baltic Sea during the 2003–2014 period. *Progr. Oceanogr.* 128, 139–171. doi: 10.1016/j.pocean.2014.08.010

Omstedt, A., Humborg, C., Pempkowiak, J., Perttilä, M., Rutgersson, A., Schneider, B., et al. (2014b). Biogeochemical control of the coupled CO_2–O_2 system of the Baltic Sea: a review of the results of Baltic-C. *Ambio* 43, 49–59. doi: 10.1007/s13280-013-0485-4

Omstedt, A., and Nyberg, L. (1996). Response of Baltic Sea ice to seasonal, interannual forcing and climate change. *Tellus A* 48, 644–662.

O'Neill, B. C., Kriegler, E., Riahi, K., Ebi, K. L., Hallegatte, S., Carter, T. R., et al. (2014). A new scenario framework for climate change research: the concept of shared socioeconomic pathways. *Clim. Change* 122, 387–400. doi: 10.1007/s10584-013-0905-2

Placke, M., Meier, H. E. M., Gräwe, U., Neumann, T., Frauen, C., and Liu, Y. (2018). Long-term mean circulation of the Baltic Sea as represented by various ocean circulation models. *Front. Mar. Sci.* 5:287. doi: 10.3389/fmars.2018.00287

Räisänen, J., Ruokolainen, L., and Ylhäisi, J. (2010). Weighting of model results for improving best estimates of climate change. *Clim. Dyn.* 35, 407–422. doi: 10.1007/s00382-009-0659-8

Remane, A., and Schlieper, C. (1971). *Biology of Brackish Water. 2nd revised Edn.* Die Binnengewässer, Band XXV. 372 Schweizerbart'sche Verlagsbuchandlung. Stuttgart: Nägele u. Obermiller.

Rennau, H., and Burchard, H. (2009). Quantitative analysis of numerically induced mixing in a coastal model application. *Ocean Dyn.* 59, 671–687. doi: 10.1007/s10236-009-0201-x

Rockel, B., Will, A., and Hense, A. (2008). The regional climate model COSMO-CLM (CCLM). *Meteorol. Zeitschr.* 17, 347–348. doi: 10.1127/0941-2948/2008/0309

Roeckner, E., Brokopf, R., Esch, M., Giorgetta, M., Hagemann, S., and Kornblueh, L., et al. (2006). Sensitivity of simulated climate to horizontal and vertical resolution in the ECHAM5 atmosphere model. *J. Clim.* 19, 3771–3791. doi: 10.1175/JCLI3824.1

Rogelj, J., Meinshausen, M., and Knutti, R. (2012). Global warming under old and new scenarios using IPCC climate sensitivity range estimates. *Nat. Clim. Change* 2, 248–253. doi: 10.1038/nclimate1385

Ryabchenko, V., Karlin, L., Isaev, A., Vankevich, R., Eremina, T., Molchanov, M., et al. (2016). Model estimates of the eutrophication of the Baltic Sea in the contemporary and future climate. *Oceanology* 56, 36–45. doi: 10.1134/S0001437016010161

Samuelsson, P., Jones, C. G., Willén, U., Ullerstig, A., Gollvik, S., Hansson, U., et al. (2011). The Rossby Centre Regional Climate model RCA3: model description and performance. *Tellus A* 63, 4–23. doi: 10.1111/j.1600-0870.2010.00478.x

Saraiva, S., Meier, H. E. M., Andersson, H., Höglund, A., Dieterich, C., Gröger, M., et al. (2018). Baltic Sea ecosystem response to various nutrient load scenarios in present and future climates. *Clim. Dyn.* doi: 10.1007/s00382-018-4330-0

Savchuk, O. P. (2002). Nutrient biogeochemical cycles in the Gulf of Riga: scaling up field studies with a mathematical model. *J. Mar. Syst.* 32, 253–280. doi: 10.1016/S0924-7963(02)00039-8

Savchuk, O. P. (2018). Large-scale nutrient dynamics in the Baltic Sea, 1970–2016. *Front. Mar. Sci.* 5:95. doi: 10.3389/fmars.2018.00095

Savchuk, O. P., Gustafsson, B. G., and Müller-Karulis, B. (2012). *BALTSEM: A Marine Model for Decision Support Within the Baltic Sea Region*. Baltic Nest Institute Technical Report No. 7, 55pp.

Schenk, F., and Zorita, E. (2012). Reconstruction of high resolution atmospheric fields for Northern Europe using analog-upscaling. *Clim. Past* 8:1681. doi: 10.5194/cp-8-1681-2012

Schernewski, G., Friedland, R., Carstens, M., Hirt, U., Leujak, W., Nausch, G., et al. (2015). Implementation of European marine policy: New water quality targets for German Baltic waters. *Mar. Policy* 51, 305–321. doi: 10.1016/j.marpol.2014.09.002

Schimanke, S., Dieterich, C., and Meier, H. E. M. (2014). An algorithm based on sea-level pressure fluctuations to identify major Baltic inflow events. *Tellus A Dyn. Meteorol. Oceanogr.* 66:23452. doi: 10.3402/tellusa.v66.23452

Schneider, B., Dellwig, O., Kulinski, K., Omstedt, A., Pollehne, F., Rehder, G., et al. (2017). "Biogeochemical cycles," in *Biological Oceanography of the Baltic Sea*, eds P. Snoeijs-Leijonmalm, H. Schubert, and T. Radziejewska (Netherlands: Springer), 87–122.

Skogen, M. D., Eilola, K., Hansen, J. L., Meier, H. E. M., Molchanov, M. S., and Ryabchenko, V. A. (2014). Eutrophication status of the North Sea, Skagerrak, Kattegat and the Baltic Sea in present and future climates: a model study. *J. Mar. Syst.* 132, 174–184. doi: 10.1016/j.jmarsys.2014.02.004

Snoeijs-Leijonmalm, P., and Andrén, E. (2017). "Why is the Baltic Sea so special to live in?" in *Biological Oceanography of the Baltic Sea*, eds P. Snoeijs-Leijonmalm, H. Schubert, and T. Radziejewska (Netherlands: Springer), 23–84.

Spilling, K., Kremp, A., Klais, R., Olli, K., and Tamminen, T. (2014). Spring bloom community change modifies carbon pathways and C:N:P: Chl *a* stoichiometry of coastal material fluxes. *Biogeosciences* 11, 7275–7289. doi: 10.5194/bg-11-7275-2014

Stevens, B., Giorgetta, M., Esch, M., Mauritsen, T., Crueger, T., Rast, S., et al. (2013). Atmospheric component of the MPI-M Earth System Model: ECHAM6. *J. Adv. Model. Earth Syst.* 5, 146–172. doi: 10.1002/jame.20015

Stigebrandt, A. (2001). "Physical oceanography of the Baltic Sea," in *A Systems Analysis of the Baltic Sea*, eds. F. V. Wulff, L. Rahm, and P. Larsson (Berlin Heidelberg: Ecological Studies, Springer), 353–372.

Tedesco, L., Piroddi, C., Kämäri, M., and Lynam, C. (2016). Capabilities of Baltic Sea models to assess environmental status for marine biodiversity. *Mar. Policy* 70, 1–12. doi: 10.1016/j.marpol.2016.04.021

Vichi, M., Lovato, T., Lazzari, P., Cossarini, G., Gutierrez Mlot, E., Mattia, G., et al. (2015). *The Biogeochemical Flux Model (BFM): Equation Description and User Manual. BFM Version 5.1*. BFM Report series N. 1. Available online at: http://bfm-community.eu, 104.

Vuorinen, I., Hänninen, J., Rajasilta, M., Laine, P., Eklund, J., Montesino-Pouzols, F., et al. (2015). Scenario simulations of future salinity and ecological consequences in the Baltic Sea and adjacent North Sea areas–implications for environmental monitoring. *Ecol. Indic.* 50, 196–205. doi: 10.1016/j.ecolind.2014.10.019

Wang, S., Dieterich, C., Döscher, R., Höglund, A., Hordoir, R., Meier, H. E. M., et al. (2015). Development and evaluation of a new regional coupled atmosphere–ocean model in the North Sea and Baltic Sea. *Tellus A Dyn. Meteorol. Oceanogr.* 67:24284. doi: 10.3402/tellusa.v67.24284

Wasmund, N., and Siegel, H. (2008). "Phytoplankton," in *State and Evolution of the Baltic Sea, 1952–2005*, eds R. Feistel, G. Nausch, and N. Wasmund (Hoboken, NJ: Wiley), 441–481.

Wilcke, R. A. I., and Bärring, L. (2016). Selecting regional climate scenarios for impact modelling studies. *Environ. Model. Softw.* 78(Supplement C), 191–201. doi: 10.1016/j.envsoft.2016.01.002

Wulff, F., Rahm, L., and Larsson, P. (eds.). (2001). "A systems analysis of the Baltic Sea," in *Ecological Studies*, Vol. 148 (Berlin; Heidelberg: Springer), 457.

Conflict of Interest Statement: The authors declare that the research was conducted in the absence of any commercial or financial relationships that could be construed as a potential conflict of interest.

Copyright © 2018 Meier, Edman, Eilola, Placke, Neumann, Andersson, Brunnabend, Dieterich, Frauen, Friedland, Gröger, Gustafsson, Gustafsson, Isaev, Kniebusch, Kuznetsov, Müller-Karulis, Omstedt, Ryabchenko, Saraiva and Savchuk. This is an open-access article distributed under the terms of the Creative Commons Attribution License (CC BY). The use, distribution or reproduction in other forums is permitted, provided the original author(s) and the copyright owner(s) are credited and that the original publication in this journal is cited, in accordance with accepted academic practice. No use, distribution or reproduction is permitted which does not comply with these terms.

frontiers in Marine Science

ORIGINAL RESEARCH
published: 22 October 2018
doi: 10.3389/fmars.2018.00384

Major Baltic Inflow Statistics – Revised

*Volker Mohrholz**

Department of Physical Oceanography and Instrumentation, Leibniz Institute for Baltic Sea Research Warnemünde, Warnemünde, Germany

Major Baltic inflow events (MBI) transport large amounts of saline water into the Baltic. They are the solely source for deep water ventilation in the central Baltic basins, and control to a large extent the environmental conditions below the permanent halocline. Available series of MBI frequency and intensity depict strong decrease of MBI frequency after the 1980s, followed by long lasting stagnation periods in the central Baltic basins. However, the expected decrease in mean salinity of the Baltic was not observed. Also the frequency of large volume changes of the Baltic has not changed, and recent model studies predict a slight increase of MBI frequency with warming climate. Using long term data series of sea level, river discharge, and salinity from the Belt Sea and the Sound a continuous series of barotropic inflows was reconstructed for the period from 1887 till present. A comparison with the MBI series of Fischer and Matthäus (1996) revealed significant differences in the period since the 1980s. The reasons for the deviations are mainly the lack of appropriate data between 1976 and 1991, and the change in observation methods afterward, which caused a bias in the inflow statistics. In contrast to earlier investigations the revised MBI series depicts no significant long term trend in MBI frequency and intensity, contradicting the hypothesis that climate change caused a decreasing MBI frequency. There exists a decadal variability of MBI with a main period of 25–30 years. Periods with reduced MBI frequency were identified. The revised MBI series was proved with observations of dissolved oxygen and salinity in the bottom layer of the Bornholm basin. Until today climate change has no obvious impact on the MBI related oxygen supply to the central Baltic Sea. The increased eutrophication during the last century is most probably the main driver for temporal and spatial spreading of suboxic and anoxic conditions in the deep layer of the Baltic Sea.

Keywords: Baltic Sea, water exchange, Major Baltic inflow, estuarine circulation, climate variability, oxygen minimum zone

OPEN ACCESS

Edited by:
Laura Tuomi,
Finnish Meteorological Institute, Finland

Reviewed by:
Jüri Elken,
Tallinn University of Technology, Estonia
Andreas Lehmann,
Helmholtz-Gemeinschaft Deutscher Forschungszentren (HZ), Germany

***Correspondence:**
Volker Mohrholz
volker.mohrholz@io-warnemuende.de

Specialty section:
This article was submitted to Coastal Ocean Processes, a section of the journal Frontiers in Marine Science

Received: *22 April 2018*
Accepted: *28 September 2018*
Published: *22 October 2018*

Citation:
Mohrholz V (2018) Major Baltic Inflow Statistics – Revised. Front. Mar. Sci. 5:384. doi: 10.3389/fmars.2018.00384

INTRODUCTION

Expanding oxygen minimum zones (OMZ) in coastal and marginal seas as well as in the tropical oceans are often discussed as indicators of ongoing climate change (Stramma et al., 2008; Kabel et al., 2012). Among the multiple drivers of OMZ advection and renewal of water below the mixed layer is crucial for the oxygen budget in the OMZ (Conley et al., 2009; Fischer et al., 2013; Neumann et al., 2017). In the Baltic Sea a strong reduction of so called Major Baltic Inflows (MBI) was observed in the early 1980s, leading to a decline of deep water renewal

(Fischer and Matthäus, 1996). Concurrently the OMZ increased in the central Baltic (Carstensen et al., 2014; Feistel et al., 2016). The relation between climate change, alteration of barotropic water exchange with the North Sea, and expanding anoxic areas in the central Baltic has been studied intensively (e.g., Meier et al., 2011; BACC II Author Team, 2015; Lehmann et al., 2017). Still, there is no clear mechanism found that describes how climate driven changes in the atmospheric circulation may cause the observed reduction of MBI frequency.

Large fresh water surplus and a very limited water exchange with the North Sea maintain the brackish water conditions in the Baltic Sea (HELCOM, 1986). High river discharges in the eastern and northern part and the inflow of high saline water through the Danish Straits establish an estuarine like overturn circulation (Meier et al., 2006). The inflowing dense saline water spreads into the deep layers and causes a strong vertical salinity gradient in the central Baltic with a pronounced halocline at about 60–80 m depth. The inflow of saline water is balanced by upwelling, diapycnal mixing and the outflow of brackish water in the surface layer. Strong stratification at the halocline limits vertical ventilation from the surface to the top mixed layer. Thus, the solely source of deep water renewal and ventilation of the Baltic Sea is the lateral advection of oxygen rich, high saline water.

The water exchange with the North Sea is hampered by the shallow and narrow connections, the Belt Sea and the Sound. The limiting cross sections are the Darss Sill in the Belt Sea and the Drogden Sill in the Sound (**Figure 1**), with sill depth of 19 m and 8 m, and cross section areas of 612 500 m^2 and 52 750 m^2, respectively. The flow through these channels is driven by barotropic and baroclinic pressure gradients in the transition area of the Baltic and the North Sea (Lass et al., 1987; Lass, 1988; Feistel et al., 2006). Accordingly, inflow events are divided in barotropic and baroclinic inflows. The latter are driven by the salinity gradient between the Baltic and the North Sea, and occur mainly with calm summer conditions. During the rest of the year the barotropic forcing exceeds the baroclinic forcing considerably. Wind forcing and air pressure differences establish sea level differences between the Kattegat and the western Baltic, which drive barotropic inflow events. To have a significant impact on the deep water conditions in the central Baltic an inflow event must transport large amounts of saline and well oxygenated water into the western Baltic. These events are usually considered as Major Baltic Inflow.

After a long lasting stagnation period an extreme MBI was observed in December 2014 (Mohrholz et al., 2015). It was accompanied by a group of medium size inflows before and after the main inflow event (Naumann et al., 2016). The inflowing saline and oxygen rich water reached the central Baltic OMZ and turned the former anoxic deep water to oxic conditions. However, the ventilation effect was of shorter duration than expected, due to observations made after MBIs of recent decades (Neumann et al., 2017). This fact initiated a revision of the MBI contribution to the oxygen supply for the deep basins of the central Baltic. Surprisingly, the review of the existing time series of MBI frequency revealed strong evidence that the MBI time series established by Fischer and Matthäus (1996; referred to as FM96) is biased. There are four major issues contradicting a significant reduction of MBI frequency during the recent decades:

1. The mean salinity of the Baltic depicts no long term trend, although the number and intensity of MBI has strongly dropped since the early 1980s (Matthäus et al., 2006).
2. Since the early 1980s the FM96 MBI time series depict a significant lack of minor MBI's, which should be the most frequent MBI group. This pointed to a bias in the MBI detection method.
3. There exists a mismatch between the MBI frequency in FM96 and the large volume change events (LVC) derived from mean sea level changes of the Baltic (Lehmann and Post, 2015; Lehmann et al., 2017).
4. And recent studies with "state of the art" numerical models predict a slightly increasing MBI frequency with warming climate and rising sea level in the transition zone between the Baltic and North Sea (Schimanke et al., 2014; Hordoir et al., 2015).

Definitions of MBI were provided by Wolf (1972); Franck et al. (1987), and most recently Fischer and Matthäus (1996). The detection of MBI based mainly on available long term salinity time series gathered in the Belt Sea and the Sound by Danish light ships. The barotropic inflow events were classified using a combination of empirical thresholds for the vertical salinity gradient, bottom salinity and duration time of inflow conditions (for details refer to the cited literature). The weak point of these definitions is the lack of a direct link to water transports, since current measurements were only occasionally available. Thus, Lehmann and Post (2015) invented the concept of "Large Volume Changes" to derive the intensity of inflow events from the related change in total water volume of the Baltic. They found a significant difference between MBI and LVC frequency, especially since the late 1980s, and attributed the decreasing MBI frequency to a negative trend in eastern types of atmospheric circulation with a concurrent increase in western circulation types (according Jenkinson and Collison, 1977). However, Rutgersson et al. (2014) did not found robust long term trends in wind forcing and precipitation in the Baltic Sea area, despite a pronounced interannual variability. Also Schimanke et al. (2014) have shown that the probability of typical meteorological forcing conditions for MBI has not changed. Only the period between 1983 and 1993 depict a lack of MBI favoring meteorological forcing conditions.

The exceptional MBI in December 2014 provided the possibility to compare different approaches for estimation of inflow volume and salt amount. Mohrholz et al. (2015) used direct salinity and current measurements at the Darss Sill, the total volume change of the Baltic and a hydrodynamic model for independent estimates of inflow intensity. Within their uncertainty limits all methods showed comparable results. Also the FM96 MBI definition was applied to two different time series in the Belt Sea (Gedser Rev and Darss Sill). The results revealed a high sensitivity of derived FM96 MBI intensity from the location of times series measurements, and provided the first hint for a reason of the supposed bias in the FM96 MBI series.

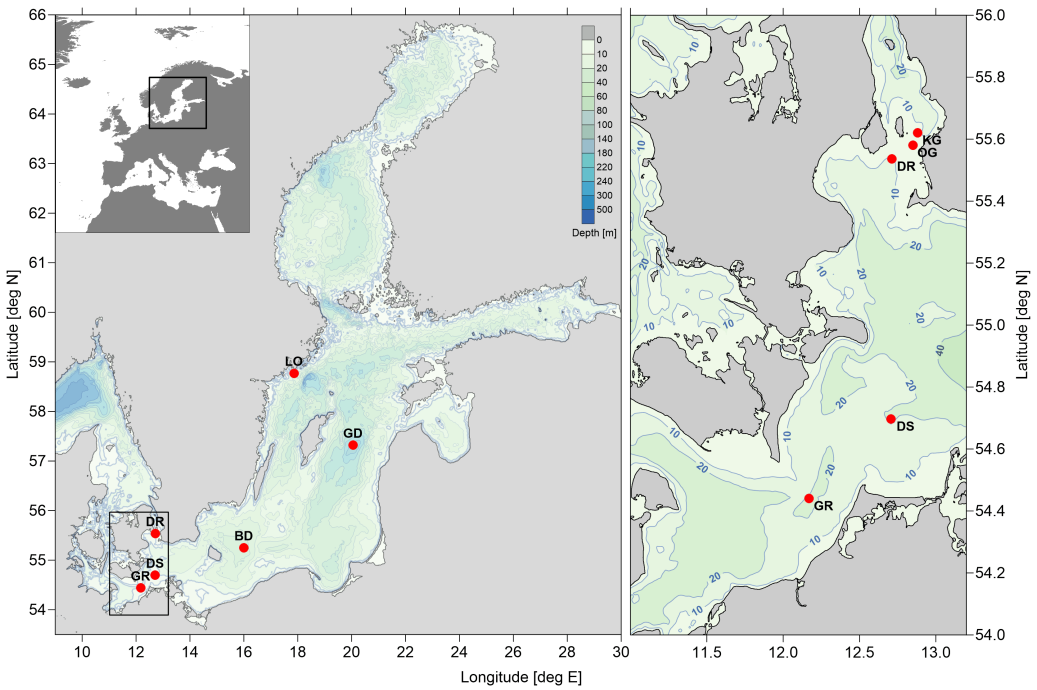


FIGURE 1 | Topography of the Baltic Sea and the location of the time series stations used in this study. Gedser Rev (GR), Darss Sill (DS), Drogden Sill (DR), Oskarsgrundet (OG), Kalksgrundet (KG), Bornholm Deep (BD), Gotland Deep (GD), Landsort (LO).

The overall objective of this study is to establish an improved continuous MBI time series for the period from 1887 till present, based on the available long term observations. The gaps of the FM96 time series for the World War I and II will be filled, and the long term trends in the frequency of barotropic inflows are investigated. The paper will supply also a critical review of the inflow frequency and strength during the recent 120 years, and deals with the problem of current MBI definition.

MATERIALS AND METHODS

Volume Transport

Intense barotropic inflow events cause a rapid increase of the total water volume V of the Baltic. Thus, the water budget of the Baltic can be used to calculate the inflow volume of saline water from the North Sea. The temporal change of the total water volume V depends on river runoff R, evaporation E, precipitation P, and the volume flow through the Danish Straits Q.

$$\frac{\partial V}{\partial t} = Q + R + E + P \tag{1}$$

Using the mean sea level η and the surface area A of the Baltic east of the Danish Straits the volume transport Q through the Danish Straits is:

$$Q(t) = \frac{1}{A}\frac{\partial}{\partial t}\eta(t) - R(t) - E - P \tag{2}$$

Evaporation and precipitation approximately balance each other (HELCOM, 1986). The climatological value of mean precipitation minus evaporation surplus is considered with a constant value of 39.7 km^3a^{-1}, neglecting the small temporal variability of this fresh water flux.

Mean Sea Level

The calculation of volume transport through the Danish straits requires consistent time series of mean Baltic Sea level and river runoff to the Baltic. The time series for the mean sea level of the Baltic was derived from observations at Landsort and Landsort Norra, published by the SMHI Opendata server (SMHI, 2018b). The station Landsort is the best representation of the mean sea level of the Baltic, well proved by several studies (Lisitzin, 1974; Jacobsen, 1980; Franck and Matthäus, 1992; Feistel et al., 2008). The station is located in the central Baltic near the knot line of the first barotropic basin mode (Wübber and Krauss, 1979; Jönsson et al., 2008). Hourly sea level data are available from November 1886 to September 2006 for the station Landsort (17.87°E 58.74°N) and from October 2004 onward for the station Landsort Norra (17.86°E 58.77°N). Both time series were detrended to remove the long term signal of eustatic and isostatic land lift. The overlapping range from October 2004 to September 2006 was used to fit both data sets to each other. The standard deviation of remaining differences between both stations was 2.04 cm for the hourly data. In the overlapping range the constructed sea level time series consist- of hourly mean values of detrended sea level data combined from both stations.

Local wind forcing on time scales up to some days are accountable for occasional strong sea level changes in the low pass filtered time series. To remove this interfering signal a threshold

filter was applied, which sets a limit for the maximum sea level change per day. The shallow and narrow Danish straits depict a limited transport capacity and act as a low pass filter for the total volume change per time (Lass, 1988). For a given sea level difference $\Delta\eta_s$ between the Kattegat and the western Baltic the transport Q can be estimated with a quadratic frictional law (Jacobsen, 1980; Omstedt, 1987).

$$Q = \sqrt{\frac{\Delta\eta_s - B}{K_f}} \tag{3}$$

Where K_f is the empirical friction coefficient for the Belt Sea or the Sound, and B is a correction offset for the sea level difference, due to the baroclinic pressure gradient along the channel. The value of B is typically in the order of some centimeters. The uncertainty of this transport estimate is about 10% (Mattsson, 1996). The bottom limits of K_f are $1.6 \cdot 10^{-10}$ s^2m^{-5} and $2 \cdot 10^{-11}$ s^2m^{-5} for the Sound and the Belt sea, respectively (Jakobsen et al., 1997, 2010). The sea level difference between the Kattegat and the western Baltic exceeds seldom 100 cm (Hela, 1944). The maximum observed sea level difference between the stations Gedser and Hornbaek since 1900 till present was 280 cm. Using the limits for K_f and a maximum sea level difference $\Delta\eta_s$ of 300 cm the top limit of transport through the Danish straits is about 45 km^3d^{-1}. This corresponds to a maximum mean sea level change of 12 cm d^{-1}, and compares to estimates given by Hela (1944) and Lass (1988). Landsort sea level changes higher than this limit are not caused by water exchange with the North Sea and were removed from the time series.

Other pronounced short term fluctuations of sea level at Landsort, that not exceed the threshold of maximum sea level change, are caused by Seiches, inertial motions, tides and partially local wind forcing. These processes are not related to the transport in the Danish straits. The slowest of these signals is the first seiche of the Baltic proper with a period of 27 h. To eliminate the short term fluctuations of the processes, which are not contribute to the total volume change, the sea level time series was low pass filtered using a 4th order Butterworth filter of 0.0347 h^{-1} (1.2 days) cut off frequency. The filtered time series of Landsort sea level was used as mean Baltic Sea level for the calculation of total volume changes.

River Discharge

The second important component of the water budget is the fresh water surplus from rivers, draining into the Baltic. On average the mean river discharge of 436 km^3 a^{-1} is nearly comparable to the total inflow of saline water from the North Sea, and about 10 times larger than the net fresh water flux from precipitation and evaporation at the sea surface. However, the river discharge depicts large seasonal and interannual variability, which is taken into account for the volume transport estimation. River discharge data were obtained from several sources. Unfortunately, they do not cover the entire time range from 1886 till today. Annual discharge data are available from 1950 till 2012 from the HELCOM fact sheets (Kronsell and Andersson, 2013). Estimates of annual river discharge from 1901 to 1949 were taken from Cyberski et al. (2000). For the period before 1901 reconstructed runoff data from Hansson et al. (2011) were used. Monthly runoff data are available from Mikulski (1982) for the years 1921–1975, and from Cyberski et al. (2000) for the years 1976–1990. From 1981 till 2017 daily discharge from HYPE model output (setup: E-HYPEv3.1.3_GFD; HYPE_version_4_10_9) is provided by SMHI (2018a). The model was calibrated with daily data from river discharge stations.

Using the data listed above, an annual discharge time series for the period 1887–2017 and a monthly time series for the period 1921–2017 were constructed. Additionally, monthly climatology of runoff for the period 1921–1940 was calculated from the Mikulski (1982) data set. The climatology and the annual discharge time series are used to calculate monthly discharge data for the period 1887–1920. This enabled a reconstruction of a monthly discharge time series for the entire period 1887–2017. Afterward, daily discharge data were interpolated from the monthly time series. A detailed statistical analysis of Baltic river discharge is beyond the scope of this study and can be found e.g., in Bergström and Carlsson (1994).

The derived time series of hourly sea level change and daily runoff are used to calculate a time series of total barotropic volume transport $Q(t)$ into the Baltic according equation (2). The climatological value of mean precipitation minus evaporation surplus is considered with a constant daily surplus of 0.109 km^3d^{-1}.

Salinity Data

The calculation of salt mass imported during an inflow requires information on the salinity of inflowing water. For some periods salinity data in the Belt Sea and the Sound are available from lightship observations, fixed stations and buoys. The time scale of the inflow processes in the order of a few days requires at least daily observations to cover an inflow event in proper resolution. For the Belt Sea, namely the Darss Sill area, daily salinity data are available from the Danish light vessel "Gedser Rev" between 1897 and 1976. This data set has two major gaps due to the world wars I and II (Feistel et al., 2008). A second data set of daily salinity observations from the MARNET station Darss Sill is available for the period 1992 till present. Fischer and Matthäus (1996) used the same data set. Salinity at both locations has been measured at varying depth and slightly different positions in the subsequent measuring periods. To estimate a consistent daily time series of mean salinity for the entire period of investigation the data were interpolated vertically to an equidistant depth vector of 1m resolution. Since the vertical salinity gradient is weak during a barotropic inflow the interpolation causes only a minor uncertainty. The interpolated salinity profiles were averaged to obtain a daily time series of mean salinity at the eastern edge of the Belt $s_B(t)$.

A bias in the salinity time series is caused by the different observation positions. The MARNET station Darss Sill is located about 47 km east of the Gedser Rev light ship position. The cross section of the Belt Sea nearly doubles from 0.461 km^2 at Gedser Rev to 0.844 km^2 at the MARNET station (Mohrholz et al., 2015). Between both stations the inflowing saline water is diluted by entrainment of brackish surface water from the Arkona Basin. Unfortunately, there exists no overlapping period

of time series observations at both positions which allows the estimation of salinity decrease. However, model results suggest a mean decrease of salinity of inflowing water of approximately 1.5 between both stations (Mohrholz et al., 2015). Thus, the mean salinity measured at the Darss Sill was increased by this offset to get a consistent time series for the entire study period.

The salinity data in the Belt Sea cover 68% of time period from 1887 to 2017. Major gaps in the time series of mean salinity exist before 1897, during both world wars (November 1915 – February 1920, and November 1939 – September 1945), and between April 1976 and November 1991. For these gaps the salinity of inflowing water has been prescribed with mean values of 18.2 and 21.7 for the Belt Sea and the Sound, respectively. Which are the mean values for 90 major inflow events between 1897 and 1976 (Fischer and Matthäus, 1996). The standard deviation of these mean values is 1.2 and 1.4. The application of constant inflow salinities causes an uncertainty of 7–8% in the total salt mass of inflow events, that occurred in periods with no salinity observations.

Salinity data for the Sound are available from light ship observations at Oskarsgrundet (55°35′N, 12°51′E) and Kalksgrundet (55°37′N, 12°53′E), published by the SMHI Opendata server (SMHI, 2018b). The data cover a period from January 1883 to December 1961 at Oskarsgrundet, and from January 1883 to December 1922 at Kalksgrundet, respectively. Both time series depict several gaps. The most comprehensive period with daily observations is from January 1883 to December 1922. Afterward the observation frequency was reduced to a 10 days interval. Another data set of salinity data in the Sound was obtained from the EMODNET data base. This time series cover the period from June 2001 to July 2010 for the station Drogden (55°32′N, 12°43′E). The station is located about 8km southeast of the historical Oskarsgrundet lightship position, but well inside the Sound (compare **Figure 1**).

Salt Transports

To calculate the transports of saline water into the Baltic the time series of total volume transport $Q(t)$ was split with a fixed ratio into the volume transports trough Belt $Q_B(t)$ and the Sound $Q_S(t)$.

$$Q(t) = r \cdot Q_B(t) + (1 - r)Q_s(t) \quad with \quad r = 0.78$$

The ratio has been analyzed by several authors and ranged usually between 75 and 80% for the Belt Sea and 25 to 20% for the Sound (e.g., Jacobsen, 1980; Mattsson, 1996). The ratios 80/20%, 78/22%, and 75/25% were applied to test its impact on the total salt mass imported during an MBI. In the following the subscripts B and S are used to indicate the similar variables for the Belt and the Sound. If the used equations are the same for both channels only the equation for the Belt is given.

Usually, there exists a salinity front between brackish Baltic surface water and the saline surface water of the Kattegat. During outflow conditions this front is located at the northern edge of the Danish Straits. Before an inflow of high saline water into the western Baltic occurs the salinity front has to be shifted beyond the Darss Sill in the Belt and the Drogden Sill in the Sound. This inflow period, till the high saline water arrives the Darss Sill, was described as precursory period of a MBI (Matthäus and Franck, 1992), which lasts usually 5–25 days. During that time the Belt Sea and the Sound is flushed with saline Kattegat water. Due to the different volumes and transport capacities of both channels the salinity front reaches the Baltic first in the Sound and some days later in the Belt Sea. Since the salinity time series have large gaps it was not possible to derive the periods, when the salinity front is located at the Baltic side of the sills, for the entire study period from these data. Instead the transports in the Belt and the Sound, derived from volume change of the Baltic, were used to estimate the approximate positions $p_B(t)$ and $p_S(t)$ of the salinity front for each channel. During inflow conditions the simulated salinity front was shifted from the Kattegat [$p(t) = 0$] toward the Baltic until it reached the Baltic edge of the channel [$p(t) = 1$], and vice versa. The front positions were calculated stepwise for each time step t, using an effective buffer volume V_{buffer} of 110 km^3 for the Belt Sea and 10 km^3 for the Sound, respectively:

$$p_B(t+1) = p_B(t)\frac{Q_B(t) \cdot \Delta t}{V_{buffer}}$$

$$with \begin{array}{ll} p_B(t+1) = 0 & for\ p_B(t+1) < 0 \\ p_B(t+1) = 1 & for\ p_B(t+1) > 1 \end{array}$$

The buffer volumes were derived from the topographic data from Seifert et al. (2001), excluding larger areas of the Kiel bight and Mecklenburg Bight in the Belt Sea. The buffer volumes compare to the brackish water inflow volumes of the precursory period of the recent MBI in December 2014 (Mohrholz et al., 2015), which were estimated with 103 and 110 km^3 for the Belt Sea using two independent calculation methods.

Time series of inflowing water volume were derived from the time series of barotropic transport in both channels:

$$V_B(t) = Q_B(t) \cdot \Delta t \quad with \quad \begin{array}{ll} V_B(t) = 0 & for\ Q_B(t) < 0 \\ V_B(t) = V_B(t) & for\ Q_B(t) >= 0 \end{array}$$

The transports of salt $S(t)$ into the Baltic were calculated by multiplying the inflowing water volume $V(t)$ with the mean salinity s for the Belt Sea and the Sound. Only transports at times when the salinity front $p(t)$ is located at the Baltic side of the cannels [$p(t) = 1$] were counted as import of saline water into the Baltic.

$$S_B(t) = V_B(t) \cdot s_B(t) \quad with \quad \begin{array}{ll} S_B(t) = 0 & for\ p_B(t) < 1 \\ S_B(t) = S_B(t) & for\ p_B(t) = 1 \end{array}$$

Detection of MBI Events

Afterward the MBIs have to be detected in the time series of inflow volume and imported salt mass. The direct application of the MBI criteria developed by FM96 is not possible, since it is based on stratification and bottom salinity in the Belt and the Sound. This method is an indirect measure for the saline transport. The criteria that an inflow must at least last for five consecutive days at the Darss Sill to be counted as MBI can be applied to our transport time series. However, it is artificial in the sense that there is no natural drop in the frequency distribution of inflow event durations at this value.

From the time series of inflow volumes single barotropic inflow events were determined by identification of all periods with continuous inward directed volume transports [V(t) > 0]. This results in a high number of short term barotropic inflow events at both channels, since the high variability of transport in the straits causes frequent flow reversals. This often splits larger inflows into several minor events. Franck et al. (1987) counted two consecutive inflow events as a single one, if the interruption between both events was shorter than 2 days and bottom salinity and stratification coefficient fit to certain limits. This was not applicable for our approach of volume and salt transports. For the decision whether subsequent inflow events belongs to a single larger inflow event the time series of sea level at Landsort was used again. The response time of the Baltic Sea level to external barotropic forcing, e.g., sea level changes in the Kattegat, is about 10 days (Lass, 1988). This is applied to identify whether consecutive inflow events belongs to a single major inflow. The mean sea level time series was low pass filtered with a Butterworth filter of 10 days cut off period. In this low pass filtered time series short term fluctuations of the Baltic mean sea level, which cause short flow reversals in the Danish straits, are removed. Now subsequent inflow events which occure during the same period of monotonic increasing sea level, derived from the 10 days low pass filtered mean sea level time series, were combined to a single inflow event. This reduced the total number of barotropic inflow events from 2781 to 2022 during the period from 1887 to 2017.

Afterward for each inflow event the start and end time of the inflow, the begin of saline overflow, the total inflow volume, the volume of saline water and the imported salt mass were calculated for both transport channels. Nearly 70% (1415) of the barotropic inflow events were strong enough to carry high saline water into the Baltic. These events consist of two types: inflows that transport high saline water exclusively through the Sound into the Baltic and inflow events with saline water inflow through both channels. For the statistical analysis and the comparison with the MBI time series of Fischer and Matthäus (1996) three subsets of inflow events were extracted. The set DD1 covers all events with an inflow of saline water for at least 1 day at the Drogden Sill in the Sound. The set DS1 contains inflow events with saline inflow via the Sound and at least 0.5 day saline inflow at the Darss Sill. All events that last at least 5 days at the Darss Sill were summarized in the set DS5, most comparable to the FM96 time series. The DS5 is a subset of DS1, which is a subset of DD1 events.

Bottom Conditions in the Central Bornholm Basin and Eastern Gotland Basin

The revised time series of MBI events were proved with data of environmental conditions in the deep layer (85–90 m) of the Bornholm Basin and the eastern Gotland Basin (200 m). Data of deep water temperature, salinity and oxygen concentration were obtained from the ICES data base (International Council for the Exploration of the Sea [ICES], 2014) and from the IOW ODIN database. The data were gathered mainly in frame of the particular national monitoring activities of the Baltic neighboring countries and during numerous research projects. Although the observation and sampling methods for temperature, salinity and oxygen concentration changed with time, all available data were merged to a single time series for each parameter. Salinity data are given in the unit of practical salinity according to TEOS-10 (IOC et al., 2010). Oxygen concentrations are given in the old unit [ml l^{-1}], since it is the original unit of the majority of the oxygen data. The time series of Bornholm basin deep water covers a period from 1960 till present, and consists of 2930 data points gathered in the vicinity of the station Bornholm deep (BY5, 55°15′N 15°59′E). The salinity time series for the eastern Gotland Basin contain data from 1877 till present. The majority of 924 data points were gathered after 1951 at or near the station Gotland deep (BY15, 57°19′N 20°03′E).

RESULTS

The sequence of barotropic inflow events were calculated for three different ratios of transport between Belt Sea and the Sound (75/25, 78/22, and 80/20) and for varying prescribed salinity at times without salinity observations (salinity Sound/Belt: 17.2/20.7, 18.2/21.7, and 19.2/22.7). The results were averaged and the uncertainty of imported salt mass for each inflow event was calculated. The total number of inflow events in the particular subsets DS5, DS1 and DD1 during the period 1897–2017 was 132, 296, and 1415, respectively. The imported salt mass of inflow events of the DS5 subset is depicted in **Figure 2** together with their uncertainty, and the salinity at 200 m in the eastern Gotland basin. The total salt mass of the strongest events ranges between 2 and 5 Gt. Extreme events with more than 4 Gt salt import were found in 1898, 1921, 1951, and 2014. The strongest event is the December inflow 1951 with 4.66 Gt salt import. The averaged properties of the inflow events of the DS5, DS1, and DD1 subsets are summarized in **Table 1**.

To estimate long term trends the number of barotropic inflows per year and the related salt import per year were calculated for the three inflow subsets. Due to their stochastic nature the event frequency as well as the annual salt import depicts large year to year fluctuations especially for the DS5 subset. Thus, the number of inflow events were merged into subsequent 5 years sections, and the salt import time series were filtered with a smoothed running mean low pass filter of 11 years cut off period. The results are shown in **Figure 3**. The annual number of inflow events of the subsets DD1 and DS1 depict only minor year to year changes. The DS5 inflow set has a pronounced interannual variability, shown in the number of inflow events for the 5 years sections. Long term averages of the number of inflow events revealed 10, 23, and 108 events in per 10 years for the subsets DS5, DS1 and DD1, respectively. Also the annually imported salt mass increases from 1.58 to 2.54, and 4.02 Gt for the three time series. The barotropic inflow number and annual salt import of the subsets DS1 and DS5 depict inter decadal fluctuations with an estimated period of 20–30 years. Local minima in the number of larger inflow events (DS5) and in the annual salt import of all subsets were found in 1905, 1930, 1960, 1987, and 2007. Local maxima were observed in 1898, 1920, 1940, 1975, and 1996. Also the year 2017 seems to be close to a local maximum, although it might not reached jet.

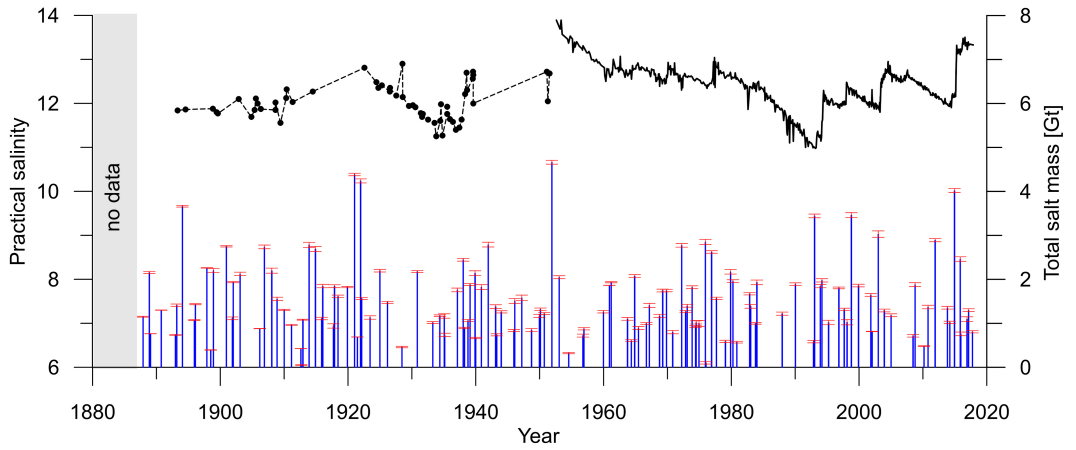


FIGURE 2 | Timing and total salt mass of barotropic inflow events of inflow set DS5 (blue bars) and their uncertainty (red range), compared to the salinity time series at 200 m depth in the central eastern Gotland basin.

TABLE 1 | Number of barotropic inflow events and averaged properties for the inflow subsets DS5, DS1, DD1, and the FM96 inflow sequence for the period 1887–2017.

	DS5	DS1	DD1	FM96
Number of inflow events	132	296	1415	115
Mean salt mass per inflow event [Gt]	1.56 ± 0.86	1.13 ± 0.74	0.37 ± 0.53	1.53 ± 0.96
Mean saline volume per inflow event [km^3]	79.55 ± 41.81	57.36 ± 36.60	18.75 ± 26.48	
Mean duration of inflow events [days]	27.6 ± 9.6	22.6 ± 9.8	15.6 ± 8.9	
Mean duration of Darss Sill overflow [days]	11.1 ± 5.2	6.4 ± 5.6	1.3 ± 3.6	9.8 ± 6.0
Mean number of inflow events per year	1.00 ± 0.79	2.26 ± 1.68	10.79 ± 1.51	0.92
Mean salt import per year [Gt]	1.58 ± 1.32	2.54 ± 1.41	4.02 ± 1.36	1.42 ± 1.60

A statistical analysis revealed no significant long term trend in any of the data sets.

The partition of saline inflow between the Belt Sea and the Sound varied between the particular inflow events (**Figure 4**). Generally, there is a shift of the contribution to imported salt mass from the Sound to the Belt Sea with increasing strength of the inflow events. For the majority of weak inflow events the ratio of salt mass passing through the Belt Sea to salt mass through the Sound is well below 1. However, there were also some weak events with a ratio exceeding 2. Events with a salt import of more than 2 Gt depicted always a ratio above 1, indicating the Belt as the main contributor to the salt import. As expected the amount of imported salt is directly correlated with the sea level change at Landsort during the active inflow, since the estimated transport in the Danish straits is derived from this sea level change. The majority of inflow events were related to a sea level change between 30 and 60 cm. Inflow events with sea level changes below 20 cm were exclusively minor events with less than 0.5Gt salt import in to the Baltic (**Figure 4**, right panel).

For the further analysis the barotropic inflows were sorted into size classes according their imported salt mass. Two different size class sets were defined, one set with 0.5 Gt resolution for the entire period from 1887 to 2017, and a second one with 1 Gt resolution for the analysis of monthly distribution. For investigation of long term variation of inflow size class distribution the inflow series were split into three subsequent 40 year periods from 1896 to 1935, 1936 to 1975, and 1976 to 2015. The frequency of inflow events per size class follows roughly an exponential distribution if all barotropic inflow events were considered (DD1). For events with saline transport at the Darss Sill (DS1 and DS5) the number of small inflow events drop by one to two order of magnitudes, whereas the higher size classes remains unchanged (**Figure 5**). The monthly distribution of number of inflow events depends also on the inflow strength. Smaller inflows via the Sound (DS1) occurs nearly equal distributed throughout the year, with a 10–20% higher frequency in winter. Considering the entire period from 1887 to 2017 about one minor barotropic inflow per month is observed through the Sound. Barotropic events which also pass the Darss Sill are confined to the winter season with a maximum frequency in December.

The inflow subsets DS1 and DS5 were compared with the time series FM96 in the three 40 year periods (**Figure 6**). The FM96 contains in total 96 MBIs in this period, which are 20 events less than the DS5 set. However, FM96 has two gaps with no data during the World Wars I and II, in total 10.5 years. During 1896 to 1935 the number of event is comparable between the series FM96 and DS5 (**Table 2**). Also the size class distribution is nearly similar, taken into account the uncertainty due to different estimation methods and the low number of inflows. The monthly distribution of inflows depicts some differences for the smaller inflows. As expected the data set DS1 contains a larger number of minor inflows than FM96 and DS5 since these events do not

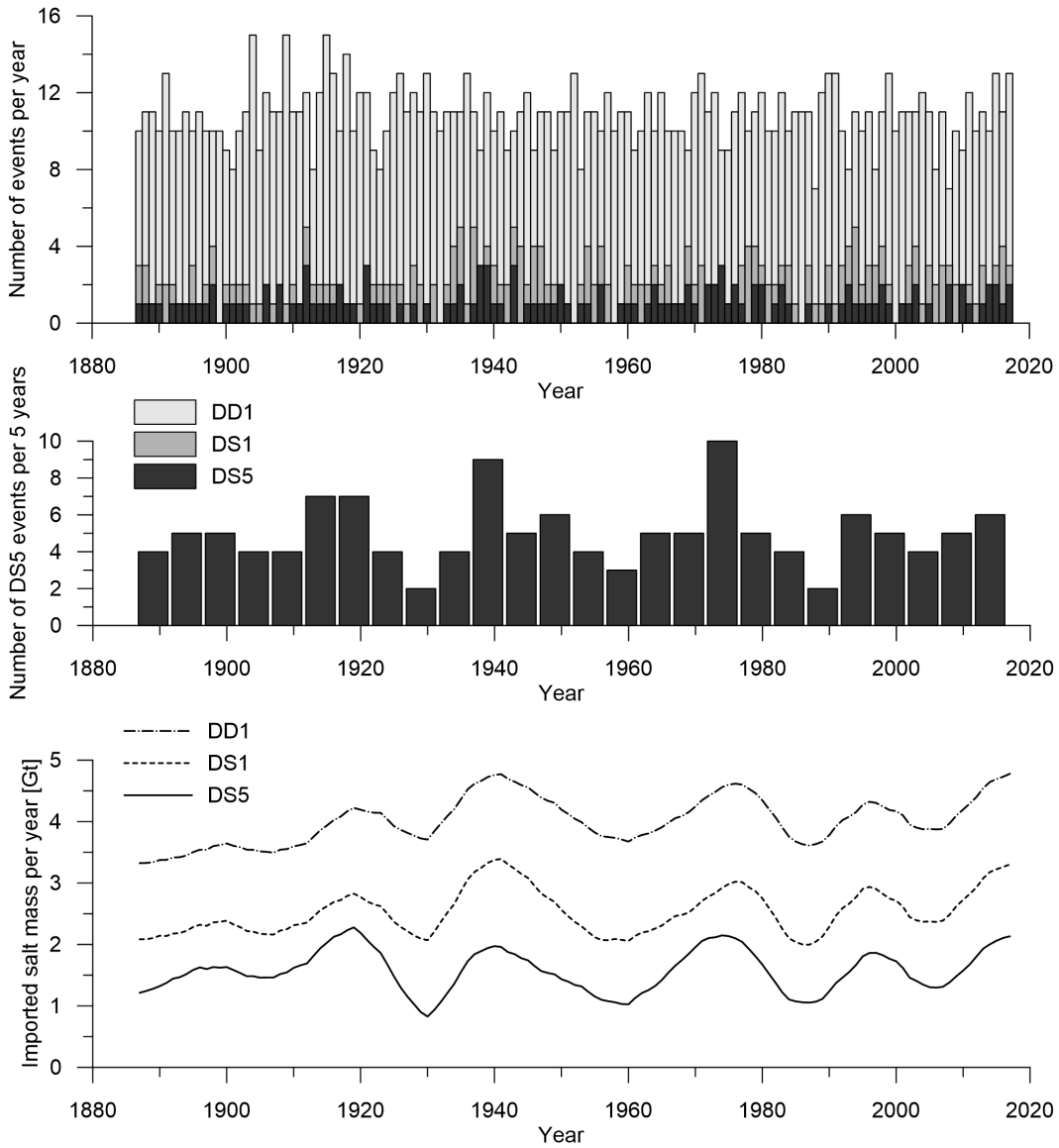


FIGURE 3 | Number of barotropic inflow events per year in the subsets DD1, DS1, and DS5 **(top)**. Number of barotropic inflow events per 5 year period in subset DS5 **(middle)** and the 11 year low pass filtered time series of salt mass annually imported by the inflow events of the subsets DD1, DS1, and DS5 **(bottom)**.

meet the 5 days duration criteria at the Darss Sill, and thus they are not classified as an MBI. However, the number of medium and large inflows compares to FM96 and DS5. For the period 1936 to 1975 the inflow distributions match the shape of the previous period. Again FM96 and DS5 depict nearly the same number of inflow events in all size classes. Also during this period the number of small inflow events in data set DS1 is higher than in FM96 and DS5. The monthly distribution of medium and large events is comparable between the three inflow series. A significant difference of FM96 and DS5 was observed for the 40 years period from 1976 to 2015. The number of inflow events in FM96 dropped from 40 and 45 events in the previous periods to only 11 for the last 40 years. This was caused mainly by a lack of minor and medium size inflow events. The time series DS5 and DS1 did not depict a similar behavior. There the number of inflows remains at the level of the preceding periods. Also their monthly distribution did not change for the third 40 year period.

To analyze the correlation between the FM96 events and the new time series the events from the subsets DS5, DS1, and DD1 were related to concurrent FM96 events. All 108 FM96 events that occurred after 1887 are present in the DD1 subset. A number of 93 and 61 of the FM96 events were found in the DS1 and DS5 subsets, respectively. The imported salt mass of inflow events from the FM96 series were correlated to the DS5 subset events. A linear fit through origin revealed a correlation coefficient R^2 of 0.8 (**Figure 7**). The FM96 events that were not contained in the DS5 subset belongs to size classes below 2 Gt. All strong and extreme events were found in both data sets.

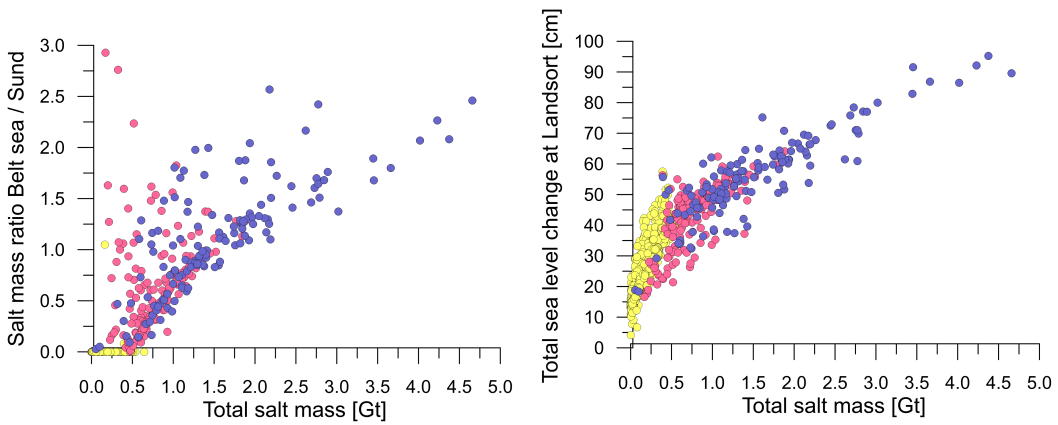


FIGURE 4 | Partition of salt import between Belt Sea and Sound during barotropic inflow events **(left)**, and relation of total sea level change at Landsort to the total salt import **(right)**. Events of the subsets DS5 marked blue, DS1 red, and DD1 yellow.

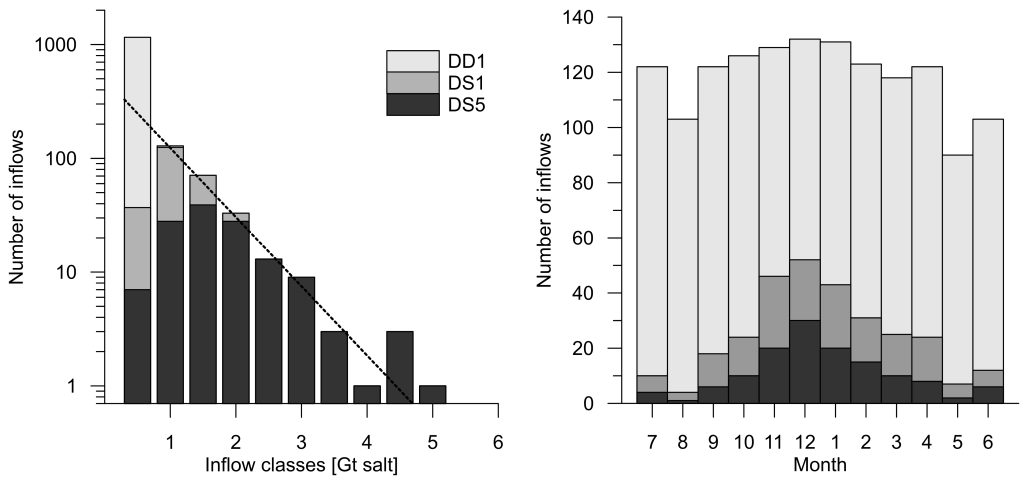


FIGURE 5 | Frequency of inflow events, sorted according their size classes **(left)**, and monthly distribution of all inflow events **(right)** of the inflow subsets DD1, DS1, and DS5.

The timing and strength of time series DS5 and DS1 inflow events were compared with the temporal behavior of salinity and oxygen concentration in the deep water layer (85–90 m) of the Bornholm basin for the period from 1960 till present. MBIs are potentially strong enough to change the environmental conditions at least in the western Baltic. Thus, the inflow events should leave their footprint in the Bornholm basin deep water properties. The salinity time series depict a saw tooth like pattern (**Figure 8**). The steep increases in deep water salinity occurred about 20–30 days after the inflow events. The jumps are followed by a phase of slowly decreasing salinity, due to diapycnal mixing and entrainment of low saline water from the overlaying top layer. The larger jumps in salinity with a change larger than 2 gkg^{-1} are related to the medium to strong inflow events of 1969, 1972, 1975, 1982/83, 1993, 2003, and 2014. However, also a number of smaller events cause jumps in the salinity. There are some medium size inflows that have almost no impact on deep water salinity in the Bornholm basin, e.g., 1964, 1973, 1984, or 1994. These events occurred during periods with high deep water salinity, established by a preceding inflow. Not every salinity jump can be related to a DS5 inflow event. Also some of the DS1 events were strong enough to change the deep water salinity considerably (e.g., 1986, 1989, 1992, 2006, and 2010). This was confined to periods with bottom salinity.

A more sensitive parameter to trace the inflow events in the Bornholm Basin is the deep water oxygen concentration. Although the sampling frequency was lower than for salinity. Nearly each inflow event of the time series DS5 and DS1 can be detected in the deep water oxygen concentration, since the biogeochemical driven oxygen decay is much faster than the diapycnal entrainment of low saline water into the deep water body. Good examples are periods with high salinity after strong inflow events like 1972, 1993 or after 2014. Then the deep water salinity was still on a high level, whereas the oxygen concentration was low enough to trace the next inflow.

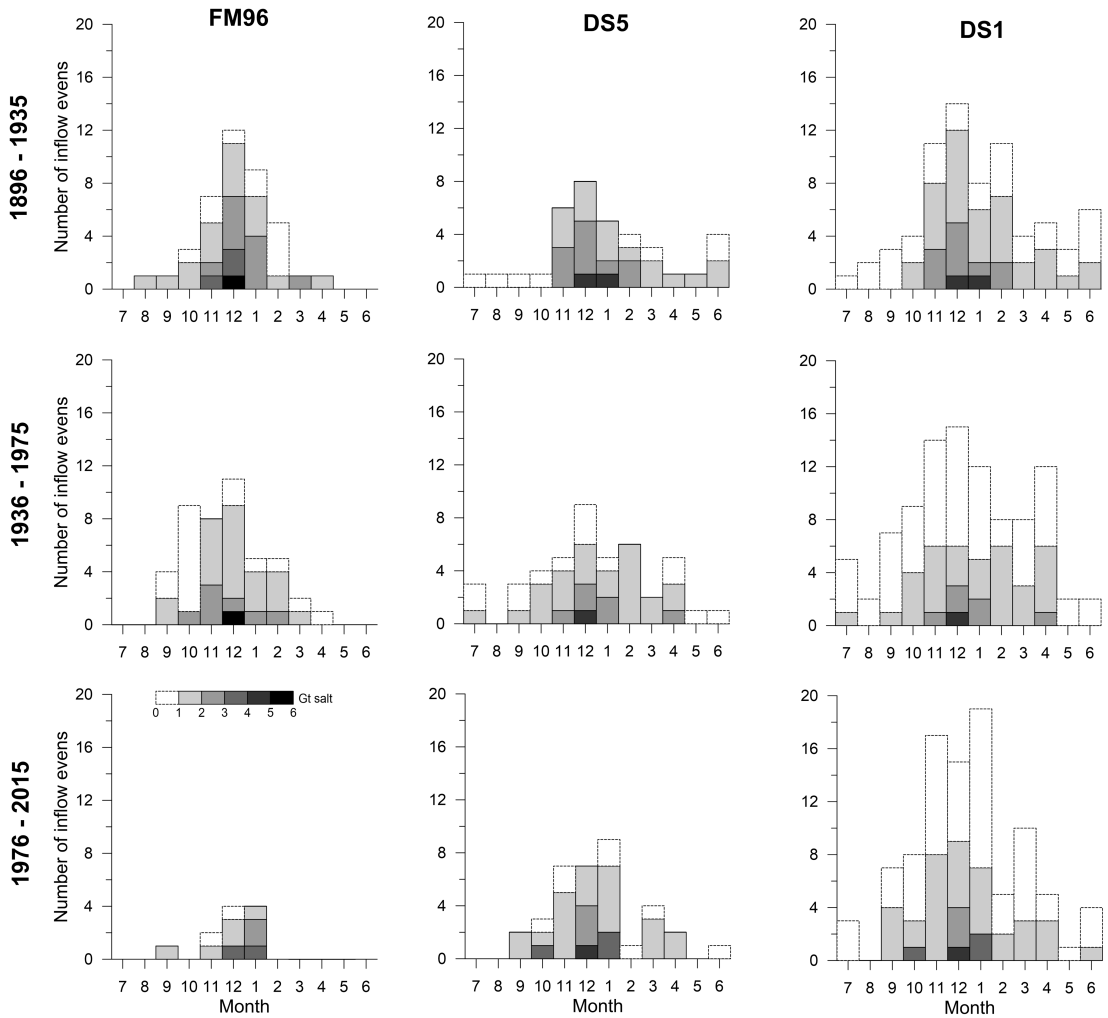


FIGURE 6 | Monthly frequency of inflow classes during the three subsequent 40-year periods of 1896–1935 **(top)**, 1936–1975 **(middle),** and 1976–2015 **(bottom)** for the inflow series FM96, DS5, and DS1.

TABLE 2 | Number of barotropic inflow events of inflow series FM96, DS5, and DS1 for three 40 year periods and different size classes.

Period	1896 –1935			1936 – 1975			1976 –2015		
Class	**FM96**	**DS5**	**DS1**	**FM96**	**DS5**	**DS1**	**FM96**	**DS5**	**DS1**
0–1 Gt	10	8	29	16	14	58	2	8	54
1–2 Gt	16	16	31	21	23	31	5	21	33
2–3 Gt	10	10	10	7	6	6	2	3	3
3–4 Gt	3	0	0	0	0	0	2	3	3
4–5 Gt	0	2	2	0	1	1	0	1	1
5–6 Gt	1	0	0	1	0	0	0	0	0
Total	**40**	**36**	**72**	**45**	**44**	**96**	**11**	**36**	**94**

DISCUSSION

Using independent and consistent time series of Baltic Sea sea level, river runoff and salinity the barotropic inflow activity of the recent 120 years was reconstructed and former gaps in the MBI series FM96 were filled. The revised inflow series contains any barotropic inflow at the Sound and the Belt Sea that lasts at least 1 day at the Drogden Sill (inflow set DD1). This is not consistent with the MBI definition of Fischer and Matthäus (1996). To compare the results of this study with the FM96 series all inflow events with at least 5 days saline inflow at the Darss Sill were selected. This group

TABLE 3 | Contribution of barotropic inflows to the total annual salt import of the Baltic.

	Volume [km^3]	Saline volume [km^3]	Salt [Gt]
Total saline water inflow (HELCOM, 1986)		481	8.18
DS5 inflows	171 ± 114	80.3 ± 65.6	1.58 ± 1.32
DS1 inflows	330 ± 158	129.5 ± 71.3	2.54 ± 1.41
DD1 inflows	892 ± 134	202.4 ± 67.6	4.02 ± 1.35
DD1 – DS5 inflows			2.44 ± 0.80
Barocline transport		279	4.2

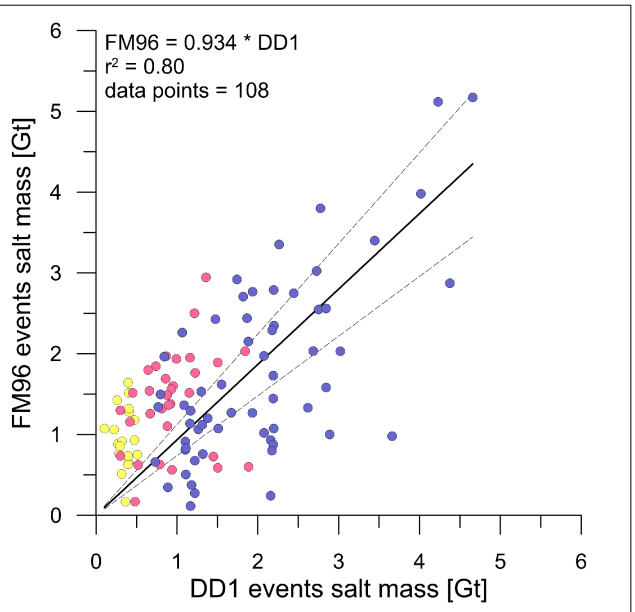


FIGURE 7 | Correlation of FM96 events and related inflow events of the subsets DS5 (blue), DS1 (red) and DD1 (yellow). A fit through origin and its 99% confidence interval is indicated by the black solid and dashed lines.

of barotropic inflows (DS5) is most similar to the classical MBI.

As expected the DS5 inflows occur mainly during the autumn and winter season from September to April with a maximum frequency between November and January, similar to the classical MBI (Matthäus and Schinke, 1994). Till 1983 both algorithms for identifying large barotropic inflows revealed nearly every MBI event, although the estimated strength differs particularly between the DS5 and the FM96 inflow series (**Figure 9**). This confirmed the applicability of the new algorithm, which uses the Landsort sea level. Since no changes in the observation methods of sea level occurs till 2006 the method should also reveal reliable data for the period after 1983. In contrast to the present knowledge from the FM96 inflow series, which assumes a strong decrease of Major Baltic Inflow frequency since the 1980s, this study shows that the frequency of Major Baltic Inflows depict no long term trend, during the last century. However, there exists a pronounced interannual variability with a time scale of 25–30 years.

The detection algorithms of large barotropic inflow events used by Fischer and Matthäus (1996) and this study based on different approaches. The classical approach used vertical salinity profiles at the Darss Sill and the Sound assuming that barotropic inflow conditions are characterized by high salinity and weak vertical stratification. Short term flow reversals during inflows are not detected by this method. The MBI detection algorithm of FM96 has two major limitations. First the MBIs were not derived directly from water transport through the Danish Straits. And secondly, the application of fixed empirical thresholds of minimum salinity and vertical stratification depends crucial on the location of measurements at the sills. However, the FM96 algorithm reveals reliable results if continuous observations of salinity and stratification in the Danish Straits are available.

The transport estimation based on the sea level change Landsort supply more direct estimations of the water exchange with the North Sea, although short term fluctuations at time scales of hours to 1.5 days were filtered out. This may lead to higher uncertainties for short inflow events, but MBI scale barotropic inflow events, with duration of at least 5 days overflow at the Darss Sill, are less affected. The calculation of imported salt mass is simple at times when salinity measurements in the Danish straits are available. The introduction of artificial salinity fronts and mean inflow salinities at the Darss Sill and Drogden Sill enables the estimation of salt import also for periods without salinity observations, although the uncertainty of salt import increases. This allowed the reconstruction of a continuous and consistent series of barotropic inflow events. The variation of transport ratio between the Belt Sea and the Sound in the observed limits has only minor impact on the strength of inflow events.

Mohrholz et al. (2015) hypothesized, that the present MBI statistic is biased since the end of the lightship observations at Gedser Rev in 1976. Especially the lack of weak and medium size inflows after 1980 contradicts the usual frequency-intensity distribution of MBIs given by Fischer and Matthäus (1996) for the period 1897 – 1976 (compare **Figure 6**). The barotropic inflow events depict an exponential frequency distribution. The smallest events have the highest frequency. The larger the events the less frequent they occur. There is no significant change in the atmospheric forcing that may explain a shift of the frequency distribution to larger inflow events.

Concurrent with the decreasing inflow activity in the FM96 inflow series around 1980 also the DS5 inflow set depicts a pronounced drop in inflow event frequency, which is attributed to the interannual variability of the inflow frequency. Unfortunately, this minimum of frequency of large inflows occurred at the same time when the continuous salinity observations at Gedser Rev were stopped. For the next decade the MBI detection was carried out using observations of the size of saline deep water body in the Arkona Basin. The data were gathered by the regular monitoring cruises and occasional project related observations of the IOW. The observation frequency was about bimonthly. Thus, minor inflow events of short duration were filtered out by the coarse spatial resolution and low sampling frequency of the observations. The low frequency of MBI in the FM96 series between 1976 and 1991 can be explained by both, the

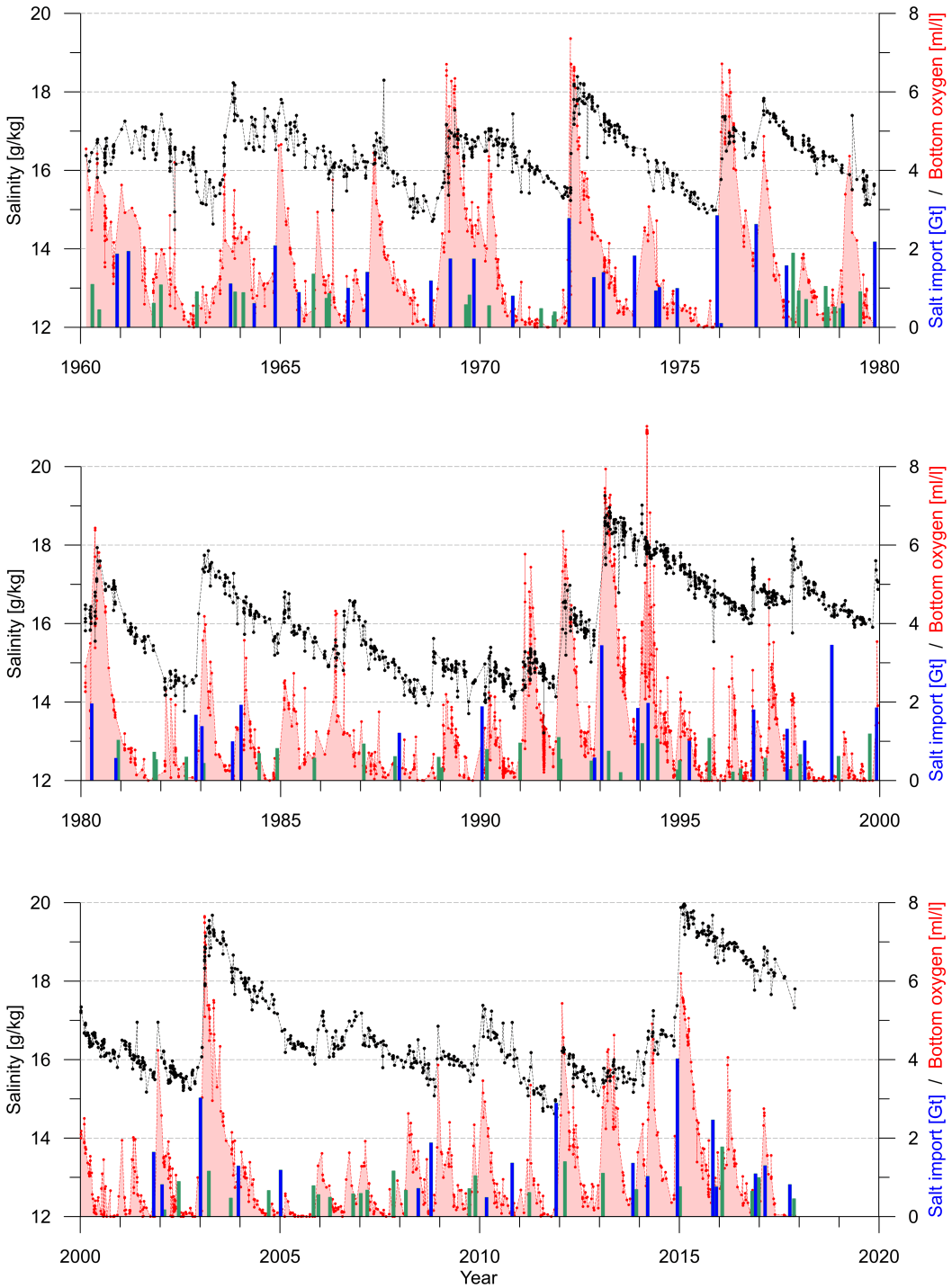


FIGURE 8 | Time series of near bottom salinity (black) and oxygen concentration (red) in the Bornholm Deep (85–90 m), overlaid with barotropic inflow events of the subsets DS5 (blue bars) and DS1 (green bars).

temporally drop in MBI frequency due to interannual variability and the end of continuous salinity observations at Gedser Rev.

In 1991 a new observation platform was established at the Darss Sill, which since then is used for continuous monitoring of the water exchange through the Belt Sea. This station is part of the German MARNET network, and is located 47 km east of the historic position of lightship Gedser Rev. The cross section area of the Belt Sea increases between both positions from 0.46 km^2 to 0.84 km^2. The MARNET station Darss Sill is located at the rim of the Arkona Basin approximately 20 km

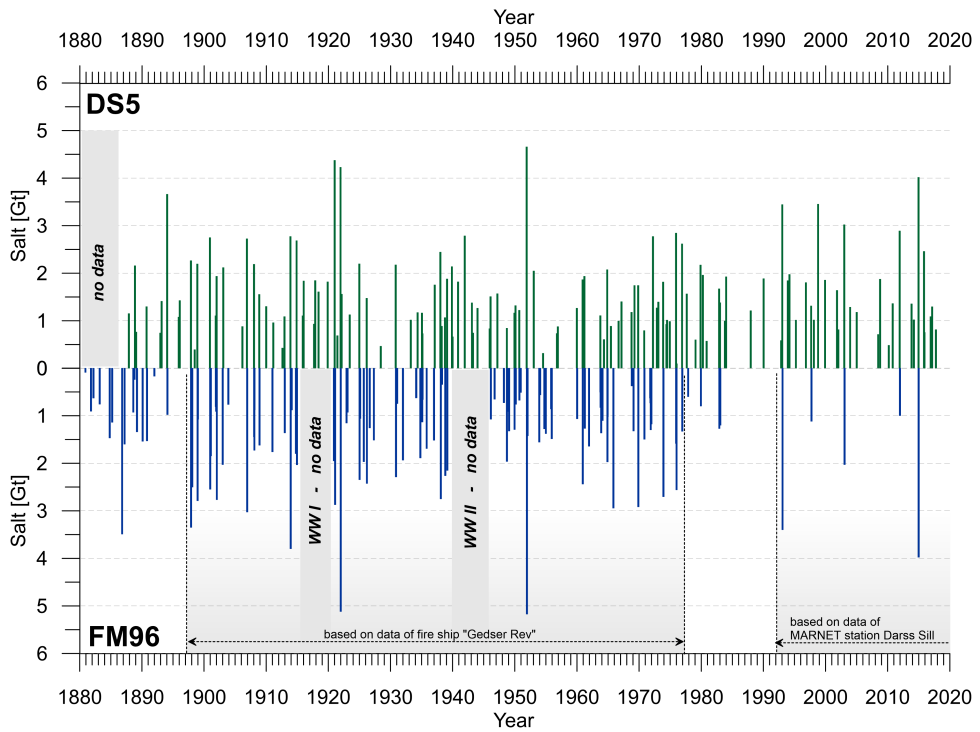


FIGURE 9 | Comparison of MBI sequence DS5 **(top)** with FM96 **(bottom)**. Gray areas indicate periods with no data. At the bottom the availability of time series observation at Gedser Rev and Darss Sill is depicted.

east of the topographic Darss Sill. On the pathway of saline water from Gedser Rev to Darss Sill and further to the MARNET Station Darss Sill entrainment of ambient brackish water reduces the salinity of the inflowing water by 1–1.5, and even the stratification changes. Due to the increasing water depth east of the topographic Darss Sill the inflowing saline water body is subducted below the brackish surface water. At the MARNET station Darss Sill the surface layer consists in the most cases of Arkona Basin surface water even during inflow conditions. Only strong inflow events as in December 2014 cover also the surface layer at the MARNET station. The bias in the FM96 inflow series after 1991 is caused mainly by the shift of continuous salinity observations to the rim of the Arkona Basin without an adjustment of the MBI identification criteria. Both the bottom mean salinity of the inflowing water at the MARNET station and the stronger stratification resulted in a strong reduction of detected inflow events. This affected especially the identification of minor inflow events, which were no longer recognized as MBI. However, also some larger barotropic inflow events failed the MBI criteria. A good example is the inflow in November 1996 which transported about 80 km^3 high saline water into the Baltic, but did not meet the MBI criteria at the Darss Sill (Matthäus et al., 1996). According to the imported salt mass of 1.5 to 1.7 Gt this inflow should be classified as a medium size MBI.

An additional indication that the salt transport into the Baltic has not changed is its stable mean salinity during the recent decades. Using well established long term averages of volume and mean salinity of the inflowing saline water of about 480 km^3 with a salinity of 17, the total salt import per year can be estimated with 8.2 Gt. The barotropic inflow events contribute approximately half of this amount with 4Gt (**Table 3**), which was confirmed also by the results of Stigebrandt (1983). The larger DS5 events which compares to the classical MBI contribute only 1.6 Gt per year with large interannual fluctuations. This is only 20% of the annual salt import to the Baltic. However, they are crucial for the deep water renewal and ventilation. The smaller barotropic inflow events (DD1 – DS5) supply on average 2.44 Gt salt to the Baltic, with a much bottom annual variability of ±0.8 Gt, and a nearly constant number of about 10 events per year. The salt import of the smaller events is on average 30% of the total salt import to the Baltic. The long term variability of salt import of barotropic inflow events is mainly caused by the variability of the DS5 events (compare **Figure 3**).

The contribution of the Belt Sea and the Sound to the total barotropic salt import depends on the size of the inflow events. If all barotropic events are recognized the Sound account for 2.79 Gt salt import per year compared to 1.23 Gt salt passing the Darss sill, which is a ratio of 69 to 31%. Lintrup and Jakobsen (1999) estimated an annual salt import through the Sound of 2.3–4 Gt, based on current and salinity observations in the years 1994 to 1997. The flow through the Sound is mainly barotropic throughout the year. Thus, the estimated salt import of 2.79 Gt per year fits to their results. The transport ratio between the Sound and the Belt Sea for only the DS5 events was 45 to 55%, with annual averages of 0.71 Gt and 0.87 Gt salt import respectively. As expected the salt transport in the

Belt Sea exceeds the Sound transport for the large barotropic events.

The classification of barotropic inflow events as MBI remains an open issue. The size class distribution of barotropic inflow events depicts a nearly exponential shape. There is no local minimum in the distribution that provides a proper reasoning for the separation between MBIs and minor barotropic events. The rule, that an MBI should last at least 5 consecutive days at the Darss sill, is also in some way artificial. As shown in **Figure 5** there were DS1 events, usually not classified as an MBI, which transports up to 2Gt salt into the Baltic. Whereas a considerable number of DS5 events are confined to size classes of 0.5 and 1.0 Gt. Lehmann and Post (2015) introduced the term "Large Volume Changes" (LVC) which are barotropic inflow events with a total volume change for the Baltic of more than 100 km^3 over a period of 40 days, regardless of the amount of salt import. This definition included the river runoff and has been revised by Lehmann et al. (2017). According to their revised definition an LVC requires a minimum net inflow of 60 km^3 from the North Sea. These LVC events have a higher frequency than the FM96 MBIs. Mohrholz et al. (2015) calculated an effective buffer volume of about 110 km^3 for the Belt Sea that must usually be replaced by saline water before the saline inflow at the Darss Sill starts. Thus, the current LVC approach seems not appropriate to replace the classical MBI definition, and it was in fact not intended by Lehmann et al. (2017). The most useful approach was already indicated by Fischer and Matthäus (1996) by using the total amount of salt import for their modified MBI classification. Although a classification of barotropic inflow events into MBI and smaller inflows might be outdated from the current point of view, one can apply the FM96 size classification without using the term MBI. Then the barotropic inflows are simply classified as weak, moderate (or medium), strong and very strong (or extreme) events using the limits of 1, 2, and 3 Gt salt import respectively. However, this is just a suggestion and has to be discussed in the scientific community. A classification like this has no relation to the ecological impact of a particular barotropic inflow. Certainly increases the probability that the saline waters of an inflow reach the deep layers of the central Baltic with its size, but also the saline stratification of the Baltic prior to the inflow has a crucial impact on the renewal and ventilation of deep water. An inclusion of ecological aspects into the MBI classification, as the oxygen supply to the deep layers of the central Baltic, appears possible and useful from the ecosystem perspective. However, it complicates the classification of inflow events to a large extent, since the required data are not available for the time before 1950. And even today the temporal and spatial resolution of the gathered data is not sufficient to trace the ecological impact of each particular inflow event.

CONCLUSION

The main results of this study are summarized as follows:

1. A continuous series of barotropic transport of saline water into the Baltic Sea was reconstructed for the period from 1887 till present, that allow a statistical analysis of the distribution of barotropic inflow events.
2. In contrast to the inflow series FM 96 the reviewed series of barotropic inflow events depict no long term trend in event frequency and the related annual salt transport during the recent 130 years.
3. The frequency of large barotropic inflows (DS5 events) has pronounced long term variability with a main period of about 25–30 years.
4. Smaller barotropic inflow events occur throughout the year with low interannual variability and supply on average 30% of the total salt transport into the Baltic.
5. The decreasing inflow frequency in the FM96 series after the 1980s can be attributed to a systematic bias caused by a lack of daily salinity observations between 1976 and 1991 and an eastward shift of observation position afterward, without an adjustment of the MBI identification criteria.
6. The observed temporal variability of barotropic inflows of saline water does not explain the increasing stagnation periods in the Baltic deep water and the spread of anoxic bottom conditions in the central Baltic. This highlights the impact of increased eutrophication as main driving factor as stated by Zillén et al. (2008); Conley et al. (2009), and several other studies.

Further research is needed to attribute the long term variability of inflow frequency to the regional climate variability and established climate indices, e.g., the NAO. Also the method for estimation of barotropic salt transport used in this study can be further improved with additional *in situ* data from the Danish straits, and independent transport calculations derived from local sea level differences between the Kattegat and the western Baltic. However, this will not alter the main conclusions given above.

DATA AVAILABILITY STATEMENT

The daily time series of total transport through the Danish Straits, derived from sea level change Landsort/Landsort Norra, and the reconstructed sequence of saline inflow events are stored in the IOW ODIN data base (https://odin2.io-warnemuende.de). These time series are provided with Creative Commons (CC) data license of type CC BY 4.0 (https://creativecommons.org/licenses/by/4.0/).

AUTHOR CONTRIBUTIONS

The author declares that the presented study is his own original research.

FUNDING

This work has been funded by institutional funds of the Leibniz Institute for Baltic Sea Research Warnemünde in frame of its research focus 3 "Changing ecosystems" and the Baltic Sea long term observation program of the institute.

ACKNOWLEDGMENTS

This study would have been impossible without the public availability of *in situ* observations provided by several institutions of the Baltic Sea neighboring countries. These data are based on the daily work of a countless number of people. Their work is greatly acknowledged. The sea level data of Landsort and Landsort Norra, the light ship observations of salinity in the Sound, and the runoff data from the HYPE model were made available by the OpenData server of the SMHI. The lightship data at Gedser Rev were published by the DMI. Additional hydrographic data from the Danish Straits, the central Bornholm basin and the eastern Gotland basin were provided by the ICES, the HELCOM, and the EMODNET data bases. The data from the MARNET station Darss Sill are gathered in frame of the German marine monitoring program, funded by the BSH and carried out by IOW.

REFERENCES

BACC II Author Team (2015). *Second Assessment of Climate Change for the Baltic Sea Basin*. Berlin: Springer International Publishing.

Bergström, S., and Carlsson, B. (1994). River runoff to the Baltic Sea: 1950-1990. *Ambio* 23, 280–287.

Carstensen, J., Andersen, J. H., Gustafsson, B. G., and Conley, D. J. (2014). Deoxygenation of the Baltic Sea during the last century. *Proc. Natl. Acad. Sci. U.S.A.* 111, 5628–5633. doi: 10.1073/pnas.1323156111

Conley, D. J., Björck, S., Bonsdorff, E., Carstensen, J., Destouni, G., Gustafsson, B. G., et al. (2009). Hypoxia-related processes in the Baltic Sea. *Environ. Sci. Technol.* 43, 3412–3420. doi: 10.1021/es802762a

Cyberski, J., Wróblewski, A., and Stewart, J. (2000). Riverine water inflows and the Baltic Sea water volume 1901-1990. *Hydrol. Earth Syst. Sci. Discuss.* 4, 1–11. doi: 10.5194/hess-4-1-2000

Feistel, R., Nausch, G., and Hagen, E. (2006). Unusual Baltic inflow activity in 2002–2003 and varying deep-water properties. *Oceanologia* 48, 21–35.

Feistel, R., Seifert, T., Feistel, S., Nausch, G., Bogdanska, B., Hansen, L., et al. (2008). "Digital supplement," in *State and Evolution of the Baltic Sea*, eds R. Feistel, G. Nausch, and N. Wasmund (Hoboken, NJ: Wiley), 625–667.

Feistel, S., Feistel, R., Nehring, D., Matthäus, W., Nausch, G., and Naumann, M. (2016). Hypoxic and anoxic regions in the Baltic Sea, 1969 - 2015. *Meereswiss Ber Warnemünde* 100:2016. doi: 10.12754/msr-2016-0100

Fischer, H., and Matthäus, W. (1996). The importance of the drogden Sill in the sound for major Baltic inflows. *J. Mar. Syst.* 9, 137–157. doi: 10.1016/S0924-7963(96)00046-2

Fischer, T., Banyte, D., Brandt, P., Dengler, M., Krahmann, G., Tanhua, T., et al. (2013). Diapycnal oxygen supply to the tropical North Atlantic oxygen minimum zone. *Biogeosciences* 10, 5079–5093. doi: 10.5194/bg-10-5079-2013

Franck, H. and Matthäus, W. (1992). Sea level conditions associated with major Baltic inflows. *Beitr. Meereskunde* 63, 65–90.

Franck, H., Matthäus, W., and Sammler, R. (1987). Major inflows of saline water into the Baltic Sea during the present century. Gerlands Beitr. *Geophys. Leipzig* 96, 517–531.

Hansson, D., Eriksson, C., Omstedt, A., and Chen, D. (2011). Reconstruction of river runoff to the Baltic Sea, AD 1500–1995. *Intern. J. Climatol.* 31, 696–703. doi: 10.1002/joc.2097

Hela, I. (1944). Über die schwankungen des wasserstandes in der ostsee mit besonderer berücksichtigung des wasseraustausches durch die dänischen gewässer. *Ann. Acad. Sci. Fenn.* 134, 1–108.

HELCOM (1986). *Water Balance of the Baltic Sea. Baltic Sea Environment Proceedings*. Helsinki: HELCOM.

Hordoir, R., Axell, L., Löptien, U., Dietze, H., and Kuznetsov, I. (2015). Influence of sea level rise on the dynamics of salt inflows in the Baltic Sea. *J. Geophys. Res. Oceans* 120, 6653–6668. doi: 10.1002/2014JC010642

International Council for the Exploration of the Sea [ICES] (2014). *The International Council for the Exploration of the Sea, Copenhagen*. Available at: http://www.ices.dk/marine-data

IOC, SCOR, IAPSO (2010). *The International Thermodynamic Equation of Seawater – 2010: Calculation and Use of Thermodynamic Properties*. Paris: UNESCO.

Jacobsen, T. S. (1980). *The Belt Project. Sea Water Exchange of the Baltic–Measurements and Methods*. Denmark: The National Agency for Environmental Protection.

Jakobsen, F., Hansen, I. S., Ottesen Hansen, N.-E., and Ostrup-Rasmussen, F. (2010). Flow resistance in the Great Belt, the biggest strait between the North Sea and The Baltic Sea. *Estuar. Coast. Shelf Sci.* 87, 325–332. doi: 10.1016/j.ecss.2010.01.014

Jakobsen, F., Lintrup, M., and Møller, J. S. (1997). Observation of the specific resistance in the Øresound. *Hydrol. Res.* 28, 217–232. doi: 10.2166/nh.1997.0013

Jenkinson, A. F., and Collison, F. P. (1977). *An Initial Climatology of Gales Over the North Sea, Synoptic Climatology Branch Memorandum*, Vol. 62. Bracknell: Meteorological Office.

Jönsson, B., Döös, K., Nycander, J., and Lundberg, P. (2008). Standing waves in the gulf of finland and their relationship to the basin-wide Baltic seiches. *J. Geophys. Res.* 113:C03004. doi: 10.1029/2006JC003862

Kabel, K., Moros, M., Porsche, C. H., Neumann, T., Adolphi, F., Andersen, T. J., et al. (2012). Impact of climate change on the Baltic Sea ecosystem over the past 1,000 years. *Nat. Clim. Change* 2, 871–874. doi: 10.1038/nclimate1595

Kronsell, J., and Andersson, P. (2013). *Total and Regional Runoff to the Baltic Sea. HELCOM Baltic Sea Environment Fact Sheets*. Available at: http://www.helcom.fi/baltic-sea-trends/environment-fact-sheets/

Lass, H. U. (1988). A theoretical study of the barotropic water exchange between the North Sea and the Baltic and the sea level variations of the Baltic. *Beitr. Meereskunde* 58, 19–33.

Lass, H. U., Schwabe, R., Matthäus, W., and Francke, E. (1987). On the dynamics of water exchange between Baltic and North Sea. *Beitr. Meereskunde* 56, 27–49.

Lehmann, A., Höflich, K., Post, P., and Myrberg, K. (2017). Pathways of deep cyclones associated with large volume changes (LVCs) and major Baltic inflows (MBIs). *J. Mar. Syst.* 167, 11–18. doi: 10.1016/j.jmarsys.2016.10.014

Lehmann, A., and Post, P. (2015). Variability of atmospheric circulation patterns associated with large volume changes of the Baltic Sea. *Adv. Sci. Res.* 12, 219–225. doi: 10.5194/asr-12-219-2015

Lintrup, M. J., and Jakobsen, F. (1999). The importance of oresund and the drogden sill for Baltic inflow. *J. Mar. Syst.* 18, 345–354. doi: 10.1016/S0924-7963(98)00018-9

Lisitzin, E. (1974). *Sea-Level Changes*. Amsterdam: Elsevier.

Matthäus, W., and Franck, H. (1992). Characteristics of major Baltic inflows - a statistical analysis. *Cont. Shelf Res.* 12, 1375–1400. doi: 10.1016/0278-4343(92)90060-W

Matthäus, W., Nehring, D., Feistel, R., Nausch, G., Mohrholz, and Lass, H. U. (2006). "The inflow of high saline water into the Baltic Sea," in *State and Evolution of the Baltic Sea, 1952–2005*, eds R. Feistel, G. Nausch, and N. Wasmund (Hoboken, NJ: Wiley), 265–309.

Matthäus, W., Nehring, D., Lass, H. U., Nausch, G., Nagel, N., and Siegel, H. (1996). The Baltic Sea in 1996 — continuation of stagnation and decreasing phosphate concentrations. *Deutsche Hydrogr. Z.* 48, 161–174.

Matthäus, W. and Schinke, H. (1994). Mean atmospheric circulation patterns associated with major Baltic inflows. *Deutsche Hydrogr. Z.* 46, 321–339. doi: 10.1007/BF02226309

Mattsson, J. (1996). Some comments on the barotropic flow through the Danish straits and the division of the flow between the Belt Sea and the Öresund. *Tellus* 48A, 456–464. doi: 10.3402/tellusa.v48i3.12071

Meier, H. E. M., Andersson, H. C., Eilola, K., Gustafsson, B. G., Kuznetsov, I., Müller-Karulis, B., et al. (2011). Hypoxia in future climates: a model ensemble study for the Baltic Sea. *Geophys. Res. Lett.* 38:L24608. doi: 10.1029/2011GL049929

Meier, H. E. M., Feistel, R., Piechura, J., Arneborg, L., Burchard, H., Fiekas, V., et al. (2006). Ventilation of the Baltic Sea deep water: a brief review of present knowledge from observations and models. *Oceanologia* 48, 133–164.

Mikulski, Z. (1982). *River Inflow to the Baltic Sea 1921–1975*. Warsaw: Polish Academy of Science.

Mohrholz, V., Naumann, M., Nausch, G., Krüger, S., and Gräwe, U. (2015). Fresh oxygen for the Baltic Sea—An exceptional saline inflow after a decade of stagnation. *J. Mar. Syst.* 148, 152–166. doi: 10.1016/j.jmarsys.2015.03.005

Naumann, M., Nausch, G., and Mohrholz, V. (2016). "A succession of four Major Baltic Inflows in the period 2014–2016 – an overview of propagation and environmental change", in *Proceedings of the 1st International Baltic Earth Secretariat Publication on Multiple drivers for Earth system changes in the Baltic Sea region* Nida, Curonian Spit, Lithuania. 9, 13–17.

Neumann, T., Radtke, H., and Seifert, T. (2017). On the importance of Major Baltic Inflows for oxygenation of the central Baltic Sea. *J. Geophys. Res. Oceans* 122, 1090–1101. doi: 10.1002/2016JC012525

Omstedt, A. (1987). Water cooling in the entrance of the Baltic Sea. *Tellus* 39A, 254–265. doi: 10.3402/tellusa.v39i3.11758

Rutgersson, A., Jaagus, J., Schenk, F., and Stendel, M. (2014). Observed changes and variability of atmospheric parameters in the Baltic Sea region during the last 200 years. *Clim. Res.* 61, 177–190. doi: 10.3354/cr01244

Schimanke, S., Dieterich, C., and Meier, H. E. M. (2014). An algorithm based on sea-level pressure fluctuations to identify major Baltic inflow events. *Tellus* 66A:23452. doi: 10.3402/tellusa.v66.23452

Seifert, T., Tauber, F., and Kayser, B. (2001). *A High Resolution Spherical Grid Topography of the Baltic Sea*, 2nd Edn, Stockholm: Baltic Sea Science Congress, 25–29.

SMHI (2018a). *Hydrological Predictions for the Environment. HYPE model setup 3-1-1*. Norrköping: SMHI.

SMHI (2018b). *Tide-Gauge Data of the Stations Landsort and Landsort Norra in Hourly Means, Reference Level RH2000*. Available at: http://opendata-download-ocobs.smhi.se

Stigebrandt, A. (1983). A Model for the exchange of water and salt between the Baltic and the Skagerrak. *J. Phys. Oceanogr.* 13, 411–427. doi: 10.1175/1520-0485(1983)013<0411:AMFTEO>2.0.CO;2

Stramma, L., Gregory, C., Johnson, G. C., Sprintall, J., and Mohrholz, V. (2008). Expanding oxygen-minimum zones in the tropical oceans. *Science* 320, 655–658. doi: 10.1126/science.1153847

Wolf, G. (1972). Salzwassereinbrüche im Gebiet derwestlichen Ostsee. *Beitr. Meereskunde* 29, 67–77.

Wübber, C., and Krauss, W. (1979). The two-dimensional seiches of the Baltic Sea. *Oceanol. Acta* 2, 435–446.

Zillén, L., Conley, D. J., Andrén, T., Andrén, E., and Björck, S. (2008). Past occurrences of hypoxia in the Baltic Sea and the role of climate variability, environmental change and human impact. *Earth Sci. Rev.* 91, 77–92. doi: 10.1016/j.earscirev.2008.10.001

Conflict of Interest Statement: The author declares that the research was conducted in the absence of any commercial or financial relationships that could be construed as a potential conflict of interest.

Copyright © 2018 Mohrholz. This is an open-access article distributed under the terms of the Creative Commons Attribution License (CC BY). The use, distribution or reproduction in other forums is permitted, provided the original author(s) and the copyright owner(s) are credited and that the original publication in this journal is cited, in accordance with accepted academic practice. No use, distribution or reproduction is permitted which does not comply with these terms.

frontiers in Marine Science

ORIGINAL RESEARCH
published: 11 July 2018
doi: 10.3389/fmars.2018.00222

Propagation of Impact of the Recent Major Baltic Inflows From the Eastern Gotland Basin to the Gulf of Finland

Taavi Liblik[1], Michael Naumann[2], Pekka Alenius[3], Martin Hansson[4], Urmas Lips[1], Günther Nausch[2], Laura Tuomi[3], Karin Wesslander[4], Jaan Laanemets[1] and Lena Viktorsson[4]*

[1] Department of Marine Systems at Tallinn University of Technology, Tallinn, Estonia, [2] Leibniz Institute for Baltic Sea Research (LG), Warnemünde, Germany, [3] Marine Research Unit, Finnish Meteorological Institute, Helsinki, Finland, [4] Oceanographic Unit, Swedish Meteorological and Hydrological Institute, Norrköping, Sweden

OPEN ACCESS

Edited by:
Isabel Iglesias, Centro Interdisciplinar de Pesquisa Marine e Ambiental (CIIMAR), Portugal

Reviewed by:
Alexander B. Rabinovich, P.P. Shirshov Institute of Oceanology (RAS), Russia
Jesus Dubert, University of Aveiro, Portugal

***Correspondence:**
Taavi Liblik
taavi.liblik@ttu.ee

Specialty section:
This article was submitted to Coastal Ocean Processes, a section of the journal Frontiers in Marine Science

Received: *30 March 2018*
Accepted: *08 June 2018*
Published: *11 July 2018*

Citation:
Liblik T, Naumann M, Alenius P, Hansson M, Lips U, Nausch G, Tuomi L, Wesslander K, Laanemets J and Viktorsson L (2018) Propagation of Impact of the Recent Major Baltic Inflows From the Eastern Gotland Basin to the Gulf of Finland. Front. Mar. Sci. 5:222. doi: 10.3389/fmars.2018.00222

Major Baltic Inflows (MBI) have a significant impact on physics, biogeochemistry, and marine life in the Baltic Sea. Spreading of the North Sea water from the Danish Straits to the Eastern Gotland Basin has been rigorously studied in recent decades. Investigations of lateral signal propagation using *in-situ* measurements, which cover the area from the Eastern Gotland Basin to the Gulf of Finland, are missing. Estonian–Swedish–German–Finnish oceanographic data from January 2014 to March 2017 were merged and analyzed to fill the gap. Recent MBIs caused considerable changes in water column properties, and salinity reached the highest values of the last 40–60 years. The arrivals of MBI waters were detected as peaks in the salinity and temperature time-series in the near-bottom layer of the Gotland Deep 4–5 months after the MBI events. Similar peaks were also identified in the Fårö Deep, Northern Deep, and Kõpu West (Northern Baltic Proper) with a further delay of 2–3, 3–5, and 4–6 months, respectively. The first impact of the 2014 December MBI occurred in the Gulf of Finland in 9 months as the arrival of the former Northern Baltic Proper deep layer water. Water renewal in the Fårö Deep occurred as a gravity current over the sill between Fårö and Gotland Deep. Deep layer water in the Northern Baltic Proper and the Gulf of Finland originated from the sub-halocline layer (110–120 m) of the Eastern Gotland Basin. The pre-condition for such mid-layer advection was a denser deep layer in the Gotland and Fårö Deep. Fresh oxygen, which arrived in the Gotland Deep in April 2015 and February 2016, was consumed in the near-bottom layer within 3–6 months. Since summer 2016, oxygenated waters occurred in the Gotland Deep in the layer from the halocline to 160 m depth. This oxygen did not reach the area further in the north, except a slight sign of ventilation of the Fårö Deep in February 2017. Thus, MBIs did not improve the oxygen conditions in the area north of the Gotland Deep and oxygen conditions rather worsened in the Northern Baltic Proper and the Gulf of Finland.

Keywords: Major Baltic Inflow, Baltic Sea, hypoxia, water masses, halocline

INTRODUCTION

The Baltic Sea is a semi-enclosed, shallow, and brackish sea with limited water exchange with the North Sea. High freshwater supply from rivers and irregular inflows of saline waters through the Danish Straits and the Sound maintain large horizontal salinity/density gradients and vertical stratification in the Baltic Sea (e.g., Myrberg and Leppäranta, 2009). Changes in freshwater flux (Hänninen and Vuorinen, 2011), despite its seasonality, accumulate, and emerge in the sea over decades (Schimanke and Meier, 2016). Strong stratification effectively restricts the direct ventilation of the deep basins below the permanent halocline at ∼70 m depth. The eutrophication of the Baltic Sea, to a large extent caused by anthropogenic enrichment of the nutrients, is expressed in increased biomass production and sedimentation resulting in oxygen depletion of the deep layers and an increase of hypoxic bottom areas (Vahtera et al., 2007; Conley et al., 2009).

There are two types of saline water inflows through the Danish Straits leading to a renewal of sub-halocline waters of the Baltic Sea. Barotropic inflows are forced by sea level differences between the Kattegat and the Arkona Basin. Strong barotropic inflows, called Major Baltic Inflows (MBIs), are the main process to ventilate deep water in the Baltic Sea (Matthäus and Franck, 1992). Special atmospheric conditions are needed to evoke an MBI—a sequence of easterly winds lasting 20–30 days followed by strong westerly winds of similar duration (Matthäus and Lass, 1995). Franck et al. (1987) analyzed long-term salinity time series (1897–1976) measured at Darss Sill area and found 5–7 MBIs per decade. Since the 1980s, MBIs have been rather rare—strong MBIs occurred in 1993 (Matthäus and Lass, 1995) and 2003 (Feistel et al., 2006) and a moderate MBI in 1997 (Hagen and Feistel, 2001). The following inflow event in December 2014 was considered as the strongest since 1951 (Mohrholz et al., 2015). During this MBI event 320 km^3 of salty and oxygen-rich water propagated into the western Baltic Sea after a 10-year stagnation period. Weaker MBIs followed in November 2015 and January–February (Naumann et al., submitted). Weaker barotropic inflows could occur several times per year and play an important role in maintaining haline stratification (Burchard et al., 2005). The second type is the baroclinic inflows forced by density gradient between the Baltic Sea and the Kattegat which usually occur during longer calm periods. If a baroclinic inflow lasts long enough, a clear signature of this inflowing water mass can be observed from the Danish Straits to the Baltic Proper (Feistel et al., 2004). Baroclinic inflows do not carry much oxygen from the North Sea, but they could pick up oxygen by entrainment with the cold intermediate layer at sills in the Baltic Sea and to some extent ventilate deeper basins (Feistel et al., 2006; Mohrholz et al., 2006).

Strong barotropic inflows cause considerable changes in environmental conditions not only in the layers they occupy, but also adjacent areas and water column above. The saltier North Sea water propagates as a dense bottom gravity current from the western Baltic to the central Baltic Sea. Strong inflows fill deep basins with high saline, oxygen-rich water, lift up the former stagnant water, and push it onwards. Transformation of water mass properties along the inflow pathway depends on advection and vertical mixing/entrainment. The impact of December 2014 MBI on the deepwater properties and dynamics in the Gotland Basin is well investigated. Schmale et al. (2016) followed the propagation of December 2014 MBI water and recorded its arrival into the Gotland Basin in the beginning of March when increasing oxygen levels in the deepest layers terminated the 10-year stagnation period. The near-bottom layer was a mixture of the inflow water, water flushed out from the near-bottom region of the neighboring Bornholm Basin, and surrounding water entrained along the pathway of the inflow. They also observed high current speed and turbulence levels in the near-bottom region along the slope and very low turbulence levels in the interior of deep basin. Holtermann et al. (2017) investigated the impact of December 2014 MBI on deepwater properties in the Gotland Basin using one-year observational data covering the inflow phase and the following stagnation period. Time series of vertical distribution of salinity and oxygen concentration allowed to separate three phases within the 5 month period starting from the end of February: (1) near-bottom propagation of saltier and moderately oxic waters, likely water masses displaced from the Bornholm Basin by the main inflow, gradually filling the 70–80 m thick near-bottom layer, (2) the main inflow pulse (duration 3–4 weeks) which doubled the oxygen concentrations and filled ∼100 m thick layer, and (3) longer period (2.5 months) of oxic intrusions detached from gravity current at intermediate depth which imported the amount of oxygen comparable with the contribution of the main inflow pulse.

Up to now, a few field observations, focused only on single, separated areas along the pathway from the Gotland Basin to the Gulf of Finland and model simulations are performed. However, investigations of signal propagation and transformation based on field measurements, which would cover the whole pathway from the Gotland Basin to the Northern Baltic Proper and the Gulf of Finland, are missing. The Northern Baltic Proper and the Gulf of Finland are considered as dynamically active regions where wind forcing is an important factor also in the deep layer dynamics. In the Gulf of Finland south-westerly wind forcing causes the reversal of estuarine circulation: surface layer flows into the gulf and deep layer out of the gulf (Elken et al., 2003). In winter (no thermal stratification), the mixing of the whole water column was accompanied by improved oxygen conditions and decreased salinity in the deep layers (Liblik et al., 2013; Lips et al., 2017). Elken et al. (2006) showed that the impact of estuarine circulation reversal extended to the Northern Baltic Proper. Northeasterly and northerly winds support estuarine circulation resulting in transport of saline, hypoxic, and phosphate-rich water from the Northern Baltic Proper to the Gulf of Finland deep layer (Liblik and Lips, 2011; Lips et al., 2017). Thus, the variable wind forcing causes large temporal variations in the deep layer water properties in the Northern Baltic Proper and the Gulf of Finland (Lehtoranta et al., 2017).

The main aim of the present work was to analyze the impact of the recent MBIs in the Northern Baltic Proper and the Gulf of Finland in 2014–2017. The following three main questions were addressed in this study: (1) If and how fast the effect of MBIs can be seen in the pathway from the Gotland Deep to the Gulf of Finland? What is the quantitative impact on heat, salt, and oxygen content in the study area? How and in which layers the signal propagates toward northeast?

DATA AND METHODS

The data analyzed in the present paper were collected in the frame of various national monitoring programs and projects by four institutions: Department of Marine Systems at Tallinn University of Technology in Estonia, Leibniz Institute for Baltic Sea Research in Germany, Swedish Meteorological and Hydrological Institute, and Finnish Meteorological Institute. Available data from research vessel cruises and moored vertical profilers (e.g., Lips et al., 2016) were used. In addition, HELCOM (Helsinki Commission) data (http://ocean.ices.dk/helcom, 31 January 2018) and historical data collected in the Department of Marine Systems were used. CTD (Conductivity, Temperature, Depth) probes with attached oxygen sensor were used to derive Conservative Temperature, Absolute Salinity (Ioc Scor Iapso, 2010) and oxygen profiles. Sensors were regularly calibrated by manufacturers; salinity and oxygen data were also calibrated against water sample analyses. Field measurements and data processing were in accordance with HELCOM Monitoring Manual (http://www.helcom.fi/action-areas/monitoring-and-assessment/manuals-and-guidelines/salinity-and-temperature/; Manual for Marine Monitoring in the COMBINE Programme of HELCOM, 2017). After processing, data were stored as vertical profiles with a step of 1 db. Density is given as potential density anomaly to a reference pressure of 0 db (σ_0; kg m^{-3}).

Vertical sections of monthly mean temperature, salinity, density, and oxygen along the pathway from the Gotland Deep to the Gulf of Finland were calculated using all available profiles for that month from the area marked with the black dashed line (**Figure 1A**). First, all vertical profiles were virtually crosswise placed to the section. Secondly, the distance of profiles from the Gotland Deep (0 km) was calculated. Next, monthly mean profiles were calculated for the horizontal grid of 5 km by averaging measured profiles within 5-km cells and filling empty cells by linear interpolation. Half-year average sections were calculated from the monthly mean fields, and half-year changes were estimated. Also, the half-year mean temperature and salinity in the water column below 80 m depth for the entire section (**Figure 1A**) were calculated. The monthly mean time-series of temperature, salinity, density, and oxygen concentration were calculated for the following six areas: Gotland Deep, Fårö Deep, Northern Deep, Kõpu West, Osmussaar, and Keri (orange boxes, **Figure 1A**) using all profiles from the particular box and month.

To estimate the total half-year mean heat content (relative to 0°C) and salt mass of the deep area (gray area, **Figure 1B**) in the water column below 80 m depth, the half-year mean profiles were extrapolated perpendicular to the section over this area using the bathymetry data with the grid step of 1.5 km (Baltic Sea Hydrographic Commission, 2013). Deeper cells on the perpendicular sections, compared to the depth at the corresponding point of the section, were filled by extrapolation. Total heat and salt content were obtained by integrating over the extrapolated area. The changes of heat content and salt mass in relation to the heat content and salt mass in January–June 2014 were calculated. Similarly, the half-year mean content of heat, salt and oxygen in the water column below 80 m depth were estimated for the following five areas: Eastern Gotland Basin, Fårö Deep, Kõpu West, Osmussaar, and Keri (**Figure 1B**). The changes of the heat, salt and oxygen content in relation to the corresponding values in January–June 2014 were calculated.

There are various hypoxia thresholds across marine benthic organisms (Vaquer-Sunyer and Duarte, 2008). In this study, hypoxia was defined as oxygen concentration <2.9 mg l^{-1} and hypoxic depth as the shallowest depth of a profile, where oxygen is <2.9 mg l^{-1}. Anoxia is defined as oxygen concentration <0.3 mg l^{-1}. Since there were small offsets in various CTD probes, oxygen values <0.3 mg l^{-1} were replaced by <0.0 mg l^{-1} when calculating oxygen content.

For correlation analysis gaps in the measured time-series were filled using linear interpolation.

RESULTS

Deep Layer Temperature, Salinity, Density, and Oxygen Distributions Along the Pathway Eastern Gotland Basin–Gulf of Finland

The thermohaline structure in the Gotland Deep at the beginning of the study period in February–March 2014 was characterized by 60–65 m thick mixed layer and the near-bottom water (at 230 m depth) with temperature, salinity, and potential density anomaly of 6.7°C, 12.2 g kg^{-1}, and 9.5 kg m^{-3}, respectively (**Figures 2a,b**, **3a**). The increase of temperature, salinity and density was continuous from the base of the mixed layer down to the near-bottom layer whereas the sharpest part of the halocline was at the depth range of 70–100 m. It is noteworthy that the halocline, which started at 70 m depth in the most of the section, was found 10 m shallower in the Gulf of Finland. The border of the hypoxic layer (the depth where oxygen falls below 2.9 mg l^{-1}) was located close to 80 m depth in the most of the study area while it was shallower in the easternmost part of the section (**Figure 3b**).

The slightly saltier (12.3 g kg^{-1}) and colder (5.9°C) and therefore denser (9.6 kg m^{-3}) water propagated into the bottom layer of the Gotland Deep by July 2014 (**Figures 2a,b**, **3a**). The changes were likely initiated by weak inflows in from the North Sea in winter 2013/2014 (Naumann et al., submitted). This new water contained also small amounts of oxygen; temporary oxygen concentrations up to 1.6 mg l^{-1} were measured within the near-bottom layer of about 20 m thickness (**Figure 5b**). The isopycnal 9.5 kg m^{-3} was observed 40 m higher, at 200 m depth (**Figure 5a**, gray dashed line). The propagation of new water mass caused the increase of salinity and density in the Fårö Deep (**Figures 3c**, **4c**), Northern Deep and onwards along the section (**Figures 2d**, **3c**). The hypoxic depth located around 70–75 m depth in the Gotland Deep and Fårö Deep area and shallowed starting from the Northern Deep to 65–70 m depth in the Gulf of Finland by July 2014 (**Figure 3d**).

In the Gotland Deep and Fårö Deep, salinity slowly increased, but in the Northern Deep and farther along the section, slightly

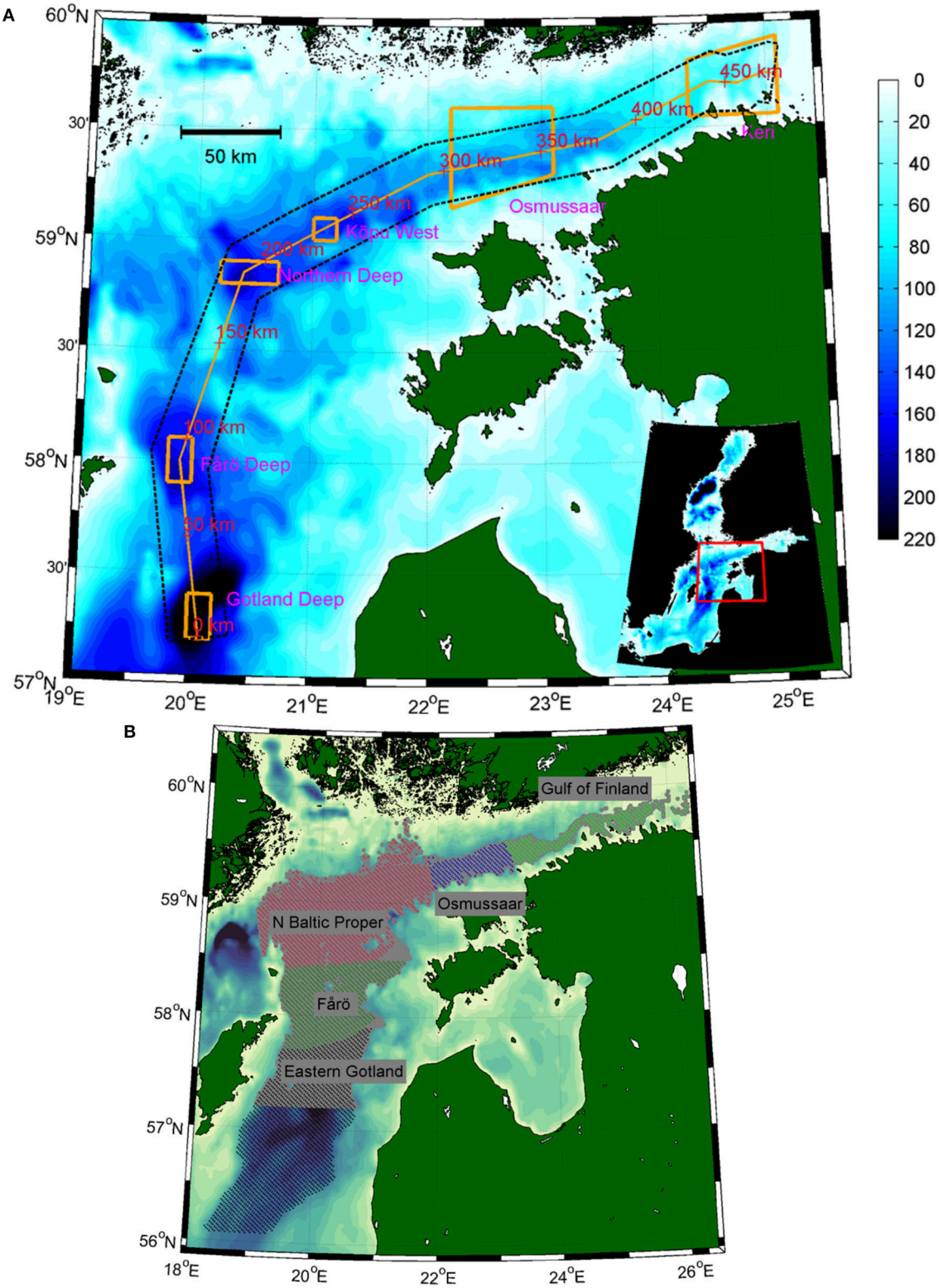


FIGURE 1 | (A) Map of the study area in the Baltic Sea (inlay). Orange line maps the pathway under investigation from the Gotland Deep to the Gulf of Finland. Black dashed lines determine the extent of cross-sections wherefrom data were collected for calculation of monthly mean parameters along the pathway. Orange boxes mark time-series areas Gotland Deep, Fårö Deep, Northern Deep, Kõpu West, Osmussaar, and Keri. Red numbers show the distance from the Gotland Deep along the pathway. **(B)** Map of the basins defined for quantification of the impact of MBIs in the water column below 80 m depth. Gray area marks the basin from the Gotland Deep to the central Gulf of Finland. Following sub-basins are defined: Eastern Gotland Basin, Fårö Basin, Northern Baltic Proper, Osmussaar area, and Gulf of Finland.

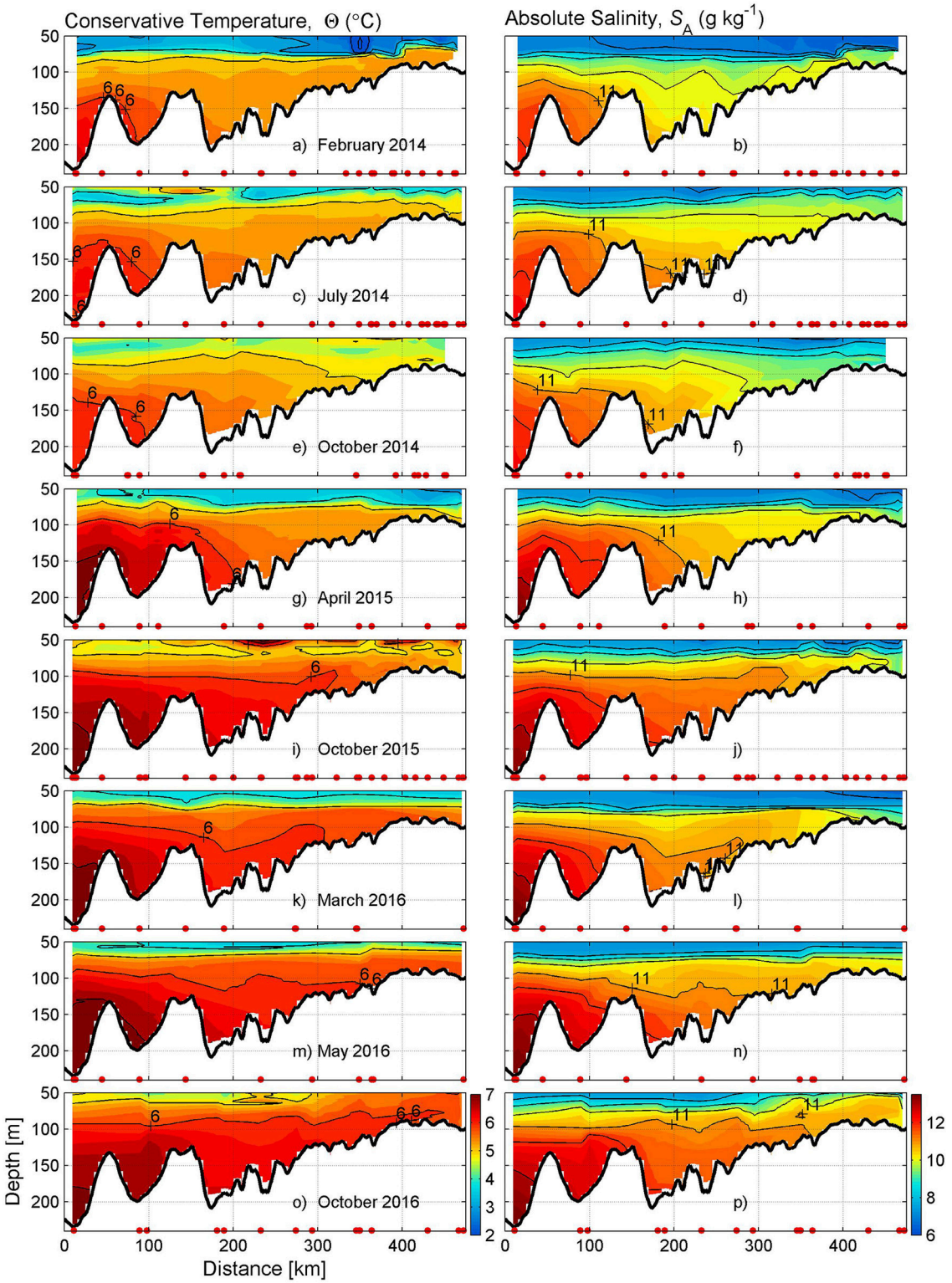


FIGURE 2 | Vertical sections of monthly mean temperature and salinity along the pathway from the Gotland Deep to the Gulf of Finland (see **Figure 1A**) in February 2014 **(a, b)**, July 2014 **(c,d)**, October 2014 **(e, f)**, April 2015 **(g, h)**, October 2015 **(i, j)**, March 2016 **(k, l)**. May 2016 **(m, n)**, October 2016 **(o, p)**. Red dots on x-axis represent the locations of the CTD stations used. Black solid isolines are shown by 1°C and 1 g kg^{-1} step.

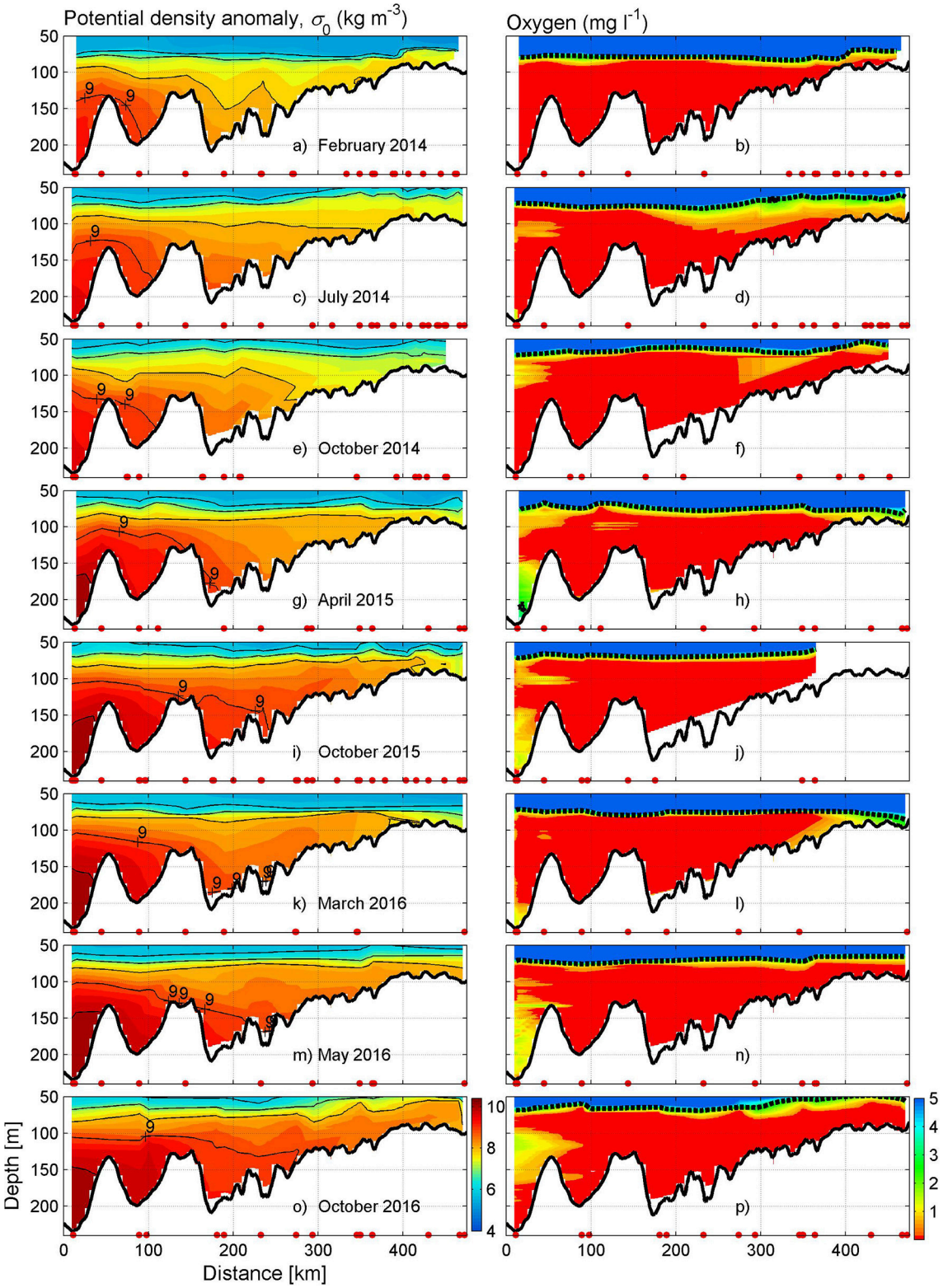


FIGURE 3 | Vertical sections of monthly mean density and oxygen along the pathway from the Gotland Deep to the Gulf of Finland (see **Figure 1A**) in February 2014 **(a, b)**, July 2014 **(c,d)**, October 2014 **(e, f)**, April 2015 **(g, h)**, October 2015 **(i, j)**, March 2016 **(k, l)**, May 2016 **(m, n)**, October 2016 **(o, p)**. Red dots on x-axis represent the locations of the CTD stations used. Black solid isolines are shown on density plots by 1 kg m^{-3} step. Black dashed line (right panels) marks the dissolved oxygen concentration of 2.9 mg l^{-1} (threshold concentration for hypoxia).

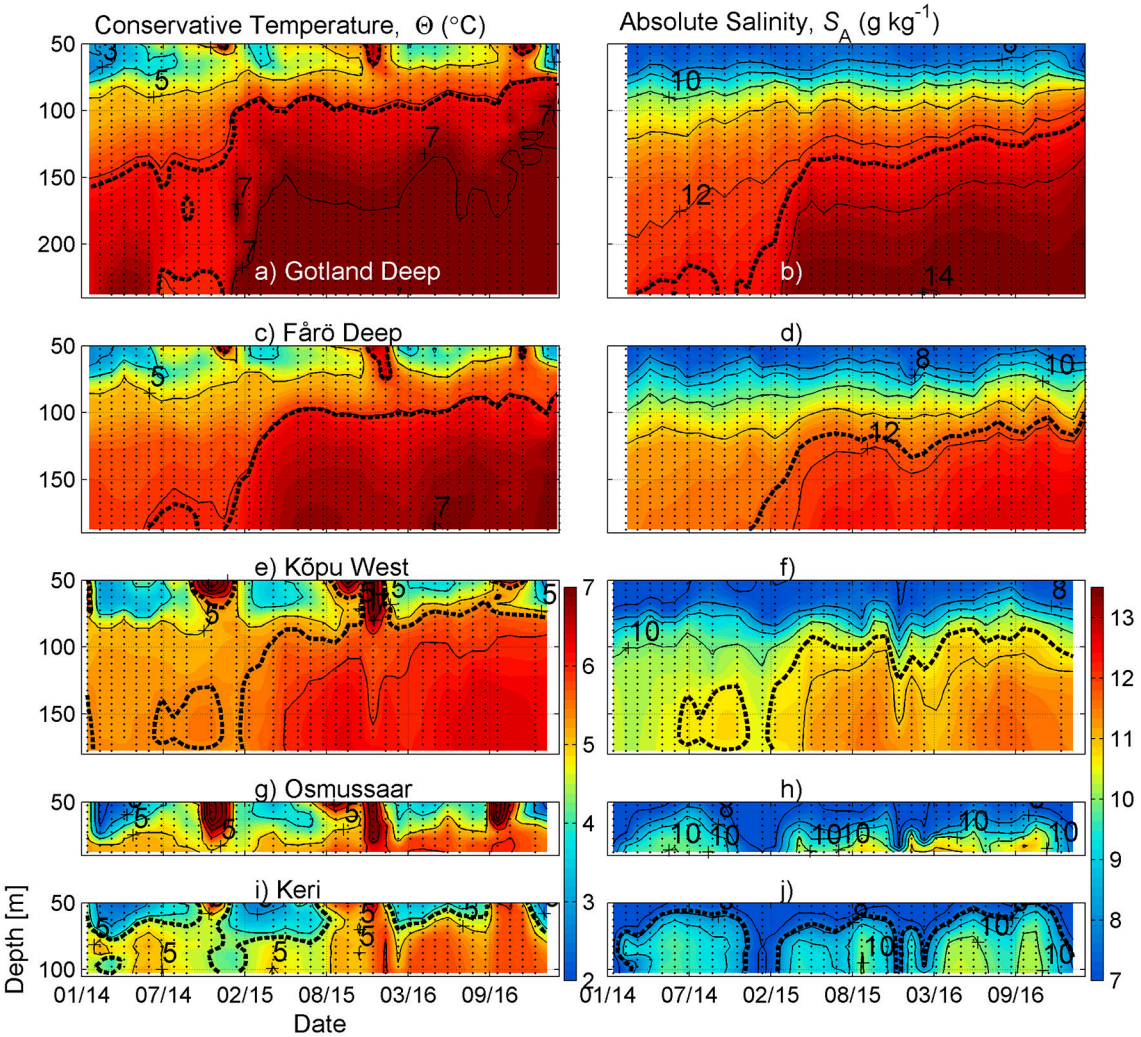


FIGURE 4 | Time-series of monthly mean temperature and salinity in the Gotland Deep **(a, b)**, Fårö Deep **(c, d)**, Kõpu West **(e, f)**, Osmussaar **(g, h)** and Keri area **(i, j)** from January 2014 to March 2017. Black solid isolines are shown by 1°C and 1 g kg^{-1} step. Black dashed lines show the near-bottom water temperature and salinity before the water of MBI in December 2014 arrived to the Gotland Deep. Vertical dashed lines represent the months with available data.

decreased from July to October 2014 (**Figure 2f**). The near-bottom water in the Gotland Deep and Fårö Deep became slightly warmer and saltier by 15 February 2015 (**Figures 2a–d**, **4c,d**) while in the north-eastern Baltic Proper (Kõpu West) and Gulf of Finland (Keri) temporal course was more variable (**Figures 2a–h**, **4g–j**). The small amount of oxygen that was observed in the Gotland Deep in July had disappeared by August 2014.

The arrival of December 2014 inflow water into the Gotland Deep in April 2015 caused a considerable increase of temperature (from 6.1 to 7.1°C), salinity (from 12.5 to 13.6 g kg^{-1}), and density (from 9.6 to 10.6 kg m^{-3}) and upward shift of isolines (**Figures 4a,b**, **5a**). High oxygen concentrations (up to 3.8 mg l^{-1}) were observed in the layer from bottom to 140 m depth (**Figure 5b**). Note that before the oxygenated water intruded, the warmer (7.5°C) water with a very low oxygen concentration was observed in the Gotland Deep in early 2015 (cf. **Figures 4a**, **5a**). Likely, this water was the old anoxic Bornholm basin water. Saltier, warmer, and denser water was also observed in the Fårö Deep and Kõpu West. Note that the increase of these parameters in the Fårö Deep and Kõpu West was much smoother and with a delay compared to the Gotland Deep (**Figure 6**). The increase of temperature, salinity and density along the pathway from Kõpu West to the Gulf of Finland was observed in April and October 2015 (**Figures 2g–j**, **3i**). There was no improvement in oxygen conditions in other basins than the Gotland Deep. Oxygen concentrations dropped close to zero in the near-bottom layer of the Gotland Deep already in September 2015 while in the depth range 170–220 m, relatively high concentrations (>1 mg l^{-1}) remained by the end of 2015.

Two moderate MBIs occurred in November 2015 and January–February 2016 (Naumann et al., submitted). The arrival of saltier and denser water into the Gotland Deep near-bottom layer can be seen in the next two snapshots in March and May 2016 (**Figures 2l,n**, **3k,m**) when salinity increased up to 14.1 g

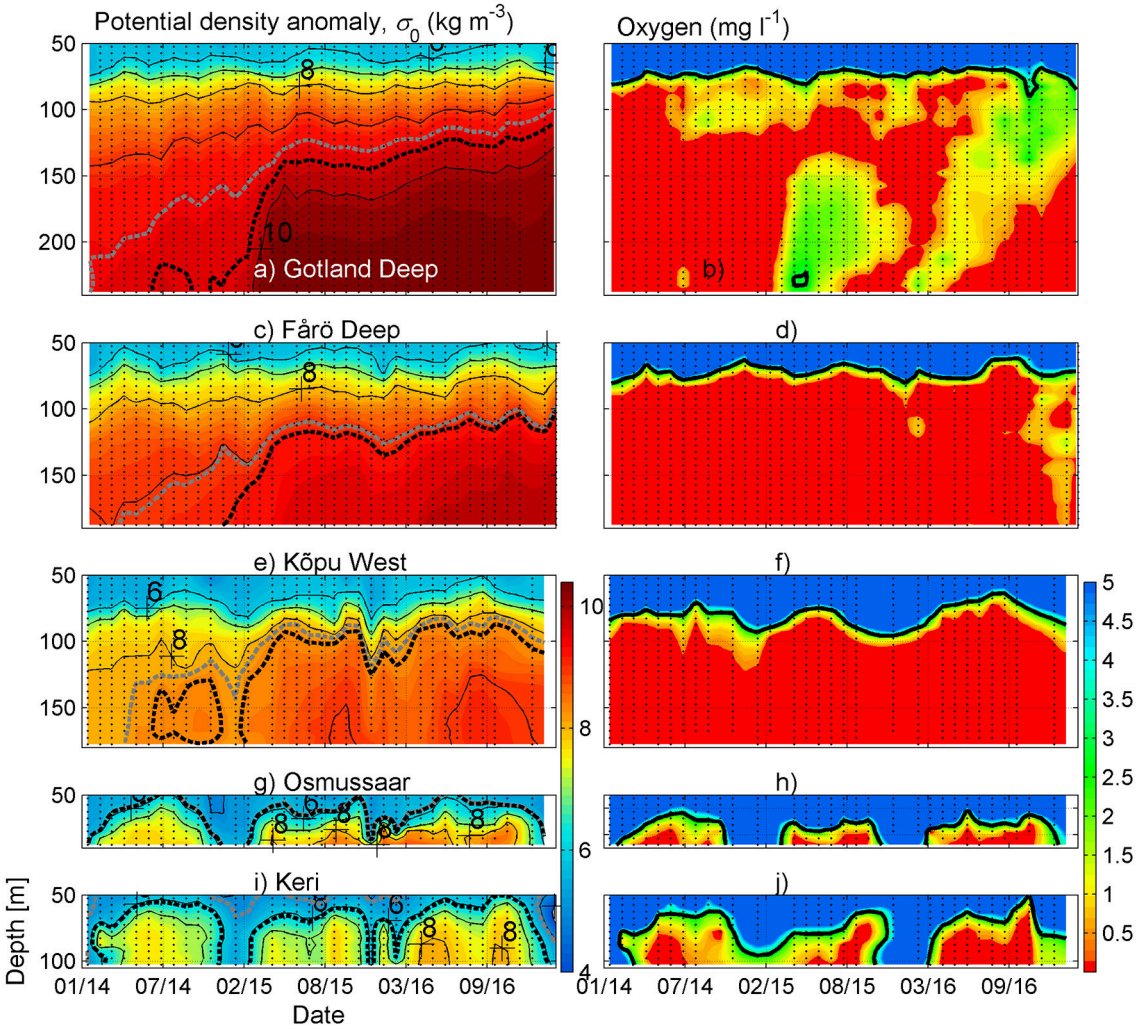


FIGURE 5 | Time-series of monthly mean density and oxygen in the Gotland Deep **(a, b)**, Fårö Deep **(c, d)**, Kõpu West **(e, f)**, Osmussaar **(g, h)** and Keri area **(i, j)** from January 2014 to March 2017. Black dashed lines (left panels) show the near-bottom water density before the water of MBI in December 2014 arrived to the Gotland Deep. Gray dashed lines show density in the beginning of our study period (February 2014). Black solid isolines are shown on density plots by 1 kg m^{-3} step. A black bold line (right panels) marks the dissolved oxygen concentration of 2.9 mg l^{-1} (threshold concentration for hypoxia). Vertical dashed lines represent the months with available data.

kg^{-1}. In the Northern Deep and farther along the pathway, first salinity decreased in the deep layer while temperature increased along the whole section (**Figures 2k,l**). By May 2016, an increase in deep layer temperature and salinity was observed along the whole pathway (**Figures 2m,n**). The Gotland Deep was occupied by oxygenated water from bottom to 130–140 m depth while the Fårö Deep had received some denser water with very low oxygen concentration (**Figures 3c,n**). Oxygen concentration in the near-bottom layer of the Gotland Deep reached to about 2 mg l^{-1}. Last snapshot in October 2016 showed the lack of oxygen again in the depth range of 170–240 m in the Gotland Deep while within the layer above (up to 90 m depth) low oxygen concentrations were detected (**Figure 3p**). No oxygen was observed in the deep basins toward the north from Gotland Deep. A remarkably thick hypoxic layer with the upper border at 50–55 m depth was found in the Gulf of Finland in October 2016 (**Figure 4h**).

Several pulses of increased oxygen concentration were observed in the depth range of 80–120 m in the Gotland Deep likely caused by transport of oxygen from the SW Baltic (**Figure 5b**). Due to the lower density of these waters, they spread above the denser deeper layers. A relatively thick oxygenated layer was observed down to 160–170 m depth in the Gotland Deep from summer to winter 2016 (**Figure 5b**). Unlike to the previous mid-layer oxygen pulses in the Gotland Deep, the sign of the lateral oxygen transport was observed in autumn 2016/17 also in the Fårö Deep (**Figure 5d**). Oxygen was also observed in the lower layers of the Fårö Deep in February 2017 (**Figure 5d**).

Note that the temporal variability of temperature, salinity and density in the deep layers of Kõpu West and particularly in the Osmussaar and Keri area was high and likely influenced by MBI events and estuarine circulation reversals forced by local wind (**Figures 2a–p**, **3a–p**, **4e,g,i**). Despite high variability, the Gulf of

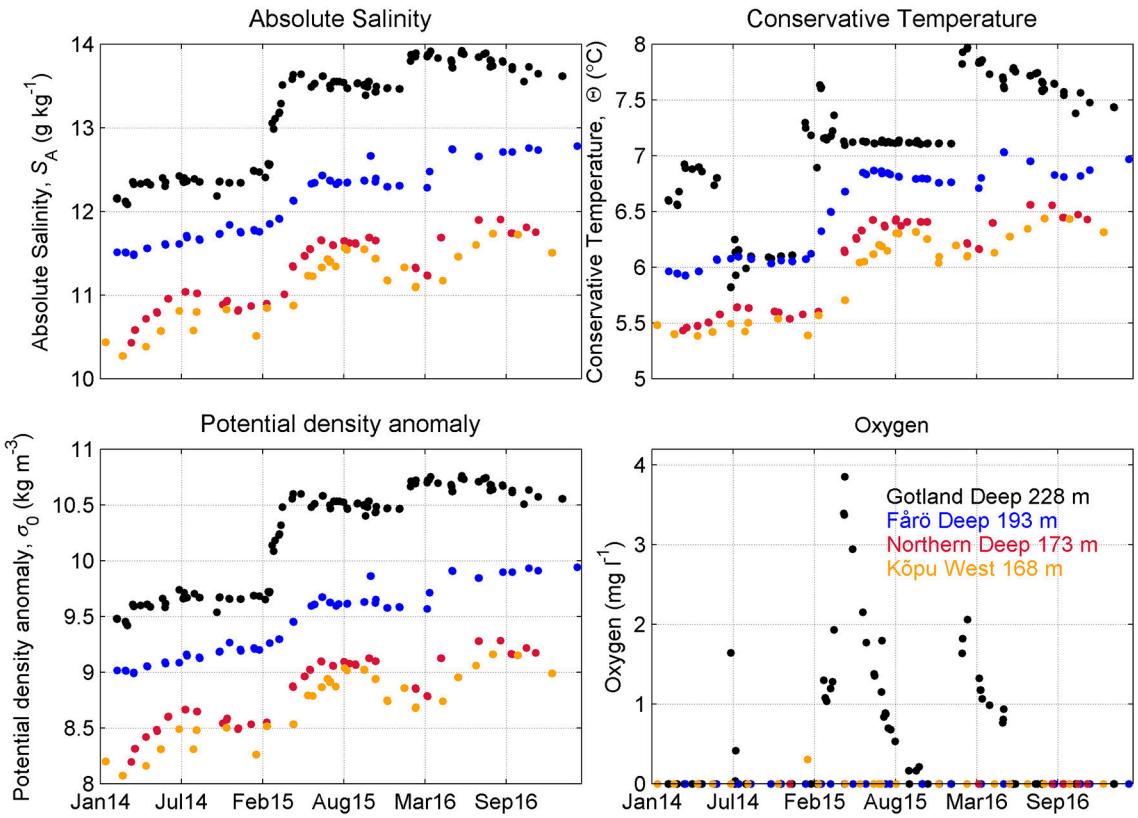


FIGURE 6 | Time series of temperature, salinity, potential density anomaly and oxygen concentration in the near-bottom layers of the Gotland Deep, Fårö Deep, Northern Deep and Kõpu West. The daily mean was calculated when there was more than one CTD cast. The depths was chosen according to the amount of available data. It means, in some cases occasional deeper measurements might show slightly higher values. For example, the highest salinity during the study period, 14.1 g kg^{-1} was observed in the Gotland Deep at 235 m depth on 16 February 2016.

Finland deep layer has been warmer and saltier in the second half of the study period. Gulf of Finland deep layer remained hypoxic most of the time (**Figure 5j**). Only occasional estuarine circulation reversal events during winters (e.g., two events in winter 2013/14, see Lips et al., 2017) temporarily (1–1.5 month) improved oxygen conditions there.

Progress of Sub-halocline Advection Along the Section

In order to assess propagation and transformation of the MBI water, we evaluated the changes in water characteristics at sills and deep basins: Gotland Deep, Fårö Deep, Northern Deep, Kõpu West, and Kõpu North. We assume that if there is a change to saltier and denser water in the deep basin, this water has to come over the previous sill along the pathway from south to north. As temporal data coverage at sills is sparse, we compare the monthly average values in the deepest part of a basin with the monthly average values from the preceding deep basin at the sill depth. For example, we compare the deepest available measurements (at 192.5 m) in the Fårö Deep with the data in the Gotland Deep at 137.5 m depth, which is the sill depth between the Gotland Deep and the Fårö Deep. If there is a correlation between the two time-series, one can expect lateral water renewal in the near bottom layer of the basin.

Baltic Proper

Salinity and temperature time-series follow each other closely (correlation coefficient $r = 0.98$ for salinity and $r = 0.94$ for temperature; $p < 0.01$) in the Fårö Deep at 192.5 m and the Gotland Deep at 137.5 m depth, the latter corresponding to the sill depth between the Gotland Deep and the Fårö Deep (**Figures 7a,b**). A smooth increase in temperature and salinity and associated 20 m uplift of the halocline was observed from February 2014 to February 2015. In spring 2015, a rapid increase in temperature and salinity occurred due to the uplift of old Gotland Deep near-bottom water caused by the arrival of December 2014 MBI water into the near bottom layer. One can note that the TS-characteristics of the near-bottom waters in the Gotland Deep and the Fårö Deep coincided with a time lag of more than 1 year (**Figure 8**), i.e., the early 2014 Gotland Deep near-bottom water reached the Fårö Deep in May–June 2015 as an effect of the December 2014 MBI. Interestingly, there is no signature of the summer 2014 cold Gotland Deep near-bottom water in the Fårö Deep. The Fårö Deep near-bottom layer received even more saline water in April–May 2016. It

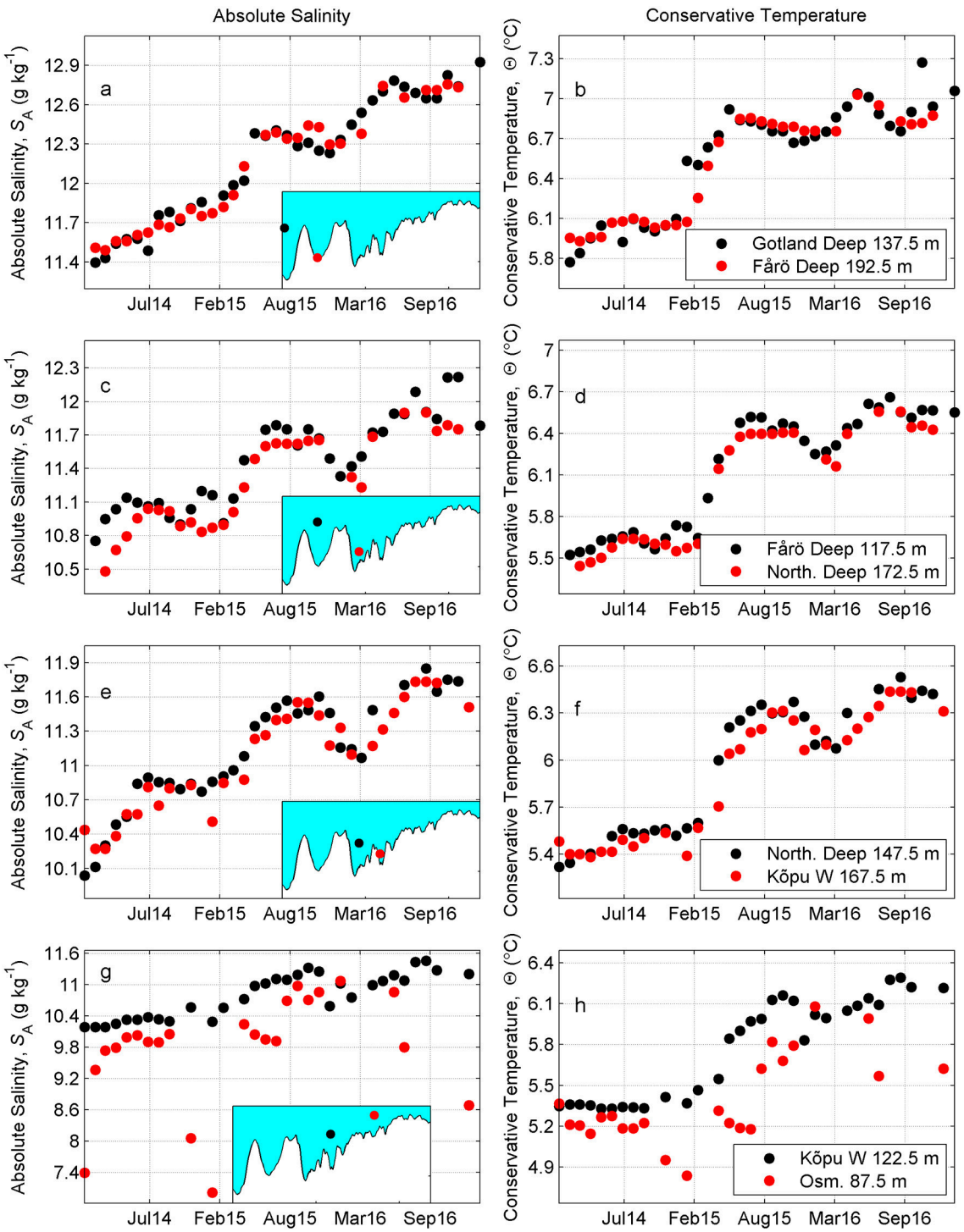


FIGURE 7 | Temporal course of monthly averaged salinity and temperature at the selected depths along pathway in the Gotland Deep **(a, b)**, Fårö Deep **(a-d)**, Northern Deep **(c-f)**, Kõpu West **(e-h)**, and Osmussaar **(g,h)**.

coincides with the arrival of the next MBI water (November 2015 and January–February 2016) to the Gotland Deep. Thus, another uplift of isopycnals in the Gotland Deep caused an overflow of denser water to the Fårö Deep. Water, which arrived to the near-bottom layer of the Fårö Deep in spring 2016 was saltier and denser than the Gotland Deep near-bottom water before the MBI in December 2014. This means that since spring 2016 the near-bottom layer of the Fårö Deep also consisted of water

that originated from the MBIs (or the Bornholm Basin). The TS-diagram suggests that since spring 2016, the Fårö Deep water contained about 2/3 of the early 2014 Gotland Deep water and 1/3 of the December 2014 MBI water. The December 2014 MBI water in the Gotland Basin was already depleted of oxygen by the end of 2016 (**Figure 5b**). Therefore, no oxygen import into the near-bottom layer of the Fårö Deep was observed.

Next, we compare salinity and temperature time series of the Northern Deep at 172.5 m and Fårö Deep at 117.5 m depth, which is the sill depth between these basins (**Figures 7c,d**). Despite the relatively long distance between the locations (100 km), concurrence is good ($r = 0.93$ for salinity and $r = 0.99$ for temperature; $p < 0.01$). Two salinity and temperature increase events in early summer 2015 and spring/summer 2016, likely as reactions to MBIs, can be detected. Also, one can see an increase in salinity from the beginning of 2014 until July 2014, likely related to the slow upward movement of the halocline in the Fårö Deep. The uplift was only 10 m during half a year, but due to the strong vertical salinity gradient at the sill depth, it was enough to increase salinity by 0.5 g kg^{-1} in the deep layers of the Northern Deep.

Water in the Northern Deep was already slightly saltier and clearly warmer in June 2015 than in the Fårö Deep before December 2014 MBI (**Figures 7c,d**). Thus, the water in the Northern Deep in June 2015 could not be purely uplifted old Fårö Deep water transported over the sill. Moreover, the CTD profiles collected prior to the MBIs showed that such water, which together with the Fårö Deep water could form the Northern Deep near-bottom layer water in June 2015, could not be found in the study area. Water with similar properties appeared in the Gotland Deep at 110–120 m depth in January 2015 and the Fårö Deep at the same depth range (110–120 m) in April–May 2015. The inspection of TS-diagrams (**Figure 8**) suggests that, at first, Fårö Deep was filled with the early 2014 Gotland Deep water. Later the new water with slightly lower density spread over the old denser water, i.e., it did not pass the deepest layers of the Fårö Deep, and reached the deep layers of the Northern Deep. Next increase in salinity and temperature in the near-bottom layer of the Northern Deep occurred from April to July 2016 (**Figure 7**). The salinity and temperature of this water mass were 11.7–11.9 g kg^{-1} and 6.4–6.6°C, respectively; and therefore, it was lighter than the near-bottom water in the Fårö Deep since June 2015. Thus, also the water that arrived in the Northern Deep in April–July 2016 did not spread along the bottom, but was buoyant, when passed the Fårö Basin.

Further along the transect Kõpu West is located in the small trench and is separated from the Northern Deep with the sill of 145–150 m depth. The three events of salinity increase, well correlated ($r = 0.94$ $p < 0.01$) with the course of salinity in the Northern Deep at sill depth were observed in the near-bottom layer of Kõpu West (**Figure 7**). Similarly to the Northern Deep, a salinity increase was observed in the near-bottom layer of Kõpu West during the first half of 2014. The next salinity increase occurred from the middle of February until the middle of August 2015, and the third increase started in March 2016 after a temporary salinity decrease by 0.5 g kg^{-1}. Likewise temperature was well-correlated between 145 and 150 m layer at Northern Deep and Kõpu West ($r = 0.97$, $p < 0.01$). At Osmussaar, the near-bottom salinity generally followed the course of salinity in Kõpu West. However occasionally lower temperatures and salinities can be observed as well, which is likely impact of estuarine circulation reversals in the Gulf of Finland. Latter events reduced the correlation between two time-series ($r = 0.51$ for salinity and $r = 0.76$ for temperature; $p < 0.05$).

Gulf of Finland

Temperature and salinity in the deep layers of the Gulf of Finland had greater variability at monthly to seasonal scale compared to the Northern Baltic Proper. Temperature and salinity in the halocline and deep layer in the Keri area did not exceed 5.3°C and 9.9 g kg^{-1}, respectively, from January 2014 to early August 2015 (**Figures 4g,i,j**). Since the end of August 2015 to mid-September 2015, salinities up to 10.2 g kg^{-1} were observed. Two periods of high salinity (>10 g kg^{-1}) in the near-bottom layer were observed in the Keri area in 2016. In April–May, salinity peaked close to 10.4 g kg^{-1} at the beginning of April and at 10.5 g kg^{-1} in mid-May. At the end of October, salinity reached to 10.77 g kg^{-1}.

There was an accompanying shift to warmer halocline along with the increase in salinity in the deep layer in 2015–2016. The same shift of TS-characteristics in the halocline can be seen in the whole study area (**Figure 9**). Unlike to the Keri area, one can see that the new warm and saltier bottom water appeared first beneath the old colder and fresher near-bottom water in Kõpu West. In monthly average bottom temperature and salinity time series, the penetration of the new water can be seen from June to October 2015 as an increase in temperature and salinity in the near-bottom layer at Kõpu West (**Figures 7**, **9**). The old bottom water was raised up to the depth of 80–90 m (**Figures 4e,f**, **5e,f**) and thus this water was available for penetration to the Gulf of Finland. TS-diagram reveals that the old near-bottom water signature remains at Kõpu West until autumn 2015. Note that the shift to a slightly saltier near-bottom water at Keri area occurred within the same time frame (August 2015). Likely the observed increase in salinity and the uplift of the halocline in the central Gulf of Finland was caused by spreading of the old near-bottom water from the Kõpu West area. This is well-supported by the comparison of TS-diagrams of the two areas—the old Kõpu West water can be the source of the near-bottom water observed at Keri in August 2015 (**Figure 9**). As conclusion, the 2014 December MBI indirectly impacted the Gulf of Finland deep layer waters already 9 months after the MBI occurred. The mean signal propagation speed from entrance of the Baltic to the entrance of the Gulf of Finland would be in the order of 3–5 cm s^{-1}.

In December 2016 very low stratification was observed (**Figure 5**) in the Gulf of Finland indicating the estuarine circulation reversal. The shift to warmer halocline had occurred in January and in spring 2016 high salinities were observed in the deep layer of the gulf. The old waters with their TS-characteristics at Keri and Kõpu West in 2014 (see dots concentrated along the lower line in TS-diagram, **Figure 9**) were not observed there after November 2015. Thus, we can suggest that the waters in the deep

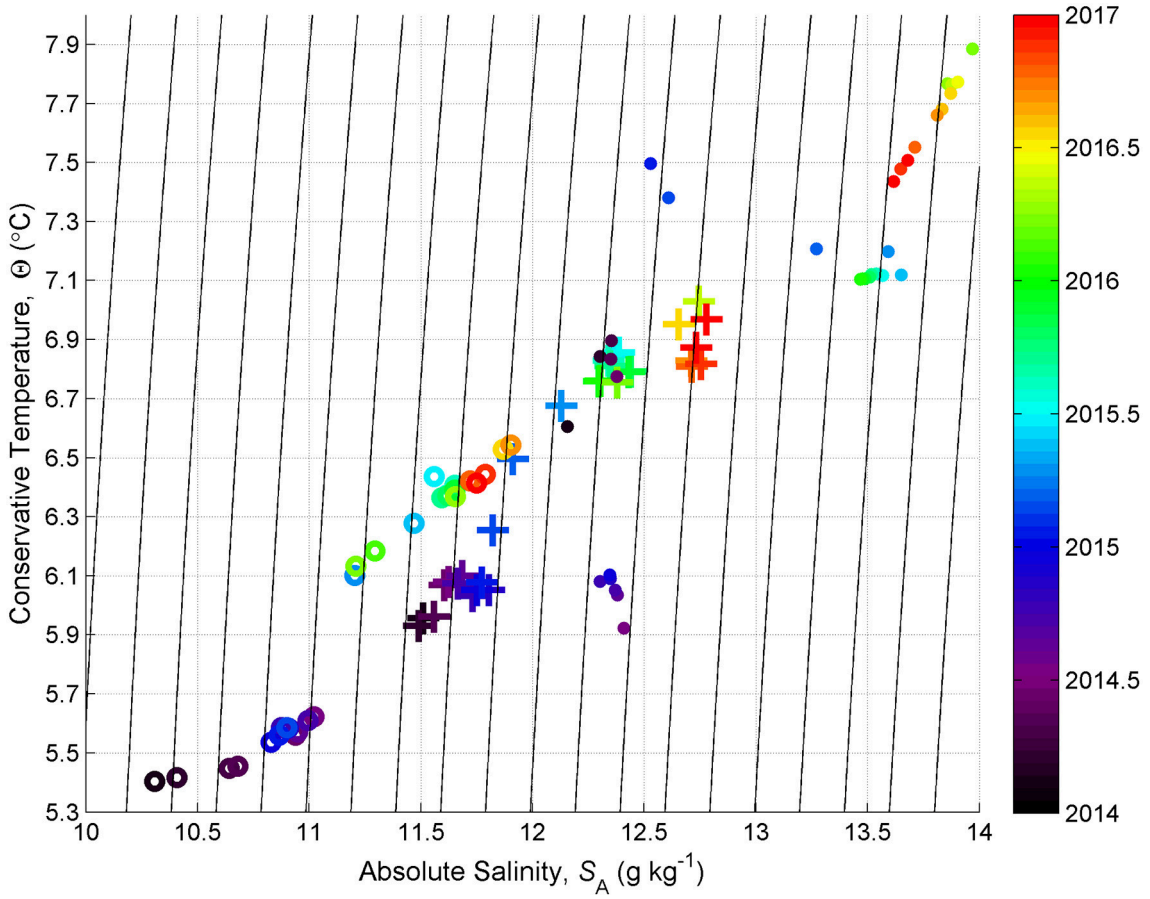


FIGURE 8 | Temporal development of near-bottom temperature-salinity in the Gotland Deep (filled circles), Fårö Deep (crosses), and Northern Deep (circles). Color scale represents time (years).

layer and halocline of the Gulf of Finland were pushed eastward and/or mixed with waters above.

Quantification of MBI Impact

In order to quantify changes in the thermohaline structure, we calculated differences in temperature and salinity along the section below 50 m depth with the 6-month time-span (**Figure 10**). The mean thermohaline fields in January–June 2014 were defined as the initial state. Changes of temperature and salinity in the section were extrapolated across the section to adjacent areas. In this way total changes in heat and salt in the area from Gotland Deep to the Gulf of Finland (gray background area in **Figure 1B**) below 80 m depth were estimated.

To quantify the impact of MBIs on the physical parameters and oxygen content in the water column below 80 m depth on basin scales, half-year changes were calculated for the whole area north from the Gotland Deep and the following sub-basins: Eastern Gotland Basin, Fårö Basin, Northern Baltic Proper, Osmussaar area, and Gulf of Finland (**Figure 1B**).

Rather small salinity changes were observed in the deep layer of the section from January–June to July–December 2014 (**Figure 10**). Strongest temperature decrease occurred in the Gotland Deep due to the arrival of denser and colder water to the bottom layer in July 2014. Increase in temperature and salinity was observed at 50–75 m depth due to the uplift of halocline. Warmer and saltier water was observed in the southern half of the section in January–June 2015. This was caused by the December 2014 MBI, concurrent uplift of isolines, and arrival of warm waters to mid-layer. Contrary, colder, and less saline deep layer was observed on the northern side of the section as a result of deeper halocline. The next half-year steps show a clear increasing tendency both in temperature and salinity. Thus, the difference in temperature and salinity between initial state (January–June 2014) to July–December 2016 show clearly higher values of salinity and temperature in the whole section.

The overall temperature and salinity increase in the area below 80 m depth from January–June 2014 to July–December 2016 was in the order of 1°C and 1 g kg^{-1}, respectively. This corresponds to the increase of 3.7×10^{18} J in heat and 1.06×10^{9} t in salt content in the whole area (**Table A1** in **Appendix**). The largest increase occurred in the period January–June 2015.

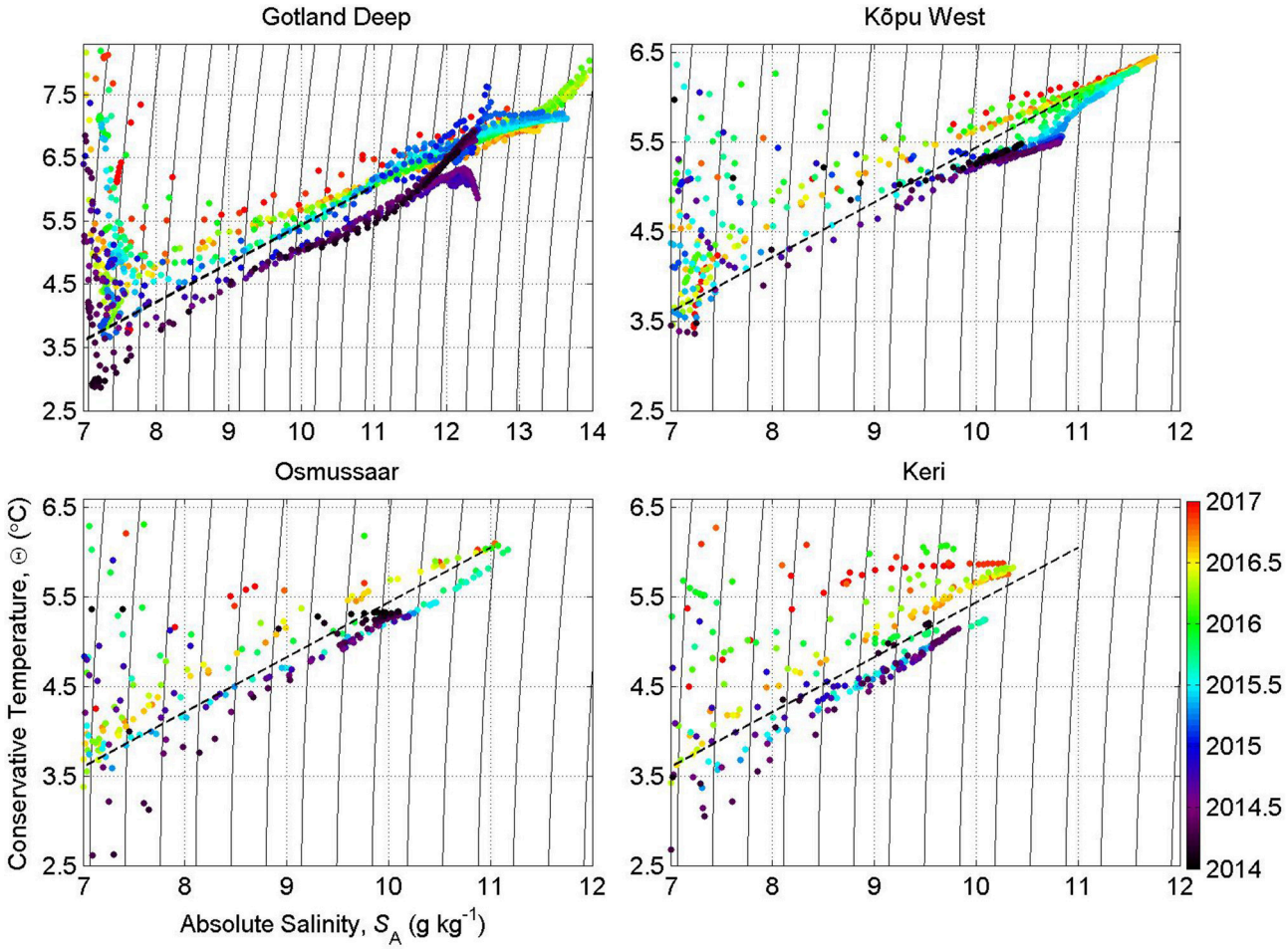


FIGURE 9 | Temporal development of temperature-salinity in the Gotland Deep, Kõpu West, Osmussaar, and Gulf of Finland (Keri). Color scale represents years. Black dashed line was added to make data in subplots better comparable. Note that limits of y-axis are different for the Gotland Deep subplot and rest of the time-series.

Heat and salt content in the Eastern Gotland Basin, Fårö Deep, and Northern Baltic Proper gradually increased in the layer below 80 m depth during 2014–2016 while the largest increase was in the Eastern Gotland Basin (**Table 1**). The heat content increase per unit volume was 4.25 × 10^{15} J km^{-3} in the Eastern Gotland Basin, 3.81 × 10^{15} J km^{-3} in the Fårö Deep, 3.29 × 10^{15} J km^{-3} in the Northern Baltic Proper, and 1.81 10^{15} J km^{-3} in the Osmussaar area by the end of study period. The salt content increase per unit volume was 11.44 × 10^5, 10.22 × 10^5, 10.50 × 10^5 t km^{-3}, and 5.75 × 10^5 t km^{-3}, respectively. It is noteworthy that contribution of >130 m layer to the total change from 80 m to bottom in the Eastern Gotland Basin, Fårö Deep, and Northern Baltic Proper were 18–24% for heat and 21–32% for salt. This share is roughly in accordance with the hypsographic curve of the area, which means that the increase in salinity and temperature was vertically rather even (**Figure 10**). By the end of study period, heat content increased up to 2.38 × 10^{15} J km^{-3} and salt content up to 5.81 × 10^5 t km^{-3} in the Gulf of Finland.

Changes in the oxygen content, compared to January–June 2014 were different in the five basins (**Table 1**). The Eastern Gotland Basin experienced an increase (although variable) in oxygen content compared to the reference state. Note that the highest increase of oxygen content (11.39 × 10^5 t) was found for the last period, July–December 2016, when the deepest layer of the basin was already out of oxygen, but relatively high oxygen concentrations were detected in the depths range 80–160 m (**Figure 5b**). Changes were rather small and variable in the Fårö Deep. Oxygen content was less than the reference state until January–June 2016, and after that, a small increase was observed. In the Northern Baltic Proper, an increase of oxygen mass was estimated until July–December 2015 due to deeper than 80 m oxycline. However, in the layer from 130 m depth to bottom, no significant increase in oxygen content was detected in the Northern Baltic Proper and Fårö Deep. In the Osmussaar area the lower oxygen values were observed in the second half of the study period. In the Gulf of Finland, there is a clear tendency whereby clearly lower oxygen values occur in the deep layer in the second half of the season. The lowest content, −19.47 ×

TABLE 1 | Changes in heat content (ΔQ_a, 10^{18} J), heat content per volume ($\Delta Q_a/V$, 10^{15} J km^{-3}), salt mass (ΔM_a, 10^8 t), salt mass per volume ($\Delta M_a/V$, 10^5 t km^{-3}), oxygen content (ΔO_a 10^5 t), and oxygen content per volume ($\Delta O_a/V$ 10^2 t km^{-3}) in the water column below 80 m depth in the Eastern Gotland Basin, Fårö Deep, Northern Baltic Proper, Osmussaar area, and Gulf of Finland area (**Figure 1B**) in relation to the heat content, salt mass, and oxygen content in January–June 2014.

	Eastern Gotland Basin		Fårö Deep		Northern Baltic Proper		Osmussaar		Gulf of Finland	
Heat content change	ΔQ_a	$\Delta Q_a/V$	ΔQ_a	$\Delta Q_a/V$	ΔQ_a	$\Delta Q_a/V$	ΔQ_a	$\Delta Q_a/V$	ΔQ_a	$\Delta Q_a/V$
Jan–Jun 2014	0.00	0.00	0.00	0.00	0.00	0.00	0.000	0.00	0.000	0.00
Jul–Dec 2014	0.39	0.47	0.00	−0.02	0.01	0.02	−0.015	−0.39	−0.022	−1.11
Jan–Jun 2015	2.76	3.31	0.40	1.61	0.52	1.09	−0.017	−0.46	−0.018	−0.90
Jul–Dec 2015	2.98	3.57	0.70	2.84	1.01	2.14	0.062	1.64	0.006	0.30
Jan–Jun 2016	3.26	3.90	0.72	2.93	1.32	2.78	0.118	3.13	0.043	2.21
Jul–Dec 2016	3.55	4.25	0.93	3.81	1.56	3.29	0.068	1.81	0.047	2.38
Salt mass change	ΔM_a	$\Delta M_a/V$	ΔM_a	$\Delta M_a/V$	ΔM_a	$\Delta M_a/V$	ΔM_a	$\Delta M_a/V$	ΔM_a	$\Delta M_a/V$
Jan–Jun 2014	0.00	0.00	0.00	0.00	0.00	0.00	0.000	0.000	0.000	0.00
Jul–Dec 2014	2.19	2.62	0.05	0.21	0.97	2.05	−0.018	−0.482	0.021	1.08
Jan–Jun 2015	5.34	6.39	0.82	3.36	1.74	3.66	−0.079	−2.100	−0.006	−0.30
Jul–Dec 2015	6.92	8.29	1.59	6.48	2.44	5.13	0.426	11.288	0.080	4.08
Jan–Jun 2016	7.95	9.53	1.28	5.23	3.55	7.48	0.524	13.892	0.052	2.68
Jul–Dec 2016	9.55	11.44	2.50	10.22	4.99	10.50	0.217	5.745	0.114	5.81
Oxygen mass change	ΔO_a	$\Delta O_a/V$	ΔO_a	$\Delta O_a/V$	ΔO_a	$\Delta O_a/V$	ΔO_a	$\Delta O_a/V$	ΔO_a	$\Delta O_a/V$
Jan–Jun 2014	0.00	0.00	0.00	0.00	0.00	0.00	0.00	0.00	0.000	0.00
Jul–Dec 2014	3.09	3.71	−0.12	−0.49	1.13	2.38	0.06	1.67	−0.267	−13.69
Jan–Jun 2015	4.01	4.80	−0.20	−0.80	2.43	5.11	0.40	10.71	−0.041	−2.11
Jul–Dec 2015	3.14	3.77	−0.13	−0.52	4.11	8.65	−0.46	−12.08	−0.252	−12.88
Jan–Jun 2016	2.49	2.98	0.36	1.49	0.03	0.06	−0.50	−13.25	0.034	1.76
Jul–Dec 2016	11.39	13.64	0.31	1.25	−1.55	−3.26	−0.43	−11.53	−0.380	−19.47

Changes are calculated for the whole volume of the basins and a unit volume.

10^5 t km^{-3} from the initial state, were found in July–December 2016.

DISCUSSION

An international measurement campaign was conducted to capture the impact of the recent MBIs and signal propagation from the Gotland Deep toward the Gulf of Finland. The water column from the bottom to the halocline in the area from the Gotland Deep to the Gulf of Finland has become warmer and saltier in the order of 1°C and 1 g kg^{-1}, respectively, after the recent MBI activity since December 2014.

Oxygen appeared in the deep layers of the Gotland Deep in spring 2015, and another pulse was registered in February 2016. Some oxygen intrusions probably arrived in the Gotland Deep before the MBIs, as H_2S concentrations started to decrease there already in February 2015 (Holtermann et al., 2017). Oxygen disappeared from the near-bottom layer after 3–6 months due to high consumption. Several pulses of oxygen were observed in the sub-halocline layers of the Gotland Deep, particularly thick layer with relatively high oxygen levels down to 160 m depth was found there since summer 2016. Although this layer in the Gotland Deep feeds the deep layer of the Fårö Deep, only low amount of oxygen was detected in the Fårö Deep in February 2017. Oxygen content rather decreased in the Northern Baltic Proper and the Gulf of Finland during the study period 2014–2016 due to shallower halocline and hypoxic depth. Unusually high bottom layer salinities and thick hypoxic bottom layer were observed in the Gulf of Finland in 2016. This result is in line with the tendencies after the previous MBIs: stronger stratification and increased hypoxia were observed in the Northeastern Baltic Sea since the mid-1990s (Laine et al., 2007; Liblik and Lips, 2011; Lehtoranta et al., 2017). In the present study, we used only oxygen measurements for the estimates of changes in the oxygen content. The inclusion of H_2S in further studies might reveal more details about the oxygen transport to the Northern Baltic Proper and the Gulf of Finland. A recent study (Kankaanpää and Virtasalo, 2017) shows that H_2S distributions are variable and sensible for physical processes in the Gulf of Finland.

The two occasions of sudden salinity increase in the Gotland Deep in April 2015 (Holtermann et al., 2017) and in February 2016 (**Figure 6**) marked arrivals of the 2014 December (Mohrholz et al., 2015) and 2015 November (Naumann et al., submitted) MBI waters. Another, 2016 January–February MBI did not reach the near bottom layer of the Gotland Deep, as it was not dense enough to replace near-bottom waters from previous MBIs in the Gotland Deep.

The two main near-bottom layer renewal events were also registered in the further basins in the north (**Figure 6**). Salinity peaked at 13.60 g kg^{-1} during the first event and 14.11 g kg^{-1} during the second event in the near-bottom layer of the Gotland Deep. Salinity was last time that high in the Gotland Deep after the 1951 MBI (Fonselius and Valderrama, 2003), which is considered the strongest inflow event in the record from 1880

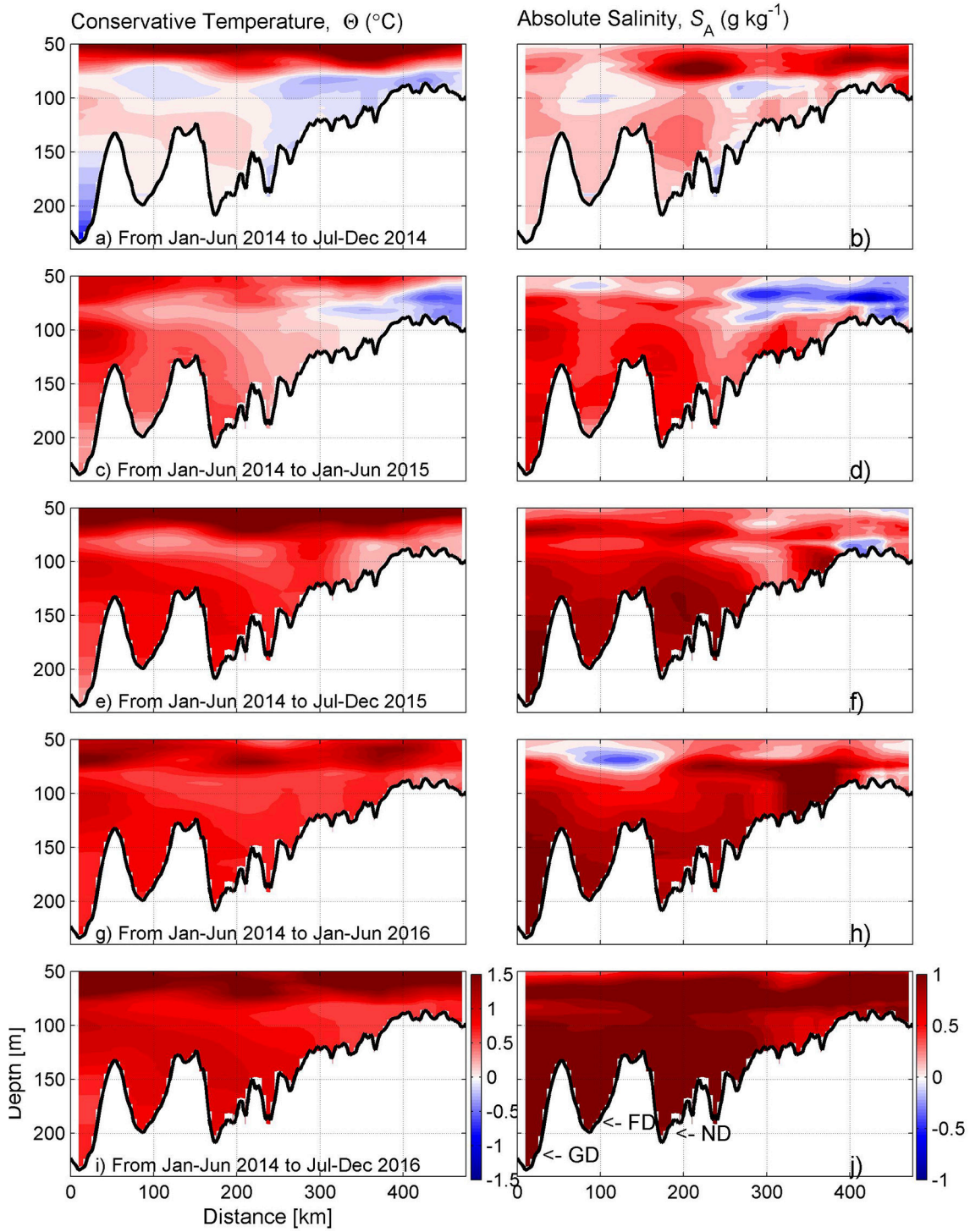


FIGURE 10 | Vertical sections of half-year averaged temperature and salinity changes relative to the mean fields in the period January-June 2014 along the pathway from Gotland Deep to the Gulf of Finland in July-December 2014 **(a, b)**, January-June 2015 **(c, d)**, July-December 2015 **(e, f)**, January-June 2016 **(g, h)**, July-December 2016 **(i, j)**. Locations of the Gotland Deep (GD), Fårö Deep (FD), and Northern Deep (ND) are shown in the lowermost right panel.

(Franck et al., 1987; Matthäus and Franck, 1992; Fischer and Matthäus, 1996; Mohrholz et al., 2015). The highest salinity values during the study period in the near bottom layer of the Fårö Deep (12.79 g kg^{-1}), Northern Deep (11.92 g kg^{-1}), and Northern Baltic Proper (Kõpu West, 11.77 g kg^{-1}) were registered in May 2016, July 2016 and August 2016, respectively.

That high salinity was last time observed in the Fårö Deep during the 1960s while in the Northern Deep and Kõpu West during the 1970s (**Figure 11**). Similar, only slightly lower salinity values were observed in the Northern Deep and Kõpu West during the mid-2000s. Salinity peaked in the Gulf of Finland at 10.77 g kg^{-1} in October 2016, which is the highest value in this area since 1974 (Alenius et al., 1998). The latest period with higher salinities (occasionally >10.5 g kg^{-1}) was observed in the Gulf of Finland in 2006–2008. In conclusion, the highest salinity was observed in the deep layers from the Gotland Deep to the Gulf of Finland in 2016 since last 40–60 years. Exceptionally high salinities comparing to historical records were also observed in the southern basins of the Baltic as consequence of 2014 December MBI (Rak, 2016).

The salinity decline rate in the deep layers of the Gotland Deep has been 1.5 g kg^{-1} during the stagnation period 1983–1993 (Reissmann et al., 2009), 0.6 g kg^{-1} from 1998 to 2002 and 0.7 g kg^{-1} from 2008 to 2014 (**Figure 11**). Therefore, the annual salinity decline in the deep layer of the Gotland Deep has been in the order of 0.12–0.15 g kg^{-1} y^{-1}. Salinity in the near-bottom layer of the Gotland Deep was 13.6 g kg^{-1} at the beginning of 2017. Thus, one might expect that even if further MBIs do not follow, deep layer salinity will not decline back to the early 2014 level (12.2 g kg^{-1}) before 2026–2029 and to pre-1993 MBI (Jakobsen, 1995) level (11.2 g kg^{-1}) not before 2033–2037.

The long-term time-series of the deep layer salinity in the Fårö Deep, Northern Deep, and Kõpu West are generally in good accordance with the Gotland Deep time-series (**Figure 11**). The best correlation between Gotland Deep and Fårö Deep salinity ($r = 0.94$; $p < 0.01$) was found, when the time lag of 3 months was used for Fårö Deep time-series. The best correlation time lags for Northern Deep ($r = 0.89$; $p < 0.01$) and Kõpu West ($r = 0.90$; $p < 0.01$) in respect to Gotland Deep were 3 months and 4 months, respectively. This result is well in accordance with our observations in 2014–2017—salinity increased by a delay of 2–3 months in the Fårö Deep, 3–5 months in the Northern Deep, and 4–6 months in Kõpu West after salinity peaked in the Gotland Deep (**Figure 6**).

The signal in these time-series is more damped and variable, particularly in the Northern Deep and Kõpu West. Moreover, some discrepancies can be found between the Gotland Deep and the other three salinity time-series. Salinity decline during the stagnation periods, first, is slower in the northern areas compared to the Gotland Deep, but after about 4–5 years of stagnation, salinity starts to decrease faster there. Discrepancies are obvious in temperature time-series (**Figure 11**). This result shows that the densest MBI water usually does not reach further from the Gotland Deep. Only several consecutive MBIs can directly reach or control temporal developments in further basins. We observed the 2014 December MBI water that first occupied the near bottom layers of the Gotland Deep in the Fårö Deep after the November 2015 and January–February 2016 MBI waters arrived in the Gotland Deep. Uplifted dense water flowed to the Fårö Deep over the sill as a gravity current. However, the MBI water that occupied the sub-halocline mid-depths in the Gotland Deep can be tracked all the way to the Gulf of Finland. In conclusion, a very strong MBI (Franck et al., 1987) that renews the water column from bottom to the halocline of the Central Baltic Sea also affects the Northern Baltic Sea, including the Gulf of Finland.

We extended the time-series from the near-bottom layer of the Fårö Deep and Gotland Deep at 137.5 m depth, which indicates the sill depth between the two basins (**Figures 7**, **12**). There is a good correlation between two historical time-series ($r = 0.91$ for salinity and $r = 0.96$ for temperature; $p < 0.01$). Coincidence is particularly strong when there is an increase in salinity, which corresponds to the periods where lateral transport of denser water over the sill between the Gotland Deep and Fårö Deep was dominant process. The declining salinity corresponds to the stagnation periods, indicating that lateral transport from the Gotland Deep to the near bottom layer of Fårö Deep did not occur. The near-bottom salinity time-series in **Figure 11** give an impression that changes in the near-bottom layer of the Fårö Deep only occur if there is a water renewal in the near-bottom layer of the Gotland Deep. The question is, do buoyant sub-halocline flows (interleaving currents from the southern Baltic to the Eastern Gotland Basin) impact the Fårö Deep as well? We checked the monthly average density time-series and found that when there was a density rise at least 0.01 kg m^{-3} in the near-bottom layer of the Fårö Deep (the layer from 175 m to bottom was integrated), the rise can also be seen in the same month 50% of cases in the sill layer between the Gotland Deep and Fårö Deep (110–150 m range in the Gotland Deep station data was integrated). The graph (**Figure 12**) suggests that the coincidence is even stronger (more than 50% of cases), but the rough method (long time-step) probably misses some events. Half (52 %) of the density rise cases, which can be simultaneously seen at the sill between the two basins and in the near-bottom layer of the Fårö Deep, can also be detected in the near-bottom layer (220–240 m layer was integrated) of the Gotland deep. This finding suggests that about half of the changes in the near bottom layer of the Fårö Deep are initiated by water renewal in the deepest layer of the Gotland Deep and consequent uplift of isopycnals. The other half are caused by the events, which cannot be seen in the deepest layer of the Gotland Deep, but can be seen in the layers above (integrated layers of 175–200, 150–175, 110–150 were checked). The density rise events occur in groups after MBIs. Thus, even if half of the cases at the sill occur because of interleaving flows, the precondition for these events is often a recent MBI. A richness of intermediate layer intrusions after the recent MBIs was detected by high-resolution observations in the Gotland Deep (Holtermann et al., 2017).

T-S analysis showed that the pre-MBI Fårö Deep bottom water did not contribute to the mixture forming the new bottom water in the Northern Deep. Warm and salty water, which arrived to the deep layers of the Northern Deep in summer 2015 (30 June 2015 profiles in the middle panel in **Figure 13**) appeared in the Gotland Deep area at the depths of 110–120 in early 2015 (10 February and 21 March 2015 profiles in the upper panel in **Figure 13**). A signature of the same warm and salty water mass was detected in the Gulf of Finland in February–March 2016.

We suggest that the MBIs create a pre-condition for the denser water transport and water renewal in the deep layers of the Northern Baltic Proper. First, MBIs create dense enough Gotland and Fårö Deep near-bottom layer, which allows relatively dense

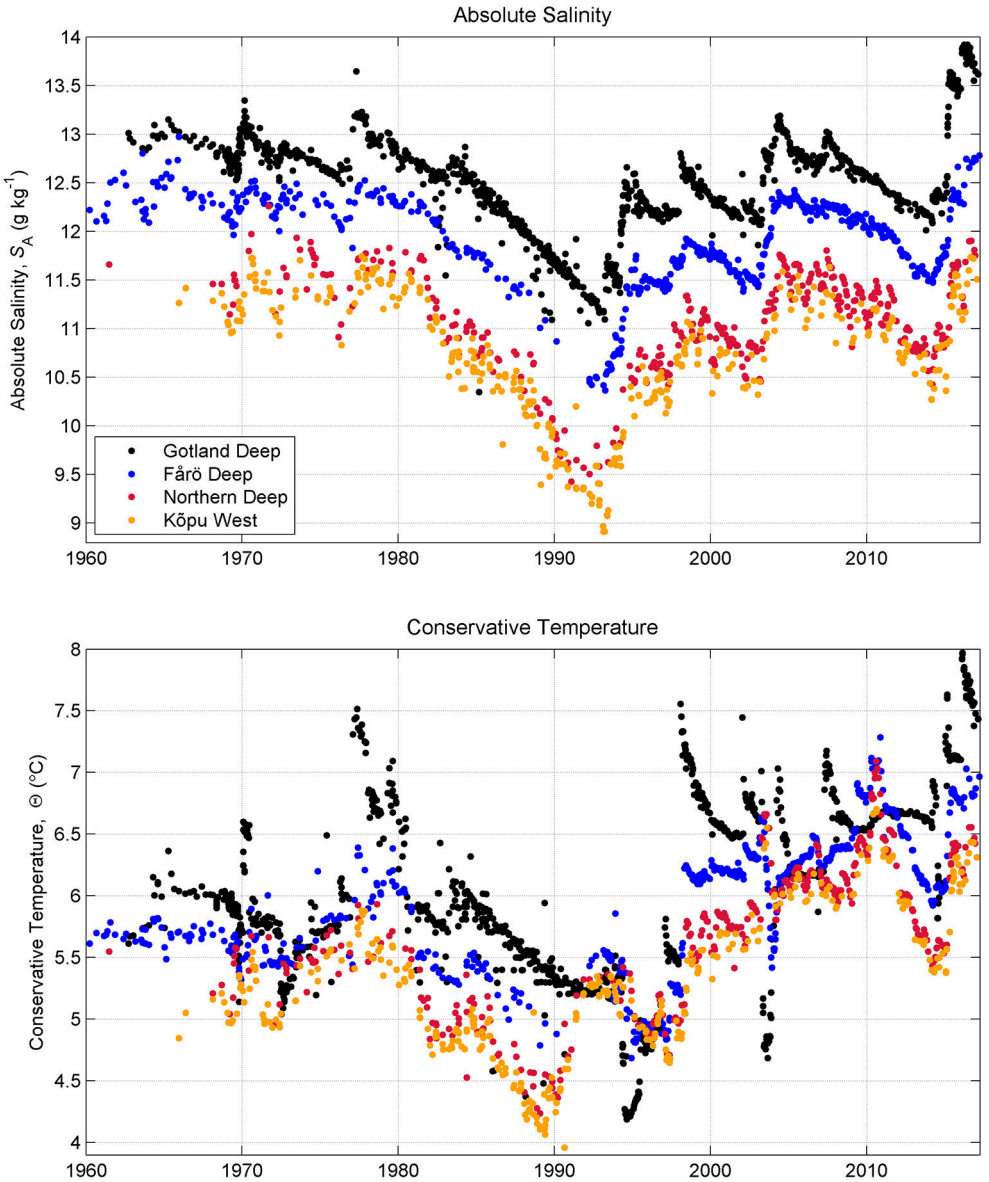


FIGURE 11 | Time series of salinity and temperature in the Gotland Deep (228 m depth), Fårö Deep (193 m depth), Northern Deep (173 m), and Kõpu West (168 m) in 1960–2017. The daily mean was calculated when there was more than one CTD cast available. Note that the deepest bin was chosen at the depth, where enough measurements were available. It means, in some cases, occasional deeper measurements might show slightly higher values. For example, the highest salinity during the study period, 14.1 g kg^{-1}, was observed in the Gotland Deep at 235 m depth on 16 February 2016.

water to pass both deep areas without a bottom touch and arrive in the deep layers of the Northern Deep and further areas. The longer time-series of temperature-salinity in the Gotland Deep at a depth of 117.5 and bottom layer (162.5 m) of the Kõpu West confirm that sub-halocline layer below 100 m in the Central Baltic Proper (Gotland Deep) likely controls the water renewal in the deep layers of the Northern Baltic Proper (**Figure 12**). There is a strong correlation between two time-series (**Figure 12**) – $r = 0.90$ for salinity and $r = 0.94$ for temperature; $p < 0.01$. The best correlation was found, when the time lag of 3–4 months was used for Kõpu West time-series. This result explains why the deep layer salinity decline is slower in the Northern Baltic Proper than in the Gotland Deep during first stagnation years. In the absence of MBIs, there is no import of salt to the deep layers of the Gotland Deep. Contrary, the sub-halocline layer of the Gotland Deep (which is the source for the deep layer water in the Northern Baltic Proper) receives salt from the deeper layers, particularly after MBIs. Secondly, after an MBI relatively dense water can advect from the southern Baltic to the north. Thus, weak barotropic (Sellschopp et al., 2006) or baroclinic inflows (Feistel et al., 2004) from the North Sea that do not affect the bottom layers in the Gotland Deep, might still

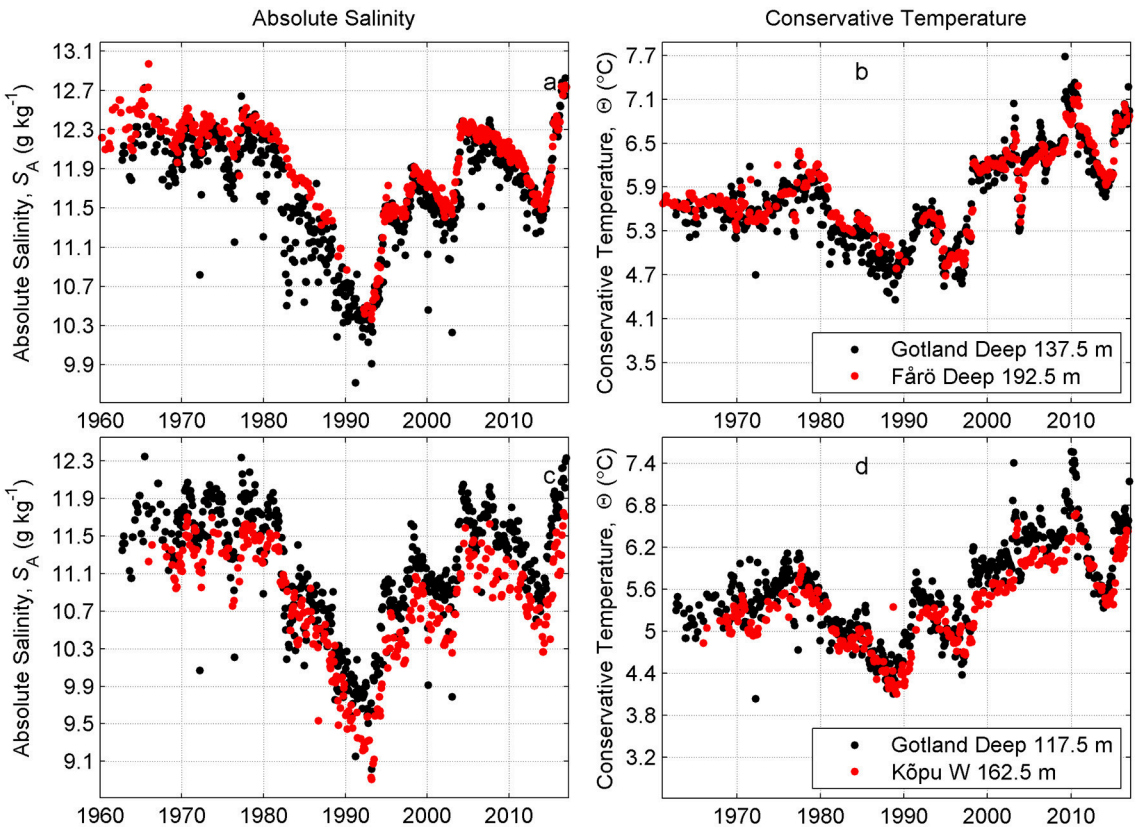


FIGURE 12 | Temporal course of monthly average salinity and temperature at the selected depths along the pathway Gotland Deep **(a-d)**, Fårö Deep **(a, b)**, and Kõpu West **(c, d)** 1960–2016.

impact the sub-halocline layers in the Central Baltic and deep layers further north. This suggestion is supported by a long-term model simulation (1961–2007), which showed that horizontally integrated low-passed northward transport with a maximum at about 100 m depth remarkably increased during MBIs and such high transport values remained in this layer of the Gotland Basin for about 5 years after the MBI (Väli et al., 2013). The further (after 4–5 years of an MBI) acceleration of the salinity decline in the deep layers of the Northern Baltic Proper and sub-halocline layer of the Gotland Deep could be explained by decreased upward vertical flux of salt due to decreased salinity in the deep layer. Secondly, if the halocline gets weaker during the stagnation period, the vertical mixing can reach deeper. Comparison of salinity data in the Gulf of Finland between stagnation period at the end of the 1980s and post-MBI period after the mid-1990s showed a considerable difference in the deep layer, but virtually same values in the cold-intermediate layer, which were explained by deeper winter mixing and concurrent salt flux during stagnation years (Liblik and Lips, 2011). Thus, the vertical flux from the deep layer to the sub-halocline layer is decreasing during the stagnation period while the vertical flux through the halocline remains the same or even increases during the stagnation period.

The first impact of the 2014 December MBI was observed in the Gulf of Finland 9 months after the MBI passed the Danish Straits. The old deep layer in the Northern Baltic Proper was replaced in the bottom layer and pushed upwards to 80–90 m depth by the new warm and salty water that arrived from the Central Baltic. The signs of the old Northern Baltic Proper (Kõpu West) deep water can be first found in the Keri T-S profile in August 2015 (profiles from 27 August 2015 shown in the lowest panel in **Figure 13**). The shift to warmer-saltier deep layer and halocline occurred in the Gulf of Finland in January–March 2016 (profiles from 24 March 2016 in the lowest panel in **Figure 13**).

Strong estuarine circulation event(s) occurred in the Gulf of Finland in December 2015. It can be seen as very weak stratification in **Figure 4i**. The reversal event resulted in a deeper and weaker halocline that can also be seen in the Northern Baltic Proper. Estuarine circulation events can reach the Northern Baltic Proper (Elken et al., 2006) and cause considerable vertical mixing of heat, salt and nutrients (Liblik et al., 2013; Lips et al., 2017). Moreover, strong SW winds that cause reversals (Elken et al., 2003) also induce erosion of the halocline by wind stirring during winters (Lass et al., 2003). The comparison of profiles in the Northern Baltic Proper in November and December 2015 shows that in the latter month the halocline deepened because both its erosion (upward vertical mixing of salt can be seen) and accumulation of the upper layer water (effect of reversal). However, the increase in salinity in the whole layer, particularly in the halocline and deep layer, can be identified in Kõpu West in

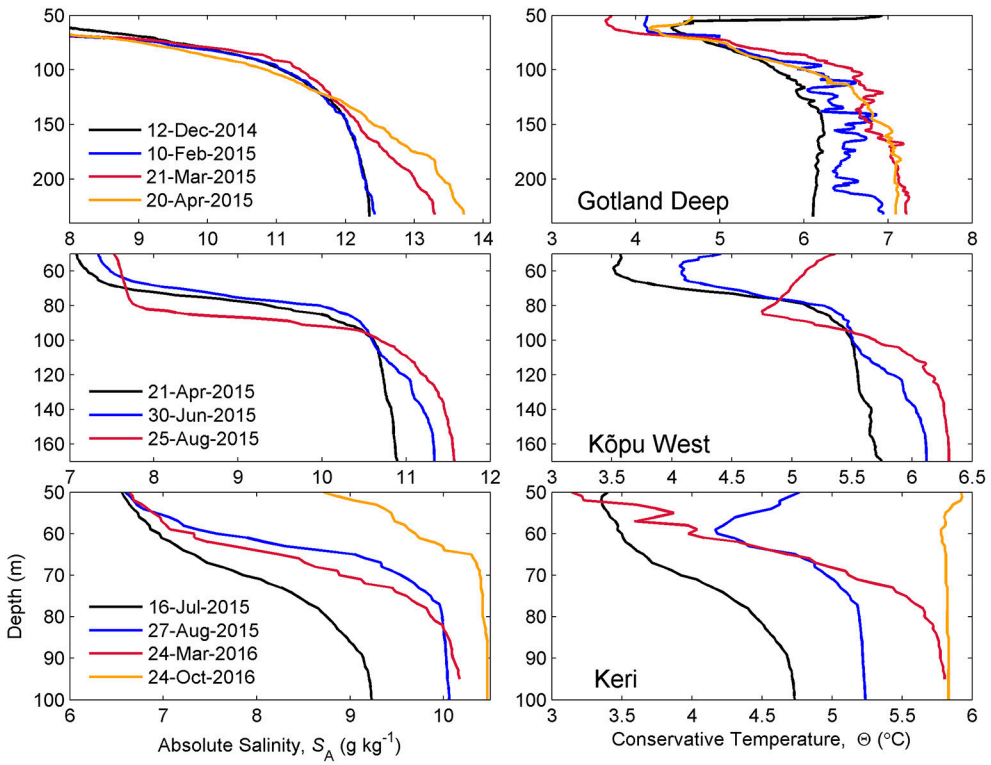


FIGURE 13 | Selected temperature and salinity profiles in the Gotland Deep, Northern Baltic Proper (Kõpu West) and the Gulf of Finland (Keri).

January 2016. The temperature-salinity characteristics of Kõpu West and Gulf of Finland show that the deep layer water that arrived in the latter basin originated from the Kõpu West. Due to sparse data, we cannot determine the exact origin depth, but the T-S diagram suggests it can originate from the deeper part of the halocline (90–100 m) or the layer below. It was suggested that salt wedge that penetrated to the Gulf of Finland in January 2012 originated from the Northern Baltic Proper from the depth of 110–115 m (Liblik et al., 2013). Since the reversal event together with wind stirring eroded only the very upper part of the halocline, but otherwise weakened the halocline and pushed it deeper, one can expect that this reversal event did not evoke, but rather postponed the warmer-saltier water mass arrival to the Gulf of Finland. Therefore, the change of temperature and salinity in the Gulf of Finland was caused by the warmer and saltier water mass that arrived in the sub-halocline layer of the Gotland Deep in early 2015 and later advected to the deep layers of the Northern Baltic Proper. As the new water in the Northern Baltic Proper accumulated from bottom to a certain depth level (110–115 m according to Liblik et al., 2013), it became available for the Gulf of Finland and penetrated there as wind conditions were favorable (Elken et al., 2003).

In summary, the Gulf of Finland receives its deep layer water from the deeper segment of the halocline in the Northern Baltic Proper. The deep layer of the Northern Baltic Proper is determined by the characteristics in the sub-halocline depth range in the Gotland Deep (**Figure 12**). Thus, despite high variability due to estuarine circulation reversals, there must be long-term correlation between the temporal changes in sub-halocline water mass in the Gotland Deep and the deep layer of the Gulf of Finland. Comparison of annual mean temperature and salinity in the depth of 117.5 m in the Gotland Deep and annual maximum in the deep layer of Osmussaar and Keri is shown in **Figure 14.** The annual maximum values, unlike the mean values, do not include such strong effect of circulation reversals. Both compared time-series show reasonable correlation, particularly in the Osmussaar vs. Gotland Deep salinity time-series ($r = 0.90$ for salinity and $r = 0.37$ for temperature; $p < 0.01$). Correlation is weaker, but significant between Keri and Gotland Deep as well ($r = 0.73$ for salinity and $r = 0.56$ for temperature; $p < 0.01$). This result once more supports our conclusion that the characteristics of sub-halocline water mass in the Central Baltic controls not only changes in the deep layer water in the Northern Baltic Proper, but also in the Gulf of Finland.

CONCLUSIONS

Recent MBIs (December 2014, November 2015 and January–February 2016) have caused considerable changes in water column structure in the area from the Gotland Deep to the Gulf of Finland. Overall temperature and salinity increase in the order of 1°C and 1 g kg^{-1} were observed in the deep layers below 80 m depth. Highest salinities since last 40–60 years were observed

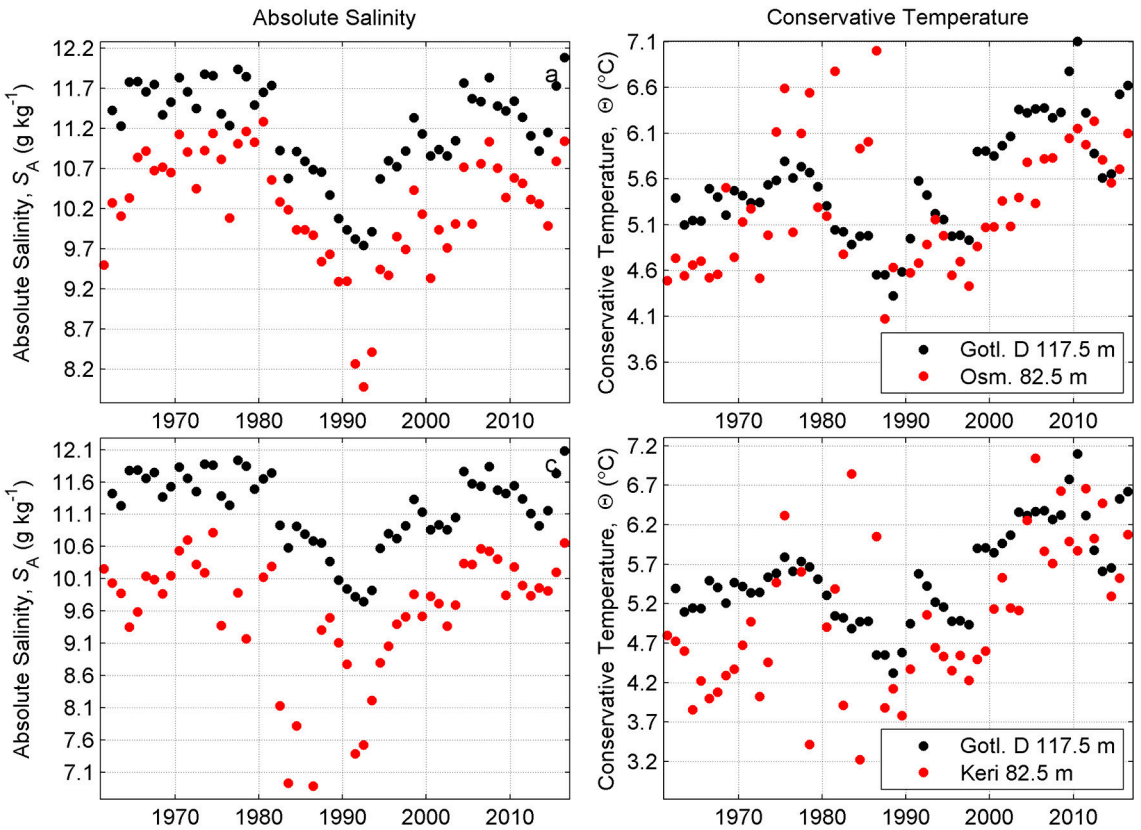


FIGURE 14 | Temporal course of yearly average salinity and temperature at 117.5 depth in the Gotland Deep, and yearly maximum salinity and temperature in the Osmussaar and Keri area.

in the whole study area. Renewal of the deep layer water was observed in the Gotland Deep in April 2015 and February 2016. The fresh oxygen was consumed by 3–6 months in the near-bottom layer. Enhanced lateral import of oxygen was registered in the mid-layer down to 160 m depth in the Gotland Deep since summer 2016. Oxygen appeared in the sub-halocline layer of the Fårö Deep in February 2017 while during the rest of the study period this area remained anoxic. Low oxygen layer thickened in the Norther Baltic Proper and the Gulf of Finland.

The arrival of December 2014 and November 2015 MBIs were detected as clear peaks in salinity and temperature in the near-bottom layers of the Gotland Deep in April 2015 and February 2016. The peaks were also detected in the further basins: in the Fårö Deep by 2–3 months delay, in the Northern Deep by 3–5 month delay, and in the Kõpu West (Northern Baltic Proper) by 4–6 month delay. The time lags were confirmed by correlation analysis of longer time-series. No clear peaks can be detected in the Gulf of Finland, but T-S analysis shows the first impact of MBI as the arrival of forward pushed former Northern Baltic Proper deep layer water in August 2015. The warmer and saltier MBI water arrived in the Gulf of Finland in February–March 2016, i.e., 14–15 months after occurrence of the December 2014 MBI.

Water renewal in the Fårö Deep occurred as gravity current over the sill between Fårö and Gotland Deep. Water that replaced near-bottom waters in the Northern Baltic Proper and in the Gulf of Finland originated from the Eastern Gotland Basin at the depth of 110–120 m. The pre-condition for such sub-halocline advection is dense enough deep layer in the Gotland Deep and the Fårö Deep. Such water renewal regimes in the deep layers of the Fårö Deep, and Northern Baltic Proper and in the Gulf of Finland are supported by long-term time-series.

In conclusion, the warm and salty water from MBIs has influenced the whole area from Gotland Deep to the Gulf of Finland.

AUTHOR CONTRIBUTIONS

TL was responsible for compiling the data, data analyzes, and writing manuscript. MN, PA, and MH were responsible for compilation of data in their institutes. All authors contributed to data collection, processing, and writing of the manuscript.

ACKNOWLEDGMENTS

We would like to thank our colleagues and research vessels crews for performing all measurements. The present work was supported by institutional research funding IUT (IUT19-6) of

the Estonian Ministry of Education and Research. Additional funding we received from the European Union Seventh Framework Programme (FP7/2007-2013) under grant agreement n° 312762 for ship time within EUROFLEETS2 (PROSID2014—Propagation of the saltwater inflow from December 2014). The continuous long-term data acquisition of the Leibniz Institute for Baltic Sea Research and Swedish monitoring programme operated by the Swedish Meteorological and Hydrological Institute contributed with their latest measurements. We thank the areviewers for their careful reading and helpful suggestions.

REFERENCES

Alenius, P., Myrberg, K., and Nekrasov, A. (1998). The physical oceanography of the Gulf of Finland: a review. *Boreal Env. Res.* 3, 97–1205.

Baltic Sea Hydrographic Commission (2013). *Baltic Sea Bathymetry Database version* 0.9.3.

Burchard, H., Lass, H. U., Mohrholz, V., Umlauf, L., Sellschopp, J., Fiekas, V., et al. (2005). Dynamics of medium-intensity dense water plumes in the Arkona Basin, Western Baltic Sea. *Ocean Dynamics* 55, 391–402. doi: 10.1007/s10236-005-0025-2

Conley, D. J., Björck, S., Bonsdorff, E., Carstensen, J., Destouni, G., Gustafsson, B. G., et al. (2009). Hypoxia-related processes in the Baltic Sea. *Environ. Sci. Technol.* 43, 3412–3420. doi: 10.1021/es802762a

Elken, J., Malkki, P., Alenius, P., and Stipa, T. (2006). Large halocline variations in the Northern Baltic Proper and associated meso-and basin-scale processes. *Oceanologia* 48, 91–117.

Elken, J., Raudsepp, U., and Lips, U. (2003). On the estuarine transport reversal in deep layers of the Gulf of Finland. *J. Sea Res.* 49, 267–274. doi: 10.1016/S1385-1101(03)00018-2

Feistel, R., Hagen, E., and Nausch, G. (2006). Unusual Baltic inflow activity in 2002–2003 and varying deep-water properties. *Oceanologia* 48, 21–35.

Feistel, R., Nausch, C., Heene, T., Piechura, J., Hagen, E., and A. F., Feistel, R., et al. (2004). Evidence for a warm water inflow into the Baltic Proper in summer. *Oceanologia* 46, 581–598.

Fischer, H., and Matthäus, W. (1996). The importance of the Drogden Sill in the Sound for major Baltic inflows. *J. Mar. Syst.* 9, 137–157. doi: 10.1016/S0924-7963(96)00046-2

Fonselius, S., and Valderrama, J. (2003). One hundred years of hydrographic measurements in the Baltic Sea. *J. Sea Res.* 49, 229–241. doi: 10.1016/S1385-1101(03)00035-2

Franck, H., Matthäus, H., and Sammler, R. (1987). Major inflows of saline water into the Baltic Sea during the present century. *Gerlands Beitr. Geophys.* 96, 517–531.

Hagen, E., and Feistel, R. (2001). Spreading of baltic deep water: a case study for the Winter 1997-1998. *Meereswiss. Ber.* 45, 99–133.

Hänninen, J., and Vuorinen, I. (2011). Time-varying parameter analysis of the baltic sea freshwater runoffs. *Environ. Model. Assess.* 16, 53–60. doi: 10.1007/s10666-010-9231-5

Holtermann, P. L., Prien, R., Naumann, M., Mohrholz, V., and Umlauf, L. (2017). Deepwater dynamics and mixing processes during a major inflow event in the central Baltic Sea. *J. Geophys. Res. Ocean.* 122, 6648–6667. doi: 10.1002/2017JC013050

Ioc Scor and Iapso (2010). The international thermodynamic equation of seawater – 2010: Calculation and use of thermodynamic properties. *Intergov. Oceanogr. Comm. Manuals Guid.* 56:196.

Jakobsen, F. (1995). The major inflow to the Baltic Sea during January 1993. *J. Mar. Syst.* 6, 227–240. doi: 10.1016/0924-7963(94)00025-7

Kankaanpää, H. T., and Virtasalo, J. J. (2017). Rapid fluctuations in the northern Baltic Sea H2S layer. *J. Mar. Syst.* 176, 24–37. doi: 10.1016/j.jmarsys.2017.07.001

Laine, A. O., Andersin, A.-B., Leini,ö, S., and Zuur, A. F. (2007). Stratification-induced hypoxia as a structuring factor of macrozoobenthos in the open Gulf of Finland (Baltic Sea). *J. Sea Res.* 57, 65–77. doi: 10.1016/j.seares.2006.08.003

Lass, H. U., Prandke, H., and Liljebladh, B. (2003). Dissipation in the Baltic proper during winter stratification. *J. Geophys. Res.* 108:3187. doi: 10.1029/2002JC001401

Lehtoranta, J., Savchuk, O. P., Elken, J., Dahlbo, K., Kuosa, H., Raateoja, M., et al. (2017). Atmospheric forcing controlling inter-annual nutrient dynamics in the open Gulf of Finland. *J. Mar. Syst.* doi: 10.1016/j.jmarsys.2017.02.001

Liblik, T., Laanemets, J., Raudsepp, U., Elken, J., and Suhhova, I. (2013). Estuarine circulation reversals and related rapid changes in winter near-bottom oxygen conditions in the Gulf of Finland, Baltic Sea. *Ocean Sci.* 9, 917–930. doi: 10.5194/os-9-917-2013

Liblik, T., and Lips, U. (2011). Characteristics and variability of the vertical thermohaline structure in the Gulf of Finland in summer. *Boreal Environ. Res.* 16, 73–83.

Lips, U., Kikas, V., Liblik, T., and Lips, I. (2016). Multi-sensor *in situ* observations to resolve the sub-mesoscale features in the stratified Gulf of Finland, Baltic Sea. *Ocean Sci.* 12, 715–732. doi: 10.5194/os-12-715-2016

Lips, U., Laanemets, J., Lips, I., Liblik, T., Suhhova, I., and Suursaar, Ü. (2017). Wind-driven residual circulation and related oxygen and nutrient dynamics in the Gulf of Finland (Baltic Sea) in winter. *Estuar. Coast. Shelf Sci.* 195, 4–15 doi: 10.1016/j.ecss.2016.10.006

Manual for Marine Monitoring in the COMBINE Programme of HELCOM. (2017). Available online at: http://www.helcom.fi/Documents/Action areas/Monitorin and assessment/Manuals and Guidelines/Manual for Marine Monitoring in the COMBINE Programme of HELCOM.pdf (Accessed December 19, 2017).

Matthäus, W., and Franck, H. (1992). Characteristics of major Baltic inflows-a statistical analysis. *Cont. Shelf Res.* 12, 1375–1400. doi: 10.1016/0278-4343(92)90060-W

Matthäus, W., and Lass, H. U. (1995). The recent salt inflow into the Baltic Sea. *J. Phys. Oceanogr.* 25, 280–286. doi: 10.1175/1520-0485(1995)025<0280:TRSIIT>2.0.CO;2

Mohrholz, V., Dutz, J., and Kraus, G. (2006). The impact of exceptionally warm summer inflow events on the environmental conditions in the Bornholm Basin. *J. Mar. Syst.* 60, 285–301. doi: 10.1016/j.jmarsys.2005.10.002

Mohrholz, V., Naumann, M., Nausch, G., Krüger, S., and Gräwe, U. (2015). Fresh oxygen for the Baltic Sea - an exceptional saline inflow after a decade of stagnation. *J. Mar. Syst.* 148, 152–166. doi: 10.1016/j.jmarsys.2015.03.005

Myrberg, K., and Leppäranta, M. (2009). "Topography and hydrography of the Baltic Sea," in *Physical Oceanography of the Baltic Sea* (Berlin; Heidelberg: Springer Berlin Heidelberg), 41–88.

Rak, D. (2016). *The Inflow in the Baltic Proper as Recorded in January–February* 2015.

Reissmann, J. H., Burchard, H., Feistel, R., Hagen, E., Lass, H. U., Mohrholz, V., et al. (2009). Vertical mixing in the Baltic Sea and consequences for eutrophication - A review. *Prog. Oceanogr.* 82, 47–80. doi: 10.1016/j.pocean.2007.10.004

Schimanke, S., and Meier, H. E. M. (2016). Decadal-to-centennial variability of salinity in the Baltic Sea. *J. Clim.* 29, 7173–7188. doi: 10.1175/JCLI-D-15-0443.1

Schmale, O., Krause, S., Holtermann, P., Power Guerra, N. C., and Umlauf, L. (2016). Dense bottom gravity currents and their impact on pelagic methanotrophy at oxic/anoxic transition zones. *Geophys. Res. Lett.* 43, 5225–5232. doi: 10.1002/2016GL069032

Sellschopp, J., Arneborg, L., Knoll, M., Fiekas, V., Gerdes, F., Burchard, H., et al. (2006). Direct observations of a medium-intensity inflow into the Baltic Sea. *Cont. Shelf Res.* 26, 2393–2414. doi: 10.1016/j.csr.2006.07.004

Vahtera, E., Conley, D. J., Gustafsson, B. G., Kuosa, H., Pitkänen, H., Savchuk, O. P., et al. (2007). Internal ecosystem feedbacks enhance nitrogen-fixing cyanobacteria blooms and complicate management in the Baltic Sea. *AMBIO A J. Hum. Environ.* 36, 186–194. doi: 10.1579/0044-7447(2007)36[186:IEFENC]2.0.CO;2

Väli, G., Meier, H. E. M., and Elken, J. (2013). Simulated halocline variability in the Baltic Sea and its impact on hypoxia during 1961-2007. *J. Geophys. Res. Ocean.* 118, 6982–7000. doi: 10.1002/2013JC009192

Vaquer-Sunyer, R., and Duarte, C. M. (2008). Thresholds of hypoxia for marine biodiversity. *Proc. Natl. Acad. Sci.U.S.A.* 105, 15452–15457. doi: 10.1073/pnas.0803833105

Conflict of Interest Statement: The authors declare that the research was conducted in the absence of any commercial or financial relationships that could be construed as a potential conflict of interest.

Copyright © 2018 Liblik, Naumann, Alenius, Hansson, Lips, Nausch, Tuomi, Wesslander, Laanemets and Viktorsson. This is an open-access article distributed under the terms of the Creative Commons Attribution License (CC BY). The use, distribution or reproduction in other forums is permitted, provided the original author(s) and the copyright owner(s) are credited and that the original publication in this journal is cited, in accordance with accepted academic practice. No use, distribution or reproduction is permitted which does not comply with these terms.

APPENDIX

TABLE 1A | The mean temperature (T_s) and salinity (S_s) along the section (see **Figure 1A**) in the water column below 80 m depth.

Period	T_s (°C)	T_a (°C)	$Q_a \times 10^{19}$ (J)	ΔQ_a (1019 J)	S_s (g kg^{-1})	S_a (g kg^{-1})	$M_a \times 10^{10}$ (t)	$\Delta M_a \times 10^{10}$ (t)
Jan–Jun 2014	5.48	5.33	2.09	0.00	10.52	10.28	1.01	0.00
Jul–Dec 2014	5.50	5.38	2.11	0.02	10.70	10.46	1.03	0.02
Jan–Jun 2015	5.94	5.81	2.28	0.19	10.98	10.76	1.06	0.05
Jul–Dec 2015	6.22	6.06	2.38	0.29	11.27	10.97	1.08	0.07
Jan–Jun 2016	6.26	6.10	2.40	0.30	11.32	10.99	1.08	0.07
Jul–Dec 2016	6.39	6.26	2.46	0.37	11.62	11.35	1.12	0.11

*The mean temperature (T_a), salinity (S_a), heat content (Q_a), and salt mass (M_a) over the area (gray area in **Figure 1B**) in the water column below 80 m depth. The changes of heat content ΔQ_a and salt mass ΔM_a in relation to the heat content and salt mass in January–June 2014.)*

frontiers in Marine Science

ORIGINAL RESEARCH
published: 17 July 2018
doi: 10.3389/fmars.2018.00248

Impact of the Major Baltic Inflow in 2014 on Manganese Cycling in the Gotland Deep (Baltic Sea)

Olaf Dellwig[1]*, *Bernhard Schnetger*[2], *David Meyer*[3], *Falk Pollehne*[4], *Katharina Häusler*[1] *and Helge W. Arz*[1]

[1] Marine Geology, Leibniz Institute for Baltic Sea Research Warnemünde (IOW), Rostock, Germany, [2] Microbiogeochemistry, Institute for Chemistry and Biology of the Marine Environment, Carl-von-Ossietzky University of Oldenburg, Oldenburg, Germany, [3] Marine Chemistry, Leibniz Institute for Baltic Sea Research Warnemünde (IOW), Rostock, Germany, [4] Biological Oceanography, Leibniz Institute for Baltic Sea Research Warnemünde (IOW), Rostock, Germany

The deep basins of the Baltic Sea, including the Gotland and Landsort Deeps, are well-known for the exceptional occurrence of sedimentary Mn carbonate. Although the details of the mechanisms of Mn carbonate formation are still under debate, a close relationship with episodic major Baltic inflows (MBIs) is generally assumed, at least for the Gotland Basin. However, the few studies on Mn cycling during MBIs suffer from a limited temporal resolution. Here we report on Mn dynamics in the water column and sediments of the Gotland Deep following an MBI that entered the Baltic Sea in December 2014. Water column profiles of dissolved Mn were obtained at a monthly to bi-monthly resolution between February 2015 and March 2017 and revealed an impact of the MBI on the Gotland Deep bottom waters beginning in March 2015. Water column profiles and budget estimates provided evidence for remarkable losses of dissolved Mn associated with the enhanced deposition of Mn oxide particles, as documented in sediment trap samples and surface sediments. In July 2015, subsequent to the nearly full oxygenation of the water column, clear signals of the re-establishment of bottom water anoxia appeared, interrupted by a second inflow pulse around February 2016. However, dissolved Mn concentrations of up to 40 μM in the bottom waters in June 2016 again indicated a pronounced reduction of Mn oxide and the escape of dissolved Mn back into the open water column. The absence of substantial amounts of Mn carbonate in the surface sediments at the end of the observation period suggested that the duration of bottom water oxygenation plays an important role in the formation of this mineral. Data from both an instrumental time series and a dated sediment core from the Gotland Deep supported this conclusion. Enhanced Mn carbonate formation occurred especially between the 1960s and mid-1970s, when several MBIs caused a long-lasting oxygenation of the water column. By contrast, Mn carbonate layers were much less pronounced or even missing after single MBIs in 1993, 2003, and 2014, each of which provided a comparatively short-term supply of O_2 to the deeper water column.

Keywords: manganese oxide, manganese carbonate, euxinia, major Baltic inflow (MBI), anoxic basin, Gotland Deep, Baltic Sea

OPEN ACCESS

Edited by:
Karol Kulinski,
Institute of Oceanology (PAN), Poland

Reviewed by:
Gennadi Lessin,
Plymouth Marine Laboratory, United Kingdom
Bradley M. Tebo,
Oregon Health and Science University, United States

***Correspondence:**
Olaf Dellwig
olaf.dellwig@io-warnemuende.de

Specialty section:
This article was submitted to Coastal Ocean Processes, a section of the journal Frontiers in Marine Science

Received: *23 March 2018*
Accepted: *27 June 2018*
Published: *17 July 2018*

Citation:
Dellwig O, Schnetger B, Meyer D, Pollehne F, Häusler K and Arz HW (2018) Impact of the Major Baltic Inflow in 2014 on Manganese Cycling in the Gotland Deep (Baltic Sea). Front. Mar. Sci. 5:248. doi: 10.3389/fmars.2018.00248

INTRODUCTION

The transition metal Mn is an essential micro-nutrient for every life-form and plays a central role in photosynthesis (Davidson and Marchant, 1987; Hansel, 2017). Redox-sensitive Mn occurs in nature in the oxidation states +2, +3, and +4, thus forming an important biogeochemical electron donor and acceptor. While the formation of solid Mn^{4+} oxides is favored in the presence of O_2, dissolved Mn^{2+} dominates under reducing conditions (Burdige, 1993). Dissolved Mn^{3+} is an important intermediate occurring in the suboxic water columns and pore waters of marine and limnic systems (Trouwborst et al., 2006; Madison et al., 2011; Dellwig et al., 2012). If reducing pore waters reach supersaturation, Ca-rich rhodochrosites containing Mn^{2+} may precipitate (Middelburg et al., 1987). The crustal abundance of Mn of ∼0.08% is low compared to ∼4% of neighboring Fe (Rudnick and Gao, 2003). However, the sensitivity of Mn to changing redox promotes the formation of massive Mn deposits in modern and ancient times; including e.g., ferromanganese crusts and nodules as well as Mn ore deposits comprising oxide, carbonate, and silicate phases (Hlawatsch et al., 2002; Nyame et al., 2003; Johnson et al., 2016). In addition to such exceptional deposits, whose mechanisms of formation are still not fully understood, sedimentary Mn signatures are also used as proxy for past redox reconstructions (Pruysers et al., 1993; März et al., 2011).

Pronounced stratification is a typical feature of restricted basins, fjords, and lakes and may promote the development of anoxic or even sulfidic (euxinic) conditions, as the limited mixing results in an insufficient O_2 supply to deeper waters (Spencer and Brewer, 1971; Jacobs et al., 1985, 1987; De Vitre et al., 1988; Skei, 1988; Murray et al., 1989; Zopfi et al., 2001; Dahl et al., 2010). At the transition between the oxygenated surface and reducing bottom waters—an area referred to as the pelagic redoxcline—intense microbial activity causes pronounced dynamics and strong gradients of nutrients and redox-sensitive metals (Dyrssen and Kremling, 1990; Taylor et al., 2001; Labrenz et al., 2007). A prominent peculiarity of redoxclines is the "Mn pump," which is initiated by the microbial oxidation of upwardly migrating dissolved Mn (Mn_{diss}) to particulate Mn oxides and their subsequent reduction as they re-enter euxinic waters either by reaction with sulfide or mediated by bacteria (Yao and Millero, 1993; Neretin et al., 2003; Tebo et al., 2004). In addition to the latter reaction between Mn and sulfide, which affects the expansion of euxinic waters, Mn may also interact with the N-cycle, as postulated by Luther et al. (1997). At pelagic redoxclines, Mn oxides are further tightly coupled to Fe and P and are believed to influence productivity by retaining certain amounts of phosphate at least over longer time-scales (Dellwig et al., 2010). Finally yet importantly, Mn oxides strongly affect trace metal cycles via scavenging and thus form an important carrier between the oxic and anoxic areas of a water body (Koschinsky et al., 2003; Dellwig et al., 2010; Yigiterhan et al., 2011).

Under reducing conditions, Mn carbonate is frequently observed in marine and lacustrine sediments as for instance in the SE Atlantic, Panama Basin, Loch Fyne, and Lake Sempach (Calvert and Price, 1970; Pedersen and Price, 1982; Gingele and Kasten, 1994; Friedl et al., 1997). Unusually high amounts of Mn carbonate are also found e.g., in manganiferous black shales deposited in the geological past (Calvert and Pedersen, 1993; Huckriede and Meischner, 1996). While missing in euxinic type-localities like the Black Sea, where euxinic bottom waters prevail since ∼7,000 years (Calvert and Pedersen, 1996; Wegwerth et al., 2018), the deep basins of the Baltic Sea are the only modern settings showing comparable and even higher Mn carbonate abundances (Suess, 1979; Lenz et al., 2015; Häusler et al., 2018). Despite their manifold occurrence, the detailed pathways of Mn carbonate formation remain unclear. Minor abundances of Mn carbonate in reducing sediments or coatings on carbonate shells may be simply explained by precipitation from supersaturated pore waters (Calvert and Pedersen, 1996). In contrast, the exceptional presence of Mn carbonate in the deep areas of the Baltic Sea requires a more complex biogeochemical and physical framework including e.g., fundamental changes in redox conditions (Huckriede and Meischner, 1996; Lepland and Stevens, 1998; Heiser et al., 2001; Lenz et al., 2015; Häusler et al., 2018). As modern type localities for intense Mn authigenesis and the formation of sedimentary Mn carbonate (Ca-rich rhodochrosite), these deeps may therefore also serve as modern analogs for sediments deposited in ancient epicontinental seas comprising manganiferous black shales and phosphorite-Mn carbonate ores (Hein et al., 1999; Jenkyns, 2010).

Although long-lasting euxinia is considered to have been characteristic of the Holocene Thermal Maximum and Medieval Climate Anomaly (e.g., Zillén et al., 2008; Jilbert and Slomp, 2013; Hardisty et al., 2016), data derived from the increased temporal resolution of (sub-)recent sedimentary records and instrumental time series suggest the occurrence of fundamental redox changes at annual to decadal scales (Neumann et al., 1997; Lenz et al., 2015; Häusler et al., 2018). Stratification of the water column fosters the development of euxinia and Black-Sea-like characteristics of the water column, such as strong bottom water Mn_{diss} enrichments, whereas irregular inflows of North Sea waters can result in the complete oxygenation of the deep basins of the Baltic Sea (Nausch et al., 2003). During these major Baltic inflows (MBIs), considerable amounts of Mn oxides are deposited on the seafloor, where, following the restoration of reducing conditions, they are presumably transformed into Mn carbonates (Huckriede and Meischner, 1996). However, a comparison of an instrumental water column time series with a sub-recent sediment record from the Gotland Basin suggested that MBIs do not necessarily result in the formation of pronounced Mn carbonate layers (Heiser et al., 2001). Rather than single MBIs, Häusler et al. (2018) identified slight bottom-water oxygenation lasting for several years as an important prerequisite of Mn carbonate formation in the Landsort Deep. In addition to experimental approaches that focus on the possible physicochemical mechanisms of Mn carbonate formation, including microbial mediation, detailed field studies during a MBI may shed light on the remarkable Mn authigenesis in the Baltic Sea. Unfortunately, studies on Mn cycling during past MBIs are extremely rare and suffer from a limited temporal resolution (Brügmann et al., 1998; Pohl

and Hennings, 1999; Turnewitsch and Pohl, 2010). However, a recent MBI entering the Baltic Sea in December 2014 (Mohrholz et al., 2015) provided the unique opportunity to follow the Mn dynamics in the Gotland Basin during an oxygenation event in detail. Water samples taken at monthly to bi-monthly intervals between February 2015 and March 2017 allowed an evaluation of Mn dynamics during the progressive oxygenation of the water column. Suspended particulate matter from a sediment trap as well as pore water samples of eight short cores were used to obtain Mn budget estimates and thus to draw conclusions on water body displacement and potential basin-internal Mn cycling. Finally, the Mn signatures of the surface sediments obtained between May 2015 and March 2017, a dated sediment core covering the past ∼70 years and instrumental water column time series are discussed in terms of the environmental conditions favoring present and past Mn carbonate formation.

MATERIALS AND METHODS

Study Site

The Baltic Sea is a brackish marginal sea comprising several basins separated by narrow sills and channels. The most prominent basins in the Baltic Proper are the Landsort Deep (∼459 m water depth), a relatively steep and narrow trench (Häusler et al., 2018), and the Gotland Basin (∼249 m water depth), with the largest areal extension and a comparatively flat center (**Figure 1**). In addition to a gradient of decreasing salinity toward the north, the water column of the Baltic Sea is permanently stratified due to the intrusion of saline waters from the North Sea and riverine freshwater inputs. The resulting restriction of vertical water-mass exchange in the deeper basins promotes a severe O_2 deficiency and the accumulation of sulfide in bottom waters (Matthäus et al., 2008).

Strong saltwater inflows from the North Sea, so-called MBIs (e.g., Matthäus and Franck, 1992), while irregular in their occurrence, enable the renewal and oxygenation of the Baltic's bottom waters. MBIs depend on certain meteorological conditions, including strong easterly winds leading to a below-normal sea level and subsequently longer-lasting westerly winds (Schinke and Matthäus, 1998). The frequency of MBIs reaching the deep basins is significantly reduced since the 1980s, possibly due to a shift in the large-scale meteorological conditions over the North Atlantic Region (Hurrell, 1995; Matthäus and Schinke, 1999; Meier and Kauker, 2003). Together with the increasing eutrophication of the Baltic Sea, especially since ∼1950, the reduced deep-water renewal has provoked the expansion of hypoxic areas (O2 <2 mL L^{-1}; Diaz and Rosenberg, 2008; Carstensen et al., 2014; Gustafsson et al., 2017).

Sampling and Sample Preparation

The samples used in this study were obtained close to the IOW monitoring station 271 (identical to station code BY15), in the central eastern Gotland Basin, during 25 cruises between 2006 and 2017 (**Table 1**). In addition, two surface sediment samples from sites MUC OD (211 m water depth) and TrKl04 (151 m water depth) were taken during Cruise POS492 in October 2015 (**Figure 1**). With the exception of pump-CTD (Strady et al., 2008) usage during cruise POS492, water column samples were obtained by a conventional CTD bottle rosette. Eight sediment cores were obtained with a multicorer device (MUC) and the pore water extracted using rhizon samplers (Seeberg-Elverfeldt et al., 2005). Samples for the determination of total dissolved Mn (Mn_{diss}) in the water column were filtered through 0.45-μM syringe filters (SFCA), whereas pore water filtration was not necessary because of a rhizon pore width of 0.1 μm. Samples for dissolved reactive Mn (dMn_{react}) were treated after Schnetger and Dellwig (2012). Water column and pore water samples were acidified to 2 vol% with concentrated HNO_3 and stored cool in acid-cleaned 2-mL reaction tubes. For sulfide analyses, 2 mL of water was fixed in 2-mL reaction tubes containing 20 μL of a 20% Zn acetate solution.

Water column samples of ∼2 L were filtered through 0.4-μm polycarbonate membrane filters for the determination of particulate Mn (Mn_{part}) in suspended particulate matter (SPM). The filters were rinsed with 60 mL of 18.2-MΩ water to remove salt and then dried at 40°C for 48 h. Time-integrated SPM samples were also obtained using a classical cone-shaped automated Kiel sediment trap with a sampling area of 0.5 m^2 (Zeitzschel et al., 1978) positioned in the central Gotland Deep (57°17.95N; 20°14.10E) at a water depth of 186 m. Sediment trap samples were recovered at a temporal resolution of 10–15 days between February 2015 and March 2017. The solid material was washed with 18.2-MΩ water and freeze-dried. A small sample aliquot was removed for scanning electron microscopy-energy dispersive X-ray spectroscopy (SEM-EDX) inspection and the remainder homogenized using an agate mortar. Sediment samples from MUC casts were sliced in intervals of 0.5–1 cm, stored frozen in Petri dishes, freeze-dried, and finally homogenized in an agate ball mill after separation of a SEM-EDX aliquot. For all solid materials, acid digestions were prepared using a HNO_3-HF-$HClO_4$ mixture in closed Teflon vessels heated to 180°C for 12 h. After evaporation of the acids to near dryness, the residues were re-dissolved, fumed off three times with 2 mL of 1+1 HCl, and finally diluted with 2 vol% HNO_3 to a volume of 50 mL (4 mL for SPM samples).

Dry bulk densities (DBDs) were estimated by dividing the weight of the dried samples by the volume of the wet samples (Brady, 1984). One short core from the MUC cast obtained in August 2012 was split lengthwise (Häusler et al., 2018) and used for X-ray fluorescence (XRF) scanning.

Analytical Methods

O_2 concentrations in the water column were determined using a SBE 911plus CTD (Sea-Bird) equipped with free-flow bottles (Hydro-Bios).

Mn_{diss} in the water column and pore waters was measured after 2-fold dilution of the samples with 2 vol% HNO_3, by inductively coupled plasma optical emission spectrometry (ICP-OES; iCAP 6300 Duo/iCAP 7300 since autumn 2016, Thermo Fisher Scientific), using external matrix-matched calibration and Sc as the internal standard. Precision (1.2%) and trueness (0.1%) were determined using 2-fold diluted international reference

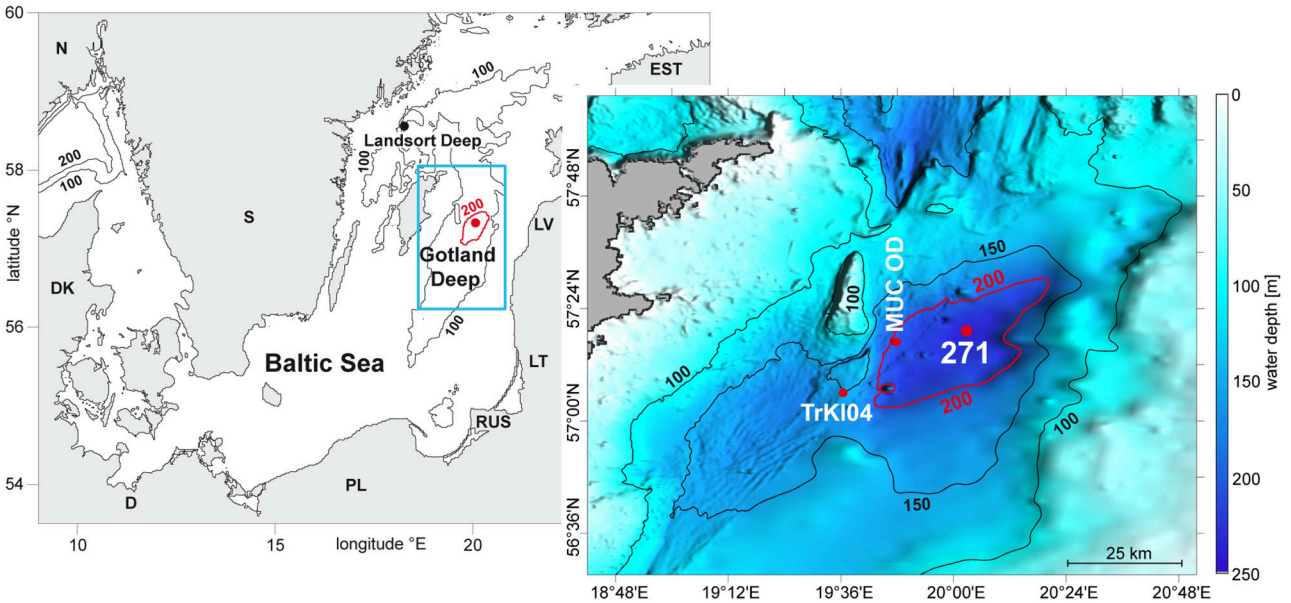


FIGURE 1 | Maps showing main sampling station 271 as well as the surface sediment stations MUC OD and TrKl04 in the central Gotland Basin. The bathymetry is described by the EMODnet Bathymetry Consortium (2016).

material SLEW-3 (National Research Council Canada) spiked with Mn.

The numerical rate estimation from concentrations model (REC; Lettmann et al., 2012) was used to estimate Mn_{diss} fluxes in the top 5 cm of the pore waters. Sediment porosity was calculated from the DBDs using an average grain density of 2.7075 g cm^{-3}. The sedimentary diffusion coefficients of Mn (Boudreau, 1997; Berg et al., 1998; Schulz, 2006) were corrected for porosity as well as temperature and salinity as determined from the CTD casts. For details, see Häusler et al. (2018).

Total sulfide concentrations in the pore water and water column samples were measured spectrophotometrically after the method of Cline (1969).

The concentrations of Al, Ca, and Mn in the acid digestions of sediments, sediment trap material, and SPM were measured by ICP-OES (iCAP 6300 Duo and iCAP 7300 since autumn 2016, Thermo Fisher Scientific) using external calibration and Sc as internal standard. The precision and trueness of the international reference material SGR-1b (USGS) were better than 2.% and −4.5%, respectively. The Pb content of the samples was determined from the same acid digestions by Q-ICP-MS (iCAP Q, Thermo Fisher Scientific) using external calibration and Ir as the internal standard. The precision and trueness of the international reference material SGR-1b (USGS) were 3.7 and −2.6%, respectively. The $^{206/207}$Pb ratios in the acid digestions of the sediment samples from the August 2012 core were also determined by Q-ICP-MS (iCAP Q, Thermo Fisher Scientific). The Q-ICP-MS was equipped with a PrepFast module (ESI), which allowed online sample dilution to a final Pb concentration of ∼1 µg L^{-1}. Following the method of Hinrichs et al. (2002), the instrument was tuned to provide the best performance for the NIST standard SRM 981. Precision and trueness were 0.04 and −0.17%, respectively.

Biogenic opal in the August 2012 short core was measured by ICP-OES (iCAP 6300 Duo, Thermo Fisher Scientific) after the extraction of 50 mg of sediment with 100 mL of 1 M NaOH for 40 min at 80°C in a shaking water bath. The precision of the in-house reference material SIBER was 4%. Si concentrations were converted into those of biogenic opal based on a conversion factor of 2.38, which considered the water content of pure biogenic opal material (diatomite).

^{137}Cs and ^{241}Am activities in the sediment samples from August 2012 were determined by gamma spectrometry (Canberra) using a planar Ge-detector GX3018-7500SL and processed using GENIE 2000 3.0 and 3.1 software (Canberra Industries Inc., USA). Counting statistics for ^{137}Cs and ^{241}Am were better than 5 and 20%, respectively. Trueness was checked against the standard reference materials IAEA-384 (^{241}Am) and IAEA-385 (^{241}Am, ^{137}Cs, decay corrected; International Atomic Energy Agency).

A parallel core from the same August 2012 MUC cast was split lengthwise (Häusler et al., 2018) and analyzed for Ca, Mn, and Ti by XRF core scanning (ITRAX XRF core scanner, Cox; Croudace et al., 2006). The sediment surface was cleaned, smoothed, and covered with a special plastic foil to minimize evaporation during the measurement. The Cr-tube operated at 30 kV and 30 mA with an exposure time of 15 s per step (step size: 200 µm).

SEM-EDX (Merlin VP Compact, Zeiss/AZtecEnergy, Oxford Instruments) was used to identify the Mn mineral phases in the sediment trap material and surface sediments. After suspension of the solid material in an ultrasonic bath and filtration through

TABLE 1 | Cruises from which sample material was obtained close to the IOW monitoring station 271 (BY15), in the central Gotland Deep (PE = R/V *Prof. Albrecht Penck*, MSM = R/V *Maria S. Merian*, M = R/V *Meteor*, EZ/EMB = R/V *Elisabeth Mann Borgese*, AL = R/V *Alkor*, POS = R/V *Poseidon*, Sal = R/V *Salme*).

Cruise	Date	Position	Water depth [m]	Device
40PE0616	14 Jul 2006	57°19.05N, 20°2.47E	237	CTD
07PE0708	13 Apr 2007	57°19.54N, 20°3.17E	241	CTD
07PE0814	4 Jul 2008	57°18.46N, 20°3.90E	243	CTD
MSM12-4b	17 Sep 2009	57°19.20N, 20°3.00E	237	CTD
M86-1b	14 Nov 2011	57°18.34N, 20°4.70E	236	CTD
06EZ1215	25 Aug 2012	57°19.29N, 20°8.15E	241	CTD/MUC
EMB95	10 Feb 2015	57°19.18N, 20°2.99E	238	CTD
AL451	3 Mar 2015	57°19.21N, 20°2.94E	234	CTD
EMB99	22 Mar 2015	57°19.19N, 20°2.84E	237	CTD
EMB100	19 Apr 2015	57°19.22N, 20°2.97E	238	CTD
EMB102	9 May 2015	57°19.24N, 20°2.86E	237	CTD
Sal2015_11	2 Jul 2015	57°19.30N, 20°3.85E	235	CTD
EMB107	21 Jul 2015	57°19.19N, 20°2.95E	237	CTD/MUC
EMB113	25 Sep 2015	57°19.20N, 20°2.90E	237	CTD
POS492	20 Oct 2015	57°19.19N, 20°2.90E	241	CTD/MUC
EMB117	11 Nov 2015	57°19.21N, 20°3.03E	238	CTD
EMB120	4 Feb 2016	57°19.20N, 20°3.05E	238	CTD
MSM51	13 Feb 2016	57°19.19N, 20°2.99E	237	MUC
EMB124	20 Mar 2016	57°19.21N, 20°3.10E	237	CTD
EMB128	15 May 2016	57°19.21N, 20°2.95E	236	CTD
AL479	9 Jun 2016	57°19.19N, 20°2.99E	238	CTD/MUC
EMB135	7 Aug 2016	57°19.05N, 20°3.11E	237	CTD
POS507	19 Oct 2016	57°18.32N, 20°4.70E	244	CTD/MUC
EMB147	12 Feb 2017	57°19.31N, 20°2.82E	236	CTD
MSM62	10 Mar 2017	57°16.83N, 20°5.87E	238	CTD/MUC

0.4-μm polycarbonate filters, the samples were fixed on Al stubs, carbon coated, and placed in a vacuum chamber. The working distance was 8.5 mm and spot analysis was done at an excitation voltage of 15 kV. Relative mineral abundances were determined by automated particle analyses, which were based on EDX element analyses of ∼2,000 particles per sample, image processing, and particle recognition. The border values for the differentiation of Mn oxide from Ca-rich Mn carbonate were: Mn >30%, Ca <6%, and Mn >30%, Ca >6%.

RESULTS

Mn Dynamics in the Water Column of the Gotland Deep Prior to the MBI of 2014

Figure 2 shows six water column profiles of dissolved and particulate Mn (Mn_{diss}, Mn_{part}), O_2, and total sulfide from the Gotland Deep at monitoring site 271 (**Figure 1**). The respective samples were taken between 2006 and 2012, during a so-called stagnation period, that is, without a substantial impact of an MBI. In July 2006, Mn_{part} was strongly enriched just above and Mn_{diss} below the redoxcline. After slightly decreasing at a water depth of around 160 m, Mn_{diss} concentrations increased again and reached a maximum of ∼26 μM in the deepest sample. Along with an upward shift of the redoxcline by ∼10 m in April 2007, Mn_{part} and Mn_{diss} enrichments were less pronounced in the suboxic waters. Below the redoxcline, Mn_{diss} remained at a nearly constant level of ∼11 μM until a sudden drop to ∼5 μM in the deepest two samples. While sulfide concentrations gradually increased with depth, to a maximum of 45 μM at 221 m, the values abruptly declined to as low as ∼2 μM just above the seafloor. In July 2008, the redoxcline occurred a few meters further upward. Mn_{diss} concentrations gradually increased with depth and remained constant at ∼10 μM below a water depth of 170 m. Sulfide concentrations also increased with water depth, reaching a maximum of 48 μM in the bottom waters. Despite lower concentrations of Mn_{part} and a bottom water sulfide level of 114 μM, the Mn_{diss} profile in September 2009 generally coincided with that of the previous cruise, in 2008. In November 2011, the sulfide concentration in the bottom waters increased to a maximum of 148 μM, while Mn_{diss} concentrations within the deeper water column remained at a similar level of ∼10 μM. In August 2012, O_2 concentrations increased strongly between water depths of 95 m and 130 m whereas the Mn_{diss} profile in deeper waters was more or less unaffected and resembled that of the previous cruises since 2008.

Mn Dynamics in the Water Column of the Gotland Deep During the MBI of 2014

Figure 3 shows O_2 and Mn_{diss} as well as available Mn_{part} and sulfide concentrations in the water column of the Gotland Deep at site 271 as determined during 18 cruises between February 2015 and March 2017. Compared to the pre-MBI profiles (**Figure 2**), the Mn_{diss} concentration during the first cruise (February 2015) was generally lower throughout the sulfidic water body. Although Mn_{diss} increased steeply, to a maximum of 6.4 μM, just below the redoxcline, its concentration in sulfidic waters gradually decreased, to 3.2 μM in the lowermost sample. Distinctly lower concentrations of sulfide, fluctuating around 20 μM, were also measured at water depths of 150–235 m. Almost 1 month later (3 March 2015), O_2 appeared in the bottom waters at concentrations ranging from 9 μM at a water depth of 208 m to 35 μM near the seafloor (231 m). In parallel, Mn_{diss} concentrations in the two deepest samples decreased to ∼1.0 μM. During the following four cruises, oxygenation of the deeper waters proceeded and Mn_{diss} was increasingly depleted. By 9 May 2015 and persisting until at least 2 July 2015, only a thin relict of the former euxinic water body remained, occurring at ∼130 m water depth. An O_2 concentration of nearly 100 μM characterized the water column from the bottom until a water depth of ∼130 m, whereas Mn_{diss} and sulfide concentrations were as low as ∼3 μM in the depth interval between 125 and 110 m.

In the same depth interval, elevated Mn_{diss} concentrations as high as 6.3, 3.4, and 2.7 μM were also determined on 21 July 2015, 26 September 2015, and 27 October 2015, respectively. The values then dropped to < 0.4 μM on 11 November 2015. Beginning with the cruise on 21 July 2015, however, the Mn_{diss} level in the bottom waters began to increase, reaching a maximum of almost 20 μM

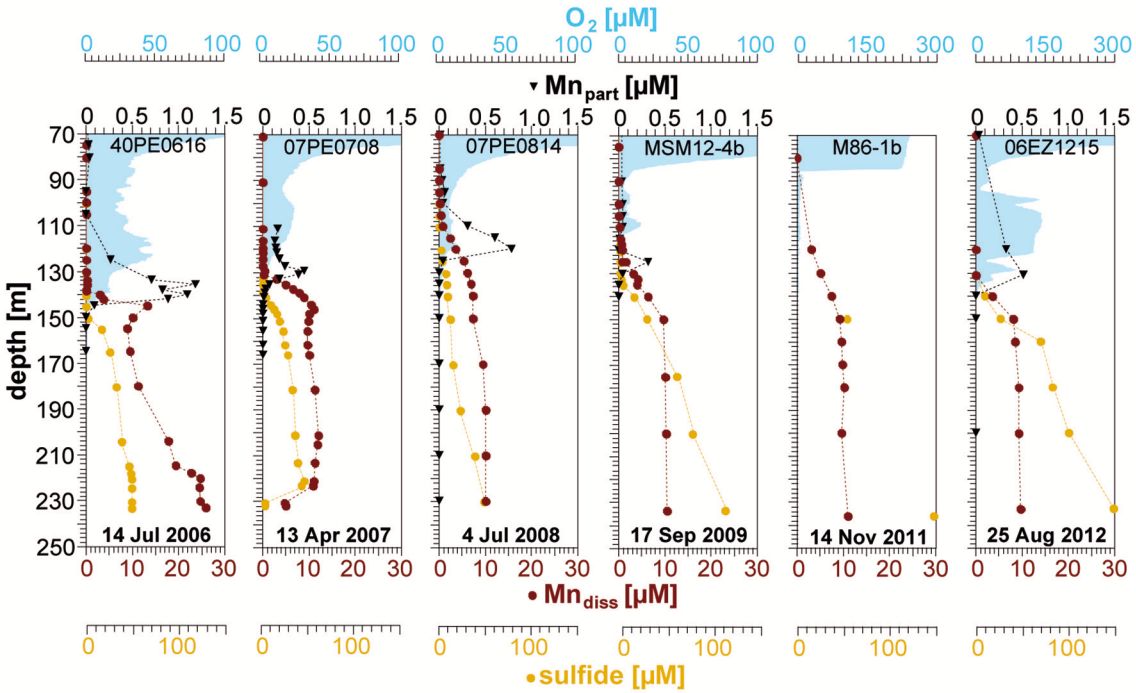


FIGURE 2 | Water column profiles of O_2, dissolved and particulate Mn, and total sulfide as determined in samples obtained from station 271 in the central Gotland Basin between 2006 and 2012.

in the deepest water samples in October and November 2015. Supernatant waters of the corresponding short cores contained up to 16 µM Mn_{diss} on 21 July 2015 and 25 µM Mn_{diss} on 27 October 2015. In samples from those two cruises, particulate Mn (Mn_{part}) concentrations showed two maxima, of 0.57 µM (128 m) and 2.9 µM (233 m), on 21 July 2015 and three maxima, of 0.98 µM (83 m), 0.65 µM (137 m), and 1.4 µM (231 m), in October 2015. Maximum sulfide concentrations were ∼0.8 µM, within the detection limit of the method used during both cruises.

On 4 February 2016, O_2 concentrations again increased in the bottom waters, reaching 76 µM. While Mn_{diss} ranged between 2 and 12 µM in these O_2-containing waters, the concentration in the still-anoxic overlying waters was 34 µM. A further decrease in the Mn_{diss} concentration was measured in the 20 March 2016 samples, and a continuing decline, to below ∼0.1 µM, throughout the almost entirely oxygenated water column in May 2016. Three weeks later (09 June 2016), the bottom waters again became anoxic at depths below 220 m. In these waters, Mn_{diss} was strongly enriched, reaching 40 µM in the supernatant waters of the corresponding short core. This trend of a re-establishment of bottom water anoxia was also reflected by increasing Mn_{diss} and sulfide concentrations during the remaining four cruises. Above the sulfide-containing waters, Mn_{part} was clearly enriched, both on 9 June 2016 and on 19 October 2016, showing a maximum concentration of 2.4 µM. On 10 March 2017, the reducing conditions extended from the bottom to a water depth of ∼180 m and Mn_{diss} and sulfide concentrations were as high as 58 and 36 µM, respectively.

Please note that Mn_{diss} represents the sum of dissolved Mn^{2+} and the intermediate Mn^{3+} species with the latter partly entirely dominating in suboxic waters (Trouwborst et al., 2006). The determination of dMn_{react} comprising mainly of Mn^{3+} (Schnetger and Dellwig, 2012) during four cruises revealed only a secondary role of Mn^{3+} under the unstable hydrodynamic conditions prevailing in the Gotland Basin (Figure S1). This finding accords with a previous study in the Baltic and Black Seas highlighting non-turbulent redoxclines as an important prerequisite for substantial Mn^{3+} accumulation (Dellwig et al., 2012).

Particulate Mn in a Sediment Trap Positioned in the Gotland Deep

Multiplying the bulk SPM fluxes of the sediment trap close to site 271 with the corresponding Mn_{part} contents allowed the calculation of Mn_{part} fluxes (Supplementary Dataset). Although the MBI reached the deepest parts of the central Gotland Basin no later than the beginning of March 2015 (**Figure 3**), Mn_{part} fluxes remained low until the end of April 2015, as determined from the sediment trap placed at a water depth of 186 m (**Figure 4**). Thereafter, a slight increase in Mn_{part} fluxes was followed by a steep rise at the end of June 2015. A malfunction of the sediment trap prevented coverage of later developments, until the end of November 2015. To estimate the Mn_{part} fluxes that might have occurred during this missing interval of the MBI, we included a dataset from an MBI in 2003 (Häusler et al., 2018). Although O_2 concentrations were slightly higher in 2003

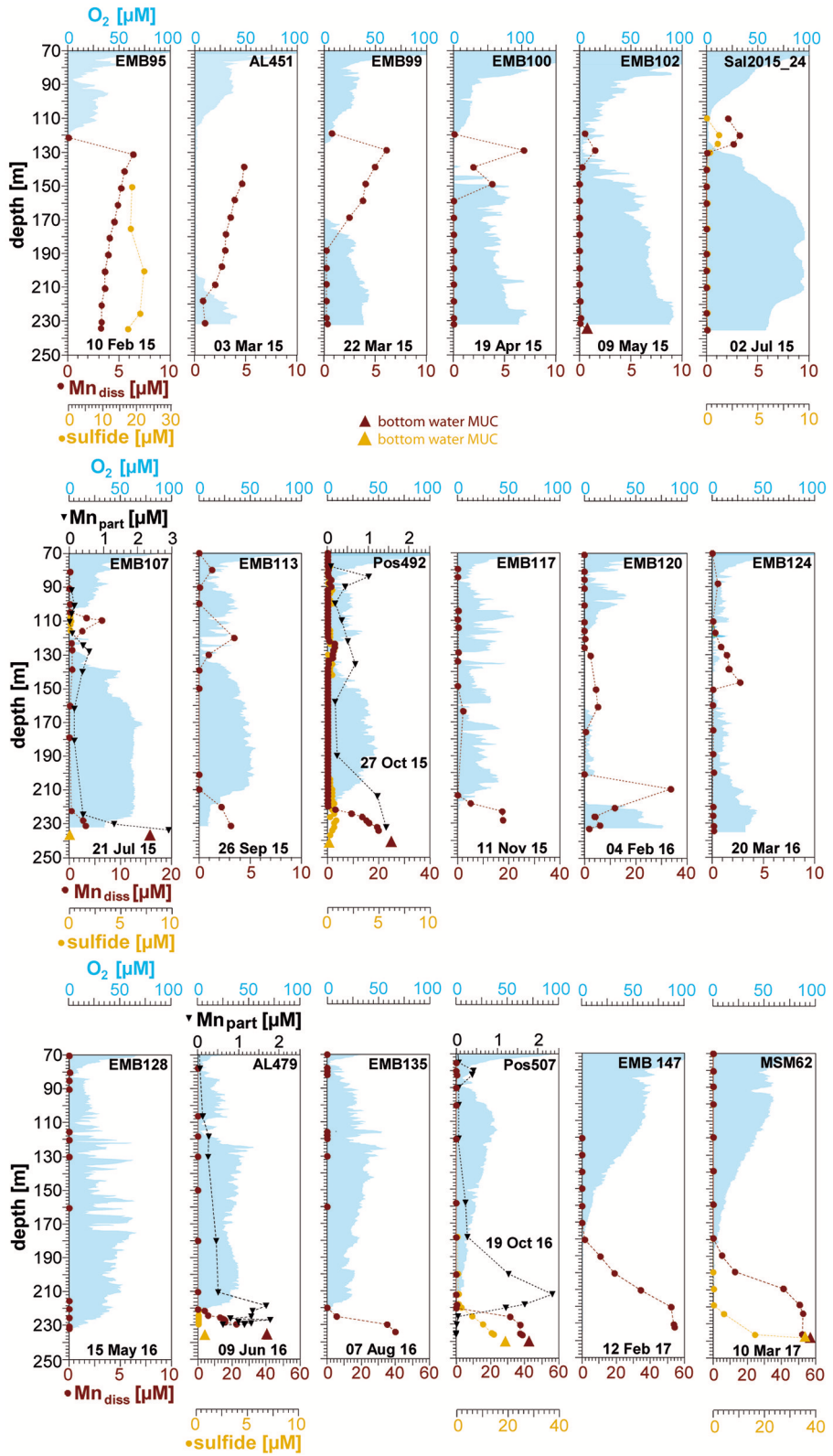


FIGURE 3 | Water column profiles of O_2, dissolved and particulate Mn, and total sulfide as determined in samples obtained from station 271 in the central Gotland Basin between February 2015 and March 2017. Large yellow and brown triangles denote sulfide and Mn_{diss} concentrations, respectively, in the supernatant water of the corresponding short cores.

than in 2015 (Figure S3), the chosen sediment trap dataset from 2003 at least represented a situation within MBI development comparable to that of 2015. Thus, the 2003 data also showed a rapid increase in Mn_{part} fluxes shortly after the onset of the MBI and a decrease to a relatively low level in the following 5 months. After the onset of a second oxygenation phase, Mn_{part} fluxes again increased steeply and strongly fluctuated until March 2017.

Surface Sediments and Pore Waters From the Gotland Deep

Eight short cores taken close to monitoring station 271 were analyzed for their sedimentary Al, Ca, and Mn contents (**Figure 5**). To eliminate dilution effects by organic matter and salt, especially in the uppermost fluffy parts, the Ca and Mn contents were normalized to the Al content. Based on the salinity of the bottom waters, the Ca contents were corrected for the pore water salt content. Because the positions of the coring locations varied between the cruises by a few nautical miles (**Table 1**), differences in the sediment records were most likely due to variable sedimentation rates. Based on a core parallelization using Pb/Al ratios indicating maximum Pb pollution between ∼1970 and 1980 (Renberg et al., 2001), in the cores from August 2012 and October 2016 older Mn enrichments occurring at a depth of ∼6 cm did not appear before 10 and 14 cm (**Figure 5** and Figure S2), respectively. Nonetheless, because all cores originated from water depths below 237 m, a comparison of the uppermost fluffy material is justified and the chosen cores can be considered as representative of the deeper central basin. The concentrations of Mn_{diss} and total sulfide in the pore water from six cores were also determined.

The short core taken in August 2012 represented pre-MBI conditions (**Figures 2**, **5**). Sedimentary Mn/Al and Ca/Al values were elevated at ∼3 cm and showed two pronounced peaks at a sediment depth of 11–13 cm, whereas no enrichments occurred in the uppermost fluffy layer overlain by euxinic bottom waters. Mn_{diss} and sulfide increased gradually with depth in the pore water, reaching highest concentrations of 190 and 996 μM, respectively, at 20 cm depth. While sedimentary Mn and Ca enrichments at the sediment-water interface (SWI) were still absent in May 2015, elevated Mn/Al and Ca/Al values were recorded in the uppermost sediment sample in July 2015. Below a slight peak at ∼1 cm in July 2015, the pore water Mn_{diss} concentrations increased with depth, finally reaching a level comparable to that seen in the profile of the pre-MBI period. By contrast, sulfide concentrations were below the detection limit until 3 cm depth and they remained lower than those of August 2012. While surface sediment Mn/Al values in the uppermost two samples were distinctly lower in October 2015, the decline in Ca/Al was less pronounced than in the core from July 2015. Sulfide was detectable below 1 cm and Mn_{diss} levels reached a distinct near-surface maximum of >400 μM. After the second oxygenation event, around January 2016, increases in Mn/Al and Ca/Al in the uppermost sediment layer were measured in February and June 2016. Pore water sulfide levels increased further in June 2016 and Mn_{diss} still showed a near-surface maximum. Mn and Ca enrichments were absent from the surface sediments collected during the remaining two cruises, in October 2016 and March 2017, and the patterns of pore water sulfide and Mn_{diss} tended to resemble those of the pre-MBI period, represented by the August 2012 core.

Pore water fluxes of Mn_{diss} across the SWI also underwent pronounced variations (**Figure 5**). While a diffusive flux of 48 μM m^{-2} d^{-1} was determined for the pre-MBI period in August 2012, distinctly higher values were estimated for subsequent cores subjected to the MBI. Parallel to the small near-surface Mn_{diss} peak, a ∼3-fold increase in the flux occurred in July 2015. Accompanying the highest Mn_{diss} concentrations and steepest gradients was an increase in the corresponding flux, which reached a maximum of 1,253 μM m^{-2} d^{-1} in October 2015. The Mn_{diss} fluxes of the remaining three cores exhibited a decreasing trend but were still above the pre-MBI level.

Surface sediments from the short cores taken during the cruises between July 2015 and March 2017 were analyzed by SEM-EDX to elucidate the nature of the Mn enrichments. Mn oxides constituted 61% of all particles analyzed in the surface sediment from July 2015, and their morphologies were similar to those of the Mn oxides in the sediment trap (**Figures 6A–C**) and in the pelagic redoxcline of the Gotland Deep during a stagnation period (Dellwig et al., 2010, 2012). By contrast, the contribution of Mn carbonates was almost negligible. A typical Mn oxide particle contained only minor amounts of Ca, resulting in a molar Mn/Ca ratio of ∼14 (**Figure 6C**). The abundance of Mn oxides significantly decreased in October 2015, whereas Mn carbonate (Ca-rich rhodochrosite) levels increased slightly (**Figure 6D**), with a distinctly lower molar Mn/Ca ratio of < 3 due to Ca incorporation. In February 2016, the percentage of Mn oxide particles again increased, to ∼61%, while the abundance of Mn carbonate remained low. Mixed particles comprising Mn oxide and Mn carbonate were also observed, as indicated by the differing Mn/Ca ratios (**Figure 6E**). In June 2016, the abundance of Mn oxides increased, as did the abundance of Mn carbonates, to almost 7% of all particles identified (**Figure 6F**). Mixed phases appeared again, with molar Mn/Ca ratios between 2.4 and 18.9. During the last two cruises, in October 2016 and March 2017, Mn oxide particles were absent and the amount of Mn carbonate was almost negligible (**Figures 6G,H**).

Sedimentary Mn Signatures in the Gotland Deep During the Past ∼60 Years

Past Mn authigenesis in the Gotland Deep was investigated based on various geochemical parameters in the short core from August 2012. XRF scanning identified several layers enriched in Mn, especially in the lower half of the laminated sediment core (**Figure 7**). The Mn contents determined by ICP-OES in samples from a parallel core of the same cast and the Mn counts from XRF scanning generally agreed well and revealed pronounced Mn enrichments of nearly 17 wt% at a sediment depth of 10–15 cm. However, compared with the discrete samples from conventional slicing at 0.5- to 1.0-cm steps, the higher resolution of 200 μm on a 1.2-cm-wide XRF measurement line captured a clearly higher variability. This methodological difference was especially critical

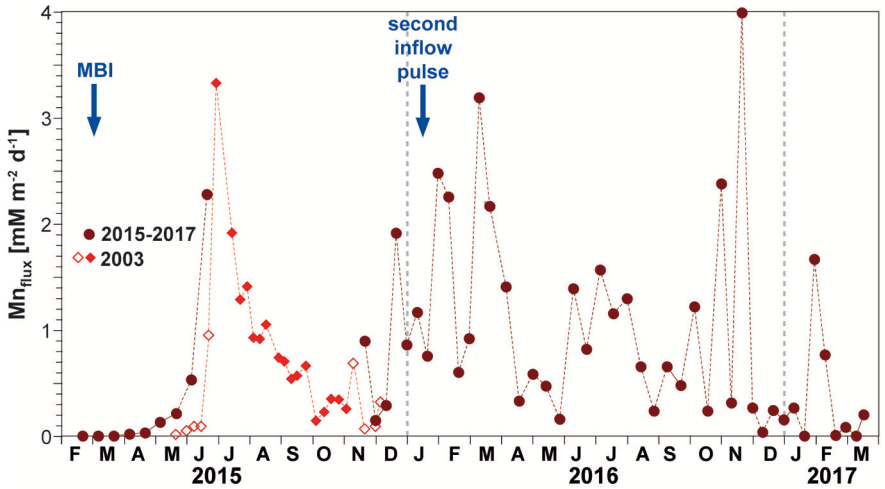


FIGURE 4 | Temporal variability of particulate Mn fluxes in a sediment trap positioned at a water depth of 186 m close to station 271 in the central Gotland Basin (brown dots: 2015–2017; open and closed red squares: 2003). Closed symbols were used for budget calculations.

for the uppermost fluffy part of the core. The slightly sloped position of the sediment material in the core liner caused a more depth-integrated sampling and prevented the registration of the two separated Mn layers, which were clearly distinguishable on the XRF scan of core depths of ∼1.5 and ∼3 cm.

A first slight increase in ^{137}Cs activity at a core depth of ∼14 cm and a peak at 11.75 cm were observed (**Figure 7**). At 9.5 cm, there was a steep rise in ^{137}Cs, with fluctuating but still elevated activities toward the core top. ^{241}Am activities were characterized by a clear maximum at a sediment depth between 14 and 11.5 cm, a single peak at 9.25 cm, and a peak between 7.75 and 8.25 cm. $^{206/207}$Pb values ranged from 1.17 to 1.21, with the lowest values at a sediment depth between ∼11 and ∼9 cm. The opal content was enriched in the topmost samples and between ∼6 and 8 cm.

DISCUSSION

Temporal Dynamics and the Fate of Mn in the Gotland Deep After the MBI of 2014

The profiles of Mn_{diss} obtained before the MBI in 2014 represent a first approximation of the conditions that prevailed during a stagnation period, that is, without the impact of substantial oxygenation events (**Figure 2**). Nonetheless, pronounced differences within the datasets were still discernible. The elevated Mn_{diss} concentrations in the bottom water in July 2006 clearly represented the remnants of the re-established euxinic conditions and the coupled reduction of deposited Mn oxides after the MBI in 2003 (Feistel et al., 2003, 2004; Turnewitsch and Pohl, 2010; Häusler et al., 2018). Conversely, the decrease in Mn_{diss} in the two lowermost samples from April 2007 was certainly due to a very short-term inflow of O_2-containing waters, documented in the time-series at site 271 (**Figures 2**, **9**; ICES, 2015). Irrespective of the rising sulfide levels in deep water, possibly attributable to a decreasing pool of reactive Fe in the sediments that exacerbated the escape of sulfide into the open water column (Lenz et al., 2015), Mn_{diss} concentrations were similar at least for the years 2008–2012 and thus suggestive of a balanced status. The Mn_{diss} level was, however, ∼2-fold higher than that in February 2015, just before the major MBI pulse of 2014 reached the Gotland Basin (**Figures 2**, **3**). The even more pronounced difference in sulfide levels can be explained by the weak oxygenation event before the major MBI, as indicated by the O_2 time series in the bottom waters from site 271 in spring 2014 (**Figure 9**; ICES, 2015). Although the average Mn_{diss} concentration in euxinic waters of 9.0 μM in August 2012 vs. 4.3 μM in February 2015 indicated substantial Mn loss, a simple inventory estimate relativizes this finding. Thus, based on the hypsography of the Gotland Basin (**Figure 9A**; Seifert and Kayser, 1995; Supplementary Dataset), the upward shift of the redoxcline by ∼10 m (**Figures 2**, **3**) significantly increased the euxinic water volume enriched in Mn, from ∼209 km^3 in 2012 to 288 km^3 in 2015. After a basin-wide extrapolation of Mn_{diss} concentrations from the water column profiles using the corresponding hypsography-based water volumes (**Figure 8**), the Mn_{diss} inventories (∼1.5 × 10^9 mol) in the euxinic water bodies were identical during the 2 years, which argues against a sustained effect of the weak pre-MBI oxygenation, at least for Mn (see Supplementary Dataset).

Increased O_2 and decreased Mn_{diss} concentrations on 3 March 2015 represented the first signals of the approaching MBI from 2014 (**Figure 3**). This date accords with an O_2 time series from a profiling mooring in the Gotland Deep (Prien and Schulz-Bull, 2016; Holtermann et al., 2017). In the following months, the main MBI phase caused the almost complete oxygenation of the water column, with only a thin remnant of the previously euxinic water body at around 120 m water depth (**Figure 3**). Correspondingly, Mn_{diss} concentrations dropped to near nanomolar levels in these oxygenated waters, thereby enhancing the formation and downward deposition of particulate Mn oxides, as documented

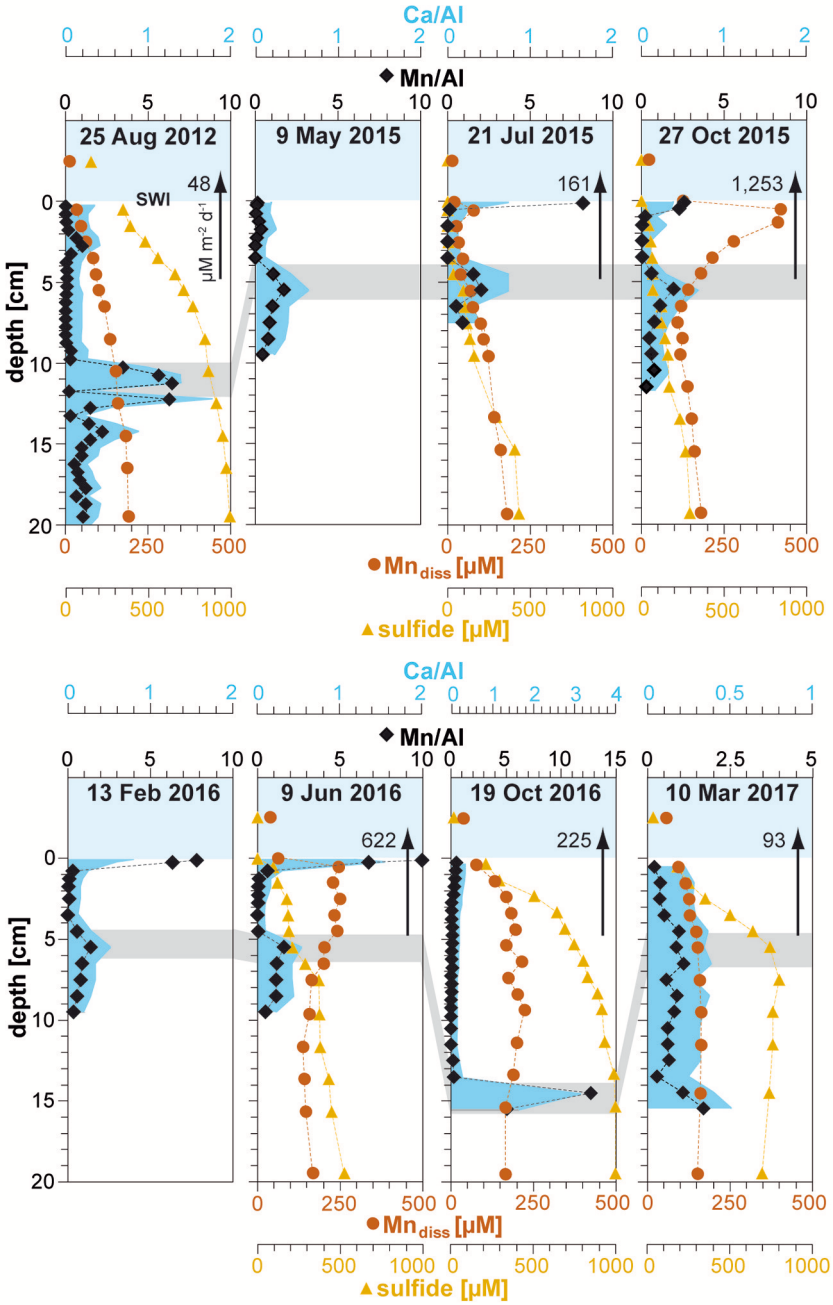


FIGURE 5 | Sedimentary Mn/Al and Ca/Al values, and Mn_{diss} and total sulfide concentrations in pore waters from short cores obtained close to station 271 in the central Gotland Basin. Numbers next to the black arrows indicate pore water fluxes of Mn_{diss} across the sediment-water interface (in $\mu M\ m^{-2}\ d^{-1}$). Gray bars indicate core parallelization based on Pb/Al ratios (Figure S3).

by the sediment trap (**Figure 4**). Although the position of the trap at a water depth of ∼186 m caused a bias between the detection of sinking Mn oxides and the onset of bottom water oxygenation, the steep increase in Mn_{part} fluxes in June 2015 reflected the considerable deposition of Mn oxides at the sediment surface. A temporal bias between the onsets of water column oxygenation and Mn oxide deposition was also apparent in the surface sediments taken close to station 271. Despite the presence of O_2 in nearly the entire water column for more than a month, there was no sign of Mn enrichment in the uppermost fluffy sediments in May 2015 (**Figure 5**). By contrast, an analysis of the core taken in July 2015 showed strongly elevated Mn/Al ratios in the uppermost sample (**Figure 5**). Particle analysis by SEM-EDX revealed a relative abundance of >60% and further supported

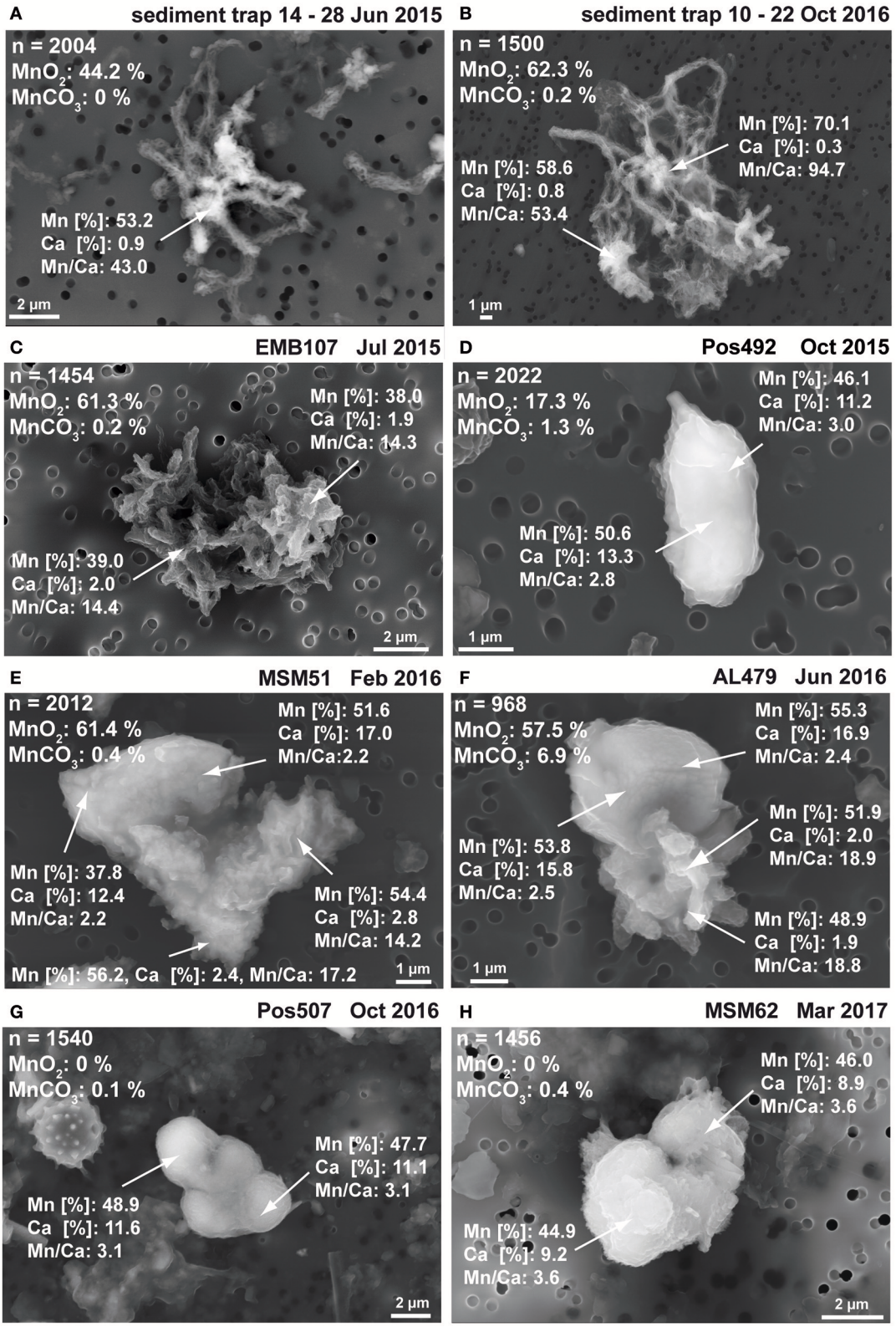


FIGURE 6 | Scanning electron microscopy with energy dispersive X-ray spectroscopy photographs and the results of particle analyses of the Mn mineral phases present in material of the sediment trap **(A, B)** and in the fluffy surface sediments **(C–H)** close to station 271 in the central Gotland Basin.

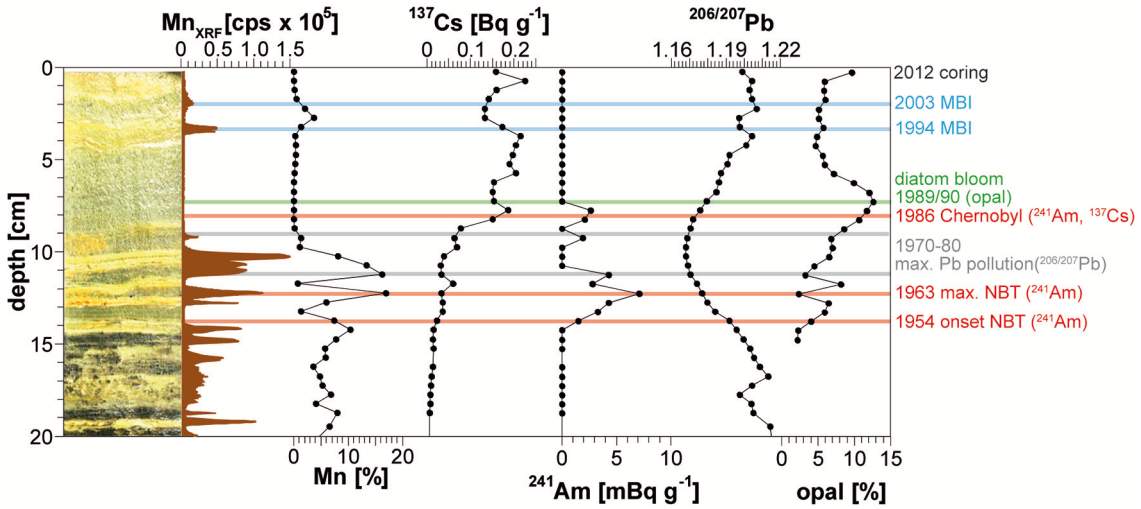


FIGURE 7 | Photograph, Mn counts (X-ray fluorescence core scanning), Mn contents (inductively coupled plasma optical emission spectrometry), activities of ^{137}Cs and ^{241}Am, $^{206/207}$Pb values, and biogenic opal contents of the short core taken in August 2012 close to station 271 in the central Gotland Basin. The data were used to identify time markers for event-stratigraphic dating of the sediment core (Supplementary Dataset).

the clear dominance of Mn oxide particles (**Figure 6C**). The similar morphologies of the Mn oxides and particles found in the sediment trap and in the pelagic redoxclines of the Baltic and Black Seas (**Figures 6A,B**; Dellwig et al., 2010) provide evidence of their origin in the water column. Because agglomeration with organic mucus reduces the density and consequently the sinking velocity of Mn oxides (<1 m d^{-1}; Glockzin et al., 2014), the elevated current velocities resulting from the intruding water masses possibly have delayed the significant deposition of these particles (Holtermann et al., 2017).

Despite the prominence of O_2 in nearly the entire water column, a first signal of the re-establishment of bottom water anoxia was already detected on 09 May 2015, by a slightly elevated Mn_{diss} concentration in the supernatant water of the short core (**Figure 3**). This shift in the bottom water redox regime was even more pronounced in the Mn_{diss} profiles from the cruises in July, September, October, and November 2015 (**Figure 3**). Elevated Mn_{diss} concentrations in the supernatant water and a peak of 81 µM in the pore water just below the Mn/Al peak at the sediment surface in July 2015 implied the onset of Mn oxide reduction and Mn_{diss} escape into the open water column (**Figures 3**, **5**). Consequently, Mn enrichment in the surface sediment decreased and a further increase in the bottom and pore water concentrations of Mn_{diss} occurred in October 2015. This liberated Mn_{diss}, however, was trapped in the bottom waters below a depth of ∼210 m, as indicated by the enhanced Mn_{part} concentrations of SPM in July and October 2015 (**Figure 3**).

The return to pronounced bottom water euxinia was interrupted by a second inflow phase that occurred between the cruises of November 2015 and February 2016. According to the ICES Dataset on Oceanography, O_2 (26 µM) first appeared, at 239 m, on 3 December 2015, (**Figure 9**), but O_2 concentrations decreased in the following cruise, to 7.6 µM, and a slight presence of ∼4 µM sulfide was even determined, on 8 January 2016. Therefore, the main onset of this second inflow pulse must have been between 8 January and 4 February 2016. While the intermediate water column in February 2016 was subjected to pronounced O_2 consumption, the intruding O_2-containing waters most likely caused an uplift of the former anoxic bottom water (**Figure 3**; Holtermann et al., 2017). The subsequent oxygenation of the water column again resulted in pronounced Mn oxide formation and deposition, as indicated by the increasing Mn_{part} fluxes in the sediment trap and the Mn_{part} enrichments in the surface sediments in February and June 2016 (**Figures 4**, **5**). Nevertheless, the rising concentrations of Mn_{diss} and sulfide in the bottom and pore waters beginning in June 2016 (**Figures 3**, **5**) again suggested a comparatively fast switch to a reducing environment in the deeper Gotland Basin. Mn_{part} concentrations as high as 2.4 µM were measured at a water depth of ∼210 m in October 2016 (**Figure 3**); however, these Mn oxides most likely dissolved in the deeper euxinic waters before reaching the seafloor, as also indicated by the absence of Mn enrichments in the corresponding surface sediments (**Figures 5**, **6**). Data from the final two cruises of February and March 2017 documented a progressive extension of euxinic bottom waters highly enriched in Mn_{diss} and the final development toward pre-MBI-like conditions (**Figures 2**, **3**).

The strong Mn_{diss} enrichments suggested a relatively rapid return to reducing near-bottom conditions within less than 3.5 months after each of the two oxygenation events. The reconstructed duration of bottom water oxygenation caused by the first inflow in winter 2014/2015 was about half as long as that determined from the instrumental O_2 time series from the deep water (below 230 m water depth) of the Gotland Basin (**Figure 9**; ICES, 2015). This difference was due to the inclusion of the supernatant water samples from the short cores in our dataset,

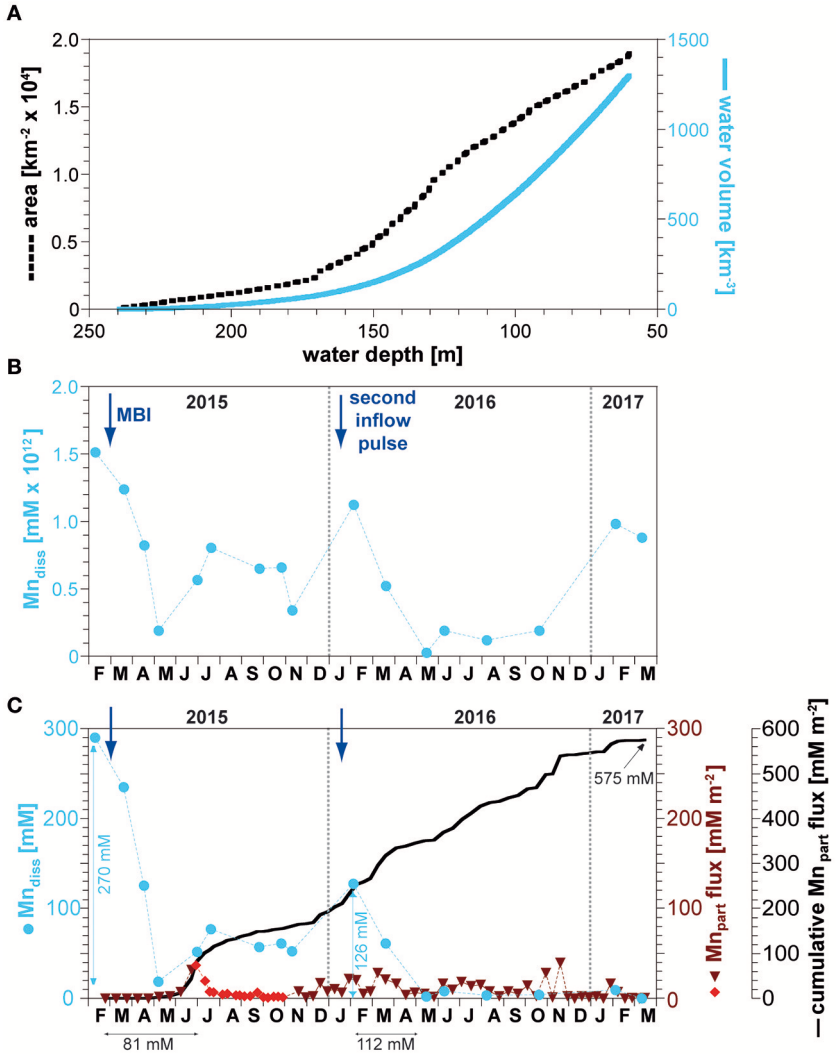


FIGURE 8 | (A) Hypsography of the Gotland Basin (Seifert and Kayser, 1995). Temporal variability of **(B)** the calculated Mn_{diss} inventories in the water column for the entire basin below a water depth of 70 m during the observation period from February 2015 until March 2017 and **(C)** comparison of Mn_{diss} inventories (blue dots) of the water body above the sediment trap (70–186 m water depth, base area 1 m^2), sum of Mn_{part} fluxes from the sediment trap for the individual sampling intervals (brown triangles: 2015–2017 red squares: 2003), and cumulative Mn_{part} flux from the sediment trap (black line, total Mn_{part} flux = 575 mM m^{-2}).

to reflect the conditions very close to the SWI. Although the MBI in 2014 was the third strongest since 1880, with a strength roughly twice as high as the previous MBI, in 2003 (Mohrholz et al., 2015), oxygenation of the Gotland Deep bottom waters was less efficient (**Figure 9**; ICES, 2015). This discrepancy was unexpected, especially given the distinctly lower sulfide level in 2015 than in 2003. Neumann et al. (2017) suggested that the larger amounts of O_2 that entered the Gotland Basin in 2003 were supported by several weaker inflows carrying additional O_2 and that the strength of an MBI is not necessarily a measure of its oxidation capacity in the deeper parts of the Baltic Sea.

Mn Balance Calculations

The water column profiles obtained in the Gotland Deep within the course of the MBI from 2014 suggest substantial losses of Mn_{diss} due to O_2 inputs and the subsequent formation of particulate Mn oxides that sank toward the sea floor (**Figures 3**, **5**, **6**). However, the relatively fast re-establishment of anoxic conditions in the pore and bottom waters also caused a reduction of deposited Mn oxides and an elevated reflux of Mn_{diss} into the water column.

Depending on the basin's topography, the water volume increases exponentially with decreasing water depth (**Figure 8A**) and concentration profiles alone cannot be used to construct elemental budgets. Nonetheless, by multiplying Mn_{diss} concentrations by the corresponding volumes of the hypsography-based water depth intervals, we calculated Mn_{diss} inventories for the entire Gotland Basin below a water depth of ~70 m (**Figure 8B**; Supplementary Dataset). The estimates were based on the assumption that the water column profiles

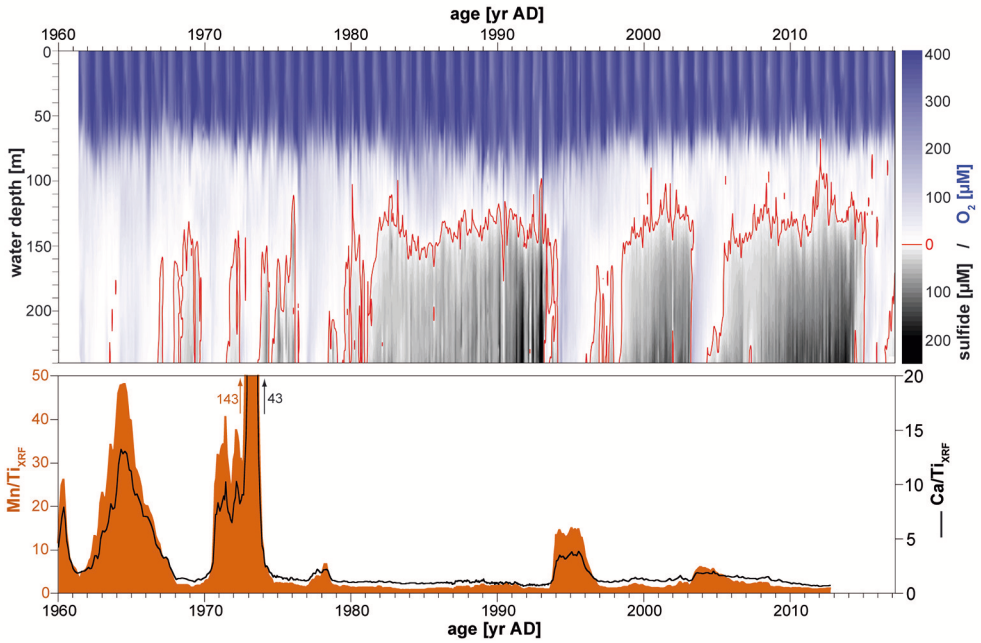


FIGURE 9 | Comparison of the instrumental time series of O_2 and total sulfide in the water column of the Gotland Deep at site 271 from 1960 to 2017 (ICES, 2015) with Mn/Ti and Ca/Ti ratios from X-ray fluorescence core scanning of a dated short core taken in August 2012.

obtained in the central deep were representative of the entire basin.

Compared with the pre-MBI situation, the inventory estimates indicated a loss of almost 90% of water column Mn_{diss} within the first 2 months after the MBI reached the Gotland Basin in the end of February 2015 (**Figure 8B**). Although the deeper parts contribute only marginally to the entire basin volume, strong Mn_{diss} enrichments in the bottom waters due to the re-establishing anoxia led to the fast recovery of the Mn_{diss} inventory, with the amounts roughly half of the pre-MBI level in the following months. Apart from the somewhat longer time span until the recharge of Mn_{diss}, a comparable behavior was also apparent after the second inflow pulse, in January 2016. The Mn_{diss} inventories from the February and March 2017 cruises, which were entirely dominated by Mn_{diss} enrichments in the deeper basin, were about two-thirds of the pre-MBI level. When considering the Mn oxides still present on surface sediments below the O_2-containing water column (above ∼170 m water depth), it is more than likely that the Mn_{diss} inventory of the Gotland Basin will further increase as euxinic conditions expand.

To allow a direct comparison between Mn_{diss} inventories and Mn_{part} fluxes from the sediment trap, Mn_{diss} inventories were also estimated for the water column above the trap (186–70 m water depth) with a base area of 1 m^2 (**Figure 8C**; Supplementary Dataset). As expected, the temporal pattern of these Mn_{diss} inventories generally resembled the total basin inventories, with two prominent phases of Mn_{diss} loss after the two inflows pulses and subsequent replenishment (**Figures 8B,C**). An exception are comparatively low Mn_{diss} values during the last two cruises in 2017 because the extension of reducing bottom waters enriched in Mn_{diss} only marginally exceeded the water depth interval considered by the inventory calculation. Compared to the Mn_{diss} inventories there was no clear relation to the Mn_{part} fluxes from the sediment trap. Thus, the delays between the increases in Mn_{part} fluxes and inflow-derived Mn_{diss} losses can be explained by slowly sinking Mn oxides particles (Glockzin et al., 2014) affected by changing hydrodynamics within the course of the inflow (Holtermann et al., 2017). In addition, the cumulative amounts of Mn_{part} found in the trap until July 2015 (81 mM) were insufficient to explain the maximum Mn_{diss} loss of ∼270 mM until May 2015. In contrast, after the second inflow pulse, Mn_{diss} loss and the cumulative Mn_{part} flux were balanced for the period between February and the end of April 2016 (**Figure 8C**). However, the total cumulative Mn_{part} flux of 575 mM m^{-2} was even twice as high as the pre-MBI Mn_{diss} inventory, which strongly argued against a simple vertical consideration of sediment trap-derived Mn_{part} fluxes.

An indication of the comparatively fast change in the bottom water toward reducing conditions causing Mn oxide dissolution came from pore water profiles that showed strong Mn_{diss} enrichments close to the SWI in October 2015 and June 2016 (**Figure 5**). This suggested that the corresponding increases in bottom water Mn_{diss} concentrations and inventories were strongly related to Mn_{diss} pore water fluxes that were distinctly higher than those prior to the MBI in 2014 (**Figures 2**, **5**). Extrapolation of the highest pore water Mn_{diss} flux of 1,253 µM m^{-2} d^{-1}, which occurred in October 2015, to the area located below a water depth of 220 m (642 km^2) and subjected to anoxic conditions resulted in an areal Mn_{diss} flux of 8×10^8 mM d^{-1}. This areal pore water flux would need ∼55 days to achieve the

calculated Mn_{diss} inventory of 4.5×10^{10} mM in the water volume below 220 m (6.6 km^3). Although this time span appears reasonable, pore water fluxes alone do not adequately explain the development of Mn_{diss} inventories especially those measured toward the end of the observation period. Even if in October 2016 and March 2017 the Mn_{diss} inventory was limited to the anoxic bottom waters below a water depth of 225 m (3.8 km^3) and 190 m (38 km^3), the time needed for the respective areal pore water fluxes (1.1×10^8 mM d^{-1} for 473 km^2 and 1.4×10^8 mM d^{-1} for 1,499 km^2) to achieve bottom water inventories of 1.3×10^8 and 8.8×10^{11} mM Mn_{diss} would have increased to 1,240 and 6,308 days, respectively. The discrepancy is undoubtedly due to the fact that the pore water fluxes determined during those two cruises in the deepest part of the basin were no longer representative of the larger basin. Along with the lack of Mn oxides at the sediment surface, the pore water profile and Mn_{diss} flux from the March 2017 cruise clearly approached pre-MBI conditions (**Figure 5**) at the deepest part of the basin. An important Mn source during these stages of the re-establishment and expansion of euxinic conditions was therefore the surface sediments from shallower water depths, where Mn oxides most likely persisted.

Several aspects strongly argue for substantial basin-internal transport of low-density Mn oxide particles (Glockzin et al., 2014) by lateral currents: (i) the temporal deviation between Mn_{diss} loss in the water column and Mn oxide sedimentation (**Figure 8C**), (ii) the rapid replenishment of the water column Mn_{diss} inventory, which cannot be explained by pore water Mn fluxes alone, (iii) the presence of Mn_{part} in oxygenated waters without a significant Mn_{diss} source, e.g., in June 2016 (**Figure 3**), (iv) the highly fluctuating pattern of Mn_{part} fluxes of the sediment trap during the second inflow phase (**Figure 4**), and (v) the discrepancy between the Mn_{diss} inventory of the water column and the Mn_{part} flux determined by the sediment trap samples (**Figure 8C**). If not already reduced by expanding euxinic waters, the enhancement of bottom currents by the MBI (Holtermann et al., 2017) most likely also re-suspended Mn oxides previously deposited in the shallower parts of the basin. Indeed, the Mn contents of the surface sediment samples from two shallower stations (MUC OD in 211 m and TrKl04 in 151 m water depth) west of site 271 (**Figure 1**) in October 2015 were 9.0and 3.1 wt%, respectively (Supplementary Dataset). The overall pathway of material transport toward the central basin finds support by several previous studies. Model results suggest an anti-clockwise direction of near-bottom currents with velocities decreasing toward the central basin (Hille et al., 2006). Along with the largest thickness of Littorina muds, the authors further report highest sedimentation rates in the deepest part of the Gotland Basin. Here, highest accumulation of TOC and heavy metals relates to physical forcing rather than biogeochemical processes (Emeis et al., 1998; Leipe et al., 2011). In addition to this physical transport of Mn_{part}, bottom currents likely also enhanced the geochemical focusing of Mn_{diss} as suggested for lakes by Schaller and Wehrli (1997).

On the other hand, Mn oxide particles may also have left the basin with the intensified deep currents during the MBI. Lower salinity in the neighboring Fårö Deep during the MBI in 2014 (Holtermann et al., 2017), however, indicate that the connection to the Gotland Basin occurred mainly via comparatively Mn-poor water masses from water intermediate depths. This has also been suggested for the downstream connection to the Landsort Deep by Häusler et al. (2018). Along with the basin's topography surrounded by sill depths of ∼130 m and less, the current patterns in the deep Gotland Basin rather argue for a pronounced basin-internal cycling of Mn (Hille et al., 2006; Holtermann et al., 2017).

Implications for Mn Carbonate Formation

Although the sediments of the deep basins of the Baltic Sea are the modern type-locality for exceptional Mn carbonate accumulation (Lenz et al., 2015; Häusler et al., 2018), our data argue against prominent Mn carbonate formation, at least in the central Gotland Deep subsequent to the MBI from 2014. Studies of the influence of previous MBIs on sedimentary Mn dynamics in the Gotland Deep require dating of the sediments to correlate instrumental time series from the water column with sediment signatures. This approach was first applied by Neumann et al. (1997), who compared dated Mn carbonate records of sub-recent sediments with the hydrographic long-term data available for the Gotland Basin. However, as recently shown for Mn-rich sediments from the Landsort Deep by Häusler et al. (2018), the application of CRS-based age modeling using ^{210}Pb (Appleby and Oldfield, 1978) is strongly compromised by the ingrowth of authigenic Mn carbonate and scavenging processes at pelagic redoxclines (Wei and Murray, 1994; Swarzenski et al., 1999). To construct an age model for the short core obtained from site 271 in 2012, we used the event-stratigraphic dating method, previously successfully applied to Mn-rich sediments from the Landsort Deep (Häusler et al., 2018) and the eastern Gotland Basin (Moros et al., 2017). Several time markers were used for the linear interpolation (**Figure 7**): the radionuclides ^{137}Cs and ^{241}Am, reflecting the onset of nuclear bomb testing in 1954 and its peak in 1963, as well as the Chernobyl accident in 1986 (Koide et al., 1977; Appleby et al., 1991), stable Pb isotopes indicating maximum Pb pollution between 1970 and 1978 (Renberg et al., 2001), a basin-wide opal layer resulting from a massive diatom bloom between 1988 and 1990 (Wasmund et al., 2011; Kabel et al., 2012), and the Mn layers that formed after the MBIs in 1994 and 2003 (Moros et al., 2017).

The XRF scan of the dated short core showed two periods of strong Mn enrichment, around 1963 and 1970 (**Figure 9**). The parallel patterns of Mn/Ti and Ca/Ti were compatible with the pronounced presence of Mn carbonate (Ca-rich rhodochrosite). A comparison with instrumental O_2/sulfide data (ICES, 2015) suggested a tight relationship between Mn carbonate and O_2-containing bottom waters, in line with the widely accepted linkage between MBIs and Mn carbonate formation (Huckriede and Meischner, 1996; Neumann et al., 1997; Sternbeck and Sohlenius, 1997). The conceptual models of those studies were based on the assumption that massive Mn oxide formation caused by MBI-related bottom water oxygenation is followed by the transformation of deposited Mn oxides into Mn carbonates during the early stages of re-establishment of anoxia. However, as noted above for the MBI from 1993 (Heiser et al., 2001), MBIs do not necessarily result in substantial Mn carbonate

formation, as was the case in our corresponding core, with its less pronounced Mn enrichments following the inflows in 1976, 1993, and especially 2003 (**Figure 9**). Although minor amounts of Mn carbonate crystals were identified in the surface sediment in June 2016 (**Figure 6F**), the fluffy layers of the cores from October 2016 and March 2017 were barren of any Mn enrichments (**Figures 5**, **6**). This finding argues against sustained Mn carbonate precipitation after the MBI from 2014. The disappearance of the freshly formed Mn carbonate in the fluffy layer samples may have been related to dissolution in the undersaturated bottom waters, as suggested by Heiser et al. (2001) for the partly missing Mn carbonate layers after the MBI in 1993.

In line with previous studies in the Gotland Basin and Landsort Deep (Neumann et al., 1997; Lenz et al., 2015; Häusler et al., 2018), the appearance of discrete Mn carbonate-rich layers in the laminated sediments implied the temporal coupling of their formation to the oxygenation events. Accordingly, a dispersed precipitation from pore waters supersaturated in Mn carbonate seems less likely. Indeed, calculation of the saturation indices for Mn carbonate from pore water data of the Gotland Deep suggests undersaturation at the SWI and supersaturation not before a sediment depth of 3–10 cm (Carman and Rahm, 1997; Heiser et al., 2001; Lenz et al., 2015). Although these studies were based on pore water data obtained during stagnation periods, with Mn_{diss} concentrations similar to those measured in our August 2012 samples (**Figure 5**), the lack of a pronounced Mn carbonate presence in the surface sediments from October 2015, when pore water Mn_{diss} concentrations were even higher close to the SWI, points to a more complex mechanism of Mn carbonate formation (**Figures 5**, **6D**), especially since fundamental changes in pore water chemistry during periods of intense (∼1960 and ∼1970) and weak to absent (e.g., the MBIs of 1993, 2003, 2014) Mn carbonate formation are rather unlikely (Lenz et al., 2015). Field data as well as experimental approaches suggest kinetic reasons and an inhibition by organics and/or phosphate as limitations on the precipitation of Ca-rich Mn carbonate in the Baltic Sea (Mucci, 1988; Jakobsen and Postma, 1989; Böttcher, 1998). Böttcher (1998) mentioned a potential role for microbial mediation, as demonstrated for other authigenic mineral phases, such as apatite and dolomite (Vasconcelos et al., 1995; Schulz and Schulz, 2005; Petrash et al., 2015).

The reduction of deposited Mn oxides as the initial step in Mn carbonate formation could occur by the upwards migration of pore water sulfide (e.g., Burdige and Nealson, 1986; Yao and Millero, 1993), but competing dissimilatory Mn reduction (e.g., Lovley, 1993) has to be considered as well. Indeed, the oxygen isotope signatures of Mn carbonates from the Gotland Basin indicated microbial involvement at least during Mn oxide reduction (Neumann et al., 2002). In incubation experiments, Aller and Rude (1988) observed the formation of Mn carbonate during microbially mediated Mn oxide reduction, in which Fe sulfides served as the reductants. In addition to Mn sulfide formation, Lee et al. (2011) reported the production of Mn carbonate by the facultative anaerobic Mn-reducing bacteria *Shewanella oneidensis* MR-1 in experiments that included Mn oxide in the medium. The enormous deposition of Mn oxides at the SWI during oxygenation events in the deeps of the Baltic Sea may therefore be accompanied by a shift in the bacterial community from sulfate- to metal-reducing phyla. A role for bacterial community dynamics during the re-establishment of anoxic conditions after the MBI from 1993 was documented by Piker et al. (1998). In that study, the sulfate reduction rates in the surface sediments (0–2 cm) in May 1995 reached distinct maxima compared to the previous oxygenated state of the bottom water in June 1994. Assuming bacterial mediation, the duration of non-euxinic conditions at the SWI may be crucial for Mn carbonate formation. In other words, the too rapid re-establishment of euxinia after a single inflow, due to excess sulfide production by sulfate-reducing bacteria, may also cause an unfavorable environment for Mn-reducing phyla potentially involved in Mn carbonate formation (Lee et al., 2011). Although there have been very few measurements allowing a description of the conditions directly at the SWI, the time series of O_2 and sulfide in the water column covering the past ∼60 years (**Figure 9**) indicated a substantial difference between Mn carbonate-rich and Mn-carbonate-poor inflow periods. Along with distinctly lower sulfide levels, bottom water oxygenation was of considerably longer duration during the Mn carbonate-rich period between the 1960s and mid-1970s (around 20 MBIs; Mohrholz et al., 2015) than was the case during the sporadic inflows entering the Gotland Basin in 1993, 2003, and 2015. This temporal aspect accords with observations in the Landsort Deep, where massive Mn carbonate formations also occurred during long-lasting periods of hypoxic (slightly oxygenated) but non-euxinic bottom water conditions (Häusler et al., 2018). In contrast to the comparatively short presence of O_2 in the bottom waters after the MBI of 2014, which fostered a considerable Mn_{diss} reflux, longer-lasting oxygenation would prevent the escape of Mn to the open water column and thus ensure a high Mn abundance at the SWI.

Although ranked as the third strongest MBI since 1880 (Mohrholz et al., 2015), the inflow from 2014 is rather of short-term relevance for Gotland basin. This is especially true when considering the fast return to an euxinic situation, which paradoxically is even promoted by the inflow of O_2-containing but also highly saline waters strengthening water column stratification. Whether this episode will have a lasting effect on nutrient and trace metal budgets remains unclear so far and asks for continuing studies. For instance, the tight relation of Mn, Fe, and P at pelagic redoxclines due to formation of mixed solid phases comprising Mn oxide, Fe oxyhydroxides, and adsorbed phosphate (Dellwig et al., 2010) was also relevant during the current inflow as indicated by elevated deposition of P- and Fe-rich particles between July 2015 and June 2016 (Figure S4). However, the absence of P enrichments at the SWI during re-establishing euxinia (October 2016 and March 2017) suggests considerable release of phosphate back into the water column. While Mn carbonates incorporate certain amounts of phosphate (Jilbert and Slomp, 2013), as seen by elevated P/Al values in older Mn-rich layers below 10 cm sediment depth (**Figure 5** and Figure S4), this P sink is currently missing.

The lack of Mn carbonate not only compromises its use as an indicator for past inflow events but also has important implications for other proxies related to Mn authigenesis. A

prominent example is Mo and its isotopes, showing strong fractionation during scavenging by Mn oxides (Wasylenki et al., 2008). The possible conservation of the altered isotope signature by sedimentary fixation of Mo released from dissolving Mn oxides may therefore result in misleading redox interpretations (Noordmann et al., 2015; Kurzweil et al., 2016; Scholz et al., 2018). Complementing studies including trace metals are required to shed more light on the possible pitfalls that may be generated by inflow events like the one in 2014 because such oxygenation events should be also of relevance for other restricted basins and fjords as well as ancient epicontinental seas that were often subjected to pronounced O_2-deficiency but also redox changes (Hein et al., 1999; Jenkyns, 2010).

CONCLUSIONS

The dynamics of Mn in the water column and sediments were studied in the Gotland Deep (central Baltic Sea) subjected to an MBI of 2014. The first signals of water column oxygenation due to the approaching inflow waters appeared at the beginning of March 2015. This was followed by an estimated loss of nearly 90% of the Mn_{diss} inventory in the water column over the following 2 months, which caused a remarkable deposition of Mn oxides. However, increased Mn_{diss} pore water concentrations and fluxes as well as elevated bottom water Mn_{diss} levels suggested the re-establishment of reducing conditions at the latest after 3.5 months. A second inflow pulse in the beginning of 2016 interrupted this development, but after less than 4 months there was a shift back to reducing bottom waters as well.

Budget calculations indicated a Mn_{diss} recovery of ∼70% of the pre-MBI level at the end of the observation period in winter 2017. The recovery could not be explained by pore water fluxes from the central basin alone. Along with the Mn_{part} fluxes determined from a sediment trap, these estimates further suggested a pronounced basin-internal cycling of Mn during and subsequent to the MBI, which may have benefitted from the circulation patterns in the Gotland Basin and concomitant sediment focusing, including the transport of solid Mn phases from shallower areas toward the central deep.

A comparison of a dated sediment Mn record with instrumental O_2/sulfide data generally confirmed the close relationship between Mn carbonate and inflow-related bottom water oxygenation. However, compared to the longer-lasting oxygenation periods in the 1960s and early 1970s, the less pronounced or even absent Mn enrichments after the single inflows in 1976, 1993, and 2003 implied unfavorable conditions for Mn carbonate formation, possibly due to the too rapid shift back to euxinic conditions. Since there was no indication for substantial Mn carbonate formation after both oxygenation pulses in 2015 and 2016 within our study period of ∼2 years, it appears rather unlikely that intensive Mn carbonate formation will take place under the currently fast re-establishing euxinic situation. This assumption compromises the use of Mn carbonate layers as a simple proxy for the identification of past MBIs. For instance, scavenged trace metals imported to an increased extent by deposited Mn oxides may serve as complementing proxies if conditions at the SWI assure their fixation. Nonetheless, the combined consideration of a previous study in the Landsort Deep (Häusler et al., 2018) and the present work in the Gotland Basin emphasizes the suitability of the deeps of the Baltic Sea as modern analogs for oxygen-deficient but comparatively dynamic systems in the geological past.

AUTHOR CONTRIBUTIONS

OD designed the study, performed ICP measurements, and wrote the manuscript. BS contributed the gamma spectroscopy data. DM organized sampling during several cruises and contributed oceanographic knowledge. FP was responsible for the sediment trap. KH contributed to the age model. HA was involved in the oceanography and the age model. All authors contributed to data analysis, discussion, and finalization of the manuscript.

ACKNOWLEDGMENTS

We are indebted to the IOW cruise leaders M. Gogina, G. Jost, K. Jürgens, J. Kuss, V. Mohrholz, M. Naumann, R. Prien, M. Schmidt, L. Umlauf, J. Waniek, N. Wasmund as well as U. Lips (Tallinn University of Technology) and R. Schneider (University of Kiel) for enabling extra CTD casts, J. Donath for water sampling during monitoring cruises, and to the captains and crews of the RVs *Alkor*, *Elisabeth Mann Borgese*, *Maria S. Merian*, *Meteor*, *Poseidon*, *Prof. A. Penck*, and *Salme*. We thank R. Bahlo and S. Plewe for the SEM-EDX support, A. Köhler for the acid digestions, U. Hehl and R. Hansen for sediment trap deployment and analyses, and T. Leipe and M. Moros for MUCs from cruises MSM51 and 62. The authors thank two reviewers for constructive comments on an earlier version of the manuscript. This work was funded by the Leibniz Association through grant SAW-2017-IOW-2 649 (BaltRap) and the IOW monitoring program. The publication of this article was funded by the Open Access Fund of the Leibniz Association.

Special thanks to our bosun Dieter Knoll, who died in late 2017.

SUPPLEMENTARY MATERIAL

The Supplementary Material for this article can be found online at: https://www.frontiersin.org/articles/10.3389/fmars.2018.00248/full#supplementary-material

REFERENCES

Aller, R. C., and Rude, P. D. (1988). Complete oxidation of solid phase sulfides by manganese and bacteria in anoxic marine sediments. *Geochim. Cosmochim. Acta* 52, 751–765. doi: 10.1016/0016-7037(88)90335-3

Appleby, P. G., and Oldfield, F. (1978). The calculation of lead-210 dates assuming a constant rate of supply of unsupported ^{210}Pb to the sediment. *Catena* 5, 1–8. doi: 10.1016/S0341-8162(78)80002-2

Appleby, P. G., Richardson, N., and Nolan, P. J. (1991). ^{241}Am dating of lake sediments. *Hydrobiologia* 214, 35–42. doi: 10.1007/BF00050929

Berg, P., Risgaard-Petersen, N., and Rysgaard, S. (1998). Interpretation of measured concentration profiles in sediment pore water. *Limnol. Oceanogr.* 43, 1500–1510. doi: 10.4319/lo.1998.43.7.1500

Böttcher, M. E. (1998). Manganese(II) partitioning during experimental precipitation of rhodochrosite–calcite solid solutions from aqueous solutions. *Mar. Chem.* 62, 287–297. doi: 10.1016/S0304-4203(98)00039-5

Boudreau, B. P. (1997). *Diagenetic Models and their Implementation: Modeling Transport and Reactions in Aquatic Sediments*. Berlin; Heidelberg: Springer-Verlag.

Brady, N. C. (1984). *The Nature and Properties of Soils, 9*. New York, NY: Macmillan Publishing Co.

Brügmann, L., Hallberg, R., Larsson, C., and Löffler, A. (1998). Trace metal speciation in sea and pore water of the Gotland Deep, Baltic Sea, 1994. *Appl. Geochem.* 13, 359–368. doi: 10.1016/S0883-2927(97)00105-4

Burdige, D. J. (1993). The biogeochemistry of manganese and iron reduction in marine sediments. *Earth Sci. Rev.* 35, 249–284. doi: 10.1016/0012-8252(93)90040-E

Burdige, D. J., and Nealson, K. H. (1986). Chemical and microbiological studies of sulfide-mediated manganese reduction. *Geomicrobiol. J.* 4, 361–387. doi: 10.1080/01490458609385944

Calvert, S. E., and Pedersen, T. F. (1993). Geochemistry of recent oxic and anoxic marine sediments: implications for the geological record. *Mar. Geol.* 113, 67–88. doi: 10.1016/0025-3227(93)90150-T

Calvert, S. E., and Pedersen, T. F. (1996). Sedimentary geochemistry of manganese; implications for the environment of formation of manganiferous black shales. *Econ. Geol.* 91, 36–47. doi: 10.2113/gsecongeo.91.1.36

Calvert, S. E., and Price, N. B. (1970). Composition of manganese nodules and manganese carbonates from Loch Fyne, Scotland. *Contribut. Mineral. Petrol.* 29, 215–233. doi: 10.1007/BF00373306

Carman, R., and Rahm, L. (1997). Early diagenesis and chemical characteristics of interstitial water and sediments in the deep deposition bottoms of the Baltic proper. *J. Sea Res.* 37, 25–47. doi: 10.1016/S1385-1101(96)00003-2

Carstensen, J., Andersen, J. H., Gustafsson, B. G., and Conley, D. J. (2014). Deoxygenation of the Baltic Sea during the last century. *Proc. Natl. Acad. Sci. U.S.A.* 111, 5628–5633. doi: 10.1073/pnas.1323156111

Cline, J. D. (1969). Spectrophotometric determination of hydrogen sulfide in natural waters. *Limnol. Oceanogr.* 14, 454–458. doi: 10.4319/lo.1969.14.3.0454

Croudace, I. W., Rindby, A., and Rothwell, R. G. (2006). ITRAX: description and evaluation of a new multi-function X-ray core scanner. *Geol. Soc. Lond. Spec. Publ.*267, 51–63. doi: 10.1144/GSL.SP.2006.267.01.04

Davidson, A. T., and Marchant, H. J. (1987). Binding of manganese by Antarctic Phaeocystis pouchetii and the role of bacteria in its release. *Mar. Biol.* 95, 481–487. doi: 10.1007/BF00409577

Dellwig, O., Leipe, T., März, C., Glockzin, M., Pollehne, F., Schnetger, B. et al. (2010). A new particulate Mn-Fe-P-shuttle at the redoxcline of anoxic basins. *Geochim. Cosmochim. Acta* 74, 7100–7115. doi: 10.1016/j.gca.2010.09.017

Dellwig, O., Schnetger, B., Brumsack, H.-J., Grossart, H.-P., and Umlauf, L. (2012). Dissolved reactive manganese at pelagic redoxclines (part II): hydrodynamic conditions for accumulation. *J. Mar. Syst.* 90, 31–41. doi: 10.1016/j.jmarsys.2011.08.007

De Vitre, R. R., Buffle, J., Perretm, D., and Baudat, R. (1988). A study of iron and manganese transformations at the O2S(-II) transition layer in a eutrophic lake (Lake Bret, Switzerland): a multimethod approach. *Geochim. Cosmochim. Acta* 52, 1601–1613. doi: 10.1016/0016-7037(88)90229-3

Dahl, T. W., Anbar, A. D., Gordon, G. W., Rosing, M. T., Frei, R., and Canfield, D. E. (2010). The behavior of molybdenum and its isotopes across the chemocline and in the sediments of sulfidic Lake Cadagno, Switzerland. *Geochim. Cosmochim. Acta* 74, 144–163. doi: 10.1016/j.gca.2009.09.018

Diaz, R. J., and Rosenberg, R. (2008). Spreading dead zones and consequences for marine ecosystems. *Science* 321, 926–929. doi: 10.1126/science.1156401

Dyrssen, D., and Kremling, K. (1990). Increasing hydrogen sulfide concentration and trace metal behavior in the anoxic Baltic waters. *Mar. Chem.* 30, 193–204. doi: 10.1016/0304-4203(90)90070-S

EMODnet Bathymetry Consortium (2016). *EMODnet Digital Bathymetry (DTM)*. EMODnet Bathymetry.

Emeis, K.-C., Neumann, T., Endler, R., Struck, U., Kunzendorf, H., and Christiansen, C. (1998). Geochemical records of sediments in the Eastern Gotland Basin—products of sediment dynamics in a not-so-stagnant anoxic basin? *Appl. Geochem.* 13, 349–358. doi: 10.1016/S0883-2927(97)00104-2

Feistel, R., Nausch, G., Heene, T., Piechura, J., and Hagen, E. (2004). Evidence for a warm water inflow into the Baltic Proper in summer 2003. *Oceanologia* 46, 581–598.

Feistel, R., Nausch, G., Matthäus, W., and Hagen, E. (2003). Temporal and spatial evolution of the Baltic deep water renewal in spring 2003. *Oceanologia* 45, 623–642.

Friedl, G., Wehrli, B., and Manceau, A. (1997). Solid phases in the cycling of manganese in eutrophic lakes: new insights from EXAFS spectroscopy. *Geochim. Cosmochim. Acta* 61, 275–290. doi: 10.1016/S0016-7037(96)00316-X

Gingele, F. X., and Kasten, S. (1994). Solid-phase manganese in Southeast Atlantic sediments: implications for the paleoenvironment. *Mar. Geol.* 121, 317–332. doi: 10.1016/0025-3227(94)90037-X

Glockzin, M., Pollehne, F., and Dellwig, O. (2014). Stationary sinking velocity of authigenic manganese oxides at pelagic redoxclines. *Mar. Chem.* 160, 67–74. doi: 10.1016/j.marchem.2014.01.008

Gustafsson, B. G., Schenk, F., Blenckner, T., Eilola, K., Meier, H. E. M., Müller-Karulis, B. et al. (2017). Reconstructing the development of Baltic Sea eutrophication 1850–2006. *Ambio* 41, 534–548. doi: 10.1007/s13280-012-0318-x

Hansel, C. M. (2017). "Chapter 2: Manganese in marine microbiology," in *Advances in Microbial Physiology 70,* ed R. K. Poole (London: Academic Press), 37–83.

Hardisty, D. S., Riedinger, N., Planavsky, N. J., Asael, D., Andrén, T., Jørgensen, B. B. et al. (2016). A Holocene history of dynamic water column redox conditions in the landsort deep, Baltic Sea. *Am. J. Sci.* 316, 713–745. doi: 10.2475/08.2016.01

Häusler, K., Dellwig, O., Schnetger, B., Feldens, P., Leipe, T., Moros, M. et al. (2018), Massive Mn carbonate formation in the Landsort deep (Baltic Sea): Hydrographic prerequisites, temporal succession and Mn budget calculations. *Mar. Geol.* 395, 260–270. doi: 10.1016/j.margeo.2017.10.010

Hein, J. R., Fan, D., Ye, J., Liu, T., and Yeh, H.-W. (1999). Composition and origin of early Cambrian Tiantaishan phosphorite–Mn carbonate ores, Shaanxi province, China. *Ore. Geol. Rev.* 15, 95–134. doi: 10.1016/S0169-1368(99)00017-7

Heiser, U., Neumann, T., Scholten, J., and Stüben, D. (2001). Recycling of manganese from anoxic sediments in stagnant basins by seawater inflow: a study of surface sediments from the Gotland Basin, Baltic Sea. *Mar. Geol.* 177, 151–166. doi: 10.1016/S0025-3227(01)00129-3

Hille, S., Leipe, T., and Seifert, T. (2006). Spatial variability of recent sedimentation rates in the Eastern Gotland Basin (Baltic Sea). *Oceanologia* 48, 297–317.

Hinrichs, J., Dellwig, O., and Brumsack, H.-J. (2002). Lead in sediments and suspended particulate matter of the German Bight: natural versus anthropogenic origin. *Appl. Geochem.* 17, 621–632. doi: 10.1016/S0883-2927(01)00124-X

Hlawatsch, S., Neumann, T., van den Berg, C. M. G., Kersten, M., Harff, J., and Suess, E. (2002). Fast-growing, shallow-water ferro-manganese nodules from the western Baltic Sea: origin and modes of trace element incorporation. *Mar. Geol.* 182, 373–387. doi: 10.1016/S0025-3227(01)00244-4

Holtermann, P. L., Prien, R., Naumann, M., Mohrholz, V., and Umlauf, L. (2017). Deepwater dynamics and mixing processes during a major inflow event in the central Baltic Sea. J. *Geophys. Res. Oceans* 122, 6648–6667. doi: 10.1002/2017JC013050

Huckriede, H., and Meischner, D. (1996). Origin and environment of manganese-rich sediments within black-shale basins. *Geochim. Cosmochim. Acta* 60, 1399–1413. doi: 10.1016/0016-7037(96)00008-7

Hurrell, J. W. (1995). Decadal trends in the North Atlantic oscillation: regional temperatures and precipitation. *Science* 269, 676–679. doi: 10.1126/science.269.5224.676

ICES (2015). *Dataset on Oceanography*. Copenhagen: The International Council for the Exploration of the Sea.

Jacobs, L., Emerson, S., and Huested, S. S. (1987). Trace metal geochemistry in the Cariaco trench. *Deep Sea Res. Part A. Oceanogr. Res. Pap*. 34, 965–981. doi: 10.1016/0198-0149(87)90048-3

Jacobs, L., Emerson, S., and Skei, J. (1985). Partitioning and transport of metals across the O2H2S interface in a permanently anoxic basin: framvaren Fjord, Norway. *Geochim. Cosmochim. Acta* 49, 1433–1444. doi: 10.1016/0016-7037(85)90293-5

Jakobsen, R., and Postma, D. (1989). Formation and solid solution behavior of Ca-rhodochrosites in marine muds of the Baltic deeps. *Geochim. Cosmochim. Acta* 53, 2639–2648, doi: 10.1016/0016-7037(89)90135-X

Jenkyns, H. C. (2010). Geochemistry of oceanic anoxic events. *Geochem. Geophys. Geosyst*. 11, Q03004. doi: 10.1029/2009GC002788

Jilbert, T., and Slomp, C. P. (2013). Iron and manganese shuttles control the formation of authigenic phosphorus minerals in the euxinic basins of the Baltic Sea. *Geochim. Cosmochim. Acta* 107, 155–169. doi: 10.1016/j.gca.2013.01.005

Johnson, J. E., Webb, S. M., Ma, C., and Fischer, W. W. (2016). Manganese mineralogy and diagenesis in the sedimentary rock record. *Geochim. Cosmochim. Acta* 173, 210–231. doi: 10.1016/j.gca.2015.10.027

Kabel, K., Moros, M., Porsche, C., Neumann, T., Adolphi, F., Andersen, T. J. et al. (2012). Impact of climate change on the Baltic Sea ecosystem over the past 1,000 years. *Nat. Clim. Change* 2, 871–874. doi: 10.1038/nclimate1595

Koide, M., Goldberg, E. D., Herron, M. M., and Langway, C. C. (1977). Transuranic depositional history in south Greenland firn layers. *Nature* 269, 137–139. doi: 10.1038/269137a0

Koschinsky, A., Winkler, A., and Fritsche, U. (2003). Importance of different types of marine particles for the scavenging of heavy metals in the deep-sea bottom water. *Appl. Geochem.* 18, 693–710. doi: 10.1016/S0883-2927(02)00161-0

Kurzweil, F., Wille, M., Gantert, N., Beukes, N. J., and Schoenberg, R. (2016). Manganese oxide shuttling in pre-GOE oceans – evidence from molybdenum and iron isotopes. *Earth Planet. Sci. Lett*. 452, 69–78. doi: 10.1016/j.epsl.2016.07.013

Labrenz, M., Jost, G., and Jürgens, K. (2007). Distribution of abundant prokaryotic organisms in the water column of the central Baltic Sea with an oxic-anoxic interface. *Aquat. Microb. Ecol.* 46, 177–190. doi: 10.3354/ame046177

Lee, J. H., Kennedy, D. W., Dohnalkova, A., Moore, D. A., Nachimuthu, P., Reed, S. B. et al. (2011). Manganese sulfide formation via concomitant microbial manganese oxide and thiosulfate reduction. *Environ. Microbiol.* 13, 3275–3288. doi: 10.1111/j.1462-2920.2011.02587.x

Leipe, T., Tauber, F., Vallius, H., Virtasalo, J., Uścinowicz, S., Kowalski, N. et al. (2011). Particulate organic carbon (POC) in surface sediments of the Baltic Sea. *Geo Mar. Lett*. 31, 175–188. doi: 10.1007/s00367-010-0223-x

Lenz, C., Jilbert, T., Conley, D. J., Wolthers, M., and Slomp, C. P. (2015). Are recent changes in sediment manganese sequestration in the euxinic basins of the Baltic Sea linked to the expansion of hypoxia? *Biogeosciences* 12, 4875–4894. doi: 10.5194/bg-12-4875-2015

Lepland, A., and Stevens, R. L. (1998). Manganese authigenesis in the Landsort Deep, Baltic Sea. *Mar. Geol.* 151, 1–25. doi: 10.1016/S0025-3227(98)00046-2

Lettmann, K. A., Riedinger, N., Ramlau, R., Knab, N., Böttcher, M. E., Khalili, A. et al. (2012). Estimation of biogeochemical rates from concentration profiles: a novel inverse method. *Estuar. Coast. Shelf Sci*. 100, 26–37. doi: 10.1016/j.ecss.2011.01.012

Lovley, D. (1993). Dissimilatory metal reduction. *Annu. Rev. Microbiol.* 47, 263–284. doi: 10.1146/annurev.mi.47.100193.001403

Luther, G. W., Sundby, B., Lewis, B. L., Brendel, P. J., and Silverberg, N. (1997). Interactions of manganese with the nitrogen cycle: alternative pathways to dinitrogen. *Geochim. Cosmochim. Acta* 61, 4043–4052. doi: 10.1016/S0016-7037(97)00239-1

Madison, A. S., Tebo, B. M., and Luther, G. W. (2011). Simultaneous determination of soluble manganese(III), manganese(II) and total manganese in natural (pore)waters. *Talanta* 84, 374–381. doi: 10.1016/j.talanta.2011.01.025

März, C., Stratmann, A., Matthiessen, J., Meinhardt, A. K., Eckert, S., Schnetger, B. et al. (2011). Manganese-rich brown layers in Arctic Ocean sediments: composition, formation mechanisms, and diagenetic overprint. *Geochim. Cosmochim. Acta* 75, 7668–7687. doi: 10.1016/j.gca.2011.09.046

Matthäus, W., and Franck, H. (1992). Characteristics of major Baltic inflows—a statistical analysis. *Cont. Shelf Res.* 12, 1375–1400. doi: 10.1016/0278-4343(92)90060-W

Matthäus, W., Nehring, D., Feistel, R., Nausch, G., Mohrholz, V., and Lass, H.-U. (2008). "The inflow of highly saline water into the Baltic Sea," in *State and Evolution of the Baltic Sea 1952–2005*, eds R. Feistel, G. Nausch, and N.Wasmund (Hoboken, NJ: John Wiley and Sons), 265.

Matthäus, W., and Schinke, H. (1999). *The Influence of River Runoff on Deep Water Conditions of the Baltic Sea*. Dordrecht: Springer, 1–10.

Meier, H. E. M., and Kauker, F. (2003). Modeling decadal variability of the Baltic Sea: 2. Role of freshwater inflow and large-scale atmospheric circulation for salinity. *J. Geophys. Res*. 108:3368. doi: 10.1029/2003JC001799

Middelburg, J. J., De Lange, G. J., and van Der Weijden, C. H. (1987). Manganese solubility control in marine pore waters. *Geochim. Cosmochim. Acta* 51, 759–763. doi: 10.1016/0016-7037(87)90086-X

Mohrholz, V., Naumann, M., Nausch, G., Krüger, S., and Gräwe, U. (2015). Fresh oxygen for the Baltic Sea — an exceptional saline inflow after a decade of stagnation. *J. Mar. Syst*. 148, 152–166. doi: 10.1016/j.jmarsys.2015.03.005

Moros, M., Andersen, T. J., Schulz-Bull, D., Häusler, K., Bunke, D., Snowball, I. et al. (2017). Towards an event stratigraphy for Baltic Sea sediments deposited since AD 1900: approaches and challenges. *Boreas* 46, 129–142. doi: 10.1111/bor.12193

Mucci, A. (1988). Manganese uptake during calcite precipitation from seawater: conditions leading to the formation of a pseudokutnahorite. *Geochim. Cosmochim. Acta* 52, 1859–1868. doi: 10.1016/0016-7037(88)90009-9

Murray, J. W., Jannasch, H. W., Honjo, S., Anderson, R. F., Reeburgh, W. S., Top, Z. et al. (1989). Unexpected changes in the oxic/anoxic interface in the black sea. *Nature* 338, 411–413.

Nausch, G., Matthaus, W., and Feistel, R. (2003). Hydrographic and hydrochemical conditions in the Gotland deep area between 1992 and 2003. *Oceanologia* 45, 557–569.

Neretin, L. N., Pohl, C., Jost, G., Leipe, T., and Pollehne, F. (2003). Manganese cycling in the Gotland Deep, Baltic Sea. *Mar. Chem*. 82, 125–143. doi: 10.1016/S0304-4203(03)00048-3

Neumann, T., Christiansen, C., Clasen, S., Emeis, K.-C., and Kunzendorf, H. (1997). Geochemical records of salt-water inflows into the deep basins of the Baltic Sea. *Cont. Shelf Res*. 17, 95–115. doi: 10.1016/0278-4343(96)00023-4

Neumann, T., Heiser, U., Leosson, M. A., and Kersten, M. (2002). Early diagenetic processes during Mn-carbonate formation: evidence from the isotopic composition of authigenic Ca-rhodochrosites of the Baltic Sea. *Geochim. Cosmochim. Acta* 66, 867–879. doi: 10.1016/S0016-7037(01)00819-5

Neumann, T., Radtke, H., and Seifert, T. (2017). On the importance of major Baltic inflows for oxygenation of the central Baltic Sea. *J. Geophys. Res. Oceans* 122, 1090–1101. doi: 10.1002/2016JC012525

Noordmann, J., Weyer, S., Montoya-Pino, C., Dellwig, O., Neubert, N., Eckert, S. et al. (2015). Uranium and molybdenum isotope systematics in modern euxinic basins: case studies from the central Baltic Sea and the Kyllaren fjord (Norway). *Chem. Geol.* 396, 182–195. doi: 10.1016/j.chemgeo.2014.12.012

Nyame, F. K., Beukes, N. J., Kase, K., and Yamamoto, M. (2003). Compositional variations in manganese carbonate micronodules from the lower proterozoic Nsuta deposit, Ghana: product of authigenic precipitation or post-formational diagenesis? *Sed. Geol.* 154, 159–175. doi: 10.1016/S0037-0738(02)00128-8

Petrash, D. A., Lalonde, S. V., González-Arismendi, G., Gordon, R. A., Méndez, J. A., Gingras, M. K. et al. (2015). Can Mn–S redox cycling drive sedimentary dolomite formation? A hypothesis. *Chem. Geol.* 404, 27–40. doi: 10.1016/j.chemgeo.2015.03.017.

Piker, L., Schmaljohann, R., and Imhoff, J. F. (1998). Dissimilatory sulfate reduction and methane production in Gotland deep sediments (Baltic Sea) during a transition period from oxic to anoxic bottom water (1993-1996). *Aquat. Microb. Ecol.* 14, 183–193. doi: 10.3354/ame014183

Pohl, C., and Hennings, U. (1999). The effect of redox processes on the partitioning of Cd, Pb, Cu, and Mn between dissolved and particulate phases in the Baltic Sea. *Mar. Chem.* 65, 41–53. doi: 10.1016/S0304-4203(99)00009-2

Pedersen, T. F., and Price, N. B. (1982). The geochemistry of manganese carbonate in Panama Basin sediments. *Geochim. Cosmochim. Acta* 46, 59–68. doi: 10.1016/0016-7037(82)90290-3

Prien, R. D., and Schulz-Bull, D. E. (2016). Technical note: GODESS—a profiling mooring in the Gotland Basin. *Ocean Sci.* 12, 899–907. doi: 10.5194/os-12-899-2016

Pruysers, P. A., de Lange, G. J., Middelburg, J. J., and Hydes, D. J. (1993). The diagenetic formation of metal-rich layers in sapropel-containing sediments in the eastern Mediterranean. *Geochim. Cosmochim. Acta* 57, 527–536. doi: 10.1016/0016-7037(93)90365-4

Renberg, I., Bindler, R., and Brännvall, M.-L. (2001). Using the historical atmospheric leaddeposition record as a chronological marker in sediment deposits in Europe. *Holocene* 11, 511–516. doi: 10.1191/095968301680223468

Rudnick, R. L., and Gao, S. (2003). 3.01 – "Composition of the Continental Crust," in *Treatise on Geochemistry*, ed K. K Turekian (Oxford: Pergamon), 1–64.

Schaller, T., and Wehrli, B. (1997). Geochemical-focusing of manganese in lake sediments – an indicator of deep-water oxygen conditions. *Aquat. Geochem.* 2, 359–378. doi: 10.1007/BF00115977

Schinke, H., and Matthäus, W. (1998). On the causes of major Baltic inflows - an analysis of long time series. *Cont. Shelf Res.* 18, 67–97. doi: 10.1016/S0278-4343(97)00071-X

Schnetger, B., and Dellwig, O. (2012). Dissolved reactive manganese at pelagic redoxclines (part I): a method for determination based on field experiments. *J. Mar. Syst.* 90, 23–30. doi: 10.1016/j.jmarsys.2011.08.006

Scholz, F., Baum, M., Siebert, C., Eroglu, S., Dale, A. W., Naumann, M. et al. (2018). Sedimentary molybdenum cycling in the aftermath of seawater inflow to the intermittently euxinic Gotland Deep, central Baltic Sea. *Chem. Geol.* 491, 27–38. doi: 10.1016/j.chemgeo.2018.04.031

Schulz, H. D. (2006). "Quantification of early diagenesis: dissolved constituents in marine pore water," in *Marine Geochemistry,* eds H. D. Schulz and M. Zabel (Berlin; Heidelberg: Springer), 85–128.

Schulz, H. N., and Schulz, H. D. (2005). Large sulfur bacteria and the formation of phosphorite. *Science* 307, 416–418. doi: 10.1126/science.1103096

Seeberg-Elverfeldt, J., Schlüter, M., Feseker, T., and Kölling, M. (2005). Rhizon sampling of porewaters near the sediment-water interface of aquatic systems. *Limnol. Oceanogr. Methods* 3, 361–371. doi: 10.4319/lom.2005.3.361

Seifert, T., and Kayser, B. (1995). A high resolution spherical grid topography of the Baltic Sea. *Mar. Sci. Rep.* 9, 72–88.

Skei, J. M. (1988). Formation of framboidal iron sulfide in the water of a permanently anoxic fjord - Framvaren, South Norway. *Mar. Chem.* 23, 345–352. doi: 10.1016/0304-4203(88)90103-X

Spencer, D. W., and Brewer, P. G. (1971). Vertical advection diffusion and redox potentials as controls on the distribution of manganese and other trace metals dissolved in waters of the Black Sea. *J. Geophys. Res.* 76, 5877–5892. doi: 10.1029/JC076i024p05877

Sternbeck, J., and Sohlenius, G. (1997). Authigenic sulfide and carbonate mineral formation in Holocene sediments of the Baltic Sea. *Chem. Geol.* 135, 55–73. doi: 10.1016/S0009-2541(96)00104-0.

Strady, E., Pohl, C., Yakushev, E. V., Krüger, S., and Hennings, U. (2008). Pump-CTD-System for trace metal sampling with a high vertical resolution. A test in the Gotland Basin, Baltic Sea. *Chemosphere* 70, 1309–1319. doi: 10.1016/j.chemosphere.2007.07.051

Suess, E. (1979). Mineral phases formed in anoxic sediments by microbial decomposition of organic matter. *Geochim. Cosmochim. Acta* 43, 339–352. doi: 10.1016/0016-7037(79)90199-6

Swarzenski, P. W., McKee, B. A., Sørensen, K., and Todd, J. F. (1999). ^{210}Pb and ^{210}Po, manganese and iron cycling across the O_2/H_2S interface of a permanently anoxic fjord: framvaren, Norway. *Mar. Chem.* 67, 199–217. doi: 10.1016/S0304-4203(99)00059-6.

Taylor, G. T., Iabichella, M., Ho, T.-Y., Scranton, M. I., Thunell, R. C., Muller-Karger, F. et al. (2001). Chemoautotrophy in the redox transition zone of the Cariaco Basin: a significant midwater source of organic carbon production, *Limnol. Oceanogr.* 46,148–163. doi: 10.4319/lo.2001.46.1.0148

Tebo, B. M., Bargar, J. R., Clement, B. G., Dick, G. J., Murray, K. J., Parker, D. et al. (2004). Biogenic manganese oxides: properties and mechanisms of formation. *Annu. Rev. Earth Planet. Sci.* 32, 287–328. doi: 10.1146/annurev.earth.32.101802.120213

Trouwborst, R. E., Clement, B. G., Tebo, B. M., Glazer, B. T., and Luther, G. W. III. (2006). Soluble Mn(III) in suboxic zones. *Science* 313, 1955–1957. doi: 10.1126/science.1132876

Turnewitsch, R., and Pohl, C. (2010). An estimate of the efficiency of the iron- and manganesedriven dissolved inorganic phosphorus trap at an oxic/euxinic water column redoxcline. *Glob. Biogeochem. Cycles* 24, GB4025. doi: 10.1029/2010GB003820

Vasconcelos, C., McKenzie, J. A., Bernasconi, S., Grujic, D., and Tiens, A. J. (1995). Microbial mediation as a possible mechanism for natural dolomite formation at low temperatures. *Nature* 377, 220–222. doi: 10.1038/377220a0

Wasmund, N., Tuimala, J., Suikkanen, S., Vandepitte, L., and Kraberg, A. (2011). Long-term trends in phytoplankton composition in the western and central Baltic Sea. *J. Mar. Syst.* 87, 145–159. doi: 10.1016/j.jmarsys.2011.03.010

Wasylenki, L. E., Rolfe, B. A., Weeks, C. L., Spiro, T. G., and Anbar, A. D. (2008). Experimental investigation of the effects of temperature and ionic strength on Mo isotope fractionation during adsorption to manganese oxides. *Geochim. Cosmochim. Acta* 72, 5997–6005. doi: 10.1016/j.gca.2008.08.027

Wegwerth, A., Eckert, S., Dellwig, O., Schnetger, B., Severmann, S., Weyer, S. et al. (2018). Redox evolution during Eemian and Holocene sapropel formation in the black sea. *Palaeogeogr. Palaeoclimatol. Palaeoecol.* 489, 249–260. doi: 10.1016/j.palaeo.2017.10.014

Wei, C.-L., and Murray, J. W. (1994). The behavior of scavenged isotopes in marine anoxic environments: ^{210}Pb and ^{210}Po in the water column of the Black Sea. *Geochim. Cosmochim. Acta* 58, 1795–1811. doi: 10.1016/0016-7037(94)90537-1

Yao, W., and Millero, F. J. (1993). The rate of sulfide oxidation by δMnO_2 in seawater. *Geochim. Cosmochim. Acta* 57, 3359–3365. doi: 10.1016/0016-7037(93)90544-7

Yigiterhan, O., Murray, J. W., and Tugrul, S. (2011). Trace metal composition of suspended particulate matter in the water column of the Black Sea. *Mar. Chem.* 126, 207–228. doi: 10.1016/j.marchem.2011.05.006

Zeitzschel, B., Diekmann, P., and Uhlmann, L. (1978). A new multisample sediment trap. *Mar. Biol.* 45, 285–288. doi: 10.1007/BF00391814

Zillén, L., Conley, D. J., Andrén, T., Andrén, E., and Björck, S. (2008). Past occurrences of hypoxia in the Baltic Sea and the role of climate variability, environmental change and human impact. *Earth Sci. Rev.* 91, 77–92. doi: 10.1016/j.earscirev.2008.10.001

Zopfi, J., Ferdelman, T. G., Jørgensen, B. B., Teske, A., and Thamdrup, B. (2001). Influence of water column dynamics on sulfide oxidation and other major biogeochemical processes in the chemocline of Mariager Fjord (Denmark). *Mar. Chem.* 74, 29–51. doi: 10.1016/S0304-4203(00)00091-8.

Conflict of Interest Statement: The authors declare that the research was conducted in the absence of any commercial or financial relationships that could be construed as a potential conflict of interest.

Copyright © 2018 Dellwig, Schnetger, Meyer, Pollehne, Häusler and Arz. This is an open-access article distributed under the terms of the Creative Commons Attribution License (CC BY). The use, distribution or reproduction in other forums is permitted, provided the original author(s) and the copyright owner(s) are credited and that the original publication in this journal is cited, in accordance with accepted academic practice. No use, distribution or reproduction is permitted which does not comply with these terms.

frontiers in Marine Science

ORIGINAL RESEARCH
published: 26 October 2018
doi: 10.3389/fmars.2018.00383

Impact of a Major Inflow Event on the Composition and Distribution of Bacterioplankton Communities in the Baltic Sea

*Benjamin Bergen[1], Michael Naumann[1], Daniel P. R. Herlemann[1,2], Ulf Gräwe[1], Matthias Labrenz[1] and Klaus Jürgens[1]**

[1] Leibniz Institute for Baltic Sea Research Warnemünde, Rostock, Germany, [2] Centre for Limnology, Estonian University of Life Sciences, Tartu, Estonia

Major Baltic inflow (MBI) events carry highly saline water from the North Sea to the central Baltic Sea and thereby affect both its environmental conditions and its biota. While bacterioplankton communities in the Baltic Sea are strongly structured by salinity, how MBIs impact the composition and distribution of bacteria is unknown. The exceptional MBI in 2014, which brought saline and oxygenated water into the basins of the central Baltic Sea, enabled the linkage of microbiological investigations to hydrographic and modeling studies of this MBI. Using sequence data of 16S ribosomal RNA (rRNA) and 16S rRNA genes (rDNA), we analyzed bacterioplankton community composition in the inflowing water and in the uplifted former bottom-water at stations reached by the MBI. Bacterial diversity data were compared with respective data obtained from previous, non-inflow conditions. Changes in bacterial community composition following the 2014 MBI were mainly apparent at the genus level. A number of specific taxa were enriched in the inflowing water, with large changes in the rRNA/rDNA ratios indicating the different activity levels between of the water masses. The relative similarity of the bacterial communities in the inflowing and uplifted waters as well as the results from an inflow-simulating numerical model showed that the inflowing water did not originate directly from the North Sea but mostly from adjacent areas in the Baltic Sea. This suggested that the inflow event led to a series of shifts in Baltic Sea water masses among the Baltic Sea basins and a gradual mixing of the water bodies. Dramatic changes in the bacterial community composition occurred when the bottom-water inflow reached the anoxic, sulfidic deep basins, resulting in an uplifting of the formerly anoxic bacterial community, dominated by *Epsilonproteobacteria*. Our study of the impact of MBIs on bacterioplankton communities therefore highlights two relevant underlying mechanisms that impact the distribution and possibly also the activities of planktonic bacteria in the Baltic Sea: (1) the successive dilution of inflowing North Sea water with ambient waters and (2) the uplifting of former bottom-water communities to higher water strata.

Keywords: bacterioplankton, Baltic Sea, Major Baltic inflow, saltwater intrusions, RNA, DNA

OPEN ACCESS

Edited by:
Elinor Andrén, Södertörn University, Sweden

Reviewed by:
Pradeep Ram Angia Sriram, UMR 6023, Laboratoire Microorganismes Génome Et Environnement (LMGE), France
Anyi Hu, Institute of Urban Environment (CAS), China

****Correspondence:***
Klaus Jürgens
klaus.juergens@io-warnemuende.de

Specialty section:
This article was submitted to Aquatic Microbiology, a section of the journal Frontiers in Marine Science

Received: *31 May 2018*
Accepted: *28 September 2018*
Published: *26 October 2018*

Citation:
Bergen B, Naumann M, Herlemann DPR, Gräwe U, Labrenz M and Jürgens K (2018) Impact of a Major Inflow Event on the Composition and Distribution of Bacterioplankton Communities in the Baltic Sea. Front. Mar. Sci. 5:383. doi: 10.3389/fmars.2018.00383

INTRODUCTION

In the land-locked Baltic Sea, water is exchanged only with the North Sea, via the straits of the Kattegat and Skagerrak. The low seawater inflow together with strong freshwater inputs from rivers, rain, and melt water accounts for the elongated, stable salinity gradient of the Baltic Sea, with high salinities in the Skagerrak (salinity > 25) and low salinities in the Gulf of Bothnia (salinity < 5) (Reissmann et al., 2009). Another result is a permanent halocline in the central Baltic Sea that prevents vertical mixing and leads to permanent stratification and subsequent oxygen deficiency in the deep basins (Reissmann et al., 2009).

Major Baltic inflow (MBI) events, forced by special atmospheric conditions, occur occasionally in the autumn and winter and carry a volume of saline water from the North Sea that is large enough to reach the central basins of the Baltic Sea (Matthäus and Franck, 1992). The inflowing water in winter typically has a higher salinity (17.5–19), a lower temperature (2–8°C), and higher oxygen content than the Baltic bottom-water (Matthäus and Franck, 1992; Omstedt et al., 2004). Several studies have shown that these inflowing, oxygenated waters can give rise to chemically and microbially mediated transformations in the deep, stratified basins, thereby affecting methane oxidation (Schmale et al., 2016), mercury species distribution (Kuss et al., 2017), manganese cycling (Dellwig et al., 2018), nutrient release from the sediments (Hall et al., 2017; Sommer et al., 2017), and macrozoobenthos communities (e.g., Laine et al., 1997), However, the mechanisms and magnitude by which MBIs change the composition, activity, and distribution of planktonic microbial communities in the Baltic Sea are currently not understood.

Nonetheless, that the Baltic Sea salinity gradient is a structuring force acting on bacterial community composition has been convincingly demonstrated in several studies (Riemann et al., 2008; ; Herlemann et al., 2011, 2016; Bergen et al., 2014), which also more generally confirmed that salinity is one of the most important determinants of the structure of microbial communities in aquatic systems (Lozupone and Knight, 2007; Nemergut et al., 2011). In estuaries, the dominant bacterial phyla/classes shift from a prevalence of *Betaproteobacteria* and *Actinobacteria* in oligohaline regions to one of *Alpha- and Gamma-proteobacteria* in higher salinity areas (e.g., Bouvier and Giorgio, 2002; Kirchman et al., 2005; Fortunato and Crump, 2011). This pattern also characterizes the Baltic Sea (Herlemann et al., 2011), where the salinity gradient is much more stable than in most estuaries. Additionally, an adapted bacterial community thrives in the brackish waters of the Baltic Sea and its composition differs significantly from that of its freshwater and marine counterparts. Because MBIs result in a major disturbance of the salinity gradient, particularly in deeper layers, and in the natural ventilation of the central basins (Matthäus and Franck, 1992), they can be expected to impact the structure of the Baltic's bacterial communities.

In December 2014, an exceptionally strong MBI occurred after the long stagnation period that followed the last MBI, in 2003. The 2014 MBI ranked as the third strongest among the recorded MBIs (Mohrholz et al., 2015). Between December 13th and 25th, a total water volume of 358 km^3 was pushed into the Baltic Sea by the continuous strong westerly winds. The inflowing water included a highly saline volume (salinity > 17) of 198 km^3 and salt transport of 3.98 Gt. During the initial inflow phase, in December 2014, a mean salinity of 20.8, a mean temperature of 7.7°C, and a dissolved oxygen concentration of 6.5 mL/L were measured in the Arkona Basin (Naumann et al., unpublished data). As previously demonstrated for other MBIs (Umlauf et al., 2007) on its way to the Baltic Sea, the highly saline inflow water mixed with ambient waters and raised the former bottom-waters, such that new and distinct water masses were formed. The large volume of highly saline water propagated quickly through the western Baltic Sea and Bornholm Basin, passing the Slupsk Sill already in February 2015. This fast propagation was supported by a series of weaker inflows that had occurred earlier in 2014. The final arrival of the water mass and the oxygenation of the Gotland Deep at 240 m water depth occurred after this study, in mid April 2015 (Naumann et al., unpublished data).

In this study, we took advantage of this strong MBI to investigate the effect of inflowing saline water on the composition of bacterioplankton within the water column. Specifically, we asked whether characteristic marine bacterial assemblages are transported by the inflow to the central basins or does the inflowing marine bacterial community become diluted through successive mixing with adjacent water masses. To answer this question, we analyzed the bacterial community composition of the inflowing and uplifted water and compared the results with data collected in 2009 under non-inflow (stagnant) conditions (Herlemann et al., 2016). Differences in community composition were determined by next-generation sequencing (NGS) of partial 16S ribosomal RNA (rRNA) and 16S rRNA genes (rDNA), which also allowed the identification of potentially active taxa. Numerical hydrodynamic modeling was used to estimate the most likely origin of the sampled water masses (Gräwe et al., 2015), and thus to identify the initial location of the bacterial community in the inflowing water masses, despite the high turbulent mixing rates. The results provided the first insights into the changes in the bacterioplankton communities that occurred in response to the different water masses during the MBI that began in 2014. Thus, we were able to show that (1) during its passage from the North Sea to the interior of the Baltic, the inflowing water mixed with adjacent water masses such that the inflowing bacterial communities became increasingly similar to those already present, and (2) the displacement (uplifting) of whole water masses caused the transport of formerly anaerobic bacterial communities into water depths where they normally do not occur.

MATERIALS AND METHODS

Sampling

Samples were taken in the Arkona Basin, Bornholm Basin, Slupsk Channel and the southwestern part of the Eastern Gotland Basin (**Figure 1**) during a cruise with the RV *Elisabeth Mann Borgese* in February 2015 (cruise EMB 95). Temperature, salinity,

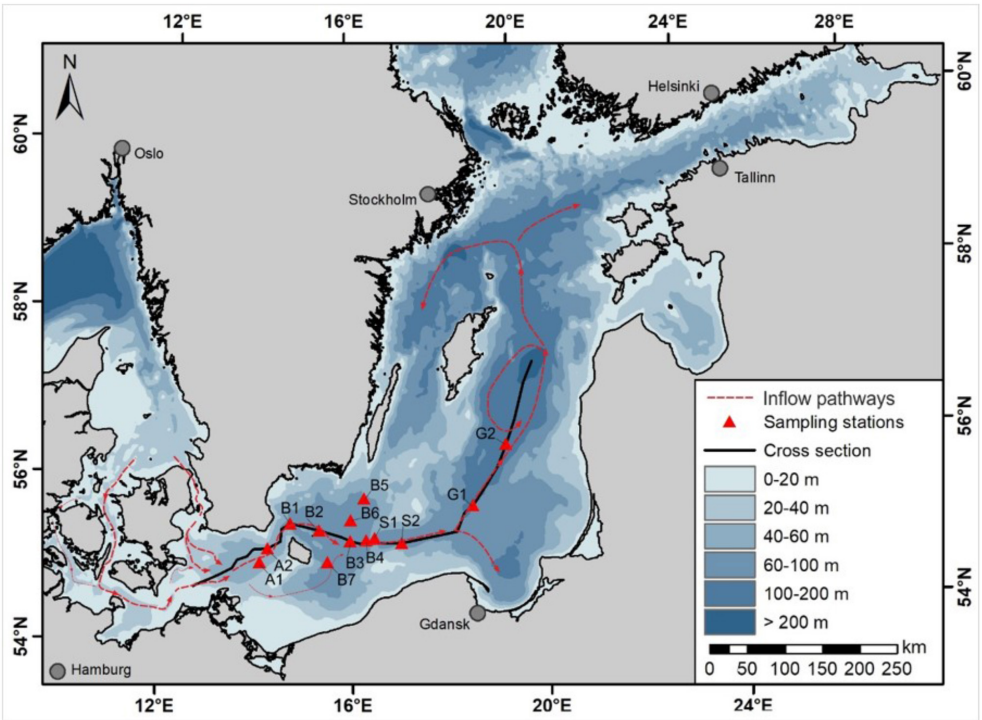


FIGURE 1 | Map of the Baltic Sea, showing the sampling stations (dots) and estimated state of the 2014 Major Baltic inflow (MBI) during the time of sampling (red lines).

oxygen, and chlorophyll fluorescence were measured using a CTD SBE911+ combined with a bottle sampler rosette, which comprised 13 10-L free-flow bottles. Sampling depths were chosen at each station according to the characteristics of the physical water mass revealed in the CTD profiles. At each station, one sample was taken from the inflowing water body and one from the uplifted bottom-water body, distinguished by different salinities, temperatures, and oxygen concentrations (**Figure 2**).

Water samples (1 L) used for DNA and RNA analysis were filtered onto 0.22-μm pore-size white polycarbonate filters. DNA and RNA were extracted according to Weinbauer et al. (2002). Concentrations of inorganic nutrients were analyzed as described by Grasshoff et al. (1983). For bacterial enumeration, subsamples (100 mL) were fixed for 1 h with 400 μl of 1% paraformaldehyde and 0.5% glutaraldehyde, shock-frozen in liquid nitrogen, and stored at −80°C until processed by flow cytometry. After staining with SYBR Green, the samples were analyzed on a FacsCalibur (Becton Dickinson) using a modification of the method of Gasol and del Giorgio (2000).

Amplicon Sequencing and Sequence Processing

For cDNA synthesis, DNA was removed from the RNA extracts by DNase I (Ambion/Applied Biosystems, Huntington, United Kingdom) digestion, following the manufacturer's protocol. RNA samples were transcribed into cDNA by a reverse transcriptase step, using the iScript Select cDNA synthesis kit (Bio-Rad, Hercules, CA, United States) with the primer 1492r. The DNA extracts and the generated cDNA for bacterial diversity analysis were sent to LGC Genomics GmbH (Berlin, Germany) for further processing. There, the primers Bakt_341F (CCTACGGGNGGCWGCAG) and Bakt_805R (GACT ACHVGGGTATCTAATCC) (Herlemann et al., 2011) were used for PCR amplification and sequences were generated on the Illumina MiSeq V3 platform in a 2 bp × 300 bp paired-end run. Pairs of forward and reverse primer-trimmed sequences were combined using BBMerge 34.48 and processed using the SILVA NGS pipeline (Quast et al., 2013; Glöckner et al., 2017) based on SILVA release version 123 (Pruesse et al., 2007). SILVA NGS performs additional quality checks according to the SINA-based alignments (Pruesse et al., 2012) with a curated seed database in which PCR artifacts or non-SSU reads are excluded. The longest read serves as a reference for the taxonomic classification in a BLAST (version 2.2.28+) search against the SILVA SSURef dataset (Quast et al., 2013). The classification of the reference sequence of a cluster (98% sequence identity) is then mapped to all members of the respective cluster and to their replicates. Best BLAST hits were only accepted if they had a (sequence identity + alignment coverage)/2 ≥ 93 or otherwise defined as unclassified. The 16S rRNA and rDNA raw sequence data have been submitted to the European Nucleotide Archive (ENA) under the Accession No. PRJEB27018.

The bacterial community composition associated with the inflow event was compared with that of a typical situation, before the MBI, in approximately the same and adjacent areas of the

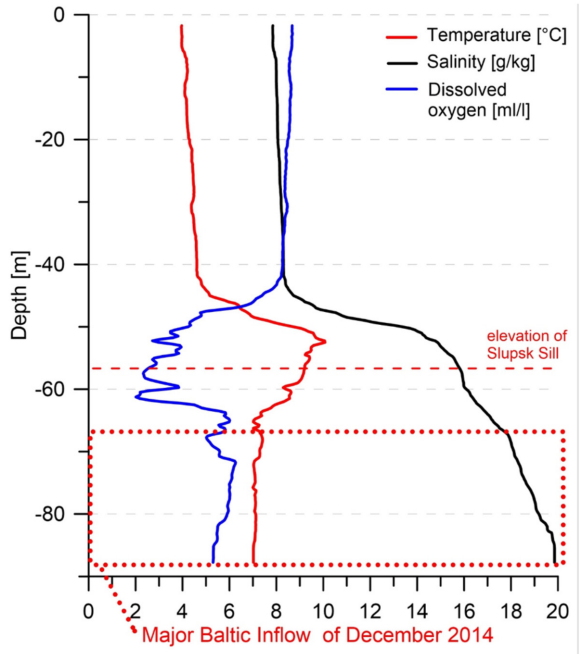


FIGURE 2 | Example of a CTD profile (station B3, Bornholm basin), used to distinguish inflowing from uplifted bottom-water. The dotted line indicates the approximate depth layer of the inflowing water with a higher salinity and oxygen concentration and a lower temperature. Warmer, former bottom-water was uplifted and crossed the Slupsk Channel (dashed line) toward the eastern Gotland basin.

Baltic Sea. For this purpose, we used sequence data from the western and central Baltic Sea obtained in February 2009 (for the positions of the 2009 stations see **Supplementary Figure 1**), as reported in Herlemann et al. (2016). DNA from the reference samples from 2009 was amplified using the same primers (Bakt_341F and Bakt_805R) as described in Herlemann et al. (2011). DNA from the 2009 samples was sequenced by Eurofins MWG GmbH on a 454 GS-FLX sequencer (Roche). For a detailed description of the amplification and 454 sequencing procedures, see Herlemann et al. (2011, 2016). To allow comparisons of the reference and inflow sequences, all sequences were processed together using the Silva NGS pipeline with standard settings.

Statistical Analyses

As the Gotland Basin samples derived from anoxic conditions and thus harbored very distinct bacterial communities, they were excluded from statistical analyses aimed at distinguishing the different bacterial communities in inflowing and uplifted waters. For all statistical tests, samples were grouped according to their origin. Explicet (Robertson et al., 2013) was used for providing bootstrapped-based subsampling for normalizing OTU counts in the bacterial alpha diversity. For this analysis all samples were reduced to 1000 reads. The difference between the bacterial communities were visualized by non-metric multidimensional scaling plots based on the Bray–Curtis dissimilarity matrix, using the software PAST (Hammer et al., 2001). For these analyses, the sum-normalized OTU abundances were combined with data from the investigation conducted during stagnant conditions in February/March 2009 (Herlemann et al., 2016). A linear discriminant analysis (LDA) effect size (LEfSe) (Segata et al., 2011)[1] was used to test for discriminatory taxa in the different water masses, inflow and uplifted waters, based on relative rDNA and rRNA abundances. Based on a normalized relative abundance table, LEfSe applies the Kruskal–Wallis rank sum test to identify OTUs with significantly different abundances and performs an LDA to estimate the effect size of each feature. In this study, an alpha value of 0.05 and an effect size threshold of three were considered to indicate statistical significance.

Physical Numerical Model

To follow the inflowing water masses and quantify their transport pathways, a three-dimensional hydrodynamic model, the General Estuarine Transport Model (GETM), was used in a multi-nested downscaling framework extending from the North Atlantic (8-km resolution) to the Western Baltic Sea (600-m resolution). The numerical model provides hourly mean values of velocity, salinity, and temperature at every grid point and reproduced the 2014 MBI in detail (Gräwe et al., 2015; Mohrholz et al., 2015). Previous studies demonstrated the utility of the GETM in simulating inflow events and in allowing statistical analyses of inflows in the western Baltic Sea (Burchard et al., 2005; Gräwe et al., 2013). Our study used the same model setup as described in Gräwe et al. (2015). Based on the output of the hydrodynamic model, a particle-tracking tool was applied that enabled the water masses to be marked and followed, including tracking of the water masses back in time to estimate the potential sources and/or origins of distinct water parcels. Backtracking was started at the sampling stations in the Bornholm Gat (TF0145) and Slupsk Channel (TF0222) and was used to analyze the origin of the inflowing water masses in greater detail.

RESULTS

Characterization of the Water Masses

The very strong inflow arising from the 2014/2015 MBI was clearly evident from the CTD profiles obtained from the Arkona Basin and Bornholm Basin; a representative example is shown in **Figure 2** (Bornholm Deep). The highly saline bottom layer (salinity $>$ 17) in the Bornholm Basin was ∼34 m thick, with a clearly higher oxygen concentration and lower temperature (**Figure 2**, dashed box) than the uplifted former bottom-water (at 50–60 m depth). This mixture of inflow water and uplifted former bottom-water ($>$8°C, salinity 12–17, 2–5 mL/L) passed the Slupsk Sill (58 m sill depth), which otherwise forms a natural barrier between the Bornholm and central Baltic basins, of which the Gotland Basin is the farthest to the northeast.

Figure 3 shows a hydrographic cross-section reaching from the Darss Sill to the Eastern Gotland Basin, including the sampling stations and sampling depths and the general situation along the "Baltic thalweg" (Burchard et al., 2005;

[1]http://huttenhower.sph.harvard.edu/lefse/

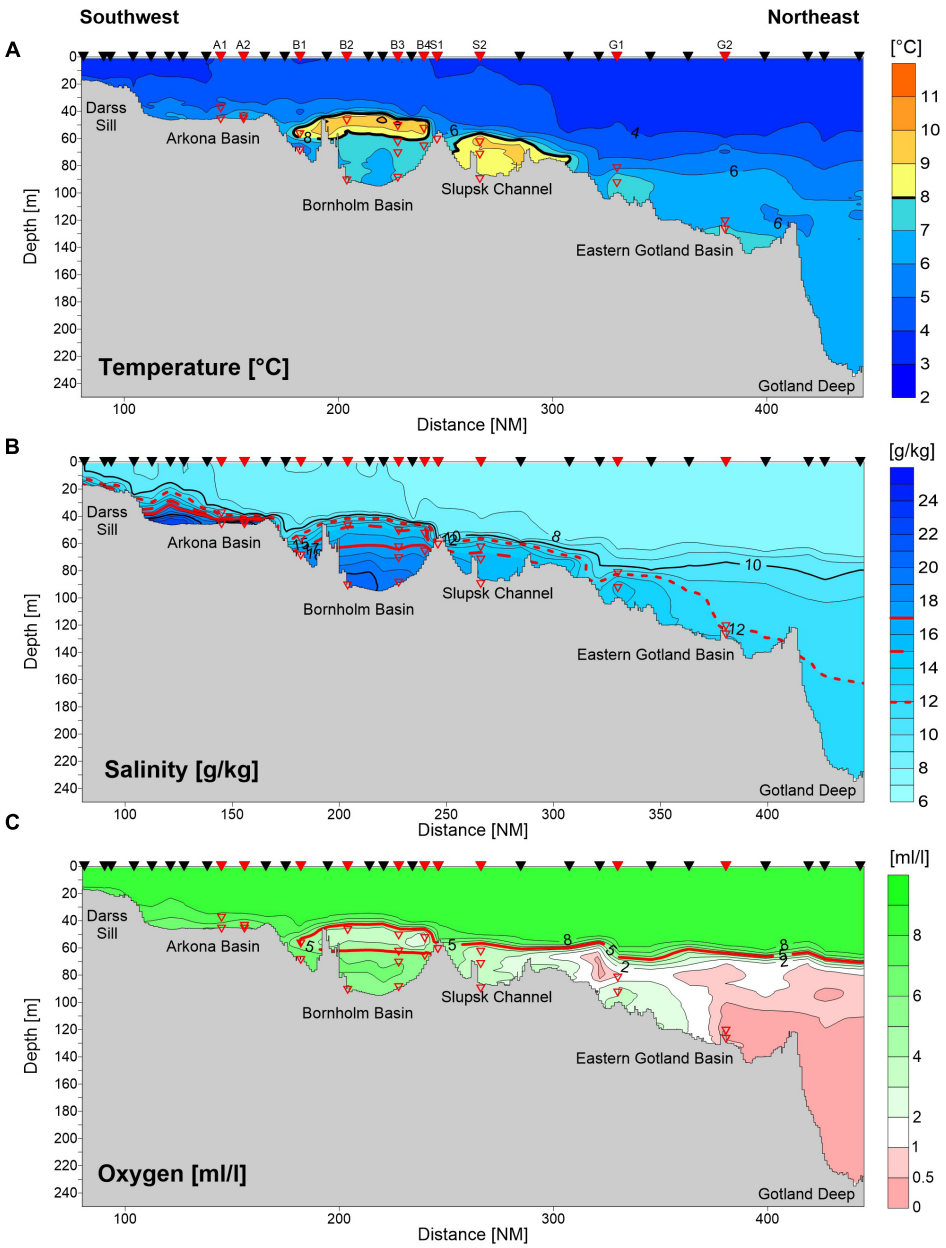


FIGURE 3 | Bathymetric map of the southwestern Baltic Sea, showing the sampling locations and inflow pathways and a vertical cross-section, also showing the sampling locations (top of graphs; black triangles: only CTD measurements; red triangles: CTD and microbiological measurements) together with temperature **(A)**, salinity **(B)**, and oxygen concentrations **(C)**.

Lilover et al., 2017) of water flowing into Baltic basins until the analyzed stage of the inflow event. During the sampling period, most of the MBI inflow water volume (about 90%) was estimated to be present in the Bornholm basin, below a water depth of 60 m (Naumann et al., unpublished data). The uplifted inflow water body, clearly apparent by its higher temperature (>7°C), lower salinity (12–15), and a lower dissolved oxygen concentration (2–4 mL/L), originated from a weak summer inflow in August of that year (Naumann et al., unpublished data). Anoxic/suboxic bottom-water in the Eastern Gotland Basin was clearly uplifted by this inflowing oxygenated, more saline water (station G1, **Figure 3C**), whereas deeper water (below 120 m depth) in the Gotland Basin remained anoxic and was not influenced at that stage of inflow propagation (station G2, **Figure 3C**).

An estimation of the flow pattern of the MBI along the stations sampled was obtained based on the features of the water masses determined from the CTD profiles and on information from previously published studies of this MBI (e.g., Gräwe et al., 2015; Mohrholz et al., 2015) (**Figure 1**). The stations first impacted by the MBI were those of the Arkoma Basin, A1 and A2, followed

by stations B1 and B2 of the Bornholm Basin. Thereafter, the MBI spread in different directions, with the central and southern stations B3 and B7 probably reached more or less simultaneously, due to the deflection of gravity currents to the right by the Coriolis force at the northern hemisphere, followed shortly thereafter by station B4, then stations B6 and S1, stations B5 and S2, and finally Gotland Basin station G1. At the bottom-water stations B5 and B6, the water probably consisted of the less-mixed original inflow water of December 2014 (temperature $< 7.4°C$, salinity > 18, dissolved oxygen > 5.2 mL/L), whereas at the bottom of the sill stations S1 and S2 (temperature $> 7.7°C$, salinity 16.6, dissolved oxygen < 4.3 mL/L) the water was composed of new inflow water strongly mixed with former bottom-water from the Bornholm Basin and Slupsk Channel, as evidenced by the higher temperatures and lower oxygen concentrations. At the time of sample collection, the inflowing water had not yet reached Gotland Basin station G2, which still had anoxic bottom-water.

As expected, salinity and temperature were higher in the inflow water and the uplifted bottom-water than in the reference water from the stagnation period in winter 2009 (**Table 1**). The higher temperature of the sampled water could be attributed to the August 2014 and December 2014 inflows. During these events, the warmed summer and autumn surface water of the Mecklenburg Bight (overflow August 2014) and Kattegat (inflow December 2014) penetrated the deep water of the Baltic basins and was warmer than the bottom-water of the previous stagnation period. The salinity and temperature values as well as the phosphate, silicate, nitrite, and nitrate concentrations of the uplifted bottom-water, especially that of the Arkona Basin, were between those of the inflow and reference waters of 2009. A comparison of the concentrations of dissolved nitrogen compounds in the Arkona and Bornholm Basins, as determined in samples from this study, with those of the reference samples from winter 2009 revealed that, due to the inflow water, the ammonia concentration was significantly lower in both basins, the nitrite concentration was lower in the Arkona Basin, and the nitrate concentration was higher in both basins (**Supplementary Figure 2**). Total prokaryotic cell numbers were in the same range, $6.6–8.0 \times 10^5$ mL^{-1}, with considerable variability between the stations but no apparent trend and with values roughly similar to those in samples from the stagnant period of 2009 (**Table 1**).

Back-Trajectory of the Water Masses

The origin of the sampled inflow water, estimated by numerical modeling and particle tracking, is depicted in the probability maps of **Figure 4**. According to the maps, the sampled water mass likely originated from a specific region in the western Baltic Sea. For the two sampling stations, located in the Bornholm Gat (A2) and Slupsk Channel (S2, see **Figure 1**), the maps show similar results for the two time slices: a main inflow period during December 13–25, 2014 and a pre-inflow stage that occurred in mid-October 2014. During the main inflow period (upper panels in **Figure 4**), the possible origin of both sampled water masses may have been the Arkona Basin and the southern Danish Belt Sea. Thus, there was a high probability that both samples were in contact with the inflowing saline water. Due to the high degree of mixing (lateral but also vertical) during the inflow, the initial start position of the sampled water masses could not be further specified. The lower maps show the position of the sampled water in October, the pre-inflow stage, and indicate an area spanning from the Skagerrak to the Danish Belt Sea, which is a common finding for such events. During this pre-inflow stage, the saline water of the Danish Belt Sea was pushed farther north into the Kattegat, due to a lowering of the water level in the Baltic Sea and the resulting outflow. Furthermore, because of the Earth's rotation, this outflowing water probably accumulated on the eastern side of the Kattegat. This specific pattern, illustrated in the lower panels of **Figure 4**, indicated that the water originated from the Danish Belt Sea and thus allowed an estimation of the origin of the sampled inflow water from this transition zone between the North Sea and the Baltic Sea.

Taxonomic Composition of the Microbial Communities in the Different Basins and in the Inflowing and Uplifted Water Bodies

We compared the bacterial community compositions of all the samples from this study (excluding the anoxic Gotland stations) with reference samples from the stagnant situation in winter 2009, which covered also those area of potential inflow water origin (Skagerrak, Belt Sea, Western Baltic) as well as the same locations as in this study (Arkona and Bornholm Basins) (Herlemann et al., 2016). The non-metric multidimensional scaling (NMDS) plot (Bray–Curtis dissimilarity) of the bacterioplankton community composition revealed a clear clustering of the respective bacterial communities according to their location (**Figure 5A**). The more saline stations from the Skagerrak, Kattegat, Belt Sea, and Western Baltic (reference 2009) were clearly separated from stations in the Arkona and Bornholm Basins. Samples from this study (**Figure 5A**, red symbols) clustered together for the Arkona and Bornholm Basins, slightly separated from samples from the reference study of 2009 (**Figure 5A**, blue symbols). The Bornholm samples from 2009 spread more widely whereas those from this study (including samples from the inflow and uplifted waters) were more tightly clustered (**Figure 5A**). A more detailed look at only the Bornholm Basin samples from this study showed the clear separation of the rRNA- and rDNA-based compositions on the first coordinate, with no overlap. Further, both the rRNA- and rDNA- based bacterial community compositions of the inflowing and uplifted water bodies were separated on the second coordinate (**Figure 5B**). To visualize the relationship between the variability in the community composition and the features of the water mass, the physicochemical parameters were plotted in the NMDS ordination as fitting environmental variables (only the Bornhom Basin, **Supplementary Figure 3**). The variation in community composition correlated with differences in salinity and oxygen (higher in the inflow water) and partly also with nutrient levels (higher in the uplifted water). Alpha diversity was significantly higher in the samples from the Arkona and Bornholm Basins obtained in this study than in all reference samples from 2009 (**Supplementary Figure 4**). A direct

TABLE 1 | Physicochemical parameters and total prokaryotic cell numbers (TCN) in the different water masses in the Arkona and Bornholm Basins.

	Salinity	Temperature (°C)	Oxygen (ml l^{-1})	Phosphate (µmol l^{-1})	Silicate (µmol l^{-1})	Nitrite (µmol l^{-1})	Nitrate (µmol l^{-1})	Ammonia (µmol l^{-1})	TCN (10^5 ml^{-1})
Arkona basin									
Inflow water (*n* = 2)	22.3 ± 0.3	6.6 ± 0.2	6.2 ± 0.4	0.92 ± 0.01	17.75 ± 0.92	0.08 ± 0.02	8.51 ± 0.27	0	7.91 ± 2.32
Uplifted bottom-water (*n* = 2)	19.2 ± 4.7	5.6 ± 1.2	6.8 ± 1.3	0.73 ± 0.05	14.6 ± 1.7	0.19 ± 0.19	5.62 ± 0.06	0	6.63 ± 0.84
Reference water 2009 (*n* = 5)	11.9 ± 2.8	2.7 ± 0.1	10.4 ± 0.3	0.62 ± 0.09	7.33 ± 2.23	0.32 ± 0.1	2.14 ± 1.16	6.82 ± 13.54	6.90 ± 1.28
Bornholm basin									
Inflow water (*n* = 10)	18.2 ± 1.2	7.2 ± 0.8	5.3 ± 0.8	1.07 ± 0.24	22.58 ± 6.8	0.07 ± 0.07	7.76 ± 0.25	0.01 ± 0.04	8.04 ± 2.02
Uplifted bottom-water (*n* = 10)	14.9 ± 1.0	8.9 ± 0.9	3.2 ± 0.9	1.27 ± 0.18	28.98 ± 4.5	0.05 ± 0.02	7.78 ± 0.69	0.02 ± 0.04	7.08 ± 0.09
Reference water 2009 (*n* = 7)	11.6 ± 2.7	6.5 ± 2.7	6.4 ± 2.9	1.66 ± 1.11	20.91 ± 7.65	0.07 ± 0.07	5.29 ± 1.63	0.61 ± 0.5	7.17 ± 1.10

Mean values ± SD.

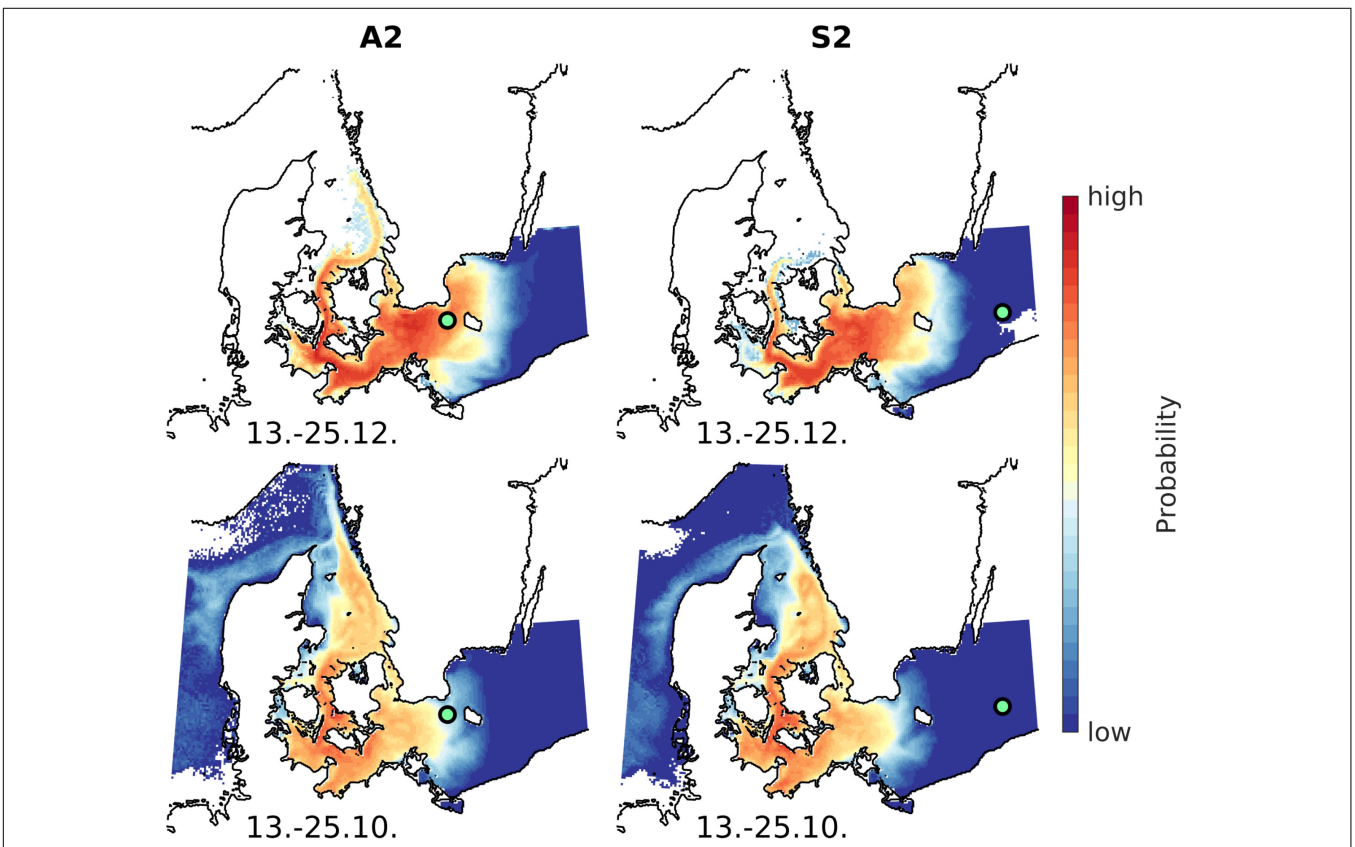


FIGURE 4 | The possible origin of the sampled inflow water in the Bornholm Gat (TFO145, left panels) and in the Slupsk Channel (TFO222, right panels) for two different time slices (upper panels: during the inflow; lower panels: 2 months prior to the inflow). The maps show the most likely origin and were estimated based on numerical modeling.

comparison of the inflowing and uplifted water masses revealed that for most stations diversity (OTU number and ShannonH) was slightly higher in the inflowing than in the uplifted water, both with the rDNA and the rRNA analyses (**Supplementary Figure 5**). Only the Gotland samples, containing anaerobic communities, deviated strongly from the other stations, showing a strongly reduced diversity (**Supplementary Figure 5**).

To elucidate the broad taxonomic changes that occurred between the inflowing and uplifted water bodies in the different basins, both 16S rDNA and 16S rRNA sequence data were examined. According to the analysis at the phylum/class level, in which the data for the different basins were pooled, 87–90% of the sequences could be assigned to these major phyla/classes; only 10–13% were unclassified or belonged to rare phylogenetic

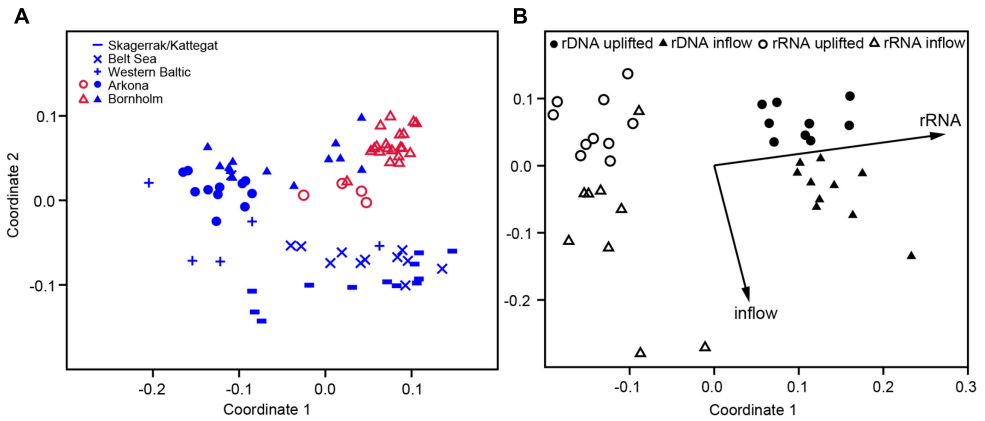


FIGURE 5 | (A) Non-metric multidimensional scaling (NMDS) plots (Bray–Curtis dissimilarity, NMDS stress = 0.1133) of bacterioplankton community composition from different basins of the Baltic Sea, based on the rDNA analysis. The blue symbols represent samples from a reference study (Herlemann et al., 2016), which included the Skagerrak/Kattegat, Belt Sea, Western Baltic, Arkona and Bornholm Basins, and the red symbols samples from this study, including the Arkona and Bornholm Basins. **(B)** NMDS plot (Bray–Curtis dissimilarity, NMDS stress = 0.1046) of bacterioplankton community composition from the Bornholm Basin (this study only) based on rRNA and rDNA analyses. Full symbols indicate DNA-based and open symbols RNA-based bacterial communities. Dots represent the uplifted water masses and triangles the inflow water. The environmental variables inflow vs. uplifted water masses and rDNA vs. rRNA were added as *post hoc* vectors to the NMDS graph, representing the correlations between the environmental variables and NMDS scores.

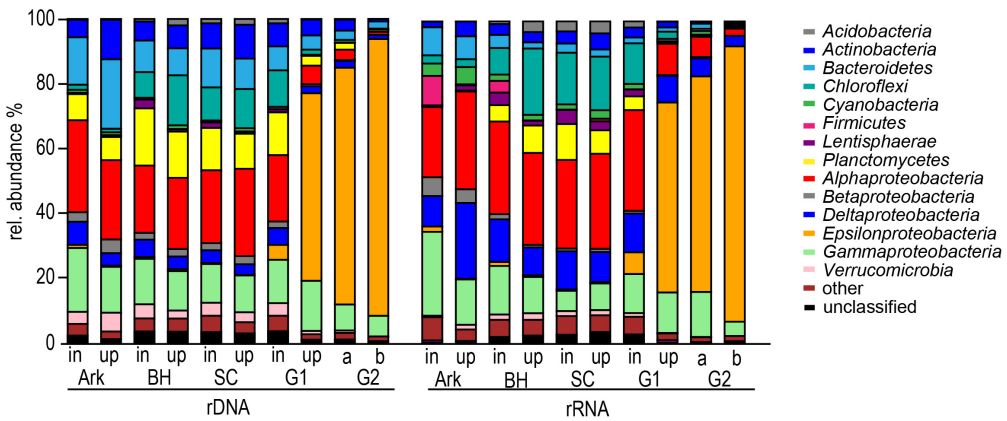


FIGURE 6 | Bacterial community composition on the phylum/class level, mean values for the stations in the Arkona Basin (Ark, $n = 2$), Bornholm Basin (BH, $n = 10$), and Slupsk Channel (SC, $n = 2$), and single values for stations G1 and G2. As the MBI had not reached G2, data from two depths are shown for this station (a: 126 m, b: 120 m).

groups (**Figure 6**). The bacterial composition at all stations until the inflow to station G1, including the Arkona Basin, Bornholm Basin, and Slupsk Channel, was comparable at this broad taxonomic resolution, and quite consistent between the rRNA- and rDNA-based analyses (**Figure 6**). *Alpha-* and *Gammaproteobacteria* were the most abundant groups in these samples, with an average relative abundance of 26 and 14%, respectively. Other important groups, with relative abundances of 5–10%, were *Deltaproteobacteria*, *Bacteroidetes*, *Planctomycetes*, *Chloroflexi,* and *Actinobacteria*. The rRNA- and rDNA-based compositions were only slightly different, with increased proportions of *Firmicutes*, *Deltaproteobacteria* and *Chloroflexi*, and decreased proportions of *Bacteroidetes* and *Planctomycetes* according to the rRNA data (**Figure 6**). The variations between the locations of the Arkona and Bornholm Basins and Slupsk Channel, and between the inflowing and uplifted waters, were rather small. However, in the Bornholm Basin, where the number of stations covered was sufficient to allow statistical tests, the inflowing and uplifted bacterial communities were significantly different at the phylum/class level ($p < 0.01$). A strikingly different community composition was apparent for the two Gotland basin stations G1 and G2, which were dominated by *Epsilonproteobacteria*. However, the water inflowing into station G1 (91 m depth), had a high overall similarity with the uplifted bottom-water from the Bornholm Basin, with a large proportion of *Alphaproteobacteria*, and only 6.8% *Epsilonproteobacteria*. By contrast, *Epsilonproteobacteria* constituted 59% of all sequences in the uplifted water at station G1 (82 m water depth). Station G2, which was not yet impacted by the MBI, was entirely dominated (85%) by *Epsilonproteobacteria* in the deeper waters (126 and

120 m) and contained only small proportions of the other phyla.

Distribution and rRNA/rDNA Ratios of Dominant OTUs

For the most abundant OTUs (>0.5% relative abundance across all stations), the relative proportions at the different stations were visualized in heatmaps. Similar trends were detected in the data from the two analyses, at the rDNA (**Supplementary Figure 6**) and rRNA level (**Figure 7**), but the latter showed a more pronounced pattern for some dominant OTUs and is therefore presented here. ANOSIM revealed significant differences at the rDNA OTU level (R = 0.721) between the inflow-water and uplifted bottom-water communities. Fifteen OTUs from various phyla were determined to be significantly enriched in the inflowing water bodies across the stations sampled (**Supplementary Table 1**). For some OTUs a characteristic alternating sequence between inflowing and uplifted waters became visible, as best seen for the OTU "unclassified SAR202 clade," belonging to the *Chloroflexi*. In the inflowing water from the Arkona Basin this OTU was present in only modest abundance whereas it became the most abundant taxon in the uplifted water of the different stations in the Bornholm Basin, indicating that it dominated the bottom-waters of this basin, before being uplifted by the inflow. Alternating abundances in the inflowing and uplifted waters were also partly visible for other taxa such as the OTUs "unclassified *Rhodospirillaceae*" and "unclassified OM27." There were also OTUs, such as the alphaproteobacterial OTU "unclassified T9d," and the OTU "unclassified WCHB1," that showed a reverse alternating pattern, with a higher abundance in the inflowing and a lower abundance in the uplifted water (**Figure 7**). A third pattern was exemplified by the OTU "unclassified Nitrospina," a widespread marine nitrite oxidizer (Lücker et al., 2013). For this as well as a few other OTUs, a successive decline in relative abundance was determined, probably linked to the dilution of inflowing with existing water masses. The OTU "unclassified SAR86," belonging to a widespread marine gammaproteobacterial group, was successively diluted and no longer detectable at stations toward the end of the Bornholm Basin (**Figure 7**). By contrast, the OTU *Nitrospina* declined with inflow propagation but was still detectable in considerable abundance in the inflowing water bodies. The epsilonproteobacterial OTU *Sulfurimonas* was present only in the Gotland Deep stations, but with a relative abundance > 55%, accompanied by only few other taxa.

The rRNA/rDNA ratios for dominant bacterial OTUs in the different water masses and stations were determined, taking into account only those OTUs with a relative abundance of all sequence reads of >0.5% at both the rRNA and rDNA levels. The overall range in rRNA/rDNA ratios for the OTUs that met these criteria was quite large (**Supplementary Table 2**). Due to the variability between stations and because data were

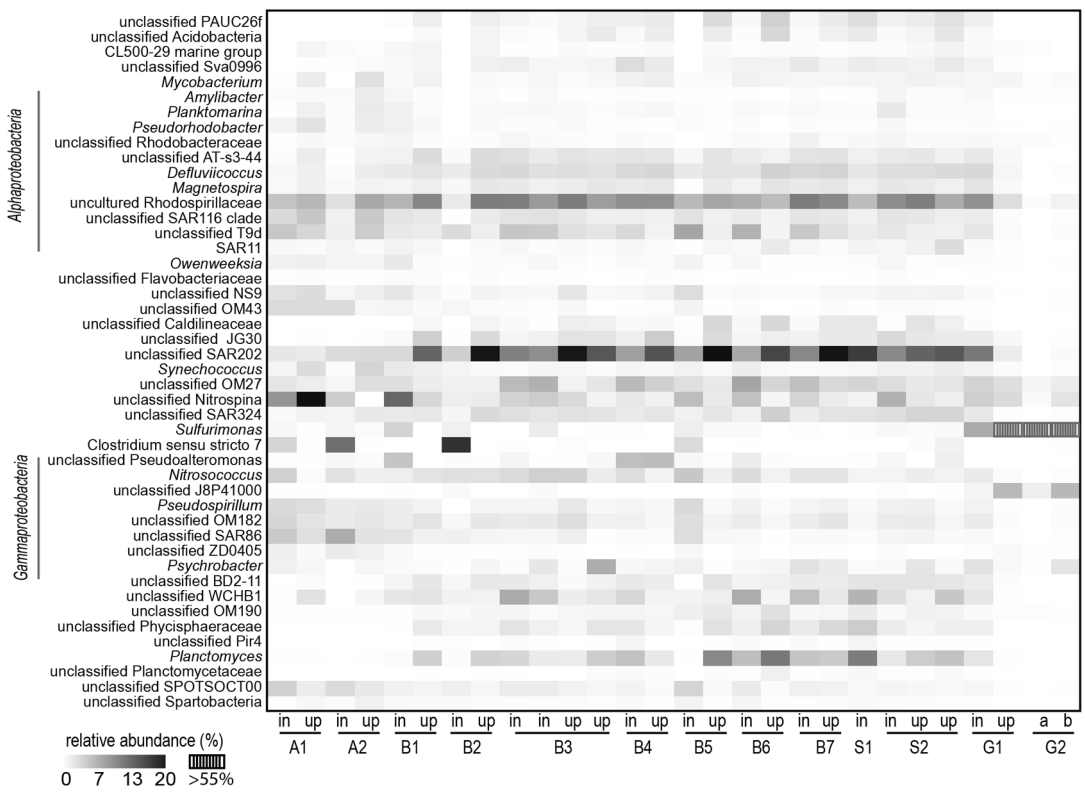


FIGURE 7 | Heatmap of the abundant (total relative abundance > 0.5%) OTUs, based on the rRNA analysis, found in the inflow and uplifted water samples of all stations.

not available for all inflow/uplift pairs, the mean values for all inflow water bodies were not significantly different from those of the uplifting water bodies for an of the OTUs (**Supplementary Table 2**). However, several OTUs underwent strong changes between the inflow and uplifted water at some stations. For example, at the two Arkona basin stations (A1, A2), in the uplifted water there was a large increase in the ratio for the OTUs "unclassified Rhodospirillaceae," "unclassified SAR116," and *Nitrospina* (**Supplementary Figure 7**). For the latter, the ratio first increased by a factor of 5–7, but it then decreased in the Bornholm basin and leveled off to values mostly in the range of 2–4.

DISCUSSION

Bacterial communities in estuaries and coastal margins differ spatially in their composition because of the prevalent gradients in salinity, nutrients, and the other components needed for bacterial growth. However, most estuaries are shaped by hydrodynamic forces, which are responsible for the mixing and characteristic short retention times of their waters. By contrast, in the Baltic Sea, the long water residence time (>5 years) (Reissmann et al., 2009) allows the adaptation of freshwater bacteria to brackish conditions (Riemann et al., 2008) and the coexistence of marine and freshwater lineages, together with presumed brackish water clades, in waters with a salinity of around 7 (Herlemann et al., 2011). Although several studies have addressed the distribution of freshwater and marine bacterial lineages in the Baltic Sea (Riemann et al., 2008; Herlemann et al., 2011, 2014; Piwosz et al., 2013; Bergen et al., 2014), the extent to which MBIs transport typical marine bacterial communities into the brackish parts of the Baltic Sea is unknown, as is the impact of inflowing water masses of relatively high salinity on the composition, distribution and activity of bacterioplankton during the transit of inflow-driven water bodies into the central Baltic Sea. This study is the first to address these questions, by taking advantage of the large MBI of 2014, investigated in detail with respect to its magnitude and temporal development, to link microbiological investigations with the hydrographic and modeling studies. Our data on the bacterioplankton communities, obtained using both rRNA- and rDNA-based community analyses, indicate a high degree of mixing of the inflowing water with the former bottom-waters, a conclusion consistent with the numerical modeling results. Moreover, we were able to show that, among the different water masses, specific bacterial taxa undergo changes in abundance and in their rRNA/rDNA ratios. We were also able to document an example of the displacement by the inflowing water of an entire bacterial assemblage into other water layers.

Characterization of the MBI Water Bodies

The development and dynamics of the 2014 MBI were investigated and followed in a series of cruises preceding our study. The data were complemented by CTD measurements of the permanent autonomous stations of the German Marine Monitoring network (MARNET), located at the Darss Sill and the Arkona Basin (Mohrholz et al., 2015), the autonomous Gotland Deep Environmental Sampling Station (GODESS) (Holtermann et al., 2017), and numerical modeling (Gräwe et al., 2015). The 2014 MBI is thus one of the best monitored MBIs in the Baltic Sea to date, with reliable estimates of inflow volume, as well as oxygen and salt transport. The data provided support for our proposed sequence of stations along which deep water transport and the uplifting of bottom-water presumably occurred (**Figure 1**).

An evaluation of the impact of the MBI on bacterioplankton communities required as a prerequisite a clear picture of the water mass transport through the western Baltic Sea and the deep basins. CTD measurements, in combination with an eddy-resolving hydrodynamic model, reproduced the timing and pattern of the inflowing saline water and revealed its successive mixing with the stagnant bottom-water on its way toward the interior of the Baltic Sea (Gräwe et al., 2015). The temporal evolution of salinity and temperature suggested that already one-third of the inflowing water had been mixed away by the time it reached the Bornholm Channel (Gräwe et al., 2015), the first sampling site of this study. The back-trajectory of the water masses sampled in the Arkona and Bornholm Basins suggested that the origin of the inflowing water was in the area between the Skagerrak and Danish Belt Sea. The widespread pattern of potential origins (**Figure 4**) indicated a high degree of mixing, both vertical and horizontal. However, given the extraordinary size of this inflow event, this strong mixing was not surprising.

When saline water enters the basins and uplifts existing bottom-water, some mixing of these water masses has to be assumed. The effects on bacterial assemblages are two-fold: first, different bacterial communities from the two water bodies are mixed; second, inputs of substrates and/or electron acceptors (oxygen, nitrate) may change the growth conditions of some taxa and modulate their activities. For the Bornholm Basin during the 2014 MBI, the situation was more complex because the uplifted bottom-water was not identical to the bottom-water present during the prolonged stagnation period in the Baltic Sea (2003–2014) that preceded the 2014 MBI. Rather, it already consisted of a mixture with the warmer water that derived from several smaller inflows into the Bornholm Basin earlier that same year (Naumann, 2015).

This study provides a snapshot of the MBI dynamics in February 2015, when the inflowing water had reached the southern edge of the Gotland Basin (station G1) but not yet the central basin. Later on, the MBI continued into the Gotland Basin and was followed by additional, smaller inflows, and two moderate MBIs in November 2015 and January–February 2016 (Naumann et al., unpublished data).

Impact of the MBI on the Composition and Distribution of the Baltic Sea Bacterial Communities on a Broad Phylogenetic Level

The relatively stable Baltic Sea salinity gradient, ranging from marine conditions in the Skagerrak to nearly limnic conditions in the Gulf of Bothnia, is an ideal natural model system to

examine how salinity impacts the composition and functions of bacterioplankton communities. Studies within the last several years have revealed that Baltic Sea salinity determines the bacterial composition at broad phylogenetic levels, with *Alpha-* and *Gamma-proteobacteria* dominating at more marine, and *Betaproteobacteria* and *Actinobacteria* at more limnic conditions (Herlemann et al., 2011). Community shifts at the phylum level occur in the brackish area of the Baltic Sea within a critical salinity range of 5–8 (Herlemann et al. (2011). Although strong seasonal shifts in bacterial composition have been documented (Andersson et al., 2009), data collected across the whole Baltic Sea imply that salinity provides a stronger phylogenetic signal in bacterial community composition than seasonality (Herlemann et al., 2016). Moreover, metagenomic analyses indicate that salinity-related changes in bacterial community composition are associated with changes in metabolic functions (Dupont et al., 2014).

These insights into bacterial composition along the salinity gradient suggest that any inflow of saline waters into the Baltic Sea will also import different (i.e., mainly marine taxa) bacterial communities into the central Baltic Sea. However, the continuous entrainment of overlying water during the passage of new, deep water from the North Sea into the Baltic Sea's basins also results in a successive dilution of the original communities. Therefore, the high similarity between the communities of the inflowing and former bottom-waters (uplifted) in the Arkona and Bornholm Basins, at least on a broad phylogenetic level (**Figure 6**), was not really surprising. This similarity was evident from not only the rDNA but also the rRNA analysis (**Figure 6B**); rRNA-based analyses have generally been used to assess the more "active" fraction of prokaryotes (e.g., Hunt et al., 2013). The successive dilution of inflowing water was also suggested by numerical modeling of the water transport (**Figure 4**). Other factors might also enhance the removal of imported marine taxa, such as inhibition due to more unfavorable conditions and losses due to viral lysis and grazing. Furthermore, the state of the deep water of the Bornholm Basin had probably already slightly changed compared to the previous stagnant conditions, due to smaller inflows of warmer water in 2014 that had mixed with old bottom-water. Despite these changes in the bottom-waters, the bacterial community compositions were rather similar to those of the reference data from 2009, as seen in the clustering of samples in the NMDS plots (**Figure 5A**). However, an inspection of only the Bornholm Basin stations, for which the most samples had been gathered, revealed obvious differences in the communities of the inflowing and uplifted water masses, both at the rDNA and the rRNA level (**Figure 5B**).

The most profound impact of the inflow water was visible in the Gotland Basin, which also represented the former stagnant water body and associated microbial communities because it had not been reached by the previous smaller inflows that occurred in 2004 (Naumann et al., unpublished data). In the Gotland Basin, a bacterial assemblage typical for the anoxic waters of the central Baltic Sea (e.g., Labrenz et al., 2007) was largely replaced by one that resembled the communities found in the adjacent oxygenated basins (Arkona, Bornholm) (**Figure 6**). *Epsilonproteobacteria*, which dominate near oxic-anoxic interfaces in the Baltic Sea and depend on the availability of sulfide and nitrate for chemoautotrophic denitrification (Grote et al., 2012), were a good indicator of the former anaerobic community. The inflowing saline water mass uplifted the former oxygen-deficient bottom-water, and thus also its anaerobic bacterial community. Interestingly, *Epsilonproteobacteria* were found, in a small proportion (5–7%), also in the inflowing water of the southern Gotland station (G1) (**Figure 6**). As this bacterial group was not detected at the (oxic) stations before G1, its proportion can be considered indicative of the degree of mixing that occurred when the inflowing water uplifted the existing bottom-water. This observation demonstrates that in addition to ventilating the Baltic Sea's deep basins (Omstedt et al., 2004) MBIs can directly shift bacterial communities to water strata where they are normally not found.

Impact of the MBI on the Composition and Distribution of the Baltic Sea Bacterial Communities on a Fine Phylogenetic Level

The *Epsilonproteobacteria* in the oxygen-deficient basins of the Baltic Sea consist nearly entirely of the *Sulfurimonas* group (Grote et al., 2012). In the oxic water column, *Sulfurimonas* spp. may serve as a strong indicator of displaced anoxic bottom-water, as this taxon is able to survive in the presence of oxygen but only proliferates around the oxic-anoxic interface (Grote et al., 2012). The previous appearance of *Sulfurimonas* in Baltic Sea surface waters, together with other anaerobic taxa, has been interpreted as the result of an upwelling event, that transported chemocline water to the surface (Lindh et al., 2015).

At a finer phylogenetic resolution (OTUs), further differences between the studied water masses became apparent, including the enrichment of several taxa in the inflow water compared to the former bottom-water (**Supplementary Table 1**). These taxa mainly belonged to *Bacteroidetes*, *Chloroflexi*, *Planctomycetes,* and *Alpha-, Delta-,* and *Gamma-proteobacteria* (**Supplementary Table 1**), with some of them related to known marine taxa (e.g., Brown et al., 2009). The SAR202 clade within the *Chloroflexi* is widespread in the mesopelagic and deep ocean (Morris et al., 2004) but has also been detected in high abundance in Baltic Sea sediments (Klier et al., 2018). This suggests an input of *Chloroflexi* cells from sediments into the water column, driven by the turbulence generated by inflowing water. The resuspension of sediments due to inflowing water has been observed (Naumann et al., unpublished data). *Planctomycetes* diversity was high in the inflow water. Members of this group have been found in the Baltic Sea, including two potential anaerobic ammonium-oxidizing phylotypes from the suboxic zone of the central Baltic (Brettar et al., 2012) and several related OTUs in the sea's brackish and marine areas (Herlemann et al., 2011). An analysis by Rieck et al. (2015) of the particle-associated bacterial communities in three salinity zones of the Baltic Sea showed a dominance of particle-associated *Planctomycetes* in the central Baltic. These *Planctomycetes* mainly consisted of the OTU CL500-3, which was also enriched in the inflow water of this study. The origin and

reason for the enrichment of this group in the inflow water are unclear but a broader distribution than previously recognized seems probable. The *Alphaproteobacteria* enriched in the inflow water mainly comprised *Rhodobacteraceae* and *Rhodospirillaceae*. Enriched *Gammaproteobacteria* were exclusively represented by *Oceanospirillales*. These groups have also been detected in marine areas of the Baltic Sea (Herlemann et al., 2011) and their immigration with the inflow water was therefore likely.

At the OTU level, interesting patterns along the inflow stations became apparent (**Figure 7**). Whereas some OTUs were successively diluted with progression of the inflow, others showed alternating abundances between the inflow and uplifted water bodies, indicating that they had occurred in higher abundance in the bottom-water and became uplifted by the inflow. The higher overall OTU richness (alpha diversity) in the Bornholm and Arkona Basins during our study compared to the reference samples from 2009, based on the rDNA analysis, also indicated that partial mixing of different water bodies with different bacterial communities increased the overall bacterial diversity (**Supplementary Figure 3**).

rRNA/rDNA Ratios

The parallel analysis of rDNA- and rRNA-based community composition also allowed calculation of the rRNA/rDNA ratios of the dominant OTUs. This ratio has been used to distinguish the different growth strategies of marine bacteria (oligotrophs vs. copiotrophs) (Lankiewicz et al., 2015), but also to decipher seasonal changes in the activity status of specific taxa as well as differences between free-living and particle-associated OTUs (Denef et al., 2016). The dominant bacterial OTUs for which a reliable sequence threshold was reached for both rRNA and rDNA all showed a considerable variation in this ratio, but within the range determined in other studies (e.g., Denef et al., 2016). Although the average values of these ratios did not significantly differ between inflowing and uplifted water bodies (**Supplementary Table 2**), the pattern across the stations suggested strong changes in some of the taxa between these water bodies (**Supplementary Figure 5**). This, together with the large changes in relative abundance along the stations (**Figure 7**) probably indicates different growth conditions in the different water bodies.

A striking example of differing rRNA/rDNA ratios was *Nitrospina*, for which large increases in its ratios in the uplifted water of the Arkona Basin were determined (**Supplementary Figure 5**). The genus *Nitrospina* is a widespread marine nitrite oxidizer, mainly below the euphotic zone and in sediments (Ngugi et al., 2015; Daims et al., 2016). This OTU may have been transported with the inflow water, and its potential activity (e.g., nitrite oxidation) was enhanced by the newly encountered nutrient conditions. Indeed, the concentrations of inorganic nitrogen compounds in the inflow water differed from those usually found in the study area (**Supplementary Figure 2**). The low concentrations of ammonia and nitrite and the high concentration of nitrate might have resulted from enhanced nitrification in the inflow water. Ammonia-oxidizing bacteria were not detected in higher abundance in our samples, but it is known that ammonia oxidation in the deeper waters of the Baltic Sea is dominated by ammonia-oxidizing archaea (Berg et al., 2015), which were not covered by our primers.

CONCLUSION

This study is the first to describe the impact of an MBI on the composition and distribution of Baltic Sea bacterioplankton. Our results provide evidence of two major mechanisms that explain the observed impact on the bacterial communities of the central Baltic Sea basins: first, successive mixing of inflowing saline water along the transit through the Baltic Sea resulted in relatively similar bacterial assemblages between inflowing and former bottom-water communities on a broad phylogenetic level. Therefore, a typical marine bacterial assemblage did not arrive by the MBI in the central Baltic Sea. However, significant community changes were apparent at the OTU level, revealing the enrichment of certain taxa with the inflowing water, different patterns of changing abundance and varying rRNA/rDNA ratios in the different water bodies. Second, the uplifting of former bottom communities, with their key indicator taxa, resulted in their displacement into different water strata. This was best illustrated by the arrival of the 2014 MBI at a station in the Gotland Basin, where the former anoxic bottom community, dominated by *Epsilonproteobacteria*, was shifted to shallower water depths. The implications of these shifts in water masses and microbial communities for microbially mediated ecosystem functions are not yet fully understood. However, they can perhaps be determined in studies that examine the functional performance of key bacterial taxa and their physiological changes in response to mixing with inflowing water or to the uplifting to new water layers with different environmental conditions.

ETHICS STATEMENT

All authors declare that the research was conducted in the absence of any commercial or financial relationships that could be construed as a potential conflict of interest. This article does not contain any studies with human participants or animals performed by any of the authors.

AUTHOR CONTRIBUTIONS

BB, MN, ML, and KJ planned, initiated, and conducted the study. MN gathered and provided hydrographic data. UG conducted the backtracking numerical model. DH helped with the analysis of bacterial diversity data. BB and KJ wrote the first draft of the manuscript. All authors discussed the results and edited the manuscript.

FUNDING

This work was funded by the Deutsche Forschungsgemeinschaft (DFG) (projects JU367/15-1, JU367/16-1 to KJ and LA1466/8-1 to ML). DH was supported by the European Regional

Development Fund and the Estonian Research Council Mobilitas Plus Top Researcher grant "MOBTT24." UG was supported by the BMBF project "Hydrodynamic observations and simulations of munition in the sea," a subproject of the collaborative project "Environmental monitoring for the delaboration of munitions in the sea" (Grant No. #03F0747C).

ACKNOWLEDGMENTS

We thank the captain and crew of the RV Elisabeth Mann Borgese for assistance in sampling during the EMB 95 cruise. The sampling campaign was done within the framework of the IOW's long-term data program, which was quickly adapted to take advantage of the special inflow situation with additional "task force inflow" sampling. We also thank Stephanie Mothes for technical assistance at sea.

SUPPLEMENTARY MATERIAL

The Supplementary Material for this article can be found online at: https://www.frontiersin.org/articles/10.3389/fmars.2018.00383/full#supplementary-material

REFERENCES

Andersson, A. F., Riemann, L., and Bertilsson, S. (2009). Pyrosequencing reveals contrasting seasonal dynamics of taxa within Baltic Sea bacterioplankton communities. *ISME J.* 4, 171–181. doi: 10.1038/ismej.2009.108

Berg, C., Vandieken, V., Thamdrup, B., and Jürgens, K. (2015). Significance of archaeal nitrification in hypoxic waters of the Baltic Sea. *ISME J.* 9, 1319–1332. doi: 10.1038/ismej.2014.218

Bergen, B., Herlemann, D. P. R., Labrenz, M., and Jürgens, K. (2014). Distribution of the verrucomicrobial clade S partobacteria along a salinity gradient in the Baltic Sea. *Environ. Microbiol. Rep.* 6, 625–630. doi: 10.1111/1758-2229.12178

Bouvier, T. C., and Giorgio, P. A. (2002). Compositional changes in free-living bacterial communities along a salinity gradient in two temperate estuaries. *Limnol. Oceanogr.* 47, 453–470. doi: 10.4319/lo.2002.47.2.0453

Brettar, I., Christen, R., and Höfle, M. G. (2012). Analysis of bacterial core communities in the central Baltic by comparative RNA–DNA-based fingerprinting provides links to structure–function relationships. *ISME J.* 6, 195–212. doi: 10.1038/ismej.2011.80

Brown, M. V., Philip, G. K., Bunge, J. A., Smith, M. C., Bissett, A., Lauro, F. M., et al. (2009). Microbial community structure in the North Pacific ocean. *ISME J.* 3, 1374–1386. doi: 10.1038/ismej.2009.86

Burchard, H., Lass, H. U., Mohrholz, V., Umlauf, L., Sellschopp, J., Fiekas, V., et al. (2005). Dynamics of medium-intensity dense water plumes in the Arkona Basin, Western Baltic Sea. *Ocean Dyn.* 55, 391–402. doi: 10.1007/s10236-005-0025-2

Daims, H., Lücker, S., and Wagner, M. (2016). A new perspective on microbes formerly known as nitrite-oxidizing bacteria. *Trends Microbiol.* 24, 699–712. doi: 10.1016/j.tim.2016.05.004

Dellwig, O., Schnetger, B., Meyer, D., Pollehne, F., Häusler, K., and Arz, H. W. (2018). Impact of the major baltic inflow in 2014 on manganese cycling in the Gotland Deep (Baltic Sea). *Front. Mar. Sci.* 5:248. doi: 10.3389/fmars.2018.00248

Denef, V. J., Fujimoto, M., Berry, M. A., and Schmidt, M. L. (2016). Seasonal succession leads to habitat-dependent differentiation in ribosomal RNA:DNA ratios among freshwater lake bacteria. *Front. Microbiol.* 7:606. doi: 10.3389/fmicb.2016.00606

Dupont, C. L., Larsson, J., Yooseph, S., Ininbergs, K., Goll, J., Asplund-Samuelsson, J., et al. (2014). Functional tradeoffs underpin salinity-driven divergence in microbial community composition. *PLoS One* 9:e89549. doi: 10.1371/journal.pone.0089549

Fortunato, C. S., and Crump, B. C. (2011). Bacterioplankton community variation across river to ocean environmental gradients. *Microb. Ecol.* 62, 374–382. doi: 10.1007/s00248-011-9805-z

Gasol, J. M., and del Giorgio, P. A. (2000). Using flow cytometry for counting natural planktonic bacteria and understanding the structure of planktonic bacterial communities. *Sci. Mar.* 64, 197–224. doi: 10.3989/scimar.2000.64n2197

Glöckner, F. O., Yilmaz, P., Quast, C., Gerken, J., Beccati, A., Ciuprina, A., et al. (2017). 25 years of serving the community with ribosomal RNA gene reference databases and tools. *J. Biotechnol.* 261, 169–176. doi: 10.1016/j.jbiotec.2017.06.1198

Grasshoff, K., Ehrhardt, M., and Kremling, K. (1983). *Methods of Seawater Analysis*, 2nd Edn. Weinheim: Verlag Chemie.

Gräwe, U., Friedland, R., and Burchard, H. (2013). The future of the western Baltic Sea: two possible scenarios. *Ocean Dyn.* 63, 901–921. doi: 10.1007/s10236-013-0634-0

Gräwe, U., Naumann, M., Mohrholz, V., and Burchard, H. (2015). Anatomizing one of the largest saltwater inflows into the Baltic Sea in December 2014. *J. Geophys. Res. Ocean* 120, 7676–7697. doi: 10.1002/2015JC011269

Grote, J., Schott, T., Bruckner, C. G., Glöckner, F. O., Jost, G., Teeling, H., et al. (2012). Genome and physiology of a model Epsilonproteobacterium responsible for sulfide detoxification in marine oxygen depletion zones. *Proc. Natl. Acad. Sci. U.S.A.* 109, 506–510. doi: 10.1073/pnas.1111262109

Hall, P. O. J., Almroth Rosell, E., Bonaglia, S., Dale, A. W., Hylén, A., Kononets, M., et al. (2017). Influence of natural oxygenation of Baltic proper deep water on benthic recycling and removal of phosphorus, nitrogen, silicon and carbon. *Front. Mar. Sci.* 4:27. doi: 10.3389/fmars.2017.00027

Hammer, Ø, Harper, D. A. T., and Ryan, P. D. (2001). PAST: paleontological statistics software package for education and data analysis. *Palaeontol. Electron.* 4:9.

Herlemann, D. P. R., Labrenz, M., Jürgens, K., Bertilsson, S., Waniek, J. J., and Andersson, A. F. (2011). Transitions in bacterial communities along the 2000 km salinity gradient of the Baltic Sea. *ISME J.* 5, 1571–1579. doi: 10.1038/ismej.2011.41

Herlemann, D. P. R., Lundin, D., Andersson, A. F., Labrenz, M., and Jürgens, K. (2016). Phylogenetic signals of salinity and season in bacterial community composition across the salinity gradient of the Baltic Sea. *Front. Microbiol.* 7:1883. doi: 10.3389/fmicb.2016.01883

Herlemann, D. P. R., Woelk, J., Labrenz, M., and Jürgens, K. (2014). Diversity and abundance of "Pelagibacterales" (SAR11) in the Baltic Sea salinity gradient. *Syst. Appl. Microbiol.* 37, 601–604. doi: 10.1016/j.syapm.2014.09.002

Holtermann, P. L., Prien, R., Naumann, M., Mohrholz, V., and Umlauf, L. (2017). Deepwater dynamics and mixing processes during a major inflow event in the central Baltic Sea. *J. Geophys. Res.* 122, 6648–6667. doi: 10.1002/2017JC013050

Hunt, D. E., Lin, Y., Church, M. J., Karl, D. M., Tringe, S. G., Izzo, L. K., et al. (2013). Relationship between abundance and specific activity of bacterioplankton in open ocean surface waters. *Appl. Environ. Microbiol.* 79, 177–184. doi: 10.1128/AEM.02155-12

Kirchman, D. L., Dittel, A. I., Malmstrom, R. R., and Cottrell, M. T. (2005). Biogeography of major bacterial groups in the Delaware estuary. *Limnol. Oceanogr.* 50, 1697–1706. doi: 10.4319/lo.2005.50.5.1697

Klier, J., Dellwig, O., Leipe, T., Jürgens, K., and Herlemann, D. P. R. (2018). Benthic bacterial community composition in the oligohaline-marine transition of surface sediments in the Baltic Sea based on rRNA analysis. *Front. Microbiol.* 9:236. doi: 10.3389/fmicb.2018.00236

Kuss, J., Cordes, F., Mohrholz, V., Nausch, G., Naumann, M., Krüger, S., et al. (2017). The impact of the major Baltic inflow of December 2014 on the mercury species distribution in the Baltic Sea. *Environ. Sci. Technol.* 51, 11692–11700. doi: 10.1021/acs.est.7b03011

Labrenz, M., Jost, G., and Jürgens, K. (2007). Distribution of abundant prokaryotic organisms in the water column of the central Baltic Sea with an oxic-anoxic interface. *Aquat. Microb. Ecol.* 46, 177–190. doi: 10.3354/ame046177

Laine, A. O., Sandler, H., Andersin, A.-B., and Stigzelius, J. (1997). Long-term changes of macrozoobenthos in the Eastern Gotland Basin and the Gulf of Finland (Baltic Sea) in relation to the hydrographical regime. *J. Sea Res.* 38, 135–159. doi: 10.1016/S1385-1101(97)00034-8

Lankiewicz, T. S., Cottrell, M. T., and Kirchman, D. L. (2015). Growth rates and rRNA content of four marine bacteria in pure cultures and in the Delaware estuary. *ISME J.* 10, 823–832. doi: 10.1038/ismej.2015.156

Lilover, M.-J., Elken, J., Suhhova, I., and Liblik, T. (2017). Observed flow variability along the thalweg, and on the coastal slopes of the Gulf of Finland, Baltic Sea. *Estuar. Coast. Shelf Sci.* 195, 23–33. doi: 10.1016/j.ecss.2016.11.002

Lindh, M. V., Sjöstedt, J., Andersson, A. F., Baltar, F., Hugerth, L. W., Lundin, D., et al. (2015). Disentangling seasonal bacterioplankton population dynamics by high-frequency sampling. *Environ. Microbiol.* 17, 2459–2476. doi: 10.1111/1462-2920.12720

Lozupone, C. A., and Knight, R. (2007). Global patterns in bacterial diversity. *Proc. Natl. Acad. Sci. U.S.A.* 104, 11436–11440. doi: 10.1073/pnas.0611525104

Lücker, S., Nowka, B., Rattei, T., Spieck, E., and Daims, H. (2013). The genome of *Nitrospina gracilis* illuminates the metabolism and evolution of the major marine nitrite oxidizer. *Front. Microbiol.* 4:27. doi: 10.3389/fmicb.2013.00027

Matthäus, W., and Franck, H. (1992). Characteristics of major Baltic inflows - a statistical analysis. *Cont. Shelf Res.* 12, 1375–1400. doi: 10.1016/0278-4343(92)90060-W

Mohrholz, V., Naumann, M., Nausch, G., Krüger, S., and Gräwe, U. (2015). Fresh oxygen for the Baltic Sea—An exceptional saline inflow after a decade of stagnation. *J. Mar. Syst.* 148, 152–166. doi: 10.1016/j.jmarsys.2015.03.005

Morris, R. M., Rappé, M. S., Urbach, E., Connon, S. A., and Rappe, M. S. (2004). Prevalence of the Chloroflexi-related SAR202 bacterioplankton cluster throughout the mesopelagic zone and deep ocean. *Appl. Environ. Microbiol.* 70, 2836–2842. doi: 10.1128/AEM.70.5.2836

Naumann, M. (2015). *Cruise Report r/v E. Mann-Borgese No. 100 – SECOS Project & MBI December 2014 Research Cruise, Leibniz-Institute for Baltic Sea Research*. Available at: http://www.io-warnemuende.de/tl_files/forschung/pdf/cruise-reports/cremb100.pdf

Nemergut, D. R., Costello, E. K., Hamady, M., Lozupone, C., Jiang, L., Schmidt, S. K., et al. (2011). Global patterns in the biogeography of bacterial taxa. *Environ. Microbiol.* 13, 135–144. doi: 10.1111/j.1462-2920.2010.02315.x

Ngugi, D. K., Blom, J., Stepanauskas, R., and Stingl, U. (2015). Diversification and niche adaptations of Nitrospina-like bacteria in the polyextreme interfaces of Red Sea brines. *ISME J.* 10, 1383–1399. doi: 10.1038/ismej.2015.214

Omstedt, A., Pettersen, C., Rodhe, J., and Winsor, P. (2004). Baltic Sea climate: 200 yr of data on air temperature, sea level variation, ice cover, and atmospheric circulation. *Clim. Res.* 25, 205–216. doi: 10.3354/cr025205

Piwosz, K., Salcher, M. M., Zeder, M., Ameryk, A., and Pernthaler, J. (2013). Seasonal dynamics and activity of typical freshwater bacteria in brackish waters of the Gulf of Gdansk. *Limnol. Oceanogr.* 58, 817–826. doi: 10.4319/lo.2013.58.3.0817

Pruesse, E., Peplies, J., and Glöckner, F. O. (2012). SINA: accurate high-throughput multiple sequence alignment of ribosomal RNA genes. *Bioinformatics* 28, 1823–1829. doi: 10.1093/bioinformatics/bts252

Pruesse, E., Quast, C., Knittel, K., Fuchs, B. M., Ludwig, W., Peplies, J., et al. (2007). SILVA: a comprehensive online resource for quality checked and aligned ribosomal RNA sequence data compatible with ARB. *Nucleic Acids Res.* 35, 7188–7196. doi: 10.1093/nar/gkm864

Quast, C., Pruesse, E., Yilmaz, P., Gerken, J., Schweer, T., Yarza, P., et al. (2013). The SILVA ribosomal RNA gene database project: improved data processing and web-based tools. *Nucleic Acids Res.* 41, 590–596. doi: 10.1093/nar/gks1219

Reissmann, J. H., Burchard, H., Feistel, R., Hagen, E., Lass, H. U., Mohrholz, V., et al. (2009). Vertical mixing in the Baltic Sea and consequences for eutrophication - A review. *Prog. Oceanogr.* 82, 47–80. doi: 10.1016/j.pocean.2007.10.004

Rieck, A., Herlemann, D. P. R., Jürgens, K., and Grossart, H.-P. (2015). Particle-associated differ from free-living bacteria in surface waters of the Baltic Sea. *Front. Microbiol.* 6:1297. doi: 10.3389/fmicb.2015.01297

Riemann, L., Leitet, C., Pommier, T., Simu, K., Holmfeldt, K., Larsson, U., et al. (2008). The native bacterioplankton community in the central Baltic Sea is influenced by freshwater bacterial species. *Appl. Environ. Microbiol.* 74, 503–515. doi: 10.1128/AEM.01983-07

Robertson, C. E., Harris, J. K., Wagner, B. D., Granger, D., Browne, K., Tatem, B., et al. (2013). Explicet: graphical user interface software for metadata-driven management, analysis and visualization of microbiome data. *Bioinformatics* 29, 3100–3101. doi: 10.1093/bioinformatics/btt526

Schmale, O., Krause, S., Holtermann, P., Power Guerra, N. C., and Umlauf, L. (2016). Dense bottom gravity currents and their impact on pelagic methanotrophy at oxic/anoxic transition zones. *Geophys. Res. Lett.* 43, 5225–5232. doi: 10.1002/2016GL069032

Segata, N., Izard, J., Waldron, L., Gevers, D., Miropolsky, L., Garrett, W. S., et al. (2011). Metagenomic biomarker discovery and explanation. *Genome Biol.* 12:R60. doi: 10.1186/gb-2011-12-6-r60

Sommer, S., Clemens, D., Yücel, M., Pfannkuche, O., Hall, P. O. J., Almroth-Rosell, E., et al. (2017). Major bottom water ventilation events do not significantly reduce basin-wide benthic N and P release in the Eastern Gotland Basin (Baltic Sea). *Front. Mar. Sci.* 4:18. doi: 10.3389/fmars.2017.00018

Umlauf, L., Arneborg, L., Burchard, H., Fiekas, V., Lass, H. U., Mohrholz, V., et al. (2007). Transverse structure of turbulence in a rotating gravity current. *Geophys. Res. Lett.* 34:08601. doi: 10.1029/2007GL029521

Weinbauer, M. G., Fritz, I., Wenderoth, D. F., and Höfle, M. G. (2002). Simultaneous extraction from bacterioplankton of total RNA and DNA suitable for quantitative structure and function analyses. *Appl. Environ. Microbiol.* 68, 1082–1087. doi: 10.1128/AEM.68.3.1082-1087.2002

Conflict of Interest Statement: The authors declare that the research was conducted in the absence of any commercial or financial relationships that could be construed as a potential conflict of interest.

Copyright © 2018 Bergen, Naumann, Herlemann, Gräwe, Labrenz and Jürgens. This is an open-access article distributed under the terms of the Creative Commons Attribution License (CC BY). The use, distribution or reproduction in other forums is permitted, provided the original author(s) and the copyright owner(s) are credited and that the original publication in this journal is cited, in accordance with accepted academic practice. No use, distribution or reproduction is permitted which does not comply with these terms.

frontiers in Marine Science

HYPOTHESIS AND THEORY
published: 26 September 2018
doi: 10.3389/fmars.2018.00342

Understanding the Coastal Ecocline: Assessing Sea–Land Interactions at Non-tidal, Low-Lying Coasts Through Interdisciplinary Research

*Gerald Jurasinski[1,2†], Manon Janssen[3†], Maren Voss[1,4], Michael E. Böttcher[1,5], Martin Brede[1,6], Hans Burchard[1,7], Stefan Forster[1,8], Lennart Gosch[3], Ulf Gräwe[7], Sigrid Gründling-Pfaff[9], Fouzia Haider[8], Miriam Ibenthal[3], Nils Karow[6], Ulf Karsten[1,9], Matthias Kreuzburg[10], Xaver Lange[7], Peter Leinweber[1,11], Gudrun Massmann[12], Thomas Ptak[13], Fereidoun Rezanezhad[14], Gregor Rehder[1,10], Katharina Romoth[15], Hanna Schade[8], Hendrik Schubert[1,15], Heide Schulz-Vogt[1,4], Inna M. Sokolova[1,8], Robert Strehse[11], Viktoria Unger[2], Julia Westphal[5] and Bernd Lennartz[1,3]**

[1] Department of Maritime Systems, Interdisciplinary Faculty, University of Rostock, Rostock, Germany, [2] Landscape Ecology, Faculty of Agricultural and Environmental Sciences, University of Rostock, Rostock, Germany, [3] Soil Physics, Faculty of Agricultural and Environmental Sciences, University of Rostock, Rostock, Germany, [4] Biological Oceanography, Leibniz Institute for Baltic Sea Research Warnemünde, Rostock, Germany, [5] Geochemistry and Isotope Biogeochemistry, Leibniz Institute for Baltic Sea Research Warnemünde, Rostock, Germany, [6] Fluid Mechanics, Faculty of Mechanical Engineering and Marine Technology, University of Rostock, Rostock, Germany, [7] Department of Physical Oceanography and Instrumentation, Leibniz Institute for Baltic Sea Research Warnemünde, Rostock, Germany, [8] Marine Biology, Faculty of Mathematics and Natural Sciences, University of Rostock, Rostock, Germany, [9] Phycology and Applied Ecology, Faculty of Mathematics and Natural Sciences, University of Rostock, Rostock, Germany, [10] Marine Chemistry, Leibniz Institute for Baltic Sea Research Warnemünde, Rostock, Germany, [11] Soil Science, Faculty of Agricultural and Environmental Sciences, University of Rostock, Rostock, Germany, [12] Hydrogeology, Carl von Ossietzky University of Oldenburg, Oldenburg, Germany, [13] Department of Applied Geology, University of Göttingen, Göttingen, Germany, [14] Ecohydrology Research Group, Water Institute and Department of Earth & Environmental Sciences, University of Waterloo, Waterloo, ON, Canada, [15] Aquatic Ecology, Faculty of Mathematics and Natural Sciences, University of Rostock, Rostock, Germany

OPEN ACCESS

Edited by:
Anas Ghadouani, The University of Western Australia, Australia

Reviewed by:
Sabine Schmidt, Centre National de la Recherche Scientifique (CNRS), France
Helena Granja, University of Minho, Portugal

***Correspondence:**
Bernd Lennartz
bernd.lennartz@uni-rostock.de

† These authors have contributed equally to this work

Specialty section:
This article was submitted to Coastal Ocean Processes, a section of the journal Frontiers in Marine Science

Received: *30 April 2018*
Accepted: *06 September 2018*
Published: *26 September 2018*

Citation:
Jurasinski G, Janssen M, Voss M, Böttcher ME, Brede M, Burchard H, Forster S, Gosch L, Gräwe U, Gründling-Pfaff S, Haider F, Ibenthal M, Karow N, Karsten U, Kreuzburg M, Lange X, Leinweber P, Massmann G, Ptak T, Rezanezhad F, Rehder G, Romoth K, Schade H, Schubert H, Schulz-Vogt H, Sokolova IM, Strehse R, Unger V, Westphal J and Lennartz B (2018) Understanding the Coastal Ecocline: Assessing Sea–Land Interactions at Non-tidal, Low-Lying Coasts Through Interdisciplinary Research. Front. Mar. Sci. 5:342. doi: 10.3389/fmars.2018.00342

Coastal zones connect terrestrial and marine ecosystems forming a unique environment that is under increasing anthropogenic pressure. Rising sea levels, sinking coasts, and changing precipitation patterns modify hydrodynamic gradients and may enhance sea–land exchange processes in both tidal and non-tidal systems. Furthermore, the removal of flood protection structures as restoration measure contributes locally to the changing coastlines. A detailed understanding of the ecosystem functioning of coastal zones and the interactions between connected terrestrial and marine ecosystems is still lacking. Here, we propose an interdisciplinary approach to the investigation of interactions between land and sea at shallow coasts, and discuss the advantages and the first results provided by this approach as applied by the research training group Baltic TRANSCOAST. A low-lying fen peat site including the offshore shallow sea area on the southern Baltic Sea coast has been chosen as a model system to quantify hydrophysical, biogeochemical, sedimentological, and biological processes across the land–sea interface. Recently introduced rewetting measures might have enhanced submarine groundwater discharge (SGD) as indicated by distinct patterns of salinity gradients in the near shore sediments, making the coastal waters in front of the study site a mixing zone of fresh- and brackish water. High nutrient loadings,

dissolved inorganic carbon (DIC), and dissolved organic matter (DOM) originating from the degraded peat may affect micro- and macro-phytobenthos, with the impact propagating to higher trophic levels. The terrestrial part of the study site is subject to periodic brackish water intrusion caused by occasional flooding, which has altered the hydraulic and biogeochemical properties of the prevailing peat soils. The stable salinity distribution in the main part of the peatland reveals the legacy of flooding events. Generally, elevated sulfate concentrations are assumed to influence greenhouse gas (GHG) emissions, mainly by inhibiting methane production, yet our investigations indicate complex interactions between the different biogeochemical element cycles (e.g., carbon and sulfur) caused by connected hydrological pathways. In conclusion, sea–land interactions are far reaching, occurring on either side of the interface, and can only be understood when both long-term and event-based patterns and different spatial scales are taken into account in interdisciplinary research that involves marine and terrestrial expertise.

Keywords: shallow coast, coastal peatland, land–sea coupling, greenhouse gas emissions, submarine groundwater discharge

SEA–LAND INTERACTIONS IN SHALLOW COASTAL AREAS UNDER ANTHROPOGENIC PRESSURE

Coastal areas are the preferred habitats of humans, and it is estimated that between half a billion and more than a billion people live in low-lying coastal regions around the world (Bollmann et al., 2010; Neumann et al., 2015). Global climate change threatens this space, while the increasing population in coastal areas puts the coasts under pressure due to construction activities (including settlements, harbors, wind farms, and coastal protection structures such as dykes and levees), agriculture, and tourism (Nicholls et al., 2007; Doney, 2010; Kummu et al., 2016). These anthropogenic activities modify the water exchange processes between land and sea.

Shallow coasts at low-lying areas are characterized by a relatively wide ecocline from land to sea. Long-term changes in sea-level as well as periodic (tides) or episodic (storm surges) events can, thus, affect large areas on both sides of the shoreline. Our understanding of the sea–land connection is focused on extreme scenarios in which the ocean is flooding the land with often dramatic consequences to the people living on the coast. Studies of sea–land interactions are often focused on estuaries where large quantities of fresh water and solutes are mixing with ocean water (e.g., Newton et al., 2014). The impact of rivers on the coastal ocean is substantial and includes excess nutrient delivery (eutrophication) (Bollmann et al., 2010), transport of essential trace compounds (metals, silica) (Martin and Whitfield, 1983; Du Laing et al., 2009), and may lead to drastic environmental changes along the salinity gradient (Kemp et al., 2005). The coastline itself is rarely considered as an exchange interface for energy, water, and substances, yet this interface is very important as it operates continuously and may have far-reaching effects on (micro-)biological and hydro-biogeochemical processes on either side of the coast (e.g., Rullkötter, 2009; Gätje and Reise, 2012).

Sea level rise is a common process observable around the world, mainly caused by ongoing climate change (Church et al., 2013). Recent studies show a rapid increase of sea level worldwide (Nerem et al., 2018), that is amplified at the southern Baltic Sea by an ongoing isostatic subsidence of the coast (Johansson et al., 2014). Taking into consideration the possible scenario of a combination of sinking coasts (Hünicke and Zorita, 2016), the rising sea levels (Grinsted et al., 2015), and future increase of winter precipitation (BACC II Author Team, 2015), we can expect that sea–land connectivity will increase in the Southern Baltic Sea region in future as the area of the coastal system increases (Nicholls et al., 2007). Understanding of the prevailing physical, biogeochemical, and biological drivers as well as of potential tipping points of such coasts in transition is crucial for our ability to sustainably balance natural conservation and anthropogenic use of the coasts. Therefore, the overarching aim of the Baltic TRANSCOAST research training group is to enhance the fundamental understanding of the interconnected physico-chemical, biogeochemical, and ecological processes along the ecocline of the shallow coast using a southern Baltic coastal site, the Hütelmoor, as a model. The aim of the present paper is to outline the hypotheses and research questions of the interdisciplinary approach of Baltic TRANSCOAST and present the first results generated by this approach as a roadmap to gain deeper insight into processes across lowland coastal transects that can be applied to investigations of similar shallow coastal systems worldwide.

THE BALTIC SEA AS A MODEL TO STUDY EXCHANGE PROCESSES AT SHALLOW COASTS WITH LOW-LYING LAND AREAS

The Baltic Sea is a young shelf sea in northern Europe (**Figure 1**) connected to the North Sea since the time of the Litorina

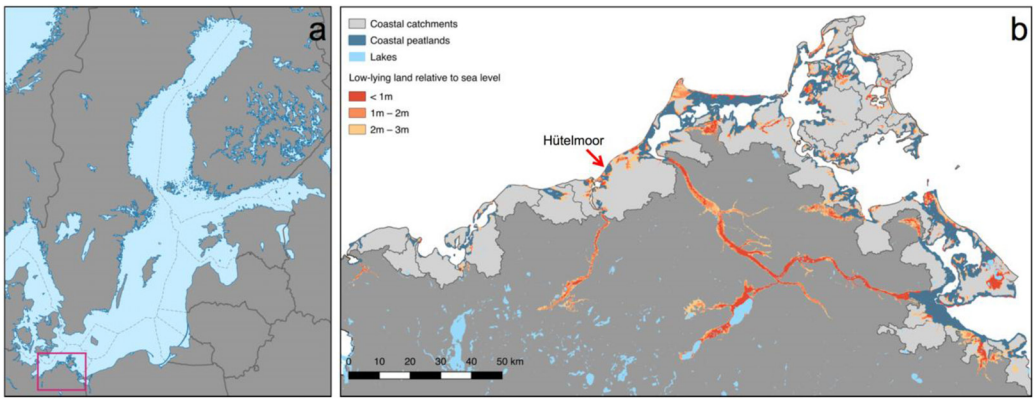


FIGURE 1 | (a) Map of the Baltic Sea with the extent of the region to the right represented by a purple rectangle; **(b)** The Baltic Sea coast in the north-east of Germany with low-lying areas and coastal peatlands. Low-lying areas reach relatively far into the land and the wide river valleys are filled with peat. Coastal peatlands occur in the lowest-lying areas (<1 m). Note the coastal catchments (light gray) that are not connected to a river basin and discharge directly into the sea. Country borders were retrieved from www.gadm.org. Base data for the map in **b** and all other maps were provided by www.geoportal-mv.de.

transgression about 8,000 years ago. The coastline of the Baltic Sea is roughly 2,000 km long (STALU-MM, 2010). The German coastal areas comprise 13,900 km^2 currently mostly protected by dykes (Bollmann et al., 2010). Along the shoreline of the Baltic Sea, cliffs alternate with low-lying areas, with the latter often including peatlands. The extent of low-lying areas increases from West to East along the Baltic Sea coast in northeastern Germany (**Figure 1**).

At low-lying coastal areas, peatlands formed by the accumulation of organic material over millennia often constitute the interface between land and water bodies (**Figure 1**). They cover an area of approx. 40,000 ha in the northeastern German federal state of Mecklenburg-Western Pomerania and play a pivotal role in buffering the exchange of water and dissolved and particulate compounds. Fundamentally, two different processes contribute to formation of the two major types of coastal peatlands along the southern Baltic Sea coast, i.e., paludification (driven by very rare flooding when the water is hindered from leaving the flooded area) or episodic flooding (weekly to monthly) with flooded periods being generally shorter than non-flooded periods. Most coastal peatlands in Mecklenburg-Western Pomerania belong to the second, episodically flooded type. The sea–land transition zone is characterized by brackish water input into the terrestrial part of the coast through underground seawater intrusion or flooding. Submarine groundwater discharge (SGD) marks transport processes into the opposite direction delivering freshwater, dissolved organic matter (DOM), and nutrients to the sea, independent from riverine export and other point sources (e.g., Andersen et al., 2007; Knee and Paytan, 2011; Donis et al., 2017). SGD also encompasses recirculating seawater and mixtures of seawater with fresh waters (e.g., Böttcher et al., 2018). The direction of exchange across the coastline depends on the prevailing pressure gradients and their physically driven dynamics.

The natural dynamics at the coastline have been altered since centuries by flood control measures such as dykes and flood walls. The exchange of water across the sea–land interface is hampered by these structures, especially at low-lying coastal segments dominated by peatlands, which would be regularly flooded under natural conditions. The establishment of coastal protection measures allowed the artificial drainage of coastal peatlands for agricultural purposes. The resulting lowering of the groundwater tables modifies the prevailing physical and chemical gradients and hinders the possible land–sea connection. The necessity of coastal protection measures is controversial and much-debated. The need for protection of people and their possessions is indisputable. However, higher levels of protection and reduced exchange between land and sea increase the vulnerability of the coast and the potential for catastrophic events. Under sea-level rise, protection of low lying areas at shallow coasts may be an effective way for ensuring wealth and health of local residents, since they could be used as buffer zones for flooding events. Some of the coastal peatlands have been or will soon be rewetted by removing the dykes. The resulting exchange of water and compounds transported by water across the coastal interface has been perceived as a natural process worthy to be conserved or re-established. Likewise, the rewetting and restoration of wet- and peatlands have become a societal priority because of the enormous ecological services restored peatlands may provide like carbon sequestration, and water and nutrient buffering (Vasander et al., 2003).

Future weather and climate scenarios obtained from downscaling of global climate models draw a differentiated picture for the southern Baltic Sea region. While dryer summers with more frequent and occasional extreme storm events are to be expected, the winters may become warmer and wetter in terms of total precipitation (BACC II Author Team, 2015). The winter half-year (i.e., November–April) is the dominant period of discharge generation in the region since in summer evapotranspiration typically causes a negative water balance. With the expected addition of precipitation in winter, more pronounced discharge rates and steeper hydraulic gradients are expected. Considering the many catchments located on the coast that do not drain through rivers (**Figure 1**), it is likely that

diffusive pathways from land to sea will become more important under future winter weather situations.

Elevated groundwater levels and associated steeper gradients toward the sea may provoke SGD (e.g., Church, 1996; Abarca et al., 2013). SGD is defined as 'any and all flow of water on continental margins from the seabed to the coastal ocean' (Burnett et al., 2003), originating, for instance, from fresh groundwater of modern terrestrial origin and/or recirculated seawater with the latter providing the main component of SGD in many places (e.g., Church, 1996; Burnett et al., 2003; Böttcher et al., 2018). Besides the hydro-geochemical measurements of dissolved substances, the patterns of Ra and other isotopes in surface waters are particularly helpful for identification and quantification of the benthic-pelagic coupling and source water contributions, respectively (e.g., Moore et al., 2011; Böttcher et al., 2014). Specifically, the pelagic presence of the short-lived ^{224}Ra isotope, which is derived from thorium decay in the sediment, indicates a recent contribution of pore waters to the water column.

Submarine groundwater discharge as a pathway for the exchange of water and associated substances has been observed along the German coastline in tidal areas like the North Sea (e.g., Moore et al., 2011; Jeandel, 2016; Reckhardt et al., 2017) and non-tidal systems like the Baltic Sea (Piekarek-Jankowska, 1996; Massel, 2001; Peltonen, 2002; Kotwicki et al., 2014; Donis et al., 2017; Böttcher et al., 2018). Biological consequences of SGD have likewise been documented (e.g., Liu et al., 2017). Most significantly, the contribution of SGD to total input loads from the land into the sea has been considered as more important than that of riverine freshwater (Kwon et al., 2014). It remains challenging to prove the occurrence of SGD at low-lying coastal segments with small hydraulic gradients. In low-gradient systems, the geological substrate and the heterogeneity of hydraulic properties of individual sedimentary layers are crucial for the establishment of local groundwater fluxes.

The hydraulic properties of the marine sediments impact the near-ground circulation and thus solute dispersion in the shallow sea water. Furthermore, the sedimentary structures, such as ripple fields, have a direct influence on the turbulence dynamics and thereby on velocity and solute concentration profiles (Smyth et al., 2002). The hydraulic properties of marine sediments are considered highly changeable because of bioturbation. The connection between groundwater exfiltration, pore water transport, and near-ground circulation of solute spreading at the sediment–water interface remains as yet poorly described. Wave action and hydrodynamic processes at the water-sediment interface cause pore water fluxes in and out of the sediment (Massel, 2001), bringing oxygen as well as organic material into deeper sediment layers, thereby modifying redox gradients and, consequently, affecting biogeochemical processes like denitrification and/or iron, manganese and sulfate reduction (Huettel et al., 1998, 2003; de Beer et al., 2005; Gao et al., 2012).

Coastal marine sediments are often characterized by coarser grains (sand and gravel), and are commonly less sorted than sediments in deeper waters (Forster et al., 2003). Sediments are often resuspended and transported along the shore; consequently, they are permeable and the upper sediment layers in coastal zones are physically unstable and very mobile habitats. Benthic-pelagic coupling in shallow water is close, and coupling becomes stronger with increasingly shallow waters. The primary production rates are typically high and occur predominantly in the pelagic zone (Schiewer and Schubert, 2004). However, benthic primary production has rarely been considered in these systems despite the micro-phytobenthos and benthic macrophytes being responsible for most of the primary production in shallow lagoons. It has been shown that seagrass and macroalgae production can exceed 100 g C m^{-2} a^{-1} (Gocke et al., 2012). Additionally, benthic diatoms may contribute up to 60 g C m^{-2} a^{-1} to primary production in the temperate climate of the northern hemisphere (Cahoon, 1999). For the southern Baltic Sea, even higher values have been measured, ranging from 75 to >100 g C m^{-2} a^{-1} (Meyercordt and Meyer-Reil, 1999). In the case of the southern Baltic Sea coast with its abundant coastal peatlands, the fluxes across the sediment water interface might be modified hydrodynamically by the presence of outcropping peat layers in the water, which may also serve as a source of carbon and nutrients to the shallow sea. These outcrops are the result of the receding shoreline over the past several thousand years because of sea-level rise (Harff et al., 2017).

BALTIC TRANSCOAST APPROACH

The coastline appears to divide terrestrial from marine ecosystems, yet in reality it forms a unique sea–land transition zone due to the exchange processes between environmental compartments create a unique sea–land transition zone. Baltic TRANSCOAST aims to quantify the extent to which the sea influences terrestrial processes and assess how the shallow sea is affected by processes operating on land, thereby unraveling the system function of shallow coasts at low-lying land areas (**Figure 2**). We suggest a systematic and interdisciplinary research approach that considers the coast as a continuum of physical and biogeochemical processes that on the one hand influence marine and terrestrial biota, and on the other hand are impacted by this biota.

The research in Baltic TRANSCOAST addresses the following main hypotheses:

(i) There is an exchange of water and matter between land and sea in both directions, on varying spatial and temporal scales at shallow coasts.
(ii) Both on land and in the sea, exchange processes influence the biogeochemical processes either directly or by impacting the biota.
(iii) The volume flux of water originating from the terrestrial side (SGD) in the shallow sea may be a low but possibly constant source of nutrients and complex organic molecules.
(iv) The impact of sea-borne water on the terrestrial side is expected to be episodic but with long lasting consequences for biogeochemical cycling.

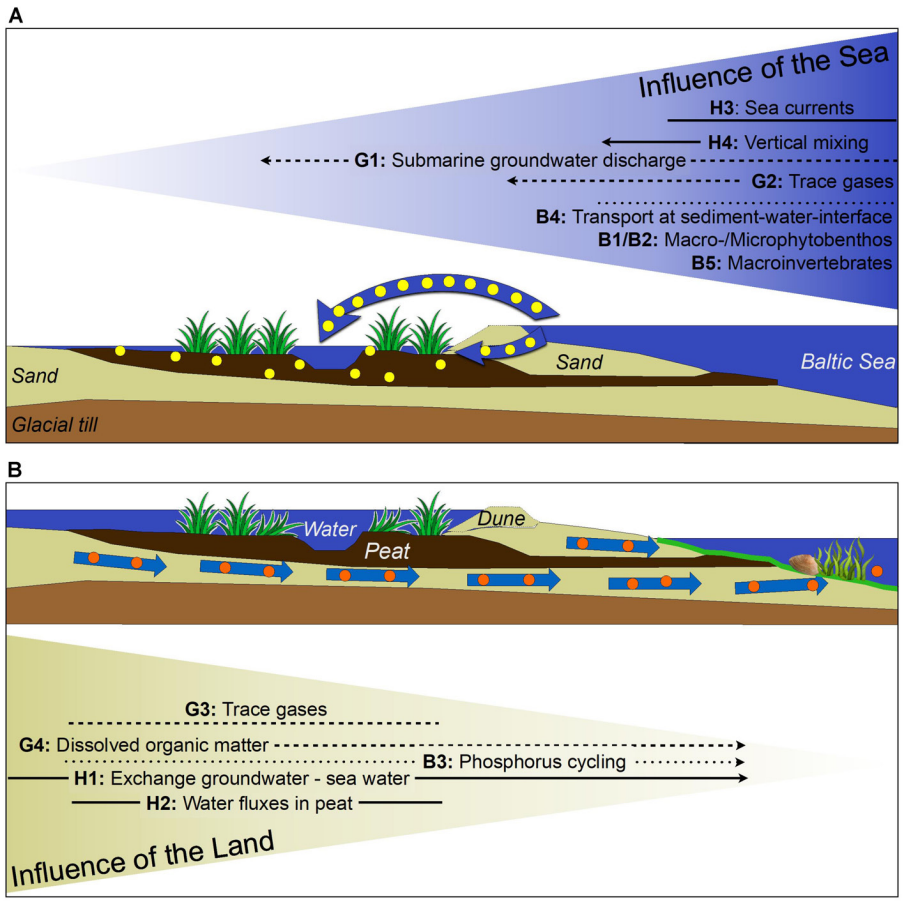


FIGURE 2 | Baltic TRANSCOAST scheme showing the spatial coverage of the different research topics (— H — hydro-physical, --- G --- biogeochemical, ···· B ···· biological) and the prevailing water and substance exchange pathways across the coast line at two different possible states: **(A)** During storm surge events brackish seawater flows into the coastal peatland (above surface and through the sediment); **(B)** When the groundwater and surface water levels at the land side are high during winter, submarine groundwater discharge (SGD) may export nutrients and dissolved organic matter (DOM) to the shallow sea (not to scale). The spread of the lines indicate the spatial coverage of the respective topic across the coastal ecocline. Arrowheads indicate that those topics have a specific focus on exchange in the direction of the arrow. Non-arrowed topics consider two-way exchange processes instead.

The research designed to test these hypotheses is arranged around three core thematic areas, i.e., hydro-physics, biogeochemistry, and biology with topics anchored in one of the thematic areas but extending into other areas (see **Figure 2**).

Hydrophysics

In non-tidal systems, the water exchange between the sea and land is driven by vertical and horizontal exchange flows generated by wind, waves, and lateral density gradients (**Figure 2**). The hydraulic properties of the prevailing strata as well as exchange processes between porous media and the above lying water column are likewise influencing the linkage between the terrestrial and the marine compartment of the ecosystem. The hydro-physics thematic area in Baltic TRANSCOAST comprises oceanographic (sea side) and groundwater (land side) modeling as well as their coupling via water levels near the shoreline. The underlying hypothesis is that water fluxes between the land and the sea are substantial even at low lying coastal areas because of changing sea levels and variations in precipitation. These water fluxes are assumed to be enhanced locally, when the heterogeneity of the underground causes a concentration of flow pathways at specific locations.

Sea level dynamics are wind-driven in non-tidal systems and modeled in Baltic TRANSCOAST by interactively coupling a General Estuarine Transport Model (GETM) with a wind wave model (Moghimi et al., 2013). Near-shore hydrodynamics are determined by wind-driven transport and the plume of the adjacent Warnow River. The groundwater dynamics are represented using the MODFLOW code and measured groundwater levels along a land–sea transect. Compared to mineral substrates, organic soils forming the peatlands are often characterized by low bulk density, high porosity, and a non-rigid organic matrix. Hydraulic and solute transport properties are highly dependent on soil structure, and thus can change upon mechanical, hydraulic, and geochemical impacts (Rezanezhad et al., 2016). Hydraulic properties of the various substrates are either tested *in situ* or measured in the lab under varying salt

concentrations. Hydrodynamic measurements and modeling are supported by geochemical stable (^{2}H, ^{18}O), non-stable isotope (Ra, ^{3}H), and noble gas (He, Ne, Rn) analyses aimed at identifying flow pathways, benthic-pelagic coupling, SGD, and groundwater residence times.

Biogeochemistry

Peat-dominated wetlands are typically water saturated and, therefore, have low redox potentials. Consequently, they have unique nutrient and carbon cycling patterns that may also alter the processes of surrounding soils and sediments. In coastal areas, the biogeochemistry of peatlands is likely altered when seawater intrudes into the peat body. For example, carbon release and/or sequestration rates may shift and/or additional sulfate may become available for alternative metabolic processes (e.g., during storm surges or via saltwater intrusion). Under the impact of SGD, biogeochemical processes, including greenhouse gas (GHG) emissions in the shallow sea, may differ substantially from non-impacted sites because of differing supplies of electron donors and acceptors (e.g., Böttcher et al., 2018). The availability and transformation of dissolved sulfate is particularly important for carbon and nutrient (e.g., nitrogen and iron) cycling. In Baltic TRANSCOAST, we investigate the pathways of carbon, nitrogen, phosphorus, and sulfate across the land-ocean interface to foster our understanding of the complex interactions of salinity, substrate availability, water and element exchange, and geochemical signal formation in soils and sediments.

We hypothesize that the occasional flooding of the peat body with brackish sea water modifies the degradation of the peat substrate and the release of DOM from the peat, with possible consequences for the reactive transport of different forms of carbon, nitrogen and phosphorus, dissolved inorganic carbon (DIC), and metals to the shallow coastal waters. The exchange of compounds between the Baltic Sea and the peatland (and vice versa) will affect microbial processes and the offshore generation and emission of trace gasses since electron acceptors and donors are transferred between the compartments (e.g., dissolved sulfate enters the peatland). Pore waters and sedimentary substrates are therefore analyzed on transects along the land–sea interface to investigate vertical profiles of concentrations and stable isotope compositions of various dissolved, solid, and gaseous compounds, as well as to characterize the underlying biogeochemical processes and the impact of microbial activities. In addition, the composition of surface waters in the peatland as well as in the shallow Baltic Sea allows for an estimate of the exchange of water and substances between the sediments/soils and the overlying water column (i.e., 'benthic-pelagic coupling').

Biology

The hydro-physical and biogeochemical conditions in the shallow coastal sea create specific environments for the biota. Salinity variations caused by freshwater input into the shallow coastal waters may impact the physiological performance, viability, biodiversity, and distribution of microbes, micro- and macroalgae, as well as zoobenthos including bioturbators such as polychaetes and/or bivalves. The input of recirculated seawater and freshwater and the nutrients therein can generate nutrient-enriched conditions in the vicinity of SGD, creating hot spots of biological productivity and shaping the local benthic communities as observed in, e.g., estuaries (Encarnação et al., 2013; Leitão et al., 2015). Changes in the activity or abundance of zoobenthos may in turn affect the sediments via feedback mechanisms such as shifts in hydraulic properties of the seabed because of a modified bioturbation activity. These processes and reactions are only poorly understood up to date and are, thus, given priority in the investigation in Baltic TRANSCOAST in the biological thematic area.

Submarine groundwater discharge and unique seabed properties (e.g., peat out-cropping) may affect the micro- and macro-phytobenthos communities. Frequent resuspension events will likely modify the benthic communities, the oxygen consumption in sediments, and the (re)growth of flora and fauna. We hypothesize that these disturbances may change the community composition of micro- and macrobenthos and influence rates of primary production by nutrient inputs from SGD and/or terrestrial runoff. In addition, benthic diatoms typically exhibit a high heterotrophic potential, and hence might benefit from DOM derived from terrestrial sources. Furthermore, direct impacts of salinity fluctuations on biota are one of the most intriguing aspects of this study. Even small changes in salinity are probably crucial for species composition in the shallow waters at the study site, with opposite effects on benthic and pelagic communities (for review see Telesh et al., 2013). Furthermore, salinity fluctuations can affect secondary productivity and energy fluxes in macrozoobenthic communities through the effects on energetic processes, oxygen consumption, and growth and bioturbation activities of key macrozoobenthos species. We test the hypotheses by determining the effects of salinity fluctuations on bioenergetics of common bioturbators (i.e., sediment-dwelling bivalves). We assess the tolerance thresholds beyond which the physiological impacts of salinity translate into reduced activity, growth and/or survival, thereby affecting the key ecological functions of bioturbation and bioirrigation. The physiological data are upscaled to community-level effects by developing physiologically realistic models of bioturbators' contributions to oxygen, nutrient, and water fluxes, as well as to the sediment reworking. The models consider the effects of environmental factors (such as temperature, salinity, or sediment characteristics) and biological traits (such as body size and/or bioenergetics status) of the bivalves.

STUDY SITE AND INSTRUMENTATION

Terrestrial Side: Low-Lying Land With Coastal Peatland

Baltic TRANSCOAST focuses on a common investigation site, the nature reserve 'Heiligensee und Hütelmoor' (in brief and in the following 'Hütelmoor'). It is located on the southern Baltic Sea coast in northeastern Germany, near the city of Rostock and the estuary of the river Warnow. The reserve stretches over an area of 540 ha with 315 ha covered by peatland. A local depression shaped by a former glacial stream (Kolp, 1957) served as basis for the development of a fen peatland that formed when the rising

sea level of the Baltic Sea caused rising groundwater levels on the landside. The climate is temperate in the transition zone between maritime and continental with an average annual temperature of 9.1°C and an average annual precipitation of 645 mm (data derived from grid product of the German Weather Service, reference climate period: 1981–2010). The evapotranspiration amounts to 620 mm in open water and 581 mm a^{-1} in reed areas (Miegel et al., 2016).

The peatland type in this site can be classified as a coastal paludification fen, and the largest portion of the peatland is covered by 1–3 m thick layers of sedge and reed peat. Due to its low elevation (−0.1 to + 0.7 m HN), the site was influenced by intermittent flooding events, resulting in the formation of thin sand layers within the peat in some areas. In the surroundings of the Heiligensee, organic or mineral lake sediments are found at the basis of the peat. Underneath the peat, 3–10 m thick basin sands form an aquifer underlain by glacial till. The peatland is surrounded by forest on mineral soils. At the eastern boundary, the peat stretches up to 100 m into the forest featuring Alder carr.

As most peatlands in northern Germany, the Hütelmoor has been artificially drained. The main ditch was installed in the 18th century and mainly served for transporting wood from the surrounding forests to the harbor (Kolp, 1957). The ditch was connected to the lower reach of the river Warnow. Originally, the area had discharged directly into the Baltic Sea via a small brook cutting through the dunes; this connection was later blocked. In accordance with intensifying agricultural production in central Europe (van Diggelen et al., 2006), large parts of the wetland complex were intensively drained in the 1970s by open ditches and then used as grassland for fodder production (i.e., mown twice a year). As a result, the mean annual water level dropped to 1.60 m below ground surface.

In the 1990s, the study site was moderately rewetted and grasses were cut once a year to keep the vegetation open. Extensive mowing supported the aims of nature conservation to preserve a resting site for migratory birds while allowing the restoration of the typical fen vegetation. The mean growing season water level during that time was close to the surface (Koebsch et al., 2013). However, water levels dropped down to 70 cm below the surface during summers, which raised concerns about ongoing aerobic peat decomposition. Therefore, a ground sill was installed in the outflow of the catchment in winter 2009/2010 which initiated a year-round shallow flooding for most areas of the study site (mean growing season water level 37 cm, values indicate flooding). The discharge from the peatland averages 44 L s^{-1}, but stops during summer months when the water level drops below the ground sill (Miegel et al., 2016). Rewetting projects are common for much of the Baltic Sea coast where nature conservation has been given priority.

Currently, the vegetation is dominated by emergent macrophytes such as Common Reed [*Phragmites australis* (Cav.) Trin.]. Especially in the second part of the vegetation period submerged aquatic species like Soft Hornwort (*Ceratophyllum submersum* L.) dominate the relatively abundant areas of open shallow water. The typical brackish water emergent macrophyte Sea Clubrush (*Bolboschoenus maritimus* L.) was almost completely displaced, whereas another brackish water species, the Softstem Bulrush [*Schoenoplectus tabernaemontani* (C.C.Gmel.) Palla], was able to increase its cover considerably in the last decade (Koch et al., 2017). Dryer areas at the boundaries to the forest are mainly colonized by the Lesser Pond Sedge (*Carex acutiformis* Ehrh.) and the Common Rush (*Juncus effusus* L.).

Drainage and agricultural use led to aeration and mineralization of the peat resulting in a highly degraded top horizon. The soil type was identified as sapric histosol before rewetting. The remaining peat body is moderately to strongly decomposed with substantial heterogeneity of physical and chemical properties. Rewetting measures and permanently high water levels (above peat surface) have led to the sealing of the soil surface because of sedimentation of fine particles. The former soil surface now resembles a lake bottom surface, with the possible formation of a gyttja (a characteristic layer composed of either organic or mineral material that can be typically found beneath fen peats, which is considered as the initiation stage of fen peat formation). The ongoing sealing process at the soil surface limits the vertical infiltration, thus, possibly changing the hydraulic functioning of the entire wetland.

A dune dyke was installed at the coastline of the fen in 1903 for coastal protection of the nearby seaside resort Markgrafenheide and was reinforced in 1963 (Miegel et al., 2016). Already before 1903 there was a natural sand dune providing a barrier between the Baltic Sea and the Hütelmoor. Due to the artificial dune dyke the peatland has been almost completely cut off from the Baltic Sea. The last notable intrusion of brackish water occurred during a storm night in November 1995 (Bohne and Bohne, 2008). Afterwards, the dune dyke was rebuilt and strengthened. It is, however, not maintained anymore since the year 2000. It is anticipated that the natural impact of the sea including episodic flooding will re-establish in the near future likely resulting in repeated input of brackish waters (on decadal time scales) with possible consequences for hydro-physical and biogeochemical processes. A recent storm flood event in January 2017, which washed away considerable parts of the dune dyke at places where it was more than 20 m wide, failed to flood the study site.

Marine Side: Shallow Coast of the Baltic Sea

A mosaic pattern of eroding cliffs and sand deposition areas are dominant along the western part of the Baltic Sea coast in northeastern Germany. Due to coastal erosion and isostatic sea level rise the coastline has shifted landwards at the study site exposing former land-based geological strata to the sea. The peat that once developed on land now extends to the sea, forming a unique habitat for micro- and macro-phytobenthos. Most of the coastal area between 0 and 10 m depth is covered by coarse-grained sediments with gravel and cobbles dominating at some sites. In the northern area of the study site, gravel and coarse sands are abundant on the sea bottom surface whereas in the south fine and medium sands dominate (for details and a map, see Kreuzburg et al., 2018). This is typical for sea floor near the coast because coastal waves and prevailing south-westerly winds generate longshore currents, displacing the small particles and

transporting them along the coast and toward greater depths. A few tens of meters away from the shoreline an underwater longshore bar has developed. This seems to be typical for the southern German Baltic coastline where no fine-grained sediments can be found (Tauber, 2012).

Roughly 10 km west from the study area, the Warnow estuary enters the Baltic Sea. The Warnow river basin is approximately 3,000 km^2 in size with elevation differences of less than 100 m as is typical for lowland catchments mainly used for agriculture (Bahnwart et al., 1998; Deutsch et al., 2006). The river mouth is located 15 km landwards where a weir prevents sea water to travel further upstream. A gauging station is located at the weir and discharge is continuously recorded. The mean outflow rate is 16.5 m^3 s^{-1} with a mean nitrate concentration of 1.78 mg N L^{-1} (or 127 μmol L^{-1})[1]. A small surface plume extends a few kilometers west – and northwards along the estuary while the salinity increases to the typical brackish values of 10–15 PSU. During the passage, inorganic nutrients are entirely consumed or mixed so that only recalcitrant substances like dissolved organic material of the plume are able to reach the study site off the Hütelmoor.

Instrumentation and Field Data Acquisition

The investigations in Baltic TRANSCOAST are carried out on a well-developed research site, the study site Hütelmoor. Some analyses within the project are based on data recorded before the project started in 2016. The investigations on the landside in the peatland have already started in 2008 with closed chamber measurements and the installation of dip wells. In 2009 an eddy covariance tower measuring CO_2 exchange was set up, which was equipped with a methane sensor in 2011 and is running continuously ever since.

In the course of Baltic TRANSCOAST, the study site has been instrumented both on land and in the sea (**Figure 3**). The investigations started in 2016 and are ongoing. The now used locations for chamber measurements are arranged in clusters around the Eddy tower (**Figure 3**) with replicates in different vegetation types including, e.g., stands of Common Reed and Common Sedge as well as areas with open water and are equipped with boardwalks and dip wells. In each cluster a peeper is installed that allows for regular sampling of pore and surface water at defined depths. GHG chamber measurements and water sampling are carried out monthly. The chambers are custom developed and flexible which allows for measuring vegetation up to 2m height while still allowing for efficient application in the field (Günther et al., 2014). During the campaigns GHG exchange (CH_4 and CO_2) is measured with either a Los Gatos Ultraportable GHG Analyzer or a Picarro GasScouter.

Groundwater monitoring wells were installed in transects across the peatland in 2016 (**Figure 3**). Each measuring point consists of up to three wells filtered in different depths (upper sand, peat, lower sand). All wells are equipped with self-registering pressure-temperature-salinity probes and are regularly sampled. The geology of the study site was assessed with 17 drillings, mostly down to the glacial till, and numerous additional peat probings. Undisturbed peat cores (250–450 cmł) for analyses of hydraulic conductivity and dissolved organic carbon (DOC) leaching in the lab were taken both in the peatland and in the peat layer cropping out into the Baltic Sea.

On the marine side, two 4.5 m long stationary pore water lances (set-up modified after Beck et al., 2007) have been installed in the sediments in front of the Hütelmoor, as well as data loggers for salinity, irradiance, and temperature in the surface water close to the groins. Pore waters are retrieved from discrete depth intervals from the stationary pore water lances (Beck et al., 2007) as well as from further stations with mobile lances on a roughly monthly basis.

At greater distance to the shore line on the marine side, sampling took place via small boats. These were equipped with temperature and conductivity sensors, sampling devices for the collection of water and sediments, and further acoustic systems. Biweekly to monthly boat-based excursions have been performed to record temperature/salinity profiles, collect water from the surface and above the sea bottom, and to retrieve sediment samples from a grid of stations (**Figure 3**). Macrophytobenthos assessment was done by Scuba-diving along transects, as described in Schubert et al. (2011). For species determination of the macrophytobenthos the key used is described elsewhere (Schubert et al., 2011), and synonymies and nomenclature follow Schories et al. (2014).

Details on sample preparation, lab analytical procedures and lab experiments are given in the results section with the respective results.

FIRST RESULTS

Our overarching hypotheses are that there is exchange of water between land and sea across the shoreline along shallow coasts at low-lying areas, that the overground and underground pathways of these exchange processes may act on different time scales, and that biotic and biogeochemical processes on the respective receiving sides of the exchange are altered. In this section we briefly describe some results of our investigations and link them to the hypotheses.

Water Fluxes and Solute Transport

Frequency of Flood Events

Recent studies report a projected increase in storm surge levels in the Baltic Sea under different regional climate scenarios (e.g., Gräwe and Burchard, 2012; Weisse et al., 2014; Soomere and Pindsoo, 2016). According to a European wide modeling study (Vousdoukas et al., 2016), the Baltic Sea shows some of the highest increases in projected extreme storm surge levels in Europe, including increased storm surge activity during all the seasons of the year, but especially during spring and summer. We analyzed how sea levels above certain thresholds relative to mean sea level have changed over the past 60 years (**Figure 4**) and found that the number of hours per year exceeding thresholds of 0.5, 0.75, and 1.00 m above mean sea level have increased. So

[1] lung.mv-regierung.de

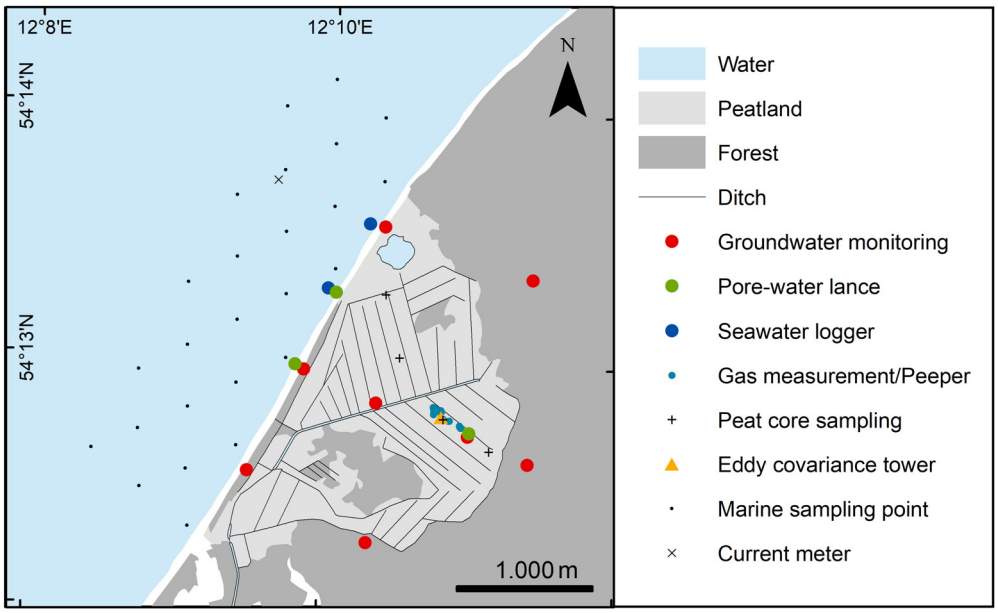


FIGURE 3 | Map of study site 'NSG Heiligensee und Hütelmoor' with instrumentation.

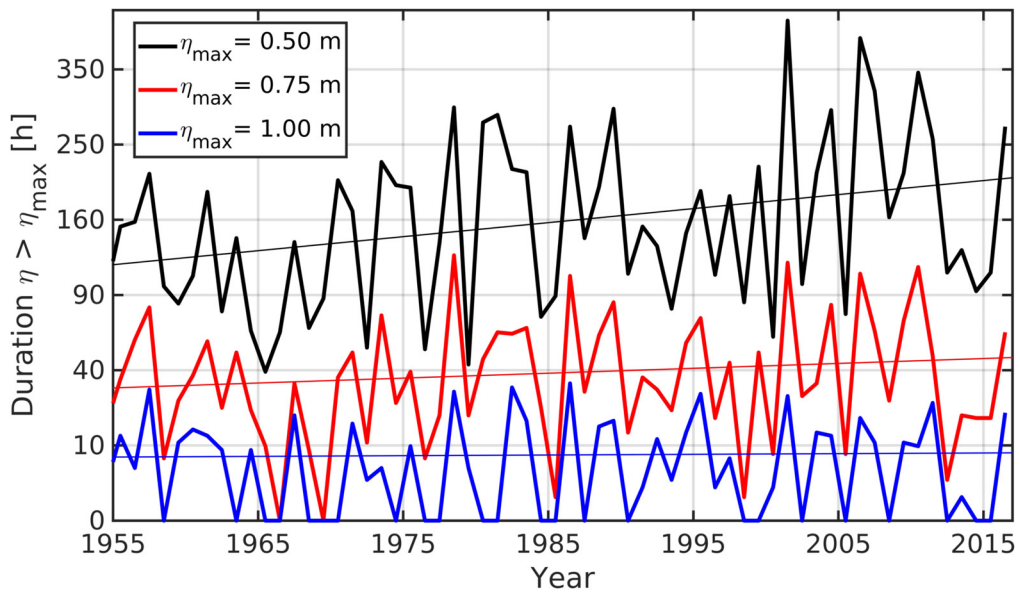


FIGURE 4 | Number of hours per year exceeding a certain mean sea level. The trend for the 0.5 m threshold above m.s.l. is significant (Southern Baltic Sea Coast). The time series of sea surface elevations were taken from the gauge at Warnemünde and were provide by the Federal Maritime and Hydrographic Agency of Germany.

far, only the trend for the 0.5 m above sea level is significant. These results suggest, that the risk for salt water intrusion (both by flooding and via the subterranean pathway) into shallow coastal areas at the southern Baltic Sea is increasing because time periods with positive hydraulic gradients from sea to land are expanding, leading to more frequent and further inland reaching salt water intrusions by underground wedges, as well as to increased risk for flooding by storm surges. Thus, an increase of land–sea interactions is to be expected for the future which is of importance to all of our main hypotheses.

Warnow River Plume

The discharge of the Warnow-river follows an annual cycle with maximum values of between 50–60 m^3 s^{-1} in February and lowest values of <5 m^3 s^{-1} in mid-summer (**Figure 5**). To realistically simulate the hydrodynamic conditions in the

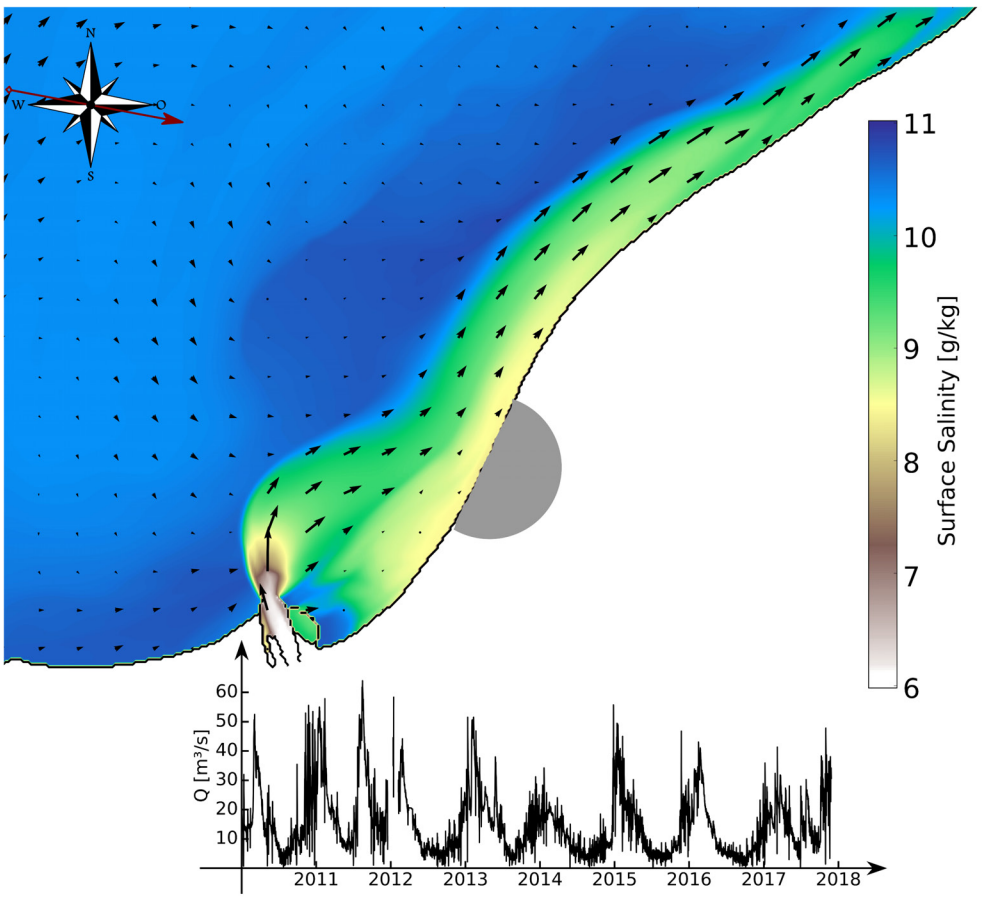


FIGURE 5 | Snapshot of simulated surface salinity outside the mouth of the Warnow estuary under westerly wind forcing. Inset: Time series of observed freshwater runoff from the river Warnow during the years 2011–2017, data provided by the Office for Agriculture and Environment Mittleres Mecklenburg.

Warnow Estuary and the adjacent coastal region including the interaction with the Baltic Sea, a nested model approach using the GETM (Burchard and Bolding, 2002) has been applied. This coastal ocean model is based on the three-dimensional hydrostatic momentum equations and transport equations for temperature, salinity, and passive marker tracers to track water masses. Due to the important role of turbulent mixing for the coastal zone, a two-equation turbulence closure model is used (Umlauf and Burchard, 2005). The model is driven by atmospheric forcing from the German Weather Service Model and lateral boundary conditions from larger-scale GETM model simulations of the entire Baltic Sea (Gräwe et al., 2015; Burchard et al., 2018), with lateral grid resolutions of about 2 km. Multiple one-way nesting is used to downscale these simulations to a lateral grid size of 20 m in the Warnow Estuary and the adjacent coast. Modeling results show that estuarine circulation causes a net inflow near the bed and an outflow near the surface of the Warnow estuary, amplifying the river discharge at the mouth by a factor of ten. According to the classification of Geyer and MacCready (2014), the almost non-tidal Warnow estuary is strongly stratified, due to its relatively low discharge and mixing. Similar to the Chesapeake Bay (Scully, 2010), which falls into the same category, its stratification is, however, strongly depending on wind forcing. Our analyses show that the estuarine discharge of the Warnow can form a river plume depending on the effects of mixing in the estuary and the strength of estuarine circulation. Plume formation is prevented when the estuarine circulation is inverted due to up-estuary wind or an inversion of the salinity gradient of Warnow river and coastal water. When leaving the estuary, the river water is deflected to the east due to earth rotation, forming a coastal current passing the Hütelmoor, as shown in **Figure 5**. This is amplified by the mainly westerly wind and may influence the measured water chemistry in front of the Hütelmoor. When assessing exchange processes between land and sea following the Baltic TRANSCOAST hypotheses, this is an important contribution that has to be acknowledged.

Hydraulic Gradients Between Land and Sea

Based on preliminary groundwater gauging data and average sea levels, a retrospective schematic of prevailing land-to-sea gradients has been developed (**Figure 6**). It is assumed that prior to human activities, water exchange processes were limited to events with either high groundwater or high sea water levels. The systematic drainage of the area resulted in negative gradients

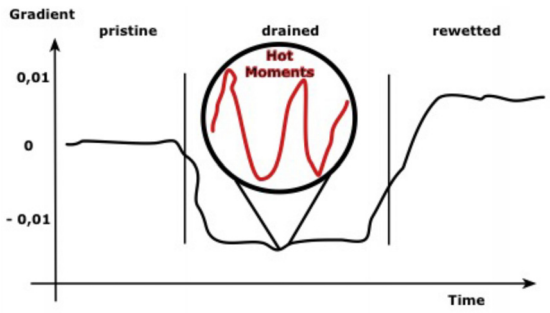


FIGURE 6 | Schematic of average land-to-sea gradients in coastal peatlands under different water management scenarios. Irrespective of the general situation, extreme events may cause higher gradients than expected.

with a possible inland migration of a subsurface salt wedge. Rewetting of the peat to levels above ground resulted in average gradients in the positive range and, although gradients are still low, freshwater SGD can be traced, at least locally. Peat shrinkage results in a soil profile that is dominated by highly degraded upper horizons, while the peat is less decomposed (lower bulk density, higher porosity) at lower depths. In the Hütelmoor, we found significant peat degradation also up to 1 m depths and below, which is possibly attributed to natural processes operational during the development of the peat. Irrespective of the general situation of the gradient, significantly higher and lower gradients than expected may occur over short periods of time. These "hot moments" are more likely to occur in the future because of a shift of the precipitation patterns toward higher winter precipitation and storm events during summer.

Seawater Intrusion

Input of seawater to the peatland can be traced by the salinity of the groundwater. While the fresh groundwater originating from the peatland's forested catchment has a salinity of about 0.3, the salinity in the Baltic Sea in the study site ranges from 8 to 18 PSU. Recent measurements in groundwater wells across the peatland yielded salinities between 3 and 5 PSU both in the peat and the underlying sand aquifer (**Figure 7A**). During a previous sampling campaign, which focused on the central areas of the study site, salinities of up to 9 PSU were locally measured in the upper peat layers (**Figure 7B**; Koebsch et al., 2013). The values show only small variations with time and demonstrate a substantial impact of seawater on the Hütelmoor hydrology and biogeochemistry, as suggested in our first and fourth hypothesis (page 4). Less pronounced seasonal oscillations are presumably due to evaporation and dilution processes. Observations at groundwater wells behind the dune dyke show that storm events with high seawater levels cause subsurface saltwater intrusions into the sands behind the dune dyke, detectable as sudden increases in salinity with subsequent gradual decrease. However, these small seawater intrusions were only observed where the dune is most narrow and could not be detected at 50 m inland of areas with wider dunes. During the decades of drainage, the hydraulic gradients between peatland and Baltic Sea were reversed (**Figure 6**), suggesting a bigger salt wedge and regular intrusions of saline waters into the peatland by surface flooding via the drainage ditches (which are connected to the Baltic Sea via the Warnow estuary) at that time (supported by Bohne and Bohne, 2008, and an unpublished Master thesis from 1995). It is assumed that the high salinities found further inland in the peatland today are still a relic of former floodings. Peat pore water depth profiles along a transect from the coastline to the forest show that at all four coring locations, except the one closest to the forest, electrical conductivity was increasing with depth, and Selle et al. (2016) describe that salinity in the peat is decreasing slowly since the last flooding in 1995. Dating of the groundwater in the sand aquifer using the $^{3}H/^{3}He$ method showed that a large part of the water infiltrated before 1950. Only near to the southeastern boundary of the peatland close to the forest, groundwater originated from the year of rewetting (2009). These observations suggest a strong legacy effect of flooding with seawater in the peatland, supporting the hypothesis that the impact of sea water on the terrestrial side is expected to have long lasting consequences for biogeochemical cycling on the land side.

Combined concentration and stable isotope analysis (C, S) indicates an intense exchange of water and or substances between

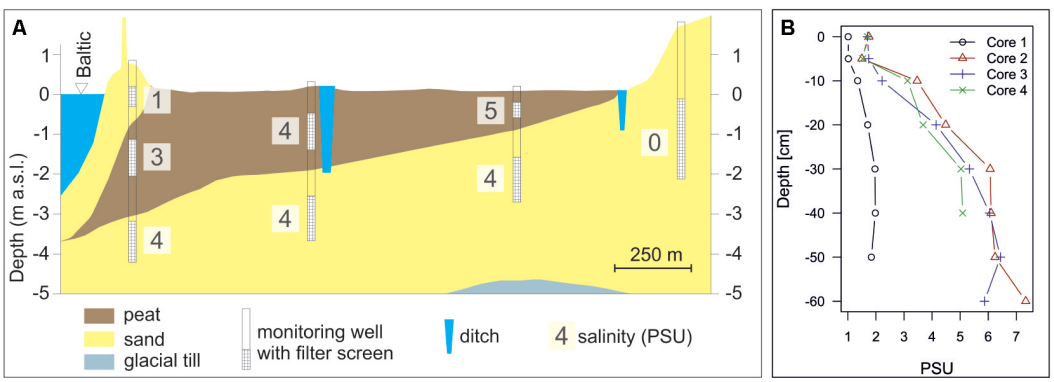


FIGURE 7 | (A) Geological profile through the peatland with salinity distribution (PSU); **(B)** Depth distribution of salinity derived from pore water sampling along a transect from the forest (Core 1) to close behind the dune dyke (Core 4) (see **Figure 3**). All cores but the one near the forest edge show increasing salinities with depth within the peat.

the soil pore water and the drainage ditches, which can also be seen in the field by enhanced concentrations of metabolites and redox-sensitive metals in surface waters. DIC was enriched in the light carbon isotope compared to Baltic seawater and dissolved sulfate that was already isotopically modified by net microbial sulfate reduction – processes that only take place within the anoxic parts of the soils. Thus, when assessing the intensity of exchange between land and sea at shallow coasts, the influence of man-made structures like ditches has to be considered since the signal on the land side will likely be the result of both exchange processes across the shoreline, and through canals and ditches, which are widespread structures on shallow coasts.

Hydraulic Conductivity of Peat

Fen peatlands and wetlands in general are transitional habitats with associated unique processes occurring between land-based mineral soils and water bodies such as rivers and oceans. However, their buffer function for water and compound fluxes depends on forcing gradients and material properties. With regards to the latter, the saturated hydraulic conductivity (Ks) is of mayor importance, especially in rewetted systems where high water tables prevail. It has been suggested that the geochemistry of pore water may influence the hydraulic properties of non-rigid organic soils. We tested the sensitivity of Ks upon shifts in salinity on peat samples in different stages of degradation (Gosch et al., 2018). The hydraulic conductivity of the undisturbed peat samples was measured with the constant head method, using water with different electrical conductivities ranging from 1 to 55 mS cm^{-1}. For details, see Gosch et al. (2018). The DOC content was measured with a DIMATOC® 2000 analyzer. Our results suggest that salinisation has only minor and non-directional impact on Ks, no matter how strongly we increased the salinity of the water. Our results showed a decrease of Ks with time, which did not depend on the water salinity but was differently shaped for different peat types (*ibid.*). Interestingly, these findings do not confirm earlier studies in which Ks was found to increase with increasing salinity (Ours et al., 1997). These studies were, however, conducted on bog peat samples whereas we have analyzed fen peat. Although systematic comparisons are missing, it is likely that Ks differs systematically between bog and fen peat since the pore structure of the peats differ strongly.

The hydraulic conductivity, as measured in percolation experiments, is to a certain extent an integrative signal of the soil pore structure (Rezanezhad et al., 2010, 2016). It can, thus, be concluded from the given results that varying salinity conditions do not necessarily modify the pore structure of peat soils as had been hypothesized. This research needs to be continued explicitly addressing pore structure employing imaging methods. A comparative computer tomography analysis on samples from the main peat body and from peat layers outcropping in the sea (continuous seawater impact) may be a promising way to study the effect of sea water on peat structure.

The Sediment–Water Interface

At the marine side of the Baltic TRANSCOAST site, approximately 80% of the area are covered by permeable sands ($k \geq 10^{-11}$ m s^{-1}; falling head permeameter). In this sandy environment, hydrodynamic forces mostly related to wave action induce pore water flows when interacting with ripples and similar sedimentary structures. Overlying water is advected into and pore water driven out of the sediment in distinct areas on spatial scales of cm to dm based on ripple dimensions. Ripples change position in response to hydrodynamic forcing. At the coast off Rostock, these changes occur on time scales ranging from minutes to days. From *in situ* experiments using stirred benthic chambers (Huettel and Gust, 1992) we found fluxes of nutrients between pore water and overlying water to increase two- to fourfold when the sediment interface was exposed to pressure gradients mimicking typical hydrodynamic conditions in the overlying water. Adding the temporal dynamics of the interface topography this suggests a highly dynamic environment with respect to salinity, oxygen, sulfide, and pore water nutrient concentrations.

The discharge of groundwater into a benthic boundary layer agitated by wave motion was implemented in a lab experiment in a water tank of 5 m × 0.8 m × 1 m (l × w × h), which was equipped with a piston type wave generator. The main water volume was seeded with 5 μm polyamide particles to observe the motion of the fluid. The groundwater was marked with fluorescent dye and infused through a permeable sea bed made of porous foam over a surface of 0.7 m × 0.6 m (l × w). The flow measurement was performed by a laser optical PIV-LIF (particle image velocimetry – laser induced fluorescence) setup. Two Flowsense cameras (Dantec Dynamics) simultaneously observe an identical field of view of 132 mm × 241 mm parallel to the flow and perpendicular to the permeable ground. The field is illuminated by a YAG laser at a 7.5 Hz double pulse rate. The LIF camera captures the fluorescent light, which is then quantitatively evaluated indicating the concentration in the groundwater. The PIV camera captures the refracted light from the tracer particles in the flow in double frames. From the particle motion the flow velocities were calculated using an adaptive PIV algorithm with a final interrogation are of 32 pixel × 32 pixel. Both measurements were performed over 6,000 frames/double frames to cover 800 s of lab time. From the time resolved flow velocity and concentration fields the concentration boundary layer and turbulent Reynolds stresses and fluxes were calculated. Concerning the boundary conditions, three scenarios were investigated to cover different levels of agitation in the coastal zone. The "calm" scenario used a period of 1.99 s and an orbital velocity of max. 0.05 m s^{-1}, the "average" scenario 2.52 s and 0.1 m s^{-1}, and the "storm" scenario 3.3 s and 0.25 m s^{-1}, respectively.

The transport coefficients derived from the fields of concentration and velocity for these scenarios can then be used in an improved modeling of the flow and transport in the benthic boundary layer under unsteady conditions. For the quantification of the transport, a 75% concentration of tracer dye was defined as the concentration boundary of the discharged groundwater (**Figure 8**). A 75% value was chosen to indicate the concentration boundary as it represents the highest gradient. This boundary was observed during a time period of 15 min. Three scenarios with increasing wave amplitude and orbital velocity were investigated. Our results from these measurements

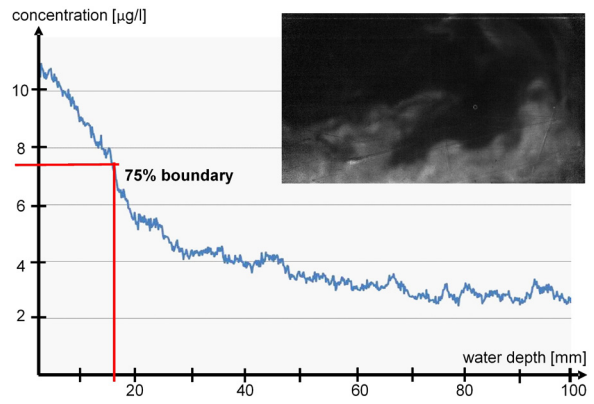


FIGURE 8 | Thickness of the groundwater boundary layer in lab experiment derived from the concentration profile of the laser induced fluorescence (LIF) tracer in the discharged groundwater. The profile was derived from a horizontal averaging of the LIF-tracer concentration maps (example map displayed above).

show that for a planar topography the vertical transport of the discharged groundwater is dominated by the diffusion velocity, whereas the horizontal transport is governed by the wave motion. Thus, with increasing wave motion the initially pure vertical transport is substituted by a horizontal efflux of the discharged groundwater. Further analysis will allow derivation of model equations of the distribution of discharged groundwater in the benthic boundary layer with respect to the wave motion and the surface topography. These experimentally validated model equations for the turbulent transport can then be used as improved boundary conditions for the numerical simulation of the distribution process on the entire coast bringing us closer to a better understanding of exchange processes on shallow coasts.

Benthic-Pelagic Exchange of Water and Substances

Offshore monitoring campaigns revealed unique patterns of hydrographic parameters in front of the Hütelmoor due to salinity changes likely originating from the influence of freshwater in front of the Hütelmoor (**Figure 9**). To investigate the seasonal and event-driven effects on the transport and biogeochemical transformation processes, vertical pore water profiles were retrieved regularly from water lances. The oxygen isotope composition of the pore water was determined with a Picarro L2140-i Laser-cavity ring-down spectroscopy system (Böttcher et al., 2014), the concentration and stable carbon isotope composition of DIC was determined by IRMS using a Gasbench II coupled to a Thermo Finnigan MAT 253 gas mass spectrometer (Winde et al., 2014; Donis et al., 2017). Dissolved sulfide was measured spectrophotometrically (Specord 40 spectrophotometer) according to Cline (1969). Dissolved phosphate and silica were measured from acidified solutions by ICP-OES (Thermo iCAP 6300 Duo Thermo Fisher Scientific).

A seasonal study of the Ra isotope distribution in surface waters showed high dynamics, and based on the detection of short-living Ra isotopes, a clear indication for fast and intense benthic-pelagic mixing of Ra-enriched pore waters into the water column. Along the shore line hydrochemical and isotopic composition of pore waters down to 5 m below sea floor were investigated regularly (**Figure 10**). The found freshening with depth indicates increasing contributions by less saline water that is also isotopically lighter than the Baltic Sea surface water. In parallel, the pore waters display the typical biogeochemical zonation with an increase in the concentrations of DIC, PO_4, NH_4, and H_2S with depth (data not shown). The carbon isotope signature of DIC indicates the addition of biogenic CO_2 derived from the mineralization of reduced carbon, probably superimposed by carbonate dissolution. Microbial sulfate reduction is the most important anaerobic process in these sediments leading to stable sulfur isotope signatures in dissolved sulfate and sulfide resembling a system in which the gross sulfate reduction is faster than the sulfide re-oxidation or diffusional/advective transport of sulfate from the bottom waters (e.g., Hartmann and Nielsen, 2012). Sulfide re-oxidation is likely limited to processes in the top part of the sediments and limited at depth due to a lack of reactive iron. The exchange of these modified pore waters with the Baltic Sea water column will lead to an SGD component acting as a source of DOM, PO_4, H_4SiO_4, NO_3 (after nitrification of NH_4), protons, and an excess of isotopically light DIC. The investigations of the long pore water profiles indicate dynamics in the pore water system which support the hypothesis that the near shore exchange through the sediment is a constant source of nutrients and complex organic molecules to the coastal sea.

Dissolved Organic Matter (DOM)

The release of DOM from peat layers from both the terrestrial and the marine side varied in leaching experiments. DOM was released in higher concentrations from the terrestrial peat as compared to the outcropping peat layers in the sea. The composition of a typical pore water DOM from peat exposed to saltwater as revealed by pyrolysis-field ionization mass spectrometry (Py-FIMS) – a non-targeted soft ionization MS method (Leinweber et al., 2009) indicated the abundance of 1% carbohydrates, 19% of phenols/lignin monomers, 5% lignin dimers, 10% lipids, 21% alkylaromatics, 0.4% mostly cyclic N-containing compounds, 2% peptides, and 4% free fatty acids (percentages as proportion of total ion intensity in the Py-FI mass spectra). This composition differs from the mean composition of other fen peat DOM samples (Leinweber et al., 2009) in larger proportions of phenols/lignin monomers, and alkylaromatics at the expense of carbohydrates, heterocyclic N-containing compounds and peptides. These differences may reflect an influence of salinity on the DOM sampled because saline waters extracted more phenols and lignin monomers and alkylaromatics than freshwater. This finding has important consequences for a future with a predicted increase in flooding events—i.e., an increase of the sea–land influence – because the remaining peat on the land side may be subject to increased physico-chemical erosion reflecting just one process where episodic sea water influxes entail long-lasting consequences for biogeochemical cycling on the land side.

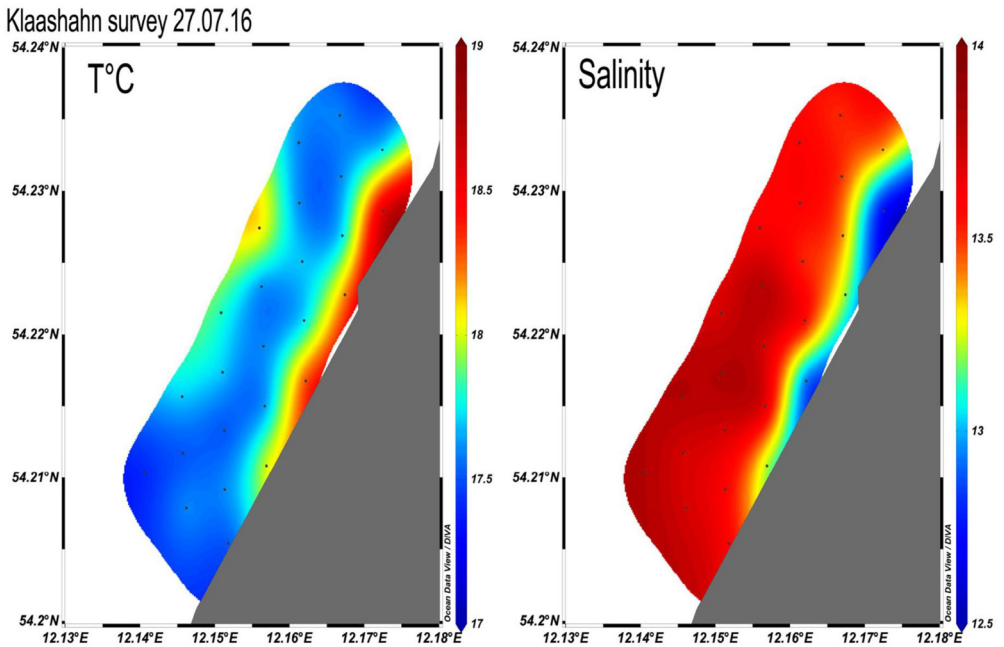


FIGURE 9 | Temperature and salinity (PSU) distribution in front of the experimental coastal peatland (summer 2016).

Greenhouse Gas Emissions

Methane Emissions in the Peatland

Due to its evolution and land management decisions in the past (first drainage, then rewetting), the studied coastal fens biogeochemistry is impacted by both fresh and saline waters. In the past, the fen must have received substantial sulfate loads from episodic flooding with brackish water and the legacies of those floodings can still be found in deeper layers of the peat. Despite the high sulfate loads, which are known to inhibit methanogenesis (Bartlett et al., 1987; Giani et al., 1996) or lead to anaerobic methane oxidation (Boetius et al., 2000), the fen became a methane source after rewetting by flooding with fresh water (Glatzel et al., 2011; Hahn et al., 2015; Koebsch et al., 2015). Our analysis of repeated pore water sampling shows that high sulfate concentrations and high methane concentrations from surface to pore waters are spatially separated (**Figure 11**) suggesting sulfate reduction and methanogenesis to happen in different depth zones and, thus, supporting the hypothesis that episodic flooding with seawater generates strong legacy effects in the biogeochemical cycling on land.

An interdisciplinary analysis of the soil profiles along a transect perpendicular to and with different distances to the shoreline using a combination of stable isotope (H, C, O, S) partitioning, analysis of microbial community structure, and diagenetic pore water modeling enabled us to get a better idea of the prevailing biogeochemical processes (Fernández-Fernández et al., 2017). We found a strong increase in salinity with depth (**Figure 7B**) at all sampling locations likely caused by residual brackish solutions. The pore water composition indicates substantial net sulfate reduction under sulfate-limited conditions at depth which find their expression in the formation of isotopically heavy iron sulfides and incorporation of sulfur into the organic matter (Fernández-Fernández et al., 2017). This zone of intense sulfur cycling is positioned below a freshened soil zone were methanogenesis takes place, which is dominated by acetotrophic Methanosaeta. Anaerobic oxidation of methane is indicated for the transitional zone. A comparison of pore water and solid phase compositional profiles suggests temporal changes of the reaction zones in the past.

We believe that the development of a shallow methanogenesis zone above a zone of intense sulfur cycling may be a specific feature of episodically flooded coastal wetlands, especially when hydrological changes cause freshening of surface waters. Interestingly this layering of a methanogenesis zone above a sulfate reduction zone is reversal of the anaerobic methane oxidation zone, observed in typical marine sediments (e.g., Boetius et al., 2000; Jørgensen and Kasten, 2006). This highlights the need for a more differentiated perspective on coastal ecosystems as commonly neglected methane sources.

Methane Emissions in the Shallow Baltic Sea

The recorded distributions of temperature and salinity in coastal waters reveal a clear impact of distinctly different waters close to shore showing cross-slope gradients with slightly reduced salinities and elevated temperatures after a short period of stagnation (**Figure 9**). To analyze the trace gas distribution at the sediment surface, water was filled bubble-free into crimp vials that were immediately sealed. Bottles with 50 ml volume received 130 µl of a saturated HgCl solution and were stored cool and dark until analysis. Trace gas concentrations were analyzed on a gas chromatograph (Shimadzu GC-2014) with an FID (flame ionization detector) for

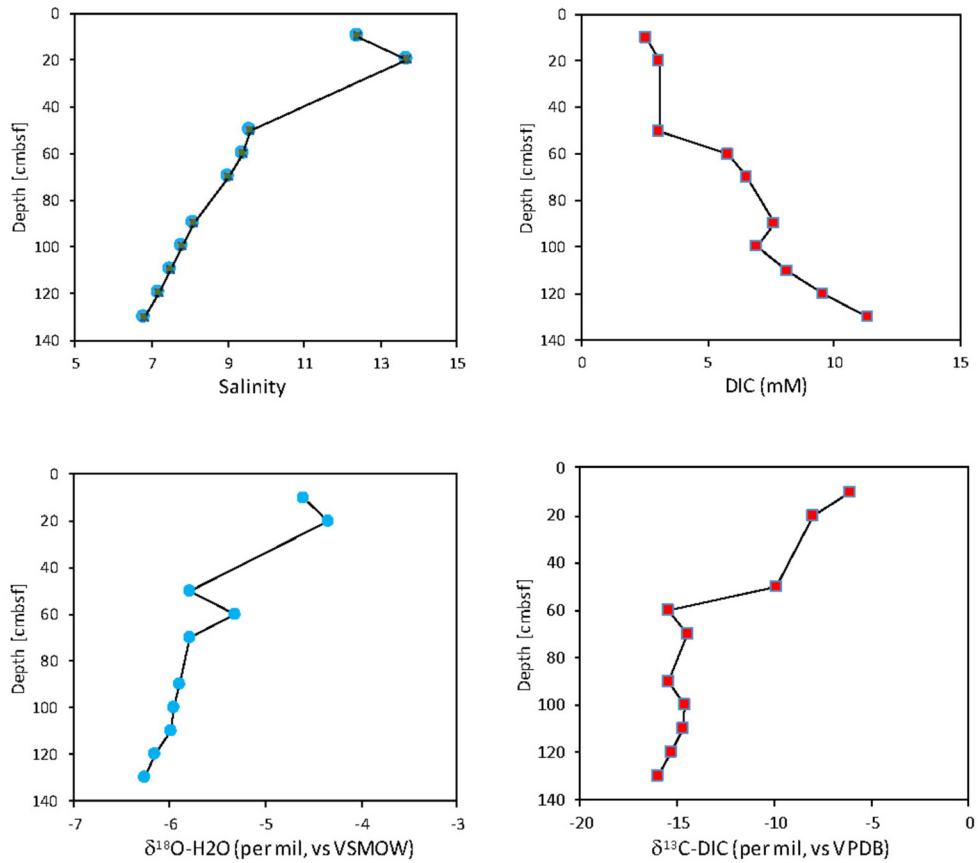


FIGURE 10 | Examples for vertical profiles of the pore water composition at a submarine groundwater discharge (SGD) impacted site (taken with a mobile pore water lance in spring 2017). Whereas the water isotopes and salinity (PSU) indicate the contribution of fresh and isotopically lighter water at depth, the dissolved carbonate system shows a clear contribution of biogenic CO_2 derived from the anaerobic mineralization of essentially marine organic matter. Dissolved sulfide, the product of microbial sulfate reduction, accumulated about 40 cm below sea floor and also phosphate and silica were substantially enriched in the pore waters when compared to surface water.

methane and ECD (electron capture detector) for nitrous oxide determination.

Interestingly, the temperature and salinity anomalies are found near the coastal area with emerging peat deposits (Kreuzburg et al., 2018) and near areas with the highest bottom water methane concentrations (mean: 25.3 ± 9.3; range: 15–55 CH_4 nmol L^{-1}, **Figure 12**). Since peat may release DOC with advection of low saline pore water (Tiemeyer et al., 2016), these coastal sediments have an increased potential of organic matter release due to hydrological dynamics. The input of peat-derived DOC likely enhances CH_4 production rates (Aravena and Wassenaar, 1993; Liu et al., 2011) in coastal surface waters. These findings match new data from the southern North Sea, where increasing concentrations and air-sea fluxes of methane were reported toward the shore in the Belgian coastal zone, in particular in areas of free gas occurrence (Borges et al., 2016). The free gas occurrence in the Belgian coastal zone has been suggested to be generated by the decomposition of a thin Pleistocene peat layer zone (Missiaen et al., 2002), which is a somewhat similar situation to ours. Thus, our results support the hypothesis that SGD is increasing the inflow of DOC and nutrients into the coastal zone and thereby instigating changes in biogeochemical cycling in the coastal sediments.

Coastal-near dynamics apparently foster the transfer of methane from the sediment toward the water column, which is usually oxidized by effective anaerobic and aerobic oxidation (Knittel and Boetius, 2009). However, our data suggest that elevated methane concentrations near the shore are hardly oxidized in the water likely due to the shallow water depth suggesting possible methane emissions from the coastal waters to the atmosphere. In the future we plan to assess whether or not this is contributing substantially to atmospheric methane fluxes.

Ecological Effects of Freshwater Fluxes and Peat Outcropping in the Baltic Sea

Macro-Phytobenthos

Salinity plays a major role for macrophytobenthos in the eutrophic southern Baltic Sea (Volkmann et al., 2016). The number of macroalgae taxa has been shown to decrease with decreasing salinity in the Baltic Sea (Schubert et al., 2011; Telesh et al., 2013), yet so far the potential role of irregular freshwater

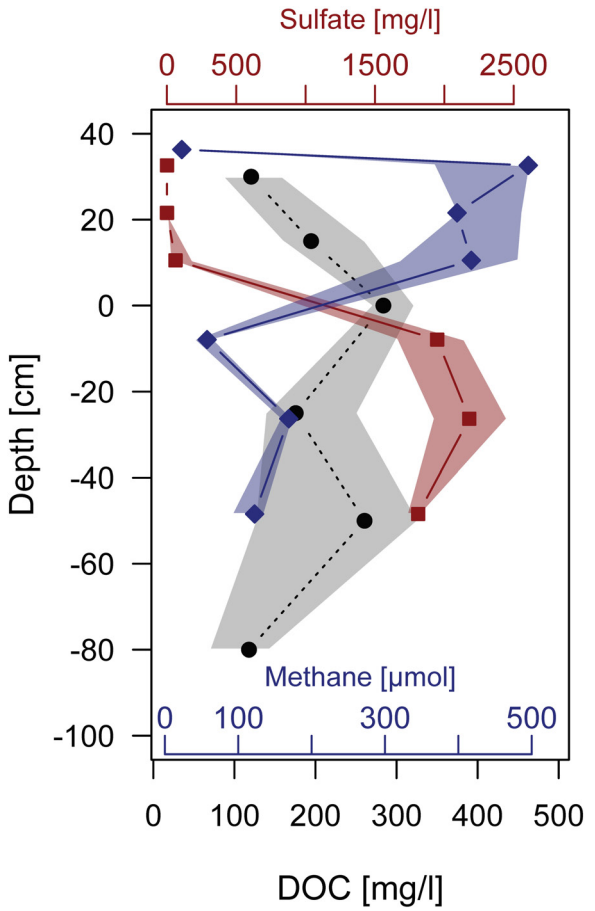


FIGURE 11 | (Pore) water profiles of DOC (black, circle), CH_4 (blue, diamond), and SO_4 (red, square) derived from repeated sampling in the central part of the peatland. Symbols denote median concentrations over monthly samples taken from May to October 2015, shaded polygons stretch from the 1st to the 3rd quartile of the distribution at the specific depths. Lines as well as shading contours are linearly interpolated between depths.

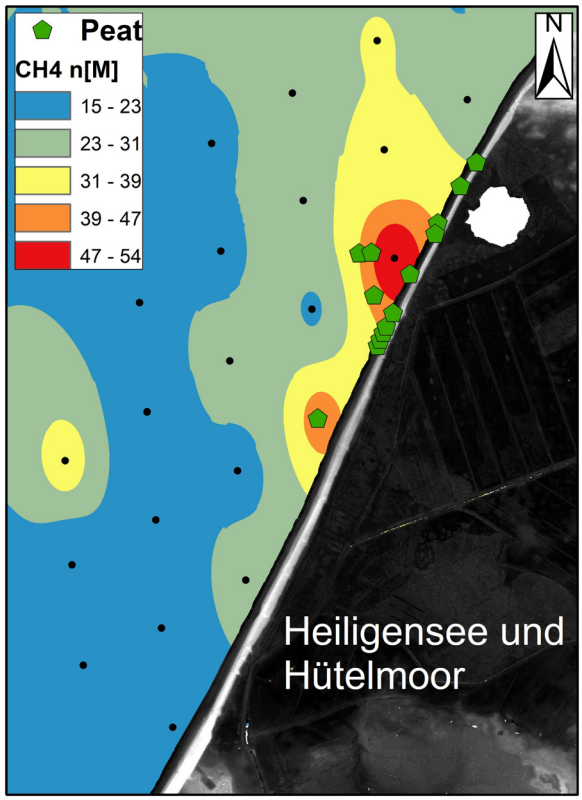


FIGURE 12 | Dissolved methane distribution in the shallow Baltic Sea in front of the study site, composite of several measurements in June 2017.

input as an additional stressor has not been studied. Frequency as well as the amplitude of variability in salinity is the decisive factor for occurrence/absence of species at a given site (Telesh et al., 2013). In this context, SGD must be seen as an additional factor of variability, impacting macro- as well as microphytobenthic community composition. Our study site is located in a critical salinity range, where small local changes in salinity may cause drastic effects in community composition. Similarity between closely neighbored communities has been shown to drop sharply in this salinity range, indicating the relatively strong effect of small perturbations (Schubert et al., 2011). Transect sampling was thus performed in front of the Hütelmoor to estimate the impact of irregular freshwater pulses on the taxonomic composition of the macrophytobenthos community.

A striking result is the almost complete absence of *Fucus* spp., the only habitat-forming species able to grow in this region of the Baltic Sea (Wahl et al., 2011). Without this species, the macroalgae community in front of the Hütelmoor is severely species-depleted, consisting mainly of branched filamentous red algae, which contribute >80% to the total biomass both in spring and autumn. Total biomass along the depth gradient showed a sharp decline below 2 m water depth (**Figure 13**, left panel), which is consistent with the steep irradiance gradient, as can be seen from the attenuation spectra (**Figure 13**, right panel). The reason for the absence of non-filamentous, perennial species as well as dominance of red algae at the depths preferentially occupied by green algae needs to be investigated by means of physiological studies of tolerance against salinity fluctuations. If the species expected to be found at these depths and/or region (such as *Fucus* spp. or green algae) turn out to be less tolerant to salinity fluctuations than those found in abundance near the Hütelmoor, this would provide a strong support for our hypothesis that land–sea exchange processes impact the relevant biota in the coastal sea.

Micro-Phytobenthos

In contrast to macroalgae, benthic diatoms are much less affected by salinity fluctuations. In a previous study, three abundant benthic diatom taxa were isolated from sandy sediments sampled at a shallow-water area (15–30-cm water depth) (54°01.490′ N; 11°32.110′ E) at the southern Baltic Sea coast, the so-called 'Boiensdorfer Werder' opposite of the island Poel and the Mecklenburg Bight, and their salinity tolerance was evaluated

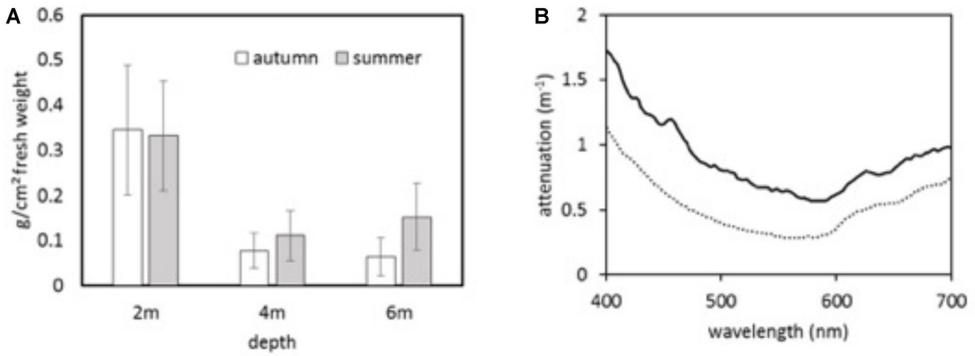


FIGURE 13 | (A) Total fresh weight of macrophytobenthos along a transect in front of the Hütelmoor in autumn and summer 2016. For each depth, six replicates were sampled by means of Scuba-diving; **(B)** Attenuation spectra recorded in July (solid line) and October (dotted line) close to the transect position. Lower attenuation in autumn is overcompensated by lower solar elevation.

(Woelfel et al., 2014). Benthic diatoms were isolated from the top 5 mm layer of the sediment cores, purified and established as unialgal cultures according the protocol of Stachura-Suchoples et al. (2016). These strains were used to measure growth and photosynthesis under various controlled abiotic conditions (Woelfel et al., 2014). Surprisingly, all species were characterized as euryhaline, growing across a wide range from almost freshwater to hypersaline conditions (1 up to 50 PSU). Consequently, these representative taxa can cope with very low *in situ* salinities, and hence SGD will most probably not have a negative osmotic effect on photosynthesis and growth.

In contrast, preliminary data on the influence of DOM in the Hütelmoor water body on benthic diatoms indicate a stimulating effect on growth of two species isolated in the shallow water in front of this fen peat site. To determine the effect of DOM in the Hütelmoor water body on heterotrophic growth in the dark, benthic diatom isolates were incubated for 10 days in darkness in 6 different chemically defined media. Afterwards the cell numbers were estimated, and the values were compared to a control. The Hütelmoor water organic compounds led to a statistically significant stimulation of growth in darkness, which suggests heterotrophic behavior. Other benthic diatoms have been experimentally characterized as mixotrophic microorganisms that photosynthesise in light and easily can switch to heterotrophy under dark conditions (Kitano et al., 1997). The heterotrophic lifestyle of benthic diatoms mainly includes the uptake of bioavailable sugars, amino acids, organic acids and other organic substrates from the environment, and some active transport mechanisms for such compounds are identified, which seem to be substrate and light regulated (Hellebust and Lewin, 1977; Armbrust et al., 2004). From an ecological standpoint, heterotrophy seems to be a very important mode of nutrition when cells are buried into the sediment because of unstable surface conditions in the shallow water habitat caused by wind, waves, and currents. Although benthic diatoms can actively move vertically in the sediment, this process requires energy and the uptake of organic substances from the peat might facilitate such movement to escape darkness. Our results suggest that SGD with increased DOM concentrations in front of the Hütelmoor may potentially increase the growth of benthic diatoms supporting the hypothesis that exchange processes alter the growth conditions on the seaside.

Zoobenthos

The multiple interconnected environmental shifts associated with SGD (such as changes in salinity, temperature, seawater chemistry, and nutrients) result in complex interactive effects on the benthic organisms inhabiting these areas that can be effectively understood by investigating the impacts on the energy fluxes through the organisms and the ecosystem (**Figure 14**). Physiological assessment of the burrowing capacity and endurance of marine bioturbators (the softshell clams *Mya arenaria*) as well as the energy costs of burrowing were conducted as described elsewhere (Haider et al., 2017). Briefly, clams were acclimated to the normal (15 PSU), low (5 PSU) and fluctuating (5–15 PSU) salinity for 3–4 weeks, and their burrowing speed and endurance was determined using video recordings during repeated forced burrowing. The respiratory activity of isolated mitochondria as well as the activity of the mitochondrial electron transfer chain in the tissue extracts were measured as proxies for the clams aerobic capacity under the resting conditions and after repeated burrowing. Energy costs of burrowing were assessed by measuring the amounts of tissue energy reserves (lipids, proteins, and carbohydrates) under resting conditions and after repeated burrowing, and the energy cost was calculated as the % of the total body reserves (expressed as energy equivalents) used to fuel a single burrowing cycle.

Sediment reworking by bioturbators is considered one of the most energy expensive modes of activity, and our estimates show that a single digging cycle of a marine bioturbator *M. arenaria* uses up on average 7% of its energy reserves (Haider et al., 2017). Thus, it is not surprising that abiotic stressors (such as low and/or fluctuating salinity characteristic of SGD) negatively affect the burrowing capacity of sediment-dwelling zoobenthos including clams, polychaetes, and echinoderms (Turner and Meyer, 1980; Lardies et al., 2001; Przeslawski et al., 2009; Haider et al., 2017). These changes may have important implications for the ecological functions of bioturbators affecting

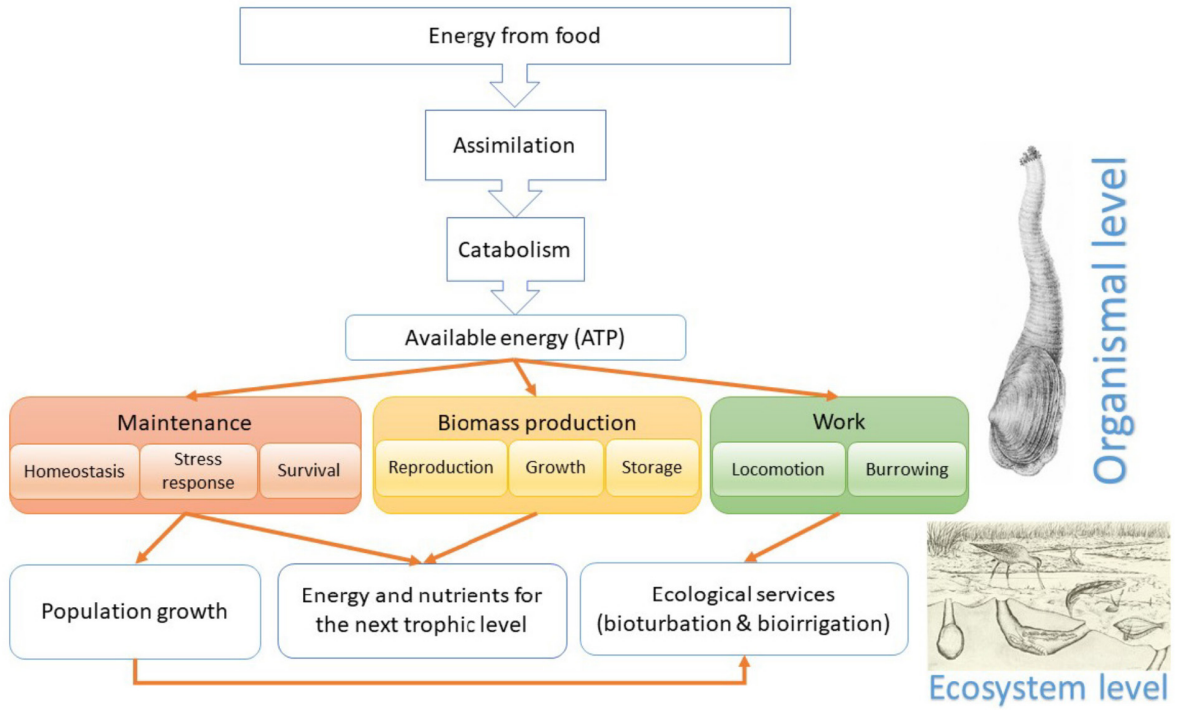


FIGURE 14 | Bioenergetics-based model integrating the physiological effects and ecological consequences of multiple stress exposures in coastal habitats. Images are obtained from the Wikimedia Commons and are in the public domain.

the sediment reworking by the resident biota and the associated influx of oxygen and nutrients into the deeper sediment layers (**Figure 14**). Furthermore, fluctuating salinities led to changes in the biochemical composition of the clam tissues (Haider et al., 2017), potentially impacting the nutritional quality of the food for the top-level predators feeding on clams in this shallow coastal ecosystem.

Currently, we are developing bioenergetically based ecological models to assess the effects of the common environmental stressors (including salinity and temperature change) on survival, growth, and digging activity of the clams by assessing the effect of these factors on energy assimilation, maintenance costs, and energy available for the biomass production. Our model considers the effects of multiple stressors (regardless of their nature) on the distribution of energy fluxes through the organism and their implications for the higher-level ecosystem functions. For example, salinity shifts caused by SGD or freshwater run-off may cause physical disturbance by hydrodynamic forces, or warming may cause physiological stress, increasing energy demand for maintenance, altering the energy and nutrient content of the tissues, and negatively affecting the capacity to do the work. Negative impacts of abiotic stressors might be modulated and partially offset by increased food supply due to the stimulation of the algal production near the freshwater influx. These changes in energy fluxes and energy trade-offs between different fitness-related functions translate into changes in ecological performance of the organisms and ecosystem services they provide (such as bioturbation or trophic energy transfer) (van der Meer, 2006; Sokolova et al., 2012; Sokolova, 2013). Such models serve as mechanistically based tools to understand and predict the complex effects of the environmental shifts caused by SGD on the local communities and ecosystem services they provide and will help us to test the hypothesis that increased inflow of water from land to sea imposes substantial changes to the marine food web.

CONCLUSIONS/OUTLOOK

A system approach, in which the coast is considered as a continuum that extents from land to sea, seems to be promising to indeed foster our understanding of the ecosystem functioning of shelf seas and low lying coastal (wet)lands. Here, we demonstrate that the interdisciplinary collaboration among both terrestrial and marine hydro-physicists, biogeochemists and biologists gives new insight into the operating processes.

Our results show that either side of the coastline is impacted by the respective other ecosystem compartment. It has to be emphasized that the mutual influence is operational despite low gradients and a non-tidal system. Although a dune functioning as a dyke between sea and land is still in place, we found evidence for earlier flooding events. Biogeochemical processes such as the production of GHGs are still affected by saltwater influx, despite the intrusion probably dating back decades. Water flux-based exchange processes within the main peat body operate at small rates, while deeper groundwater fluxes and at the border

of the peatland might be more relevant. Considering the land area along the Baltic Sea coast that is discharging directly into the sea (catchments unconnected to main draining rivers), we conclude that biogeochemical and resulting biological processes in the shallow sea might be regulated to a great extent by nutrient and complex organic matter fluxes originating from (peat) land.

In the future, rate measurements of *in situ* transformations in the carbon-sulfur cycles and dating of the different water sources will allow for a better mechanistic understanding of the actual processes and the flow of water as an important driver for element transport. A model-based analysis linked to physical properties of the land and sea side will allow depicting larger scale (1–10 km) water fluxes as a basis for balance calculations of nutrients and other relevant compounds, while bioenergetically based ecological models assessing the effects of the common environmental stressors on marine biota will complete the system view onto the coastal ecocline.

AUTHOR CONTRIBUTIONS

GJ, MJ, BL, MV, MEB, MB, HB, SF, UK, PL, GR, HS, HS-V, and IS developed the idea and elaborated the concept. LG, SG-P, FH, MI, NK, MK, XL, KR, HAS, RS, VU, and JW provided experimental or numerical data and organized and conducted the data analyses together with UG, GM, TP, FR, and GJ. BL, GJ, MJ, and MV led the manuscript writing, with contributions from all authors.

FUNDING

This study was conducted within the framework of the Research Training Group Baltic TRANSCOAST funded by the DFG (Deutsche Forschungsgemeinschaft) under grant number GRK 2000/1. This is Baltic TRANSCOAST publication no. GRK2000/00XX.

ACKNOWLEDGMENTS

MEB and JW wish to thank I. Schmiedinger, R. I. Liskow, C. Burmeister, R. Bahlo, and A. Köhler (IOW) for their invaluable biogeochemical and stable isotope geochemical and SEM-EDX laboratory support. H. Nikolai (ICBM Wilhelmshaven) is thanked for the expert support with the manufacturing and *in-situ* establishment of the pore water lances. U. Mallast, W. S. (Billy) Moore, N. Moosdorf, J. Scholten, and J. Sültenfuß are thanked for their continuous active support with Rn, Ra, and dating investigations. **Figure 14** uses images from the following sources: Mya arenaria by J. A. Herklots, 'De Weekdieren van Nederland', https://commons.wikimedia.org/w/index.php?curid=1748721; Internet Archive Book Images, https://commons.wikimedia.org/w/index.php?curid=43541209.

REFERENCES

Abarca, E., Karam, H., Hemond, H. F., and Harvey, C. F. (2013). Transient groundwater dynamics in a coastal aquifer: the effects of tides, the lunar cycle, and the beach profile. *Water Resour. Res.* 49, 2473–2488. doi: 10.1002/wrcr.20075

Andersen, M. S., Baron, L., Gudbjerg, J., Gregersen, J., Chapellier, D., Jakobsen, R., et al. (2007). Discharge of nitrate-containing groundwater into a coastal marine environment. *J. Hydrol.* 336, 98–114. doi: 10.1016/j.jhydrol.2006.12.023

Aravena, R., and Wassenaar, L. I. (1993). Dissolved organic carbon and methane in a regional confined aquifer, southern Ontario, Canada: carbon isotope evidence for associated subsurface sources. *Appl. Geochem.* 8, 483–493. doi: 10.1016/0883-2927(93)90077-T

Armbrust, E. V., Berges, J. A., Bowler, C., Green, B. R., Martinez, D., Putnam, N. H., et al. (2004). The genome of the diatom *Thalassiosira pseudonana*: ecology, evolution, and metabolism. *Science* 306, 79–86. doi: 10.1126/science.1101156

BACC II Author Team (2015). *Second Assessment of Climate Change for the Baltic Sea Basin. Regional Climate Studies*. Berlin: Springer.

Bahnwart, M., Hübener, T., and Schubert, H. (1998). Downstream changes in phytoplankton composition and biomass in a lowland river-lake system (Warnow River, Germany). *Hydrobiologia* 391, 99–111. doi: 10.1023/A:1003558209411

Bartlett, K. B., Bartlett, D. S., Harriss, R. C., and Sebacher, D. I. (1987). Methane emissions along a salt marsh salinity gradient. *Biogeochemistry* 4, 183–202. doi: 10.1007/BF02187365

Beck, M., Dellwig, O., Kolditz, K., Freund, H., Liebezeit, G., Schnetger, B., et al. (2007). In situ pore water sampling in deep intertidal flat sediments. *Limnol. Oceanogr. Methods* 5, 136–144. doi: 10.4319/lom.2007.5.136

Boetius, A., Ravenschlag, K., Schubert, C. J., Rickert, D., Widdel, F., Gleseke, A., et al. (2000). A marine microbial consortium apparently mediating anaerobic oxidation methane. *Nature* 407, 623–626. doi: 10.1038/35036572

Bohne, B., and Bohne, K. (2008). "Monitoring zum Wasserhaushalt einer auf litoralem Versumpfungsmoor gewachsenen Regenmoorkalotte - Beispiel Naturschutzgebiet "Hütelmoor" bei Rostock," in *Aspekte der Geoökologie*, ed. O. Stüdemann (Berlin: Weißensee Verlag), 313–338.

Bollmann, M., Bosch, T., Colijn, F., Ebinghaus, R., Froese, R., Güssow, K., et al. (2010). *World Ocean Review: Living with the Oceans*. Hamburg: Maribus GmbH.

Borges, A. V., Champenois, W., Gypens, N., Delille, B., and Harlay, J. (2016). Massive marine methane emissions from near-shore shallow coastal areas. *Sci. Rep.* 6:27908. doi: 10.1038/srep27908

Böttcher, M. E., Lipka, M., Winde, V., Dellwig, O., Böttcher, E. O., Böttcher, T. M. C., et al. (2014). "Multi-isotope composition of freshwater sources for the southern North and Baltic Sea," in *Proceedings of the 23rd SWIM Conference*, Husum, 46–49.

Böttcher, M. E., Mallast, U., Massmann, G., Moosdorf, N., Müller-Petke, M., and Waska, H. (2018). "Coastal-Groundwater interfaces (submarine groundwater discharge)," in *Ecohydrological Interfaces*, ed. S. Krause (New York, NY: Wiley).

Burchard, H., and Bolding, K. (2002). *GETM, A General Estuarine Transport Model. Scientific Documentation*. Brussels: European Commission.

Burchard, H., Bolding, K., Feistel, R., Gräwe, U., MacCready, P., Klingbeil, K., et al. (2018). The Knudsen theorem and the Total Exchange Flow analysis framework applied to the Baltic Sea. *Prog. Oceanogr.* 165, 268–286. doi: 10.1016/j.pocean.2018.04.004

Burnett, W. C., Bokuniewicz, H., Huettel, M., Moore, W. S., and Taniguchi, M. (2003). Groundwater and pore water inputs into the coastal zone. *Biogeochemistry* 66, 3–33. doi: 10.1023/B:BIOG.0000006066.21240.53

Cahoon, L. B. (1999). The role of benthic microalgae in neritic ecosystems. *Oceanogr. Mar. Biol. Annu. Rev.* 37, 47–86.

Church, J. A., White, N. J., Domingues, C. M., Monselesan, D. P., and Miles, E. R. (2013). Sea level and ocean heat-content change. *Int. Geophys.* 103, 697–725. doi: 10.1016/B978-0-12-391851-2.00027-1

Church, T. M. (1996). A groundwater route for the water cycle. *Nature* 380, 579–580. doi: 10.1038/380579a0

Cline, J. D. (1969). Spectrophotometric determination of hydrogen sulfide in natural waters. *Limnol. Oceanogr.* 14, 454–458. doi: 10.4319/lo.1969.14.3.0454

de Beer, D., Wenzhöfer, F., Ferdelman, T. G., Boehme, S. E., Hüttel, M., van Beusekom, J. E. E., et al. (2005). Transport and mineralization in North Sea sandy intertidal sediments, Sylt-Rømø Basin, Wadden Sea. *Limnol. Oceanogr.* 50, 113–127. doi: 10.4319/lo.2005.50.1.0113

Deutsch, B., Mewes, M., Liskow, I., and Voss, M. (2006). Quantification of diffuse nitrate inputs into a small river system using stable isotopes of oxygen and nitrogen in nitrate. *Org. Geochem.* 37, 1333–1342. doi: 10.1016/j.orggeochem.2006.04.012

Doney, S. C. (2010). The growing human footprint on coastal and open-ocean biogeochemistry. *Science* 328, 1512–1516. doi: 10.1126/science.1185198

Donis, D., Janssen, F., Liu, B., Wenzhöfer, F., Dellwig, O., Escher, P., et al. (2017). Biogeochemical impact of submarine ground water discharge on coastal surface sands of the southern Baltic Sea. *Estuar. Coast. Shelf Sci.* 189, 131–142. doi: 10.1016/j.ecss.2017.03.003

Du Laing, G., Rinklebe, J., Vandecasteele, B., Meers, E., and Tack, F. M. (2009). Trace metal behaviour in estuarine and riverine floodplain soils and sediments: a review. *Sci. Total Environ.* 407, 3972–3985. doi: 10.1016/j.scitotenv.2008.07.025

Encarnação, J., Leitão, F., Range, P., Piló, D., Chícharo, M. A., and Chícharo, L. (2013). The influence of submarine groundwater discharges on subtidal meiofauna assemblages in south Portugal (Algarve). *Estuar. Coast. Shelf Sci.* 130, 202–208. doi: 10.1016/j.ecss.2013.04.013

Fernández-Fernández, L., Westphal, J., Schmiedinger, I., Kreuzburg, M., Bahlo, R., Koebsch, F., et al. (2017). Sulfur isotope biogeochemistry of soils from an episodically flooded coastal wetland, southern Baltic Sea. *Geophys. Res. Abstr.* 19:EGU2017-14335.

Forster, S., Bobertz, B., and Bohling, B. (2003). Permeability of sands in the coastal areas of the southern Baltic Sea: mapping a grain-size related sediment property. *Aquat. Geochem.* 9, 171–190. doi: 10.1023/B:AQUA.0000022953.52275.8b

Gao, H., Matyka, M., Liu, B., Khalili, A., Kostka, J. E., Collins, G., et al. (2012). Intensive and extensive nitrogen loss from intertidal permeable sediments of the Wadden Sea. *Limnol. Oceanogr.* 57, 185–198. doi: 10.1371/journal.pone.0104517

Gätje, C., and Reise, K. (2012). *Ökosystem Wattenmeer - Austausch-, Transport- und Stoffumwandlungsprozesse / The Wadden Sea Ecosystem - Exchange, Transport and Transformation Processes*. Berlin: Springer.

Geyer, W. R., and MacCready, P. (2014). The estuarine circulation. *Annu. Rev. Fluid Mech.* 46, 175–197. doi: 10.1146/annurev-fluid-010313-141302

Giani, L., Dittrich, K., Martsfeld-Hartmann, A., and Peters, G. (1996). Methanogenesis in saltmarsh soils of the North Sea coast of Germany. *Eur. J. Soil Sci.* 47, 175–182. doi: 10.1111/j.1365-2389.1996.tb01388.x

Glatzel, S., Koebsch, F., Beetz, S., Hahn, J., Richter, P., and Jurasinski, G. (2011). Maßnahmen zur minderung der treibhausgasfreisetzung aus mooren im mittleren mecklenburg. *Telma Beih.* 4, 85–106.

Gocke, K., Lenz, J., Westphal, H., Koppe, R., Rheinheimer, G., and Hoppe, H.-G. (2012). Diel variations in microbial activity in hypertrophic coastal waters. *Hydrol. Wasserbewirtschaftung* 56, 48–58.

Gosch, L., Janssen, M., and Lennartz, B. (2018). Impact of the water salinity on the hydraulic conductivity of fen peat. *Hydrol. Process.* 32, 1214–1222. doi: 10.1002/hyp.11478

Gräwe, U., and Burchard, H. (2012). Storm surges in the Western Baltic Sea: the present and a possible future. *Clim. Dyn.* 39, 165–183. doi: 10.1007/s00382-011-1185-z

Gräwe, U., Holtermann, P., Klingbeil, K., and Burchard, H. (2015). Advantages of vertically adaptive coordinates in numerical models of stratified shelf seas. *Ocean Model.* 92, 56–68. doi: 10.1016/j.ocemod.2015.05.008

Grinsted, A., Jevrejeva, S., Riva, R. E., and Dahl-Jensen, D. (2015). Sea level rise projections for northern Europe under RCP8. 5. *Clim. Res.* 64, 15–23. doi: 10.3354/cr01309

Günther, A., Schenzle, E., and Jurasinski, G. (2014). *Flexible Chambers for Greenhouse Gas Measurements in Tall Vegetation - A Construction Manual*. Available at: http://bit.ly/2GLLy8O

Hahn, J., Glatzel, S., Köhler, S., and Jurasinski, G. (2015). Greenhouse gas exchange in a coastal fen in the first year after flooding - a systems shift. *PLoS One* 10:e0140657. doi: 10.1371/journal.pone.0140657

Haider, F., Sokolov, E. P., and Sokolova, I. M. (2017). Effects of mechanical disturbance and salinity stress on bioenergetics and burrowing behavior of the soft shell clam *Mya arenaria*. *J. Exp. Biol.* 221(Pt 4):jeb172643. doi: 10.1242/jeb.172643

Harff, J., Furmanczyk, K., and von Storch, H. (2017). *Coastline Changes of the Baltic Sea from South to East: Past and Future Projections*. Berlin: Springer. doi: 10.1007/978-3-319-49894-2

Hartmann, M., and Nielsen, H. (2012). δ34S values in recent sea sediments and their significance using several sediment profiles from the western Baltic Sea. *Isotopes Environ. Health Stud.* 48, 7–32. doi: 10.1080/10256016.2012.660528

Hellebust, J. A., and Lewin, J. (1977). "Heterotrophic nutrition," in *The Biology of Diatoms*, ed. D. Werner (Berkeley, CA: University of California Press), 169–197.

Huettel, M., and Gust, G. (1992). Solute release mechanisms from confined sediment cores in stirred benthic chambers and flume flows. *Mar. Ecol. Prog. Ser.* 82, 187–197. doi: 10.3354/meps082187

Huettel, M., Røy, H., Precht, E., and Ehrenhauss, S. (2003). Hydrodynamical impact on biogeochemical processes in aquatic sediments. *Hydrobiologia* 494, 231–236. doi: 10.1023/A:1025426601773

Huettel, M., Ziebis, W., Forster, S., and Luther, G. W. (1998). Advective transport affecting metal and nutrient distributions and interfacial fluxes in permeable sediments. *Geochim. Cosmochim. Acta* 62, 613–631. doi: 10.1016/S0016-7037(97)00371-2

Hünicke, B., and Zorita, E. (2016). Statistical analysis of the acceleration of Baltic mean sea-level rise, 1900-2012. *Front. Mar. Sci.* 3:125. doi: 10.3389/fmars.2016.00125

Jeandel, C. (2016). Overview of the mechanisms that could explain the 'Boundary Exchange' at the land-ocean contact. *Philos. Trans. R. Soc. A Math. Phys. Eng. Sci.* 374:20150287. doi: 10.1098/rsta.2015.0287

Johansson, M. M., Pellikka, H., Kahma, K. K., and Ruosteenoja, K. (2014). Global sea level rise scenarios adapted to the Finnish coast. *J. Mar. Syst.* 129, 35–46. doi: 10.1016/j.jmarsys.2012.08.007

Jørgensen, B. B., and Kasten, S. (2006). "Sulfur cycling and methane oxidation," in *Marine Geochemistry*, eds H. D. Schulz and M. Zabel (Berlin: Springer), 271–309.

Kemp, W. M., Boynton, W. R., Adolf, J. E., Boesch, D. F., Boicourt, W. C., Brush, G., et al. (2005). Eutrophication of Chesapeake Bay: historical trends and ecological interactions. *Mar. Ecol. Prog. Ser.* 303, 1–29. doi: 10.3354/meps303001

Kitano, M., Matsukawa, R., and Karube, I. (1997). Changes in eicosapentaenoic acid content of *Navicula saprophila*, *Rhodomonas salina* and *Nitzschia* sp. under mixotrophic conditions. *J. Appl. Phycol.* 9, 559–563.

Knee, K. L., and Paytan, A. (2011). "Submarine groundwater discharge: a source of nutrients, metals, and pollutants to the coastal ocean," in *Treatise on Estuarine and Coastal Science 4*, eds E. Wolanski and D. S. McLusky (London: Academic Press), 205–233.

Knittel, K., and Boetius, A. (2009). Anaerobic oxidation of methane: progress with an unknown process. *Annu. Rev. Microbiol.* 63, 311–334. doi: 10.1146/annurev.micro.61.080706.093130

Koch, M., Koebsch, F., Hahn, J., and Jurasinski, G. (2017). From meadow to shallow lake: monitoring secondary succession in a coastal fen after rewetting by flooding based on aerial imagery and plot data. *Mires Peat* 19:11. doi: 10.19189/MaP.2015.OMB.188

Koebsch, F., Glatzel, S., and Jurasinski, G. (2013). Vegetation controls methane emissions in a coastal brackish fen. *Wetl. Ecol. Manag.* 21, 323–337. doi: 10.1007/s11273-013-9304-8

Koebsch, F., Jurasinski, G., Koch, M., Hofmann, J., and Glatzel, S. (2015). Controls for multi-scale temporal variation in ecosystem methane exchange during the growing season of a permanently inundated fen. *Agric. For. Meteorol.* 204, 94–105. doi: 10.1016/j.agrformet.2015.02.002

Kolp, O. (1957). *Die Nordöstliche Heide Mecklenburgs*. Berlin: Deutscher Verlag der Wissenschaften.

Kotwicki, L., Grzelak, K., Czub, M., Dellwig, O., Gentz, T., Szymczycha, B., et al. (2014). Submarine groundwater discharge to the Baltic coastal zone: impacts on the meiofaunal community. *J. Mar. Syst.* 129, 118–126. doi: 10.1016/j.jmarsys.2013.06.009

Kreuzburg, M., Ibenthal, M., Janssen, M., Rehder, G., Voss, M., Naumann, M., et al. (2018). Submarine continuation of peat deposits from a coastal peatland in the southern Baltic Sea and its Holocene development. *Front. Earth Sci.* 6:103. doi: 10.3389/feart.2018.00103

Kummu, M., De Moel, H., Salvucci, G., Viviroli, D., Ward, P. J., and Varis, O. (2016). Over the hills and further away from coast: global geospatial patterns of human and environment over the 20th-21st centuries. *Environ. Res. Lett.* 11:034010. doi: 10.1088/1748-9326/11/3/034010

Kwon, E. Y., Kim, G., Primeau, F., Moore, W. S., Cho, H.-M., Devries, T., et al. (2014). Global estimate of submarine groundwater discharge based on an observationally constrained radium isotope model. *Geophys. Res. Lett.* 41, 8438–8444. doi: 10.1002/2014GL061574

Lardies, M. A., Clasing, E., Navarro, J. M., and Stead, R. A. (2001). Effects of environmental variables on burial depth of two infaunal bivalves inhabiting a tidal flat in southern Chile. *J. Mar. Biol. Assoc. U.K.* 81, 809–816. doi: 10.1017/S0025315401004635

Leinweber, P., Jandl, G., Eckhardt, K.-U., Schlichting, A., Hofmann, D., and Schulten, H.-R. (2009). "Analytical pyrolysis and soft-ionization mass spectrometry," in *Biophysico-Chemical Processes Involving Natural Nonliving Organic Matter in Environmental Systems*, eds N. Senesi, B. Xing, and P. M. Huang (Hoboken, NJ: John Wiley & Sons), 539–588. doi: 10.1002/9780470494950.ch14

Leitão, F., Encarnação, J., Range, P., Schmelz, R. M., Teodósio, M. A., and Chícharo, L. (2015). Submarine groundwater discharges create unique benthic communities in a coastal sandy marine environment. *Estuar. Coast. Shelf Sci.* 163, 93–98. doi: 10.1016/j.ecss.2015.06.007

Liu, D. Y., Ding, W. X., Jia, Z. J., and Cai, Z. C. (2011). Relation between methanogenic archaea and methane production potential in selected natural wetland ecosystems across China. *Biogeosciences* 8, 329–338. doi: 10.5194/bg-8-329-2011

Liu, J., Su, N., Wang, X., and Du, J. (2017). Submarine groundwater discharge and associated nutrient fluxes into the Southern Yellow Sea: a case study for semi-enclosed and oligotrophic seas - implication for green tide bloom. *J. Geophys. Res. Oceans* 122, 139–152. doi: 10.1002/2016JC012282

Martin, J. M., and Whitfield, M. (1983). "The significance of the river input of chemical elements to the ocean," in *Trace Metals in Sea Water*, ed. C. Wong (Boston, MA: Springer), 265–296.

Massel, S. R. (2001). Circulation of groundwater due to wave set-up on a permeable beach. *Oceanologia* 43, 279–290.

Meyercordt, J., and Meyer-Reil, L. A. (1999). Primary production of benthic microalgae in two shallow coastal lagoons of different trophic status in the southern Baltic Sea. *Mar. Ecol. Prog. Ser.* 178, 179–191. doi: 10.3354/meps178179

Miegel, M., Graeff, T., Selle, B., Salzmann, T., Franck, C., and Bronstert, A. (2016). Untersuchung eines renaturierten Niedermoores an der mecklenburgischen Ostseeküste - Teil I: systembeschreibung und hydrologische Grundcharakterisierung (Investigation of a renatured fen on the Baltic Sea coast of Mecklenburg - Part I: system description and basic hydrological characterisation). *Hydrol. Wasserbewirtschaftung* 60, 242–258.

Missiaen, T., Murphy, S., Loncke, L., and Hernriet, J.-P. (2002). Very high-resolution seismic mapping of shallow gas in the Belgian coastal zone. *Cont. Shelf Res.* 22, 2291–2301. doi: 10.1016/S0278-4343(02)00056-0

Moghimi, S., Klingbeil, K., Gräwe, U., and Burchard, H. (2013). A direct comparison of a depth-dependent radiation stress formulation and a vortex force formulation within a three-dimensional coastal ocean model. *Ocean Model.* 70, 132–144. doi: 10.1016/j.ocemod.2012.10.002

Moore, W. S., Beck, M., Riedel, T., Rutgers van der Loeff, M., Dellwig, O., Shaw, T. J., et al. (2011). Radium-based pore water fluxes of silica, alkalinity, manganese, DOC, and uranium: a decade of studies in the German Wadden Sea. *Geochim. Cosmochim. Acta* 75, 6535–6555. doi: 10.1016/j.gca.2011.08.037

Nerem, R. S., Beckley, B. D., Fasullo, J. T., Hamlington, B. D., Masters, D., and Mitchum, G. T. (2018). Climate-change-driven accelerated sea-level rise detected in the altimeter era. *Proc. Natl. Acad. Sci. U.S.A.* 115, 2022–2025. doi: 10.1073/pnas.1717312115

Neumann, B., Vafeidis, A. T., Zimmermann, J., and Nicholls, R. J. (2015). Future coastal population growth and exposure to sea-level rise and coastal flooding-a global assessment. *PLoS One* 10:e0118571. doi: 10.1371/journal.pone.0118571

Newton, A., Icely, J., Cristina, S., Brito, A., Cardoso, A. C., Colijn, F., et al. (2014). An overview of ecological status, vulnerability and future perspectives of European large shallow, semi-enclosed coastal systems, lagoons and transitional waters. *Estuar. Coast. Shelf Sci.* 140, 95–122. doi: 10.1016/j.ecss.2013.05.023

Nicholls, R. J., Wong, P. P., Burkett, V. R., Codignotto, J. O., Hay, J. E., McLean, R. F., et al. (2007). "Coastal systems and low-lying areas. Climate change 2007: impacts, adaptation and vulnerability," in *Contribution of Working Group II to the Fourth Assessment Report of the Intergovernmental Panel on Climate Change*, eds M. L. Parry, O. F. Canziani, J. P. Palutikof, P. J. van der Linden, and C. E. Hanson (Cambridge: Cambridge University Press), 315–356.

Ours, D. P., Siegel, D. I., and Glaser, P. H. (1997). Chemical dilation and the dual porosity of humified bog peat. *J. Hydrol.* 196, 348–360. doi: 10.1016/S0022-1694(96)03247-7

Peltonen, K. (2002). *Direct Groundwater Inflow to the Baltic Sea*. Copenhagen: TemaNord.

Piekarek-Jankowska, H. (1996). Hydrochemical effects of submarine groundwater discharge to the Puck Bay. *Geogr. Pol.* 67, 103–120.

Przeslawski, R., Zhu, Q., and Aller, R. (2009). Effects of abiotic stressors on infaunal burrowing and associated sediment characteristics. *Mar. Ecol. Prog. Ser.* 392, 33–42. doi: 10.3354/meps08221

Reckhardt, A., Beck, M., Greskowiak, J., Schnetger, B., Böttcher, M. E., Gehre, M., et al. (2017). Cycling of redox-sensitive elements in a sandy subterranean estuary of the southern North Sea. *Mar. Chem.* 188, 6–17. doi: 10.1016/j.marchem.2016.11.003

Rezanezhad, F., Price, J. S., Quinton, W. L., Lennartz, B., Milojevic, T., and Van Cappellen, P. (2016). Structure of peat soils and implications for water storage, flow and solute transport: a review update for geochemists. *Chem. Geol.* 429, 75–84. doi: 10.1016/j.chemgeo.2016.03.010

Rezanezhad, F., Quinton, W. L., Price, J. S., Elliot, T. R., Elrick, D., and Shook, K. R. (2010). Influence of pore size and geometry on peat unsaturated hydraulic conductivity computed from 3D computed tomography image analysis. *Hydrol. Process.* 24, 2983–2994. doi: 10.1002/hyp.7709

Rullkötter, J. (2009). The back-barrier tidal flats in the southern North Sea—a multidisciplinary approach to reveal the main driving forces shaping the system. *Ocean Dyn.* 59, 157–165. doi: 10.1007/s10236-009-0197-2

Schiewer, U., and Schubert, H. (2004). Carbon budget and pelagic community compositions at two coastal areas that differ in their degree of eutrophication, in the Southern Baltic Sea. *Estuar. Coast. Shelf Sci.* 61, 89–100. doi: 10.1016/j.ecss.2004.04.006

Schories, D., Kuhlenkamp, R., Schubert, H., and Selig, U. (2014). Rote Liste und Gesamtartenliste der marinen Makroalgen (Chlorophyta, Phaeophyceae et Rhodophyta) Deutschlands. *Nat. Biol. Vielfalt* 70, 179–229.

Schubert, H., Feuerpfeil, P., Marquardt, R., Telesh, I. V., and Skarlato, S. O. (2011). Macroalgal diversity along the Baltic Sea salinity gradient challenges Remane's species-minimum concept. *Mar. Pollut. Bull.* 62, 1948–1956. doi: 10.1016/j.marpolbul.2011.06.033

Scully, M. E. (2010). Wind modulation of dissolved oxygen in Chesapeake Bay. *Estuaries Coast.* 33, 1164–1175. doi: 10.1007/s12237-010-9319-9

Selle, B., Graeff, T., Salzmann, T., Oswald, S. E., Walther, M., and Miegel, K. (2016). Untersuchung eines renaturierten Niedermoores an der mecklenburgischen Ostseeküste - Teil II: salzdynamik und Wasserhaushalt (Investigation of a renatured fen catchment on the Baltic Sea coast of Mecklenburg - Part II: salt dynamics and water balance). *Hydrol. Wasserbewirtschaftung* 60, 259–268.

Smyth, C., Hay, A. E., and Zedel, L. (2002). Coherent Doppler profiler measurements of near-bed suspended sediment fluxes and the influence of bed forms. *J. Geophys. Res. Oceans* 107, 19-1–19-20. doi: 10.1029/2000JC000760

Sokolova, I. M. (2013). Energy-limited tolerance to stress as a conceptual framework to integrate the effects of multiple stressors. *Integr. Compar. Biol.* 53, 597–608. doi: 10.1093/icb/ict028

Sokolova, I. M., Frederich, M., Bagwe, R., Lannig, G., and Sukhotin, A. A. (2012). Energy homeostasis as an integrative tool for assessing limits of environmental stress tolerance in aquatic invertebrates. *Mar. Environ. Res.* 79, 1–15. doi: 10.1016/j.marenvres.2012.04.003

Soomere, T., and Pindsoo, K. (2016). Spatial variability in the trends in extreme storm surges and weekly-scale high water levels in the eastern Baltic Sea. *Cont. Shelf Res.* 115, 53–64. doi: 10.1016/j.csr.2015.12.016

Stachura-Suchoples, K., Enke, N., Schlie, C., Schaub, I., Karsten, U., and Jahn, R. (2016). Contribution towards a molecular taxonomic reference library of Arctic benthic marine diatoms from Kongsfjorden. *Polar Biol.* 39, 1933–1956. doi: 10.1007/s00300-015-1683-2

STALU-MM (2010). *Regelwerk Küstenschutz Mecklenburg-Vorpommern, 2-1 Küstenlängen in Mecklenburg-Vorpommern. Staatliches Amt für Landwirtschaft und Umwelt Mittleres Mecklenburg url*. Available at: http://service.mvnet.de/_php/download.php?datei_id=155707

Tauber, F. (2012). "Meeresbodensedimente in der deutschen Ostsee: Mecklenburger Bucht - Darß, Karte Nr. 2934," in *Maßstab 1 : 100 000*, ed. Bundesamt für Seeschifffahrt und Hydrographie (Hamburg: Bundesamt für Seeschifffahrt und Hydrographie).

Telesh, I., Schubert, H., and Skarlato, S. (2013). Life in the salinity gradient: discovering mechanisms behind a new biodiversity pattern. *Estuar. Coast. Shelf Sci.* 135C, 317–327. doi: 10.1016/j.ecss.2013.10.013

Tiemeyer, B., Albiac Borraz, E., Augustin, J., Bechtold, M., Beetz, S., Beyer, C., et al. (2016). High emissions of greenhouse gases from grasslands on peat and other organic soils. *Glob. Change Biol.* 22, 4134–4149. doi: 10.1111/gcb.13303

Turner, R. L., and Meyer, C. E. (1980). Salinity tolerance of the brackish-water echinoderm *Ophiophragmus filograneus* (Ophiuroidea). *Mar. Ecol. Prog. Ser.* 2, 249–256. doi: 10.3354/meps002249

Umlauf, L., and Burchard, H. (2005). Second-order turbulence closure models for geophysical boundary layers. A review of recent work. *Cont. Shelf Res.* 25, 795–827. doi: 10.1016/j.csr.2004.08.004

van der Meer, J. (2006). Metabolic theories in ecology. *Trends Ecol. Evol.* 21, 136–140. doi: 10.1016/j.tree.2005.11.004

van Diggelen, R., Middleton, B., Bakker, J., Grootjans, A., and Wassen, M. (2006). Fens and floodplains of the temperate zone: present status, threats, conservation and restoration. *Appl. Veg. Sci.* 9, 157–162. doi: 10.1111/j.1654-109X.2006.tb00664.x

Vasander, H., Tuittila, E.-S., Lode, E., Lundin, L., Ilomets, M., Sallantaus, T., et al. (2003). Status and restoration of peatlands in northern Europe. *Wetl. Ecol. Manag.* 11, 51–63. doi: 10.1023/A:1022061622602

Volkmann, C., Halbedel, S., Voss, M., and Schubert, H. (2016). The role of dissolved organic and inorganic nitrogen for growth of macrophytes in coastal waters of the Baltic Sea. *J. Exp. Mar. Biol.* 477, 23–30. doi: 10.1016/j.jembe.2016.01.005

Vousdoukas, M. I., Voukouvalas, E., Annunziato, A., Giardino, A., and Feyen, L. (2016). Projections of extreme storm surge levels along Europe. *Clim. Dyn.* 47, 3171–3190. doi: 10.1007/s00382-016-3019-5

Wahl, M., Jormalainen, V., Eriksson, B. K., Coyer, J. A., Molis, M., Schubert, H., et al. (2011). Stress ecology in Fucus: abiotic, biotic and genetic interactions. *Adv. Mar. Biol.* 59, 37–105. doi: 10.1016/B978-0-12-385536-7.00002-9

Weisse, R., Bellafiore, D., Menéndez, M., Méndez, F., Nicholls, R. J., Umgiesser, G., et al. (2014). Changing extreme sea levels along European coasts. *Coast. Eng.* 87, 4–14. doi: 10.1016/j.coastaleng.2013.10.017

Winde, V., Böttcher, M. E., Escher, P., Böning, P., Beck, M., Liebezeit, G., et al. (2014). Tidal and spatial variations of DI13C and aquatic chemistry in a temperate tidal basin during winter time. *J. Mar. Syst.* 129, 396–404. doi: 10.1016/j.jmarsys.2013.08.005

Woelfel, J., Schoknecht, A., Schumann, R., and Karsten, U. (2014). Growth and primary production characteristics of three benthic diatoms from the brackish Southern Baltic Sea in relation to varying environmental conditions. *Phycologia* 53, 639–651. doi: 10.2216/14-019.1

Conflict of Interest Statement: The authors declare that the research was conducted in the absence of any commercial or financial relationships that could be construed as a potential conflict of interest.

Copyright © 2018 Jurasinski, Janssen, Voss, Böttcher, Brede, Burchard, Forster, Gosch, Gräwe, Gründling-Pfaff, Haider, Ibenthal, Karow, Karsten, Kreuzburg, Lange, Leinweber, Massmann, Ptak, Rezanezhad, Rehder, Romoth, Schade, Schubert, Schulz-Vogt, Sokolova, Strehse, Unger, Westphal and Lennartz. This is an open-access article distributed under the terms of the Creative Commons Attribution License (CC BY). The use, distribution or reproduction in other forums is permitted, provided the original author(s) and the copyright owner(s) are credited and that the original publication in this journal is cited, in accordance with accepted academic practice. No use, distribution or reproduction is permitted which does not comply with these terms.

frontiers in Marine Science

ORIGINAL RESEARCH
published: 08 June 2018
doi: 10.3389/fmars.2018.00201

Impact of Macrofaunal Communities on the Coastal Filter Function in the Bay of Gdansk, Baltic Sea

Franziska Thoms[1], Christian Burmeister[1], Joachim W. Dippner[1], Mayya Gogina[1], Urszula Janas[2], Halina Kendzierska[2], Iris Liskow[1] and Maren Voss[1]*

[1] Department for Marine Biology, Leibniz Institute for Baltic Sea Research, Warnemünde, Germany, [2] Department of Experimental Ecology of Marine Organisms, Institute of Oceanography, University of Gdańsk, Gdańsk, Poland

During three cruises to the Bay of Gdansk, Baltic Sea, the fauna, porewater and bottom water were sampled at stations parallel to the shore and along a transect offshore. Diffusive porewater fluxes were calculated and related to the total net fluxes (TNF) of nutrients. The TNF comprise all nutrients that reach the bottom water from the sediment including diffusive nutrient efflux, discharge from macrozoobenthos and microbial activity. They were determined during *in situ* incubations using a benthic chamber lander, which is rarely done in coastal research. The lander restricts the physical influence of currents and waves on the sediments and only allows nutrient fluxes due to bioturbation by natural communities. Strong benthic-pelagic coupling in the shallow coastal zone suggested a crucial filter function for the bioturbated coastal sediments, which are separated from muddy deep sediments with little or no fauna at a depth of 50 m; in between is a small intermediate zone. While diffusive fluxes were highest at intermediate and offshore stations, TNF were highest at sandy coastal stations, where reservoirs of dissolved nutrients were small and sediments almost devoid of organic material. The greatest impact of macrofauna on sedimentary fluxes was found at stations whose communities were dominated by deep-burrowing polychaetes. The largest TNF were measured directly at the mouth of the Vistula River, where riverine food and nutrients supplies were highest. Macrofauna communities and sediment variables can thus serve as descriptive indicator to estimate the extent of the coastal filter. Finally, based on the total areal size of the different sediment types, annual efflux for the complete coastal zone of the Gdansk Bay was estimated to be 6.9 kt N, 19 kt Si, and 0.9 kt P. Compared to the muddy offshore area, which is twice as large, these amounts were similar for P and threefold higher for N and Si.

Keywords: bioturbation, chamber lander, macrofaunal communities, nutrient fluxes, porewater fluxes, coastal filter, coastal sediments, Baltic Sea

OPEN ACCESS

Edited by:
Karol Kulinski,
Institute of Oceanology (PAN), Poland

Reviewed by:
Jan Marcin Weslawski,
Institute of Oceanology (PAN), Poland
Nafsika Papageorgiou,
Hellenic Centre for Marine Research, Greece

****Correspondence:***
Franziska Thoms
franziska.thoms@io-warnemuende.de

Specialty section:
This article was submitted to Marine Ecosystem Ecology, a section of the journal Frontiers in Marine Science

Received: *07 December 2017*
Accepted: *18 May 2018*
Published: *08 June 2018*

Citation:
Thoms F, Burmeister C, Dippner JW, Gogina M, Janas U, Kendzierska H, Liskow I and Voss M (2018) Impact of Macrofaunal Communities on the Coastal Filter Function in the Bay of Gdansk, Baltic Sea. Front. Mar. Sci. 5:201. doi: 10.3389/fmars.2018.00201

INTRODUCTION

Eutrophication and anoxia threaten large stretches of the world's coastal zones, including those of the Baltic Sea (Diaz and Rosenberg, 2008; Conley et al., 2011). Although most nutrients from rivers are sequestered in the coastal zone, as suggested in the Baltic Sea by the $\delta^{15}N$ budget (Voss et al., 2005), little is known about the processes that impact the recycling of dissolved and particulate

organic matter or the contribution of the related transport processes. The current definition of coastal zones takes into account their high nutrient turnover rates, the product of intensive benthic-pelagic coupling (Dürr et al., 2011). In addition, shallow coastal zones are impacted by wind waves and swell, both of which strengthen benthic-pelagic coupling via sediment resuspension in the breaker zone (Phillips, 1966). Besides physical mixing, the reworking of substrates by macrofauna (bioturbation) modifies natural gradients in the system and alters the exchange of nutrients between sediment and water, which in turn changes the bioavailability of nutrients (e.g., Graf and Rosenberg, 1997; Aller and, 1998). Microbial processes such as denitrification and nitrification are closely related to nutrient availability and are responsible for the efficiency of the coastal filter (Asmala et al., 2017). The highest remineralization potential due to microbes was shown to occur in sediments, and the highest production of particulate organic matter (POM) in the euphotic zone (Andersen and Kristensen, 1992).

The direct impact of macrofauna on nutrient turnover is via detrital food consumption and the predation of secondary consumers on primary consumers. Since most marine invertebrates are ammonotelic, the excreted metabolic waste products are ammonia and ammonium (e.g., Gardner et al., 1993; Wright, 1995; Devine and Vanni, 2002); thus, the benthic ammonium pool is either enlarged or eventually transported into the overlying water. Bioturbation, defined as the mechanical work of macrofauna in or on the sediment, impacts nutrient turnover processes indirectly, through the exchange of solutes and particles across the sediment-water interface through burrows and tubes (bioirrigation), particle mixing, biodeposition, and bioresuspension (Graf and Rosenberg, 1997; Aller and, 1998; Bouma et al., 2009; Laverock et al., 2011).

The impact of fauna on nutrient turnover and release has mainly been studied in lab experiments, which have shown an influence of this process on solute exchange. Higher ammonium concentrations in the bottom water of bioturbated sediments than in sediments with no macrozoobenthic activity were reported by Karlson (2007). However, differences between species have been demonstrated. For example, *Corophium volutator* and *Hediste diversicolor* doubled the ammonium efflux while *Cerastoderma* spp. did not have a positive effect on ammonium release (Pelegri and Blackburn, 1994; Mermillod-Blondin et al., 2004). Reworking by macrofauna increases the availability of nitrate in the sediment and thereby stimulates denitrification, which removes nitrogen from the system (Gilbert et al., 1998). However those effects vary depending on the species (Heisterkamp et al., 2012). The authors showed that the occurrence of the polychaete *H. diversicolor* increased nitrification rates in the system due to the ammonium supply, resulting in nitrogen retention. To understand the main net effect of fauna on nutrient removal or retention in the environment requires measurements of all related processes in combination with both, information on the structure of the faunal community and efflux data. Furthermore, an accurate investigation of the effect of macrozoobenthos and bioturbation on the change in nutrient availability must include a consideration of the differences between sedimentary nutrient fluxes in the presence and absence of fauna.

Artificial core experiments with rebuilt sediment column or modified infauna can provide information on an animal's effect on nutrient release from the sediment but not on net fluxes, as these involve the natural microbial and macrofauna community. For example, denitrification can only be quantified in naturally layered sediment cores with strong gradients in oxygen and nitrate, which are usually not obtained in cores rebuilt in the lab. Further, the mutual impact on the activity of one benthic species by another can be positive, neutral or negative; accordingly, the effect of bioturbation in a natural benthic community is less investigated and might be never simply the sum of the bioturbation effects of a single species or of a few individuals. Thus, while artificial core experiments yield valuable information on general processes, they do not necessarily allow the quantification of real-life fluxes. Even *in situ* cores may not include a representative, natural, undisturbed fraction of the benthic community, as a typical core 10 cm in diameter may include a community in which 200 ind/m^2 of its residents have been disturbed or damaged during the retrieval. Contrary, only 50 ind/m^2 are disturbed using cores 30 cm in diameter (Glud and Blackburn, 2002). Moreover, large individuals, for example bivalves or starfish, are often accidently excluded from measurements performed in small cores, even if in the field they are major contributors to nutrient exchange and oxygen consumption (Glud et al., 1998). Consequently, current knowledge of the impact of entire communities on nutrient cycling in the field remains deficient.

Chamber lander incubations are an appropriate tool to study nutrient release from sediments while excluding the influence of physical advection on vertical nutrient fluxes, but including the effect of a natural benthic community. In this study, a chamber lander system was used to address the following questions: What is the difference between *in situ* TNF and diffusive fluxes at the same station? How is the flux impacted by different benthic communities from the same site? To answer these questions, we compared data on the classical diffusive fluxes determined in 10-cm diameter cores with chamber lander data by following a holistic approach that considered all potential fluxes. We hypothesized that, due to the presence of fauna, TNF would be higher in near-coastal sediments than offshore and that an effect of deep burrowing animals will be visible in the *in situ* approach. Finally, we evaluated the coastal filter function of the Bay of Gdansk with respect to the presence of macrozoobenthos.

MATERIALS AND METHODS

Study Area

The study area is located in the Polish part of the Bay of Gdansk in the southern Baltic Sea. The Vistula River is one of the largest rivers draining into the Baltic Sea. It contributes 90% of the total inflow to the Bay of Gdansk (Witek et al., 2003), with an annual

Abbreviations: TNF, total net fluxes; AF, amplification factor; LOI, loss on ignition.

N load of ∼98 kt (recalculated from data of Pastuszak and Witek, 2012).

Samples were collected during three 10- to 15-day cruises with the "RV Elisabeth Mann Borgese" and "RV Alkor" in 2014 (July), 2015 (February), and 2016 (March) covering summer, winter, and spring, respectively. Measurements and samples were taken at 19 different stations (10–111 m water depth) (**Figure 1**). Due to inflows from the Vistula River, the salinity is in the range of 0–12, with salinities of almost 0 directly at the mouth and as 12 in the bottom water of the Gdansk Deep. Water temperatures in summer were between 18°C at the surface and 5°C in the bottom water. In winter and spring, temperatures varied between 3 and 6°C. The Vistula plume is variable and wind-driven, in a complex manner. In a steady state the plume is transported eastwards parallel to the coast.

To cover all types of sediments, cores were taken along two transects; one extending directly offshore from the mouth of the river to the Gdansk Deep and the other parallel to the coast. This allowed coastal stations (down to 50 m water depth) to be distinguished from offshore stations (60–110 m water depth). Station VE07 (50 m water depth) differed from the other stations in that the values of the collected data were between those of the other stations; it was therefore considered as an intermediate station. The properties of the sediment at station VE07 suggested the presence of sandy as well as muddy components with a high organic matter content, such that an exact description of the sediment type was not possible.

The Bay of Gdansk has an area of 1,141 km^2 where the water depth is <50 m and 2,153 km^2 where the depth is >50 m. Its mostly well-sorted sediments are of different types and the entire area is characterized by a distinct patchiness (**Figure 1**). The three main sediment types were: fine sand (type 1), medium sand (type 2), and mud/silt (type 3). The areas covered by sediment types 1–3 were calculated using the program ArcGIS 10 (ESRI 2011) together with the WGS_1984_UTM_Zone_33N Projected Coordinate System.

Sediment and Porewater

At each sampling station, five sediment cores each 10 cm in diameter were taken using a multicorer. At coarse-grained sandy stations, multicorer sampling was not possible; instead, the sediments were sampled using Haps corers (KC Denmark) and subsampled with the same 10-cm diameter cores used for the multicorer, to ensure the same volumes. All cores had undisturbed surfaces and clear water on top. Until the cores were processed, they were kept cold and dark. Two of the cores were immediately used for porewater retrieval via rhizon sampling (Seeberg- Elverfeldt et al., 2005). The first milliliter was used to rinse the rhizon and 4 ml were stored frozen at −20°C for later nutrient analysis. Only the porewater samples from the winter cruise (2015) were measured onboard directly after sampling. The rhizons from rhizosphere had a membrane 5 cm in length and with a pore size of 0.12–0.18 µm; they were kept in ultra-pure water for 15 min before they were used in the sampling, to obtain suction during the filtration. Three of the cores from each site were sectioned into 0.5-cm slices in the upper 3 cm, 1-cm slices down to 10 cm, and 2-cm slices down to a sediment depth of 20 cm. The samples were kept frozen at −20°C until the analysis. Subsamples of each slice were used for the determination of water content and porosity, organic matter content, and grain size. Samples used to determine the water content were freeze-dried for 2.5 days, at which time they had reached a constant weight, and then weighed to determine the weight loss. The percentage of each sample composed of water is defined as the porosity. The organic matter content of the dry samples was measured as the

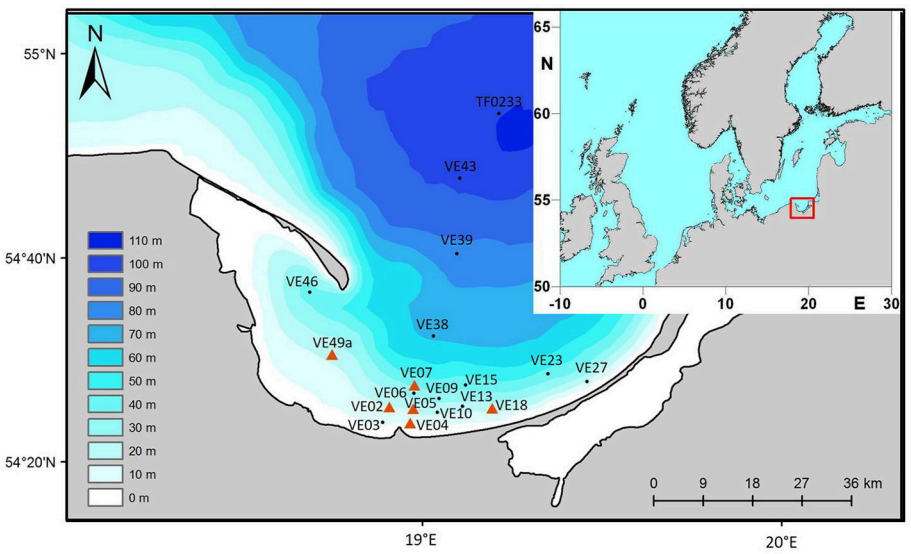


FIGURE 1 | Location of the sampling stations in the Bay of Gdansk, southern Baltic Sea. The inlay shows a map of Northern Europe, the rectangle marks the Bay of Gdansk.

loss of ignition (LOI) after heating in a muffle furnace at 550°C for 5 h.

The grain size in each slice was analyzed using a Cilas gradistrat 1180 laser granulometer according to a procedure based on a laser multi-angle analysis to measure particle diameter in the range of 0.04–1,000 μm. Particles >1,000 μm were retained by a sieve and not registered quantitatively, but they made up only a small fraction of the sample. The sediment-type designations used herein are based on the median grain size of each sample.

The $\delta^{15}N$ values in the upper 3 cm of the sediment were analyzed using a Thermo Scientific Delta V Advantage (Thermo) isotope mass spectrometer combined with a Conflo IV (Thermo) interface and a Flash 2000 (Thermo) elemental analyzer. Each sample was dried for at least 2 days at 50°C and then homogenized with mortar and pestle. For mud and sand samples, 5 and 100 mg were weighed, placed in tin caps, and pressed into pellets. To measure the organic C content, a parallel sample was first acidified by adding ∼10 μl of HCl (2N) and then processed as described for the $\delta^{15}N$ samples except that silver caps were used.

Benthic Chamber Lander Incubations

In situ incubations to measure benthic nutrient fluxes across the sediment-water interface were done with the automated mini-chamber lander system (Unisense, DK). The first deployment was in February 2015, at station VE02; all other stations (VE04, VE05, VE07, VE49a, and VE18) were sampled in March 2016. The incubation chamber was square, with rounded corners, and Teflon-coated to avoid reactions between ambient oxygen and the stainless steel cover of the chamber. The adjustable feet and changeable weights on the lander frame enabled the chamber to penetrate the sediment to a depth of ∼5 cm. The chamber proportions were 30 × 30 × 35 cm (width × length × height) and its sediment penetration depth was 5 cm. The enclosed incubation volume is large enough (27 L) to avoid oxygen depletion. The sediment area covered by the chamber was 900 cm^2. The chamber size was favorable toward smaller chambers and cores, as the inaccuracy in measurements of oxygen uptake was 10% (few fauna) or 20% (abundant fauna), in contrast to core incubations in which the inaccuracy is 26 and 41%, respectively (Glud and Blackburn, 2002). The chamber lid was open during launch but autonomously closed after an acclimatization time defined in the program. The water inside the chamber was stirred during the whole sampling period at 15 rpm to ensure sample homogeneity. Preliminary tests showed that a homogenous water sample was obtained after 5 min of stirring. No resuspension effects from the bottom could be detected. Up to 12 water samples of 55 ml each were removed directly from the chamber using polypropylene syringes operated by an integrated water-sampling rosette. During the 12- to 15-h incubation used for each deployment, the first water sample was taken directly at the beginning of the incubation, and subsequent samples every 65–75 min. Oxygen inside the chamber was measured using an optode to monitor the total oxygen uptake and thus the chamber tightness. Only one small port in the chamber lid was kept open to ensure a pressure balance while retrieving the samples. The oxygen concentration profiles showed that the open port was not large enough for environmental water to enter the chamber and thereby disturb the measurements. The samples were incubated overnight, including at least 2 h before dusk and after dawn. The water samples were filtered through a syringe GF filter (Whatman) and frozen at −20°C directly after retrieval of the lander system.

Nutrient Analysis

Nutrients of all samples (porewater, bottom water, lander incubation) were measured colorometrically according to Grasshoff et al. (1999) using a SEAL analytical QuAAtro continuous segmented flow analyzer. Methods for NO_2^- and NO_3^- determination were adapted for the SEAL based on a procedure developed by NIOZ (Grasshoff et al., 1999). NH_4^+ levels were measure using sodium salicylate, which results in the formation of the same color complex obtained with the phenol reagent. To address different nutrient concentration ranges six-point- calibrations were done at different quantification limits. For porewater samples, the quantification limits were as follows: 0.25 μmol PO_4^{3-}/l, 0.05 μmol NO_2^-/l, 0.5 μmol NO_3^-/l, 1.5 μmol NH_4^+/l, and 2 μmol SiO_2/l. For bottom water samples from the field and from the lander incubations, the quantification limits were the following: 0.25 μmol PO_4^{3-}/l, 0.05 μmol NO_2^-/l, 0.5 μmol NO_3^-/l, 0.5 μmol NH_4^+/l, and 1 μmol SiO_2/l. We did not find significant increase in SiO_2 concentrations when samples were filtered through GF/F, which was done for pore waters only. However, we took care to process samples as fast as possible. All nutrient samples were frozen at −20°C directly after sampling until used in the measurements, except the porewater samples of the winter cruise in 2015, which were analyzed onboard immediately after sampling.

Flux Calculations

Diffusive nutrient fluxes were calculated according to Fick's first law of diffusion:

$$J = -D_S \left(\frac{c(z + \Delta z) - c(z)}{\Delta z} \right) \quad (1)$$

where J is the flux (mmol m^{-2} d^{-1}), D_s the effective diffusion coefficient, c the concentration of a nutrient, z the sampling depth, and Δz the distance between two sampling depths. Fluxes were calculated using steady porewater nutrient profiles. If the profile shows vertical oscillation, a 1-2-1- filter was used to obtain steady profiles. The effective diffusion coefficient for each nutrient in the respective sediment was calculated according to Equation (2), using the diffusion coefficients for dissolved nutrients in water (D_0) (Iversen and Jørgensen, 1993; Schulz and Zabel, 2006). Porosity (Φ) was calculated according to Flemming and Delafontaine (2000) where n reflects a coefficient for the sediment type.

$$D_S = \frac{D_0}{1 + n(1 - \Phi)} \quad (2)$$

For each diffusive flux calculation, two parallels were considered. The TNF were used to calculate the flux during the incubation.

Finally, the fluxes were extrapolated to 1 m^2 based on the chamber volume of 27 l.

Macrofauna

At each station, at least four parallel samples were taken with a 0.1 m^2 Van Veen grab, sieved with a 1-mm mesh sieve, and preserved in 4% borax-buffered formalin. At least four parallel fauna samples were taken at each site while the ship was remained in a fixed position. The grab samples covered an area of several tens of square meters. It was therefore assumed that the average fauna sample also represented the fauna in the incubation chamber. The fauna was sorted and identified to the lowest taxonomic level using a stereomicroscope. Individuals were counted and weighed to determine their abundance and biomass (biomass data not shown in this study). To relate the fauna to sediment properties and nutrient fluxes. The faunal species were grouped according to their burrowing depth and irrigation behavior (e.g., Davey, 1994; Zettler et al., 1994; Pelegri and Blackburn, 1995), as these are the most relevant features for solute exchange between sediment and water.

Statistics

Principal Component Analyses (PCA) and cluster analysis were applied using the software Statistica (Statistica System Reference, 2012). An agglomerative cluster analysis was computed with the variables sediment surface grain size, LOI and water depth using Euclidian distance norm (**Figure 3** right). Functional traits of the macrofauna, sediment properties and nutrient fluxes are subject of a PCA computing the eigenvalues and eigenvectors of the correlation matrix to analyses the dominant relationship in the coastal system (**Figure 8**).

A canonical correlation analysis (CCA) was performed between the leading eigenvectors of benthic animals, TNFs, and sediment variables (depth, grain size, LOI) using statistical downscaling methods (von Storch et al., 1993). This method has been applied e.g., to macrozoobenthos communities in the German Bight (Kröncke et al., 2013) or in the Gulf of Riga (Dippner and Ikauniece, 2001) and details on the method were given in Heyen and Dippner (1998).

RESULTS

Source of Particulate Organic Nitrogen

The organic material in the sediment was characterized by high $\delta^{15}N$ values (8.6 ± 0.8‰) at stations with a water depth of <50 m. The highest values were at the shallowest stations near the river mouth. The $\delta^{15}N$ values of the sediments at stations deeper than 50 m, including the intermediate station VE07, were lower (6.3 ± 0.9‰). A comparison of the $\delta^{15}N$ values of POM from the Vistula River (8‰) and the surface waters of the offshore station farthest from the river mouth (station TF0233, 5‰) suggested a riverine impact on the organic matter at coastal sediments, but a declining influence offshore (**Figure 2** left). This relationship was less obvious in $\delta^{13}C$ values of the surface sediment. The $\delta^{13}C$ values were higher at coastal stations (−26.8 ± 0.8‰) and slightly lower (−25.8 ± 0.5‰) further offshore (**Figure 2** right), a trend typical for coastal sediments. In fine and medium sand the standard deviation for $\delta^{15}N$ values was ±0.63‰ and ±0.6‰ for $\delta^{13}C$ values. For mud the standard deviation was of ±0.29‰ for $\delta^{15}N$ values and of ±0.53‰ for $\delta^{13}C$ values.

Sediment Characteristics and Organic Matter

The properties of the well sorted sediment samples suggested the patchiness of fine and medium sand, with smaller areas covered by medium- and coarse-grained silt emerging in shallower areas. All of the sediments from the offshore stations with a water depth >50 m were muddy, while those from coastal stations had lower organic matter content and higher grain size. Fine and medium sand had an average standard deviation of ±23.15 μm for and mud an average standard deviation of ±4.35 μm. The median grain size and organic matter content of the surface sediments correlated with the water depth, based on R^2 values of 0.88 and 0.92 for the winter and spring cruises, respectively. **Figure 3A** displays surface values only. Further analyses indicated the same structure in the vertical up to a depth of 20 cm (not shown). For the three parallel cores at each station we found an average standard deviation of ±0.89% dry sample at sandy sites and of ±1.6% dry samples at muddy stations. The division in three main group is also supported by a cluster analysis (**Figure 3**). The cluster analysis underlines that especially the deep muddy stations and the coastal medium sand stations of both years group together, the fine sand stations build the third main cluster. Station VE07_2015 groups to the offshore stations while the same station sampled in 2016 groups to the fine sand stations. That may illustrate its variability and the intermediate character between sands and muds at 50 m depth.

Porewater Nutrient Concentrations and Fluxes in the Cores

The nutrient concentrations did not differ in magnitude during the different seasons. Porewater nutrient concentrations are closely related to the sediment type and, in general, higher concentrations of SiO_2, PO_4^{3-}, and NH_4^+ are found in the porewaters of muddy sediments than in those of sandy, shallower sediments. The properties of the porewater from the near-surface sediment layers were quite similar and in the lower ranges at all stations (<10 μmol/l for PO_4^{3-} and NH_4^+, <1 μmol/l for NO_2^-, ∼5 μmol/l for NO_3^-, and 10–50 μmol/l for SiO_2). In deeper sediment layers the differences were more pronounced (see Supplementary Figure 1). The porewater concentrations of SiO_2, PO_4^{3-}, and NH_4^+ were highest at muddy offshore stations, but much lower at coastal stations. The maximum NH_4^+ concentration was between 2,000 and 3,000 μmol/l, while the maximum PO_4^{3-} values were as high as 360 μmol/l, and those of SiO_2 up to 1,500 μmol/l. At coastal sites, the maximum NH_4^+ concentration was in the range of 100–200 μmol/l, measured in deeper waters. The PO_4^{3-} concentrations at all coastal stations were as high as 50 μmol/l, with summer values being slightly higher than winter and spring values. The SiO_2 concentration in coastal waters was between 200 and 500 μmol/l. The porewater nutrient concentrations at the intermediate station VE07 were mostly between those of the coastal and offshore stations. Coastal

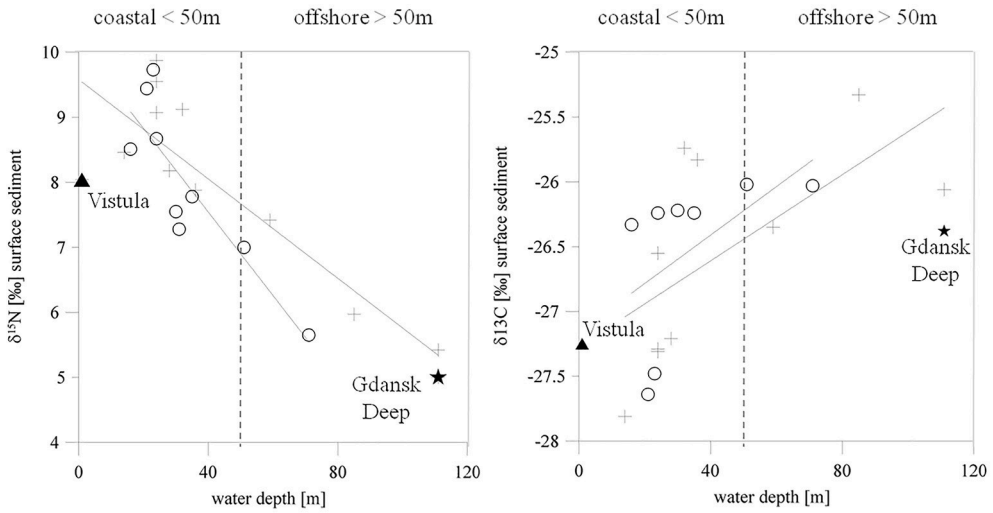


FIGURE 2 | $\delta^{15}N$ **(left)** and $\delta^{13}C$ **(right)** values of the organic matter from the upper surface sediments as a function of water depth. Crosses mark winter 2015 and circles spring 2016 data. The straight lines show the regression. The filled triangle represents Vistula River POM, and the filled star the surface-water POM at the deep-water station TF0233.

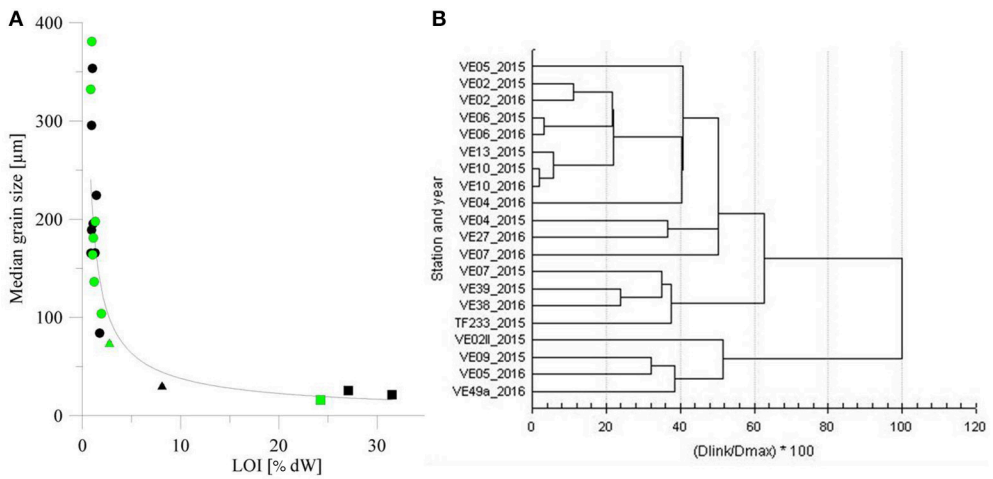


FIGURE 3 | (A) Correlation of the loss on ignition (LOI, in % dW) and the median grain size for samples collected during winter cruise AL449 (black) and spring cruise EMB123 (green). Dots indicate the coastal stations, triangles the intermediate stations, and squares the offshore stations. **(B)** Cluster analysis of surface grain size, surface LOI, and water depth of all stations against the distance value (D) in percent.

stations VE04 and VE03, located close to the river mouth, showed small deviation from the general patterns whereas their porewater nutrient concentrations were lower than those at the offshore stations. Measurable NO_3^- and NO_2^- concentrations were detected only in sandy sediments; at muddy sites the concentration of both nutrients was below the detection limit (see Supplementary Figure 1).

The concentration gradients were related to different fluxes, with higher diffusive fluxes of SiO_2, NH_4^+, and PO_4^{3-} at muddy stations (except stations VE03 and VE04). Most fluxes did not differ in magnitude between seasons, thus indicating a stable condition of the sediment porewater. A significant difference occurred at station VE07, where the diffusive flux values in winter were 3–14 times higher than those in spring. Diffusive SiO_2 fluxes at the coastal stations were between 0.01 and 0.14 mmol m^{-2} d^{-1}, with the exception of station VE03, located close to the river mouth, where the flux was 2.11 mmol m^{-2} d^{-1} (0.62 mmol m^{-2} d^{-1} for NH_4^+), and station VE46, with a flux of 0.22 mmol m^{-2} d^{-1} (0.21 mmol m^{-2} d^{-1} for NH_4^+). The latter station with muddy sediment in Puck Bay was largely influenced by sediment type and not by depth alone. At the muddy offshore stations, SiO_2 fluxes were 0.44–0.66 mmol m^{-2} d^{-1}. NH_4^+ fluxes were in the range of 0.002–0.62 mmol m^{-2} d^{-1}, with a mean of 0.06 mmol m^{-2} d^{-1}. At station VE07, the diffusive NH_4^+

flux was 0.06–0.18 mmol m^{-2} d^{-1} and at the offshore stations 0.21–0.87 mmol m^{-2} d^{-1}. For PO_4^{3-}, the fluxes were between 0.004 and 0.03 mmol m^{-2} d^{-1} (except VE03: 0.06 mmol m^{-2} d^{-1}, and VE46: 0.01 mmol m^{-2} d^{-1}) at coastal stations, between 0.005 and 0.07 mmol m^{-2} d^{-1} at the intermediate station, and between 0.01 and 0.68 mmol m^{-2} d^{-1} at the offshore stations. In muddy sediments, diffusive NO_3^- and NO_2^- fluxes could not be calculated, but the values determined were in the range of −0.01 to −0.006 mmol m^{-2} d^{-1} indicating a flux into the sediment (Supplementary Table 1).

Nutrient and Oxygen Fluxes in Chamber Lander Incubations

Chamber lander incubations were only possible in shallow water down to a depth of 50 m.

Continuous oxygen consumption was determined in all sediments but only down to a minimum of 299.63 µmol/l. The most rapid decrease in the oxygen concentration was at station VE04, near the mouth of the Vistula River, where the flux was −31.48 mmol m^{-2} d^{-1}. The oxygen fluxes at stations VE02 and VE05 were only half as high. At the eastern and western stations VE18 and VE49a, oxygen consumption was slightly lower: 12.43 and 11.26 mmol m^{-2} d^{-1}, respectively. At station VE07, the oxygen concentration inside the chamber dropped very slowly, as indicated by a flux of −2.37 mmol m^{-2} d^{-1} (**Figure 4**).

Net nutrient fluxes were high at all sandy stations and lower at the intermediate muddy station. At all stations, nutrient concentrations increased over time, except for NO_3^- at station VE04 and NO_2^- at station VE49a, where the respective concentrations decreased over time. Generally, at all stations the highest initial concentrations were those of NO_3^- and SiO_2 whereas NO_2^- and PO_4^{3-} concentrations remained low throughout the incubations (**Figure 5**). The strongest concentration changes were those of NH_4^+ at the coastal stations, where initial concentrations were 0.5–2.2 µmol/l but increased to 1.3–6.8 µmol/l by the end of the incubation. At VE07, the concentrations of all nutrients fluctuated during the incubation. Large changes in the PO_4^{3-} and NO_2^- concentrations over time were not detectable at any of the coastal stations. Fluctuations in nutrient concentration during the incubations caused TNF with respect to the start and end values that were lower than the fluxes over the short term, in some cases. A decrease in the concentration of NO_3^- from 8.2 to 7.3 µmol/l after 11 h (**Figure 5**) was measured at station VE04 (see Supplementary Material).

The data obtained from the chamber Lander incubations were used to calculate the TNF. Based on the nutrient concentrations inside the chamber, all fluxes were positive, with two exceptions, at stations VE04 and VE49a, where the total NO_3^- flux and the total NO_2^- flux, respectively, were negative, which may indicate a flux into the sediment. The TNF was lowest at station VE07 in nearly all cases, while at the sandy stations the TNFs were high. The highest averaged fluxes were those of SiO_2, and the lowest positive fluxes those of NO_3^- at all stations. The fluxes at all stations ranged between 0.01 and 0.16 mmol m^{-2} d^{-1} for PO_4^{3-}, from −0.77 to 0.91 mmol m^{-2} d^{-1} for NO_3^-, and from 0.08 to 3.04 mmol m^{-2} d^{-1} for NH_4^+. The maximum flux of all incubations occurred at station VE04, where the NH_4^+ flux was 3.04 mmol m^{-2} d^{-1}; this value exceeded even the SiO_2 flux (2.61 mmol m^{-2} d^{-1}) (**Figure 6**).

Comparison of TNF and Diffusive Fluxes

Considering all nutrient fluxes, an amplification factor (AF) is defined as the relation of TNF to the diffusive fluxes, which showed a band- width of 1.3–303. The highest AF of 303 occurred in NO_3^- at station VE05. This was the only station where a positive diffusive flux of NO_3^- was measured. The second highest flux was that of SiO_2 (AF of 11.9–255). For PO_4^{3-} and NH_4^+, the AF were quite similar at the different stations: 10–16 and 1.3–32.5, respectively. In nearly every case, the AF for the intermediate station VE07 were lower than those of the coastal stations. For the coarse sands at stations VE18 and VE49a, the TNF of SiO_2 was lower than at the other stations, but the AF were higher (**Figure 6**), which may have been related to the presence of fauna (see below).

Macrofaunal Composition

The individual abundances of macrofauna and the species richness decreased with larger distance to the shore and to the mouth of the Vistula River (**Figure 7**). The highest abundances were measured at stations VE02, VE04, and VE05, closest to the river mouth, followed by stations VE18 and VE49a, east and west of it. The abundance at the intermediate station VE07 was approximately one-third of the average abundances at the coastal stations. At station TF0233 (**Table 1**), representing the Gdansk Deep, the absence of any fauna was consistent with the lack of oxygen in these waters. Small, surface-living animals, dominated by the surface-grazing snail *P. ulvae*, contributed numerous individuals but little biomass. Shallow- and deep-burrowing animals accounted for a large percentage of the macrofaunal community at coastal stations. The macrofaunal communities in the Bay of Gdansk were dominated by following species: the amphipod *C. volutator* at station VE02, the soft-shell clam *Mya arenaria* at station VE04, and the polychaete *Marenzelleria* spp. at station VE05. Station VE07 was dominated by shallow-burrowing animals, mostly the small clam *M. baltica* and the amphipods *P. femorata* and *M. affinis*. This station lacked deep-burrowing animals, in contrast to the coastal stations, and harbored only a few individuals of *Marenzelleria* spp. and *P. elegans*. Excluding the highly abundant *P. ulvae* at the coastal stations, the overall abundance of shallow-burrowing individuals at station VE07 was only half or less of that of the sediment infauna at the coastal stations. Only two of the three offshore stations were inhabited by macrofauna: at station VE39 (5 individuals per m^2) and at station VE38 (32 individuals per m^2). At the latter station, the macrofaunal community comprised *M. baltica* and *B. sarsi*, both of which are surface-living and shallow-burrowing species. Generally, mollusks and polychaetes dominated over crustaceans in the waters of the Bay of Gdansk (**Table 1**).

Finally, we performed a principal component analysis (PCA) to figure out dependencies between high of $SiO2_2$ TNF, SiO_2 factors and different variables (**Figure 8**). The dominant

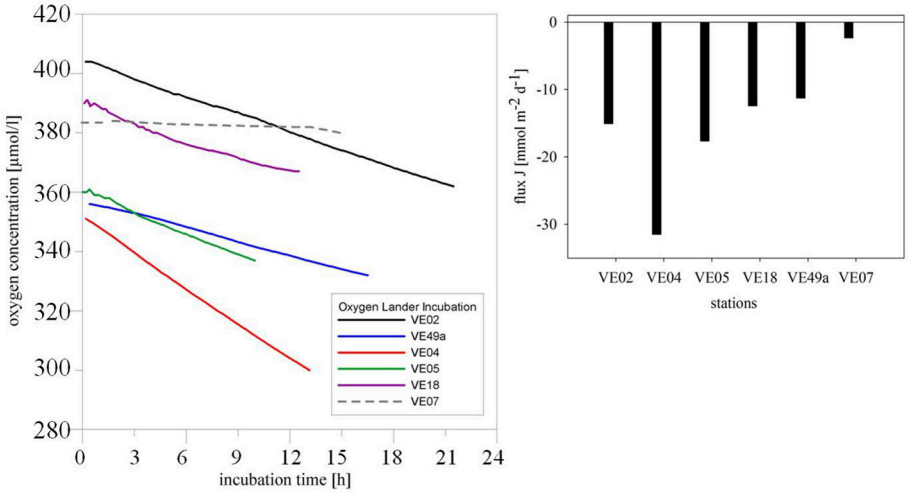


FIGURE 4 | Change in the oxygen concentrations in the chamber over time. Solid lines in black (VE02), blue (VE49a), red (VE04), green (VE05), and violet (VE18) indicate the coastal stations, and the dashed gray line the intermediate station VE07 **(left)**. Oxygen consumption at the different stations is expressed as the flux (mmol m^{-2} d^{-1}) **(right)**.

pattern with an amount of explained variance of 78% in the first two modes indicated a clear dependence between AF and deep burrowing tube dwellers as well as a strong negative correlation between AF and SiO_2 inventory in the sediment. Further, the high of TNF is depending on more diverse variables such as most of the remaining groups of fauna which built the major portion of the macrozoobenthos community. The water depth is negatively correlated with the TNF.

The CCA pattern of the dominant eigenvectors of sediment variables and TNFs were uncorrelated ($r = -0.17$) and a negative Brier based skill score indicated a poor potential predictability (Livezey, 1995). In contrast, a significantly high correlation occurred in the CCA between benthic animals and TNFs (**Figure 9**).

Extrapolation of the Data to the Whole Bay of Gdansk

Diffusive and total nutrient fluxes were estimated based on the area covered by each representative sediment type (**Figure 10**), for coastal and for offshore areas. The annual diffusive and total fluxes of NH_4^+-N from the sediment into the bottom water in the coastal zone of the Bay of Gdansk were 0.31 and 6 kt, respectively. For PO_4^{3-}-P, the annual diffusive and total fluxes were 0.11 and 0.84 kt, respectively. The largest annual diffusive and total fluxes were those of SiO_2-Si: 0.92 and 18.83 kt, respectively. Adding the total annual NO_3^--N efflux (0.74 kt) or that of NO_2^--N (0.16 kt) yielded a balance of 6.9 kt N per year originating from the sediment and entering the bottom water in the Bay of Gdansk's coastal zone. For the offshore area, the total fluxes were consistent with the diffusive fluxes of the muddy stations. Extrapolation of NH_4^+- N, SiO_2- Si, and PO_4^{3-} -P to the entire offshore area resulted in annual fluxes of 2.96, 6.8, and 0.9 kt, respectively.

DISCUSSION

Characterization of the Coastal Zone: Zonation of the Study Site

In contrast to other studies on coastal zone nutrient cycling, most of which investigated lagoons or semi-enclosed bights, the focus of our study was an open bay with strong environmental gradients. This region was divided into sub-areas based on the grain size, LOI, and stable isotope data ($\delta\ ^{15}N$, $\delta\ ^{13}C$) of the sediments and the POM, thus separating an area shallower than 50 m depth, covered mainly by fine and medium sand, from offshore muddy sediments. That is a typical feature of coastal zones, as shown, for example, by Reid et al. (2005) for the US Atlantic coast, Wilson et al. (2008) for various regions in the world ocean and by Leipe et al. (2011) for the southern Baltic Sea. Waters with a depth of <50 m may be the natural border for a close benthic-pelagic coupling. If the impact of wind-induced waves reaches the bottom, fine-grained material is resuspended into the water column and transported parallel to the coast by the long- shore current (Longuet- Higgins, 1970). The consequence is that the shallow areas are covered by coarser- grained sediment. The $\delta^{15}N$ and $\delta^{13}C$ values suggested a strong impact of Vistula-River-derived organic matter on the sea bottom near the river mouth and dilution of the signal further offshore, while the higher $\delta\ ^{15}N$ values were an indicator of land-derived material (Voss et al., 2005). Even if the Vistula River plume propagated quasi geostrophic balanced, parallel to the coast, the sediments of the entire coastal zone showed an intense $\delta^{15}N$ signal. Under oxygen availability, even the fine fraction in sandy sediments may be used more efficiently than the muddy sediments (Leipe et al., 2017). However, in our study the fine fraction was not analyzed separately, such that information on the organic carbon content of sediment <63 µm was not available. At the muddy stations, the grain size of the complete

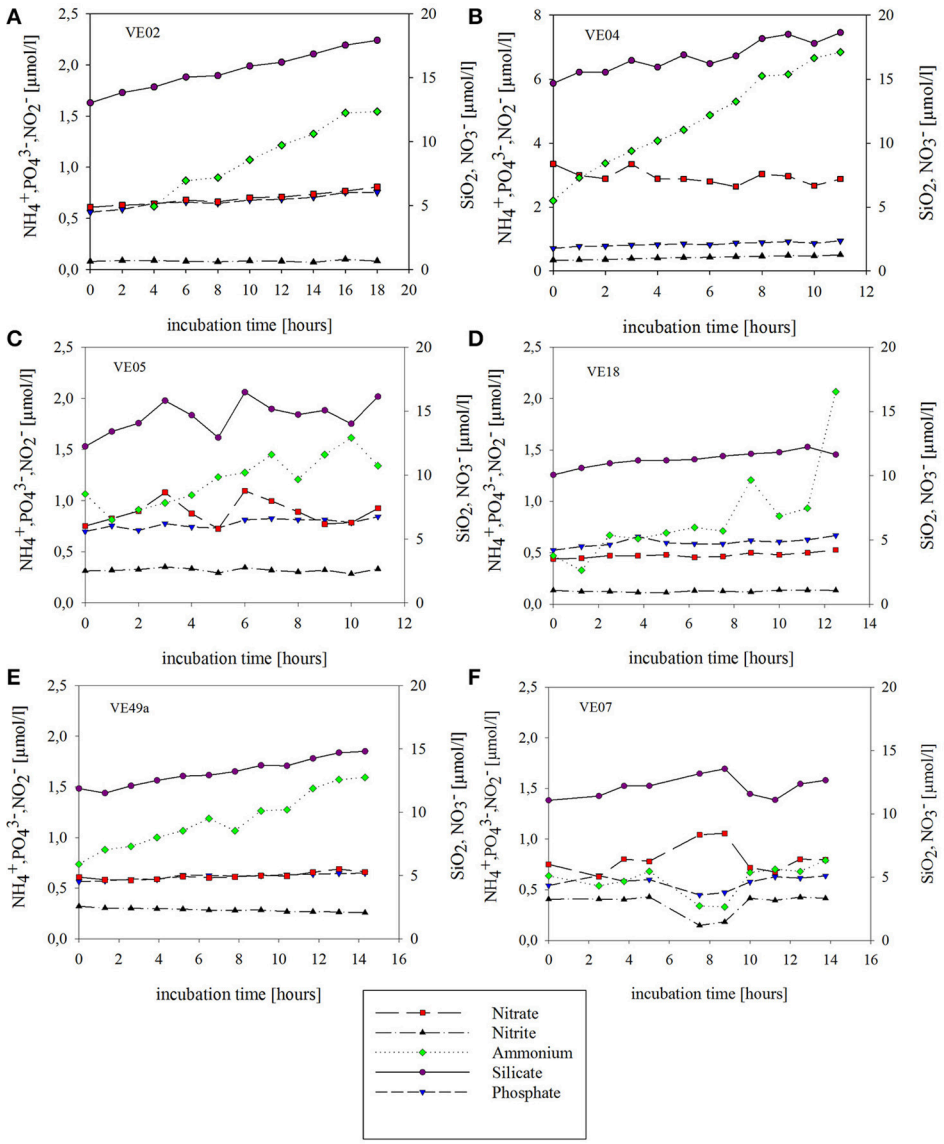


FIGURE 5 | Concentration changes over time during the chamber lander incubations of sediment and bottom water at five sandy coastal stations **(A–E)** and one muddy intermediate station **(F)**. Symbols indicate the time points at which the water samples were taken (via syringes) and the concentration of each nutrient at each time point. The lines connecting the time points show the tendency of the concentration development. SiO_2 is indicated in purple, NH_4^+ in green, NO_3^- in red, NO_2^- in black, and PO_4^{3-} in blue.

sediment volume could be assigned to the fine fraction. Fauna may play an important role in changing the bioavailability of this organic fraction. Leipe et al. (2017) described an effect of the fine fraction of the sandy sediments of the Oderbank (Germany), showing that sand and mud provide nearly the same amount of organic carbon. Thus, the organic and fine fractions in sandy sediments are readily available to the fauna and microbes and thus potentially fully degraded by them, whereas this is not the case in mud. The offshore macrofaunal abundance showed a pattern similar to that of the sediment characteristics (**Figure 7**).

Species richness and individual abundances were separated by the 50-m depth contour. Since the sediment type determines the settlement of macrofauna, most species will be found in the sandy sediment or in sand-mud mixtures, with few species and low abundances in pure mud (Künitzer et al., 1992). Denisenko et al. (2003) reported that community structure is highly influenced by the total organic carbon content and the water depth of shallow waters. While at deeper stations the settling of POM from the pelagial may be restricted by stratification, at coastal sites larger amounts of potential food reach the bottom and can lead to the development

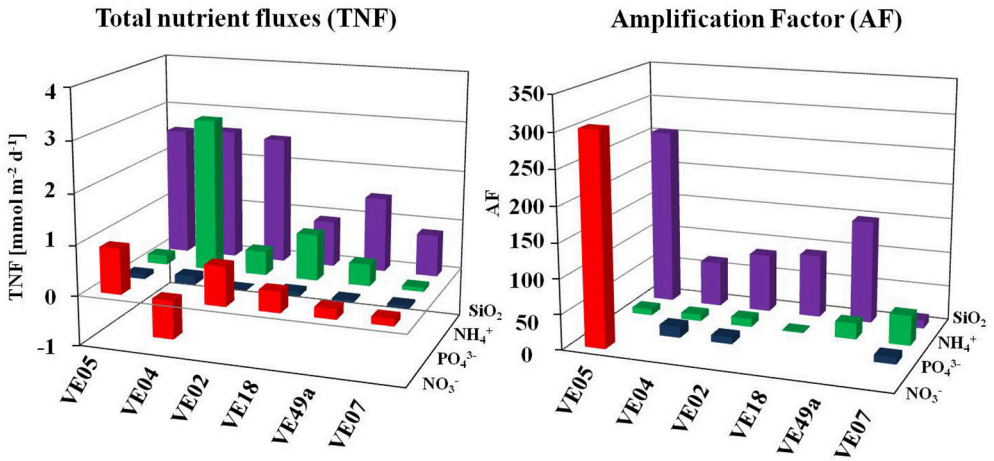


FIGURE 6 | Left TNF at each station for NH_4^+, NO_3^-, PO_4^{3-} and SiO_2. AF is shown on the **right** site.

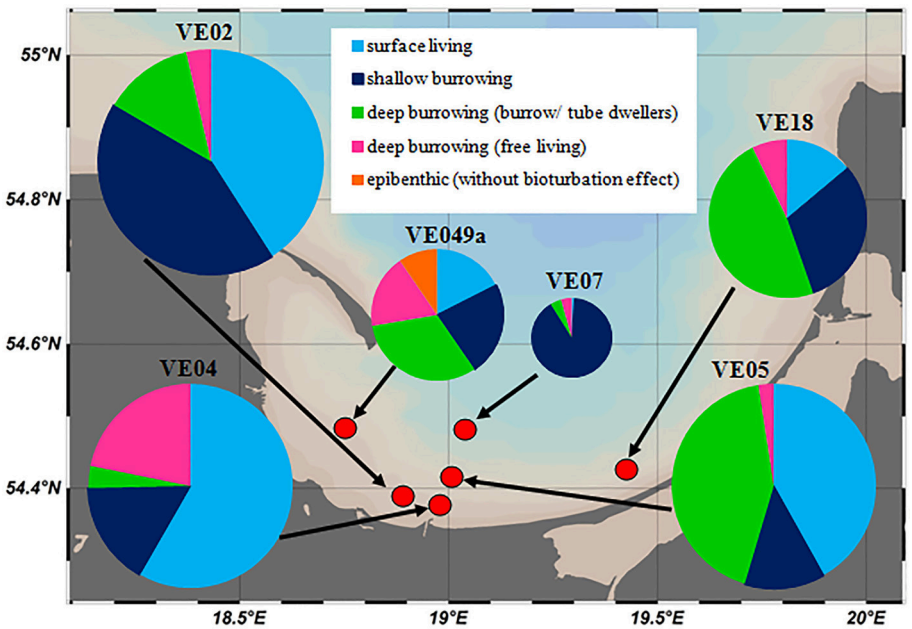


FIGURE 7 | Overview of the proportional occurrence and distribution of functional groups of macrozoobenthos at the six chamber lander incubation stations. The sizes of the pie charts reflect the total individual abundances at the stations, given in **Table 1**.

of a greater infauna biomass. Additionally, biodeposition induced by deposit feeders increases the introduction of carbon and nitrogen to the benthic system (Norkko et al., 2001).

Therefore, in the absence of tides, the factor limiting macrofaunal occurrence is oxygen availability (Warwick and Uncles, 1980), as stable stratification in the deep basins can lead to oxygen deficiency or anoxia at the bottom. Janas et al. (2004) measured H_2S concentrations as high as 443 µmol/l in the sediment of a 51-m-deep station. The oxygen supply was lower at this station than at a station with a depth of 37 m, where the maximum H_2S concentration was ∼13 µmol/l. A stable macrofaunal community, characterized by the relatively high-level reproduction of animals, can develop only under permanent oxygen conditions (Jørgensen, 1980; Rosenberg et al., 1992; Diaz and Rosenberg, 1995). Accordingly, the largest number of individuals was detected at shallow stations VE02, VE04, and VE05, fewer at intermediate station VE07, and none in the hypoxic Gdansk Deep (**Figure 7** and **Table 1**).

Previous studies revealed the dominance of different species in the macrozoobenthos communities of the Bay of Gdansk (e.g., Janas et al., 2004) and their close relationship to sediment type.

TABLE 1 | Macrofaunal abundances and individual composition at each chamber lander incubation site and the three offshore stations.

Burrowing behavior	Species	VE02	VE04	VE05	VE18	VE49a	VE07	VE38	VE39	TF0233
				Coastal			Interm.		Offshore	
Surface living	*Mytilus edulis*	0	7	0	0	131	0	0	0	0
	Saduria entromon	0	0	0	0	0	20	0	0	0
	Diastylis rathkei	0	0	7	41	69	0	0	0	0
	Peringia ulvae	2,994	3,738	2,519	783	292	0	0	0	0
	Cerastoderma glaucum	0	0	195	20	3	0	0	0	0
	Gammarus salinus	0	0	0	0	10	0	0	0	0
	Gammarus zaddachi	0	0	0	0	5	0	0	0	0
	Jaera	0	0	0	0	5	0	0	0	0
Total		2,994	3,747	2,723	381	394	20	0	0	0
Shallow burrowing	*Limecola (Macoma) baltica*	174	1,041	348	141	343	935	39	0	0
	Portoporeia femorata	0	0	0	0	0	324	0	0	0
	Monoporeia affinis	0	0	0	13	0	225	0	0	0
	Corophium volutator	2,931	7	478	215	46	0	0	0	0
	Bylgides sarsi	0	0	0	13	5	0	32	5	0
Total		3,105	1,050	826	845	515	1,484	72	5	0
Deep burrowing (burrow/tube dwellers)	*Hediste diversicolor*	442	225	123	369	118	0	0	0	0
	Marenzelleria spp.	422	0	1,935	814	599	44	0	0	0
	Pygospio elegans	88	0	734	141	3	31	0	0	0
Total		952	225	2,792	1,324	719	75	0	0	0
Deep burrowing (free living)	*Mya arenaria*	0	1140	24	118	26	0	0	0	0
	Halicryptus spinulosus	0	0	0	0	0	72	0	0	0
	Prostoma obscura	36	0	3	0	0	0	0	0	0
	Oligochaeta	52	263	130	79	381	0	0	0	0
Total		262	1,403	157	197	407	72	0	0	0
Epibenthic (no bioturbatio)	*Amphibalanus improvisus*	0	0	0	0	215	0	0	0	0
Total		0	0	0	0	215	0	0	0	0
Total ind. per station		7,140	6,420	6,496	2,747	2,250	1,652	72	5	0

All numbers refer to individuals per square meter. All data are for the year when the chamber lander was deployed (winter 2015 for VE02; all other data are from spring 2016, also for the offshore stations).

The high abundances of the grazing snail *P. ulvae* at all coastal stations provided an indication that settling POM comprises a major food source. The filter-feeding bivalve *M. arenaria* was prominent at station VE04, presumably due to the ample food supply near the mouth of the Vistula River. The occurrence of perennial, omnivorous predators such as *H. diversicolor* and *Marenzelleria* spp. (data not shown) evidenced the permanent presence of this food supply and the associated prey animals. At the intermediate station VE07, mostly surface-living or shallow-burrowing animals were detected, probably because of the noticeable occurrence of H_2S in the upper sediments. *M. baltica* has a high tolerance of both low oxygen concentrations and the presence of H_2S (Long et al., 2008), which together probably account for it being one of the dominant species. Hence, species distribution can also be used to define the extent of the coastal zone.

Patterns of Nutrient Release and the Impact of Macrofauna

Oxygen as a Measure of Benthic Activity

The rates of oxygen consumption in coastal zones of the Bay of Gdansk was in the range of 11.24–31.48 μmol O_2 m^{-2} d^{-1}, indicating the higher biological activity at the coastal stations than at the intermediate station VE07, where the rate was 2.37 μmol O_2 m^{-2} d^{-1} (**Figure 4**). Although in terms of their

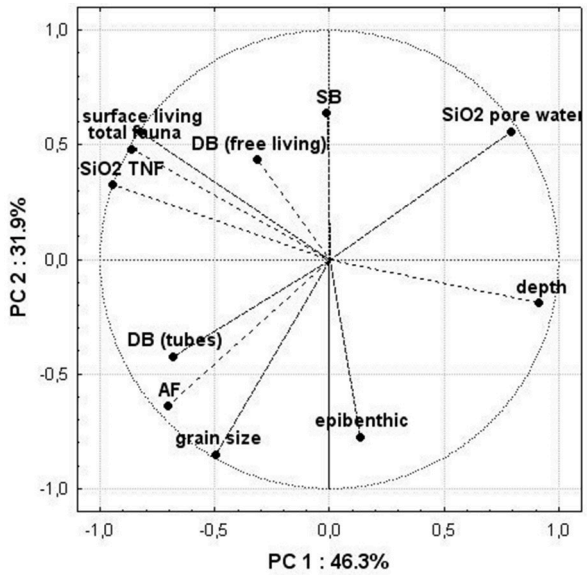


FIGURE 8 | Results of the principle component analysis (PCA). The eigenvectors of the correlation matrix are shown as lines. The variables included in the PCA are DB, deep burrowing fauna; SB, shallow burrowing fauna; epibenthic, epibenthic fauna; depth, water depth at the stations; total fauna, total amount of individuals of all groups at the station.

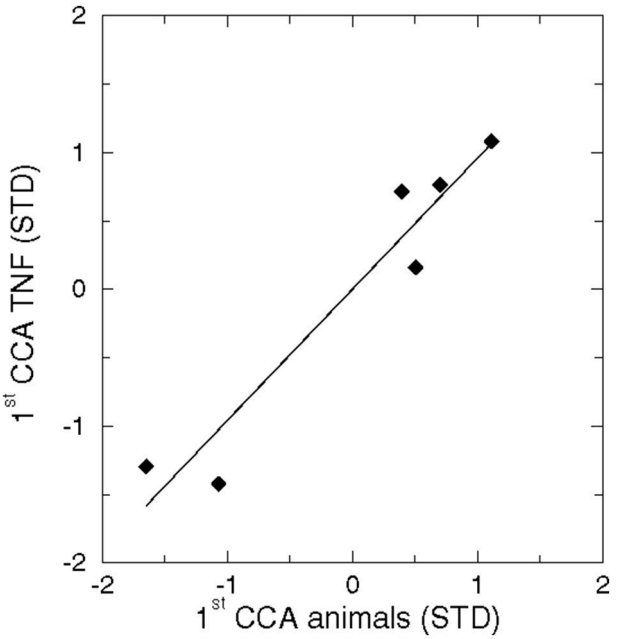


FIGURE 9 | Correlation between the 1st CCA pattern of benthic animals and the 1st CCA pattern of TNFs ($r = 0.96$, $n = 6$, $p < 0.01$).

size bacteria use more oxygen than macrozoobenthos and are the largest sink for oxygen, because of their large numbers in the (muddy) sediment (Schwinghamer, 1981), macrofaunal respiration uses more oxygen at once. Our data showed a much higher total net oxygen flux into the sediment at the sandy coastal stations than at the intermediate station (**Figure 4**). This was caused by intense macrofaunal activity at coastal sites, due to individual abundances and a reworking of the sediment, the rate of which exceeded that of oxygen consumption (Moodley et al., 1998) by bacterial activity at the intermediate, muddy station. The deep-burrowing species *H. diversicolor* and *M. viridis* alone caused a doubling of benthic oxygen consumption (Kristensen et al., 2011). Thus, as a measure of the activity of benthic communities, oxygen consumption differentiates the coastal from the intermediate zone (Moodley et al., 1998).

Comparison of Fluxes

The nutrient inventory of the sediments matched that previously described for the porewaters of different sediment types (Devol and Christensen, 1993; Mortimer et al., 1999; Tuominen et al., 1999). While the sands lacked nutrient reservoirs, except of NO_3^- and NO_2^-, in muddy sediments significantly high amounts of SiO_2, NH_4^+, and PO_4^{3-} were measured, increasing with depth (**Figure 11**, Supplementary Figure 1). This accounted for the higher diffusive efflux in muddy than in sandy sediments (Supplementary Table 1).

Consistent with our findings regarding O_2 consumption, the TNF showed the greater release of nutrients from the coastal zone than from offshore and intermediate stations, attributable to active reworking of the sediments by macrofauna. The efflux of dissolved nutrients was generally higher at sandy sites (**Figure 6**), even though fewer dissolved nutrients were stored in the sedimentary reservoirs (**Figure 11**, Supplementary Figure 1). The food supply at the sediment surface is a driving factor in sediment reworking. Duport et al. (2006) reported a positive linear relationship between the density of *H. diversicolor* and sediment reworking and showed a significant effect of the abundance of animals on particle transport into the sediment similar to our own observations. In addition, the irrigation activity increases with their increasing density. This behavior promotes the transport of particles and organic matter into the sediment (Ouellette et al., 2004). Moreover, irrigation and degradation leave no time for storing the dissolved nutrients in amounts comparable to those at the offshore stations. Produced or released nutrients as well as settled POM cannot accumulate in the sediment because they are used immediately. Rusch et al. (2006) already reported muddy, diffusion dominated sediments to offer the highest amount of POM degeneration only at the surface. By contrast, their experiments showed that the permeable sands of the shelf area are effective biocatalytical filters with high microbial degradation rates due to percolation of POM loaded water down to 10 cm sediment depth.

The mismatch between the output and inventory of the sediments can also be explained by the fine fraction of the sediments itself (Leipe et al., 2017). Deep-burrowing fauna in the Bay of Gdansk, such as *Marenzelleria* ssp. and *H. diversicolor*, bury organic matter but also make buried POM available to microbial degradation processes by particle mixing and surface increment. Burrow walls constitute an increased sediment surface. Their ventilation provides habitats

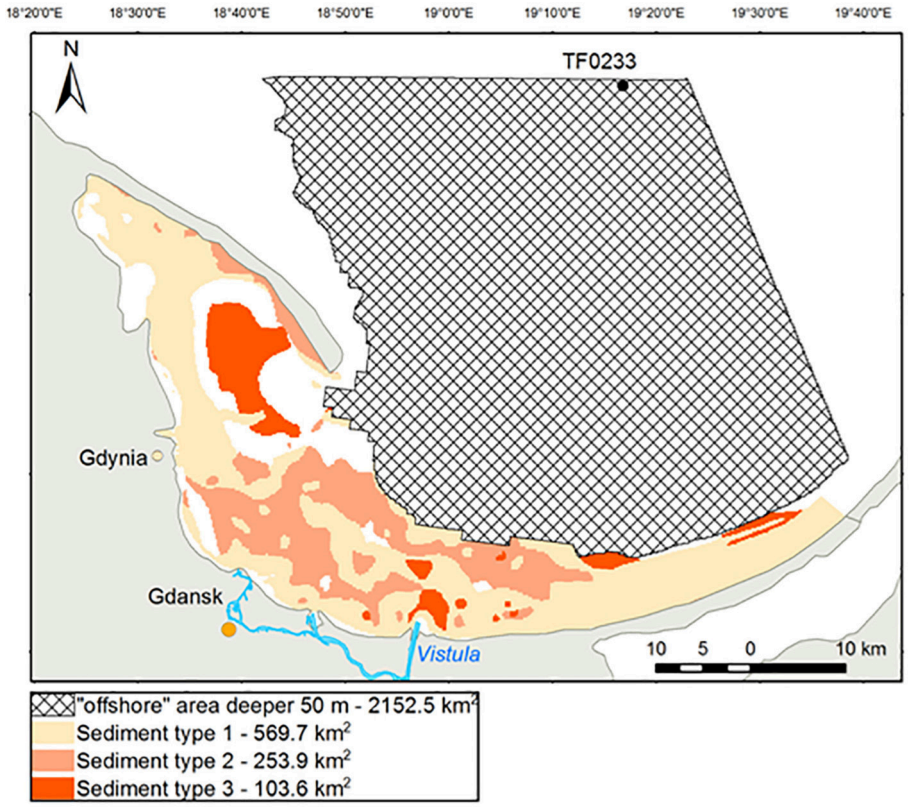


FIGURE 10 | Sediment type distribution. Type 1 = fine sand (VE04 and VE02), type 2 = medium sand (VE05, VE18, and VE49a), type 3 = mud (VE07). The shaded area indicates the offshore region (water depth of 50–100 m) which were excluded from the classification.

for microbes dependent on oxygen for the remineralization of organic matter. Thus, remineralization rates are enhanced in ventilated sediments. For example, a 300% increase of the oxygenated surface was reported for sediments inhabited by *H. diversicolor* (Davey, 1994) and a 6–11% increase of oxygenated sediment volume was shown for *M. viridis* (Jovanovic et al., 2014). The latter transports oxygenated water into the sediment most of the time, but the deeper parts of the burrows are oxygen depleted due to intense use of oxygen in aerobic microbial processes (Quintana et al., 2011; Jovanovic et al., 2014). Renz and Forster (2014) also reported the sediment water interface as the largest sink for oxygen in *M. viridis* and *M. neglecta* burrows due to increased nitrification activity. By contrast, at muddy, less-bioturbated stations remineralizing microbes can use only the organic material at the sediment surface, where oxygen from the bottom water is present. The higher volume of reworked sandy sediment and the larger bioturbation depth may thus compensate for the low organic carbon content that is due to a dilution of the fine fraction per volume. Also dissolved nutrients are transported by deep burrowing fauna like *Marenzelleria* spp. (Quintana et al., 2011; Jovanovic et al., 2014; Renz and Forster, 2014). Based solely on the efflux caused by bioirrigation of the reservoirs, higher fluxes from the sediment may be reached by large numbers of animals processing small amounts of nutrients repeatedly (Duport et al., 2006; De Backer et al., 2011) than by only a few animals processing large amounts less often.

Impact of Faunal Communities on Flux Modification

Amplification Factors and the Magnitude of TNF

The effects of physical advection by currents and wave action can be excluded from our TNF calculations because the incubated bottom water was completely enclosed by the chamber. The steadily decreasing oxygen concentrations inside the chamber ruled out the influence of the surrounding water (**Figure 4**). However, if physical advection as an impact on total fluxes is also considered, then our calculated fluxes may be slightly underestimated. Especially for permeable sands in shelf areas it is known that waves and currents can influence the fluid flow through the bottom. Bottom topography may also play a role, thus it was reported that sand ripple structures caused an increase of the sediment solute volume by a factor of 2.1 and the solute flux down to 2.7 cm sediment depth was enhanced by a factor of 1.9 due to pressure gradients (Huettel et al., 1996). Thus, advective solute flow in permeable sediment water layers is able to control the removal and offer of POM for degradation processes (Rusch et al., 2006; Rocha, 2008). This might be supported by hydraulic wave pumping where pressure

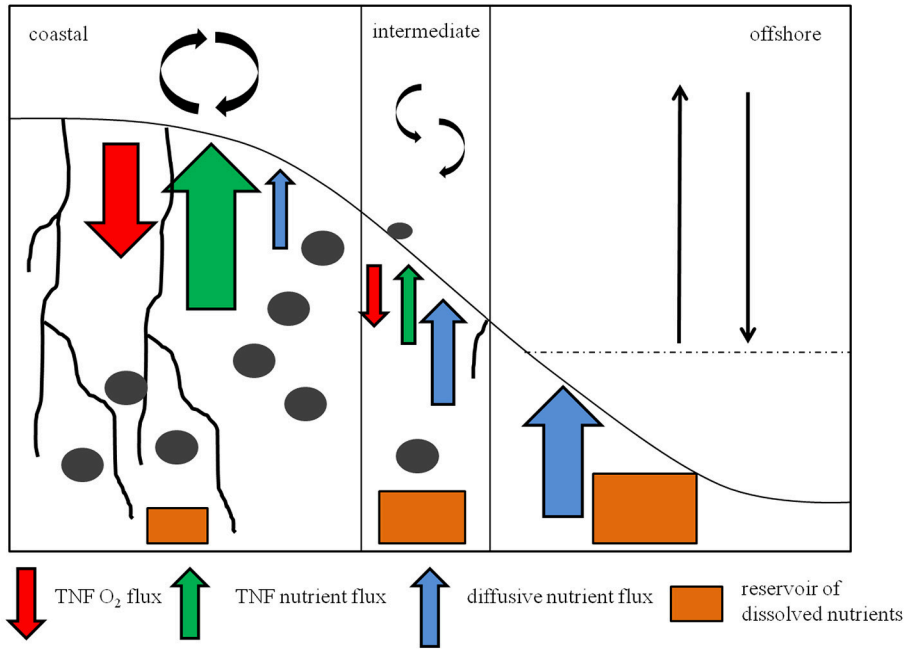


FIGURE 11 | Schematic overview of the sedimentary conditions and trends in fluxes at coastal, intermediate and offshore stations. Black irregular lines in the sediment symbolize deep burrowing tube- dwellers. Gray ellipses symbolize burrowing animals. The red arrows mean the total net flux of O_2 to avoid misunderstandings, green arrows mean the TNF of nutrients, blue arrows mean the diffusive flux of nutrients. Orange boxes stand for the nutrient inventory inside the sediment. The size of these symbols stands for the high of the fluxes and the size of the nutrient inventories in the field.

gradients caused by wave influence cause an increased porewater flow through the sediment (Santos et al., 2012). Ahmerkamp et al. (2017) additionally showed that the increased oxygen supply caused by current velocities and depending on the sediment grain size requires higher microbial degradation rates in the sediment. They reported an oxygen penetration depth of 1–6 cm in coarse sands (210–540 μm) and an oxygen flux of 8 mmol to 34 mm m^{-2} d^{-1} only caused by physical transport and sediment characteristics. For our efflux calculations in the Bay of Gdansk this would mean a doubling in fluxes when physical advection contributes. Therefore, the complete efflux of the nutrient inventory in the sediment would take average only 0.8 days than 1.66 days as calculated from our incubation measurement. The physical advection might enhance the degradation potential of the sediments and cause a leaching of solutes from the permeable sands. Hence, the nutrient cycling in the coastal zone might probably be faster in reality than we estimated.

SiO_2 is not governed by any microbial turnover processes; rather, total net SiO_2 fluxes are a measure of macrofaunal influence because dissolved SiO_2 can be treated as an inert tracer of bioturbation (Boudreau, 1997). All of the other nutrients contributed to turnover processes during the chamber lander incubations. This would explain why the highest AF occurred in the total net SiO_2 fluxes, which were larger than the respective diffusive fluxes (**Figure 6**). Thus, the intrinsic effluxes of nutrients that undergo microbial transformation or use were probably underestimated. Consequently, in estimating the macrofaunal contribution to nutrient exchange, it might be more important to evaluate those factors of the TNF that cause it to exceed the diffusive fluxes than to focus on the fluxes themselves. An examination of the AF and TNF of different nutrients as a function of the dominant species of the benthic communities revealed interesting features related to their individual life strategies as following described. At station VE18, deep-burrowing *Marenzelleria* spp. and *H. diversicolor* dominated the community, with 814 and 369 ind. m^{-2}, respectively. The total net SiO_2 flux at that station was only a few mmol m^{-2} d^{-1} higher than at station VE07, where the abundances of these species were 44 and 0 ind. m^{-2}, respectively. The second largest factor enhancing sedimentary SiO_2 fluxes was at station VE18, where *M. viridis* might have reached a bioturbation depth of ∼25 cm (maximum: 30 cm) (Zettler et al., 1994). Davey (1994) showed that the burrow systems of *H. diversicolor* reached a depth of 8 cm (small individuals) to 35 cm (large individuals). Thus, the establishment of deep NH_4^+ reservoirs (1,620 μmol/l; station VE04) in the sediment was possible. *Marenzelleria* spp. irrigates nutrients dissolved in the porewater even more efficiently than does *H. diversicolor* (Kristensen et al., 2011), as demonstrated by the AF identified in our study that were especially high at stations where *Marenzelleria* spp. dominated the polychaete community (VE05, VE18, VE49a; **Figure 6**).

At station VE02, the large population of *C. volutator* may have accounted for a total NH_4^+ flux that was 12 times higher than the diffusive flux, in contrast to the enhancement at station VE04 (AF 9.5). Together with the large populations of *H. diversicolor, C. volutator* may be capable of increasing the NH_4^+ flux to

this extent (Pelegri and Blackburn, 1994; Mermillod-Blondin et al., 2004). Moreover, the different excretion rates of the macrozoobenthos feed the NH_4^+ pool (Blackburn and Henriksen, 1983; Gardner et al., 1993). For example, Tuominen et al. (1999) showed that a population of *M. affinis* can enlarge the NH_4^+ flux in a system by up to 10%, due to excretion products. We speculate that at station VE04, where we found the highest NH_4^+ TNF of 3.04 mmol m^{-2} d^{-1} and where the food supply was likely also high, excretion by the filter-feeding clam *M. arenaria* and the facultative deposit-feeding clam *M. baltica*, might also have contributed to the high flux since both were present at high abundances (1,140 and 1,041 ind. m^{-2}, respectively). High excretion rates of *Mya arenaria* have long been known (Allen and Garrett, 1970) and filter-feeding clams are able to control phytoplankton stocks in shallow bights (Officier et al., 1982)

Additionally, remineralization stimulated by fauna might have increased the ammonium pool (Davey, 1994). At stations VE04, VE05, and VE18, where deep-burrowing polychaetes were found (**Table 1**) alongside high positive ammonium fluxes (**Figure 5** and Supplementary Table 1), an increased oxygenated surface presumably caused ammonium effluxes of 0.65–3.04 mmol m^{-2} d^{-1}. In studies of deep-sea sediment without fauna, the fluxes of NH_4^+ differed from the fluxes at coastal sites. Berelson et al. (1990), for example, found that during a 4-day chamber lander incubation in the deep sea NH_4^+ was below the detection limit. By contrast, we found detectable concentration changes (**Figure 5**) and TNF values measurable in mmol m^{-2} d^{-1} (**Figure 6**) after <1 day of incubation in shallow waters. At station VE04, where the reservoirs of dissolved nutrients were higher than at the other coastal stations (Supplementary Figure 1), deep-burrowing fauna may have created a high flux due to bioirrigation. This would suggest that *H. diversicolor* (225 ind. m^{-2} at VE04) was responsible for a doubling of the NH_4^+ flux (Mermillod-Blondin et al., 2004) and therefore half of the increase at station VE04 (AF 9.5; **Figure 6**).

Total net PO_4^{3-} fluxes were quite low and the calculated AF were in a similar range at all stations. This may have been caused by the precipitation reaction of phosphate with Fe(III)- ions to iron phosphate under aerobic conditions in the bottom water (Froehlich et al., 1982). Because of the low concentration of PO_4^{3-} in the bottom water, the amount exiting the sediment might react in the oxygenated water immediately.

The CCA expresses the high influence of fauna on the TNF (**Figure 9**). In contrast, a second CCA showed that the TNF are uncorrelated to sediment properties and therefore not predictable. That means that the TNF are directly depending on the fauna community, which in turn depends on the sediment characteristics and location as discussed above. Thus, for a prediction of TNF the macrofauna community, the abundances in the functional groups and the availability of food sources must be considered.

Further, only the AF expresses the contribution of the macrofaunal community to flux modification in the coastal filter, not the high nutrient flux itself. This clearly implies that a comparison between total and diffusive fluxes is essential. The results suggest that it is mainly the occurrence and abundance of deep-burrowing polychaetes in a community that account for the enlargement of nutrient fluxes in the sediment, even if other species belong to the community in high abundances. The PCA showed that the depth of the sediments, which reflects the near to the shore and river mouth, and the faunal community are important determinants of the magnitude of the nutrient fluxes (**Figure 8**). The results further suggest that sediments consisting of well-mixed sand and mud and located in very shallow waters near the mouth of a river create the best conditions for turnover processes whereas sediments of mud alone seem to inhibit them. This might be why according to our data, oxygen consumption, TNF, and infauna occurrences were highest at stations nearest the mouth of the Vistula River and decreased progressively with increasing proximity to the offshore stations. The coastal zone therefore seems to buffer the highest loads of the Vistula River directly at the entry to the bay.

Flux Modification at the Study Site by Different Species According to Microbial Turnover Processes

NH_4^+ is produced in the dissimilatory nitrate reduction that occurs in anoxic sediment layers (Laverock et al., 2011) or during microbial degradation of organic matter. Both processes feed the NH_4^+ pool, either in the oxic zone of the sediment or bottom water or in the deeper, anoxic regions (Laverock et al., 2011). Conversely, an important NH_4^+-consuming process might be nitrification that occurs in oxygenated bottom water, and oxic sediment layers, or at the oxic-anoxic interfaces of tubes and burrows where ammonium may be converted to nitrate which may then be used during denitrification (e.g., Kristensen and Blackburn, 1987; Jäntti and Hietanen, 2012). In the absence of calculations of the rates of assimilation, remineralization, excretion, or nitrification, the process(es) with the strongest influence on NH_4^+ production and transformation could not be determined.

While there was a net NO_3^- efflux from the sediments at all stations except VE04 where a negative NO_3^- flux appeared. This may imply a consumption of NO_3^- during denitrification in the sediments, which was assumed for all stations at the beginning of the incubation. Previous studies showed that *H. virens* activity stimulated the coupling of nitrification and denitrification by 2.3- to 2.4-fold (Kristensen and Blackburn, 1987). This may also have been due to the high NH_4^+ supply, as a substrate for nitrification, at VE04. Karlson et al. (2005) showed that an increased NO_3^- supply from the bottom water supported sediment denitrification in cores inhabited by *M. affinis*. This was also the case for *H. diversicolor* in the study of Pelegri and Blackburn, 1995. Karlson et al. (2005) further proposed that, in the absence of appropriate denitrification rates, the high negative total NO_3^- flux in bioturbated cores reflected the high rates of dissimilatory nitrate reduction to ammonium. For all stations where NO_3^- accumulated in the bottom water, we speculated that nitrification was significantly higher than denitrification in the sediments or bottom water. Further, it may be that these processes were more weakly coupled than at station VE04. An

example was provided by the large increase in the total net NO_3^- efflux at stations VE05 and VE02, which exceeded the diffusive porewater fluxes by an AF of 303 (VE05) despite the considerable amount of deep-burrowing tube and burrow dwellers inhabiting the sediments of these stations. While at station VE04 the conditions for denitrifiers were potentially good, due to the sediment characteristics near the river mouth, station VE05 lacked substrates for heterotrophs and probably included anoxic sediment areas that hindered the removal of NO_3^- from the system (Hellemann et al., 2017). This result is supported by a study of Henriksen et al. (1983), which showed that NH_4^+ is oxidized to NO_3^- in burrow environments before it reaches the water column via bioirrigation. The opposite was probably true at station VE07, where the sedimentary conditions might have favored NO_3^- removal, but deep-burrowing animals were absent (**Table 1**, **Figure 7**). At that station, sedimentary denitrification and bottom water nitrification might have been nearly uncoupled, such that the removal processes were not enhanced.

The Coastal Filter Function and Bioturbation

Sediments of the coastal zone are generally a source of nutrients (**Figures 5**, **6**), although variable for nitrate (this study **Figure 6**; Devol and Christensen, 1993; Sumei et al., 2004). For example, in sediments of the continental margin of the eastern Pacific, the TNF of SiO_2 and NO_3^- were up to three times higher than the diffusive fluxes (Devol and Christensen, 1993). The AF determined in this study for sediments of the coastal zone were, in the case of SiO_2, much higher (11.9–148, **Figure 6**), and provide an example of the potential differences in the enhancement of fluxes, as determined in the studies published thus far. Using chamber lander incubations, Berelson et al. (1990) showed that deep-sea sediments are a source of nutrients but the diffusive fluxes of the porewater were considered to be the main source of SiO_2 and NO_3^- effluxes. The fluxes measured in their study were, on average, only a small fraction of those measured in the present study at the Bay of Gdansk. Forja et al. (1994) reported SiO_2 and NH_4^+ fluxes in the Mediterranean that were 6- to 13-fold higher than measured in this work; the difference can perhaps be explained by seasonal temperature changes (Forja et al., 1994). By contrast, in the core incubations in Bohai Sea, Sumei et al. (2004) did not find significant seasonal differences in the NO_3^- and SiO_2 fluxes. Our study, however, was limited to winter and spring with the chamber Lander incubations for TNF calculation.

According to our calculations, 10% of the nitrogen in the Bay of Gdansk is introduced by inputs from the Vistula River reaching the bottom water system each year after being filtered and partly removed through the sediment in the coastal zone. The coastal filter is probably not a "one-way street" from the river through the sediments to the open Baltic Sea. More likely, a cycling process takes places as long as nutrients reach the bioturbated sediments and mixed water columns. Each nutrient cycle reduces bioavailability because every turnover process, including ingestion and digestion by fauna and microbial transformation, results in the transformation of nutrients to biomass. The retention of nutrients in the coastal zone would therefore lead to the temporal removal of nutrients bound in biomass. Coastal zones with long residence times and large numbers of bioturbating, deep-burrowing infauna may offer the best nutrient-filter function. Bioturbation is therefore not only a tool for determining the extent of the coastal filter but also an indispensable component thereof.

SUMMARY

In this study, a significant, direct increase in the TNF compared to the diffusive fluxes in bioturbated sediments was determined, thus demonstrating that the sediments were a source of nearly all of the examined nutrients. The smaller increase in the TNF at the intermediate station reflected the lower level of bioturbation activity of infauna in those sediments than in the sediments of the coastal stations. The increase in the TNF differed for the different nutrients, with the highest TNF being that of SiO_2. Consistent with the enhancement of fluxes due to bioturbation, stations close to the mouth of the Vistula River had the highest NH_4^+ fluxes overall. In contrast, the stations with the largest number of deep-burrowing animals had the largest AF. Thus, the abundance (dominance) of burrow dwellers may determine the bioturbation effect of the whole community on the benthic system (**Figures 6**, **8**, **9**).

Our findings suggest that, each year, 6.9 kt N, 0.9 kt P, and 19 kt Si exit coastal sediments in the Bay of Gdansk and enter new transformation cycles in other parts of the marine system. For nitrogen, this is ∼10% of the amount annually reaching the bay from the Vistula River.

In the offshore region of the Bay of Gdansk, the area of which is approximately twice that of the coastal zone (<50 m water depth), only 2.96 kt N, 6.8 kt Si, and 0.9 kt P exit the sediments each year. Thus, when extrapolated to the total area, the contribution of the coastal zone is roughly twice that of the offshore area.

AUTHOR CONTRIBUTIONS

FT designed the study together with MV, did the sediment sampling, chamber lander, and porewater sampling and most of the analysis and the calculations and wrote the paper. MV additionally contributed to the text. UJ and HK did the macrofauna sampling and counting and contributed to the text. IL did the mass-spectrometric analyzes, CB performed the nutrient analyzes. MG conducted the area calculation and map design and contributed to the text. JD run the statistical analysis and contributed to the text.

ACKNOWLEDGMENTS

We thank David Meyer (Leibniz Institute for Baltic Sea Research Warnemünde) for helpful discussions and comments. Thanks

also to the captains and crews of RV Elisabeth Mann Borgese and RV Alkor for their help with sampling. Thanks to all BONUS-COCOA colleagues. The BONUS COCOA project was funded by BMBF grant number FKZ 03F063A. Finally we thank two reviewers for their helpful and constructive comments.

SUPPLEMENTARY MATERIAL

The Supplementary Material for this article can be found online at: https://www.frontiersin.org/articles/10.3389/fmars.2018.00201/full#supplementary-material

REFERENCES

Ahmerkamp, S., Winter, C., Krämer, K., de Beer, D., Janssen, F., Friedrich, J., et al. (2017). Regulation of benthic oxygen fluxes in permeable sediments of the coastal ocean. *Limnol. Oceanogr*. 62, 1935–1954. doi: 10.1002/lno.10544

Allen, J. A., and Garrett, M. R. (1970). The excretion of ammonia and urea by *Mya arenaria* L. (Mollusca: Bivialvia). *Comp. Biochem. Phys. A* 39, 633–642. doi: 10.1016/0300-9629(71)90185-X

Aller, R. C., and Aller J. Y. (1998). The effect of biogenic irrigation intensity and solute exchange on diagenetic reaction rates in marine sediments. *J. Mar. Res*. 56, 905–936. doi: 10.1357/002224098321667413

Andersen, F. Ø., and Kristensen, E. (1992). The importance of benthic macrofauna in decomposition of microalgae in a coastal marine sediment. *Limnol. Oceanogr*. 37, 1392–1403. doi: 10.4319/lo.1992.37.7.1392

Asmala, E., Carstensen, J., Conley, D. J., Slomp, C. P., Stadmark, J., and Voss, M. (2017). Efficiency of the coastal filter: nitrogen and phosphorous removal in the Baltic Sea. *Limnol. Oceanogr*. 62, 222–238. doi: 10.1002/lno.10644

Berelson, W. M., Hammond, D. E., O'Neill, D., Xu, X.-M., Chin, C., and Zukin, J. (1990). Benthic fluxes and pore water studies from sediments of the central equatorial north Pacific: nutrient diagenesis. *Geochim. Cosmochim. Acta* 54, 3001–3012. doi: 10.1016/0016-7037(90)90117-4

Blackburn, T. H., and Henriksen, K. (1983). Nitrogen cycling in different types of sediment from Danish waters. *Limnol. Oceanogr*. 28, 477–493. doi: 10.4319/lo.1983.28.3.0477

Boudreau, B. P. (1997). *Diagenetic Models and Their Implementation*. Berlin Heidelberg: Springer.

Bouma, T. J., Olenin, S., Reise, K., and Ysebaert, T. (2009). Ecosystem engineering and biodiversity in coastal sediments: posing hypothesis. *Helgol. Mar. Res*. 63, 95–106. doi: 10.1007/s10152-009-0146-y

Conley, D. J., Carstensen, J., Aigars, J., Axell, P., Bonsdorff, E., Eremenia, T., et al. (2011). Hypoxia is increasing in the coastal zone of the Baltic Sea. *Environ. Sci. Technol*. 45, 6777–6783. doi: 10.1021/es201212r

Davey, J. T. (1994). The architecture of the burrow of *Nereis diversicolor* and its quantification in relation to sediment-water exchange. *J. Exp. Mar. Biol. Ecol*. 179, 115–129. doi: 10.1016/0022-0981(94)90020-5

De Backer, A., van Coillie, F., Montserrat, F., Provoost, P., van Colen, C., Vincx, M., et al. (2011). Bioturbation effects of *Corophium volutator*: importance of density and behavioural activity. *Estuar. Coast. Shelf Sci*. 91, 306–313. doi: 10.1016/j.ecss.2010.10.031

Denisenko, S. G., Denisenko, N. V., Lehtonen, K. K., Andersin, A.-B., and Laine, A. O. (2003). Macrozoobenthos of the Pechora Sea (SE Barents Sea): community structure and spatial distributions in relation to environmental conditions. *Mar. Ecol. Prog. Ser*. 258, 109–123. doi: 10.3354/meps258109

Davey, J. T. (1994). The architecture of the burrow of Nereis diversicolor and its quantification in relation to sediment-water exchange. *J. Exp. Mar. Bio. Ecol.* 179, 115–129.

Devine, J. A., and Vanni, M. J. (2002). Spatial and seasonal variation in nutrient excretion by benthic invertebrates in a eutrophic reservoir. *Freshw. Biol.* 47, 1107–1121. doi: 10.1046/j.1365-2427.2002. 00843.x

Devol, A. H., and Christensen, J. P. (1993). Benthic fluxes and nitrogen cycling in sediments of the continental margin of the eastern North Pacific. *J. Mar. Res*. 51, 345–372. doi: 10.1357/0022240933223765

Diaz, R. J., and Rosenberg, R. (1995). Marine benthic hypoxia: a review of its ecological effects, and the behavioural responses of benthic macrofauna. *Oceanogr. Mar. Biol*. 33, 245–303.

Diaz, R. J., and Rosenberg, R. (2008). Spreading dead zones and consequences for marine ecosystems. *Science* 321, 926–929. doi: 10.1126/science.1156401

Dippner, J. W., and Ikauniece, A. (2001). Long-term zoobenthos variability in the Gulf of Riga in relation to climate variability. *J. Mar. Syst*. 30, 155–164. doi: 10.1016/S0924-7963(01)00055-0

Duport, E., Stora, G., Tremblay, P., and Gilbert, F. (2006). Effects of population density on the sediment mixing induced by the gallery- diffuser *Hediste (Nereis) diversicolor* O.F. Müller, 1776. *J. Exp. Mar. Biol. Ecol.* 336, 33–41. doi: 10.1016/j.jembe.2006.04.005

Dürr, H. H., Laruelle, G. G., van Kempen, C. M., Slomp, C. P., Meybeck, M., and Middelkoop, H. (2011). Worldwide typology of nearshore coastal systems: defining the estuarine filter of river inputs to the oceans. *Estuar. Coasts* 3, 441–458. doi: 10.1007/s12237-011-9381-y

Flemming, B. W., and Delafontaine, M. T. (2000). Mass physical properties of muddy intertidal sediments: some applications, misapplications and non- applications. *Cont. Shelf Res.* 20, 1179–1197. doi: 10.1016/S0278-4343(00)00018-2

Forja, J. M., Blasco, J., and Gómez- Parra, A. (1994). Spatial and seasonal variation of *in situ* benthic fluxes in the Bay of Cadiz (south- west Spain). *Estuar. Coast. Shelf Sci*. 39, 127–141. doi: 10.1006/ecss.1994.1053

Froehlich, P. N.,Bender, M. L., Luedtke, N. A., Heath, G. R., and De Vries, T. (1982). The marine phosphorus cycle. *Am. J. Sci*. 282, 474–511. doi: 10.2475/ajs.282.4.474

Gardner, W. S., Briones, E. E., Kaegi, E. C., and Rowe, G. T. (1993). Ammonium excretion by benthic invertebrates and sediment-water nitrogen flux in the Gulf of Mexico near the Mississippi River outflow. *Estuar. Coast* 16, 799–808. doi: 10.2307/1352438

Gilbert, F., Stora, G., and Bonin, P. (1998). Influence of bioturbation on denitrification activity in Mediterranean coastal sediments: an *in situ* experimental approach. *Mar. Ecol. Prog. Ser*. 163, 99–107. doi: 10.3354/meps163099

Glud, R. N., and Blackburn, N. (2002). The effects of chamber size on benthic oxygen uptake measurements: a simulation study. *Ophelia* 56, 23–31. doi: 10.1080/00785236.2002.10409486

Glud, R. N., Holby, O., Hoffmann, F., and Canfield, D. E. (1998). Benthic mineralization and exchange in arctic sediments. *Mar. Ecol. Prog. Ser*. 173, 237–251. doi: 10.3354/meps173237

Graf, G., and Rosenberg, R. (1997). Bioresuspension and biodeposition: a review. *J. Mar. Syst*. 11, 269–278. doi: 10.1016/S0924-7963(96)00126-1

Grasshoff, K., Kremling, K., and Ehrhardt, M. (1999). *Methods of Seawater Analysis, 3rd Edn.* Weinheim: Wiley-VCH.

Heisterkamp, I. M., Kamp, A., Schramm, A. T., de Beer, D., and Stief, P. (2012). Indirect control of the intracellular nitrate pool of intertidal sediment by the polychaete *Hediste diversicolor*. *Mar. Ecol. Prog. Ser*. 445, 181–192. doi: 10.3354/meps09464

Hellemann, D., Tallberg, P., Bartl, I., Voss, M., and Hietanen, S. (2017). Denitrification in an oligotrophic estuary: a delayed sink for riverine nitrate. *Mar. Ecol. Prog. Ser*. 583, 63–80. doi: 10.3354/meps12359

Henriksen, K., Rasmussen, M. B., and Jensen, A. (1983). Effect of bioturbation on microbial nitrogen transformations in the sediment and fluxes of ammonium and nitrate to the overlying water. *Environ. Biogeochem*. 35, 193–205.

Heyen, H., and Dippner, J. W. (1998). Salinity variability in the German Bight in relation to climate variability. *Tellus* 50, 545–556. doi: 10.3402/tellusa.v50i4.14532

Huettel, M., Ziebis, W., and Forster, S. (1996). Flow- induced uptake of particulate matter in permeable sediments. *Limnol. Oceanogr*. 41, 309–322. doi: 10.4319/lo.1996.41.2.0309

Iversen, N., and Jørgensen, B. B. (1993). Diffusion coefficients of sulfate and methane in marine sediments: influence of porosity. *Geochim. Cosmochim. Acta* 57, 571–578. doi: 10.1016/0016-7037(93)90368-7

Janas, U., Wocial, J., and Szaniawska, A. (2004). Seasonal and annual changes in the macrozoobenthic populations of the Gulf of Gdansk with respect to hypoxia and hydrogen sulphide. *Oceanologia* 46, 85–102.

Jäntti, H., and Hietanen, S. (2012). The effects of hypoxia on sediment nutrient cycling in the Baltic Sea. *Ambio* 42, 161–169. doi: 10.1007/s13280-011-0233-6

Jørgensen, B. B. (1980). Seasonal oxygen depletion in the bottom waters of a danish fjord and its effect on the benthic community. *Oikos* 34, 68–76. doi: 10.2307/3544551

Jovanovic, Z., Larsen, M., Quintana, C. O., Kristensen, E., and Glud, R. N. (2014). Oxygen dynamics and porewater transport in sediments inhabited by the invasive polychaete *Marenzelleria viridis*. *Mar. Ecol. Prog. Ser*. 504, 181–192. doi: 10.3354/meps10737

Karlson, K. (2007). Diurnal bioturbating activities of *Monoporeia affinis*: effects on benthic oxygen and nutrient fluxes. *Mar. Ecol. Prog. Ser*. 331, 195–205. doi: 10.3354/meps331195

Karlson, K., Hulth, S., Ringdahl, K., and Rosenberg, R. (2005). Experimental recolonisation of Baltic Sea reduced sediments: survival of benthic macrofauna and effects on nutrient cycling. *Mar. Ecol. Prog. Ser*. 294, 35–49. doi: 10.3354/meps294035

Kristensen, E., and Blackburn, T. H. (1987). The fate of organic carbon and nitrogen in experimental marine sediment systems: influence of bioturbation and anoxia. *J. Mar. Res*. 45, 231–257. doi: 10.1357/002224087788400927

Kristensen, E., Hansen, T., Delefosse, M., Banta, G. T., and Quintana, C. O. (2011). Contrasting effects of the polychaetes *Marenzelleria viridis* and *Nereis diversicolor* on benthic metabolism and solute transport in sandy coastal sediment. *Mar. Ecol. Prog. Ser*. 425, 125–139. doi: 10.3354/meps09007

Kröncke, I., Reiss, H., and Dippner, J. W. (2013). Effects of cold winters and regime shifts on macrofauna communities in the southern North Sea. *Estuar. Coast. Shelf Sci.* 119, 79–90. doi: 10.1016/j.ecss.2012.12.024

Künitzer, A., Basford, D., Craeymeersch, J. A., Dewarumez, J. M., Dörjes, J., Duineveld, G. C. A., et al. (1992). The benthic infauna of the North Sea: species distribution and assemblages. *J. Mar. Sci*. 49, 127–143. doi: 10.1093/icesjms/49.2.127

Laverock, B., Gilbert, J. A., Tait, K., Osborn, A. M., and Widdicombe, S. (2011). Bioturbation: impact on the marine nitrogen cycle. *Biochem. Soc. Trans*. 39, 315–320. doi: 10.1042/BST0390315

Leipe, T., Naumann, M., Tauber, F., Radtke, H., Friedland, R., Hiller, A., et al. (2017). Regional distribution patterns of chemical parameters in surface sediments of the south- western Baltic Sea and their possible causes. *Geo. Mar. Lett*. 37, 593–606. doi: 10.1007/s00367-017-0514-6

Leipe, T., Tauber, F., Vallius, H., Virtasalo, J., Uścinowicz, S., Kowalski, N., et al. (2011). Particulate organic carbon (POC) in surface sediments of the Baltic Sea. *Geol. Mar. Lett*. 31, 175–188. doi: 10.1007/s00367-010-0223-x

Livezey, R. E. (1995). "The evaluation of forecast," in *Analysis of Climate Variability*, eds H. Von Storch and A. Navarra(Berlin: Springer Verlag), 177–196.

Long, C. W., Brylawski, B. J., and Seitz, R. D. (2008). Behavioral effects of low dissolved oxygen on the bivalve *Macoma balthica*. *J. Exp. Mar. Biol. Ecol*. 359, 34–39. doi: 10.1016/j.jembe.2008.02.013

Longuet- Higgins, M. S. (1970). Longshore currents generated by obliquely incident sea waves 1. *J. Geophys. Res*. 75, 6778–6789. doi: 10.1029/JC075i033p06778

Mermillod-Blondin, F., Rosenberg, R., François-Carcaillet, F., Norling, K., and Maulaire, L. (2004). Influence of bioturbation by three benthic infaunal species on microbial communities and biogeochemical processes in marine sediment. *Aquat. Microb. Ecol*. 36, 271–284. doi: 10.3354/ame036271

Moodley, L., Heip, C. H. R., and Middelburg, J. J. (1998). Benthic activity in sediments of the northwestern Adriatic Sea: sediment oxygen consumption, macro- and meiofauna dynamics. *J. Sea Res*. 40, 263–280. doi: 10.1016/S1385-1101(98)00026-4

Mortimer, R. J. G., Davey, J. T., Krom, M. D., Watson, P. G., Frickers, P. E., and Clifton, R. J. (1999). The effect of macrofauna on porewater profiles and nutrient fluxes in the intertidal zone of the Humber Estuary. *Estuar. Coast. Shelf Sci*. 48, 683–699. doi: 10.1006/ecss.1999.0479

Norkko, A., Hewitt, J. E., Thrush, S. F., and Funnell, G. A. (2001). Benthic- pelagic coupling and suspension- feeding bivalves: linking site- specific sediment flux and biodeposition to benthic community structure. *Limnol. Oceanogr*. 46, 2067–2072. doi: 10.4319/lo.2001.46.8.2067

Officier, C. B., Smayda, T. J., and Mann, R. (1982). Benthic filter feeding: a natural eutrophication control. *Mar. Ecol. Prog. Ser*. 9, 203–210. doi: 10.3354/meps009203

Pastuszak, M., and Witek, Z. (2012). "Discharges of water and nutrients by the Vistula and Oder rivers draining Polish territory," in *Temporal and Spatial Differences in Emission of Nitrogen and Phosphorus from Polish Territory to the Baltic Sea,* eds M. Pastuszak and J. Igras (Gdynia: National Marine Fisheries Research Institute; Institute of Soil Science and Plant Cultivation; Fertilizer Research Institute), 309–346.

Pelegri, S. P., and Blackburn, T. H. (1994). Bioturbation effects of the amphipod *Corophium volutator* on microbial nitrogen transformations in marine sediments. *Mar. Biol*. 121, 253–258. doi: 10.1007/BF00346733

Pelegri, S. P., and Blackburn, T. H. (1995). Effect of bioturbation by *Nereis* sp., *Mya arenaria* and *Cerastoderma* sp. on nitrification and denitrification in estuarine sediments. *Ophelia* 42, 289–299. doi: 10.1080/00785326.1995.10431509

Phillips, O. M. (1966). *The Dynamic of the Upper Ocean*, *2nd Edn*. Cambridge, NY: Cambridge University Press.

Ouellette, D., Desrosiers, J.-P. G., Gilbert, F., Poggiale, J.-C., Blier, P.U., and Stora, G. (2004). Effects of temperature on *in vitro* sediment reworking processes by a gallery diffusor, the polychaete Neanthes virens. *Mar. Ecol. Prog. Ser*. 266, 185–193. doi: 10.3354/meps266185

Quintana, C. O., Hansen, T., Delefosse, M., Banta, G., and Kristensen, E. (2011). Burrow ventilation and associated porewater irrigation by the polychaete *Marenzelleria viridis*. *J. Exp. Mar. Biol. Ecol*. 397, 179–187. doi: 10.1016/j.jembe.2010.12.006

Reid, J. M., Reid, J. A., Jenkins, C. J., Hastings, M. E., Williams, S. J., and Poppe, L. J. (2005). *usSEABED: Atlantic Coast Offshore Surficial Sediment Data Release.* (Reston, VA:U.S. Geological Survey Data Series 118, version 1.0).

Renz, J., and Forster, S. (2014). Effects of bioirrigation by the three sibling species of *Marenzelleria* spp. on solute fluxes and porewater nutrient profiles. *Mar. Ecol. Prog. Ser*. 505, 145–159. doi: 10.3354/meps10756

Rocha, C. (2008). Sandy sediments as active biogeochemical reactors: compound cycling in the fast lane. *Aquat. Microb. Ecol*. 53, 119–127. doi: 10.3354/ame01221

Rosenberg, R., Loo, L.-O., and Möller, P. (1992). Hypoxia, salinity and temperature as structuring factors for marine benthic communities in a eutrophic area. *Neth. J. Sea Res*. 30, 121–129. doi: 10.1016/0077-7579(92)90051-F

Rusch, A., Huettel, M., Wild, C., and Reimers, C. (2006). Benthic oxygen consumption and organic matter turnover in organic- poor, permeable shelf sands. *Aquat. Geochem*. 12, 1–9. doi: 10.1007/s10498-005-0784-x

Santos, I. R., Eyre, B. D., and Huettel, M. (2012). The driving forces of porewater and groundwater flow in permeable coastal sediments: a review. *Estuar. Coast Shelf Sci*. 98, 1–15. doi: 10.1016/j.ecss.2011.10.024

Schulz, H. D., and Zabel, M., (2006). *Marine Geochemistry*, *2nd Edn.* Berlin Heidelberg: Springer.

Schwinghamer, P. (1981). Characteristic size distributions of integral benthic communities. *Can. J. Fish. Aquat. Sci*. 38, 1255–1263. doi: 10.1139/f81-167

Seeberg- Elverfeldt, J., Schlüter, M., Feseker, T., and Kölling, M. (2005). Rhizon sampling of pore waters near the sediment- water interface of aquatic systems. *Limnol. Oceanogr. Methods* 3, 361–371. doi: 10.4319/lom.2005.3.361

Statistica System Reference (2012). StatSoft. Inc., Tulsa, USA.

Sumei, L., Jing, Z., Hongtao, C., and Raabe, T. (2004). Benthic nutrient recycling in shallow coastal waters of the Bohai Sea. *Chin. J. Oceanol. Limnogr*. 22, 365–372. doi: 10.1007/BF02843630

Tuominen, L., Mäkelä, K., Lehtonen, K. K., Haahti, H., Hietanen, S., and Kuparinen, J. (1999). Nutrient fluxes, porewater profiles and denitrification in sediment influenced by algal sedimentation and bioturbation by *Monoporeia affinis*. *Estuar. Cost. Shelf Sci*. 49, 83–97. doi: 10.1006/ecss.1999.0492

von Storch, H., Zorita, E., and Cubasch, U. (1993). Downscaling of global climate change estimates to regional scales: an application to Iberian rainfall in wintertime. *J. Clim.* 6, 1161–1171. doi: 10.1175/1520-0442(1993)006<1161:DOGCCE>2.0.CO;2

Voss, M., Liskow, I., Pastuszak, M., Rüβ, D., Schulte, U., and Dippner, J. W. (2005). Riverine discharge into a coastal bay: a stable isotope study in the Gulf of Gdansk, Baltic Sea. *J. Mar. Syst*. 57, 127–145. doi: 10.1016/j.jmarsys.2005.04.002

Warwick, R. M., and Uncles, R. J. (1980). Distribution of benthic macrofauna associations in the Bristol Channel in relation to tidal stress. *Mar. Ecol. Prog. Ser*. 3, 97–103. doi: 10.3354/meps003097

Wilson, A. M., Huettel, M., and Klein, S. (2008). Grain size and depositional environment as predictors of permeability in coastal marine sands. *Estuar. Coast. Shelf Sci.* 80, 193–199. doi: 10.1016/j.ecss.2008.06.011

Witek, Z., Humborg, C., Savchuk, O., Grelowski, A., and Łysiak-Pastuszak, E. (2003). Nitrogen and phosphorus budgets of the Gulf of Gdansk (Baltic Sea). *Estuar. Coast. Shelf Sci.* 57, 239–248. doi: 10.1016/S0272-7714(02)00348-7

Wright, P. A. (1995). Nitrogen excretion: three end products, many physiological roles. *J. Exp. Biol.* 198, 273–281.

Zettler, M. L., Bochert, R., and Bick, A. (1994). Röhrenbau und Vertikalverteilung von *Marenzelleria viridis* (*Polychaeta: Spionidae*) in einem inneren Küstengewässer der südlichen Ostsee. *Rostock. Meeresbiol. Beitr.* 2, 215–225.

Conflict of Interest Statement: The authors declare that the research was conducted in the absence of any commercial or financial relationships that could be construed as a potential conflict of interest.

The reviewer JW and handling Editor declared their shared affiliation.

Copyright © 2018 Thoms, Burmeister, Dippner, Gogina, Janas, Kendzierska, Liskow and Voss. This is an open-access article distributed under the terms of the Creative Commons Attribution License (CC BY). The use, distribution or reproduction in other forums is permitted, provided the original author(s) and the copyright owner are credited and that the original publication in this journal is cited, in accordance with accepted academic practice. No use, distribution or reproduction is permitted which does not comply with these terms.

frontiers in Earth Science

ORIGINAL RESEARCH
published: 27 July 2018
doi: 10.3389/feart.2018.00103

Sub-marine Continuation of Peat Deposits From a Coastal Peatland in the Southern Baltic Sea and its Holocene Development

Matthias Kreuzburg[1], Miriam Ibenthal[2], Manon Janssen[2], Gregor Rehder[1], Maren Voss[3], Michael Naumann[4] and Peter Feldens[5]**

[1] Marine Chemistry, Leibniz-Institute for Baltic Sea Research, Warnemünde, Germany, [2] Soil Physics, Faculty of Agricultural and Environmental Sciences, University of Rostock, Rostock, Germany, [3] Biological Oceanography, Leibniz-Institute for Baltic Sea Research, Warnemünde, Germany, [4] Physical Oceanography and Instrumentation, Leibniz-Institute for Baltic Sea Research, Warnemünde, Germany, [5] Marine Geology, Leibniz-Institute for Baltic Sea Research, Warnemünde, Germany

Coastal low-lying areas along the southern Baltic Sea provide good conditions for coastal peatland formation. At the beginning of the Holocene, the Littorina Sea transgression caused coastal flooding, submergence and erosion of ancient coastlines and former terrestrial material. The present Heiligensee and Hütelmoor peat deposits (located near Rostock in Northern Germany) were found to continue more than 90 m in front of the coastline based on on- and offshore sediment cores and geo-acoustic surveys. The seaward areal extent of the coastal peatland is estimated to be around 0.16–0.2 km^2. The offshore boundary of the former peatland roughly coincides with the offshore limit of a dynamic coast-parallel longshore bar, with peat deposits eroded seawards. While additional organic-rich layers were found further offshore below a small sand ridge system, no connection to the former peatlands can be established based on ^{14}C age and C/N ratios. The preserved submerged peat deposits with organic carbon contents of 37% in front of the coastal peatland Heiligensee and Hütelmoor was radiocarbon-dated to 6725 ± 87 and 7024 ± 73 cal yr BP, respectively, indicating an earlier onset of the peatland formation as presently published. The formation time of the peat layers reveals information about the local sea level rise. The local sea level curve derived from our ^{14}C-dated organic-rich layers is in general agreement to nearby sea level reconstructions (North Rügen and Fischland, Northern Germany), with differences explained by slightly varying local isostatic movements.

Keywords: coastal peatland, Holocene development of the southern Baltic Sea, shallow water hydroacoustic surveys, Heiligensee and Hütelmoor, submerged peatland, radiocarbon age dating of submerged peat deposits, peatland formation, sub-marine continuation of a coastal peatland

OPEN ACCESS

Edited by:
Elinor Andrén, Södertörn University, Sweden

Reviewed by:
Fabio Matano, Consiglio Nazionale Delle Ricerche (CNR), Italy
Ole Bennike, Geological Survey of Denmark and Greenland, Denmark

****Correspondence:***
Matthias Kreuzburg
matthias.kreuzburg@io-warnemuende.de
Peter Feldens
peter.feldens@io-warnemuende.de

Specialty section:
This article was submitted to Quaternary Science, Geomorphology and Paleoenvironment, a section of the journal Frontiers in Earth Science

Received: *30 April 2018*
Accepted: *05 July 2018*
Published: *27 July 2018*

Citation:
Kreuzburg M, Ibenthal M, Janssen M, Rehder G, Voss M, Naumann M and Feldens P (2018) Sub-marine Continuation of Peat Deposits From a Coastal Peatland in the Southern Baltic Sea and its Holocene Development. Front. Earth Sci. 6:103. doi: 10.3389/feart.2018.00103

INTRODUCTION

Shallow coastal areas and shorelines are important for social, economical, and scientific purposes, for example development of coastlines, land usage, and infrastructure, archeology, sediment dynamics, and biogeochemical fluxes (Small and Nicholls, 2003; Valiela, 2009; Wong et al., 2014). Soft coastlines around the globe increasingly suffer from adverse processes such as erosion, flooding and submergence. Sea level rise and climate change will increasingly stress and shape coastal urban living areas and ecosystems in the future (Vestergaard, 1997; Stigge et al., 2005; Thorne et al., 2007; Furmanczyk and Dudzinska-Nowak, 2009; Nicholls and Cazenave, 2010). In the Baltic Sea, present

shorelines were shaped during the Littorina Sea period since ∼8,000 cal yr BP (Björck, 1995; Lemke, 1998) following the last glacial maximum (LGM).

Ongoing coastal dynamic processes such as wave and current induced erosion, sediment transport and accumulation have influenced the evolution of coastlines immensely (Lehfeldt and Milbradt, 2000; Schlungbaum and Voigt, 2001; Harff et al., 2009). These processes have led to coastline displacement due to land-loss or land reclamation and therefore changed spatial extensions of coastal ecosystems and habitats. One of the most vulnerable coastal areas is low-lying coastal wetlands. These wetlands are highly endangered by sea water intrusion, erosion and submergence (Vestergaard, 1997; Nicholls and Cazenave, 2010; Wong et al., 2014). Along the Baltic Sea, about 1,800 km^2 of coastal wetland is influenced by saltwater intrusion (Sterr, 2008). Sea level rise is further expected to result in a loss of wetland areas in inland direction provided that accumulation of sediments is lower than erosion and the vertical growth rate is below that of sea level rise (Vestergaard, 1997; Lampe and Janke, 2004). During the post-glacial evolution of the southern Baltic Sea and the accompanying sea level rise (Lampe, 2005) sub-marine terraces of ancient shorelines developed (Kolp, 1990). With the onset of the Littorina transgression around 8000 calibrated years before present (cal yr BP) (Lampe, 2002; Reimann et al., 2011) the southern Baltic sea level rose rapidly to around 2 m below present sea level. Around 5,800 cal yr BP, the sea level stabilized and has remained largely stable in this local area since 4,000 cal yr BP. Where preserved, the age and position of basal peat deposits, as formed in former coastal wetlands, can be used to obtain information about past sea level (Milliman and Emery, 1968; Gehrels and Anderson, 2014).

The Holocene sea level rise in the Baltic Sea deviates strongly from the eustatic sea level rise and can vary widely locally. This was, and partly still is, caused by different effects of isostatic adjustment (Köster, 1961). The current isostatic movements result in a subsidence of the southern Baltic Sea coast by about 0.1–0.2 cm yr^{-1} (Lampe, 2005; Rosentau et al., 2007; Lampe et al., 2011), and an approximate relative sea level rise of 0.1–0.12 cm yr^{-1} (Dietrich and Liebsch, 2000) increasing the pressure caused by the eustatic sea level rise on the local coastal wetlands and also affecting the presence of bedforms in shallow waters.

In this study, we investigate the shallow offshore continuation of a coastal wetland at the southern coast of the Baltic Sea, using a combination of hydroacoustic methods, geologic surveys and physical and geochemical characterization of surface sediments and sediment cores. Our first objective is to determine the surface and subsurface structure offshore the wetland area and its former extension into the Baltic Sea. The second objective is to reconstruct the Holocene dynamic of the wetland formation and erosion.

STUDY SITE

The study site is a shallow coastal area (0–10 m depth) that adjoins an approximately 3 km long coastline of the nature reserve "Heiligensee und Hütelmoor" located northeast of Rostock-Warnemünde, northern Germany (**Figure 1**). The southwest-northeast striking coastline between the investigated area and the Fischland-Darß peninsula (**Figure 1**) is heavily exposed to the prevailing westerly wind conditions, mainly originating from low pressures crossing the northern Atlantic. Alongshore currents lead to sediment transport in a northeastern direction, accumulating along the barrier spit of the Fischland-Darß peninsula (Lampe et al., 2011). At the study site, a dune dike separates the coastline from the landside, which is a partly degraded peatland, extending 1.59 km in the north-south direction and 1.38 km in the east-west direction (Koebsch, 2013). To the east, the wetland is surrounded by the Rostocker Heide, a forest area with sandy soils >2 meter above mean sea level (m amsl). The formation onset of this low-lying (−0.1 to +0.7 m amsl) wetland is described to begin between 5,400 and 3,900 cal yr BP (Voigtländer et al., 1996; Bohne and Bohne, 2008). Following the glacial retreat, a post-glacial river delta (named the Ur-Recknitz) discharging into a glacial lake led to the partial erosion of glacial till and subsequent deposition of fine sand (Kolp, 1957). The constant rise of the sea level caused by the Littorina transgression, as well as the subsequent rise of the groundwater level resulted in organic material accumulation on top of the sands and led to the formation of the peatland (Dahms, 1991). Today, the onshore peat layer is up to 3 m thick (Voigtländer et al., 1996) behind the dune, and gradually thins out toward the surrounding forest. The peat consists of moderately to strongly decomposed Carex and Phragmites. Underneath, the peat layer is underlain by 3–10 m thick sediments of fine sands and glacial till. In the area surrounding Lake Heiligensee, lake sediments are found underneath the peat. The peatland was artificially drained by open ditches, with an intensive drainage starting in the 1970s, which caused a severe degradation of the upper peat horizons and subsidence of the soil surface. The peatland has been rewetted in 2010.

Within the last decades, the wetland has experienced multiple different ecological stages due to diverse anthropogenic influences (Voigtländer et al., 1996). Average coastal retreat rates between 1907 and 1971 were 114 cm yr^{-1} in the north (Rebentrost, 1973) and 20–25 cm yr^{-1} in the south of Lake Heiligensee (Kolp, 1957). To counter the continuing coastal erosion, an artificial dune dike was constructed in 1903 and rebuilt in 1963 (Miegel et al., 2016) to separate the low-lying areas from the Baltic Sea (Voigtländer et al., 1996; Bohne and Bohne, 2008). However, the area experienced several wash-over events, the latest in 1995, which required the reconstruction of the dune dike in 1996. With the aim of land renaturation, protection and maintenance of the dune system was abandoned in the year 2000. Since then, the coastline has been subjected to coastal erosion with coastal retreat rates of 120–210 cm yr^{-1} (Generalplan Küsten und Hochwasserschutz, Mecklenburg-Vorpommern). Estimation by Voigtländer et al. (1996) stated that since the onset of peatland formation, coastal erosion led to approximately 3 km of wetland-loss toward eastern direction. This results in outcropping peat-layers along the beach, which are then exposed to wave erosion along the seaward edge of the wetland following the abrasion of covering sand layers by storms.

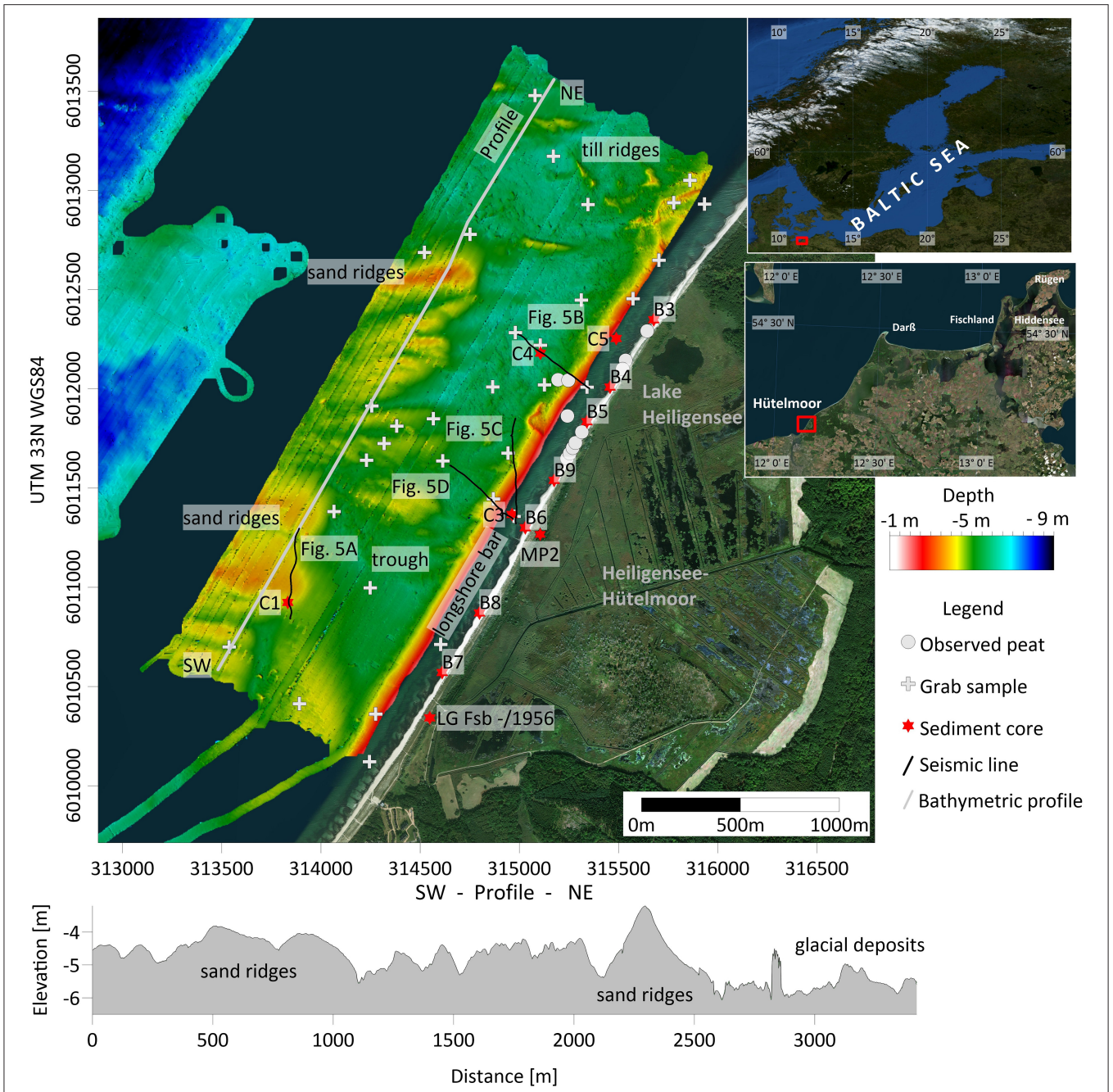


FIGURE 1 | (Top) Bathymetry and location of the study area along the southwestern Baltic Sea coast. White line parallel to the shore in SW-NE direction indicates the bathymetric cross section shown underneath. The positions of sediment cores (red stars) and grab samples (white crosses) are also indicated. The black lines show the locations of the seismic profiles. The longshore bar was identified from the parametric echosounder data (INNOMAR, see Methods). **(Bottom)** Bathymetric SW-NE transect at the upper shoreface indicating the distribution of the main geological units.

METHODS

Acquisition of Geophysical Data

Bathymetric and backscatter intensity data were collected with a Norbit iwbms multibeam echo sounder, which was pole-mounted on the research boat Klaashahn. Data in shallow waters (1.5–7 m) were recorded in June 2016 and July 2017. The Norbit iwbms uses an 80 kHz wide chirp signal centered at 400 kHz and an opening angle of 130–155°, set depending on water depth. Navigation data were acquired using an Applanix Surfmaster inertial navigation system utilizing the EGNOS correction. Total navigation accuracy is about 0.5 m both in the latitude and longitude direction. In addition to continuous sound velocity measurements at the multibeam transducer head, water

column sound velocity was measured using an SVP probe. The preparation of bathymetric data was completed using the Hypack (2016) software. Data processing included a quality control, the automatic, and manual removal of spikes, the correction of roll and pitch offsets, as well as the application of water column SVP profiles. Data were then gridded to a resolution of 0.5 m. Backscatter intensity data were processed using mbsystem (Caress and Chayes, 1995). A correction for the angular varied gain, including the multibeam residual beam pattern, was applied using mbbackangle. The backscatter data were passed through a gaussian low-pass filter to reduce speckle noise and gridded to a resolution of 0.5 m.

Seismic data were acquired using an INNOMAR standard parametric echo sounder during the June 2016 survey. In total, seismic data were acquired for the area covering a distance of 30 km. The system was pole-mounted on the Klaashahn research vessel. Data were recorded at frequencies of 8, 10, and 15 kHz, of which the 15 kHz frequency is shown in this study. A low pass swell filter was applied to remove heave artifacts caused by a malfunctioning motion sensor. However, due to the rapid movements of the small vessel, the wave impact could not be entirely removed. Two-way-travel time were converted to depths using a sound velocity of 1,480 m/s.

Ground Truthing

For seafloor ground truthing of the backscatter data, twelve 30 cm sediment cores were taken during scientific-diver missions and 20 surface sediment grab samples were taken from a boat. Deeper vertical ground truthing of the seismic data was achieved using 4 sediment cores (**Figure 1**) retrieved from maximum sediment depths of 280 cm with hand-pulling extraction tools from the BOREAS drilling platform (Lampe et al., 2009). The closed probe heads (STITZ) of 1 and 2 m, respectively were fitted with customized PVC liners of Ø46 mm for core extraction.

In total 7 sediment cores on land were taken with a percussion driller (Rammkernsonde). Open metal rods of Ø40 mm were used to sample sediment cores to a depth of −3.5 m below sea level (bsl). To assess the peat thickness in more detail, peat probings were conducted in the shallow coastal water. A Ø1 cm metal rod was pushed through the peat and stopped by the sand layer. All drilling and sampling locations were leveled with a real-time kinematic and differential GPS (Leica Viva Net-Rover).

Grain Size Distribution

Given the sandy composition of the analyzed sediments, no chemical pretreatment was performed. The grain size distribution of surface sediments (grab samples) was determined from sub-samples (∼150 g) of homogenized sediments. Dry sieving was conducted with DIN standard ISO 3310-1 sieves. Fractions <0,063 mm were lost during washing and were determined by weight difference compared to the total weight after washing and drying. Fractions >2 mm were retained. Automated sieving was conducted by a computer-controlled sieving tower (AS200) and a coupled Sartorius balance.

The grain size distribution of the sediment cores was determined by laser diffraction using an CILAS 1180, as not enough material for traditional sieving was available. Grain sizes larger than 1 mm cannot be measured with this method. To allow a comparison between the grain size distributions obtained with both methods, the first mode is used as the central statistical parameter. The mode is unaffected by removing the fine (mechanical sieving) or coarse (optical grain size distribution) sediment fraction, and can be used for bimodal sediments. All grain sizes are shown using the PHI scale, with PHI = – log2d, where d is the grain size in mm.

Geochemical Analyses and ^{14}C Dating

Organic carbon contents (C_{org}, after digestion with HCl) and stable isotope analyses of $\delta^{13}C$ of bulk material were performed on 2 onshore- and 3 offshore sediment cores using an infrared Elemental Analyzer Multi EA 2000 CS. Oven-dried samples were ground in an agate motor mill and homogenized. Splits of 10–20 mg powdered, homogenized sample were weighed in tin (C_{inorg}) and silver (C_{org}) containers (Nieuwenhuize et al., 1994). Stable isotope analyses of $\delta^{13}C$ was performed using an Isotope Ratio Mass Spectrometer (IRMS, Thermo Fisher Scientific), connected to an elemental analyzer via an open split interface. The $\delta^{13}C$ (‰) represents the isotope ratio of $^{13}C/^{12}C$ between the sample and a standard. The reference gas was ultra-pure CO_2 from a bottle calibrated against international standards (IAEA-C3, IAEA-C6, NBS 22) at the Leibniz-Institute for Baltic Sea Research (IOW). Calibration for carbon quantities was done with the reagent acetanilide. The lab internal standard was peptone (Merck) with a standard deviation of <0.2‰. AMS ^{14}C age control of plant material, shells, wood and bulk organic carbon dating (**Table 1**) was done by the commercial testing laboratory Beta Analytics (https://www.radiocarbon.com). Calibration of ^{14}C ages was done following Reimer et al. (2013).

RESULTS

Onshore

The general sediment sequence in a transect along the beach (**Figure 2**) shows a fine basin sand, at some spots followed by gyttja that presumably formed in former local depressions, and a peat layer on top. The peat is covered by marine medium to coarse, partly gravelly sands at the beach, and partly covered by dune sand further inland. In the north-eastern part of the transect, up to 2.5 m of silty to clayey sediments of gray-blueish to whitish color are found between the fine sands and the gyttja. The elevation of the peat surface along the transect decreases from NE to SW from 0.15 m bsl in core B5 to 2.84 m bsl in core B8. In addition, peat thickness tends to decrease in the same direction. The maximum peat thickness of 1.55 m (B9) and 1.4 m (B4) are found on top of gyttja. The minimum peat thickness of 0.1 m is found at B8. Further inland, the peat layer clearly extends southwards of core B7, indicating partial erosion of peat along the coastline. Additional peat probing conducted between B3 and B5 further seaward in shallow water depths (<0.5 m) indicate that the peat surface dips seawards. Sediment core MP2 (**Figure 1**) was retrieved near the position of B6 but further landward behind the dune dike. Here, the peat layer is found between depths of −0.7 and −3 m bsl with a 10 cm thick layer of gyttja below the base of the peat. The peat layer (and gyttja) at the beach (B6) was

TABLE 1 | Available age control ^{14}C in the study area. Age intervals are given at a 95.4% confidence interval.

Core ID	Core depth (cm)	Lat (N)	Long (E)	^{14}C age (yr BP)	cal yr BP	Material	C/N	$\delta^{13}C$ (‰)	C_{org} (%)
C1.1	190	54.212455	12.144969	8,040 ± 30	8,586 ± 256	Shell (Marine)	–	–	–
C1.2	190	54.212455	12.144969	4,430 ± 30	4,972 ± 137	Gyttja	11.97	−25.2	5.12
C3.1	150	54.216839	12.161998	5,900 ± 30	6,725 ± 87	Peat	36.4	−27.1	37.5
C3.2	165	54.216839	12.161998	6,160 ± 30	7,024 ± 73	Wood	15.2	−28.6	8.1
B9	305	54.218463	12.16515E	5,950 ± 30	6,769 ± 128	Gyttja	71.46	−30.5	50.25
B6.1	300	54.216265	12.163076	3,290 ± 30	3,516 ± 87	Peat	60.7	−28.08	51.06
B6.2	308	54.216265	12.163076	5,150 ± 30	5,918 ± 45	Gyttja	1.46	−27.92	19.83

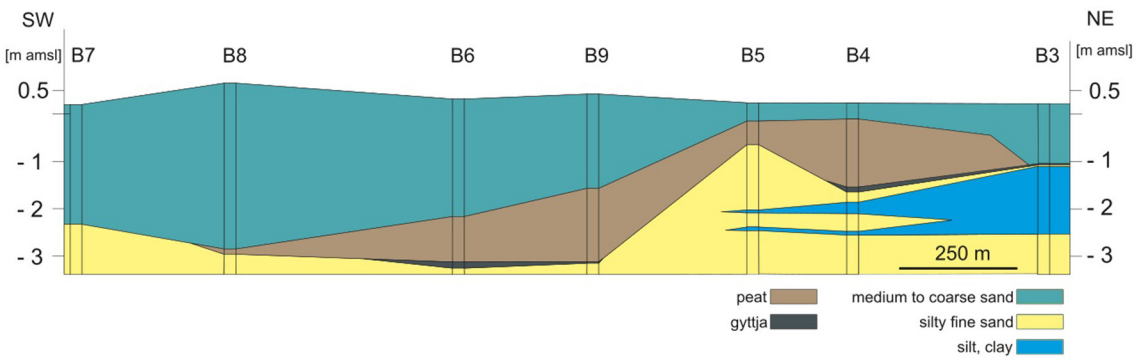


FIGURE 2 | Geological profile along the beach with drilling locations (B3–B9); sediment depth in meter above mean sea level (m amsl). Refer to **Figure 1** for coring locations.

also found to continue toward the hinterland behind the dune dike (MP2, **Figure 1**).

Offshore

Bathymetry

The bathymetric map (**Figure 1**) shows a series of sand ridges emerging seaward of a flat trough-like area. The SW/NE-elongated local trough extends roughly 1.2 km and is bound by nearshore sand bars in the east, and sand ridges in the southwest. The trough broadens in northern direction. Water depth in the broad northern part of the trough mostly exceeds ∼6 m. Here, numerous boulders and glacial till ridges, which have been observed during diver missions, are found. Several east-west to northwest-southeast oriented elevations of 450 m in length and up to 1.2 m in height are crossing the northern part of the trough. West and south-west of the trough, decreasing water depths are observed toward the sea. Here, a number of east-west oriented sand ridges 0.6–1.5 m in height, mostly 75–250 m in width, with one ridge reaching a width of 375 m, and up to 320 m observed length are located oblique (40–60°) to the coastline in water depths of 3–4 m. The maximum length of the ridges can be constrained to 1 km based on bathymetric data available further offshore (**Figure 1**). Generally, the ridges slope gently with angles mostly <0.5°. Although not all sand ridges follow the pattern, a slight asymmetry is observed, with wider and less inclined northern to north-western faces of the ridges (profile in **Figure 1**). In combination with the seismic data, a shore-parallel longshore bar can be identified that precedes the entire beach face. The longshore bar height is ∼1 m, while its width is 50–100 m.

Seafloor Composition

Backscatter mosaics ground-truthed with grab samples and short sediment cores allowed differentiation of three major facies types of seafloor in the study area (**Figure 3**): well sorted fine sand, medium sand with low gravel percentage, and poorly sorted coarse sand and gravel. The well-sorted fine sand is characterized by low backscatter intensities with a generally smooth and homogenous texture. It is mainly observed in the southern and south-western part of the study area in water depths of 4–6 m, forming the sand ridges in the south and south-west. The area covered by well-sorted fine sands may be further differentiated. While difficult to differentiate in acoustic data of the used frequency, available ground truthing data suggest a combined clay and silt fraction of ∼5% in the trough (**Figure 1**) separating the sand ridges and the beach face. The clay and silt fraction is absent within the sand ridges. In contrast, the sand ridges show a higher percentage of the medium to coarse sand fraction of ∼5%. Seafloor comprising medium sand with a low gravel percentage is characterized by medium backscatter intensities and is primarily observed along the runnels in-between the sand ridges, and fringing the boundaries of coarser sediment deposits. Seafloor composed of poorly sorted coarse sand and gravel (gravel content of up to 50%) is characterized by high backscatter intensities,

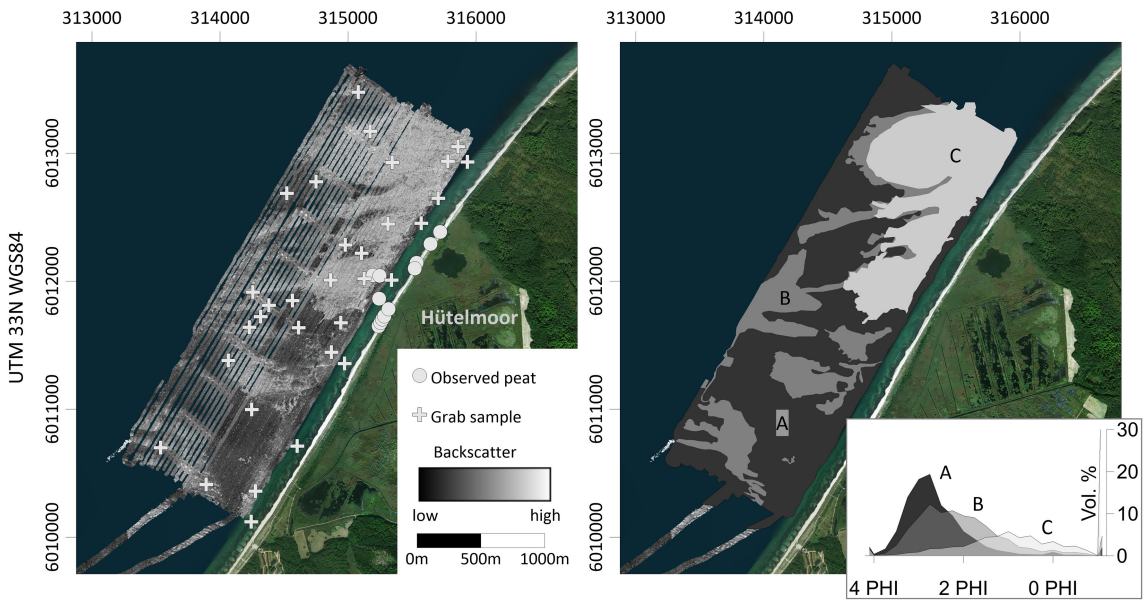


FIGURE 3 | (Left) Available backscatter data with grab samples for surficial ground truthing and near-coastal peat observations. **(Right)** Manual clustering of the backscatter data into three seafloor facies A–C. Representative grain size distributions for each facies are displayed, with A fine sand (black), B gravelly medium sand (gray), and C gravelly coarse sand (light gray). The insert in the **(Right)** panel indicates the grain size distribution (PHI-scale) in Vol %.

with numerous stones, boulders and uncovered glacial till. These deposits are observed in the north-eastern part of the study area (**Figure 3**).

Sediment Cores

Locations for sediment cores were selected based on thin seismic reflections, located parallel to the sediment surface at 3 m bsl and interpreted as the submerged extension of the peat sequence. Sediment core C1 was recovered in a water depth of 6.5 m (**Figure 4**, for location see **Figure 1**). At the base of the core from 280 to 248 cm depth, a sediment sequence composed of fine sand and scattered shell fragments was recovered, followed above by decimeter thick coarse and fine sand units, discontinued by layers of fine sand above. Following a sharp boundary, at 190 cm core depth two dark, 5- and 3 cm thick gyttja layers with shell fragments are separated by well-sorted fine sands. Two radiocarbon ages from the lower organic layer were determined from one sample (**Table 1**). The samples have different ages, with 8,586 ± 256 cal yr BP for marine shells fragments (Peringia ulva, Macoma Baltica) and 4,972 ± 137 cal yr BP for the bulk organic sediments (C_{org} 5.12%, $\delta^{13}C$ −25.2‰, C/N-ratio 11.97).

Sediment core C3 (**Figure 4**) has a total length of 197 cm, and was recovered in a water depth of 1.8 m. The lowest unit (171–197 cm) is mostly composed of fine sand featuring dark layers with C_{org} of 0.4%, $\delta^{13}C$ of −27.2‰ and C/N-ratios of 11.6. It is followed by a gyttja layer (C_{org} 8.1%, $\delta^{13}C$ −28.6‰, C/N-ratios 15.2) containing wooden fragments, which were dated to 7,024 ± 73 cal yr BP (C3.2) and a decimeter thick peat layer at 146–160 cm depth. Peat material (C3.1) has been dated to 6,725 ± 87 cal yr. Organic carbon contents of 36.9 and 37.5% (C_{org}), stable isotopic signatures of ($\delta^{13}C$) −28.9 and −27.1‰ and C/N ratios of 21.3 and 36.4 were measured in this peat layer. The peat layer itself is a horizon of a pure freshwater habitat representing a former preserved land surface. Separated by an erosional boundary, sediments above the peat are mostly composed of fine to medium marine sands with little change in grain size distribution.

Sediment core C4, with a total length of 120 cm, was retrieved in a water depth of 5.3 m. The bottom part (113–120 cm) is composed of glacial till. Sediments above the till, separated by a sharp boundary, alternate between fine and medium sands. Surface sediments (4–12 cm) are composed of dark coarse sand including coarse gravel of 2–3 cm diameter, sharply followed by dark fine sands. Sediment core C5 was retrieved in a water depth of 1 m and has a total length of 117 cm. The bottom sediment in C5 is composed of medium sand containing fine gravels with low sphericity. Above a diffuse transition, it is followed by two distinct layers of minerogenic lake sediments at 110–93 and 88–62 cm that are separated by a well-sorted fine sand layer of ∼5 cm thickness. Above, a coarsening upwards trend of medium to coarse sands prevails. At 38 cm a black layer of ∼3 mm thickness with C_{org} of 1.22%, $\delta^{13}C$ of −24.36‰, and C/N of 10.66 is observed.

Subsurface Structure

Subsurface information is derived from seismic reflection data (**Figure 5**, for location see **Figure 1**) and ground truthing by sediment cores of various lengths. Glacial till that commonly forms the acoustic basement for high-frequency seismic surveys in the Baltic Sea, forms the substratum of the observed stratigraphy. The glacial till is generally dipping from North to South. In addition, its top is slightly inclined toward the offshore

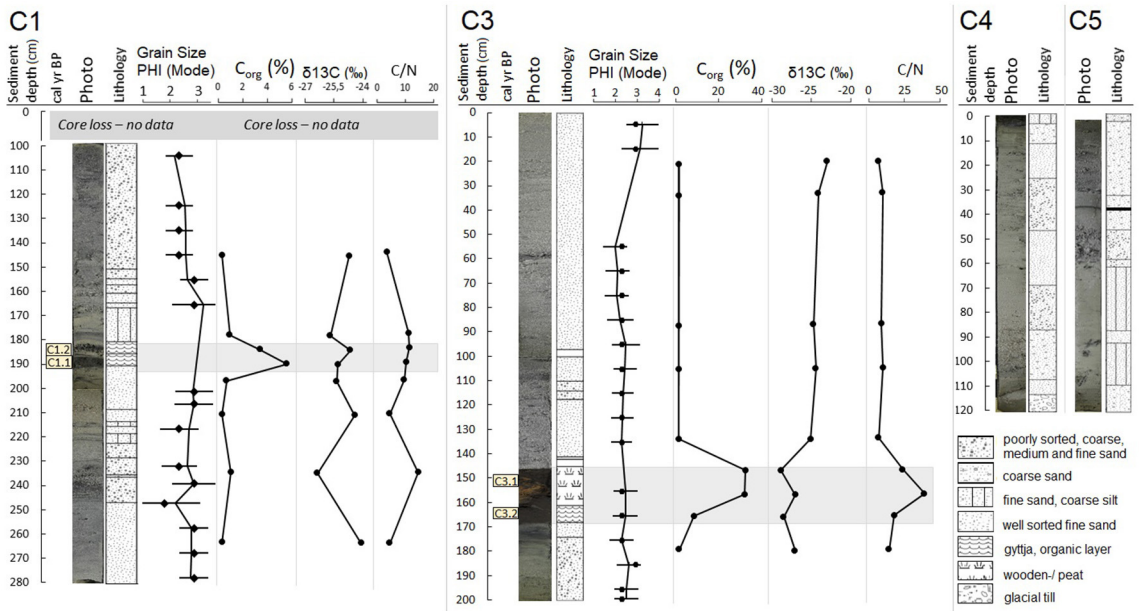


FIGURE 4 | Sediment depths (cm), radiocarbon age-dating, photographs, lithology, grain size distribution, organic carbon content (%), isotope ratio $\delta^{13}C$ (‰), Carbon/Nitrogen ratios (C/N) of the 4 offshore sediment cores (C1, C3, C4, C5) retrieved from the study site.

direction and is marked by steep irregularities, corresponding to outcropping till ridges observed in the bathymetric data. The burial depth of the till surface controls the accommodation space available for the overlying sediments. Acoustically homogeneous to transparent material (**Figures 5A–D**, labeled with medium sand) partly fills the irregularities. Where these materials outcrop at the seafloor, medium sand with low gravel percentage is retrieved in grab samples (**Figure 5B**). Layered sedimentary units (marked with H in **Figures 5A–D**) thin as till deposits emerge in the north of the research area. Based on ground truthing with sediment cores C1 and C3, the layered sediments are of Holocene age. They are characterized by high amplitudes and frequently show internal reflectors indicating different layers of sediment. In several locations, a chaotic and disturbed appearance of the Holocene deposits prevails, and individual reflectors cannot be followed. The Holocene sequence includes organic sediments and peat that have been retrieved in sediment cores C1 and C3. At the exact location of the sediment cores, the peat layer is difficult to recognize in the seismic data. Thin reflections located roughly parallel to the sediment surface at a depth of ∼3 m bsl (**Figures 5B–D**) are interpreted as corresponding to the peat sequence observed in the cores at the same depth. The peat layer continues with decreased reflection intensities beneath the longshore sand bar observed in bathymetric data, where it terminates unconformably against its seaward base (**Figures 5B–D**). Its continuation landwards of the coring position cannot be reliably determined due to the shallow multiple. In the seismic data, the longshore sand bar shows faintly visible internal, offshore-directed lamination. It has medium to low acoustic transparency, and a maximum observed thickness of ∼1.5 m. In the western and south-western part of the investigated area, sand ridges composed of fine sand (**Figure 5A**) unconformably overlie the layered deposits beneath. The sand ridges are characterized by a homogeneous, transparent signature with hardly any internal reflections. They reach an observed thickness of ∼1 m at maximum. Showing the same acoustic characteristics but located further north, isolated lenses of fine sand with a thickness of <1 m are deposited on top of the medium sand (**Figure 5B**). Several profiles in the near-coastal-zone of the central study area are cross-cutting a shore-parallel sand bar.

DISCUSSION

Geomorphological Setting

The combination of high resolution hydro-acoustics, subsurface information and sediment composition analyses confirms large heterogeneities between the northern and the southern shoreline as well as the offshore sand ridge area. Well- sorted fine sands prevailingly cover the southern trough area and form the sand ridges, medium sands with low gravel percentage separate the sand ridges and the northern plain area where glacial deposits are located close to the seafloor surface. In contrast, increasing sedimentation of medium to fine sand results in decreasing water depths and sheltered environments toward the south, indicated by internal lamination of Holocene deposits (**Figures 5B–D**) in the seismic data.

The sand ridges are a prominent geomorphological feature in this nearshore study site. Shoreface connected sand ridges are widespread on continental shelves, and are best described in the eastern Atlantic and in the Dutch and German part of the North Sea (van de Meene and van Rijn, 2000; Zeiler et al., 2008). Sand

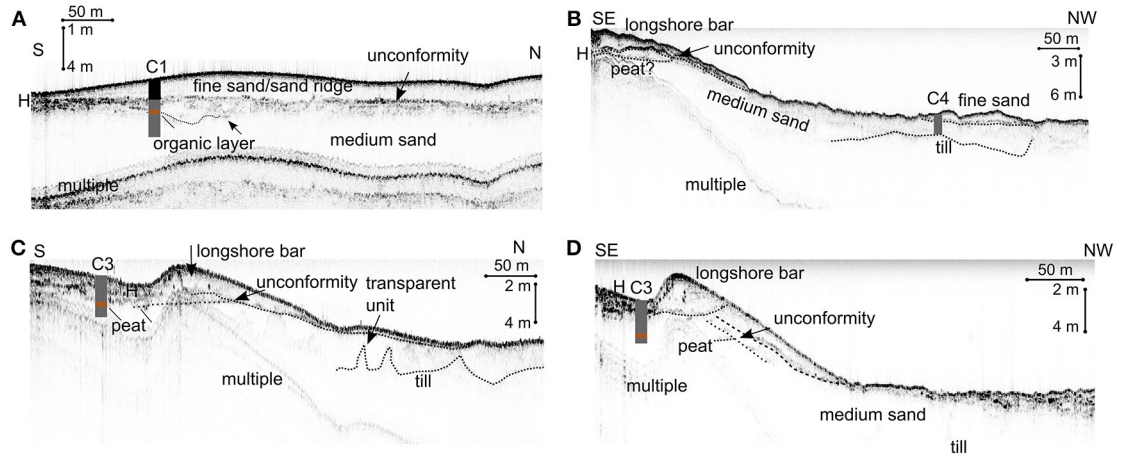


FIGURE 5 | Seismic data of profiles **(A–D)**. Sediment cores to prove the ground truthing are indicated. The position of core C3 was extrapolated to the nearest shot points of seismic lines **(C,D)**. The distance to line **(C)** is 25 m, and the distance to line **(D)** is 15 m. Refer to **Figure 1**. for location of the seismic lines.

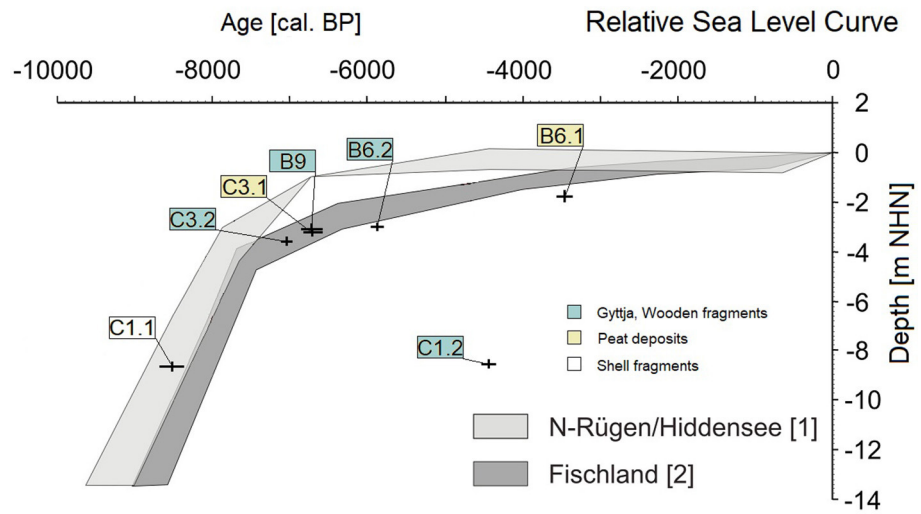


FIGURE 6 | Local Holocene sea level curve based on Lampe et al. (2010) with age/depth relationships obtained in this study.

ridges are formed both by tidal currents (negligible in the Baltic Sea) as well as by wind/storm generated longshore currents, and they can persist for several thousand years (Snedden and Dalrymple, 1999). However, no reports of shoreface connected sand ridges in the southern Baltic Sea exist to our knowledge. A main reason for the local scarcity of sand ridges is the heterogeneous and patchy sediment composition in the Baltic Sea compared to other shelf regions causing sediment-starved conditions (Schwarzer, 2010; Feldens et al., 2015). Thus, the Baltic Sea lacks sufficient sand supply for the formation of sand ridges in most regions. Still, the sand ridges observed offshore the Hütelmoor is interpreted as a small sand ridge field. The ridges downdrift tip is oriented toward the coast, in agreement with dominant SW-NE directed longshore currents. The variable length-to-width ratio (∼ 2 to 10), which is lower here by the Hütelmoor than in comparable nearshore ridges (Pendleton et al., 2017), low height (Nnafie et al., 2014), and shallow base may indicate a frequent reworking of the fine sand ridges by background wave action, while formation of the ridges requires intense storm activity (Swift et al., 1978). The time of formation of the sand ridges offshore the Hütelmoor can be constrained by the available ^{14}C date within core C1 and the seismic data. Since the base of the sand ridges forms an unconformity to the material of core C1 (**Figure 5A**), they have to be formed subsequently to the deposition of the youngest dated material below at 3,582–3,450 cal yr BP at a time when the Baltic Sea sea level reached its present value and was approximately nearly stable (**Figure 6**).

The entire beach area is preceded by a longshore bar (**Figure 1**) consisting of fine to medium sand and is the result of nearshore sedimentation processes. Longshore bars are common

on micro-tidal sandy beaches, and are characterized by a steep slope facing the beach and a smoother, longer, offshore-facing slope (Guillén and Palanques, 1993; Zhang et al., 2011). The stability and position of longshore bars are influenced by coastal dynamics such as wave energy and sea level variations. Sea level rises cause a higher wave energy and an upwards movement (Wright and Short, 1984; Lippmann and Holman, 1990). In exchange, the shape of the longshore bar controls the amount of energy that reaches the beachface and thus controls sediment erosion or accumulation. Preserved mid-Holocene peat deposits (6,725 ± 87 cal yr BP) at the base of the longshore bar (C3.1) archive information about associated paleo-landscapes, pre-existing floodplains, habitat migration, sediment stability and its seasonal equilibrium morphology (Gerdes et al., 2003; Westley and Dix, 2006; Plets et al., 2007). The sub-marine extension and formation time of the peat deposits is discussed in the following section.

Sub-marine Extension of the Peat Deposits

Corresponding to the geometry of the till deposits in the study area, peat deposits in the northern part are located in more shallow depths of ∼1 m bsl (cores B4 and B5, **Figure 2**). As these peat deposits are observed at the beach face ("observed peat" in **Figure 1**) they become increasingly exposed to coastal dynamics. Ongoing peat erosion near Lake Heiligensee (**Figure 1**) caused by a washover event was reported in spring 1995 (Krüger, 1995), and minor erosion can be observed regularly after storm surges, when peat blocks with dimensions of several decimeters are washed up on the beach. The offshore continuation of the peat layer is limited, as no corresponding deposits have been found in core C5. Peat deposits might extend below the longshore bar, as a corresponding reflector below its base (**Figure 5B**) shows similar acoustic characteristics to reflections ground truthed near core C3. A former sub-marine extension of the peat layer in the northern part of the study area is further supported by core C5. The core contains alternating layers of minerogenic lake sediments and fine sand, with a corresponding sediment sequence found below the peat deposits in core B4 (Gerdes et al., 2003).

Peat deposits in the southern and central part of the study site are better preserved due to their deeper burial (**Figure 2**). The elevation difference between the peat base in B9 in the south and in B4 in the north is ∼2 m. The southern peat deposits could be sampled both on- and offshore. Due to a comparable age of formation (discussed in section Formation Time and Local Sea Level Rise), the same sediment sequences of silty fine sand, gyttja and peat (**Figure 7**) with similar depths of these layers both on- and offshore, and corresponding horizontal reflections in the seismic data, the sub-marine peat is interpreted as a seaward extension of the peat deposits on land (**Figure 7**). Seismic data imply a seaward extension of the peat layer that was detected in C3 to the seaward dipping base of the longshore sand bar (**Figures 5C,D**), with no indication of peat deposits underneath the offshore sand ridges (core C1). Peat burial depth and thickness declines again toward south-west, and peat deposits are absent in core B7 (**Figure 2**). Onshore, peat sediments re-appear in sediment core Ig Fsb -/1956 (**Figure 1**) further south, containing peat deposits of 85 cm thickness. The reason for the hiatus found in the vicinity of B7 is most likely a single large storm surge in 1954, which eroded the covering sand layer and caused washover and erosion of peat blocks across a length of 100 m (Kolp, 1957). The sub-sedimentary, areal continuation of peat deposits under the nearshore sandbar can be roughly defined by the seismic data (**Figures 5B–D**), indicating spatial offshore extensions in the central and field observations along the northern part of the study site. Assuming a continuous deposit of the peat along the shoreline and homogeneous offshore extension, limited by the seaward extension of the longshore sand bar, a coherent submerged area of 0.16–0.2 km^2 can be estimated.

Formation Time and Local Sea Level Rise

The onset of the Heiligensee and Hütelmoor peatland formation was ascribed to Atlantic period in 5,400 yr BP (Bohne and Bohne, 2008). Submerged peat detritus (basal organic/gyttja) sampled in this study shows that the peatland development started as early as 7,024 ± 73 cal yr BP (sample C3.2). Albeit not dated, due to their base situated at 1 m bsl, peat deposits in the northern part of the study area are presumed to be younger compared to the dated peat deposits situated at a depth around 3 m bsl. An earlier formation of the peatland during the early Littorina transgression may be possible, with indications by the organic-rich layer retrieved in core C.1, but is rather unlikely. Despite the fact that the material was certainly reworked due to widely differing ages (**Figure 6**), the measured C/N ratios (11.97), $\delta^{13}C$ isotope values (−25.2‰) and the observation of marine shell fragments of the bulk material support the assumption that the increase of organic carbon content (C_{org} from 0.6 to 5.1%) within the organic layer of C1 is of marine-derived matter (Stein, 1991).

Near the shoreline, submerged gyttja deposits are overlain by peat layers dated to 6,725 ± 87 cal yr BP (C3.1). The variable presence of the gyttja—a lake sediment—is attributed to its formation in local depressions. The Hütelmoor is generally classified as a paludification mire, which formed as a consequence of a rising groundwater. However, at the same time, depressions turned into lakes within the wetland, where lacustrine sediments were deposited, and which were eventually filled up with peat by terrestrialization. The silty and clayey sediments found underneath the gyttja in the northern part of the beach are interpreted as clastic lacustrine or fluvio lacustrine sediments due to their high content of silt or clay and their position between the basin sand and the gyttja. A continuous basal sediment sequence in C3 suggests the autochthonous formation of the sediments, showing sand deposited under freshwater conditions, followed by gyttja deposited during wetland conditions and peat accumulation during the Littorina transgression. Basal peat deposits are frequently used to constrain past sea levels (Lampe and Janke, 2004; Rößler et al., 2011; Heinrich et al., 2017). In principle, the available ^{14}C ages agree with and support the local Fischland and North Rügen Holocene sea level rise curves (**Figure 6**) established by Lampe et al. (2010), but with a slight tendency toward lower sea level as determined by samples B6.1 and B6.2. The observed trend of lower reconstructed sea levels from the north (North of Rügen) to the south (this study) agrees well with different isostatic uplift rates (Lampe, 2005), with the North of Rügen experiencing uplift, and the more south Hütelmoor subsiding along the isostatic equilibrium line.

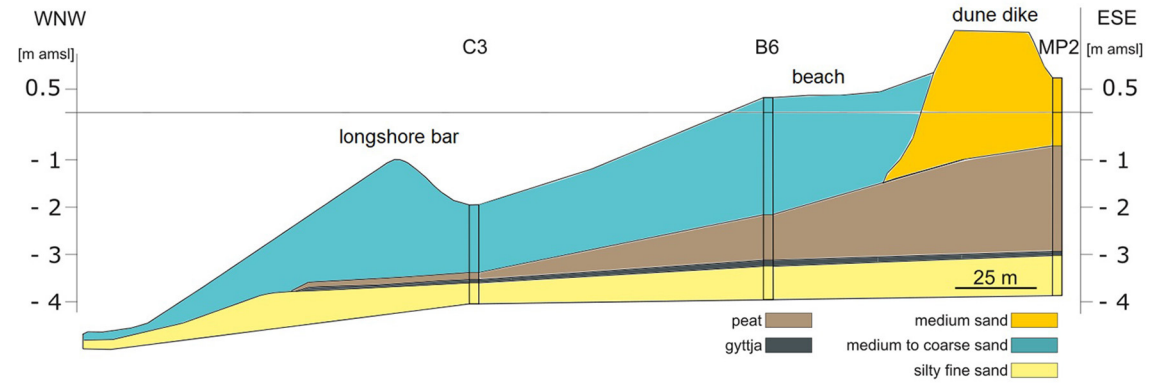


FIGURE 7 | Geological profile perpendicular to the coast with drilling locations (MP2, B6, C3—compare **Figure 1** for core locations) with sediment depths in m amsl. The information of sub-sedimentary peat continuation is based on ground truthing with core C3 and the continuation of internal reflectors in the seismic profiles.

The sharp and erosional upper boundary of both on- and offshore peat sediments indicates a sudden flooding of the former peatland. According to Meyers (1997) a C/N ratio of 20 or higher indicates terrigenous organic material and is evident within the submerged peat (C/N = 21.3 in 147 cm and 36.4 in 157 cm). In addition, a sudden increase of mean $\delta^{13}C$ isotope values from -27.9 ± 0.95 in the peat and sand deposits below the erosive boundary to -24.3 ± 0.8 in marine sands above suggests a shift from a terrestrial, freshwater environment to a marine saltwater environment (Bickert, 2000). Under the assumption of a coherent peatland system, the former erosion event of the palaeo-landscape can be constrained to a maximum age of 3,516 ± 87 cal yr BP (B6.1) and indicates a subsequent formation of the coastal longshore bar. Thereafter, the erosion of the sub-marine basal peat deposits was largely dependent on the position and stability of the longshore bar. The time frame and depth of the sampled peat deposits coincide with a period of continuously decreasing sea level rise (from >0.1 cm yr^{-1} to 0.05–0.08 cm yr^{-1}) starting around 7000 BP, allowing peat formation (~0.05–0.13 cm yr^{-1}) to keep up with the rising water table (van der Linden et al., 2008; Lampe et al., 2010, 2011). The center of the peatland was relocated from the present offshore area to the current location of the Hütelmoor. This is confirmed by peat detritus and peat of similar thickness deposited above on- and offshore basin sands in B6.2 (5,918 ± 45 cal BP), B9 (6,769 ± 128 cal BP), and C3.2 at a similar depth, respectively.

CONCLUSION

The combination of geological, geochemical and geophysical data provide a powerful method to reconstruct the coherent formation and former extension of the peatland in the working area, with peat deposits being now found across the on-/offshore zone. Slightly different formation ages are controlled by morphological differences. The large scale spatial distribution of the Hütelmoor peatland deposits since ~7,000 cal yr BP is controlled by the accommodation space above the glacial till substratum. The present offshore extension of the peat deposits is limited to the seaward base of the shore parallel sandbar. The formation of the peatland coincides with a slowdown of the sea level rise around ~7,000 cal yr BP, starting with the deposition of basal gyttja at 7,024 ± 73 cal yr BP and the deposition of peat at 6,725 ± 87 cal yr BP. As a function of coastline stability, erosion and flooding of the peatland have led and will lead to submergence of former terrestrial, high-organic material, shifting from terrestrial to marine ecosystems. It can be assumed that submerged peat layers are also present in front of other coastal peatlands along the southern Baltic Sea coast.

AUTHOR CONTRIBUTIONS

MK wrote the manuscript and conducted the geological offshore surveys. MI worked on the geological profiles, wrote the onshore descriptions and greatly supported the discussion. MJ greatly supported the research and writing of all sections of the manuscript. GR and MV supported the research and contributed to the writing of the manuscript. MN supported the geological offshore surveys and discussion on Holocene development. PF recorded hydroacoustic data and wrote the manuscript.

ACKNOWLEDGMENTS

This study was conducted within the framework of the Research Training Group Baltic TRANSCOAST funded by the DFG (Deutsche Forschungsgemeinschaft) under grant number GRK 2000/1. This is Baltic TRANSCOAST publication no. GRK2000/0012. We thank our colleagues from the GRK Baltic TRANSCOAST as well as Iris Liskow (IOW), who carried out high-quality geochemical analyses. We are grateful to Sebastian Lorenz and Jürgen Becker (University Greifswald) for support with the BOREAS-platform and the IOW-crews of the research vessels Klaashahn and Elisabeth Mann Borgese, the IOW-Scientific Divers and the support by the trainees Caroline Coccoli, Isabelle Wittstock, Florian Schneider, and Charlotte Westhoven. Further, we thank the Landesamt für Umwelt, Naturschutz und Geologie MV (LUNG) for providing detailed core data.

REFERENCES

Bickert, T. (2000). "Influence of geochemical processes on stable isotope distribution in marine sediments," in *Marine Geochemistry*, eds H. D. Schulz and M. Zabel, (Berlin; Heidelberg: Springer), 309–333.

Björck, S. (1995). A review of the history of the Baltic Sea, 13.0-8.0 ka BP. *Q. Int.* 27, 19–40. doi: 10.1016/1040-6182(94)00057-C

Bohne, B., and Bohne, K. (2008). *Monitoring zum Wasserhaushalt einer auf litoralem Versumpfungsmoor gewachsenen Regenmoorkalotte—Beispiel Naturschutzgebiet "Hütelmoor" bei Rostock*. Berlin: Aspekte der Geoökologie;Weißensee Verlag.

Caress, D. W., and Chayes, D. N. (1995). "New software for processing sidescan data from sidescan-capable multibeam sonars," in *Proceedings of the IEEE Oceans* 95 *Conference* (San Diego, CA), 997–1000.

Dahms, P. (1991). *Studie Wasserregulierung Hütelmoor*. Rostock: Unveröffentlichte Studie des StAUN Rostock.

Dietrich, R., and Liebsch, G. (2000). Zur variabilität des meeresspiegels an der küste von mecklenburg-vorpommern. *Z. Geol. Wiss.* 28, 615–624.

Feldens, P., Diesing, M., Schwarzer, K., Heinrich, C., and Schlenz, B. (2015). Occurrence of flow parallel and flow transverse bedforms in Fehmarn Belt (SW Baltic Sea) related to the local palaeomorphology. *Geomorphology* 231, 53–62. doi: 10.1016/j.geomorph.2014.11.021

Furmanczyk, K., and Dudzinska-Nowak, J. (2009). Effects of extreme storms on coastline changes: a southern Baltic example. *J. Coast. Res.* 1637–1640.

Gehrels, W. R., and Anderson, W. P. (2014). Reconstructing Holocene sea-level change from coastal freshwater peat: a combined empirical and model-based approach. *Mar. Geol.* 353, 140–152. doi: 10.1016/j.margeo.2014.04.004

Gerdes, G., Petzelberger, B. E. M., Scholz-Böttcher, B. M., and Streif, H. (2003). The record of climatic change in the geological archives of shallow marine, coastal, and adjacent lowland areas of Northern Germany. *Q. Sci. Rev.* 22, 101–124.

Guillén, J., and Palanques, A. (1993). Longshore bar and trough systems in a microtidal, storm-wave dominated coast: the Ebro Delta (Northwestern Mediterranean). *Mar. Geol.* 115, 239–252. doi: 10.1016/0025-3227(93)90053-X

Harff, J., Graf, G., and Bobertz, B. (2009). Dynamics of natural and anthropogenic sedimentation (DYNAS). *J. Mar. Sys.* 75, 315–316. doi: 10.1016/j.jmarsys.2008.04.008

Heinrich, C., Anders, S., and Schwarzer, K. (2017). Late Pleistocene and early Holocene drainage events in the eastern Fehmarn Belt and Mecklenburg Bight, SW Baltic Sea. *Boreas* 47, 754–767. doi: 10.1111/bor.12298

Koebsch, F. (2013). Dynamics of CH4 and CO_2 exchange in a Brackish Fen. *Q. Sci. Rev.* 22, 101–124.

Kolp, O. (1957). *Die Nordöstliche Heide Mecklenburgs*. Berlin: VEB Deutscher Verlag Der Wissenschaften.

Kolp, O. (1990). The Ancylus lake phase of the post-glacial evolution of the Baltic Sea. *Quaest. Geograph.*13, 69–86.

Köster, R. (1961). Junge eustatische und tektonische Vorgänge im Küstenraum der südwestlichen Ostsee. *Meyniana* 11, 23–81.

Krüger (1995). *Untersuchung zur Salzbeeinflussung überflutungsgefährdeter, forstlich genutzter Flächen im Naturschutzgebiet Hütelmoor-Heiligensee.* Rostock: Dipliomarbeit am Fachbereich Landeskultur und Umweltschutz der Universität Rostock.

Lampe, R. (2002). *Holocene Evolution of the South-Western Baltic Coast: Geological, Archaeological and Palaeo-Environmental Aspects: Field Meeting of INQUA Subcommission V Sea-Level Changes and Coastal Evolution, Western Europe, Western Europe, September 22-27, (2002)*. Greifswald: Ernst-Moritz-Arndt-Universität.

Lampe, R. (2005). Lateglacial and Holocene water-level variations along the NE German Baltic Sea coast: review and new results. *Q. Int.* 133–134, 121–136. doi: 10.1016/j.quaint.2004.10.005

Lampe, R., Endtmann, E., Janke, W., and Meyer, H. (2010). Relative sea-level development and isostasy along the NE German Baltic Sea coast during the past 9 ka. *E&G Q. Sci. J.* 59, 3–20. doi: 10.3285/eg.59.1-2.01

Lampe, R., and Janke, W. (2004). The Holocene sea level rise in the Southern Baltic as reflected in coastal peat sequences. *Polish Geol. Ins. Spec. Pap.* 11, 19–30.

Lampe, R., Lorenz, S., Janke, W., Meyer, H., Küster, M., Hübener, T., et al. (2009). *Zur Landschafts- und Gewässergeschichte der Müritz: Umweltgeschichtlich Orientierte Bohrungen 2004 - 2006 Zur Rekonstruktion der Nacheiszeitlichen Entwicklung*. Greifswald: Geozon Science Media.

Lampe, R., Naumann, M., Meyer, H., Janke, W., and Ziekur, R. (2011). "Holocene evolution of the southern baltic sea coast and interplay of sea-level variation, isostasy, accommodation and sediment supply," in *The Baltic Sea Basin, Central and Eastern European Development Studies (CEEDES)*, eds J. Harff, S. Björck, and P. Hoth (Berlin; Heidelberg: Springer), 233–251.

Lehfeldt, R., and Milbradt, P. (2000). "Longshore sediment transport modeling in 1 and 2 dimensions, in: advances in Hydro-science and engineering," in *Proceedings of the 4th International Conference on Hydro-Science and Engineering Abstract* (Seoul).

Lemke, W. (1998). Sedimentation und paläogeographische Entwicklung im westlichen Ostseeraum (Mecklenburger Bucht bis Arkonabecken) vom Ende der Weichselvereisung bis zur Litorinatransgression. *Meereswissenschaftliche Berichte* 31, 156.

Lippmann, T. C., and Holman, R. A. (1990). The spatial and temporal variability of sand bar morphology. *J. Geophys. Res.* 95:11575. doi: 10.1029/JC095iC07p11575

Meyers, P. A. (1997). Organic geochemical proxies of paleoceanographic, paleolimnologic, and paleoclimatic processes. *Org. Geochem.* 27, 213–250. doi: 10.1016/S0146-6380(97)00049-1

Miegel, K., Graeff, T., Selle, B., Salzmann, T., Franck, C., and Bronstert, A. (2016). Untersuchung eines renaturierten Niedermoores an der mecklenburgischen Ostseeküste - Teil I: Systembeschreibung und hydrologische Grundcharakterisierung (Investigation of a renatured fen on the Baltic Sea coast of Mecklenburg - Part I: system description and basic hydrological characterisation). *Hydrol. Wasserbew.* 60, 242–258. doi: 10.5675/HyWa_2016,4_1

Milliman, J. D., and Emery, K. O. (1968). Sea levels during the past 35,000 years. *Science* 162, 1121–1123. doi: 10.1126/science.162.3858.1121

Nicholls, R. J., and Cazenave, A. (2010). Sea-level rise and its impact on coastal zones. *Science* 328, 1517–1520. doi: 10.1126/science.1185782

Nieuwenhuize, J., Maas, Y. E. M., and Middelburg, J. J. (1994). Rapid analysis of organic carbon and nitrogen in particulate materials. *Mar. Chem.* 45, 217–224. doi: 10.1016/0304-4203(94)90005-1

Nnafie, A., de Swart, H. E., Calvete, D., and Garnier, R. (2014). Effects of sea level rise on the formation and drowning of shoreface-connected sand ridges, a model study. *Cont. Shelf Res.* 80, 32–48. doi: 10.1016/j.csr.2014.02.017

Pendleton, E. A., Brothers, L. L., Thieler, E. R., and Sweeney, E. M. (2017). Sand ridge morphology and bedform migration patterns derived from bathymetry and backscatter on the inner-continental shelf offshore of Assateague Island, USA. *Cont. Shelf Res.* 144, 80–97. doi: 10.1016/j.csr.2017.06.021

Plets, R., Dix, J., Bastos, A., and Best, A. (2007). Characterization of Buried inundated Peat on Seismic (Chirp) data, inferred from core information. *Archaeol. Prospection* 14, 261–272. doi: 10.1002/arp.318

Rebentrost, G. (1973). *Beschreibung von Rückgangserscheinungen der Rostocker Heide in den Letzten Jahren auf der Strecke Uhlenflucht bis Stromgrabenmündung*. Rostock: Akademie der Wissenschaften der DDR, Institut für Meereskunde Warnemünde.

Reimann, T., Tsukamoto, S., Naumann, M., and Frechen, M. (2011). The potential of using K-rich feldspars for optical dating of young coastal sediments-A test case from Darss-Zingst peninsula (southern Baltic Sea coast). *Q. Geochronol.* 6, 207–222. doi: 10.1016/j.quageo.2010.10.001

Reimer, P. J., Bard, E., Bayliss, A., Warren, B. J., Blackwell, P. G., Ramsey, C. B., et al. (2013). Intcal13 and marine13 radiocarbon age calibration curves 0–50,000 years cal bp. *Radiocarbon* 55, 1869–1887. doi: 10.2458/azu_js_rc.55.16947

Rosentau, R., Meyer, M., Harff, J., Dietrich, R., and Richter, A. (2007). Relative sea level change in the Baltic Sea since the Littorina Transgression. *Z. Geol. Wiss.* 35, 3–16.

Rößler, D., Moros, M., and Lemke, W. (2011). The Littorina transgression in the southwestern Baltic Sea: new insights based on proxy methods and radiocarbon dating of sediment cores. *Boreas* 40, 231–241. doi: 10.1111/j.1502-3885.2010.00180.x

Schlungbaum, G., and Voigt, B. (2001). "Die Darß-Zingster Bodden-ein junges Gewässersystem in einer noch nicht alten Landschaft,"in *Die Darß-Zingster Bodden. Monographie Einer Einzigartigen Küstenlandschaft*. (Stralsund: Meer und Museum), 5–16.

Schwarzer, K. (2010). Aggregate resources and extraction in the baltic sea: an introduction. *J. Coast. Res.* 165–172.

Small, C., and Nicholls, R. J. (2003). A global analysis of human settlement in coastal zones. *J. Coast. Res.* 19, 584–599. doi: 10.2307/4299200

Snedden, J. W., and Dalrymple, R. W. (1999). Modern shelf sand ridges: from historical perspective to a unified hydrodynamic and evolutionary model. *Soc. Sediment. Geol.* 64, 13–28.

Stein, R. (1991). "Accumulation of organic carbon in Baffin Bay and Labrador Sea sediments (ODP-Leg 105)," in *Accumulation of Organic Carbon in Marine Sediments: Results from the Deep Sea Drilling Project/Ocean Drilling Program* (DSDP/ODP) (Berlin Heidelberg: Springer), 40–84.

Sterr, H. (2008). Assessment of vulnerability and adaptation to sea-level rise for the coastal zone of germany. *J. Coast. Res.* 24, 380–393. doi: 10.2112/07A-0011.1

Stigge, H. J., Weiss, D., Biermann, S., Weigt, R., Redieck, M., and Schade, A. (2005). *Dokumentation der Sturmflut vom 3. und 4. November 1995 an der Küste von Mecklenburg Vorpommern* (Schwerin: Verlag Rediecke & Schade GmbH), 17–20.

Swift, D. J. P., Parker, G., Lanfredi, N. W., Perillo, G., and Figge, K. (1978). Shoreface-connected sand ridges on american and european shelves: a comparison. *Estuarine Coast. Mar. Sci.* 7, 257–273. doi: 10.1016/0302-3524(78)90109-3

Thorne, C., Evans, E., and Penning-Rowsell, E. (2007). *Future Flooding and Coastal Erosion Risks*. London: Thomas Telford, p350.

Valiela, I. (2009). *Global Coastal Change*. Hoboken, NJ: John Wiley & Sons.

van de Meene, J. W. H., and van Rijn, L. C. (2000). The shoreface-connected ridges along the central Dutch coast—part 1: field observations. *Cont. Shelf Res.* 20, 2295–2323. doi: 10.1016/S0278-4343(00)00048-0

van der Linden, M., Barke, J., Vickery, E., Charman, D. J., and van Geel, B. (2008). Late holocene human impact and climate change recorded in a north swedish peat deposit. *Palaeogeogr. Palaeoclimatol. Palaeoecol.* 258, 1–27. doi: 10.1016/j.palaeo.2007.11.006

Vestergaard, P. (1997). Possible impact of sea-level rise on some habitat types at the Baltic coast of Denmark. *J. Coast. Conserv.* 3, 103. doi: 10.1007/BF02908185

Voigtländer, U., Schmidt, J., and Scheller, W. (1996). *Pflege-und Entwicklungsplan NSG.* Schwerin: Heiligensee und Hütelmoor.

Westley, K., and Dix, J. (2006). Coastal environments and their role in prehistoric migrations. *J. Marit. Archaeol.* 1, 9–28. doi: 10.1007%2Fs11457-005-9004-5

Wong, P. P., Losada, I. J., Gattuso, J.-P., Hinkel, J., Khattabi, A., McInnes, K. L., et al. (2014). Coastal systems and low-lying areas. *Clim. Change* 2104, 361–409. doi: 10.1017/CBO9781107415379.010

Wright, L. D., and Short, A. D. (1984). Morphodynamic variability of surf zones and beaches: a synthesis. *Mar. Geol.* 56, 93–118. doi: 10.1016/0025-3227(84)90008-2

Zeiler, M., Schwarzer, K., and Ricklefs, K. (2008). Seabed morphology and sediment dynamics. *Die Küste* 74, 31–44.

Zhang, W., Harff, J., and Schneider, R. (2011). Analysis of 50-year wind data of the southern Baltic Sea for modelling coastal morphological evolution – a case study from the Darss-Zingst Peninsula. *Oceanologia* 53, 489–518. doi: 10.5697/oc.53-1-TI.489

Conflict of Interest Statement: The authors declare that the research was conducted in the absence of any commercial or financial relationships that could be construed as a potential conflict of interest.

Copyright © 2018 Kreuzburg, Ibenthal, Janssen, Rehder, Voss, Naumann and Feldens. This is an open-access article distributed under the terms of the Creative Commons Attribution License (CC BY). The use, distribution or reproduction in other forums is permitted, provided the original author(s) and the copyright owner(s) are credited and that the original publication in this journal is cited, in accordance with accepted academic practice. No use, distribution or reproduction is permitted which does not comply with these terms.

frontiers in Marine Science

ORIGINAL RESEARCH
published: 07 December 2018
doi: 10.3389/fmars.2018.00472

Continuous and High Transport of Particles and Solutes by Benthos in Coastal Eutrophic Sediments of the Pomeranian Bay

Martin Powilleit and Stefan Forster*

Institute of Biological Sciences – Marine Biology, University of Rostock, Rostock, Germany

We present results on bioirrigation and reworking of sediments by benthic macrofauna in sediments of the Pomeranian Bay (southern Baltic Sea), that were obtained ∼22 years ago. The investigation took place at four stations ranging from 9 to 19 m water depth, which we observed between 1993 and 1995 over the course of 30 months. In order to assess exchange of solutes across and particles from the sediment–water interface with the underlying sediments, we used bromide as *ex situ* tracer for bioirrigation and chlorophyll a equivalents as *in situ* tracer for particle reworking. Using models to interpret tracer distributions in the sediment, we compare the magnitudes of small scale, diffusion-like, versus relatively large-scale, non-local, transport modes. Our results indicate a spatial differentiation of the bay: the coastal station most heavily impacted by eutrophication close to the Oder River mouth showed medium reworking and intense bioirrigation combined with lower chlorophyll concentrations throughout the sediment. This contrasts with high surface pigment concentrations at the shallow Oder Bank station, indicating benthic primary production and intense particle mixing. Medium local particle reworking at the northwestern station and medium mean solute transport rates characterized the two deeper stations in the northern Bay. The bromide tracer experiments, which exclusively depict animal activity, showed significant biological solute transport to ∼10 cm sediment depth within 3 days. Non-biological transport mechanisms in the field (resuspension, fishing activity, and pore water advection) might additionally affect the *in situ* tracer chlorophyll a – depth distributions. This tracer, too, indicates mixing within the uppermost 10 cm of the sediment within ∼2–3 months. In general, experimentally obtained solute transport constants were higher than most values reported previously (surface α: 155 year^{-1}) and particle reworking was at the high end of reported values as well. Thus, benthic fauna is responsible for an intense bioturbation in Pomeranian Bay. Specifically, high bioirrigation rates were associated with high density and biomass of deep burrowing polychaetes. Recently published rates of particle reworking in the same area are on the same order of magnitude as ours obtained two decades ago. This finding is consistent with the species composition which generally remained the same.

Keywords: macrozoobenthos, bioturbation, bioirrigation, chloropigments, Baltic Sea

OPEN ACCESS

Edited by:
Elinor Andrén,
Södertörn University, Sweden

Reviewed by:
Robert Lafite,
Université de Rouen, France
Cintia Organo Quintana,
University of Southern Denmark, Denmark

****Correspondence:***
Martin Powilleit
martin.powilleit@uni-rostock.de

Specialty section:
This article was submitted to Coastal Ocean Processes, a section of the journal Frontiers in Marine Science

Received: *25 April 2018*
Accepted: *23 November 2018*
Published: *07 December 2018*

Citation:
Powilleit M and Forster S (2018) Continuous and High Transport of Particles and Solutes by Benthos in Coastal Eutrophic Sediments of the Pomeranian Bay. Front. Mar. Sci. 5:472. doi: 10.3389/fmars.2018.00472

INTRODUCTION

Bioturbation activity by benthic fauna influences early diagenetic processes, which are important for organic matter decomposition in benthic habitats. In estuarine regions with high nutrient inputs and intense matter cycling a well-developed macrofauna community plays a key role in organic matter degradation before final burial of the material in deeper sediment layers. Depending on the organisms' densities, body size, mode of locomotion, and feeding type as well as the seasonal and interannual variability of benthic communities, the transport intensities vary considerably between sites (e.g., Lee and Swartz, 1980).

Transport processes in the solute phase (bioirrigation) primarily determine the oxidation status of the sediment by a downward transport of dissolved oxygen from the water column into the sediment and a release of reduced/adsorbed compounds like ammonia, phosphate, hydrogen sulfide, or methane (e.g., Aller, 1982). Particle reworking by fauna (particulate phase transport) often causes a rapid downward transport of labile fresh organic material derived from the water column (e.g., Graf, 1992), a slower transport of inorganic particles in the same direction, and may be responsible for the release of particle-associated contaminants due to changing redox conditions (e.g., Emerson et al., 1984; Kersten, 1988). Bioturbation is considered sensitive to anthropogenic drivers (Griffiths et al., 2017), but its effects on ecosystem functioning remain unclear. The present study adds to the understanding of variability and drivers of bioturbation in a comparatively shallow marine system.

Tracer studies using either artificial or natural tracer substances are used to quantify transport processes by benthic animals. In order to compare methods and transport mechanisms involved in different habitats, mathematical simulations of reworking and bioirrigation may be applied using diffusive and/or advective (non-local) transport modes (e.g., Berner, 1980; Aller, 1982; Aller and Yingst, 1985; Boudreau, 1986a,b; Martin and Banta, 1992; Sun et al., 1994; Soetaert et al., 1996; Gerino et al., 1998). Inert bromide ions are the most common solute tracers used. Still the number of studies with application to natural benthic communities is scarce (e.g., Martin and Banta, 1992; Forster et al., 1995, 2003b; Kauppi et al., 2018). Thus, both magnitude of solute exchange and the factors responsible for the transport still need further investigation. Particle tracer studies are more frequent and a whole suite of particles (minerals, various radionuclides, artificial particles, and chlorophyll) have been used (compare, e.g., Boudreau, 1997; Bradshaw et al., 2006). In the sediment chlorophyll is a highly attractive and labile substance and may therefore be particularly suited to trace bioturbation.

A few studies, mostly from the Baltic Sea, (Powilleit et al., 1994; Quintana et al., 2007; Hedman et al., 2011; Renz and Forster, 2013) combine particle and solute tracer studies. The combined studies of transport in these two phases representing the sediment has provided insight in the relative importance of solute versus particle movement, however, mostly in single species experiments. Studies using natural communities and both solute and particle tracers might reveal patterns of bioturbation (e.g., seasonal, geographic, external factors, other), since their common driver is the benthos. Bioturbation studies from the Baltic Sea are rare and often give information restricted to single species (e.g., Mahaut and Graf, 1987; Brey, 1989; Schaffner et al., 1992; Powilleit et al., 1994; Renz and Forster, 2013, 2014). The investigation presented here was conducted in the Pomeranian Bay, a coastal region in southern Baltic Sea influenced by the Oder River. A benthos sampling program started in April 1993 to generate an overview of the status of the macrozoobenthos. The communities were characterized by low species richness and a strong gradient in zoobenthic biomass with highest values in the coastal south western part (Powilleit et al., 1995; Kube, 1996; Kube et al., 1996a,c).

The aim of this study was to quantify particle reworking and bioirrigation at different sites within a relatively homogeneous area of the Pomeranian Bay. The study employed bromide as *ex situ* tracer for dissolved compounds (Martin and Banta, 1992) and sedimentary pigments as *in situ* tracer for organic particle movement (e.g., Sun et al., 1991, 1994; Boon and Duineveld, 1998; Morys et al., 2016). Different transports were compared on the basis of mixing coefficients derived from simulation processes with transport models. We identified dominant benthic species and modes of transport involved in different areas of the relatively homogeneous eutrophic shallow habitat to assess the importance of benthic fauna on biodegradation and transport processes. Finally, we compare our findings from the 90s to a recent investigation on particle reworking in this area by Morys et al. (2016, 2017).

The Study Area

The Pomeranian Bay, southern Baltic Sea, is a shallow bay situated north of the Oder river estuary between Germany and Poland. The total area covers approximately 6000 km^2 taking the 20 m isobath as the northern boundary to the adjacent Arkona and Bornholm Basins. Water depth is <20 m with the central part the Oder Bank measuring water depths of only 7 to 9 m (**Figure 1**). Well to very well sorted fine sandy sediments prevail (Bobertz and Harff, 2004) with the exception of the Sassnitz Channel region in the north-western part where sediments are increasingly silty and less well sorted. Except for station 952, which is close but not in the channel, all of our station are located on the relatively homogeneous sandy grounds of the bay.

The major discharge of large freshwater input and nutrients into the Pomeranian Bay and source of eutrophication originates from the Oder River, which was one of the most contaminated rivers in Central Europe, through Szczecin Lagoon (Lampe, 1993; Siegel et al., 1996). Discharge loads follows the coast to the north-west or northeast direction depending on the predominant wind direction (Schernewski et al., 2001; Siegel et al., 2005). Tauber and Emeis (2005) substantiated that transport of fine material, nutrients and discharge from the Oder River predominantly occurs in the form of suspended fluffy material into the adjacent Arkona Basin in the north, while sandy bottoms remain stationary for many years.

Mean salinity varied from 7.8 near the Oder mouth to 8.5 near the Sassnitz Channel (Kube et al., 1996a) (**Table 1**). Sediments are typical of nutrient-poor sands, with median grain sizes ranging from 165 to 190 μm which were associated with low silt fractions (<1% of total mass) and values of loss on ignition (LOI) < 0.6%

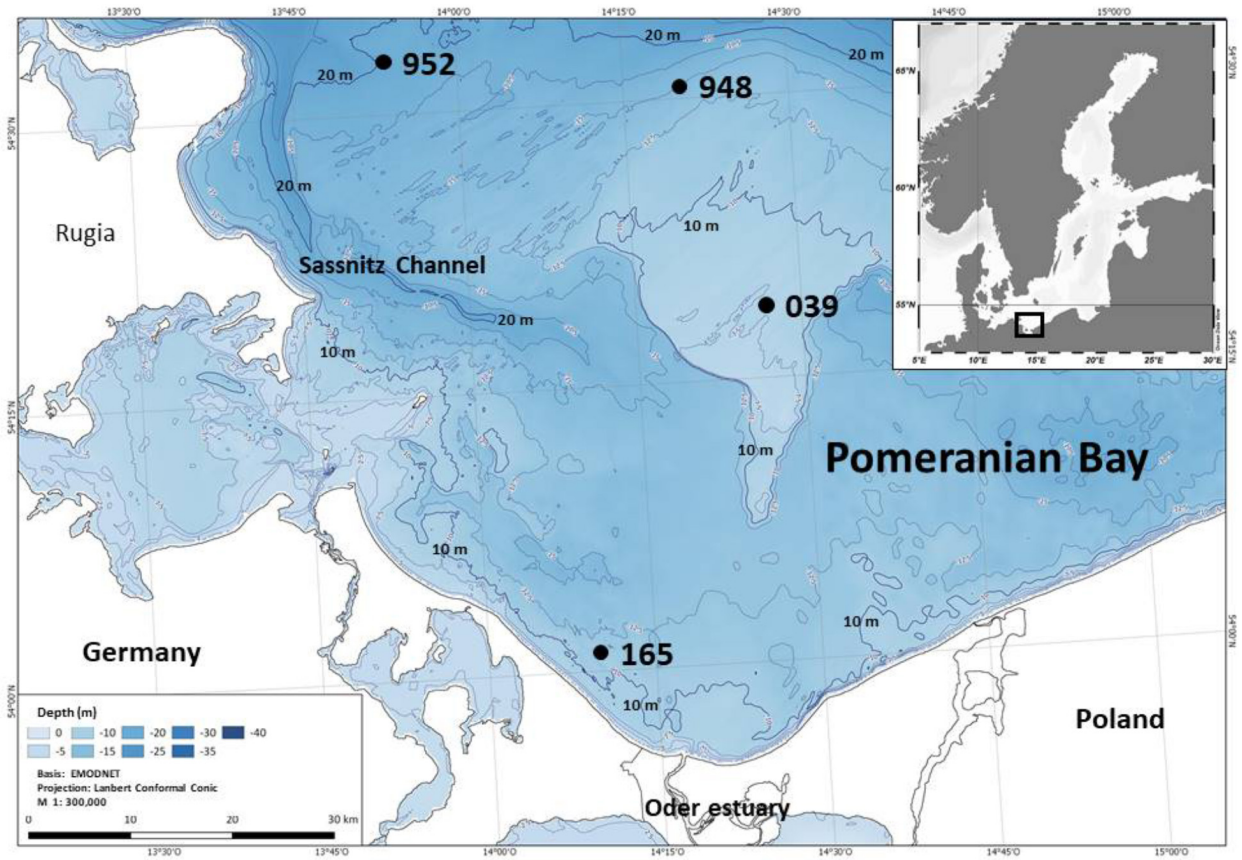


FIGURE 1 | Map of the investigation area, Pomeranian Bay, and its location in the southern Baltic Sea. Stations are located at different water depths between 9 and 19 m across the shallow bay consisting of well sorted fine sands. The deeper channel system with more heterogeneous and considerably finer sediment is not part of the sampling scheme.

TABLE 1 | Abiotic and biotic characteristics of the four stations in Pomeranian Bay.

Station	165	952	948	039
Geographic position	54° 00,70 N 14° 12,20 E	54° 33,00 N 13° 50,50 E	54° 31,90 N 14° 26,20 E	54° 20,30 N 14° 31,30 E
Water depth (m)	11	19	15	9
Salinity	7.8	8.5*	8.4	8.2
Median grain size (μm)	173	165**	190**	167
Species richness	14	8	10	13
Species density (ind./m^2)	11748	1582	3842	7833
Species biomass (g AFDW/m^2)	65.31	5.54	15.02	20.61
Biomass dominants (g AFDW/m^2)	*Mya* 51.7 *Marenzelleria* 4.2 *Limecola* 2.8 *Nereis* 0.8	*Mytilus* 5.2 *Limecola* 0.2	*Mya* 8.6 *Limecola* 4.5 *Marenzelleria* 0.5 *Cerastoderma* 0.5	*Mya* 12.7 *Limecola* 5.1 *Cerastoderma* 0.5 *Nereis* 0.3
Diversity (Shannon index H')	2.82	1.32	2.65	2.40
Evenness (Pielou's index J)	0.74	0.44	0.80	0.65

*Sediment parameters cited after Kube et al. (1996a). Biological macrofauna data derived from Van-Veen grab samples April 1993 (means, n = 3). *Single measurement on 23 April 1993. **Tauber (pers. communication).*

dry mass, reflecting low organic contents. We did not observe substantial deviations of median grain size at station 952 despite its location close the Sassnitz Channel.

The total number of benthic infauna species in the Pomeranian Bay was 35 (Powilleit et al., 1995). About 10 typical estuarine species (e.g., *Peringia ulvae, Mya arenaria, Limecola*

balthica, Pygospio elegans, Nereis diversicolor, and *Marenzelleria* spp.) have an occurrence of nearly 90% and dominate the species inventory (Powilleit et al., 1995). Additionally these sediments often contain mobile clumps of the blue mussel *Mytilus* sp. and associated fauna, which resulted in benthic communities a bit more variable in terms of species diversity and biomass (Powilleit et al., 1995). Water depth, sediment characteristics, and the food supply in the bottom water were considered to be the most important factors controlling the distribution of macrofauna (Kube et al., 1996b). In the mid-nineties, when this study was conducted, highest macrofauna biomasses (up to 150 g AFDW m^{-2}) were found in the estuarine region near the river mouth with dominance of suspension feeding bivalves. Pronounced gradients in macrofauna biomass existed from this coastal zone to outer parts of the Pomeranian Bay with biomasses of only 1 g AFDW m^{-2} (Powilleit et al., 1995).

The four stations of this study represent main macrofauna assemblages in the investigation area which could be separated by multivariate analyses (Powilleit et al., 1995) and basically these macrofauna distribution pattern still persist (e.g., Glockzin and Zettler, 2008; Darr et al., 2014a,b): the organically enriched southwestern coastal part close to the mouth of the Oder river (station 165, 11 m water depth), the shallow and exposed Oder Bank (station 039, 9 m), the northern part of Pomeranian Bay (station 948, 15 m) and the transition zone in the deep channel region in the northwestern part of the bay (station 952, 19 m), which is connected to the Arkona Basin (see Powilleit et al., 1995).

MATERIALS AND METHODS

Collection and Sample Treatment

Between April 1993 and October 1995 sediment samples of four sampling locations were taken with a box corer (0.0225 m^2) and additionally with a van Veen grab for macrofauna analyses in April 1993 (0.1 m^2) in the Pomeranian Bay (**Figure 1**). Box core samples were subsampled on board for sediment pigment analyses (five or six sampling dates per station), for laboratory tracer experiments (up to 10 subcores per station and sampling date), and for sediment analyses using Plexiglas® cores of 10 cm inner diameter.

Bioirrigation Experiments

To determine the exchange of solutes at the sediment–water interface we performed laboratory tracer experiments of 3 days duration on land using sediment cores from the respective four sampling sites. The activity of organisms (with fauna, $n = 3$ replicate cores) was compared to the molecular diffusive transport of the tracer in previously deep frozen cores without living fauna ($n = 1$; i.e., defaunated) at each station.

Sediment cores were kept in a temperature controlled water tank in the dark and aerated individually. This aeration also maintained a well-mixed water column and no additional stirring was applied in order to not induce advective pore water flows. Sodium bromide (NaBr) was used as a chemical inert tracer for solute transport and added from a stock solution to the well-mixed overlying water (∼1 liter) to each sediment cores. The concentration at the start of the experiment was set to ∼10 mM Br^-, with later measurements confirming the exact concentrations.

We analyzed water samples for bromide at the start and the end of the experiment by iodometric titration according to Kremling (1983). At the end of the experiments the sediments were sectioned into slices of 0.5 cm intervals (0–3 cm) and 1 cm intervals (3 – max. 12 cm) and pore water extracted by centrifugation (Saager et al., 1990). Concentrations of bromide were analyzed using the same titration method. During the slicing procedure all macrofauna sufficiently large to be seen by the naked eye were noted and dominant bioirrigators identified. Porosity was determined as the difference between wet weight and dry weight after drying subsamples of known volume (1.0 cm^3) at 60°C for 12 h (for details see Powilleit et al., 1994).

Bromide experiments on previously frozen defaunated cores were used as controls for the biologically enhanced transports.

Sediment Pigment Content

Sediment cores of the four stations 165, 039, 952, and 948 were sliced into ten 1 cm slices on board immediately after sampling and stored deep frozen until laboratory analyses. For chlorophyll a equivalent and phaeopigment determinations about 2 cm^3 sediment subsamples of these slices ($n = 1$) were extracted in 8 cm^3 of 90% acetone for at least 1 h with repeated vigorous shaking (Vortex) of the tubes that were kept dark and refrigerated. Pigment levels were measured by fluorescence before and after acidification on a Turner Designs Model 10 AU fluorometer according to Edler (1979) adapted to sediments. The extracted sediment was then dried at 60°C and weighed. Pigment concentrations are expressed as μg pigment cm^{-3} of sediment.

Water content, porosity and organic matter content were determined by weighing and as LOI in 1 cm sediment slices after combustion at 520°C.

Modeling

We used different standard transport models to compare and quantify biogenic transports, i.e., bioirrigation and particle reworking. These models interpret the depth distribution of tracer in the sediment by accounting for transport and, in the case of chlorophyll, reaction processes (details below). In case of bromide, molecular diffusion and non-local irrigation mimic the transport; no reaction of bromide occurs. For chloropigment profiles the model includes sedimentation, chloropigment degradation and diffusive mixing of sediments, a diffusion analogy. Model derived depth distributions of the respective tracers are compared to the measured tracer distributions from our experiments. A best fit finally yields the transport parameters describing bioirrigation and reworking of particles.

Chloropigment distributions with sediment depth, generated *in situ*, were simulated with a hierarchical family of steady state transport-reaction models published by Soetaert et al. (1996). Each member of the hierarchy, starting from a simple advection/decay model, includes all processes of the previous

model. Model 1 simply includes sedimentation and decay of chloropigments. Model 2 adds diffusive particle mixing as biological transport (D_B) and model 3 the direct injection of particles as a non-local transport into a specific deeper sediment layer, L (for details see Soetaert et al., 1996; Morys et al., 2016, 2017). We performed degradation experiments immediately after sampling and obtained site specific decay rates of chloropigments in the range of 0.1008 and 0.121 day^{-1}. We used a sedimentation rate of 2.74×10^{-5} cm day^{-1} determined by Leipe et al. (1995) for the nearby Arkona Basin and the Oder Haff in our modeling procedure. Best fits to our data were obtained mainly by the models 1 and 2. In one instance model 3 including the additional non-local injection flux to depth L gave the best fit.

Since chlorophyll profiles were generated *in situ*, reworking and non-local transports may be of other than biological origin as well.

We investigated solute exchange driven by macrofauna using Br^- ions as tracer (Martin and Banta, 1992; Anderson et al., 2006) and calculated exchange coefficients from solute tracer profiles following (Forster et al., 2003b). Briefly, bioirrigation was formulated as a non-local irrigation function (α) of sediment depth (z) which was fit to the data. In the model vertical molecular diffusive transport of tracer into the pore water is enhanced by adding radial diffusion around burrow structures as envisioned by Aller (1980) and Boudreau (1984). This procedure takes into account site-specific porosity. Parameters in equation 1 are concentrations (C) in the overlying water (C_{olw}) and at depth (C_z) in the sediment, molecular diffusivity (Ds) and constants α_0 and α_1.

$$\frac{\partial C}{\partial t} = Ds\frac{\partial^2 C}{\partial z^2} + \alpha(Colw - Cz) \quad (1)$$

$$\alpha = \alpha_0 \exp(-z\alpha_1) \quad (2)$$

While the constants α_0 and α_1 (given in **Supplementary Table 1**) obtained by the modeling procedure describe the decline of solute transport activity as a function of depth, a discrete value may be calculated for any depth by inserting the two constants into the original exponential function. Below we use these discrete values, irrigation constants averaged over 5 cm depth intervals (e.g., α_{0-5}), for an easier comparison among stations.

RESULTS

Sediments

Between April 1993 and October 1995 sediment temperatures at the study sites ranged between 4.3 and 17.1°C with only slight differences between sites at any given date due to water depth. Structural sediment parameters were basically homogeneously distributed all over the Bay (e.g., median grain size) with little spatial variations even in the channel region in the north-west. Porosity varied slightly between 0.36 (station 039) and 0.40 (station 952). Organic matter contents in surface sediments were generally very low at all stations investigated (<0.3 to 0.1% dw) with slightly higher values in the south-western coastal area and small seasonal variations.

Bioirrigation Experiments

Laboratory experiments revealed that bioirrigation activity by the benthic fauna increased the solute exchange across the sediment/water interface considerably compared to molecular diffusion. Bromide concentrations declined much slower in all inhabited cores compared to defaunated controls at all stations (**Figure 2**), indicating an increased solute transport depicted here by the non-local irrigation function α. Nevertheless, all control experiments, allowing only for molecular diffusion as a transport mechanism, still indicated α_{0-5} ranging from 32 to 42 $year^{-1}$ but high attenuation with depth (**Table 2** and **Supplementary Table 1**). If calculated for each cm interval, α declined to values <10 $year^{-1}$ within the top 3 cm in these diffusive defaunated controls (data not shown).

At all stations with the exception of 039 (shallow central Oder Bank) the solute tracer concentrations indicate a minimum depth of 10 or 11 cm to which sediments are influenced by the bioirrigation activity of the benthic community. Solute transport was highest at station 165 in the southwest (**Table 2**; $\alpha_{0-5} = 155 \pm 22$ $year^{-1}$) with the dominant species *Marenzelleria* spp., *Nereis diversicolor,* and *Mya arenaria* in the sediment cores. The deepest location (952) in the northwestern part of the investigation area was next in bioirrigation intensity, with the dominant species *L. balthica*, *Marenzelleria* spp. and *N. diversicolor*. We calculated much smaller exchange coefficients at stations 039 on Oder Bank and 948 in the deeper northern region with medium sized *M. arenaria* and small sized *L. baltica* (**Table 2**). Here means in the upper 5 cm of the sediments were $\alpha_{0-5} \sim$ 70–76 $year^{-1}$ (**Table 2**).

In situ Pigment Profiles

When looking at seasonal changes in the sediment chloropigment content of all stations the highest concentrations were measured at the shallowest station 039 at the Oder Bank with values between 1.9 and 4.6 μg cm^{-3} (**Figure 3**). April and September 1994 show the highest concentrations. The northern station 948 reveals surface chlorophyll concentrations of about 2 μg cm^{-3}. Both stations showed decreasing values with depths and accordingly model 2 (diffusion-like mixing) reveals the best fit results in most cases (**Figure 3** includes the results of the simulations). For the only time in September 1994 at station 039 model 3, which includes a non-local tracer injection term, resulted in the best fit to the measured chloropigment concentrations.

Low chlorophyll concentrations characterized the sediment at the deepest station 952 (<0.5 μg cm^{-3}) except for a spring peak in the surface sediment layer in 1995. Similarly the coastal station 165 was without pronounced seasonality (<0.9 μg cm^{-3}). Here pigment profiles differ considerably from the other two stations due to several smaller subsurface peaks and no concentration gradient with depth. Accordingly in the modeling of chlorophyll profiles (at a significance level of 1%) model 1 gave the best fits at these two stations indicating that only sedimentation and no biological transport took place. Only in two cases at station 952

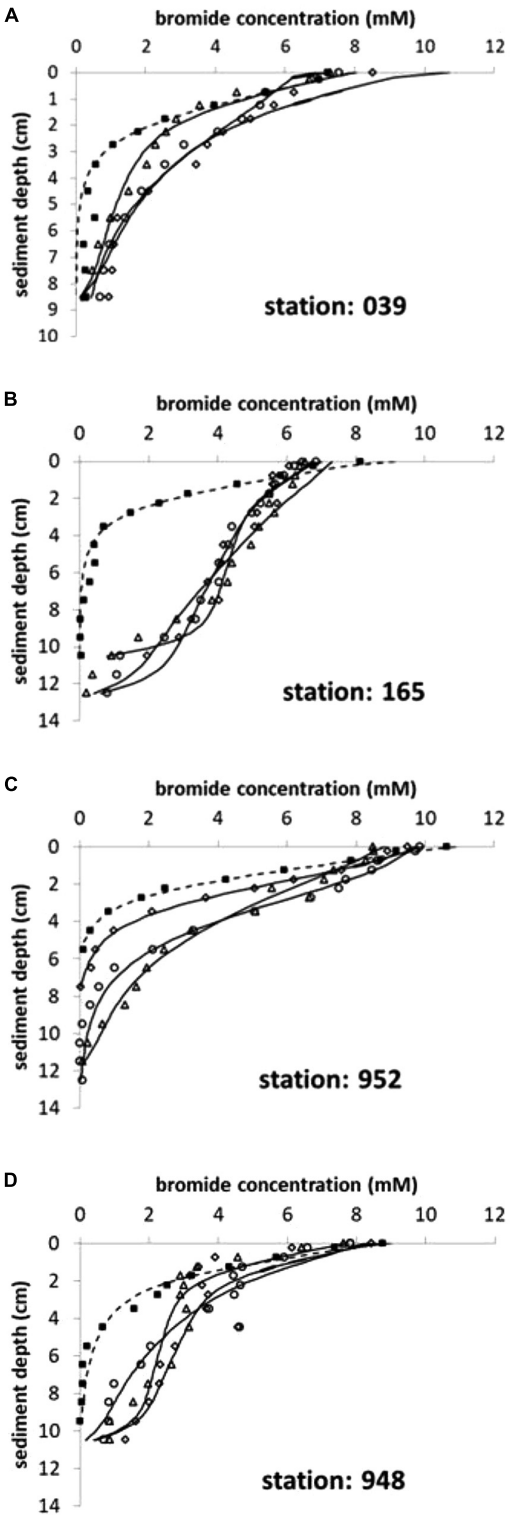


FIGURE 2 | (A–D) Bromide concentration profiles in sediment cores after 3 days of incubation. Four stations in the Pomeranian Bay are shown with one control (squares; dashed line) and three replicate cores containing active fauna (core 1: triangles, core 2: circles, core 3: diamonds; solid lines). Lines depict the modeled tracer distribution with depth according to equation (2) and (3) using α_0 and α_1 values given in **Supplementary Table 1**.

(April and October 1995) modeling resulted in model 2, which includes sedimentation and diffusive mixing ($D_B < 0.8$ cm^2 day^{-1}). Highest diffusive bioturbation coefficients D_B occurred at station 039 (up to 30.8 cm^2 day^{-1}) and station 948 (up to 8.0 cm^2 day^{-1}) (**Figure 3**).

Generally, the coastal station 165 is characterized by the highest mean pigment inventory of 32.7 μg 10 cm^{-3} (μg cm^{-2} 10 cm^{-1}) whereas station 948 shows the lowest mean of 23.6 μg 10 cm^{-3} (**Figure 4**). Station 165 and station 952 showed inventories of chlorophyll equivalents and phaeopigments generally typical for many sediments located at greater water depths, where degraded chlorophyll deposits at the sediment surface. Here phaeopigments clearly dominate the inventories (19–35 μg 10 cm^{-3}) during all seasons with only low contents of chlorophyll equivalents (<6 μg 10 cm^{-3}) indicating older organic material in the sediments. Considerably different pigment inventories, with similar medium contents of both components (9–24 μg 10 cm^{-3}) and slightly higher chlorophyll equivalent values, characterized the sediment at the Oder Bank station 039. Slightly higher phaeopigment values, but also of similar magnitude in both components, prevail at the northern station 948 (**Figure 4**).

DISCUSSION

In this study we investigated solute and particle transport by benthic fauna into the sediments of the Pomeranian Bay. Bromide (bioirrigation) tracers are used *ex situ* under laboratory conditions which essentially makes the benthic fauna in the sediment the only possible agents causing solute transport. This may be different for the particle tracer employed, natural chlorophyll pigments occurring *in situ*. Here, in principle hydrodynamic action and bottom fishing gear may affect observed depth distributions in addition to fauna. Compared to such episodic physical events, however, bioturbation causes a more continuous transport. The *ex situ* tracer shows intense solute exchange by benthic animals to ∼10 cm sediment depth at all stations. Biological solute transport to this depth occurs within the experimental duration of 3 days. While physical transport mechanisms may add to natural chloropigment transport, this tracer, too, indicates mixing within the uppermost 10 cm of the sediment within at least ∼2–3 months (tracer life-time). We conclude that in Pomeranian Bay benthic fauna facilitates solute exchange on very short timescales (3 days) and particle reworking on short time scales of a few weeks. Especially in late summer, a period often characterized by low mixing and stagnant conditions in a stratified water column, the transports induced by fauna play a key role in biodegradation for instance due to the transport of oxygen into the sediment.

While relatively homogeneous in sediment structure, the existing differences in fauna composition among stations also show up in the biological transports investigated here. We identified one hot spot in bioirrigation activity (165, southern Bay) and one in particle reworking (039, Oder Bank). A qualitative judgment as to which location is characterized by the higher tracer transport and which by lower may be

TABLE 2 | Water depth, incubation temperature, and bioirrigation constants calculated for various depth intervals and dominant bioirrigating fauna in the bromide tracer experiments.

Station	165		952		948		039	
Water depth (m)	11		19		15		9	
	July 1993		October 1994		November 94		April 93	
Temperature (°C)	14		14		9		6	
	Natural	Defaunated	Natural	Defaunated	Natural	Defaunated	Natural	Defaunated
α_{0-5} (year^{-1})	155 ± 22	32	140 ± 33	42	70 ± 18	32	76 ± 35	35
α_{5-10} (year^{-1})	83 ± 15	1	11 ± 10	0	31 ± 9	2	11 ± 1	0
α_{10-15} (year^{-1})	56 ± 21	0	2 ± 3	0	19 ± 11	0	3 ± 1	0
α_{0-10} (year^{-1})	121 ± 5	17	79 ± 19	22	51 ± 6	18	46 ± 19	18
Dominant bioirrigators	*Marenzelleria, Mya, Nereis*		Small *Limecola*		*Marenzelleria, Nereis, Limecola*		Medium-sized *Mya*	

Results for irrigation constants were determined in sediment cores inhabited by the original fauna (n = 3) and in one control core with defaunated sediments at four sandy stations of the Pomeranian Bay. Bioirrigation coefficients α_0 and α_1 obtained by modeling according to equations (1) and (2) are provided in the ***Supplementary Table 1****. Bioirrigation constants given here for the depth intervals were calculated as an average of α-values calculated using equation (2) for every cm interval into the sediment.*

simply based on the shapes of tracer depth profiles and the tracer penetration depth. This approach uses the experimental results directly and is not affected by factors such as decay constants or model boundary conditions. Since we also modeled the depth distributions a quantitative comparison is also possible. Both qualitative and quantitative criteria were used to establish sequences of decreasing biological transport (**Table 3**). An important and reassuring result of this comparison is that, in principle, the sequences of biological transport intensities among the stations compared is the same. High particle reworking and relatively little bioirrigation characterize the central Oder Bank station 039. The southern location 165 near the Oder river mouth shows an opposite trend with very high solute transport and an unusual chloropigment tracer distribution, which we will discuss below.

Station 948, characteristic for the open northern area of the Pomeranian Bay sandy flats, and the Oder Bank station 039 have balanced ratio of chlorophyll a versus phaeopigments in common. In this, they differ from typical sediments where degradation of chloropigment leads to much higher phaeopigment than chlorophyll a concentrations (Josefson et al., 2012). At both these offshore locations light can penetrate to the seafloor (own observations at 039) such that we interpret generally higher pigment concentrations here (**Figures 3**, **4**) as a sign of benthic primary production by microphytobenthos. Location 952 at the northwestern channel with considerable bioirrigation and reworking reflects conditions at 165, Oder river mouth, without pronounced benthic primary production and accordingly relatively high phaeopigment contents. It seems that different conditions with respect to the food supply, here indicated by benthic phototrophs, in addition to the slight differences in fauna community affect biological transports.

Magnitudes of Solute Transport

The bioirrigation coefficients for all four stations are high, in fact α_{0-10} of 121 ± 5 year^{-1} is one of the highest value reported for benthic communities in literature so far (**Figure 5**). The benthic community in the coastal part of Pomeranian Bay caused very high irrigation transport when compared to bromide tracer results and exceed those from Buzzards Bay, United States, fourfold (Martin and Banta, 1992), the southern North Sea results by Forster et al. (1995) threefold and those obtained from the western Baltic Sea by a factor 2.5 (Powilleit et al., 1994; Schlüter et al., 2000). All solute exchange profiles (**Figure 2**) indicate transport to depths far below 3 cm that are reached in control diffusion experiments, in which alpha declines to values <10 year^{-1} below 3 cm already. Bromide, and similar solutes like sulfate, oxygen, or DOM, can reach 10 cm depth within 3 days, while reduced substances, NH_4^+ or HS^-, may be transported upward by the same principle (Aller, 1980; Boudreau, 1984). Since the shallow water sands of Pomeranian Bay are permeable (Forster et al., 2003a), water flows above the sediment will be able to induce advective pore water movement (Huettel et al., 1996), whenever the weather conditions permit. There are no measurements of the magnitude such advective flows available from this area. Advective downwelling typically reaches 3–5 cm deep within 24 h (Huettel and Gust, 1992). Given this velocity water from the sediment surface would potentially reach 10 cm depth during ∼2 days. We may thus conclude that biological solute transport will continuously mix dissolved substances to sediment depths which are comparable to those likely mixed intermittently by pore water advection.

Bioirrigation is caused mainly by feeding activities of polychaetes that generate bulky profiles with high bromide concentrations below 6 cm depth and reaching to more than 10 cm (165, 948). Higher bioirrigation coefficients were also determined in experiments exclusively containing *Marenzelleria* spp. or *Heteromastus filiformis* (Quintana et al., 2007; Renz and Forster, 2013). The later authors determined a rate of 130 year^{-1} on 1273 individuals per m^2. At station 165, depicting high community bioirrigation rates, a high abundance of *Marenzelleria* spp. of 2400 individuals m^{-2} was found in 1993, while at the other locations it ranged from 50 to 130 individuals m^{-2}. The species then called *M. cf. viridis* might today be identified as *M. viridis* or *M. neglecta*, the latter being the dominant *Marenzelleria* species in the Pomeranian Bay today. Since these two sibling species perform similarly in bioirrigation activity it is only important to state in this context that the smaller *M. arctia* does not inhabit the area. Direct observations revealed that *Marenzelleria* spp. waved its tentacles during feeding and

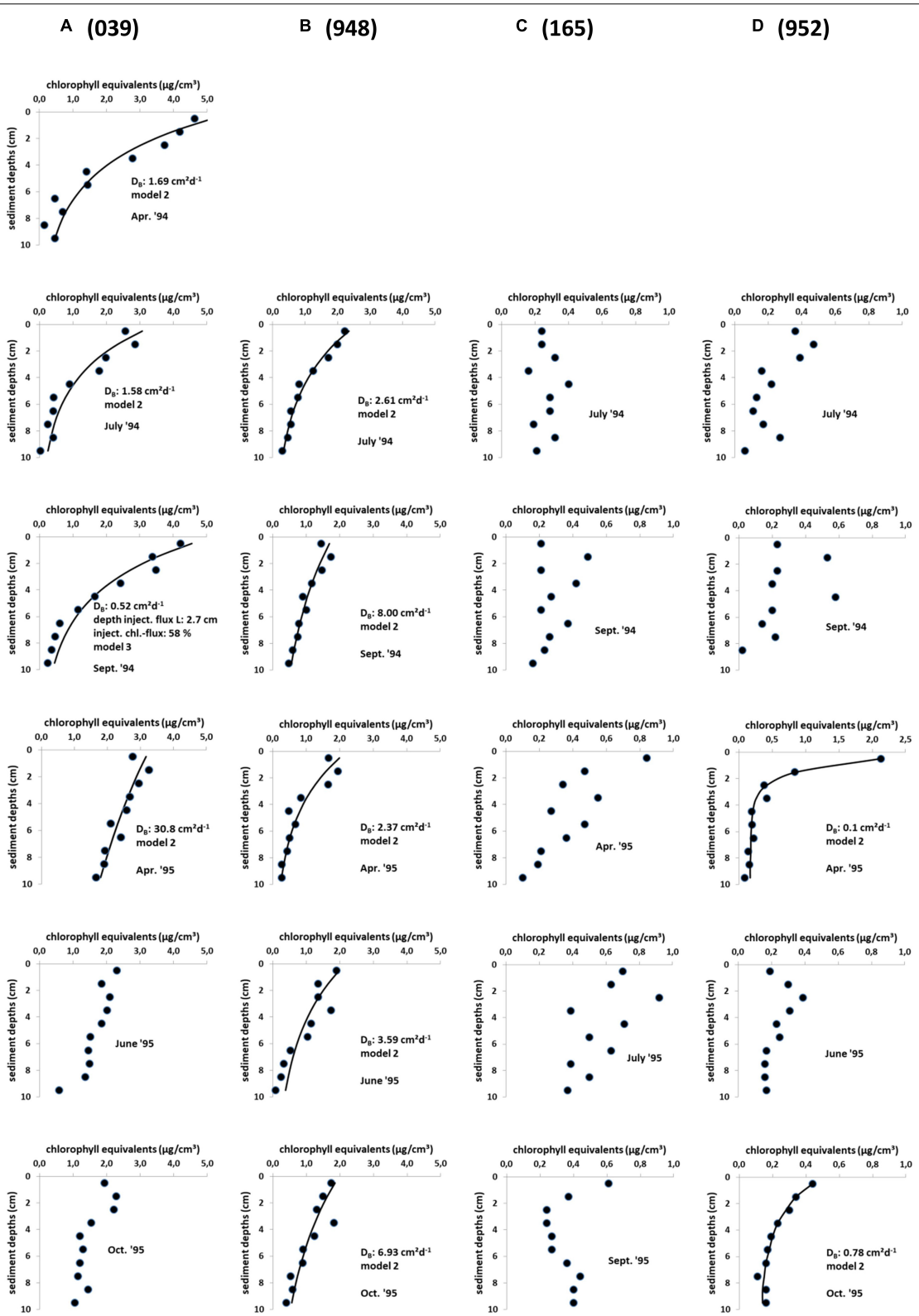


FIGURE 3 | (A–D) *In situ* chlorophyll equivalent concentration profiles (dots) in sediment cores of stations 039 **(A)**, 948 **(B)**, 165 **(C)**, and 952 **(D)** in the Pomeranian Bay with active fauna between April 1994 and October 1995. Solid lines indicate the simulations with the diffusion/non-local bioturbation models 2 and 3, which include bioturbative (diffusive) mixing only in model 2 or an additional non-local transport term of the pigment flux directly into a certain sediment depth L in model 3 (Soetaert et al., 1996).

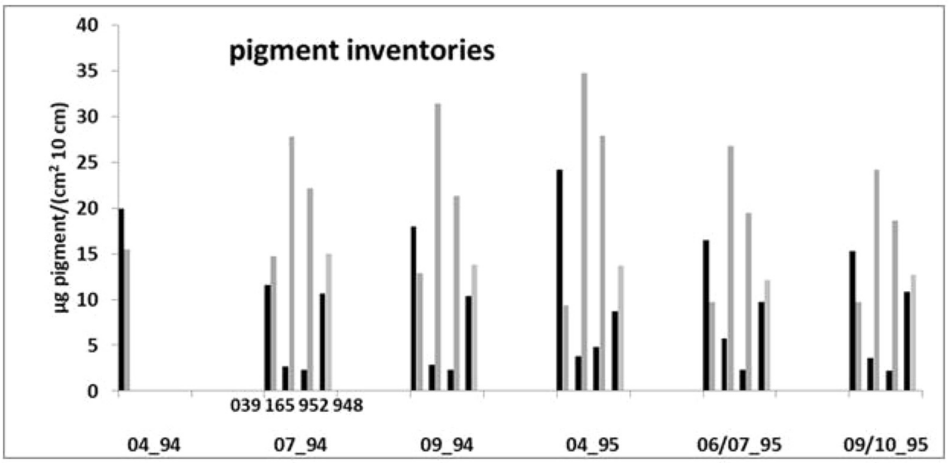


FIGURE 4 | Chlorophyll equivalent and phaeopigment inventories of the upper 10 cm sediment ($\mu g\ cm^{-2}\ 10\ cm^{-1}$) of the stations 039, 165, 952, and 948 in the Pomeranian Bay between April 1994 and October 1995.

TABLE 3 | Summary of bioturbation intensities observed in Pomeranian Bay.

Bromide penetration depth	165 > 948 > 039, 952 South > north > bank, channel
Bromide α_{0-10}	165 > 952 > 039, 948 South > channel > bank, north
Chlorophyll displacement depth	039 > 948 > 952, 165 Bank > north > channel, south
Chlorophyll D_B	039 > 948 > 952, 165 (unclear) Bank > north > channel, south

A sequence of decreasing or equal intensities is given for each tracer, both in qualitative terms observed from the trace's depth distribution (penetration and displacement depth) and quantitatively based on modeled transport coefficients.

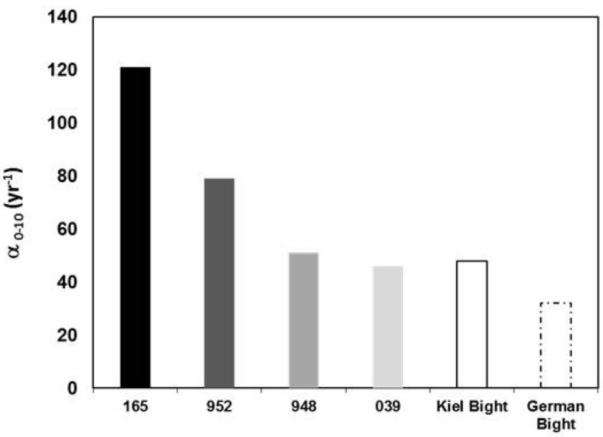


FIGURE 5 | Irrigation rate constants integrated from 0 to 10 cm sediment depth using α_0 and α_1. Results from this study on Pomeranian Bay are compared to studies employing the same depth dependent analyses of the irrigation rate constant from Kiel Bight (Schlüter et al., 2000) and the German Bight (Forster et al., 2003b) and previous data for comparison.

moved vertically in its burrow especially during defecation, enabling a noticeable solute transport into deeper sediment layers by ventilation activity. Irrigation by the other dominant polychaete *H. diversicolor* may additionally explain the high exchange coefficients observed in the Pomeranian Bay (Davey et al., 1990; Riisgård, 1991; Clavero et al., 1994; Vedel et al., 1994; Davey and Watson, 1995). This species, too, was twice as abundant (360 individuals m^{-2}) at 165 compared to the other locations. In addition siphon movements by adult, filter-feeding specimens of the bivalve *Mya arenaria* and crawling of *Limecola balthica* and medium-sized *M. arenaria* were observed and could be another cause of a considerable solute transport in the upper 6 cm of the sediment. Our results show that exceptionally high bioirrigation and high particle reworking rates can occur even in the absence of conspicuous and strong bioturbators like *Arenicola marina* (Meysman et al., 2006). In this context the role of *M. arenaria* awaits further exploration.

Comparing *in situ* temperatures and irrigation rates in **Table 2** one might suspect temperature to cause high rates. In 1994 at 952 (14°C) and 948 (9°C) irrigation rates in the top 5 cm are twice as high at the elevated temperature, suggesting a relation similar to the temperature dependency of metabolism (Q_{10}). In subsequent depth intervals 5–10 cm and 10–15 cm, however, the coefficients are higher at station 948 despite its lower temperature. This hints at the surficially active small *Limecola* found at 952. However, our data are not sufficient to extract, support or reject a Q_{10} value. Forster et al. (2003b) observed that bioirrigation was high and nearly the same in January (∼7°C) and in October (∼14°C) 1988/89 in a North Sea community. In that data set bioirrigation was relatively low and of the same intensity both in August (∼16°C) and February (∼5°C), when abundance of organisms was low at both dates and likely more important than temperature for the intensity of solute exchange. Similarly from the present data set we see that temperature may affect the irrigation activity of benthos, but not only and probably not predominantly so. Bioirrigation may also be influenced by factors such as food supply or hypoxia, but the structure (abundance,

biomass, identity) of the benthic community seems the most relevant one.

Particle Transport Derived From Sedimentary Pigments

The general pattern found with the natural particle tracer chlorophyll is that particle reworking is highest on the central Oder Bank, followed by the northern area of the Bay and lower at the northwestern channel and southern Oder mouth area. Reworking rates determined ranged from 0.5 to 30 cm^2 day^{-1} at 039 and from 2.4 to 8 cm^2 day^{-1} at 948. At station 952 we could detect reworking rates only twice with small values <1 cm^2 day^{-1}, while no reworking was found at station 165 (see below). These reworking rates are among the highest reported so far (Boudreau, 1997).

There are several reasons that may explain why chlorophyll derived reworking rates are high compared to those obtained using other particle tracer. As food particles, cells or cell fragments containing chloropigments are clearly more attractive than indifferent tracers, such as luminophores, glass beads, or radioactive tracers adsorbed to the organic matrix on mineral grains. These trace average sediment particles and not the most attractive portion, which chlorophyll may represent.

In models that incorporate two or more transport mechanisms the allocation of tracer to local and non-local processes affects the magnitude of D_B, too. In our data there is only one situation (September 1994, station 039) where the model software suggested non-local transport to a sediment depth L of 2.7 cm. According to the model, this flux constitutes more than half of the total chlorophyll transported into the sediment by bioturbation, with the remaining 42% left to diffusive mixing, D_B. In fact, this coincides with the lowest D_B determined at station Oder Bank. In the same area Morys et al. (2017) detected more incidences of non-local transport.

We cannot exclude additional transport of chlorophyll by physical mechanisms occurring only in the field, such as sediment resuspension and mixing by waves (Jenness and Duineveld, 1985) or advective particle transport (Grant, 1983; Huettel et al., 1996). Whatever the mechanism, chlorophyll tracer is found at 4–6 cm depth (extreme >10 cm) and reaches this depth during its life time of a few months. Thus, particles in sediments of the Pomeranian Bay are transported an order of magnitude slower than solutes.

At station 165, Oder river mouth, we found no bioturbation when using the interpretation software "mixing." We suggest that in this situation the model approach is not suitable for an extraction of reworking rates. In temperate regions, like the Pomeranian Bay, primary production follows a relatively regular seasonal pattern with a maximum in spring and a smaller secondary fall maximum (e.g., Graf, 1992; Sun et al., 1994). The chloropigment inventories at the study sites in general follow this pattern with slightly higher spring values (**Figure 4**). Morys et al. (2017) suggested surface feeding and consequently reduced foraging (reworking) activity, when chlorophyll was higher concentrated at sediment surface. Murray et al. (2017) provide an example of highest reworking rates at medium, not at maximum levels of food concentration in the bottom water with the polychaete *H. diversicolor*.

Knowing that at 165 many organisms with high total biomass were present, we propose the following explanation for a lack of chlorophyll pigments in the sediment. All major fauna elements here, *Marenzelleria* spp., *Nereis diversicolor, Limecola balthica*, *and Mya arenaria*, are well capable of suspension feeding and prefer to feed on fresh labile organic particles from the water column and/or sediment surface (e.g., Riisgård, 1991). At the high biomass of up to 150 g AFDW m^{-2} and density of large organisms present, the community may have essentially taken all food from the interfacial water layer by suspension feeding and effectively prevented chloropigment containing material from settling onto the sediment. With particle tracer missing in the sediment (compare low concentrations at all times at 165), the model software could only interpret the depth distribution as no bioturbation (model 1). In fact, at the 5% confidence level, which we did not use in this study, mixing interprets those depth distributions as exceedingly high D_B, which also shows that under these conditions the model framework is useless without additional information available. Possibly experiments reported by Webb (1993) with *L. balthica* in subtidal sediments without benthic primary production relate to the same mechanism, since they did not show any clear effect on sedimentary chlorophyll *a* concentrations. We consider 165 to be reworked by the abundant fauna, however, unable to extract quantitative information.

Comparing Then and Now

Our result stem from a study performed between 1993 and 1995. In recent studies on particle reworking (Morys et al., 2016, 2017; Morys, 2016) the authors sampled the location "Oder bank" at 16 m depth. It is closest to our station 948 (15 m depth) visited about 22 years before. A comparison of particle transport is possible since they also determined rates using chlorophyll as a tracer. Between summer 2014 and fall 2015 reworking rates determined at five occasions with 6–23 sediment cores analyzed each time, ranged from 0.4 and 3.9 cm^2 day^{-1} (Morys, 2016). Only in winter 2014 D_B were exceptionally low (0.005 cm^2 day^{-1}) (Morys et al., 2016). Our D_B at station 948 range from 2.4 to 8.0 cm^2 day^{-1} ($n = 5$) with no sign of non-local transport. Morys (2016) and Morys et al. (2016, 2017) did find substantially more non-local transport. In conclusion, particle transport seen today seems as intense as two decades ago when judged based on diffusive reworking of sediments. There may be a change in the nature of transport, i.e., more non-local rather than diffusive reworking, but due to the sample numbers in the 1990s and only partially comparable abundance/biomass data between both periods this aspect does not allow for a profound comparison.

Continuously high rates of particle reworking are consistent with the fauna inventory (community composition and dominant species), which has not changed profoundly since then, despite the obvious variations of abundance and biomass in time and space. Since reworking today is on the same order of magnitude as that two decades ago, the biological transport at the sea bed may not have changed so far in response of the reduction of nutrient inputs to the coastal zone (Schernewski et al., 2011;

Wasmund et al., 2011). While chlorophyll concentrations in the waters of the Pomeranian Bay decline (Wasmund et al., 2011), the eutrophic state is probably still high. Benthic-pelagic coupling and nutrients cycling between seabed and water column buffers the system, so that a lag in a possible response may be expected. If bioturbation is predominantly dependent on the benthic community structure, as we suggest, continued research focusing on effects of species identity and abundance seem paramount.

AUTHOR CONTRIBUTIONS

MP conducted all experiments, sample and data analysis as well as particle modeling. SF conducted bromide modeling, contributed to tables, and graphics. Both authors contributed equally to writing and editing.

FUNDING

This study was conducted at the Leibniz Institute for Baltic Sea Research Warnemünde (IOW) and at the University of Rostock and supported by the Federal Ministry of Research and Technology (BMBF) under grant number: 03F0105B.

ACKNOWLEDGMENTS

We wish to thank U. Wolff, K. Fennel, and A. Khalili for their help during modeling as well as G. Graf and J. Renz for helpful comments on the draft version. G. Nausch and B. Koine kindly provided sediment data. Special thanks are due to C. Peters for her assistance during field and laboratory work. This manuscript also profited from two helpful reviews.

SUPPLEMENTARY MATERIAL

The Supplementary Material for this article can be found online at: https://www.frontiersin.org/articles/10.3389/fmars.2018.00472/full#supplementary-material

REFERENCES

Aller, R. C. (1980). Quantifying solute distributions in the bioturbated zone of marine sediments by defining an average microenvironment. *Geochim. Cosmochim. Acta* 44, 1955–1965. doi: 10.1016/0016-7037(80)90195-7

Aller, R. C. (1982). "The effects of macrobenthos on chemical properties of marine sediment and overlying water," in *Animal Sediment Relations*, eds P. L. McCall and M. J. S. Tevesz (New York, NY: Plenum Press), 53–102.

Aller, R. C., and Yingst, J. Y. (1985). Effects of the marine deposit-feeders *Heteromastus filiformis* (polychaeta), *Macoma baltica* (bivalvia) and *Tellina texana* (Bivalvia) on averaged sedimentary solute transport, reaction rates, and microbial distributions. *J. Mar. Res.* 43, 615–645. doi: 10.1357/002224085788440349

Anderson, M. J., Ellingsen, K. E., and Mcardle, B. H. (2006). Multivariate dispersion as a measure of beta diversity. *Ecol. Lett.* 9, 683–693. doi: 10.1111/j.1461-0248.2006.00926.x

Berner, R. A. (1980). *Early Diagenesis, a Theoretical Approach*. Princeton, NJ: Princeton Univ. Press.

Bobertz, B., and Harff, J. (2004). Sediment facies and hydrodynamic setting: a study in the south western Baltic Sea. *Ocean Dyn.* 54, 39–48. doi: 10.1007/s10236-003-0061-8

Boon, A. R., and Duineveld, G. C. A. (1998). Chlorophyll a as a marker for bioturbation and carbon flux in southern and central North Sea sediments. *Mar. Ecol. Progr. Ser.* 162, 33–43. doi: 10.3354/meps162033

Boudreau, B. P. (1984). On the equivalence of nonlocal and radial-diffusion models for porewater. *J. Mar. Res.* 42, 731–735. doi: 10.1357/002224084788505924

Boudreau, B. P. (1986a). Mathematics of tracer mixing in sediments: I. spacially-dependent, diffusive mixing. *Am. J. Sci.* 286, 161–198. doi: 10.2475/ajs.286.3.161

Boudreau, B. P. (1986b). Mathematics of tracer mixing in sediments: II. nonlogical mixing and biological conveyor belt phenomena. *Am. J. Sci.* 286, 199–238. doi: 10.2475/ajs.286.3.199

Boudreau, B. P. (1997). *Diagenetic Models and Their Implementation: Modelling Transport and Reactions in Aquatic Sediments*. Berlin: Springer.

Bradshaw, C., Kumblad, L., and Fagrell, A. (2006). The use of tracers to evaluate the importance of bioturbation in remobilising contaminants in Baltic sediments. *Estuar. Coastal Shelf Sci.* 66, 123–134. doi: 10.1016/j.ecss.2005.08.002

Brey, T. (1989). The impact of physical and biological factors on structure and dynamics of the sublitoral Macoma -community in Kiel Bay. *Ber. Inst. Meereskd* 186:248.

Clavero, V., Niell, F. X., and Fernandez, J. A. (1994). A laboratory study to quantify the influence of nereis diversicolor O.F.Müller in the exchange of phosphate between sediment and water. *J. Exp. Mar. Biol. Ecol.* 176, 257–267. doi: 10.1016/0022-0981(94)90188-0

Darr, A., Gogina, M., and Zettler, M. L. (2014a). Detecting hot-spots of bivalve biomass in the south-western Baltic Sea. *J. Mar. Syst.* 134, 69–80. doi: 10.1016/j.jmarsys.2014.03.003

Darr, A., Gogina, M., and Zettler, M. L. (2014b). Functional changes in benthic communities along a salinity gradient- a western Baltic case study. *J. Sea Res.* 85, 315–324. doi: 10.1016/j.seares.2013.06.003

Davey, J. T., and Watson, P. G. (1995). The activity of *Nereis diversicolor* (Polychaeta) and its impact on nutrient fluxes in estuarine waters. *Ophelia* 41, 57–70. doi: 10.1080/00785236.1995.10422037

Davey, J. T., Watson, P. G., Bruce, R. H., and Frickers, P. E. (1990). An instrument for the monitoring and collection of the vented burrow fluids of benthic infauna in sediment microcosms and its application to the polychaetes *Hediste diversicolor* and *Arenicola marina*. *J. Exp. Mar. Biol. Ecol.* 139, 135–149. doi: 10.1016/0022-0981(90)90043-C

Edler, L. (1979). Recommendations on methods for marine biological studies in the baltic sea Phytoplankton and Chlorophyll. *Baltic Mar. Biol.* 5, 1–38.

Emerson, S., Jahnke, R., and Heggie, D. (1984). Sediment-water exchange in shallow water estuarine sediments. *J. Mar. Res.* 42, 709–730. doi: 10.1016/j.marenvres.2018.09.013

Forster, S., Bobertz, B., and Bohling, B. (2003a). Permeability of sands in the coastal areas of the southern Baltic Sea: mapping a grain-size related sediment property. *Aquat. Geochem.* 9, 171–190. doi: 10.1023/B:AQUA.0000022953.52275.8b

Forster, S., Khalili, A., and Kitlar, J. (2003b). Variation of nonlocal irrigation in a subtidal benthic community. *J. Mar. Res.* 61, 335–357. doi: 10.1357/002224003322201223

Forster, S., Graf, G., Kitlar, J., and Powilleit, M. (1995). Effects of bioturbation in oxic and hypoxic conditions: a microcosm experiment with a North Sea sediment community. *Mar. Ecol. Prog. Ser.* 116, 153–161. doi: 10.3354/meps116153

Gerino, M., Aller, R. C., Lee, C., Cochran, J. K., Aller, J. Y., Green, M. A., et al. (1998). Comparison of different tracers and methods used to quantify bioturbation during a spring bloom: 234-Thorium, luminophores and chlorophyll a. *Estuar. Coast. Shelf Sci.* 46, 531–547. doi: 10.1006/ecss.1997.0298

Glockzin, M., and Zettler, M. L. (2008). Spatial macrozoobenthic distribution patterns in relation to major environmental factors- a case study from the Pomeranian Bay (southern Baltic Sea). *J. Sea Res.* 59, 144–161. doi: 10.1016/j.seares.2008.01.002

Graf, G. (1992). Benthic-pelagic coupling: a benthic view. *Oceanogr. Mar. Biol. Annu. Rev.* 30, 149–190. doi: 10.1007/s11356-015-4997-2

Grant, J. (1983). The relative magnitude of biological and physical sediment reworking in an intertidal community. *J. Mar. Res.* 41, 673–689. doi: 10.1357/002224083788520469

Griffiths, J. R., Kadin, M., Nascimento, F. J. A., Tamelander, T., Törnroos, A., Bonaglia, S., et al. (2017). The importance of benthic–pelagic coupling for marine ecosystem functioning in a changing world. *Glob. Change Biol.* 23, 2179–2196. doi: 10.1111/gcb.13642

Hedman, J. E., Gunnarsson, J. S., Samuelsson, G., and Gilbert, F. (2011). Particle reworking and solute transport by the sediment-living polychaetes *Marenzelleria neglecta* and *Hediste diversicolor*. *J. Exp. Mar. Biol. Ecol.* 407, 294–301. doi: 10.1016/j.jembe.2011.06.026

Huettel, M., and Gust, G. (1992). Solute release mechanisms from confined sediment cores in stirred benthic chambers and flume flows. *Mar. Ecol. Prog. Ser.* 82, 187–197. doi: 10.3354/meps082187

Huettel, M., Ziebis, W., and Forster, S. (1996). Flow-induced uptake of particulate matter in permeable sediments. *Limnol. Oceanogr.* 41, 309–322. doi: 10.4319/lo.1996.41.2.0309

Jenness, M. I., and Duineveld, G. C. A. (1985). Effects of tidal currents on chlorophyll a content of sandy sediments in the southern North Sea. *Mar. Ecol. Prog. Ser.* 21, 283–287. doi: 10.3354/meps021283

Josefson, A. B., Norrko, J., and Norrko, A. (2012). Burial and decomposition of plant pigments in surface sediments of the Baltic Sea: role of oxygen and benthic fauna. *Mar. Ecol. Prog. Ser.* 455, 33–49. doi: 10.3354/meps09661

Kauppi, L., Bernard, G., Bastrop, R., Norkko, A., and Norkko, J. (2018). Increasing densities of an invasive polychaete enhance bioturbation with variable effects on solute fluxes. *Nat. Sci. Rep.* 8:7619. doi: 10.1038/s41598-018-25989-2

Kersten, M. (1988). "Geobiological effects on the mobility of contaminants in marine sediments," in *Pollution of the North Sea*, eds W. Salomons (Berlin: Springer), 36–58.

Kremling, K. (1983). "Determination of major constituents," in *Methods of Sea Water Analysis*, ed. K. Grasshoff (Weinheim: Verlag Chemie), 247–268.

Kube, J. (1996). The ecology of macrozoobenthos and sea ducks in the Pomeranian Bay. *Meereswiss Ber. Warnemünde* 18, 1–128.

Kube, J., Peters, C., and Powilleit, M. (1996a). Spatial variation in growth of *Macoma balthica* and *Mya arenaria* (Mollusca, Bivalvia) in relation to environmental gradients in the Pomeranian Bay (southern Baltic Sea). *Arch. Fish. Mar. Res.* 44, 81–93.

Kube, J., Powilleit, M., and Warzocha, J. (1996b). The importance of hydrodynamic processes and food availability for the structure of macrofauna assemblages in the Pomeranian Bay (Southern Baltic Sea). *Arch. Fuer Hydrobiol.* 138, 213–228.

Kube, J., Zettler, M. L., Gosselck, F., Ossig, S., and Powilleit, M. (1996c). Distribution of *Marenzelleria viridis* (Polychaeta: Spionidae) in the Southwestern Baltic Sea in 1993/94 - ten years after introduction. *Sarsia* 81, 131–142.

Lampe, R. (1993). Environmental state and material flux in the western part of the Oder river estuary - results and consequences. *Petermanns Geogr. Mitt.* 137, 275–282.

Lee, H., and Swartz, R. C. (1980). Biological processes affecting the distribution of pollutants in marine sediments. part 2: biodeposition and bioturbation. contaminants and sediments. *Anal. Chem. Biol.* 2, 555–606.

Leipe, T., Neumann, T., and Emeis, K.-C. (1995). Schwermetallverteilung in holozänen Ostseesedimenten -untersuchungen im Einflußbereich der Oder. *Geowissenschaften* 13, 470–478.

Mahaut, M. L., and Graf, G. (1987). A luminophore tracer technique for bioturbation studies. *Oceanol. Acta* 10, 323–328.

Martin, W. R., and Banta, G. T. (1992). The measurement of sediment irrigation rates: a comparison of the Br – tracer and 222Rn/ 226Ra disequilibrium techniques. *J. Mar. Res.* 50, 125–154. doi: 10.1357/002224092784797737

Meysman, F. J. R., Galaktionov, O. S., Gribsholt, B., and Middelburg, J. J. (2006). Bioirrigation in permeable sediments: advective pore-water transport induced by burrow ventilation. *Limnol. Oceanogr.* 51, 142–156. doi: 10.4319/lo.2006.51.1.0142

Morys, C. (2016). *Particle Dynamics in Sediments of the Western Baltic Sea.* Ph.D. thesis, University Rostock, Rostock

Morys, C., Forster, S., and Graf, G. (2016). Variability of bioturbation in various sediment types and on different spatial scales in the southwestern Baltic Sea. *Mar. Ecol. Progr. Ser.* 557, 31–49. doi: 10.3354/meps11837

Morys, C., Powilleit, M., and Forster, S. (2017). Bioturbation in relation to the depth distribution of macrozoobenthos in the southwestern Baltic Sea. *Mar. Ecol. Progr. Ser.* 579, 19–36. doi: 10.3354/meps12236

Murray, F., Solan, M., and Douglas, A. (2017). Effects of algal enrichment and salinity on sediment particle reworking activity and associated nutrient generation mediated by the intertidal polychaete *Hediste diversicolor*. *J. Exp. Mar. Biol. Ecol.* 495, 75–82. doi: 10.1016/j.jembe.2017.06.002

Powilleit, M., Kitlar, J., and Graf, G. (1994). Particle and fluid bioturbation caused by the priapulid worm *Halicryptus spinulosus* (v.Seibold). *Sarsia* 79, 109–117. doi: 10.1080/00364827.1994.10413551

Powilleit, M., Kube, J., Maslowski, J., and Warzocha, J. (1995). Distribution of macrobenthic invertebrates in the Pomeranian Bay (Southern Baltic) in 1993/1994. *Bull. Sea Fish. Inst.* 3, 75–87.

Quintana, C. O., Tang, M., and Kristensen, E. (2007). Simultaneous study of particle reworking, irrigation transport and reaction rates in sediment bioturbated by the polychaetes *Heteromastus* and *Marenzelleria*. *J. Exp. Mar. Biol. Ecol.* 352, 392–406. doi: 10.1016/j.jembe.2007.08.015

Renz, J. R., and Forster, S. (2013). Are similar worms different? a comparative tracer study on bioturbation in the three sibling species *Marenzelleria arctia*, *M. viridis*, and *M. neglecta* from the Baltic Sea. *Limnol. Oceanogr.* 58, 2046–2058. doi: 10.4319/lo.2013.58.6.2046

Renz, J. R., and Forster, S. (2014). Effects of bioirrigation by the three sibling species of *Marenzelleria* spp. on solute fluxes and porewater nutrient profiles. *Mar. Ecol. Progr. Ser.* 505, 145–159. doi: 10.3354/meps10756

Riisgård, H. U. (1991). Suspension feeding in the polychaete *Nereis diversicolor*. *Mar. Ecol. Prog. Ser.* 70, 29–37. doi: 10.1016/j.marpolbul.2016.02.033

Saager, P. M., Sweerts, J.-P., and Ellermeijer, H. J. (1990). A simple pore-water sampler for coarse, sandy sediments of low porosity. *Limnol. Oceanogr.* 35, 747–751. doi: 10.4319/lo.1990.35.3.0747

Schaffner, L. C., Jonsson, P., Diaz, R. J., Rosenberg, R., and Gapcynski, P. (1992). Benthic communities and bioturbation history of estuarine and coastal systems: effects of hypoxia and anoxia. *Sci. Total Environ. Suppl.* 21–24, 1001–1016. doi: 10.1016/B978-0-444-89990-3.50087-0

Schernewski, G., Neumann, T., Opitz, D., and Venohr, M. (2011). Long-term eutrophication history and ecosystem changes in a large Baltic river basin – estuarine system. *Transit. Waters Bull.* 5, 21–49.

Schernewski, G., Neumann, T., Podsetchine, V., and Siegel, H. (2001). Spatial impact of the Oder river plume on water quality along the south-western Baltic coast. *Int. J. Hyg. Environ. Health* 204, 143–155. doi: 10.1078/1438-4639-00086

Schlüter, M., Sauter, E., Hansen, H. P., and Suess, E. (2000). Seasonal variations of bioirrigation in coastal sediments: modelling of field data. *Geochim. Cosmochim. Acta* 64, 821–834. doi: 10.1016/S0016-7037(99)00375-0

Siegel, H., Gerth, M., and Schmidt, T. (1996). Water exchange in the pomeranian bight investigated by satellite data and shipborne measurements. *Cont. Shelf Res.* 16, 1793–1817. doi: 10.1016/0278-4343(96)00012-X

Siegel, H., Seifert, T., Schernewski, G., Gerth, M., Ohde, T., Reißmann, J., et al. (2005). Discharge and transport processes along the German Baltic Sea Coast. *Ocean Dyn.* 55, 47–66. doi: 10.1007/s10236-005-0110-6

Soetaert, K., Herman, P. M. J., Middelburg, J. J., Heip, C., Destigter, H. S., Van Weering, T. C. E., et al. (1996). Modeling 210Pb-derived mixing activity in ocean margin sediments: diffusive versus nonlocal mixing. *J. Mar. Res.* 54, 1207–1227. doi: 10.1357/0022240963213808

Sun, M., Aller, R. C., and Lee, C. (1991). Early diagenesis of chlorophyll-a in Long Island Sound sediments: a measure of carbon flux and

particle reworking. *J. Mar. Res.* 49, 379–401. doi: 10.1357/002224091784995927

Sun, M. Y., Aller, R. C., and Lee, C. (1994). Spatial and temporal distributions of sedimentary chloropigments as indicators of benthic processes in Long Island Sound. *J. Mar. Res.* 52, 149–176. doi: 10.1357/0022240943076768

Tauber, T., and Emeis, K.-C. (2005). Sediment mobility in the Pomeranian Bight (Baltic Sea): a case study based on sidescan-sonar images and hydrodynamic modelling. *Geo. Mar. Lett.* 25, 221–229. doi: 10.1007/s00367-004-0207-9

Vedel, A., Andersen, B. B., and Riisgard, H. U. (1994). Field investigations of pumping activity off the facultatively filter-feeding polychaete nereis diversicolor using an improved infrared phototransducer system. *Mar. Ecol. Progr. Ser.* 103, 91–102. doi: 10.3354/meps103091

Wasmund, N., Schöppe, C., Göbel, J., and von Weber, M. (2011). Chlorophyll-a in den Deutschen Ostseegewässern. *Meeresumwelt aktuell Nord- und Ostsee 2011/2*. Available at: http://www.blmp-online.de/Seiten/Berichte.html

Webb, D. G. (1993). Effect of surface deposit-feeder (*Macoma balthica* L.) density on sedimentary chlorophylla concentrations. *J. Exp. Mar. Biol. Ecol.* 174, 83–96. doi: 10.1016/0022-0981(93)90252-J

Conflict of Interest Statement: The authors declare that the research was conducted in the absence of any commercial or financial relationships that could be construed as a potential conflict of interest.

Copyright © 2018 Powilleit and Forster. This is an open-access article distributed under the terms of the Creative Commons Attribution License (CC BY). The use, distribution or reproduction in other forums is permitted, provided the original author(s) and the copyright owner(s) are credited and that the original publication in this journal is cited, in accordance with accepted academic practice. No use, distribution or reproduction is permitted which does not comply with these terms.

frontiers in Marine Science

ORIGINAL RESEARCH
published: 05 September 2018
doi: 10.3389/fmars.2018.00305

Phosphorus Contents Re-visited After 40 Years in Muddy and Sandy Sediments of a Temperate Lagoon System

Maximilian Berthold[1], Dana Zimmer[2], Volker Reiff[1] and Rhena Schumann[1]*

[1] Biological Station Zingst, Institute of Biological Sciences, Department of Mathematics and Natural Sciences, University of Rostock, Rostock, Germany, [2] Marine Chemistry, Leibniz Institute for Baltic Sea Research, Warnemünde, Germany

Worldwide, coastal water bodies suffer from anthropogenically elevated nutrient inputs, which led to eutrophication. Sediments in eutrophic systems are assumed to be an important internal nutrient source. The total phosphorus (TP) concentration (mg g^{-1} dry mass) is widely used as a proxy for the sediment nutrient load. 2-D distribution maps of TP concentrations are used for management plans, where areas of high TP values are marked in red. However, the sediment density is lowered at increasing water content, which can lead to different TP stocks per g m^{-2}. The aim of this study was, to do a re-evaluation of TP concentrations and stocks in the model ecosystem of the Darß-Zingst Bodden chain, a typical lagoon system of the southern Baltic Sea. Sediment cores were taken at eight stations along transects from shallow to deeper parts of the lagoon. Samples were analyzed for TP, water and organic content, as well as density. This data set was compared to results from a sediment survey during the time of highest nutrient inputs (40 years ago) at the same sampling stations. TP concentrations from 40 years ago and today were in the same range. The highest TP concentrations (up to 0.6 mg TP g^{-1} dry mass) were found in the deeper basins and lowest concentrations in the shallow areas of the lagoon (down to 0.05 mg TP g^{-1} dry mass). However, normalization over dry bulk density (DBD) reversed some results. The highest TP stocks (up to 5 g TP m^{-2}) were then found in the shallow areas and lowest stocks (down to 0.2 g TP m^{-2}) in the deeper parts of the lagoon. Some stations did not exhibit any differences of TP at all, even after including the DBD. These findings suggest that there seems to be no up-, or downward trend in nutrient concentrations of sediments even after 25 years of reduced external nutrient inputs. Furthermore, TP stocks point to possible diffuse P entry pathways that counteract external nutrient reductions. These findings can have an impact on possible countermeasures for ecosystems rehabilitation, like sediment removal or nutrient reductions in the adjacent land.

Keywords: phosphorus concentration, sediment, brackish lagoon, dry bulk density, Baltic Sea, organic content

OPEN ACCESS

Edited by:
Karol Kulinski,
Institute of Oceanology (PAN), Poland

Reviewed by:
Dirk De Beer,
Max-Planck-Gesellschaft (MPG), Germany
Sarah Elizabeth Reynolds,
University of Portsmouth, United Kingdom

****Correspondence:***
Maximilian Berthold
maximilian.berthold@uni-rostock.de

Specialty section:
This article was submitted to Marine Biogeochemistry, a section of the journal Frontiers in Marine Science

Received: *29 April 2018*
Accepted: *10 August 2018*
Published: *05 September 2018*

Citation:
Berthold M, Zimmer D, Reiff V and Schumann R (2018) Phosphorus Contents Re-visited After 40 Years in Muddy and Sandy Sediments of a Temperate Lagoon System. Front. Mar. Sci. 5:305. doi: 10.3389/fmars.2018.00305

Abbreviations: DBD, dry bulk density; DM, dry mass; DZBC, Darß-Zingst Bodden chain; LOI, loss on ignition; TP, total phosphorus; WC, water content.

INTRODUCTION

Along with the Green Revolution in agriculture in the last 50–75 years in the developed countries, ecosystems worldwide are strongly influenced by high anthropogenic nutrient inputs especially nitrogen (N) and phosphorus (P) (e.g., Smil, 2000; Liu et al., 2008; Schröder et al., 2010; Childers et al., 2011; Lu and Tian, 2017). Even the most optimistic future scenarios point to an overall increased use of P worldwide (Van Vuuren et al., 2010), i.e., overall use will most likely still lead to increased P inputs into aquatic ecosystems, despite of examples of reverse trends by effective reduction of P entering aquatic systems (e.g., Civan et al., 2018). Moreover, Yan et al. (2016) pointed to the fact that P seems to accumulate faster than N in aquatic systems, which means that even reduced P loads can still increase the P background within systems. This accumulated P has short and long-term effects in aquatic ecosystems. In the short term, the primary production within a system increased on a recurring annual basis. On a longer timeframe, P accumulates in sediments, where it can be remobilized occasionally (e.g., Ruttenberg, 2003). Consequently, P is trapped in the biological cycles until it is precipitated in more or less biologically insoluble forms. Such increases of insoluble forms of P in sediments are well described worldwide (e.g., Heathwaite, 1994; Jensen et al., 1995). Elevated P pools are still a burden for restoration, as they can be released massively during suboxia in near-bottom water layers or at a slower rate by diffusion. Such release situations are well described for, e.g., the Baltic proper and sediments of the Baltic coastal zones (Pitkänen et al., 2001). If P is released, it starts to refuel primary production again and the system will remain in its current state (Vahtera et al., 2007). Furthermore, Duarte et al. (2009) described this elevated P background as a main cause, why restoration will not work and ecosystems fail to return to the reference status upon nutrient reduction.

The Baltic Sea is such a highly anthropogenically impacted brackish water body, where the drainage basin (∼1,739,000 km^2, Nilsson, 2006) is around four times larger than the sea (∼412,500 km^2) itself. The nutrient loads into the Baltic Sea increased from the 1950s until peak values around 1980 followed by a decrease continuing up to present (Gustafsson et al., 2012). However, the inputs amounted to 1,056,922 tons of N and 41,163 tons of P in 1995 and 825,825 tons N and 30,949 tons P in 2014 (HELCOM, 2018). Nevertheless, P inputs into water bodies by point sources were reduced during the mid-1980s and are permanently low in German coastal water bodies since then. Therefore, this input reduction of up to 80% (Nausch et al., 2011) could meanwhile have impacted P stocks in sediments of the coastal water bodies. Coastal lagoon systems are of special interest, as they cover 5% of the entire Baltic coastal zone, but account for 10% of the P burial and half of the denitrification of all coastal ecosystems in the Baltic Sea (Asmala et al., 2017). Therefore, such lagoon systems can act as nutrient filter for the open Baltic Sea by trapping nutrients within their system. However, these reduced P inflows take only the reduction of direct river-borne P into account, but Germany's federal state agencies indicated that diffuse P inputs became increasingly important during the last decades (BMUB and BMEL, 2016). In this context, Karstens et al. (2016) showed the impact of the adjacent land use on the wetland sediments in coastal systems, and Berthold et al. (2018a) described the possible direct export of P from adjacent wetlands into coastal water bodies. These diffuse P input could strongly affect the spatial distribution of P accumulation especially in dependency from coastal distance.

A well-described typical shallow lagoon system of the southern Baltic Sea is the DZBC (e.g., Schiewer, 2007), where a synoptic sediment study was conducted 40 years ago (e.g., Schlungbaum, 1982; Schlungbaum et al., 1994). At that time, sediment samples were taken in every lagoon part in a 500 to 1,000 m sampling grid in shallow and deep areas. Certain P hotspots were shown, often in deeper waters (e.g., Nausch and Schlungbaum, 1984). The sampling coincided with the peak of riverine TP inputs of up to 80 t a^{-1} during 1976 to 1980. Highest TP values were found in the deeper parts between 2 mg P g^{-1} DM in the inner lagoon, and up to 1 mg P g^{-1} DM in the outer lagoon. The LOI ranged between <1 and 40% (Nausch, 1981) depending on the sampling depth. Afterward, TP inputs by rivers were steadily reduced by 75% and are now for the last 20 years constant at 20 t a^{-1} (LUNG, 2013). Interestingly, these P reductions did not reduce turbidity, or phytoplankton biomass within the system, but the light limitation of phytoplankton seems to be so stable that small, light-efficient cyanobacteria (Schiewer, 2007; Albrecht et al., 2017) remain dominant. The original annual periodicity of phytoplankton composition disappeared, leaving the DZBC in a state of permanent high turbidity since the end of the 1980s (Schiewer, 2007). Such results indicate, that other P sources than direct inputs by rivers might explain the permanent high phytoplankton biomass. However, the DZBC is also described to possess a nutrient filter function, as the water exchange rate with the surrounding open Baltic sea is low (0.15 a^{-1} Schiewer, 2007), and the sediments sorption capacity for P is high (0.05–1.1 mg P g^{-1} DM, Schlungbaum, 1982). Furthermore, the particulate matter in this lagoon system has a high TN:TP (15-year median: 36–47:1, mol:mol) ratio, compared to other coastal water bodies of this region (Berthold et al., 2018b). This finding means that sedimented particulate material had a relatively low P status. Moreover, the sedimentation rate in this lagoon system is postulated to be between 1 (Lampe et al., 2013) and 5 mm a^{-1} (Nausch, 1981). Therefore, we hypothesized that the lowered P inputs had already an effect on the first centimeters of the sediment and re-evaluation of sediment P loads might reflect lowered P inputs into the lagoon. Such re-evaluations of sediments are exceptionally important, as the EU-Water Framework Directive and society have to consider the necessary time-spans for reducing anthropogenic impacts in aquatic ecosystems.

As mentioned, P concentrations (in mg g dry $mass^{-1}$ or % of DM) in sediments are assumed to be important indicators for the total P load in an aquatic system and they are often used to create heat maps where hot spots of P- and other element-concentrations are described (e.g., Leipe et al., 2017). This approach could be questionable because sediment density can vary strongly due to the texture and water and organic matter content (Avnimelech et al., 2001; Köster and Meyer-Reil, 2001; Verstraeten and Poesen, 2001; Faas and Wartel, 2006) strongly

affecting P stock in the sediment volume. Moreover, P stocks per m^{-2} seemed to be ecologically much more important, because the exchange at the sediment/water contact zone happens per area.

Due to the potential spatial and temporal differences in P loads of the sediments in the DZBC, sediments were sampled in transects in a right angle from the coastline, i.e., from shallow to the deeper areas across all lagoon basins. These samples were analyzed for bulk density, water and organic matter content and TP concentrations. From theses analyses, P stocks of sediment were calculated per area. All of these data were compared to the historical sample data 40 years ago. With this approach we want to answer the questions (1) if there is a gradient of increasing TP in the sediment from shore to deeper waters – both on a concentration or on a stock basis and (2) if surface TP changed within 40 years in line with decreasing P inputs into the lagoon system and the Baltic Sea.

MATERIALS AND METHODS

Sampling Area

The DZBC is a temperate lagoon system with consecutively connected lagoon basins. The innermost lagoon parts Saaler Bodden (SB) and Bodstedter Bodden (BoB) are oligohaline (salinity 1–4) and highly eutrophic (Schiewer, 2007). The two outer lagoon parts Barther Bodden (BB) and Grabow (GB) are less influenced by riverine nutrient inputs (salinity 5–12) and less turbid (secchi depth up to 100 cm). Sampling spots were chosen for a gradient from shallow areas, proximate to the coastline to deeper parts of the lagoon. Two different spots were chosen per lagoon part. Additionally, samples from the outer southern Baltic coast line were taken as comparison. Those stations were located in Kühlungsborn, Zingst, island of Hiddensee and island of Usedom (**Figure 1**).

Sampling

The sedimentation rate in this lagoon system is postulated to be between 1 (Lampe et al., 2013) and 5 mm a^{-1} (Nausch, 1981). We used the lower sedimentation rate as a conservative approach to test our hypothesis. The time between the first sampling in 1977 and 2017 equals for 4 cm of increased sediment height. P inputs are on a constant low level for more than 27 years (=2.7 cm, LUNG, 2013). We sampled the upper first 1.4 cm (first 5 ml of a syringe), which is half of the sediment increase.

Sediment samples in the DZBC were taken with a sediment corer (10 cm diameter) (Hydrobios) between the water depths of 0.5 and 3.5 m, depending on the sampling site. Geographic coordinates for start and end point of each transect can be found in **Supplementary Table 1**. Sediment samples from the outer coast line were taken by divers, which used hand-held sediment corer with only 5 cm diameter. Six to eight sediment cores were taken along transects per sampling spot from shore to open water. Samples from the outer coast were taken with hand-held sediment tubes (10 cm diameter) by divers starting at water depths of 20 cm up to 5 m water depth. Three sub-samples of the first 1.4 cm were taken with a cylinder, which had a fixed volume, from the sediment cores. All samples were taken in 2017, except for a transect near Dabitz in the GB, which was already sampled in 2013 and included as an additional station. Additionally, sediment from this transect was separated in the horizons of 0–1, 1–2, and 2–5 cm.

Determination of Dry Bulk Density, Water, and Organic Matter Content

The fixed volume of a cylinder (syringe, 5 ml volume) was used to calculate DBD (g cm^{-3}) after drying. Sub-samples were weighed wet, dried at 105°C for 24 h, and weighed dry again. The difference was used to calculate the WC (%) and DBD. Afterward, the sub-samples were combusted at 550°C for 4 h in a muffle furnace (Heraeus). The sediment ash of the sub-samples were weighed again after cooling down in a desiccator. The difference was used to calculate the organic content as LOI of the sediment. At least, the sub-samples of the sediment ash were pooled again and grinded in a powder mill (5,000 rpm, 2 min, Fritsch). The final grain size was between 1 and 10 μm. The dust was used for subsequent TP analyses.

Determination of Total Phosphorus

Ten to 50 mg of sediment ash were weighed in perfluoroalkoxy-polymer (PFA) tubes (AHF Analysentechnik) and suspended in 15 ml of ultrapure, phosphate-free water (power plant Rostock). Subsequently, 1.5 ml of acid persulfate was added, the samples were tightly closed and oxidized at 90°C for 24 h (Berthold et al., 2015). Afterward, the complete sample was neutralized and filtered (GF/F filter, Whatman). TP was determined with molybdenum blue according to Hansen and Koroleff (1999) with a photometer (Hach DR3900, 5 cm cuvette) at 885 nm. All sediment samples were digested and measured in quadruplicates.

The synoptic sediment study from 40 years ago collected amongst other parameters, WC, LOI, and TP concentrations. DBD was only sampled on a random basis and results were averaged for sediments with an LOI of <5% (1.5 g cm^{-3}) and >5% (1.0 g cm^{-3}). These mean DBD values were used to estimate the total P stock (in g P cm^{-2}) in the first cm of the sediments of the lagoon system (Nausch, 1981). Instead, we took the historic values of WC and TP concentrations (only available as range) to re-calculate DBD and areal TP stocks (Equation 1) as such a relationship was missing in the studies from 40 years ago (see the section "Discussion"). The equation for areal TP stocks (g m^{-2}) was calculated out of the TP concentrations (mg P g^{-1} DM sediment) and the relationship of WC (%) to sediment density (**Figure 2A**). The relationship of areal TP stocks to sediment densities are rather widely distributed (**Figure 4**), which affects this approach.

$$\text{Totalphosphorus}\,(\text{g}\cdot\text{m}^{-2}) = (3.47\cdot e^{-0.035\cdot WC\%})\cdot \text{TP}\,(\text{mg}\cdot\text{g}^{-1}\,\text{dry mass}^{-1})\cdot 10 \quad (1)$$

Quality Management and Statistics

Determination (quantification) limit for TP was 0.22 μmol l^{-1} by the blank method in the digestate. Sediment samples

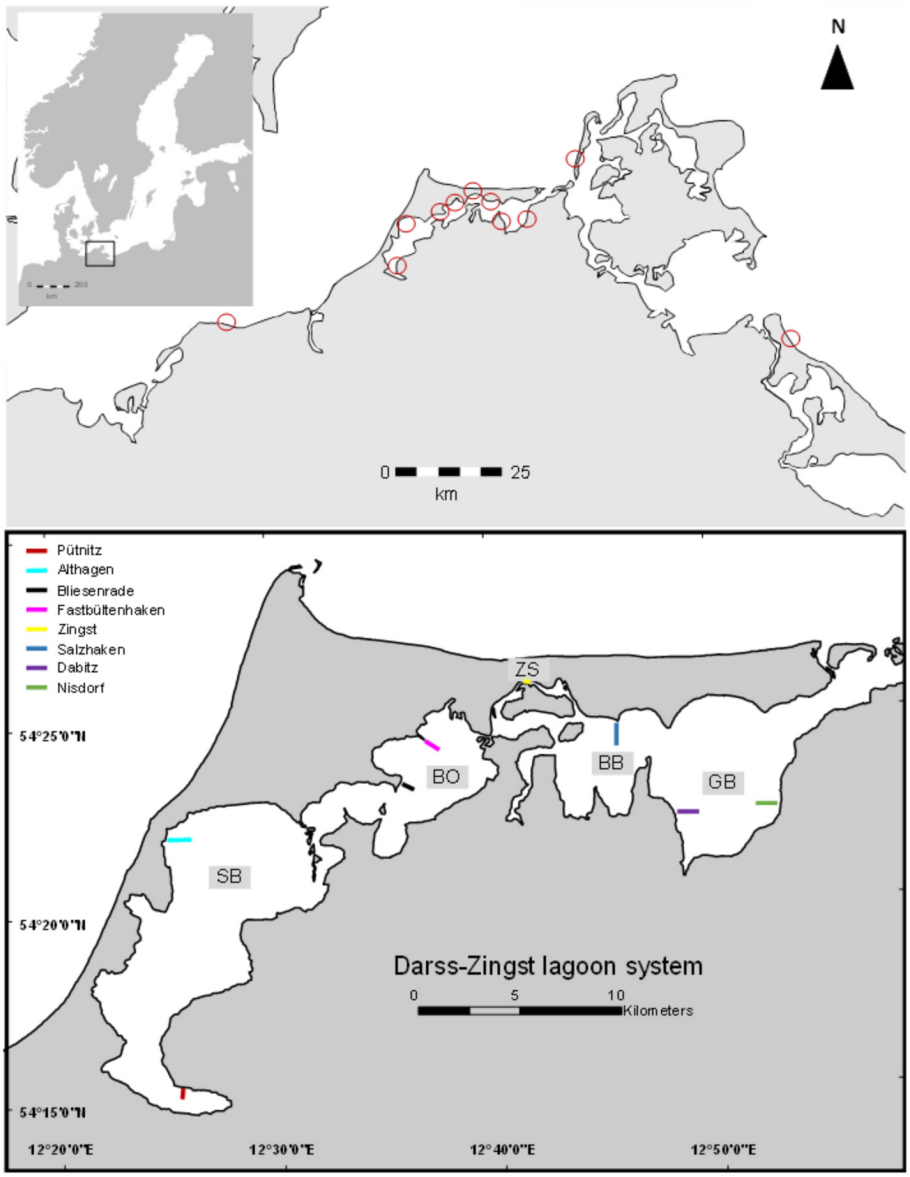


FIGURE 1 | Map of the sampling area (drawn with ArcGIS version 10.2). Colored bars indicate samplings spots of conducted transects. GPS coordinates can be found in the **Supplementary Table 1**.

were prepared to be above that limit and reach at least 2 μmol l^{-1} in the extract. The combined standard deviation was 11.8% for TP determination, which combines the random error of replicate samples and all standard values measured over the whole investigation period. This value describes reproducibility of both (samples and standards, i.e., random error of both).

SigmaPlot 13.0 was used for statistical analysis. Shapiro–Wilk tested all data for normal distribution. A Spearman Rank Order test was used for correlations. The principal component analysis (PCA) for the separation of sampling sites was computed for the water depth (in m), the LOI (in %), the DBD (in g cm^{-3}), the total P concentration (in mg TP g^{-1}) and the total P stocks of the first cm (in g TP cm^{-2}) of the sediment samples using STATISTICA 6.0 (StatSoft, Inc., 2001).

RESULTS

Characteristics and P-Content of Sediment Samples

The water depth of the 64 sediment samples of the eight transects ranged from 0.4 to 4 m. The WC ranged between 17 and 88% and the LOI between 0.036 and 23% LOI (**Figure 2**). Sediment samples from the outer coastline had a WC between 14 and 20%

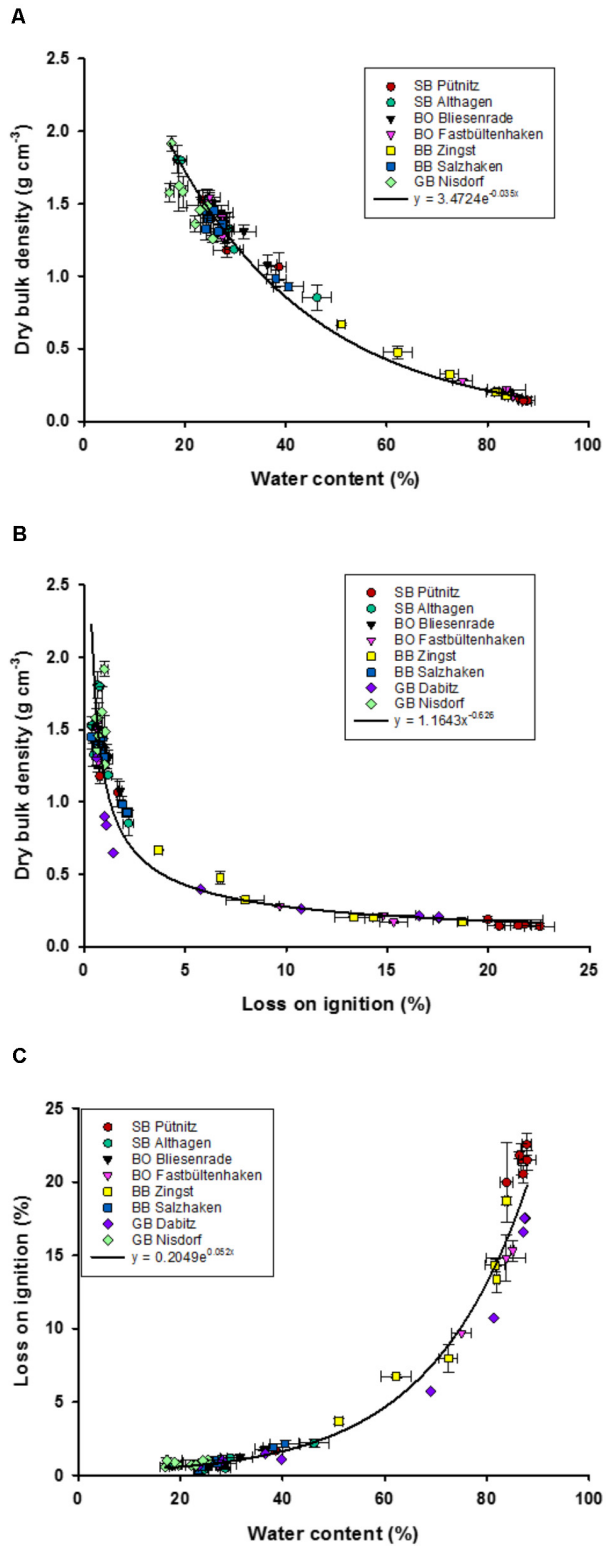


FIGURE 2 | Relationships of dry bulk density (g dry mass cm^{-3}) to water content (%) **(A)**, and loss on ignition (%) **(B)**, and water content (%) to loss on ignition (%) **(C)**, in the upper sediment (1.4 cm). Fits were chosen to represent all data points, and not the highest coefficients of determinations (R^2). Error bars are standard deviation of three replicate measurements.

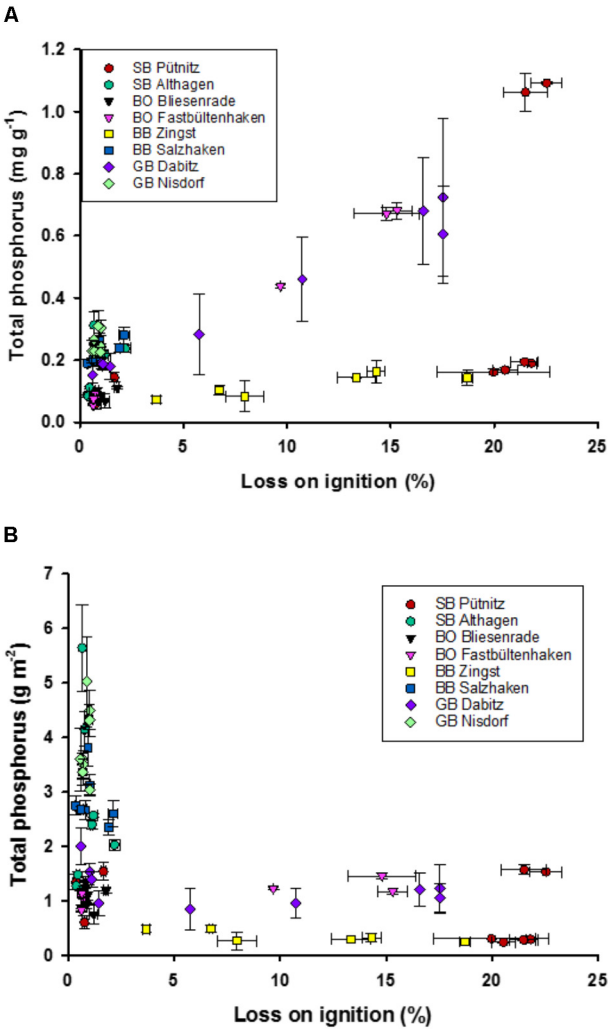


FIGURE 3 | Relationship of total phosphorus concentration (TP) in g P dry $mass^{-1}$ **(A)** and areal TP stock in g P m^{-2} **(B)** to loss on ignition (%). Error bars are standard deviation of three replicate measurements for organic content and four for TP.

and a DBD of 1.4 to 1.7 g cm^{-3} (**Supplementary Figure 1**). At least one out of four samples had an LOI higher than 5%, while one third of those samples had a DBD below 1 g cm^{-3} (**Figure 2**). WC and LOI were significantly positively correlated (r = 0.91) and both negatively with DBD (r = –0.84 and – 0.74, respectively). Additionally, the sediment characteristics were different in shallow and deeper waters, since the water depth correlated significantly with WC (r = 0.52), LOI (r = 0.67), and DBD (r = –0.48).

The median of the P concentrations ranged from 0.05 to 1.1 mg TP g dry $mass^{-1}$ and those of the P stocks from 0.24 to 5.6 g P cm^{-2} in the first cm of the sediment. The highest TP concentrations were found at higher LOI (**Figure 3A**). However, there was a huge variability, as some sediments with a high LOI had very low TP concentration per g DM. Low TP concentrations were measured at increasing DBD, i.e., lower WC

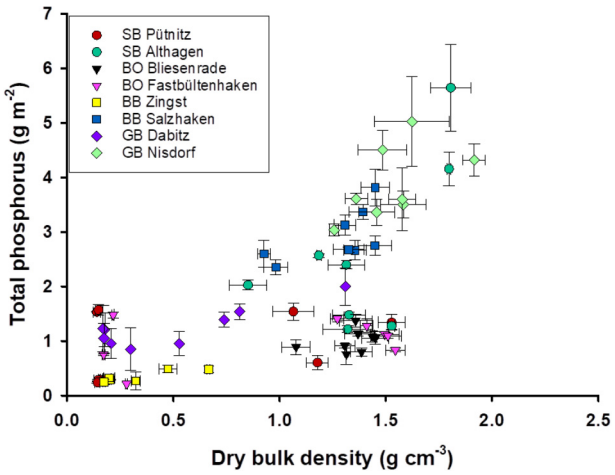


FIGURE 4 | Total phosphorus stock (g P m^{-2}) and dry bulk density (g dry mass cm^{-3}). Error bars are standard deviation of three replicate measurements for DBD and four for TP.

and OC. In contrast, TP stocks were very variable at low LOI (**Figure 3B**). Nonetheless, LOI correlated significantly with both, TP concentrations (r = 0.4) and areal TP stocks (r = –0.42). Most of the samples with a low TP concentration and high WC and LOI originated from the station Zingst and were close to a harbor whereas others were from Pütniz, the innermost lagoon basin.

There was less variation in TP stocks at lower DBDs compared to sampling sites with higher DBD (**Figure 4**). For example, samples from the lagoon part BoB had high areal TP stocks, compared to samples of lower DBD from deeper parts. In contrast, there were also samples with a DBD comparable to BoB (i.e., GB and BB), but those had three- to six-times higher areal TP stocks. Comparable TP stocks of 0.6–2.9 g TP m^{-2} at DBD's from 1.3 to 1.6 were found at the outer coastline (**Supplementary Figure 2**). Interestingly, the stations with very high areal TP stocks were at the southern site of the lagoon, which is at the coast of the main land and receives riverine water. It becomes apparent that even stations in the most eutrophic part of the lagoon, i.e., SB and BoB, have comparably low areal TP stocks. The stations Fastbültenhaken and Bliesenrade, which are in the middle of the lagoon system, had the lowest variations, even though all samples originated from different depths. There were also outliers present in the innermost and outermost lagoon, i.e., Altenhagen and Nisdorf. Areal TP stocks of up to 6 g m^{-2} were found, but at water depths of around 2 m and with low LOI. DBD correlated positively and significantly with the areal TP stocks. Dabitz (GB) was the only transect with low as well as high DBD. At the same depth range the stations at the outer coast only varied in areal TP, but not in DBD (**Supplementary Figure 1**).

Spatial Separation of Sampling Sites

Water depth, LOI, DBD, TP concentrations and TP stocks were included in the PCA to visualize separation of sampling sites in a two-dimensional plot (**Figure 5**). The first two PCs of the PCA explained together 82% and the first three PCs 95% of the variance between samples (**Figure 5**). Generally, the stronger the correlation of a factor to a specific PC (**Table 1**) the more the samples are shifted to the outward. Therefore, especially correlations of about ≥0.7 are highly important for separation of samples whereas correlations <0.5 are of low importance. Additionally, a negative correlation to a PC shifted samples to the left (PC 1) or downward (PC2) and a positive correlation to the right (PC1) or upward (PC2) (**Figure 5**). According to correlations (>0.9) of factors to PC1 (**Table 1**): the higher the LOI the more the samples are shifted to the right and the higher the DBD the samples are shifted to the left. The water depth had a correlation of 0.672 and the TP concentration of 0.635 to the PC1. That means that the deeper the water and the higher the TP concentrations the more the samples are shifted to the right but due to the lower correlations compared to LOI and DBD the shift is not so strong. The correlation of the TP stock to PC1 is the lowest of all factors and shifted to the opposite direction compared to the TP concentration (Tab. 1). However, TP concentrations and TP stocks were highest positively correlated to PC2 (**Table 1**). That means that samples with higher TP concentrations and/or TP stocks are shifted downward.

It is clearly visible that the sediment samples of Nisdorf (green triangles) and Salzhaken (yellow squares) and in parts those of Althagen (red triangles) are separated from the other sampling transects by shifting downward on the left side of the diagram (**Figure 5**). The shifting of these three transects was mainly caused by highest P stocks (1.2–5.6 g TP m^{-2}) in combination with generally higher DBD (0.85–1.92 g cm^{-3}) and lower LOI (0.36–2.19%) in contrast to the other transects (**Figures 2–5**). For the other transects the TP stocks ranged from 0.24 to 2.0 g TP cm^{-2}, the DBD from 0.14 to 1.53 g cm^{-3} and the LOI from 0.36 to 22.5% (**Figure 5**). The transect Zingst (blue circles) was completely separated from Nisdorf, Salzhaken, and Althagen because the samples of Zingst had low TP stocks (maximum 0.49 g TP cm^{-2}), low DBDs (maximum 0.67 g cm^{-3}) and high LOIs (3.7–18.7%).

Sampling points of the transect Pütnitz (lilac circles) are widely spread at the score plot (**Figure 5**) because TP stocks (0.24–1.57 g TP cm^{-2}), DBD (0.14–1.53 g cm^{-3}), LOI (0.36–22.5%) and TP concentrations (0.06–1.09 mg TP g^{-1}) varied strongly between samples (compare **Figures 2**, **4**). Additionally, the six samples from Pütnitz transect with the highest LOI (minimum 20%) had the lowest DBD (maximum 0.19 g cm^{-3}) in contrast to the three samples with lowest LOI (maximum 1.7%) and highest DBD (minimum 1.07 g cm^{-3}). The spreading of the sampling points of the transect Dabitz (brown squares) was caused by the combination of high LOI (minimum 10%) with high TP concentration (minimum 0.46 mg TP g^{-1}) and low DBD (maximum 0.26 g cm^{-3}) in four of the samples whereas in the other five samples the low LOI (maximum 5.8%) was combined with low TP concentrations (maximum 0.28 mg TP g^{-1}) and higher DBD (minimum 0.39 g cm^{-3}). The sampling points of the transect Bliesenrade (gray squares) clustered together because the sediment samples varied less and were very similar to each other (LOI: 0.63–1.78%, DBD: 1.08–1.45 g cm^{-3}, TP

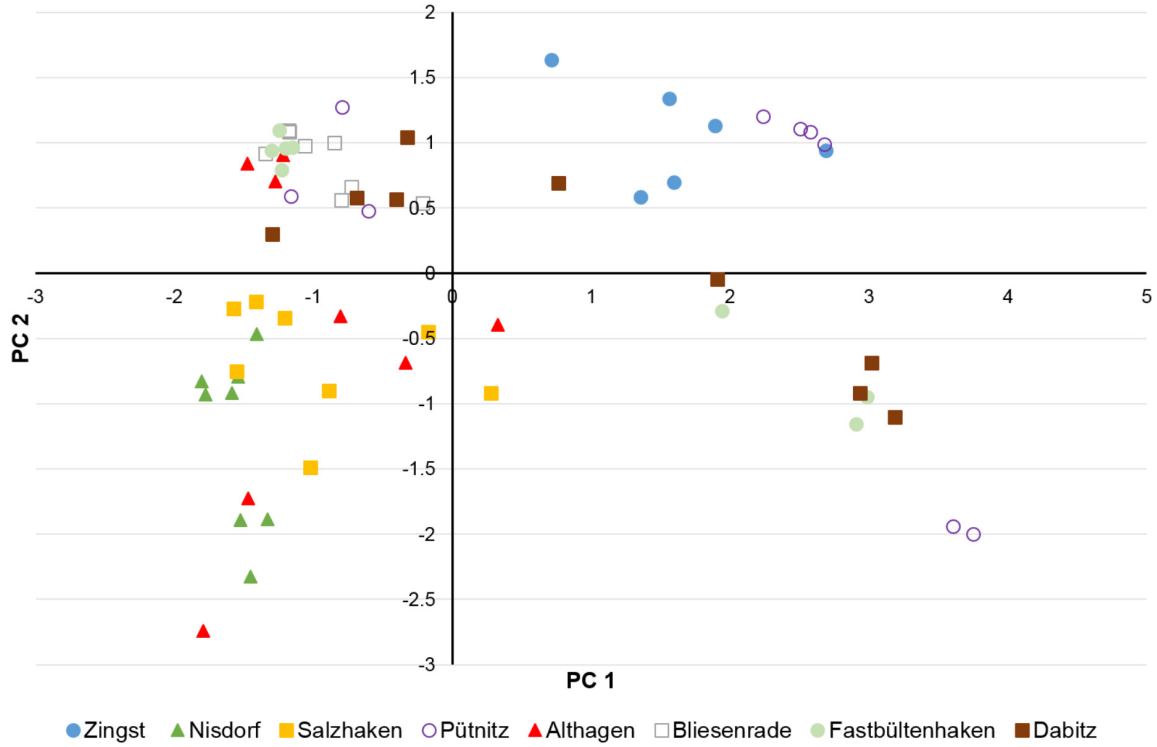


FIGURE 5 | Score plot of the principle component analysis (PCA) of water depth, DBD, concentration of LOI and TP and TP stocks in the first cm of the sediment samples of the transects near Zingst, Nisdorf, Salzhaken, Pütnitz, Althagen, Bliesenrade, Fastbültenhaken, and Dabitz.

concentration: 0.06–0.10 mg TP g^{-1}, TP stocks: 0.75–1.37 g TP cm^{-2}).

There was a general trend of increasing LOI and TP concentrations but decreasing DBD and nearly constant TP stocks with increasing water depth for all samples of all transects (**Supplementary Figure 3**). The nearly constant TP stocks can be attributed to the opposite trends in the different transects because in the transects Zingst, Nisdorf, Althagen, Bliesenrade, and Fastbültenhaken the TP stocks increased but for the transects Salzhaken, Pütnitz, and Dabitz the TP stocks decreased with water depth. Correlations between water depth and the sediment parameters were found for the transect Dabitz. In this transect, the sediment samples were additionally evaluated at three sediments depth at each sampling point. The TP concentrations in Dabitz ranged between 0.13 and 0.76 mg TP g DM^{-1} with increasing values at deeper waters. Additionally, stations below 1 m water depth had an increasing WC and LOI of up to 87% and 17%, respectively. In contrast, highest TP stocks were found nearshore and were decreasing with distance from land (**Figure 6**), even though the first centimeter was comparably between all stations. The nearshore cores (water depth 0.5–0.7 m) had a TP stock peak in 1–2 cm, even though DBD was highest from 2 to 5 cm sediment depth. This result indicates a P enrichment. Furthermore, combined TP stocks of all horizons were at those nearshore stations at least two times higher, compared to stations below 1 m water depth. The LOI decreased per depth from around 2 to 0.5% at the shallow stations (except at 0.6 m). Samples below 1 m water depth had no clear depth gradient for TP stocks, DBD or OC.

TABLE 1 | Correlation of the parameters water depth, organic matter content (OC %), dry bulk density (DBD in g cm^{-3}), total concentration of P (TP in mg g^{-1}) and total P stocks in the first cm (TP in g m^{-2}) with the principle components PC 1 to PC 5.

Parameter	PC 1	PC 2	PC 3	PC 4	PC 5
water depth in m	−0.672	−0.268	0.686	0.072	−0.028
OC in %	0.942	−0.01	−0.141	−0.264	−0.151
DBD in g cm^{-3}	−0.951	−0.172	0.075	0.054	−0.239
TP mg g^{-1}	0.635	−0.634	−0.364	0.222	−0.032
TP g m^{-2} 1 cm^{-1}	−0.534	−0.814	0.048	−0.207	0.087

DISCUSSION

Evaluation of P-Content in Sediments

The TP concentration (mg g^{-1}) found in the upper sediments of this study were in a comparable range with other sediments (**Table 2**) of the DZBC (Berghoff et al., 2000), the south-western Baltic Sea (Leipe et al., 2017) and the Gulf of Finland (Lehtoranta and Pitkänen, 2003). However, higher TP concentrations compared to those of our study were detected in sediments of the Archipelago Sea (Conley and Johnstone (1995) and the

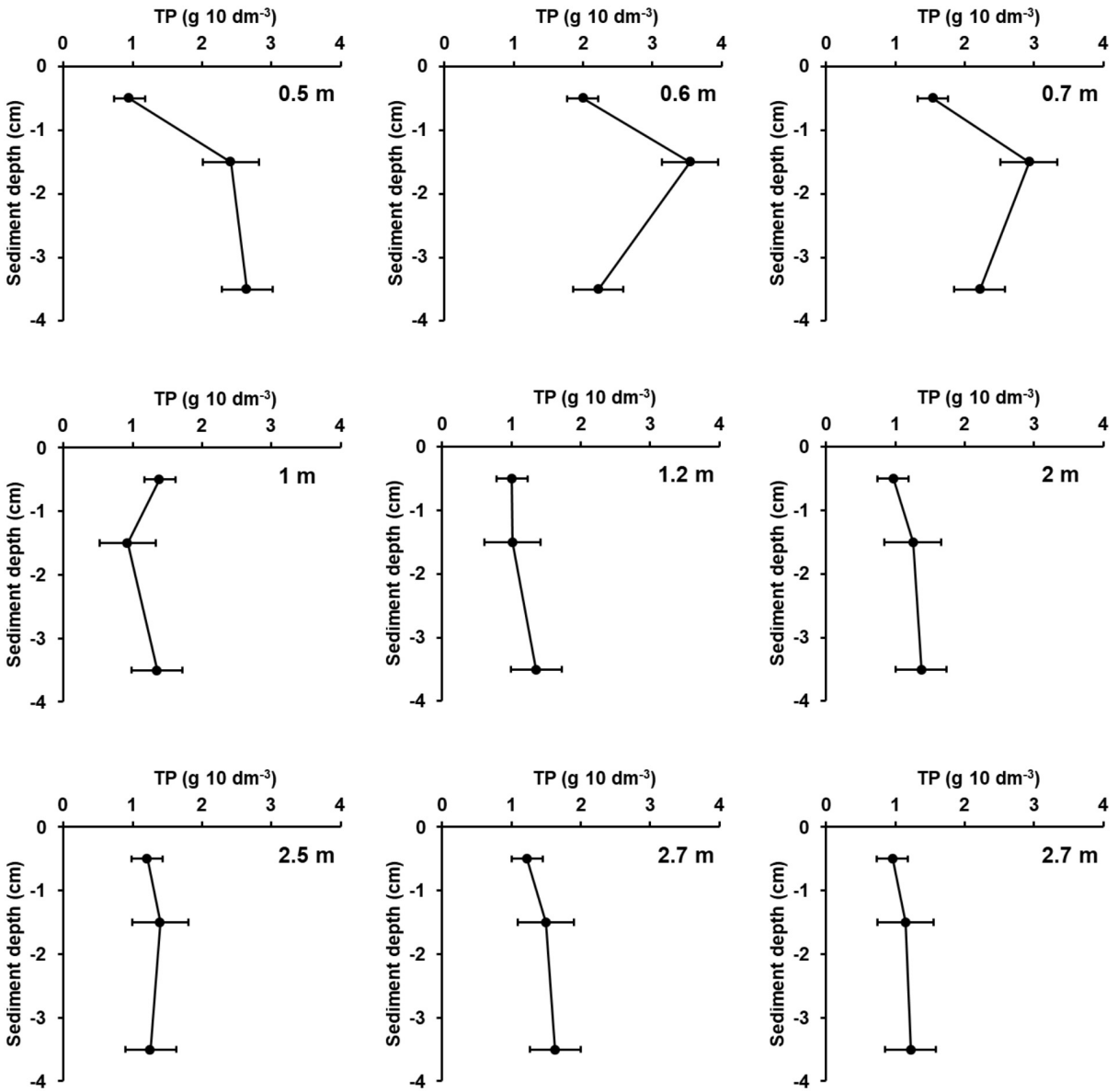


FIGURE 6 | Total phosphorus stocks (g TP 10 dm^{-3}, 1 cm slices) within the upper 5 cm of sediment in Dabitz (Grabow). Sediment was sampled in a transect at nine stations and separated in three horizons, 0–1, 1–2, 2–5 cm. The horizon in 3.5 cm depth was a mixed sample of 2–5 cm. Water depth is shown within the diagrams. Station 8 and 9 are spatial separated but in the same water depth. Error bars are standard deviation of four measurement replicates.

Landsort Deep (Dijkstra et al., 2016). The LOI (or calculated POC content) found in this study was within the same range as in other studies, but with one of the highest values found in the DZBC. Leipe et al. (2011) found a similar non-linearity between POC and DBD as found in this study. Furthermore, they described that with increasing POC content particles get smaller, whereas mud content <63 µm increases. Simultaneously, WC increases as well, i.e., the amount of water per area increases. Furthermore, the smaller particles have a higher area:volume ratio, compared to bigger particles, which increases P adsorbing capacities (Borggaard, 1983). These results mean, that in areas with fine sediment, like in basins, P concentrations are likely to be higher per g sediment, but decrease per area (Carman and Jonsson, 1991). However, we did not find a high correlation of LOI to TP concentrations, as described by, e.g., McComb et al. (1998) for the Peel-Harvey estuarine system. This result indicate, that there are possibly other factors influencing the TP concentration besides organic content.

The graphical summary in **Figure 7** points to this additional problem. The share of the solid phase on the wet mass density strongly decreases with increasing WC. Even though the LOI increases from 0.05 to 17% of the solid phase, it only increases from 0.3 to 2% of the complete sediment volume in the WC rich sediments. It seems unreasonable to assume

TABLE 2 | Overview of commonly found sediment parameter in combination with total phosphorus (TP) concentrations.

Water bodies	Location	TP (mg g^{-1} DM)	Org. C (%)	LOI (%)	DBD (g cm^{-3})	Reference
Baltic Sea	Darss-Zingst lagoon	0.05–1.1	0.1–7.4*	0.4–22.5	0.1–1.9	This study
Baltic Sea	South-western Baltic Sea	0–1.5	0–6			Leipe et al., 2017
Baltic Sea	Landsort Deep, Baltic Sea	0.93–2.0	3–6			Dijkstra et al., 2016
Baltic Sea	Grabow in Darss-Zingst lagoon	0.1–0.35		< 1–6.5	0.4 – < 1.6	Bitschofsky, 2016
Baltic Sea	Archipelago Sea, Stockholm Sweden	1.34				Conley and Johnstone, 1995
Baltic Sea	Gulf of Finland, estuary of river Neva	0.7–1.1		9.1–25		Lehtoranta and Pitkänen, 2003
Baltic Sea	Baltic proper	0.9–1.5		2.7–20.7		Carman and Wulff, 1989

LOI, loss on ignition; Org. C, organic carbon; DBD, dry bulk density. The values marked with one asterisk were calculated out of the relationship of POC content (%) to LOI (%) according to Leipe et al. (2010) for Baltic Sea sediments.

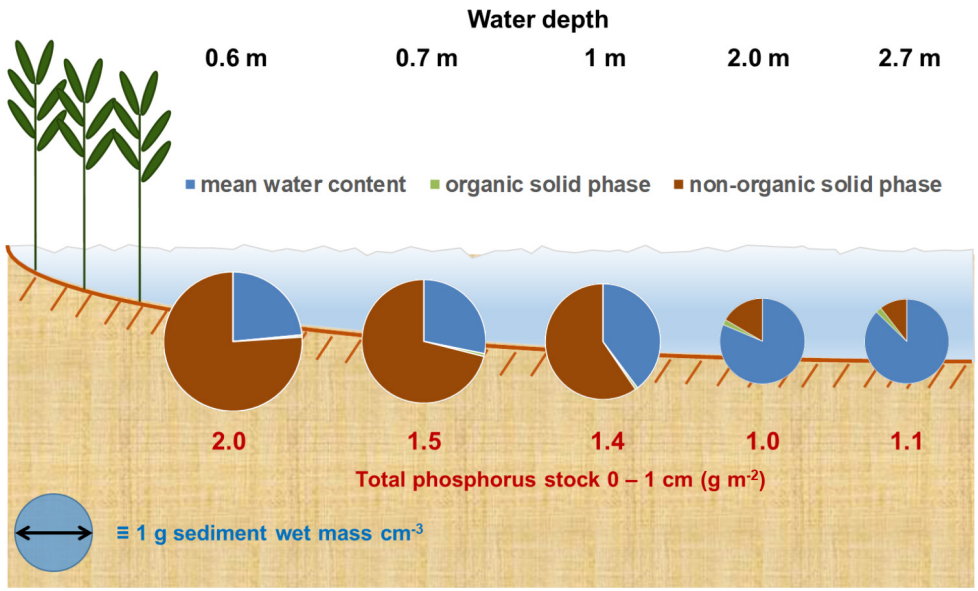


FIGURE 7 | Graphical summary of sediment properties development along the exemplary transect in the Grabow. Sediments wet bulk density is direct proportional to the circle's diameter. Organic solid phase was calculated as share of the whole solid phase per wet sediment volume.

that this small increase represents completely organic bound P. Furthermore, several authors point to the high pore-water concentrations in such apparently LOI rich sediments (e.g., Søndergaard et al., 1992; Kraal et al., 2013; Bitschofsky, 2016), whereas pore-water concentrations in sediments low on LOI have lower or non-determinable pore-water concentrations (e.g., Bitschofsky, 2016). For example, Bitschofsky (2016) determined 3–5 µmol l^{-1} dissolved inorganic phosphate in the pore-water of the DZBC at 2 m water depth. A sediment core with 85% WC would have 80–130 ng PO_4 cm^{-3}. The water evaporates during drying, but P is adsorbed to the solid phase and is determined as TP. However, TP ranged from 90 to 140 ng cm^{-3} in this study and is only slightly higher than the assumed pore-water concentration per sediment volume. This assumption brings up the question how P is actually bound in such water rich sediments. Up-to-date analysis methods like synchrotron-based XAS might be necessary to evaluate this question.

Nonetheless, several locations in the Baltic Sea have areal TP stocks between 1.6 g TP m^{-2} (Lehtoranta, 2003) and 4.9 g TP m^{-2} (Puttonen et al., 2014). Those sites showed high TP stocks even at very low DBD, compared to a maximum of 2 g TP m^{-2} at stations with low DBD in the DZBC. Contrary to these studies, the highest TP stocks were observed in sediments with low LOI and high DBD in this study (up to 6 g m^{-2}, see **Figure 3B**, station Althagen, Nisdorf). Such findings were also described by Carman and Wulff (1989), who found 9.5 g TP m^{-2} in highly dense sediments (WC – 29% LOI 2.7%, 0–1 cm), but only 1.15 g TP m^{-2} in less dense sediments (WC 91%, LOI 20.7%, 0–1 cm) in the Baltic Proper. This discrepancy highlights the importance of the factor sediment density, as small changes in TP concentrations affect TP stocks due to the non-linear relation (**Figure 3**). Furthermore, these contrary results suggest that knowledge of P loading and cycling within the system is necessary besides the sediment parameter.

Origin of P in Sediments – Location of Sampling Transects

In the PCA Nisdorf, Salzhaken and Althagen clustered together (**Figure 5**), resulting from similar higher TP stocks and DBDs but

lower LOI compared to the other transects. Similarity of these samples is surprising, since these stations are from completely different lagoon parts (**Figure 1**). However, the hinterland of these transects in Nisdorf and Althagen is intensively used for agriculture whereas that of Salzhaken is mainly used as pasture. This agricultural usage and possibly higher TP input could explain similarity of these transects and enriched of P stocks. Heathwaite (1994) described that runoff, transported suspended matter, N, and P loading increased by a factor of 8–9 from heavily grazed pasture areas intro the adjacent land. This increased nutrient inflow was found in the lake sediments as increased allogenic fraction. Generally, P can be transported into the water by agricultural drainage especially during storm events (e.g., Zimmer et al., 2016), by direct soil erosion with soil particles or by submarine groundwater discharge (Knee and Paytan, 2012). However, it has to be pointed out that phosphorus is strongly adsorbed to soil particles especially amorphous Fe-(hydr)oxides (Cornell and Schwertmann, 2004; Fink et al., 2016; Gypser et al., 2017) and only low percentages of P are extractable by water and/or anion exchange resin (e.g., Koch et al., 2018). That means that transport of P in a dissolved form with drainage water or by groundwater discharge might be restricted especially to extreme storm events, to sandy soils with low P sorption capacity or to soils with high P loads (e.g., Tiemeyer et al., 2009; Knee and Paytan, 2012; Zimmer et al., 2016). Therefore, it is assumed that P loading of the shallow sediments in the DZBC resulted mainly from soil erosion by water and transport of P loaded soil particles from adjacent agricultural land. This assumption is supported by the unchanged positive P accumulation in German agricultural used soils (1.8 kg ha^{-1} a^{-1}), as described by van Dijk et al. (2016). A change of P stock in the sediments would be less likely with permanent diffuse P loadings, besides the reduced point sources. However, transport proportions of P adsorbed to soil particles and dissolved P into the sediment cannot be estimated at this point. There is no data available on P specific ground water fluxes or soil erosion in this area.

The effects of usage of the adjacent land on P stocks in sediment is further visible in the separation from the above mentioned transects and the clustering in the PCA (**Figure 5**) of the transects Bliesenrade and Fastbültenhaken. The adjacent land of both transects are without agricultural usage and have comparably low areal TP stock at similar DBDs. The transects Zingst, Pütnitz, and Dabitz are partly separated from the transects of Nisdorf, Salzhaken, and Althagen (**Figure 5**). At theses transects the land is used as harbor area, former airport with close river connection and agricultural used adjacent land. All these land usages might explain an overall increased P stock, as in the other areas. However, it is interesting, that Zingst, Pütnitz, and Dabitz represent a nutrient gradient, i.e., high TP (4 $\mu mol\ l^{-1}$) concentration in the water column in Pütnitz against low TP (2 $\mu mol\ l^{-1}$) in Dabitz (Berthold et al., 2018b). This result might imply that besides the water column as important P source for the sediment, the adjacent land and subsequent run-off is important as well. The transects in Dabitz and Fastbültenhaken exhibited a wide range in the PCA (**Figure 5**) pointing to strong differences between sampling points within both transects. At both stations a sharp increase in LOI and TP concentration but decrease in DBD was observed with increasing water depth (**Supplementary Figure 3**). The transect in Dabitz is located in the western lagoon GB where water exchange with the open Baltic Sea is highest. Fastbültenhaken is in the middle part of the lagoon and is likely subject to changing fresh- and seawater exchange. The clustering of both stations can be a result of different sediment accumulation, due to hydrological conditions. A hydrological model for the DZBC lagoon is missing, therefore no statements are possible regarding underwater currents.

Changes in Sediment P in the Last 40 Years and Ecological Evaluation

The data set from 40 years ago presented a wide range of TP concentrations between 0.05 and 1.5 mg TP g^{-1} DM (Nausch, 1981) (**Table 3**). The LOI ranged between 0.6 and >30% in the whole system, where deeper basins (up to 4 m depth) had not exclusively higher LOI values (possible range 1–30%). This distribution was most likely a result of underwater currents and sediment transports. The percentage of mineral sediments (<5% LOI) of the separate lagoon parts ranged between 60% (GB) and 40% (SB). In the present study had a share of 80% of the sediments were mineral sediments. However, these percentage is not representative as straight sampling transects

TABLE 3 | Total phosphorus (TP) (stock in g P m^{-2} 0–1 cm, and concentration in mg P g dry $mass^{-1}$) from 40 years ago (40-year BP – before present) compared with today at the same sampling spots.

Location	Sampling depth	TP (mg g^{-1}) 40-year BP	TP (g m^{-2})* 40-year BP	TP (mg g^{-1}) today	TP (g m^{-2}) today
Saaler Bodden	Shallow	0.1–0.2	1.7–2.4	0.05–0.1	1.2–1.5
	Deep	0.8–1.5	1.7–2.0	0.2–1.2	0.3–1.6
Bodstedter Bodden	Shallow	0.1–0.3	1.2–1.8	0.05–0.1	0.8–1.4
	Deep	0.4–0.8	0.8–1.7	0.4–0.7	0.8–1.5
Barther Bodden	Shallow	0.1–0.3	0.6–3.6	0.2	2.7–3.4
	Deep	0.3–0.4	0.9–1.8	0.2–0.3	2.3–2.6
Grabow	Shallow	0.1–0.2	1.4–4.0	0.2–0.3	3.0–5.0
	Deep	0.5–0.8	0.8–1.7	0.5–0.7	1.0–1.2

*Data is derived from Nausch (1981). *Values are assumed from Nausch (1981) with calculated dry bulk densities derived from water content (%) and TP (mg g^{-1} DM, only in ranges). Sampling depth: shallow (<1 m), deep (>2 m).*

were used, rather than a sampling grid. Furthermore, Nausch (1981) sampled 100 sediment cores per lagoon part, whereas the present study had only a maximum of 17 per lagoon part. Generally, the TP concentrations of Nausch (1981) and the present study are comparable for the range and depth distribution (**Table 3**). However, the original data set is only available as a range in tables and figures in the cited publication. DBD cannot be attributed to special samples, only to charts and averages. An uncertainty of the TP stock resulted from the missing exact values for the DBD from the old data sets. Sediment density should always be present within publications, as well as GPS coordinates, or deposited at data bases for future comparisons. This data set will be made accessible via PANGAEA[1]. Methodology of TP extraction was comparable, as the different digestion methods in these studies (HCl) and today (acid persulfate) were equally efficient (Berthold et al., 2015).

Generally, the results suggest that a significant P reduction within 40 years was not verifiable. The TP concentration ranges of the upper sediment layers did not change within the last 40 years. For example, sediment samples of the deeper parts (>1 m) were in the same range as already described by Nausch (1981) (**Table 3**). However, some stations from 2017 had TP concentrations at the lower range compared to 40 years before present. In general, the results found in this study and from 40 years ago are comparable. This similarity of old and new concentrations and stock is somewhat surprising as P inputs were at least reduced by 60 t P a^{-1} (LUNG, 2013). There were around 290 t P bound in the sediments (0–1 cm), if the mean P stocks of the whole system are re-calculate from 1980. The total P stored in the sediments nowadays is 257 t P, if it is assumed that (1) values of this study were representative for most sediments in the system and (2) that sediment characteristics did not change dramatically, i.e., the percentage of mineral to mud sediments remained constant. Some lowered ranges of TP occurred mainly in BoB and SB, which may reflect lower influxes from the Recknitz River. The reduction in TP influxes was largest in the Recknitz decreasing from 50 to 10 t a^{-1} during 1980 through 2010 (LUNG, 2013). No matter if the sediment P load decreased or not, the most important proportion of P in the sediment is the portion of P which normally interacts with the water column.

The interactions between the water column and the sediment depend also on the potential of P being released into or exported from the water column. This potential is higher in suboxic waters regardless of the areal TP. In fact, the State Agency for this region (LUNG, 2013) reported that all inner coastal water bodies of the southern German Baltic coast are oxygen-saturated even above the sediments, i.e., >6 mg O_2 l^{-1}. One pathway for PO_4 in oxic waters is co-precipitation with calcite (Gunduz et al., 2011) or the formation of iron-rich colloids with PO_4 (Gunnars et al., 2002). Such PO_4-colloids are removed by 40% within ca. 40 h in brackish waters (salinity of around 6) (Gunnars et al., 2002). These results suggest that the oxic environment is favoring net P export from the water column into the sediment. Furthermore, Lampe et al. (2013) described that a wind speed of >8 m/s (5 Bft), or a ground flow velocity of >0.4 m s^{-1} is necessary to induce resuspension events in the inner lagoon part SB. This wind speed happened only 7% of the time in, e.g., 2011 and a TP export via particulate matter into the Baltic Sea amounted only to 3 t a^{-1} (Lampe et al., 2013). However, this export is hard to quantify due to frequent water level changes. A regular occurring resuspension can increase the overall cycling of P between the water column and sediment and might gradually even out the TP concentrations in the growing sediments. Nonetheless, these results indicate that abiotic and biotic particles will be trapped within the lagoon and therefore lead to a TP deposition. Even the deeper basins of other lagoon parts (e.g., station Dabitz, GB) were probably permanently affected by transport of fine material down the slope (Håkanson, 1977), which would explain the absent TP peaks in the sediment horizons (**Figure 6**). This would support the low export rates and the sediment sink function for TP.

There is the possibility that especially high areal TP stocks in shallow areas are subject to frequent TP release events, as they are populated with macrozoobenthos. For example, the burrowing polychaetes *Hediste diversicolor* can reach average population densities of 700 Ind. m^{-2} in the shallow areas (<2 m, max. 7000 Ind. m^{-2}) of the BB and GB. This species was not found below 2 m or in the less saline lagoon parts, i.e., BoB and SB (Arndt, 1989). The burrows of *H. diversicolor* can increase the water-sediment surface by a factor of 3 as well as the nutrient exchange to the overlying water through their ventilation activity (Davey and Watson, 1995). Additionally, *Marenzelleria* spp. established stable populations since the early 1990s (Zettler, 1996) in this lagoon system with 2,000 to 8,000 Ind. m^{-2} in all lagoon parts (Zettler, 1997). *Marenzelleria* can simultaneously shift and increase the PO_4 porewater concentrations in the upper 5 cm sediment depth to the sediment surface by around 5 µmol PO_4 l^{-1} in sandy sediments (Renz and Forster, 2014). Both polychaetes, *Marenzelleria* and *H. diversicolor* have comparable irrigation rates of 12 l m^{-2} d^{-1} at population densities of 3,200 and 800 Ind. m^{-2}, respectively (Hedman et al., 2011). Thus, *Marenzelleria* spp. can replace *H. diversicolor* and expand the bioirrigation activity into the inner lagoon waters. *Chironomidae* occur in high abundances in the SB and BoB with 2,000 to 5,000 Ind. m^{-2} (Arndt, 1994; Zettler, 1997). They appear to be absent in the BB and GB, which means that bioirrigation by these species for deeper lagoon parts can be neglected. Deeper parts of the lagoon may have lower areal TP stocks as well as less P release by animals. The areal P release probably remains lower in deeper parts even if an average diffusive flux of 28.3 ± 15.2 µmol PO_4 l^{-1} m^{-2} d^{-1} is considered compared to a non-determinable, perhaps lower flux in shallow, unpopulated sediments (Bitschofsky, 2016).

However, these transport fluxes were not commonly monitored, as PO_4 concentrations in the water column were on median 0.1 µmol PO_4 l^{-1}, which is close to the determination limit (0.05 µmol l^{-1}) (Berthold et al., 2018b). One cause can be the luxury consumption of PO_4 by phytoplankton (e.g., Taft et al., 1975). A PO_4 increase would be missed analytically and phytoplankton may still be permanently fertilized. This low, but permanent fertilization might explain the missing ecosystem

[1]https://doi.pangaea.de/10.1594/PANGAEA.892498

improvement regarding a lower phytoplankton biomass and turbidity within the lagoon (Schiewer, 2007; Berthold et al., 2018b). This possible fertilization effect in the shallow areas is even more concerning, as phytoplankton and submerged macrophytes are not subject to light limitation in these areas, i.e., they can use available nutrients directly for growth and biomass increase, instead of storage. On an area base, TP stocks are much higher here and may fertilize phytoplankton and macrophytes considerably. On the other side, the low PO_4 concentrations within the system could also be caused by the high macrozoobenthos population. One major shift within the system was the aforementioned *Marenzelleria* colonization. The increased water-sediment contact surface in worm burrows could also lower water P concentrations through oxic precipitation and increased remineralization as described earlier. Additionally, a present light limitation (Schiewer, 2007) would always cap phytoplankton biomass, regardless of available P. Therefore, it is reasonable to assume that the P reduction caused only a phytoplankton adaptation to the reduced P availability, like postulated in Sas (1989) for lakes. The reduction of P might have triggered the species composition change (Schiewer, 2007) to small cell cyanobacteria with high volume to surface ratios, which are highly competitive in nutrient uptake (e.g., Friebele et al., 1978). This change could also explain the high TN:TP ratios (36–50) throughout the year found in this lagoon system (Berthold et al., 2018b), as cyanobacteria always show high N:P ratios (Finkel et al., 2010). As conclusion, the net P flux to the sediment might have stayed the same, as seen by the constant TP levels in the sediment, but the decreased P inputs were buffered by a changing species composition and inventory.

Such observations are important for management and restoration actions within eutrophic coastal water bodies. Therefore, future restoration measures shall not predominantly focus on apparently high TP concentrations (mg g^{-1} DM) in the sediment, but rather on diffuse sources in the very shallow areas of coastal water bodies. Those areas can have a greater impact than assumed so far.

CONCLUSION

Analysis of different characteristics of sediment samples, especially TP content, from different transects in the DZBC pointed to the importance of the land use near the transect, affecting the earlier and present day diffuse P input especially in such an almost closed water system such as the DZBC. However, strong differences between sampling points within a transect seem to call for additional effects of P- and/or sediment distribution such as DZBC internal sediment transport or biological sediment mixing by plants and animals. The sampling of sediment cores with parallel analysis of volume percentage of water, DBD and density specific calculation of P stock underlines the importance of sample preparation and area specific P stocks to evaluate ecological relevant P stocks in sediments. Furthermore, it seems reasonable, that the P stocks did not change in 40 years due to a constant P flux into the sediments and increased bioturbation by invasive species. The phytoplankton composition might have adapted to the lower available P concentrations within the water column and bypassed an ecosystem improvement by, e.g., lower turbidity. Therefore, it can be highlighted that P stock specific evaluation of sediments can draw a different picture of spatial P distribution compared to simple P concentrations in the solid sediment phase. Nevertheless, sediment core analysis have to be extended to separate TP analysis of pore water in the sediment volume and analysis of TP and total concentrations of Al, Ca, Fe, and Mn in the solid phase to get deeper insights into the proportions of dissolved P and adsorbed P as well as in binding partners of P in sediments. This knowledge is urgent necessary to evaluate the potential of P release and its real contribution to eutrophication in shallow lagoon systems and the Baltic Sea. Such enhanced analyses especially of the solid sediment phase from sediment cores from such transects could also contribute to improve the understanding in which diffuse ways P is mainly imported from the adjacent land into the water body. Additionally, a hydrological model seems necessary to determine, where particulate material is transported. This model would help to evaluate, if the lagoon sediment is a permanent P sink, or if particulate matter is transported with a delay into the Baltic Sea.

AUTHOR CONTRIBUTIONS

MB and VR planned and conducted the sampling. DZ performed the statistics. MB and RS performed the calculations. MB wrote the manuscript with extensive contributions of DZ, VR, and RS. RS conducted a substantial part of the phosphorus analytics.

FUNDING

This work was done in the context of the BACOSA II project (funded by the German Ministry for Education and Research, funding 03F0737A). This research was performed within the scope of the Leibniz ScienceCampus Phosphorus Research Rostock. We acknowledge financial support by Deutsche Forschungsgemeinschaft and Universität Rostock within the funding programme Open Access Publishing.

ACKNOWLEDGMENTS

Heike Lippert and Ronny Weigelt supplied us with sediment cores from the outer coast line. Brandt Coleman, Kana Kuriyama, Samira Roshan Khanipour, and Elena Samolov helped with the analytical work. We thank the reviewers with their comments and constructive criticism, which improved the manuscript, as well as the editorial and guest editorial board of this special issue.

SUPPLEMENTARY MATERIAL

The Supplementary Material for this article can be found online at: https://www.frontiersin.org/articles/10.3389/fmars.2018.00305/full#supplementary-material

REFERENCES

Albrecht, M., Pröschold, T., and Schumann, R. (2017). Identification of Cyanobacteria in a eutrophic coastal lagoon on the Southern Baltic Coast. *Front. Microbiol.* 8:923. doi: 10.3389/fmicb.2017.00923

Arndt, E. A. (1989). "Ecological, physiological and historical aspects of brackish water fauna distribution," in *European Marine Biology Symposium*, 23rd Edn, eds J. S. Ryland and P. A. Tyler (Denmark: Olsen & Olsen), 327–338.

Arndt, E. A. (1994). Struktur und Dynamik des Makrozoobenthos in der Darß-Zingster Boddenkette im Laufe der Letzten 25 Jahre unter besonderer Berücksichtigung der Makrozoobenthos — Ent-wicklung im Saaler Bodden von 1986-1990. *Rostocker Meeresbiol. Beit.* 2, 93–119.

Asmala, E., Carstensen, J., Conley, D. J., Slomp, C. P., Stadmark, J., and Voss, M. (2017). Efficiency of the coastal filter: nitrogen and phosphorus removal in the Baltic Sea. *Limnol. Oceanogr.* 62, 222–238. doi: 10.1002/lno.10644

Avnimelech, Y., Ritvo, G., Meijer, L. E., and Kochba, M. (2001). Water content, organic carbon and dry bulk density in flooded sediments. *Aquac. Eng.* 25, 25–33. doi: 10.1016/S0144-8609(01)00068-1

Berghoff, S., Schlungbaum, G., and Selig, U. (2000). Phosphorus in sediments from coastal waters of Mecklenburg-Vorpommern (southern Baltic sea). *Proc. Mar. Sci.* 2, 161–173. doi: 10.1016/S1568-2692(00)80013-3

Berthold, M., Karsten, U., von Weber, M., Bachor, A., and Schumann, R. (2018b). Phytoplankton can bypass nutrient reductions in eutrophic coastal water bodies. *Ambio* 47, 146–158. doi: 10.1007/s13280-017-0980-0

Berthold, M., Karstens, S., Buczko, U., and Schumann, R. (2018a). Potential export of soluble reactive phosphorus from a coastal wetland in a cold-temperate lagoon system: buffer capacities of macrophytes and impact on phytoplankton. *Sci. Total Environ.* 616–617, 46–54. doi: 10.1016/j.scitotenv.2017.10.244

Berthold, M., Zimmer, D., and Schumann, R. (2015). A simplified method for total phosphorus digestion with potassium persulphate at sub-boiling temperatures in different environmental samples. *Rostocker Meeresbiol. Beiträge* 25, 7–25.

Bitschofsky, F. (2016). *Phosphorus Dynamics in Sediments of Darß-Zingst Bodden Chain, a Eutrophic Estuary in the Southern Baltic Sea*. Available at: http://rosdok.uni-rostock.de/resolve/id/rosdok_disshab_0000001782

BMUB, and BMEL (2016). *Nitrate Report 2016 - Shared Report of the Federal Ministry for Environment, Nature Conversation, Building and Nuclear Safety and the Federal Ministry of Food and Agriculture*. Bonn: BMUB.

Borggaard, O. K. (1983). Effect of surface area and mineralogy of iron oxides on their surface charge and anion adsorption properties. *Clays Clay Miner.* 31, 230–232. doi: 10.1346/CCMN.1983.0310309

Carman, R., and Jonsson, P. (1991). Distribution patterns of different forms of phosphorus in some surficial sediments of the Baltic Sea. *Chem. Geol.* 90, 91–106. doi: 10.1016/0009-2541(91)90036-Q

Carman, R., and Wulff, F. (1989). Adsorption capacity of phosphorus in Baltic Sea sediments. *Estuar. Coast. Shelf Sci.* 29, 447–456. doi: 10.1016/0272-7714(89)90079-6

Childers, D. L., Corman, J., Edwards, M., and Elser, J. J. (2011). Sustainability challenges of phosphorus and food: solutions from closing the human phosphorus cycle. *Bioscience* 61, 117–124. doi: 10.1525/bio.2011.61.2.6

Civan, A., Worrall, F., Jarvie, H. P., Howden, N. J. K., and Burt, T. P. (2018). Forty-year trends in the flux and concentration of phosphorus in British rivers. *J. Hydrol.* 558, 314–327. doi: 10.1016/j.jhydrol.2018.01.046

Conley, D. J., and Johnstone, R. W. (1995). Biogeochemistry of N, P and Si in Baltic Sea sediments: response to a simulated deposition of a spring bloom. *Mar. Ecol. Prog. Ser.* 122, 265–276. doi: 10.3354/meps122265

Cornell, R. M., and Schwertmann, U. (2004). *The Iron Oxides: Structure, Properties, Reactions, Occurences and Uses*, 2nd Edn. Weinheim: Wiley-VCH, doi: 10.1002/3527602097

Davey, J. T., and Watson, P. G. (1995). The activity of *Nereis diversicolor* (Polychaeta) and its impact on nutrient fluxes in estuarine waters. *Ophelia* 41, 57–70. doi: 10.1080/00785236.1995.10422037

Dijkstra, N., Slomp, C. P., and Behrends, T. (2016). Vivianite is a key sink for phosphorus in sediments of the Landsort Deep, an intermittently anoxic deep basin in the Baltic Sea. *Chem. Geol.* 438, 58–72. doi: 10.1016/j.chemgeo.2016.05.025

Duarte, C. M., Conley, D. J., Carstensen, J., and Sanchez-Camacho, M. (2009). Return to neverland: shifting baselines affect eutrophication restoration targets. *Estuaries Coast.* 32, 29–36. doi: 10.1007/s12237-008-9111-2

Faas, R., and Wartel, S. (2006). Rheological properties of sediment suspensions from eckernförde and kieler förde bays, western Baltic Sea. *Int. J. Sediment. Res.* 21, 24–41.

Fink, J. R., Inda, A. V., Tiecher, T., and Barrón, V. (2016). Iron oxides and organic matter on soil phosphorus availability. *Ciênc. Agrotecnol.* 40, 369–379. doi: 10.1590/1413-70542016404023016

Finkel, Z. V., Beardall, J., Flynn, K. J., Quigg, A., Rees, T. A. V., and Raven, J. A. (2010). Phytoplankton in a changing world: cell size and elemental stoichiometry. *J. Plankton Res.* 32, 119–137. doi: 10.1093/plankt/fbp098

Friebele, E. S., Correll, D. L., and Faust, M. A. (1978). Relationship between phytoplankton cell size and the rate of orthophosphate uptake: in situ observations of an estuarine population. *Mar. Biol.* 45, 39–52. doi: 10.1007/BF00388976

Gunduz, B., Aydin, F., Aydin, I., and Hamamci, C. (2011). Study of phosphorus distribution in coastal surface sediment by sequential extraction procedure (NE Mediterranean Sea, Antalya-Turkey). *Microchem. J.* 98, 72–76. doi: 10.1016/j.microc.2010.11.006

Gunnars, A., Blomqvist, S., Johansson, P., and Andersson, C. (2002). Formation of Fe (III) oxyhydroxide colloids in freshwater and brackish seawater, with incorporation of phosphate and calcium. *Geochim. Cosmochim. Acta* 66, 745–758. doi: 10.1016/S0016-7037(01)00818-3

Gustafsson, B. G., Schenk, F., Blenckner, T., Eilola, K., Meier, H. E. M., Müller-Karulis, B., et al. (2012). Reconstructing the development of baltic sea eutrophication 1850-2006. *Ambio* 41, 534–548. doi: 10.1007/s13280-012-0318-x

Gypser, S., Hirsch, F., Schleicher, A. M., and Freese, D. (2017). Impact of crystalline and amorphous iron- and aluminum hydroxides on mechanisms of phosphate adsorption and desorption. *J. Environ. Sci.* 70, 175–189. doi: 10.1016/j.jes.2017.12.001

Håkanson, L. (1977). The influence of wind, fetch, and water depth on the distribution of sediments in Lake Vänern. Sweden. *Can. J. Earth Sci.* 14, 397–412. doi: 10.1139/e77-040

Hansen, H. P., and Koroleff, F. (1999). "Determination of nutrients," in *Methods of Seawater analysis*, eds K. Grasshoff, K. Kremling, and M. Ehrhardt (Weinheim: Wiley-VCH), 159–251. doi: 10.1002/9783527613984.ch10

Heathwaite, A. L. (1994). Chemical fractionation of lake sediments to determine the effects of land-use change on nutrient loading. *J. Hydrol.* 159, 395–421. doi: 10.1016/0022-1694(94)90269-0

Hedman, J. E., Gunnarsson, J. S., Samuelsson, G., and Gilbert, F. (2011). Particle reworking and solute transport by the sediment-living polychaetes Marenzelleria neglecta and *Hediste diversicolor*. *J. Exp. Mar. Bio. Ecol.* 407, 294–301. doi: 10.1016/j.jembe.2011.06.026

HELCOM. (2018). Sources and pathways of nutrients to the Baltic Sea. *Balt. Sea Environ. Proc.* 153:48.

Jensen, H. S., Mortensen, P. B., Andersen, F. O., Rasmussen, E., and Jensen, A. (1995). Phosphorus cycling in a coastal marine sediment, Aarhus Bay, Denmark. *Limnol. Oceanogr.* 40, 908–917. doi: 10.4319/lo.1995.40.5.0908

Karstens, S., Buczko, U., Jurasinski, G., Peticzka, R., and Glatzel, S. (2016). Impact of adjacent land use on coastal wetland sediments. *Sci. Total Environ.* 550, 337–348. doi: 10.1016/j.scitotenv.2016.01.079

Knee, K. L., and Paytan, A. (2012). *Submarine Groundwater Discharge: A Source of Nutrients, Metals, and Pollutants to the Coastal Ocean*. New York, NY: Elsevier, doi: 10.1016/B978-0-12-374711-2.00410-1

Koch, M., Kruse, J., Eichler-Löbermann, B., Zimmer, D., Willbold, S., Leinweber, P., et al. (2018). Phosphorus stocks and speciation in soil profiles of a long-term fertilizer experiment: evidence from sequential fractionation, P K-edge XANES, and31P NMR spectroscopy. *Geoderma* 316, 115–126. doi: 10.1016/j.geoderma.2017.12.003

Köster, M., and Meyer-Reil, L. A. (2001). Characterization of carbon and microbial biomass pools in shallow water coastal sediments of the southern Baltic Sea (Nordrügensche Bodden). *Mar. Ecol. Prog. Ser.* 214, 25–41. doi: 10.3354/meps214025

Kraal, P., Burton, E. D., Rose, A. L., Cheetham, M. D., Bush, R. T., and Sullivan, L. A. (2013). Decoupling between water column oxygenation and benthic

phosphate dynamics in a shallow eutrophic estuary. *Environ. Sci. Technol.* 47, 3114–3121. doi: 10.1021/es304868t

Lampe, R., Baudler, H., Schumann, R., and Buckmann, K. (2013). *Restaurierung der Darß-Zingster Boddenkette (DZBK) – Bilanzierung des Wasser- und Detritusaustausches in der DZBK*. Greifswald: University of Greifswald.

Lehtoranta, J. (2003). Dynamics of sediment phosphorus in the brackish Gulf of Finland. *Monogr. Boreal Environ. Res.* 24, 5–58.

Lehtoranta, J., and Pitkänen, H. (2003). Binding of phosphate in sediment accumulation areas of the eastern Gulf of Finland. Baltic Sea. *Hydrobiologia* 492, 55–67. doi: 10.1023/A:1024869929510

Leipe, T., Naumann, M., Tauber, F., Radtke, H., Friedland, R., Hiller, A., et al. (2017). Regional distribution patterns of chemical parameters in surface sediments of the south-western Baltic Sea and their possible causes. *Geomarine Lett.* 37, 593–606. doi: 10.1007/s00367-017-0514-6

Leipe, T., Tauber, F., and Vallius, H. (2011). Particulate organic carbon (POC) in surface sediments of the Baltic Sea. *Geomarine Lett.* 31, 175–188. doi: 10.1007/s00367-010-0223-x

Leipe, T., Tauber, F., Vallius, H., Virtasalo, J., Uścinowicz, S., Kowalski, N., et al. (2010). Particulate organic carbon (POC) in surface sediments of the Baltic Sea. *Geomarine Lett.* 31, 175–188.

Liu, Y., Villalba, G., Ayres, R. U., and Schroder, H. (2008). Global phosphorus flows and environmental impacts from a consumption perspective. *J. Ind. Ecol.* 12, 229–247. doi: 10.1111/j.1530-9290.2008.00025.x

Lu, C., and Tian, H. (2017). Global nitrogen and phosphorus fertilizer use for agriculture production in the past half century: shifted hot spots and nutrient imbalance. *Earth Syst. Sci. Data* 9, 181–192. doi: 10.5194/essd-9-181-2017

LUNG (2013). *Development and Status of Nutrient Loads in the Coastal Water Bodies of Mecklenburg-Vorpommern*. Güstrow: Berichte zur Gewässergüte.

McComb, A. J., Qiu, S., Lukatelich, R. J., and McAuliffe, T. F. (1998). Spatial and temporal heterogeinity of sediment phosphorus in the Peel-Harvey estuarine system. *Estuar. Coast. Shelf Sci.* 47, 561–577. doi: 10.1006/ecss.1998.0389

Nausch, G. (1981). Die Sedimente der Darß-Zingster Boddengewässer - Zustandsanalyse und Stellung im Phosphorkreislauf. DissOnline Universität Rostock.

Nausch, G., Bachor, A., Petenati, T., Voss, J., and Von Weber, M. (2011). Nutrients in the German coastal waters of the Baltic Sea and adjacent areas (in German). *Meeresumwelt Aktuell Nord und Ostsee* 2011, 1–16.

Nausch, G., and Schlungbaum, G. (1984). Sedimentchemische Untersuchungen in Küstengewässern der Deutschen Demokratischen Republik Teil 17. Spezielle Untersuchungen zur Dynamik der Oberflächensedimente eines flachen Boddengewässers (Barther Bodden). *Acta Hydrochim. Hydrobiol.* 12, 61–72. doi: 10.1002/aheh.19840120112

Nilsson, S. (2006). *International River Basins in the Baltic Sea Region. Report of the BSR INTERREG III B Programme*. Available at: http://www.baltex-research.eu/material/downloads/riverbasins.pdf [accessed April 15, 2017].

Pitkänen, H., Lehtoranta, J., and Räike, A. (2001). Internal nutrient fluxes counteract decreases in external load: the case of the estuarial Eastern Gulf of Finland, Baltic Sea. *Ambio* 30, 195–201. doi: 10.1579/0044-7447-30.4.195

Puttonen, I., Mattila, J., Jonsson, P., Karlsson, O. M., Kohonen, T., Kotilainen, A., et al. (2014). Distribution and estimated release of sediment phosphorus in the northern Baltic Sea archipelagos. *Estuar. Coast. Shelf Sci.* 145, 9–21. doi: 10.1016/j.ecss.2014.04.010

Renz, J. R., and Forster, S. (2014). Effects of bioirrigation by the three sibling species of Marenzelleria spp. on solute fluxes and porewater nutrient profiles. *Mar. Ecol. Prog. Ser.* 505, 145–159. doi: 10.3354/meps10756

Ruttenberg, K. C. (2003). "The Global Phosphorus Cycle," in *Treatise on Geochemistry*, eds H. D. Holland and K. K. Turekian (Oxford: Pergamon), 585–643. doi: 10.1016/B0-08-043751-6/08153-6

Sas, H. (1989). "The relation between inlake-P concentration and algal biomass indicators (subsystem 2)," in *Lake Restoration by Reduction of Nutrient Loading: Expectations, Experiences, Extrapolations*, eds H. Sas, J. Ahlgren, H. Bernhardt, B. Boström, J. Clasen, and C. Forsberg (Sankt Augustin: RicharzAcademia Verlag), 102–148.

Schiewer, U. (2007). "Darß-Zingst Boddens, Northern Rügener Boddens and Schlei," in *Ecology of Baltic Coastal Waters*, eds U. Schiewer, M. M. Caldwell, G. Heldmaier, R. B. Jackson, O. L. Lange, and H. A. Mooney (Berlin: Springer), 35–86.

Schlungbaum, G. (1982). Sedimentchemische Untersuchungen in den Küstengewässern der DDR. *Teil* 10: Die Rolle der Stoffaustauschprozesse an der Sediment/Wasser-Kontaktzone eutropher Flachgewässer und Möglichkeiten zur Untersuchung am Beispiel des Phosphatkreislaufes — ein Überblick am Beispiel der Darß-Zingster Boddenkette. 10, 119–134. doi: 10.1002/aheh.19820100204

Schlungbaum, G., Nausch, G., and Baudler, H. (1994). Sedimentstruktur und Sedimentdynamik in den Darß-Zingster Boddengewässern. *Rostock. Meeresbolog. Beitr.* 2, 27–40.

Schröder, J. J., Cordell, D., Smit, A. L., and Rosemarin, A. (2010). *Sustainable use of phosphorus. Wageningen*. Available at: http://ec.europa.eu/environment/natres/pdf/phosphorus/sustainable_use_phosphorus.pdf

Smil, V. (2000). Phosphorus in the environment: natural flows and human interferences. *Annu. Rev. Energy Environ.* 25, 53–88. doi: 10.1146/annurev.energy.25.1.53

Søndergaard, M., Kristensen, P., and Jeppesen, E. (1992). Phosphorus release from resuspended sediment in the shallow and wind-exposed Lake Arresø, Denmark. *Hydrobiologia* 228, 91–99. doi: 10.1007/BF00006480

Taft, J. L., Taylor, W. R., and McCarthy, J. J. (1975). Uptake and release of phosphorus by phytoplankton in the Chesapeake Bay estuary, USA. *Mar. Biol.* 33, 21–32. doi: 10.1007/BF00394997

Tiemeyer, B., Kahle, P., and Lennartz, B. (2009). Phosphorus losses from an artificially drained rural lowland catchment in North-Eastern Germany. *Agric. Water Manag.* 96, 677–690. doi: 10.1016/j.agwat.2008.10.004

Vahtera, E., Conley, D. J., Gustafsson, B. G., Kuosa, H., Pitkänen, H., Savchuk, O. P., et al. (2007). Internal ecosystem feedbacks enhance nitrogen-fixing cyanobacteria blooms and complicate management in the Baltic Sea. *Ambio J. Hum. Environ.* 36, 186–194. doi: 10.1579/0044-7447(2007)36[186:IEFENC]2.0.CO;2

van Dijk, K. C., Lesschen, J. P., and Oenema, O. (2016). Phosphorus flows and balances of the European Union Member States. *Sci. Total Environ.* 542, 1078–1093. doi: 10.1016/j.scitotenv.2015.08.048

Van Vuuren, D. P., Bouwman, A. F., and Beusen, A. H. W. (2010). Phosphorus demand for the 1970-2100 period: a scenario analysis of resource depletion. *Glob. Environ. Chang.* 20, 428–439. doi: 10.1016/j.gloenvcha.2010.04.004

Verstraeten, G., and Poesen, J. (2001). Variability of dry sediment bulk density between and within retention ponds and its impact on the calculation of sediment yields. *Earth Surf. Process. Landf.* 26, 375–394. doi: 10.1002/esp.186

Yan, Z., Han, W., Peñuelas, J., Sardans, J., Elser, J. J., Du, E., et al. (2016). Phosphorus accumulates faster than nitrogen globally in freshwater ecosystems under anthropogenic impacts. *Ecol. Lett.* 19, 1237–1246. doi: 10.1111/ele.12658

Zettler, M. L. (1996). Successful establishment of the spionid polychaete. *Arch. Fish. Mar. Res.* 43, 273–284.

Zettler, M. L. (1997). Population dynamics, growth and production of the neozoon Marenzelleria cf. viridis (Verrill, 1873) (Polychaeta: Spionidae) in a coastal water of the southern Baltic Sea. *Aquat. Ecol.* 31, 177–186. doi: 10.1023/A:1009903521182

Zimmer, D., Kahle, P., and Baum, C. (2016). Loss of soil phosphorus by tile drains during storm events. *Agric. Water Manag.* 167, 21–28. doi: 10.1016/j.agwat.2015.12.017

Conflict of Interest Statement: The authors declare that the research was conducted in the absence of any commercial or financial relationships that could be construed as a potential conflict of interest.

Copyright © 2018 Berthold, Zimmer, Reiff and Schumann. This is an open-access article distributed under the terms of the Creative Commons Attribution License (CC BY). The use, distribution or reproduction in other forums is permitted, provided the original author(s) and the copyright owner(s) are credited and that the original publication in this journal is cited, in accordance with accepted academic practice. No use, distribution or reproduction is permitted which does not comply with these terms.

frontiers in Marine Science

ORIGINAL RESEARCH
published: 08 November 2018
doi: 10.3389/fmars.2018.00413

Solute Reservoirs Reflect Variability of Early Diagenetic Processes in Temperate Brackish Surface Sediments

Marko Lipka[1], Jana Woelfel[2], Mayya Gogina[3], Jens Kallmeyer[4], Bo Liu[1†], Claudia Morys[5], Stefan Forster[6] and Michael E. Böttcher[1]**

[1] Geochemistry and Stable Isotope Biogeochemistry Group, Marine Geology, Leibniz Institute for Baltic Sea Research (LG), Warnemünde, Germany, [2] Trace Gas Biogeochemistry, Marine Chemistry, Leibniz Institute for Baltic Sea Research (LG), Warnemünde, Germany, [3] Benthology, Biological Oceanography, Leibniz Institute for Baltic Sea Research (LG), Warnemünde, Germany, [4] Section 5.3 Geomicrobiology, Helmholtz Center Potsdam German Geophysical Research Center (GFZ), Helmholtz Association of German Research Centers (HZ), Potsdam, Germany, [5] Estuarine and Delta Systems, Royal Netherlands Institute for Sea Research (NIOZ), Den Burg, Netherlands, [6] Institute for Biosciences - Marine Biology, University of Rostock, Rostock, Germany

Coastal marine sediments are a hotspot of organic matter degradation. Mineralization products of early diagenetic processes accumulate in the pore waters of the sediment, are subject of biological uptake and secondary biogeochemical processes and are released back into the water column via advective and diffusive fluxes across the sediment-water interface. Seven representative sites in the shallow coastal area of the southern Baltic Sea (15–45 m water depth), ranging from permeable sands to fine grained muds, were investigated on a seasonal basis for their key mineralization processes as well as their solid phase and pore water composition to identify the drivers for the variability of early diagenetic processes in the different sediment types. The sandy sediments showed about one order of magnitude lower organic carbon contents compared to the muds, while oxygen uptake rates were similar in both sediment types. Significantly higher oxygen uptake rates were determined in two near-shore muddy sites than in a deeper coastal muddy basin, which is due to higher nutrient loads and the corresponding addition of fresh algal organic matter in the near-shore sites. Pore water concentration profiles in the studied sediments were usually characterized by a typical biogeochemical zonation with oxic, suboxic, and sulfidic zones. An up to 15 cm thick suboxic zone was sustained by downward transport of oxidized material in which dissolved iron and phosphate indicate an intensive reduction of reactive Fe with the release of adsorbed phosphorus. While the geochemical zonation was stable over time in the muds of the studied deeper basin, high variability was observed in the muds of a near-coastal bay probably mainly controlled by sediment mixing activities. The sediments can be characterized by essentially two factors based on their near-surface benthic solute reservoirs: (1) their organic matter mineralization and solute accumulation efficiency and (2) their redox-state. Benthic solute reservoirs in the pore waters of the top decimeter were generally higher in the muddy than in the sandy sediments as the

OPEN ACCESS

Edited by:
Elinor Andrén,
Södertörn University, Sweden

Reviewed by:
Boris Chubarenko,
P.P. Shirshov Institute of Oceanology (RAS), Russia
Björn Grüneberg,
Brandenburg University of Technology Cottbus-Senftenberg, Germany

***Correspondence:**
Marko Lipka
marko.lipka@posteo.de
Michael E. Böttcher
michael.boettcher@io-warnemuende.de

†Present Address:
Bo Liu,
Section Marine Geochemistry, Alfred Wegener Institute Helmholtz Center for Polar and Marine Research, Bremerhaven, Germany

Specialty section:
This article was submitted to Coastal Ocean Processes, a section of the journal Frontiers in Marine Science

Received: *30 April 2018*
Accepted: *17 October 2018*
Published: *08 November 2018*

Citation:
Lipka M, Woelfel J, Gogina M, Kallmeyer J, Liu B, Morys C, Forster S and Böttcher ME (2018) Solute Reservoirs Reflect Variability of Early Diagenetic Processes in Temperate Brackish Surface Sediments. Front. Mar. Sci. 5:413. doi: 10.3389/fmars.2018.00413

more permeable sands were prone to an intensive exchange between pore water and bottom water. The three studied muddy sites showed great dissimilarities with respect to their predominating redox-sensitive metabolites (dissolved iron, manganese, and sulfide). Surface-near advective transport like irrigation of permeable sands and rearrangement of cohesive muds had a particularly strong influence on early diagenetic processes in the studied sediments and were probably the most important cause for the spatiotemporal variability of their benthic solute reservoirs.

Keywords: Baltic Sea, pore water, benthic solute reservoirs, nutrients, sediment mixing, surface sediment, advective transport, early diagenesis

1. INTRODUCTION

Coastal seas constitute only about 1.7 % of the oceans surface area but provide around 18 % of total oceanic net primary production (Field, 1998). The seabeds serve as the main locations of modification and accumulation of particulate matter incorporated into the sediments on deposition (Rullkötter, 2006). Coastal sediments are inherently highly dynamic systems; they display highest sedimentation rates, are affected by waves or near-shore currents and beyond that continuously exposed to human interventions (Talley et al., 2011).

Mineralization of organic material is carried out by microorganisms using oxygen, nitrate, manganese/iron (oxyhydr)oxides, or sulfate as terminal electron acceptors (Froelich et al., 1979). Thermodynamically, oxygen is the most favorable terminal electron acceptor for microbial degradation of organic matter. Due to transport limitations and low saturation concentration of oxygen in sea water, its availability in marine sediments is often limited to the top millimeters to centimeters depending on sediment permeability, irrigation and bioturbation activity (Revsbech et al., 1980; Glud, 2008). Below the thin oxic zone, anaerobic bacteria use alternative electron acceptors to decompose organic matter. Sulfate reduction is the most important anaerobic degradation process in reduced marine sediments (Jørgensen, 1982; Howarth, 1984; Isaksen and Jørgensen, 1996). Highest sulfate reduction activities were observed in estuarine and shallow sea ecosystems, accounting for 20–40 % of the global sulfate reduction (Skyring, 1987). Microbial sulfate reduction is reported to contribute to the organic matter mineralization in continental shelf sediments by more than 50 % (Jørgensen, 1982; Canfield et al., 1993; Wang and Van Cappellen, 1996; Bowles et al., 2014).

Post-depositional processes, including the consumption of terminal electron acceptors, the release of mineralization products (dissolved inorganic carbon, nitrogen, and phosphorus) into the sedimentary interstitial waters, as well as subsequent reactions of produced metabolites (hydrogen sulfide, dissolved iron, and manganese) are reflected by the chemical composition of the solid phase and associated pore waters. Since marine organic matter is mainly composed of carbon, nitrogen, and phosphorus, its mineralization releases dissolved inorganic carbon, nitrogen, and phosphorus into the sediment pore waters. The dissolved substances in the pore water migrate upward and downward along concentration gradients via diffusion and other transport mechanisms. Non-diffusive transport processes like burrowing animals (bioturbation and bioirrigation), hydro-irrigation or anthropogenic influences (bottom trawling or ship anchors) effectively relocate particles and pore water in the surface sediments (Eggleton and Thomas, 2004; Kristensen et al., 2012). These processes, collectively referred to as "advective processes" in this study, transport organic matter and reactive metals into and pore water solutes out of the sediments (Huettel et al., 1996; Huettel and Rusch, 2000; Rusch and Huettel, 2000).

The pore water chemistry of marine sediments is largely influenced by the presence of iron and manganese minerals, which are widely distributed in the environment and common in marine sediments. These minerals are introduced into the marine system via rivers and over the air and play a major role as electron shuttle in suboxic processes, especially iron with its diverse binding forms in different oxidation states (Haese, 2006). Iron and manganese naturally occur in two oxidation states, reduced Mn(II) and Fe(II) (ferrous iron) and oxidized Mn(III/IV) and Fe(III) (ferric iron). Ferric iron phases are highly reactive toward sulfide. Sedimentary iron may also be associated with clay minerals, however, these iron phases are less reactive to microbial activity or reactivity toward hydrogen sulfide than iron (oxyhydr)oxides (Poulton et al., 2004). Also some sulfate reducing bacteria are known to contribute to Fe-reduction in coastal marine sediments (Lovley et al., 1993; Reyes et al., 2016). Thus, in reactive iron-rich layers (suboxic zone) dissolved sulfide is hardly present in pore waters although sulfate reduction occurs; instead dissolved iron accumulates in the suboxic zone (Canfield, 1989; van de Velde and Meysman, 2016). Therefore, the occurrence of dissolved Fe^{2+} in the pore waters marks the suboxic zone, which forms a buffer between the often very thin oxic and the sulfidic zone. This zone has ecosystematic relevance for benthic flora and fauna, which do not tolerate hydrogen sulfide (Wang and Chapman, 1999). Buried Mn-oxides can be reduced by Fe^{2+}, liberating Mn^{2+} into the interstitial waters (Postma and Appelo, 2000) and also ammonia oxidation by Mn-oxides was suggested (Hyacinthe et al., 2001). Mn^{2+} and Fe^{2+} in return can be reoxidized on contact with nitrate or oxygen. Schippers and Jørgensen (2001) discovered a mechanism of anoxic pyrite oxidation by MnO_2 via an Fe(II)/Fe(III)-shuttle, so that no direct contact between the two solid phases is required. Via this redox cascade, most of the produced sulfide is reoxidized by oxidizing agents like iron (oxyhydr)oxides, manganese oxides, nitrate, and finally oxygen (Aller and Rude, 1988; Canfield et al., 1993; Schippers and Jørgensen, 2002).

Consequently, the geochemical composition of the pore waters is determined by microbial organic matter mineralization, transport processes at the sediment-water interface and secondary reactions within the surface sediments. Multi-element pore water solute analysis allows for a detailed biogeochemical characterization of the studied sediments. Pore water concentration profiles are usually used to calculate diffusive solute fluxes across the sediment-water interface or to identify zones of biogeochemical transformations and estimate the transformation rates in the sediment. The accuracy of the result of such estimates highly depends on the depth resolution of the surveyed pore water concentration profiles, which is often limited due to methodological constraints. The conclusions that can be drawn from such calculations are correspondingly confined. In this study we derive a different parameter from pore water concentration profiles, the benthic solute reservoir. To our knowledge, a quantification of the benthic solute reservoirs, i.e. the accumulated amount of dissolved substances in the upper centimeters of the sediment, has not yet been used to characterize sediments regarding their early diagenetic processes. Near-surface benthic solute reservoirs are sum parameters for the characterization of porous sediments concerning biogeochemical reactions and transport processes. Unlike diffuse fluxes or transformation rates, the calculation of benthic solute reservoirs is robust even with lower sampling resolution and less dependent on the pore water concentration profile shape at the dynamic sediment-water interface , i.e., due to short-term changes in bottom waters. Instead, the multi-element benthic solute reservoirs directly reflect mineralization activity, subsequent biogeochemical reactions and transport processes in the considered depth interval.

This study aims to quantify the variability of solute reservoirs in the surface sediments of different sediment types of the southern Baltic Sea and to identify the reasons for the variability in the different early diagenetic processes in surface sediments, including organic matter mineralization, secondary biogeochemical reactions and transport processes.

Previous biogeochemical studies in the Baltic Sea have mostly concentrated on the deep anoxic basins, Gdansk Bay, and the Gulf of Finland. However, the southern Baltic Sea offers a gradient system, that allows to compare muds and sands under different salinity regimes and, as a consequence, differing benthic fauna. In addition to spatial variability, there are also great temporal dynamics in temperature, salinity, and oxygen availability in this shallow coastal area. Most studies on benthic ecosystem services lack such seasonal aspects. The Baltic Sea is also under great pressure from anthropogenic activity (e.g., nutrient input via rivers, shipping traffic). Potential environmental controlling factors responsible for spatial variability or temporal dynamics in the benthic solute reservoirs of the studied coastal surface sediments are discussed.

2. METHODS

2.1. Study Area

The study area is situated in the southern Baltic Sea region (**Figure 1**). This coastal region is characterized by shallow water depths (<50 m), diverse sediment conditions (grain size distribution and organic matter content) and a strong salinity gradient from west (~20) to east (~8). There are two recent sediment accumulation areas, the *Bay of Mecklenburg* and the *Arkona Basin*, with maximum water depths of 26 and 49 m, respectively. In the accumulation areas, about 90 % of the sediment dry weight are clastic components, organic matter makes up ~10 % of the dry weight (Leipe et al., 2011). The occurrence of sandy sediments in the southern Baltic Sea is concentrated along the coasts and in larger areas between the *Bay of Mecklenburg* and the *Arkona Basin* as well as on the *Oder Bank*, a wide flat east of Rügen island (**Figure 1**). The sandy sites are characterized by fine and medium sands (125–500 μm) and low organic carbon contents (<1 % of the dry weight; Leipe et al., 2011).

Seven study sites in the German Baltic Sea region were intensively studied (**Figure 1** and **Table 1**) on a seasonal basis during ten ship-based expeditions between July 2013 and March 2016 (R/V Alkor: 2014-03; R/V Elisabeth Mann Borgese: 2014-06, 2015-01, 2015-04, 2015-08, and 2016-03; R/V Poseidon: 2014-09; R/V Maria S. Merian: 2016-01; see **Supplementary Material** for a detailed list of cruise expeditions). The sites are representative of the major depositional environments. Major events of the year, namely spring- and autumn algal blooms, stagnation periods with bottom water hypoxia and winter dormancy were covered. Two sites within the *Bay of Mecklenburg* were sampled, M-M1 in the inner bay and M-M2 in the outer bay.

The sampling site M-A was situated in the deepest part of the basin inside the exclusion zone for shipping around a monitoring station (**Figure 1**).

Sandy sediments were investigated at two near-coastal sites (S-S and S-D) between the main accumulation areas and on the *Oder Bank* (S-O), a non-depositional sand flat northwest of the *Oder River* mouth (**Figure 1**). The *Oder Bank* sediments are very organic-poor, occasionally overlain by thin fluff (Emeis et al., 1998). A strong variability in sediment type and benthic communities is reported by Laima et al. (1999) for the *Oder Bank*.

An intermediate sediment type with low permeability (comparable to mud) and low organic matter contents (similar to the studied sandy substrates) was studied at the silty I-T site, situated in a shallow bay at the shoulder of northern Rügen. This site is affected by sediment rearrangement during storms (Laima et al., 2001).

2.2. Sediment Sampling

Up to eight parallel short sediment cores were collected with a multicorer in acrylic tubes of 60 cm length and 10 cm internal diameter. Special care was taken to discard sediment cores potentially disturbed during sample collection indicated by e.g., a lower lying or inclined sediment water interface and missing characteristic structures like ripples or macrozoobenthos induced structures in the surface sediments compared to the parallel cores.

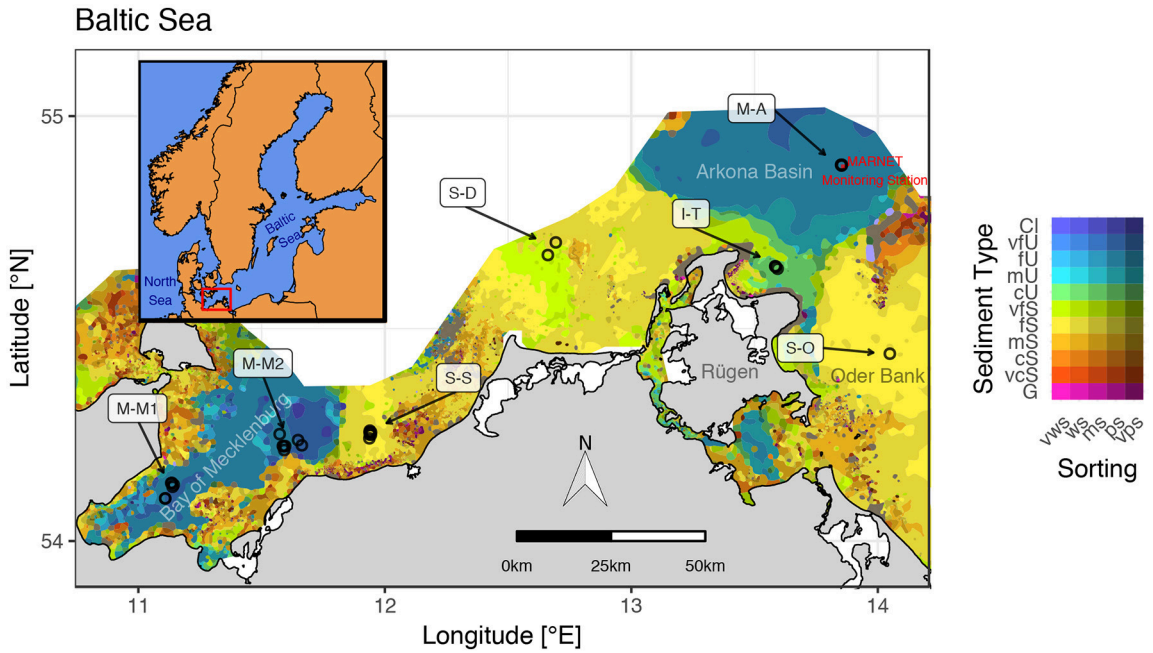


FIGURE 1 | Sampled sites and sediment type distribution in the southern Baltic Sea. Sediment distribution map is redrawn from Tauber (2014). Abbreviations in the legend follow the Wentworth classes: Cl, clay; U, silt; S, sand; G, gravel with graduations of very fine (vf), fine (f), medium (m), and coarse (c). Sediment sorting classes range from very well sorted (vws) over moderately sorted (ms) to very poorly sorted (vps). The red area in the *Arkona Basin* marks the 500 m exclusion zone around a BSH MARNET monitoring station.

TABLE 1 | Sampling sites, their sediment types and typical bottom water temperature, salinity and oxygen concentration investigated in the present study.

Site	Type	Lat. [°N]	Long. [°E]	Depth [m]	T [°C]	Sal	Oxygen [mL/L]
M-M1	Mud	54.1193	11.1336	24	4–14	18–23	1–7
M-M2	Mud	54.2284	11.6069	28	4–14	20–24	0–7
S-S	Sand	54.2531	11.9399	19	4–14	16–22	2–8
S-D	Sand	54.6879	12.6774	22	5–15	13–19	3–8
I-T	Silt	54.6448	13.5870	29	4–16	9–10	5–8
M-A	Mud	54.8848	13.8528	48	5–15	13–24	2–6
S-O	Sand	54.4401	14.0568	17	2–18	8–9	5–9

2.3. Sediment Solid Phase Analysis

Sediment surface chlorophyll *a* (ChlA) contents, a proxy for organic carbon export to the sediments, were analyzed in 6–18 parallel cores per site during four cruises in 2014-09, 2015-01, 2015-04, and 2015-08. According to the method described in Morys et al. (2016), sediment samples of the top 5 mm were extracted for chlorophyll with 96 % ethanol and the extracts were analyzed photometrically.

Sediment samples were retrieved from short cores in 1–2 cm slices. The outer 1 cm rim was immediately trimmed off each slice to avoid cross contamination from adjacent horizons. Sediment slices were transferred into plastic tubes and frozen at –20 °C immediately for subsequent laboratory analysis.

For the classification of the study sites into permeable and impermeable sediments, the dry bulk density (DBD) of the sediment samples was estimated from the water content (determined by weight loss upon vacuum freeze-drying) with the empirical relationship suggested by Flemming and Delafontaine (2000). Sediment porosity was calculated from the water content ($m_{wet} - m_{dry}$), the salt corrected sediment dry weight (m_{solid}) based on the methods suggested by Dadey et al. (1992), the DBD and the density of sea water (ρ):

$$\phi = \frac{V_{water}}{V_{total}} = \frac{m_{water}/\rho}{m_{solid}/DBD} = \frac{(m_{wet} - m_{dry}) \cdot DBD}{\rho \cdot m_{solid}}$$

Sediment permeability was directly measured on sub-cores using a falling head permeameter (Schaffer and Collins, 1966). Hydraulic conductivity, K, was derived from seven to ten consecutive readings of the falling head vs. time, averaged for each measurement (standard deviation ±3–20 % of the mean). Permeability (k) was calculated from hydraulic conductivity

measurements (K) with the following equation:

$$k = \frac{K \cdot \mu}{\rho \cdot g}$$

where μ is the dynamic viscosity, ρ density of sea water, and g the gravitational acceleration.

For a general characterization of the biogeochemical composition of sediments, freeze-dried sediment samples were analyzed for total carbon (TC), total nitrogen (TN), and total sulfur (TS) contents with a CHNS-O *Elemental Analyser EuroEA 3052* from *EuroVector*. Combustion was catalyzed by added *divanadium pentoxide*, the resulting gaseous products were chromatographically separated and measured via infrared spectrophotometry.

Total inorganic carbon (TIC) was determined with a *Macro-Elemental Analyser multi EA* (*Analytik Jena*) by transferring inorganic carbon with 40–50 % phosphoric acid into CO_2, which was then measured by infrared spectrophotometry.

Total organic carbon (TOC) contents were calculated from the difference of TIC and TC contents.

Sedimentary C, N, and S contents were corrected for salinity, compiled and provided by Dennis Bunke (available in Bunke et al., 2018).

Reactive iron (Fe^*) contents were analyzed on freeze dried sediment samples, extracted with 0.5 M HCl solution under constant gentle agitation for 1 h (Kostka and Luther, 1994). Filtered extracts (0.45 µm *Minisart* syringe filters) were analyzed either via photometric analysis (Stookey, 1970) or by inductively coupled plasma optical emission spectrometry (ICP-OES) analysis (*iCAP 6300 Duo Thermo Fisher Scientific*).

Precision and detection limits are given in the **Supplementary Material**.

2.4. Oxygen Uptake

Total oxygen uptake (TOU) is a proxy for the total mineralization activity of a sediment and was studied via *ex-situ* sediment core incubations monitoring oxygen concentrations in the overlying bottom waters. Intact short cores were incubated at constant temperature (5 or 10 °C, depending on ambient bottom water temperature) and under dark conditions for 5–10 d. The bottom water was slowly stirred via magnetic stirrers driven by a rotating magnet outside the core.

Bottom water oxygen concentrations were monitored in high resolution (sampling rate of < 60 s) using in-core attached optode spots with a FIBOX oxygen sensor spot system (*Presens*, Regensburg, Germany). Two-point sensor calibration was performed with aerated sea water (100 % atmospheric saturation) and sea water mixed with sodium dithionite (0 % oxygen). Linear oxygen decline ($R^2 > 0.85$, $p < 0.1$) during oxic (> 89 µM O_2) and hypoxic (< 89 µM O_2) incubation phases were used to calculate TOU rates in the respective incubation phases as follows:

$$TOU = -\frac{\Delta c(O_2)}{\Delta t} \cdot h$$

where $\frac{\Delta c(O_2)}{\Delta t}$ is the concentration gradient over time (slopes of linear model fits) and $h = V/A$ is the height of the water column overlying the sediment in the incubated core (with constant surface area of the core $A = 78.5\ cm^2$).

For an assessment of the influence of macrozoobenthos on the investigated processes, species abundance and biomass were determined after the incubation. Sediment cores were carefully washed on board through a 1 mm mesh sieve and the >1 mm fraction was stored in 4 % buffer formalin solution. Macrozoobenthos species were then sorted in the laboratory, identified at the highest possible taxonomic resolution (species level with the exception of genus *Phoronis* and family *Naididae*) following the World register of Marine Species (WoRMS), counted and weighted. Overall 30 taxa were recorded in 41 incubated cores. Species abundance and biomass was standardized to the area of 1 m^2.

2.4.1. Sulfate Reduction Activity

In order to determine the proportion of anaerobic processes in the total mineralization gross sulfate reduction rates (SRR) were analyzed by the ^{35}S radio-tracer injection technique (Jørgensen, 1978) in the laboratories of the German Research Centre for Geosciences (GFZ). Intact sediment short cores for the analysis were sampled during a summer (August 2015) and a winter (January 2016) campaign from sandy (S-S and S-O) and muddy (M-M1, M-M2, and M-A) sites and stored with supernatant water and head space of air at 4 °C until start of the experiments (November 2015 and February 2016). Rates of ^{35}S-sulfide formation were measured by incubation experiments with $^{35}SO_4^{2-}$ radio-labeled sediments after Fossing (1995) and Kallmeyer et al. (2004).

Sediment incubations were performed either in glass tubes (6 cm long and ~1 cm inner diameter, November 2015) or in sub-cores (3.5 cm inner diameter, February 2016). Transfer of sediment sub-samples into glass tubes was carried out in an inert gas (Ar) atmosphere two days before the start of the incubation experiments. Sub-sampling via sub-cores occurred right before the tracer injection with small liners having silicone-filled injection ports arranged vertically at 1 cm intervals down to 15 cm.

Volumes of 15 µL $^{35}SO_4^{2-}$ tracer solution (*Hartmann Analytic GmbH*, Braunschweig, Germany) with a specific activity of 2.6–5.2 kBq μL^{-1} were injected into each glass tube or injection port so that each sediment sub-sample or sub-core interval contained a radiotracer activity of about 39–78 kBq.

Sub-cores or glass tubes were incubated under dark conditions at near *in-situ* temperature (chosen on the basis of field measurements in the bottom water) for 8 h (at 10 °C in November 2015) or 14.5 h (at 4 °C in February 2016). The sediment sub-cores were sliced into 1 cm (upper 5 cm) or 2 cm (5–15 cm) sections after incubation. Sediment slices or contents of incubated glass tubes were immediately mixed with a 20 % ZnAc solution to fix sulfides and inhibit further sulfate reduction activity.

The cold chromium distillation procedure (Kallmeyer et al., 2004) was used to recover radio-labeled sulfide from the sediment. Radioactivity of ^{35}S was determined using a liquid scintillation counter (*Packard 2500 TR*) with a counting window of 4–167 keV.

2.5. Pore Water Sampling

Immediately after recovery of the sediment short cores, pore water samples were extruded from about 1, 2, 3, 4, 5, 7, 9, 11, 15, and 20 cm below as well as from bottom water right above the sediment-water interface through pre-drilled holes using Rhizons (Rhizosphere, Wageningen, The Netherlands; Seeberg-Elverfeldt et al., 2005) attached to clean syringes (Winde et al., 2014). About 10 mL pore water were extracted from each depth after discarding the first 1–2 mL. Additional filtering of the water samples was not necessary, as the Rhizon samplers consist of microporous tubes with a pore width of 0.2 μm. The water samples were transferred into different sample containers for later analysis: Without delay, 2 mL of pore water were fixed with 5 vol.% Zn-acetate solution for later analysis of sulfide concentration. Samples for major and trace element analysis were filled into pre-conditioned (with 2 % nitric acid) 2 mL sample tubes and acidified to 2 vol.% HNO_3 for conservation. Three milliliters Exetainers (pre-cleaned with 2 % nitric acid, subsequently washed with MilliQ water) prepared with 25 μL saturated mercury chloride solution were filled with no head space for later analysis of dissolved inorganic carbon (DIC).

2.6. Water Analysis

Dissolved Na, Si, S, Fe, Mn, and P in the water samples were analyzed with an ICP-OES (*iCAP 6300 Duo Thermo Fisher Scientific*). Water samples were diluted with 2 % HNO_3 to a target salinity of 3, 6, or 12 depending on the salinity of the samples, estimated from bottom water salinity (measured with a ship based CTD system, e.g., *911+*, *Sea-Bird Electronics*, USA). Measurements were validated with the certified seawater reference standards *CASS-5* or *SLEW-3* (*National Research Council of Canada*, Ottawa, Canada). An additional reference standard mixed with spike solution containing P, Fe, and Si was routinely used, since concentrations of these elements can be distinctly higher in pore water samples than in the reference material (Kowalski et al., 2013).

Dissolved ammonium (NH_4^+) concentrations were analyzed shipboard using standard photometric methods (Grasshoff et al., 2009) on a *QuAAtro* multianalyser system (*Seal Analytical*, Southampton, UK) within hours after sampling and checked with a multi-ion standard solution (*Bernd Kraft GmbH*, Duisburg, Germany; Winde et al., 2014).

Dissolved inorganic carbon (DIC) was measured by means of continuous-flow isotope-ratio-monitoring mass spectrometry (CF-irmMS) using a *Thermo Finnigan MAT 253* gas mass spectrometer coupled to a *Thermo Electron Gas Bench II* via a *Thermo Electron Conflo IV* interface. In an aliquot of the water samples, DIC was transferred to gaseous CO_2 by the manual injection of supersaturated phosphoric acid into *Exetainers* in a thermo-constant *Gas Bench*. Solutions were allowed to react for at least 18 h before introduction into the mass spectrometer (Winde et al., 2014). Aqueous $NaHCO_3$ solutions and solid carbonates were used for concentration calibration.

Dissolved sulfide concentrations in pore waters were determined in 5- to 100-fold diluted samples by the methylene blue technique (Cline, 1969) using a *Spekol 1100* spectrophotometer (*Analytik Jena*).

Precision, accuracy and detection limits of the analysis are given in the **Supplementary Material**.

2.7. Calculations and Statistics

Calculations and statistical analysis were conducted using R version 3.4.2 (R Core Team, 2016). Averages are given as mean ± one standard deviation. To test for statistical significance of the difference between means of group samples, *Bartlett's test* was used to check the homogeneity of variances, normality was checked with *Shapiro-Wilk test* on the *ANOVA* residuals. As *ANOVA* assumptions were not met, the *Kruskal–Wallis H test*, a non-parametric alternative to one-way *ANOVA*, and *Dunn's post-hoc test*, was performed. Unless otherwise stated, hypotheses were tested at a 0.05 level of significance.

Benthic solute reservoirs were calculated from the pore water concentration gradients of the respective solutes as the integrated concentration in the top 10 cm. This corresponds to the cumulated substance quantity in this layer. An integration depth of 10 cm was chosen to avoid the exclusion of some short sandy cores from the comparative analysis.

Principal component analysis (PCA) were performed on benthic solute reservoirs (DIC, H_2S, Fe^{2+}, Mn^{2+}, NH_4^+, PO_4, and H_4SiO_4). Data was zero-centered and scaled to unitary variance before the analysis.

3. RESULTS

3.1. Sediment Solid Phase

3.1.1. Porosity and Permeability

Sediment porosity in the southern Baltic Sea sampling sites was >80 % in muddy sites and ~40 % in sandy sites (**Figure 2**). Porosity profiles showed highest values at the sediment-water interface and decreased with depth due to compaction.

The sandy sites S-O and S-S display permeability values (k_i) of $10 \cdot 10^{-12}\ m^2$ and $4.2 \cdot 10^{-12}\ m^2$ respectively, while permeability in the muddy sites M-A, M-M1, and M-M2 was 2–3 orders of magnitude lower ($k_i = 4.5 \cdot 10^{-14}\ m^2$, $8.2 \cdot 10^{-14}\ m^2$, and $3.6 \cdot 10^{-14}\ m^2$, respectively). S-D and I-T were not analyzed for permeability, but they displayed porosity values (**Figure 2**) and grain size distributions (pers. comm. Dennis Bunke, IOW) comparable to the S-O and M-A sediments, respectively. Hence, the sandy sites S-S, S-D, and S-O can be classified as permeable while the muddy and silty sites M-M1, M-M2, M-A, and I-T must be considered impermeable.

3.1.2. Surface Sediment Chlorophyll

Chlorophyll *a* (ChlA) contents in the top 5 mm of the studied sediments, representing input of fresh organic matter to the sediments, ranged between 2 and 17 $\mu g\ cm^{-2}$ during four cruises between 2014-09 and 2015-08 capturing different seasons (**Figure 9**). Surface sediment ChlA contents were overall lowest at the sandy site S-O ($3.8 \pm 1.1\ \mu g\ cm^{-2}$), significantly higher in the M-A muds ($5.1 \pm 1.7\ \mu g\ cm^{-2}$) and S-S sands ($5.5 \pm 2.6\ \mu g\ cm^{-2}$) and highest at the muddy sites M-M1 ($10.3 \pm 3.5\ \mu g\ cm^{-2}$) and M-M2 ($9.4 \pm 3.0\ \mu g\ cm^{-2}$). The silty site I-T was only analyzed once during this study and

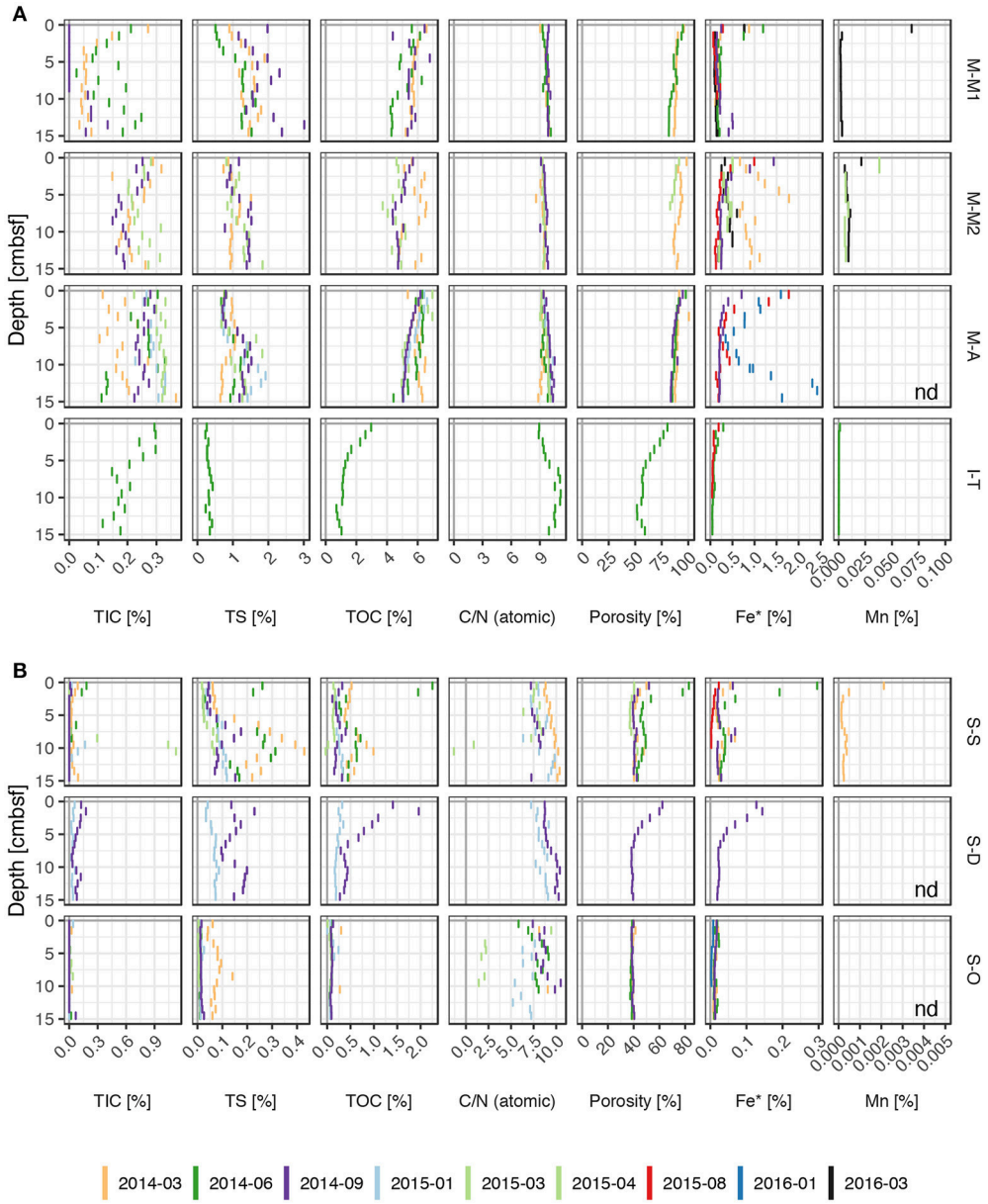


FIGURE 2 | Depth dependent dry mass content of sediment total inorganic carbon (TIC), total organic carbon (TOC), atomic TOC:TN ratio, reactive iron (Fe*), and acid extractable manganese (Mn) in **(A)** silty/muddy and **(B)** sandy sediments. Each bar represents one sediment sample, bar heights indicate the sampling interval. nd, not determined.

showed comparatively high ChlA contents (8.9 ± 0.6 μg cm^{-2}) statistically indistinguishable from the M-M1 and M-M2 muds.

3.1.3. Sediment Solid Phase Composition

Muddy sediments (M-M1, M-M2, and M-A) were statistically indistinguishable in their TIC, TS, and TOC contents of the top 15 cm, indicating a largely homogeneous geochemical composition. However, the muds were characterized by about an order of magnitude higher mean contents of TOC (5.5 ± 0.7 %) compared to the sandy sites (S-S, S-D, and S-O) with TOC contents of 0.3±0.3 % in the top 15 cm (**Figure 2**). The sandy sites occasionally showed surface peaks of more than 2 % (e.g., S-D in September 2014 and S-S in June 2014), indicating temporally or spatially variable input of organic matter. Sedimentary TOC/TN-ratios generally increased with depth, suggesting a preferred degradation of organic nitrogen compounds, thus depletion of N in the more refractory organic matter fraction.

The silty site I-T showed mud-like composition in the top parts of the sediments and a more sand-like composition at depth. Besides, the depth gradients of TOC and the TOC/TN-ratio were large compared to the other sites, indicating a non-steady-state during the single sampling occasion.

Reactive iron and manganese contents of up to approximately 2.5 and 0.07 %, respectively, were measured in the studied muds and about an order of magnitude lower contents were found in the organic-poor sands and silts (**Figure 2**). Fe^{*} and acid extractable Mn usually showed peak contents at the sediment surface exponentially decreasing with depth within the top 2–7 cm. Occasionally, another peak with contents above the background value occurred below. While pyrite does not belong to the still reactive iron fraction (Fe^{*}), as it is not dissolved during acid extraction, amorphous mono-sulfide (FeS) does (Haese, 2006). Fe-sulfides may additionally contribute to the reactive iron fraction due to reoxidation prior to extraction (Böttcher and Lepland, 2000).

3.2. Organic Matter Mineralization

3.2.1. Total Oxygen Uptake

Total oxygen uptake (TOU) is a measure of organic matter mineralization in sediments underlying oxygenated bottom water. The initial TOU rates of the studied sediments in the southern Baltic Sea ranged from 1.5 to 15.5 mmol m^{-2} d^{-1} (**Figure 3**). These rates are at the lower end of previously reported values in coastal muddy and sandy sediments, which vary widely from 4 to ~50 mmol m^{-2} d^{-1} (Jørgensen, 1977; Balzer, 1984; Jørgensen and Revsbech, 1989; Mackin and Swider, 1989; Jensen et al., 1995; Conley et al., 1997; Rysgaard et al., 2001; Janssen et al., 2005; Almroth et al., 2009; Bonaglia et al., 2014).

During summer, bottom water conditions were often already hypoxic or the transition to hypoxic situations occurred during the incubations. Considering only incubation phases with oxic bottom water conditions, average TOU were 5.1 ± 2.2 mmol m^{-2} d^{-1} and 4.9 ± 3.8 mmol m^{-2} d^{-1} in muddy and sandy sites, respectively (statistically not distinguishable). Within the studied muds, TOU in the sites M-M1 and M-M2 of the muddy *Bay of Mecklenburg* were significantly higher (7.3 ± 3.0 mmol m^{-2} d^{-1} and 5.9 ± 1.1 mmol m^{-2} d^{-1}, respectively) than in the muddy site M-A (3.6 ± 0.8 mmol m^{-2} d^{-1}). Oxygen uptake rates of the studied sandy sites S-S and S-O (3.8 ± 1.7 mmol m^{-2} d^{-1} and 5.3 ± 4.7 mmol m^{-2} d^{-1}, respectively) were statistically not distinguishable.

Exceptionally high infauna biomass was responsible for particularly high total oxygen uptake rates in one of the cores in April 2015 (**Figure 4**). The differences within the muds did not correlate with macrozoobenthos abundance or biomass, although very low bioturbation potential of the enclosed macrozoobenthos in the incubation cores of the site M-M1 prevailed. More details on benthic infauna and their influence on the biogeochemistry of the studied sediments can be found in Gogina et al. (in review) (this issue).

3.2.2. Gross Sulfate Reduction

The proportion of sulfate reduction, the most important anaerobic degradation process in reduced marine sediments, was investigated via gross sulfate reduction rate analysis in the studied sediments. The radio-tracer experiments revealed microbial sulfate reduction in all cores, muddy and sandy, with volumetric rates ranging from ~1 to ~100 nmol cm^{-3} d^{-1} (**Figure 5**). Sulfate reduction rates (SRR) of ~100 nmol cm^{-3} d^{-1} are typical for organic-rich, muddy sediments in eutrophic coastal environments, while much lower rates are usually found in continental slope and deep sea sediments (Canfield et al., 2005). The downward decreasing trend of SRR was not due to sulfate limitation but indicates exhaustion of labile organic pools with depth (Boudreau and Westrich, 1984) and a decrease in cell numbers of active sulfate reducing bacteria (Llobet-Brossa et al., 2002; Al-Raei et al., 2009). Sharp local maxima in the top mm below the sediment-water interface followed by a broad sulfate

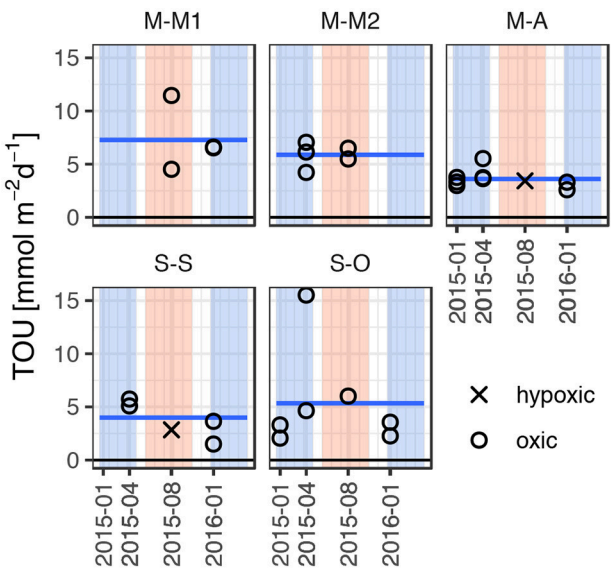


FIGURE 3 | Seasonal record of total oxygen uptake (TOU) rates in southern Baltic Sea sediments obtained via core incubation. Summer (June–October) and winter (January–April) season are highlighted by red and blue shaded areas, respectively. Horizontal blue lines represent the mean total oxygen uptake rate over all incubations for each site.

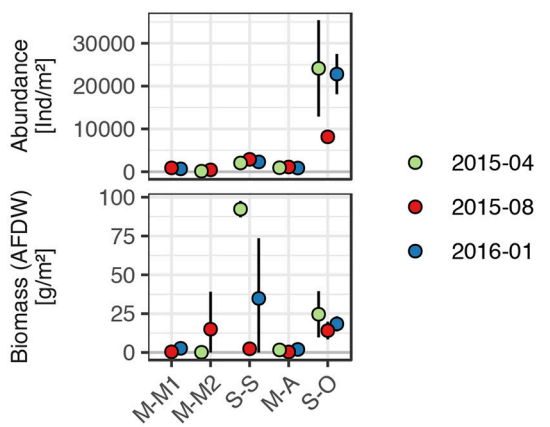


FIGURE 4 | Total macrozoobenthos abundance and biomass (ash free dry weight) in the incubated short cores. Points and errorbars represent means ± one standard deviation of 2 to 4 cores.

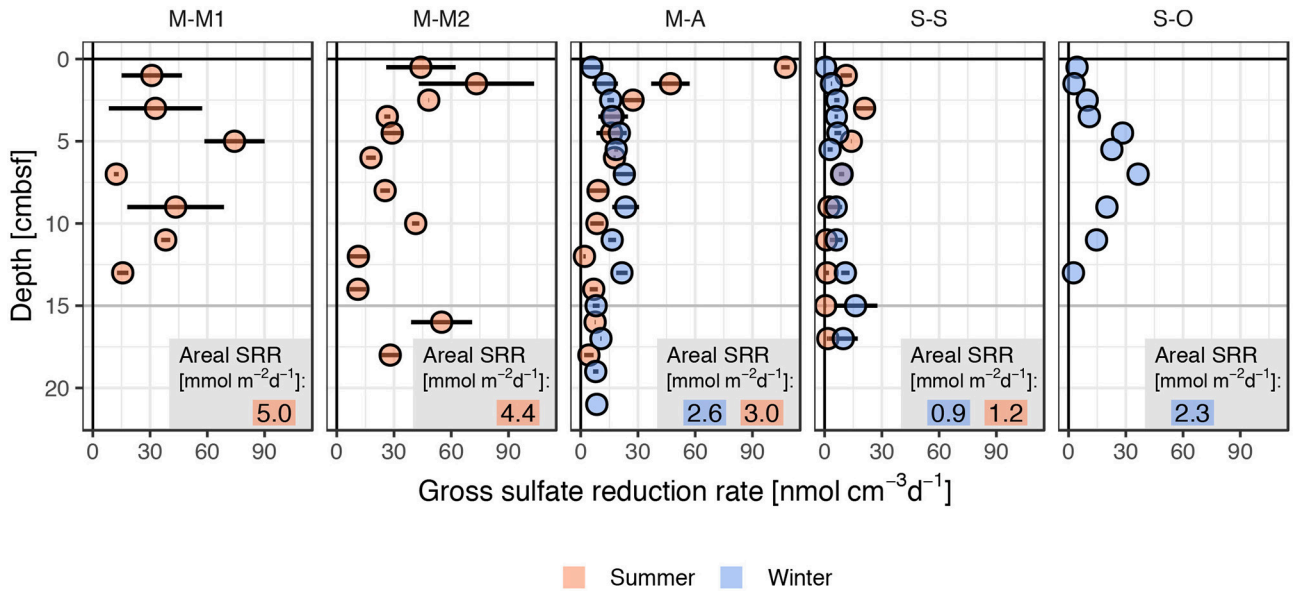


FIGURE 5 | Vertical distribution of sulfate reduction rates measured in muddy (M-A, M-M1, and M-M2) and sandy (S-S and S-O) study sites in summer and winter. Values are given as mean and range of two replicates except for S-O, where only one core was incubated. Areal SRR [*mmol* m^{-2} d^{-1}] are shown separately for summer and winter as depth-integrated sulfate reduction rates in the top 15 cm of the sediments.

reduction zone below are frequently reported in the literature (Moeslund et al., 1994; Kristensen, 2000; Sawicka et al., 2012).

Highest rates (~100 nmol cm^{-3} d^{-1}) at the surface of M-A muddy sediments during summer 2015 may be explained by increased organic matter supply from algal bloom detritus. M-M1 and M-M2 sediments, however, did not show a clear depth dependence in sulfate reduction but overall higher values in depths >5 cm compared to the site M-A.

Overall lowest values were measured in the sandy site S-S.

Depth integrated SRR in the top 15 cm measured during this study ranged from 0.9 to 5.0 mmol m^{-2} d^{-1} (**Figure 5**). These measures are in good agreement with average sulfate reduction rates for non-depositional (1.1 mmol m^{-2} d^{-1}) and depositional (4.7 mmol m^{-2} d^{-1}) shelf sediments compiled by Canfield et al. (2005). Thode-Andersen and Jørgensen (1989) reported integrated sulfate reduction rates (top 15 cm) in fine grained organic-rich coastal sediments (Aarhus Bay, Denmark) of 1.1–3.8 mmol m^{-2} d^{-1}, which matches the measured SRR at site M-A (2.6 and 3.0 mmol m^{-2} d^{-1}) but is distinctly lower than the values observed for the sites M-M1 and M-M2 (4.4 and 5.0 mmol m^{-2} d^{-1}; **Figure 5**). In the central deep basin of the Baltic Sea, the *Gotland Deep* with organic-rich silty sediments and usually anoxic bottom waters, depth integrated SRR (20 cm) of 4.8 mmol m^{-2} d^{-1} (Al-Raei & Böttcher, unpubl. results) and 3.8–7.6 mmol m^{-2} d^{-1} (Piker et al., 1998) were reported. These measures are comparable to southern Baltic Sea SRR found at muddy sites in this study. Considerably higher rates (13.5 mmol m^{-2} d^{-1} in top 20 cm) were observed in the *Landsort Deep* (Al-Raei et al. unpublished). Both sites are located in the deep basins with temporarily anoxic bottom waters and were anoxic at the time of sampling. Hence, sulfate reduction was most likely the dominating mineralization pathway here.

Werner et al. (2006) reported integrated SRR (top 15 cm) of ~2.2 mmol m^{-2} d^{-1} for the Janssand intertidal sand flat (Spiekeroog, North Sea, Germany), which is close to the value observed in the sandy S-O sediments during this study. In contrast, integrated sulfate reduction rates of 1.9–34 mmol m^{-2} d^{-1} were reported for the top 15 cm of temperate intertidal sediments in the German Wadden Sea of the southern North Sea (Böttcher et al., 2000; Kristensen, 2000). Al-Raei et al. (2009) reported seasonally dynamic integrated SRR in North Sea intertidal surface sediments (top 15 cm) ranging from ~6 – 30 mmol m^{-2} d^{-1} (mixed type sediments) to ~1 – 16 mmol m^{-2} d^{-1} (sands). Although obtained from a coastal sea in the same climate zone in sediments with similar TOC contents, these rates are considerably higher than those found in the Baltic Sea sediments during this study. In the compilation of sulfate reduction rates from different marine depositional settings (Canfield et al., 2005), intertidal sediments showed two to tenfold higher values compared to the listed shelf sediments.

3.3. Pore Water Profiles

The pore water concentration profiles (**Figure 6**) were consistent with the typical pore water zonation below mostly oxic bottom waters (Jørgensen and Kasten, 2006). Differences between the profile shapes of parallel cores are usually small compared to the temporal variability of the pore water profiles so that spatial homogeneity can be assumed within the individual sites. Most pronounced in muddy sediments (**Figure 6A**), pore water profiles in the top 20 cm were dominated by intense net sulfate reduction, indicated by decreasing SO_4^{2-} and increasing H_2S concentrations with increasing depth.

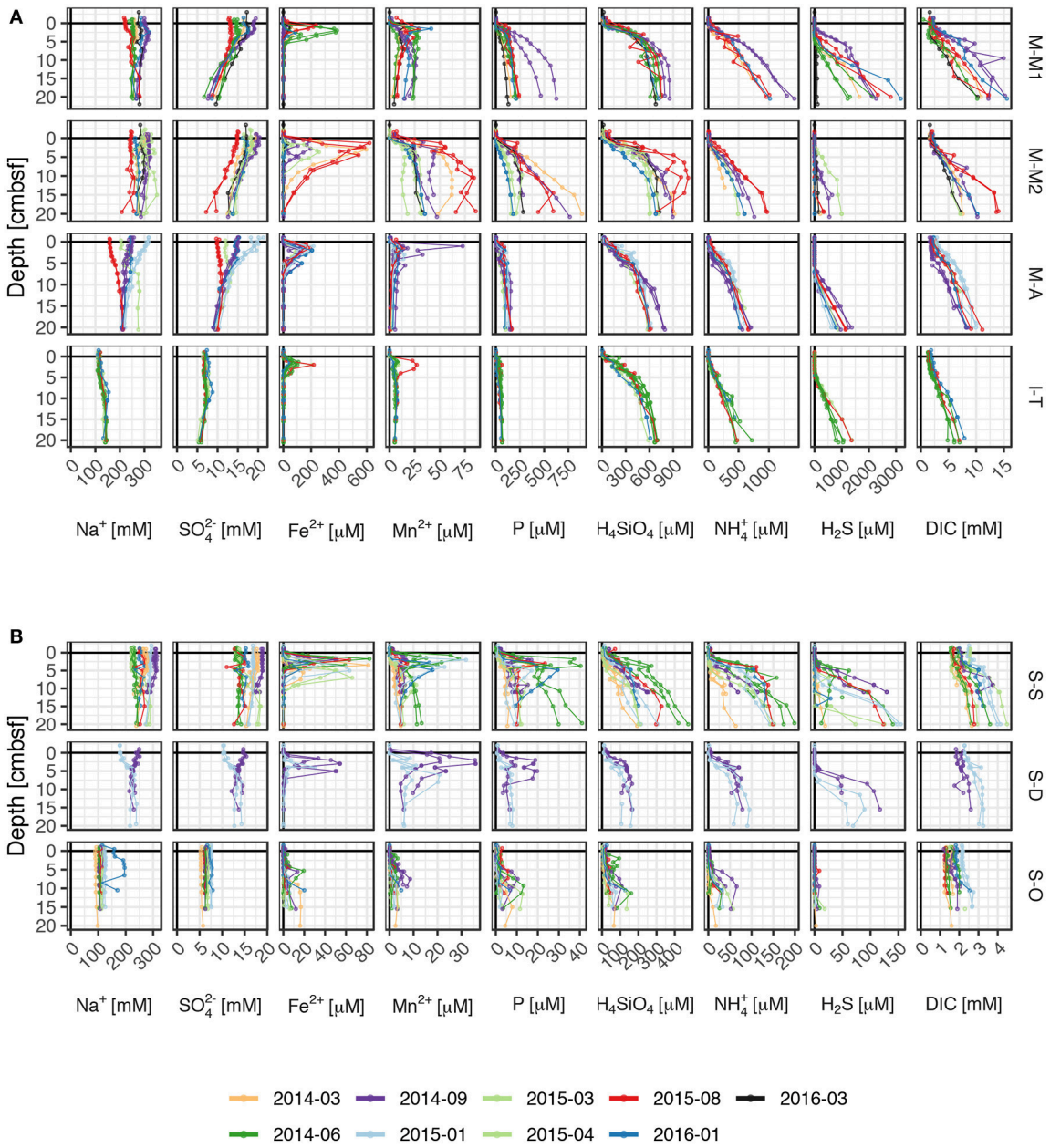


FIGURE 6 | Multi-parameter pore water concentration profiles in **(A)** soft sediments and **(B)** sandy sediments.

Active manganese and iron reduction were indicated by the presence of dissolved manganese (Mn^{2+}) and iron (Fe^{2+}) in the pore waters. The appearance of H_2S consistently coincided with Fe^{2+} depletion at depth. All organic matter mineralization processes released dissolved inorganic carbon (DIC, mainly HCO_3^- at pH 8), ammonium (NH_4^+) and phosphate (mainly as HPO_4^{2-} at pH 8) into the interstitial waters.

Orders of magnitude lower concentrations were found in sandy and organic-poor sediments (**Figure 6B**). No decrease in sulfate with depth and only low concentrations of dissolved sulfide (up to 150 µM) were found at depths >10 cm. Active manganese and iron reduction was indicated by increased Fe^{2+} and Mn^{2+} concentrations and also primary mineralization products (DIC, NH_4^+, H_4SiO_4, and PO_4) accumulated at depth to a lesser extent.

3.4. Benthic Solute Reservoirs

Especially the primary products of organic matter mineralization dissolved inorganic carbon (DIC), dissolved inorganic nitrogen (DIN, mainly NH_4^+), and dissolved inorganic phosphorus (DIP, mainly PO_4), accumulate in surface sediment interstitial waters

(**Figure 6**). Also sulfide (H_2S) concentrations were usually high in pore waters of the muddy sites, as sulfate reduction is an important process in the studied muds (**Figure 5**). Consequently, these solutes showed orders of magnitudes higher concentrations in the pore waters compared to the overlying water column, forming substantial solute reservoirs in the surface sediments (**Figure 7**). Benthic reservoirs of all considered solutes (H_4SiO_4, NH_4^+, PO_4, DIC, sulfide, Fe^{2+}, and Mn^{2+}) in the top 10 cm surface sediment were generally higher in studied muds than in the sandy study sites, while the silty site I-T showed intermediate values (**Figure 7**).

Benthic solute reservoirs were largest in the organic-rich and impermeable muds, smaller in the intermediate silt and close to zero in the sandy sediments (**Figure 7**). DIC formed by far the largest benthic solute reservoirs (about 450 mmol m^{-2} in the muds), followed by H_4SiO_4 and NH_4^+ (about 42 and 25 mmol m^{-2} in the muds; C:Si:N = 106:10:6). This is approximately in line with the Redfield-Brzezinski compositions of marine organic matter or diatoms, assuming that organic matter mineralization products are released into the pore waters with a ratio of C:Si:N:P = 106:15:16:1 (Redfield, 1958; Brzezinski, 1985). Smaller Si and N reservoirs compared to C in the pore waters may be attributed to limited solubility of biogenic silica and ammonium reoxidation via nitrification. Phosphate reservoirs, on the other hand, were on average 15 mmol m^{-2} in the muds (C:Si:N:P = 106:10:6:4). Due to a higher degradability of organic P and N components, these can be preferentially released relative to C during the initial stages of organic matter mineralization. In the long run, however, metabolites are often released in stoichiometric relation of the bulk composition of reactive organic matter (Burdige, 2006). High PO_4 reservoirs relative to DIC indicate the release of adsorbed P from reactive Fe phases rather than through mineralization of organic matter.

The redox-sensitive pore water constituents (sulfide, Fe^{2+}, and Mn^{2+}) only accumulate to considerable reservoirs in the fine-grained sediments.

A Principal Component Analysis (PCA) based on the benthic solute reservoirs (DIC, NH_4^+, PO_4, H_4SiO_4, sulfide, Fe^{2+}, and Mn^{2+}) of the studied sediments revealed that the first two principal components explain 89 % of the observed variance (**Figure 8B**) allowing for a virtually undistorted two-dimensional visualization of the dissimilarity between the study sites at different points in time (**Figure 8A**). Sandy sites clearly cluster on the left and muddy sites on the right hand side of the y-axis, while silt situates between these two clusters (**Figure 8A**). Variability, represented by the size of the spanned areas in **Figure 8A**, was highest in the muds and considerably smaller within the sandy sites. Strikingly, the individual sites are almost completely distinguishable in the PCA plot (**Figure 8A**). The results were practically independent of the chosen sediment depth over which the substance quantities were cumulated to benthic solute reservoirs (tested on values between 5 and 20 cm). Using benthic solute reservoirs of the top 15 cm as a basis for the PCA analysis (instead of 10 cm), the number of available data (especially from sandy sites) is reduced but results are generally very similar (see **Supplementary Material**).

4. DISCUSSION

4.1. Organic Matter Mineralization

Oxygen uptake of 5.0 ± 2.9 mmol m^{-2} d^{-1} and depth integrated (top 15 cm) gross sulfate reduction rates of 0.9–5.0 mmol m^{-2} d^{-1} indicate active organic matter mineralization with substantial contribution of sulfate reduction in the studied muddy and sandy sediments. The study sites differed primarily in their sediment type which is reflected most clearly in their varying permeability and organic matter contents. Organic matter content in sediments can be described as a reactive continuum, where rapid degradation of freshly deposited organic matter takes place near the sediment surface, while a large fraction of deeper buried organic matter is rather refractory (Berner, 1980). Sands have often been treated as generally unreactive sediments due to their lack of TOC and reactive substances. However, recent studies show that substantial mineralization of highly degradable organic matter occurs in sandy sediments while accumulation of aged material and mineralization products is prevented by advective transport processes (Boudreau et al., 2001; Huettel et al., 2014). Huettel and Gust (1992) and Ziebis et al. (1996) demonstrated strong advective pore water flushing down to several centimeters sediment depth caused by boundary layer flows over a rough sea floor. Such bedform-induced interfacial flows also lead to uptake of particulate organic matter into permeable shelf sediments (Huettel et al., 1996; Huettel and Rusch, 2000; Rusch and Huettel, 2000), which is the source of the reactive organic matter for mineralization processes. Occasionally increased TOC contents throughout the top 2–5 cm in the studied sandy sediments indicate such short-term incorporation of organic matter (**Figure 2**, e.g., S-S in 2014-06 or S-D in 2014-09).

Significantly increased TOU rates and SRR were measured in the *Bay of Mecklenburg* (M-M1 and M-M2) compared to the *Arkona Basin* (M-A), although TOC contents of the different muds were statistically indistinguishable (**Figure 2**). However, statistically significant higher ChlA contents were detected at the sediment surface of sites M-M1 and M-M2 (9.5 ± 3.1 μg cm^{-2} and 8.3 ± 3.3 μg cm^{-2}) than at site M-A (4.6 ± 1.7 μg cm^{-2}) during four cruises of this study (**Figure 9A**). There was also significant correlation between the oxygen uptake rates and the ChlA contents in the top 0.5 cm of the studied muds (**Figure 9B**). Consequently, differences in mineralization intensity between the studied muds were rather controlled by spatially varying input of readily degradable organic matter than by the standing TOC stock. This is in accordance with several studies after which the supply of labile organic material from the water column is a main factor controlling mineralization rates in sediments (Middelburg, 1989; Graf, 1992; Middelburg et al., 1993; Arndt et al., 2013).

4.2. Benthic Solute Reservoirs in Different Sediment Types

The PCA analysis of the benthic solute reservoirs revealed that the variability between the studied sediments can be expressed by

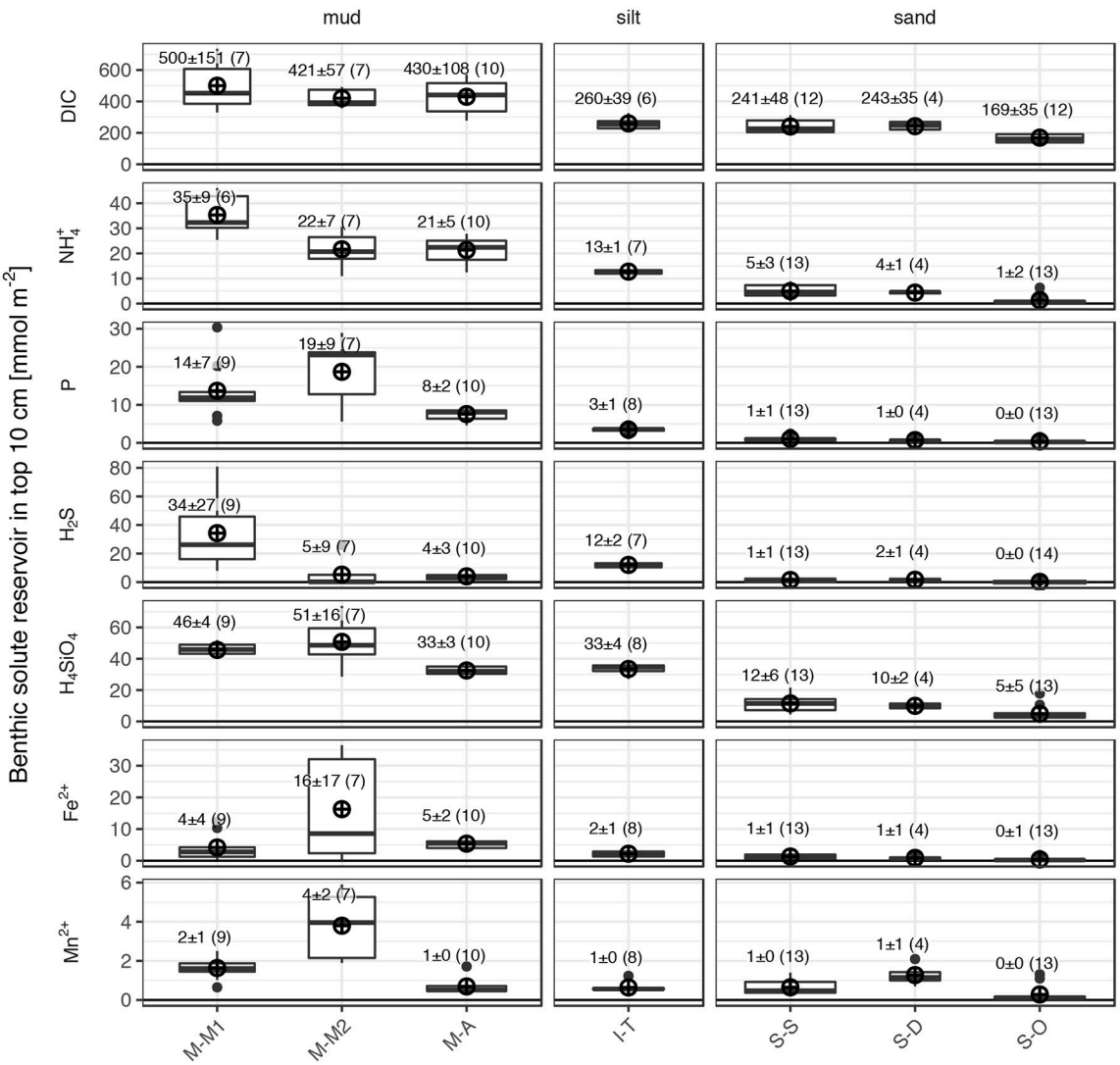


FIGURE 7 | Benthic solute reservoirs of the top 10 cm of the southern Baltic Sea sediments calculated from the pore water profiles shown in **Figure 6** and visualized by boxplots. Each boxplot summarizes the data from multiple pore water profiles for each site and parameter. The lower and upper hinges of the boxes correspond to the 25 and 75th percentiles, the line within the boxes represents the median. The whiskers extend from the hinges to the largest and smallest value inside the 1.5-fold inter-quartile range. Labeled ⊕ mark the arithmetic mean reservoir size of each subset (± one standard deviation, number of cores in brackets).

essentially two principal components. The principal component *PC1* alone explained 68 % of the variability (**Figure 8B**). All considered parameters substantially contributed to this component but the primary organic matter mineralization products DIC, NH_4^+, PO_4, and H_4SiO_4 dominate (**Figure 8C**). As similar rates of organic matter mineralization were observed in sand and mud, similar amounts of mineralization products must be released into the pore waters. The significantly smaller reservoirs in the studied sands therefore indicate the removal of mineralization products from the pore space back into the water column via advective transport processes. *PC1* can therefore be regarded as a factor representing the degree of organic matter mineralization and subsequent release of dissolved substances into the pore waters and the potential of the sediment to accumulate these solutes in form of benthic reservoirs. This mineralization and solute accumulation efficiency factor was above average in low-permeable and organic-rich muds and below average in the sands (**Figure 8A**).

Although substantial gross sulfate reduction (**Figure 5**) and oxygen uptake (**Figure 3**) rates were observed at site S-O, these sands showed the lowest benthic solute reservoirs of all studied sites (**Figure 7**), significantly lower than the other studied sands. Thus, the S-O sands were least accumulative for benthic solute reservoirs. This is in accordance with the comparatively highest porosity (**Figure 2**) and permeability values of the S-O sediments, which facilitates the exchange with the bottom water in the presence of advective processes. S-S and S-D clustered indistinguishably further right in the

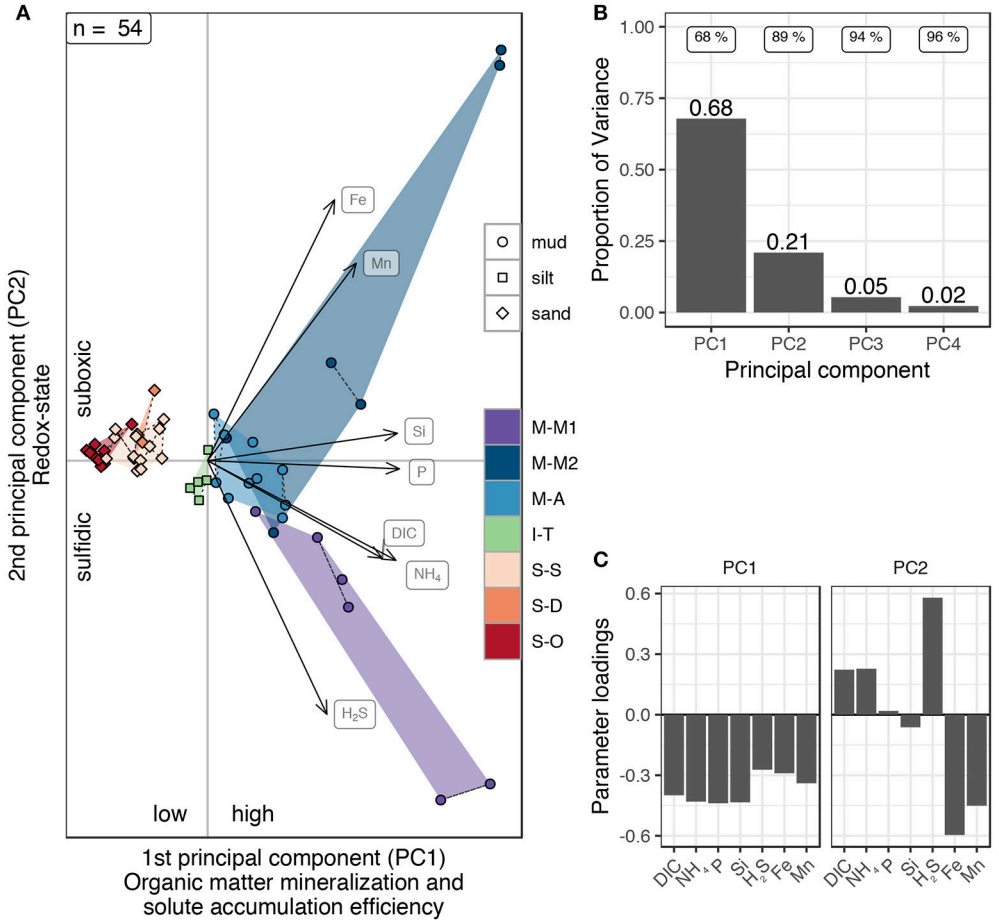


FIGURE 8 | Principal component analysis (PCA) of southern Baltic Sea benthic solute reservoirs in the top 10 cm. **(A)** Each dot represents the mean benthic solute reservoir of *DIC*, NH_4^+, PO_4, H_4SiO_4, sulfide, Fe^{2+}, and Mn^{2+} from parallel cores of each sampling campaign. Shaded areas envelop the expansion of variability of each study site in the two-dimensional space. Dashed lines connect points of the same sampling time. **(B)** Explained variance by different principal components. The first principal component alone explains 68 % and cumulative proportions of the first two principal components explain 89 % of the total variance. **(C)** Loadings of the major two components of the principal component analysis. All considered parameters substantially contribute to PC1. PC2 is loaded with the redox sensitive parameters dissolved sulfide (H_2S), Fe^{2+}, and Mn^{2+} (note the anticorrelation between H_2S and dissolved metals Fe^{2+} and Mn^{2+}) with minor contributions of *DIC* and NH_4^+.

PCA plot (**Figure 8A**), indicating a higher organic matter mineralization and/or solute accumulation potential. Since S-S clearly showed lower oxygen uptake rates (**Figure 3**) and gross sulfate reduction rates (**Figure 5**) compared to S-O sediments, these differences must be attributed to a higher benthic-pelagic solute exchange at the S-O sediment-water interface rather than lower mineralization activity. M-A muds and I-T silts situated in central positions on the x-axis of the PCA plot (**Figure 8A**), suggesting an average organic matter mineralization and/or solute accumulation potential. Although the I-T silt had intermediate TOC contents (**Figure 2**), ChlA contents were significantly higher in I-T than M-A sediments which might indicate higher mineralization rates at this site. Then, the comparatively low reservoirs would suggest a lowered solute accumulation potential than in the studied muds, especially the site M-A. However, since neither the permeability nor the mineralization rates were analyzed at site I-T, it remains unclear whether a different mineralization efficiency or solute accumulation potential of the silty sediment had the larger influence on the difference to the muds.

Further right in the PCA plot, the muddy M-M1 and M-M2 sediments spanned a wide range, indicating great temporal and/or spatial variability. The highest benthic reservoirs were stored in these organic-rich muds, which are impermeable, located in regions with rather calm deposition conditions and therefore less prone to pore water irrigation. M-M1 sediments showed significantly higher pore water sulfide reservoirs in the top 10 cm compared to the other studied muds, which can be partly explained with the comparatively high sulfate reduction rates at this site (**Figure 5**). The differences between the benthic solute reservoirs of the sites M-M1 and the M-M2 were highest and the reservoirs were overall largest during summer (the

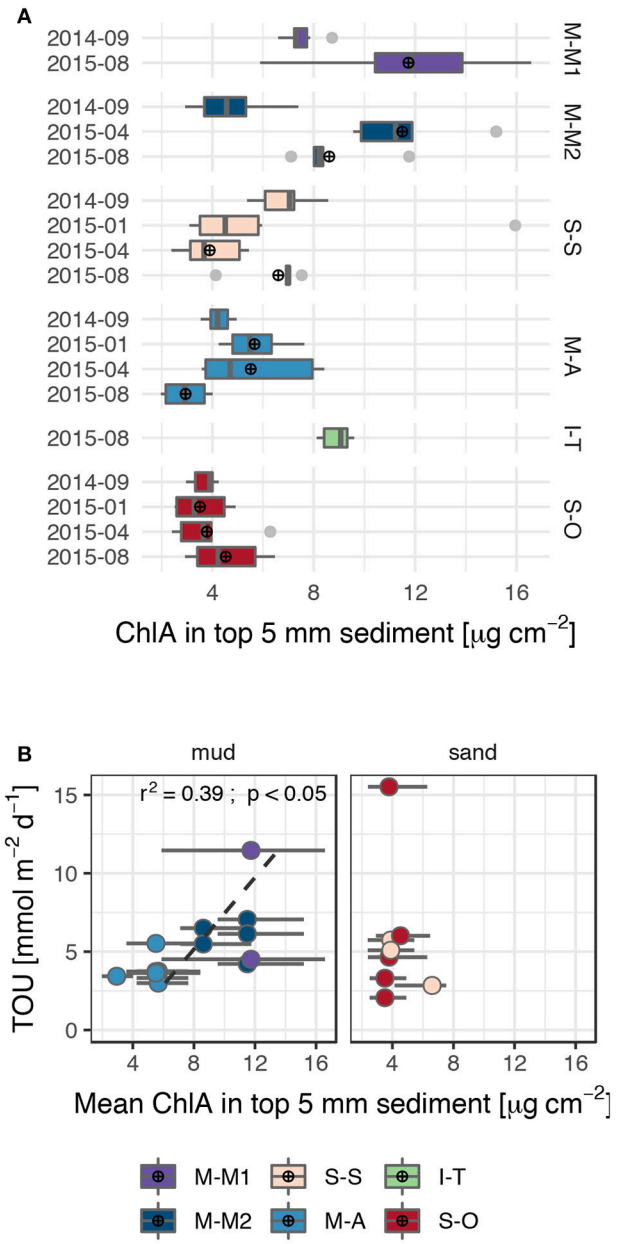


FIGURE 9 | (A) Chlorophyll *a* contents in the top 5 mm surface sediments. Each boxplot summarizes data from multiple sediment cores of one cruise. The left and right hinges of the boxes correspond to the 25 and 75th percentiles, the line within the boxes represents the median. The whiskers extend from the hinges to the largest and smallest value inside the 1.5-fold inter-quartile range. Arithmetic means of the groups used in **(B)** are marked by a ⊕. **(B)** Total oxygen uptake rates vs. mean chlorophyll *a* contents in the top 5 mm of the studied muddy and sandy sediments. Horizontal lines represent the range of values from which the arithmetic mean was calculated.

point pairs furthest to the right in **Figure 8A**). This was likely supported by the higher temperatures during summer in the comparatively shallow stations of the *Bay of Mecklenburg* and can therefore be regarded as seasonal effect.

The second principal component (*PC2*, **Figure 8A**) explained further 21 % of the variance (**Figure 8B**) and was mainly loaded with the redox sensitive parameters sulfide, Fe^{2+} and Mn^{2+} with minor contributions of DIC and NH_4^+ (**Figure 8C**). Negative correlation between sulfide and the reactive metals Fe and Mn was due to the close redox coupling between these elements. The existence of free Fe^{2+} and sulfide in the pore water are mutually exclusive, as the two species precipitate as FeS. Considerable reservoirs of Fe^{2+} and Mn^{2+} can only form by reduction of reactive metal (oxyhydr)oxides where these oxidized phases are frequently or continuously buried by sediment mixing processes, otherwise dissolved sulfide accumulates instead. The variability of near-surface reactive iron contents was likely controlled by particulate inputs from the water column, suggesting an intensive benthic-pelagic Fe turnover. The overall low contents of reactive iron and manganese in the top 10 cm sediments at site M-M1 compared to M-M2 and M-A (**Figure 2**) suggest that this location was decoupled from this cycling for example due to hydrodynamic reasons or hindered bioturbation. Morys et al. (2016) examined the same sites that are covered in this study and found lowest intensities of sediment mixing and also lowest macrozoobenthos abundance and biomass at the M-M1 site. Furthermore, overall highest ChlA contents and SRR values were detected in M-M1 sediments (**Figure 5**) which shifts the suboxic zone closer to the sediment-water interface and narrows it as well. Due to the lack of reaction partners for secondary redox-reactions below the suboxic zone, dissolved sulfide could accumulate in the interstitial waters to high concentrations, while the benthic solute reservoirs in the top 10 cm of the sites M-M2 and M-A were rather controlled by suboxic processes.

Therefore, by the second principal component, mainly the muddy sediments were further classified according to their predominating redox metabolites in the top 10 cm. Highest dissimilarities were evident between summer situations of the adjoining sites M-M1 (sulfidic) and M-M2 (suboxic).

The multi-parameter PCA analysis on the basis of southern Baltic Sea benthic solute reservoirs allowed to clearly differentiate between the studied sites and indicated wide disparities between the different sediment types but also within the studied muds, reflecting fundamental differences in sedimentation conditions, mineralization activity and mixing processes.

4.3. Environmental Control Factors

4.3.1. Bottom Water Salinity Oscillation

The southern Baltic Sea is highly affected by frequent salt water inflows from the North Sea so that the bottom water salinity is usually subject to temporal variability. The *Arkona Basin* is the deepest basin in the southern Baltic Sea study area, deep enough that regular storms do not affect the sediment surface, but shallow enough that seasonal temperature changes reach the bottom waters and also the surface sediments (Leipe et al., 2008). The salinity in the *Arkona Basin* is influenced by the freshwater inflows of the nearby entering *Oder River* as well as by salt water inflows from the North Sea. A stable stratification of the water column in the basin is the consequence of these water sources with different salinity. A major Baltic inflow event occurred at the end of 2014 (Mohrholz et al., 2015) and the resulting

bottom water salinity changes were recorded at the monitoring station *MARNET Arkona* (BSH, 2016). The site M-A, situated close to the *MARNET* monitoring buoy (**Figure 1**), was visited four times during this study between January 2015 and January 2016 after the major Baltic inflow. Bottom water temperature and salinity during these visits ranged from ~5–15 °C and 13–24 respectively, reflecting the variability that is known from the decade-long measurement series at the *Arkona Basin MARNET* station (BSH, 2016). Bottom water salinity variability during this study was clearly higher in the *Arkona Basin* (13–24) than in the *Bay of Mecklenburg* (18–24). These bottom water salinity changes were observed to also affect the pore waters in more than 10 cm depth below the sediment-water interface (e.g., **Figure 6**: Na^+ profiles at site M-A). Pore water concentration profiles of dissolved sodium, representing pore water salinity, quantitatively reflect the influence of bottom water salinity variability on pore water concentration gradients. Considerably higher salinity and thus also higher sulfate concentrations (about 15 mM) were available in the interstitial waters of the top 5 cm during January 2016 compared to September 2015 (about 10 mM sulfate). This implies a strongly enhanced concentration of sulfate, the educt for sulfate reduction, in the top 5 cm of the sediments. Still, gross sulfate reduction rates were higher in the summer situation (**Figure 5**), when bottom water salinity was lowest, compared to the winter situation with much higher bottom water salinity. In addition, generally little variability could be found in the depth gradients of dissolved hydrogen sulfide and the concentrations of organic matter mineralization products (DIC and ammonium) during four visits of the site M-A close to the *MARNET* station (**Figure 6**: site M-A). Despite the serious changes in environmental parameters, the organic matter mineralization derived pore water solutes at site M-A were in a steady-state during this study. Accordingly, we can assume that neither the considerable changes in temperature nor in salinity were the cause for the great spatiotemporal variability in the studied muds of sites M-M1, M-M2, and M-A.

4.3.2. Sediment Mixing

Reactive iron contents considerably above the estimated background levels were detected far below the diffusive oxygen penetration depth of ~1.5–4 mm (**Figure 2**), indicating an active downward transport of oxidized material. The Fe^* profiles often showed a characteristic shape with a maximum close to the sediment water interface, a minimum at ~5–10 cm depth and a second, often broader peak below. Decreasing contents of reactive Fe and Mn with depth (**Figure 2**) indicate active reduction of the oxidized phases, either sulfide-mediated or via microbial dissimilatory metal reduction (Lovley, 1991; Reyes et al., 2017). Released Fe^{2+} and Mn^{2+} migrate up and down along pore water concentration gradients (**Figure 6**) and precipitate as oxides or (oxyhydr)oxides on contact with oxygen near the sediment surface. Precipitation reactions are more likely to occur in the sediment than in the water column, because they are favored by iron and manganese oxide particles and microbially mediated (Thamdrup et al., 1994). Precipitation on contact with hydrogen sulfide from sulfate reduction, either as iron monosulfide (FeS) or pyrite (FeS_2), forms solid phase sulfur reservoirs at depth (**Figure 2**). This characteristic shape, a sharp maximum at the sediment surface, a broader minimum below followed by a second peak at depth, was also found for FeS precipitation in a model study by van de Velde and Meysman (2016), who simulated bioturbation in an idealized coastal muddy sediment. The lower peak was situated at the suboxic-sulfidic interface, where downward diffusing dissolved Fe^{2+} and upward diffusing sulfide meet. Expansion and shrinking of the suboxic zone lead to a vertical shift of the suboxic/sulfidic transition zone so that increased iron sulfide contents are distributed over a broader interval. Manganese is less reactive toward sulfide and therefore remains in solution at depth.

Also profiles of sedimentary mercury (Hg) reflect severe sediment disturbance in the M-M2 sediments (Bunke et al., in review). This type of profile can be found in the sediments of the M-A and S-S site (Bunke et al., 2018, Bunke et al., in review). Going from bottom to top, undisturbed sediments show natural background Hg values at depth ($\leq 50\ \mu g\ kg^{-1}$), a steep increase marking the beginning of the industrialization (about 1900) and a Hg maximum followed by constantly decreasing contents toward the sediment-water interface due to again reduced pollution (Leipe et al., 2013). Also the site M-M1 was characterized by a sharp maximum with highest mercury contents at 18 cm depth. This site is located near a known dumping site of industrial waste material, highly enriched in various contaminants including heavy metals (Kersten et al., 2005; Leipe et al., 2005). However, sediments at the site M-M2 do not show typical Hg gradients, but display instead a thoroughly mixed zone with virtually constant Hg contents in the top ~20–25 cm. Here, the transition from natural background to the anthropogenically affected zone might not mark the beginning of the industrial Hg pollution but the depth down to which sediments were thoroughly mixed, suggesting that these sediments were affected by deep-reaching (25–30 cm) and intensive rearrangement at least once after deposition.

4.3.2.1. Causes of sediment mixing

The site M-A is an aphotic muddy sediment dominated by *Limecola balthica* (Schiele et al., 2015), a surficial modifier penetrating muds and sands up to 5–6 cm deep (Gogina and Zettler, 2010). Morys et al. (2016) found *Limecola balthica*, *Artica islandica*, and *Scoloplos armiger* being the dominant species in M-A muds and responsible for sediment mixing. Advective transport processes across the sediment-water interface include the sediment reworking and water irrigation by the activity of benthic infauna (Aller, 1982; Ziebis et al., 1996; Kristensen et al., 2005) and other processes. Under oxygenated bottom waters, bioturbation, including the transport of both particles and solutes by living organisms either by local (diffusion analog transport) or non-local (directed convective transport) mixing processes, may be the most important sediment mixing process. Layers influenced by bioturbation usually reach 5–10 cm depth, rarely up to 15 cm in surface sediments of coastal marine environments (Aller and Rude, 1988; Aller, 1990, 1994).

However, sediment rearrangement can also be triggered by other processes than bio-mixing. At the site M-M2, Hg profiles indicate intensive sediment rearrangement with mixing depths

of more than 20 cm, which is too deep for most bioturbating infauna. The seabed in this region shows lots of bottom trawl traces, which are clearly recognizable by Side-Scan sonar (Bunke et al., in review). Hopkins (2004) observed imprints in Baltic Sea muddy bottoms of about 0.5–1.0 m depth and 1.0–1.5 m width. It is so far unknown how long these traces last, but significant sediment reworking through bottom trawling must be assumed. Bunke et al., (in review) suggest anthropogenic mixing activity (fishery) as a major sediment rearrangement process in the southern Baltic Sea. Since the bottom trawls mix the sediments only locally, this mixing process may also explain the remarkable redox-dynamics in the M-M2 sediments. In view of the large number of traces and the intensity of the impact on the seabed, anthropogenic mixing via trawl fishery may be the main sediment mixing process at this site.

The site M-A was the by far most constant of all studied sites in this study regarding the sediment pore water signatures in the top 15 cm (**Figure 6**). The study site is located inside the exclusion zone for ship traffic of the *Arkona Basin MARNET* monitoring station (**Figure 1**). It can be assumed that this site is rather unaffected by marine traffic as sidescan sonar recordings in this region revealed essentially no traces of bottom trawl fishing (personal communication Franz Tauber, IOW).

4.3.2.2. Effects of sediment mixing

Significantly higher mineralization rates (TOU and SRR) were measured in the coastal near sites of the *Bay of Mecklenburg* than in the deeper *Arkona Basin*. Increased mineralization activity of the coastal near muds of the *Bay of Mecklenburg* is attributed to enhanced input of fresh organic matter during algal blooms. However, also bioturbation affects early diagenetic processes by modifying the overall reactivity of the sediments (Meysman et al., 2006; Karlson et al., 2007; Kristensen et al., 2012). In sediments underlying oxygenated bottom water, most of organic matter decomposition takes place within the bioturbated zone, and mixing induced redox-oscillation enhances organic matter decomposition compared to constant oxic or anoxic conditions (Aller, 1994). Regular mixing leads to the incorporation of fresh organic matter and oxidants and a continuous removal of inhibitory metabolites which leads to an overall increased degradation of organic material (Aller, 1998). This applies not only to bioturbation but in principle to all sediment mixing processes.

We observed both, downward shifts of the sulfide appearance depth (**Figure 6**) and subsurface reactive iron reservoirs (**Figure 2**) in the sediments of the muddy sites M-M2 and M-A and also at the sandy site S-S. A model study by van de Velde and Meysman (2016) demonstrated the opposing impact of pure particle transport (bio-mixing) and pore water flushing (bio-irrigation) on the development of a suboxic zone in coastal marine sediments. The authors conclude that bio-mixing strongly promotes redox-reactions and cycling of Fe and S, so that stronger and deeper mixing of the top sediment column leads to downward shifts of the sulfide appearance depth and to larger reactive iron reservoirs in the sediment. van de Velde and Meysman (2016) further conclude that bio-irrigation rather removes reduced solutes from the pore water, preventing Fe and S from being recycled within the sediment column and resulting in an overall loss of both solid phase and dissolved Fe and S in irrigated sediments. The sandy site S-O seems to correspond to this pattern as it always showed low sedimentary TS and Fe^* contents (**Figure 2**) and mostly also particularly small pore water concentrations. The site S-O may thus act as a flow reactor with effective transportation of involved reactants, both educts and products, through the surface sediments.

Interestingly, the site M-M1 showed only small subsurface Fe^* contents (**Figure 2**), shallow sulfide appearance depths (**Figure 6**), and overall highest mineralization rates (TOU: **Figure 3** and SRR: **Figure 5**) and benthic solute reservoirs (**Figure 7**). Thus, neither bio-mixing nor bio-irrigation seems to play an important role here although it is near the presumably mixing controlled site M-M2. Particularly low bioturbation potentials were reported for this region, which was attributed to regularly recurring hypoxia and a resulting reduced infauna abundance (Morys et al., 2016).

In the muddy sediments, benthic solute phosphate reservoirs were considerably higher than mineralization of organic matter with the common element ratios of marine organic matter would suggest (subsection 3.4). At comparatively lowest benthic DIC and NH_4^+ reservoirs, the M-M2 station showed the highest phosphate reservoirs of the investigated muds (**Figure 7**). Sedimentary iron oxides control phosphate reservoirs in pore water and solid phase by reversible and irreversible adsorption (Froelich et al., 1982; Sundby et al., 1992; Jensen et al., 1995; Slomp et al., 1996a,b). These reactive iron phases form a barrier against diffusive phosphate transport toward the sediment-water interface, leading to an accumulation of P in the coastal surface sediments (Haese, 2006). As long as the reactive iron phases are not completely reduced or saturated with phosphate, the "iron curtain" efficiently retains phosphate in the sediments. Saturation of the adsorptive surface in the sediments with phosphate is only reached at pore water phosphate concentrations of 10–15 mM (Carman and Wulff, 1989), which is far above the observed concentrations in this study and is thus not likely. Strongly mixed muddy sites like the M-M2 site may thus be an effective sink for P in coastal Baltic Sea sediments.

5. CONCLUSION AND OUTLOOK

Oxygen uptake and sulfate reduction rates were similar in muds and sands, observed variability could essentially be attributed to spatially heterogeneous organic matter inputs. Multi-element pore water concentration gradients in the muds mainly reflected sulfate reduction and consecutive redox-reactions. Suboxic zones of varying extents suggested active downward transport of oxidized material. Coastal basin muds showed most stable geochemical zonation over time, while near-shore bay muds were remarkably dynamic. Orders of magnitude lower pore water concentrations were detected in the sandy sediments, indicating strong and frequent irrigation of the top centimeters, while mineralization products only accumulated below.

The studied sands were, hence, not unreactive substrates but usually rather unable to preserve the mineralization products.

Sands may have a huge importance in coastal marine systems but are underrepresented in most studies and methodologically difficult to investigate. Early diagenetic processes and the impact of intense benthic-pelagic exchange in such shallow marine environments is still poorly understood. Further studies are needed to better understand the driving forces in these environments and their impact on the coastal marine system.

The studied sediments of the southern Baltic Sea showed great dissimilarities with respect to their pore water compositions. Multi-parameter benthic solute reservoirs were shown to reflect early diagenetic processes in surface sediments, including organic matter mineralization, redox-reactions and transport processes. In contrast to diffusive fluxes and transformation rates, parameters usually calculated from pore water profiles, the benthic solute reservoir is an integrated size over a relevant depth range and thus robust against outliers and coarse resolution. In combination with multi-dimensional statistical analysis, namely the principal component analysis (PCA), we were able to clearly differentiate between the studied sites and to identify the processes mainly responsible for the differences between them. The studied sediments differed mainly by (1) their organic matter mineralization and solute accumulation efficiency and (2) their redox-state, reflecting fundamental differences in their sedimentation conditions and mixing processes. The supply of organic matter to the sea floor controlled the overall mineralization activity, while the sediment permeability determined the solute accumulation efficiency of the near-surface sediments.

Strong bottom water salinity variability clearly affected the pore water concentration gradients of the surface sediments but showed no noticeable effects on early diagenetic processes. However, highest dissimilarities were evident between two adjacent sites in a coastal muddy bay. Their varying redox-states could be traced back to different intensities of burial of oxidized material through sediment mixing.

Altogether, advective processes had a particularly strong influence on early diagenetic reactions and benthic solute reservoirs in the top sediments both by irrigation of permeable sands and by rearrangement of cohesive muds. Thus, they are probably the most important cause for spatial and temporal variability of coastal sediments and an important controlling factor for the release/retention of pollutants (e.g., heavy metals) and nutrients (e.g., P) in coastal sediments. In addition to bioturbation, anthropogenic effects can also be considered as potential mixing processes. The influence of sediment rearrangement through bottom trawl fishing on the biogeochemistry of coastal sediments is not sufficiently understood and must be further studied, since a large portion of coastal sediments is regularly affected by trawling equipment.

AUTHOR CONTRIBUTIONS

MB, SF, ML, and JW designed the study. ML performed the sediment and pore water sampling and analysis, the gross sulfate reduction analysis, the benthic solute reservoirs calculations, statistical analysis, and wrote the manuscript. JW and ML conducted core incubation experiments and their evaluation. MG sampled and analyzed benthic macrofauna. JK planned and supervised the gross sulfate reduction analysis at the GFZ. BL developed the reaction-transport models and performed the modeling to evaluate enhanced vertical solute fluxes across the sediment-water interface. CM sampled and analyzed surface sediment ChlA contents. SF performed sediment permeability analysis. All authors contributed to revisions.

FUNDING

This study was supported by German BMBF during the KÜNO projects SECOS-I and -II (03F0666 and 03F0738 A–C), thanks to MB, SF, and Leibniz Institute for Baltic Sea Research. The publication of this article was funded by the Open Access Fund of the Leibniz Association.

ACKNOWLEDGMENTS

We acknowledge the help of Dennis Bunke, Christian Burmeister, Florian Cordes, Andreas Frahm, Michael Glockzin, Axel Kitte, Anne Köhler, Gerhard Lehnert, Tobias Marquardt, Céline Naderipour, Sascha Plewe, Ines Scherff, and Iris Schmiedinger during field sampling and laboratory analysis. The authors wish to thank the captains and crews of R/V Elisabeth Mann Borgese, R/V Poseidon, R/V Alkor, and R/V Maria S. Merian. We wish to thank Boris Chubarenko and Björn Grüneberg for careful reviews that helped to improve the manuscript. Furthermore, Elinor Andrén is thanked for the editorial handling.

SUPPLEMENTARY MATERIAL

The Supplementary Material for this article can be found online at: https://www.frontiersin.org/articles/10.3389/fmars.2018.00413/full#supplementary-material

REFERENCES

Aller, R. C. (1982). "The Effects of Macrobenthos on Chemical Properties of Marine Sediment and Overlying Water," in *Animal-Sediment Relations. Topics in Geobiology,* Vol 100, eds P. L. McCall and M. J. S. Tevesz (Boston, MA: Springer).

Aller, R. C. (1990). Bioturbation and manganese cycling in hemipelagic sediments. *Philos. Trans. R. Soc. Lond. A Math. Phys. Eng. Sci.* 331, 51–68. doi: 10.1098/rsta.1990.0056

Aller, R. C. (1994). Bioturbation and remineralization of sedimentary organic matter : effects of redox oscillationl. *Chem. Geol.* 114, 331–345.

Aller, R. C. (1998). Mobile deltaic and continental shelf muds as suboxic, fluidized bed reactors. *Mar. Chem.* 61, 143–155. doi: 10.1016/S0304-4203(98)00024-3

Aller, R. C., and Rude, P. D. (1988). Complete oxidation of solid phase sulfides by manganese and bacteria in anoxic marine sediments. *Geochim. Cosmochim. Acta* 52, 751–765. doi: 10.1016/0016-7037(88)90335-3

Almroth, E., Tengberg, A., Andersson, J. H., Pakhomova, S. V., and Hall, P. O. J. (2009). Effects of resuspension on benthic fluxes of oxygen, nutrients,

dissolved inorganic carbon, iron and manganese in the Gulf of Finland, Baltic Sea. *Continent. Shelf Res.* 29, 807–818. doi: 10.1016/j.csr.2008.12.011

Al-Raei, A. M., Bosselmann, K., Böttcher, M. E., Hespenheide, B., and Tauber, F. (2009). Seasonal dynamics of microbial sulfate reduction in temperate intertidal surface sediments: controls by temperature and organic matter. *Ocean Dyn.* 59, 351–370. doi: 10.1007/s10236-009-0186-5

Arndt, S., Jørgensen, B. B., LaRowe, D. E., Middelburg, J. J., Pancost, R. D., and Regnier, P. (2013). Quantifying the degradation of organic matter in marine sediments: a review and synthesis. *Earth Sci. Rev.* 123, 53–86. doi: 10.1016/j.earscirev.2013.02.008

Balzer, W. (1984). Organic matter degradation and biogenic element cycling in a nearshore sediment (Kiel Bight). *Limnol. Oceanogr.* 29, 1231–1246. doi: 10.4319/lo.1984.29.6.1231

Berner, R. A. (1980). *Early Diagenesis: A Theoretical Approach*. Princeton, NJ: Princeton University Press.

Bonaglia, S., Deutsch, B., Bartoli, M., Marchant, H. K., and Brüchert, V. (2014). Seasonal oxygen, nitrogen and phosphorus benthic cycling along an impacted Baltic Sea estuary: Regulation and spatial patterns. *Biogeochemistry* 119, 139–160. doi: 10.1007/s10533-014-9953-6

Böttcher, M. E., Hespenheide, B., Llobet-Brossa, E., Beardsley, C., Larsen, O., Schramm, A., et al. (2000). The biogeochemistry, stable isotope geochemistry, and microbial community structure of a temperate intertidal mudflat: an integrated study. *Continent. Shelf Res.* 20, 1749–1769. doi: 10.1016/S0278-4343(00)00046-7

Böttcher, M. E., and Lepland, A. (2000). Biogeochemistry of sulfur in a sediment core from the west-central Baltic Sea: evidence from stable isotopes and pyrite textures. *J. Mar. Syst.* 25, 299–312. doi: 10.1016/S0924-7963(00)00023-3

Boudreau, B. P., Huettel, M., Forster, S., Jahnke, R. A., McLachlan, A., Middelburg, J. J., et al. (2001). Permeable marine sediments: Overturning an old paradigm. *Eos* 82, 133–136. doi: 10.1029/EO082i011p00133-01

Boudreau, B. P., and Westrich, J. T. (1984). The dependence of bacterial sulfate reduction on sulfate concentration in marine sediments. *Geochim. Cosmochim. Acta* 48, 2503–2516. doi: 10.1016/0016-7037(84)90301-6

Bowles, M. W., Mogollón, J. M., Kasten, S., Zabel, M., and Hinrichs, K.-U. (2014). Global rates of marine sulfate reduction and implications for subsea-floor metabolic activities. *Science* 344, 889–891. doi: 10.1126/science.1249213

Brzezinski, M. A. (1985). The si:C:N ratio of marine diatoms: Interspecific variability and the effect of some environmental variables. *J. Phycol.* 21, 347–357. doi: 10.1111/j.0022-3646.1985.00347.x

BSH (2016). *Station Arkona Basin*. Available online at: https://www.bsh.de/DE/DATEN/Meeresumweltmessnetz/_Module/Stationen_mit_Frame/arkona_extern_node.html (Accessed November 18, 2016).

Bunke, D., Leipe, T., and Arz, H. (2018). *Geochemical Depth Profiles of Modern Sediments in the South-Western Baltic Sea*. Available online at: http://iowmeta.io-warnemuende.de/geonetwork/srv/ger/catalog.search#/metadata/IOW-GIS-SECOS-52 (Accessed March 6, 2018).

Burdige, D. J. (2006). *Geochemistry of Marine Sediments*. doi: 10.1086/533614

Canfield, D. E. (1989). Sulfate reduction and oxic respiration in marine sediments: implications for organic carbon preservation in euxinic environments. *Deep Sea Res.* 36, 121–138.

Canfield, D. E., Kristensen, E., and Thamdrup, B. (2005). *Aquatic Geomicrobiology, 1st Edn*. London: Elsevier Academic Press.

Canfield, D. E., Thamdrup, B., and Hansen, J. W. (1993). The anaerobic degradation of organic matter in Danish coastal sediments: iron reduction, manganese reduction, and sulfate reduction. *Geochim. Cosmochim. Acta* 57, 3867–3883. doi: 10.1016/0016-7037(93)90340-3

Carman, R., and Wulff, F. (1989). Adsorption capacity of phosphorus in Baltic Sea sediments. *Estuar. Coast. Shelf Sci.* 29, 447–456. doi: 10.1016/0272-7714(89)90079-6

Cline, J. D. (1969). Spectrophotometric determination of hydrogen sulfide in natural waters. *Limnol. Oceanogr.* 14, 454–458. doi: 10.4319/lo.1969.14.3.0454

Conley, D. J., Stockenberg, A., Carman, R., Johnstone, R. W., Rahm, L., and Wulff, F. (1997). Sediment-water nutrient fluxes in the Gulf of Finland, Baltic Sea. *Estuar. Coast. Shelf Sci.* 45, 591–598. doi: 10.1006/ecss.1997.0246

Dadey, K., Janecek, T., and Klaus, A. (1992). Dry-bulk Density: Its uses and determination. *Proc. Ocean Drill. Program Sci. Results* 126, 551–554.

Eggleton, J., and Thomas, K. V. (2004). A review of factors affecting the release and bioavailability of contaminants during sediment disturbance events. *Environ. Int.* 30, 973–980. doi: 10.1016/j.envint.2004.03.001

Emeis, K. C., Neumann, T., Endler, R., Struck, U., Kunzendorf, H., and Christiansen, C. (1998). Geochemical records of sediments in the Eastern Gotland Basin – products of sediment dynamics in a not-so-stagnant anoxic basin? *Appl. Geochem.* 13, 349–358. doi: 10.1016/S0883-2927(97)00104-2

Field, C. B. (1998). Primary production of the biosphere: integrating terrestrial and oceanic components. *Science* 281, 237–240. doi: 10.1126/science.281.5374.237

Flemming, B. W., and Delafontaine, M. T. (2000). Mass physical properties of muddy intertidal sediments: some applications, misapplications and non-applications. *Continent. Shelf Res.* 20, 1179–1197. doi: 10.1016/S0278-4343(00)00018-2

Fossing, H. (1995). "S-35-radiolabeling to probe biogeochemical cycling of sulfur," in *Geochemical Transformations of Sedimentary Sulfur*, eds. M. A. Vairavamurthy and M. A. A. Schoonen (Washington, DC: American Chemical Society), 348–364.

Froelich, P. N., Bender, M. L., Luedtke, N. A., Heath, G. R., and DeVries, T., (1982). The marine phosphorus cycle. *Am. J. Sci.* 282, 474–511.

Froelich, P. N., Klinkhammer, G. P., Bender, M. L., Luedtke, N. A., Heath, G. R., Cullen, D., et al. (1979). Early oxidation of organic matter in pelagic sediments of the eastern equatorial Atlantic: suboxic diagenesis. *Geochim. Cosmochim. Acta* 43, 1075–1090. doi: 10.1016/0016-7037(79)90095-4

Glud, R. N. (2008). Oxygen dynamics of marine sediments. *Mar. Biol. Res.* 4, 243–289. doi: 10.1080/17451000801888726

Gogina, M., and Zettler, M. L. (2010). Diversity and distribution of benthic macrofauna in the Baltic Sea. Data inventory and its use for species distribution modelling and prediction. *J. Sea Res.* 64, 313–321. doi: 10.1016/j.seares.2010.04.005

Graf, G. (1992). "Benthic-pelagic coupling: a benthic view," in *Oceanography and Marine Biology: An Annual Review,* eds H. Barnes and M. Barnes (Aberdeen: University Press), 149–190.

Grasshoff, K., Kremling, K., and Ehrhardt, M. (2009). *Methods of Seawater Analysis*. Weinheim: John Wiley & Sons.

Haese, R. R. (2006). "The Biogeochemistry of Iron," in *Marine Geochemistry*, eds. H. D. Schulz and M. Zabel (Berlin: Springer-Verlag), 207–240.

Hopkins, C. C. E. (2004). The dangers of bottom trawling in the Baltic Sea. A Report for Coalition Clean Baltic. *Aquat Mar. Advisers.* 1, 1–14. Available online at: https://www.ccb.se/wp-content/uploads/2014/06/bottom_trawling.pdf

Howarth, R. W. (1984). The ecological significance of sulfur in the energy dynamics of salt marsh and coastal marine sediments. *Biogeochemistry* 1, 5–27. doi: 10.1007/BF02181118

Huettel, M., Berg, P., and Kostka, J. E. (2014). Benthic exchange and biogeochemical cycling in permeable sediments. *Annu. Rev. Mar. Sci.* 6, 23–51. doi: 10.1146/annurev-marine-051413-012706

Huettel, M., and Gust, G. (1992). Impact of bioroughness on interfacial solute exchange in permeable sediments. *Mar. Ecol. Prog. Ser.* 89, 253–267. doi: 10.3354/meps089253

Huettel, M., and Rusch, A. (2000). Transport and degradation of phytoplankton in permeable sediment. *Limnol. Oceanogr.* 45, 534–549. doi: 10.4319/lo.2000.45.3.0534

Huettel, M., Ziebis, W., and Forster, S. (1996). Flow-induced uptake of particulate matter in permeable sediments. *Limnol. Oceanogr.* 41, 309–322. doi: 10.4319/lo.1996.41.2.0309

Hyacinthe, C., Anschutz, P., Carbonel, P., Jouanneau, J. M., and Jorissen, F. J. (2001). Early diagenetic processes in the muddy sediments of the bay of biscay. *Mar. Geol.* 177, 111–128. doi: 10.1016/S0025-3227(01)00127-X

Isaksen, M. F., and Jørgensen, B. B. (1996). Adaptation of psychrophilic and psychrotrophic sulfate-reducing bacteria to permanently cold marine environments. *Appl. Environ. Microbiol.* 62, 408–414.

Janssen, F., Faerber, P., Huettel, M., Meyer, V., and Witte, U. (2005). Pore-water advection and solute fluxes in permeable marine sediments (I): Calibration and performance of the novel benthic chamber system Sandy. *Limnol. Oceanogr.* 50, 768–778. doi: 10.4319/lo.2005.50.3.0768

Jensen, H. S., Mortensen, P. B., Andersen, F. O., Rasmussen, E., and Jensen, A. (1995). Phosphorus cycling in a coastal marine sediment, Aarhus Bay, Denmark. *Limnol. Oceanogr.* 40, 908–917. doi: 10.4319/lo.1995.40.5.0908

Jørgensen, B. B. (1977). Distribution of Colorless Sulfur Bacteria a Coastal Marine Sediment. *Mar. Biol.* 28, 19–28.

Jørgensen, B. B. (1978). A comparison of methods for the quantification of bacterial sulfate reduction in coastal marine sediments. *Geomicrobiol. J.* 1, 11–27. doi: 10.1080/01490457809377721

Jørgensen, B. B. (1982). Mineralization of organic matter in the sea bed—the role of sulphate reduction. *Nature* 296, 643–645. doi: 10.1038/296643a0.

Jørgensen, B. B., and Kasten, S. (2006). "Sulfur cycling and methane oxidation," in *Marine Geochemistry*, eds. H. D. Schulz and M. Zabel (Berlin; Heidelberg: Springer), 271–309.

Jørgensen, B. B., and Revsbech, N. P. (1989). Oxygen uptake, bacterial distribution, and carbon-nitrogen-sulfur cycling in sediments from the Baltic Sea-North Sea transition 1937. *Ophelia* 31, 29–49. doi: 10.1080/00785326.1989.10430849

Kallmeyer, J., Ferdelman, T. G., Weber, A., Fossing, H., and Jørgensen, B. B. (2004). A cold chromium distillation procedure for radiolabeled sulfide applied to sulfate reduction measurements. *Limnol. Oceanogr. Methods* 2, 171–180. doi: 10.4319/lom.2004.2.171

Karlson, K., Bonsdorff, E., and Rosenberg, R. (2007). The impact of benthic macrofauna for nutrient fluxes from Baltic Sea sediments. *Ambio* 36, 161–167. doi: 10.1579/0044-7447(2007)36

Kersten, M., Leipe, T., and Tauber, F. (2005). Storm disturbance of sediment contaminants at a hot-spot in the Baltic sea assessed by ²³⁴Th radionuclide tracer profiles. *Environ. Sci. Technol.* 39, 984–990. doi: 10.1021/es049391y

Kostka, J. E., and Luther, G. W. (1994). Partitioning and speciation of solid phase iron in saltmarsh sediments. *Geochim. Cosmochim. Acta* 58, 1701–1710. doi: 10.1016/0016-7037(94)90531-2

Kowalski, N., Dellwig, O., Beck, M., Gräwe, U., Neubert, N., Nägler, T. F., et al. (2013). Pelagic molybdenum concentration anomalies and the impact of sediment resuspension on the molybdenum budget in two tidal systems of the North Sea. *Geochim. Cosmochim. Acta* 119, 198–211. doi: 10.1016/j.gca.2013.05.046

Kristensen, E. (2000). Organic matter diagenesis at the oxic/anoxic interfacein coastal marine sediments, with emphasis on the role of burrowing animals. *Hydrobiologia* 426, 1–24. doi: 10.1023/A:1003980226194

Kristensen, E., Haese, R. R., and Kostka, J. E. (eds) (2005). *Interactions Between Macro-and Microorganisms in Marine Sediments*. Washington, DC: Wiley.

Kristensen, E., Penha-Lopes, G., Delefosse, M., Valdemarsen, T., Quintana, C. O., and Banta, G. T. (2012). What is bioturbation? the need for a precise definition for fauna in aquatic sciences. *Mar. Ecol. Prog. Ser.* 446, 285–302. doi: 10.3354/meps09506

Laima, M. J., Matthiesen, H., Christiansen, C., Lund-Hansen, L. C., and Emeis, K. C. (2001). Dynamics of P, Fe and Mn along a depth gradient in the SW Baltic Sea. *Boreal Environ. Res.* 6, 317–333. Available online at: http://www.borenv.net/BER/pdfs/ber6/ber6-317s.pdf

Laima, M. J., Warszawy, P., and Christiansen, C. (1999). Near-bottom fluxes and composition of suspended matter in the Pomeranian Bay. *Oceanologia* 41, 335–353.

Leipe, T., Harff, J., Meyer, M., Hille, S., Pollehne, F., Schneider, R., et al. (2008). "Sedimentary Records of Environmental Changes and Anthropogenic Impacts during the Past Decades," in *State and Evolution of the Baltic Sea, 1952–2005*, eds. G. Nausch, R. Feistel, and N. Wasmund (Hoboken, NJ: Wiley & Sons).

Leipe, T., Kersten, M., Heise, S., Pohl, C., Witt, G., Liehr, G., et al. (2005). Ecotoxicity assessment of natural attenuation effects at a historical dumping site in the western Baltic Sea. *Mar. Pollut. Bull.* 50, 446–459. doi: 10.1016/j.marpolbul.2004.11.049

Leipe, T., Moros, M., Kotilainen, A., Vallius, H., Kabel, K., Endler, M., et al. (2013). Mercury in Baltic Sea sediments-Natural background and anthropogenic impact. *Chem. Erde Geochem.* 73, 249–259. doi: 10.1016/j.chemer.2013.06.005

Leipe, T., Tauber, F., Vallius, H., Virtasalo, J., Uścinowicz, S., Kowalski, N., et al. (2011). Particulate organic carbon (POC) in surface sediments of the Baltic Sea. *Geo Mar. Lett.* 31, 175–188. doi: 10.1007/s00367-010-0223-x

Llobet-Brossa, E., Rabus, R., Böttcher, M. E., Könneke, M., Finke, N., Schramm, A., et al. (2002). Community structure and activity of sulfate-reducing bacteria in an intertidal surface sediment : a multi-method approach. *Inter Res. Aquat. Microb. Ecol.* 29, 211–226. doi: 10.3354/ame029211

Lovley, D. R. (1991). Dissimilatory Fe (III) and Mn (IV) Reduction. *Microbiol. Rev.* 55, 259–287.

Lovley, D. R., Roden, E. E., Phillips, E. J., and Woodward, J. C. (1993). Enzymatic iron and uranium reduction by sulfate-reducing bacteria. *Mar. Geol.* 113, 41–53. doi: 10.1016/0025-3227(93)90148-O

Mackin, J. E., and Swider, K. T. (1989). Organic matter decomposition pathways and oxygen consumption in coastal marine sediments. *J. Mar. Res.* 47, 681–716.

Meysman, F. J. R., Middelburg, J. J., and Heip, C. H. (2006). Bioturbation: a fresh look at Darwin's last idea. *Trends Ecol. Evol.* 21, 688–695. doi: 10.1016/j.tree.2006.08.002

Middelburg, J. J. (1989). A simple rate model for organic matter decomposition in marine sediments. *Geochim. Cosmochim. Acta* 53, 1577–1581. doi: 10.1016/0016-7037(89)90239-1

Middelburg, J. J., Vlug, T., and Nat, F. J. van der, W. A. (1993). Organic matter mineralization in marine systems. *Global Planet. Change* 8, 47–58.

Moeslund, L., Thamdrup, B., and Jørgensen, B. B. (1994). Sulfur and iron cycling in a coastal sediment: radiotracer studies and seasonal dynamics. *Biogeochemistry* 27, 129–152. doi: 10.1007/BF00002815

Mohrholz, V., Naumann, M., Nausch, G., Krüger, S., and Gräwe, U. (2015). Fresh oxygen for the Baltic Sea – An exceptional saline inflow after a decade of stagnation. *J. Mar. Syst.* 148, 152–166. doi: 10.1016/j.jmarsys.2015.03.005

Morys, C., Forster, S., and Graf, G. (2016). Variability of bioturbation in various sediment types and on different spatial scales in the southwestern Baltic Sea. *Mar. Ecol. Prog. Ser.* 557, 31–49. doi: 10.3354/meps11837

Piker, L., Schmaljohann, R., and Imhoff, J. F. (1998). Dissimilatory sulfate reduction and methane production in Gotland Deep sediments (Baltic Sea) during a transition period from oxic to anoxic bottom water (1993-1996). *Aquat. Microb. Ecol.* 14, 183–193. doi: 10.3354/ame014183

Postma, D., and Appelo, C. A. J. (2000). Reduction of Mn-oxides by ferrous iron in a flow system: Column experiment and reactive transport modeling. *Geochim. Cosmochim. Acta* 64, 1237–1247. doi: 10.1016/S0016-7037(99)00356-7

Poulton, S. W., Krom, M. D., and Raiswell, R. (2004). A revised scheme for the reactivity of iron (oxyhydr)oxide minerals towards dissolved sulfide. *Geochim. Cosmochim. Acta* 68, 3703–3715. doi: 10.1016/j.gca.2004.03.012

R Core Team (2016). *R: A Language and Environment for Statistical Computing*. Available online at: https://www.r-project.org/.

Redfield, A. C. (1958). The biological control of chemical factors in the environment. *Am. Sci.* 46, 230A–221.

Revsbech, N. P., Sorensen, J., Blackburn, T. H., and Lomholt, J. P. (1980). Distribution of oxygen in marine sediments measured with microelectrodes. *Limnol. Oceanogr.* 25, 403–411. doi: 10.4319/lo.1980.25.3.0403

Reyes, C., Dellwig, O., Dähnke, K., Gehre, M., Noriega-Ortega, B. E., Böttcher, M. E., et al. (2016). Bacterial communities potentially involved in iron-cycling in baltic sea and north sea sediments revealed by pyrosequencing. *FEMS Microbiol. Ecol.* 92:fiw054. doi: 10.1093/femsec/fiw054

Reyes, C., Schneider, D., Thürmer, A., Kulkarni, A., Lipka, M., Sztejrenszus, S. Y., et al. (2017). Potentially active iron, sulfur, and sulfate reducing bacteria in skagerrak and bothnian bay sediments. *Geomicrobiol. J.* 34, 840–850. doi: 10.1080/01490451.2017.1281360

Rullkötter, J. (2006). "Organic Matter: The Driving Force for Early Diagenesis," in *Marine Geochemistry*, eds. H. D. Schulz and M. Zabel (Berlin; Heidelberg: Springer), 125–168. doi: 10.1007/3-540-32144-6_4

Rusch, A., and Huettel, M. (2000). Advective particle transport into permeable sediments–evidence from experiments in an intertidal sandflat. *Limnol. Oceanogr.* 45, 523–533. doi: 10.4319/lo.2000.45.3.0525

Rysgaard, S., Fossing, H., and Jensen, M. M. (2001). Organic matter degradation through oxygen respiration, denitrification, and manganese, iron, and sulfate reduction in marine sediments (the Kattegat and the Skagerrak). *Ophelia* 55, 77–91. doi: 10.1080/00785236.2001.10409475

Sawicka, J. E., Jørgensen, B. B., and Brüchert, V. (2012). Temperature characteristics of bacterial sulfate reduction in continental shelf and slope sediments. *Biogeosciences* 9, 3425–3435. doi: 10.5194/bg-9-3425-2012

Schaffer, G., and Collins, H.-J. (1966). "Eine methode zur messung der infiltrationsrate im felde," in *Z. f. Kulturtechnik und Flurbereinigung,* Vol. 7, (Berlin, Hamburg; P. Parey), 193–199.

Schiele, K. S., Darr, A., Zettler, M. L., Friedland, R., Tauber, F., Weber, M. von, et al. (2015). Biotope map of the German Baltic Sea. *Mar. Pollut. Bull.* 96, 127–135. doi: 10.1016/j.marpolbul.2015.05.038

Schippers, A., and Jørgensen, B. B. (2001). Oxidation of pyrite and iron sulfide by manganese dioxide in marine sediments. *Geochim. Cosmochim. Acta* 65, 915–922. doi: 10.1016/S0016-7037(00)00589-5

Schippers, A., and Jørgensen, B. B. (2002). Biogeochemistry of pyrite and iron sulfide oxidation in marine sediments. *Geochim. Cosmochim. Acta* 66, 85–92. doi: 10.1016/S0016-7037(01)00745-1

Seeberg-Elverfeldt, J., Schluter, M., Feseker, T., and Kolling, M. (2005). Rhizon sampling of porewaters near the sediment-water interface of aquatic systems. *Limnol. Oceanogr. Methods* 3, 361–371. doi: 10.1016/S0012-821x(02)01064-6

Skyring, G. W. (1987). Sulfate reduction in coastal ecosystems. *Geomicrobiol. J.* 5, 295–374. doi: 10.1080/01490458709385974

Slomp, C. P., Epping, E. H. G., Helder, W., and Raaphorst, W. V. (1996a). A key role for iron-bound phosphorus in authigenic apatite formation in North Atlantic continental platform sediments. *J. Mar. Res.* 54, 1179–1205. doi: 10.1357/0022240963213745

Slomp, C. P., Van Der Gaast, S. J., and Van Raaphorst, W. (1996b). Phosphorus binding by poorly crystalline iron oxides in North Sea sediments. *Mar. Chem.* 52, 55–73. doi: 10.1016/0304-4203(95)00078-X

Stookey, L. L. (1970). Ferrozine—a new spectrophotometric reagent for iron. *Anal. Chem.* 42, 779–781. doi: 10.1021/ac60289a016

Sundby, B., Gobeil, C., Silverberg, N., and Mucci, A. (1992). The phosphorus cycle in coastal marine sediments. *Limnol. Oceanogr.* 37, 1129–1145. doi: 10.4319/lo.1992.37.6.1129

Talley, L. D., Pickard, G. L., Emery, W. J., and Swift, J. H. (2011). *Descriptive Physical Oceanography: An Introduction.* Amsterdam; Boston: Elsevier-Academic Press.

Tauber, F. (2014). "Regionalized classification of seabed sediments in the German Baltic Sea. BALTIC 2014," in *The 12th Colloquium on Baltic Sea Marine Geology, Warnemünde, September 08-12, 2014,* Abstract Vol. 79. Available online at: www.io-warnemuende.de/conference-bsg2014-schedule.html?file=tl_files/conference/bsg2014/pdf/abstract_volume0809.pdf

Thamdrup, B., Glud, R. N., and Hansen, J. W. (1994). Manganese oxidation and in situ manganese fluxes from a coastal sediment. *Geochim. Cosmochim. Acta* 58, 2563–2570. doi: 10.1016/0016-7037(94)90032-9

Thode-Andersen, S., and Jørgensen, B. B. (1989). Sulfate reduction and the formation of 35S-labeled FeS, FeS2, and S0 in coastal marine sediments. *Limnol. Oceanogr.* 34, 793–806. doi: 10.4319/lo.1989.34.5.0793

van de Velde, S., and Meysman, F. J. R. (2016). The Influence of Bioturbation on Iron and Sulphur Cycling in Marine Sediments: A Model Analysis. *Aquat. Geochem.* 22, 469–504. doi: 10.1007/s10498-016-9301-7

Wang, F., and Chapman, P. M. (1999). Biological implications of sulfide in sediment - A review focusing on sediment toxicity. *Environ. Toxicol. Chem.* 18, 2526–2532. doi: 10.1002/etc.5620181120

Wang, Y., and Van Cappellen, P. (1996). A multicomponent reactive transport model of early diagenesis: application to redox cycling in coastal marine sediments. *Geochim. Cosmochim. Acta* 60, 2993–3014. doi: 10.1016/0016-7037(96)00140-8

Werner, U., Billerbeck, M., Polerecky, L., Franke, U., Huettel, M., Beusekom, J. E. E. van, et al. (2006). Spatial and temporal patterns of mineralization rates and oxygen distribution in a permeable intertidal sand flat (Sylt, Germany). *Limnol. Oceanogr.* 51, 2549–2563. doi: 10.4319/lo.2006.51.6.2549

Winde, V., Böttcher, M. E., Escher, P., Böning, P., Beck, M., Liebezeit, G., et al. (2014). Tidal and spatial variations of DI13C and aquatic chemistry in a temperate tidal basin during winter time. *J. Mar. Syst.* 129, 396–404. doi: 10.1016/j.jmarsys.2013.08.005

Ziebis, W., Huettel, M., and Forster, S. (1996). Impact of biogenic sediment topography on oxygen fluxes in permeable seabeds. *Mar. Ecol. Prog. Ser.* 140, 227–237. doi: 10.3354/meps140227

Conflict of Interest Statement: The authors declare that the research was conducted in the absence of any commercial or financial relationships that could be construed as a potential conflict of interest.

Copyright © 2018 Lipka, Woelfel, Gogina, Kallmeyer, Liu, Morys, Forster and Böttcher. This is an open-access article distributed under the terms of the Creative Commons Attribution License (CC BY). The use, distribution or reproduction in other forums is permitted, provided the original author(s) and the copyright owner(s) are credited and that the original publication in this journal is cited, in accordance with accepted academic practice. No use, distribution or reproduction is permitted which does not comply with these terms.

frontiers in Marine Science

ORIGINAL RESEARCH
published: 15 November 2018
doi: 10.3389/fmars.2018.00415

Nutrient Retention in the Swedish Coastal Zone

Moa Edman[1], Kari Eilola[1], Elin Almroth-Rosell[1], H. E. Markus Meier[1,2], Iréne Wåhlström[1] and Lars Arneborg[1]*

[1] Swedish Meteorological and Hydrological Institute, Norrköping, Sweden, [2] Department of Physical Oceanography and Instrumentation, Leibniz Institute for Baltic Sea Research Warnemünde, Rostock, Germany

In this study, the average nutrient filter efficiency of the entire Swedish coastline is estimated to be about 54 and 70% for nitrogen and phosphorus, respectively. Hence, significantly less than half of the nutrient input from land (defined as river discharge and point sources) can be assumed to be exported from coastal waters to the open sea. However, some coastal areas retained more than 100% of the land load and thus, also filter the open Baltic Sea water. These areas with effective filtering of nutrients have low land load per unit coastal area. The filter efficiency was calculated from a 30-years model simulation (1985–2014) of water exchanges and nutrient cycling within the Swedish coastal zone. The average model skill was evaluated to be good or acceptable compared to observations. In addition to the entire Swedish coast, the retention of total nutrient loads in seven larger coastal sub-regions and selected key sites representing different coastal types was also estimated. The modeled long term nutrient retention was found to be associated with the physical characteristics of a water body, such as the surface area, but also the mean depth and residence time of water. In addition, high retention efficiency is associated with high ratio of sediment nutrient content to pelagic nutrient concentrations. On interannual timescales temporal changes in the coastal nutrient pool can have a large influence on perceived nutrient retention. At one site, the phosphorus filter efficiency was actually negative, i.e., the coastal zone transported more phosphorus to the open Baltic Sea than it received from land. The nutrient removal is most efficient close to land, where the area specific retention efficiency is the highest. The variability of both the filter and retention efficiency between coastal regions was found to be large, with a range of approximately 4–1,200% and 0.1–8.5%, respectively.

Keywords: Baltic Sea, nitrogen, phosphorus, retention, coastal, numerical modeling

OPEN ACCESS

Edited by:
Teresa Radziejewska, University of Szczecin, Poland

Reviewed by:
Angel Menendez, Instituto Nacional del Agua, Argentina
Elżbieta Łysiak-Pastuszak, Institute of Meteorology and Water Management, Poland

****Correspondence:***
Moa Edman
moa.edman@smhi.se

Specialty section:
This article was submitted to Coastal Ocean Processes, a section of the journal Frontiers in Marine Science

Received: *29 March 2018*
Accepted: *17 October 2018*
Published: *15 November 2018*

Citation:
Edman M, Eilola K, Almroth-Rosell E, Meier HEM, Wåhlström I and Arneborg L (2018) Nutrient Retention in the Swedish Coastal Zone. Front. Mar. Sci. 5:415. doi: 10.3389/fmars.2018.00415

INTRODUCTION

Most of the Swedish coast boarders the brackish, semi-enclosed Baltic Sea while the Swedish West Coast is connected to the Kattegat and Skagerrak system that acts as a transitional zone between the North Sea and the Baltic Sea. The Baltic Sea is shallow with a mean water depth of 54 m [Gotland Deep and Landsort Deep are about 250 and 459 m, respectively; see Seifert and Kayser (1995)]. It is characterized by large vertical and horizontal salinity gradients (e.g., Leppäranta and Myrberg, 2009) from the entrance up to the Bothnian Bay. The Baltic Sea is connected to the Kattegat through the Danish straits of Öresund, the Great Belt, and the Little Belt where the entrance area is very

shallow. The average depth of the Kattegat and Belt Sea amounts to only 19 m and the sills in the Öresund (Drogden Sill) and Belt Sea (Darss Sill) are 7 and 18 m deep, respectively. Due to the limited water exchange between the Baltic Sea and North Sea the volume averaged salinity of the Baltic Sea amounts to only 7–8 g kg^{-1} (e.g., Meier and Kauker, 2003). Further north of the Kattegat, in the Skagerrak, both water depth and salinity increase considerably.

The Baltic Sea drainage basin is large in comparison to the Baltic Sea and the southern part of the drainage area includes heavily populated areas such as the Polish and German coasts. The catchment area belongs to 14 different countries and about 85 million people are living in the drainage basin (Helcom, 2017). As a consequence, the Baltic Sea receives high anthropogenic nutrient loads (e.g., Gustafsson et al., 2012; Carstensen et al., 2014). Together with a long water residence time, and restricted ventilation of the deep water caused by permanent salinity stratification, oxygen deficiency is a common problem in large parts of the Baltic proper (Conley et al., 2009) and even in the coastal zone (Conley et al., 2011). Today large parts of the sea bottom in the Baltic Sea are dead, i.e., higher forms of life do not occur, because the dissolved oxygen concentrations of the bottom water are below 2 ml l^{-1}. Such low oxygen conditions are called hypoxia. Changes in the coastal zones of the Baltic Sea due to high nutrient loads are region specific and manifested, e.g., by increased occurrence of hypoxia, reduced nutrient retention, increased growth of opportunistic filamentous algae and drifting algae mats, as well as changes in species composition and the increased occurrence of cyanobacteria (e.g., Norkko and Bonsdorff, 1996; Rönnberg and Bonsdorff, 2004; Cossellu and Nordberg, 2010; Conley et al., 2011).

All inputs from land first enter the coastal zone and depending on the nutrient transports and transformations in this zone, not all reach the open sea. The coastal zone often filters some of the land nutrient input (Almroth-Rosell et al., 2016; Asmala et al., 2017) since the biogeochemical processes that remove or retain nutrients can act faster in this area due to the shallow depth creating closer connection between input, water and sediment. Such processes are, for instance, the uptake of nutrients due to primary production (temporary storage), the permanent burial in the sediment of organic material, reduction of nitrate to molecular nitrogen (denitrification) and the uptake of dissolved molecular nitrogen by nitrogen fixing algae. Hence, nutrient transports that exit the coastal zone are often much smaller than the riverine nutrient loads that enter the coastal zone. The effectiveness of the coastal zone in removing nutrients is very important for open sea eutrophication. However, the coastal zone is often not considered in modeling efforts on coastal seas. For example, most three-dimensional circulation models of the Baltic Sea and other large coastal seas are too coarse to resolve coastal zone environments such as coastal wetlands, river estuaries, and embayments such as small fjords, archipelagos and lagoons properly. Typical horizontal grid resolutions of present Baltic Sea models are 3–5 km (e.g., Neumann et al., 2002; Eilola et al., 2009). Gräwe et al. (2015) studied saltwater inflows with a nested model using a horizontal resolution of even 600 m in the nest. For a model inter-comparison of state-of-the-art coupled physical-biogeochemical models the reader is referred to Eilola et al. (2011).

The Swedish Coastal zone Model (SCM) has previously been used to calculate nutrient retention in the Stockholm archipelago (Almroth-Rosell et al., 2016). That study showed that only around 30% of the land load to the archipelago actually reached the Baltic Sea, while the remaining fraction was temporarily withheld or permanently removed within the coastal zone. Together, the removal and withholding constitute the coastal retention that filter the nutrient loads from land. The retention acts on any constituent, in this context nutrients, i.e., nitrogen (N) and phosphorus (P), disregarding if they originate from the Baltic Sea or directly from land. The coastal filter refers to the filtering of land load. Almroth-Rosell et al. (2016) showed that the area specific retention efficiency (i.e., the fraction of the total nutrient supply that is retained per area unit) was highest in the inner part of the archipelago, while the filter efficiency increased as the coastal area that receives the nutrient load increased.

Asmala et al. (2017) compiled available information about nitrogen (denitrification) and phosphorus (burial) removal rates from coastal systems around the Baltic Sea and analyzed their spatial variation and regulating environmental factors. They estimated from an up-scaling of their data that the coastal filter of the entire Baltic Sea removes 16% of nitrogen and 53% of phosphorus inputs from land. They also concluded, in agreement with Almroth-Rosell et al. (2016), that archipelagos are important phosphorus traps and account for 45% of the coastal P removal, while covering only 17% of the coastal areas. Similarly, their estimates indicated that the coastal region around the Baltic Proper alone accounted for 50% of the total Baltic Sea denitrification in their study, even though it contributed only 25% of the total area. Especially the lagoons and the open coasts were pointed out as very efficient coastal filters for nitrogen removal due to denitrification.

For management purposes the Swedish coastline is divided into five water districts (WDs), shown in **Figure 1A**. Water district four (WD4) consists of very different types of coastline, such as the open coasts around Skåne and Gotland contrasted with the Blekinge archipelago. Thus, this water district is sometimes divided into three smaller, more homogeneous, regions as will be done in this study. The definition of the coastal zone and coastal waters in the SCM follows Article 2 (7) in the Water Framework Directive European Parliament Council of the European Union (2000). This generally includes all waters from the shoreline to within one nautical mile from the baseline.

The present study will investigate retention efficiency, the coastal filter function and how it is related to environmental indicators along the entire Swedish coastline. The analysis will show how nutrient retention and some associated parameters vary along the coast, and also start to unravel which physical and environmental factors affect the retention in a water body. Understanding how effectively, and why, different coastal sites act as filter for land derived nutrients may help to upscale the results of more detailed studies at specific sites along the Baltic Sea coast.

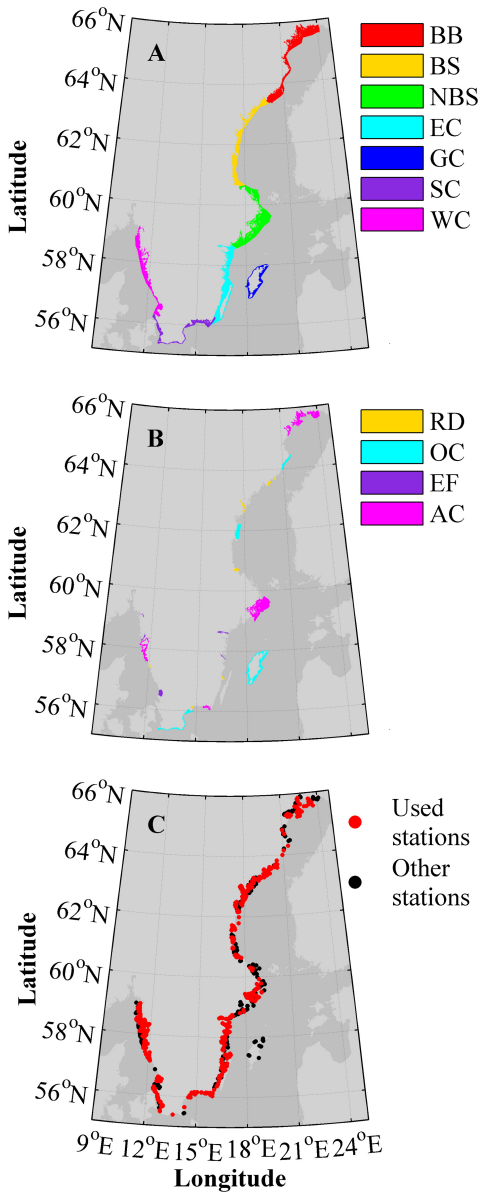


FIGURE 1 | Maps of the Swedish coastline with abbreviations in the legends according to **Table 1**. **(A)** The seven major regions, i.e., the five water districts (WD1, WD2, WD3, WD4, and WD5) where WD4 is divided in three parts. **(B)** The key sites colored after type. **(C)** The coastal monitoring stations available in the SHARK database for the 1995–2014 period.

This work was part of the BONUS COCOA project[1], which investigated the transports and transformations of nutrients in the coastal zone of the Baltic Sea.

MATERIALS AND METHODS

To facilitate for the reader, the most frequently used abbreviations and definitions, including units, are listed in **Table 1**.

[1]https://www.bonusportal.org/projects/viable_ecosystem_2014-2018/cocoa

TABLE 1 | List of abbreviations and units.

Abbreviation	Full expression	Unit
WD	Water district	–
MR	Major region	–
PNR	Permanent net removal	t yr^{-1}
ΔM	Change in temporary storage	t yr^{-1}
R_{tot}	Total retention = $PNR + \Delta M$	t yr^{-1}
$Load_{land}$	Load from land = Point sources + land runoff	t yr^{-1}
$Load_{tot}$	Total load = $Load_{land}$ + atmospheric deposition + advection from open sea + exchange with other water bodies	t yr^{-1}
E_R	Retention efficiency = $PNR/Load_{tot}$	%
E_F	Filter efficiency = $R_{tot}/Load_{land}$	%
V_S	Apparent removal rate, expressed as a Settling Velocity	m yr^{-1}
Blr	Benthic Loss Rate	day^{-1}
τ	Water residence time	day
A	Flat bottom area, equivalent to the surface area of a model basin	km^2
H	Mean depth = *V*/*A*	m
Rho	Spearman rank correlation coefficient	–
r	Pearson correlation coefficient	–
C	Cost function	–

Retention

Retention is the withholding of matter within a region and is usually calculated as the external input to the area minus the export. This definition of retention includes both a withholding of matter but also internal removal or additions. To be able to set our results in a literature context we use the same definition in this study.

The approach described in the previous paragraph follows the concept of temporal and permanent retention introduced by Almroth-Rosell et al. (2016). They defined the total retention (R_{tot}) as the sum of permanent net removal (*PNR*, i.e., permanent retention) and changes in temporary storage (ΔM, i.e., temporary retention). *PNR* of nutrients is calculated from the models' biogeochemical process rates, i.e., sinks and sources in the nutrient budgets. For phosphorus this only includes sediment burial while for nitrogen sediment burial, denitrification in water and sediment and fixation of dinitrogen (N_2) are included. The temporary retention is calculated as the annual change in nutrient storage in the water bodies, with the nutrient storage calculated as the sum of vertically integrated pelagic and sediment pools.

Retention Efficiency and Effective Coastal Filter

The retention discussed in Section "Retention" is expressed as annually retained tons of nitrogen and phosphorus. To better understand what these numbers entail they are set in relation to the load. We use both the total load ($Load_{tot}$) and the load from land ($Load_{land}$). $Load_{land}$ is defined as the supply from

rivers, surface runoff, groundwater and point sources. $Load_{tot}$ is defined as the sum of $Load_{land}$, surface deposition, advective transports from the open sea and sound transports within the model domain. Note that the groundwater nutrient flux is not well known and thus, the groundwater output from the runoff model is difficult to estimate and also, as a consequence, to validate.

The retention efficiency (E_R) is the fraction of the total load that is permanently removed,

$$E_R = \frac{PNR}{Load_{tot}} \quad (1)$$

The nutrient filter (the filter efficiency, E_F) is the retained fraction of land load only (from rivers, surface runoff, ground water and point sources)

$$E_F = \frac{R_{tot}}{Load_{land}} \quad (2)$$

The filtering efficiency is calculated from the total retention since we are interested in estimating the long-term average nutrient filter around the Swedish coast, which should also include any possible long-term net effects of temporary retention. However, *PNR* is used to calculate E_R since the highly variable temporary retention (Almroth-Rosell et al., 2016) would be a hindrance in the following analyze.

Occasionally retention needs to be normalized to the horizontal area of water bodies or regions. This will be indicated in the text.

Theory of Steady State Retention

In order to understand what governs the retention efficiency in a specific water body we explore the concept of steady state retention as discussed in Eilola et al. (2017). For this we assume a well-mixed basin with a flat bottom with area (A) that is supplied with a bioactive tracer with the freshwater from land and with inflowing water from the adjacent sea. The bioactive tracer may be exported to the adjacent sea and also be removed due to *PNR* (Wulff and Stigebrandt, 1989). Especially, we investigate the functioning of *PNR* and retention efficiency in a case study where the bioactive tracer is a nutrient (nitrogen or phosphorus), which is also used for primary production of organic matter in a productive layer at the surface of the sea. Since we focus on shallow coastal areas we assume that the internal loss of the bioactive tracer mainly is due to permanent loss of nutrients in the sediment caused by, e.g., burial and/or denitrification.

The basis for the analysis is the mass conservation equation where changes in the pools depend on nutrient supplies, exports and the internal losses *PNR*. For simplicity, we investigate the steady state conditions where changes in the nutrient pools are assumed to be small. In accordance with Wulff and Stigebrandt (1989), we use the concept of an apparent removal rate, i.e., a fraction of the bioactive tracer mass in the water is removed with an apparent removal rate V_S. Thus, *PNR* within the system is dependent on $V_S \cdot C_{pel} \cdot A$, where C_{pel} is the mean pelagic nutrient concentration.

We use mass conservation

$$V \cdot \frac{dC_{pel}}{dt} = Q_0 \cdot C_0 + Q_2 \cdot C_2 - Q \cdot C_{pel} - PNR \quad (3)$$

and assume a steady state to calculate the concentration C_{pel}

$$C_{pel} = \frac{Q_0 \cdot C_0 + Q_2 \cdot C_2}{Q + V_S \cdot A}. \quad (4)$$

Here V is the volume of water in the basin, dC_{pel}/dt the change in concentration of the nutrient with time (equal to zero in steady state), Q_0 is the freshwater supply from land and C_0 is the concentration of the nutrient in the inflowing freshwater (including here also the supplies from atmosphere and point sources), Q_2 is the inflowing water from adjacent basins, C_2 the concentration of the nutrient in the inflowing water and Q is the outflowing water.

The retention efficiency (Eq. 1) can be written as

$$E_R = \frac{PNR}{Q_0 \cdot C_0 + Q_2 \cdot C_2} \quad (5)$$

Using Eq. 4 this can be rewritten as

$$E_R = \frac{1}{1 + \frac{H}{V_S \cdot \tau}}, \quad (6)$$

where $H = V/A$ is the mean depth and τ is the water residence time defined by:

$$\tau = \frac{V}{Q}. \quad (7)$$

According to Eq. 6 E_R is a function of mean depth (m), water residence time (days) and apparent removal rate (m day^{-1}).

Since internal losses are assumed to take place mainly at the sea floor, the apparent removal rate (V_S) is related to the benthic loss rate, *Blr* (day^{-1}), in the sediment, i.e., $PNR = V_S \cdot C_{pel} \cdot A = Blr \cdot M_{sed} \cdot A$, where C_{pel} is the concentration in the water column (mmol m^{-3}). Thus, V_S can be expressed as a function of the mean vertically integrated mass in the sediment M_{sed} (mmol m^{-2}) and the C_{pel} (Eq. 8) for any bioactive tracer,

$$V_S = Blr \cdot \frac{M_{sed}}{C_{pel}}. \quad (8)$$

Here the benthic loss rate is related to the burial and denitrification rates, i.e., the deposition of bioactive tracer to the sediment and redox-state as well as the benthic release rate. It is dependent on many local factors such as the supplies to the sub-basin, the productivity and mineralization in the basin, which depend on the temperature, deep water stagnation, and potentially other factors.

Determining Dependence of E_R on Hydrological and Environmental Factors

According to the theory described in Section "Theory of Steady State Retention," the retention efficiency of the coastal zone is determined by water depth and residence time as well as on the apparent removal rate V_S that depends on the environmental state in water and sediment. Previous studies (Nixon et al., 1996; Billen et al., 2011; Hayn et al., 2014; Almroth-Rosell et al., 2016) have shown the dependency only on hydrographical factors.

The modeled water bodies are of variable size and since PNR, and thus E_R, is largely determined by burial and denitrification,

also the association strength to the sediment area of the water bodies will be investigated. E_R is calculated for each modeled water body according to Eq. 1 and residence times are derived from the model calculations (see section "Calculation of Residence Times"). Mean depths are calculated from the hypsography of the water bodies, i.e., total water volume divided by surface area.

To investigate the association strength between V_S and different environmental indicators, Eq. 6 is solved for V_S, i.e.,

$$V_S = \frac{H \cdot E_R}{\tau \cdot (1 - E_R)}. \quad (9)$$

V_S can then be calculated for each water body. When V_S is known *Blr* can be calculated by solving Eq. 8 for *Blr*,

$$Blr = V_S \cdot \frac{C_{pel}}{M_{sed}}. \quad (10)$$

The environmental indicators that will be tested are: the ratio between the nutrient content in the sediment and in the water column (Eq. 8), the total nutrient content; the inorganic nutrients (dissolved inorganic nitrogen, DIN and dissolved inorganic phosphorus, DIP); N:P ratios; the hypoxic area; salinity; stratification strength; annual surface temperature and the effect of loads. The stratification strength is tested since it can indicate stagnant bottom water, hypoxic areas could be a proxy for denitrification rates, and DIN and DIP are often available from monitoring. DIN and DIP values are only taken from winter months, i.e., December, January and February. The selection of factors is a combination of what is given by theory, environmental factors that are known to have an impact on the environmental state and variables that are readily available.

The Coastal Zone Model System

The Swedish Coastal zone Model (SCM) is a multi-basin, one dimensional model based on the equation solver PROgram for Boundary layers in the Environment (PROBE; Svensson, 1998), coupled to the Swedish Coastal and Ocean Biogeochemical model (SCOBI; Marmefelt et al., 1999; Eilola et al., 2009). The model system was developed to calculate physical and biogeochemical states in Swedish coastal waters bodies. The set-up used in the present study includes 653 coupled basins covering the entire Swedish coast. The basins follow the water bodies defined by the water framework directive and mainly follow natural topographic constraints. The water exchange in the straits between the main water bodies is calculated from the baroclinic pressure gradients. The net flow through the sounds will be the same as the river discharge from land in order to preserve volume since the volume changes caused by precipitation and evaporation are neglected. The water exchange over the boundary between the coastal zone and the open sea is assumed to be in geostrophic balance, because normally this boundary is open with a width greater than the internal Rossby radius. The hydro-dynamical part of the SCM is integrated with high temporal resolution (10 min time step for hydrodynamics). Thus, changes in the physical characteristics, including, e.g., diurnal variations, freshwater and nutrient supplies, water exchanges and transports of substances between the sub-basins are resolved. The time step of the biogeochemical module (SCOBI) in SCM amounts to 1 h, which is sufficient to resolve biogeochemical sources and sinks in the sub-basins.

For this study, the model has been run for the 1985–2014 period. Below, the two main components of the model system, the forcing and set-up are described briefly. For more details the reader is referred to Almroth-Rosell et al. (2016) and other cited publications.

The PROBE Numerical Model

The physical model PROBE calculates horizontally averaged concentration profiles of all the state variables, including temperature and salinity. It calculates horizontal velocities, advection and mixing (Svensson, 1998). The surface mixing is calculated by a k–ε turbulence model, light transmission as well as ice formation growth and decay are also included in the model. The vertical resolution is half a meter in the uppermost layers, 1 m in the 4–70 m interval, and 2 m between 70 and 100 m. Below 100 m the layer thickness increases to 5 m and to 10 m below 250 m. The general differential equation solved for each dependent, laterally averaged variable, ϕ, in each basin can be written as

$$A\frac{\partial \phi}{\partial t} = \frac{\partial}{\partial z}(A\Gamma_\phi \frac{\partial \phi}{\partial z} - Q_z\phi) + q_{in}\phi_{in} - q_{out}\phi + AS_\phi + \frac{\partial A}{\partial z}J_{\phi bot}. \quad (11)$$

Here t is time, z vertical coordinate, A horizontal area, Γ_ϕ vertical exchange coefficient, S_ϕ source and sink terms per volume, $J_{\phi bot}$ bottom flux per bottom area, Q_z vertical volume flux, and q_{in} and q_{out} horizontal volume fluxes per meter depth to and from the basin through connecting straits. From volume conservations the latter three variables are related through

$$Q_z = \int_{-H_{max}}^{z} (q_{in} - q_{out})dz \quad (12)$$

where H_{max} is the maximum depth of the basin. The sources and sinks determined by the biogeochemical model are added and subtracted from S_ϕ.

The SCOBI Model

The SCOBI model describes the dynamic biogeochemistry of marine waters (Eilola et al., 2009). Nine pelagic and two benthic variables are described in the SCM. In the pelagic zone, three different phytoplankton groups (diatoms, flagellates and others, and cyanobacteria), one zooplankton group, one pool for detritus and three inorganic nutrients pools (nitrate, ammonium, and phosphate) are represented. The model also calculates oxygen and hydrogen sulfide concentrations, which are represented by "negative oxygen" equivalents (1 ml H_2S l^{-1} = −2 ml O_2 l^{-1}) (Fonselius and Valderrama, 2003). For the benthic layer the amounts of stored nitrate and phosphate are calculated. SCOBI has been used and validated in several studies, both coupled to the PROBE-Baltic (Marmefelt et al., 1999) and to the three dimensional Rossby Center Ocean model (RCO; e.g., Meier et al., 2011).

Burial, denitrification and N_2-fixation are the processes that affect the permanent retention in the model. The burial is parameterized from the concentration of nutrients in the active sediment layer (i.e., approximately 2–5 cm) and a burial rate constant that defines how large a fraction of the sediment nutrient content (mmol/m^2) that is to be buried in each time step. A burial constant is set for each water district. There is an additional burial of nitrogen due to a small amount of N-adsorption to sediment particles. For nitrogen, also denitrification contributes to the permanent removal. On the other hand, N_2-fixation adds organic N to the system in favorable conditions (i.e., a salinity below 10 and low N:P ratios, not active on the West Coast) and thus counteracts the removal of nitrogen, i.e., N_2 fixation causes negative retention of nitrogen. Denitrification is incorporated in the model in both the free water mass and in sediments. The pelagic denitrification is regulated by the redox state of water and the availability of nitrogen, while the benthic denitrification is regulated by bottom water oxygen concentrations and sediment nitrogen regeneration/mineralization.

One should note that the assimilation of nutrients taking place at the seafloor on illuminated sediments could affect water-sediment fluxes (Hoefsloot, 2017), and thus retention, but this is not yet explicitly described in the SCM.

For further details of the SCOBI model the readers are referred to Eilola et al. (2009); Almroth-Rosell et al. (2011), Eilola et al. (2011), and Almroth-Rosell et al. (2015).

Model Forcing

The SCM-SCOBI model system is forced by weather, atmospheric deposition of nutrients, the conditions in the sea outside the coastal zone, and discharge of freshwater and nutrients from land. The initial values for both the pelagic zone and the sediment are derived from spin-up simulations.

The weather variables are taken from the gridded Lars Mueller database (3-hourly meteorological synoptic monitoring station data) at the Swedish Meteorological and Hydrological Institute (SMHI) up until 2010. After that the forcing is based on MESAN model output (Häggmark et al., 2000). The insolation and all the radiation and heat fluxes across the water-air interface are calculated by the PROBE model. Atmospheric depositions of nitrogen species (NHX and NOX) are a climatic estimate based on a 3 year simulation (2001–2003) by the MATCH model (Robertson et al., 1999). For the deposition of phosphate a literature value of 0.5 mg m^{-2} month^{-1} is used (Areskoug, 1993).

Observations alone are inadequate to force the models open Baltic Sea and Kattegat boundaries since the temporal resolution is too low (monthly) and the information is incomplete (e.g., lacking information on zooplankton, phytoplankton and detritus). Hence, the lateral boundary of the outer archipelago to the open Baltic Sea is set by vertical mean profiles calculated by 1D PROBE set-up for each open sea area including assimilation of monitoring data.

The land derived forcing is divided in two types; discharge of water and nutrients as well as point sources representing sewage plants and industries. The discharge is given by the S-HYPE model (Lindstrom et al., 2010) and consists of river water, ground water and surface run-off from the drainage area surrounding each coastal basin. No reduction of river nutrients due to retention at river-mouths is assumed in this model setup. The loads from point sources mainly consist of nutrient loads reported in VISS[2] and data collected via personal communication with local and regional management boards to enhance time resolution for larger sewage plants. Thus, the loads from the point sources have varying time resolution.

Model Output Treatment

Model Skill Evaluation

Since the sub-basins of the model are horizontally averaged and the model system is forced by coarse-resolution weather and boundary conditions that may deviate from the actual situation, it is not realistic to expect reproduction of detailed synoptic features or patchy properties in the model results. Instead we focus the evaluation on averaged modeled and measured values during 1996–2014. To capture the characteristics of the basins we look at vertical profiles and seasonal cycles of salinity and the biogeochemical parameters in the surface and deep waters. Salinity represents the general circulation in the coastal zone and biogeochemical cycling is evaluated by nutrients and oxygen in the deep water while nutrients and salinity are evaluated in the surface water.

Since many monitoring stations in the coastal zone have poor data coverage either in the vertical or in time, a sub-set of the model results are extracted to represent the timing and vertical/annual location of the monitoring data. Model data is extracted for a week (±3 days) around any time of measurement and for ±3 m vertically around the measured depths. This allows for the usage of scarce monitoring data and still keeping the model output comparable. Observational data from all stations in a water body have also been combined to give better observational data coverage. Using several stations from different location also shows the horizontal range that can occur within a water body, which reduces the problem of comparability that can occur if only one monitoring station being placed in the outskirts of a water body is used.

The observational data used for validation are open access and extracted from SHARKweb[3]. The used stations are indicated in **Figure 1C**. The quality flags included in the data base output have been used to exclude data that the data host does not trust, e.g., values flagged as bad or suspected.

To give an overview of the model skill in the just over 200 basins included in the evaluation and avoid relying only on subjective visual inspection of the results, two dimensionless skill metrics, the Pearson correlation coefficient (r) and the mean of a cost function (C) (Eilola et al., 2009) are used (Eq. 13 and 14).

$$r = \frac{\sum_{i=1}^{n}(P_i - \bar{P})\,(O_i - \bar{O})}{\pm\sqrt{\sum_{i=1}^{n}(P_i - \bar{P})^2 \;\sum_{i=1}^{n}(O_i - \bar{O})^2}} \tag{13}$$

[2]http://viss.lansstyrelsen.se/

[3]http://www.smhi.se/klimatdata/oceanografi/havsmiljodata/marina-miljoovervakningsdata

$$C = \frac{\sum_{i=1}^{n} \left| \frac{P_i - O_i}{sdt(O_i)} \right|}{n}, \quad (14)$$

where i is the depth level or seasonal point in time in the vertical profiles or seasonal variations, respectively. The correlation coefficient compares the similarity in the shape of the vertical profiles and seasonal cycles between measured data (O_i) and model results (P_i) by evaluating the Pearson correlation (Eq. 13). The mean cost function value indicates the proximity of the model to measurements by normalizing the off-set between them with the standard deviation of the observations. If the average model results fall within the standard deviation of what is observed, C will be below one. For two data sets with identical shape, r will be 1 and if there is no correlation, r has values around zero. Similar approaches has previously been used in Edman and Omstedt (2013) and Edman and Anderson (2014) and is based on the recommendations given by Oschlies et al. (2010).The normality of the observational and model data-sets has been evaluated with the Lilliefors test (Lilliefors, 1967).

The estimation of r is problematic if the data distribution is too homogeneous, e.g., a well-mixed water body would give a straight vertical salinity profile without much spread in data and thus, make the analysis sensitive to any small, insignificant differences between the observed and modeled output distributions. Likewise, if the standard deviation of observed data is low, e.g., nutrient concentrations in summer surface waters are often below or close to the detection level and are thus set to the same default low values, the calculation of C becomes very high. Both situations would give indications of bad quality even if the actual problem would not be the model but the evaluation technique combined with the inherent quality of the data sets. Thus, for r computations the maximal spread in averaged observational data is set to be at least 10% of the average concentration of both model results and observations. For C, the standard deviation of observational data has to be at least 10% of the average concentration calculated from both model and observations, for the computation to be done.

Averages of the measured data have been calculated for occurrences of dense data distribution during the year and vertically, and the model output has been averaged for the same time and depth ranges. The evaluation has been performed for depth profiles of salinity (S), DIN, DIP, oxygen (O_2), seasonal surface variation of DIN and DIP as well as the bottom annual variation of O_2. For all vertical profiles the evaluation has been volume weighted so that more relevance is assigned to the accuracy in the large surface volumes of the water bodies.

Clustering of Water Bodies

Not all properties are valid or valuable to be calculated for individual water bodies, for example the coastal filter only makes sense to be calculated for a larger area that participates in the filtering of land load from rivers. Hence, besides calculating average results for the individual water bodies and for the entire coast, two more approaches are used in this study.

The first approach is to analyze the model results clustered together in seven major regions (MRs) (**Figure 1A** and **Table 1**): the Bothnian Bay coast (WD1, BB), the Bothnian Sea coast (WD2, BS), the Northern Baltic Sea coast (WD3, NBS), the East Coast (WD4, EC), the Gotland Coast (WD4, GC), the South Coast (mainly Skåne) (WD4, SC) and the West Coast (WD5, WC). The division is based on the five water districts that are used in Swedish coastal management and related to the different characteristics of the off shore water bodies. As described above, WD4 is divided into three parts; Gotland, Skåne and the rest of the east Swedish coast up to water district three. This approach should capture major differences or gradients along the coast, mainly based on off shore conditions, but also influenced by freshwater properties draining into each major area.

To investigate the influence of coastal type and freshwater conditions, the second approach is focused on specific key sites based on the coastal environments proposed in the BONUS COCOA project. The sites have been selected manually to give a few sites representing each of the coastal environments: archipelagos (AC), river dominated (RD), open coast (OC), or embayments, mainly fjords (EF) (**Figure 1B** and **Table 1**).

Calculation of Residence Times

The residence time is the average time that a water parcel resides within a defined water volume. In the present study, the residence time is calculated in three different ways:

(1) For the individual water bodies, i.e., the model basins, the average water age is calculated by the model using a concept that is described in detail by Engqvist et al. (2006). The values used in this study are the 20-year vertical volume weighted averages. Since the basins are calculated as horizontally homogeneous, the age can be used as a measure for the residence time because residence time (or average transit time) and average age are identical in case of well-mixed reservoirs, i.e., reservoirs that contain water parcels of all ages (Bolin and Rodhe, 1973).

(2) For larger clusters, containing several model basins, the equality between water age and residence time is no longer valid and we calculated the residence time as the total water volume in the cluster divided by the total outflow.

(3) To compare the filter efficiency calculated in this study to literature values, a third approach is applied where the freshwater residence time (τ_{qf}) is calculated as the freshwater volume in a cluster divided by the freshwater inflow it receives. This method follows the freshwater fraction method discussed by Sheldon and Alber (2006). A freshwater tracer is used to determine the freshwater volume. The filter efficiency refers to the filtering of nutrients carried by freshwater and thus, the flushing of the freshwater fraction is the relevant residence time.

Association Strength of Retention With Ambient Factors

To understand which factors that determine the retention in the coastal zone, the strength of association between nutrient retention and several ambient variables needs to be tested. However, the null hypothesis that retention values in the

water bodies are normally distributed was rejected by a Lilliefors test (Lilliefors, 1967) thus, we cannot use the common Pearson correlation. Instead, the Spearman rank correlation will be used to evaluate association strength. The correlation coefficient is denoted *Rho*. The Spearman rank correlation, or Spearman's *Rho*, does not require normally distributed samples and it also evaluates the monotonic relationship between two data-sets rather than their linear relationship. Since the association between the nutrient retention and ambient variables is not necessarily linear, the evaluation of monotonic relationships, i.e., the values should have a strict increase or decrease in the data-set, is better for this evaluation. A limit of $p < 0.05$ is used to determine significance.

RESULTS

Model Skill Evaluation

The model skill averaged over salinity, DIN, DIP, and oxygen, expressed as *C* and *r*, is acceptable in all water districts (**Figure 2**, numbers colored after WD). However, at the Bothnian Bay coast (WD1) the data coverage is still poor and thus it is hard to evaluate the model quality with any certainty, especially for oxygen. When the variables are evaluated separately within the WDs (**Figure 2**, colored markers) the averaged salinity bias in the north (i.e., WD1 and WD2) is not within two standard deviations of the measurement data, i.e., not acceptable. Neither is the model's skill to simulate oxygen in WD3. All other variables are simulated with an acceptable skill.

However, for specific basins (not shown) the results are sometimes very poor (or very good). Especially the shape of nutrient distributions, represented by $(1-r)$, compares poorly to what is observed in some basins. It is mainly the vertical correlation that causes too large biases (not shown). However, for this study it is more important that the levels are right, which is indicated by the *C*-values, and for the nutrient distributions only five basins have biases that are not acceptable (not shown). The averages shown in **Figure 2** are all good or acceptable with regard to *C* in all water districts.

Overview of Land Loads, Physical Characteristics and the Temporal Variability of the Coastal Nutrient Pool

The averaged mean depth in the water bodies along the coast (**Figure 3A**) is about 20 m but ranges from 0 to 60 m. The shallow areas are typically close to the coast, in fjords and bays, with some exceptions such as the deep Gullmars Fjord on the West Coast and parts of the Stockholm archipelago. The deepest locations are found in the northern parts of the Swedish West Coast and outer rim of the Bothnian Sea coast. Also locations in the outer part of the Stockholm archipelago and the northern tip of Gotland have relatively large mean depths.

Residence times in the model (**Figure 3B**) are most commonly between 1 and 10 days and tend to co-vary with the mean depth, i.e., deeper basins tend to have longer residence times. However, there are exceptions, e.g., the northern part of the West Coast where the residence times in the outer part of the coastal zone are comparable to the averaged residence time in WD1, even if the area is very deep. Some of the more open areas between the mainland and the Öland Island, as well as the outer waters of the Bothnian Bay coastal stretch, have residence times of up to 25–30 days, while the shallow inner areas of the coastal zone can have either very short residence times of as small as 1 day or less, or up to 30–40 days.

The nutrient load normalized to the areas (**Figures 3C,D**) shows that the relative load is lowest to the south-east Swedish coast, especially Gotland. The pressure of anthropogenic nutrients is highest at the West Coast followed by the Bothnian Bay. Almost one third of the nitrogen (32%) and phosphorus (29%) from land and air to the Swedish coastal zone is discharged to the West Coast (not shown). The spatial distribution of the normalized nitrogen and phosphorous loads are similar. The normalized load ranges between 0.1 and 10 t nitrogen per km^2 and 0–0.3 t phosphorus per km^2, annually.

The development of the nitrogen and phosphorus pools over the 30 years of the model run is illustrated in **Figure 4**. The phosphorus pool decreases on the west and south-eastern coastal stretches but increases in the coastal zone bordering the Bothnian Sea. At the Bothnian Bay and the Northern Baltic proper coasts, the pool at the end of the run is very similar to the initial values in 1985. However, in both areas the values decrease in the period in between and then rise again in recent years. The recent increase in the modeled pools is most likely due to increased phosphorus content in the open sea forcing. For nitrogen, the general patterns are the same as for phosphorus, but for individual years the behavior of the nitrogen and phosphorus pools differs.

Estimations of the Coastal Filter Efficiency

The filter efficiency of nitrogen and phosphorus in relation to the depth to residence time ratio (H/τ_{qf}) is shown in **Figure 5**. This relation has previously been used in earlier studies (Nixon et al., 1996; Billen et al., 2011; Hayn et al., 2014; Almroth-Rosell et al., 2016). The present study adds the entire Swedish coast, the seven MRs and the smaller key sites. Most of the key sites and MRs investigated in this study have the same dependence on H/τ_{qf} as seen in previous studies. The association is negative and the range is rather wide. The range depends on the different environmental conditions of the studied areas.

Retention, Retention Efficiency and Filter Efficiency in the Swedish Coastal Zone

The average, annual retention for the Swedish coast is approximately 71 Kt nitrogen and 2.9 Kt phosphorus (**Table 2**). The nutrient filter capacity of the entire Swedish coast is estimated to be about 60% (approximately 53% for nitrogen and 69% for phosphorus) and thus, less than half of the input from land can be assumed to be exported from the coastal zone to the open sea. However, the differences between the water districts are large. The lowest filtering of land nitrogen occurs in the coastal zone of the Gulf of Bothnia while the

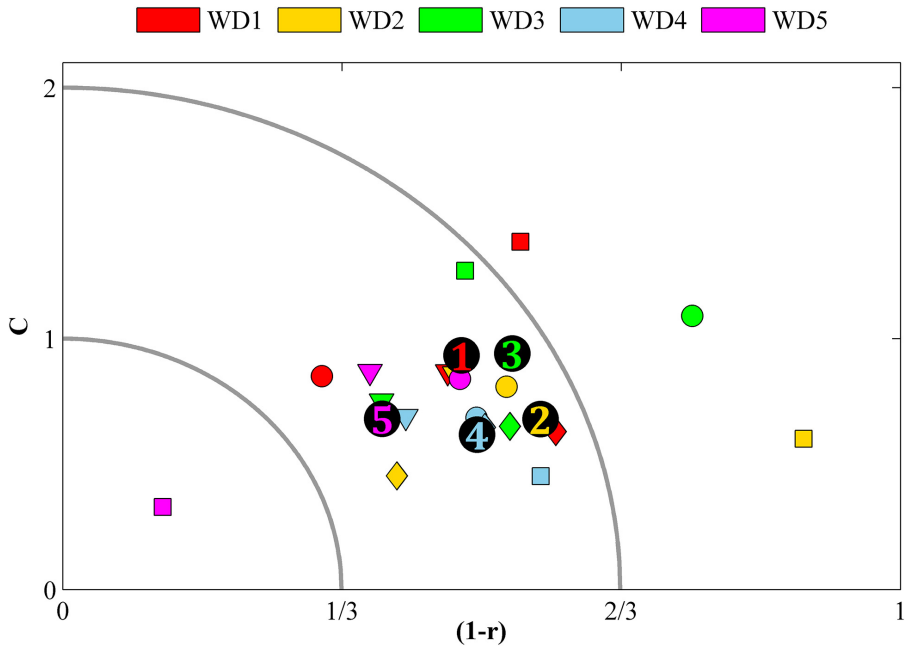


FIGURE 2 | Model bias shown as combination of correlation bias (1–*r*) and mean bias *C* in the five WDs. Colored markers denote the averaged bias for a single variable (square = salinity, round = oxygen, diamond = DIN and triangle = DIP) in a WD. Numbers mark the average bias in a water district (all variables included). Markers inside the outer quarter circle has a combined *C* and 1–*r* bias that indicate that the model skill is acceptable and markers within the inner quarter circle indicate good model skill. Markers outside the quarter circles indicate too large biases.

lowest phosphorus filtering is calculated for the Swedish West and South Coasts. The Gotland Coast, WD3 including the Stockholm archipelago, and the East Coast in WD4 all retain more than 100% of the land and air load they receive. Thus, these areas have a net import and retention of open Baltic Sea nutrients and filter not only the land load but also the Baltic Sea water.

The total retention is divided in temporary retention, i.e., the nutrient storage changes in the coastal zone, and the permanent retention caused by net removal of nitrogen through denitrification and permanent burial in sediments (**Table 2**). For the modeled period the permanent retention is always positive but the temporary retention is negative for all areas except the Bothnian Sea coast.

However, the absolute value of the long term temporary retention is almost always smaller than the long term permanent retention and as a consequence, the total retention values are positive. The only exception in this study is a stretch of open coastline in the south of Sweden (**Table 3**, key sites) where the total retention of phosphorus is negative. For nitrogen the temporary retention is typically 1–2 orders of magnitude smaller than *PNR*. For phosphorus, the values are typically one order of magnitude smaller, only occasionally are they of the same order of magnitude as *PNR*. Thus, the total retention of phosphorus is more affected by the negative temporary retention than nitrogen.

The 20-year average nutrient retention in individual water bodies range between approximately 0–0.25 t P km^{-2} and 0–7 t N km^{-2} annually for phosphorus and nitrogen, respectively (**Figure 6**). In **Figure 6**, the nutrient retention has been normalized to the sediment areas of the water bodies to avoid that their different sizes affects the visual impact of the results. The nitrogen retention is highest on the west coast and in certain near shore basins on the east coast, e.g., water bodies in the inner Stockholm archipelago. Phosphorus retention is highest along the Bothnian Sea shore, especially in the water bodies bordering the Baltic Sea. Overall, the phosphorus retention is high in some near shore protected bays but not in all such locations. There is also a tendency that low retention of both nutrients occurs in basins in-between the open Baltic Sea and the inner bays and estuaries.

The retention efficiency, i.e., the percentage of retained total load, in the individual water bodies in the Swedish coastal zone, shows the same general spatial patterns for both nutrients (**Figure 7**). The nutrient removal is most efficient close to land, in bays, fjords and archipelagos.

Filter Efficiency at Key Sites

Judging from the average values from each type of area, archipelagos and open coastlines tend to be the most effective nutrient filters (**Table 3**). However, due to the large variability within each coastal type this result does not give strong support to any general patterns of filter efficiency. For open coastlines, the averaged E_F is over 100% and for archipelagos, 36 and 38%, for phosphorus and nitrogen, respectively. River dominated areas without archipelagos have slightly lower filter capacity (20% phosphorus and 16% nitrogen), but the variability is large. For embayments the filter is usually more efficient for nitrogen,

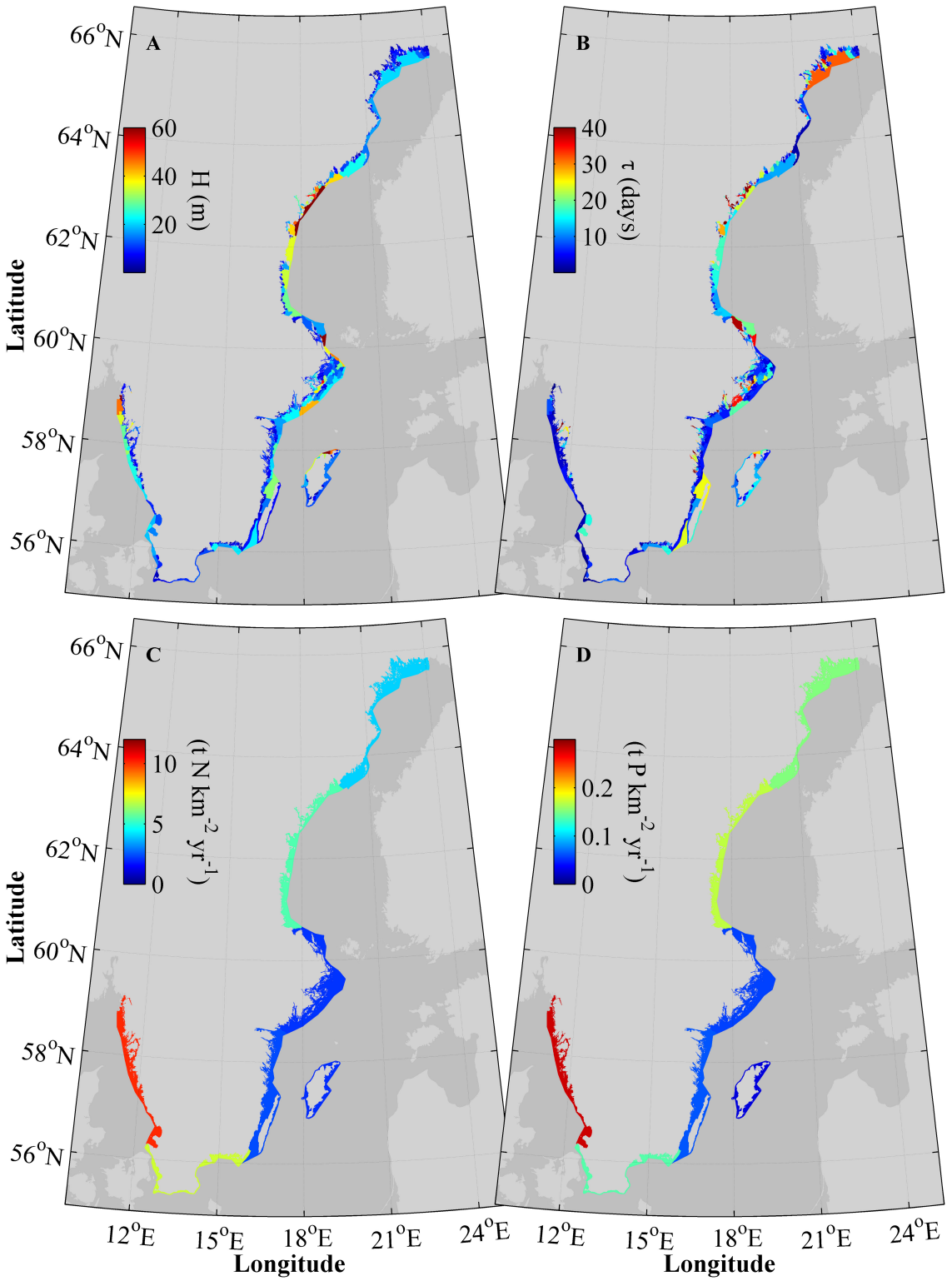


FIGURE 3 | Mean depth, *H*, **(A)** and average age, τ, **(B)** for the individual water bodies along the coast, and land load (S-HYPE and point sources) normalized to area **(C,D)** for the seven MRs.

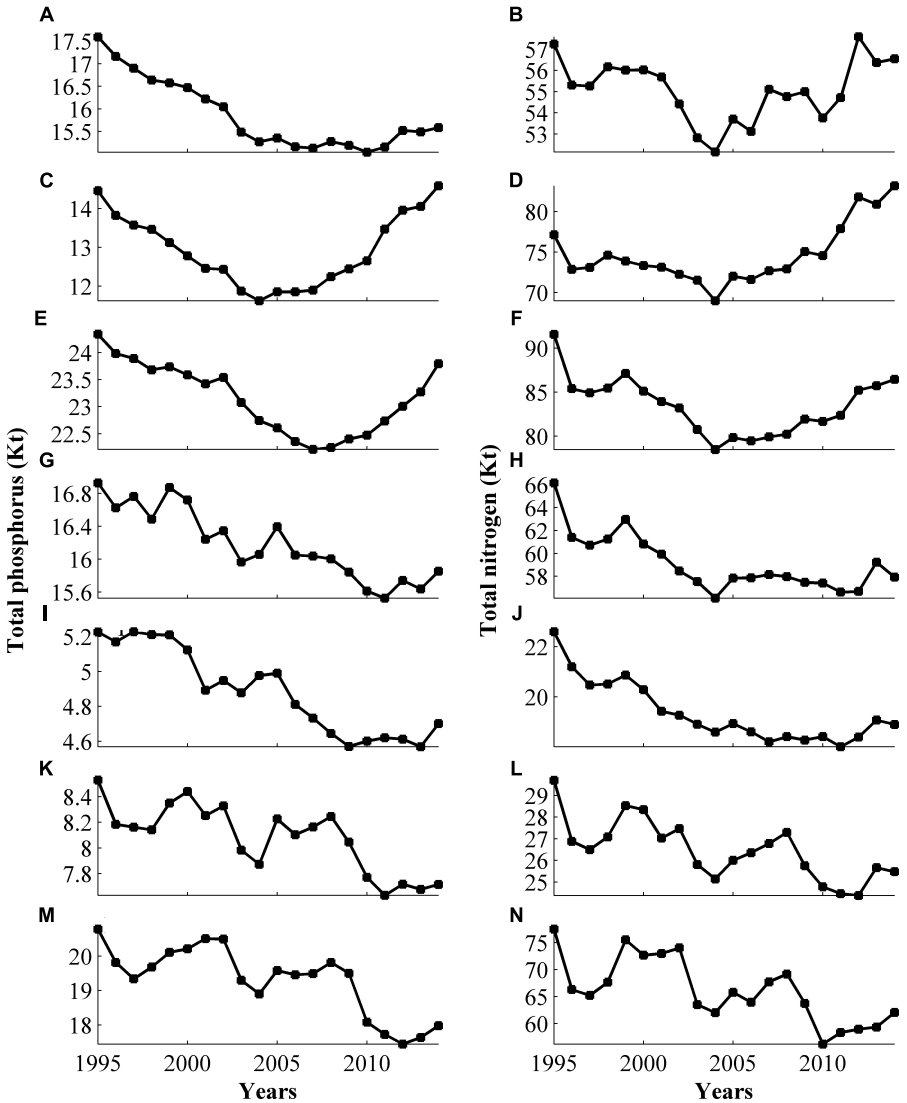


FIGURE 4 | Annually averaged nutrient reservoirs in the Bothnian Bay **(A,B)**, the Bothnian Sea **(C,D)**, the Northern Baltic Sea **(E,F)**, the East Coast **(G,H)**, Gotland **(I,J)**, the South Coast **(K,L)**, and the West Coast **(M,N)**, expressed in Kt. The reservoir is the sum of the vertically integrated pelagic and benthic nutrient in dissolved inorganic, and organic and particulate organic forms.

while the other coastal types show no difference between the nutrients.

The most effective river dominated site is the Öre estuary where approximately 33–45% of the nutrients from land are retained or removed in the coastal zone close to land. These are higher percentages than calculated for the Norrbotten and Göteborg archipelagos. The high values for the open coastlines are an effect of extremely high values for the northern Bothnian Sea coast.

Temporal and Permanent Components of Total Nutrient Retention

This section describes how the modeled total retention (R_{tot}) is associated to temporal storage (ΔM) and *PNR* and also how these two components relate to each other. In **Figures 8A,B** each small colored dot represents 20 annual averages within a basin. The squares in the same figures represent data-sets of a 20-year average from each basin within a larger area. The squares thus show how the average R_{tot} is associated to averaged ΔM and *PNR* within either an MR or the entire Swedish coast.

Long-Term Average Retention

The average R_{tot} (**Figures 8A,B**, colored squares) is very strongly associated to *PNR*. This was expected and agrees with previous result in Almroth-Rosell et al. (2016) and Section "Estimations of the Coastal Filter Efficiency" in this paper where it is stated that the average *PNR* is usually at least one order of magnitude larger than the absolute average ΔM. The association of the average R_{tot} to ΔM is instead negative with the exception of

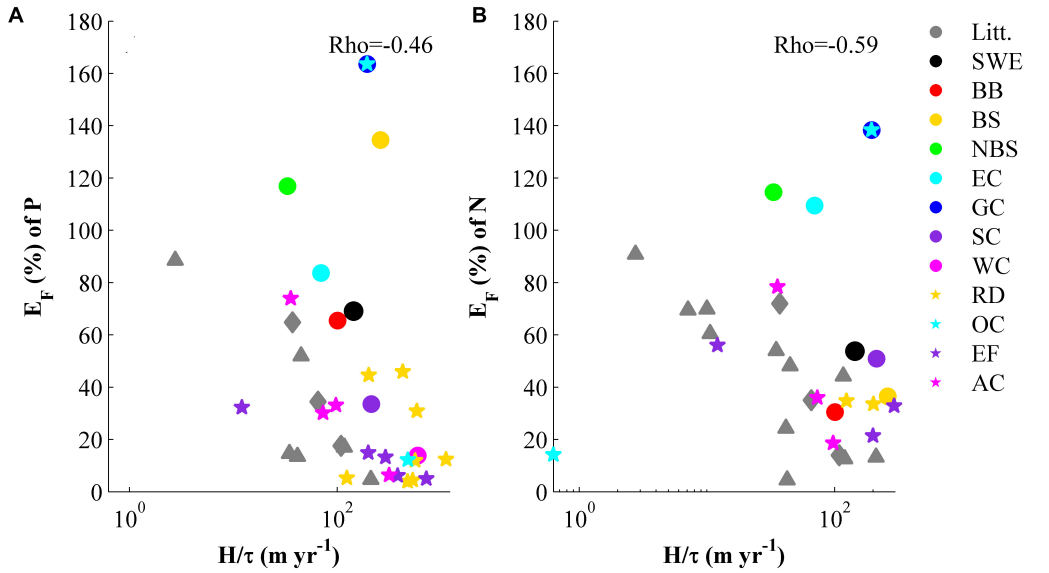


FIGURE 5 | Filter efficiency, E_F, of phosphorous **(A)** and nitrogen **(B)**, versus the ratio between the depth and the residence time (H/τ). The literature data (gray triangles) are from Nixon et al. (1996); Billen et al. (2011), Hayn et al. (2014) and the gray diamonds are values from Almroth-Rosell et al. (2016). The colored dots and stars are from this study (abbreviations in the legend according to **Table 1**).

TABLE 2 | Averaged (1995–2014) depth (H), residence time (τ), total retention (R_{tot}), permanent net removal (PNR), temporary changes in nutrient storage (ΔM), retention efficiency (E_R) and filter efficiency (E_F) in the seven major regions.

	H (m)	τ (days)	R_{tot} (ton yr^{-1})	PNR (ton yr^{-1})	ΔM (ton yr^{-1})	E_R (%)	E_F (%)
Nitrogen							
Entire Swedish coast	20.9	6.5	70645.3	72368.9	−1723.6	0.7	53.8
Bothnian Bay	16.1	7.6	8022.3	8161.8	−139.5	0.6	30.5
Bothnian Sea	35.5	12.8	9153.5	9037.2	116.3	0.7	36.5
Northern Baltic	20.5	7.3	12720.4	12978.8	−258.4	0.7	114.6
East coast	16.1	8.4	10410.3	10779.9	−369.6	0.9	109.5
Gotland	18.7	10.7	3287.8	3481.7	−194.0	1.0	138.4
Southern coast	12.8	2.2	7428.9	7593.9	−165.0	0.5	50.9
West Coast	23.9	3.5	19622.1	20335.6	−713.4	0.7	46.9
Phosphorous							
Entire Swedish coast	20.9	6.5	2946.0	3227.8	−281.8	0.4	69.1
Bothnian Bay	16.1	7.6	691.8	792.9	−101.1	2.0	65.5
Bothnian Sea	35.5	12.8	1084.3	1066.7	17.7	1.8	134.6
Northern Baltic	20.5	7.3	446.6	450.1	−3.4	0.4	116.9
East coast	16.1	8.4	273.7	307.4	−33.7	0.3	83.7
Gotland	18.7	10.7	67.0	84.6	−17.6	0.3	163.6
Southern coast	12.8	2.2	127.0	158.4	−31.4	0.1	33.6
West Coast	23.9	3.5	255.5	367.8	−112.2	0.1	13.9

the Bothnian Sea and northern Baltic Sea coasts. Neither of the latter coastal stretches seem to have any association (open squares in **Figure 8A**) between R_{tot} and ΔM for phosphorus. The Bothnian Sea coast has a positive association between R_{tot} of nitrogen and ΔM (yellow square in **Figure 8B**), contrary to all the other investigated regions. This gives that the average R_{tot} within a water body is usually determined by its PNR rate, but also that water bodies with less changes in nutrient storage are more likely to have a high total retention, but the cause for this is not yet determined. It was also found (not shown) that a system with a higher total load tends to have a lower, most likely negative, average temporary retention compared with systems with a lower total load. This may be caused by load reductions from large point sources during the investigated period and thus, it is not a generally applicable result.

TABLE 3 | Averaged (1995–2014) depth (H), residence time (τ), retention efficiency (E_R) and filter efficiency (E_F) at the key sites, with averages for each coastal type in bold numbers.

	H (m)	τ (days)	E_R (%)	E_F (%)	E_R (%)	E_F (%)
			Nitrogen		Phosphorous	
River dominated areas:						
Kalix estuary	5.7	3.9	3.3	7.8	8.5	11.9
Umeå estuary	7.6	2.1	1.7	5.7	3.5	12.4
Öre estuary	11.1	10.5	1.5	33.5	3.4	44.6
Ångermanälven estuay	26.9	8.3	1.1	10.1	4.2	45.9
Gävle bay estuary	16.3	10.2	2.2	10.4	5.7	30.9
Emån estuary	5.5	2.4	0.6	9.4	0.2	4.4
Mörrum estuary	8.6	1.5	0.5	14.5	0.1	4.0
Kungälv bay estuary	7.6	11.0	5.3	34.8	1.2	5.2
	11.2	**6.2**	**2.0**	**15.8**	**3.4**	**19.9**
Open coastlines:						
Southern Bothnian Bay	8.2	5.6	0.1	14.1	0.4	−102.5
Northern Bothnian Sea	35.4	16.9	0.8	297.6	2.1	1218.4
Gotland Island	18.7	10.7	1.0	138.4	0.3	163.6
Southern Skåne coast	9.7	2.5	0.6	26.1	0.1	12.2
	18.0	**8.9**	**0.6**	**119.1**	**0.7**	**322.9**
Embayments (fjords):						
Bråviken Bay	11.0	4.2	1.5	21.4	0.6	14.9
Gamlebyviken Bay	9.6	14.7	3.2	56.1	1.1	32.2
Laholm Bay	12.1	15.5	5.7	32.8	1.1	13.2
Gullmars fjord	33.5	13.4	2.1	32.7	0.5	5.0
Idre fjord	12.9	4.7	2.5	24.7	0.5	6.2
	15.8	**10.5**	**3.0**	**33.5**	**0.8**	**14.3**
Archipelagos:						
Norrbotten archipelago	8.2	5.8	1.2	18.6	4.2	33.1
Stockholm archipelago	16.3	5.8	0.7	78.4	0.4	74.0
Blekinge archipelago	5.1	4.3	0.9	36.0	0.3	30.1
Göteborg archipelago	10.0	2.8	1.2	17.7	0.3	6.4
	9.9	**4.7**	**1.0**	**37.7**	**1.3**	**35.9**

Interannual Variability of Retention

On inter-annual timescales (**Figures 8A,B**, colored dots) the total retention in a water body is generally associated with ΔM, in contrast to the results in Section "Long-Term Average Retention." This result is in agreement with Almroth-Rosell et al. (2016). For phosphorus the association is very strong for all basins but for nitrogen the association is insignificant at some locations, especially around Gotland (blue dots) and the South Coast (purple dots). These basins with low inter-annual association of R_{tot} to ΔM tend to have stronger inter-annual association of R_{tot} to PNR instead. This gives that annual fluctuations of R_{tot} within a water body are most likely caused by changes in the amount of nutrient it holds. However, for nitrogen there can also be an influence of an increased removal rate (i.e., increased denitrification or burial). On inter-annual timescales a majority of the modeled water bodies tended to have a positive temporary retention if the load increases to a basin (not shown).

The Impact of Sediment Area on Permanent Retention

Changes in a water body's nutrient content are usually negatively associated to PNR within the MRs (colored Rho values in **Figures 8C,D**), but for the coast as a whole, the association is weaker than for the individual regions. It is likely that the negative association between ΔM and PNR is caused by both being associated to the size of the water bodies. The correlation between PNR and sediment area is strong (not shown) with Rho of 0.89 for both phosphorus and nitrogen. The results are clearly grouped after water district and the correlation is stronger when the association is evaluated separately for MRs. The differences between the water districts are caused by the use of different burial rate constants. ΔM is negatively associated to the sediment area (A) (not shown), i.e., smaller water bodies tend to have larger fluctuations in their nutrient storage. The correlation of ΔM with A is strong for most MRs, with the exception for Bothnian Sea coast and the northern Baltic Sea coast were the association was weak or slightly positive. The resulting association of ΔM with A

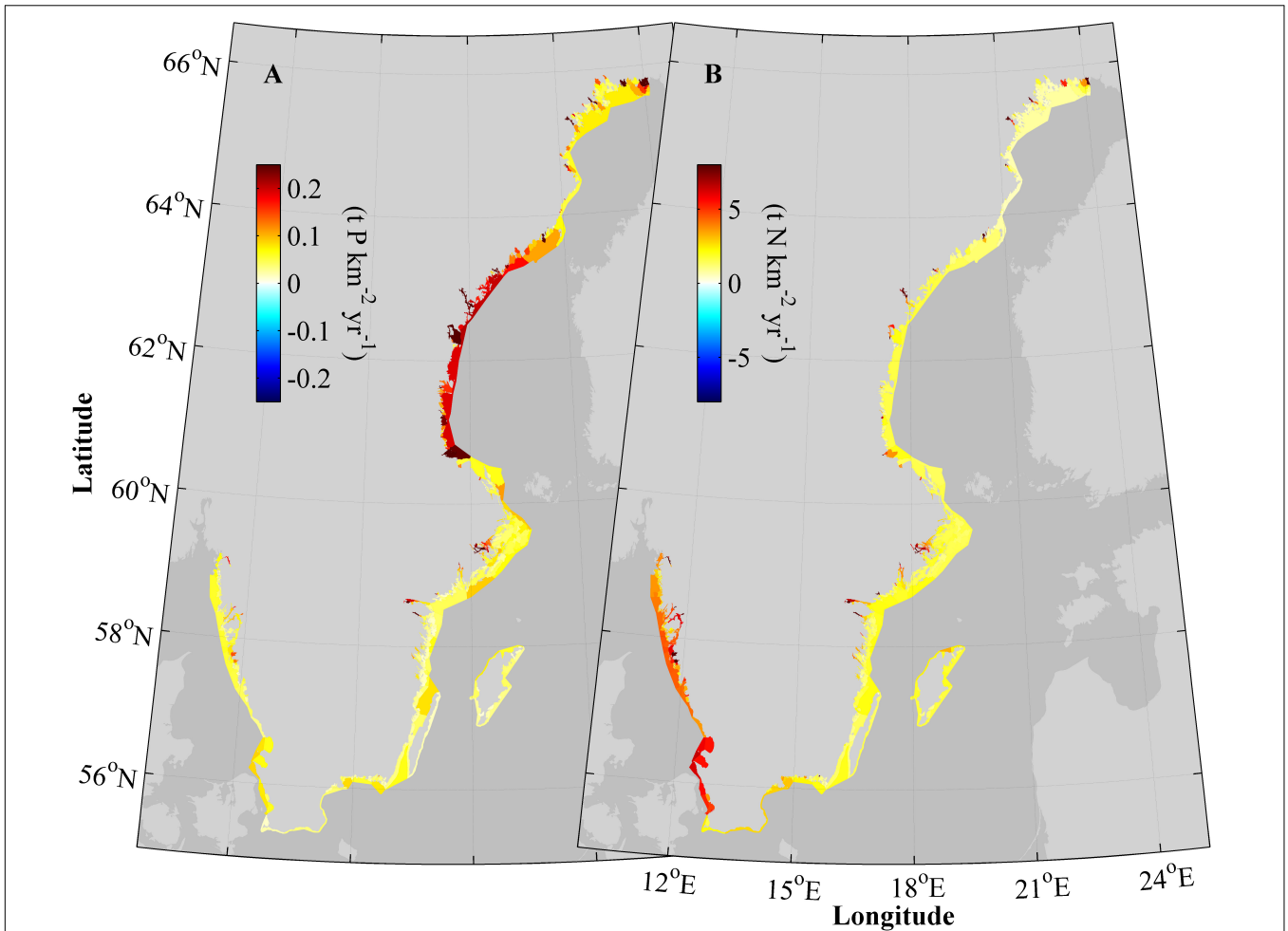


FIGURE 6 | A 20 years average (1995–2014) of total retention, R_{tot}, of phosphorous **(A)** and nitrogen **(B)** normalized to area and in all modeled water bodies.

for the coast as a whole is −0.50 and −0.63 for phosphorus and nitrogen, respectively.

Estimating Retention Efficiency From the Physical Characteristics of Water Bodies and Environmental Indicators

The retention efficiency (E_R) does not have strong association to a water body's surface area (**Figures 9A,B**), even if *PNR* does. Instead E_R is positively associated with τ (**Figures 9E,F**) and also negatively associated with H (**Figures 9C,D**), even if the latter association is weaker. When the two properties are combined as τ/H or according to Eq. 9, the correlation increases (**Figures 9G–J**) with a *Rho* of 0.71 and 0.75 for phosphorus and nitrogen, respectively. The use of Eq. 9 does not strengthen the association for either of the nutrients (**Figures 9I,J**) in comparison with the simpler expression τ/H. This is true also when the MRs are evaluated separately.

The apparent removal rate (V_S) seems to have similar associations with the environmental factors for both nutrients and will be evaluated together (**Figure 10**). Where important differences occur they will be mentioned. The averaged V_S for the Swedish coast was estimated to 0.025 m day^{-1} for phosphorus and to 0.022 m day^{-1} for nitrogen with ranges of 0–0.43 m day^{-1} and 0–0.16 m day^{-1} for phosphorus and nitrogen, respectively. For nitrogen, V_S tends to be higher on the West Coast while for phosphorus the highest average is calculated for the Bothnian Bay.

The theory in Section "Theory of Steady State Retention" for a steady state water body suggested that the M_{sed}:C_{pel} ratio would affect the retention efficiency and the results in **Figures 10A,B** affirm this assumption. The M_{sed}:C_{pel} ratio stands out as positively associated with retention efficiency for both nutrients in all MRs. The association is strong and homogeneous across the MRs. For the coast as a whole E_R of nitrogen is also strongly associated to the nitrogen M_{sed}:C_{pel} ratio and likewise E_R of phosphorus associates strongly to the phosphorus M_{sed}:C_{pel} ratio. However, for the coast as a whole the nutrient retention does not cross-associate.

V_S has a weaker, but homogeneous, positive association with stratification strength, the maximum hypoxic area and with all expressions of nutrient concentration. Thus, the permanent

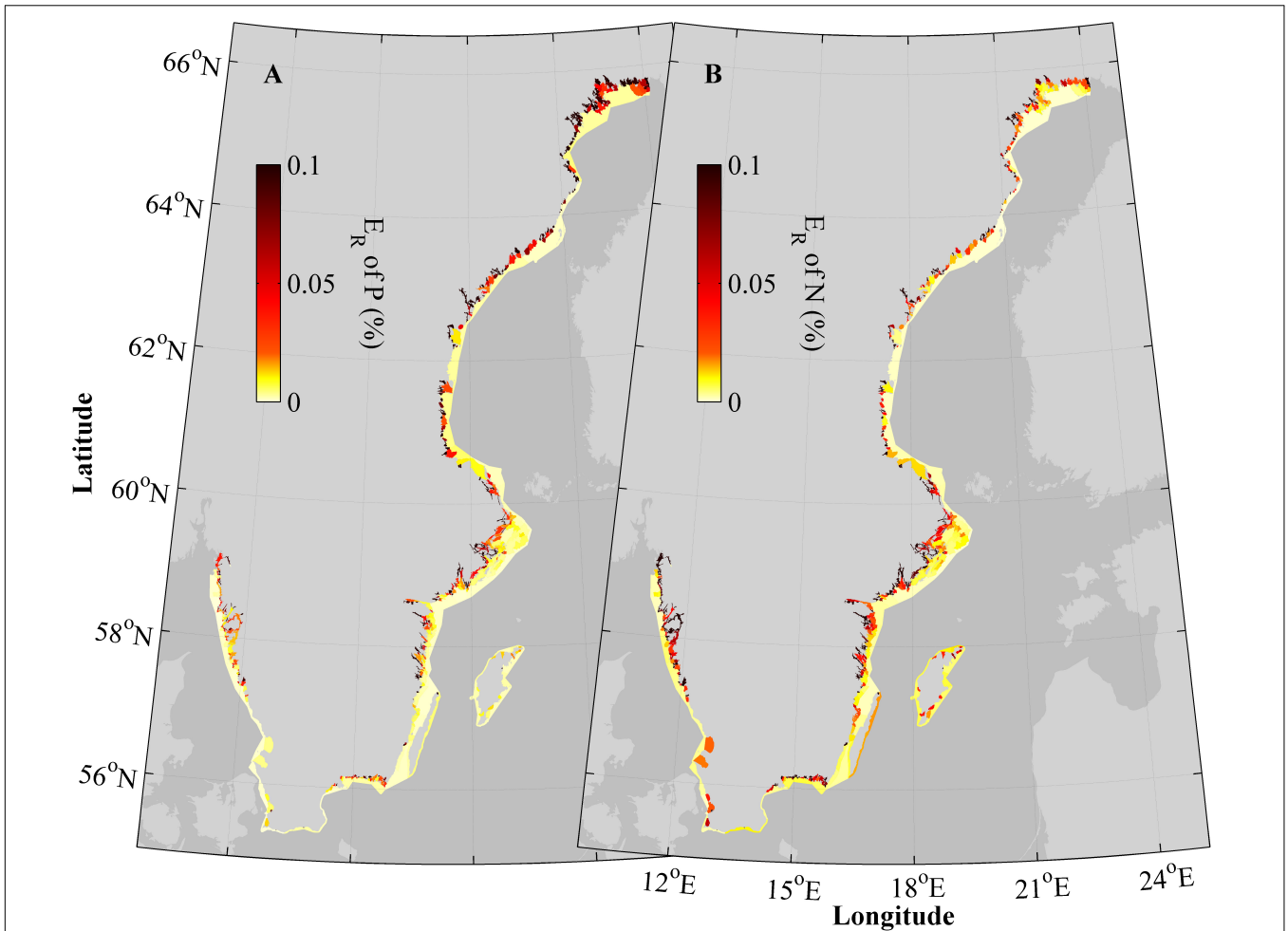


FIGURE 7 | A 20 years average (1995–2014) of total retention efficiency, E_R, of phosphorous **(A)** and nitrogen **(B)** in all modeled water bodies.

retention of both nitrogen and phosphorus generally tends to increase with eutrophication. For the entire coast (black triangles in **Figure 10**), V_S can be differently associated with some environmental indicators than what is seen for the MRs when they are evaluated separately. This is due to model settings and climate differences along the coast that affect some indices. This concerns DIP, DIN:DIP, pelagic Ntot:Ptot, surface temperature and salinity.

The only clearly negative association, i.e., indicated by a significant association in a majority of the evaluated regions and without contradictory results, in **Figure 10** is the V_S of nitrogen that is negatively associated to the pelagic DIN:DIP factor in all MRs. Thus, the modeled retention of nitrogen is more effective at lower N:P ratios, i.e., when there is no overabundance of nitrogen. When looking into the details of the association (not shown), the same tendency is found for phosphorus V_S. For the remaining environmental indices the correlation is either insignificant or the association to retention efficiency seem to vary between the regions (the colored dots are scattered and/or of different sign).

The same analyze was performed for *Blr*, calculated from re-arrangement of Eq. (10) (not shown) but fewer clear associations were found. The analyze gave no clear indication of which environmental condition that are associated with high benthic loss rates of phosphorus but for nitrogen associations to M_{sed}:C_{pel}, both inorganic and total nutrient rations and high surface temperatures were found. The associations to nutrient ratios were positive in all MRs except for the Bothnian Bay coastline where the association was positive up to an N:P of about 50 but decreased after that point. For phosphorus an average *Blr* was calculated to be 4e-10 day^{-1} and for nitrogen 1e-9 day^{-1}.

DISCUSSION

Model Validation

Properties such as integrated internal nutrient losses and retention efficiency are easily extracted from a numerical model since all the biogeochemical transformation rates are calculated for each water body. Thus, a modeling approach gives a homogeneous and more complete data-set than observations. However, model results will always be dependent on the

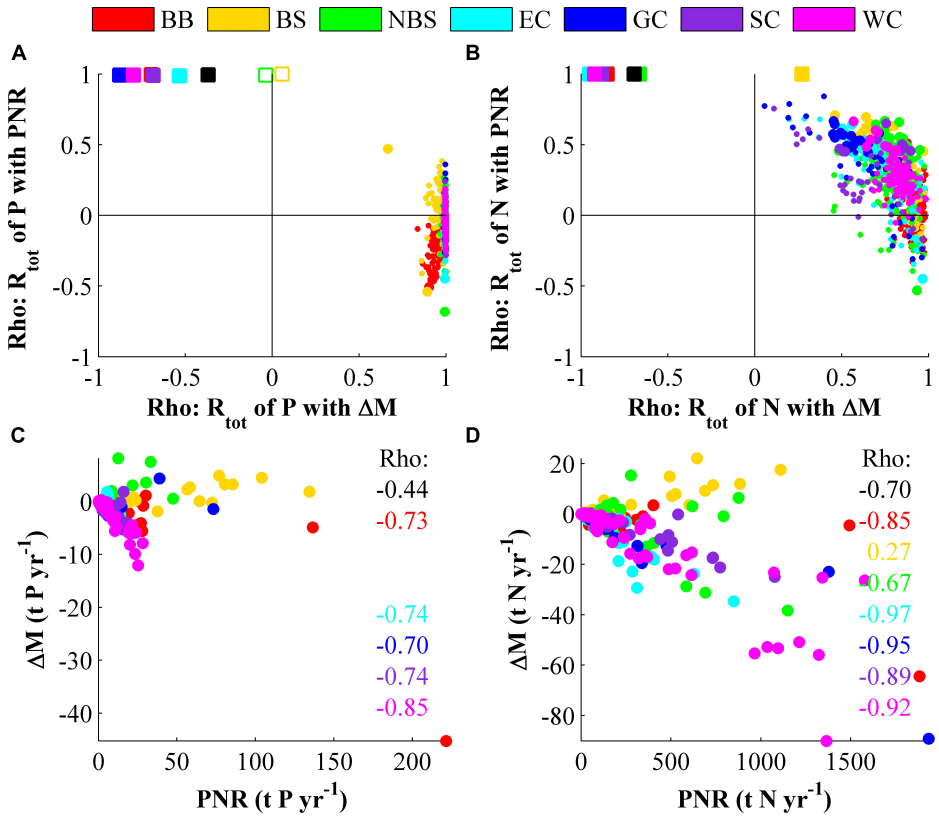


FIGURE 8 | Association strength (Spearman's rank correlation, *Rho*) of total retention (R_{tot}), internal losses (*PNR*) and changes in nutrient storage (ΔM). **(A,B)** Each marker represents a data-set for which the association strength of R_{tot} to *PNR* and ΔM has been calculated. The correlations in data-sets consisting of inter-annual variations within basins are shown as colored dots and correlation of 20-years averages are shown as colored squares. Smaller dots and open or missing squares denote that the correlation was insignificant ($p > 0.05$) for one correlation coefficient. **(C,D)** Show 20-year averaged values from each basin. Statistically significant ($p < 0.05$) *Rho* values are printed in the figure.

parameterizations that describe the biogeochemical processes and by definition a model will never cover everything that can occur in reality. Also the forcing and boundary conditions may be crucial for the results. The essential question is if it is good enough to answer the question at hand. Although, the validation shown in this paper indicates that the average skill of the model is acceptable, it also shows that for individual basins it can be poor. Thus, the results cannot be expected to be valid for every local situation, but still good enough to extract system understanding. Also the limitations associated with measurements, e.g., restrictions in time and location, as well as differences in vertical distribution at the different stations within a single basin make it difficult to evaluate the models' quality. One area mentioned explicitly in the results is the Gotland coastline. Unfortunately not enough validation data were available for this area and hence, not a single water body could be validated. The model calculations for the Gotland coastline gave very high retention and generally extreme values, and since no validation is available these results should be treated with precaution.

Uncertainty of Biogeochemical Processes

It must also be noted that some biogeochemical processes are still missing in the model formulation. For example, the assimilation of nutrients by macrophytes and benthic microphytes is not explicitly described in SCM. In the model, these nutrient uptakes are partly compensated for by pelagic production and subsequent sedimentation. The difference between production that falls onto sediment and a production that takes place directly on illuminated seafloor is uncertain. Benthic microalgae do play an important role for total primary production capacity, e.g., in the northern Baltic Sea (Ask et al., 2016). According to Sundbäck et al. (2004) microphytobenthic (MPB) nitrogen assimilation often exceeds nitrogen removal by denitrification, partly because MPB activity suppresses denitrification and benthic production by MPB, and thus affects nutrient pathways in the sediment. Perennial macrofauna retains assimilated nutrients interannually and the uptake can be substantial. The effect on nutrient retention does, however, depend on the type of macroplants. To cause a permanent removal of nutrients macrofauna needs to produce refractory organic material, which can increase the removal by

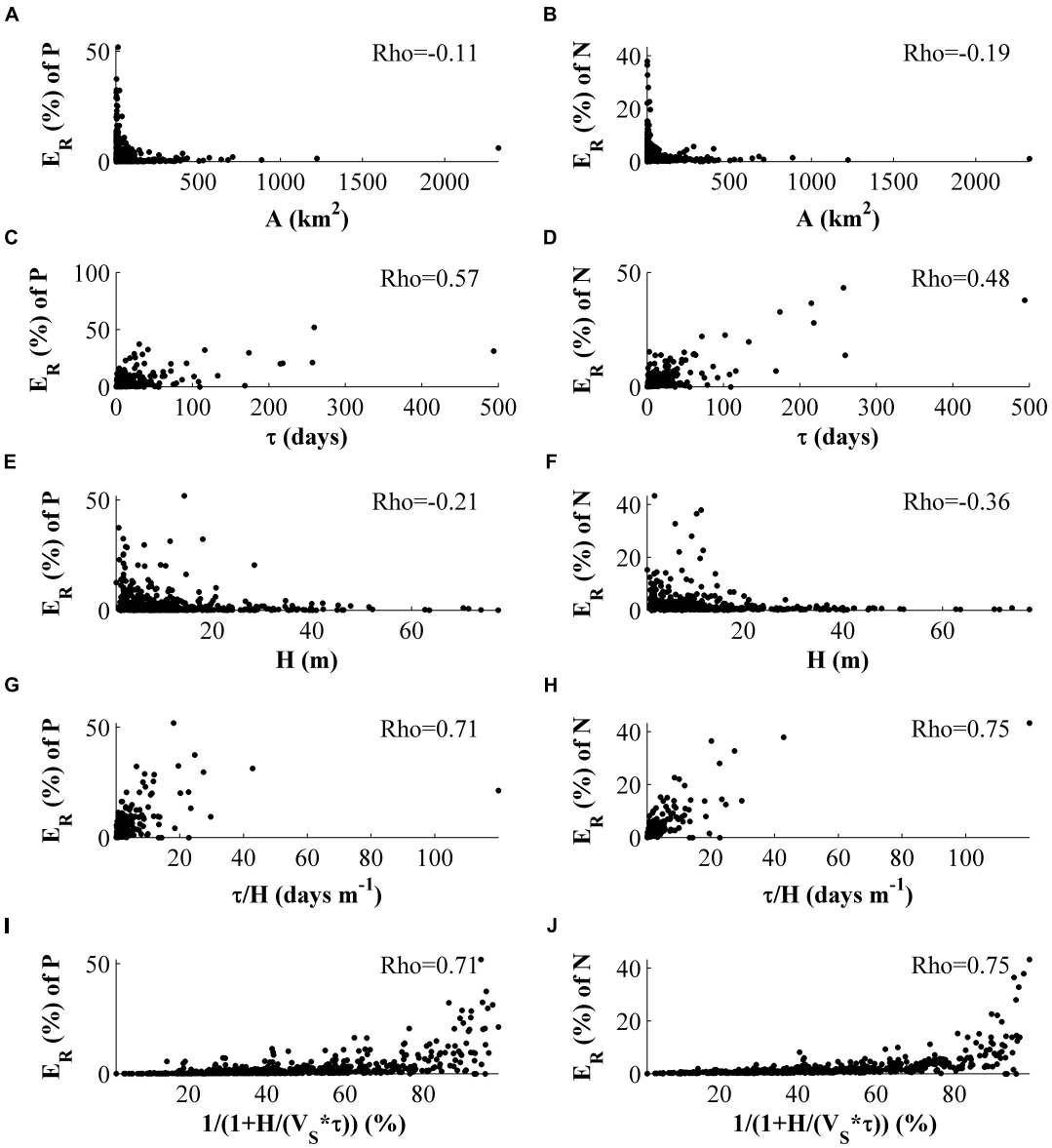


FIGURE 9 | Association of E_R (*PNR* in percent of total load per area) with physical characteristics of the basins, i.e., surface area (*A*) **(A,B)**, residence time (τ) **(E,F)** and mean depth (*H*) **(C,D)**, in different formulations **(G,H,I,J)**. V_S is set to 1. Only statistically significant ($p < 0.05$) *Rho* values are printed in the figure.

burial but plants might also outcompete bacteria for nitrogen and thus, decrease denitrification (McGlathery et al., 2007). Macroalgae that are advected with the water or are decomposed on an annual basis will affect retention only temporary.

In order to fully evaluate and understand the relative role of MPB and macro faunal production on the long-term retention of supplied nutrients, a module that takes into account the many effects of both macrophytes and benthic microphytes is needed. This model development and its evaluation were outside the scope and main focus of this study. Also, modeled sediment concentrations should ideally be evaluated against measurements. This work is ongoing, but sediment nutrient data are scarce, as shown by Hoefsloot (2017).

Nutrient Retention Along the Swedish Coastline

In this study, the Swedish coastal zone retains the largest amount of nitrogen per area on the west coast while the highest amount of phosphorus per area is retained along the Bothnian Sea shore (**Figure 7**). The filter and retention efficiencies on the West Coast are either comparable or lower than the rest of the Swedish coastal zone (**Table 2**), even though the West Coast has a slightly higher V_S. Thus, it can be concluded that the high total retention on the West Coast is not due to a more effective removal but rather to high nutrient load, likely the land loads (**Figures 3C,D**). Since the West Coast has low E_R for phosphorus, the high load does not result in an equally high retention of this nutrient.

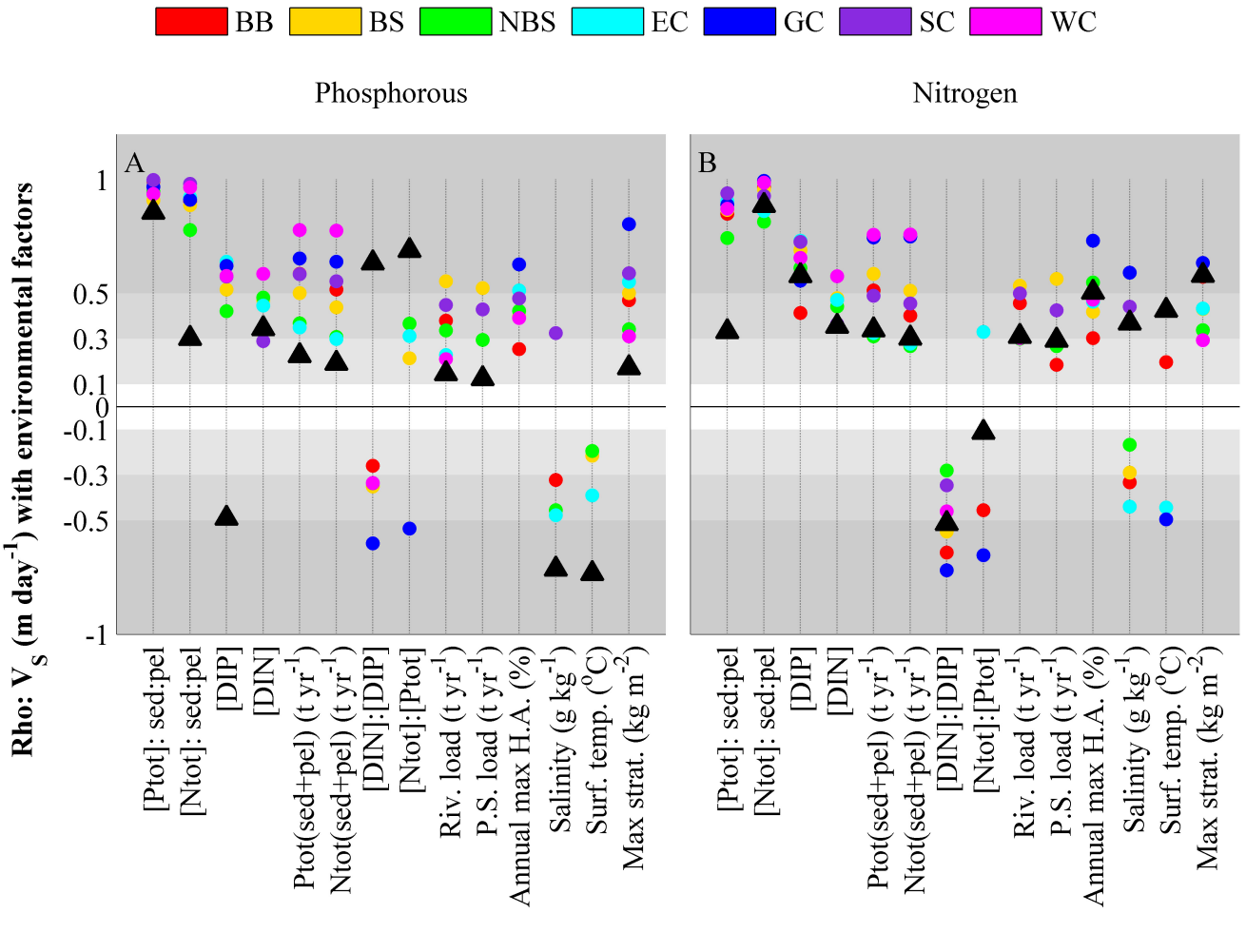


FIGURE 10 | Spearmans rank correlation coefficients for the 20 years averaged V_S for phosphorous **(A)** and nitrogen **(B)** tested against environmental factors. All environmental factors are taken as 20-year averages from the model set-up, input or output. Concentrations are denoted with brackets and are expressed in mmol m^{-3} for the water mass and mmol m^{-2} for the sediment. DIN and DIP represents winter values (November–January). In the labels, hypoxic area has been abbreviated with H.A and point sources with P.S. Colored dots shows correlations within one of the MRs and black triangles denote the correlation of all water bodies along the Swedish coast. Insignificant correlations ($p > 0.05$) are not shown.

In contrast, the high phosphorus retention along the Bothnian Sea (WD2) shore is not due to high loads but to a high *PNR*. This is further intensified by a positive temporal retention, i.e., the area both removes phosphorus effectively but has also a build-up of phosphorus in the SCMs water and sediment storage during the evaluated period. The high *PNR* is due to the models high burial rate constant in WD2.

The high R_{tot} in some areas close to land, e.g., the inner Stockholm archipelago, are likely due to a combination of high loads and high E_R in many enclosed near shore locations while the higher retention in basins bordering the open sea is due to the load supplied from the open Baltic Sea.

Both *PNR* and ΔM were found to be associated to the size of the water bodies. For *PNR* the cause is that the burial of matter depends on the amount of sediment area available, i.e., a larger water body can bury a larger amount of nutrients. The proximity to land, and thus to the natural and anthropogenic forced variability of the land load, is likely to be the reason behind the positive association of ΔM with the surface area of water bodies. The smaller water bodies close to land are likely to have larger fluctuations in their nutrient load and thus, their nutrient content tends to vary more over time.

The Stockholm Archipelago Key Site

The Stockholm archipelago is included both as part of WD3 and as a key site. The WD3 has more than 100% filtration efficiency, while the filter efficiency at the Stockholm key site is lower and comparable to the numbers presented in Almroth-Rosell et al. (2016). The higher filtration for the larger WD3 area is in line with Almroth-Rosell et al. (2016), who concluded that filtration efficiency increased with increasing area as long as it receives roughly the same load. This is the case in WD3, and

especially the Stockholm archipelago, since most of the land load is received from the lake Mälaren outlet in the innermost parts of the archipelago.

Effects of Temporary Retention

Another result that was mentioned already in Almroth-Rosell et al. (2016) is that estimated retention values are sensitive to trends in nutrient storage during the period. Usually these fluctuations of the nutrient pool are one or two orders of magnitude less than the permanent retention, but occasionally (e.g., the open coastline in the south of the Bothnian Bay in **Table 3**) these trends in nutrient storage significantly affect the calculation of the nutrient filter efficiency. Hence, the effect of the build-up of, or release from, the nutrient pool in water and sediment needs to be considered whenever nutrient retention is estimated from data that are restricted in time, especially in water bodies or regions in the inner coastal zone. Evaluations based on a short timespan will only give a snapshot of information and thus, has restricted usability. This is especially important for phosphorus for which the temporal retention can be of the same order of magnitude as the permanent retention and thus, the momentary retention can vary greatly from the long term average.

Long term changes in the nutrient storage of the coastal zone are caused partly by changes in the nutrient load from land but it also depends on the influx of nutrients from the Baltic Sea. The nutrient levels of the open Baltic Sea are regulated by both land loads and internal nutrient release and loss due to fluctuating oxygen concentrations in deep waters. Hence, both anthropogenic factors, such as increased eutrophication and more recently, the mitigation of eutrophication, but also the natural hypoxic/anoxic periods of the Baltic Sea can affect long-term nutrient trends in the coastal zone.

Reversely, the open Baltic Sea is also impacted by changes in the coastal zone since alterations of the coastal nutrient filter impact the effective nutrient load that reach the Baltic Sea, which will also affect the Baltic Seas' eutrophic state and hence, the oxygen conditions.

Estimating Coastal Retention Efficiency and Filter Efficiency

The geographical area of the coastal filter estimation in this study and in Asmala et al. (2017) overlaps, but differs in extent, and the methodology differ substantially, i.e., numerical biogeochemical modeling versus synthesis and extrapolation of measured data. However, these studies agree on several characteristics of the nutrient filter in coastal zone of the Baltic Sea.

Asmala et al. (2017) estimated that the coastal filter around the entire Baltic Sea removes 16% of the nitrogen and 53% of the phosphorus inputs from land. This may be compared to our estimate of the filter efficiency for the Swedish coastal zone of about 54 and 70% for nitrogen and phosphorus, respectively. The calculated filter efficiency from our study are higher, but agree with Asmala et al. (2017), as well as with Almroth-Rosell et al. (2016), in the sense that the coastal zone is a more efficient filter for phosphorus than for nitrogen and that the coastal filter has an important function in retaining and removing nutrients in the Baltic Sea. In Savchuk (2018), this high filter efficiency for phosphorus in the coastal zone is questioned when set in context of the overall nutrient budget of the Baltic Sea. However, the numbers derived for the entire Baltic Sea area by Asmala et al. (2017) is based on a limited set of data and more research is needed to connect the perspectives of the coastal zone and the Baltic Sea as a whole. The high filter efficiency in our study is derived for the Swedish coastline and more detailed studies are needed to extrapolate the results to other coastal areas in the Baltic Sea.

Both the results presented here and in Asmala et al. (2017) indicate that archipelagos and open coastlines tend to be more efficient nutrient filter than other coastal types, but both modeling and measured data also suggest that the spread in removal rates and filter efficiency is very large. In this study, the variation within each type is greater than the differences between the type averages and we suggest that the variation is most likely due to retention efficiency having a strong dependency on physical characteristics such as residence times and mean depth. These factors are not necessarily consistent within a coastal type. The physical characteristics give a rough estimation of the retention efficiency, but environmental factors, such as M_{sed}:C_{pel}:, can give a range of *PNR* values for water bodies that have similar H and τ. Even though the values in **Figure 5** are taken from several different studies, from different coastal types and produced with different methods, there is a correlation between physical factors and nutrient retention.

The identical association strengths found between H/τ and Eq. (6) (**Figures 9G–J**) are due to the fact that Eq. 6 does not include anything new compared to τ/H as long as V_S is assumed constant. The same factors are combined differently resulting in another type of distribution, which is not taken into account when Spearman's *Rho* is used instead.

The Impact From Environmental Conditions on Nutrient Retention Efficiency

To get an improved estimation of retention the environmental conditions also need to be taken into account. Theory for a steady state water body suggests that the ratio between the nutrient content in sediment and the concentrations in water could be used to estimate V_S and this study affirms that it is a good approach to estimate retention efficiency also for transient systems. Thus, Eq. 9 and 10 together offers a way to estimate E_R for any water body. The theory does, however, disregard the specification of the load. It gives the retention of the total load, i.e., both land and air load but also the exchange with other areas and the open sea, and does not clearly state the relation to filtering of land load, which is often of interest. However, Asmala et al. (2017) found denitrification rates to be positively associated to nitrate concentrations and sediment organic carbon (%), which suggested a dependence on similar factors as is suggested here, i.e., association of V_S to the M_{sed}:C_{pel} ratio.

The environmental factors evaluated in **Figure 10** should also be assumed to interact, e.g., the strength of stratification

will affect the likelihood of stagnant deep water and hence, also the likelihood of a basin experiencing hypoxia and anoxia. Also DIN and DIP levels can elevate the risk of low oxygen levels and are of course related to the amounts of total N and P. One should note that both the benthic loss rate and the apparent removal rate might be model dependent and the applicability to other data-sets is therefore not known. However, the average values listed in this work includes a variety of hydrological, climate and anthropogenic conditions, and thus, the values are not specific for any such environmental setting.

An expected result would be that the hypoxic fraction was a better indicator of retention potential than what is suggested by the results in **Figure 10** and the analyze of *Blr's* association with environmental indices. The expectation is based on an assumed relation between denitrification rates and hypoxic conditions and also release of phosphorus from the sediments at anoxia. However, even though these relations most likely affect retention to some extent, they seem to be overshadowed by the association of retention and retention efficiency with factor concerning all water bodies, i.e., physical dimensions, nutrient levels, nutrient ratios and temperatures. To investigate the effects from oxygen deficiencies the selection of water bodies needs to be aimed at that question specifically.

The seasonal variations in temperature are shown to be significantly associated to nitrogen retention caused by denitrification in Eilola et al. (2017). In the present study, the correlation is less pronounced since an annually averaged temperature is used (**Figure 10**). This could also be the case for other ambient parameters that have their largest variation on the annual time scale, e.g., seasonal oxygen deficiencies.

CONCLUSION

This modeling study gives an overview of nutrient retention for the entire Swedish coast and covers an array of coastal types in different climates and anthropogenic settings. The work also attempts to not only describe and quantify nutrient removal, but to relate it to some driving factors, i.e., to aid modeling of open coastal and shelf seas, such as the Baltic Sea. In a near shore context the parameterization of what happens to constituents in the fresh to saline continuum is of importance.

The main conclusions from this study are as follows:

- The Swedish coastal zone filters about 60% (approximately 53% for nitrogen and 69% for phosphorus) of the nutrients it received from land and air and thus, less than half of the input from land can be assumed to be exported from the coastal zone to the open sea.
- The northern and eastern Baltic Sea coasts, including the Stockholm archipelago, all retain more than 100% of the land and air load they receive. Thus, they also filter the Baltic Sea water.
- The nutrient removal is most efficient close to land.
- Nutrient retention cannot strictly be estimated only from the coastal type of the water body since the long term retention efficiency depends mainly on physical characteristics, i.e., mean depth and residence time, which vary independently of the coastal type.
- The inherent physical retention is modified by the ambient environmental state of the water body. Higher nutrient retention was found to be associated primarily with high M_{sed}:C_{pel} ratios. This ratio is in turn related to the ambient state of a water body, but it consists of factors that are feasible to measure, and thus offers opportunities to monitor changes in the retention efficiency of the coastal zone.
- On interannual timescales, the retention in a water body changes due to changes in its nutrient storage, i.e., the water body withholds or releases nutrients due to interannual variations and long term trends.
- The long-term retention efficiency can be well estimated from expressions derived from a steady state situation, even if the system shows a trend in it's nutrient content. The area specific retention can also be reasonably well estimated from a simple expression based on physical properties.
- The most effective filtering of nutrients occurs in areas with low land load normalized to the area that receives them, e.g., the southern part of the Swedish East Coast.

DATA AVAILABILITY

The raw data supporting the conclusions of this manuscript will be made available by the authors, without undue reservation, to any qualified researcher.

AUTHOR CONTRIBUTIONS

ME formulated the first draft of the concept for the study, performed the model run, and analyzed the model output. ME also wrote the main share of the manuscript. HM, KE, and EA-R contributed to the conception and design of the study and to the writing of the manuscript, adding important intellectual content. IW and LA contributed to the writing of the manuscript, also adding important intellectual content. All co-authors read and approved the submitted manuscript version.

FUNDING

The research presented in this study was part of the Baltic Earth Programme (Earth System Science for the Baltic Sea region, see http://www.baltex-research.eu/balticearth) and is part of the BONUS COCOA (Nutrient COcktails in COAstal zones of the Baltic Sea) project, which has received funding from BONUS, the Joint Baltic Sea Research and Development Programme (Art 185), funded jointly from the European Union's Seventh Programme for research,

technological development and demonstration and from the Swedish Research Council for Environment, Agricultural Sciences and Spatial Planning (FORMAS), grant no. 2013–2056. Additional financing has been received from the Swedish Agency for Marine and Water Management grant 1:12 Environmental management of marine and inland waters, tasks performed in accordance with regulation (204:660) regarding water quality considerations.

REFERENCES

Almroth-Rosell, E., Edman, M., Eilola, K., Meier, H. E. M., and Sahlberg, J. (2016). Modelling nutrient retention in the coastal zone of an eutrophic sea. *Biogeosciences* 13, 5753–5769. doi: 10.5194/bg-13-5753-2016

Almroth-Rosell, E., Eilola, K., Hordoir, R., Meier, H. E. M., and Hall, P. O. J. (2011). Transport of fresh and resuspended particulate organic material in the Baltic Sea — a model study. *J. Mar. Syst.* 87, 1–12. doi: 10.1016/j.jmarsys.2011.02.005

Almroth-Rosell, E., Eilola, K., Kuznetsov, I., Hall, P. O. J., and Meier, H. E. M. (2015). A new approach to model oxygen dependent benthic phosphate fluxes in the Baltic Sea. *J. Mar. Syst.* 144, 127–141. doi: 10.1016/j.jmarsys.2014.11.007

Areskoug, H. (1993). *Nedfall av Kväve och Fosfor till Sverige, Östersjön och Västerhavet*. Report No. 4148. Solna: Swedish Environmental Protection Agency.

Ask, J., Rowe, O., Brugel, S., Strömgren, M., Byström, P., and Andersson, A. (2016). Importance of coastal primary production in the northern Baltic Sea. *Ambio* 45, 635–648. doi: 10.1007/s13280-016-0778-5

Asmala, E., Carstensen, J., Conley, D. J., Slomp, C. P., Stadmark, J., and Voss, M. (2017). Efficiency of the coastal filter: nitrogen and phosphorus removal in the Baltic Sea. *Limnol. Oceanogr.* 62, S222–S238. doi: 10.1002/lno.10644

Billen, G., Silvestre, M., Grizzetti, B., Leip, A., Garnier, J., Voss, M., et al. (2011). "Nitrogen flows from European regional watersheds to coastal marine waters," in *European Nitrogen Assessment Sources, Effects and Policy Perspectives*, eds M. A. Sutton, C. M. Howard, and J. W. Erisman (Cambridge: Cambridge University Press), 271–297. doi: 10.1017/CBO9780511976988.016

Bolin, B., and Rodhe, H. (1973). A note on the concepts of age distribution and transit time in natural reservoirs. *Tellus* 25, 58–62. doi: 10.3402/tellusa.v25i1.9644

Carstensen, J., Conley, D., Bonsdorff, E., Gustafsson, B., Hietanen, S., Janas, U., et al. (2014). Hypoxia in the Baltic Sea: biogeochemical cycles, benthic fauna, and management. *AMBIO* 43, 26–36. doi: 10.1007/s13280-013-0474-7

Conley, D., Bjorck, S., Bonsdorff, E., Carstensen, J., Destouni, G., and Gustafsson, B. (2009). Hypoxia-related processes in the Baltic Sea. *Environ. Sci. Technol.* 43, 3412–3420. doi: 10.1021/es802762a

Conley, D. J., Carstensen, J., Aigars, J., Axe, P., Bonsdorff, E., Eremina, T., et al. (2011). Hypoxia is increasing in the coastal zone of the Baltic Sea. *Environ. Sci. Technol.* 45, 6777–6783. doi: 10.1021/es201212r

Cossellu, M., and Nordberg, K. (2010). Recent environmental changes and filamentous algal mats in shallow bays on the Swedish west coast—A result of climate change? *J. Sea Res.* 63, 202–212. doi: 10.1016/j.seares.2010.01.004

Edman, M., and Omstedt, A. (2013). Modeling the dissolved CO2 system in the redox environment of the Baltic Sea. *Limnol. Oceanogr.* 58, 74–92. doi: 10.4319/lo.2013.58.1.0074

Edman, M. K., and Anderson, L. G. (2014). Effect on pCO 2 by phytoplankton uptake of dissolved organic nutrients in the central and Northern Baltic Sea, a model study. *J. Mar. Syst.* 139, 166–182. doi: 10.1016/j.jmarsys.2014.06.004

Eilola, K., Gustafsson, B. G., Kuznetsov, I., Meier, H. E. M., Neumann, T., and Savchuk, O. P. (2011). Evaluation of biogeochemical cycles in an ensemble of three state-of-the-art numerical models of the Baltic Sea. *J. Mar. Syst.* 88, 267–284. doi: 10.1016/j.jmarsys.2011.05.004

Eilola, K., Lindqvist, S., Almroth-Rosell, E., Edman, M., Wåhlström, I., Bartoli, M., et al. (2017). *Linking Process Rates with Modelling Data and Ecosystem Characteristics*. Report Oceanography No. 61. Norrköping: Swedish Meteorological and Hydrological Institute.

Eilola, K., Meier, M. H. E., and Almroth, E. (2009). On the dynamics of oxygen, phosphorus and cyanobacteria in the Baltic Sea; a model study. *J. Mar. Syst.* 75, 163–184. doi: 10.1016/j.jmarsys.2008.08.009

Engqvist, A., Döös, K., and Andrejev, O. (2006). Modeling water exchange and contaminant transport through a Baltic coastal region. *AMBIO* 35, 435–447. doi: 10.1579/0044-7447(2006)35[435:MWEACT]2.0.CO;2

European Parliament Council of the European Union. (2000). *Directive 2000/60/EC of the European Parliament and of the Council of 23 October 2000 Establishing a Framework for Community Action in the Field of Water Policy*. Available at: http://data.europa.eu/Eli/dire/2000/60/O: Official Journal of the European Communities L 327

Fonselius, S., and Valderrama, J. (2003). One hundred years of hydrographic measurements in the Baltic Sea. *J. Sea Res.* 49, 229–241. doi: 10.1016/S1385-1101(03)00035-2

Gräwe, U., Naumann, M., Mohrholz, V., and Burchard, H. (2015). Anatomizing one of the largest saltwater inflows into the Baltic Sea in December 2014. *J. Geophys. Res.* 120, 7676–7697. doi: 10.1002/2015JC011269

Gustafsson, B., Schenk, F., Blenckner, T., Eilola, K., Meier, H. E. M., Müller-Karulis, B., et al. (2012). Reconstructing the development of Baltic Sea Eutrophication 1850–2006. *AMBIO* 41, 534–548. doi: 10.1007/s13280-012-0318-x

Häggmark, L., Ivarsson, K. I., Gollvik, S., and Olofsson, P. O. (2000). Mesan, an operational mesoscale analysis system. *Tellus A* 52, 2–20. doi: 10.3402/tellusa.v52i1.12250

Hayn, M., Howarth, R., Marino, R., Ganju, N., Berg, P., Foreman, K. H., et al. (2014). Exchange of nitrogen and phosphorus between a shallow lagoon and coastal waters. *Estuaries Coast.* 37, 63–73. doi: 10.1007/s12237-013-9699-8

Helcom. (2017). *First Version of the 'State of the Baltic Sea' Report – June 2017 – to be Updated in 2018*. Avaliable at: http://stateofthebalticsea.helcom.fi

Hoefsloot, I. (2017). *Validation of Modelled Benthic Nutrients in the Swedish Coastal Zone Model and the Effects of Microphytobenthos Implementation*. Utrecht: Utrecht University.

Leppäranta, M., and Myrberg, K. (2009). *Physical Oceanography of the Baltic Sea*. Berlin: Springer Science & Business Media. doi: 10.1007/978-3-540-79703-6

Lilliefors, H. W. (1967). On the kolmogorov-smirnov test for normality with mean and variance unknown. *J. Am. Stat. Assoc.* 62, 399–402. doi: 10.1080/01621459.1967.10482916

Lindstrom, G., Pers, C., Rosberg, J., Stromqvist, J., and Arheimer, B. (2010). Development and testing of the HYPE (Hydrological Predictions for the Environment) water quality model for different spatial scales. *Hydrol. Res.* 41, 295–319. doi: 10.2166/nh.2010.007

Marmefelt, E., Arheimer, B., and Langner, J. (1999). An integrated biochemical model system for the Baltic Sea. *Hydrobiologia* 393, 45–56. doi: 10.1023/A:1003541816177

McGlathery, K. J., Sundbäck, K., and Anderson, I. C. (2007). Eutrophication in shallow coastal bays and lagoons: the role of plants in the coastal filter. *Mar. Ecol. Prog. Ser.* 348, 1–18. doi: 10.3354/meps07132

Meier, H., and Kauker, F. (2003). Modeling decadal variability of the Baltic Sea: 2. Role of freshwater inflow and large-scale atmospheric circulation for salinity. *J. Geophys. Res.* 108:3368. doi: 10.1029/2003JC001799

Meier, M., Eilola, K., and Almroth, E. (2011). Climate-related changes in marine ecosystems simulated with a 3-dimensional coupled physical-biogeochemical model of the Baltic Sea. *Clim. Res.* 48, 31–55. doi: 10.3354/cr00968

Neumann, T., Fennel, W., and Kremp, C. (2002). Experimental simulations with an ecosystem model of the Baltic Sea: a nutrient load reduction experiment. *Global Biogeochem. Cycles* 16:1033. doi: 10.1029/2001GB001450

Nixon, S. W., Ammerman, J. W., Atkinson, L. P., Berounsky, V. M., Billen, G., Boicourt, W. C., et al. (1996). "The fate of nitrogen and phosphorus at the land-sea margin of the North Atlantic Ocean," in *Nitrogen Cycling in the North Atlantic Ocean and its Watersheds*, ed. R. Howarth (Berlin: Springer), 141–180. doi: 10.1007/978-94-009-1776-7_4

Norkko, A., and Bonsdorff, E. (1996). Rapid zoobenthic community responses to accumulations of drifting algae. *Mar. Ecol. Prog. Ser.* 131, 143–157. doi: 10.3354/meps131143

Oschlies, A., Blackford, J., Doney, S. C., and Gehlen, M. (2010). "Modelling considerations," in *Guide to Best Practices for Ocean Acidification Research*

and Data Reporting, eds U. Riebesell, V. J. Fabry, L. Hansson, and J.-P. Gattuso (Luxembourg City: Publications Office of the European Union), 233–242.

Robertson, L., Langner, J., and Engardt, M. (1999). An Eulerian limited-area atmospheric transport model. *J. Appl. Meteorol.* 38, 190–210. doi: 10.1175/1520-0450(1999)038<0190:AELAAT>2.0.CO;2

Rönnberg, C., and Bonsdorff, E. (2004). Baltic Sea eutrophication: area-specific ecological consequences. *Hydrobiologia* 514, 227–241. doi: 10.1023/B:HYDR.0000019238.84989.7f

Savchuk, O. P. (2018). Large-scale nutrient dynamics in the Baltic Sea, 1970–2016. *Front. Mar. Sci.* 5:95. doi: 10.3389/fmars.2018.00095

Seifert, T., and Kayser, B. (1995). *A High Resolution Spherical Grid Topography of the Baltic Sea*. Rostock: Institut fur Ostseeforschung.

Sheldon, J. E., and Alber, M. (2006). The calculation of estuarine turnover times using freshwater fraction and tidal prism models: a critical evaluation. *Estuaries Coasts* 29, 133–146. doi: 10.1007/bf02784705

Sundbäck, K., Linares, F., Larson, F., Wulff, A., and Engelsen, A. (2004). Benthic nitrogen fluxes along a depth gradient in a microtidal fjord: the role of denitrification and microphytobenthos. *Limnol. Oceanogr.* 49, 1095–1107. doi: 10.4319/lo.2004.49.4.1095

Svensson, U. (1998). PROBE program for boundary layers in the environment system description and manual. *SMHI Rep. Oceanogr.* 24:42.

Wulff, F., and Stigebrandt, A. (1989). A time-dependent budget model for nutrients in the Baltic Sea. *Global Biogeochem. Cycles* 3, 63–78. doi: 10.1029/GB003i001p00063

Conflict of Interest Statement: The authors declare that the research was conducted in the absence of any commercial or financial relationships that could be construed as a potential conflict of interest.

Copyright © 2018 Edman, Eilola, Almroth-Rosell, Meier, Wåhlström and Arneborg. This is an open-access article distributed under the terms of the Creative Commons Attribution License (CC BY). The use, distribution or reproduction in other forums is permitted, provided the original author(s) and the copyright owner(s) are credited and that the original publication in this journal is cited, in accordance with accepted academic practice. No use, distribution or reproduction is permitted which does not comply with these terms.

frontiers in Marine Science

ORIGINAL RESEARCH
published: 28 February 2019
doi: 10.3389/fmars.2019.00076

Two Non-indigenous Dreissenids (*Dreissena polymorpha* and *D. rostriformis bugensis*) in a Southern Baltic Coastal Lagoon: Variability in Populations of the "Old" and a "New" Immigrant

Brygida Wawrzyniak-Wydrowska[1], Teresa Radziejewska[1], Anna Skrzypacz[1] and Adam Woźniczka[2]*

[1] Palaeoceanology Unit, Faculty of Geosciences, University of Szczecin, Szczecin, Poland, [2] National Marine Fisheries Research Institute, Gdynia, Poland

OPEN ACCESS

Edited by:
Hendrik Schubert, University of Rostock, Germany

Reviewed by:
Sven Dahlke, University of Greifswald, Germany
Martin Powilleit, University of Rostock, Germany

***Correspondence:**
Brygida Wawrzyniak-Wydrowska
brygida.wydrowska@usz.edu.pl

Specialty section:
This article was submitted to Coastal Ocean Processes, a section of the journal Frontiers in Marine Science

Received: *05 June 2018*
Accepted: *11 February 2019*
Published: *28 February 2019*

Citation:
Wawrzyniak-Wydrowska B, Radziejewska T, Skrzypacz A and Woźniczka A (2019) Two Non-indigenous Dreissenids (Dreissena polymorpha and D. rostriformis bugensis) in a Southern Baltic Coastal Lagoon: Variability in Populations of the "Old" and a "New" Immigrant. Front. Mar. Sci. 6:76. doi: 10.3389/fmars.2019.00076

Dreissena polymorpha and *D. rostriformis bugensis* are freshwater Ponto-Caspian bivalve species, at present widely distributed in Europe and North America. In the Szczecin Lagoon (a southern Baltic coastal lagoon), the quagga was recorded for the first time in 2014 and found to co-occur with the zebra mussel, a long-time resident of the Lagoon. As the two species are suspected of being competitors where they co-occur, their population dynamics was followed at a site the new immigrant was discovered (station ZS6, northern part of the Lagoon) by collecting monthly samples in 2015–2017. The abundance and biomass of the two congeners showed wide fluctuations, significant differences being recorded between months within a year and between years. The abundance and biomass proportions between the two congeners changed from an initial domination of the newcomer quagga until mid-2015 to a persistent domination of the zebra mussel throughout the remainder of the study period. Both the abundance and biomass of the two dreissenids showed a number of significant associations with environmental variables, notably with salinity, chlorophyll *a* content, and temperature. The co-occurrence of the two dreissenids in the Lagoon is discussed in the context of their invasion stage; it is concluded that while the quagga seems to have achieved the "outbreak" stage, the zebra mussel, an "accommodated" invader present prior to the quagga immigration, reverted to that stage.

Keywords: non-indigenous species, zebra mussel, quagga, lagoon, Baltic Sea

INTRODUCTION

Co-occurrence of congeneric species, observed in many ecosystems, is of interest for both theoretical and practical reasons (Gotelli, 2000; Sfenthourakis et al., 2005; Veech, 2014). It is generally assumed that co-occurrence may lead to co-existence (HilleRisLambers et al., 2012) as a result of competitive interactions, whereby the sympatric occurrence of the two congeners is

possible on account of their resource partitioning (Walter, 1991) both in space (spatial separation, e.g., Pigot and Tobias, 2013; the use of different food resources, e.g., Labropoulou and Eleftheriou, 1997) and in time (different timing of reproduction; e.g., Dettman et al., 2003). Co-existence of congeners is of a special importance when a non-indigenous species (a "newcomer") appears in an area already occupied by a congener with an established population (the "resident"). The increasing rate of species migrations and biological invasions worldwide (Lockwood et al., 2007; Nentwig, 2008; Rilov and Crooks, 2009) present an opportunity to follow the course of events associated with immigration of one species to an area already colonized by a congener. Such an opportunity presented itself in 2014 when the quagga (*Dreissena rostriformis bugensis* Andrusov, 1897) was first recorded in the Szczecin Lagoon, a coastal water body at the southern Baltic Sea coast, which already supported a population of a congener, the zebra mussel [*D. polymorpha* (Pallas, 1771)] (Woźniczka et al., 2016).

The two dreissenids are freshwater Ponto-Caspian bivalves of a considerable invasive potential (Nalepa and Schloesser, 1993; Karatayev et al., 1997, 2014a; Nalepa and Schloesser, 2014), which have colonized European and North American waters (Zhulidov et al., 2004, 2010; Karatayev et al., 2014a, 2015). The zebra mussel expansion in Europe began at the turn of the 18th century (Thienemann, 1950), much earlier than the onset of the *D. rostriformis bugensis* spread in the 1940s (e.g., Orlova et al., 2004; Popa and Popa, 2006; Molloy et al., 2007; Bij de Vaate, 2010; Stańczykowska et al., 2010; Zhulidov et al., 2010; Heiler et al., 2013; Matthews et al., 2014). In the Szczecin Lagoon, *D. polymorpha* has been present since the time regular biological observations in the area began in the 19th century. Despite its non-indigenous species status (Olenin et al., 2017), the zebra mussel has become a permanent and abundant component of the Lagoon's biota (Wolnomiejski and Witek, 2013). When the quagga was first recorded in the Lagoon, it was already abundant and co-occurring with *D. polymorpha* (Woźniczka et al., 2016).

Numerous literature data from Europe and North America demonstrate that the sudden appearance of *D. rostriformis bugensis,* like previously that of *D. polymorpha*, can lead to ecosystem alteration and changes in indigenous communities (Karatayev et al., 1997; Ricciardi and MacIsaac, 2000; Nalepa et al., 2010). Both in North America and in its native area, it took *D. rostriformis bugensis* a relatively short time (5–10 years) to displace *D. polymorpha* (e.g., Mills et al., 1996; Orlova et al., 2004; Ricciardi and Whoriskey, 2004; Karatayev et al., 2015). The zebra mussel's replacement by *D. rostriformis bugensis* in the Great Lakes was explained by invoking a number of possible mechanisms. One involves genetic adaptations of *D. rostriformis bugensis* to colonize new areas, which makes it possible for the species to migrate from deeper cooler waters to shallow areas (Mills et al., 1996; Karatayev et al., 2015). It has also been suggested that reproduction of *D. rostriformis bugensis* begins at temperatures lower than those needed by *D. polymorpha*, that is earlier in the season, which facilitates the former species' success in the "race" to colonize suitable areas (Roe and MacIsaac, 1997; Claxton and Mackie, 1998). Still other hypotheses refer to differences between the two species in their filtration rates, feeding and energy efficiency. According to Diggins (2001), the filtration rate of *D. rostriformis bugensis* is higher than that of *D. polymorpha*, which is advantageous for the former, particularly under limited food resources. In addition, the energy efficiency of *D. rostriformis bugensis* is higher than that of *D. polymorpha*, resulting in a higher growth rate at a high food supply (Baldwin et al., 2002; Stoeckmann, 2003). Is it then likely that the zebra mussel, an "old" immigrant and the resident in the Szczecin Lagoon, might be replaced by *D. rostriformis bugensis*?

To assess (and possibly predict) effects of species, particularly immigrants, upon communities and ecosystems, the functional approach is regarded as especially valuable at present (Flynn et al., 2011; Karatayev et al., 2015). Functionally, the two congeners are considered interchangeable in terms of their community or ecosystem effects (Keller et al., 2007; Ward and Ricciardi, 2007; Higgins and Vander Zanden, 2010; Kelley et al., 2010; Karatayev et al., 2015). They are fairly similar in their life traits (e.g., a high reproductive potential, free-swimming planktonic larvae, sessile mode of life effected by byssus attachment to the substrate, efficient filtration) (Karatayev et al., 2015). Consequently, they are successful colonizers and invaders, and may reach a dominant status in a newly settled area. On the one hand, they are perceived as representing the most invasive freshwater species in the northern hemisphere (Nalepa and Schloesser, 1993, 2014; Karatayev et al., 2014a, 2015). On the other, the dreissenid presence in water bodies is ecologically important as the bivalves, on account of their mode of life and suspension feeding, contribute significantly to the functioning of aquatic ecosystems (e.g., Fréchette and Bourget, 1985; Stańczykowska and Planter, 1985; Smit et al., 1993; Stewart et al., 1998; Daunys et al., 2006; Radziejewska et al., 2009; Nalepa and Schloesser, 2014; Karatayev et al., 2015). Both dreissenids are the so-called ecosystem engineers as, at a mass occurrence, their aggregations form complex three-dimensional structures consisting of both live individuals and empty shells, generating microhabitats and enhancing biodiversity of the associated sessile and motile benthos (Karatayev et al., 2002; Vanderploeg et al., 2002; Gutierrez et al., 2003; Hecky et al., 2004; Zaiko et al., 2009). The bivalves' filter-feeding reduces the eutrophication symptoms by eliminating suspended particulates from the water column, whereas their feces and pseudofaeces deposited on the bottom supply organic matter to the sediment and boost microbial processes in it (Izvekova and Lvova-Katchanova, 1972; Stewart et al., 1998, 1999; Bially and MacIsaac, 2000; Ward and Ricciardi, 2007; Stańczykowska et al., 2010).

Although the two species are similar, they are by no means identical. To understand their ecology and effects on ecosystems they live or have appeared in, it is necessary to obtain insights into their distribution and population dynamics (Karatayev et al., 2015). Therefore, as an initial step toward exploring effects of the new immigrant on its resident congener and on the recipient ecosystem in general, this study focused on following the dynamics of the two dreissenid populations in the Lagoon in terms of their abundance and biomass from the time point when the new immigrant was first recorded in the Lagoon.

MATERIALS AND METHODS

Area of Study

The Szczecin Lagoon (**Figure 1**), one of the three southern Baltic Sea lagoons, is a major part of the Odra River estuarine system (Wolnomiejski and Witek, 2013). It is divided into two sub-basins, the Kleines Haff in the west (in Germany) and the Wielki Zalew ("Great Lagoon") in the east (in Poland). From the south, the Lagoon is fed by the Odra River; in the north, it is connected – via three straits (the Peene, Świna and Dziwna) – with the Pomeranian Bay in the Baltic Sea. The Lagoon is a brackish transitional water body the hydrography of which is shaped by the interplay of riverine runoff from the Odra and periodic intrusions of the seawater from the Pomeranian Bay. As a result, the Lagoon's salinity changes in time and space (in the south–north direction) from PSU 0.3 to 4.5 (Radziejewska and Schernewski, 2008). With its mean depth of 3.8 m, the Lagoon is a shallow water body; the maximum natural depth is 8.5 m, whereas the artificially dredged navigation channel leading to the port of Szczecin is 10.5 m deep (Radziejewska and Schernewski, 2008). The central part of the Wielki Zalew is surrounded by a belt of sandy shallows (1–1.5 m depth) which extend from the shores into the Lagoon; steep slopes of the shallows descend to the muddy areas of the central basin (Wolnomiejski and Witek, 2013). Both the shallows and their slopes have been known to support dense aggregations of *D. polymorpha* (Wiktor, 1969; Wolnomiejski and Witek, 2013) and – as it turned out in 2014 – also mixed aggregations of *D. polymorpha* and *D. rostriformis bugensis* (Woźniczka et al., 2016).

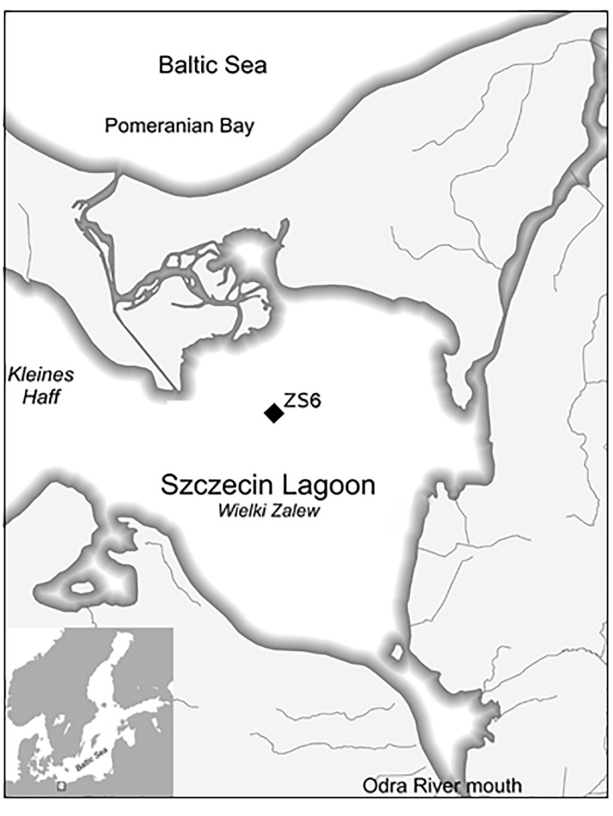


FIGURE 1 | Area of study and location of sampling station in the Szczecin Lagoon.

The Szczecin Lagoon has been for years subjected to a heavy anthropogenic pressure, with all the consequences, including pronounced eutrophication (Radziejewska and Schernewski, 2008). It is also used as a busy shipping area, with navigation lanes leading to the large Baltic Sea ports of Świnoujście and Szczecin. The estuarine system of the Lagoon is also connected – via the Odra and a network of canals – with the European waterways, including the catchments of the Vistula and Elbe, and indirectly with those of the Rhein and Danube. The location of the Lagoon and the busy ship's traffic has resulted in a fairly high contribution of non-indigenous species to the Lagoon's biota (Gruszka, 1999; Wawrzyniak-Wydrowska and Gruszka, 2005; Radziejewska and Schernewski, 2008; Wolnomiejski and Witek, 2013), the estuary itself constituting potentially a source area for further spread of those species in the Baltic Sea catchment (Gruszka, 1999).

Following the first record of *D. rostriformis bugensis* in November 2014, the two dreissenids were sampled monthly (March to November or December) in 2015, 2016, and 2017 at station ZS6 in the northern part of the Lagoon (**Figure 1**). Due to water level changes in the Lagoon, the station depth varied between 3 and 4.5 m.

Sampling

The bivalves were sampled with a 625 cm^2 Van Veen grab, three samples being collected at each site on each sampling occasion. The three samples were sieved individually on an 0.5 mm mesh size sieve and the sieving residue was fixed with buffered 10% formalin. The samples were then sorted, the bivalves were identified and counted, and subsequently dried for 12 h at 105°C and weighed to determine the dry-weight based biomass.

Synoptically with dreissenid sampling, environmental variables of the water column (temperature, salinity, pH, dissolved oxygen content, chlorophyll *a* content) and the sediment (silt/clay and organic matter content) were determined; these measurements are summarized in **Table 1**.

The near-bottom (0.5 m above the bottom) water temperature, salinity, pH, dissolved oxygen content, and chlorophyll *a* content (a measure of the quantity of biogenic suspended particulates and a proxy of phytoplankton biomass) were measured with an ENDECO YSI 6600 device equipped with appropriate sensors. To characterize the sediment, the silt/clay fraction (a MALVERN 300 laser grain size analyser, 0.3–200 μm) and the organic matter content (loss on ignition at 550°C; Bale and Kenny, 2005) in a sediment sample collected separately with the Van Veen grab were determined.

Statistical Treatment

The near-bottom water characteristics (temperature, salinity, pH, chlorophyll *a* content, dissolved oxygen content) were processed with the Principal Components Analysis (PCA) to identify those variables which accounted for most of the variation in the data set. The PCA was run, on log-transformed and normalized values, using the Statistica v. 12 software (Statistica, Poland).

TABLE 1 | Sampling dates and characteristics of the near-bottom water layer (temperature, salinity, pH, chlorophyll *a* content, dissolved oxygen content) and sediment (organic matter and silt/clay contents) at the Szczecin Lagoon station ZS6 sampled in 2014–2017.

	Near-bottom water					Sediment	
Date	**Temp. (°C)**	**Salinity (PSU)**	**pH**	**Chlorophyll *a* (μg dm^{-3})**	**O_2 (mg dm^{-3})**	**Organic matter (% sediment dry weight)**	**Silt/clay (% sediment dry weight)**
November 20, 2014	8.1	2.1	8.1	5.0	9.9	13.7	49.5
July 07, 2015	22.5	1.8	8.8	7.9	11.1	18.8	48.1
August 11, 2015	20.6	2.2	8.7	5.6	8.9	15.4	51.3
September 14, 2015	16.2	2.9	7.7	7.1	10.5	4.0	44.7
October 20, 2015	9.2	3.2	8.2	7.3	10.8	0.5	42.4
November 26, 2015	5.3	3.2	8.7	4.9	11.8	12.6	39.3
March 05, 2016	3.1	2.3	7.7	6.2	14.0	5.0	43.6
April 12, 2016	9.2	1.5	7.6	54.4	14.4	17.5	48.6
May 19, 2016	13.8	1.1	8.3	19.9	11.3	10.6	46.3
June 15, 2016	18.2	1.7	8.0	4.4	9.2	23.2	60.5
July 16, 2016	18.3	2.8	7.7	5.7	9.0	17.5	48.4
August 23, 2016	18.5	2.0	8.0	6.1	7.9	15.7	53.2
September 30, 2016	15.2	2.1	7.8	2.5	8.7	4.4	43.1
October 24, 2016	7.8	2.2	7.7	2.8	10.7	10.5	43.7
November 21, 2016	3.8	2.5	8.0	3.3	12.2	14.8	59.8
December 18, 2016	1.6	2.8	7.5	3.5	13.1	19.2	49.7
March 09, 2017	2.7	1.5	8.1	13.6	13.7	21.0	50.4
April 04, 2017	8.4	1.0	9.0	28.3	16.2	22.7	51.0
May 03, 2017	8.2	1.3	8.3	17.4	12.6	20.9	48.5
June 19, 2017	16.7	1.4	8.5	12.4	10.5	21.0	44.3
July 27, 2017	17.1	2.0	8.4	4.8	9.2	20.1	47.8
August 28, 2017	16.9	1.4	8.3	4.5	9.8	15.0	49.4
September 26, 2017	12.7	1.3	8.1	4.6	11.1	20.0	62.3
October 24, 2017	10.0	1.3	9.0	3.7	10.2	22.3	59.1
November 29, 2017	2.4	1.4	8.3	3.7	13.5	6.2	45.5
December 28, 2017	1.5	1.0	8.2	3.0	13.6	19.3	56.9

Differences in the two dreissenids' population metrics of interest for this study (abundance and biomass) were assessed using the three-level nested ANOVA for uneven groups. The first level (group effect) involved the abundance or biomass of a species, and the null hypothesis tested was that the mean abundances or biomasses did not differ significantly between the species. The second level (sub-group effects) tested the null hypothesis of there being no significant differences in mean abundance or biomass between the years within species. The third level (sub-sub-group effects) tested the null hypothesis of no significant differences in mean abundance or biomass between months within a year. The analyses were run, using the algorithm available at http://www.biostathandbook.com/nestedanova.html (McDonald, 2014) on log(x+1)-transformed abundance and biomass data.

Relationships between the bivalve abundance or biomass, as the dependent variables, and the near-bottom water characteristics mentioned before, as the independent or explaining variables, were explored using the multiple regression analysis (Stanisz, 2007). When some of the variables were co-linear or non-significant, step-wise regression (forward or backward) was applied. The forward step-wise regression involves gradual adding, to the list of the explaining variables, of those variables which affect the dependent variable the most. The procedure was repeated until the best model was obtained. The backward step-wise regression involves gradual removal from the model, consisting of all the potential variables, of those variables which, at a given step, were the least important for the dependent variable, until the best model is obtained (Stanisz, 2007). The regression was run for t0 (environmental data collected synoptically to bivalve sampling) and for $t-1$ (environmental data preceding the actual abundance or biomass value by a time lag of 1 month). The analyses were conducted with the Statistica v. 12 software (Statistica, Poland).

RESULTS

Environment

The near-bottom water temperature (**Table 1**) in each year varied seasonally, from 1.5°C in December 2017 to 22.5°C in July 2015. A between-year comparison showed each season of 2015 to be warmer than the respective seasons of 2016 and 2017.

The near-bottom water salinity (**Table 1**) ranged from PSU 1.0 in April and December 2017 to PSU 3.2 in October and November 2015. In 2015, salinities were somewhat higher than in other years. Noteworthy were markedly reduced salinities at ZS6 in 2016, even in the autumn (PSU 1–1.4) when northerly and north-westerly winds, usually prevalent at that time, are known to enhance seawater intrusions into the Lagoon (Meyer and Lampe, 1999; Bangel et al., 2004).

The near-bottom water pH (**Table 1**) ranged from 7.5 in December 2016 to a maximum of 9.0 recorded in October 2017.

The near-bottom chlorophyll *a* content was found to range from about 2.5 (September 2016) to 54.4 μg dm^{-3} (April 2016) and varied markedly in time (between months and years) (**Table 1**). Regarding the temporal variability (between-months differences), a similar general pattern was observed in 2016 and 2017 (the measurements in both years were taken from March until December), with a pronounced peak in spring (April and May). The chlorophyll *a* content in April 2016, however, was almost twice that in April 2017. In addition, much higher chlorophyll *a* contents were recorded in individual months of 2015, compared to the respective records in other years.

The near-bottom mean dissolved oxygen contents (**Table 1**) varied from 7.9 (August 2016) to 14.4 mg dm^{-3} (April 2016). No instances of oxygen deficiency were recorded, although the contents observed in August 2016 were fairly low, compared to the oxygen situation at other times.

The sediment showed a very high silt/clay content, from 39.3% in November 2015 to 62.3% in September 2017 (**Table 1**), and contained some admixture of fine sand. The sediment was usually strongly enriched in organic matter (from 0.5% in October 2015 to 23.2% in June 2016) (**Table 1**), the enrichment being dependent on sedimentation of organic material from the water column (Radziejewska et al., in prep.) and hence a distinct between-month variation. The enrichment was noticeably higher in 2017 than in the two previous years.

The PCA of the environmental variables (**Figure 2**) showed the characteristics of the water column in its near-bottom part to change primarily in time. The sampling events were grouped mainly along the principal component 1 (PC1), and a separation between "warm" (June, July, and September, on the right-hand side of PC1) and "cold" (April, March, October, and November on the left) months is fairly distinct in the plot. PC1, which accounted for 50.4% of the total variation in the data, combined the near-bottom water temperature and the dissolved oxygen content. The second principal component (PC2), accounting for 22.7% of variation in the data, combined salinity, pH and the chlorophyll *a* content, and separated the sampling events temporally as well, with the "warm" months being grouped above the main axis and the "cold" ones below it.

Dreissenid Abundance

The mean abundance of *D. polymorpha* at ZS6 was found to range from 1573.3 ± 351.39 (September 2015) to 101642.7 ± 9192.73 ind. m^{-2} (October 2016) (**Supplementary Table S1**). After a period of rather low abundances lasting until July 2016, a boom was observed in August–September, followed by a decline resulting in abundances being fairly leveled-out, albeit at a level much higher than that observed prior to August 2016, throughout 2017.

The mean abundance of *D. rostriformis bugensis* was found to range from 3141.3 ± 1719.71 ind. m^{-2} (July 2017) to 26869.3 ± 2644.91 ind. m^{-2} (August 2015)

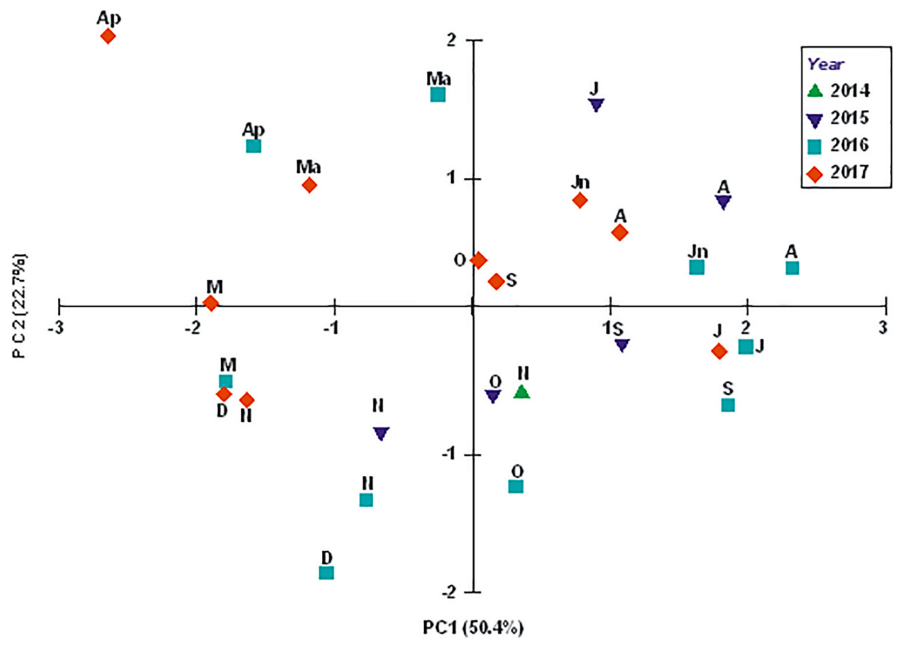


FIGURE 2 | Environmental variables-based PCA plot for sampling events (months of 2014, 2015, 2016, and 2017) at station ZS6. Letters next to symbols denote months (M, March; Ap, April; Ma, May; Jn, June; J, July; A, August; S, September; O, October; N, November; and D, December).

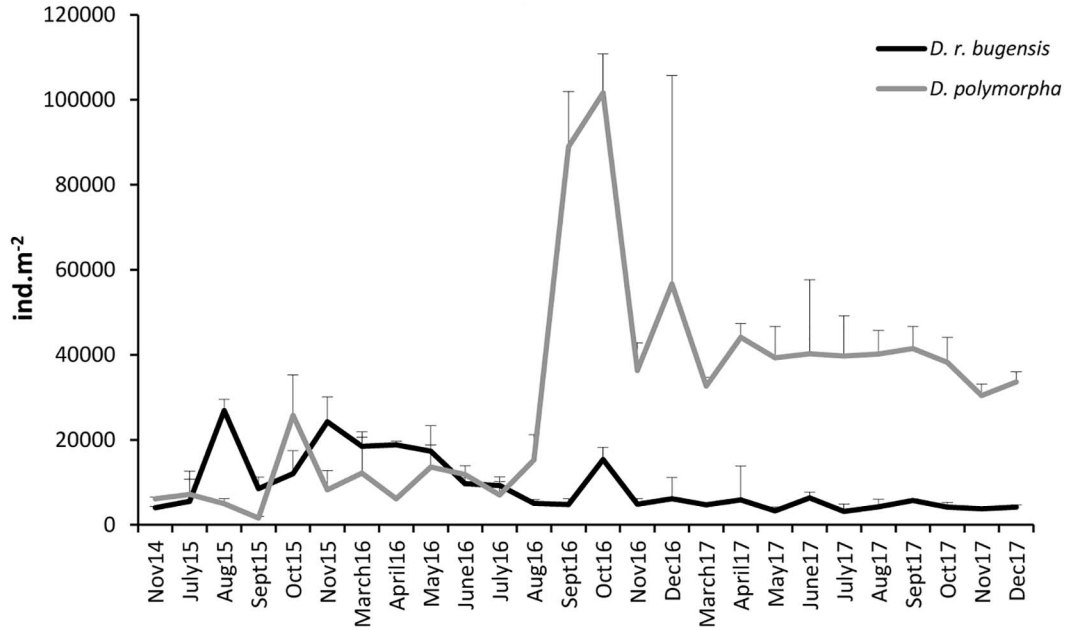


FIGURE 3 | Changes in mean abundances of *D. polymorpha* and *D. r. bugensis* in 2014–2017 at station ZS6; error bars denote standard deviations.

(**Supplementary Table S1**). Like those of the zebra mussel, the quagga abundance fluctuated considerably over time (**Figure 3**), the fluctuations being particularly dynamic in 2015–2016. The quagga population peaked in August 2015 and again in May 2016, to decline thereafter down to fairly low levels maintained throughout 2017.

When analyzed together, the abundances of the two dreissenids at ZS6 were observed to change out of synchrony (correlation coefficient $r = -0.15$) (**Figure 3**), with peak abundances coinciding (albeit at very different levels) only in October 2016. Initially (from August 2015 until July 2016), the quagga was a dominant congener (the abundance ratio of ca. 6:4 in favor of *D. rostriformis bugensis*), but as of August 2016 the zebra mussel took over, its abundances being several times higher than those of the quagga.

Differences in abundance between the two species proved non-significant (group effect, $p > 0.05$) (**Table 2**). On the other hand, differences in abundance between years in each species (sub-group effect) proved highly significant ($p < 0.01$), very highly significant differences ($p < 0.001$) being observed between months in each year (**Table 2**).

Dreissenid Abundance Versus Environmental Variables

The regression analysis for dreissenid abundance at t0 and $t-1$ (abundance time-lagged by 1 month relative to records of environmental characteristics) (**Table 3**) showed significant associations ($p < 0.05$; $p < 0.001$) for *D. polymorpha*. In 2015, the significant variable was the chlorophyll *a* content at t0 (a very high coefficient of determination, 0.92; model $p < 0.05$), no significant associations being found for $t-1$. In 2016, the zebra mussel abundance showed to be significantly related to temperature; however, the model with one variable explained as little as 45% of the variation in the abundance. No significant association was found for $t-1$. In 2017, the significant variables explaining 89% ($p < 0.001$) of the variability in abundance were the temperature and salinity. The 2017 time-lagged model included salinity and chlorophyll *a* which explained 68% ($p < 0.05$) of the variability in abundance.

The *D. rostriformis bugensis* abundance at ZS6 showed significant associations with environmental variables in 2016 only, the significant variables including the near-bottom water temperature, chlorophyll *a* and dissolved oxygen contents which, taken together, explained 72% ($p < 0.01$) of the variability in abundance at t0.

Dreissenid Biomass

The mean dry weight biomass of *D. polymorpha* at ZS6 was found to range from 123.4 ± 55.30 (April 2016) to 2603.3 ± 504.91 g m^{-2} (July 2017) (**Figure 4**). Like the abundances, the biomass fluctuated extensively throughout the period of study (**Figure 4**): after a biomass peak in October 2015, a steep decline was observed and a low biomass prevailed until September 2016 when

TABLE 2 | Three-level nested ANOVA (among-species difference as the group effect) for abundances of *D. polymorpha* and *D. rostriformis bugensis*.

Groups and sub-groups	*F*	*p*
Group effect (species)	$F(1,100) = 3.57$	$p > 0.05$
Subgroup effect (years within species)	$F(4,100) = 5.12$	$p < 0.01$
Sub-subgroup effect (months within year)	$F(44,100) = 8.28$	$p < 0.001$

TABLE 3 | Multiple regression analysis for relationships between dreissenid abundances (*D.p.*, *D. polymorpha*; *D.r.b.*, *D. rostriformis bugensis*) and environmental variables (at t0 and $t-1$) in the near-bottom water layer; significant regression coefficients shown only.

Species/year	Temperature	Salinity	pH	Chlorophyll *a*	O_2	R^2	Model *p*
D.p.							
2015 t0	ns	ns	ns	0.92*	ns	0.84	$p < 0.05$
2016 t0	0.67*	ns	ns	ns	ns	0.45	$p < 0.05$
2017 t0	1.02*	0.49***	ns	ns	ns	0.89	$p < 0.001$
2017 $t-1$	ns	0.59*	ns	0.79*	ns	0.68	$p < 0.05$
D.r.b.							
2016 t0	1.10*	ns	ns	0.63*	1.39	0.72	$p < 0.01$

*ns, regression coefficient non-significant; * regression coefficient significant ($p < 0.05$); *** regression coefficient very highly significant ($p < 0.001$).*

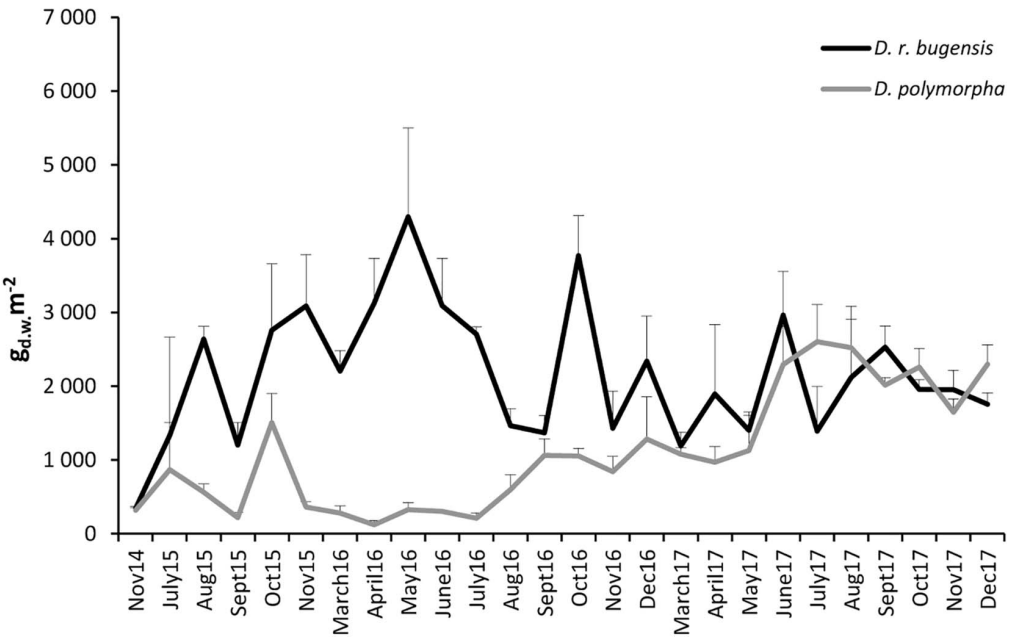


FIGURE 4 | Changes in mean biomasses of *D. polymorpha* and *D. r. bugensis* in 2014–2017 at station ZS6; error bars denote standard deviations.

the biomass started to increase steadily until the summer of 2017 (July–August).

The mean dry weight biomass of *D. rostriformis bugensis* was found to range from 345.6 ± 7240 (November 2014) to 4297.8 ± 1202.20 g m^{-2} (May 2016) (**Figure 4**). Like those of the zebra mussel, the quagga biomass fluctuated during the period of study (**Figure 4**), with pronounced peaks in May 2016, October 2016, and June 2017.

The biomasses of the two congeners at ZS6 were observed to follow different paths of variation, without any synchrony (correlation coefficient $r = -0.09$) (**Figure 4**). The quagga biomasses were higher (initially very much so) than the biomass of the zebra mussel until May 2017, when the two congeners – notwithstanding some differences, particularly in July – showed fairly similar biomasses.

Like in the case of abundance, between-species changes in biomass proved non-significant (group effect, $p > 0.05$) (**Table 4**). On the other hand, each species showed very highly significant biomass differences between years (sub-group effect; $p < 0.001$) and between months within a year (sub-subgroup effect; $p < 0.001$) (**Table 4**).

Dreissenid Biomass Versus Environmental Variables

The regression analysis for dreissenid biomass at t0 and $t-1$ (biomass time-lagged by 1 month relative to records of environmental characteristics) (**Table 3**) showed no significant associations between the *D. polymorpha* biomass and environmental variables in 2015. In 2016 and 2017, the near-bottom water temperature, chlorophyll *a* and dissolved oxygen contents at t0 were found to account jointly for 70 ($p < 0.05$) and 89% ($p < 0.001$) of the biomass variation, respectively.

The *D. rostriformis bugensis* biomass, like that of *D. polymorpha*, showed significant associations with environmental variables in 2016 and 2017 only. The time-lagged biomass in 2016 was found to be significantly related to the dissolved oxygen content (47% of the variability explained),

TABLE 4 | Three-level nested ANOVA (among-species difference as the group effect) for biomasses of *D. polymorpha* and *D. rostriformis bugensis*.

Groups and sub-groups	*F*	*p*
Group effect (species)	$F(1,100) = 4.45$	$p > 0.05$
Subgroup effect (years within species)	$F(4,100) = 9.75$	$p < 0.001$
Sub-subgroup effect (months within year)	$F(44,100) = 6.29$	$p < 0.001$

the near-bottom temperature being a significant variable at t0 in 2017 (57%, $p < 0.05$).

DISCUSSION

Dreissenid Abundance and Biomass

The abundances and biomasses of both dreissenids were found to fluctuate extensively. Such wide fluctuations seem to be well known from dreissenid populations worldwide (Strayer and Malcom, 2006; Stańczykowska et al., 2010) and are typical of sessile bivalve populations in general (e.g., Ardisson and Bourget, 1991). In the Szczecin Lagoon, the zebra mussel population abundances and biomass have been observed to fluctuate since the time when observations of the population in the Lagoon began (the early 1950s) (Wiktor, 1962, 1969). In the 1950s–1960s, the zebra mussel was a very abundant component of the Szczecin Lagoon biota, the abundances being estimated at more than 110 thou. ind. m^{-2} (Wiktor, 1962, 1969). In the 1980s, the *D. polymorpha* abundance in the Lagoon was reported to decline, and the population was even thought to have disappeared from the area (Piesik, 1992; Masłowski, 1993). The population decline at that time was associated with increased anthropogenic pressure, primarily the progressing eutrophication (Piesik, 1992). However, surveys conducted in 2000–2004 (Woźniczka and Wolnomiejski, 2005) showed *D. polymorpha* to be still an abundant component of the Lagoon's biota and to occur primarily on the slopes of shallows (depth range of 2.5–4.5 m) with average abundances of several thousand ind. m^{-2}. And yet, the 2005 survey (Wolnomiejski and Woźniczka, 2008) revealed a distinct (even fourfold) decline in the Lagoon's zebra mussel population. The authors quoted ascribed the decline to the habitat's trophic capacity being exceeded due to excessive growth of the population in the preceding years, which resulted in the food resources being depleted by intensive filtration of the large population. This "population boom and bust" is fairly common in various sessile populations (Strayer and Malcom, 2006). Considerable fluctuations in the *D. polymorpha* abundance were reported from the Kleines Haff (the eastern part of the Szczecin Lagoon), too: Fenske et al. (2010) found that, between 1993 and 2007, the zebra mussel abundance and biomass declined and the area occupied by the bivalves shrank. And yet, Stańczykowska et al. (2010) regarded the *D. polymorpha* population in the Lagoon as "stable," i.e., persistent, the fluctuations of abundance notwithstanding. Even with large differences from 1 year to the next, the fluctuations are, in the opinion of Stańczykowska et al. (2010), typical of eutrophic areas. The short-term instability, such as observed in the abundances of *D. polymorpha* in this study (3 years of observations) could then be a part of the normal longer-term pattern of variability in the area.

Changes in abundance and biomass of *D. rostriformis bugensis* have been studied much less extensively than those of the zebra mussel. Nevertheless, a large variability has been reported as well, ascribed (particularly with regard to the abundance) to an invasion stage and the depth of the bivalve's occurrence in a reservoir (Mills et al., 1996; Zhulidov et al., 2004; Jones and Ricciardi, 2005; Nalepa et al., 2009, 2010; Wong et al., 2012).

Fluctuations in the abundance of sessile bivalve populations, including those of dreissenids, have been explained by invoking effects of internal and/or external drivers. The former involve primarily recruitment and mortality (e.g., Cockrell et al., 2015; Polsenaere et al., 2017) and intra-specific competition (e.g., Naddafi et al., 2010; D'Hont et al., 2018) as mechanisms of population regulation (Krebs, 1995). In the *D. polymorpha* population studied here, recruitment might have played a role, as the abundance peaks coincided with the appearance of new cohorts, visible as increased numbers of small (<8 mm) individuals in the population (Wawrzyniak-Wydrowska et al., in prep.). However, the timing of the new individuals' appearance differed between years, as the peaks occurred in different months (cf. **Figure 3**).

External drivers include abiotic environmental factors and biotic pressures. The former, at least the suite of environmental factors analyzed in this study, did not produce a uniform pattern of responses: abundance correlated with different parameters each year, and the biomass was significantly related to the near-bottom water temperature, chlorophyll *a* content, and dissolved oxygen content (cf. **Tables 3**, **5**).

Certain associations inferred from results of the multiple regression analysis (cf. **Tables 3**, **5**) are amenable to a more in-depth exploration. For example, in 2015 and 2017, the zebra mussel abundance produced significant relationships with chlorophyll *a*, a proxy of phytoplankton biomass and the trophic status of a water body. As shown in a number of studies (Dorgelo, 1993; Sprung, 1995a,b; Schneider et al., 1998), the trophic status as well as the quality and density of the bioseston (which includes the phytoplankton) strongly affects the growth rate of *D. polymorpha*, the bivalves growing better under eutrophic than meso-oligotrophic conditions, and Jantz and Neumann (1992) reported a highly significant correlation between the zebra mussel growth rate and the chlorophyll *a* content. As suspension feeders, the two dreissenids rely on ambient phytoplankton for food. In a eutrophic water body such as the Szczecin Lagoon, the phytoplankton densities are usually high (Wolnomiejski and Witek, 2013), so the filter feeders should not experience food limitation. However, the phytoplankton in the Lagoon frequently features the presence of cyanobacteria, and cyanobacteria blooms of different intensity are a regularly observed effect. It may be conceivable that the presence of cyanobacteria limits the availability of phytoplankton as food for both dreissenids. Bierman et al. (2005) demonstrated selective rejection of cyanobacteria from the phytoplankton food ingested by the zebra mussel, while Fernald et al. (2007) found high cyanobacterial biomasses to be associated with low

TABLE 5 | Multiple regression analysis for relationships between dreissenid biomasses (*D.p.*, *D. polymorpha*; *D.r.b.*, *D. rostriformis bugensis*) and environmental variables (at t0 and *t*−1) in the near-bottom water layer; significant regression coefficients shown only.

Species/year	Temperature	Salinity	pH	Chlorophyll *a*	O_2	R^2	Model *p*
D.p.							
2016 t0	1.29*	ns	ns	0.78*	1.21*	0.70	$p < 0.05$
2017 t0	0.52*	ns	ns	0.79**	0.55*	0.89	$p < 0.001$
D.r.b.							
2016 *t*−1	ns	ns	ns	ns	1.06*	0.47	$p < 0.05$
2017 t0	0.77*	ns	ns	ns	ns	0.57	$p < 0.05$

*ns, regression coefficient non-significant; * regression coefficient significant ($p < 0.05$); ** regression coefficient highly significant ($p < 0.01$).*

zebra mussel filtration rate (and hence a weakened feeding ability). Paradoxically, the presence of the zebra mussel may even promote cyanobacteria (Nogaro and Steinman, 2013; Gaskill and Woller-Skar, 2018). As demonstrated by Boegehold et al. (2018) in a laboratory study, reproduction potential, spawning and fertilization success of the quagga was greatly reduced in the presence of cyanobacteria. Although no effects of cyanobacteria on *in situ* reproduction of invasive dreissenids have been identified yet, there is a possibility of reproductive consequences for wild populations.

Salinity emerged as another environmental factor producing significant associations with the abundance of *D. polymorpha* (cf. **Table 3**). Although the two species show a low salinity tolerance, *D. polymorpha* is somewhat more tolerant (up to above PSU 6) than *D. rostriformis bugensis* (<PSU 5) (Karatayev et al., 1998, 2014a; Garton et al., 2014), hence a significant association of the factor with the zebra mussel abundance.

The near-bottom water temperature was still another environmental variable that could be associated with fluctuations in the two species' abundances and biomass. Generally, *D. polymorpha* has a wider temperature tolerance than *D. rostriformis bugensis*, with the upper limit being reported as 33 and 31°C, respectively, the lower limit being set at 0°C for both species (McMahon, 1996; Karatayev et al., 1998, 2014a). The temperature range recorded in the Lagoon during the period of study (1.5–22.5°C) would hardly be limiting for either species. The temperature could, however, affect the timing of the onset of reproduction and larval settlement (Karatayev et al., 1998, 2014a; Garton et al., 2014). The associations between the dreissenids' abundances and biomass, produced by the multiple regression, were, however, weaker than those involving the salinity and chlorophyll *a* content.

The dissolved oxygen content in the Szczecin Lagoon does not seem to be a factor limiting the dreissenid occurrence in the area, as the near-bottom water was generally well-oxygenated throughout the period of study (cf. **Table 1**). The water column in the Lagoon, a shallow reservoir, is usually well-mixed, and hypoxia has been occasional only (Wolnomiejski and Witek, 2013). As the multiple regression analysis identified dissolved oxygen content to form significant associations with the dreissenid abundance/biomass in 2016 and 2017, it is possible that the association was a result of the lower-than-usual oxygen contents recorded in August 2016 at ZS6 (cf. **Table 1**).

Among the external biotic pressures affecting the dreissenid populations, predation by waterfowl and fish (Mörtl et al., 2010; Wong et al., 2013) and parasitic infestations (Molloy et al., 1997; Karatayev et al., 2000; Mastitsky and Gagarin, 2004; Tyutin, 2005) have been most frequently referred to. The zebra mussel and quagga individuals sampled in the Lagoon were found to be parasite-free (Żbikowska, pers. comm.). On the other hand, the waterfowl predation could be an important factor affecting the population size and inducing its fluctuations. The zebra mussel in the Lagoon is known to be a food resource, particularly in winter, for the tufted duck (*Aythya fuligula*), the coot (*Fulica atra*) and the greater scaup (*Aythya marila*) (Piesik, 1974, 1983; Fenske et al., 2013; Marchowski et al., 2015), all abundant in the area. The fish predators include the roach (*Rutilus rutilus*), white bream (*Blicca bjoerkna*), vimba (*Vimba vimba*). and the invasive round goby (*Neogobius melanostomus*) (Kublickas, 1959; Fenske et al., 2013), a species that has already formed a local reproducing population in the River Odra estuary (Czugała and Woźniczka, 2010). The evidence from other areas (Naddafi and Rudstam, 2014; Foley et al., 2017) indicates, however, that the round goby predation, preferential with respect to the quagga where the bivalve's abundance has exceeded that of the zebra mussel, seems to affect the population demography (size structure) rather than the abundance. Other zebra mussel predators in the Lagoon include the crayfish *Orconectes limosus* and the Chinese mitten crab (*Eriocheir sinensis*) (Fenske et al., 2013). On the other hand, as reported from the Dutch lakes IJsselmeer and Markermeer, even where the two congeners co-occur, the quagga is selectively preyed upon by the wintering tufted duck, scaup, pochard and goldeneye, and is their main food item in the area (Noordhuis et al., 2010; Van Eerden and De Leeuw, 2010). However, no estimates of predation impact on either dreissenid in the Lagoon are available as yet.

Predation on dreissenid larvae may be another external biotic driver affecting the population size and inducing fluctuations in both abundance and biomass. Dreissenid larvae are known to be ingested by large planktonic copepods (e.g., Liebig and Vanderploeg, 1995) as well as by the conspecific adult bivalves (e.g., MacIsaac et al., 1991). The lack of data on this mechanism of population regulation underscores the importance of long-term observations on invasive species (Lucy, 2006).

Another line of reasoning with which to seek the underpinnings of wide fluctuations in the population size of new immigrants/invaders invokes generalizations concerning

stages of invasion. Based on 12 years of observations of the zebra mussel in Ireland, Zaiko et al. (2014) developed a generalized scheme of invasion progression, whereby the arrival of an invader is followed by its establishment, expansion, outbreak (with sub-stages of late expansion, peak abundance, and early decline), and eventually accommodation; they provided also direct (semi-quantitative) and indirect (qualitative) characteristics of each stage. Zaiko et al. (2014), like Strayer and Malcom (2006), stressed the importance of long-term observations for an appropriate assessment of invader population fluctuations. Following this line of reasoning and referring to older data (Wiktor, 1962, 1969; Piesik, 1992; Masłowski, 1993; Woźniczka and Wolnomiejski, 2005; Wolnomiejski and Woźniczka, 2008), it may be assumed that *D. polymorpha* had reached the accommodation phase in the Lagoon prior to the appearance of *D. rostriformis bugensis*. It is likely that immigration of the quagga has perturbed the zebra mussel accommodation, as abundance fluctuations as well as certain demographic traits (Wawrzyniak-Wydrowska et al., in prep.) and asynchrony between changes in abundance and biomass point to the population reverting periodically to various sub-stages of the outbreak. According to the classification of Zaiko et al. (2014), the stage of the *D. rostriformis bugensis* invasion in the Lagoon can be regarded as the outbreak, with its sub-stages (late expansion, peak abundance, and decline) detectable throughout the study. It will be interesting to follow further developments in the status of the two populations in the lagoon, to find out, *inter alia,* whether the pattern known from other areas where longer-term observations have been made (Zaiko et al., 2014; D'Hont et al., 2018) would be repeated in the Lagoon.

"New" Versus "Old" Immigrant

For an immigration of a non-indigenous species to be successful in a new area, that species has to survive there, establish a population and persist (Olenin et al., 2017). This may be difficult when the area has already been colonized by a congener. Species within the same genera are usually similar to each other in many respects (Brionez-Fourzán, 2014); for example, they share a trophic level, for which reason competitive exclusion is expected to take place (Scott, 2009). However, closely related congeners do co-occur in many systems, which is evidently the case of the two dreissenids in the Szczecin Lagoon. Since it was first revealed in the Lagoon in 2014 (Woźniczka et al., 2016), *D. rostriformis bugensis* has apparently fulfilled the three conditions of success spelled out above: the species survived in the Lagoon, established a population (with sub-populations sampled in this study), and seems to have persisted. Thus, it presents an interesting case of co-occurring, at a local scale, with a congener representing the same trophic level. The emerging question is whether the two congeners will co-exist in the Lagoon. As stated by Chesson (2000), the essential criterion for coexistence is the "invasibility"; this criterion requires that a species be able to increase in abundance, from a low level, whereas the other species maintains its typical abundance (Brionez-Fourzán, 2014).

The 3 years of observations reported here seem to confirm that the invasibility criterion has been fulfilled, as the quagga did increase in abundance (cf. **Figure 3**). After its first record at ZS6 in November 2014, the abundance ratio of the two dreissenids was in favor of the zebra mussel (4:6) and remained so in the first half of 2015 (until July). Subsequently, until May 2016, the proportion shifted in favor of the quagga, to change again to a more or less even ratio (June and July 2016), following which the quagga abundance declined and the ratio changed again in favor of the zebra mussel (75–95% of the combined dreissenid abundance). A similar ratio (85–92%), in favor of the zebra mussel, was maintained throughout 2017.

Since the onset of observations the quagga was a clear dominant in terms of biomass, despite a marked decline in its abundance in the consecutive months of 2015 and 2016. Even at the peak zebra mussel numerical domination in October 2016 (the *D. polymorpha* abundance was 7.5 times that of *D. rostriformis bugensis*), the quagga biomass was 3.5 times that of the zebra mussel. In 2017, despite a marked decline in the quagga abundance, the biomass ratio was more or less even. This effect was resulted from the quagga population being dominated by larger (older) bivalves (Wawrzyniak-Wydrowska et al., in prep.).

The changes in population sizes of the two dreissenids are to some extent consistent with a general pattern of events following an invasion (see above). The quagga is still at the early stage of invasion, although probably not at the initial phase, because – when first recorded (November 2014) – the individuals found were of a size suggesting they were about 3 years old, so the immigration must have occurred earlier. Nevertheless, the early stage of invasion implies a lower adaptability to the conditions of the Szczecin Lagoon. The differences between the two species may, on the one hand, reflect internal regulation mechanisms, and on the other, may be an outcome of feedbacks resulting from inter-specific competition for space and food as well as cyclicity in reproductive potential and settlement success (Strayer and Malcom, 2006; Pace et al., 2010; D'Hont et al., 2018).

CONCLUSION AND OUTLOOK

In 2014–2017, we followed the dynamics, in terms of abundance and biomass, of two non-indigenous dreissenids, *D. polymorpha* and *D. rostriformis bugensis* co-occurring at a station in the Szczecin Lagoon. We managed to observe how the latter clearly established itself in the area, was co-occurring and possibly was entering co-existence with the former. We consider it important to record changes in both populations at the initial stage of the new immigrant's establishment, the more so that *D. rostriformis bugensis* shows – like in other areas where more long-term data are available (e.g., D'Hont et al., 2018) – signs of becoming dominant over the already established *D. polymorpha*. It, however, remains to be seen what the two populations are being driven by in the Szczecin Lagoon.

Considering the "known unknowns" in the co-occurrence of the two dreissenids in the Lagoon, it seems necessary to continue observations on changes in their populations and to explore their respective population structures. Longer-term studies on

demography of both species will be helpful in shedding light on interactions between them and in forming predictions regarding the fate of the two species in the area. It will be particularly interesting to learn whether the quagga will be persistently successful in colonizing the Lagoon, as was the case in other areas it migrated into where, in a relatively short time of 5–10 years, it outcompeted the zebra mussel (e.g., Mills et al., 1996; Orlova et al., 2004; Ricciardi and Whoriskey, 2004; Karatayev et al., 2015), although the latter may still persist and feature prominently in the Lagoon's ecosystem, as it has done in. e.g., Lake Erie (cf. Karatayev et al., 2014b).

AUTHOR CONTRIBUTIONS

BW-W developed the plan of research. BW-W, AW, and AS conducted the field work. BW-W, AS, and AW processed the samples. BW-W and TR analyzed the data. All authors contributed to writing the manuscript.

FUNDING

This study was supported by the Faculty of Geosciences, University of Szczecin, Szczecin, Poland within the framework of the statutory funds for research.

ACKNOWLEDGMENTS

Thanks are due to our skipper, Mr. Mieczysław Ziarkiewicz, for his much-appreciated assistance with sampling. We appreciate greatly the input received from three reviewers whose comments helped us to improve the manuscript.

SUPPLEMENTARY MATERIAL

The Supplementary Material for this article can be found online at: https://www.frontiersin.org/articles/10.3389/fmars.2019.00076/full#supplementary-material

REFERENCES

Ardisson, P. L., and Bourget, E. (1991). Abundance, growth, and production estimation of the blue mussel *Mytilus edulis* on moored navigation buoys in the estuary and northwestern gulf of St. Lawrence. *Can. J. Fish. Aquat. Sci.* 48, 2408–2419. doi: 10.1139/f91-282

Baldwin, B. S., Mayer, M. S., Dayton, J., Pau, N., Mendilla, J., Sullivan, M., et al. (2002). Comparative growth and feeding in zebra and quagga mussels (*Dreissena polymorpha* and *Dreissena bugensis*): implications for North American lakes. *Can. J. Fish. Aquat. Sci.* 59, 680–694. doi: 10.1139/f02-043

Bale, A. J., and Kenny, A. J. (2005). "Sediment Analysis and Seabed Characterisation," in *Methods for the Study of Marine Benthos*, 3 Edn, eds A. Eleftheriou and A. McIntyre (Oxford: Blackwell Science), 43–86. doi: 10.1002/9780470995129.ch2

Bangel, H., Schernewski, G., Bachor, A., and Landsberg-Uczciwek, M. (2004). "Spatial pattern and long-term development of water quality in the Oder Estuary," in *The Oder Estuary – Against the Background of the European Water Framework Directive*, eds G. Schernewski and T. Dolch (Rostock: Institut für Ostseeforschung Warnemünde), 17–65.

Bially, A., and MacIsaac, H. J. (2000). Fouling mussels (*Dreissena* spp.) colonize soft sediments in lake erie and facilitate benthic invertebrates. *Freshw. Biol.* 43, 85–97. doi: 10.1046/j.1365-2427.2000.00526.x

Bierman, V. J. Jr., Kaur, J., DePinto, J. V., Feist, T. J., and Dilks, D. W. (2005). Modeling the role of zebra mussels in the proliferation of blue-green algae in saginaw bay, lake huron. *J. Great Lakes Res.* 31, 32–55. doi: 10.1016/S0380-1330(05)70236-7

Bij de Vaate, A. (2010). Some evidence for ballast water transport being the vector of the quagga mussel (*Dreissena rostriformis bugensis* Andrusov, 1897) introduction into Western Europe and subsequent upstream dispersal in the River Rhine. *Aquat. Invasions* 5, 207–209. doi: 10.3391/ai.2010.5.2.13

Boegehold, A. G., Johnson, N. S., Ram, J. L., and Kashian, D. R. (2018). Cyanobacteria reduce quagga mussel (*Dreissena rostriformis bugensis*) spawning and fertilization success. *Freshw. Sci* 37, 510–518. doi: 10.1086/698353

Brionez-Fourzán, P. (2014). Differences in life-history and ecological traits between co-occurring *Panulirus* spiny lobsters (Decapoda, Palinuridae). *ZooKeys* 457, 289–311. doi: 10.3897/zookeys.457.6669

Chesson, P. (2000). Mechanisms of maintenance of species diversity. *Annu. Rev. Ecol. Evol. Syst.* 31, 343–366. doi: 10.1146/annurev.ecolsys.31.1.343

Claxton, W. T., and Mackie, G. L. (1998). Seasonal and depth variations in gametogenesis and spawning of *Dreissena polymorpha* and *Dreissena bugensis* in eastern Lake Erie. *Can. J. Zool.* 76, 2010–2019. doi: 10.1139/z98-150

Cockrell, M. L., Bernhardt, J. R., and Leslie, H. M. (2015). Recruitment, abundance, and predation on the blue mussel (*Mytilus edulis*) on northeastern estuarine rocky shores. *Ecosphere* 6:art18. doi: 10.1890/ES14-00176.1

Czugała, A., and Woźniczka, A. (2010). The River odra estuary – another baltic sea area colonized by the round goby *Neogobius melanostomus* Pallas, 1811. *Aquat. Invasions* 5(Suppl. 1), S61–S65. doi: 10.3391/ai.2010.5.S1.014

Daunys, D., Zemlys, P., Olenin, S., Zaiko, A., and Ferrarin, C. (2006). Impact of the zebra mussel *Dreissena polymorpha* invasion on the budget of suspended matter in a shallow lagoon ecosystem. *Helgol. Mar. Res.* 60, 113–120. doi: 10.1007/s10152-006-0028-5

Dettman, J. R., Jacobson, D. J., Turner, E., Pringle, A., and Taylor, J. W. (2003). Reproductive isolation and phylogenetic divergence in neurospora: comparing methods of species recognition in a model eukaryote. *Evolution* 57, 2721–2741. doi: 10.1111/j.0014-3820.2003.tb01515.x

D'Hont, A., Gittenberger, A., Hendriks, A. J., and Leuven, R. S. E. W. (2018). Drivers of dominance shifts between invasive ponto-caspian dreissenids *Dreissena polymorpha* (Pallas, 1771) and *Dreissena rostriformis bugensis* (Andrusov, 1897). *Aquat. Invasions* 13, 449–462. doi: 10.3391/ai.2018.13.4.03

Diggins, T. P. (2001). A seasonal comparison of suspended sediment filtration by quagga (*Dreissena bugensis*) and zebra mussels (*D. polymorpha*). *J. Great Lakes Res.* 27, 457–466. doi: 10.1016/S0380-1330(01)70660-0

Dorgelo, J. (1993). "Growth and population structure of the zebra mussel (*Dreissena polymorpha*) in Dutch lakes different in trophic state," in *Zebra Mussels: Biology, Impacts, and Control*, eds T. F. Nalepa and D. W. Schloesser (Ann Arbor, MI: Lewis Publishers), 79–94.

Fenske, C., Dahlke, S., Riel, P., and Woźniczka, A. (2010). "Dynamics of mussel beds in the Szczecin Lagoon," in *From Brazil to Thailand – New Results in Coastal Research*, eds K. Schwarzer, K. Schrottke, and K. Stattegger (Rostock: EUCC - Die Küsten Union Deutschland e.V), 51–58.

Fenske, C., Zaiko, A., Wozniczka, A., Dahlke, S., and Orlova, M. I. (2013). "Variation in length-frequency distributions of zebra mussels (*Dreissena polymorpha*) within and between three Baltic Sea subregions Szczecin Lagoon, Curonian Lagoon, and Gulf of Finland," in *Quagga and Zebra Mussels: Biology, Impacts and Control*, eds T. F. Nalepa and D. W. Schlosser (Boca Raton, FL: CRC Press Taylor), 725–740.

Fernald, S. H., Caraco, N. F., and Cole, J. J. (2007). Changes in cyanobacterial dominance following the invasion of the zebra mussel *Dreissena polymorpha*: long-term results from the hudson river estuary. *Estuaries Coasts* 30, 163–170. doi: 10.1007/BF02782976

Flynn, D. F. B., Mirotchnick, N., Matthew, M. J., Palmer, J. I., and Naeem, S. (2011). Functional and phylogenetic diversity as predictors of

biodiversity–ecosystem-function relationships. *Ecology* 92, 1573–1581. doi: 10.1890/10-1245.1

Foley, C. J., Andree, S. R., Pothoven, S. A., Nalepa, T. F., and Höök, T. O. (2017). Quantifying the predatory effect of round goby on saginaw bay dreissenids. *J. Great Lakes Res.* 43, 121–131. doi: 10.1016/j.jglr.2016.10.018

Fréchette, M., and Bourget, E. (1985). Energy flow between the pelagic and benthic zones: factors controlling particulate organic matter available to an intertidal mussel bed. *Can. J. Fish. Aquat. Sci.* 42, 1158–1165. doi: 10.1139/f85-143

Garton, D. W., McMahon, R., and Stoeckmann, A. M. (2014). "Limiting Environmental Factors and Competitive Interactions between Zebra and Quagga Mussels in North America," in *Quagga and Zebra Mussels: Biology, Impacts, and Control*, 2nd Edn, eds T. F. Nalepa and D. W. Schloesser (Boca Raton, FL: CRC Press), 695–703.

Gaskill, J. A., and Woller-Skar, M. M. (2018). Do invasive dreissenid mussels influence spatial and temporal patterns of toxic *Microcystis aeruginosa* in a low-nutrient Michigan lake? *Lake Reserv. Manag.* 34, 244–257. doi: 10.1080/10402381.2018.142358

Gotelli, N. J. (2000). Null model analysis of species co-occurrence patterns. *Ecology* 81, 2606–2621. doi: 10.1890/0012-9658(2000)081[2606:NMAOSC]2.0.CO;2

Gruszka, P. (1999). The river odra estuary as a gateway for alien species immigration to the baltic sea basin. *Acta Hydrochim. Hydrobiol.* 27, 374–382. doi: 10.1002/(SICI)1521-401X(199911)27:5<374::AID-AHEH374>3.0.CO;2-V

Gutierrez, J. L., Jones, C. G., Strayer, D. L., and Iribarne, O. O. (2003). Mollusks as ecosystem engineers: the role of shell production in aquatic habitats. *Oikos* 101, 79–90. doi: 10.1034/j.1600-0706.2003.12322.x

Hecky, R. E., Smith, R. E. H., Barton, D. R., Guilford, S. J., Taylor, W. D., Charlton, M. N., et al. (2004). The nearshore phosphorus shunt: a consequence of ecosystem engineering by dreissenids in the laurentian great lakes. *Can. J. Fish. Aquat. Sci.* 61, 1285–1293. doi: 10.1139/f04-065

Heiler, K. C. M., Bij de Vaate, A., Ekschmitt, K., von Oheimb, P. V., Albrecht, C., and Wilke, T. (2013). Reconstruction of the early invasion history of the quagga mussel (*Dreissena rostriformis bugensis*) in Western Europe. *Aquat. Invasions* 1, 53–57. doi: 10.3391/ai.2013.8.1.06

Higgins, S. N., and Vander Zanden, M. J. (2010). What a difference a species makes: a meta-analysis of dreissenid mussel impacts on freshwater ecosystems. *Ecol. Monogr.* 80, 179–196. doi: 10.1890/09-1249.1

HilleRisLambers, J., Adler, P. B., Harpole, W. S., Levine, J. M., and Mayfield, M. M. (2012). Rethinking community assembly through the lens of coexistence theory. *Annu. Rev. Ecol. Evol. Syst.* 43, 227–248. doi: 10.1146/annurev-ecolsys-110411-160411

Izvekova, E. I., and Lvova-Katchanova, A. A. (1972). Sedimentation of suspended matter by *Dreissena polymorpha* Pallas and its subsequent utilization by Chironomidae larvae. *Pol. Arch. Hydrobiol.* 19, 203–210.

Jantz, B., and Neumann, D. (1992). "Shell growth and population dynamics of *Dreissena polymorpha* in the River Rhine," in *The Zebra Mussel Dreissena Polymorpha. Limnologie till*, eds D. Neumann and H. A. Jenner (Stuttgart: Gustav Fischer Verlag), 49–66.

Jones, L. A., and Ricciardi, A. (2005). Influence of physicochemical factors on the distribution and biomass of invasive mussels (*Dreissena polymorpha* and *Dreissena bugensis*) in the St. Lawrence River. *Can. J. Fish. Aquat. Sci.* 62, 1953–1962. doi: 10.1139/f05-096

Karatayev, A. Y., Burlakova, L. E., Molloy, D. P., and Volkova, L. K. (2000). Endosymbionts of *Dreissena polymorpha* (Pallas) in Belarus. *Int. Rev. Hydrobiol.* 85, 543–559. doi: 10.1002/1522-2632(200011)85:5/6<543::AID-IROH543>3.0.CO;2-3

Karatayev, A. Y., Burlakova, L. E., and Padilla, D. K. (1997). The effects of *Dreissena polymorpha* (Pallas) invasion on aquatic communities in Eastern Europe. *J. Shellfish Res.* 16, 187–203.

Karatayev, A. Y., Burlakova, L. E., and Padilla, D. K. (1998). Physical factors that limit the distribution and abundance of *Dreissena polymorpha* (Pall.). *J. Shellfish Res.* 17, 1219–1235.

Karatayev, A. Y., Burlakova, L. E., and Padilla, D. K. (2002). "Impacts of zebra mussels on aquatic communities and their role as ecosystem engineers," in *Invasive Aquatic Species of Europe: Distribution, Impacts and Management*, eds E. Leppäkoski, S. Gollasch, and S. Olenin (Dordrecht: Kluwer Academic Publishers), 433–446.

Karatayev, A. Y., Burlakova, L. E., and Padilla, D. K. (2014a). "General overview of zebra and quagga mussels what we do and do not know," in *Quagga and Zebra Mussels: Biology, Impacts, and Control*, 2nd Edn, eds T. F. Nalepa and D. W. Schloesser (Boca Raton, FL: CRC Press), 695–703.

Karatayev, A. Y., Burlakova, L. E., Pennuto, C., Ciborowski, J., Karatayev, V. A., Juette, P., et al. (2014b). Twenty five years of changes in Dreissena spp. populations in Lake Erie. *J. Great Lakes Res.* 40, 550–559. doi: 10.1016/j.jglr.2014.04.010

Karatayev, A. Y., Burlakova, L. E., and Padilla, D. K. (2015). Zebra versus quagga mussels: a review of their spread, population dynamics, and ecosystem impacts. *Hydrobiologia* 746, 97–112. doi: 10.1007/s10750-014-1901-x

Keller, R. P., Drake, J. M., and Lodge, D. M. (2007). Fecundity as a basis for risk assessment of nonindigenous freshwater molluscs. *Conserv. Biol.* 21, 191–200. doi: 10.1111/j.1523-1739.2006.00563.x

Kelley, D. W., Herborg, L. M., and MacIsaak, H. J. (2010). "Ecosystem changes associated with *Dreissena* invasions: recent developments and emerging issues," in *The Zebra Mussel in Europe*, eds G. van der Velde, S. Rajagopal, and A. Bij de Vaate (Leiden: Backhuys Publishers), 199–209.

Krebs, C. J. (1995). Two paradigms of population regulation. *Wildlife Res.* 22, 1–10. doi: 10.1071/WR9950001

Kublickas, A. (1959). "Feeding of benthophagous fish in the Curonian lagoon," in *Kursiu Marios*, eds K. Jankevicius, I. Gasiûnas, A. Gediminas, V. Gudelis, A. Kublickas, and I. Maniukas (Vilnius: Lithuanian Academy of Sciences), 463–521.

Labropoulou, M., and Eleftheriou, A. (1997). The foraging ecology of two pairs of congeneric demersal fish species: importance of morphological characteristics in prey selection. *J. Fish Biol.* 50, 324–340. doi: 10.1111/j.1095-8649.1997.tb01361.x

Liebig, J. R., and Vanderploeg, H. A. (1995). Vulnerability of *Dreissena polymorpha* larvae to predation by great lakes calanoid copepods: the importance of the bivalve Shell. *J. Great Lakes Res.* 21, 353–358. doi: 10.1016/S0380-1330(95)71046-2

Lockwood, J. L., Hoopes, M. F., and Marchetti, M. P. (2007). *Invasion Ecology*. Hoboken, NJ: Blackwell Publishing.

Lucy, F. (2006). Early life stages of *Dreissena polymorpha* (zebra mussel): the importance of long-term datasets in invasion ecology. *Aquat. Invasions* 1, 171–182. doi: 10.3391/ai.2006.1.3.12

MacIsaac, H. J., Sprules, W. G., and Leach, J. H. (1991). Ingestion of small-bodied zooplankton by zebra mussels (*Dreissena polymorpha*): can cannibalism on larvae influence population dynamics? *Can. J. Fish Aquat. Sci.* 48, 2051–2060. doi: 10.1139/f91-244

Marchowski, D., Neubauer, G., Ławicki, Ł, Woźniczka, A., Wysocki, D., Guentzel, S., et al. (2015). The importance of non-native prey, the zebra mussel *Dreissena polymorpha*, for the declining greater scaup *Aythya marila*: a case study at a key european staging and wintering site. *PLoS One* 10:e0145496. doi: 10.1371/journal.pone.0145496

Masłowski, J. (1993). Long-term changes in the bottom macrofauna of the Szczecin Lagoon (north-western Poland). *Acta Hydrobiol.* 35, 341–355.

Mastitsky, S. E., and Gagarin, V. G. (2004). Nematodes which infect the mollusc *Dreissena polymorpha* (Bivalvia: Dreissenidae) in Narochanskie Lakes. Vestnik Belorusskogo Gosudarstvennogo Universiteta. *Seriya* 2, 22–25.

Matthews, J., Van der Velde, B., Bij de Vaate, A., Collas, F. P. L., Koopman, K. R., and Leuven, R. S. E. W. (2014). Rapid range expansion of the invasive quagga musselin relation to zebra mussel presence in The Netherlands and Western Europe. *Biol. Invasions* 16, 23–42. doi: 10.1007/s10530-013-0498-8

McDonald, J. H. (2014). *Handbook of Biological Statistics*, 3rd Edn. Baltimore, MD.: Sparky House Publishing.

McMahon, R. F. (1996). The physiological ecology of the zebra mussel, *Dreissena polymorpha*, in North America and Europe. *Am. Zool.* 36, 339–363. doi: 10.1016/j.fsi.2016.06.054

Meyer, H., and Lampe, R. (1999). The restricted buffer capacity of a south baltic estuary – the oder estuary. *Limnologica* 29, 242–248. doi: 10.1016/S0075-9511(99)80008-5

Mills, E. L., Rosenberg, G., Spidle, A. P., Ludyanskiy, M., Pligin, Y., and May, B. (1996). A review of the biology and ecology of the quagga mussel (*Dreissena bugensis*), a second species of freshwater dreissenid introduced to North America. *Am. Zool.* 36, 271–286. doi: 10.1093/icb/36.3.271

Molloy, D. P., Bij de Vaate, A., Wilke, T., and Giamberini, L. (2007). Discovery of *Dreissena rostriformis bugensis* (Andrusov 1897) in Western Europe. *Biol. Invasions* 9, 871–874. doi: 10.1007/s10530-006-9078-5

Molloy, D. P., Karatayev, A. Y., Burlakova, L. E., Kurandina, D. P., and Laruelle, F. (1997). Natural enemies of zebra mussels: predators, parasites and ecological competitors. *Rev. Fish. Sci.* 5, 27–97. doi: 10.1080/10641269709388593

Mörtl, M. S., Werner, K., and Rothhaupt, O. (2010). "Effects of predation by wintering water birds on zebra mussels and on associated macroinvertebrates," in *The Zebra Mussel in Europe*, eds G. Van der Velde, S. Rajagopal, and A. Bij de Vaate (Leiden: Backhuys Publishers), 239–249.

Naddafi, R., Pettersson, K., and Eklöv, P. (2010). Predation and physical environment structure the density and population size structure of zebra mussels. *J. N. Am. Benthol. Soc.* 29, 444–453. doi: 10.1899/09-071.1

Naddafi, R., and Rudstam, L. G. (2014). Predation on invasive zebra mussel, *Dreissena polymorpha*, by pumpkinseed sunfish, rusty crayfish, and round goby. *Hydrobiologia* 721, 107–115. doi: 10.1007/s10750-013-1653-z

Nalepa, T. F., Fanslow, D. L., and Lang, G. A. (2009). Transformation of the offshore benthic community in Lake Michigan: recent shift from the native amphipod *Diporeia* spp. to invasive mussel *Dreissena rostriformis bugensis*. *Freshw. Biol.* 54, 466–479. doi: 10.1111/j.1365-2427.2008.02123.x

Nalepa, T. F., Fanslow, D. L., and Pothoven, S. A. (2010). Recent changes in density, biomass, recruitment, size structure, and nutritional state of *Dreissena* populations in southern Lake Michigan. *J. Great Lakes Res.* 36, 5–19. doi: 10.1016/j.jglr.2010.03.013

Nalepa, T. F., and Schloesser, D. W. (1993). *Zebra Mussels Biology, Impacts, and Control*. Boca Raton, FL: Lewis Publishers.

Nalepa, T. F., and Schloesser, D. W. (2014). *Quagga and Zebra Mussels: Biology, Impacts, and Control*, 2nd Edn. Boca Raton, FL: CRC Press.

Nentwig, W. (2008). "Pathways in Animal Invasion," in *Biological Invasion*, ed. W. Nentwig (Berlin: Springer), 11–27.

Nogaro, G., and Steinman, A. D. (2013). Influence of ecosystem engineers on ecosystem processes is mediated by lake sediment properties. *Oikos* 123, 500–512. doi: 10.1111/j.1600-0706.2013.00978.x

Noordhuis, R., van Erden, M. R., and Roos, M. (2010). "Crash of zebra mussel, transparency and water bird populations in Lake Markermeer," in *The Zebra Mussel in Europe*, eds G. van der Velde, S. Rajagopal, and A. bij de Vaate (Leiden: Backhuys Publisher), 265–277.

Olenin, S., Gollasch, S., Lehtiniemi, M., Sapota, M., and Zaiko, A. (2017). "Biological invasions"," in *Biological Oceanography of the Baltic Sea*, eds P. Snoeijs-Leijonmalm, H. Schubert, and T. Radziejewska (Dordrecht: Springer Science+Business Media), 193–232. doi: 10.1007/978-94-007-0668-2_5

Orlova, M. I., Muirhead, J., Antonov, P. I., Shcherbina, G. K., Starobogatov, I., Biochino, G. I., et al. (2004). Range expansion of quagga mussels *Dreissena rostriformis bugensis* in the Volga River and Caspian Sea basin. *Aquat. Ecol.* 38, 561–573. doi: 10.1007/s10452-004-0311-y

Pace, M. L., Strayer, D. L., Fischer, D., and Malcom, H. M. (2010). Recovery of native zooplankton associated with increased mortality of an invasive mussel. *Ecosphere* 1, 1–10. doi: 10.1890/ES10-00002.1

Piesik, Z. (1974). The role of crayfish *Orconectes limosus* (Raf.) in extinction of *Dreissena polymorpha* subsisting on steelon-net. *Pol. Arch. Hydrobiol.* 21, 401–410.

Piesik, Z. (1983). Biology of *Dreissena polymorpha* (Pall.) settling on stylon nets and the role of this mollusk in eliminating the seston and the nutrients from the water-course. *Pol. Arch. Hydrobiol.* 30, 353–361.

Piesik, Z. (1992). The biological and ecological role of the fouling organisms inhabiting artificial substrates in various types of water. *Rozpr. Stud. Uniw. Szczecińskiego* 12, 127–128.

Pigot, A. L., and Tobias, J. A. (2013). Species interactions constrain geographic range expansion over evolutionary time. *Ecol. Lett.* 16, 330–338. doi: 10.1111/ele.12043

Polsenaere, P., Soletchnik, P., Le Moine, O., Gohin, F., Robert, S., Pépin, H.-F., et al. (2017). Potential environmental drivers of a regional blue mussel mass mortality event (winter 2014, Breton Sound, France). *J. Sea Res.* 123, 39–50. doi: 10.1016/j.seares.2017.03.005

Popa, O. P., and Popa, L. O. (2006). The most westward European occurrence point for *Dreissena bugensis* (Andrusov 1897). *Malacol. Bohemoslov.* 5, 3–5.

Radziejewska, T., Fenske, C., Wawrzyniak-Wydrowska, B., Woźniczka, A., and Gruszka, P. (2009). The zebra mussel (*Dreissena polymorpha*) and the benthic community in a coastal Baltic lagoon: another example of enhancement? *Mar. Ecol.* 30, 138–150. doi: 10.1111/j.1439-0485.2009.00313.x

Radziejewska, T., and Schernewski, G. (2008). "The Szczecin (Oder-) Lagoon," in *Ecology of Baltic Coastal Waters Series*, ed. U. Schiewer (Heidelberg: Springer-Verlag), 115–129. doi: 10.1007/978-3-540-73524-3_5

Ricciardi, A., and MacIsaac, H. J. (2000). Recent mass invasion of the North American Great Lakes by Ponto-Caspian species. *Trends Ecol. Evol.* 15, 62–66. doi: 10.1016/S0169-5347(99)01745-0

Ricciardi, A., and Whoriskey, F. G. (2004). Exotic species replacement: shifting dominance of dreissenid mussels in the soulanges canal, upper St. Lawrence River, Canada. *J. N. Am. Benthol. Soc.* 23, 507–514. doi: 10.1899/0887-3593(2004)023<0507:ESRSDO>2.0.CO;2

Rilov, G., and Crooks, J. A. (2009). *Biological Invasions in Marine Ecosystems, Ecological, Management, and Geographic Perspectives*. Berlin: Springer Science. doi: 10.1007/978-3-540-79236-9

Roe, S. L., and MacIsaac, H. J. (1997). Deepwater population structure and reproductive state of quagga mussels (*Dreissena bugensis*) in Lake Erie. *Can. J. Fish. Aquat. Sci.* 54, 2428–2433. doi: 10.1139/f97-151

Schneider, D. W., Madon, S. P., Stoeckel, J. A., and Sparks, R. E. (1998). Seston quality controls zebra mussel (*Dreissena polymorpha*?) energetics in turbid rivers. *Oecologia* 117, 331–341. doi: 10.1007/s004420050666

Scott, L. E. (2009). *Co-occurrence with a Congeneric Species Predicts Life History and Morphological Diversification in the Mexican Livebearing fish Poelicopsis baenschi*. M.Sc. Thesis, Brigham Young University, Brigham.

Sfenthourakis, S., Tzanatos, E., and Giokas, S. (2005). Species co-occurrence: the case of congeneric species and a causal approach to patterns of species association. *Glob. Ecol. Biogeogr.* 15, 39–49. doi: 10.1111/j.1466-822X.2005.00192.x

Smit, H., Bij de Vaate, A., Reeders, H. H., Van Nes, E. H., and Noordhuis, R. (1993). "Colonization, ecology, and positive aspects of zebra mussels (*Dreissena polymorpha*) in The Netherlands," in *Zebra Mussels Biology, Impacts and Control*, eds T. F. Nalepa and D. Schloesser (Boca Raton, FL: CRS Press), 55–77.

Sprung, M. (1995a). Physiological energetics of the zebra mussel *Dreissena polymorpha* in lakes I. Growth and reproductive effort. *Hydrobiologia* 304, 117–132. doi: 10.1007/BF02579417

Sprung, M. (1995b). Physiological energetics of the zebra mussel *Dreissena polymorpha* in lakes III. Metabolism and net growth efficiency. *Hydrobiologia* 304, 147–158. doi: 10.1007/BF02579419

Stańczykowska, A., Lewandowski, K., and Czarnoleski, M. (2010). "Distribution and densities of *Dreissena polymorpha* in Poland – past and present" in *The Zebra Mussel in Europe*, eds G. Van der Velde, S. Rajagopal, and A. Bij de Vaate (Leiden: Backhuys Publishers), 119–126.

Stańczykowska, A., and Planter, M. (1985). Role of mussel *Dreissena polymorpha* (Pall.) in N and P cycles in a lake ecosystem. *Ekol. Pol.* 33, 345–354.

Stanisz, A. (2007). Przystępny kurs statystyki z zastosowaniem STATISTICA PL na przykładach z medycyny. *StatSoft Polska Kraków* 2, 137–166.

Stewart, T. W., Gafford, J. C., Miner, J. G., and Lowe, R. L. (1999). *Dreissena*-shell habitat and antipredator behavior: combined effects on survivorship of snails co-occurring with molluscivorous fish. *J. N. Am. Benthol. Soc.* 18, 274–283. doi: 10.2307/1468465

Stewart, T. W., Miner, J. G., and Lowe, R. L. (1998). Quantifying mechanisms for zebra mussel effects on benthic macroinvertebrates: organic matter production and shell-generated habitat. *J. N. Am. Benthol. Soc.* 17, 81–94. doi: 10.2307/1468053

Stoeckmann, A. (2003). Physiological energetics of Lake Erie dreissenid mussels: a basis for the displacement of *Dreissena polymorpha* by *Dreissena bugensis*. *Can. J. Fish Aquat. Sci.* 60, 126–134. doi: 10.1139/f03-005

Strayer, D. L., and Malcom, H. (2006). Long term demography of a zebra mussel (*Dreissena polymorpha*). *Freshw. Biol.* 51, 117–130. doi: 10.1111/j.1365-2427.2005.01482.x

Thienemann, A. (1950). The transport of aquatic animals by birds. *Binnengewasser* 18, 156–159.

Tyutin, A. V. (2005). "Aboriginal parasitic systems following invasions of new aquatic species in the Rybinsk Reservoir (the Upper Volga, Russia)," in *Proceedings of the Second International Symposium "Alien Species in Holarctic (Borok-2)*, eds Y. Y. Dgebuadze and Y. V. Slynko (Borok: CAB International), 131–132.

Van Eerden, M. R., and De Leeuw, J. (2010). "How *Dreissena* sets the winter scene for water birds: Dynamic interaction between diving ducks and zebra mussel,"

in *The Zebra Mussel in Europe*, eds G. van der Velde, S. Rajagopal, and A. bij de Vaate (Leiden: Backhuys Publisher), 251–264.

Vanderploeg, H. A., Nalepa, T. F., Jude, D. J., Mills, E. L., Holeck, K. T., Liebig, J. R., et al. (2002). Dispersal and emerging ecological impacts of ponto-caspian species in the Laurentian Great Lakes. *Can. J. Fish. Aquat. Sci.* 59, 1209–1228. doi: 10.1139/f02-087

Veech, J. A. (2014). The pairwise approach to analysing species co-occurrence. *J. Biogeogr.* 41, 1029–1035. doi: 10.1111/jbi.12318

Walter, G. H. (1991). What is resource partitioning? *J. Theor. Biol.* 150, 137–143. doi: 10.1016/S0022-5193(05)80327-3

Ward, J. M., and Ricciardi, A. (2007). Impacts of *Dreissena* invasions on benthic macroinvertebrate communities: a meta-analysis. *Divers. Distrib.* 13, 155–165. doi: 10.1111/j.1472-4642.2007.00336.x

Wawrzyniak-Wydrowska, B., and Gruszka, P. (2005). Population dynamics of alien gammarid species in the River Odra estuary. *Hydrobiologia* 539, 13–25. doi: 10.1007/s10750-004-3081-6

Wiktor, J. (1962). Quantitative and qualitative investigations of the Szczecin Firth bottom fauna. Part II. *Pr. Mor. Inst. Ryb. Gdynia* 11, 81–112.

Wiktor, J. (1969). The biology of *Dreissena polymorpha* (Pall.) and its biological importance in the Firth of Szczecin. *Stud. Mat. Mor. Inst. Ryb. Gdynia* A, 1–88.

Wolnomiejski, N., and Witek, Z. (2013). *The Szczecin Lagoon Ecosystem: The Biotic Community of the Great Lagoon and its Food Web Model*. London: Versita Ltd. doi: 10.2478/9788376560502

Wolnomiejski, N., and Woźniczka, A. (2008). A drastic reduction in abundance of *Dreissena polymorpha* Pall. in the Skoszewska Cove (Szczecin Lagoon, River Odra estuary): effects in the population and habitat. *Ecol. Quest.* 9, 103–111. doi: 10.2478/v10090-009-0025-9

Wong, W. H., Gerstenberger, S., Baldwin, W., and Moore, B. (2012). Settlement and growth of quagga mussels (*Dreissenia rostriformis bugensis* Andrusov, 1897) in Lake Mead, Nevada-Arizona, USA. *Aquat. Invasions* 7, 7–19. doi: 10.3391/ai.2012.7.1.002

Wong, W. H., Gerstenberger, S. L., Hatcher, M. D., Thompson, D. R., and Schrimsher, D. (2013). Invasive quagga mussels can be attenuated by redear sunfish (*Lepomis microlophus*) in the Southwestern United States. *Biol. Control.* 64, 276–282. doi: 10.1016/j.biocontrol.2012.11.006

Woźniczka, A., Wawrzyniak-Wydrowska, B., Radziejewska, T., and Skrzypacz, A. (2016). The quagga mussel (*Dreissena rostriformis bugensis* Andrusov, 1897) – another ponto-caspian dreissenid bivalve in the southern Baltic catchment: the first record from the Szczecin Lagoon. *Oceanologia* 58, 154–159. doi: 10.1016/j.oceano.2015.12.002

Woźniczka, A., and Wolnomiejski, N. (2005). Zebra mussel *(Dreissena polymorpha* Pall.) in the river odra estuary: the current status. *5th Baltic Sea Sci. Congr. Sopot Poland* 373–374.

Zaiko, A., Minchin, D., and Olenin, S. (2014). "The day after tomorrow": anatomy of an 'r' strategist aquatic invasion. *Aquat. Invasions* 9, 145–155. doi: 10.3391/ai.2014.9.2.03

Zaiko, A., Olenin, S., and Daunys, D. (2009). Habitat engineering by the invasive zebra mussel *Dreissena polymorpha* (Pallas) in a boreal coastal lagoon: impact on biodiversity. *Helgol. Mar. Res.* 63, 85–94. doi: 10.1007/s10152-008-0135-6

Zhulidov, A. V., Kozhara, A. V., Scherbina, G. H., Nalepa, T. F., Protasov, A., Afanasiev, S. A., et al. (2010). Invasion history, distribution, and relative abundances of *Dreissena bugensis* in the Old World: a synthesis of data. *Biol. Invasions* 12, 1923–1940. doi: 10.1007/s10530-009-9641-y

Zhulidov, A. V., Pavlov, D. F., Nalepa, T. F., Scherbina, G. H., Zhulidov, D. A., and Gurtovaya, T. Y. (2004). Relative distributions of *Dreissena bugensis* and *Dreissena polymorpha* in the lower don river system, Russia. *Int. Rev. Hydrobiol.* 89, 326–333. doi: 10.1002/iroh.200310727

Conflict of Interest Statement: The authors declare that the research was conducted in the absence of any commercial or financial relationships that could be construed as a potential conflict of interest.

The handling Editor is currently organizing a Research Topic with one of the authors TR, and confirms the absence of any other collaboration.

Copyright © 2019 Wawrzyniak-Wydrowska, Radziejewska, Skrzypacz and Woźniczka. This is an open-access article distributed under the terms of the Creative Commons Attribution License (CC BY). The use, distribution or reproduction in other forums is permitted, provided the original author(s) and the copyright owner(s) are credited and that the original publication in this journal is cited, in accordance with accepted academic practice. No use, distribution or reproduction is permitted which does not comply with these terms.

frontiers in Marine Science

ORIGINAL RESEARCH
published: 10 April 2018
doi: 10.3389/fmars.2018.00131

Assessment of the Influence of Dredge Spoil Dumping on the Seafloor Geological Integrity

Joonas J. Virtasalo[1]*, *Samuli Korpinen*[2] *and Aarno T. Kotilainen*[1]

[1] *Marine Geology, Geological Survey of Finland (GTK), Espoo, Finland,* [2] *Marine Research Center, Finnish Environment Institute (SYKE), Helsinki, Finland*

The European Marine Strategy Framework Directive requires the development of suitable indicators for regular reporting on the environmental state and achievement of a good environmental status of EU's marine waters by 2020. The development of indicators for determining seafloor integrity and its possible disturbance by human activities have so far largely ignored the geological properties of seafloor. This paper presents a study of Vuosaari and Uusikaupunki-D offshore dumping sites in Finland, the northern Baltic Sea. Full coverage multibeam bathymetry and relative backscatter data, and a number of sediment cores were collected over the sites. The areas covered by dumped dredge spoil stand out in the multibeam images because of their irregular surface and elevated backscatter. The short gravity cores were studied for lithology, and in 1-cm slices for ^{137}Cs activity, organic content, and grain size distribution. The dumped material is represented in the cores by the gravelly mud lithofacies with massive texture and angular coarse particles. The dumped material is coarser, less sorted and has higher kurtosis compared to natural sediment due to the admixing of blasted rock during the dredging activities, and limited sorting during fall through the water column upon dumping. Dispersed dredge spoil, which was suspended in the water column during the dumping activities or reworked from the dumped material mounds and redistributed along the seafloor soon thereafter, was deposited over a wide area as a thin layer that is not necessarily readily identifiable by visual inspection in the cores. Cesium activity helped distinguish the dumped material from the ^{137}Cs-enriched natural sediments deposited after the 1986 Chernobyl disaster. Considering that the dumped material at many of the coring sites in the Vuosaari dumping area is covered by natural sediment, it probably is largely stable. In contrast, dumped material at the shallower Uusikaupunki-D site has slumped down to an adjacent channel and is likely being redistributed by near-bottom currents. Based on the findings of the study, a protocol for the assessment of the geological integrity of seafloor, its anthropogenic change due to dumping, and its potential recovery is proposed, as required by the Marine Strategy Framework Directive.

Keywords: impact study, seafloor integrity, dredged material dumping, sediment, grain size, multibeam echosounder, Baltic Sea, Finland

OPEN ACCESS

Edited by:
Ulrich Volkmar Bathmann, Leibniz Institute for Baltic Sea Research (LG), Germany

Reviewed by:
Vanesa Magar, Centro de Investigación Científica y de Educación Superior de Ensenada, Mexico
Ian Townend, CoastalSEA, United Kingdom

***Correspondence:**
Joonas J. Virtasalo
joonas.virtasalo@gtk.fi

Specialty section:
This article was submitted to Coastal Ocean Processes, a section of the journal Frontiers in Marine Science

Received: *30 January 2018*
Accepted: *28 March 2018*
Published: *10 April 2018*

Citation:
Virtasalo JJ, Korpinen S and Kotilainen AT (2018) Assessment of the Influence of Dredge Spoil Dumping on the Seafloor Geological Integrity. Front. Mar. Sci. 5:131. doi: 10.3389/fmars.2018.00131

INTRODUCTION

Disposal of dredged material (dumping) is a notable issue in coastal zone management, which may represent a major anthropogenic disturbance to the structure and functioning of the seabed, albeit often at very local scales (e.g., Olenin, 1992; Essink, 1999; Bolam et al., 2006; Powilleit et al., 2006; Korpinen et al., 2012). Although open water disposal is often the primary alternative due to economic considerations, dumping effects should be evaluated in order to determine the potential impact on human health, marine ecosystems, and other legitimate uses of the sea. Guidelines and procedures have been established by intergovernmental bodies and international organizations (e.g., OSPAR, 2014; HELCOM, 2015; IMO, 2015) with an aim at reducing the adverse effects of dumping operations. Environmentally acceptable offshore dumping requires the careful evaluation of a number of issues, including the prior characterization of material to be dredged considering the prerequisite that the dredged material is clean or low contaminated, the selection of a suitable dumping site with regard to the stability of the dumped material mounds on the seafloor (depositional site) or its resuspension by currents and transportation to adjacent locations (dispersive site), and the monitoring of environmental effects caused by dumping during and after the operations.

The European Marine Strategy Framework Directive (MSFD) demands regular reporting on the environmental state and the achievement of a Good Environmental Status (GES) of the EU's marine waters by 2020. Eleven descriptors were constituted and associated criteria and indicators were defined to interpret the GES (European Commission, 2017). The Descriptor 6 (seafloor integrity) of GES is targeted to assess the degree to which the seafloor is adversely affected by human activities. Indicators for determining the seafloor integrity and its change are being developed (e.g., Rice et al., 2012; Berg et al., 2015; Teixeira et al., 2016); however, these efforts are focused on the biological (e.g., macrofauna) and hydrochemical (e.g., dissolved oxygen) aspects of the seafloor ecosystem. As yet, there is no consensus on assessment methods to estimate effects of anthropogenic pressures, as required by the recently adopted GES criteria (European Commission, 2017). Even though an approach has been proposed in the Baltic Sea (Korpinen et al., 2013; HELCOM, 2017), determination of the physical (geological) integrity of a seafloor, or its change, is still in an early phase. This lack of geological indicators for the seafloor physical integrity further reverberates in the current consideration of suitable ecosystem service indicators (Broszeit et al., 2017). In this contribution, geological integrity is understood as the integrity of geological properties of the seafloor surface sediment, with respect to its ability to provide a habitable substrate for the indigenous macrozoobenthic community.

Only few studies have considered the physical sedimentary impacts of offshore dumping, and the physical recovery of the seafloor substrate after the cessation of dumping activities. Stronkhorst et al. (2003) observed a recovery of sediment texture a year after the cessation of activities at a dumping site in the North Sea, near the port of Rotterdam. Wienberg and Hebbeln (2005) observed a recovery of seafloor dune morphology and redistribution of dumped material from a dumping site within few months in the Weser Estuary, North Sea. Du Four and Van Lancker (2008) observed a restoration of seafloor morphology and sediment texture within 1 year at a dumping site near the Zeebrugge harbor, also in the North Sea. Marmin et al. (2016) observed a partial recovery of seafloor morphology and the admixing of dumped fine sand with coarser natural sediments after 14 months at an experimental dumping site in the Bay of Seine, the English Channel. All these studies are from tidal high-energy sandy seafloor environments, where the dumped dredge spoil is intensively reworked and redistributed along the seafloor. The physical sedimentary impacts of dumping activities, as well as the process of the possible recovery of the seafloor substrate, are expected to be different in wave-dominated coastal areas with minimal tidal amplitude and soft muddy sediments. Indeed, Lepland et al. (2009) observed restricted spread of dumped mixture of mud, sand and gravel, and loading-induced compaction of underlying natural organic-rich mud at a dumping site in Oslofjord, Norway. Stockmann et al. (2009) and Tauber (2009) observed minimal change in the volume of experimentally dumped mounds of glacial till and mixed till, silt and sand, but modest smoothing of the surface roughness by reworking of fine-grained material to local depressions and the development of sandy lags on local elevations during 3 years in the Mecklenburg Bight, southern Baltic Sea.

The purpose of this study is to develop observation techniques and criteria for the assessment of the geological integrity of seafloor, its anthropogenic change due to dumping, and recovery as required by the MSFD. The assessment techniques are based on multibeam seafloor surveys as well as sedimentary ^{137}Cs activity, organic content and grain size distribution parameters determined for sub-sample slices of sediment cores. Those data can be routinely collected in order to facilitate the establishment of robust and cost-effective monitoring programmes that are required to make future assessments of the status of the marine environment. Findings from the study are used for producing a graphical illustration of the assessment process. Grain-size data have been successfully used previously for inferring sediment sources and depositional sub-environments (e.g., Folk and Ward, 1957; Stevens et al., 1996; Bobertz and Harff, 2004; Kairyte and Stevens, 2015), as well as anthropogenic influence such as the redistribution of dumped dredge spoil on the seafloor (Okada et al., 2009; McLaren and Teear, 2014). This study focuses on two offshore dumping areas in Finland, Vuosaari in the south coast and Uusikaupunki-D in the west coast (**Figures 1**, **2**), which provide test cases for discriminating dumped dredge spoil and naturally deposited sediments.

STUDY AREA

The southern coastal sea areas (archipelagos) of Finland are characterized by a mosaic of numerous islands and small bays. These areas have been identified as seabed heterogeneity (i.e., geodiversity) hotspots in the Baltic Sea (Kaskela and Kotilainen, 2017). High primary productivity and sluggish near-bottom

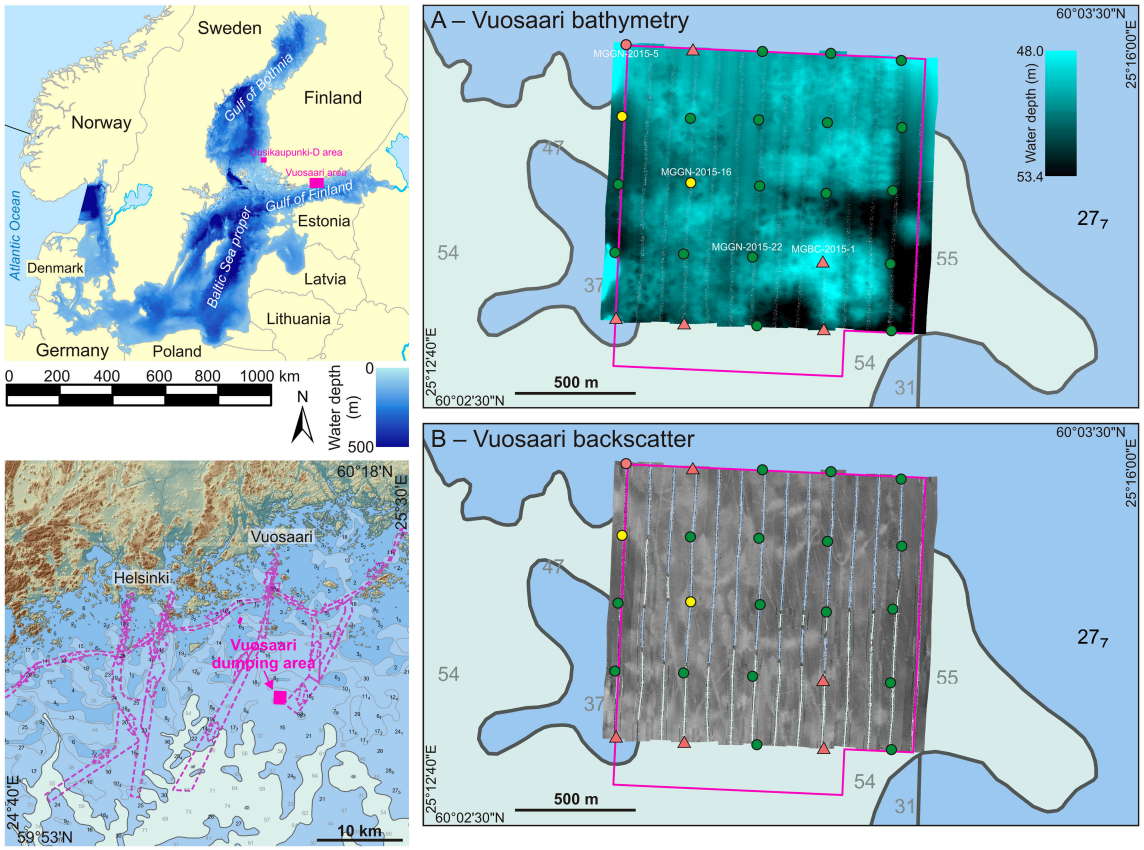


FIGURE 1 | Maps of the Baltic Sea and the Helsinki sea area. **(A)** Multibeam bathymetric image over the Vuosaari dumping area. **(B)** Multibeam relative backscatter image over the Vuosaari dumping area. Magenta line indicates the permitted dumping area. Circle symbol: Gemax short gravity coring site. Triangle symbol: box coring site. Symbol colors: green, organic-rich mud (natural seafloor); red, dumped dredge spoil; yellow, mixture of organic-rich mud and dumped dredge spoil. Coordinate system ETRS-TM35FIN. Base map: ESRI Inc. (Redlands) data & maps of 2005. Bathymetric data: BALANCE project (www.helcom.fi). Nautical chart: S-57 Finnish Transport Agency 2017. Topographic map: National Land Survey of Finland digital elevation model 2 m 2017.

water exchange in these patchy sea areas frequently result in seasonal and longer-lasting hypoxia in local sub-basins (Virtasalo et al., 2005; Jokinen et al., 2015). The waters are annually covered by sea ice for 2–4 months, and the ice season usually ends in April (Seinä and Peltola, 1991). The sea is essentially non-tidal, but irregular water level fluctuations of up to +2.5 m occur due to variations in wind and air pressure.

The Finnish south coast was covered during the last (Weichselian) glacial maximum by the Fennoscandian continental ice-sheet, which retreated northwestwards ca. 13 thousand years ago (Stroeven et al., 2016). The ice-margin retreat was followed by the successive deposition of till, outwash, glaciolacustrine varved silt–sand and clay, postglacial lacustrine silty clay, and brackish-water organic-rich mud (Virtasalo et al., 2007, 2014). The glaciolacustrine and postglacial lacustrine sediments were deposited in deep freshwater as drapes with comparably uniform thicknesses. The superimposed brackish-water muds were deposited after the marine flooding and the establishment of brackish-water conditions with estuarine circulation in the Baltic Sea basin at ca. 7.6 thousand years ago (Eronen et al., 2001; Virtasalo et al., 2007). The brackish-water muds have lower consistency due to the increased organic-matter delivery from amplified primary production, and were thus deposited as asymmetric sediment drifts, influenced by near-bottom currents and wave action (Virtasalo et al., 2007).

The Vuosaari offshore dumping area came into use in 2003, when the construction of the Vuosaari harbor began near the city of Helsinki. The 2.3 km^2 rectangular dumping area is located ca. 20 km south from the Finnish coastline, in the northern part of a local depression with water depths between 50 and 60 m (**Figure 1**). The site is below fairweather wave-base but above storm wave-base (Kohonen and Winterhalter, 1999). The natural seafloor, before the dumping activities, was covered by a thin (<1 m) surface layer of organic-rich brackish-water mud, which sharply overlies a 2–10 m thick layer of organic-bearing brackish-water mud with thin sand–silt stripes. In the downward order, these sediments are underlain by postglacial lacustrine silty clays, glaciolacustrine varved sand–silt and clay, and till. The crystalline bedrock surface is buried down to 60 m below the seafloor, but till

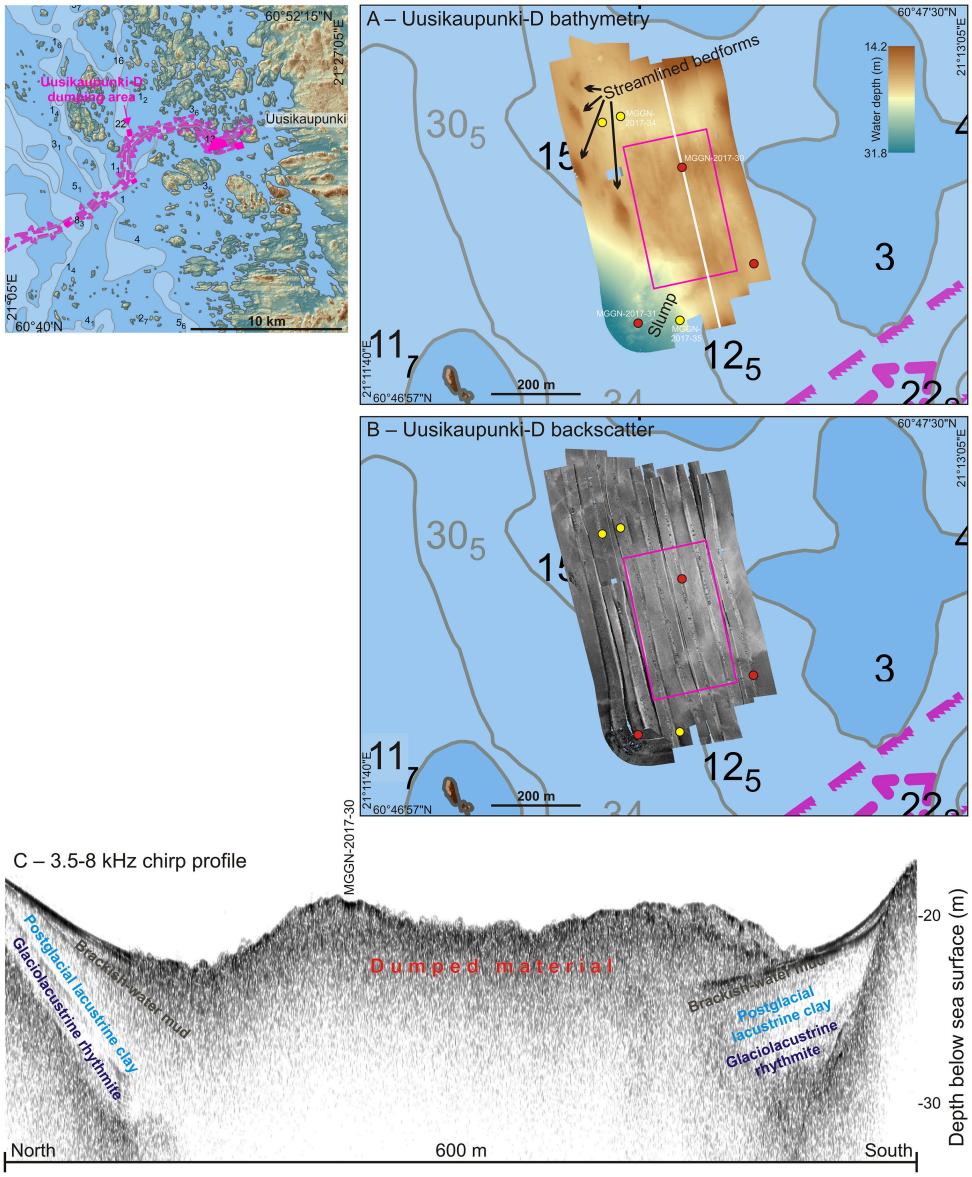


FIGURE 2 | Maps of the Uusikaupunki sea area. **(A)** Multibeam bathymetric image over the Uusikaupunki-D dumping area. **(B)** Multibeam relative backscatter image over the Uusikaupunki-D dumping area. Magenta line indicates the permitted dumping area. White line indicates the CHIRP sub-bottom transect in **(C)**. Circle symbol: Gemax short gravity coring site. Symbol colors: green, organic-rich mud (natural seafloor); red, dumped dredge spoil; yellow, mixture of organic-rich mud and dumped material. **(C)** 3.5–8 kHz CHIRP sub-bottom profile over the dumping area. The interpretation of seismo-acoustic units in the profile follows Virtasalo et al. (2007, 2014). Coordinate system ETRS-TM35FIN. Base map: ESRI Inc. (Redlands) data & maps of 2005. Bathymetric data: BALANCE project (www.helcom.fi). Nautical chart: S-57 Finnish Transport Agency 2017. Topographic map: National Land Survey of Finland digital elevation model 2 m 2017.

and bedrock outcrops flank the dumping area in the east, west, and north (Rantataro, 1997).

The most active phase of dredging and dumping in Vuosaari was 2004–2006. The dumping ceased with the completion of the harbor construction works in 2008, when 6.14 million hopper m^3 of dredge spoil had been dumped (Vatanen et al., 2012). The dredged sediments in the Vuosaari harbor area were characterized by a thin (<1 m) surface layer of organic-rich (LOI 5.7%) brackish-water mud that was underlain by a few meters of organic-bearing (LOI 2.8%) brackish-water mud. Till, boulders, and crystalline bedrock were exposed locally, and the dredged material also included blasted rock from the necessary demolitions. Contaminated sediments were stabilized in banks in the harbor area and not transported to the offshore dumping area. Environmental monitoring studies show that PCB contents were below detection limit and metal contents were at the background level except Cd that was slightly elevated in seafloor sediments at the dumping area in 2009 (Vatanen et al., 2012).

The Uusikaupunki-D offshore dumping area was in use in 2013–2014, when the shipping lane to the Uusikaupunki harbor was deepened from a draft of 10 to 12.5 m. The 0.062 km^2 rectangular dumping area is located ca. 9 km west from the coastline, in a small depression with water depths between 22 and 25 m (**Figure 2**). The site is more or less at the fairweather wave-base. The natural seafloor in the depression before the activities was composed of a thin (<10 cm) surface layer of organic-rich brackish-water mud (LOI 6.6%), which sharply overlies compact sandy mud (Vatanen et al., 2014). The dumping area is surrounded from west, north, and east by ridges of slightly harder sediment with LOI between 2.8 and 3.6%. Altogether 0.563 million hopper m^3 of dredge spoil, composed mainly of silt with minor till and blasted rock, were dumped to the area. A sediment trap study, carried out during the dumping operations, shows that suspended solids were transported to a maximum range of 600 m from the site (Vaittinen and Vartia, 2016). Turbidity peaks resulting from the dumping activities typically cleared within 45 min. Contaminated sediments in the dredged areas were stabilized in the Uusikaupunki harbor area, and not transported to the Uusikaupunki-D dumping area.

MATERIALS AND METHODS

The fieldwork at the Vuosaari offshore dumping area was carried out during 2 weeks in August 2015, whereas the Uusikaupunki-D area was studied in June 2017 (**Figures 1**, **2**). Multibeam seafloor surveys were run at 5 knots along predetermined transect lines using a 200 kHz Atlas Fansweep 20 multibeam echo sounder onboard r/v Geomari of the Geological Survey of Finland. Seismo-acoustic sub-bottom profiles were collected simultaneously using Meridata 28 kHz pinger and Massa TR-61A 3.5–8 kHz compressed high-intensity radar pulse (CHIRP) systems. The parallel survey lines were spaced at 100 m intervals in Vuosaari and at 50 m intervals in Uusikaupunki-D to permit full multibeam coverage, and orientated N-S on the basis of typical wind (wave) direction. Sound velocity and temperature profiles of the water column were measured during the survey using a Reson SVP 15T profiler. Multibeam bathymetric data were collected and processed with Hypack, and visualized with Fledermaus 7.4.4b software. A relative backscatter mosaic was produced using a GeoCoder algorithm. Sub-bottom profile data were processed and interpreted using Meridata MDPS software. The seismo-acoustic units and corresponding sediment types were interpreted following Virtasalo et al. (2007, 2014): *glaciolacustrine rhythmite*—a draped unit of fairly uniform thickness that is characterized by parallel internal reflectors of high amplitude; *postglacial lacustrine clay*—a draped unit of fairly uniform thickness that is characterized by parallel internal reflectors of low amplitude; *brackish-water mud*—an asymmetric drift unit of variable thickness that is characterized by downlapping and onlapping internal reflectors of low amplitude.

Sediment cores were collected in a predetermined 5 × 5 grid pattern (altogether 25 sites) in Vuosaari (**Figure 1**, **Table 1**), whereas in the smaller Uusikaupunki-D area, six sites were cored with an aim to capture the natural seafloor types present as well as the dumped material (**Figure 2**, **Table 1**). At each site, three cores were collected by two pulls using a twin barrel Gemax short gravity corer (core diameter 9 cm), which is designed for retrieving cores with undisturbed surfaces of soft sediments. One core of the first pull was cut in half lengthwise and cleaned for sedimentological description and digital photography, whereas the other core and a third core from the second pull were sectioned using a rotary device into 1 cm subsamples. After description and photography, the cleaned surface of the core MGGN-2017-34 from Uusikaupunki-D was sampled in a 28 × 5 × 2 cm plastic box for high-resolution digital X-ray imaging using a GE phoenix v|tome|x s micro-computed-tomography device supplied by GE phoenix (Wunstorf, Germany). At four sites in Vuosaari, where the substrate was too hard for the gravity corer to penetrate, a custom-made box corer, 20 × 20 cm in cross section, was used. One side of each box core was cleaned for sedimentological description and photography, after which the cores were sliced into 2 cm thick subsamples using a knife. All subsamples were stored refrigerated in plastic bags until laboratory analysis.

Subsample slices of the first-pull gravity cores were analyzed for ^{137}Cs activity in order to determine the amount of sediment in each core that was deposited after the fallout from the 1986 Chernobyl nuclear disaster. The ^{137}Cs activity of fresh subsamples was measured for 60 min using an EG&G Ortec ACE™-2K gamma spectrometer equipped with a four-inch NaI/TI detector at the Geological Survey of Finland (Ojala et al., 2017). The cores were analyzed starting from the uppermost 1-cm subsample slice and progressing downwards until near-zero (background) activity levels were measured in at least three consecutive subsamples. Weight loss on ignition (LOI) was analyzed for the same subsamples after the ^{137}Cs analysis for the entire length of the gravity cores, and for the uppermost 2 cm subsamples of the box cores. LOI was determined by weighing subsamples after drying at 105°C for 16 h and weighing again after ignition at 550°C for 2 h (Bengtsson and Enell, 1986).

Grain size distribution was analyzed for selected 1-cm subsample slices of the second-pull gravity cores at the commercial laboratory Labtium Ltd. The uppermost (seafloor) subsample was selected for analysis in each core, as well as representative subsamples of each lithofacies present in the core (for lithofacies descriptions, see Results section). The subsamples were freeze dried prior to sieving by ISO 3110/1 test sieves. The <63 μm size fraction was further analyzed down to 0.6 μm using a Micromeritics Sedigraph III 5120 X-ray absorption sedimentation analyzer. The sieving results were merged with sedimentation data in Sedigraph software. Grain size distribution parameters (mean grain-size, sorting [graphic standard deviation], skewness, and kurtosis) were calculated according to the geometric Folk and Ward (1957) graphical measures implemented in GRADISTAT 4.0 software (Blott and Pye, 2001). Clay is defined as grains finer than 2 μm, whereas mud is clay and silt (<63 μm), sand is 63 μm to 2 mm, gravel is 2–64 mm, and boulder 64–2,048 mm (Blott and Pye, 2012).

TABLE 1 | Coring locations, water depths, recoveries, and the types of coring equipment used.

Core	Sampling date	Latitude (WGS84)	Longitude (WGS84)	Water depth (m)	Gear	Recovery (cm)
VUOSAARI OFFSHORE DUMPING AREA						
MGGN-2015-5	18 Aug. 2015	60°03.370N	25°13.585E	49.8	G	21
MGBC-2015-2	25 Aug. 2015	60°03.363N	25°13.898E	50.6	B	8
MGGN-2015-7	18 Aug. 2015	60°03.363N	25°14.226E	50.7	G	51
MGGN-2015-8	18 Aug. 2015	60°03.363N	25°14.547E	50.7	G	50
MGGN-2015-9	19 Aug. 2015	60°03.350N	25°14.879E	49.7	G	36
MGGN-2015-10	19 Aug. 2015	60°03.201N	25°13.576E	51.9	G	38
MGGN-2015-11	19 Aug. 2015	60°03.201N	25°13.896E	50.5	G	29
MGGN-2015-12	19 Aug. 2015	60°03.202N	25°14.217E	51.0	G	6
MGGN-2015-13	19 Aug. 2015	60°03.199N	25°14.540E	50.6	G	46
MGGN-2015-14	21 Aug. 2015	60°03.192N	25°14.890E	51.4	G	19
MGGN-2015-15	21 Aug. 2015	60°03.041N	25°13.566E	52.0	G	46
MGGN-2015-16	21 Aug. 2015	60°03.049N	25°13.906E	51.2	G	40
MGGN-2015-17	21 Aug. 2015	60°03.046N	25°14.231E	51.1	G	47
MGGN-2015-18	24 Aug. 2015	60°03.033N	25°14.543E	51.9	G	8
MGGN-2015-19	24 Aug. 2015	60°03.044N	25°14.855E	51.6	G	31
MGGN-2015-20	24 Aug. 2015	60°02.881N	25°13.559E	51.6	G	32
MGGN-2015-21	25 Aug. 2015	60°02.881N	25°13.882E	51.2	G	24
MGGN-2015-22	25 Aug. 2015	60°02.878N	25°14.206E	51.1	G	32
MGBC-2015-1	25 Aug. 2015	60°02.873N	25°14.535E	49.6	B	9
MGGN-2015-23	26 Aug. 2015	60°02.871N	25°14.855E	52.3	G	34
MGBC-2015-3	26 Aug. 2015	60°02.727N	25°13.571E	50.2	B	2
MGBC-2015-4	26 Aug. 2015	60°02.719N	25°13.892E	51.5	B	6
MGGN-2015-24	26 Aug. 2015	60°02.717N	25°14.235E	52.3	G	25
MGBC-2015-5	26 Aug. 2015	60°02.714N	25°14.548E	52.2	B	4
MGGN-2015-25	27 Aug. 2015	60°02.714N	25°14.867E	53.4	G	27
UUSIKAUPUNKI-D OFFSHORE DUMPING AREA						
MGGN-2017-29	24 Aug. 2017	60°47.318N	21°12.203E	21.0	G	23
MGGN-2017-30	24 Aug. 2017	60°47.272N	21°12.410E	18.0	G	40
MGGN-2017-31	24 Aug. 2017	60°47.079N	21°12.341E	28.5	G	37
MGGN-2017-32	24 Aug. 2017	60°47.164N	21°12.608E	20.2	G	43
MGGN-2017-34	25 Aug. 2017	60°47.327N	21°12.247E	21.6	G	31
MGGN-2017-35	25 Aug. 2017	60°47.088N	21°12.439E	25.8	G	11

G = Gemax short twin-barrel gravity corer, B = box corer.

RESULTS

Vuosaari Offshore Dumping Area

Multibeam bathymetric image shows a gently undulating seafloor with water depths between 48 and 53 m over the 1,200 × 1,200 m survey area (**Figure 1A**). Numerous small irregular pits and mounds, a few meters to tens of meters in diameter, characterize the bottom topography. Relative backscatter displays a more complex picture of the seafloor with bright streaks and diffuse patches on a dark background (**Figure 1B**). The bright tone corresponds to relatively hard substrate that produces stronger acoustic backscatter, i.e. the presumed dumped material.

Of the 25 predefined coring sites, 20 were successfully sampled with the Gemax short gravity corer. Gemax did not penetrate successfully at the remaining five sites because of hard seafloor substrate, and the box corer was used instead for sampling. In the backscatter image, the box coring sites plot on the bright patches of hard seafloor (**Figure 1B**).

The four lithofacies that were identified in the studied sediment cores have been described in detail in previous studies in the area (Virtasalo et al., 2007, 2014). The key features of the lithofacies are recapitulated here in the upward stratigraphic order.

Postglacial lacustrine silty clay facies is represented by the lower half of the gravity core MGGN-2015-22 (**Figure 3A**). The facies is composed of poorly layered organic-bearing (<3.5% LOI) gray silty clay with black spots and mottling by iron monosulfides.

Brackish-water organic-bearing silt-striped mud is the most characteristic facies of the studied cores (**Figure 3**). The facies is gray with thin silt stripes and diffuse dark mottling by iron monosulfides, and small macrofauna burrows in particular in the

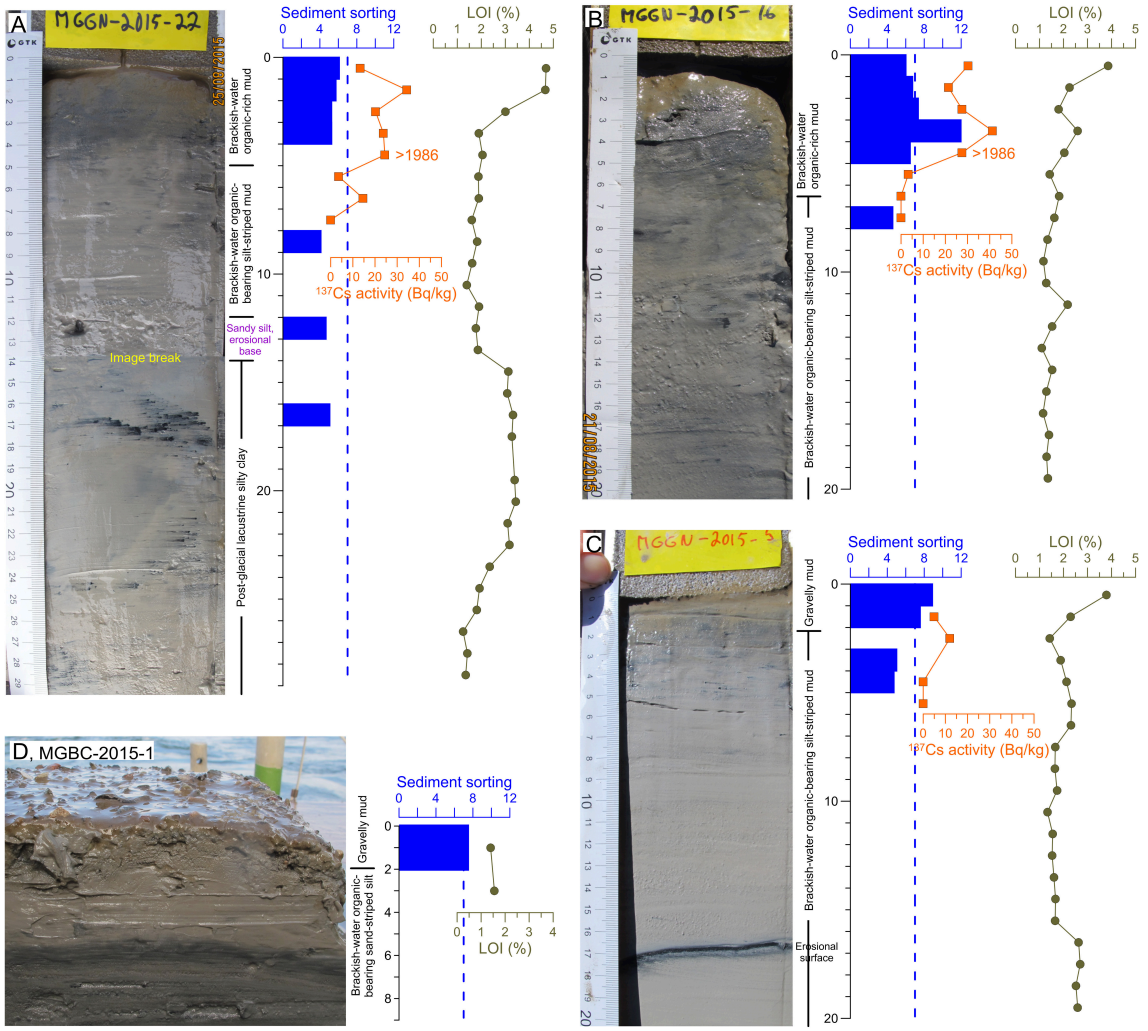


FIGURE 3 | Digital images and the plots of grain size sorting, ^{137}Cs activity and weight loss on ignition (LOI) of selected sediment cores from the Vuosaari dumping area. **(A)** Gravity core MGGN-2015-22. **(B)** Gravity core MGGN-2015-16. **(C)** Gravity core MGGN-2015-5. **(D)** Box core MGBC-2015-1. Dashed vertical line indicates the local threshold sorting value of 7 for dumped dredge spoil. The core locations are indicated in **Figure 1A**.

upper part of the cores. The facies also contains clay balls and less frequent sand stripes. The contact to the underlying postglacial lacustrine silty clays in MGGN-2015-22 is erosional and with a 2 cm thick basal sandy silt layer that gradates upward to the brackish-water mud (**Figure 3A**). This basal sandy silt layer is a transgressive shelf sand sheet, which is a widespread stratigraphic feature in the region, resulting from the mid-Holocene marine flooding of the Baltic Sea Basin (Virtasalo et al., 2016).

Brackish-water organic-rich mud is the uppermost and loosest facies in most of the studied cores (**Figures 3A,B**). The facies is olive green and intensely mottled by small macrofauna burrows. The sediment is soft and with a high water content and LOI of c. 4% or higher. The basal contact to the brackish-water organic-bearing silt-striped mud is sharp to bioturbated. When at the core top, the facies has a ca. 1 cm thick fluffy brown oxidized surface layer that may locally have high sand content.

Gravelly mud facies is found at the top of the gravity core MGGN-2015-5, as well as in all of the box cores (**Figures 3C,D**). The gray-colored mud facies has a massive texture and contains angular to jagged gravel-sized particles and small boulders. The facies is relatively hard because of the coarse grains present, which probably is the reason for the poor success with gravity coring. The basal contact is sharp and with frequent load structures (**Figure 3D**). When at the core top, the facies often has a fluffy brown oxidized surface layer.

Cesium-137 activity in the sediment cores from the Vuosaari dumping area is low (<100 Bq/kg, **Figure 3**) compared to the present values exceeding 1,000 Bq/kg in the sediments that were deposited off the Finnish south coast soon after the 1986 Chernobyl nuclear disaster (e.g., Jokinen et al., 2015; Vallius, 2015). Furthermore, the ^{137}Cs curves do not display well-developed activity peaks that would denote the year of fallout.

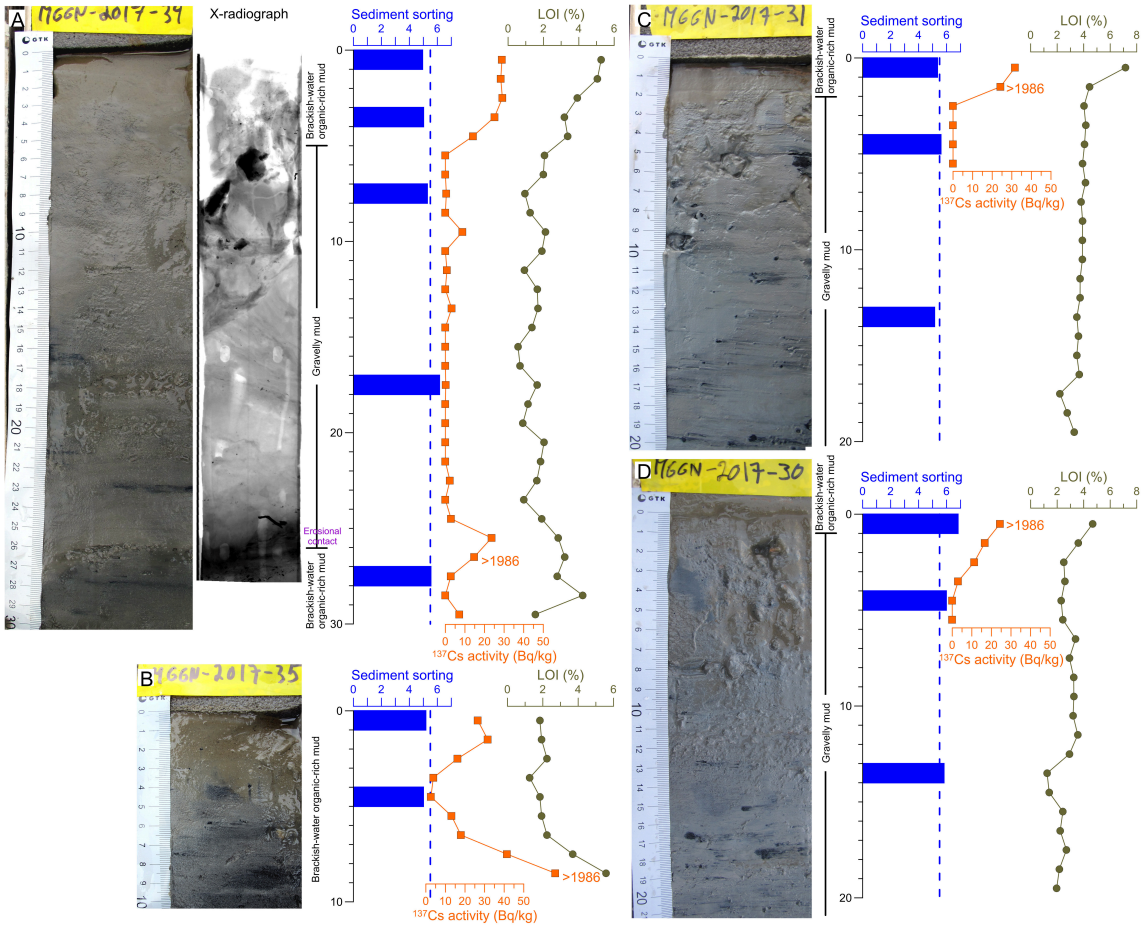


FIGURE 4 | Digital images and the plots of grain size sorting, ^{137}Cs activity and weight loss on ignition (LOI) of selected sediment cores from the Uusikaupunki-D dumping area. **(A)** Gravity core MGGN-2017-34. **(B)** Gravity core MGGN-2017-35. **(C)** Gravity core MGGN-2017-31. **(D)** Gravity core MGGN-2017-30. Dashed vertical line indicates the local threshold sorting value of 5.5 for dumped dredge spoil. The core locations are indicated in **Figure 2A**.

Therefore, the ^{137}Cs values above the pre-fallout values with the threshold of c. 20 Bq/kg are taken as indicative of sediments younger than 1986. Indeed, the overall comparably low ^{137}Cs activity, together with the low consistency and low thickness (<6 cm) of the ^{137}Cs-enriched sediment surface layer, suggest that the ^{137}Cs-enriched sediments in the studied cores were deposited sometime after 1986, possibly during the past few years.

Sediments from the Vuosaari dumping area are composed of mixed grain sizes, as is shown by the poor to very poor sorting of the sub-samples, and there is a strong relationship between improved sorting and smaller grain size (**Figure 5A**). In particular, there is a very poorly sorted sub-population with values of larger than 7 and mean grain sizes exceeding 12 μm. Most of the sub-samples have a balanced grain size distribution (symmetrical skewness), but several sub-samples are dominated by coarse particles (coarse/negative skewed) and some by fine particles (fine/positive skewed; **Figure 5B**). Kurtosis of the most grain size distributions is platykurtic (negative), but there is a leptokurtic (positive) sub-population with primarily heavy-tailed distributions (DeCarlo, 1997). The predominantly symmetrical skewness with a wide range of values is indicative of fluctuating energy levels with intermittent erosion and deposition of particles from mixed sediment sources (Duane, 1964). The coarsest, worst sorted and leptokurtic subsamples are interpreted to be from dumped material; these grain size characteristics reflect admixing of coarse grains and little sorting during fall through the water column.

Uusikaupunki-D Offshore Dumping Area

Multibeam bathymetric image over the survey area shows a relatively flat seafloor with water depths between 18 and 21 m, except streamlined bedforms that rise up to 15 m water depth, and a NW-SE trending channel with water depths of more than 30 m in the southwest (**Figure 2A**). The seafloor is notably smooth, except the dumping area that has irregular topography at the meter scale. A slump in the southwest documents the flow of material to the channel. Relative backscatter image shows patchy texture with generally brighter tones over the dumping area and also to the north and east of the area, indicating a harder consistency of the dumped material compared to the

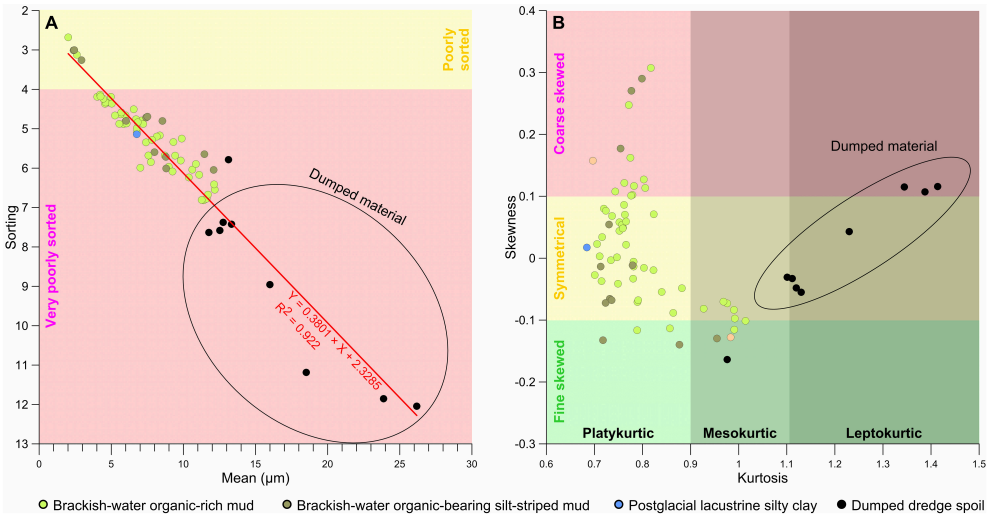


FIGURE 5 | Plots for the total-sample size distributions of **(A)** sorting and mean, and **(B)** skewness and kurtosis from the Vuosaari dumping area. Sample classes follow lithofacies classification described in the text. The sorting, skewness, and kurtosis class limits follow geometric Folk and Ward (1957) graphical measures as modified by Blott and Pye (2001).

natural seafloor, and that not all dumped material actually sit on the permitted dumping area (**Figure 2B**). The dumped material mounds are well distinguishable in the sub-bottom profiles based on the poor penetration of the seismo-acoustic signal and the irregular surface morphology (**Figure 2C**).

The two lithofacies present in the cores from the Uusikaupunki-D dumping area are similar to those in the Vuosaari area. Their key characteristics are as follows:

Brackish-water organic-rich mud is the uppermost and loosest facies in the studied cores (**Figure 4**). The facies is olive green and intensely mottled by small macrofauna burrows. The primary physical sedimentary structure is preserved locally in short thin-bedded intervals with smothered bed contacts. Diffuse dark patches of presumably iron monosulfide are present. The sediment is soft, and its organic content of ca. 3% is higher than in the underlying sediments but lower than in brackish-water organic-rich mud in the Vuosaari dumping area. The facies comprises the whole core MGGN-2017-35 (**Figure 4B**), where it is underlain by a compact sand layer at the 12 cm depth that was not penetrated by the Gemax corer. The facies is present in the basal part of MGGN-2017-34 below the depth of ca. 26 cm where it is sharply truncated from top, as well as in the uppermost 5 cm of that core (**Figure 4A**). When at the core top, the facies has a ca. 1 cm thick fluffy brown oxidized surface layer.

Gravelly mud facies is found in almost all of the studied cores. The gray-colored facies has a massive structure with local dark monosulfide spots and patches (**Figure 4**). The grain size is dominated by mud, but the presence of larger grains including angular to jagged gravel (**Figure 6C**) results in comparably hard consistency. The facies is present in MGGN-2017-34 between 26 and 5 cm, where it has an erosional contact to the underlying brackish-water mud (**Figure 4A**). X-radiograph of this interval shows that the sediment is strongly deformed and includes rotated sediment clasts. Dislocated sediment clasts are also present in MGGN-2017-31 (**Figure 4C**). When at the core top, the facies often has a fluffy brown oxidized surface layer.

Cesium-137 activity in the Uusikaupunki-D cores (<100 Bq/kg, **Figure 4**) is at the similar low level than in the Vuosaari dumping area. Together with the low consistency and low thickness (<6 cm) of the ^{137}Cs-enriched sediment surface layer, this suggests that the ^{137}Cs-enriched sediments in the cores were deposited during the past few years. Notably, ^{137}Cs-enriched brackish-water organic-rich mud is erosionally overlain by gravelly mud at 26 cm in MGGN-2017-34 (**Figure 4A**). The underlying brackish-water mud layer is younger than 1986, and the gravelly mud layer was emplaced on it during dumping activities. The gravelly mud layer has since been buried by 5 cm of organic-rich brackish-water mud.

Sorting of the sediment subsamples is very poor, which is similar to the majority of subsamples from Vuosaari (**Figure 6A**). The relationship between improved sorting and smaller grain size is weaker than in the Vuosaari subsamples. The grain size distributions are symmetrical or fine skewed, except a couple of subsamples that are coarse skewed (**Figure 6B**). Kurtosis of the subsamples is mostly platykurtic. There is a very poorly sorted sub-population with values exceeding 5.5 and with kurtosis higher than 0.72; these subsamples are interpreted to be from dumped material, with their grain size distributions reflecting admixing of coarse grains and minimal sorting during fall through the water column.

DISCUSSION

Two offshore dumping areas, Vuosaari in the south coast and Uusikaupunki-D in the west coast of Finland, have been studied with an aim to develop observation techniques and criteria

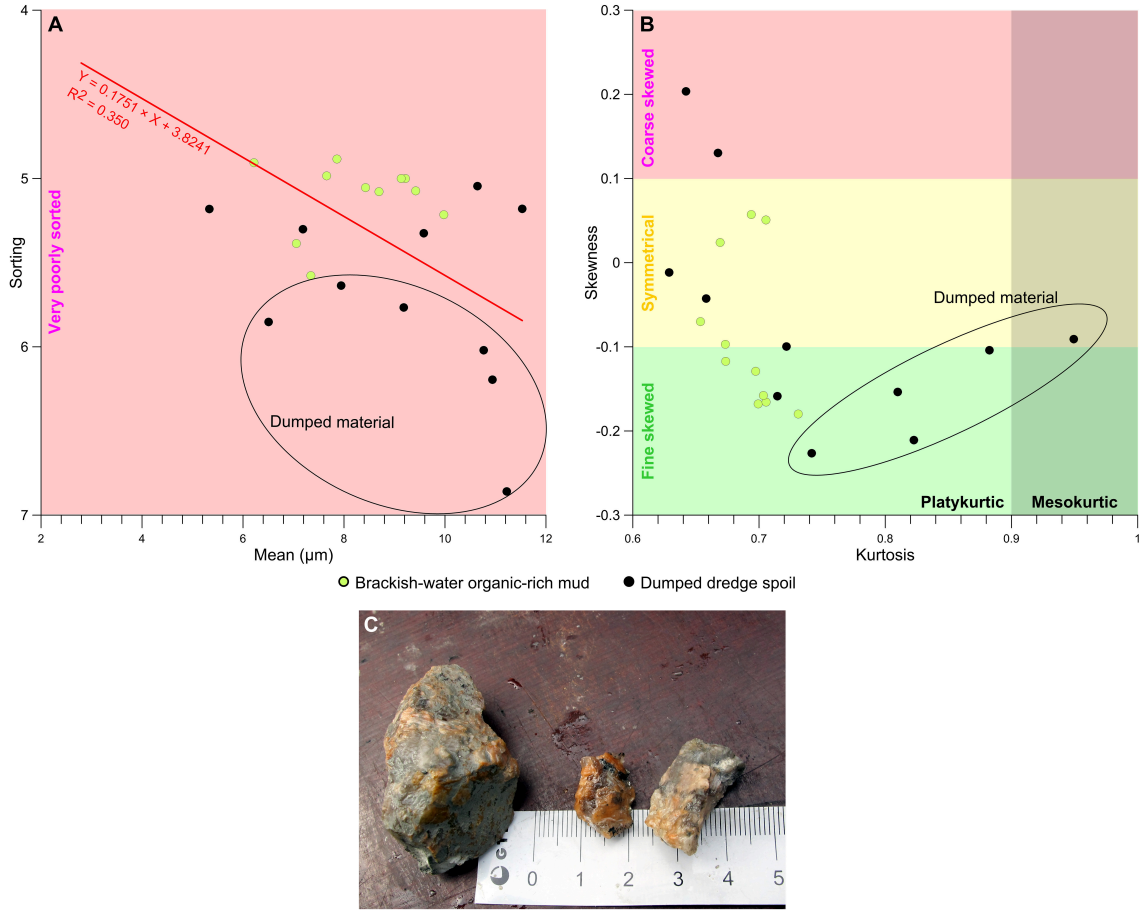


FIGURE 6 | Plots for the total-sample size distributions of **(A)** sorting and mean, and **(B)** skewness and kurtosis, and **(C)** a picture of blasted rock fragments from the Uusikaupunki-D dumping area. Sample classes follow lithofacies classification described in the text. The sorting, skewness, and kurtosis class limits follow geometric Folk and Ward (1957) graphical measures as modified by Blott and Pye (2001).

for the assessment of the geological integrity of seafloor, its anthropogenic change due to dumping, and recovery as required by the MSFD. Full coverage multibeam bathymetry and relative backscatter data as well as a number of sediment cores have been analyzed over the dumping areas.

Sedimentary Environment

Adequate knowledge about sedimentary environment of an offshore dumping area is necessary for understanding the fate of the dumped dredge spoil, which can be resuspended by currents and transported to adjacent locations (dispersive site), or buried by natural sediment deposition (depositional site).

Based on the analysis of sediment cores, the Vuosaari dumping area is net depositional area, although the sediment deposition is slow and episodic. The local seafloor is composed of brackish-water silt-striped organic-bearing mud that is covered with a thin layer of soft brackish-water organic-rich mud (**Figure 3**). The silt stripes and less frequent sand stripes in the organic-bearing mud indicate that episodic strong near-bottom currents result in seafloor erosion and the deposition of thin silt and sand layers from traction transport. The poor sorting and the predominantly symmetrical skewness of both the organic-bearing and organic-rich brackish-water mud (**Figure 5**) further indicate importation of particles from mixed sediment sources (Duane, 1964; Stevens et al., 1996). These particles originate from till, glaciofluvial sand formations, glaciolacustrine varved silt–sand and clay, postglacial lacustrine silty clay and previously deposited brackish-water mud in the area (Rantataro, 1997; Virtasalo et al., 2007, 2014). This observation is in line with previous studies, which show that resuspension accounts for a considerable proportion of deposition in the regressive coastal sea areas of the northern Baltic Sea (Jokinen et al., 2015; Rasmus et al., 2015; Nuorteva and Kankaanpää, 2016).

The comparably low ^{137}Cs activity and the lack of well-developed peaks in the ^{137}Cs curves from the Vuosaari gravity cores (**Figure 3**) suggest that the thin surficial organic-rich mud layer was deposited during the past few years, and that the contact to the underlying more compact silt-striped organic-bearing mud is likely to be unconformable. Recent studies show that ^{137}Cs is still being redistributed and deposited in significant amounts in the Finnish coastal sea areas (Jokinen et al., 2015; Vallius, 2015). The exact cause of increased organic-content in

the recently deposited mud is not known, but it may be related to the recent increase in organic sedimentation as a consequence of eutrophication (Bonsdorff et al., 1997; Weckström, 2006; Tuovinen et al., 2010).

The Uusikaupunki-D dumping area shows characteristics of both dispersive and depositional site. The presence of streamlined bedforms on the relatively shallow seafloor indicate strong reworking by waves and near-bottom currents (**Figure 2A**). The seafloor is covered with a patchy and comparably thin (<20 cm) layer of brackish-water organic-rich mud. The underlying, older and more compact sandy mud, postglacial lacustrine and glaciolacustrine sandy–silty clays, and till are exposed in the surrounding ridges and local elevations. The very poor sorting and mostly symmetrical skewness of the thin organic-rich brackish-water mud blanket indicate that it to a large part is composed of material reworked from previously deposited local sediments (Duane, 1964; Stevens et al., 1996). The low ^{137}Cs activity and the lack of well-developed peaks in the ^{137}Cs curves further indicate that the brackish-water mud blanket was deposited during the recent past and may to a large degree be semi-permanent. These findings are in agreement with a recent study by Vatanen et al. (2014), which shows that recent sediment deposition in the area is minor and restricted to shallow local depressions.

Dumped Material

At the Vuosaari offshore dumping area, the mounds of dumped dredge spoil, possibly enhanced by scouring around the individual mounds (Du Four and Van Lancker, 2008), result in irregular seafloor topography (**Figure 1A**). In addition, the dumped dredge spoil stands out bright among natural sediments in the multibeam backscatter image because of its harder consistency and irregular surface morphology (**Figure 1B**). In the studied sediment cores, the dumped material is represented by the gravelly mud facies with massive texture and angular to jagged coarse particles, and an unconformable contact to the underlying sediments (**Figure 3**). The dumped material in general is coarser, less sorted and of higher kurtosis compared to natural sediment (**Figure 5**), as a result of the admixing of coarser grains during the dredging operations, and limited sorting during fall through the water column upon dumping. Dumped dredge spoil also has lower ^{137}Cs activity than natural seafloor sediments because most of the dredged sediments are older than the 1986 Chernobyl disaster. During the 7 years after the cessation of dumping activities, the dumped material at many of the coring sites has been covered by few centimeters of younger sediments, which shows that it is largely stable in the Vuosaari dumping area.

The Uusikaupunki-D dumping area is located in a small depression, which has been filled to the level of the surrounding till and hard mud ridges. The seafloor topography at the dumping area is irregular and the dumped material has brighter tone in the multibeam backscatter image compared to the surrounding natural seafloor, which has been smoothed and streamlined by current activity (**Figure 2**). The dumped material has a mixed texture with dislocated mud clasts, which is different from Vuosaari and probably results from the shorter fall through the shallow water column upon dumping (**Figures 4A,C**). The poor sorting and higher kurtosis of dumped material compared to natural sediment is similar to Vuosaari, and further indicates the admixing of coarser grains during dredging and minimal sorting during fall through the water column (**Figure 6**). Irregularities in the dumped material surface will likely be leveled off and the eroded material dispersed in the surrounding area by strong near-bottom currents (Tauber, 2009). Mean current velocities, measured 2 m above seafloor during 4 weeks in October 2014, occasionally exceeded 30 cm/s (Vaittinen and Vartia, 2016), which is well above the threshold for erosion of the muddy seafloor (Rasmus et al., 2015). A sediment core shows that the dumped material has been covered by 1 cm layer of natural sediment during the 3 years after the dumping activities, but the site would need to be revisited after a few years to determine the permanence of this very thin covering layer. In addition, dumped material has slumped down to the adjacent channel (**Figure 2A**), where it likely will be transported further by strong near-bottom currents.

The dumped material is not always readily identifiable to the naked eye. In the core MGGN-2015–16 from Vuosaari, a poorly-sorted thin layer of dumped material at 3–4 cm is difficult to tell apart from brackish-water sediments immediately above and below based on the visual inspection alone (**Figure 3B**). Similarly, in the core MGGN-2017-35 from Uusikaupunki-D, upward decreasing organic content and a nadir in ^{137}Cs activity at 3–5 cm indicate a significant share of admixed old material (**Figure 4B**). The admixed dumped material probably was dispersed in the water column during the dumping activities, or resuspended from a dumped material mound and transported along the seafloor by near-bottom currents soon thereafter (Truitt, 1988; Du Four and Van Lancker, 2008; Marmin et al., 2016).

Assessment of Seafloor Geological Integrity

In Europe, the GES of seafloor integrity is assessed through the terms "physical loss of seabed" and "adverse effects from physical disturbance to seabed" (European Commission, 2017). These two stressors are defined by changes in the seabed substrate and morphology, and distinguished by recovery time; seabed that requires more than 10 years to recover is considered as "physically lost" in the GES assessment.

In order to address the requirement for the assessment of the physical loss and disturbance of seabed substrate and morphology, an assessment protocol for the geological integrity of seafloor substrate in the context of offshore dumping is proposed (**Figure 7**). The proposed assessment protocol is based on the successful discrimination of dumped dredge spoil and naturally deposited sediments by the observation techniques used in the two offshore dumping areas. In this approach, geological integrity is understood as the capability of seafloor to provide a habitable substrate for indigenous benthic communities. The proposed protocol includes two assessment methods. *Seabed seismo-acoustic survey* allows quick identification of dumped material mounds and their areal coverage on the seafloor, and repeated surveys permit the assessment of their possible reworking and burial (e.g., Stockmann et al., 2009; Tauber,

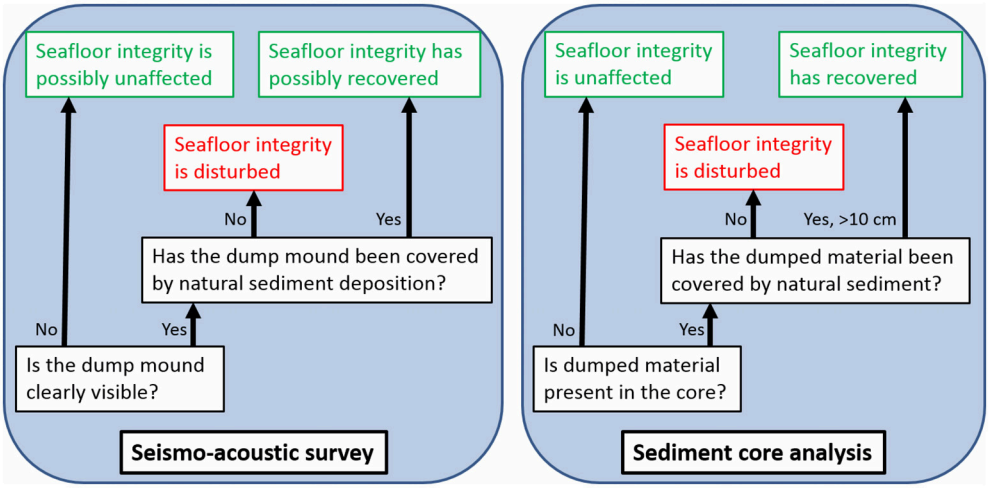


FIGURE 7 | The proposed assessment protocol of the seafloor geological integrity. Seismo-acoustic surveys permit the estimation of the areal coverage of dumped material, whereas sediment core analysis is more informative about the degree of physical change in seafloor substrate and the state of possible recovery. These methods should preferably be used in parallel with more weight given on the sediment core data.

2009). *Sediment core analysis* permits ground-truthing of seismo-acoustic data, and detailed determination of the thickness and quality of the dumped material layer and its possible burial by natural sediment at the coring locations. The two methods ideally should be used in parallel with more weight given on the sediment core analysis.

In the proposed assessment protocol (**Figure 7**), the burial of dumped dredge spoil by natural sediment is considered as a prerequisite for the recovery of the seafloor geological integrity. This is obviously possible at depositional dumping areas only, whereas at dispersive sites the dumped material will remain exposed and be redistributed along the seafloor, as is commonly the case with dumping sites in tidal high-energy sandy seafloor environments (e.g., Stronkhorst et al., 2003; Wienberg and Hebbeln, 2005; Du Four and Van Lancker, 2008; Marmin et al., 2016), and largely also in the Uusikaupunki-D dumping area. The required thickness of the natural sediment cover for the recovery will depend on the species specific requirements in the local macrobenthic community, and will differ considerably between locations. Already a relatively thin layer of natural sediment may make the seafloor appear as a natural substrate for macrofauna in the northern Baltic Sea, where the macrozoobenthic communities are dominated by small organisms with shallow burrowing depths due to considerable environmental stress caused by low salinity with further aggravation in areas of oxygen deficiency (Elmgren et al., 1984; Bonsdorff et al., 1996; Laine et al., 2007; Virtasalo et al., 2011). Therefore, the burial of dumped material by 10 cm of natural sediment is proposed as a rule-of-thumb criterion for the recovery of the seafloor geological integrity that is applicable over wide areas in the northern Baltic Sea.

In the case the dumped material is not buried by natural sediment (dispersive site), the new macrozoobenthic community that may establish on the site will differ from the undisturbed one, and a new steady state will appear. The magnitude of change in the macrozoobenthic community will depend on how closely the dumped material mounds resemble the natural seafloor in terms of e.g., grain size, organic content, and consistency (e.g., Bolam et al., 2006; Powilleit et al., 2006; Barrio Froján et al., 2011). The re-establishment of the macrozoobenthic community often takes a few years if analyzed by univariate indices but at least 5 years when analyzed by multivariate analyses of the species composition (Bolam et al., 2006; Barrio Froján et al., 2011). By the strictest (and likely unrealistic) interpretation of the "physical loss," the geological integrity of seafloor in such a case would be lost forever unless restored by human intervention (European Commission, 2017). However, a seafloor that does provide a habitat to an indigenous macrozoobenthic community, although different from the earlier one, should hardly be considered "lost." Therefore, the "physical loss" may require a practical definition, which could be based on macrozoobenthic or other biological condition of the site. This method could contain an estimate of the potential ecological value of such an artificial habitat. It should be noted that its ecological value is not necessarily less than that of a natural seafloor.

In addition to the seafloor geological properties, the re-establishment of a macrozoobenthic community is controlled by other abiotic factors such as oxygen saturation. The macrozoobenhic community at the Vuosaari offshore dumping area disappeared because of the dumping activities, but the accurate impact of dumping in the reduction is difficult to estimate due to the episodic hypoxia that had set in just before the dumping operations (Vatanen et al., 2012). In the surrounding areas 0.6–1.2 km from the site, the communities were only slightly affected. In 2009, a year after the cessation of dumping and under improved oxygen conditions, macrozoobenthic density increased to the level of the surrounding areas and the community included the amphipod *Monoporeia affinis*, the

bivalve *Macoma balthica*, the priapulid *Halicryptus spinulosus*, and the invasive polychaete *Marenzelleria* spp. The shallower Uusikaupunki-D dumping area, in contrast, is generally well oxygenated, but no macrozoobenthic studies on the effects of dumping have been carried out there (Vatanen et al., 2014).

Sediment core analysis is the only means of gaining detailed information about the geological integrity of seafloor, its change due to human activities such as dumping, and its possible recovery. The analysis requires scrutiny, such as the analysis of 1 cm vertical subsamples of gravity cores with geochronological control that is carried out here (**Figures 3**, **4**). A similar analysis is not possible when the sediment samples are collected by grab samplers, which are typically used for macrozoobenthic sampling and mix the sediment structure to a large extent (e.g., Olenin, 1992; Powilleit et al., 2006; Okada et al., 2009; McLaren and Teear, 2014; Marmin et al., 2016). The selection of the monitoring method can, however, be determined on the basis of the known characteristics of the site. In case the dumping history is known and the site is of dispersive type, then sediment core analysis may not be required and macrozoobenthic sampling may be sufficient. Such knowledge about the sites will considerably decrease monitoring costs.

CONCLUSIONS

Knowledge about reference conditions before significant human influence is needed to determine the seafloor physical (geological) integrity, and to set targets for achieving good environmental status of the EU's marine waters within the MSFD (European Commission, 2017). Techniques and concepts presented in this paper provide a means for discriminating uncontaminated dumped dredge spoil from sediments that were deposited naturally at a dumping area, both before the dumping activities and after them in the possible case that recovery has taken place. The analysis of grain size distribution parameters and lithofacies characteristics of sediment cores allows the identification of (1) dumped dredge spoil *sensu stricto* that rapidly and with minimal sorting fell through the water column during the dumping activities, and (2) dispersed dredge spoil that was suspended in the water column during the dumping activities, or reworked from the dumped material mounds and redistributed along the seafloor soon after the dumping activities, and deposited over a wider area as a thin layer that is not necessarily readily identifiable to the naked eye. Radiochronological techniques such as ^{137}Cs dating help distinguish the dumped material in sediment cores.

Following the proposed assessment protocol (**Figure 7**), multibeam data indicate the presence of dumped material mounds at the Vuosaari dumping area, and sediment core analyses document shallow burial of the dumped material by natural sediment deposition at some of the coring locations. These findings show that slow recovery of the seafloor geological integrity is taking place at the area. However, the dumped material has not been buried by at minimum 10 cm of natural sediment, meaning that the seafloor has not yet fully recovered at any of the coring sites during the seven years after the dumping activities. It remains to be seen whether the seafloor is "adversely affected" or "physically lost" according to the GES assessment. The dump mounds are visible in multibeam data over the Uusikaupunki-D dumping area, as well. Sediment core analyses show that little natural sediment has deposited on the dumped material during the 3 years since the dumping activities ceased. Taking into the consideration the highly dynamic sedimentary environment of the Uusikaupunki-D dumping area, the seafloor would seem "physically lost."

Anthropogenic disturbance studies should be accompanied by detailed geological investigation, in order to comprehensively assess the consequent physical changes in the structure and consistency of the seafloor substrate. The proposed assessment protocol for the seafloor geological integrity is meant to give a more accurate overview of the extent of disturbance and the possible physical recovery of the seafloor substrate after dumping operations. The protocol can be used to support studies of the re-establishment of macrozoobenthic communities.

AUTHOR CONTRIBUTIONS

JV: responsible for the sample collection, analysis, and the results; SK: contributed to writing about EU directives and benthic ecology, and to the development of the assessment protocol; AK: support in sample collection and interpretation of results.

ACKNOWLEDGMENTS

We acknowledge the crew of our r/v Geomari and those who assisted in the sediment sampling. Kimmo Alvi prepared the multibeam images. Jukka Kuva produced the X-radiograph in **Figure 4A**. This work has been partially supported by the Strategic Research Council at the Academy of Finland, project SmartSea (grant 292 985).

REFERENCES

Barrio Froján, C. R. S., Cooper, K. M., Bremner, J., Defew, E. C., Wan Hussin, W. M. R., and Paterson, D. M. (2011). Assessing the recovery of functional diversity after sustained sediment screening at an aggregate dredging site in the North Sea. *Estuar. Coast. Shelf Sci.* 92, 358–366. doi: 10.1016/j.ecss.2011.01.006

Bengtsson, L., and Enell, M. (1986). "Chemical analysis," in *Handbook of Holocene Palaeoecology and Palaeohydrology*, ed D. E. Berglund (Chichester, UK: Wiley), 423–451.

Berg, T., Fürhaupter, K., Teixeira, H., Uusitalo, L., and Zampoukas, N. (2015). The Marine Strategy Framework Directive and the ecosystem-based approach – pitfalls and solutions. *Mar. Pollut. Bull.* 96, 18–28. doi: 10.1016/j.marpolbul.2015.04.050

Blott, S. J., and Pye, K. (2001). GRADISTAT: a grain size distribution and statistics package for the analysis of unconsolidated sediments. *Earth Surf. Process. Landforms* 26, 1237–1248. doi: 10.1002/esp.261

Blott, S. J., and Pye, K. (2012). Particle size scales and classification of sediment types based on particle size distributions: review

and recommended procedures. *Sedimentology* 59, 2071–2096. doi: 10.1111/j.1365-3091.2012.01335.x

Bobertz, B., and Harff, J. (2004). Sediment facies and hydrodynamic setting: a study in the south western Baltic Sea. *Ocean Dyn.* 54, 39–48. doi: 10.1007/s10236-003-0061-8

Bolam, S. G., Rees, H. L., Somerfield, P., Smith, R., Clarke, K. R., Warwick, R. M., et al. (2006). Ecological consequences of dredged material disposal in the marine environment: a holistic assessment of activities around the England and Wales coastline. *Mar. Pollut. Bull.* 52, 415–426. doi: 10.1016/j.marpolbul.2005.09.028

Bonsdorff, E., Blomqvist, E. M., Mattila, J., and Norkko, A. (1997). Long-term changes and coastal eutrophication. examples from the Åland Islands and the Archipelago sea, Northern Baltic sea. *Oceanol. Acta* 20, 319–329.

Bonsdorff, E., Diaz, R. J., Rosenberg, R., Norkko, A., and Cutter, G. R. Jr. (1996). Characterization of soft-bottom benthic habitats of the Åland Islands, northern Baltic Sea. *Mar. Ecol. Prog. Ser.* 142, 235–245. doi: 10.3354/meps142235

Broszeit, S., Beaumont, N. J., Uyarra, M., Heiskanen, A.-S., Frost, M., Somerfield, P. J., et al. (2017). Whan can indicators of good environmental status tell us about ecosystem services?: reducing efforts and increasing cost-effectiveness by reapplying biodiversity indicator data. *Ecol. Indic.* 81, 409–442. doi: 10.1016/j.ecolind.2017.05.057

DeCarlo, L. T. (1997). On the meaning and use of kurtosis. *Psychol. Methods* 2, 292–307. doi: 10.1037/1082-989X.2.3.292

Duane, D. B. (1964). Significance of skewness in recent sediments, western Pamlico Sound, North Carolina. *J. Sediment. Petrol.* 34, 864–874.

Du Four, I., and Van Lancker, V. (2008). Changes of sedimentological patterns and morphological features due to the disposal of dredge spoil and the regeneration after cessation of the disposal activities. *Mar. Geol.* 255, 15–29. doi: 10.1016/j.margeo.2008.04.011

Elmgren, R., Rosenberg, R., Andersin, A.-B., Evans, S., Kangas, P., Lassig, J., et al. (1984). Benthic macro- and meiofauna in the Gulf of Bothnia (northern Baltic). *Finnish Mar. Res.* 250, 3–18.

Eronen, M., Glückert, G., Hatakka, L., van de Plassche, O., van der Plicht, J., and Rantala, P. (2001). Rates of Holocene isostatic uplift and relative sealevel lowering of the Baltic in SW Finland based on studies of isolation contacts. *Boreas* 30, 17–30. doi: 10.1080/030094801300062248

Essink, K. (1999). Ecological effects of dumping of dredged sediments; options for management. *J. Coast. Conserv.* 5, 69–80. doi: 10.1007/BF02802741

European Commission (2017). Commission Decision (EU) 2017/848 of 17 May 2017 laying down criteria and methodological standards on good environmental status of marine waters and specifications and standardised methods for monitoring and assessment, and repealing Decision 2010/477/EU. *Off. J. Eur. Union* L125, 43–74.

Folk, R. L., and Ward, W. C. (1957). Brazos river bar: a study in the significance of grain size parameters. *J. Sediment. Petrol.* 27, 3–26. doi: 10.1306/74D70646-2B21-11D7-8648000102C1865D

HELCOM (2015). *HELCOM Guidelines for Management of Dredged Material at Sea and HELCOM Reporting Format for Management of Dredged Material at Sea*. Helsinki: HELCOM Baltic Marine Environment Protection Commission.

HELCOM (2017). *First version of the 'State of the Baltic Sea' report – June 2017 – to be Updated in 2018*. Helsinki: HELCOM Baltic Marine Environment Protection Commission. Available online at: http://stateofthebalticsea.helcom.fi

IMO (2015). *Guidelines for Low Cost, Low Technology Assessment of Dredged Material*. London: International Maritime Organization.

Jokinen, S. A., Virtasalo, J. J., Kotilainen, A. T., and Saarinen, T. (2015). Varve microfabric record of seasonal sedimentation and bottom flow-modulated mud deposition in the coastal northern Baltic Sea. *Mar. Geol.* 366, 79–96. doi: 10.1016/j.margeo.2015.05.003

Kairyte, M., and Stevens, R. L. (2015). Composite methodology for interpreting sediment transport pathways from spatial trends in grain size: a case study of the Lithuanian coast. *Sedimentology* 62, 681–696. doi: 10.1111/sed.12156

Kaskela, A. M., and Kotilainen, A. T. (2017). Seabed geodiversity in a glaciated shelf area, the Baltic Sea. *Geomorphology* 295, 419–435. doi: 10.1016/j.geomorph.2017.07.014

Kohonen, T., and Winterhalter, B. (1999). Sediment erosion and deposition in the western part of the Gulf of Finland. *Baltica* 12, 53–56.

Korpinen, S., Meidinger, M., and Laamanen, M. (2013). Cumulative impacts on seabed habitats: an indicator for assessments of good environmental status. *Mar. Pollut. Bull.* 74, 311–319. doi: 10.1016/j.marpolbul.2013.06.036

Korpinen, S., Meski, L., Andersen, J. H., and Laamanen, M. (2012). Human pressures and their potential impact on the Baltic sea ecosystem. *Ecol. Indic.* 15, 105–114. doi: 10.1016/j.ecolind.2011.09.023

Laine, A. O., Andersin, A.-B., Leiniö, S., and Zuur, A. F. (2007). Stratification-induced hypoxia as a structuring factor of macrozoobenthos in the open Gulf of Finland (Baltic Sea). *J. Sea Res.* 57, 65–77. doi: 10.1016/j.seares.2006.08.003

Lepland, A., Bøe, R., Lepland, A., and Totland, O. (2009). Monitoring the volume and lateral spread of disposed sediments by acoustic methods, Oslo Harbor, Norway. *J. Environ. Manage.* 90, 3589–3598. doi: 10.1016/j.jenvman.2009.06.013

Marmin, S., Lesueur, P., Dauvin, J. C., Samson, S., Tournier, P., Gallicher Lavanne, A., et al. (2016). An experimental study on dredge spoil of estuarine sediments in the Bay of Seine (France): a morphosedimentary assessment. *Cont. Shelf Res.* 116, 89–102. doi: 10.1016/j.csr.2016.01.010

McLaren, P., and Teear, G. (2014). A Sediment Trend Analysis (STA®) in support of dredged material management in Lyttelton Harbour, Christchurch, New Zealand. *J. Coast. Res.* 30, 438–447. doi: 10.2112/JCOASTRES-D-13-00136.1

Nuorteva, J., and Kankaanpää, H. T. (2016). Relocation of soft mud deposits: an example from the Archipelago Sea, northern Baltic Sea. *Mar. Geol.* 380, 148–162. doi: 10.1016/j.margeo.2016.08.002

Ojala, A. E. K., Luoto, T. P., and Virtasalo, J. J. (2017). Establishing a high-resolution surface sediment chronology with multiple dating methods – testing ^{137}Cs determination with Nurmijärvi clastic-biogenic varves. *Quat. Geochronol.* 37, 32–41. doi: 10.1016/j.quageo.2016.10.005

Okada, T., Larcombe, P., and Mason, C. (2009). Estimating the spatial distribution of dredged material disposed of at sea using particle-size distributions and metal concentrations. *Mar. Pollut. Bull.* 58, 1164–1177. doi: 10.1016/j.marpolbul.2009.03.023

Olenin, S. (1992). "Changes in a south-eastern Baltic soft-bottom community induced by dredged spoil dumping," in *Proceedings 12th Baltic Marine Biologist Symposium*, eds E. Bjørrnestad, L. Hagerman, and K. Jensen (Fredensborg: Olsen & Olsen), 119–123.

OSPAR (2014). *OSPAR Guidelines for the Management of Dredged Material at Sea, Agreement 2014-06*. London: OSPAR Commission.

Powilleit, M., Kleine, J., and Leuchs, H. (2006). Impacts of experimental dredged material disposal on a shallow, sublittoral macrofauna community in Mecklenburg Bay (western Baltic Sea). *Mar. Pollut. Bull.* 52, 386–396. doi: 10.1016/j.marpolbul.2005.09.037

Rantataro, J. (1997). *Itä-Tontun ja Soratontun Hiekka-Alueiden Sekä Eesti-Luodon Eteläpuolisen Läjitysalueen Akustis-Seismiset Tutkimukset*. Espoo: Geological Survey of Finland.

Rasmus, K., Kiirikki, M., and Lindfors, A. (2015). Long-term field measurements of turbidity and current speed in the Gulf of Finland leading to an estimate of natural resuspension of bottom sediment. *Boreal Environ. Res.* 20, 735–747.

Rice, J., Arvanitidis, C., Borja, A., Frid, C., Hiddink, J. G., Krause, J., et al. (2012). Indicators for sea-floor integrity under the European Marine Strategy Framework Directive. *Ecol. Indic.* 12, 174–184. doi: 10.1016/j.ecolind.2011.03.021

Seinä, A., and Peltola, J. (1991). Duration of the ice season and statistics of fast ice thickness along the Finnish coast 1961–1990. *Finnish Mar. Res.* 258, 1–46.

Stevens, R. L., Bengtsson, H., and Lepland, A. (1996). Textural provinces and transport interpretations with fine-grained sediments in the Skagerrak. *J. Sea Res.* 35, 99–110. doi: 10.1016/S1385-1101(96)90739-X

Stockmann, K., Riethmüller, R., Heineke, M., and Gayer, G. (2009). On the morphological long-term development of dumped material in a low-energetic environment close to the German Baltic coast. *J. Mar. Syst.* 75, 409–420. doi: 10.1016/j.jmarsys.2007.04.010

Stroeven, A. P., Hättestrand, C., Kleman, J., Heyman, J., Fabel, D., Fredin, O., et al. (2016). Deglaciation of Fennoscandia. *Quat. Sci. Rev.* 147, 91–121. doi: 10.1016/j.quascirev.2015.09.016

Stronkhorst, J., Ariese, F., van Hattum, B., Postma, J. F., de Kluijver, M., Den Besten, P. J., et al. (2003). Environmental impact and recovery at two disposal sites for dredged material in the North Sea. *Environ. Pollut.* 124, 17–31. doi: 10.1016/S0269-7491(02)00430-X

Tauber, F. (2009). Sidescan sonar survey of a dumping site in the Mecklenburg Bight (south-western Baltic Sea). *J. Mar. Syst.* 75, 421–429. doi: 10.1016/j.jmarsys.2008.04.006

Teixeira, H., Berg, T., Uusitalo, L., Fürhaupter, K., Heiskanen, A.-S., Mazik, K., et al. (2016). A catalogue of marine biodiversity indicators. *Front. Mar. Sci.* 3:207. doi: 10.3389/fmars.2016.00207

Truitt, C. L. (1988). Dredged material behavior during open-water disposal. *J. Coastal Res.* 4, 389–397.

Tuovinen, N., Weckström, K., and Virtasalo, J. J. (2010). Assessment of recent eutrophication and climate influence in the Archipelago Sea based on the subfossil diatom record. *J. Paleolimnol.* 44, 95–108. doi: 10.1007/s10933-009-9390-z

Vaittinen, T., and Vartia, M. (2016). *Sedimentation Study for Sea Banking During the Uusikaupunki Sea Route Deepening Project*. Research Reports of the Finnish Transport Agency 22/2016.

Vallius, H. (2015). Sediment and carbon accumulation rates off the southern coast of Finland. *Baltica* 28, 81–88. doi: 10.5200/baltica.2015.28.08

Vatanen, S., Haikonen, A., and Kervinen, J. (2014). *Uudenkaupungin Väylän ja Sataman Ruoppaus- Ja Läjityshankkeen vesistö- Ja Kalataloustarkkailu – Ennakkotarkkailu Sekä Rakentamisen Aikainen Tarkkailu Vuonna 2013*. Klaukkala: Kala- ja vesitutkimus Oy.

Vatanen, S., Haikonen, A., and Piispanen, A. (2012). *Vuosaaren Sataman Rakentamisen Aikaisen (2003–2008) Vesistö- Ja kalataloustarkkailun Yhteenvetoraportti*. Klaukkala: Kala- ja vesitutkimus Oy.

Virtasalo, J. J., Bonsdorff, E., Moros, M., Kabel, K., Kotilainen, A. T., Ryabchuk, D., et al. (2011). Ichnological trends along an open-water transect across a large marginal-marine epicontinental basin, the modern Baltic Sea. *Sediment. Geol.* 241, 40–51. doi: 10.1016/j.sedgeo.2011.09.010

Virtasalo, J. J., Endler, M., Moros, M., Jokinen, S. A., Hämäläinen, J., and Kotilainen, A. T. (2016). Base of brackish-water mud as key regional stratigraphic marker of mid-Holocene marine flooding of the Baltic Sea Basin. *Geo-Marine Letters* 36, 445–456. doi: 10.1007/s00367-016-0464-4

Virtasalo, J. J., Hämäläinen, J., and Kotilainen, A. T. (2014). Toward a standard stratigraphical classification practice for the Baltic Sea sediments: the CUAL approach. *Boreas* 43, 924–938. doi: 10.1111/bor.12076

Virtasalo, J. J., Kohonen, T., Vuorinen, I., and Huttula, T. (2005). Sea bottom anoxia in the Archipelago Sea, northern Baltic Sea implications for phosphorus remineralization at the sediment surface. *Mar. Geol.* 224, 103–122. doi: 10.1016/j.margeo.2005.07.010

Virtasalo, J. J., Kotilainen, A. T., Räsänen, M. E., and Ojala, A. E. K. (2007). Late-glacial and post-glacial deposition in a large, low relief, epicontinental basin: the northern Baltic Sea. *Sedimentology* 54, 1323–1344. doi: 10.1111/j.1365-3091.2007.00883.x

Weckström, K. (2006). Assessing recent eutrophication in coastal waters of the Gulf of Finland (Baltic Sea) using subfossil diatoms. *J. Paleolimnol.* 35, 571–592. doi: 10.1007/s10933-005-5264-1

Wienberg, C., and Hebbeln, D. (2005). Impact of dumped sediments on subaqueous dunes, outer Weser Estuary, German Bight, southeastern North Sea. *Geo-Mar. Let.* 25, 43–53. doi: 10.1007/s00367-004-0202-1

Conflict of Interest Statement: The authors declare that the research was conducted in the absence of any commercial or financial relationships that could be construed as a potential conflict of interest.

Copyright © 2018 Virtasalo, Korpinen and Kotilainen. This is an open-access article distributed under the terms of the Creative Commons Attribution License (CC BY). The use, distribution or reproduction in other forums is permitted, provided the original author(s) and the copyright owner are credited and that the original publication in this journal is cited, in accordance with accepted academic practice. No use, distribution or reproduction is permitted which does not comply with these terms.

frontiers in Marine Science

ORIGINAL RESEARCH
published: 23 October 2018
doi: 10.3389/fmars.2018.00388

Influence of Surfactant Concentration and Temperature Gradients on Spreading of Crude-Oil at Sea*

Katarzyna Boniewicz-Szmyt[1]* *and Stanisław Józef Pogorzelski*[2]

[1] Department of Physics, Gdynia Maritime University, Gdynia, Poland, [2] Physics and Informatics, Faculty of Mathematics, Institute of Experimental Physics, University of Gdańsk, Gdańsk, Poland

Spreading kinetics measurements were carried out on crude oils surfactant-containing sea water of well-controlled thermo elastic surface properties in laboratory conditions. It was found that oil lens expansion rates, predicted from the classical surface tension-driven spreading theory, were higher by a factor of 6–9 than those experimentally derived for Baltic collected sea water. Previously, in order to explain such a discrepancy, the initial spreading coefficient S_0–entering the lens radius vs. time dependence was replaced with the temporal one S_t dependent on the water phase surface viscoelasticity of Boniewicz-Szmyt and Pogorzelski (2008). Now, natural surfactant concentration and temperature gradients perpendicular to the surface were shown to drive a particular cell-like flow at the surface microlayer, as a result of the classic and thermal Marangoni phenomenon. The balance of interfacial forces was taken as: $-\mu\partial U_s/\partial z = \partial\gamma/\partial T\cdot\partial T/\partial x+\partial\gamma/\partial c\cdot\partial c/\partial x$ where: μ is the dynamic viscosity, U_s—the velocity, z and x axes oriented perpendicularly and horizontally to the main flow direction, T, γ, c are the temperature, surface tension, and concentration of surfactants. Computations performed on original seawater (Baltic Sea) systems, shown that the natural surfactant concentration term $\partial\gamma/\partial c$ is several times lower than the thermal $\partial\gamma/\partial T$ one (Boniewicz-Szmyt and Pogorzelski, 2016). Such a surface tension gradients induce the Benard-Marangoni instability, for high enough the so-called Marangoni numbers that could significantly slow down the spreading process. On the basis of thermo-physical model liquids properties, the critical temperature difference ΔT_c required to initiate the process under an evaporative cooling condition was evaluated. In this just concept study, the preliminary results suggest that the vertical processes are involved, and that a realistic model of oil dispersion should include vertical velocity shears appearing in the final surface tension-driven stage of oil pollution development.

Keywords: surface tension-driven spreading, spreading kinetics, Marangoni effect, Benard-Marangoni circulation, evaporative temperature gradients

OPEN ACCESS

Edited by:
Karol Kulinski,
Institute of Oceanology (PAN), Poland

Reviewed by:
Carlo Saverio Iorio,
Free University of Brussels, Belgium
Jacek Piskozub,
Institute of Oceanology (PAN), Poland

***Correspondence:**
Katarzyna Boniewicz-Szmyt
kbon@am.gdynia.pl

Specialty section:
This article was submitted to Coastal Ocean Processes, a section of the journal Frontiers in Marine Science

Received: *16 April 2018*
Accepted: *03 October 2018*
Published: *23 October 2018*

Citation:
Boniewicz-Szmyt K and Pogorzelski SJ (2018) Influence of Surfactant Concentration and Temperature Gradients on Spreading of Crude-Oil at Sea. Front. Mar. Sci. 5:388. doi: 10.3389/fmars.2018.00388*

INTRODUCTION

The kinetics of spreading various liquid hydrocarbons (including crude oil and petroleum substances) on the surface of the original seawater were investigated using video-microscopy and dynamic tensometry under laboratory conditions. The aqueous phase, containing natural surfactants, formed on the surface an adsorption layer with specific viscoelastic properties, which were determined by means of supplementary measurements with the Langmuir technique (Boniewicz-Szmyt and Pogorzelski, 2016). The classic spreading theory, so-called laminar flow theory of the boundary layer (Camp and Berg, 1987; Craster and Matar, 2006) is applicable to the system of immiscible, insoluble, and chemically pure liquids and predicts the rate of expansion of the oil spot 6–9 times higher than that was observed in previous studies (Boniewicz-Szmyt and Pogorzelski, 2008). The form of the dependence: oil lens radius vs. time $r_L \sim K\, t^n$, shows the power-law character. However, the exponent n proved to be close to ¾ for non-volatile substances but was lower oscillating around ½ for volatile hydrocarbons (Dussaud and Troian, 1998). The K constant is a function of the viscoelasticity of water phase (in particular, the dilational elasticity modulus E_{AW}). The change in the exponent n, from the initial value ¾ to ½, appeared as an inflection point in the dependence $r_L(t)$ for volatile substances, occurred after a certain time t (of the order seconds), from the moment of oil substance deposition, which pointed to the activation of the additional underestimated fluid flow mechanism. As a first step made to eliminate the discrepancy between the experimentally measured and theoretically predicted oil on water spreading velocity, the existing model was corrected by replacing the static spreading coefficient S_0 with the dynamic one S_t (Boniewicz-Szmyt and Pogorzelski, 2008). That explained only the observed stopping of the expansion of oil lens edge when S_t attained 0, and revealed the dependence $r_L(E_{AW})$.

The aim of the work is to determine the effect of surface tension gradients induced by inhomogeneities in the distribution of natural seawater surfactant concentrations, and temperature gradients in the upper surface micro-layer on the flow of fluids in the course of oil substance spreading process. The Benard-Marangoni circulation in the near-surface region results from the so-called Marangoni effect (Chauvet et al., 2012). Surface tension gradients cause Benard-Marangoni instability and creation the extremely dissipative, turbulent of cell-like fluid flow, in thin layers (several millimeters) of volatile petroleum products, during the spreading process, in the final stage of the process, where surface tension forces play a main role surface (Perfetti and Iorio, 2014). It was assumed that the evaporation process of volatile hydrocarbons with a sufficiently high evaporation rate E (gs^{-1}), can initiate the appearance of circulation cells in the expanding oil layer if the threshold temperature difference ΔT_c (between the lower and upper surface of the expanding lens layer) is attained. It appears for the so-called Marangoni number exceeding the critical value (Chauvet et al., 2012). The required ΔT was determined for model hydrocarbons on the basis of their physico-thermal properties and thermo-elastic surface parameters of the original seawater (Boniewicz-Szmyt and Pogorzelski, 2016). The directly performed the evaporative hydrocarbon surface cooling measurements (using a thermal infrared sensor) allowed us to conclude that $\Delta T \sim E$ and the induced temperature gradients are sufficiently high to initiate the Benard-Marangoni dissipative flow accompanying the oil substance spreading at seawater.

Even though the classical spreading equations developed by Fay form the basis for the most spreading algorithms in use in oceanographic practice, it is well-established that oil spreading cannot be fully explained by these relations (Fingas, 2012, 2013). As a consequence, many of the formalisms used in crude oil spill models are often quite simple and attempt to describe only the gross evolution of the oil slick, ignoring finer scale processes.

Surface Tension-Driven Spreading—Theory and Problem Formulation

Earlier spreading dynamics studies of non-volatile, insoluble thin oil layers on a thick liquid layer showed that the leading edge of the expanding lens moves with time like $t^{3/4}$, according to the laminar theory of the boundary layer (Camp and Berg, 1987; Craster and Matar, 2006). However, we have evidenced that the leading edge of volatile, immiscible spreading films also advances as a power law in time i.e., t^n but with $n \sim 1/2$ (Boniewicz-Szmyt and Pogorzelski, 2008) in the form:

$$r_L(t) = K\left[\frac{{S_0}^{1/2}}{(\mu\rho)^{1/4}}\right] t^n, \tag{1}$$

where μ and ρ are the viscosity and density of the substrate liquid, respectively, and K is an experimental constant dependent on the dilational viscoelasticity E_{AW} of the sea water surface (Figure 7 in Boniewicz-Szmyt and Pogorzelski, 2008).

Whether or not oil or surface active material will spread depends on the sign of the spreading coefficient S_0 (Boniewicz-Szmyt et al., 2007). Its positive value means a spontaneous process (Adamson and Gast, 1997):

$$S_0 = \gamma_{AW} - \gamma_{OA} - \gamma_{OW}, \tag{2}$$

where γ_{AW} is the surface tension of the air/water interface, γ_{OA} is the surface tension of air/oil interface, and γ_{OW} is the interfacial tension of water/oil interface. Spreading liquid films and water subphase can contain surface active materials like: detergents, fatty acids, phospholipids, and resins and asphaltens (in crude oil, Bauget et al., 2001). Any deformation of an elastic film-covered (of elasticity modulus E_{AW}) water surface either by shear or dilational compression will be resisted by the corresponding surface tension change:

$$\Delta\gamma_f = E_{AW}\left(\frac{\Delta A}{A}\right), \tag{3}$$

where $\Delta A/A$ is the relative film area change.

As a result, if surface active material is already present at the air/water interface, the rate of spreading dr_L/dt and the area over which the oil spreads are reduced. The compression of the initial layer of surface active material resulting from oil drop spreading leads to a further time-dependent decrease of S_0. The initial

spreading coefficient S_0 in Equation (1) should be corrected, and takes the form (Boniewicz-Szmyt and Pogorzelski, 2008):

$$S_t = S_0 - \Delta\gamma_f, \tag{4}$$

where S_t is the temporal spreading coefficient.

Solutal and Thermal Marangoni Effect

Spontaneous flow toward regions of high surface tension, so-called Marangoni flow, is a very fast transport process whose speed is mediated by the surface tension gradients (Pearson, 1958).Temperature gradients ΔT and differences in concentration of Δc surfactants (thermal and classic Marangoni effect) lead to tangential interfacial stresses and development of circulating cells (Chauvet et al., 2012).

The direction of fluid circulation in the liquid layer, with the horizontal $\Delta T_{||}$ and the vertical temperature gradient $\Delta T_{\perp}$ (Unny and Niessen, 1969), along with the concentration gradients of surface active substances (Li and Mao, 2001), is shown in **Figure 1**.

Under equilibrium conditions, shear stresses induced by surface tension gradients are balanced by viscous stresses, which leads, in two dimensions: x-horizontal and z-vertical coordinates, to the Equation (Mao et al., 2008):

$$\mu\frac{\partial U_s}{\partial z} = -\frac{\partial\gamma}{\partial T}\cdot\frac{\partial T}{\partial x} - \frac{\partial\gamma}{\partial c}\cdot\frac{\partial c}{\partial x}, \tag{5}$$

where U_s is the velocity of surface flow (m s^{-1}), μ the dynamic viscosity (Pa s), $\partial\gamma/\partial T = \gamma_T$ the surface entropy (mN m^{-1} K^{-1}), $\partial\gamma/\partial c = \gamma_c$ the surfactant activity (mN $m^2 mol^{-1}$).

The current surface tension of γ liquid, in the presence of non-uniform spatial distribution of the surface active substance concentration (c – c_0), and temperature differences (T – T_0) is described by the relationship:

$$\gamma = \gamma_0\left[1 - \gamma_T\left(T - T_0\right) - \gamma_c\left(c - c_0\right)\right]. \tag{6}$$

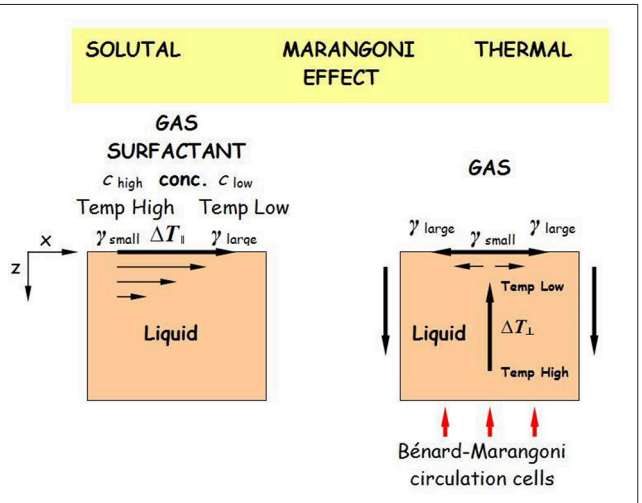


FIGURE 1 | Mechanism of surface tension-driven flow (modified after Hibiya and Ozawa, 2013).

The final effect of the Marangoni mechanism depends on the physico-thermal properties of the liquid as well as on the surface activity of a surfactant.

The linear velocity U_s of the outermost surface regions, under the temperature gradient perpendicular to the mean spreading flow direction, in circulation cells, for a layer of thickness d of the liquid describes the relationship (Berg, 2009):

$$U_s = \frac{1}{4}\frac{\frac{\partial\gamma}{\partial T}\frac{\partial T}{\partial x}d}{\mu}. \tag{7}$$

For d ($\sim$ milimeters), $U_s = 0.1$–0.3 cms^{-1}.

In order to form the Benard-Marangoni convection cell, the system must exceed the critical Rayleigh or Marangoni numbers (i.e., any one of them) both of which are proportional to the vertical temperature differences, and are defined in the form (Toussaint et al., 2008):

Number Marangoni **Number Rayleigh**

$$Ma = \frac{\partial\gamma}{\partial T}\cdot\frac{\Delta T d}{\rho\nu\kappa}, \qquad Ra = \frac{\alpha g\Delta T d^3}{\nu\kappa}, \tag{8}$$

where γ is the surface tension (mN m^{-1}), ΔT the temperature difference (K), ρ the liquid density (kgm^{-3}), ν the kinematic viscosity (m^2s^{-1}), κ the thermal diffusivity (m^2s^{-1}), d the fluid layer thickness (m), α the thermal volume expansion coefficient (K^{-1}), g is acceleration due to gravity (ms^{-2}).

The following critical values of the numbers are usually reported for the formation of circulation cells: $Ma_c = 81$; $Ra_c = 680$ (Toussaint et al., 2008).

Since the numbers: $Ma \sim d$ and $Ra \sim d^3$, the critical temperature differences (from Equation 8) are related to d as: $(\Delta T_{crit})_{Ma} \sim d^{-1}$ and $(\Delta T_{crit})_{Ra} \sim d^{-3}$. For thin layers ($d$ of the order of millimeters), the temperatures remain to each other in the following relationship $(\Delta T_{crit})_{Ma} << (\Delta T_{crit})_{Ra}$, which means that the Marangoni mechanism associated with surface tension gradients requires much lower temperature to activate than the Rayleigh mechanism attributed to the convective movements caused by vertical liquid density differences (Sefiane and Ward, 2007). Even small temperature differences (of 0.3 K), easily achieved in spreading of volatile hydrocarbons, are capable of creating the circulation cells (Toussaint et al., 2008). Critical temperatures ΔT_c have been estimated on the physical and thermal properties of the model substances and subsequently compared with those measured in the evaporation rate experiment. In order to evaluate the threshold ΔT_c required to initiate the B-M circulation, for a non-volatile model liquid a separate experiment was performed.

It is worth noting that with the increase of ΔT, the flow of liquid in B-M cells, initially stable and regular, takes on the oscillatory character, until it finally becomes completely turbulent, as illustrated in **Figure 2** (Yoda, 2007).

MATERIALS AND METHODS

Research Material

In oil substance spreading dynamics studies on the water phase, four types of crude oil were used (Romashkino,

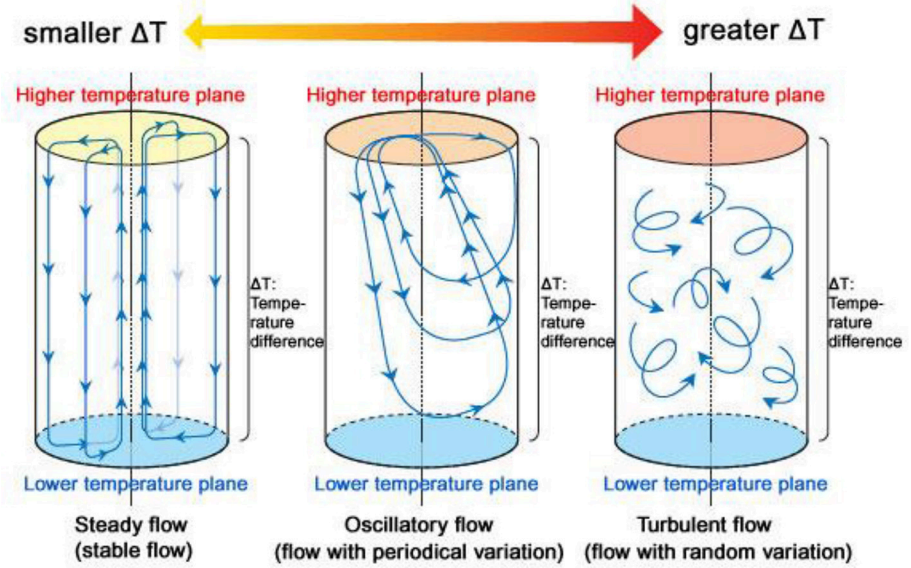


FIGURE 2 | The temperature effect on B-M flow pattern. The initial steady flow turns into a flow with periodical variations called an oscillatory flow, and then the flow becomes completely disordered named a turbulent flow with an increase of temperature difference ΔT (Yoda, 2007).

Flotta, Petrobaltic, Podkarpacka), and pure hydrocarbons of differentiated volatility (silicon oil, ethanol and acetone) as model substances deposited at the sea water collected in coastal waters (Gulf of Gdansk, Baltic Sea). Physical and thermal parameters of the studied hydrocarbons were obtained from table reference data (Bejan, 2004; Riazi, 2005; Jones, 2010), while the thermo-elastic properties of air/water (A/W) and air/oil (A/O) interfaces have been determined in our previous studies (Boniewicz-Szmyt and Pogorzelski, 2016). They were used as input data for the theoretical estimation of the threshold value ΔT_c.

Kinetics Measurements of Oil Spreading on Water

Spreading dynamics of model of hydrocarbons on the surface of original sea water samples were performed in a thermostated measuring tank using the video cameras, computer-aided image recording system, as described in detail together with the conditions of experiment methodology in Boniewicz-Szmyt and Pogorzelski (2008).

B-M Circulation Imaging, Temperature Distribution, and Evaporation Rate Measurements

The scheme of the experimental set-up used for non-contact, continuous recording and spatial mapping of the temperature difference ΔT between the free surface of the liquid and the base of the layer, using the IR sensor camera, is shown in **Figure 3** (adapted after Pasquetti et al., 2002).

In the first stage of the experiment, the non-volatile liquid layer (silicone oil) was heated from below using a heating bottom mat in order to introduce a controlled vertical temperature gradient ($\Delta T \sim 2$ K for a liquid thickness $d = 2.4$ mm), recording the development of the circulation cells.

In the case of volatile substances, the differential temperature ΔT was measured simultaneously during the evaporation process and the weight sample decrease as a function of time was recorded with an electro balance to calculate the evaporation rate $E = (dm/dt)$. The images were graphically analyzed (ImageJ program) to determine the specific cell flow features and the spatial distribution of the sample surface temperature.

RESULTS AND DISCUSSION

Spreading of Oil Substances Over Sea Water

The spreading kinetics of different crude oils and their derivatives were already presented and discussed in detail elsewhere (Boniewicz-Szmyt and Pogorzelski, 2008). The r_L-time dependences, discussed here as an example, can be found in **Figures 4**, **6** in Boniewicz-Szmyt and Pogorzelski (2008), for crude oil products where the "switch over" time, marked with the arrow, was ranging from $t = 0.5$–20 s clearly dependent on the substance volatility. The similar $r_L = 4.86\ t^{0.49}$ relation was found by Dussaud and Troian (1998), for toluene.

An exemplary radius time history $r_L(t)$, for 1-mm^{3}m drops crude oil (Petrobaltic) spreading on sea water collected in Orlowo is depicted in **Figure 4** on logarithmic scales, which is characteristic for all the tested volatile liquids.

In the initial part (short times), the dependence follows the power-law function (Equation 1) with the exponent $n = 3/4$, applicable to non-volatile liquids. As the evaporation process progresses, after time $t = 0.91$ s, the exponent n becomes closer to ½, characteristic for volatile liquids (Toussaint et al.,

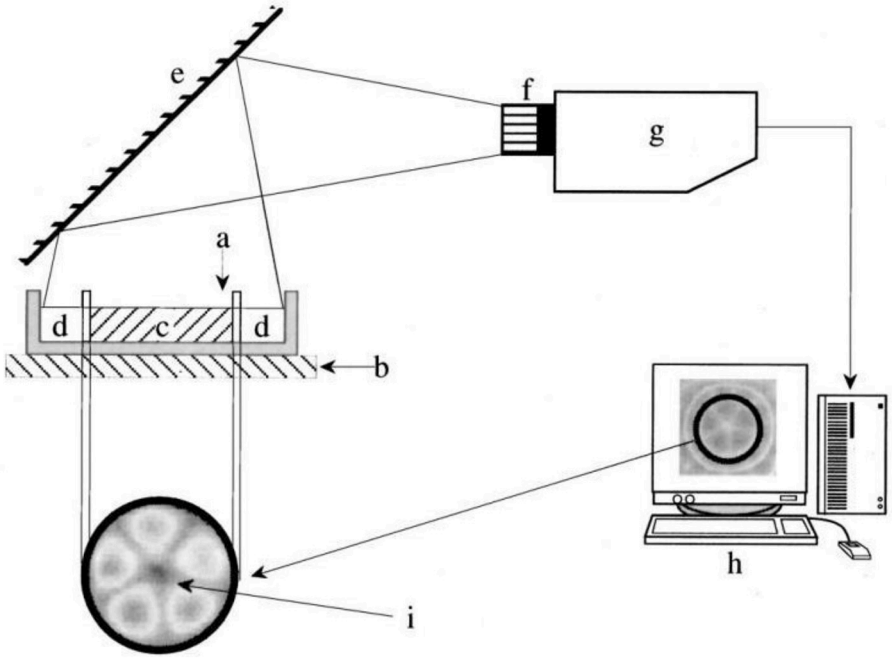


FIGURE 3 | Diagram of experimental set-up for B-M cellular flow studies: a—free surface of test liquid, b—heated plate with temperature controller, resting on analytical electro balance, c—probe liquid in Peltier dish, d—container, e—inclined aluminum mirror, f—long-focus lens, g—IR camera (infrared light range, 3–5 μm sensor wavelength, $\Delta T \sim 20$ mK resolution), h—computer with data acquisition and image analysis, i—exemplary image of liquid surface with cellular temperature spatial distribution (modified after Pasquetti et al., 2002).

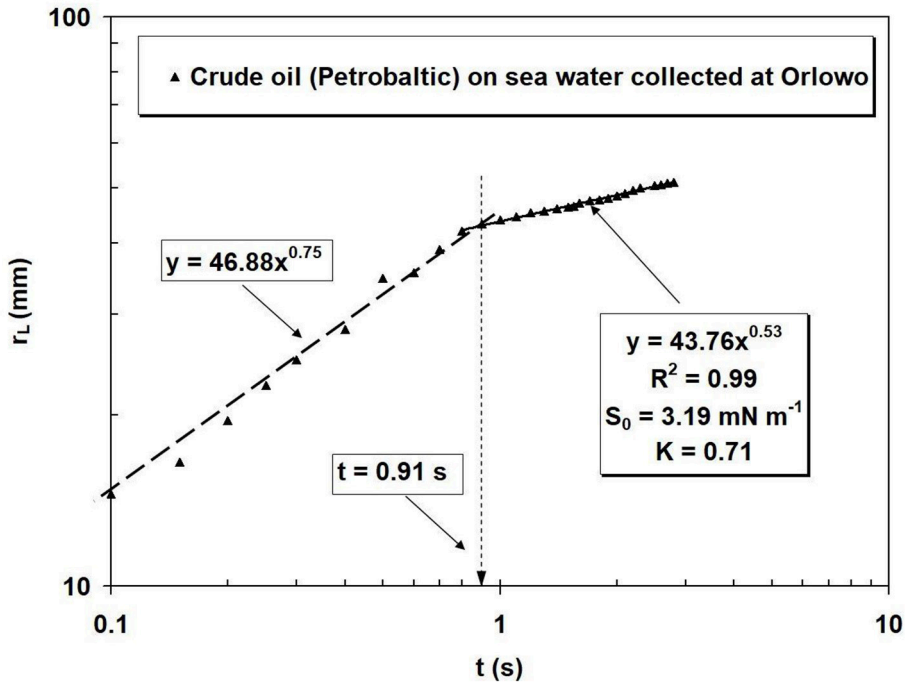


FIGURE 4 | Radius r_L vs. time for 1 mm^3m volume crude oil (Petrobaltic) drop on sea water collected at Orlowo (Gulf of Gdansk, Baltic Sea). The solid line (–) corresponds to the time dependence with $n = 3/4$, whereas the dashed (- - - -) one results from the best-fit least-squares approximation applied to the experimental data. A vertical line points to the "switch over" time, at which the transition from "nonvolatile" to "volatile" spreading regime starts.

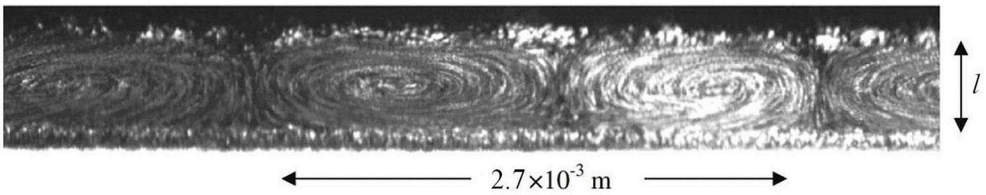


FIGURE 5 | Toluene spreading experiment visualized with aluminum dust particles and laser scattering technique, layer thickness $l = 0.8$ mm. B-M cells dimension ~ 3.3 × *l* (Toussaint et al., 2008).

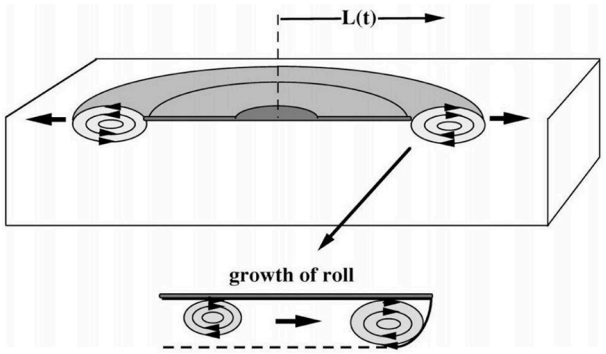


FIGURE 6 | Sub-surface flow in the water phase observed during volatile oil film spreading. Below a magnified view of stretched roll which produces flat thermal layer therein (Dussaud and Troian, 1998).

2008). The observed effect can result from the initiation of a specific flow analogous to the B-M circulation caused by surface cooling as a result of intensive evaporation of the volatile substance. Moreover, differences in the liquid vapor pressure or the spreading coefficient seem only to affect the speed of advance but not the value of spreading exponent (Dussaud and Troian, 1998). There is an evidence of an particular thermal boundary layer created in the base liquid. This thermal layer corresponds to the development of a vertical temperature gradient induced in the liquid support during the rapid spreading and evaporation process. The observed decrease of the spreading exponent found in volatile films can be attributed to the presence of a Benard-Marangoni type convective roll which develops beneath the leading edge. This strong circulation pattern may be the additional source of dissipation required to diminish the spreading exponent (Dussaud and Troian, 1998).

In the experiments, using a reflected laser beam for visualization of the flow, during the spreading process a thin layer of the volatile liquid (toluene), the picture of this phenomenon was evidenced (**Figure 5**).

This allows to propose the model of spreading a thin layer of insoluble but volatile oil substance on the water phase in the form illustrated in **Figure 6**.

This kind of fluid circulation is caused by evaporation and the accompanied process of surface cooling, during the rapid spreading of the film, resembles B-M circulation flow. This leads to the induction of an additional mechanism of fluid flow energy dissipation and subsequently to slow down the spreading process, as evidenced previously in Boniewicz-Szmyt and Pogorzelski (2008).

The standard Fay oil spill spreading model at sea divides the process into three stages: the gravity-inertial phase, gravity viscous phase, and viscous-surface tension phase (Lehr and Simecek-Beatty, 2000). It appears that it is difficult to construct a spreading formula applicable in all circumstances, while the Fay formulas may be theoretically sound, they have performed poorly in experimental and actual spills. For example, the extend of spread *R(t)* was proposed to obey the power law with respect to time: $R(t) = m\ t^n$, where m is the pre-exponential constant (Njobuenwu and Abowei, 2008). For an elongated ellipse along the wind direction oil spill shape, the non-symmetrical spreading was found, and in the case of minor and major axes relations $r_L \sim t^{0.5}$ and $r_L \sim t^{1.0}$, respectively were reported (Giwa and Jimoh, 2010). However, if the spreading was caused by a first stage shear diffusion process then the elongation would be proportional to $t^{1.5}$, while a second stage process would cause it to grow as $t^{0.5}$. The numerical results suggest that the observed spreading is a mixture of the two processes (Elliott, 1986). The realistic model of oil spreading should include the shear diffusion that is associated with vertical shears resulting also from small-scale processes like Benard-Marangoni phenomenon.

B-M Circulation vs. Thermo-Physical Properties of Hydrocarbons

The B-M circulation experiments presented here, for a non-volatile model liquid, were necessary to evaluated the threshold ΔT_c, which turned out to be much higher (a few K) than evaluated for the volatile liquids. That explains the result of the our previous kinetics studies performed also for crude oil products (non-volatile), where the "swith over" time was not observed as attributed to the transition from $r_L \sim t^{¾}$ to $t^{0.5}$ (Boniewicz-Szmyt and Pogorzelski, 2008).

A thermo-graphic image of the non-volatile liquid layer surface (silicone oil with a layer thickness $d = 2.1$ mm, placed in a cylinder vessel with an inner diameter $D = 7.4$ cm, bottom heated by a regulated electric device) observed for the surface-bottom temperature difference $\Delta T = 2.5$ K, is shown in **Figure 7A**.

By means of the image analysis procedure (Find Edges function in ImageJ program), hexagonal structures of B-M (**Figure 7B**) can be clearly visualized, whose characteristic cell

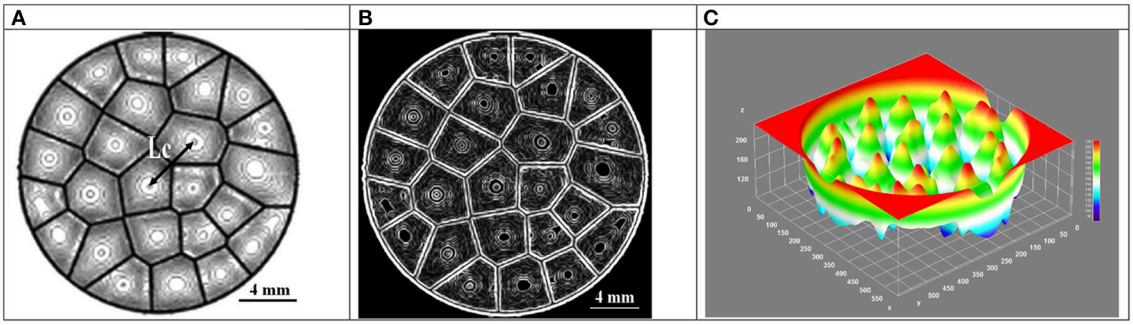


FIGURE 7 | (A) Circulation cells in silicone oil layer ($d = 2.1$ mm) heated from below $\Delta T = 2.5$ K, $L_C = 2.3 \times d = 4.9$ mm. **(B)** "Find Edges" procedure (ImageJ program) applied to the picture. **(C)** 3D thermograph of liquid temperature distribution after onset of B-M circulation. Cooler and wormer regions are indicated with blue and red colors, respectively. When the pattern is fully developed, it becomes an almost perfect array of regular hexagons, arranged in a honeycomb.

sizes L_C (distance between the centers), remained in relation to the layer thickness $L_C = 2.3 \times d$, consistent with the theoretical models and results of experiments (Chauvet et al., 2012). The gray intensity of black and white images is proportional to the temperature of the sample area that allowed to create a 3D image of the temperature distribution on the surface of the liquid (**Figure 7C**; Interactive 3D surface plot, ImageJ program), which exhibited the B-M pattern. Colder (blue) regions with higher surface tension are adjacent to warmer areas (red), where the surface tension is lowered. The surface tension gradient introduces an imbalance of forces, which causes liquid flow. The warmer fluid flows upward in the convection cell centers, while it is directed downwards at the hexagonal boundaries. When the mechanism reaches the steady state, the surface becomes an area entirely covered with almost ideal honey-like hexagons (Merkt and Bestehorn, 2003; Mancini and Maza, 2004).

The condition required to onset the B-M circulation is to achieve the threshold ΔT_c.

An interesting relationship between the Rayleigh and Rayleigh numbers can be obtained: Ra/Ma = (constant values characteristic of the probe liquid) $\times$ d^2, as a result the relative importance of the two effects involved in the B-M convection depends on the thickness of the liquid layer (Maroto et al., 2007). It is evident that the convection is controlled by surface tension forces for small thicknesses of the liquid layer. So surface tension effects are the predominant, although buoyancy forces become gradually important when the thickness of the liquid is increased. The critical ΔT_c temperature computed as a function of a model non-volatile liquid layer thickness (see **Figure 5B** in Maroto et al., 2007), established a decrease of the critical temperature gradient with the increment of the thickness of the liquid layer similarly as found in our experiments. Moreover, the temperature vertical gradient increase can make the flow beneath the expanding spill edge completely turbulent, as shown in **Figure 2**, and could be observed for the realistic case of low-temperature liquid spread over the warmer subphase.

The temperature difference ΔT_{cool} induced by the cooling process depends on the physical and thermal properties of the hydrocarbon related to the rate of evaporation (Chauvet et al., 2012; Machrafi et al., 2013).

The process of hydrocarbon evaporation considered in a larger spatial scale (at-sea) leads to the particular surface effects (Zhang, 2006), as illustrated in **Figure 8**.

In the case of evaporating liquid layers, there are local internal fluctuations and external disturbances (wind stresses, currents, and others) of random nature at the sea surface. A local increase in evaporation rate results in the drop of local temperature, and therefore creates a local increase of surface tension. The fluid from the adjacent area will be dragged toward this high surface tension region. The liquid coming from the surrounding area would push the local surface upward and make the surface ripples and corrugations. Meanwhile, the surface flow is communicated to the bulk of the fluid as a result of its shear viscosity and drags part of the bulk fluid upward. As it is known that the surface ripples and corrugations will enhance the local evaporation process, reinforcing the surface gradient in temperature and tension, and will amplify the local increase in the evaporation rate. Consequently, the evaporation rate at ridges of the cell surface would be higher than E at the center of the cell. The fluid transiting across the surface is cooled during its way and will sink at the region of the lowest temperature and the B-M circulation pattern is established. The isotherms and circulation flows in a cell are sketched in **Figure 8**.

The ocean surface is typically something like 0.1–0.6°C cooler than the temperature just below the surface. This "skin" or ultra-thin region is less than a 1 mm thick (Gentemann et al., 2009). Such a sea surface temperature (*SST*) difference can be quantified as:

$$\Delta T_c = SST_{skin} - T_{depth} = -0.14 - 0.3e^{(-U/3.7)}, \qquad (9)$$

where U is the wind speed in (ms^{-1}), as reported in Woods et al. (2014). For moderate winds i.e., $U = 6$ ms^{-1}, $\Delta T_c = -0.19$°C. This value is higher than the threshold values ΔT_{B-M} theoretically predicted on the basis of thermophysical properties of all the considered liquids (see **Table 1**).

Threshold B-M Circulation Temperature vs. Volatile Hydrocarbon Properties

The evaporation rate $E = (dm/dt)$ was derived from the experimental curve (sample mass vs. evaporation time), depicted

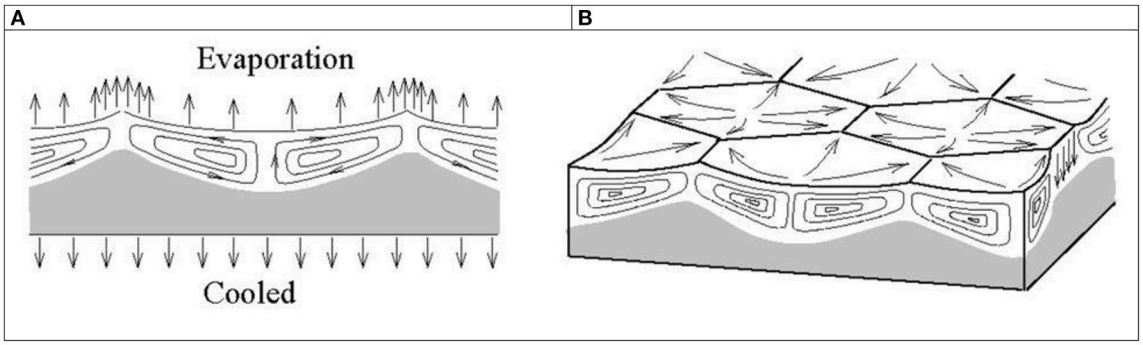


FIGURE 8 | Temperature gradient circulating flow in an evaporating liquid layer cooled: **(A)** circulating flow induced by evaporation; **(B)** tessellation on the layer surface (Zhang, 2006).

TABLE 1 | Thermal and physical properties of studied liquids vs. critical threshold temperature difference ΔT_{B-M} predicted to onset B-M circulation in thin layers at ambient conditions ($T = 23°C$) and experimental evaporative cooling ΔT_{cool}.

No.	Substance	ρ	μ	$-\partial\gamma/\partial T$	α	κ	L	ΔT_{B-M}	ΔT_{cool}
		(kg m^{-3})	(Pa s) × 10^{-3}	(N m^{-1} K^{-1}) × 10^{-3}	(K^{-1}) × 10^{4}	(m^2 s^{-1}) × 10^{6}	(J kg^{-1}) × 10^{3}	(K)	(K)
1.	Silicone oil nonvolatile	959	1.64	0.045	7.67	1.14	–	0.04	–
2.	Ethanol medium volatile	791	1.07	0.083	9.15	0.13	918	0.05	1.3–2.1
3.	Acetone highly volatile	792	0.33	0.101	8.11	0.14	517	0.02	2.5–4.3
4.	Hydrofluoro-ether highly volatile	1,482	0.61	0.103	8.34	4.88	119	0.03	0.5–3.4
5.	Crude oil Romashkino (light)	848	4.71	0.159	8.01	0.08	256	0.12	0.9–1.5
6.	Crude oil Petrobaltic (light)	806	5.17	0.188	8.15	0.07	268	0.14	0.5–0.7
7.	Crude oil Flotta (medium)	874	6.57	0.141	7.12	0.06	223	0.08	0.4–0.7
8.	Crude oil Polish (light)	864	3.36	0.176	8.54	0.07	278	0.07	0.6–1.1

in **Figure 9**, for a very volatile hydrocarbon (acetone). In the initial stage, E-values equal to 0.16 ± 0.03 g min^{-1} quickly decreased to 0.08 ± 0.01 g min^{-1} as the air over the sample layer becomes saturated with acetone vapor at longer times. For liquids with medium volatility (ethanol), under the same experimental conditions, $E = 0.032 \pm 0.008$ g min^{-1}.

Theoretical work points to the following dependence for the threshold ΔT_{cool} on the physico-thermal parameters of the evaporating liquid related to E (Merkt and Bestehorn, 2003; Chauvet et al., 2012):

$$\Delta T_{cool} \sim \mathrm{Ed} = \frac{ELd}{\lambda_l S}, \tag{10}$$

where E is the evaporation rate, d is the liquid layer thickness, L is the latent heat of evaporation, λ_l is the liquid thermal conductivity (gas $\lambda_g << \lambda_l$ liquid), S is the vessel cross-section area.

It is of particular value to quantify the evaporation rate of crude oil in at-sea conditions since it affects the threshold ΔT_{cool}. Evaporation is an important component in oil spill models (Fingas, 2012, 2013). The factors significant to evaporation include time and temperature. The difficulty in studying oil evaporation is that crude oil is a mixture of hundreds of compounds and oil composition varies from source to source and also over time. Evaporation equations are the principal physical change equations applied in spill models. The immediate layer of air above the evaporation surface, might be as thin as <1 mm, is called the boundary layer and in the case of water regulates the evaporation rate. Under low wind speed conditions or low turbulence, the air immediately above the water becomes saturated and evaporation slows. Under all experimental and environmental conditions, oil and petroleum products were not found to be boundary layer-regulated (Fingas, 2012). That is confirmed by a strong correlation between oil mass and evaporation rate (see **Figure 6** in Fingas, 2012). The at-sea experiments showed a classical relationship between the water evaporation rate and the wind speed: $E \sim U^{0.78}$ (Fingas, 2013). **Figures 1–4** in Fingas (2012) demonstrate that the evaporation rates for oils and even the light products, gasoline and heavy crude oil do not increase significantly with increasing wind. A comparison of the maximum evaporation rates for a few oils, gasoline, and water, measured under the wind-free condition showed that some oil rates exceeded that for water by as much as an order of magnitude ($E_{\mathrm{water}} = 0.034$, light crude oil ASMB = 0.075, and Gasoline = 0.34 g min^{-1} (Fingas, 2012) being in agreement with the E data obtained in this study. Further experiments performed by Yang and Wang (1997)

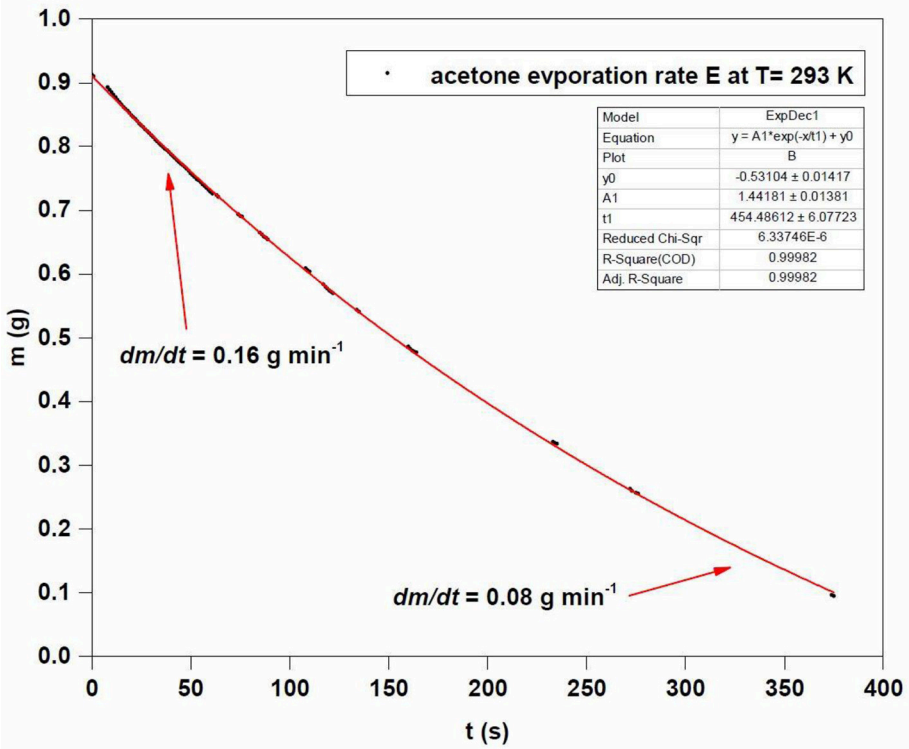


FIGURE 9 | Evaporating sample mass vs. time dependence, and Acetone evaporation rate $E = dm/dt$ at $T = 23°C$.

showed that a film could be formed on evaporating oils and this compact, solid-like film significantly retarded evaporation. The evaporation rate turned out to be reduced fivefold after the surface film formation. An important factor of evaporation regulation is also the saturation concentrations which are collected in **Table 1** of Fingas (2013), for water and several oil components. The saturation concentration of water is about two orders of magnitude less than the saturation concentration of volatile oil components such as pentane.

On the other hand, the direct measurement of ΔT_{cool} indicated the power-law like dependence: $\Delta T_{cool} = \mathrm{A}{\cdot}E^{\mathrm{B}}$, where A and B constants appeared to be dependent both on the thermal properties of hydrocarbons and air stream velocity over the evaporating surface. For evaporating crude oil and petroleum products, E is a wind speed U related quantity as found in field studies (Fingas, 2012).

The thermal and physical quantities that characterize the test liquids and raw crude oils together with the threshold values of ΔT_{B-M} (calculated from the theoretical model) and ΔT_{cool} measured experimentally in the evaporation process are summarized in **Table 1.** Temperature differences ΔT_{cool} registered in the process of evaporation for model liquids of significant volatility were of the order of 1.3–3.4 K but almost two times lower values (0.4–1.5 K) were found for crude oils. However, they are several times higher than the threshold ΔT_{B-M} theoretically-predicted values required for the B-M flow pattern to be initiated.

To sum up, the crude oil spreading at the final stage of the pollution expansion, when the surface tension forces play a main role is attributed to generation of subsurface turbulence dissipative flow of circular nature that leads to the slower velocity of the expanding oil front edge in reference to value predicted from the classical boundary-layer flow theory.

Apart from the thermal Marangoni effect, there is also the classic one, caused by the gradients of the concentration of natural surfactants present in the sea surface microlayer. The tangential stresses resulting from the both effects describe the dependence (Li and Mao, 2001; Pasquetti et al., 2002; Mao et al., 2008):

$$\tau_z = \frac{\partial \gamma}{\partial c} \cdot \frac{\partial c}{\partial z} + \frac{\partial \gamma}{\partial T} \cdot \frac{\partial T}{\partial z}. \tag{11}$$

The first term (attributed to classical surfactant effect) $\partial\gamma/\partial z$, reaches values from the range 5.32–10.45 mN m^{-2}, while the second one (thermal effect) in the Equation (11) is of the order of 52.6–274.2 mN m^{-2}, which is 10–30 times greater than that in the case of the surfactant-mediated effect, as found in thermo-elastic studies of Baltic Sea coastal waters (Boniewicz-Szmyt and Pogorzelski, 2016). The M-B circulation may be a very effective and still underestimated process of mixing, redistribution or enrichment of the micro-layer of the sea in various fractions of dissolved organic matter (DOM), in which temperature

gradients (Marangoni's thermal effect) play a principal role, while the natural sea water surfactant effect is of secondary importance.

CONCLUSIONS

It is suggested that the decrease in the spreading exponent n (from ¾ to ½) in the relation $r_L(t)$, observed for the volatile hydrocarbon films, occurring after 1–3 s from the moment of initiating the spread phenomenon, can result from the creation of Benard-Marangoni-type convective rolls which develop beneath the leading edge under particular conditions (sufficient evaporation rate, ΔT_{coll} cooling effect temperature difference between the free surface of the layer and the base). This highly dissipative nature of fluid flow, observed only in the case of volatile stretched films, leads to a significant decrease in the rate of expansion.

Large temperature gradients present in thin (∼mm) liquid layers lead to perpendicular components of the U_s fluid velocities (0.1–0.3 cms^{-1}) that are responsible for the development of turbulent fluid circulation below the expanding film.

The threshold temperature difference ΔT_{B-M} required for the activation of B-M circulation pattern, determined on the basis of the thermo-physical properties of model substances, can be achieved by surface cooling for each of the tested hydrocarbon and the crude oils ($\Delta T_{B-M} << \Delta T_{cool}$).

The B-M circulation experiments performed here, for a non-volatile model liquid, established the threshold ΔT_c, which turned out to be much higher (a few K) than evaluated for the volatile liquids of the same layer thicknesses. For non-volatile crude oil products, the evaporative cooling mechanism of the B-M circulation is unlikely to appear, and the general dependence $r_L \sim t^{¾}$ is obtained at the latest stage of the oil spill spreading, where the "switch over" time was not observed as attributed to the transition from $r_L \sim t^{3/4}$ to $t^{0.5}$.

The temperature difference ΔT_{cool}, is a function of the evaporation rate $\Delta T_{cool} = \mathrm{A}\cdot E^{\mathrm{B}}$, where constants A and B depend on the velocity of the air stream over the evaporating liquid surface.

The generation of the Marangoni fluid flow mechanism in the upper per sea water microlayer is attributed mainly to temperature gradients with a minor role played by natural surfactant concentration gradients.

Fay's empirical formulas from layer-averaged Navier-Stokes equations and their later derivatives are still sometimes considered as the state-of-the-art in oil slick modeling literature. As argued in this preliminary study, the vertical fine processes are involved, and that a realistic model of oil dispersion should include vertical velocity shears.

In such a concept study, surface tension-dependent phenomena pointed to here are of universal concern in several physicochemical systems of oceanographic concern taking place at the interfaces (natural sea surface film formation, for instance) and turned out to be still underestimated effects.

AUTHOR CONTRIBUTIONS

KB-S collected data in the field experiment, evaluated surface film parameters, performed correlation analyses, searched for literature background interpretation, and wrote manuscript. SP formulated work concept, created theoretical background, analyzed, and discussed results.

FUNDING

Support for this work was provided by the University of Gdansk (DS 530-5200-D-464-17).

REFERENCES

Adamson, A. W., and Gast, A. P. (1997). *Physical Chemistry of Surfaces*. New York, NY: John Wiley and Sons.

Bauget, F., Langevin, D., and Lenormand, R. (2001). Dynamic surface properties of asphaltenes and resins at the oil-water interface. *J. Colloid Interface Sci.* 239, 501–508. doi: 10.1006/jcis.2001.7566

Bejan, A. (2004). *Convection Heat Transfer*. New York, NY: Wiley and Sons.

Berg, S. (2009). Marangoni-driven spreading along liquid-liquid interfaces. *Phys. Fluids* 21, 032105–032112. doi: 10.1063/1.3086039

Boniewicz-Szmyt, K., and Pogorzelski, S. J. (2008). Crude oil derivatives on sea water: signatures of spreading dynamics. *J. Mar. Syst.* 74, S4S1–S5S1. doi: 10.1016/j.jmarsys.2007.11.015

Boniewicz-Szmyt, K., and Pogorzelski, S. J. (2016). Thermoelastic surface properties of seawater in coastal areas of the Baltic Sea. *Oceanologia* 58, 25–38. doi: 10.1016/j.oceano.2015.08.003

Boniewicz-Szmyt, K., Pogorzelski, S. J., and Mazurek, A. (2007). Hydrocarbons on sea water: steady-state spreading signatures determined by an optical method. *Oceanologia* 49, 413–437.

Camp, D. W., and Berg, J. C. (1987). The spreading of oil on water in the surface tension regime. *J. Fluid Mech.* 184, 445–462.

Chauvet, F., Dehaeck, S., and Colinet, P. (2012). Threshold of Benard-Marangoni instability in drying liquid films. *Europhys. Lett.* 99:34001. doi: 10.1209/0295-5075/99/34001

Craster, R. V., and Matar, O. K. (2006). On the dynamics of liquid lenses. *J. Colloid Interface Sci.* 303, 503–516. doi: 10.1016/j.jcis.2006.08.009

Dussaud, A. D., and Troian, S. M. (1998). Dynamics of spontaneous spreading with evaporation on a deep fluid layer. *Phys. Fluids* 10, 23–38.

Elliott, A. (1986). Shear diffusion and the spread of oil in the surface layers of the North Sea. *Dt.Hydrogr.Z.* 39, 113–137.

Fingas, M. F. (2012). Studies on the evaporation regulation mechanisms of crude oil and petroleum products. *Adv. Chem. Eng. Sci.* 2, 246–256. doi: 10.4236/aces.2012.22029

Fingas, M. F. (2013). Modeling of oil and petroleum evaporation. *J. Petrol. Sci. Res.* 2, 104–115.

Gentemann, C. L., Minnett, P. J., and Ward, B. (2009). Profiles of ocean surface heating (POSH): a new model of upper ocean diurnal warming. *J. Geophys. Res.* 114:C0C7017. doi: 10.1029/2008J88JC0C004825

Giwa, A., and Jimoh, A. (2010). Development of models for the spreading of crude oil. *AU J.T.* 14, 66–71.

Hibiya, T., and Ozawa, S. (2013). Effect of oxygen partial pressure on the Marangoni flow of molten metals. *Cryst. Res. Technol.* 48, 208–213. doi: 10.1002/crat.201200514

Jones, J. C. (2010). *Hydrocarbons- Physical Properties and Their Relevance to Utilization*. Houston, TX: Jones and Ventus Publishing ApS.

Lehr, W. J., and Simecek-Beatty, D. (2000). The relation of Langmuir circulation processes to the standard oil spill spreading, dispersion, and transport. *Spill Sci. Technol. Bull.* 6, 247–253. doi: 10.1016/S1353-2561(01)00043-3

Li, X. J., and Mao, Z. S. (2001). The effect of surfactant on the motion of buoyancy-driven drop at intermediate Reynolds numbers: a numerical approach. *J. Colloid Interface Sci*. 240, 307–322. doi: 10.1006/jcis.2001.7587

Machrafi, H., Sadoun, N., Rednikov, A., Dehaeck, S., Dauby, P. C., and Colinet, P. (2013). Evaporation rates and Benard-Marangoni supercriticality levels for liquid layers under an inert gas flow. *Microgravity Sci. Technol*. 25, 251–265. doi: 10.1007/s12217-013-9355-8

Mancini, H., and Maza, D. (2004). Pattern formation without heating in an evaporative convection experiment. *Europhys. Lett*. 66, 812–818. doi: 10.1209/epl/i2003-10266-0

Mao, Z., Lu, P., Zhang, G., and Yang, C. H. (2008). Numerical simulation of the Marangoni effect with interphase mass transfer between two planar liquid layers. *Chin. J. Chem. Eng*. 16, 161–170. doi: 10.1016/S1004-9541(08)60057-9

Maroto, J. A., Perez-Munuzuri, V., and Romero-Cano, M. S. (2007). Introductory analysis of Benard-Marangoni convection. *Eur. J. Phys*. 28, 311–320. doi: 10.1088/0143-0807/28/2/016

Merkt, D., and Bestehorn, M. (2003). Benard-Marangoni convection in a strongly evaporating fluid. *Physica D* 185, 196–208. doi: 10.1016/S0167-2789(03)00234-3

Njobuenwu, D. O., and Abowei, M. F. N. (2008). Spreading of oil spill on placid aquatic medium. *Leonardo J. Sci.* 7, 11–24.

Pasquetti, R., Cerisier, P., and LeNiliot, C. (2002). Laboratory and numerical investigations on Benard-Marangoni convection in circular vessels. *Phys. Fluids* 14, 227–228. doi: 10.1063/1.1424307

Pearson, J. R. A. (1958). On convection cells induced by surface tension. *J. Fluid Mech*. 4, 489–496.

Perfetti, C., and Iorio, C. S. (2014). Evaporation induced thermal patterns in fluid layers: a numerical study. *J. Electr. Cool. Therm. Cont.* 4:52049. doi: 10.4236/jectc.2014.44011

Riazi, M. R. (2005). *Characterization and Properties of Petroleum Fractions*. Philadelphia, PA: ASTM International.

Sefiane, K., and Ward, C. A. (2007). Recent advances on thermocapillary flows and interfacial conditions during the evaporation of liquids. *Adv. Colloid Interface Sci*. 134–135, 201–223. doi: 10.1016/j.cis.2007.04.020

Toussaint, G., Bodiguel, H., Dumenc, F., Guerrier, B., and Allain, C. (2008). Experimental characterization of buoyancy- and surface tension-driven convection during the drying of a polymer solution. *Int. J. Heat Mass Transfer* 51, 4228–4237. doi: 10.1016/j.ijheatmasstransfer.2008.02.006

Unny, T., and Niessen, P. (1969). Thermal instability in fluid layers in the presence of horizontal and vertical temperature gradients. *J. Appl. Mech*. 36, 121–128.

Woods, S., Minnett, P. J., Gentemann, C. L., and Bogucki, D. (2014). Influence of the ocean cool skin layer on global air-sea CO_2O flux estimates. *Remote Sens. Environ.* 145, 15–24. doi: 10.1016/j.rse.2013.11.023

Yang,W. C., and Wang, H. (1997). Modelling of oil evaporation in aqueous environment. *Water Res.* 11, 879–887.

Yoda, Y. (2007). *Research Report NSR*. Japan Chemical Society.

Zhang, N. (2006). "Surface tension-driven convection flow in evaporating liquid layers," in *Surface Tension-Driven Flows and Applications*, ed R. Savino (Trivandrum: Research Signpost), 147–170.

Conflict of Interest Statement: The authors declare that the research was conducted in the absence of any commercial or financial relationships that could be construed as a potential conflict of interest.

Copyright © 2018 Boniewicz-Szmyt and Pogorzelski. This is an open-access article distributed under the terms of the Creative Commons Attribution License (CC BY). The use, distribution or reproduction in other forums is permitted, provided the original author(s) and the copyright owner(s) are credited and that the original publication in this journal is cited, in accordance with accepted academic practice. No use, distribution or reproduction is permitted which does not comply with these terms.

frontiers in Marine Science

ORIGINAL RESEARCH
published: 05 September 2018
doi: 10.3389/fmars.2018.00313

Secondary Microplastics Generation in the Sea Swash Zone With Coarse Bottom Sediments: Laboratory Experiments

Irina Efimova[1], *Margarita Bagaeva*[1], *Andrei Bagaev*[1,2], *Alexander Kileso*[3] *and Irina P. Chubarenko*[1]*

[1] Shirshov Institute of Oceanology, Russian Academy of Sciences, Moscow, Russia, [2] Federal State Budget Scientific Institution "Marine Hydrophysical Institute of RAS," Sevastopol, Russia, [3] Department of Geography of the Ocean, Immanuel Kant Baltic Federal University, Kaliningrad, Russia

Marine beaches worldwide are nowadays exposed to significant contamination by plastics. On the Baltic beaches, polyethylene, polypropylene, and polystyrene are most abundant. We investigate the generation of microplastics particles (MPs, characteristic size from 0.5 to 5 mm) from larger plastic items in the sea swash zone using a laboratory rotating mixer filled with water and natural coarse beach sediment (marine pebbles). Inclination of the axis of rotation and the volume of the material were adjusted in such a way that mixing resembled a breaking wave in the swash zone. Plastic samples used were of the types most commonly found on the sea beaches. Experimental 2 × 2 cm-large plastic items made of low-density polyethylene (LDPE) were manufactured from common new garbage bags (thickness 5 μm); those made of polypropylene (PP) and polystyrene (PS) were produced from single-use tableware; samples of foamed plastics were presented by cubes (with 2-cm sides) cut out of standard building insulator sheets (foamed PS). Four sets of 24-h-long experiments were conducted (for each type of plastic separately), with step-wise (every 3 h) examination of the generated MPs mass, number of particles, and their qualitative characteristics such as shape, quality of the surface, general behavior while mixing, etc. Statistically significant dependencies are obtained for the increase in mass and in number of MPs with time for all four used kinds of plastics. Brittle solid PS is shown to be the most productive in terms of both mass and number of MPs generated. Anisotropic springing PP is the most resistant. Tensile tearing of LDPE and fragmentation of foamed PS to compounding bubbles/spherules show the variety of mechanisms involved in fragmentation of plastics in the swash zone. Increase in MPs mass and the number of MPs particles with time, as well the link between them, are important for field monitoring and numerical modeling. Potentially shape-selective operation of sieves during sampling and sorting of MPs particles of various shapes is discussed.

Keywords: secondary microplastics, mechanical degradation, swash zone, pebble beach, mass of microplastics vs. number of particles

OPEN ACCESS

Edited by:
Haibo Zhang,
Zhejiang Agriculture and Forestry University, China

Reviewed by:
Monica F. Costa,
Universidade Federal de Pernambuco, Brazil
André Ricardo Araújo Lima,
Universidade Federal de Pernambuco, Brazil

***Correspondence:**
Irina P. Chubarenko
irina_chubarenko@mail.ru

Specialty section:
This article was submitted to Marine Pollution, a section of the journal Frontiers in Marine Science

Received: *31 May 2018*
Accepted: *15 August 2018*
Published: *05 September 2018*

Citation:
Efimova I, Bagaeva M, Bagaev A, Kileso A and Chubarenko IP (2018) Secondary Microplastics Generation in the Sea Swash Zone With Coarse Bottom Sediments: Laboratory Experiments. Front. Mar. Sci. 5:313. doi: 10.3389/fmars.2018.00313

INTRODUCTION

Contamination of marine environments by microplastic particles (MPs) is an unfortunate sign of the development of the Anthropocene epoch on the Earth (Waters et al., 2016): mankind significantly influences its habitat. Unprecedented amounts of plastic objects, their wreckage and smaller plastic particles are nowadays found everywhere in the World Ocean, from Pole to Pole (Nerland et al., 2014) and from shorelines to the deep sea (Barnes et al., 2009; Browne et al., 2011). Fast expansion of this kind of contamination has its roots in the plastics durability and movability. MPs are small (1–5 mm Arthur et al., 2009) and relatively light [in comparison with natural sediments (Chubarenko et al., 2016)]. Transport properties and fate of MP particles depend on their shape, size, and density, all of which vary with time spent in the environment (Chubarenko et al., 2016; Khatmullina and Isachenko, 2016). This makes it difficult to analyse their impact on ecosystems and to model their behavior.

Two types of MPs are usually distinguished by their origin: primary and secondary MPs. The so-called primary MPs is produced as such and appears in marine environment either by chance (like pre-production pellets, abundant in the environment in 1970–1990s Ryan et al., 2009; Karapanagioti, 2012) or with waste waters (like residuals of used scrubbers, cosmetics, etc.). These particles typically have rounded or amorphous 3d shapes, a quite definite size range (e.g., in the US—74–420 μm Beach, 1972), are made of PE, PP, or PS (Zitko and Hanlon, 1991; Gregory, 1996; Hintersteiner et al., 2015; Lassen et al., 2015; Napper et al., 2015; Duis and Coors, 2016), and location of their sources is usually quite predictable. Thus, contamination by primary MPs is relatively easier to tackle, and effective preventive measures against it are already undertaken. The so-called secondary MPs come from destruction of larger objects which have ended up in the marine environment for some reason or another. Given the large amount of macroplastics entering the environment, it is generally assumed that most MPs in the environment are secondary MPs (Andrady, 2011; Hidalgo-Ruz et al., 2012; Duis and Coors, 2016).

Disintegration of common polymers in the terrestrial environment is mainly driven by UV radiation (Andrady, 2011; Duis and Coors, 2016): as a result of photo-oxidative degradation, plastic becomes brittle and eventually fragments. High temperature, thaw-freeze cycles, weathering–all these facilitate plastic degradation, which leads to relatively effective plastic fragmentation on land, and also on the beach surface. In water, the majority of destructive for plastic environmental conditions are absent or at least not as effective (Shah et al., 2008; Barnes et al., 2009; Andrady, 2011), making degradation much slower. As for today's knowledge, plastics are not biodegraded to considerable extent under environmental (especially marine) conditions (Andrady, 2011; Duis and Coors, 2016), and mineralisation of plastics appears to be extremely slow as well (Shah et al., 2008; Andrady, 2011). In the sea, however, new mechanisms appear (Shah et al., 2008; Chubarenko et al., 2016), most effective being mechanical abrasion by sediments and fragmentation in the sea swash and wave breaking zone, especially during stormy events (Chubarenko and Stepanova, 2017; Chubarenko et al., 2018; Efimova and Chubarenko, 2018). Here, properties and qualities of the generated MP particles are very difficult to predict, which does not make this question less important. In this work, in order to single out the effect of interaction with sediments in the swash zone, we consider only mechanical degradation of newly made materials, not discussing their degradation on the beach due to weathering, UV-exposure, oxidation, or any other destructive conditions. As abrasive material, potentially most effective in mechanical degradation under marine environmental conditions, we have selected natural pebbles, collected on the Baltic Sea beaches. This selection is based on the results of our fragmentation experiments carried out with different marine sediments–sand, granules, small, and large pebbles (to be submitted to "Environmental Pollution"). Natural beaches, consisting of gravel, pebbles, and cobbles (known as coarse clastic beaches) can be found along many mid- and high-latitude (formerly glaciated) coasts of England, Iceland, Canada, etc. (e.g., Carter and Orford, 1993), while segments with coarser beach sediments can be commonly found around capes and near cliffs all over the world.

Modern production trends accounted for the selection of plastics used in the reported laboratory experiments. Most common polymers produced worldwide in, e.g., 2012 were polyethylene (PE, 30%) and polypropylene (PP, 19%), followed by polyvinyl chloride (11%) and polystyrene (PS, 7%) (Plastics Europe, 2013). From 288 million tons of plastics produced in 2012, 57 million tons (20%) were produced in Europe (Plastics Europe, 2016). Following worldwide trends, plastic demand in Europe similarly contains about 30% of PE, about 19% of PP, and about 7% of PS (Plastics Europe, 2014).

Monitoring of coastal zones worldwide shows that the types of plastics typically found on the beaches and in sea/ocean coastal zones tend to reflect the most commonly used plastics (Andrady, 2011; Li et al., 2016). For example, a study from Italy (Vianello et al., 2013) found the most predominant microplastics to be PE (48%) and PP (34%). Frias et al. (2014) found PE, PP, and polyacrylates (PA) dominating along the Portuguese coast. On the beaches of Hawaii, PE (85%) and PP (14%) are dominating (Carson et al., 2011). In Claessens et al. (2011), the analyzed granules in coastal and offshore sediments consisted of PP, PS, and PP. Esiukova (2017) found that foamed PS is the most common type of MPs over the beaches of the south-eastern Baltic Sea. Consequently, ingestion by living creatures follows the same plastic-type distribution; (e.g., Goldstein and Goodwin, 2013) revealed that MPs ingested by gooseneck barnacles (*Lepas anatifera, Lepas pacifica, Lepas* sp.) were PE (58%), PP (5%), and PS (1%). Thus, in aquatic environments PE, PP, and PS are the most frequently found polymers, while fragments, films and styrofoam spherules are among the most commonly found particle types.

About a half of the produced plastic is used in low-value products designed for disposable single-use (Plastics Europe, 2013). The majority of the beach litter consists of single-use PP cups, PS plates, and PE bags (**Figure 1**). Foamed PS spherules are also mentioned in many studies dedicated to beach MPs (e.g., Claessens et al., 2011; Duis and Coors, 2016; Esiukova, 2017). Below we analyse the process and the results of the



FIGURE 1 | Common types of plastic litter on the beaches of the Baltic Sea: **(A)** polyethylene (LDPE) garbage bags, **(B)** polystyrene (PS) single-use plates, **(C)** polypropylene (PP) single-use beverage glasses, and **(D)** building insulations sheets (foamed PS) **(D)**. Photos by I. Chubarenko. In the center–respective laboratory samples prepared for the experiment.

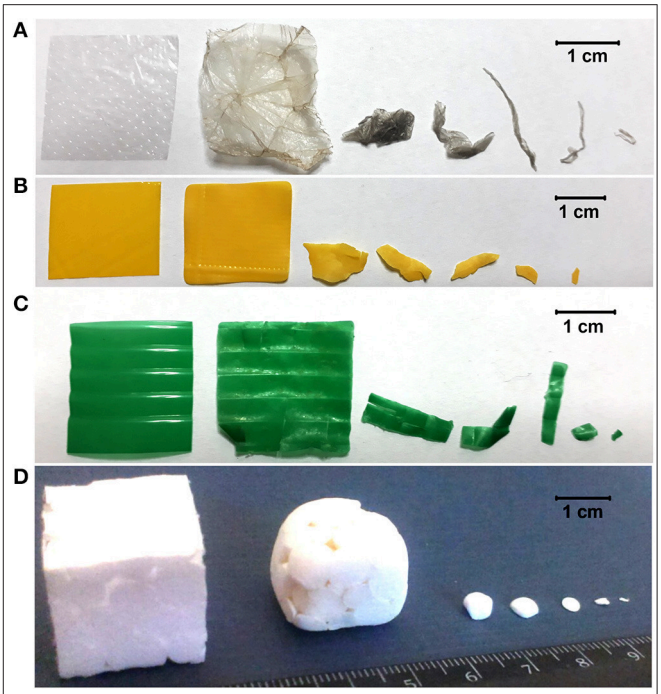


FIGURE 2 | Large plastic items (LPIs, 2 cm each side) of LDPE **(A)**, PP **(C)**, and PS in its solid **(B)** and foamed **(D)** form, and examples of macro- and microplastic items present after 24 h of mixing with pebbles and water.

degradation of larger plastic items (LPIs, with the characteristic length scale of 2 cm) made of new, bought on the market PP cups, PS plates, low-density PE (LDPE) garbage bags, and building insulation sheets (foamed PS), which were placed for 24 h into the laboratory rotating mixer together with natural 4–6.4 cm large marine pebbles and water, simulating wave breaking on the water's edge of the beach. Purely qualitative description is provided first on how fast and what kind of particles are produced from particular plastic samples. It is followed by a quantitative analysis of stepwise (every 3 h) weighing and calculation of the number of MPs particles generated. Comparison of degradation processes of different plastics and application of the results to the marine environment are provided.

MATERIALS AND METHODS

Selection of the Plastics and the Objects

The following types of plastics were selected for the degradation experiments: LDPE, PP, and PS in its solid and foamed form. There are three reasons for this selection: (i) these are the most popular plastics produced worldwide (Andrady and Neal, 2009), (ii) they are most abundant on marine beaches (Andrady, 2011; Engler, 2012), and (iii) the preference was given to those kinds of objects which might have the most different ways of mechanical destruction (flexible LDPE film; springing PP; brittle solid PS; foamed PS composed of individual spherules). They are mechanically degraded in different ways: PE tears in flakes and fibers, PS breaks up into pieces and needles (strips/strings), PP cracks into oblong plates, and foamed PS scatters into beads (see **Figure 2**). So we used LDPE garbage bags (thickness—5 μm; material density—0.92 g cm^{-3}), PS single-use plates (10 μm; 1.05 g cm^{-3}), PP single-use beverage glasses (6 μm; 0.86 g cm^{-3}), and building heat insulation plates made of foamed PS (20 mm; 0.011 g cm^{-3}), see **Figure 1** in the center. Square 2 × 2 cm LPIs were cut from bags and tableware, while foamed PS plates were cut into 2 × 2 × 2 cm cubes (**Figure 2**).

Laboratory Set-Up and Procedure

Problems related to wear of polymers are of great importance in a wide range of applications, including industry, practical use of machines and mechanisms, longevity of commercial products, and many others (e.g., Lancaster, 1969; Viswanath and Bellow, 1995; Pejaković et al., 2015, to name a few). Quite often, their solutions rely on case-specific laboratory wear tests, like comparative examination of polymers on abrasive papers, metal gauze, rough metal surfaces, a rubber, steel, or dry-sand wheels, etc. Some of the tests aim at evaluation of the weight or volume loss of the plastic material (e.g., ASTM D4060 test, www.intertek.com/polymers/testlopedia/taber-abrasion). The same very approach can be used in our case, since the loss of material from large plastic items means the generation of smaller plastic particles. The difference is in the case-specific testing conditions, which in our case will reproduce the considered "natural" external load as close as possible.

The swash zone is the most dynamic part of the nearshore zone, where pebbles are moved by wave action (asymmetric wave motion e.g., Elfrink and Baldock, 2002), thus providing an effective "mill" for plastics. On natural beaches, a swash zone is a zone which is intermittently wet and dry showing relatively large velocities (up to 3 m/s for long waves on steep beaches

Van Rijn, 2013) during the uprush and backwash phases of the saw-tooth swash wave cycle due to bore propagation and bore collapse (Van Rijn, 2013). The pebbles are moved up the beach to the run-up limit by strong bores (uprush) and moved down the beach close to the line of the steepest beach slope by the backwash (less strong due to percolation) plus gravity, resulting in a saw-tooth movement (Van Rijn, 2013). In order to reproduce the main features of this process in a laboratory, we modified the standard concrete mixer, removing the metallic blades and adjusting the angle of inclination of the axis as described below.

Natural marine pebbles (40 kg, fraction 4–6.4 cm) collected on the Baltic Sea beach, tap water (20 l), and prepared LPIs of one of the selected plastics (200 g of either LDPE, or PS, or PP, or 50 g of foamed PS) were placed into the prepared laboratory mixer with an inclined axis of rotation (**Figure 3**). There were no metallic blades inside the mixer, to ensure fragmentation of plastics by pebbles only. Every 3 h of mixing, the plastics were filtered out of the mixture and washed through a nest of 10 sieves with the mesh sizes from 5 to 0.5 mm (with the 0.5-mm step). We didn't put a pan underneath the nest to collect the smallest particles, letting them flow out with the water. After that, the remaining plastic particles were dried, weighted, examined, and placed back into the mixer for the next 3 h. Based on this methodology, we consider as MPs here those particles that passed through the 5-mm sieve, but remained within the nest of sieves. In the used set (TransAnalit, standard set C30/50), the sieves with 5.0, 4.5, 4.0, 3.0, 1.5 mm meshes had round openings, while those with 3.5, 2.5, 2.0, 1.0, 0.5 mm meshes were wire woven (i.e., with square openings). This is taken into account during the analysis of the results and pointed out directly in all the graphs and calculations where both kinds of sieves are used together. The use of the set of sieves instead of the two sieves selecting just the size range of MPs (0.5 and 5 mm) is motivated by minimisation of possible errors during weighting and, especially, the particle number calculations. When weight and number of MPs were small, they were picked up from the sieves by tweezers, calculated directly during the collection, and weighted using analytical laboratory scales (Sartogosm MB-210A, working range 1 mg−210 g, precision 0.0001 g). If the weight and number of particles were large enough (e.g., for macro-plastic fraction), the laboratory scales (ACOM JW-1-2000, working range 5–2,000 g, precision 0.1 g) were applied, and the number of MPs were obtained via calculation of the particles of given size fraction in the sub-sample weighted on the analytical scales. Maximum estimated error of weighting of MPs is eventually defined by the precision of laboratory scales and makes up about 1 g; due to gradual increase of mass of MPs the calculated errors for initial runs made up 15–20%, while for final runs it was <1%. For calculation of the number of MPs, maximum bias was contributed by the precision of laboratory scales in the cases when calculation of particles in sub-samples was required (for PS and last runs for LDPE); final accuracy of estimation of the number of particles in such cases was about 10^3 particles, or <3% of the total number of MPs particles.

The distribution of mass and number of fragments by size fraction and their evolution with time during 24 h were analyzed for every kind of plastics, as well as photos were taken for further analysis of the particles' shapes. Qualitative changes and the behavior of plastic materials were described in protocols.

Frequency of rotation (0.5 Hz) of the mixer, inclination of its axis (α∼40° from vertical), and the amount of the working material inside the mixer were adjusted in a way to provide a sort of a surging wave, with swash runup at the side A (**Figure 4**) and swash return at the side B (see also **Video S1**). The resulting angle of inclination of the surface of pebbles (β∼30°) adjusted itself quite soon after the start of rotation to be in equilibrium with

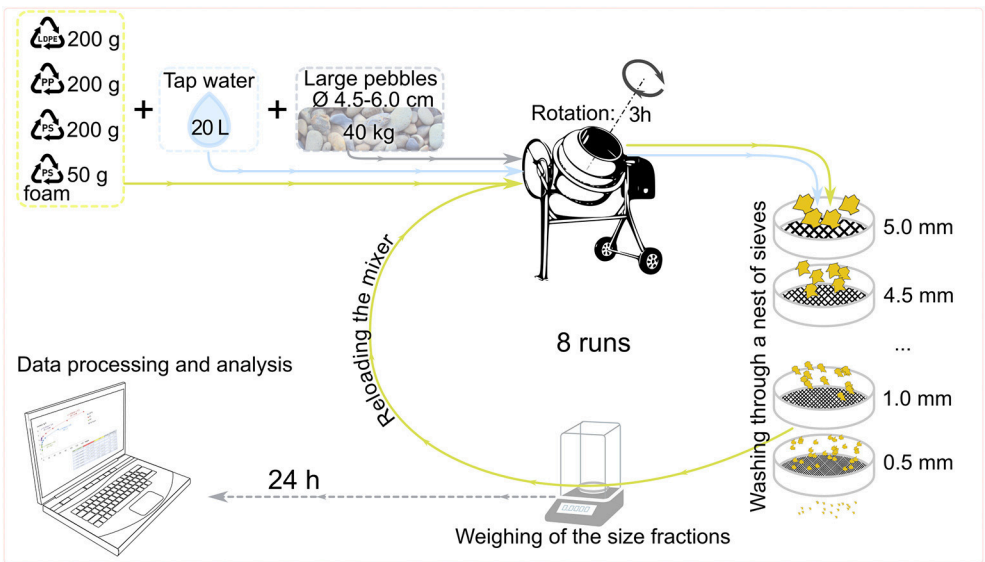


FIGURE 3 | The main stages of the experimental procedure.

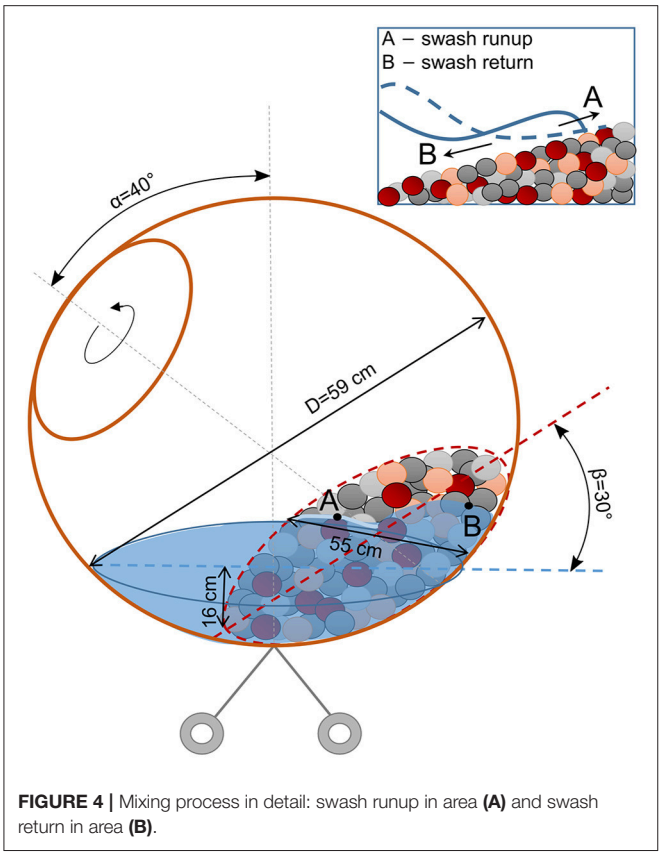


FIGURE 4 | Mixing process in detail: swash runup in area **(A)** and swash return in area **(B)**.

the given "wave energy," and some pebbles rolling downslope at the rising site B. Measured porosity of the "beach material" amounted to about 0.32. The experiments were carried out at room temperature.

RESULTS AND DISCUSSION

Qualitative Behavior of Plastics

Wear and friction are complex subjects where the results depend highly on many factors, including of course the properties of the material under examination (e.g., Lancaster, 1969; Viswanath and Bellow, 1995). This way, variations in the mechanical properties of polymers affect the wear process for a given counterface characteristics. Cutting is the most important for rigid polymers, while fatigue (or sometimes tensile tearing)-for the more elastic polymers (Lancaster, 1969). Given a wide range of polymers found on marine coasts, as well as the variability of the given polymer properties due to additives used, current environmental conditions, and/or time spent in marine environment, we find it important to report the qualitative features of the behavior of the plastics/products selected for this study. This may (i) assist the application of the obtained results to other polymers/objects, which exhibit similar (e.g., brittle, plastic, elastic) properties, (ii) shed some light onto relative roles of ductile, plastic, or elastic deformations in the swash-zone fragmentation process of the considered materials, and (iii) help in understanding of the key physical mechanisms at work under highly complex swash-zone mixing. For practical use in field observations, such qualitative descriptions link the type of plastics on the beach with the shape of the generated MPs and illuminate how (and how fast) the properties of different plastics change with time of fragmentation.

LDPE Film

Polyethylene was chosen as a representative of flexible, elastic polymer material, prone to surface fatigue and tensile tearing. It is also known to have quite low resistance against abrasion (Pejaković et al., 2015).

Garbage bags (thickness−5 μm) from the local supermarket were taken to produce LPIs of LDPE film. Considering the initial weight of samples to be 200 ± 0.1 g, measured material density of 0.92 g cm^{-3}, and a number of pieces in a subsample, the initial total amount of square 2 × 2 cm film LPIs was about 110 thousand items.

Being flexible and elastic, the LDPE samples behave during the experiment quite specifically. After 1 h of mixing with heavy pebbles, the films began bending two- or four-fold, but still remained larger than 5 mm and consequently–in the macro-size fraction. Square LPI pieces became crumpled, with a wrinkled surface. The total weight of dried samples slightly increased due to attaching small fractions of paint from the mixer's walls and crumbs from pebbles. After 9 h of mixing, films started drowning (i.e., they were floating submerged, under the surface). During the washing through the set of sieves, a part of samples flowed through the 5-mm sieve, thus formally getting in the class of MPs. However, the films on the 4.5, 4, 3.5, 3-mm sieves were not broken/ragged, but bent in elongated flattened tubes. On the 2.5-mm sieve and smaller, the particles were thin stretched-out threads (see **Figure 2A**). After 24 h, the total mass of dried samples was 5% larger than at the beginning, indicating that the part of particles smaller than 0.5 mm is negligible; 31% of the total mass of the dried samples passed through the 5-mm sieve, thus falling into the class of MPs. Increase in mass of the samples of the MPs class with time of mixing was significantly nonlinear, with a substantial jump after 20 h (see **Figure 5A**). Toward the end of the experiment, the LDPE-material of the samples became very soft, almost inelastic (non-stretching), wrinkled, and weary. Rough edges of the LDPE particles point at the ductile mechanism of failure, and indicate large plastic deformations. Such deformations require a large amount of energy absorption before failure (Mehmood et al., 2012), suggesting that higher-energy environmental conditions are more effective in generation of secondary LDPE MPs. Worn surface of the films reflects contribution of mechanical abrasion as well, which, however, has not yet contributed to the generation of MPs during 24 h of the experiment.

Solid PS

Solid PS is a brittle, hard material. The "rippled" bottom parts of common PS disposable plates were used to cut out square 2 × 2 cm LPI-pieces. After the first 3 h of mixing with pebbles, the surface of LPIs became significantly smoother. The main types of LPI-shape distortion included broken corners, triangular chips, and torn off thin strips. All the original LPIs got wrinkled, bent, fractured or twisted. The shapes of the pieces were getting

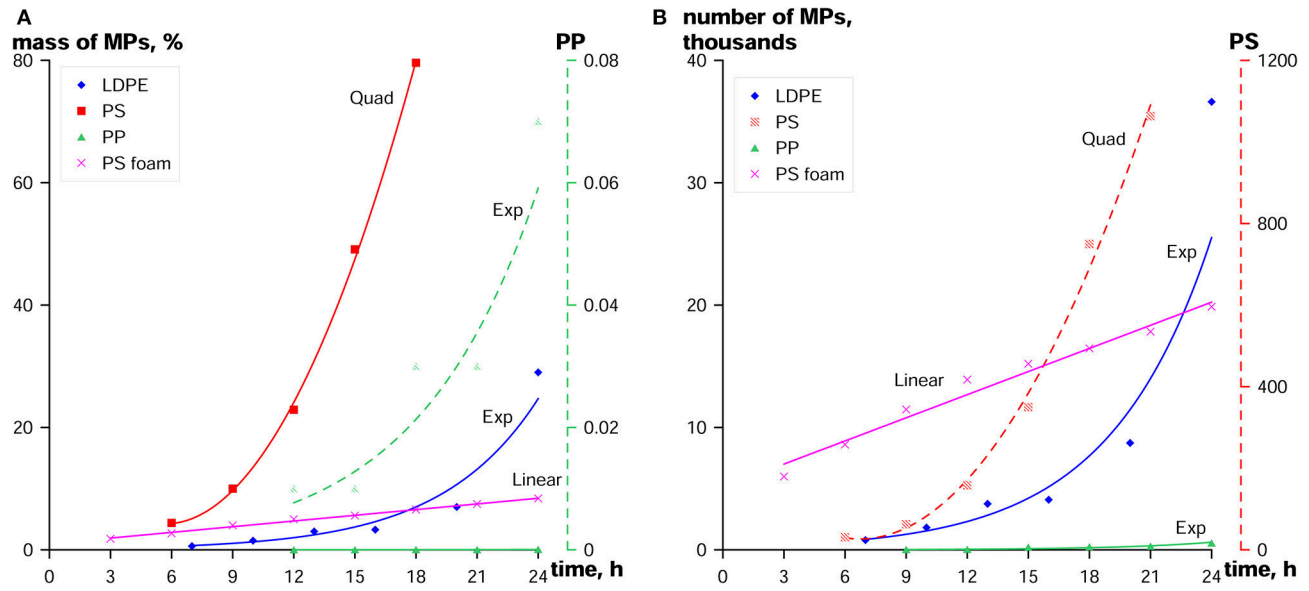


FIGURE 5 | Increase in **(A)** mass (in per cent of the total mass of the given plastic) and **(B)** number of MPs particles with time of the experiment for four types of plastic materials. Initial mass of LPIs of LDPE, PS, and PP was 200 g, of PS-foam–50 g. Additional axes at the right-hand side, the dashed graphs, and pale markers show: **(A)** enlarged exponential best fit for the mass of PP MPs; data and graph at the same scale with other plastics are shown by green triangular markers/solid line; **(B)** best fit for the number of solid PS MPs at much compressed scale.

TABLE 1 | Results of statistical analysis of exponential, quadratic, and linear models for relationship between the mass of microplastics and time of degradation of large plastic items in laboratory mixer.

Material	*F*-test		*p*-level for *F*	a (± SE)	b (± SE)	c (± SE)	A (%)	SE
	F	F_{crit}						
EXPONENTIAL REGRESSION ($y = a\,e^{bx}$)								
LDPE	38.01	7.71	**0.0035**	0.16 ± 0.03	0.21 ± 0.02		**24.12**	**3.73**
PS	65.36	10.13	0.0039	1	0.25 ± 0.01		8.67	7.53
PP	34.98	10.13	**0.0096**	0.001 ± 1.4E−07	0.17 ± 0.03		**23.05**	**0.01**
PS foam	63.62	5.99	0.00009	1.83 ± 0.36	0.07 ± 0.01		11.14	0.73
QUADRATIC REGRESSION ($y = a\,x^2 + b\,x + c$)								
LDPE	16.38	9.55	0.02	0.17 ± 0.06 (ns)	−3.77 ± 1.79 (ns)	20.922 ± 12.67 (ns)	106.38	4.04
PS	941.95	19	**0.001**	0.5 ± 0.04	−5.7 ± 1.03	20.5 ± 5.7 (ns)	**2.75**	**1.43**
PP	**12.13**	19	0.08	0.0005 ± 1.68 (ns)	−0.01 ± 1.21 (ns)	0.09 ± 1.03 (ns)	17.74	0.01
PS foam	873.06	5.79	4E-07	−0.002 ± 0.001 (ns)	0.37 ± 0.03	0.7 ± 0.2	2.2	0.15
LINEAR REGRESSION ($y = a\,x + b$)								
LDPE	8.35	7.71	0.04	1.4 ± 0.49	−13.68 ± 7.82 (ns)		195.23	6.88
PS	37.34	10.13	0.009	6.32 ± 1.03	−42.6 ± 13.16		62.24	9.81
PP	13.36	10.13	0.04	0.005 ± 0.001	−0.05 ± 0.02 (ns)		40.76	0.01
PS foam	1325.74	5.79	**2.86E-08**	0.31 ± 0.01	0.99 ± 0.13		**3.3**	**0.17**

For the F-test, both the obtained value, F, for the particular model and the critical value, F_{crit} (for the level of significance $\alpha = 0.05$) are provided; failed F-test case is highlighted by red color. Levels of significance (p) of the F-value of the ANOVA of the regression, the mean error of approximation (A), and the standard error of the regression (SE) are taken into account while choosing the best regression law. The best model for every kind of plastic is highlighted by green color/bold font and shown on ***Figure 5A****. Statistics and coefficients (a, b, c) for three regression models are shown for all four kinds of the used plastics, with non-significant (ns) coefficients shown in red.*

TABLE 2 | Results of statistical analysis of exponential, quadratic, and linear models for relationship between the number of MPs particles and time of degradation of large plastic items in laboratory mixer.

Material	*F*-test		*p*-level for *F*	a (± SE)	b (± SE)	c (± SE)	A (%)	SE
	F	F_{crit}						
EXPONENTIAL REGRESSION ($y = a\,e^{bx}$)								
LDPE	34.71	7.71	**0.004**	0.21 ± 0.04	0.2 ± 0.02		**23.13**	**4.91**
PS	34.74	7.71	0.004	7.47 ± 0.74	0.25 ± 0.01		13.14	150.15
PP	14.29	7.71	**0.019**	0.004 ± 0.0005	0.21 ± 0.04		**31.36**	**0.1**
PS foam	49.48	5.99	0.0004	6.32 ± 0.36	0.05 ± 0.007		9.9	1.67
QUADRATIC REGRESSION ($y = a\,x^2 + b\,x + c$)								
LDPE	16.27	9.55	0.02	0.21 ± 0.07 (ns)	−4.81 ± 2.27 (ns)	26.67 ± 16.06 (ns)	104.3	5.12
PS	227.26	9.55	**0.0005**	5.22 ± 0.8	−70.18 ± 21.7	262.51 ± 133.8 (ns)	**8.17**	**43.69**
PP	20.63	9.55	0.018	0.001 ± 0.001 (ns)	−0.01±0.04 (ns)	0.02 ± 0.3 (ns)	24.81	0.07
PS foam	374.86	5.79	4E-06	−0.015 ± 0.004	1.03 ± 0.11	3.16 ± 0.63	2.28	0.45
LINEAR REGRESSION ($y = a\,x + b$)								
LDPE	8.24	7.71	0.05	1.77 ± 0.62	−17.27±9.92 (ns)		191.67	8.73
PS	35.72	7.71	0.004	70.62 ± 11.82	−550.99 ± 170.62		116.18	148.29
PP	36.81	7.71	0.004	0.03 ± 0.005	−0.31 ± 0.09		58.14	0.07
PS foam	232.75	5.99	**5E-06**	0.63 ± 0.04	5.12 ± 0.63		**5.61**	**0.81**

For the F-test, both the obtained value, F, for the particular model and the critical value, F_{crit} (for the level of significance $\alpha = 0.05$) are provided. Levels of significance (p) of the F-value of the ANOVA of the regression, the mean error of approximation (A), and the standard error of the regression (SE) are taken into account while choosing the best regression law; the best model for every kind of plastic is highlighted by green color/bold font and shown on ***Figure 5B****. Statistics and coefficients (a, b, c) for three regression models are shown for all four kinds of the used plastics, with non-significant (ns) coefficients shown in red.*

more and more diverse, displaying all kinds of irregularity, e.g., segments, flakes, strips, crumbs, etc. After 15 h of mixing, about 50% of LPIs could still be identified visually as "original squares," although obviously wrecked and crippled. Three hours later this number decreased to 20% only. The "original squares" disappeared completely from the remaining mass of LPIs after 21 h of mixing.

A remarkable feature of PS fragmentation process was sudden acceleration of growth of MPs mass after 20 h of mixing, manifesting the material fatigue. If during the first 9 h the LPIs mass was decreasing relatively slowly (minus 2%–4%—7% of the total mass per 3 h), as much as 48% of the LPIs mass was lost between 15 and 18 h. Still, even after 24 h of mixing there were a few LPI flakes (0.4 g) left. At the same time, the total mass of PS in the mixer after 24 h has decreased by 18% in comparison to the initial LPIs' mass, showing that about one third of the material had been fragmented to tiny pieces smaller than 0.5 mm. The same process of fast fragmentation of PS leads also to the shift in the MPs size distribution: after 21 h of mixing, a massive shift from larger 5–3.5 mm fractions to smaller 3–0.5 mm occurred. Overall, the experiments showed fast brittle failure of solid PS LPIs.

PP

Polypropylene is a springing, mechanically rugged plastic material. For the reported experiment, te LPIs (2 × 2 cm) were prepared from the side walls of single-use PP beverage glasses. Since plastic glasses are produced by stretching from the PP sheet, the material of the side walls is mechanically anisotropic: it fractures preferentially along the direction of stretching, see photo in **Figure 1C**. On the glasses used in the experiment, the walls were manufactured with wavy "ridges" perpendicular to the stretching lines (**Figure 2C**). This makes the walls more resistant to fracture. Still, however, the preferential direction of fracture of LPIs was obvious, and the main type of the generated MPs was a 2-cm long narrow strip (**Figure 2C**). All the LPIs obtained after the experiment were cracked, bent, broken or twisted one way or another, and the diversity of the shapes of MPs increased with time of fragmentation.

Among the plastics examined in the experiments, PP appeared to have maximum longevity: after 24 h of energetic abrasion by pebbles, about 97.6% of LPIs could still be visually identified as the "original squares" (>5 mm), although they were softer, more flexible, with smoother, and matte surface.

With its material density of 0.86 g cm^{-3}, PP is positively buoyant. Nevertheless, during the experiment lots of LPIs and smaller fragments were found submerged, being captured in-between and underneath the pebbles.

Thus, a brittle fragmentation is characteristic of PP, and the specific feature of the used PP single-use glasses is anisotropy of their response to mechanical forcing by pebbles. It is worth noting that stretching of the glass out of the plastic sheet is a common technology, applied not only to PP (e.g., also to PS). However, anisotropic behavior of the very PP material is also mentioned in publications (e.g., Mehmood et al., 2012).

Foamed PS

The foamed (or expanded) PS is a rigid, tough, closed-cell foam, made of pre-expanded polystyrene beads. It has a very low density of 0.011 g cm^{-3}, so during the mixing process it mostly

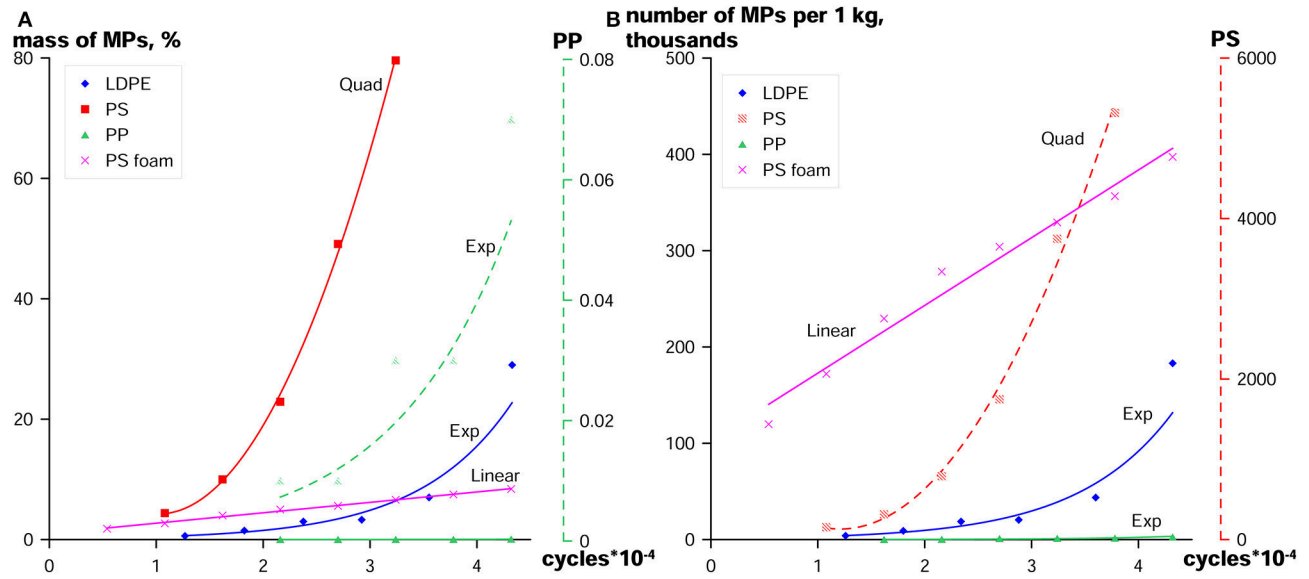


FIGURE 6 | Dependence of **(A)** mass (in per cent of the total mass of the given plastic) and **(B)** number of MPs particles, generated from 1 kg of LPIs, on the number of "wave periods." Analogously to **Figure 5**, additional axes at the right-hand side, the dashed graphs, and pale markers show: **(A)** enlarged exponential best fit for the mass of PP MPs; data and graph at the same scale with other plastics are shown by green triangular markers / solid line; **(B)** best fit for the number of solid PS MPs at much compressed scale.

TABLE 3 | Results of statistical analysis of exponential, quadratic, and linear models for relationship between the mass of MPs and dimentionless time of the degradation experiment.

Material	*F*-test		*p*-level for *F*	a (± SE)	b (± SE)	c (± SE)	A (%)	SE
	F	F_{crit}						
EXPONENTIAL REGRESSION ($y = a\,e^{bx}$)								
LDPE	45.4	7.71	**0.0025**	0.15 ± 0.03	1.16 ± 0.11		**22.66**	**3.44**
PS	65.36	10.13	0.0039	1	1.37 ± 0.07		8.67	7.53
PP	34.98	10.13	**0.0097**	0.001 ± 0.0001	0.92 ± 0.18		**23.05**	**0.008**
PS foam	63.62	5.99	0.0002	1.83 ± 0.35	0.39 ± 0.04		11.14	0.73
QUADRATIC REGRESSION ($y = a\,x^2 + b\,x + c$)								
LDPE	20.45	9.55	0.018	5.1 ± 1.57	−21.18 ± 8.9 (ns)	21.08 ± 11.41 (ns)	103.88	3.65
PS	941.95	19	**0.001**	15.46 ± 1.32	−34.68 ± 4.74	20.5 ± 5.7 (ns)	**2.75**	**1.43**
PP	**12.13**	19	0.07	0.01 ± 0.009 (ns)	−0.07 ± 0.06 (ns)	0.09 ± 0.09 (ns)	17.74	0.01
PS foam	873.06	5.79	4E-06	−0.07 ± 0.04 (ns)	2.05 ± 0.19	0.7 ± 0.2	2.2	0.15
LINEAR REGRESSION ($y = a\,x + b$)								
LDPE	8.56	7.71	0.04	7.92 ± 2.71	−14.07 ± 7.85 (ns)		201.64	6.82
PS	37.34	10.13	0.009	35.09 ± 5.74	−42.6 ± 13.16		62.24	9.81
PP	13.36	10.13	0.04	0.03 ± 0.007	−0.05 ± 0.02 (ns)		40.76	0.01
PS foam	1324.74	5.79	**2.86E-08**	1.73 ± 0.05	0.99 ± 0.13		**3.25**	**0.17**

For the F-test, both the obtained value, F, for the particular model and the critical value, F_{crit} (for the level of significance $\alpha = 0.05$) are provided; failed F-test case is highlighted by red color. Levels of significance (p) of the F-value of the ANOVA of the regression, the mean error of approximation (A), and the standard error of the regression (SE) are taken into account while choosing the best regression law; the best model for every kind of plastic is highlighted by green color/bold font and shown on ***Figure 6A****. Statistics and coefficients (a, b, c) for three regression models are shown for all four kinds of the used plastics, with non-significant (ns) coefficients shown in red.*

TABLE 4 | Results of statistical analysis of exponential, quadratic, and linear models for relationship between the number of MPs particles and dimensionless time of degradation experiment.

Material	*F*-test		*p*-level for *F*	a (±SE)	b (±SE)	c (±SE)	A (%)	SE
	F	F_{crit}						
EXPONENTIAL REGRESSION ($y = a\,e^{bx}$)								
LDPE	34.71	7.71	**0.004**	1	1.13 ± 0.12		**23.13**	**24.54**
PS	34.67	7.71	0.004	37.31 ± 2.05	1.37 ± 0.08		13.15	751.27
PP	14.28	7.71	**0.019**	0.02 ± 0.003	1.19 ± 0.21		**31.36**	**0.51**
PS foam	49.48	5.99	0.0004	126.38 ± 2.77	0.29 ± 0.04		9.9	33.47
QUADRATIC REGRESSION ($y = a\,x^2 + b\,x + c$)								
LDPE	16.27	9.55	0.02	32.69 ± 11.14 (ns)	−133.51 ± 63.05 (ns)	133.36 ± 80.3 (ns)	104.3	25.61
PS	227.27	9.55	**0.0005**	804.7 ± 122.61	−1949.26 ± 603.67	1312.24 ± 668.74 (ns)	**8.17**	**218.45**
PP	20.63	9.55	0.018	0.21 ± 0.18 (ns)	−0.34 ± 1.09 (ns)	0.12 ± 1.52 (ns)	24.81	0.33
PS foam	374.86	5.79	4E-06	−8.97 ± 2.4	113.94 ± 11.95	63.22 ± 12.66	2.28	9.07
LINEAR REGRESSION ($y = a\,x + b$)								
LDPE	8.24	7.71	0.045	49.21 ± 17.14	−86.35 ± 49.6 (ns)		191.67	43.64
PS	35.72	7.71	0.0039	1961.55 ± 328.22	−2754.93 ± 853.09		116.25	741.45
PP	36.81	7.71	0.004	0.91 ± 0.15	−1.56 ± 0.47		58.14	0.34
PS foam	232.75	5.99	**5.01E-06**	70.33 ± 4.61	102.46 ± 12.57		**5.61**	**16.13**

For the F-test, both the obtained value, F, for the particular model and the critical value, F_{crit} (for the level of significance $\alpha = 0.05$) are provided. Levels of significance (p) of the F-value of the ANOVA of the regression, the mean error of approximation (A), and the standard error of the regression (SE) are taken into account while choosing the best regression law; the best model for every kind of plastic is highlighted by green color/bold font and shown on ***Figure 6B****. Statistics and coefficients (a, b, c) for three regression models are shown for all four kinds of the used plastics, with non-significant (ns) coefficients shown in red.*

kept floating on the water surface. For the experiment, we used the standard 2-cm thick building heat insulation plates, which were cut with a hot nichrome wire into PS LPIs–small cubes with each side of 2 cm. Overall, 50 g of PS LPIs gave about 600 such cubes. Already after the first 3 h-run, some changes in the cubes' shapes were observed: the edges of the cubes became more clipped, attrited, there were individual spherules of PS or their parts (trimmed parts of the edges of a cube left after the cube's been cut) in the water. Despite very high buoyancy, a lot of small parts of the PS spherules were found under the water stuck to the pebbles.

The LPIs broke down slowly, becoming smoother and more polished at the corners, and some were torn to pieces. Individual PS particles acquired a variety of shapes, demonstrating the material's compounds–spherules of different sizes. At the end of the experiment about 72.8% of the PS was still LPIs, most of which were generally cubic in shape (**Figures 2**, **5**).

Thus, high buoyancy of foamed PS keeps its particles on the water surface, preventing effective fragmentation by moving pebbles. The main way of fragmentation of PS-foam LPIs is detaching of individual beads.

Summary of Qualitative Features

Inter-comparison of the mechanical degradation processes of different types of plastics, as well as of the specific features of the generated MPs particles leads to several conclusions. The most important one is that each type of the selected plastics/objects generated specific MPs particles. The slightly positively buoyant LDPE LPIs were transferred to the MPs class first due to folding in two or four. They effectively captured paint flakes, shards of pebbles, or other smallest suspended particles. This way, they became negatively buoyant quite soon and thus more effectively destroyed by rolling pebbles. Only then, they began fragmenting, stretching in oblong forms, became inelastic, thereby badly tearing and crumpling. Solid PS LPIs were destroyed in hard MPs of various shapes: segments, crumbs, flakes, and strips. After about 20 h of mixing, the PS MPs became suddenly very brittle, and crumbled into the smallest particles at the slightest touch. Samples of PP appeared to be the most resistive to fragmentation in comparison with others; they showed anisotropy, fragmenting into rectangular strips with sharp edges. The breaking lines were most probably defined by the production technique rather than the material fatigue. Foamed PS, being composed of individual spherules of different diameters, was first fragmented to its compounds.

At the same time, there are common tendencies in changes of plastic quality and behavior of samples during the experiment. All the plastic materials, sooner or later, became rippled and faded, worn, and crumpled, without glossy non-wettable coating. A very important observation is that all of the samples, disregarding the initial density, tend to get submerged with time and finally clog below the pebbles. The solid PS LPIs, which were the only negatively buoyant plastics in the experiments, still floated at the beginning of the experiment due to surface tension of water and non-wettability of a newly-made plastic surface. However, already after 10 min of mixing they did sink–and

throughout the rest of the experiment were distributed among the pebbles, with a clear tendency to clog between and below them. The slightly positively buoyant LDPE (both macro- and micro-) items got submerged after 9 h, with the same tendency to concentrate among the lowest pebbles. The more buoyant PP and especially foamed PS LPIs stayed floating for the entire experiment, however the majority of MPs particles tended to penetrate among/beneath the pebbles as deep as possible (the smaller the particle was the deeper it could be found). In fact, the analogous physical so-called Brazil nut effect could be mentioned here: while shaking the container with loose items (a basket with berries or a truck with stones)–larger items tend to move upwards, leaving smaller ones below (https://en.wikipedia.org/wiki/Granular_convection). The effect for items (stones, berries, etc.) of similar density but different size is usually explained by the advantage in gravitational energy: smaller items settle in-between larger ones leading to a more compact medium, whose integral center of mass is eventually lower. In our case, with the mixture of heavy stones and light plastics, this effect is not so straightforward and in general could not be foreseen. Still, the same explanation works as well: pebbles with smaller plastics in-between and beneath them are more compact than pebbles with plastics on top of them, and thus–gravitationally more advantageous.

This fact of clogging of plastics under the stones in the mixing experiment suggests the analogous behavior on natural beaches. This is in agreement with observations: e.g., McWilliams et al. (McWilliams et al., 2017) found that at rocky shores of Fogo Island, Newfoundland and Labrador, a lot of plastics were found below the sediment surface.

Mass of MPs and the Number of Particles

Increase in the MPs Mass and the Number of Particles With Time

The particles were classified as MPs here if they had passed through the sieve with 5-mm mesh, but had been retained by one of the sieves with a smaller mesh size–down to 0.5 mm. For every plastic type, the mass of this 0.5–5 mm fraction was measured every 3 h. **Figure 5A** summarizes the results, while **Figure S2** shows the generation of each type of microplastic separately and in more detail. The results show that solid PS samples (i.e., single-use PS tableware) are the most "productive": they were practically completely fragmented between 21 and 24 h of the experiment. Of LDPE samples (thin garbage bags), only 31% was transferred to MPs after 24 h, followed by foamed PS (building insulation)–with about 8% of MPs, and PP (single-use cups), where <0.1% of initial mass was transferred to MPs.

Experimental data show an increase in mass and number of MPs with time for all the used materials; they are presented on **Figures 5**, **6**. The data are provided in the **Table S1** of the **Supplementary Material**. In order to describe the relations analytically, three model hypotheses for the fit curves were examined statistically: exponential, quadratic, and linear. Analytical dependencies were obtained using the method of least squares. The adequacies of the obtained models were determined by ANOVA (*F*-test). Because of a small number of samples for each experiment the significance for each coefficient in the obtained regression formulas was additionally tested using the Student's *t*-test. **Table 1** shows the results of *F*-test and *p*-level analyses for all the fit curves. For the generation of MPs mass, the exponential regression can be considered as the best model for LDPE and PP (SE = 3.73, $p = 0.0035$ and SE = 0.01, $p = 0.0096$, correspondingly; here, SE is the standard error of the regression, and p is the significance of the *F*-value of the ANOVA of the regression). For PS, the quadratic regression is slightly better (SE = 1.43, $p = 0.001$) than the exponential one (SE = 7.53, $p = 0.0036$), however they both successfully pass the *F*-test. For the foamed PS, the best model is the linear regression (SE = 0.17, $p = 2.86\text{E-}08$).

Physically, linear dependence of mass of MPs, M, on time is equivalent to $dM/dt = const$, i.e., constant rate of production of MPs mass. This mirrors the fragmentation of foamed-PS LPIs first to their basic compounds–the bubbles of MPs size range. Since the material is highly buoyant, it is less affected by heavy moving pebbles. Twenty-four hours of the experiment are not enough to make a conclusion about further fragmentation of individual bubbles, however the change of the linear fragmentation model at further stages can be foreseen. Quadratic model for brittle solid PS ($M \sim t^2$) leads to an increase in the growth rate of MPs mass with time, $dM/dt \sim t$, probably related to the observed material fatigue. Exponential law of the MPs mass growth with time seems to indicate that the process of fragmentation involves several wear mechanisms, e.g., tensile tearing plus surface abrasion for ductile LDPE, or cutting plus surface abrasion for springing anisotropic PP.

The obtained results allow for some useful comparative evaluations. This way, fragmentation of 50% of the initial macroplastic mass to MPs under experimental conditions will take about 15/28/29 h for PS/LDPE/PS foam, correspondingly. As for PP, it showed the slowest degradation rate, and evaluation of half-fragmentation time on the base of this experiment is hardly reliable.

The projection of these results to evaluation of the corresponding time intervals and fragmentation rates at natural conditions is not straightforward, because too many factors influence mechanical mixing at the beach face. First of all, these are the wave energy, the wave period, and the grain size of the beach sediment, as well as the beach face inclination angle and percolation of the beach sediment (e.g., Komar and Allan, 2010). The use of real time of the experiment gives obviously an underestimation for real-sea conditions, since surface waves with a period of 2 s are definitely too weak to roll pebbles and fragment plastics. As zero-approach, one may use the number of cycles of the mixer (see **Figure 6**) as a kind of the "dimensionless time," and recalculate the increase in mass of MPs with time using a typical wave period for the given region instead of the period of rotation of the mixer. One may suggest considering environmental conditions with only moderate wave energy, capable of rolling only some pebbles at the beach face. The established inclination of the "beach face" in the mixer (about 1:2) also suggests the prototype with low wave energy conditions: natural clastic beaches have the slopes of about 1:4–1:10, with steeper slopes for milder external conditions (Carter and Orford, 1993). For the Baltic Sea, for example, the wave period could be

about 5–6 s (Leppäranta and Myrberg, 2009), or about 3 times as large as the period of rotation in the above experiments. Thus, a rough estimate of intensity of mechanical fragmentation in the swash zone with coarse bottom sediments under rather moderate wind-wave conditions gives about 2–4 days for disintegration of 50% of the mass of PS and LDPE into MPs, and 10% of the mass of foamed PS. Disintegration of PP samples should last much longer.

In the majority of field monitoring data, the number of MPs particles is reported instead of the integral MPs mass. Thus, analysis of increase in the number of MPs particles is important as well. This is why, in order to calculate the number of MPs particles as exactly as possible, the nest of 9 sieves with different mesh sizes (from 0.5 to 4.5 mm) was used every 3 h and with every type of plastic. After washing of all the plastic material through the nest after each run, the number of particles on every sieve was either calculated directly (if it was not too high), or estimated using calculation of particles in the weighted sub-sample. The obtained increase in number of MPs particles with time is shown in **Figure 5B**, with the results of statistical analysis provided in **Table 2**. The best fit models for different plastics are similar to those obtained for the increase in mass: the exponential relation for LDPE and PP (SE = 4.91, $p = 0.004$ and SE = 0.1, $p = 0.0019$, correspondingly), the quadratic law for solid PS (SE = 43.69, $p = 0.0005$); for the foamed PS, quadratic and linear regressions are close (SE = 0.45, p = 4E-06 and SE = 0.81, p = 5E-06, correspondingly). In total, as calculated at the nest of sieves, the number of MPs particles of LDPE/PS/PP/PS-foam generated after 24 h is estimated as about $3.6{\cdot}10^4/1.1{\cdot}10^6/5.5{\cdot}10^2/2.0{\cdot}10^4$ particles, correspondingly. Note that the total mass of solid PS decreased during the experiment to 82% of the initial mass, showing that about 18% of mass was transferred to the nano-sized particles.

In order to simplify any probable evaluations for real-beach cases, **Figure 6** displays the same data as **Figure 5**, as dependent on the number of rotational cycles, which could be treated as the number of wave periods characteristic of the observation site. For vertical axes, the mass of the generated MPs is shown in per cent from the available mass of plastic LPIs, and the number of generated MPs particles is re-calculated per 1 kg of the particular plastic. **Tables 3**, **4** provide the results of statistical analyses of the three hypothesized models. Finally, for convenience, **Table 5** summarizes the analytical expressions for the best models from **Tables 3**, **4**.

The approximations summarized in **Table 5** are applicable only during a certain time span. It begins from about 5 thousand of cycles, which is equivalent to about 3 h of the laboratory experiment, or about 9 h of fragmentation in the swash zone under waves of 6 s-wave period and moderate wave energy. The upper time limit for the models' applicability is defined by the condition, that there still should be *enough* larger objects for fragmentation. The only material passing this limit during the experiments was solid PS: after 18 h of fragmentation, when only 11.5% of the initial PS LPIs mass remained as large objects, the rate of growth of MPs mass began decreasing. Thus, the condition for the upper time limit might be formulated as follows: the approximations are valid until the mass of the large objects is no <15% of the mass of the plastic initially available for fragmentation. For real beach applications and numerical modeling, this limitation can be considered together with an external supply of larger plastic objects.

Mass vs. Number of Particles

The laboratory experiment provides an opportunity to build up a correlation between the mass and the number of particles, that is of significant interest for both observational and modeling applications. Since for all the types of plastics both mass and number of particles grow similarly with time, a close-to-linear relationship between these variables might be expected (**Figure 7**). This result could not be foreseen in advance, because the distribution of particles by size (discussed below in Section Methodical Problems of Use of Sieves for Particles of Various Shapes) is different for different plastics, while in the same mass the number of smaller particles is larger. In view of further numerical modeling, field applications, analytical evaluations, etc., the simplest relationships are desirable, so we report here the obtained linear approximations. Their statistical significance is confirmed by *F*-test analysis and provided in **Table 6**. **Figure 7** and **Table 7** present the relation between the fraction of mass, converted to MPs, and the number of the MPs particles generated after fragmentation of 1 kg of plastics. These dependencies indirectly contain the duration of the fragmentation process (see **Table 5**): they show how many MPs particles will be generated when the certain per cent of available LPIs are fragmented. In particular, it follows from the equations of **Figure 7** and **Table 7** that the same mass of solid PS is 8 times more productive than LDPE in terms of the generated MPs particles. While building the approximations, we excluded data of the last stages of fragmentation of solid PS particles (21 and 24 h): at that stages of fragmentation there might not be enough LPIs to supply the MPs generation. For PP, the data points cover only initial stages of fragmentation of this hard plastic; however for some applications the relationship still may be useful. In contrast to other polymers, for foamed PS the free term b of a linear regression is also significant; this may be an indication that fragmentation of this material to individual spherules begins with some delay. The approximations are valid for the total MPs mass of more than 1 g.

Methodical Problems of Use of Sieves for Particles of Various Shapes

Size distributions of the number of MPs particles generated from different types of plastics in our experiments (see **Figure S1**) are not directly suitable for mathematical analysis and highlight several methodical issues.

Firstly, our (standard) set of metallic sieves with mesh sizes from 0.5 to 5 mm (with 0.5 mm step) contained both perforated sieves with round openings (1.5, 3.0, 4.0, 4.5, 5.0 mm), and woven wire sieves with square openings (0.5, 1.0, 2.0, 2.5, 3.5 mm). As the analysis shows, the sieves with round openings retain much more particles, and re-calculation of the number of particles via the relative area of the openings (Allen, 2003) does not lead to sensible results. **Figure S3** shows size distributions of different plastics using all the sieves together (a), only perforated sieves (b), and only woven wire sieves (c). The first size distribution is rather

TABLE 5 | Summary of the best fit models for different plastics from **Tables 3**, **4**.

	Mass of MPs, $M_{\%}$ Mean error of the approximation, A (%)	**Number of MPs particles, *N* (in thousands) Mean error of the approximation, A (%)**
LDPE	$M_{\%} = 0.15\, e^{1.16n}$ A = 23%	$N = e^{1.13n}$ A = 23%
PS	$M_{\%} = 15.46\, n^2 - 34.68\, n$ A = 3%	$N = 804.7\, n^2 - 1946.26\, n$ A = 8%
PP	$M_{\%} = 0.001\, e^{0.92n}$ A = 23%	$N = 0.02 \cdot e^{1.19n}$ A = 31%
PS foam	$M_{\%} = 1.73\, n + 0.99$ A = 3%	$N = 70.33\, n + 102.46$ A = 6%

Dependence of the mass of MPs (0.5–5 mm); $M_{\%}$ (expressed in per cent of the initial mass); and the number of MPs particles (in thousands); N, generated from 1 kg of LPIs, on the dimensionless time; n (the number of rotation cycles in the experiment, or the number of "wave periods" in field applications, multiplied by 10^{-4}) for the types of plastics used in the experiments. The corresponding mean errors of the approximations, A (in per cent), are also shown.

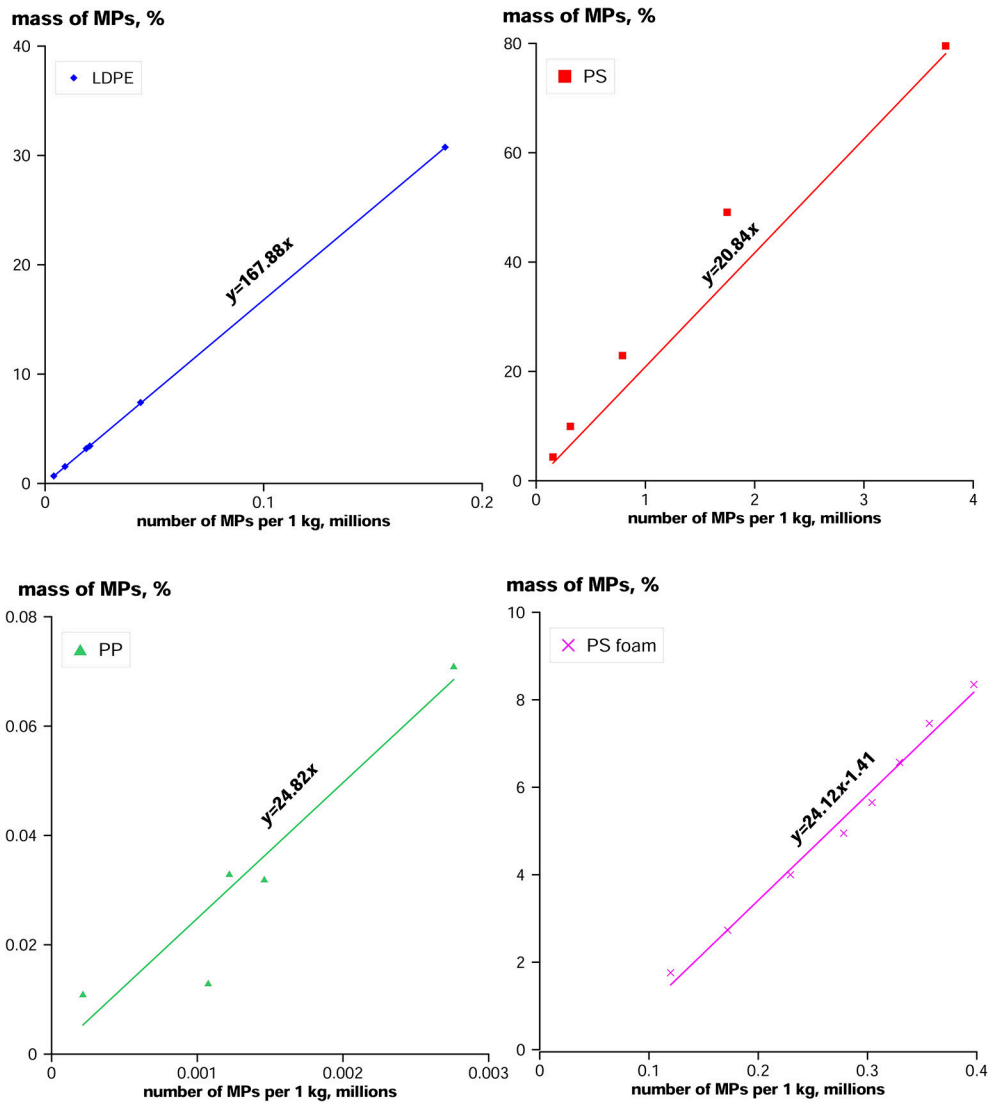


FIGURE 7 | Correlation of the fraction of mass converted to MPs and the number of MPs particles generated from 1 kg of LPIs of LDPE, PS, and PP (for solid PS, data for 21 and 24 h are not included due to possibly too small remaining amount of LPIs available for fragmentation).

TABLE 6 | Parameters of linear regression ($y = a\,x + b$) for a relationships between the mass of MPs and the number of MPs particles.

Material	a (± SE)	*p*-level for a	b (± SE)	*p*-level for b	*p*-level for *F*-test
LDPE	167.88 ± 0.18	8.531E-12	0.02 ± 0.01	0.16 (ns)	8.53E-12
PS	20.84 ± 1.87	0.0015	5.03 ± 3.53	0.25 (ns)	0.0015
PP	24.82 ± 4.87	0.015	−0.001 ± 0.008	0.87 (ns)	0.015
PS foam	24.12 ± 1.03	4.04E-07	−1.41 ± 0.3	0.003	4.04E-07

P is the significance of the F-test value of the regression; (ns) indicates non significant coefficients.

TABLE 7 | Relations between the mass of MPs (0.5–5 mm); $M_{\%}$, expressed in per cent of the initial mass of LPIs; and the number of MPs particles; *N*, expressed in millions; generated from 1 kg of LPIs; for the types of plastics used in the experiments.

LDPE	*M (in %)* = 164.88 *N* (*in millions*) A = 0.66%
Solid PS	*M (in %)* = 20.84 *N* (*in millions*) A = 26.38%
PP	*M (in %)* = 24.82 *N* (*in millions*) A = 37.11%
Foamed PS	*M (in %)* = 24.12 *N* (*in millions*)–1.41 A = 4.71%

The corresponding mean errors of the approximations, A (in per cent), are also shown.

chaotic, whilst the other two are more smooth, but significantly different. In broader context, this means that data obtained from different kinds of sieves should be compared with caution, and the type of the sieves used must be reported together with the data. Since *in situ* the most typical methods for sampling of MPs are nets and trawls, woven wire sieves should be preferred also for wet sieving.

Secondly, the sieves of different types seem to be "shape-selective." Natural sediments, like sand, granules, etc., are 3-dimensional and rounded, and the nest of sieves gives a reliable result on the particles' size distribution regardless of the type of the sieve. MPs have various shapes, and the use of different types of sieves may introduce certain misbalance between the particles of different shapes. Our experiments show that elongated, flexible and, especially, fibrous MPs particles are much better retained by woven wire sieves. Fibrous particles (in our case–LDPE fragments, see **Figure 2A** right-hand part) get entangled, and are easily retained by woven wire sieves with the mesh size of about 10 times as large as the fiber diameter, but they easily flow through perforated plates. This way, a lot of thin flexible LDPE fragments in our experiments were retained by the woven wire sieves with the largest mesh size (see **Figure S1A**). As for long flat rigid particles (PP in our case, see **Figure 2C** right-hand panel), they are difficult to wash through, because they tend to stay flat-side down at the sieve surface even when their width permits to flow through. Eventually in our experiments, only for PS particles (both in solid and foamed modifications) wet sieving showed quite reliable results, and exactly these plastics produce more or less "rounded" MPs particles (**Figures 2B,D**). These outcomes suggest that using nets in the field, woven wire sieves for beach sediments, or woven filters in laboratory, we may retain disproportionally more fibrous and elongated rigid particles in comparison to 3-dimensional and rounded ones.

Size-distribution curves for solid and foamed PS (**Figures S1B,D**), which have more or less rounded particle' shapes, are quite smooth and less dependent on the sort of the sieve. They show an obvious gradual increase in mass of all the fractions in the first half of the experiment, and then a sudden decrease for larger MPs, related with the decrease in the number of LPI available for degradation and the fatigue of the working material. Quite surprisingly, the maximum number of particles at any time of the experiment is observed in the range of 1–2 mm, i.e., practically the same as in the distribution of MPs floating on the surface of the ocean (Cózar et al., 2014). Distribution curves for LDPE and PP (**Figures S1A,C**) are irregular and show direct influence of the kind of the sieve.

CONCLUDING REMARKS

The swash zone of the sea is an area where mechanical fragmentation of plastic objects and the corresponding generation of secondary microplastics (MPs) are the most intense. The performed experiments have shown both qualitative and quantitative trends in the behavior of plastic materials under laboratory conditions mimicking natural wave runup/rundown on the beach face. A detailed description of qualitative modifications of the samples during the fragmentation process is important for further analysis of their behavior and fate in marine environment, while the obtained quantitative dependencies are intended to support analytical evaluations and further numerical modeling.

For the most typical beach litter objects–polystyrene (PS) and polypropylene (PP) single-use tableware, polyethylene (LDPE) bags, and foamed polystyrene isolation sheets–statistically significant regressions are obtained for an increase in mass of MPs and the number of MPs particles in the sea swash zone with coarse bottom sediments. The hardest for mechanical degradation among the selected plastics is PP. Foamed PS, being composed of small spherules, tends first to disintegrate into individual bubbles, which then are further fragmented into pieces. Most productive in terms of mechanical fragmentation is solid PS: as much as 99.8% of its initial mass was transferred to MPs and nano-sized particles within the 24 h of the experiment, producing about $5{\cdot}10^3$ micro-particles and uncountable amount of nano-particles out of every gram of plastic.

Despite different distribution of the number of MPs particles Vs. their size for the selected plastics, the relation between the mass and the total number of the generated MPs particles can be approximated by statistically significant linear dependencies.

Qualitative observations during the experiments provide information both on the variability of the appearance of particles

of different plastic types and on their characteristic behavior during the fragmentation process. An important outcome for field studies is the observed tendency of clogging of MPs particles beneath the sediment cover.

The obtained results are obviously "the case study" of the mechanical fragmentation of particular plastic objects in particular sediments, however they are thought to be useful for general evaluations of contamination of marine environment by MPs, for field monitoring, and for developing of proper parameterizations in numerical modeling.

AUTHOR CONTRIBUTIONS

IE performed experiments with PP and foamed PS, wrote the text, and designed the figures. MB performed experiments with solid PS. AB analyzed experimental results. AK performed statistical analysis of the hypothesized dependencies obtained and designed corresponding figures and tables. IC designed the experiments, performed the experiments with LDPE, and worked with the text.

ACKNOWLEDGMENTS

The investigations are supported by the Russian Foundation for Basic Research via grant number 18-55-76001 (as a part of ERA.Net RUS Plus S&T project 429 BalticLitter). Laboratory research facilities are maintained within the framework of the state assignment of FASO Russia (theme No. 0149-2018-0012). Development of parameterisations for numerical modeling is motivated by the work of IC within the WG 153 of the Scientific Committee on Oceanic Research (SCOR) which is supported by Grant OCE-1546580 to SCOR from the U.S. National Science Foundation.

SUPPLEMENTARY MATERIAL

The Supplementary Material for this article can be found online at: https://www.frontiersin.org/articles/10.3389/fmars.2018.00313/full#supplementary-material

REFERENCES

Allen, T. (2003). "Chapter 4: particle size analysis by sieving," in *Powder Sampling and Particle Size Determination*, eds T. Allen (Cape St. Francis: Elsevier), 208–250.

Andrady, A. L. (2011). Microplastics in the marine environment. *Mar. Pollut. Bull.* 62, 1596–1605. doi: 10.1016/j.marpolbul.2011.05.030

Andrady, A. L., and Neal, M. A. (2009). Applications and societal benefits of plastics. *Philos. Trans. R Soc. B* 364, 1977–1984. doi: 10.1098/rstb.2008.0304

Arthur, C., Baker, J., and Bamford, H. (2009). *Proceedings of the International Research Workshop on the Occurrence, Effects and Fate of Microplastic Marine Debris. Sept 9–11, 2008,* Vol. 2009. NOAA Technical Memorandum NOS-OR&R-30.

Barnes, D. K., Galgani, F., Thompson, R. C., and Barlaz, M. (2009). Accumulation and fragmentation of plastic debris in global environments. *Philos. Trans. R Soc. B* 364, 1985–1998. doi: 10.1098/rstb.2008.0205

Beach, W. J. (1972). *United States Patent 3,645,904 for Skin Cleaner*. Patented February 29, 1972.

Browne, M. A., Crump, P., Niven, S. J., Teuten, E., Tonkin, A., Galloway, T., et al. (2011). Accumulation of microplastic on shorelines woldwide: sources and sinks. *Environ. Sci. Technol.* 45, 9175–9179. doi: 10.1021/es201811s

Carson, H. S., Colbert, S. L., Kaylor, M. J., and McDermid, K. J. (2011). Small plastic debris changes water movement and heat transfer through beach sediments. *Mar. Pollut. Bull.* 62, 1708–1713. doi: 10.1016/j.marpolbul.2011.05.032

Carter, R. W. G., and Orford, J. D. (1993). The morphodynamics of coarse clastic beaches and barriers: a short- and longterm perspective. *J. Coast Res*. 158–179.

Chubarenko, I., Bagaev, A., Zobkov, M., and Esiukova, E. (2016). On some physical and dynamical properties of microplastic particles in marine environment. *Mar. Pollut. Bull.* 108, 105–112. doi: 10.1016/j.marpolbul.2016.04.048

Chubarenko, I., Esiukova, E., Bagaev, A., Isachenko, I., Demchenko, N., Zobkov, M., et al. (2018). "Chapter 6. Behaviour of Microplastics in Sea Coastal Zone," in *Microplastic Contamination in Aquatic Environments, 1st Edn.,* ed E. Zeng (Amsterdam: Elsevier), 175–223.

Chubarenko, I., and Stepanova, N. (2017). Microplastics in sea coastal zone: lessons learned from the Baltic amber. *Environ Poll.* 224, 243–254. doi: 10.1016/j.envpol.2017.01.085

Claessens, M., De Meester, S., Van Landuyt, L., De Clerck, K., and Janssen, C. R. (2011). Occurrence and distribution of microplastics in marine sediments along the Belgian coast. *Mar. Pollut. Bull.* 62, 2199–2204. doi: 10.1016/j.marpolbul.2011.06.030

Cózar, A., Echevarría, F., González-Gordillo, J. I., Irigoien, X., Ubeda, B., Hernández-León, S., et al. (2014). Plastic debris in the open ocean. *Proc. Natl. Acad. Sci. U. S. A.* 111, 10239–10244. doi: 10.1073/pnas.1314705111

Duis, K., and Coors, A. (2016). Microplastics in the aquatic and terrestrial environment: sources (with a specific focus on personal care products), fate and effects. *Environ. Sci. Eur.* 28:22. doi: 10.1186/s12302-015-0069-y

Efimova, I. V., and Chubarenko, I. P. (2018). Fragmentation of plastic garbage in the surf zone of the sea: a laboratory experiment on the example of expanded polystyrene. *Ser. Earth Sci.* 18, 10–13. doi: 10.18500/1819-7663-2018-18-1-10-13

Elfrink, B., and Baldock, T. (2002). Hydrodynamics and sediment transport in the swash zone: a review and perspective. *Coast Eng.* 45, 149–167. doi: 10.1016/S0378-3839(02)00032-7

Engler, R. E. (2012). The complex interaction between marine debris and toxic chemicals in the ocean. *Environ. Sci. Technol.* 46, 12302–12315. doi: 10.1021/es3027105

Esiukova, E. (2017). Plastic pollution on the Baltic beaches of Kaliningrad region, Russia. *Mar. Pollut. Bull.* 2, 1072–1080. doi: 10.1016/j.marpolbul.2016.10.001

Frias, J. P., Otero, V., and Sobral, P. (2014). Evidence of microplastics in samples of zooplankton from Portuguese coastal waters. *Mar. Environ. Res.* 95, 89–95. doi: 10.1016/j.marenvres.2014.01.001

Goldstein, M. C., and Goodwin, D. S. (2013). *Gooseneck barnacles* (Lepas spp.) ingest microplastic debris in the North Pacific Subtropical Gyre. *Peer J* 1:e184. doi: 10.7717/peerj.184

Gregory, M. R. (1996). Plastic 'scrubbers' in hand cleansers: a further (and minor) source for marine pollution identified. *Mar. Pollut. Bull.* 32, 867–871.

Hidalgo-Ruz, V., Gutow, L., Thompson, R. C., and Thiel, M. (2012). Microplastics in the marine environment: a review of the methods used for identification and quantification. *Environ. Sci. Technol.* 46, 3060–3075. doi: 10.1021/es2031505

Hintersteiner, I., Himmelsbach, M., and Buchberger, W. W. (2015). Characterization and quantitation of polyolefin microplastics in personal-care products using high-temperature gel-permeation chromatography. *Anal. Bioanal. Chem.* 407, 1253–1259. doi: 10.1007/s00216-014-8318-2

Karapanagioti, H. K. (2012). "Floating plastics, plastic pellets, and organic micropollutants in the Mediterranean Sea," in *Life in the Mediterranean Sea: a Look at Habitat Changes*, ed N. Stambler (New York, NY: Nova Science Publishers), 557–593.

Khatmullina, L., and Isachenko, I. (2016). Settling velocity of microplastic particles of regular shapes. *Mar. Pollut. Bull.* 114, 871–880. doi: 10.1016/j.marpolbul.2016.11.024

Komar, P. D., and Allan, J. C. (2010). ""Design with Nature" strategies for shore protection—The construction of a cobble berm and artificial dune in an Oregon State Park," in *2010, Puget Sound Shorelines and the Impacts of Armoring—Proceedings of a State of the Science Workshop*, Vol. 5254, eds H. Shipman, M. N. Dethier, G. Gelfenbaum, K. L. Fresh, and R. S. Dinicola (Tillamook, OR: U.S. Geological Survey Scientific Investigations Report), 117–126.

Lancaster, J. K. (1969). Abrasive wear of polymers. *Wear* 14, 223–239. doi: 10.1016/0043-1648(69)90047-7

Lassen, C., Hansen, F. S., Magnusson, K., Norén, F., Hartmann, B., and N. I., Jensen, R. P., et al. (2015). *Microplastics—Occurrence, Effects and Sources of Releases to the Environment in Denmark. Environmental project No. 1793*. Copenhagen: Environment Protection Agency, Ministry of Environment and Food of Denmark.

Leppäranta, M., and Myrberg, K. (2009). *Physical Oceanography of the Baltic Sea*. Chicester: Springer.

Li, W. C., Tse, H. F., and Fok, L. (2016). Plastic waste in the marine environment: a review of sources, occurrence and effects. *Sci. Total Environ.* 2016, 333–349. doi: 10.1016/j.scitotenv.2016.05.084

McWilliams, M., Liboiron, M., and Wiersma, Y. (2017). Rocky shoreline protocols miss microplastics in marine debris surveys (Fogo Island, Newfoundland and Labrador). *Mar. Pollut. Bull.* 129, 480–486. doi: 10.1016/j.marpolbul.2017.10.018

Mehmood, N., Mao, T., and Bhupati, G. (2012). *Fracture Mechanical Trouser Tear Testing in Thin Polymer Films (Experiments Along with Numerical simulations)*. Master's Degree Thesis. School of Engineering, Department of Mechanical Engineering. Blekinge Institute of Technology. Available online at: https://www.researchgate.net/publication/235934734_Fracture_Mechanical_Trouser_Tear_Testing_in_Thin_Polymer_Films_Experiments_Along_with_Numerical_simulations (Accessed July 30, 2018).

Napper, I. E., Bakir, A., Rowland, S. J., and Thompson, R. C. (2015). Characterisation, quantity and sorptive properties of microplastics extracted from cosmetics. *Mar. Pollut. Bull.* 99, 178–185. doi: 10.1016/j.marpolbul.2015.07.029

Nerland, I. L., Halsband, C., Allan, I., and Thomas, K. V. (2014). *Microplastics in Marine Environments: Occurrence, Distribution and Effects*. Oslo: Norwegian Institute for Water Research.

Pejaković, V., Jisa, R., and Franek, F. (2015). Abrasion resistance of selected commercially available polymer materials. *Tribol Finnish J. Tribol.* 33, 21–7. Available Online at: https://journal.fi/tribologia/article/view/69241

Plastics Europe (2013). *Plastics - the Facts 2013, an Analysis of European Plastics Production Demand and Waste Data*. Available online at: http://www.plasticseurope.org/en/resources/publications/103-plastics-facts-2013

Plastics Europe (2014). *Plastics - the Facts 2014, an Analysis of European Plastics Production, Demand and Waste Data*. Available online at: http://plasticker.de/Kunststoff_News_23931_PlasticsEurope_Plastics_the_Facts_2014_erschienen.

Plastics Europe (2016). *Plastics - the Facts 2016, an Analysis of European Plastics Production Demand and Waste Data*. Available online at: http://www.plasticseurope.org/en/resources/publications/3-plastics-facts-2016

Ryan, P. G., Moore, C. J., van Franeker, J. A., and Moloney, C. L. (2009). Monitoring the abundance of plastic debris in the marine environment. *Philos. Trans. R. Soc. Lond. B.* 364, 1999–2012. doi: 10.1098/rstb.2008.0207

Shah, A. A., Hasan, F., Hameed, A., and Ahmed, S. (2008). Biological degradation of plastics: a comprehensive review. *Biotechnol. Adv.* 26, 246–265. doi: 10.1016/j.biotechadv.2007.12.005

Van Rijn, L. C. (2013). *Erosion of Gravel/Shingle Beaches and Barriers*. Available online at: http://www.leovanrijn-sediment.com/papers/Gravelbeaches2013.pdf

Vianello, A., Boldrin, A., Guerriero, P., Moschino, V., Rella, R., Sturaro, A., et al. (2013). Microplastic particles in sediments of Lagoon of Venice, Italy: first observations on occurrence, spatial patterns and identification. *Estuar. Coast. Shelf Sci.* 130, 54–61. doi: 10.1016/j.ecss.2013.03.022

Viswanath, N., and Bellow, D. G. (1995). Development of an equation for the wear of polymers. *Wear* 181–183, 42–9. doi: 10.1016/0043-1648(94)07055-5

Waters, C. N., Zalasiewicz, J., Summerhayes, C., Barnosky, A. D., Poirier, C., Gałuszka, A., et al. (2016). The Anthropocene is functionally and stratigraphically distinct from the Holocene. *Science* 351, 138–147. doi: 10.1126/science.aad2622

Zitko, V., and Hanlon, M. (1991). Another source of pollution by plastics: skin cleaners with plastic scrubbers. *Mar. Pollut. Bull.* 22, 41–42.

Conflict of Interest Statement: The authors declare that the research was conducted in the absence of any commercial or financial relationships that could be construed as a potential conflict of interest.

Copyright © 2018 Efimova, Bagaeva, Bagaev, Kileso and Chubarenko. This is an open-access article distributed under the terms of the Creative Commons Attribution License (CC BY). The use, distribution or reproduction in other forums is permitted, provided the original author(s) and the copyright owner(s) are credited and that the original publication in this journal is cited, in accordance with accepted academic practice. No use, distribution or reproduction is permitted which does not comply with these terms.

Advantages of publishing in Frontiers

OPEN ACCESS
Articles are free to read for greatest visibility and readership

FAST PUBLICATION
Around 90 days from submission to decision

HIGH QUALITY PEER-REVIEW
Rigorous, collaborative, and constructive peer-review

TRANSPARENT PEER-REVIEW
Editors and reviewers acknowledged by name on published articles

Frontiers
Avenue du Tribunal-Fédéral 34
1005 Lausanne | Switzerland

Visit us: www.frontiersin.org
Contact us: info@frontiersin.org | +41 21 510 17 00

REPRODUCIBILITY OF RESEARCH
Support open data and methods to enhance research reproducibility

DIGITAL PUBLISHING
Articles designed for optimal readership across devices

FOLLOW US
@frontiersin

IMPACT METRICS
Advanced article metrics track visibility across digital media

EXTENSIVE PROMOTION
Marketing and promotion of impactful research

LOOP RESEARCH NETWORK
Our network increases your article's readership